STARS and NEBULA - New Generations of Hydroprocessing Catalysts for the Production of Ultra Low Sulfur Diesel

Sonja Eijsbouts, Frans Plantenga, Bob Leliveld, Yoshimasa Inoue and Katsuhisa Fujita**

Akzo Nobel Catalysts B.V., Research Centre Amsterdam,
P.O.Box 37650, 1030 BE Amsterdam, The Netherlands
and
*Nippon Ketjen Co., Ltd., R&D Center,
17-4, Isoura-cho, Niihama, Ehime, Japan

Introduction

EU, Japan and US have decided to lower sulfur in diesel to the 10 – 15 ppm level in very near future. This means that that refiners have to apply more and more severe hydroprocessing (more reactor volume, higher pressure and temperature), i.e. have to invest heavily in new hydrodesulfurization (HDS) capacity and start desulfurizing streams that were not treated before. To do this in the most efficient and economic way is a major challenge for the refiners, catalyst and process designers.

Type 2 Active Sites

The last few hundred ppm sulfur leftover after "normal" hydrotreating is present in much less reactive molecules: alkyl-substituted dibenzothiophenes. These molecules not only react slower but their reaction mechanism is also different, involving first a hydrogenation of the aromatic part of the molecule followed by a desulfurization step (rather than direct hydrogenolysis). This hydrogenation pathway has led to the development of a new generation of catalysts, whereby another type of active sites, Type 2, was maximized. Type 2 sites are generated by careful tuning of the metal-support interaction and are thought to be more effective for hydrogenation reactions. Two Type 2 catalysts, Ni-Mo KF848-STARS and Co-Mo KF757-STARS are commercially available.

Special Features of Type 2 Catalysts. The lower metal-support interaction leads to a different sulfidation behavior of the Type 2 catalysts. The sulfidation is complete at lower temperature (**Figures 1 and 2**) and proceeds through a different Mo intermediate (Mo^{5+}) (**Figure 2**) in Type 2 catalysts compared to conventional catalysts, containing typically a mixture of Type 1 and 2 sites.

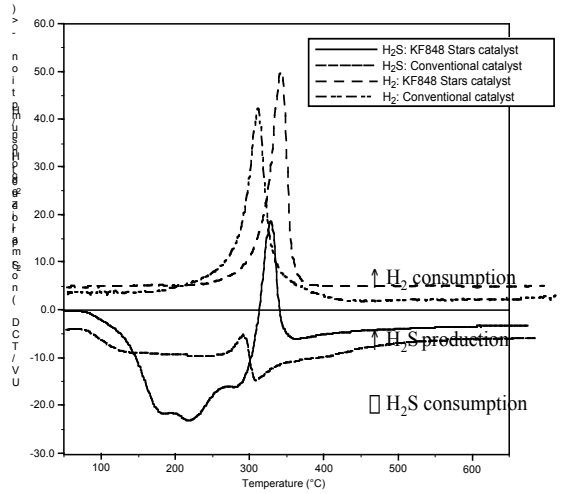

Figure 1. Temperature Programmed Sulfidation (TPS) patterns of conventional Ni-Mo KF843 and Ni-Mo KF848-STARS catalysts.

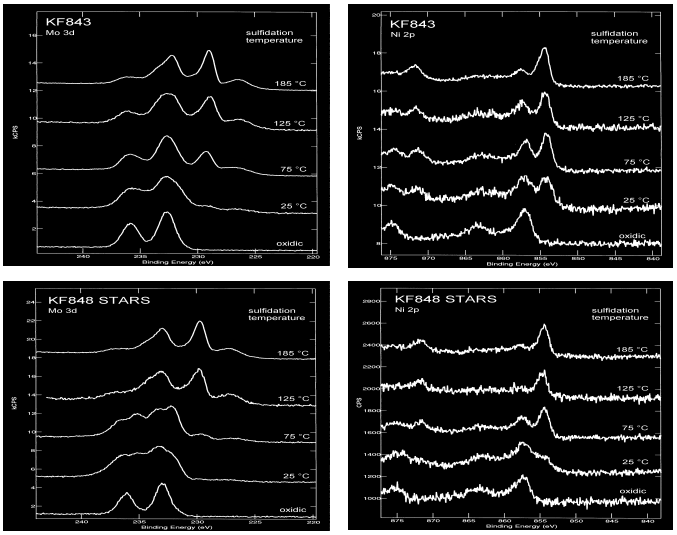

Figure 2. X-ray Photoelectron Spectroscopy (XPS) spectra of conventional Ni-Mo KF843 and Ni-Mo KF848-STARS catalysts.

Performance of Type 2 Catalysts. The incorporation of Type 2 sites leads to a higher activity of Ni-Mo (**Figure 3**) and Co-Mo catalysts. While traditionally Co-Mo catalysts were used for HDS, Ni-Mo catalysts are applied for some process conditions (higher pressure) nowadays. The reason is that the activity ranking of a Ni-Mo Type 2 changes compared to a Co-Mo Type 2 catalyst as a function of the hydrogen pressure and operating severity (**Figure 4**).

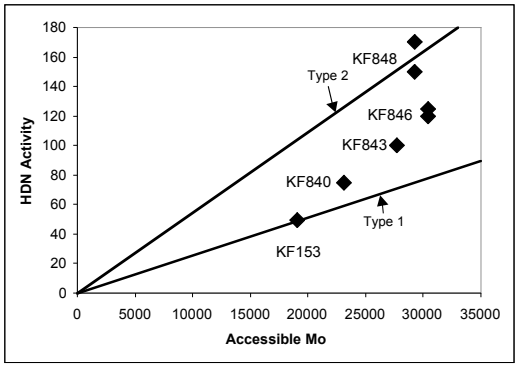

Figure 3. HDN activity (VGO) of conventional Ni-Mo (KF153, KF840, KF843 and KF846) and Ni-Mo KF848-STARS Catalysts.

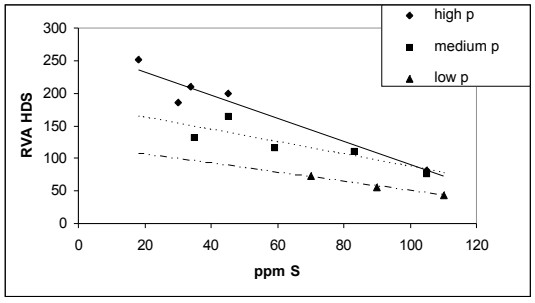

Figure 4. Changing activity ranking of Ni-Mo versus Co-Mo catalysts due to changing reaction mechanism in diesel HDS at different reaction pressures. Relative volume activity (RVA) HDS of KF848 is calculated versus the KF757 reference.

NEBULA Catalyst

The opportunities are even bigger with the NEBULA catalyst[1], a joint development of Akzo Nobel with ExxonMobil, which is a totally novel hydroprocessing catalyst not made according to today's technology of alumina carriers with impregnated metals. NEBULA is such an improvement in activity, that it enables refiners to produce ultra low sulfur diesel in most high-pressure units that have been designed for the production of 500 ppm S (**Figure 5**).

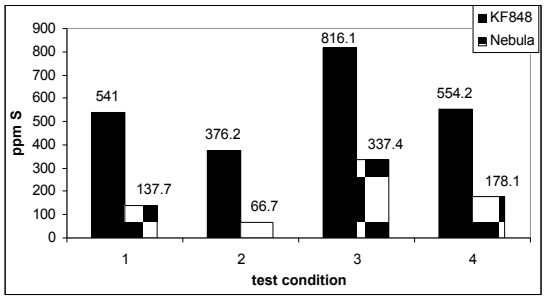

Figure 5. HDS performance of NEBULA and KF848 in diesel HDS.

Besides using NEBULA for treating the diesel fractions, NEBULA can contribute to the production of low S diesel when used in VGO pretreatment, preceding the hydrocracking and FCC units (**Figures 6-8**). Just like in diesel HDS, KF757 has a good performance at higher product S levels. KF848 and especially NEBULA outperform KF757 at low product S levels. As really low product S levels can be obtained only at low product N levels (**Figure 9**), not only the HDS but also the hydrodenitrogenation (HDN) and hydrogenation (HDA) activities are improved.

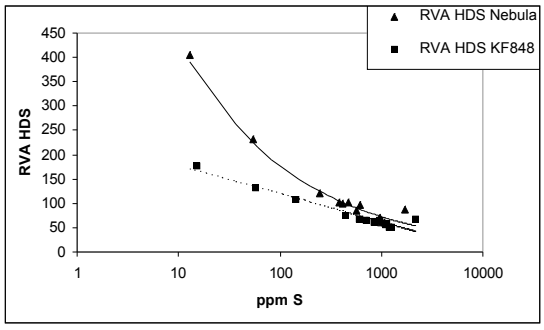

Figure 6. HDS performance of NEBULA and KF848 in VGO hydrotreating. RVA HDS is calculated versus the KF757 reference.

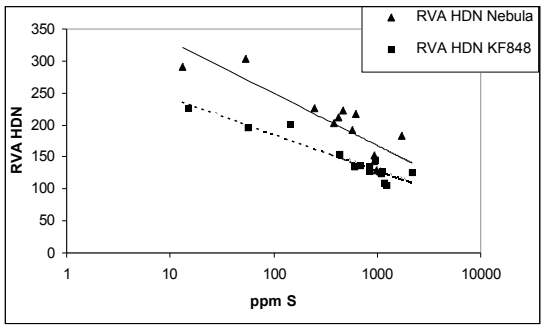

Figure 7. HDN performance of NEBULA and KF848 in VGO hydrotreating. RVA HDN is calculated versus the KF757 reference.

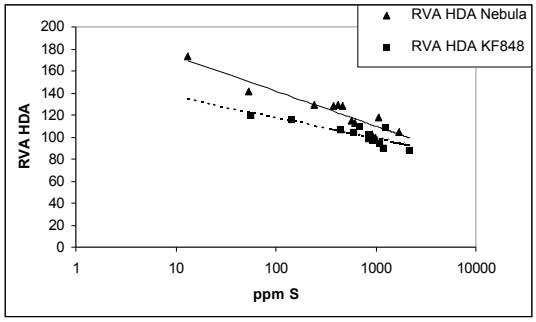

Figure 8. HDA performance of NEBULA and KF848 in VGO hydrotreating. RVA HDA is calculated versus the KF757 reference.

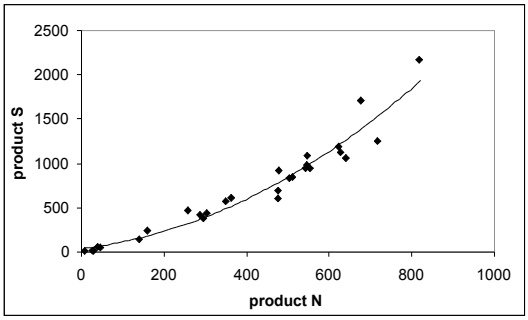

Figure 9. Product S and N level of hydrotreated VGO corresponding to Figures 6 – 8.

Summary Catalyst Development

Figure 10 shows the development of the "traditional" hydroprocessing catalysts and the new catalyst generations, "STARS and NEBULA technology".

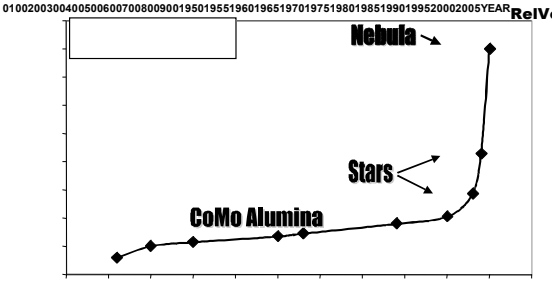

Figure 10. Development of hydrotreating catalyst in past 50 years.

Already with the move to STARS, a new development S-curve was started. At present, the end point of the graph is NEBULA, a catalyst with breakthrough activity that reaches four times the activity of the conventional catalysts. Nowadays, NEBULA is finding its place in the refinery processes. NEBULA catalyst not only helps to use the existing units to meet the future product specifications. It also helps to maintain the product specifications while increasing the cycle length by running the units at less severe conditions (e.g. lower temperature) or while increasing the unit throughput at normal operating conditions.

References

1. D. Pappal; NPRA Annual meeting, March 23-25, 2003, AM-03-59.

CHARACTERISTICS OF NOVEL TITANIA CATALYST PREPARED BY MULTI-GELATION METHOD IN DEEP-DESULFURIZATION CONDITION

Shinichi Inoue[*1], *Akihiro Muto*[*1], *Hidehiko Kudou*[*1], *Takeo Ono*[*2]

*1: PEC Chiyoda Laboratory
(Research & Development Center, Chiyoda Corporation)
1-1 Minamiwatarida-cho, Kawasaki-ku, Kawasaki, 210-0855, Japan
E-mail : sinoue@ykh.chiyoda.co.jp

*2 : Ono Professional Engineer Office
1-38 Furuichiba, Saiwai-ku, Kawasaki 211-0952, Japan

Introduction

Japanese refiners started providing cleaner diesel fuel of 50ppm sulfur content in the spring 2003. Furthermore, the movement of new regulation reinforcement is anticipated to reduce sulfur content in diesel oil under 10 or 15ppm by 2008. Thus, excellent hydrodesulfurization catalyst is so desired. During the last decade, titania supported molybdena catalysts have attracted increasing attention. Several articles dealing with titania outlined a higher intrinsic activities than on the conventional alumina support. However, titania catalyst was not commercially used because TiO_2 is regarded having a small specific surface area less than 50-60m^2/g and poor thermal stability.

The novel manufacturing technology of structure controlled titania support catalyst was proposed for the further improvement of diesel fuel in ultra deep hydrodesulfurization[1)]. The multi-gelation method has a good performance for controlling pore structures, i.e., pore size distributions as shown in Figure 1.

In this study, we investigated the denitrogenation activities of controlled meso-porous titania catalyst prepared by the multi-gelation method.

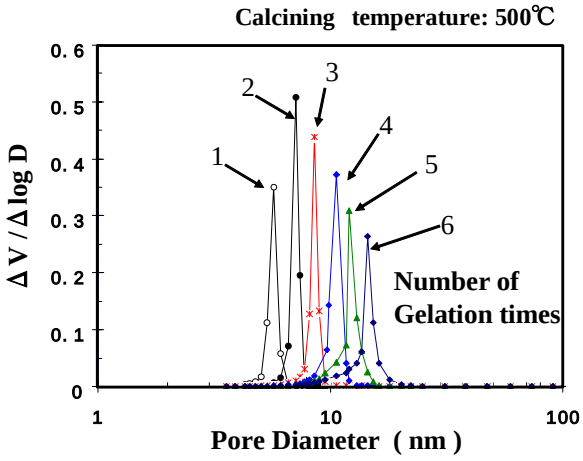

Figure 1. Pore Distributions of TiO_2 Controlled by Multi-Gelation Method

Experimental

1) Preparation Method of TiO_2 Support

Multi-gelation method is the procedure to produce the inorganic oxides gel by swinging of pH of solution dexterously several times. This method can be employed in preparation of hydrous titanium. It can control a particle size of TiO_2 uniformly with a designed pore size. Figure 2 shows the preparation flow diagram of the multi-gelation method to synthesize TiO_2. The raw materials are acidic $TiCl_4$ and basic ammonia solutions. Hydroxyl gel of TiO_2 was synthesized by swinging pH from $TiCl_4$ and ammonia solutions. $TiCl_4$ and ammonia solutions were supplied to the gelation vessel alternately, and hydrous titanium was synthesized. Particles of hydrous titanium were controlled in desirable particle size by alternately supplying $TiCl_4$ or ammonia solution. And hydrous titanium was washed by water to remove ammonium chloride. After filtration, TiO_2 as a catalyst or a catalyst carrier was molded to cylindrical shapes by the extruder, for example. And it was dried at 120 °C and is calcined at 500 °C in the standard procedure.

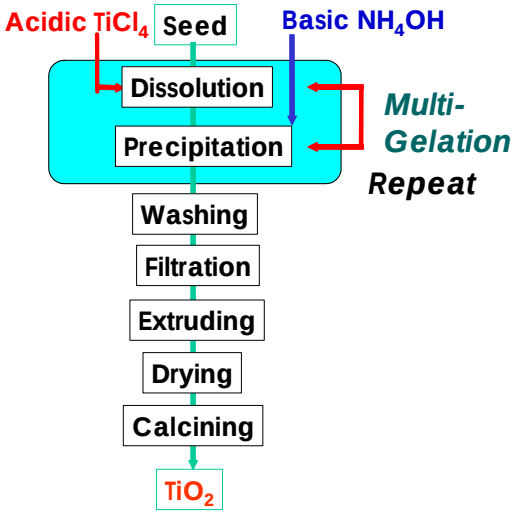

Figure 2. Preparation Flow Diagram of TiO_2 by Multi-Gelation Method

2) Catalysts

TiO_2 supports properties used in this study are as follows: Specific surface area is 162m^2/g, average pore diameter is 9nm whose pH swing number is 3 times. The CoMo/TiO_2 catalysts were prepared by gel impregnation method: TiO_2 gel was impregnated with ammonium heptamolybdate and Cobalt nitride as required. This was followed by drying at 120°C for 3h and calcination in air at 500°C for 3h.

3) Measurement of HDS and HDN activity

The HDS and HDN experiments were carried out with a fixed-bed reactor. The cata1yst was presulfided with the feed oil spiked by DMDS. Typical reaction conditions were as follows: H_2/Oil ratio 250, LHSV 2 h^{-1}, reaction pressure 5 MPa, Reaction temperature 330 - 350°C. The Middle-East straight run gas oil with 1.3wt% sulfur was used as feed stock.

Results and Discussion

1) Hydrodesulfurization Activity

The activity of the proprietary TiO_2 catalyst compared with the conventional CoMo/alumina catalyst for 500 ppm HDS are shown in Figure 3. This Figure also shows the reactivity of CoMo/TiO_2 catalyst prepared using conventional TiO_2 carrier with 60 m^2/g of surface area. It is important to mention that the catalytic activity of the TiO_2 supported prepared by multi-gelation method with high surface area and good pore distribution is much higher than that of the catalyst using conventional TiO_2 support with low surface area. Furthermore, it also shows that the new TiO_2 catalyst has 2 times higher hydrodesulfurization activity than that of the commercial alumina catalyst.

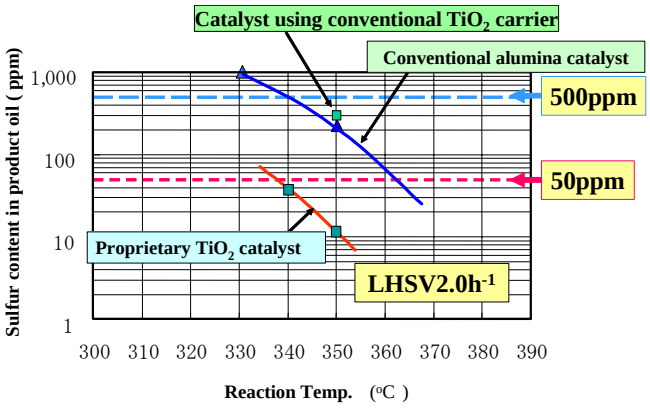

Figure 3. HDS Performance of Proprietary TiO_2 Catalyst

2) Characteristic of denitrogenation activities

It was found another remarkable characteristic of TiO_2 catalyst that the titania catalyst has high denitrogenation selectivity. Figure 4 shows the correlation between desulphurization rate and nitrogen removal rate of TiO_2 and commercial alumina catalysts. Comparing at the same decarburization rate, denitrogenation selectivity of CoMo/TiO_2 catalyst is much higher than Commercial CoMo and NiMo alumina catalyst.

Figure 5 shows the correlation between nitrogen removal rate and chemical hydrogen consumption of titania and commercial alumina catalysts. In spite of high denitrogenation selectivity, it is clear that the hydrogen consumption of titania catalyst is about 10Nm^3/kl lower than the commercial CoMo and NiMo alumina catalysts at the range of high nitrogen conversion rate.

Generally, it is considered that denitrogenation reaction passed through a hydrogenation of aromatic ring with nitrogen. It is considered that the hydrogenation reaction rate of titania catalyst for the other aromatic compound is slower than that of alumina catalysts.

Accordingly, hydrogenation of aromatic is restrained as much as possible, and it may be said that CoMo/titania catalyst is more economic catalyst for desulfurization and denitrogenation.

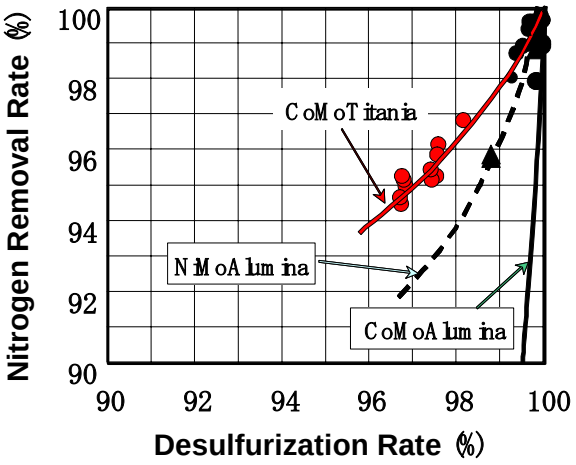

Figure4. Correlation between desulfurization rate and nitrogen removal rate

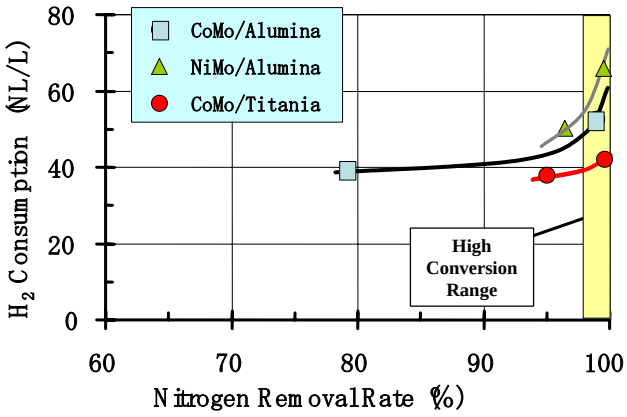

Figure 5. Correlation between nitrogen removal rate and H_2 consumption

Conclusions

It was confirmed that TiO_2 with high specific surface area by the novel multi-gelation method showed good performance of catalytic activity, especially denitrogenation activities, in ultra-deep hydrodesulfurization condition. Therefore, the proprietary TiO_2 catalyst is good candidates for the hydrodesulfurization or hydrotreating processes.

Acknowledgement. This work has been entrusted by the New Energy and Industrial Technology Development Organization under a subsidy of the Ministry of Economy, Trade and Industry of Japan.

Reference

1) Inoue, S., Kudou, H., Muto, A., Ono, T,
The 255th ACS National Meeting in Fuel Symposia
New Orleans, LA, March 23-27, 2003 Spring

CATALYTIC POTENTIAL OF CARBON-SUPPORTED NiMo-SULFIDE FOR ULTRA-DEEP HYDRODESULFURIZATION OF DIESEL FUEL

Masato Kouzu, Yasunori Kuriki, Hamdy Farag, Kinya Sakanishi, Yosikazu Sugimoto, and Ikuo Saito

National Institute of Advanced Industrial Science and Technology (AIST), Tsukuba Center, Ibaraki 305-8565, Japan

Introduction

The regulation of sulfur content in diesel fuel to around 10 ppm is coming closer to the reality in a couple of years for the suppression of air pollution in urban areas. To achieve such ultra-deep hydrodesulfurization(HDS) of diesel fuel without new investment in petroleum refineries, further improvements in HDS catalytic performance are required in terms of the much higher activity and selectivity for HDS of refractory sulfur compounds such as 4,6-dimethyldibenzothiophene(4,6-DMDBT).

Enhancing dispersion of the active components is one of the approaches to modify the HDS catalyst. In the case of conventional alumina-supported CoMo and NiMo catalysts, the dispersion of the active components such as CoMoS and NiMoS phases is hardly enhanced due to the strong polarity and the limited surface area of the alumina support.[1] Carbon supports such as active carbons and carbon blacks have been reported to have the potentials for enhancing the dispersion of the active sulfides because of the weak polarity and the higher surface area.[2] Solar et al. quantitatively measured the surface functional groups of some active carbons to analyze the dispersion of the active component.[3] It has been also reported that CoMo and NiMo sulfides on active carbons can be superior to the conventional alumina-supported ones in the activity and selectivity for HDS of DBT derivatives, suggesting that carbon-supported Mo sulfides may enhance hydrogenative HDS route.[4,5]

The most important key for ultra-deep HDS of diesel fuel is to selectively desulfurize refractory alkyl-DBT derivatives through the hydrogenative HDS, because the hydrogenation of neighboring aromatic ring of alkyl-DBT derivatives accelerates C-S bond scission. Hence, it is expected that NiMo sulfide supported on active carbon with high surface area can be one of the potential catalysts for the achievement of ultra-deep HDS of diesel fuel.

In the present study, HDS reactions of 4,6-DMDBT as a model feedstock and real gas oil are performed over NiMo sulfide catalysts supported on a particular active carbon (NiMo/C) by using a micro-autoclave and a down-flow tubular reactor with fixed-bed, respectively, in order to clarify the catalytic potential of NiMo/C in comparison to a conventional NiMo/alumina catalyst.

Experimental

Catalyst preparation. A commercially available active carbon powder with the surface area of 3,000m^2/g was used as the support material of NiMo/C prepared. Ni and Mo were simultaneously impregnated on the active carbon by incipient wetness procedure using methanol solution of the organic salts, Ni acetate tetrahydrate and MoO_2 acetylacetonate. Ratio of Ni/Mo was kept constant at 0.2 on the basis of their weight. The impregnating procedures were repeated to the prescribed amount of the active components, followed by atmospheric drying at 80℃ between the each step. Amounts of Ni and Mo impregnated were analyzed by ICP-AES measurement.

Prepared precursor of NiMo/C was sulfided at 400℃ under atmospheric gas flow of H_2S/H_2 mixture in off-site, prior to the activity measurement. Both the porosity and the morphology were measured by N_2 adsorption and TEM observation, respectively, in the final sulfide form of the catalyst.

Activity measurement. A micro-autoclave inserted into electric furnace of vertically shaking type was used for a reaction of the model feedstock. The model feedstock was composed of DBT (2.0%), 4,6-DMDBT (0.2%), 1-MN (5.0%) in decane solvent. After 5ml of the model feedstock, 30 mg of the catalyst and 3MPa of H_2 gas were charged into the autoclave, the reaction was conducted at 320℃. The processed model feedstock was subjected to GC-FID and GC-MS to calculate the conversion ratio and the product yield.

Following the above activity measurement, a reaction of the real feedstock was carried out in a down-flow tubular reactor. The real gas oil feedstock contained 12,300ppm-S and 120ppm-N. 4 ml of the catalyst was packed into the reactor with silicon carbide of the diluent. After set-up of the reactor unit, the temperature was made to increase from ambient to 330℃ for 16h in the flow of the real feedstock with 2% dimethyldisulfide. Then, the HDS reaction was operated at 330-350℃ with LHSV of 1.5-3.0 h^{-1}. The hydrogen gas pressure and the volumetric hydrogen gas/oil ratio were kept at 5MPa and 250Nl/l, respectively. The HDS rate constant was analyzed using 1.3th order kinetics.

A commercially available NiMo catalyst supported on alumina (NiMo/Al) was subjected to these activity measurements as the reference to evaluate the catalytic potential of NiMo/C.

Results and Discussion

A variety of NiMo/C catalysts were prepared to analyze the dispersion of the active component on the active carbon. **Table 1** summarizes effect of the amounts of the active components on the conversion of 4,6-DMDBT in the reaction of the model feedstock.

Table 1. Conversion of 4,6-DMDBT and DBT in the reaction of the model feedstock at 320℃ for 1.0h

Catalyst	NiMo/C				(NiMo/Al)
Ni [wt%]	2	3	4	5	3
Mo[wt%]	10	15	20	25	15
4,6-DMDBT					
Converting ratio [%]	30.7	37.1	49.3	53.6	17.9
Rate Const. [h^{-1}]	0.42	0.59	0.82	0.78	0.22
C_2BP [%]	2.1	1.6	2.1	2.3	1.6
C_2CHB [%]	11.7	15.8	30.3	30.7	5.1
C_2BCH [%]	2.9	6.3	6.3	10.2	1.2
DBT					
Converting ratio [%]	71.5	78.9	91.1	90.2	43.8
Rate Const. [h^{-1}]	1.45	1.76	2.50	2.15	0.63
BP [%]	41.0	43.4	49.7	45.7	26.8
CHB [%]	26.6	30.8	37.7	40.6	14.0
BCH [%]	1.8	3.2	3.1	3.3	0.4

The conversion of 4,6-DMDBT was enhanced with the increase of the amount of the active component, although the converting ratio reached the peak at 20%-Mo. 4,6-DMDBT was mainly converted into C_2-CHB via the hydrogenative HDS route. Except for 25%-Mo, the reaction rate constant on 1st order kinetics increased in proportion to the amount of the active component. The maximum reaction rate constant, at 20%-Mo, was above 4 times as large as NiMo/Al. It is supposed that the enhanced dispersion was kept constant until the amount of impregnated Mo reached at 20%

The positive effect of the amount of the active component was evident, also, in the conversion of DBT. 60-70% of DBT was converted into CHB via the hydrogenative HDS route.

TEM images gave the evident information on the enhanced dispersion of the active component in NiMo/C, as shown in **Figure 1**. Layered structure of the active component was visible in NiMo/Al, whereas not visible in NiMo/C, indicating the higher dispersion of the active component in NiMo/C. A small portion of layered structure of NiMo/C may be formed at the external slit on the active carbon. Although the active component was not appreciable in TEM image, Ni and Mo were detected in EDX spectrum at the same measuring field. It is an evidence that the higher dispersion of the active phases may be achieved on NiMo/C catalyst. The invisible active component on the active carbon was independent of the amount impregnated, which was consistent with the reaction rate constant for converting 4,6-DMDBT mentioned above.

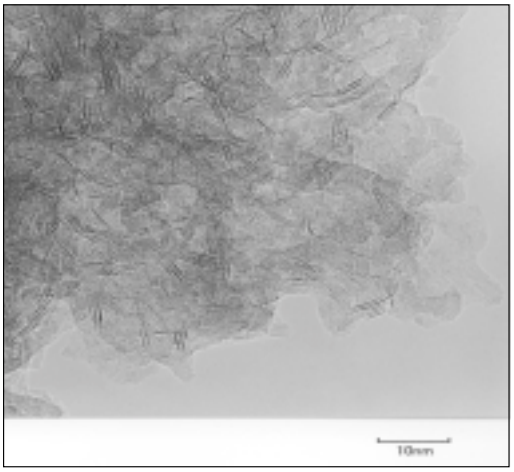

(a) NiMo/Al

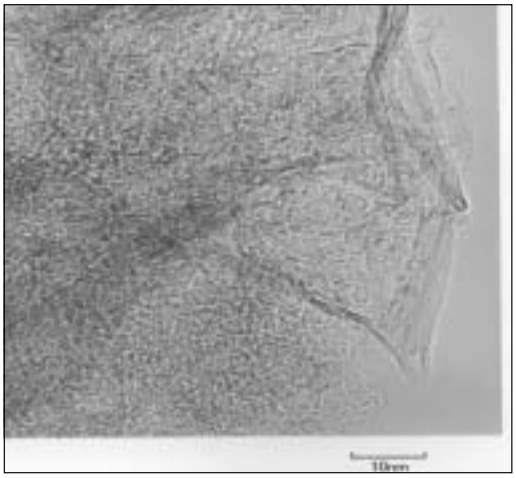

(b) NiMo/C, 4%Ni-20%Mo

Figure 1. TEM images of NiMo/Al and NiMo/C catalysts (1.5million magnification)

The reaction of the real gas oil feedstock was carried out over the best NiMo/C that contained 4%Ni and 20%Mo. **Figure 2** shows the reaction temperature versus the residual sulfur content.

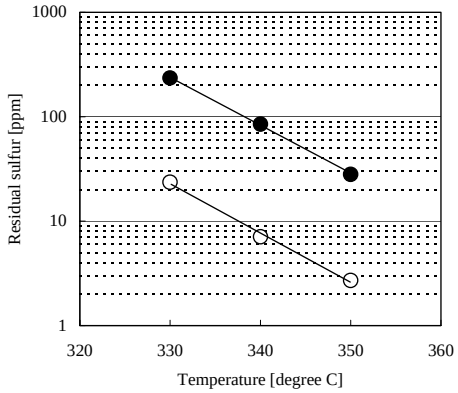

Figure 2. Reaction temperature *vs*. residual sulfur content in the reaction of the real feedstock under hydrogen pressure of 5MPa with LHSV of $1.5h^{-1}$. ○, NiMo/C (k_{HDS}@330℃: $1.59h^{-1}$); ●, NiMo/Al (k_{HDS}@330℃: $0.68h^{-1}$)

NiMo/C achieved 10ppm-S level at 337℃, whereas not completed over NiMo/Al under the present operating conditions. It is revealed that NiMo/C can be also advantageous catalyst for the ultra-deep HDS of real diesel fuel. The HDS rate constant over NiMo/C was above 2 times higher than that over NiMo/Al. This was consistent with the reaction rate constant for converting 4,6-DMDBT in the reaction of the model feedstock, taking into difference in the bulk density consideration.

Conclusions

Catalytic potential of NiMo/C prepared using an active carbon powder with the surface area of 3,000 m^2/g was evaluated in order to achieve the ultra-deep HDS of diesel oil. The reaction rate constant for converting 4,6-DMDBT was enhanced in proportion to the amount of the active component in a reaction of model feedstock at 320℃, although the reaction rate constant reached the peak at 20%-Mo. The maximum rate constant over NiMo/C was 4 times larger than that over NiMo/Al. TEM observation showed the much higher dispersion of the active species on NiMo/C. The best NiMo/C containing 4%Ni and 20%Mo achieved 10ppm-S at 337℃ in a reaction of the real gas oil feedstock using a down-flow tubular reactor, whereas was not completed over NiMo/Al under the same condition. The HDS rate constant over NiMo/C was above 2 times higher than that over NiMo/Al. Hence, NiMo/C can be a candidate for the innovative catalyst for the ultra-deep HDS.

Acknowledgement. The work has been entrusted by the New Energy and Industrial Technology Development Organization under a subsidy of the Ministry of Economy, Trade and Industry.

References

1. Grange, P., *Catal. Rev-Sci. Eng*., **1980**, *21*, 135
2. Rodriguez-Reinoso, F., *Carbon*, **1998**, *36*, 3, 159
3. Solar, J. M., Derbyshire, F. J., DeBeer, V. H., Randvic, L. R., *J. Catal*.,**1991**, *129*, 330
4. Hamdy, F., Whitehurst, D. D., Sakanishi, K., Mochida, I., *Catal. Today*, **1999**, *50*, 9
5. Sakanishi, K., Nagamatsu, T., Mochida, I., Whitehurst, D.D., *J. Mol.Catal. A:Chemical*, **2000**, 155, 101.

SONO-SYNTHESIS AND CHARACTERIZATION OF NANOPHASE HYDRODESULFURIZATION CATALYSTS

Christopher L. Marshall[1], Devinder Mahajan[2], A. Jeremy Kropf[1], Manuela Serban[1], Norma B. Castagnola[1], and Jonathan C. Hanson[3]

[1]ChemicalTechnology Division, Argonne National Laboratory, Argonne, Illinois 60439-4837
[2]Energy Sciences and Technology Department, Brookhaven National Laboratory, Upton, New York 11973-5000 USA and Department of Materials Science and Engineering, Stony Brook University, Stony Brook, New York 11794-2275 USA
[3]Department of Chemistry, Brookhaven National Laboratory, Upton, New York 11973-5000 USA

Introduction

The generation of microporous and small-particle chalcogenides for catalytic hydrodesulfurization (HDS) of transportation fuels and heavy crude is of interest. However, currently employed commercial wet chemical synthesis techniques result in large sheets of MoS_2. A few recent reports include preparation of supported MoS_2 on alumina catalyst with a Co promoter, sonolysis of $Mo(CO)_6/Co(CO)_3NO$ /wide-pore Al-MCM-41 in decalin to produce nano particles of Mo and Co oxides on an alumina support that was further treated to form the HDS catalyst, and sonochemical preparation of supported nano HDS catalysts, Co-Mo-S/ Al_2O_3, Ni-Mo-S/ Al_2O_3, and Co-Ni-Mo-S/ Al_2O_3. These catalysts were shown to exhibit several-fold higher HDS activity than comparable micrometer-sized commercial catalysts.

Results and Discussion

A convenient synthesis of nano-size HDS catalytic materials in several-gram quantities is the main focus of the present activity at Brookhaven National Laboratory (BNL) and Argonne National Laboratory (ANL). Several hydrocarbon solvents have been evaluated to optimize "cavitation" that is critical to produce nano Mo metal particles by decomposition of molybdenum hexacarbonyl. Further in situ complexation of nano Mo with elemental sulfur yields nano MoS2. With a known ratio of $Co_2(CO)_8/Mo(CO)_6$, the method produces nano Co/MoS_2. Sonolysis of $Mo(CO)_6$ in the presence of γ-Al_2O_3 produced supported nano Mo, i.e., nano MoS_2/γ-Al_2O_3. The yields of all three nano-sized materials are >90% based on the starting $Mo(CO)_6$.

The prepared samples are being characterized at the National Synchrotron Light Source (NSLS) at BNL and the Advanced Photon Source (APS) at ANL. The measurement of these materials is a challenge. Preliminary x-ray diffraction (XRD) data show that the prepared materials indeed are nano-size. Transmission electron microscopy (TEM) (with a resolution of 0.16 nm) is being used to measure the morphology and particle size of the samples.

The nano-scale materials exhibit temperature-programmed reduction (TPR) profiles that are about 75°C higher than the commercially available catalyst. Adding cobalt to the molybdenum has no effect on the temperature of the reduction but does lower the overall amount of hydrogen adsorption. The MoS_2 nanophase materials are highly reactive and susceptible to oxidation in air. Running x-ray adsorption near edge spectroscopy (XANES) at the APS in temperature- programmed oxidation (TPO) mode (**Figure 1**) shows that the native material oxidizes at the relatively low temperature of 365°C. The addition of Co to the nanophase MoS_2 material

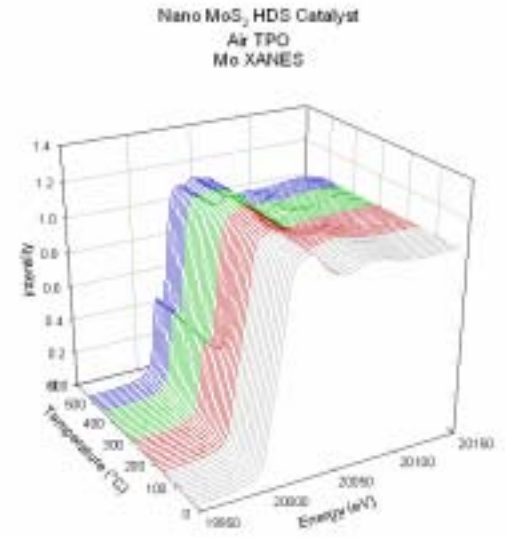

Figure 1 – Temperature programmed oxidation followed by Mo XANES.

(necessary for HDS catalytic activity) removes some of this oxidation instability. Principle component analysis (PCA) (**Figure 2**) provides us with an estimate of the amount of a specific component at any given temperature.

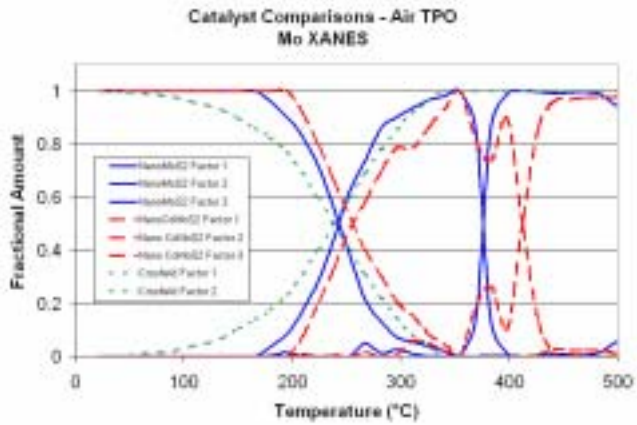

Figure 2. Principle Component Analysis of the types of Mo during TPO of commercial and nano-phase MoS_2.

HDS activity of several supported metals has been correlated with the temperature programmed reduction (TPR) peak. The TPR for the nano-MoS_2 and nano-Co/MoS_2 materials is significantly higher than that of the supported materials. The fact that the temperature of the TPR reduction peak was almost the same as nano-MoS_2 implies that there was not a combination of these two phases. In addition, the width of the TPR peak for the nano-sized materials (nano-MoS_2 and nano-Co/MoS_2) is significantly broader than the commercial catalyst. The wider TPR peak for the sonochemically-generated materials implies that there is a much broader distribution of active sites in the nanophase materials versus the commercially prepared catalyst. This would result in a wider variety of active sites and is probably the

reason for the lower activity for the sonochemically prepared materials.

Preliminary HDS activity evaluation studies show lower activity for the nano-CoS-MoS_2 compared to the nano-MoS_2. This was surprising but is mirrored in the TPR data. The activity of the unsupported nanosized catalysts, however, is much higher than the commercial micron-sized counterparts. This enhancement comes from the increased surface area of the nanoparticles. In the micron-sized catalysts, diffusion in between the long rafts of MoS_2 is mass transport limited, so it is expected that most of the activity comes from the 'rims' and 'edges.' Incorporation of Co to MoS_2 increases the activity of the catalyst. In preliminary studies, the catalytic activities are compared at commercially operated temperature that may not be the optimized temperature for nanosized MoS2-based catalysts.

A major problem with hydrodesulfurization is the hydrogenation of olefins, which leads to loss of research octane number (RON). The rate of olefin hydrogenation is much faster than HDS, but competitive adsorption of S at the active site strongly inhibits the hydrogenation reaction. At low S levels, olefin hydrogenation takes over. To model these olefins in our HDS runs, 1-octene (1 wt.%) was added to the liquid feed and the HDS tests were run again. Interestingly, the sonochemically synthesized nanophase catalysts are less active for olefin hydrogenation than their commercial counterparts. This observation contrasts the expected result that the hydrogenation function in nanosized catalysts should increase because nanosizing increases the number of edge sites. Work is in progress to further decrease the hydrogenation function with concomitant increase in the HDS activity of the synthesized nanophase materials.

Acknowledgement. This work was performed under the auspices of the U. S. Department of Energy, under contract number W-31-109-ENG-38.

ZEOLETIC SUPPORT OF HDS CATALYSTS FOR DEEP HYDRODESULFURIZATION TO ACHIEVE 10PPM SULFUR LEVEL

Naoyuki Kunisada, Ki-Hyouk Choi, Yozo Korai, Isao Mochida, and K. Nakano+*

*Institute of Material Chemistry and Engineering, Kyushu University,
Kasuga-Koen, Kasuga, Fukuoka 816-8580, JAPAN
+ Catalysts & Chemicals Ind. Co. Ltd, JAPAN

*e-mail: mochida@cm.kyushu-u.ac.jp

INTRODUCTION

NOx, SOx and particulate matters exhausted from diesel engine which combusts gas oil as fuel has provided a sincere social problem all over the world. The drastic reduction of sulfur in gas oil is expected to reduce those environmental pollutants and burden for diesel engines. Removing sulfur species deeply from gas oil has two difficulties; the first one is very low reactivity of some refractory sulfur species in gas oil such as 4,6-dimethyldibenzothiophene (4,6-DMDBT), 4,6,x-trimethyldibenzothiophene (4,6,x-TMDBT) having methyl group at 4 and 6 positions, the second is the strong inhibitors in feed oil and the products such as H_2S, NH_3, nitrogen species and aromatic compounds[1,2]. Hence deep HDS of these refractory sulfur species in gas oil can be achieved rather easily by the first and second stages of the catalysts when H_2S removal is performed between stages. Another approach is to develop catalysts of higher activity. Larger amount or better dispersion of sulfides have potential possibility for higher activity. Nevertheless severe conditions appear necessary.

The present authors prepared a two layer catalyst bed to achieve desulfurization without H_2S (NH_3) removal between layers. The functions of the catalysts in each layer are defined as follows. 1st layer : complete removal of reactive sulfur species and 95% removal of refractory sulfur species. 2nd layers : remaining refractory sulfur species (around 400-500ppm) must be removed to less than 10ppm in the presence of H_2S and NH_3. In the present study, several types of zeolite containing supports for HDS catalysts are prepared to be examined in the first and second layers.

Zeolite support has been reported to provide high HDS activity and resistivity against H_2S. However it loses activity and accelerates the cracking of paraffin substrate. Hence, it is the present target to reduce the deactivation and cracking activity with maintain HDS activity and resistivity.

EXPERIMENTALS

a, Gas oil samples

Straight Run Gas Oil (SRGO) and Hydrodesulfurized Straight Run Gas Oil (HSRGO) were used as typical feedstocks for the first and second layer catalysts, respectively in this study. The SRGO contains 11780ppm while the HSRGO contains 340ppm of sulfur. Furthermore, the SRGO contains 155ppm while the HSRGO contains 20ppm of nitrogen.

b, Catalysts

The catalysts used in this study were CoMo and NiMo supported on alumina(-A), silica-alumina(-SA), alumina-zeolite composite(-AZ, -ACZ), silica-alumina-zeolite composite(-SAZ), modified zeolite alumina(-ACZ) which were manufactured by a commercial catalyst vendor. **Table 1** shows their surface area, average pore size measured by BET and NH_3 desorbed amount measured by NH_3-TPD.

c, Hydrotreatment

SRGO and HSRGO were hydrotreated over the catalyst at 340ºC under 50kg/cm^2 of H_2 for first layer, 50 kg/cm^2 H_2 with H_2S (1.67%) and 50 kg/cm^2 H_2 with H_2S (1.67%) added ethylenediamine (15ul) for second layer in a 100ml autoclave.

The ratio of catalyst to feed was 1g/10g. Catalyst was presulfided at 360ºC under the stream of H_2S(5%)/H_2 mixture for 2hr before the catalytic reaction.

Table.1 Catalysts properties

	Surface area (m^2/g)	Pore volume (cm^3/g)	NH_3-Desorbed area (mmol/g-cat.)
CoMoA	191	0.41	0.48
NiMoA	175	0.34	0.62
CoMoSA	221	0.41	0.56
NiMoSA	242	0.39	0.49
CoMoAZ	265	0.34	0.81
NiMoAZ	262	0.35	0.66
NiMoSAZ	271	0.33	0.85
CoMoSAZ	274	0.32	0.82
NiMoACZ	129	0.36	0.58

RESULTS

a, HDS of SRGO

Figure 1 shows remaining sulfur chromatograms of SRGO after HDS over NiMo- and CoMo-A, NiMo- and CoMo-SA, NiMo- and CoMo-AZ, NiMo- and CoMo-SAZ, and NiMo-ACZ catalysts at 340ºC under 50 kg/cm^2 H_2. NiMo-AZ shows the highest activity among nine catalysts, and its remaining sulfur content is less than 300ppmS. Although NiMo-ACZ, having smaller surface area, shows low activity, zeolite containing catalysts having larger surface area except for NiMo-ACZ tend to show higher activity than SA- and A-series catalysts for HDS of SRGO that contained major reactive sulfur species. The HDS at this stage removed all reactive sulfur species and about 95% of refractory sulfur species to achieve sulfur level of 500ppm.

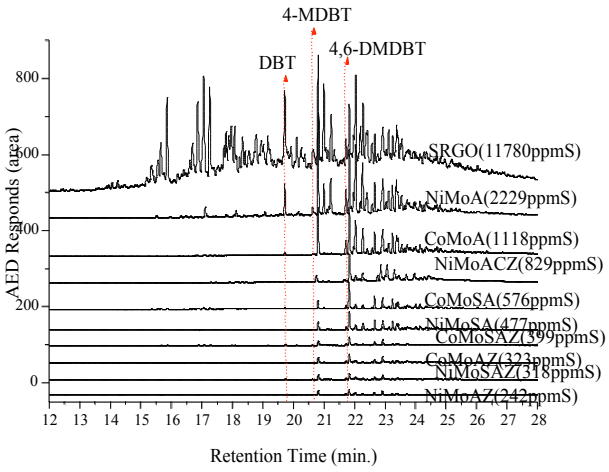

Figure 1. HDS of SRGO over several NiMo and CoMo catalysts

d, HDS of HSRGO in the presence of H_2S and NH_3

Figure 2 shows HDS of H-SRGO in the presence of both H_2S and NH_3. **Figure 3** shows GC-AED carbon chromatograms after HDS of HSRGO in the presence of both H_2S and NH_3. NiMo-A of large pore was found very active for HDS of refractory sulfur species in the presence of H_2S and NH_3 to achieve less than 6ppmS. In contrast, CoMo-A, NiMo-SA and CoMo-SA were less active. NiMo-AZ and CoMo-AZ were much inhibited by addition H_2S and NH_3. NiMo-ACZ, NiMo-SAZ and CoMo-SAZ having strong acidity were found very active as a second layer catalyst.

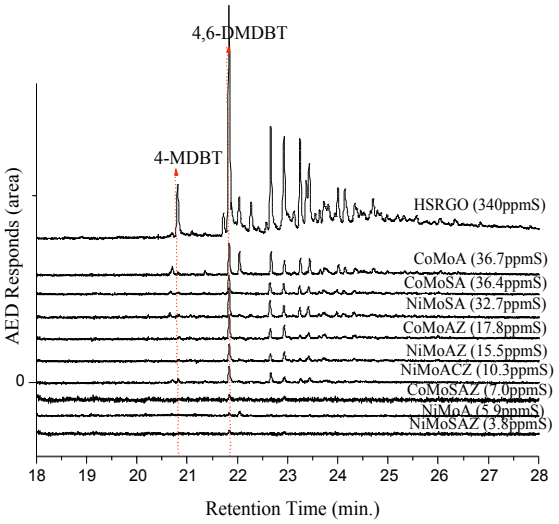

Figure 2. GC-AED sulfur chromatograms on HDS of H-SRGO in the presence of H_2S and NH_3

Acidic catalyst can crack and isomerize hydrocarbons. As can be seen in **Figure 3**, a number of products were found at a range of shorter retention time as a result of hydrocracking. Such products were the most remarkable on alumina-zeolite supported catalysts. In contrast NiMo-ACZ containing zaolite catalyst showed higher activity didn't crack for isomerize hydrocarbons at all. Although the strength of acidity of NiMo-ACZ can be demonstrated, cracking of hydrocarbons is not distinct.

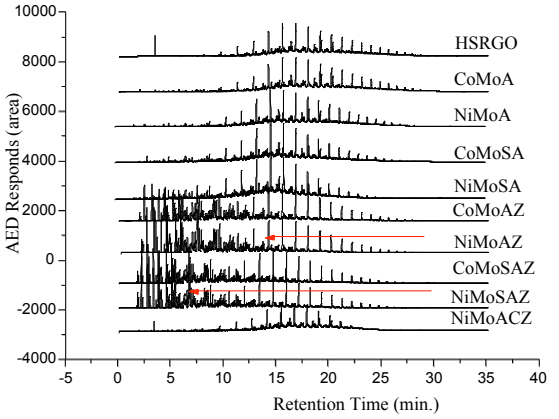

Figure 3. AED Carbon Chromatograms of HDS over some Acidic Catalysts

DISCUSSIONS

The present study revealed that the two layers of the best HDS catalysts with appropriate activity under respective conditions can be a logical approach to achieve deep HDS of gas oil.

The first layer catalyst must eliminate 100% of reactive sulfur species, first of all. Hence, the catalyst must have larger surface area, slightly smaller pore being allowed for the larger surface area. Acidity helps higher activity. 95% of refractory sulfur species must be also eliminated. Its content is still in relatively large range, being less influenced by inhibitors. Moderate acidity is helpful for the hydrogenative HDS.

The second layer catalyst eliminates the refractory sulfur species of 100-500ppm to less than 10ppm in the presence of H_2S and NH_3. The catalyst must have larger pores to accept the refractory sulfur species of tri aromatic rings with methyl groups more than di aromatic rings. Acidity is important to enhance HDS of the refractory sulfur species in the hydrogenation route by moderate H_2S inhibition. Zeolite containing CoMo and NiMo showed higher activity in SRGO, HSRGO+H_2S+NH_3. On the other hand, zeolite having strong acidity is easily deactivated and can crack and isomerizes hydrocarbons. ACZ catalyst showed very high activity in HDS of HSRGO, while it didn't crack the substrate so much. Therefore, modified zeolite-alumina catalyst may have longer life time than any other zeolite containing catalyst, with have high cracking activity.

Appropriate sets of two catalysts with successive layers are very active to achieve regulated Sulfur level of gas oil. It is always discussed whether CoMo or NiMo is better catalyst for the first and second layers. The support and supporting procedure appear very influential and hence we can not tell which is better at this stage. Nevertheless high dispersion in designed shape of the sulfides must be practiced in any supports.

ACKNOWLEDGEMENT

This work has been entrusted by the New Energy and Industrial Technology Development Organization under a subsidy of the Ministry of Economy, Trade and Industry of Japan.

REFERENCE

1. Isoda, T.; Ma, X.; Mochida, I. *Sekiyu Gakkaishi,* **1994**, *37*, 506.
2. Whitehurst, D. D.; Isoda, T.; Mochida. I, *Adv. Catal.*, 1998, *42*, 345.
3. Isoda, T.; Ma, X.; Mochida, I. *Sekiyu Gakkaishi,* 1995, *25*, 38.

DIBENZOTHIOPHENE HYDRODESULFURIZATION OVER BULK UNPROMOTED AND COBALT PROMOTED MoS_2 CATALYSTS

Hamdy Farag; Kinya Sakanishi; Masato Kouzu; Akimitsu Matsumura; Yoshikazu Sugimoto and Ikuo Saito

Institute for Energy Utilization, AIST
Tsukuba West 16-1 Onogawa, Ibaraki 305-8569, Japan

Introduction

Environmental concerns are the driving force behind the growing interest of removing sulfur compounds from middle distillate fuels. To encounter the strict of nowadays regulation of sulfur content superior, catalyst is needed. Polyaromatic sulfur compounds are confirmed to be the real obstacle for deep hydrodesulfurization (HDS) reaction. They are the leftover species after deep HDS. These species react through consecutive and sequence reaction in which the selectivity plays a role in the reaction mechanism. In respect to this, catalyst designers encounter two options; one is to search for a catalyst in which the hydrogenation is the pioneer feature of its activity and the other is an ascertained catalyst for the hydrogenolysis of C-S bond. MoS_2 based catalysts are widely applied for HDS reactions. The role of cobalt in promoting MoS_2 supported catalysts has been extensively studied and the synergetic effect is well established.1,2 Nevertheless, the impact of cobalt addition to bulk MoS_2 on the selectivity trend of HDS is not clear yet. A better understanding how cobalt may modify the bulk MoS_2 catalyst will provide researchers with fruitful information about how such inclusions promote the HDS activity in case of supported Mo-catalysts. In this piece of work we address some experimental insight work on the comparison between behavior of bulk and supported Mo-catalysts. In addition, it may contribute the linkage between the catalytic activity and selectivity in HDS reaction. Kinetic treatments that focus on the selectivity change of HDS of dibenzothiophene (DBT) are prescribed.

Experimental

Bulk MoS_2 was synthesized through heat annealing in presence of continuous flow of 10v/v% H_2S/H_2 gas mixture. Detail of preparation and characterization of this catalyst is stated elsewhere3. The obtained highly crystalline MoS_2 phase was further ground fine particle around nanometer sizes. This form of MoS_2 was applied to be a primary support for cobalt addition. Alcoholic solution of cobalt (II) acetate was impregnated to MoS_2 at ambient temperature. This mixture was exposed to ultrasonic for 10min. Then the sample was dried at 80°C under vacuum condition. Thereafter, the catalyst was pre-sulfided at 400°C by flow of 10v/v H_2S/H_2 gas mixture. CoS phase synthesized via heat annealing of cobalt (II) acetate with gas flow of 10v/v%H_2S/H_2.

The HDS catalytic activity of DBT was investigated through the use of a batch magnetically stirrer micro-autoclave reactor. All reaction runs were examined at 340°C and 3MPa H_2. Some reaction runs were carried out after addition of copper powder which serves as a scrubber of the continuous production of H_2S during HDS. Reaction products were tracked by the aid of GC-FID and GC-MS.

Results and Discussion

The main HDS products from DBT obtained over the studied catalysts are biphenyl (BP) and Phenylcyclohexane (PC) in addition to the well-known intermediate of H4-DBT. However, it is unique of the MoS_2 and/or Co-promoted bulk MoS_2 catalysts that traces of fragmented products like alkylated derivatives of benzene or even naphthalene is formed. The presence of these species could be explained due to a series of consecutive hydrogenation reactions that takes place over this kind of catalysts. Table 1 shows the catalysts characterization and the product distribution of DBT HDS at ca. 50% conversion level. Fixed conversion level was adopted because the selectivity of these consecutive and parallel reactions varies with the conversion level.

Table 1. Activity of Bulk MoS_2 Promoted Cobalt Catalysts for DBT HDS.

Catalyst	Co wt%	Level of H_2S[a]	HDS*	Selectivity at 50% conv. level		
				BP	PC	H4-DBT
CoS	100	High	2	24.4	21.6	3.9
MoS_2	0	Low	24	22.3	25.3	2.4
MoS_2	0	High	83	8.2	28.5	13.3
MCS-I	2	High	38	28.5	16.4	5.1
MCS-II	10	High	33	28.5	16.3	5
MCS-III	16	Low	17	43.2	6.2	0.7
MCS-III	16	High	33	28.6	16.7	5.2

*$s^{-1}.g.cat.^{-1}.10^{-4}$, (340°C & 3MPa H_2), ± 3%

The HDS activity of CoS is very low compared with MoS_2 catalyst. One may notice the sharp decrease in activity for Co-promoted MoS_2 catalysts. Unlike the supported CoMo catalysts, Co addition to bulk MoS_2 has a negative effect on the HDS activity. In addition the selectivity of DBT HDS was changed dramatically based on the level of H_2S in the reaction medium. **Figures** 1,2 and 3 show the activity and selectivity behavior of the MoS_2 and Co-promoted MoS_2 catalysts. To explain the connection between cobalt inclusions and the changes in HDS activity, one must look at their impact on the selectivity trend.

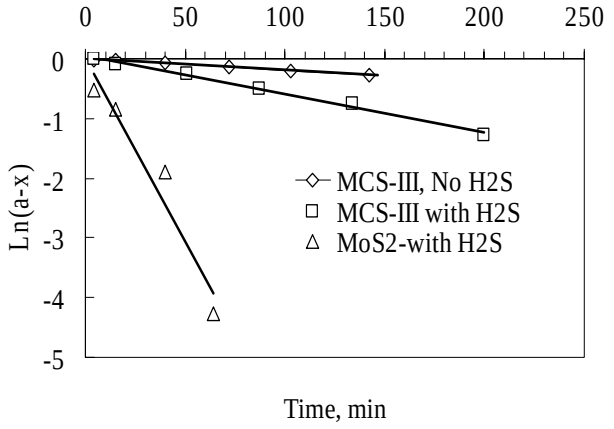

Figure 1. Pseudo-first order plots of DBT HDS over MoS_2 and MCS-III catalysts with or without copper addition.

It is interesting to note the drastic change in selectivity in presence or absence of Co. The obvious decrease of activity with Co inclusions to MoS_2 is markedly linked in a direct proportion relation with the change made on the selectivity behavior. This raises the consolidation between selectivity and activity in HDS reaction4. Another interesting feature of the present results is the effect of H_2S on the selectivity and activity of DBT HDS. Figures 3 and 4 show the effect of H_2S level on the HDS selectivity of DBT over MCS-III catalyst. H_2S level is defined as whether copper are included or not into the reaction medium. It is evident that H_2S promote the reaction via the acceleraton of the hydrogenation route. Nevertheless, the contribution from the direct hydrogenolysis route is still significant. DBT HDS showed pseudo-first order behavior and the influence of H_2S on the activity is clarified on **Figure** 1. **Figures** 2 and 3 illustrate the selectivity changes over MoS_2 and MSC-III catalyst. The hydrocracked fragments products were assumed to result from PC.

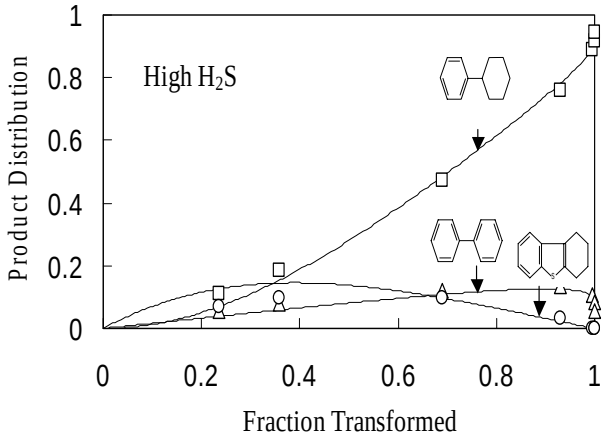

Figure 2. HDS selectivity Curves of DBT (MoS_2, 340 °C & 3MPa H_2).

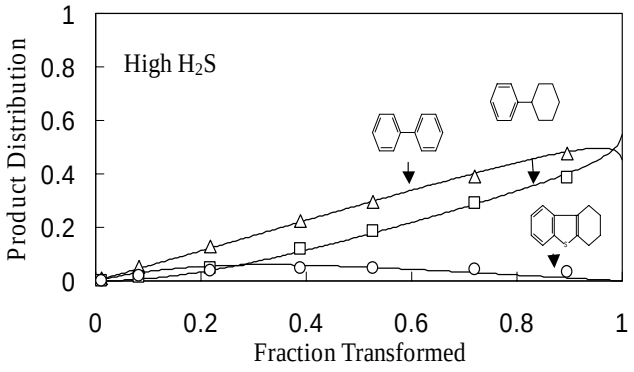

Figure 3. HDS selectivity Curves of DBT (MCS-III, 340 °C & 3MPa H_2).

The decrease in activity of MoS_2 after inclusion of Co is suggested to be due to the negative synergetic effect that has been widely known for these supported catalysts. In other words, the synergy in the present bulk sulfides is not helpful for HDS activity. It seems that this synergy rule the HDS reaction via more contribution of the direct desulfurization route leading to BP species. The reaction through this route is reported to undergo geometrical difficulty to reach the prospected catalytic active sites. In this respect, it is suggested that the catalytic activity is linked with two distinct active sites. The inclusions of Co to the MoS_2 catalyst replaced some of the usable hydrogenation sites in MoS_2 catalyst. Consequently, these sites will no longer be active for hydrogenation. The obtained new sites forward the reaction to the direct desulfurization route.

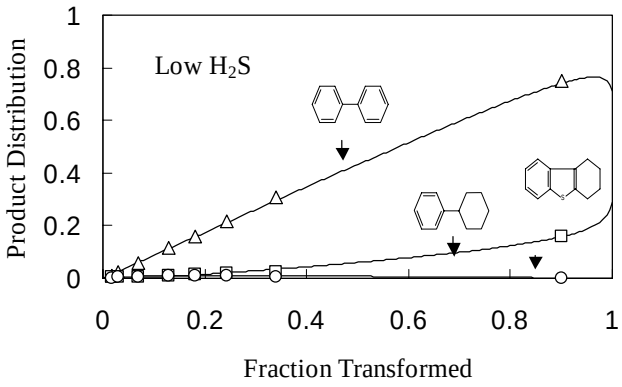

Figure 4. HDS product distribution curves of DBT over MCS-III catalyst, the run with added copper powder. (340°C & 3MPa H_2)

In summary, the results show the close correlation between activity and selectivity in HDS reaction and how cobalt modified the HDS reaction mechanism occurred over MoS_2 catalyst.

Acknowledgment. This work has been entrusted by the New Energy and Industrial Technology Development organization under a subsidy of the Ministry of Economy, Trade and Industry.

References

1. Prins, R., Adv.Catal. **2002**, 46, 399.
2. Rossini, S., Catalysis Today **2003**, 77, 467.
3. Farag, H., Energy & Fuel **2002**, 16, 944.
4. Nava, H.; Ornelas, C.; Aguilar, A.; Berhault, G.; Fuentes, S.; Alonso, G., Catal.Lett. **2003**, 86(4), 257.

IN SITU FT-IR STUDY OF CO HYDROGENATION ON A MOLYBDENUM NITRIDE CATALYST

Dong Liu, Yunqi Liu, Tao Zhou, Chenguan Liu, Guohe Que

INTRODUCTION

Free ammonia had been replaced with N_2/H_2 gases, the production of molybdenum nitride and Co-promoted molybdenum nitride, which had more sufficient specific surface area, had been obtained from the two-stage temperature-programmed reduction of molybdenum oxides with the mixture of N_2/H_2 gases. The new synthetic molybdenum nitride and co-promoted molybdenum nitride is very sensitive to air, so it should be pre-treated in the cell—namely the new synthetic molybdenum nitride should be retarded-oxidized by oxygenic inert gas on their surface and a thin layer of CoMoNx will be formed on their surface. CoMoNx on surface layer will invert to molybdenum nitride due to hydrogenation at 673K, and will improve their hydrodesulfurization activity. Because hydrofining catalysts will be influenced by H2S in the hydrodesulfurization process, they should possess high activity and cracking activity (desulfurization activity). It is difficult to distinguish which is better between hydrogenation activity and cracking activity for molybdenum nitride catalysts when organosulfur is adopted to evaluate activity, because H_2S in production will bring some disturbance on surface structure of catalysts. The CO hydrogenation activity was measured by FT-IR in-situ method. Mo_2N and CoMoNx were prepared and used in the experiment, and compared their effect on CO hydrogenation activity with MoS_2.

EXPERIMENTAL

Catalysts preparation

The production of molybdenum nitride and co-promoted molybdenum nitride were obtained from the two-stage temperature-programmed reduction of molybdenum oxides with the mixture of N_2/H_2 gases. The BET specific surface areas of molybdenum nitride and Co-promoted molybdenum nitride (atomic ratio of Co and Co+Mo is 0.25) are 165 and 158 m^2/g respectively. MoS_2 (99.9%) was produce by Beijing chemical reagent company.

Method of in situ FT-IR study on CO hydrogenation

CO hydrogenation was carried out in a self-designed IR cell described as Figure 1. The IR cell was made of quartz, the length and high of optical path were ascertained by Magna-750 Fourier Transform Infrared spectrometer. The IR cell (a hollow cell) adding with water inlet and outlet tube were constituted into a whole circular cooling system to protect windows. Heating zone, made up to groove shape to keep insulation of resistance heater, was situated in the middle of the cell. Heating power was 350W. A self-supporting disc (13mm diameter) was prepared by compressing the powder obtained by Catalysts (1% Mo_2N, MoS_2 or CoMoNx mixed with 99% Υ-Al_2O_3). This disc was mounted in a self-designed IR quartz cell described as Figure 1. A thermocouple well was indwelled in the middle of the IR cell around the catalysts disc. Actual temperature about catalysts (reaction temperature) was measured by the thermocouple. Programmed temperature control instrument, joined with all heating zone and temperature detector in the IR cell, will control the temperature. Air inlet and air outlet were installed on two end of the cell that were adopted with KBr plate and were connected with air inlet channel and outlet channel of in-situ systems by vacuum silicone grease.

Partial pressure of CO, H_2 are 1.01×10^4 and 2.02×10^4Pa respectively in the CO hydrogenation experiment, reaction temperature is 673K unless otherwise stated.

The catalyst disc was degassed under vacuum for 1hr at 673 K, then was pre-reduced in-situ in high-purity H_2 at 2×10^3Pa for 2hr. In-situ IR spectra of the disc in CO, H_2 at the quoted temperatures and pressures were recorded with a Nicolet Magna-750 Fourier Transform Infrared spectrometer. The resolution was $4cm^{-1}$, the scanning area was 4000~400 cm^{-1}, the scanning frequency was 256.

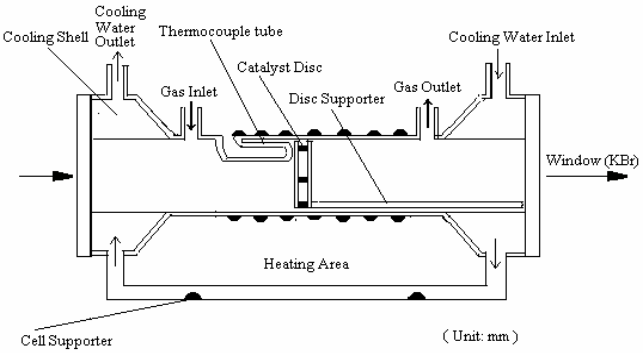

Figure 1. In-situ FT-IR Quartz Cell

Figure 1b. Disc Quartz Supporter

RESULTS AND DISCUSSION

CONFIRMATION OF REACTION PRODUCT

It was confirmed by IR spectrum of methane standard gas (99.99%) that there was methane in the reaction product. Figure2 show the IR spectrum of methane standard gas and the reaction product of CO and H_2. There were two broad infrared bands at 3020 and $1310cm^{-1}$ emerged on the IR spectrum of methane standard gas, which were coincided with two infrared bands on the IR spectrum of reaction products of CO and H_2. It showed that there might be methane existed in the reaction products of CO and H_2. It means that gaseous CO_2 in the IR cell might cause the bands at $2200\sim2400cm^{-1}$ and the band at $1400\sim1600cm^{-1}$ may be due to H_2O, H_2O is one of the reaction products of CO hydrogenation. On the existing of H_2, the main reaction is hydrogenation, but the disproportionation of CO may have occurred (to form CO_2 and C). This experiment mainly observes and studies the hydrogenation activity about molybdenum nitride catalyst. CH_4 is main hydrogenation product in the reaction of CO probe molecule hydrogenation and CH_4 did not react to form C_2 further, which showed the high selectivity of CO hydrogenation on the surface of molybdenum nitride catalyst.

Figure3 shows the effect on the IR spectra about reaction products that are formed by CO hydrogenation reaction on the surface of molybdenum nitride catalyst different time. It shows obviously that methane IR spectra peak area will increase while the reaction time increasing when we compare IR spectra peak area on different time. The peak area will characterize the hydrogenation activity of catalysts instead of the concentration of reaction products because it is proportionate with concentration of reaction products, when we deal with the experimental data.

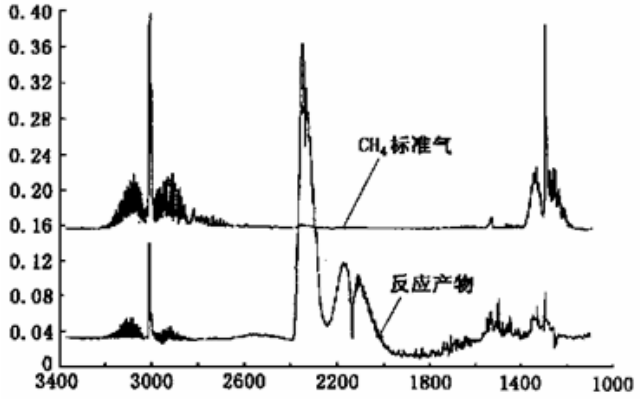

Figure 2. Spectra of the production of CO hydrogenation and pure methane

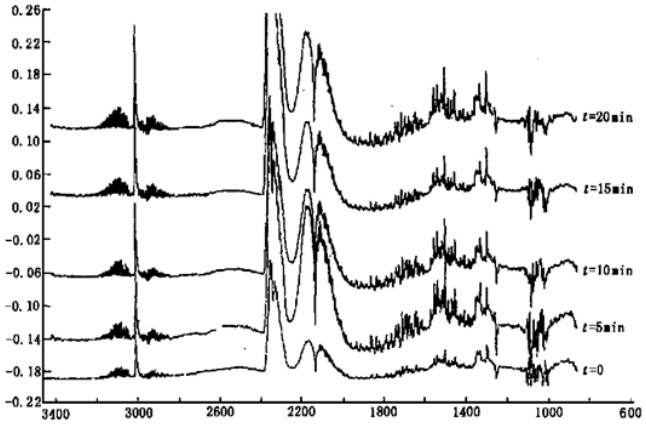

Figure 3. Spectra of the production of CO hydrogenation on Mo_2N

INFLUENCE FACTORS OF HYDROGENATION ACTIVITY ON THE (Co-PROMOTED) MOLYBDENUM NITRIDE CATALYST

H_2-reduction pretreatment

In order to find the influence factors of CO hydrogenation activity about molybdenum nitride catalyst, we compared CO hydrogenation activity on different time about Mo_2N and CoMoNx catalysts before H_2-reduction pretreatment with after H_2-reduction pretreatment, and compared them with CO hydrogenation activity of MoS_2 catalysts. The result shows in the table1. Table1 shows:① It is the same result to Mo_2N and CoMoNx catalysts that CO hydrogenation activity will be reduced after catalysts were hydrogenation reduction;② CO hydrogenation activity will be increased by adding Co into molybdenum nitride catalyst;③ Hydrogenation activity of passivated molybdenum nitride catalysts is lower than that of MoS_2 catalysts. The reason is the surface structure of passivated molybdenum nitride catalysts is high dispersing molybdenum nitride oxide due to introduce O_2 after molybdenum nitride catalysts were passivated (figure 4-a). Oxides atom and hydrogen atom dissociated from hydrogen molecule formed to –OH, which improve the acidity of catalysts and reduce the metallic property of catalysts (hydrogenation activity) (figure4 (b)). Catalytic hydrogenation promoter of Co is mainly depended on its the ability of high-activated hydrogen, and at the same time its lower hydrogen adsorptivity improve hydrogenation activity of catalysts, because Co addition improve the quantity of hydrogen fugacity.

Reaction temperature

Figure2 shows CO hydrogenation activity of Mo_2N and CoMoNx catalysts on different reaction temperature and reaction time (showed by CH_4 peak area). While reaction temperature increasing, CO hydrogenation activity increases obviously. In the proper temperature range, addition of Co will improve hydrogenation activity.

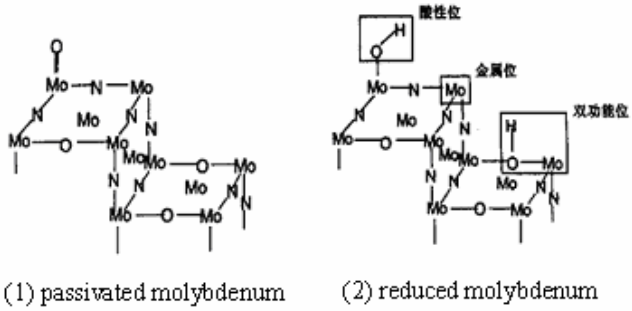

Figure 4. The surface layer structure of Mo_2N

CONCLUSIONS

The production of molybdenum nitride and Co-promoted molybdenum nitride has been obtained from the temperature-programmed reduction of molybdenum oxides with the mixture of N_2-H_2 gases. The BET surface areas of molybdenum nitride and Co-promoted molybdenum nitride are 165 and 158m^2/g respectively. The CO hydrogenation activity was measured by FT-IR in-situ method. It is showed high activity and selectivity of methane formation. It is the same result to Mo_2N and CoMoNx catalysts that CO hydrogenation activity will be reduced after catalysts were hydrogenation reduction. Addition of Co will improve hydrogenation activity; Hydrogenation activity of passivated molybdenum nitride catalysts is lower than that of MoS_2 catalysts.

REFERENCE

(1) OYAMAST, Prepartion and catalytic properties of transition metal carbides and nitrides[J]. Catalysis Today, 1992, 15:179-200
(2) M. Lin, Practical FT-IR Spectroscopy, Publishing House of Chinese Environment, Beijing, 1991.
(3) A. Jayasooriya, M.A. Chesters, M.W. Howard, et al., Surf.Sci. 93 (1980) 526.
(4) W.M. Mandy and H.R. Colin, J. Catal. 141 (1993) 355.
(5) M.R. Prairie, J.G. Highfield and A. Renken. Chemical Engineering Science, 46 (1991) 113
(6) B. Robert and C. Sophia, Surf. Sci, 87 (1991) 1791

Ab initio Study of Interaction of a Model Nitrile Polymer with Various Model Fuel Molecules

Dominic R. Alfonso and Anthony V. Cugini

National Energy Technology Laboratory, Pittsburgh, PA 15236, USA

Introduction

The extensive use of polymeric materials in various diverse industries has generated increased interest in the study of polymers particularly on how they will perform in a chemical environment. For example, many synthetic polymers are able to swell in suitable solvents, thus significantly altering their properties. This often is the first step in a degradation process that may ultimately lead to deterioration of the performance of the material in service, resulting in increased downtime for the system and costly maintenance procedures. However, there are polymer applications that rely on the polymers ability to be at least partially swollen and without swelling many technological applications of polymers would not be possible. In systems where flammable liquids are employed, the failure of O-rings (used in fuel line connections) to swell can cause tank seals to fail. It is therefore of practical interest to understand the mechanism of solvent-induced swelling.

The swelling behavior of polymers in a fluid can be examined experimentally in a variety of ways. [1-3] These include weight gain immersion time studies, modifications of hardness, volume and tensile strength, and dynamic mechanical thermal analysis (DMTA) to measure changes in the dynamic properties of the polymer as a function of temperature. Unfortunately, it is difficult to obtain direct mechanistic information about the swelling process on a molecular level using these approaches. It is well established that swelling of polymers involves mutual dissolution of two completely miscible substances accompanied by an increase in the dimension of the polymer. [4] The mechanism of swelling is therefore related to the competition of intermolecular and intramolecular bond in polymer on the one hand and in the polymer-solvent system on the other hand. Fundamental investigations into the interaction between the polymer and the fluid have important bearing in the understanding of the swelling process.

Quantum mechanical modeling has become a useful tool for obtaining a complete microscopic understanding of the polymer-fluid interactions under controlled conditions. A number of *ab initio* investigations using a small molecule analogue approach have been reported. [4,5] The validity of this approach was investigated for a model nitrile polymer (isobutyronitrile) interacting with a variety of model fuel molecules. The most common commercially available O-rings are based on nitrile polymers. Mixtures of nitrile polymers and numerous hydrocarbon based fuels (3-GP-11 naval distillate fuel and JP-5 aviation turbine fuel) have been studied experimentally. [3] Diffusion coefficients and weight gain were measured and correlated with the swelling behavior of nitrile polymers. Nevertheless, to date there is no clear understanding of the interaction of nitrile polymer with hydrocarbon based fluids from *ab initio* calculations. In this paper, we present the first results of molecular modeling for isobutyronitrile-fuel molecules systems at selected quantum mechanical levels of theory.

Computational Details

As can be seen, the method most widely used to model intermolecular interactions which takes into account the effect of electron correlation at relatively low computational cost is the second order Møller-Plesset (MP2) theory.[6] Density Functional Theory (DFT) within the B3LYP approach [7] has been shown to yield reliable predictions of the geometries and stabilization energies of some hydrogen bonded and ionic complexes. However, DFT poorly reproduces dispersion interactions and other weak forces. On the other hand, local correlation methods such as the local MP2 (LMP2) method [8] have recently emerged as alternatives for the study of intermolecular interactions. The LMP2 method is virtually free from basis set superposition error (BSSE). In addition, LMP2 offers significant computational savings over MP2. The method has been applied to study interactions between a variety of systems such as amino acid backbone and side chain analogues.

All MP2 calculations were performed using the program Gaussian 98. [9] LMP2 single point energy calculations were performed with the program Molpro. [10] Full geometry optimizations for various combinations of the model nitrile polymer and fuel molecules were carried out at the MP2 level of theory with the 6-31G* basis set. Single point energy evaluations for each combination of the model polymer and a fuel molecule at the LMP2/cc-pVDZ and LMP2/cc-pVTZ level of theory were carried out for geometries optimized at the MP2/6-31G* level. Calculations were carried out using isobutyronitrile ($(CH_3)_2CHCN$) as a model nitrile polymer. The number of atoms in the model polymer cluster was chosen to be as large as possible in order to adequately represent the extended bulk system while at the same time, remaining computationally tractable. We employed CH_4, C_2H_2, C_2H_4, C_2H_6 and C_6H_6 as model fuel molecules

Results and Discussion

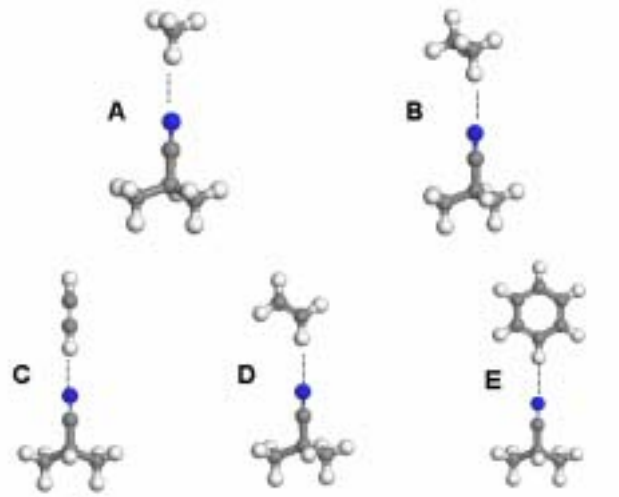

Figure 1. LMP2/6-31G* optimized geometries for isobutyronitrile – hydrocarbons considered in this work. Gray, white and blue balls denote carbon (C), hydrogen (H) and nitrogen (N) atoms, respectively.

Figure 1 shows the MP2/6-31G* optimized geometry of the various complexes considered in this work. In all cases, the C-H bond of the hydrocarbons prefers to point to the CN fragment of isobutyronitrile. The computed H··N distances are 2.759 (**A**), 2.742 (**B**), 2.315 (**C**), 2.616 (**D**) and 2.548 Å (**E**). For all cases, the C-N distances in the model polymer are unchanged compared to that in the isolated model polymer (1.18 Å).

Table 1 shows the LMP2 binding energies of the studied complexes. The uncorrected binding energy ($E_{uncorrected}$) were obtained by subtracting the energy of two fully optimized monomers

from the energy of the dimer. The LMP2 interaction energies were corrected for BSSE at the Hartree-Fock (HF) level. The BSSE-corrected interaction energy ($E_{corrected}$) is determined as follows:

$$E_{corrected} = (E[AB] - E[A]_{mon} - E[B]_{mon}) + E_{BSSE} \quad (1)$$

$$E_{BSSE} = (E[A]_{dim} - E[A]_{dim}^{*} + E[B]_{dim} - E[B]_{dim}^{*}) \quad (2)$$

where E[AB] is the energy of the dimer, E_{mon} is the energy of the individually optimized monomer and E_{BSSE} is the correction for the BSSE. E_{dim} and E_{dim}^{*} represent the energies of the monomers in their dimer optimized geometries for the basis set of the monomer and dimer, respectively.

Table 1. Interaction Energies (kcal/mol) at the LMP2 level of theory

complex	basis set	$E_{uncorrected}$	E_{BSSE}	$E_{corrected}$
A	cc-pvDZ	-1.086	0.405	-0.681
	cc-pvTZ	-0.767	0.132	-0.635
B	cc-pvDZ	-1.083	0.416	-0.667
	cc-pvTZ	-0.836	0.133	-0.702
C	cc-pvDZ	-3.684	0.612	-3.072
	cc-pvTZ	-3.254	0.209	-3.045
D	cc-pvDZ	-1.558	0.448	-1.111
	cc-pvTZ	-1.283	0.158	-1.124
E	cc-pvDZ	-1.960	0.485	-1.475
	cc-pvTZ	-0.997	0.182	-0.816

For the complex of isobutyronitrile with aliphatic, ethylenic and acetylenic hydrocarbons, we find a slight change (ranging from 0.013 to 0.046 kcal/mol) in the binding energies when the the basis set size increased from from cc-pvDZ to cc-pvTZ at the LMP2 level. The only exception to this trend is the isobutyronitrile -benzene complex. As may be seen, significant differences in the interaction energies occur, indicating that this complex to be especially sensitive to the basis set protocol. One encouraging conclusion that can be made by analyzing Table 3 is that BSSE becomes small when cc-pvTZ basis set is used, thus making unnecessary BSSE correction in the case of LMP2/cc-pvTZ calculations.

Our calculations have identified key differences between the interaction of saturated and unsaturated hydrocarbons with isobutyronitrile. The interaction of C_2H_4, C_2H_2 and C_6H_6 with isobutyronitrile is stronger compared to CH_4 and C_2H_6. The larger attraction of aromatic, ethylenic and acetylenic C-H bonds with the CN moiety can be attributed to the substantial bond dipoles in these *sp* and sp^2 C-H bonds. These bond dipoles have attractive dipole-dipole interactions with the CN fragment of the model polymer. The corresponding interaction between aliphatic C-H bond in CH_4 and C_2H_6 is weaker.

Hiltz *et al.* have carried out a DMTA study of swelling behavior of a variety of elastomers in naval distillate fuel (3-GP-11) and aviation turbine fuel (JP-5). [3] For nitrile elastomer, the rubber showed the biggest weight gain following exposure to JP-5 compared to 3-GP-11. They suggested that one of the factors that influence the uptake of hydrocarbons by the elastomer is the structure of the hydrocarbon. As JP-5 contains 25 % aromatic hydrocarbons, the higher solubility of the rubber in this fuel can be attributed to this factor. Our molecular modeling computations have brought to light differences in the interaction of saturated and unsaturated hydrocarbons considered in this work with isobutyronitrile. Based on the assumption that the swelling process is determined by solvent-polymer interactions, our calculations show larger interaction energy for complexes composed of unsaturated hydrocarbons such as the aromatic compound benzene. Comparing all compounds investigated, one may further assume that the swelling property of nitrile rubber increases as the interaction energies increases. To obtain further insight into the swelling properties of the nitrile rubber, purely thermodynamical investigations obviously do not yield complete information. For this reason, additional investigations into the dynamic behavior with molecular dynamics simulations will lead to a better understanding of the different swelling behavior.

Conclusions

Interactions of isobutyronitrile with CH_4, C_2H_2, C_2H_4, C_2H_6 and C_6H_6 were examined using *ab initio* calculations at the LMP2 level of theory. In all cases, a C-H bond of the hydrocarbons prefer to point to the CN fragment of isobutyronitrile. Computations at the cc-pvDZ and cc-pvTZ level have identified key differences between the interaction of saturated and unsaturated hydrocarbons with isobutyronitrile. The attraction of aromatic, ethylenic and acetylenic C-H bonds with the CN moiety are larger and attributed to the substantial dipoles in these *sp* and sp^2 C-H bonds. These molecular modeling computations have brought to light differences between the interaction of isobutyronitrile and saturated and unsaturated hydrocarbons which may help to explain why certain fuels swell nitrile elastomers and others do not.

Acknowledgement. We thank Kurt Rothenberger, Kenneth Jordan, Richard Christie and Evgeny Mishakin for helpful comments. Computations were performed on a computer cluster at the National Energy Technology Laboratory.

References

(1) Harogoppad, S. B.; Aminabhavi, T. M. *Polym. Commun*. **1991**, 32, 120.
(2) Harogoppad, S. B.; Aminabhavi, T. M. *Polymer*, **1991**, 32, 870.
(3) Hiltz, J. A.; Morchat, R. M.; Keough, I. A. *Thermochimica Acta*, **1993**, 226, 143.
(4) See for example, Kast, K. M.; Reiling, S.; Brickmann, *J. Mol. Struct*. **1998**, 453, 169.
(5) Akbulut, M.; Ermler, W. C.; Kalyon, D. M. *Comp. Theor. Poly. Sci*. **1997**, 7, 75.
(6) Moller, C.; Plesset, M. S. Phys. Rev. 1934, 46, 618.
(7) Becke, A. D. *J. Chem. Phys*. **1993**, 98, 1372.
(8) Saebo, S.; Tong, W.; Pulay, P. *J. Chem. Phys*. **1993**, 98, 2170.
(9) Frisch, M. J. *et al*., Gaussian 98, revision A.9; Gaussian Inc.: Pittsburgh, PA 1998.
(10) Hetzer, G.; .Pulay, P.; Werner, H. -J. *Chem. Phys. Lett*. **1998**, 290, 143.

EFFECT OF MONOMERIC SEQUENCE ON NANOPHASE-SEGREGATED STRUCTURE AND WATER TRANSPORT IN NAFION 117

Seung Soon Jang, Valeria Molinero, Tahir Çağın, and William A. Goddard III

Materials and Process Simulation Center MC 139-74, California Institute of Technology, Pasadena, CA 91125

Introduction

Nafion is a polyelectrolyte consisting of nonpolar N=(CF_2-CF_2) and polar-ionizable P=(O-CF_2-$CF(CF_3)$)$_2$-CF_2-CF_2-SO_3H) segment. Hydrated Nafion 117 with an average of 6.5 hydrophobic tetrafluoroethylene units per vinyl ether sulfonate unit is widely used for membranes in fuel cell operations due to its relatively high proton conductivity, mechanical and electrochemical stability. Although the ratio of hydrophobic to hydrophilic monomers is well known, the monomeric sequence in the Nafion polymer is not well characterized and its affect has not been included as a design variable to improve fuel cell performance. There is a general consensus supported by experiments[1-7] and simulations[8] that hydrated Nafion has a nanosegregated structure consisting of hydrophobic and hydrophilic domains. Notwithstanding, the details of the segregated morphology remain unclear and highly debated. In this work we explore in particular the effect of monomer sequence on the structure and transport in hydrated Nafion 117 by Molecular Dynamics (MD) simulations. Our goal is to elucidate the effect of the monomeric sequence of polar (P) and nonpolar (N) monomeric units in Nafion on the phase-segregated morphology and water/hydronium transport.

Simulation Methods

In order to assess the monomeric sequence effect on the properties of our interest, we prepared two model samples of Nafion 117 (equivalent weight 1150) chains. One has a $(N_7P)_{10}$ sequence in which the vinyl ether sulfonate unit comes every 7 tetrafluoroethylene units. This structure is characterized by a degree of randomness value (DR) of 1.1, and the ionizable monomeric unit is uniformly distributed along the chain. The Second polymer structure considered is a diblock copolymer with a $N_{70}P_{10}$ sequence in which the 10 vinyl ether sulfonate units gather at the end of a chain of 70 tetrafluoroethylene units. This latter structure has a DR=0.1. The distance between contiguous sulfonate groups in a fully extended chain is ~22 Å for DR=1.1 and ~6 Å for DR=0.1.

The simulation cells consist of four identical ionized Nafion chains of a given DR with 560 water molecules and 40 hydronium molecules, corresponding to 20 wt % water content.

MD simulations were performed at two temperatures, 300 and 353 K, relevant for fuel cell operation under isobaric-isothermal conditions using LAMMPS.[9,10] The Dreiding force field was partially modified to handle perfluorocarbon compounds, water and hydronium.[11] The equations of motion were integrated using the Verlet algorithm with a 1 fs time steps and the PPPM method[12] was used to evaluate the electrostatic interactions. After an equilibration cycle, each system was simulated for additional 2 nanoseconds to obtain the equilibrium structural properties and to determine the water and hydronium diffusion.

Results and Discussion

I. Structure: Nanophase segregation. We observed water-polymer segregation for both temperatures and monomer sequences (Fig. 1). We found all sulfonate groups to be in the water nanophase, consistent with the experimental observation of complete dissociation for the sulfonic moiety in hydrated Nafion.[13,14] The hydrophilic domain forms a percolated nanophase and its shape is far from spherical which is in good agreement with Falk's work.[15]

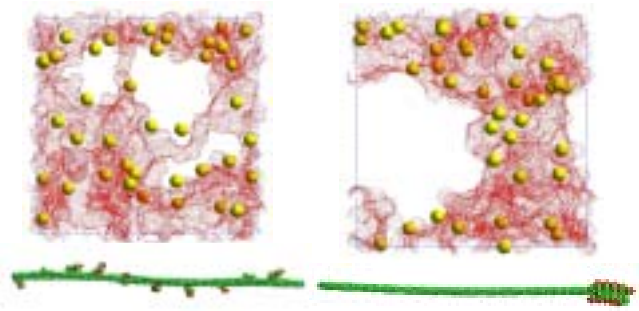

(a) DR=1.1 (b) DR=0.1

Figure 1. Nanostructure of hydrated Nafion. White domains are mainly occupied by Nafion backbone. Spheres represent the sulfur atoms. The surface formed by the dense dots is the Nafion/water interface in both figures.

Nanostructure of hydrated Nafion. White domains are mainly occupied by Nafion backbone. Spheres represent the sulfur atoms. The surface formed by the dense dots is the Nafion/water interface in both figures.

We have computed the fraction of water molecules in the first solvation sphere of the hydronium and sulfonate ions. They constitute 49 and 43% of the total for the DR=1.1 and DR=0.1, respectively, at 353 K. These findings are consistent with the existence of bulk-like water in the IR spectrum of hydrated Nafion with this water content.[14]

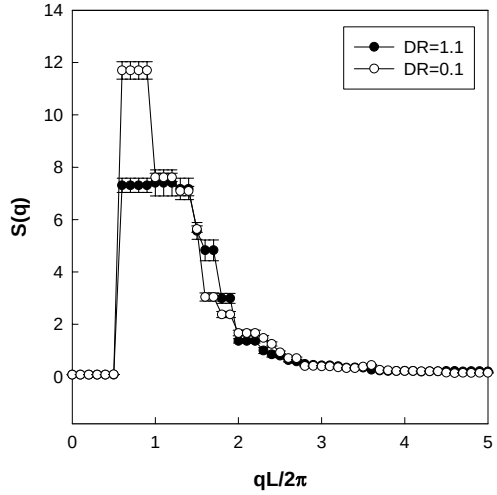

Figure 2. Structure factor profile for hydrated Nafion with 20 wt % of water content. S(q) was computed following the method of Ref.[16].

There are noticeable differences, nevertheless, in the spatial distribution of these "bulk" waters for the two monomer sequences: while for the DR=1.1, the "bulk" waters are dispersed all along the hydrophilic nanophase, they are lumped together in the structures for the blocky polymer of DR=0.1. The structure factor, S(q) at 353 K is shown in Fig. 2. We observe that at low q, the intensity of S(q) for the blocky Nafion of DR=0.1 is stronger than the DR=1.1, which means that the blocky Nafion of DR=0.1 has better developed phase-

segregated structure. Another point of noteworthy is that the S(q) at q ranging from 1.5 to 2.0 decays faster in DR=0.1 than in DR=1.1. This difference is attributed to the thickness of interface between water and polymer. In other words, the DR=0.1 system has sharper and thinner interface than the DR=1.1.

The blockiness of the sulfonate groups in the polymer chain also has a clear effect on the radial distribution function between sulfonate groups, $g_{ss}(r)$, as shown in Fig. 3. Notice that although S-S distances in the extended polymer chains are as different as 22 and 6 Å for the DR=1.1 and DR=0.1, respectively, the sulfonate groups are at comparable distances when the polymer is folded in the system. Still, the polymer with DR=0.1 has more S-S neighbors below 8 Å than the DR=1.1. Fig.3 displays the intrachain contribution to $g_{ss}(r)$, along with the total one. We observe that the most important contribution at low distances to $g_{ss}(r)$ of the blocky, DR=0.1, Nafion comes from S in the same chain, while this is not the case for the DR=1.1 system.

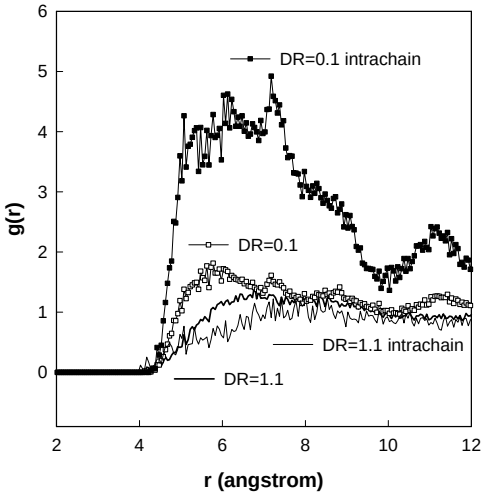

Figure 3. Sulfur-Sulfur Radial distribution function (g(r)) for hydrated Nafion 117 with 20%wt water at 353 K for two sequences of polar/nonpolar monomers. The thick lines show the total g(r), while the thin lines display only the contribution of the distribution of S that belong to the same polymer chain, averaged over the four chains in each cell.

II. Diffusion of Water and hydronium. The diffusion coefficients for water at 300 K are 0.65×10^{-5} for DR=0.1and 0.67×10^{-5} for DR=1.1, and at 353 K, 1.59×10^{-5} cm^2/s for DR=0.1 and 1.47×10^{-5} cm^2/s for DR=1.1 calculated using the time dependence of mean square displacement. These values compare well with the experimental values: 0.5×10^{-5} and 1.25×10^{-5} cm^2/s at 300 and 353 K, respectively.[17] In this simulation study, we don't find any significant effect of nanophase-segregated structure caused by the monomeric sequence.

The calculated diffusion constants for hydronium ion at 300 K are 0.17×10^{-5} cm^2/s for DR=0.1 and 0.29×10^{-5} cm^2/s for DR=1.1, and at 353 K, 0.28×10^{-5} cm^2/s for DR=0.1 and 0.33×10^{-5} cm^2/s for DR=1.1, showing hydronium diffusion is not much affected by the monomeric sequence. Another point of noteworthy is that these hydronium diffusion constants are smaller than the experimental values (2.0×10^{-5} cm^2/s at 298 K[18]). The diffusion constant of hydronium in this study should not be compared with the experiments because we are computing only the vehicular transport of H_3O^+ and the measured proton transport includes an additional process, namely the hopping of the bare H^+ between water molecules.

Conclusions

For both temperatures and sequences, Nafion with 20 wt % water shows a clearly segregated structure with water and polymer domains. Water domains are far from spherical, indicating that minimization of the interfacial area is not the determining factor as was assumed in simplified models.[1] The monomer sequence of the polyelectrolyte has an effect on the extent of segregation: The more blocky sequence has better phase segregation.

The vehicular transport of water and hydronium are not affected significantly by the monomeric sequence. Further investigation on these systems is required to assess whether the different arrangement of the sulfonate groups in the interface for the DR=0.1 and DR=1.1 have an effect on the rate of proton hopping, and hence controlling of the overall proton migration.

Acknowledgement

This research was partially supported by General Motors The facilities of the Materials and Process Simulation Center are also supported by DOE (ASCI ASAP), NSF (CHE), MURI-ARO, MURI-ONR, General Motors, ChevronTexaco, Seiko-Epson, Beckman Institute, and Asahi Kasei.

References

(1) Gierke, T. D.; Munn, G. E.; Wilson, F. C. *J. Polym. Sci., Polym. Phys. Ed.* **1981**, *19*, 1687.
(2) Hsu, W. Y. *Macromolecules* **1983**, *16*, 745.
(3) Yeager, H. L.; Steck, A. *J. Electrochem. Soc.* **1981**, *128*, 1880.
(4) Verbrugge, M. W.; Hill, R. F. *J. Electrochem. Soc.* **1990**, *137*, 893.
(5) Gebel, G. *Polymer* **2000**, *41*, 5829.
(6) Rollet, A.-L.; Gebel, G.; Simonin, J.-P.; Turq, P. *J. Polym. Sci.: Part B: Polym. Phys.* **2001**, *39*, 548.
(7) Rollet, A.-L.; Diat, O.; Gebel, G. *J. Phys. Chem. B* **2002**, *106*, 3033.
(8) Vishnyakov, A.; Neimark, A. V. *J. Phys. Chem. B* **2001**, *105*, 9586.
(9) Plimpton, S. J. *J. Comp. Phys.* **1995**, *117*, 1.
(10) Plimpton, S. J.; Pollock, R.; Stevens, M. In *the Eighth SIAM Conference on Parallel Processing for Scientific Computing*: Minneapolis, 1997.
(11) Jang, S. S.; Blanco, M.; Goddard, W. A.; Caldwell, G.; Ross, R. B. *Macromolecules*, *in print*.
(12) Hockney, R. W.; Eastwood, J. W. *Computer simulation using particles*; McGraw-Hill International Book Co.: New York, 1981.
(13) Laporta, M.; Pegoraro, M.; Zanderighi, L. *Phys. Chem. Chem. Phys.* **1999**, *1*, 4619.
(14) Gruger, A.; Regis, A.; Schmatko, T.; Colomban, P. *Vibr. Spectro.* **2001**, *26*, 215.
(15) Falk, M. *Can. J. Chem.* **1980**, *58*, 1495.
(16) Jo, W. H.; Jang, S. S. *J. Chem. Phys.* **1999**, *111*, 1712.
(17) Okada, T.; Xie, G.; Meeg, M. *Electrochim. Acta* **1998**, *14*, 2141.
(18) Kreuer, K. D. *J. Membr. Sci.* **2001**, *185*, 29.

Density Functional Theory Study of Adsorption and Decomposition of H_2S on Pd(111), Cu(111) and PdCu(110)

Dominic R. Alfonso, Anthony V. Cugini and Dan Sorescu

National Energy Technology Laboratory, Pittsburgh, PA 15236

Introduction

Inorganic nonporous membranes composed of Pd have been used for a number of hydrogenation and dehydrogenation applications.[1] Because of their potential to cause equilibrium shift as well as the production of a pure hydrogen stream, they can be used in membrane reactors for facilitating equilibrium limited reactions such as hydrogen purification. Numerous potential processes for utilizing fossil fuel resources would involve separation of hydrogen from other gases in a reaction system. Unfortunately, sulfur impurities in a fossil fuel based feedstream has been found to have adverse effects on the performance of a Pd membrane.[2] It has been reported that these materials poison very easily even at ppm-levels of H_2S. [3]

There is surprisingly little fundamental information available on the mechanism by which sulfur compounds such as H_2S poison the membrane. A major challenge in the area of membrane purification of hydrogen is the development of materials that either resist poisoning of sulfur compounds, or that adsorb a limited amount of sulfur compounds without drastically inhibiting their hydrogen permeability. Recently, Pd alloyed with a second metal, such as Cu, has appeared as a promising material for hydrogen separation.[4] Some PdCu alloys are reported to exhibit enhanced resistance to H_2S poisoning compared to the constituent metallic systems. But little is known about the effect of alloying Pd with Cu on the poisoning process. A fundamental knowledge of the interaction of H_2S with the surfaces that constitute these membranes has an important bearing in the accomplishment of this goal.

In the present paper, we report results of a theoretical investigation of interaction of H_2S with Pd(111) and Cu(111) surfaces from gradient-corrected plane wave Density Functional Theory (DFT) using a periodic supercell approach. We identify the most stable binding site, decomposition pathways and decomposition energy barriers. Previous experiments show that the role of H_2S as a poison is to deposit sulfur adatoms, which are the true poison.[5] The adsorption and decomposition of H_2S on the corresponding PdCu(110) surface will also be investigated and the results compared to its pure metal counterparts. One particular aim is to analyze trends in adsorption energies and reaction barriers.

Computational Details

The calculations were performed with the Vienna *ab initio* simulation package (VASP). [6] Ionic cores are described by ultra soft pseudopotential[7] and the Kohn-Sham one-electron valence states are expanded in a basis of plane waves. The exchange correlation energy is described at the level of spin polarized generalized gradient approximations (GGA) in the implementation of Perdew *et al.* (PW91). [8]

To model the Pd (111), Cu (111) and PdCu (110) surfaces, we used periodic supercells. First, the bulk Pd, Cu and PdCu were geometrically optimized in order to determine the lattice constants. Our calculated lattice constant for bulk fcc Pd, fcc Cu and bcc PdCu are 3.965, 3.641 and 3.031 Å, respectively, in excellent agreement with experiments (3.883, [9] 3.606 [10] and 2.960 Å, [10] respectively). After optimization of the bulk crystal, the (111) or (110) was exposed assuming a bulk terminated structures, followed by construction a three dimensional periodic supercell with a vacuum of 12 Å on the top of the free surface.

For all the surfaces investigated, we utilized a slab consisting of three layers. 4×4 surface cells were used for Pd(111) and Cu(111) (16 atoms/layer) whereas the surface cell for PdCu(110) is 4×5 (18 atoms/layer). Adsorbate was adsorbed on one side of the slabs and all the atoms except the bottom layer were allowed to relax. This corresponds to a coverage of roughly θ=0.06 ML for all the surfaces considered here. The geometrical optimizations were done using a dynamical-quenching like technique and the structural parameters were considered as converged when the atomic forces were less than 0.03 eV/Å. For the Brillouin zone integration, a 3 × 3 Monkhorst-Pack *k*-point grid [11] and cutoff of 234 eV was used for the plane wave basis set.

Results and Discussion

H_2S on Pd(111). Our calculations predict no reconstruction of the bare Pd(111) with respect to the (111) face of the bulk in agreement with experiments and several theoretical studies.[12] H_2S binds molecularly on the surface through its sulfur atom in an atop configuration with its molecular plane nearly parallel to the surface (Fig. 1). In this configuration, all the atoms of the adsorbate interact with the surface. The S-Pd distance is 2.37 Å and the binding energy is 0.71 eV.

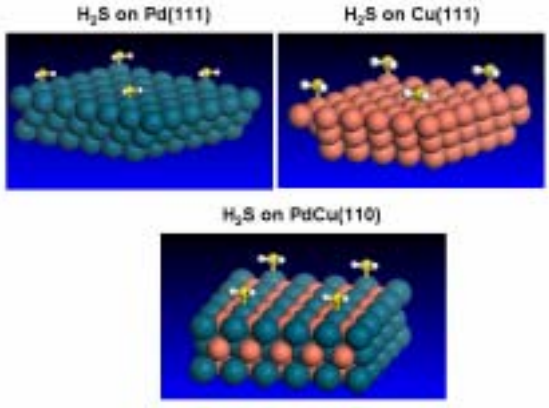

Figure 1. Schematic representation of H_2S on Pd(111), Cu(111) and PdCu(110) surfaces.

For the dissociative adsorption of H_2S starting with S-H scission leading to adsorbed SH and and hydrogen, $H_2S_{(surface)} \rightarrow SH_{(surface)} + H_{(surface)}$, the energy released is 0.88 eV. Thus this reaction is an energetically favorable process. SH binds through sulfur in a bridge (di-σ) configuration with the S-H axis nearly parallel to the surface while the abstracted hydrogen is adsorbed on a neighboring three-fold hollow site. The abstraction of hydrogen from adsorbed SH yielding an adsorbed atomic sulfur and hydrogen, $SH_{(surface)} \rightarrow S_{(surface)} + H_{(surface)}$, is also found to be energetically favorable. The energy released for this reaction is 0.72 eV. The generated S and H are both adsorbed on the three-fold hollow sites Thus from a thermochemical point of view, the complete H_2S decomposition pathway on Pd(111), $H_2S_{(gas)} \rightarrow S_{(surface)} + 2H_{(surface),}$, starting from H_2S adsorption and proceeding via sequential hydrogen abstraction is exothermic (ΔE=2.31 eV).

We calculate the binding energies of all reaction intermediates. The binding energy of SH is 3.02 eV and the S-Pd and H-Pd distances are 2.31 and 1.97 Å, respectively. H adsorbed preferentially on the three-fold hollow site on the surface and the binding energy is 0.50 eV with respect to gas phase H_2. A diffusion barrier of H between the adjacent three-fold sites *via* the bridge site is about 0.16 eV which indicates that H is quite mobile on the surface. The S

binding energy is predicted to be 4.85 eV. Note that atomic S and SH form strong bonds on the ideal Pd(111) surface but the bonding interaction of H_2S is relatively weak.

The reaction pathway for the initial abstraction of hydrogen from the adsorbed H_2S was studied using the Nudged Elastic Band (NEB) method. [13] Linear interpolations between the reactant and product states (eight images including the endpoints) were employed as initial guesses for the reaction coordinates and the coordinates were then relaxed with a constrained molecular dynamics algorithm. The transition state is approximated by the image of the highest energy on the optimized reaction coordinate. As a hydrogen is abstracted from the adsorbed H_2S, the SH fragment tilts toward the surface and ends in a bridge configuration. The reaction coordinate is also composed of rotation of the S-H bond towards a surface Pd atom. The energy barrier for this step is 0.35 eV. The energy barrier for the second dissociation step found from Bond Order Potential (BOP) [14] method is just slightly higher. NEB optimization of the reaction pathway for the final S-H scission process is currently underway to confirm this finding.

H_2S on Cu(111). Similar to the bare Pd(111) surface, the surface relaxation for Cu(111) was found to be weak. We predicted about 0.5 % inward relaxation of the top layer. The most stable adsorption configuration of H_2S on Cu(111) is similar to that on Pd(111) (Fig. 1). The S-Cu distance is 2.44 Å and the binding energy is 0.26 eV which is smaller than the corresponding binding on Pd(111). The $H_2S_{(surface)} \rightarrow SH_{(surface)} + H_{(surface)}$ and the $SH_{(surface)} \rightarrow S_{(surface)} + H_{(surface)}$ reactions on Cu(111) are also found to be downhill processes (ΔE=0.87 and ΔE=0.53 eV, respectively). The complete decomposition of H_2S, $H_2S_{(gas)} \rightarrow S_{ssurface)} + 2H_{(surface)}$, is also energetically favorable with ΔE=1.66 eV.

The binding energies of the reaction intermediates were evaluated. Similar to the Pd(111) case, the SH fragments preferred the bridge sites (E_{bind}=2.76 eV) while S and H atoms are adsorbed on the three-fold hollow sites (E_{bind}=4.66 eV and 0.20 eV, respectively). The initial hydrogen abstraction from adsorbed H_2S follows a similar pathway found on the corresponding Pd(111) case. The predicted energy barrier for the first dissociation step from NEB calculations is about 0.47 eV. Qualitatively, this seems to agree with existing experimental data which shows that at low temperature (~120 K), H_2S adsorbs molecularly on the Cu(111) surface.[5] Significant dissociation was observed when the system was heated to 200 K. Upon dissociation, sulfur adatoms were found on the surface which are stable to heating in vacuum or H_2. The BOP method predicts that the energy barrier for the second dissociation step is just slightly higher (Optimization of the reaction pathway for the final S-H scission process is currently underway to confirm this result). Thus, based on our thermochemical and energy barrier calculations the corresponding decomposition of H_2S on Pd(111) should be easier than on the Cu(111) surface.

H_2S on PdCu(110). The close packed surface of PdCu which crystallizes in the ordered bcc $Pd_{50}Cu_{50}$ like structure (with Cu content of about 40 atomic %) at low temperature.[10] It was reported that the composition of the uppermost layers of the closely packed (110) surface can be similar or different from the bulk depending on the preparation procedure. [15] To model the substrate whose topmost layer are similar to the bulk, a regular (110) surface bcc surface was adopted in this work. Each layer consists of equal numbers of Pd and Cu atoms. The calculated equilibrium surface structure of the surface shows the top layer Pd and Cu atoms relaxed inwards toward the bulk by 2.0 % and 2.2 % of the bulk layer spacing, respectively. The most stable adsorption configuration of H_2S on PdCu(110) is similar to that on Pd(111) and Cu(111). H_2S binds molecularly on the surface through its sulfur atom in an atop configuration (over Pd) with its molecular plane nearly parallel to the surface The S-Pd distance is 2.39 Å and the binding energy is 0.68 eV which is comparable to the corresponding binding on Pd(111).

The $H_2S_{(surface)} \rightarrow SH_{(surface)} + H_{(surface)}$ and the $SH_{(surface)} \rightarrow S_{(surface)} + H_{(surface)}$ reactions on PdCu(110) are also found to be downhill processes (ΔE=0.89 and ΔE=0.72 eV, respectively). The binding energies of the intermediates are 2.97 eV (SH), 4.74 eV (S) and 0.56 eV (H). The complete decomposition of H_2S, $H_2S_{(gas)} \rightarrow S_{(ssurface)} + 2H_{(surface)}$, is also energetically favorable (ΔE=2.35 eV). The predicted energy barrier for the first dissociation step from NEB calculations is about 0.35 eV. Similarly, the BOP method predicts that the energy barrier for the second dissociation step is just slightly higher. Our present results indicate that the ease with which H_2S decomposition occurs on PdCu(110) and Pd(111) is comparable.

Conclusions

We present gradient-corrected DFT studies of H_2S adsorption and decomposition on Pd(111), Cu(111) and PdCu(110) surfaces. In all cases, H_2S is adsorbed molecularly and the binding energies follow the trend: Pd(111) ~ PdCu(111) > Cu(111). The reaction steps, intermediates and transition states for the decomposition process starting from the most stable adsorption configuration of H_2S and proceeding via sequential hydrogen abstraction are identified. The bonding of S-containing species, S and SH, is stronger on Pd(111) and PdCu(110) than on Cu(111). The activation energies for initial S-H scission are relatively small (>0.5 eV) and follow the trend: Cu(111) > Pd(111) ~ PdCu(110). We confirm that the role of H_2S as a poison is to deposit sulfur adatoms, which are the true poison.

Acknowledgement. Computations were performed at the Pittsburgh Supercomputer Center.

References

(1) Lewis, F. *The Palladium Hydrogen System*, Academic Press: London, 1967; Gryyaznov, V. M. *Platin. Metals. Rev.* **1986**, 30, 68.
(2) Rodriguez, J. A.; Hrebek, J. *Acc. Chem. Res.* **1999**, 32, 719.
(3) Lee. J.; Rhee, H. *J. Catal.* **1998**, 177, 208
(4) Piper, J. *J. Appl. Phys.* **1966**, 37, 715; Knapton, A. G. *Platin. Met. Rev.* **1977**, 21, 44.; Weiss, A.; Ramaprabhu, S.; Rajalakshmi, N. *Z. Phys. Chem.* **1997**, 199, 165.
(5) Campbell, C. T. *Surf. Sci.* **1987**, 183, 100.
(6) Kresse, G.; Furthmuller, J. *Phys. Rev. B* **1996**, 54, 11169.
(7) Vanderbilt, D. H. *Phys. Rev. B* **1990**, 41, 7892; Kresse, G.; Hafner, J. *J. Phys. Condens. Matter* **1994**, 6, 8245.
(8) Perdew, J. P.; Wang, Y. *Phys. Rev. B* **1986**, 33, 8800; Perdew, J. P.; Chevary, J. A..; Vosko, S. H.; Jackson, K. A.; Pederson, M.; Singh, D. J.; Fiolhais, C. *Phys. Rev. B* **1992**, 46, 6671.
(9) Coles, B. R. *J. Inst. Metals* **1956**, 84, 346.
(10) Villar, A. P.; Calvet, L. D. *Pearson's Handbook of Crystallographic Data for Intermetallic Phases,* ASM International; Materials Park, OH, 1991.
(11) Monkhorst, H. J.; Pack, J. D. *Phys. Rev. B* **1976**, 13, 5188.
(12) Somorjai, G. A. *Surface Chemistry and Catalysis,* John Wiley & Son: New York, 1994; Lopez, N.; Nørskov, J. K. *Surf. Sci.* **2001**, 477, 59; Watson, G. W.; Wells, R. P. K.; Willock, D. J.; Hutchings, G. J. *J. Phys. Chem.* **2001**, 105 4889.
(13) Mills, G.; Jönsson H.; Schenter, G. *Surf. Sci.* **1995**, 324, 305.
(14) Sellers, H.; Shustorovich, E. *Surf. Sci.* **1996**, 356, 209.
(15) Loboda-Cackovic, *Vacuum* **1997**, 48, 571.

THERMODYNAMIC CONSISTENCY IN MICROKINETIC DEVELOPMENT OF SURFACE REACTION MECHANISMS

Ashish B. Mhadeshwar[a,c], Hai Wang[b,c], and Dionisios G. Vlachos[a,c]

[a] Department of Chemical Engineering
[b] Department of Mechanical Engineering
[c] Center for Catalytic Science and Technology
University of Delaware
Newark, DE 19716

Introduction

Microkinetic analysis has evolved into a promising tool for modeling surface reactions since it has been well established by Dumesic and coworkers.[1] A key advantage of the microkinetic analysis is that a mechanism developed at certain conditions is expected, in many cases, to capture system features under significantly different conditions. The rate parameters are typically obtained using input from surface science experiments or theoretical estimates using semi-empirical techniques and quantum mechanical density functional theory calculations, and sometimes using statistical mechanics through transition state theory. Due to the uncertainty resulting through the theoretical estimates of rate parameters, experimental measurements, and heterogeneity of real catalysts, some tuning/optimization of parameters is typically necessary for quantitative model predictions.

In mechanism development and rate parameter fitting or optimization, an issue often overlooked is thermodynamic consistency at both the enthalpic and entropic levels. This issue has been brought up in several instances,[1-4] but there is no strategy available for testing and ensuring thermodynamic consistency of an arbitrary complex reaction network. As a result, while a few published mechanisms are thermodynamically consistent, most literature mechanisms are not. Enthalpic inconsistency gives incorrect solutions to the energy conservation equation, which translates to incorrect predictions of heat exchange and conversion/selectivity. Entropic inconsistency directly translates to fundamental inconsistency in the pre-exponential factors. Finally, entropic and enthalpic inconsistency distorts the underlying equilibrium constant, which affects the prediction of equilibrium states.

In this work, we review the criteria of thermodynamic consistency and demonstrate cases of thermodynamic inconsistency in previously published reaction mechanisms. We then present an optimization approach, coupled with statistical mechanics and semi-empirical techniques, which ensures thermodynamic consistency of the entire mechanism. We present a proof-of-concept analysis using the reaction model of H_2 oxidation on Pt as an example. Similar examples of syngas production from methane and hydrogen production from ammonia will also be presented.

Thermodynamic Constraints and Reaction Basis Set

In general, for any i^{th} reaction in a mechanism, the following equations form the basis of the enthalpic and entropic constraints.

$$E_i^f - E_i^b = \Delta H_i \qquad \text{and} \qquad A_i^f / A_i^b = e^{\Delta S_i / R},$$

where *f* and *b* stand for the forward and backward steps, *A* is the pre-exponential factor, *E* is the activation energy, R is the universal gas constant and ΔH and ΔS are the enthalpy change and entropy change of the reaction, respectively. If we consider a set of linearly independent reactions of size *L* in a reaction mechanism consisting of *I* number of reactions ($L \le I$), it forms a basis in the reaction network. The basis set is usually not unique but its size *L* is unique. The rest of the reactions are linear combinations of the basis set. They are termed linearly dependent reactions of the network and the constraints on them can be expressed as

$$E_i^f - E_i^b = \Delta H_i = \sum_{j=1}^{L} c_{ij} \Delta H_j = \sum_{j=1}^{L} c_{ij} \left(E_j^f - E_j^b \right), \quad i = L+1, I$$

$$\ln\left(A_i^f / A_i^b \right) = \frac{\Delta S_i}{R} = \sum_{j=1}^{L} c_{ij} \frac{\Delta S_j}{R} = \ln \prod_{j=1}^{L} \left(A_j^f / A_j^b \right)^{c_{ij}}, \quad i = L+1, I,$$

where c_{ij} are the coefficients of i^{th} linearly decomposed reaction onto the reaction basis. Equations corresponding to the catalytic reaction mechanism analog are also derived and will be presented (not shown here).

Examples of Thermodynamic Consistency

Literature mechanisms. Three literature mechanisms, viz. ethylene dehydrogenation on Pt[5], ammonia synthesis on Fe[6], and hydrogen oxidation on Pt[4] are tested for thermodynamic consistency. **Figure 1** shows the equilibrium constants of few reactions given by the surface reaction rate parameters normalized by the equilibrium constants determined by the more accurate gas-phase thermochemistry. The ratio of equilibrium constants is unity or close to unity if a reaction mechanism is thermodynamically consistent. It is seen that the equilibrium constants for ethylene hydrogenation differ by 8 orders of magnitude. The equilibrium constant for the H_2 oxidation reaction cycle matches well with the corresponding gas phase equilibrium constant, although this is a result of cancellation of errors. This is illustrated using a different reaction cycle of water decomposition in the H_2 oxidation mechanism in **Figure 1** where the equilibrium constants differ by 2 orders of magnitude.

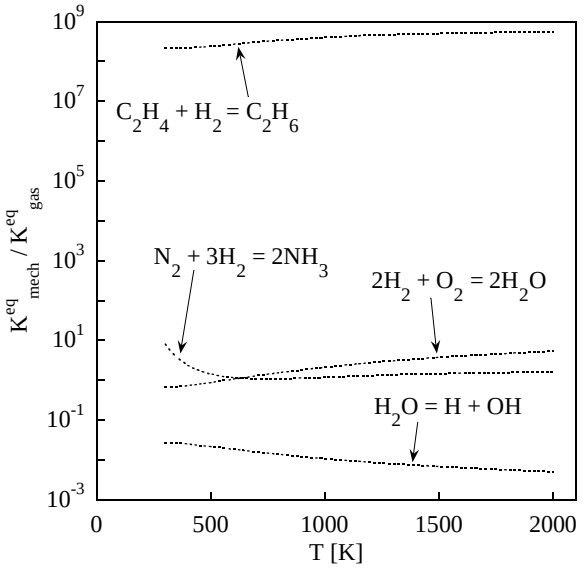

Figure 1. Equilibrium constant of a surface reaction cycle over the corresponding overall gas phase reaction versus temperature.

Effect of temperature. The ratio of the equilibrium constants changes by a factor of approximately 2.5, 5, 8, and 5.5 for ethylene hydrogenation, ammonia synthesis, hydrogen oxidation, and water decomposition reactions, respectively (see **Figure 1**), which can result in large errors in equilibrium conversion. This indicates the

need for ensuring thermodynamic consistency as a function of temperature when temperature varies over a wide range.

Optimization Strategies

The quantitative relations given by the above equations can be used in rate parameter optimization as implicit constraints in the least-squares objective function. Alternatively, the constraints can be explicitly placed on the rate parameters. Minimization is carried out using the IMSL subroutine zxmwd.[7] As the heats of chemisorption and activation energies are generally more readily available than the pre-exponential factors, for demonstration purposes, we choose to keep activation energies fixed and optimize the pre-exponential factors only. Enthalpic consistency is taken care of through the use of Bond Order Conservation (BOC)[8] and our derived statistical mechanics formulae.

a) Implicit thermodynamic constraints: simple Arrhenius equation. The pre-exponential factors are assumed to be independent of temperature (except for sticking coefficients which vary with temperature as described by kinetic theory for the collision flux). However, the fundamental limitation lies in the use of simple Arrhenius equation to describe the reaction rate constant, and can be removed by using a modified Arrhenius equation.

b) Implicit thermodynamic constraints: modified Arrhenius equation. To rigorously account for the temperature variation in entropic consistency, we propose to use the modified Arrhenius expression with temperature dependent pre-exponential factors. Along with the pre-exponential factors, the temperature exponents are also optimized. This case captures the experimental data more accurately, but the method is CPU intensive.

c) Explicit thermodynamic constraints: modified Arrhenius equation. Here we select the entropies of the adsorption/desorption steps as the independent variables. During the optimization process, the ratios of pre-exponential factors of the remaining reaction steps are calculated using explicit, algebraic constraints. A significant gain in CPU is observed due to fewer optimization parameters. However, experimental data is moderately captured due to overconstraining of the system.

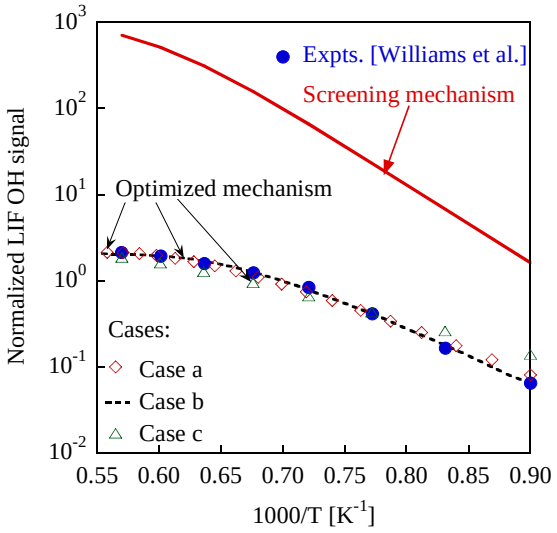

Figure 2. Prediction of the screening H_2 oxidation mechanism on polycrystalline Pt against the experimental LIF data of Williams et al.[9] (solid line). Predictions using three sets of optimized parameters of the H_2/O_2/Pt mechanism against the experimental data are also shown, corresponding to the three cases discussed.

Figure 2 shows the performance of the surface reaction mechanism obtained using the three approaches discussed above, against experimental data of Williams et al.[9] The resulting equilibrium constants of the overall H_2 oxidation and water decomposition reactions over their gaseous counterparts are shown in **Figure 3** for all cases. Finally, all surface reaction mechanisms are presented (not shown here) in surface CHEMKIN format.

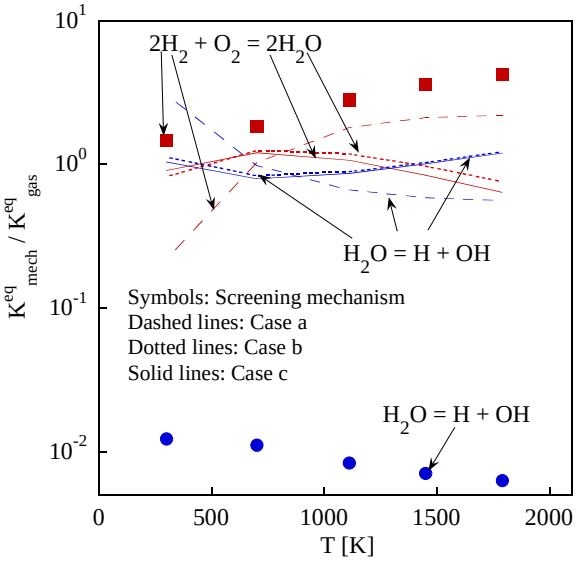

Figure 3. Ratio of the equilibrium constants of the surface reaction mechanism over the gas-phase one versus temperature for two selected examples, the overall reaction of H_2 oxidation and water decomposition (the entire mechanism is also thermodynamically consistent).

Acknowledgment

This work was prepared with the support of the U. S. Department of Energy, under Award No. DE-FC26-00NT41027. However, any opinions, findings, conclusions, or recommendations expressed herein are those of the authors and do not necessarily reflect the views of the DOE.

References

(1) Dumesic, J. A.; Rudd, D. F.; Aparicio, L. M.; Rekoske, J. E.; Trevino, A. A., The Microkinetics of Heterogeneous Catalysis, American Chemical Society: Washington, D.C., 1993.
(2) Stoltze, P., *Prog. Surf. Sci.*, **2000**, *65*, 65-150.
(3) Schmitz, G., *J. Chem. Phys.*, **2000**, *112*, 10714-10717.
(4) Aghalayam, P.; Park, Y. K.; Vlachos, D. G., *AIChE J.*, **2000**, *46*, 2017-2029, *This paper was selected in the highlights of Chem. Eng. Progress (paper of the month), p., Oct. issue, 2000.*
(5) Rekoske, J. E.; Cortright, R. D.; Goddard, S. A.; Sharma, S. B.; A., D. J., *J. Phys. Chem.*, **1992**, *96*, 1880-1888.
(6) Dumesic, J. A.; Trevino, A. A., *J. Catal.*, **1989**, *116*, 119-129.
(7) Visual-Numerics, IMSL FORTRAN subroutines for mathematical applications, 1997.
(8) Shustorovich, E.; Sellers, H., *Surf. Sci. Rep.*, **1998**, *31*, 1-119.
(9) Williams, W. R.; Marks, C. M.; Schmidt, L. D., *J. Phys. Chem.*, **1992**, *96*, 5922-5931.

Development of Automatic Chemical Reaction Mechanism Generation Software Using Object-Oriented Technology

Jing Song, Sumathy Raman, Joanna Yu, Catherina D Wijaya, George Stephanopoulos, and William H. Green

Department of Chemical Engineering,

Massachusetts Institute of Technology,

77 Massachusetts Avenue, Cambridge, MA 02139, USA

Introduction

Computer-aided reaction mechanism generation has been employed by many groups to model multi-component reacting mixtures, in processes such as pyrolysis and fuel combustion (Chinnick, et al., 1988; Hillewaert, et al. 1988; Chevalier, et al. 1990; Froment, 1991; DiMaio and Lignola, 1992; Quann and Jaffe, 1992; Broadbelt, et al., 1994; Blurock, 1995; Broadbelt, et al., 1995; Ranzi, et al., 1995; Broadbelt, et al., 1996; Prickett and Mavrovouniotis 1997a, 1997b, 1997c; Susnow, et al., 1997; Warth, et al., 2000). Good model-generation software is desired to quickly build more detailed and reasonably-structured reaction mechanisms with better kinetics parameters. With the efforts from those groups, people have successfully represented the chemical structures and properties of reaction systems and generated large reaction mechanisms. However, some common shortcomings in the existing software prevent their wide usage in chemical reaction simulations. For example, many fewer reaction patterns are considered in such software than should be; furthermore, the thermal and kinetics parameters are not specific enough to account for different types of reaction pathways. How to extend the model generation software to accommodate more types of chemical reactions and/or allow users to create their own desired reaction types easily and how to systematically integrate the available thermal and kinetics data from different sources remained unsolved before this work.

Many previous chemical software applications were developed in procedural languages, like Fortran and C. Although those languages are good for calculation efficiency, they make it difficult to satisfy the important requirements of ease of maintenance, reusability and extendibility, when we design and develop software applications for large complex systems. In recent years, object-oriented technology has been rapidly developed to satisfy those basic requirements of good software. Corresponding modeling languages, such as unified modeling language (UML), and programming languages, such as C++, Java, and C#, have been widely used in developing better-structured software. In this work, we made use of those advanced research fruits to develop a well-structured, reusable and extendable automatic reaction mechanism generation software, RMG.

Representing Chemical Structures by Graphs

Graphs, as fundamental data structures, and their associated algorithms have been widely used for uniquely representing chemical structures and estimating chemical properties in most chemical application software.

In RMG, we also used 2-dimensional graph data structures representing individual chemical species and chemical functional groups. The estimation of all the species features, such as symmetry number, resonance isomer structures, and cycle identification, etc. are implemented based on basic graph operations. The thermal properties are estimated by a group additivity method proposed by Benson (1968). Unlike chemical species with the unique graph representation, functional group describes a special group of chemical species with the same chemically functional centers. Introducing functional group object into reaction generation software allows one to easily define the reaction pattern later. Moreover, we developed a key matching algorithm to quickly identify the sub-graph relationship between species and functional groups and between two functional groups, which speed recognition of all the chemical reaction patterns existing in any species.

Defining Reaction Families

In most existing reaction model generation software, the reaction family definitions are hard-coded; this makes it very difficult for users to change the existing reaction families and to add any new ones. In RMG, we define the reactant families by drawing their functional groups and indicating the graph mutations happening to the reactants through the course of the reaction. Therefore, new reaction families can be easily input through a graphical interface, without the need for the user to modify the source code. This makes it much easier for normal users other than software developers to vary the present reaction family specification, to define new families of reactions, and to document the exact assumptions behind the models they construct. In this work, thirty-three primary reaction families, including eighteen forward families and fifteen reverse ones, are defined; this is the richest set of reaction families ever compiled. The summarization of all the reaction families is shown in table 1.

Table 1. Reaction Families Defined in RMG

Forward Reaction Family (Reverse Reaction Family)
(1) Inter-molecular Hydrogen Abstraction
(2) Radical Addition to Multiple Bond (Beta Scission)
(3) Radical Addition to CO (CO Elimination from Carbonyl)
(4) Radical Recombination (Bond Dissociation)
(5) Bi-radical Recombination to Form Cyclic Structure (Ring open)
(6) Disproportionation (Molecular Addition)
(7) 1,2 Insertion (1,1 Elimination)
(8) 1,3 Insertion (1,2 Elimination)
(9) 1+2 Cyclo-addition (Three-Ring Cleavage)
(10) 2+2 Cyclo-addition (Four-Ring Cleavage)
(11) Diels-Alder Addition (Retro Diels-Alder Addition)
(12) Keto-Enol Tautomerism (Enol-Keto Tautomerism)
(13) Intra-molecular Hydrogen Migration
(14) Intra-Molecular Addition across Multiple Bond to Form an Exo-Cyclic Radical (Ring Open for Exo-Cyclic Radical)
(15) Intra-Molecular Addition across Multiple Bond to Form an Endo-Cyclic Radical (Ring Open for Endo-Cyclic Radical)
(16) Cyclic Ether Formation from Alkyl-Hydroperoxy Radical (OH Addition to Cyclic Ether)
(17) Intra-Molecular Hydroxyl Migration
(18) HO_2 Elimination from Peroxy Radical

Constructing Thermal Groups and Reaction Kinetics database by Hierarchical Tree

With the technology described above, we are able to enumerate all the reactions occurring among any chemical species. However, a more important question still remains unanswered: how to get the best reaction kinetics parameter for a generated reaction?

Owing to the work of many experimental and computational chemical kinetics groups, now there are a large number of good-quality reaction kinetics data available. However, in much previous model generation software, only a small number of data are used to account for a huge group of reactions. Such approach is due in part to the high running time cost to construct and search through a huge kinetics database.

In this work, we construct systematically our reaction family kinetics database by a hierarchical tree structure, which can hold a large number of kinetics data for different subfamilies. Consequently, the cost for searching tree-structured database is reduced from O(N) to O(logN), where N is the overall number of kinetics data in one database. This dramatic reduction in data retrieving time makes it possible to break one big reaction family into numerous subfamilies with more precise parameters (e.g. accounting for nearest-neighbor effects on the rates); therefore, more precise kinetics data will be assigned to each individual reaction. So far, we have built and maintained the kinetics database into hierarchical-tree structure for all the reaction families. However, the database we constructed is not limited to its present status, and it is easy for anybody to extend the tree structure by adding new sub-nodes and their corresponding kinetics data. We also have filled in the kinetics database mainly with high level quantum chemistry calculation results from our group, (Sumathi, et al., 2001 and 2002; Wijaya, C.D., et al., 2003), and from the Livermore group (Curran, et al., 2002).

Similarly, the thermo-chemical group data are also stored and recalled for group additivity estimation of the thermal properties of each species. The thermal group data are originally from Benson's estimation, and the database could be extended in the same way as the reaction kinetics database.

Iterative Mechanism Generation Algorithm

This work adopted the rate-based reaction path screening method proposed by Susnow, et al. (1997) to identify the reactions and species required to satisfy the user-defined accuracy requirements. Since this reaction pathway screening algorithm greatly depends on the kinetics parameters of each competing reaction path, building a big and well-structured kinetics database seems to be more crucial in such circumstance. This, from another aspect, proves the importance of our hierarchical tree solution to building large and detailed kinetics databases. This work also implements the valid parameter range analysis algorithms, presented in Song et al. (2002), to construct robust chemical reaction mechanism under a wider range of reaction system conditions.

Applying Object-oriented Technology in RMG Design and Development

Object-oriented technology is the most advanced breakthrough in software engineering methodology in last decade, and it has been rapidly improved and broadly applied in most software applications. To assist in the development of good architecture for object-oriented software, unified modeling language, UML, has been broadly used.

Introduction to Unified Modeling Language (UML). UML is a modeling language to help build an unambiguous and well-structured blueprint of a software at the design stage. With a graphic visualization, UML not only specifies the static relations between objects inside system, but also defines the dynamic communications between different parts of software at different time. With the aid of UML, people in the different stages of software development, such as design, implementation, test, and maintenance, can talk to each other with the same design language for a better communication with much less misunderstanding. There are many commercial implementation tools of UML, for example, Rose from Rational and Rhapsody from I-Logix.

Design and Implementation of RMG in UML. The automatic reaction mechanism generation software developed by our group, RMG, is fully designed and implemented in UML. Rhapsody in J is the UML tool we adopted in this work. There are four major packages in RMG, chemUtil, chem, rxn, and rxnSystem. ChemUtil defines the basic data structure objects, Graph and Tree, used in RMG; Chem defines the fundamental chemical components such as Atom, Bond, Electron, etc.; Rxn describes the common structure of Reactions in RMG, as well as the reaction generator from defined reaction families; RxnSystem performs the iterative reaction mechanism generation algorithm and the simulation of a homogeneous reaction system. Since RMG is designed and implemented in an object-oriented manner, it is easily extended and re-factored further. For instance, although the present species model is a 2-dimensional graph, it can be later extended into a 3-dimensional model by simply adding coordinates of graph nodes. Beside designed in UML, all the packages are written in Java and also documented in the standard Java Doc format.

Applications

Applications of RMG for automatically generating chemical reaction mechanisms for a complex liquid-fuel combustion process are studied.

Conclusion

In this work, we successfully designed and developed a new chemical reaction mechanism generation Java software, RMG, using object-oriented technology. Two advanced technologies, graph representation of reaction families and a hierarchy tree-structured database for retrieving thermal and kinetics parameters, have been proposed and implemented.

Acknowledgement. We acknowledge financial support from Alstom Power, the National Science Foundation, and US Department of Energy.

References

(1) Blurock, E. S. J. Chem. Inf. Comput. Sci., **1995**, 35, 607.
(2) Benson, S.W., Thermochemical kinetics, **1968**, John Wiley & Sons, Inc.
(3) Broadbelt, L. J.; Stark, S. M.; Klein, M. T. *Ind. Eng. Chem. Res.* **1994**, *33*, 790.
(4) Broadbelt, L. J.; Stark, S. M.; Klein, M. T. *Ind. Eng. Chem. Res.* **1995**, *34*, 2566.
(5) Broadbelt, L. J.; Stark, S. M.; Klein, M. T. *Computers Chem. Engng.* **1996**, *20*, 113.
(6) Chevalier, C.; Warnatz, J.; Melenk, H. *Ber. Bunsenges. Phys. Chem.* **1990**, *94*, 1362.
(7) Chinnick, S. J.; Baulch, D. L.; Ayscough, P. B. *Chemometrics and Intelligent Laboratory Systems*. **1988**, 5, 39.
(8) Curran, H.J.; Gaffuri, P.; Pitz, W.J.; Westbrook, C.K.. *Combustion and Flame*, **2002**, 129, 253.
(9) DiMaio, F. P.; Lignola, P. G. *Chem. Eng. Sci.*, **1992**, 47, 2713.
(10) Froment, G. F. *Chemical Reactions in complex systems: the Mobil Workshop*, **1991,** A. V. Sapre and F. J. Krambeck. New York, Van Nostrand Reinhold.
(11) Hillewaert, L. P.; Dierickx, J. L.; Froment, G. F. *AIChE J.*, **1988**, 34, 17.
(12) Prickett, S. E.; Mavrovouniotis, M. L. *Comp. Chem. Engn*, **1997a**, 21, 1219.
(13) Prickett, S. E.; Mavrovouniotis, M. L. *Comp. Chem. Engn*, **1997b**, 21, 1237.
(14) Prickett, S. E.; Mavrovouniotis, M. L. *Comp. Chem. Engn*, **1997a**, 21, 1325.
(15) Quann, R. J.; Jaffe, S. B. *Ind. Eng. Chem. Res.* **1992**, 31, 2483.
(16) Song, J.; Stephanopoulos G.; Green, W.H., *Chem. Eng. Sci.*, **2002**, 57, 4475.
(17) Susnow, R. G., Dean, A. M., Green, W. H., Peczak, P. and Broadbelt, L. J. *J. Phys. Chem. A*, **1997**, 101, 3731.
(18) Warth, V., Battin-Leclerc, F., Fournet, P. A., Glaude, P. A., Come, G. M. and Scacchi, G. *Computers and Chemistry*, **2000**, 24, 541.
(19) Sumathi, R.; Carstensen, H.-H.; Green, W. H. *J. Phys. Chem. A*, **2001**, 105, 6910.
(20) Sumathi, R.; Carstensen, H.-H.; Green, W. H. *J. Phys. Chem. A*, **2001**, 105, 8969.
(21) Sumathi, R.; Carstensen, H.-H.; Green, W. H. *J. Phys. Chem. A*, **2002**, 106, 5474.
(22) Sumathi, R.; Green, W. H. *Theor. Chem. Acc.*, **2002**, 108, 187-213.
(23) Wijaya, C.D.; Sumathi, R.; Green Jr., W. H. *J. Phys. Chem. A*, **2003**, (in press).

Modeling the Negative Temperature Coefficient in the Low Temperature Oxidation of Light Alkanes

Timothy A. Barckholtz

Corporate Strategic Research
ExxonMobil Research and Engineering
1545 Route 22 East
Annandale, NJ 08801
tim.barckholtz@exxonmobil.com

Introduction

A distinguishing feature of the low temperature ignition of many molecules is a "negative temperature coefficient", or NTC. At very low temperatures, as the temperature is raised, the ignition delay of a fuel is decreased. However, for many fuels, at a certain temperature the ignition delay reverses course and becomes longer as the temperature is raised. At some higher temperature, generally about 50 - 100 K higher than the onset of the NTC, the ignition delay begins to decrease again. Propane and butane each have a distinct and large NTC.

The aim of the work reported here was to model this ignition chemistry at the fundamental level, incorporating all necessary species and reactions. The resultant mechanism is fully pressure dependent and completely thermodynamically reversible. The mechanism reproduces with good accuracy the NTC in propane and butane. Reduced versions of the mechanism allowed for a detailed analysis of the cause of the NTC.

Mechanism Details

The core of the mechanism is derived from the GRI mechanism[1]. While significant additions have been made to extend the mechanism to C_4 fuels, we restrict ourselves here to discussion of the parts of the mechanism that are most relevant to the low temperature oxidation of propane and butane.

The key species for the modeling of the NTC are the propylperoxy radicals and their isomers. For these species, the thermodynamics were calculated using *ab initio* and density functional techniques as reported earlier for the ethyl systems[2]. The high pressure rate constants for the unimolecular reactions of the RO_2• intermediates were also calculated using *ab initio* and DFT, similar to earlier work. Rates for the addition of a second O_2 molecule to C•CCOOH, CC•COOH, and C2•COOH are comparable to those for the first O_2. For the rate constant of the reaction between the alkyl radicals and O_2 we use the rate given by Miller and Klippenstein for the ethyl radical[3].

The pressure dependence of these reactions was modeled using modified strong collision theory, similar to previous work. For the ethylperoxy system, there were not significant differences between the rates calculated using modified strong collision theory and those calculated with the more sophisticated master equation[4], and we prefer to continue to use the simpler and faster method. Many additional reactions of the species involved in the reactions were included in the mechanism. These reactions are too numerous to list here and did not play a significant role in the conclusions presented here.

Results: Propane

The mechanism for propane was compared to several experimental data sets. Fig. 1 shows one such comparison, the induction period for the static reactor experiments from Drexel[5] at 600 Torr for four different equivalence ratios. The calculations were performed under zero-dimensional, nearly isothermal, constant volume assumptions. The induction period in the modeling was determined as the time taken to achieve a 0.1% rise in the pressure.

The model achieves nearly quantitative agreement with the experiment regarding the minimum and the maximum of the NTC, the discrepancy being only about 10 K. The general shapes of the curves are also in very good agreement. Residual differences between the model and experiments can be largely attributed to the length duration of the experiments (nearly 30 minutes for the longest cases) and the assumptions made in the modeling (i.e., nearly isothermal, no wall chemistry, etc.).

The model was also compared to results from a rapid compression machine[6], a high pressure flow reactor[7], and numerous high temperature experiments. In all cases, the model performed with similar quality to the results shown in Fig. 1. For the comparison to the high pressure flow tube data, the formaldehyde concentration was overpredicted, while the carbon monoxide concentration was underpredicted. However, the sum of their concentration was predicted well, indicating a flaw in the modeling of the oxidation of CH_2O to CO. Further comparisons and more detailed results will be published soon.

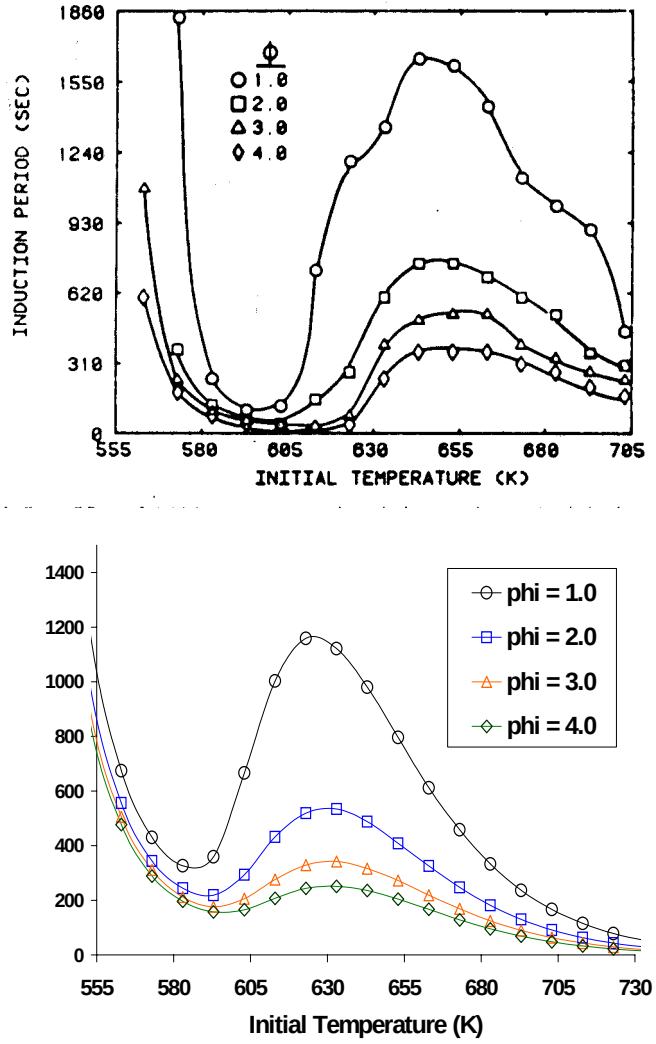

Figure 1. . Comparison between the induction times for propane at 600 Torr (top: experimental, reference 5; bottom: modeling) for four different equivalence ratios.

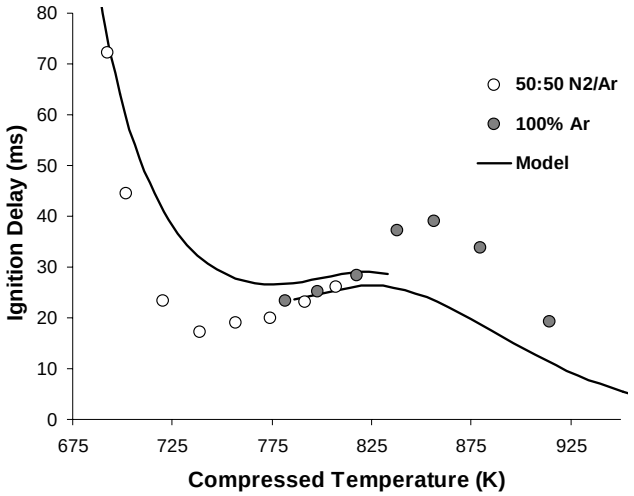

Figure 2. . Comparison between the ignition times for butane in a rapid compression machine[8]. The experiments were performed for two different gas mixtures containing different concentrations of N_2 and Ar, thus the two different data points and modeling lines.

Results: Butane

The mechanism for butane was also compared to several experimental data sets, all with good success. Fig. 2 shows one of the comparisons, to the rapid compression machine data of Minetti et al.[8]. Three different equivalence ratios were examined, but only the stoichiometric data and model is shown in the figure. The comparisons and conclusions are nearly identical for the lean and rich mixtures.

As the figure shows, the model obtains reasonable agreement with the overall ignition timing, but is too flat in the region near the NTC. This indicates that the chain branching in the model before the NTC is slightly too slow, and that the chain termination step that leads to the uptick in the NTC is also slightly too slow, or occurs at a lower temperature than in reality. Slight adjustments in the potential energy surface of the R + O2 system would probably alleviate many of the discrepancies between the model and the experimental data.

Discussion: Origins of the NTC

A detailed analysis of the mechanism leads to the following conclusions regarding the orgin of the NTC in the ignition of light alkanes.

$T < T_{min}$

At colder conditions than the minimum in the ignition curve, chain branching occurs via the reaction sequences similar to

$CCC\bullet + O_2 = CCCOO\bullet$
$CCCOO\bullet = C\bullet CCOOH$
$C\bullet CCOOH + O_2 = C(OO\bullet)CCOOH$
$C(OO\bullet)CCOOH = C(OOH)CC\bullet OOH$
$C(OOH)CC\bullet OOH = C(OOH)CCHO + OH\bullet$
$\underline{C(OOH)CCHO = C(O\bullet)CCHO + OH\bullet}$
Net : $CCC\bullet + 2\ O_2 = C(O\bullet)CCHO + 2\ OH\bullet$

which is chain branching by producing 3 radicals from only 1. (Note that the first two reactions may proceed directly via a chemical activation mechanism; i.e., $CCC\bullet + O_2 = C\bullet CCOOH$. Such reactions are explicitly included in the kinetic model via the modified strong collision calculations).

$T_{min} < T < T_{max}$

In the region near the NTC itself, the reaction sequence listed above continues to operate, but an additional reaction begins to become fast,

$CCCOO\bullet = C_3H_6 + HO_2$

This reaction competes with the chain branching reaction. Due to the fast recombination of HO_2radicals, yielding H_2O_2 and O_2, the concerted elimination to olefin and HO_2 is actually chain terminating. This leads to the longer ignition delays and a maximum in the ignition curve.

$T > T_{max}$

Finally, at temperatures greater than the maximum in the NTC, the hydrogen peroxide formed via the recombination of HO_2 radicals becomes unstable, leading to two OH radicals. Thus, the concerted elimination channel is no longer chain terminating, but chain propagating. This leads to a shorter ignition delay, and a downturn in the ignition curve.

All of these peroxy reactions are highly pressure dependent, due to their unimiolecular nature. The decomposition of H_2O_2 is also pressure dependent. Thus, the location of, and even existence of, the NTC in an alkane ignition is a complicated function of both temperature and pressure. We are continuing our research into this area with a focus on the pressure dependence of the rates, and the influence this dependence has on ignition timing in real-world systems, such as internal combustion engines.

Acknowledgement. We thank Joe Bozzelli for many helpful comments and for providing the initial calculations of the peroxy radical isomerization reactions.

References

(1) Bowman, C. T., Hanson, R. K., Davidson, D. F., Gardiner, Jr, W. C., Lissianski, V., Smith, G. P., Golden, D. M., Frenklach, M., and Goldenberg, M, http://www.me.berkeley.edu/gri_mech
(2) Bozzelli, J. W. and Sheng, C., *J. Phys. Chem. A*, **2002**, *106*, 1113.
(3) Miller, J. A. and Klippenstein, S. J. *Int. J. Chem. Kinet.*, **2001**, *33*, 654.
(4) Sheng, C. Y., Bozzelli, J. W., Dean, A. M., and Chang, A.Y, *J. Phys. Chem. A*, **2002**, *106*, 7276.
(5) Wilk, R. D., Cernansky, N. P., and Cohen, R. S., *Combust. Sci. Tech.*, **1984**, *49*, 41.
(6) Gallagher, S. M.; Curran, H. J.; Wurmel, J.; Simmie, J. M. *Proc. 3rd Joint Meeting, US Sections of the Combustion Institute,* Paper PM02.
(7) Koert, D. N., Miller, D. L., and Cernansky, N. P., *Combust. Flame*, **1994**, *96*, 34.
(8) Minetti, R.; Ribacour, M.; Carlier, M.; Fittschen, C.; Sochet, L. R. *Combust. Flame*, **1994**, *96*, 201.

CHEMISTRY-AIDED DESIGN OF FUTURE CLEAN FUELS

Edward L. Sughrue and Uday T. Turaga

Bartlesville Technology Center, ConocoPhillips Company, Bartlesville, OK 74004

Introduction

During most of the last century, refining research focused on maximizing the production of fuels and petrochemicals from a barrel of petroleum and improving the properties of fuels to meet the demands of the automakers' newer engines. This produced a number of processes such as catalytic cracking, alkylation, and catalytic naphtha reforming [1]. Societal demands for a cleaner environment and the resulting Clean Air Act in 1970 shifted the focus of refining research and catalyzed the advent of clean fuels, which first appeared in the form of lead-free gasoline.

The Increasing Stringency of the Regulatory Ladder

Lead removal was the first in a series of developments influencing the evolution of gasoline. These developments are described in the regulatory ladder shown in Figure 1. Lead removal is at the foot of the ladder followed by reformulated gasoline (RFG) with lower vapor pressure and the addition of oxygenates. We are currently at the step mandating gasoline sulfur content less than 30 ppm. At higher steps in the ladder, even lower sulfur levels such as 10 ppm or less could be mandated. The elimination of benzene and methyl *tertiary*-butyl ether (MTBE) from gasoline will likely be formalized in the near future. Similarly, addition of renewable fuels such as ethanol is anticipated. At the top of the ladder is the Driveability Index (DI), which is being discussed increasingly in the context of a more consistent fuel.

The arrows at the top of the ladder in Figure 1 imply that new clean fuels regulations will continue beyond those discussed here which are critical but not exhaustive. The ladder represents the increasing difficulty of producing clean fuels that meet increasingly stringent regulations. Each new regulation places a new constraint on the properties of allowable fuels. The property constraints in turn limit what can be blended into the gasoline pool thus defining what refining processes can produce. For example, the loss in octane because of the phase-out of lead was offset by catalytic naphtha reforming, alkylation, and the addition of MTBE.

Clean Fuels from Fuel Composition and Properties

Relating the properties of a fuel to its composition reveals the impact that regulations have on both fuel and refinery process chemistry. For example, reducing fuel vapor pressure impacts the amount of C_4 and C_5 hydrocarbons allowed in the fuel. Similarly, any reductions in DI reduce the permissible amounts of C_9 and C_{10} aromatics in gasoline. Removing these light hydrocarbons or heavy aromatics reduces gasoline's octane and also demands a home for the now orphan streams. While C_9 aromatics have high octane numbers, they have poor cetane values and make inferior quality diesel. Therefore, after removal from gasoline, their alternative use is as fuel gas and fuel oil, both of which are not high-value markets.

Fuel composition and properties also enable insight for the design of tools and techniques to produce clean fuels. One such example relates to hydrodesulfurization of diesel fuels. Analytical methods were developed in the early 1990s to routinely identify—accurately and quantitatively—the types of sulfur molecules present at ppm levels. Concurrently reaction kinetics for different sulfur compounds had been accurately described [2]. Combining analytical measurements with fundamental kinetics led to the development of sophisticated reactor and process models. Currently, at ConocoPhillips, catalyst hydrodesulfurization activity data from a standardized laboratory reactor test is combined with the feed sulfur distributions and other compositional properties in a reactor model to predict product sulfur concentrations, hydrogen consumption, and catalyst life for new and existing hydrodesulfurization units. This approach facilitates the determination of optimal solutions for low-sulfur diesel at each of our 15 different refineries.

Low-Sulfur Gasoline Without Octane Loss

Detailed compositional analyses combined with reaction kinetics have also proven useful in the production of low-sulfur gasoline. Regulations mandating low-sulfur gasoline raised the issue of removing sulfur without losing octane. Most of the sulfur in gasoline is associated with the gasoline produced in the catalytic cracker. This gasoline also contains 20-30% olefins, which contribute to the fuel's octane. Attempts to reduce sulfur through hydrodesulfurization of gasoline results in the hydrogenation of olefins to paraffins causing significant loss of octane. A comparison of the distribution of sulfur and olefins by boiling points shows that a higher percentage of the olefins boil below 180 ºF while most of the sulfur compounds boil above 250 ºF. This led some to fractionate the light end off gasoline feedstocks followed by hydrotreatment of only the heavy fraction.

While such a strategy might work for sulfur specifications of 30 ppm, the prospect of intensifying regulations specifying sulfur content to levels as low as 10 ppm calls for a greater understanding of the olefin-sulfur interactions. It is interesting to note that although 50% of the olefins in gasoline are in the C_5 fraction, the hydrogenation of olefins in the C_6 and C_7 fraction results in greater octane loss (Figure 2). For example the hydrogenation of methyl-2-butene to iso-pentane actually increases road octane from 90 to 91.5, while the hydrogenation of 2-methyl-2-hexene reduces octane from 87 to 44. It may also be noted that thiophene boils very near the C_7 olefins. Furthermore, at high olefin concentrations, Langmuir-Hinshelwood kinetics of olefin hydrogenation predict a rate dependence on olefins closer to zero than one. This implies that leaving the C_5 olefins in the feed to compete with the C_7 olefins for hydrogenation sites will actually reduce octane loss.

It is therefore clear that desulfurization through separation or fractionation has limited potential for effective desulfurization. In light of this, a different set of investigations were begun to answer the question, "Is it possible to remove sulfur without significant hydrogenation?" These investigations resulted in ConocoPhillips's proprietary S Zorb Sulfur Removal Technology, which uses certain metal combinations capable of adsorbing and decomposing thiophenic sulfur with only minimal olefin saturation and without forming any hydrogen sulfide. The ability to accomplish desulfurization without the formation of hydrogen sulfide is a critical advantage of the S Zorb Sulfur Removal Technology over hydrotreating. Hydrogen sulfide, produced during hydrotreating, is known to react with olefins and form mercaptans, thereby enhancing product sulfur.

The Utility of Olefins Beyond Octane Loss

While retention of olefins for the sake of gasoline octane is good, future clean fuel issues demand increased understanding and value for olefins. Of the different types of hydrocarbons available to petroleum and fuel chemists, olefins are the most reactive and undergo a suite of reactions including alkylation, dimerization, and

cracking at conditions much milder than demanded by corresponding paraffins, aromatics, and naphthenes. For example, C_9 and C_{10} aromatics can be alkylated with C_5 and C_7 olefins to produce diesel-range material with acceptable cetane numbers. Similarly, dimerization of C_5 olefins could reduce vapor pressure. Olefins offer such versatility and flexibility, which need better understanding and creative utilization to unlock issues that will dominate the future of clean fuels.

Conclusions

The future of cleans fuels will continue to be both challenging and full of opportunities for creative chemists and chemical engineers. A critical tool toward the development of processes and products for producing clean fuels will be a strong understanding of the fundamentals of fuel chemistry. Recent advances in analytical techniques, kinetic modeling of fuel components, catalysis and materials, and reactor engineering will enable the production of a new generation of clean fuels.

References

1. Martino, G.; Courty, P.; and Marcilly, C. In *Handbook of Heterogeneous Catalysis*; Ertl, G.; Knozinger, H.; and Weitkamp, J.; Eds.; VCH: Berlin, Germany, **1997**; pp. 1801-1818.
2. Girgis, M. J. and Gates, B. C. *Ind. Eng. Chem. Res.* **1991**, *30*, 2021-2058.

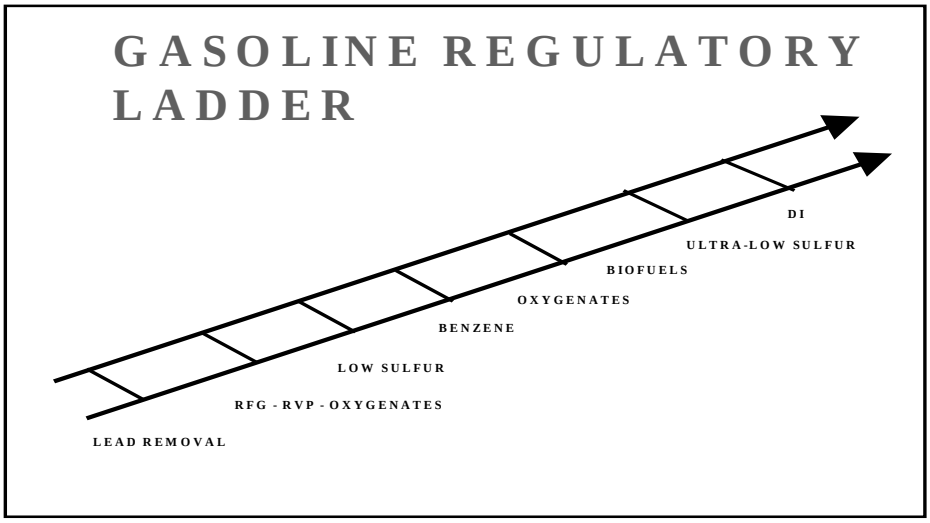

Figure 1. The issues that constitute the increasingly stringent regulatory ladder.

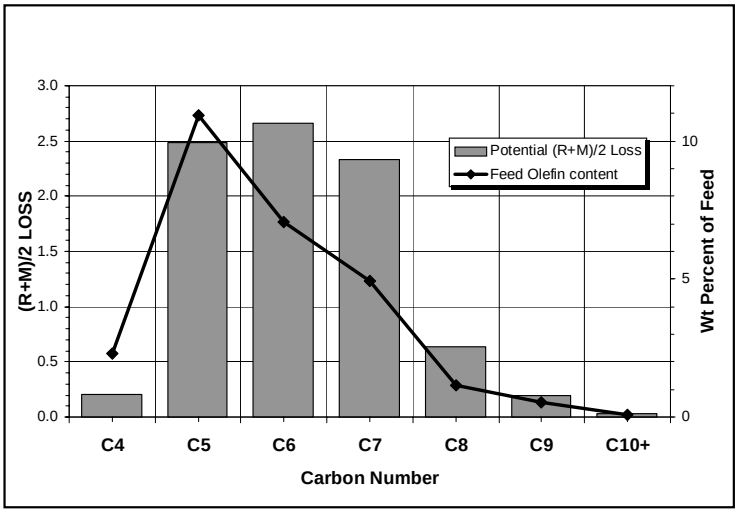

Figure 2. Olefins distribution and potential octane loss for gasoline.

ADSORPTIVE DESULFURIZATION OF DIESEL FUEL OVER A METAL SULFIDE-BASED ADSORBENT

*Xiaoliang Ma, Lu Sun, and Chunshan Song**

Clean Fuels and Catalysis Program, The Energy Institute and Department of Energy and Geo-Environmental Engineering, The Pennsylvania State University, 209 Academic Projects Building, University Park, PA 16802
*E-mail: csong@psu.edu

Introduction

Ultra-deep removal of sulfur from diesel fuel is important for environmental protection and fuel cell applications (1,2). The current hydrodesulfurization technology is difficult to reduce the sulfur content in diesel fuel to less than 10 ppmw, because the remaining sulfur compounds in the current commercial diesel fuel are the refractory sulfur compounds, the alkyl dibenzothiophenes with one and/or two alkyl groups at the 4- and/or 6-positions (1,3,4). On the other hand, the conventional hydrodesulfurization technology has to be operated at high temperature and high pressure with hydrogen, resulting in high cost for the ultra-deep hydrodesulfurization. Selective adsorption desulfurization is a promising technology for the ultra-deep desulfurization of diesel fuel. We are exploring a new approach at Penn State called selective adsorption for removing sulfur (PSU-SARS), for ultra-deep removal of sulfur from liquid hydrocarbon fuels (1, 2, 5-11).

The major challenge to our proposed approach is to selectively adsorb sulfur compounds onto the surface of the solid adsorbent but leave the coexisting hydrocarbons including aromatic and olefinic hydrocarbons as well as saturated hydrocarbons, untouched. On the other hand, for the industrial applications one of the key points in the adsorptive desulfurization process is to develop the adsorbent that can be regenerated easily. We envision that the interaction between the sulfur compounds and the adsorption sites on the adsorbent should be selective and suitable in strength. The too strong interaction between them will cause a difficulty in the subsequent regeneration process, while the too weak interaction probably results in a low adsorption selectivity and low capacity. In the present approaches we attempted to develop a metal-sulfide-based adsorbent that not only can selectively adsorb the sulfur compounds but also can be easily regenerated without using hydrogen gas.

Experimental

Two model diesel fuels (MD-1 and MD-2) were used in the present study. MD-1 contains the same molar concentration (3.9 mmol/L) of dibenzothiophene (DBT), 4-methyldibenzothiophene (4-MDBT) and dimethyldibenzothiophene (4,6-DMDBT), and 1-methylnaphalene (1-MNA). MD-2 contains only one sulfur compound, DBT. The total sulfur concentration in MD-1 and MD-2 is 486 and 200 ppmw, respectively. MD-1 and MD-2 also contain 10 wt% of n-butylbenzene for mimicking the aromatics in the real diesel. The detailed composition of the model diesel fuels is listed in Table 1 and 2. The sulfur compounds and hydrocarbons contained in the fuels were purchased from Aldrich without further treatment before use.

The adsorbent used in the present study was Adsorbent-6, which was prepared from CoMo oxides supported on γ-alumina (CoMo/γ-Al_2O_3; CoO: 3wt%; MoO3: 14wt%; Surface area: 183 m^2/g; Pore volume: 0.4755 ml/g; Average pore size: 102 Å). CoMo/γ-Al_2O_3 was sulfided at 350 ˚C with 10 vol % H_2S in H_2 at a flow rate of 200 ml/min for 4 h. The sulfided CoMo/γ-Al_2O_3 was cooled to room temperature under the same atmosphere, and then, kept into hexane before use. Adsorbent-6 was obtained by treating the sulfide CoMo/γ-Al_2O_3 with H_2 at 300 ˚C for 60 min. About 2 g of the sulfided CoMo/γ-Al_2O_3 was parked into a stainless steel column with internal diameter of 4.6 mm and length of 150 mm. The adsorbent bed volume was 2.49 ml. H_2 gas was passed through the column at ambient pressure and a flow rate of 20 ml/min. After the treatment, the column temperature was reduced to the assigned temperatures for the adsorption.

The adsorption experiments were performed at ambient pressure without using H_2 gas. The model diesel fuel was fed into the column and flowed up through the adsorption bed. The flow rate was 0.2 ml/min, corresponding to a LHSV of 4.8 h^{-1}. The treated model fuel was collected for analysis. The regeneration of the spent adsorbents was accomplished by washing the adsorbent with a polar solvent followed by heating the adsorbent to remove the remaining solvent. The polar solvent was pumped through the adsorbent bed at 60 ˚C and a LHSV of 4.8 h^{-1}. After washing, the adsorbent bed was heated to 300 ˚C under a nitrogen flow at 20 ml/min for 1 h, and then, was cooled to the assigned temperature for the subsequent adsorptive desulfurization.

Analysis of concentration of sulfur compounds in the treated MD-1 was performed by using GC with a capillary column, XTI-5 (Restek) 30 m x 0.25 mm x 0.25 μm, and a flame ionization detector (FID). An Antek 9000 Series Sulfur Analyzer (detection limit 0.5 ppmw) was used for determining sulfur concentration in the treated MD-2.

Results and Discussion

Figure 1 shows the molar concentration of sulfur compounds and 1-MNA at the outlet as a function of the effluent amount for the adsorptive desulfurization of MD-1 over Adsorbent-6 at 50 ˚C. The first break-through compound was 1-MNA with a break-through point at 0.2 g/g (gram of MD-1 per gram of adsorbent) and a saturation point at 1.6 g/g. The second one was 4,6-DMDBT with a break-through point at 0.4 g/g. The concentration of 4,6-DMDBT was kept below 0.2 mmol/l before the effluent amount reached 2.5 g/g, and then, increased quickly to the saturation point at 4.4 g/g. Break-through point of 4-MDBT was at 2.5 g/g with a saturation point at 5.0 g/g. The last break-through compound was DBT with a break-through point at 3.5 g/g and a saturation point at > 5.5 g/g. It is clear that Adsorbent-6 has much higher selectivity to adsorb DBTs compared to aromatics represented by 1-MNA. As is well known, 1-MNA has a higher π-electron density on its aromatic ring than that of DBTs (9), although the aromatic ring size of the former is smaller than that of the latter. It is clear that interaction between the S atom and the adsorption sites plays an important role in the competitive adsorption between DBTs and 1-MNA. From a comparison of DBT, 4-MDBT and 4,6-DMDBT, the adsorption selectivity increases in the order of 4,6-DMDBT < 4-MDBT < DBT, implying that the methyl groups at the 4 and 6-positions inhibit the interaction between the S atom and the adsorptive sites on the adsorbent, which results in the decrease in the adsorption capacities of 4,6-DMDBT and 4-MDBT.

It should be noted the system we used is based on selective adsorption, not reaction. No detectable biphenyls and cyclohexylbenzenes type products were found in the effluent, indicating that no HDS reaction takes place at such conditions.

Adsorption desulfurization of MD-2 over Adsorbent–6 was conducted at 50 ˚C under ambient pressure. The total sulfur concentration at outlet as a function of the treated MD-2 amount is shown in Figure 2. When the treated MD-2 amount was less than 2.5 g/g, the sulfur concentration at outlet was less than 10 ppmw. After 2.5 g/g of the effluent amount, the sulfur concentration increased sharply with increasing the effluent amount. Adsorbent-6 was saturated when the effluent amount reached about 8 g/g. The adsorptive capacity corresponding to the break-through point at 10 ppmw sulfur level and the saturation point was 0.65 and 0.77

milligram of sulfur per gram of adsorbent (mg-S/g-A), respectively. Adsorption desulfurization of MD-2 over Adsorbent–6 at 150 ˚C was also conducted, but the performance was poorer than that at 50 ˚C. This indicates that lower temperature is better for the adsorptive desulfurization over this type of adsorbents, in contrast to the nickel-based adsorbents (12).

After regeneration of the spent adsorbent, the adsorption performance of the regenerated adsorbents was tested. The adsorption break-through curves for the regenerated adsorbents are shown in Figure 2 in comparison with the curve for the fresh adsorbent. It shows clearly that the break-through curves for the 1st regenerated adsorbent and the 2nd regenerated adsorbent coincide well with that for the fresh adsorbent, especially when the treated MD-2 amount is less than 4 g/g. The adsorption capacity corresponding the break-through point at 10 ppmw sulfur level for the 1st regenerated adsorbent and the 2nd regenerated adsorbent is 0.65 and 0.66 mg-S/g-A, respectively. It implies that the spent adsorbent can be regenerable, and almost all adsorption capacity in the adsorbent can be recovered by our developed method.

Acknowledgments. We gratefully acknowledge the financial support by US Department of Energy and US Department of Defense.

References

1. Song, C., Ma, X., Appl. Catal. B., 41 (1-2), 207-238 (2003).
2. Song, C. *Catalysis Today*, , 77 (1), 17-50 (2002).
3. Ma, X., Sakanishi, K., Mochida, I., Ind. Eng. Chem, Res. 33, 218 (1994).
4. Gates, B.C., Topsoe, H., Polyhedron 16, 3213 (1997).
5. Ma, X, Sun, L., and Song, C., *Catal. Today*, 77, 107-116 (2002).
6. Velu, S., Ma, X., and Song, C., *Am. Chem. Soc. Div. Petr. Chem. Prepr.*, 48 (2), 58-59 (2003).
7. Velu, S., Watanabe, S., Ma, X., and Song, C., *Am. Chem. Soc. Div. Petr. Chem. Prepr.*, 48 (2), 56-57 (2003).
8. Ma, X., Sprague, M., Sun, L., and Song, C., Ultra-Deep Desulfurization of Gasoline and Diesel for Fuel Cell Applications by SARS Adsorbent and Process. Materials Research Society Fall 2002 National Meeting, Boston, Dec. 2-6, 2002
9. Ma, X., Sprague, M., Sun, L., and Song, C., *Am. Chem. Soc. Div. Fuel Chem. Prep.*, 47, 452 (2002).
10. Velu, S., Ma, X., and Song, C., Zeolite-Based Adsorbents for Desulfurization of Jet Fuel by Selective Adsorption. *Am. Chem. Soc. Div. Fuel Chem. Prep.*, 47, 457 (2002).
11. Ma, X., Sun, L., Yin, Z. and Song, C., *Am. Chem. Soc. Div. Fuel Chem. Prep.*, 46 (2), 648-649 (2001).
12. Ma, X., Velu, S., Sun, L., and Song, C., *Am. Chem. Soc. Div. Fuel Chem. Prep.*, 48, (2003), in submission.

Table 1 Composition of MD-1

No.	Name	Concentration		
		wt %	mmol/l	ppmw
	Sulfur compounds			
1	DBT	0.095	3.93	165
2	4-MDBT	0.099	3.81	160
3	4,6-DMDBT	0.107	3.85	162
	Total Sulfur		11.59	486
4	Naphthalene (99%)	0.067		
5	2-methylnaphthalene (98%)	0.074	3.85	
6	n-Hexadecane(99+%)	39.97		
7	n-Dodecane(99+%)	39.50		
8	n-Tetradecane (99+%)	0.109		
9	Decalin(99+%)	9.988		
10	t-Butylbenzene(99%)	9.988		

Table 2 Composition of MD-2

No.	Name	Concentration		
		wt %	mmol/l	ppmw
1	DBT (99+%)	0.115	4.84	200
2	1-Methylnaphthalene(97%)	0.090	4.89	
3	n-Hexadecane(99+%)	88.67		
4	n-Tetradecane (99+%)	0.122		
5	n-Butylbenzene(99%)	10.01		
	Others	1.00		

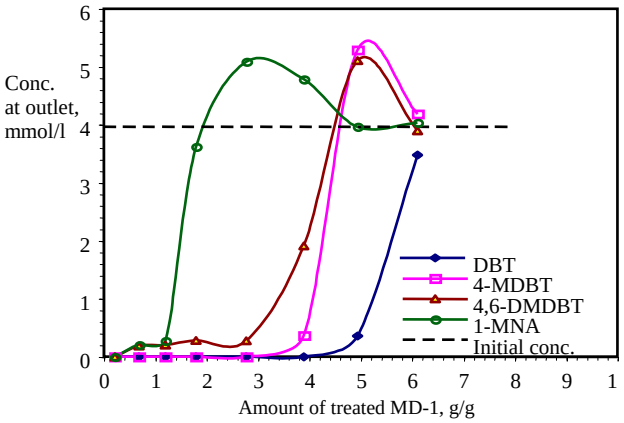

Figure 1. Break-through curves of MD-1 over Adsorbent-6

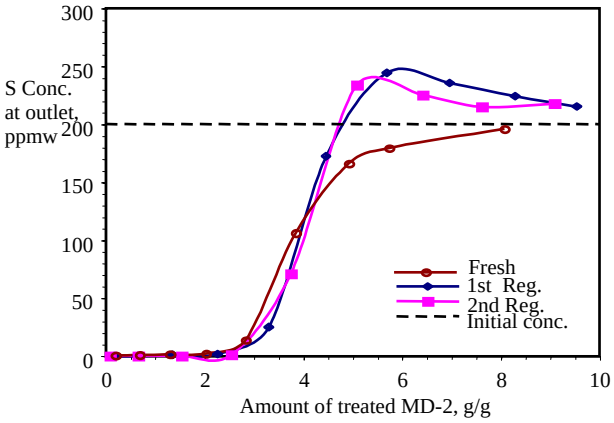

Figure 2. Break-through curves of MD-2 over fresh and regenerated adsorbents at 50˚C

ADSORPTIVE REMOVAL OF SULFUR COMPOUNDS FROM NAPHTHA FRACTIONS BY USING CARBON ADSORBENTS

Kinya Sakanishi, Hamdy Farag, Shinya Sato, Akimitsu Matsumura, and Ikuo Saito*

National Institute of Advanced Industrial Science and Technology (AIST), Tsukuba West, Ibaraki 305-8569, Japan

Introduction

Ultra-deep desulfurization of gasoline and diesel fuels is aimed to produce sulfur-free fuels or their sulfur contents below 10 ppm for the environmental protection in urban areas. To develop fuel cell vehicles in the future, olefin and aromatic compounds as well as sulfur compounds are to be removed to extremely low levels of less than percent levels of the former two compounds and tens of ppb levels of sulfur compounds.[1-3]

Hydrodesulfurization(HDS) of gasoline and diesel fuels has been widely applied in petroleum refineries for the production of such sulfur-free fuels, however, reduction of sulfur levels below 10 ppm is hardly achieved by conventional catalysts under HDS process conditions.[4] Much higher activity and selectivity of HDS catalysts should be designed for the removal of refractory sulfur compounds in petroleum light products.

Adsorptive removal processes of sulfur compounds from petroleum distillates have been also developing for the complete capture to achieve the sulfur levels below ppm order. Some of such adsorptive sulfur removal procedures are expected to produce sulfur-free gasoline and diesel fuels because of their simple and energy-saving manner without hydrogen consumption. Although variable kinds of adsorbents have been screened for the achievement of sulfur-free fuel production, effects of coexisting aromatic compounds on the adsorption selectivity of sulfur compounds are not fully elucidated.

Carbon adsorbents such as active carbon and active carbon fiber are one of the most promising materials for the selective removal of sulfur compounds at relatively low temperatures around room temperatures due to their extremely high surface area and very uniform pore size distribution with weak polarity.[5]

In the present study, some of mesoporous carbon adsorbents are investigated to estimate their adsorption capacity and selectivity for sulfur compounds such as benzothiophene(BT) and 2-methyl-benzo-thiophene(2MBT) and in their mixture with some aromatic compounds as model feedstocks. In addition, a real naphtha fraction is also treated with active carbons of different surface areas and particle sizes with or without dilution with n-hexane solvent. Mesoporous active carbons of finer particles are revealed to be preferable for the selective adsorption of two-ring sulfur compounds such as BT and 2MBT.

Experimental

Some properties of carbon adsorbents used in the present study are summarized in Table 1. Three types of active carbons(MaxSorb, Diahope, and Alkali-activated carbon prepared from Marlim Brazilian vacuum residue: MarVR-AC) and a carbon black(Ketjen Black) are selected for the comparison of adsorption capacity and selectivity. All of the active carbons were ground to < 60 mesh and dried at 333 K under vacuum prior to the adsorption experiment.

A simple model feedstock of BT(0.05 g) in 10 cc n-heptane was prepared for the evaluation of adsorption capacity. A series of model solutions of toluene(T), naphthalene(N), 1-methylnaphthalene(1MN), and 2-methylbenzothiophene(2MBT) were prepared for the evaluation of adsorption selectivity. These solutions were mixed with 0.5 g of carbon adsorbent and stirred for 1 h at room temperature.

10 g of a real naphtha fraction supplied from Japan Energy Co.(sulfur content: ca.300 ppm; b.p. range: 70-151℃) and its 10 wt% solution diluted with n-hexane were also treated with 0.1 g of active carbon for checking the adsorption ability of carbon adsorbents.

Model solutions and real naphtha fractions were analyzed by GC-AED before and after the adsorption treatment.

Results and Discussion

First of all, detection limit of sulfur compounds by GC-AED was examined by changing the measurement conditions such as split ratios, injection amounts, and gas flow rates with a series of standard BT solutions in their concentrations of 87.2 ppm, 7.44 ppm, 0.84 ppm, 0.071 ppm, and 8.7 ppb. It is revealed that about 0.05 ppm(50 ppb) of BT can be detected by GC-AED measurement by adjusting the split ratio to 1:1 and the injection amount to 2 ul. GC-AED can be a powerful tool for the detection of tens ppb level of sulfur compounds, enabling us to check the quality of nearly sulfur-free fuels.

Adsorption capacity of carbon adsorbents for BT is summarized in Table 1. Among the carbon adsorbents examined in the present study, the adsorption capacity was in the order of Diahope [0.083 (g-BT / g-adsorbent)] > Ketjen Black [0.062] > MaxSorb [0.056]> MarVR-AC [0.041]. It seems that relatively mesoporous active carbons may be preferable for the selective adsorption of BT.

Table 1
Some properties of carbon adsorbents and their adsorption capacity for benzothiophene (BT) *

Carbons	S.A. (m^2/g)	Av.pore dia. (nm)	Pore vol. (ml/g)	Ads. for BT (g / g)
MaxSorb (active carbon)	3370	0.37	1.88	0.056
Diahope (active carbon)	1150	1.2	0.70	0.083
Ketjen Black (carbon black)	1270	< 0.3	1.39	0.062
MarVR-AC (active carbon)	2150	1.9	1.05	0.041

* BT 0.05 g in 10cc n-heptane with 0.5 g carbon at r.t for 1 h

Adsorption selectivity of each model compound on Diahope powder was summarized in Table 2. Roughly speaking, adsorption ratio of each substrate increase with its molecular molecular weight or molecular size, however, it is suggested that sulfur compounds may be more selectively adsorbed on Diahope powder.

Table 2 Adsorption selectivity of each model compound*

	Adsorption (%)
Toluene	**10**
Naphthalene (Np)	**31**
1-methylnaphthalene(1MN)	**25**
Benzothiophene（BT）	**83**
2-methylbenzothiophene(2MBT)	**89**

* 0.05 g of each substrate in 10 cc n-heptane with 0.5 g Diahope(< 60 mesh) at r.t. for 1h

Adsorption selectivity of mixed model compounds on Diahope powder was summarized in Table 3. Adsorption ratios of sulfur compounds decreased significantly with increased adsorption ratios of two-ring aromatic compounds, indicating large interference of similar-sized aromatic compounds against sulfur compounds. It is noted that a single ring aromatic compound of toluene may not be adsorbed so much as two-ring aromatic compounds, suggesting that a majority of one-ring aromatic compounds in gasoline and naphtha fractions may not interfere with the adsorption of sulfur compounds.

Table 3 Adsorption selectivity of mixed model compounds*

	Adsorption (%)
Toluene	8.5
Naphthalene (Np)	39
1-methylnaphthalene(1MN)	35
Benzothiophene（BT）	54
2-methylbenzothiophene(2MBT)	62

* 20% of five model solutions mixed and treated with 0.5 g Diahope(< 60 mesh) at r.t. for 1h

According to the sulfur-chromatograms of the naphtha feedstock analyzed by GC-AED before and after the adsorption treatment, the original naphtha fraction mainly consisted of alkylated thiophene derivatives with a small amount of benzothiophene and its alkylated derivatives, and the benzothiophene derivatives were selectively removed by the adsorption treatment, although such two-ring aromatic sulfur compounds are relatively minor components.

Table 4 compares the adsorption behaviors of two active carbons of Diahope and MaxSorb with two levels of particle sizes of < 60 mesh and 60-100 mesh for neat naphtha fraction. It is revealed that a very small amount of sulfur compounds as low as a few percents were adsorbed in all the cases examined in the present study regardless of the carbon types and particle sizes. The recovery yield of the naphtha feedstock was also as low as 80%, indicating the difficulty in the selective adsorption of sulfur compounds and in the effective recovery of non-adsorbed species from the carbon adsorbents.

Table 4 Adsorption treatment of neat naphtha fraction using active carbon powders*

Adsorbent	Adsorbed S(%)	Recovery(%)
Diahope (< 60 mesh)	2.8	79
Diahope (60 - 100 mesh)	1.9	83
Maxsorb (< 60 mesh)	3.5	78
Maxsorb (60 – 100 mesh)	2.1	81

* 10 g of neat naphtha solution was stirred with 0.1 g active carbon at r.t. for 1h

Table 5 summarizes the adsorption amount of sulfur compounds from real naphtha fraction when it was diluted with n-hexane to 10wt% before the adsorption treatment. Although the adsorbed amount of sulfur compounds remained low even if the naphtha fraction was diluted to 10%, finer particles of the active carbons gave slightly higher adsorption capacity. MaxSorb gave the larger adsorption capacity for sulfur compounds in real naphtha feedstock in comparison to Diahope, probably due to its higher surface area and pore volume regardless of their particle sizes.

In addition, recovery yields of the naphtha fraction after the adsorption treatment were always above 90 %, suggesting that n-hexane solvent may not only improve the adsorption efficiency of sulfur compounds by enhancing the diffusion into the pore structure of the carbon adsorbent, but also facilitate the separation and recovery of non-adsorbed species from the carbon adsorbent.

Table 5 Adsorption treatment of 10wt% naphtha fraction diluted with n-hexane by using active carbon powders*

Adsorbent	Adsorbed S(%)	Recovery(%)
Diahope (< 60 mesh)	11	95
Diahope (60 - 100 mesh)	9.5	97
Maxsorb (< 60 mesh)	21	92
Maxsorb (60 – 100 mesh)	16	93

* 10 g of naphtha solution(10wt%) was stirred with 0.1 g active carbon at r.t. for 1h

Table 6 summarizes the adsorption behaviors of mixed sulfur compounds which consists of each 1wt% of 2-methylthiophene (2MT), ethylphenylsulfide(EPS), benzothiophene(BT), and 2-methylbenzo-thiophene(2MBT), and diphenylsulfide(DPS) dissolved in n-hexane solvent. Two-ring aromatic sulfur compounds were more selectively adsorbed on Diahope powder, reflecting from their molecular sizes in the order of BT < 2MBT < DPS. It is suggested that microporous carbon adsorbents may be favorable for the removal of one-ring sulfur compounds such as 2MT and EPS. Otherwise, the conventional catalytic hydrodesulfurization treatments are preferable for the removal of such one-ring aromatic sulfur compounds because of their much higher reactivity under the milder conditions compared to two-ring and three-ring aromatic sulfur compounds.

Table 6 Adsorption selectivity of mixed sulfur model compounds *

	Adsorption (%)
2-methylthiophene(2MT)	21
Ethylphenylsulfide (EPS)	33
Benzothiophene（BT）	52
2-methylbenzothiophene(2MBT)	59
Diphenylsulfide(DPS)	68

* 1wt % of five model sulfur compounds dissolved in n-hexane solvent mixed with 0.5 g Diahope(< 60 mesh) at r.t. for 1h

Conclusion

The present study revealed that relatively mesoporous active carbons with finer particle size may be preferable for the selective adsorption of two-ring sulfur compounds such as BT and 2MBT contained in the naphtha fraction. Hydrogenative removal of one-ring sulfur compounds with the adsorption treatment had better be combined for the more effective and optimized desulfurization procedures.

Acknowledgment

The work has been entrusted by the New Energy and Industrial Technology Development Organization under a subsidy of the Ministry of Economy, Trade and Industry.

References

1. Song, C., *Prepr. ACS Div. Fuel Chem.*, **2002**, 47(2), 438.
2. Ma,X., Sun, L., Song,C., *Catalysis Today*, **2002**, 77(1), 107.
3. Ma, X., Sprague, M., Sun, L., Song, C., *Prepr. ACS Div. Petrol. Chem.*, **2002**, 47(1), 48.
4. Whitehurst, D.D., Isoda, T., Mochida, I., *Advan.Catal*., **1998**, 42, 345
5. Sano, Y., Choi, K., Korai, Y., Mochida, I., *Prepr. ACS Div. Fuel Chem.*, **2003**, 48(1), 138

REGENERABLE ADSORBENTS FOR THE ADSORPTIVE DESULFURIZATION OF TRANSPORTATION FUELS FOR FUEL CELL APPLICATIONS

*S. Velu, Shingo Watanabe, Xiaoliang Ma, and Chunshan Song**

Clean Fuels and Catalysis Program, The Energy Institute, and
Department of Energy and Geo-Environmental Engineering
The Pennsylvania State University
209 Academic Project Building, University Park, PA 16802
*E-mail: csong@psu.edu

Introduction

The requirement of ultra-clean transportation fuels, particularly, gasoline and diesel, has resulted in a continuing worldwide effort to dramatically reduce the sulfur levels in them. The presence of sulfur in these fuels is a very serious environmental concern because on combustion in the internal combustion engines, the sulfur is converted into toxic SOx. The Government agencies in various countries have implemented more stringent regulations for refineries to produce gasoline and diesel fuels with reduced sulfur content. For instance, the U.S EPA recently issued a new Tier II regulation that mandates refineries to reduce the sulfur content of gasoline from the current average of 300 ppmw to 30 ppmw by 2005-2006 and to cut down the sulfur content of highway diesel fuel from the current limit of 500 ppmw to 15 ppmw by 2006. Lowering the sulfur content in transportation fuels not only reduces the SOx emission, but it also contributes to reducing the emissions of other noxious gases such as NOx and hydrocarbons by allowing the automotive catalytic converters to work better.

The need for the production of ultra-clean gasoline and diesel fuel is further motivated by the rapid development of fuel cells for mobile, stationary and portable power application for which the sulfur levels need to be further reduced down to 1 ppmw. Hydrodesulfurization (HDS) using sulfided Ni-Mo or Co-Mo catalyst at high temperature and high pressure is a conventional method being employed by the refineries to produce low sulfur gasoline and diesel in order to meet the environmental regulations.[1,2] However, the process is inefficient to produce ultra-clean transportation fuels, particularly for fuel cell applications. Alternative methods such as adsorptive desulfurization, oxidative and extractive desulfurization, biodesulfurization, etc. are being developed in recent years to produce ultra-low-sulfur gasoline and diesel fuels.

Among the alternative methods, adsorptive desulfurization is a promising approach and several new processes, such as IRVAD and Philips S-Zorb processes have been reported recently.[3,4] The challenges in the adsorptive desulfurization include the following: (i) the adsorbent should be selective to remove only sulfur compounds without adsorbing the aromatics and olefins present the fuel; (ii) for on-board or on-site fuel cell applications, the adsorptive desulfurization should be performed at close to the ambient temperature; and (iii) the adsorbent should be regenerable for subsequent use.

A new process concept is being developed in our laboratory at PSU known as selective adsorption for removing sulfur (PSU-SARS) for the adsorptive desulfurization of gasoline, diesel and jet fuel.[1,2,5,6] Here we report what may be characterized as the "sense and grab" and "sense and shoot" approaches employed for selectively removing organic sulfur compounds present in these fuels. In the former approach, the sulfur compounds are selectively adsorbed onto certain adsorbents. The adsorbed sulfur compounds are recovered and the adsorbents are regenerated either by solvent washing or by oxidative regeneration. In the "sense and shoot approach", the sulfur compounds adsorbed onto the adsorbents are decomposed because of the occurrence of surface reactions with adsorbents. The sulfur is retained on the surface of the adsorbent and the remaining organic moiety is added to the fuel. The performance of the adsorbents is regained by reductive regeneration or a combined oxidative and reductive regeneration. In this communication we show few examples for our approaches for the desulfurization of diesel fuels and regeneration of adsorbents by solvent washing and reductive regeneration methods.

Experimental

A wide variety of materials, including metal ions loaded on zeolites or mesoporous materials, mixed metal oxides, hydrotalcite-like anionic clays, metal modified activated carbon, supported metals, etc were tested as adsorbents. Most of these materials were synthesized in our laboratory as described elsewhere.[1,2,5,6] Either a model fuel containing thiophene (as representative for gasoline) or 4,6-Dimethyldibenzothiophene (4,6-DMDBT; as representative for diesel fuel) or commercial real gasoline / diesel fuels were used as a feedstock. The adsorbent was packed in a stainless steel column with an internal diameter of 4.6 mm and length of 150 mm. The adsorbent bed volume was 2.49 ml. Adsorbents such as zeolite-based, activated carbon and mixed oxides were initially activated at 200˚C in N_2 flow to remove any adsorbed gases and then cooled down to the adsorption temperature (60˚C). Sulfur-free n-decane was fed into the column using a HPLC pump at a rate of 0.2 ml/min. (LHSV = 4.8 h^{-1}) for about 10 min to remove entrapped gases and then switched to the sulfur containing feed with the same space velocity. Samples were collected periodically and their total sulfur contents were determined using an Antek 9000 Series Sulfur Analyzer (detection limit 0.5 ppmw). A GC equipped with a sulfur selective pulsed flame photometric detector (PFPD) was used to identify the nature of sulfur compounds present in the feed and effluent.

Regeneration of spent adsorbent was performed by solvent washing, oxidative or reductive regeneration. In the solvent washing method, a 1:1 mixture of methanol and toluene was flowed through the adsorbent bed at 70˚C until the sulfur in the washing solvent became undetectable. The oxidative regeneration was effected by treating the spent adsorbent by flowing air at 300˚C for 2-3 h while the reductive regeneration was performed by flushing the adsorbent with H_2 gas at 500˚C for 2-3 h.

Result and Discussion

The sulfur compounds present in gasoline, jet fuel and diesel are derivatives of thiophene (T), benzothiophene (BT) and dibenzothiophene (DBT), respectively. The reactivity of these sulfur compounds in the HDS reaction decreases in the order; thiophene (100) > benzothiophene (30) ≥ dibenzothiophene (30) > MDBT (5) > DMDBT (1).[7,8] The GC chromatograms obtained using a sulfur selective PFPD for two kinds of low sulfur diesel received from commercial sources are shown in Fig. 1. As can be seen, the 4,6-DMDBT is present as a major sulfur compound even in the diesel fuel containing below 10 ppmw of sulfur. This is the most refractory sulfur compound and is very difficult to remove by the existing the HDS process because of the steric hindrance exerted by the presence of methyl groups at the 4 and 6 positions.

In order to develop regenerable adsorbents for the desulfurization of diesel fuels, a wide variety of new adsorbents based on zeolites, mixed metal oxides, activated carbon and supported metal compounds have been tested using a model diesel fuel containing 220 ppmw of sulfur as 4,6-DMDBT in a

mixture of decane and hexadecane solvents. The breakthrough curves for the adsorptive removal of 4,6-DMDBT from the model diesel fuel at 60˚C over transition metal oxides supported on MCM-41 mesoporous material and activated carbon are shown in Fig. 2. It is interesting to note that in both cases, the 4,6-DMDBT has been completely removed. The MCM-41-based adsorbent exhibits a breakthrough capacity of 3.5 mg of sulfur per g of adsorbent while the transition metal supported on activated carbon shows very high breakthrough capacity of 12.6 mg/g of adsorbent.

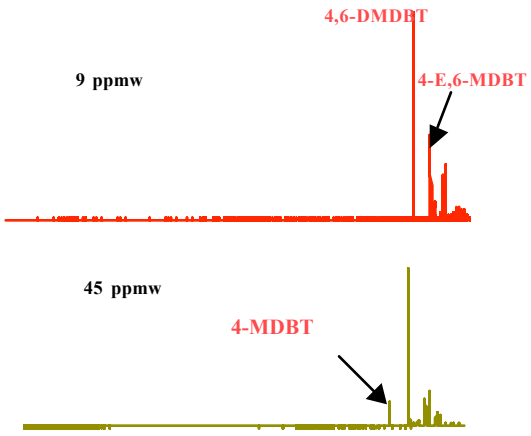

Fig. 1. Sulfur selective GC PFPD Chromatogram of low sulfur diesel fuels containing 9 ppmw and 45 ppmw sulfur

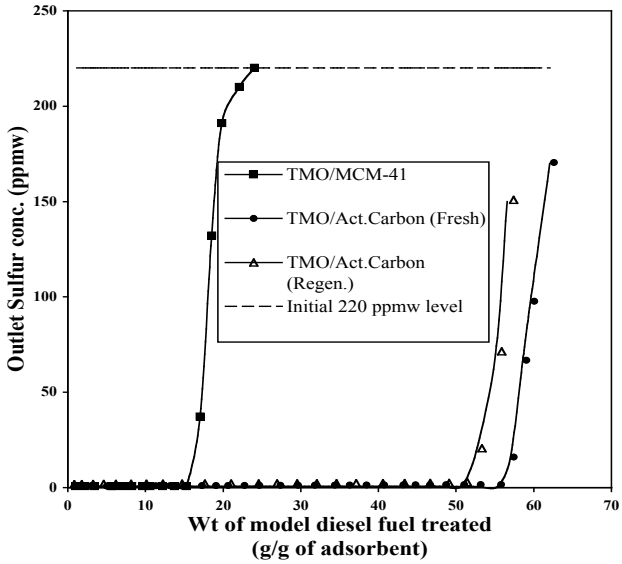

Fig. 2. Breakthrough curves for the adsorptive desulfurization of a model diesel fuel containing 4,6-DMDBT at 60˚C over Transition metal oxides supported on MCM-41 and activated carbon. LHSV = 4.8 h^{-1}

Attempt has been made to regenerate these adsorbents by flushing with a 1:1 mixture of methanol and toluene at 70˚C. In order to estimate the amount of solvent required to completely recover the 4,6-DMDBT and to regenerate the adsorbent for subsequent use, the fractions of the solvent have been collected and analyzed using the total sulfur analyzer. The profile for recovering the 4,6-DMDBT by solvent washing from the spent activated carbon-based adsorbent is shown in Fig.3. The sulfur content in the initial few fractions exceeded 1000 ppmw and then decreases exponentially. The results indicate that most of the sulfur compounds could be recovered using 20 cc of the solvent per g of adsorbent. However, about 100 cc of the solvent is required under the present experimental condition for the complete removal of all the sulfur compounds adsorbed on this particular adsorbent.

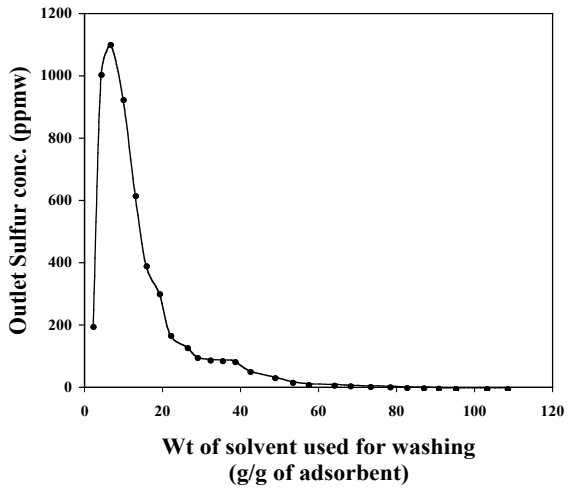

Fig.3. Profile for recovering the adsorbed 4,6-DMDBT by solvent washing from the spent activated carbon-based adsorbent at 70˚C

After the solvent washing, the regenerated adsorbent has been flushed with N_2 gas (40 ml/min) for about 1 h at 300˚C in order to remove any adsorbed solvent molecules. Desulfurization of model diesel fuel over regenerated adsorbent has been performed under the same experimental condition as that of fresh sample and the sulfur breakthrough curve obtained on the regenerated sample is shown in Fig. 2 itself along with that of fresh samples. The breakthrough curves of fresh and regenerated samples are close to coincidence and this indicates that solvent washing can regenerate the adsorbent almost completely. This observation infers that the adsorbent simply grabs the sulfur sulfur compound (4,6-DMDBT) from the fuel and holds it by some weak interactions without destroying. Flushing with solvent is sufficient to break such weak interactions.

There are several advantages of solvent washing for the regeneration of spent adsorbent. For instance, the organic sulfur compounds can be recovered by separating them from the solvent and the concentrated sulfur compounds can be treated in small HDS reactors to remove sulfur and the remaining organic moiety can be blended with the fuel.[1,2] Regeneration by solvent washing is an environmentally benign method because it avoids the emissions of SOx generated by oxidative regeneration or H_2S generated in the reductive regeneration.

In the "sense and shoot" approach, model and real diesel fuels have been treated over adsorbents such as Ni supported on SiO_2-Al_2O_3, and nano-composite materials derived from hydrotalcite-like anionic clays. These materials exhibit better adsorption performance at relatively elevated temperature of around 200˚C. This indicated that the sulfur compounds over these adsorbents are removed by surface reactions rather than weak interactions. Experiments using model fuels revealed that the sulfur compounds are destroyed and converted into

corresponding organic moiety although no hydrogen gas has been used during the adsorption.

Fig.4 shows the breakthrough curves for the adsorptive desulfurization of a low sulfur diesel fuel containing 45 ppmw of sulfur shown in Fig. 1. (bottom panel). In addition to the 4,6-DMDBT, the fuel contained 4-ethyl-6methyl dibenzothiophene (4-E,6-MDBT) which is even more refractory than the 4,6-DMDBT because of the presence of ethyl group instead of methyl group in the 4th position. The results indicate that the adsorbent is capable of sensing the sulfur compounds from this very dilute feed (feed containing only 45 ppmw of sulfur) and removing them completely (below 1 ppmw) by the surface reaction. The adsorbent has been regenerated by treating with H_2 gas at 500˚C for 1-2 h and then reused for the subsequent run. The breakthrough curves of the regenerated adsorbent in two cycles, also shown in Fig.4, indicate that the adsorption performance can be completely regained by the reductive regeneration.

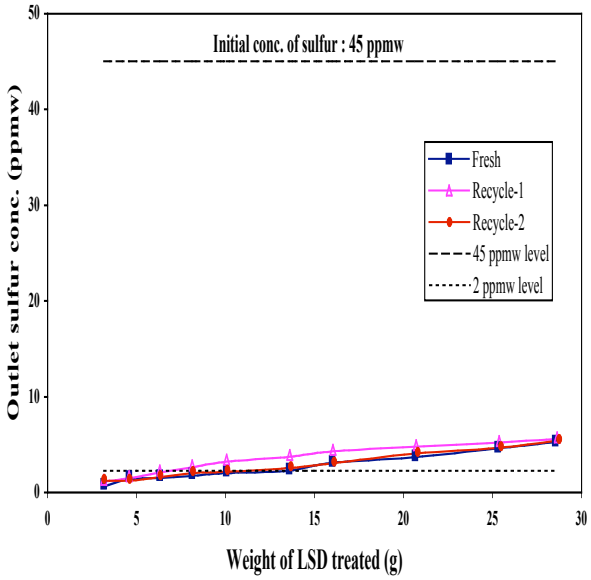

Fig. 4. Breakthrough curves for the adsorptive desulfurization of low sulfur diesel containing 45 ppmw of sulfur over a Ni-based adsorbent at 200˚C. LHSV = 4.8 h^{-1}

Several other adsorbents are currently being evaluated using the "sense and grab" and "sense and shoot" approaches in order to develop highly efficient and regenerable adsorbents for the production of ultra-clean gasoline, diesel and jet fuel for refinery and fuel cell applications and the detailed results will be reported.

Conclusions

New regenerable adsorbents based on zeolites, mesoporous materials, activated carbon, supported metal, etc, are being developed for the selective removal of organic sulfur compounds present in gasoline, diesel and jet fuels using "sense and grab" and "sense and shoot" approaches. In the former approach, certain adsorbents such as metal oxide supported on activated carbon simply grabs the 4,6-DMDBT present in the model diesel fuel at 60˚C and hold it by some weak interactions without chemical reaction. The adsorbed sulfur compound could be recovered by solvent washing and the adsorbent could be completely regenerated for subsequent use. On the other hand, in the sense and shoot approach, the adsorbent such as supported Ni metal, adsorbs the sulfur compounds at elevated temperature. The adsorbed sulfur compounds are decomposed and the remaining organic moiety is added to the fuel. The adsorbent could be regenerated by reductive regeneration at 500˚C using hydrogen gas.

Acknowledgements

This work was supported in part by the US department of Energy and in part by the US department of Defense.

References

(1) Song, C.; Ma, X. *Applied Catalysis B: Environmental*, **2003**, 41, 207; Song, C., *Catalysis Today*, **2002**, 77 (1), 17.
(2) Ma, X.: Sun, L.; Song, C. *Catal.Today*, **2002**, 77, 107.
(3) Irvin R.L. Process for Desulfurizing gasoline and hydrocarbon Feedstocks, U.S. Patent 5730860, 1998
(4) For Philips S-Zorb process, see http://www.fuelstechnology.com/szorbgas.htm
(5) S. Velu, Xiaoliang Ma and Chunshan Song, *Preprint Paper – American Chemical Society,* Division Fuel Chemistry **2002**, *47(2),* 447-448.
(6) Xiaoliang Ma, Michael Sprague, Lu Sun and Chunshan Song, *Preprint Paper – American Chemical Society,* Division Fuel Chemistry **2002**, *47(2),* 452-453.
(7) Gates, B. C.; H. Topsoe, *Polyhedron*. **1997**, 16, 3213.
(8) Ma, X.; Sakanishi, K.; Mochida, I. *Ind. Eng. Chem. Res.* **1996**, 35, 2487.

SYNTHESIS OF HIGH-PERFORMANCE NAPHTHENIC KEROSENE FROM SELECTED REFINERY NAPHTHA FEEDSTOCKS

F.V. Hanson, R. Aggrawal, D. Bhat, J.V. Fletcher, and W. Zmierczak

Department of Chemical & Fuels Engineering, University of Utah
Salt Lake City, Utah 84112

Introduction

A recently developed process for the synthesis of naphthenic kerosene (NK) from selected refinery naphtha feedstocks can provide an opportunity to produce high-performance jet fuel/rocket propellant compositions accommodating the next generation of aircraft, and reusable space access vehicles, which must use the high-temperature performance fuel to cool critical engine components.[1] The process is based on newly elucidated chemistry of naphthenes (alkylated cyclopentanes and cyclohexanes), which embraces several types of the following simultaneously occurring catalytic reactions:[2]

1. Self-condensation (dehydrodimerization and dehydrotrimerization) of alkylcyclopentanes to alkylsubstituted decalins and some alkylsubstituted tricyclic naphthenes, *e.g.*,

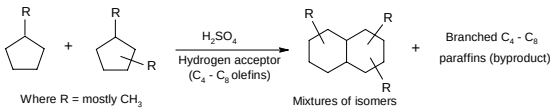

2. Self-condensation (dehydrodimerization) of alkylcyclohexanes to alkylsubstituted bicyclohexyls (dodecahydrobiphenyls), *e.g.*,

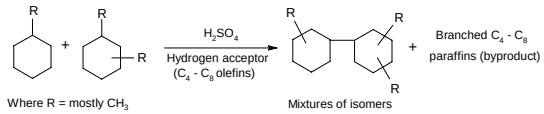

3. Dispersive alkylation of monocyclic napthenes by C_4 - C_8 olefins to polyalkylcyclohexanes, *e.g.*,

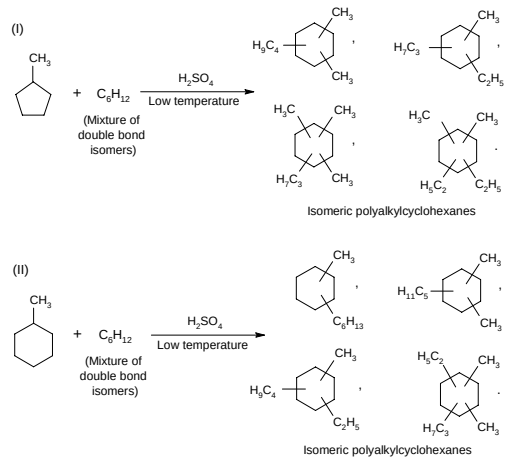

The reactions occur at low temperatures in the presence of concentrated H_2SO_4 as a catalyst and reaction medium. The product obtained contains alkylated bicyclic (and some tricyclic) naphthenes, *i.e.*, alkylated decalins, some alkylated bicyclohexyls, alkylated perhydrophenanthrenes, alkylated hydrindanes, and polyalkylated cyclohexanes. Olefins and sulfur-containing compounds present in the naphthenic reaction mixtures act as hydrogen acceptors. It results in production of highly-branched paraffinic gasoline components as a byproduct and exhaustive hydrodesulfurization.

Experimental

Semi-batch experimental process runs to produce naphthenic kerosene were performed using:

(a) mixtures of two naphthenic model compounds, *i.e.*, methyl cyclopentane (MCP) and methylcyclohexane (MCH) of variable composition, with 1-hexene as olefinic hydrogen acceptor (initial temperature, 7 °C, increasing to 12 ºC; olefin addition rate, 0.3 g/min; molecular naphthenes/olefin ratio, 2.0; total reaction time, 120 minutes; and, H_2SO_4/naphthenes wt ratio, 4); and

(b) refinery naphthene-rich naphthas *i.e.*, heavy virgin naphtha (HVN) and intermediate virgin naphtha (IVN) with olefinic light catalytically cracked naphtha (LCCN) (initial temperature, 7 °C, increasing to 12 °C during the run; LCCN addition rate, 1g/min; calculated molecular naphthenes/olefins ratio, 2.0; total reaction time, 77 minutes ; and, H_2SO_4/naphthenes wt ratio, 4).

The reaction runs were performed in a semi-batch stirred tank reactor system (a three-neck flask), equipped with a mechanical stirrer, a reflux condenser, and a metering pump for introducing the reactants and a remote temperature controlled water bath. A mixture of a liquid catalyst (concentrated H_2SO_4) and the naphthenic component was placed in the reactor, and the olefinic component was added dropwise to the reaction mixture. Contact between the acid phase and the hydrocarbon phase was maintained by vigorous stirring.

Reaction feeds and products obtained were analyzed using a HP-6890 gas chromatograph equipped with an HP-1 capillary column, flame ionization and mass spectrometer detectors. Sulfur analysis was also carried out to determine the feeds and products sulfur content using Horiba sulfur analyzer, SLFA-800.

Results and Discussion

Results of conversions to NK products for relevant model naphthenes (MCP + MCH variable mixtures) and 1-hexene as a hydrogen acceptor in the initial reaction runs are summarized in **Figure 1**.[3]

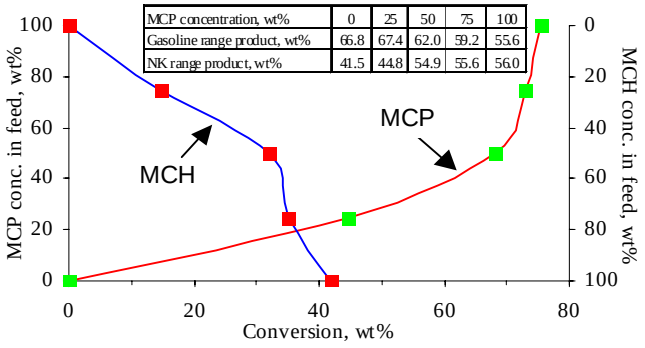

Figure 1. Conversion of MCP and MCH (variable compositions) to naphthenic kerosene range components.

In addition, the table in the figure shows the contents of gasoline and NK fractions (overlapped) in products obtained during the model compounds reaction runs.

Similar (not optimized) runs were performed with refinery naphtha feeds under similar process conditions.[3,4] The chemical type composition of the naphthas, summarized in **Table 1,** in general, indicated their potential suitability for use as feed in the NK process. The only undesirable components were arenes, which undergo undesirable reactions of sulfonation, and alkylation with olefins.

Table 1. Distribution of naphtha components by chemical type

Component type	HVN, wt%	IVN, wt%	LCCN, wt%
Olefins	00.0	00.1	39.2
n-Paraffins	19.6	33.6	01.6
Isoparaffins	19.5	32.5	33.5
Naphthenes	35.6	20.0	09.0
Arenes	25.2	13.2	16.6
Unidentified	00.1	00.6	00.1

Two reaction runs were carried out with the use of naphthene-rich intermediate virgin (HVN) and heavy virgin (IVN) naphthas in combination with olefinic (hydrogen acceptor) light catalytically cracked naphtha (LCCN). The stoichiometric naphthenes/olefins ratio for dehydrodimerization (DHD) reactions in the reaction mixture was determined on the basis of detailed GC/MS analysis of these feeds. The obtained conversions of the naphthenic components in naphtha feeds to NK products, *i.e.*, 25.3 wt% for HVN, and 14.9 wt% for IVN were considerably lower as compared to the model compound runs. Also, reduction in sulfur concentration by ~ 80 wt% was found.[3]

The comparison of the compositions of feeds and reaction products obtained in these runs is summarized in **Figures 2 and 3**.[4] **Figure 2** shows the changes in (overlapped) gasoline (b.p. < 225 ºC) and naphthenic kerosene (b.p. > 150 ºC) range product distributions relative to the feed. The increase in the content of NK range products obtained in the runs with HVN and IVN was 15.3 wt%, and 16.7 wt% respectively. It was mostly due to dehydrodimerization (DHD), dehydrotrimerization (DHT), and dispersive alkylation of naphthenes, and alkylation of arenes.

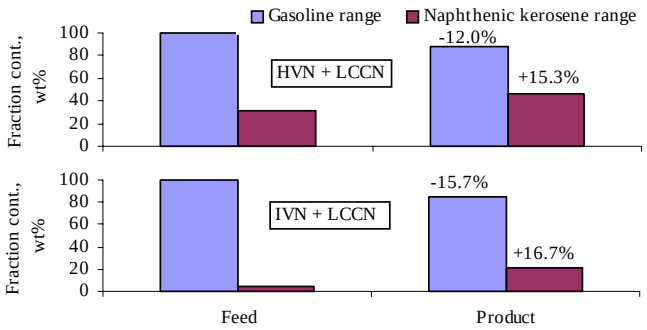

Figure 2. Comparison of the change of gasoline and naphthenic kerosene range fraction distributions in feeds and reaction products obtained in the refinery naphtha runs.

The comparison of feeds and products from the refinery naphtha runs, in terms of chemical type distribution, were obtained by using PIONA (n-paraffins, isoparaffins, olefins, naphthenes and arenes distribution) analysis techniques.[4] The results obtained demonstrated in **Figure 3** show that the olefinic component of LCCN is highly reactive under the process conditions as reflected by the high conversion of olefins in the feed (92 wt% with HVN and 97 wt% with IVN) in DHD, dispersive alkylation of naphthenes, alkylation of arenes, and dimerization.

The total increase in naphthenes was a result of their dispersive alkylation, whereas the increase in branched paraffins was related to hydrogen transfer to LCCN-derived olefin molecules and their concurrent skeletal isomerization. The lower then expected

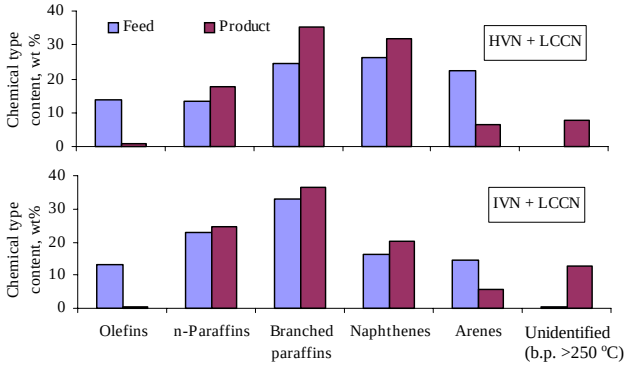

Figure 3. Comparison of the change in different chemical type component distributions in feeds and reaction products obtained in the refinery naphtha runs.

conversions of the naphthenic components in these reaction runs in combination with almost complete conversion of olefins can be ascribed to the competitive reactions of alkylation of arenes and dimerization of olefins, which resulted in reduction of olefinic hydrogen acceptors.

Reduction in concentration of arenes in the reaction mixture was caused by their retention in the sulfuric acid phase.

Conclusions

Studies using model compounds and refinery naphthas have shown the significant conversion of naphthenes to the naphthenic kerosene type compounds simultaneously with an improvement in desirable gasoline fraction properties.

Manipulation of process conditions, *i.e.*, feed to olefin ratios, and H_2SO_4 concentration, temperature, contacting time, *etc.*, and feed composition *via* cut selection and feed pretreatment, can be used to control the conversion of naphthenes and the selectivity of the process toward maximizing high performance naphthenic kerosene products. Virgin naphthas high in naphthenes and low in aromatics are the preferred feedstocks. Cracked naphthas high in olefins are the preferred hydrogen acceptors.

Sulfuric acid is suitable as a catalyst and as a reaction medium provided that aromatics in the feed are low. The sulfur content of the refinery naphthas can be dramatically reduced under the process conditions studied.

Acknowledgements

The authors acknowledge the financial support of BP Air and the Petroleum Research Center at the University of Utah. Professor Joseph S. Shabtai is thanked for many stimulating discussions related to the chemistry of the process.

References

1. Lander, H.R., Maurice, L.Q., Harrison, W.E. III, and Edwards, T., Proc. of XIV Int. Symp. on Air Breathing Engines (ISABE), Paper IS-253, Florence, Italy, **1999**.
2. Shabtai, J., Zmierczak, W., and Tsai, C.H., Proc. of XIV Int. Symp. on Air Breathing Engines (ISABE), Paper IS-7070, Florence, Italy, **1999**.
3. Aggrawal, R., M.S. Thesis, University of Utah, **2003**.
4. Bhat, D., M.S. Thesis, University of Utah, **2003**.

OXIDATIVE DESULFURIZATION OF DIESEL FUELS BY MOLECULAR OXYGEN

Satoru Murata, Kazutaka Murata, Koh Kidena, and Masakatsu Nomura

Department of Applied Chemistry, Faculty of Engineering, Osaka University, 2-1 Yamada-oka, Suita, Osaka 565-0871, Japan

Introduction

Deep desulfurization of petroleum-derived fuels is nowadays the most important technology in petroleum industry. Sulfur-containing compounds in the fuels are converted to sulfur oxide, *i.e.* SOx, during their combustion. Therefore, amounts of *S*-compounds were strictly limited. For example, regulation of sulfur amounts in diesel fuels in Japan is 500 wtppm, and the value will be reduced to 50 wtppm in 2005 and 10 wtppm in 2008. Petroleum-refining and catalyst-making companies, therefore, are trying to develop new and efficient desulfurization processes and highly active catalysts.

In 1990s, an epoch making process was proposed, *so-called*, oxidative desulfurization (ODS). ODS consists of two processes: the former one is oxidation of sulfur-containing compounds in feeds and the latter is removal of oxidized *S*-compounds from the feeds. ODS has several advantages compared with a classical hydrodesulfurization process: (1) reaction conditions are very mild such as ambient pressures and temperatures, (2) there are high potentials for desulfurization of sterically hindered thiophene derevatives, and (3) expensive hydrogen is not required. Oxidants examined were peroxyacetic acid, hydrogen peroxide-acetic or formic acids, hydrogen peroxide-polyoxometalte, etc.[1] Photoirradiation of DBT in the presence of sensitizer or catalyst under molecular oxygen was also examined.[2] The authors are very interested in oxidation with peroxy carboxylic acids, because reaction proceeds rapidly and selectively. However, large scale-storage and usage of peroxide are somewhat dangerous.

Transition metal-catalyzed co-oxidation of aldehydes and organic substrates with molecular oxygen may solve the above problems. Co-oxidation of aldehydes and alkenes are well known, and extensively studied by several authors. The reaction is believed to proceed *via* two steps, autoxidation of aldehydes to peroxy acids and oxidation of alkenes to oxyranes by peroxy acids produced *in situ* (**eq .1**).[3]

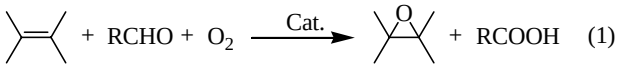

(1)

Therefore, the authors examined the co-oxidation of aldehydes and *S*-containing compounds such as dibenzothiophene (DBT) by molecular oxygen to develop a new system for deep desulfurization of petroleum-derived fuels.

Experimental

Typical procedure for oxidation of model compounds was as follows: A mixture of cobalt(II) acetate (0.05 mmol), *n*-octanal (4 mmol), DBT (1 mmol), and benzene (10 mL) was stirred at 40 ^{o}C under ambient pressure of oxygen. Time-profiles of DBT conversion was monitored by gas chromatographic analysis.

Results and Discussion

A benzene solution of DBT was employed for model of diesel fuels. A mixture of benzene, cobalt acetate, DBT, and *n*-octanal was stirred at 40 ^{o}C for 15 min under ambient pressure of oxygen, DBT being oxidized to the corresponding sulfone in an almost quantitative yield (**eq. 2**, R=*n*-C_7H_{15}).

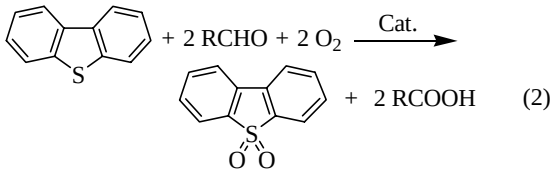

(2)

In order to check the stoichiometry of this reaction, the following experiments were conducted: A benzene solution containing cobalt acetate (0.05 mmol), DBT (1 mmol), and *n*-octanal (1 mmol) was stirred at 40 ^{o}C for 15 min under oxygen, GC-analysis of the products indicating formation of 1 mmol of *n*-octanoic acid and 0.5 mmol of DBT sulfone, and recovery of 0.5 mmol of DBT. In the absence of either cobalt catalyst or aldehyde, the reaction did not proceed and DBT was recovered almost quantitatively. These results indicate that the stoichiometry of the reaction obey the **equation 2**.

Several metal salts and aldehydes were examined as catalysts and sacrificial materials for this reaction, respectively, the results being summarized in **Table 1**. This indicates that both cobalt(II) acetate and chloride are the most suitable catalysts among the metal salts employed and aliphatic aldehydes with 6-10 carbons and benzaldehyde could be used instead of *n*-octanal.

Table 1. Oxidation of DBT with molecular oxygen in the presence of several transition metal salts and aldehydes.

Metal salt	Aldehyde	Conv. of DBT (mol%)
$Co(OAc)_2$	*n*-octanal	> 99
$CoCl_2$	*n*-octanal	> 99
$Mn(OAc)_2$	*n*-octanal	> 99
$Ni(OAc)_2$	*n*-octanal	54
CuCl	*n*-octanal	35
none	*n*-octanal	0
$Co(OAc)_2$	*none*	0
$Co(OAc)_2$	*n*-hexanal	> 99
$Co(OAc)_2$	*n*-decanal	96
$Co(OAc)_2$	benzaldehyde	93
$Co(OAc)_2$	cinnamaldehyde	0

Then, the authors tried to desulfurization of commercial diesel oil by this method. The commercial oil (100 mL) was treated with cobalt acetate (0.1 mmol) and *n*-octanal (16 mmol) at 40 ^{o}C for 16 h under oxygen. Oxidized *S*-compounds were removed from the feed by adsorption with alumina. Concentration of sulfur could be reduced from 193 wtppm (in the original feed) to <5 wtppm by these treatments. The results may indicate that this brand-new ODS process has a potential to meet a future regulation of sulfur in the diesel fuel.

Acknowledgements. The authors thank Dr. Ikushima (Petroleum Energy Center, Japan) and Mr. Nagai (Taiyo Oil Co., Ltd.) for their helps concerning analysis of sulfur contents in the oils.

References.

(1) Aida, T. Yamamoto, D. *Prepr. Pap.-Am. Chem. Soc., Div. Fuel Chem.* **1994**, *39*, 623; Babich, I. V.; Moulijn, J. A. *Fuel* **2003**, *82*, 607.

(2) Hirai, T.; Ogawa, K.; Komasawa, I. *Ind. Eng. Chem. Res.* **1996**, *35*, 586; Matsuzawa, S.; Tanaka, J.; Sato, S.; Ibusuki, T. *J. Photochem. Photobiol.* **2002**, *149*, 183.

(3) Kholdeeva, O. A.; Grigoriev, V. A.; Maksimov, G. M.; Fedotov, M. A.; Golovin, A. V.; Zamaraev, K. I. *J. Mol. Catal. A*, **1996**, *114*, 123; Nam, W.; Kim, H. J.; Kim, S. H.; Ho, R. Y. N.; Valentine, J. S. *Inorg. Chem.* **1996**, *35*, 1045; Komiya, N.; Naota, T.; Oda, Y.; Murahashi, S.-I. *J. Mol. Catal. A*, **1997**, *117*, 21.

NOVOZYM435 -CATALYZED TRANSESTERIFICATION OF SOYBEAN OIL FOR BIODIESEL PRODUCTION IN A SOLVENT-FREE MEDIUM

Wei Du, Yuan-yuan Xu, De-hua Liu*

Department of Chemical Engineering, Tsinghua University, Beijing 100084, P. R. China

Biodiesel, generally classified as fatty acid alkyl esters, has become more attractive recently because of its environmental benefits. Although biodiesel has been successfully produced chemically at present, there are several associated problems to restrict its development, such as glycerol recovery and removal of inorganic salt. The disadvantages caused by chemical catalysts are largely prevented by using lipases as the catalysts and enzymatic production of biodiesel fuel has drawn considerable attention in recent years.

For large-scale production of biodiesel, the repeated use of lipase is one of the major issues. In this paper, effects of some key issues (such as temperature, alcohol/oil ratio, glycerol removal etc.) on the enzymatic reaction during biodiesel production have been studied and within the optimized conditions, lipase expressed good stability in continuous batch operation in the production of biodiesel.

Effect of temperature, oil/alcohol molar ratio and by-product glycerol were studied during Lipozyme TL IM-catalyzed continuous batch operation when short chain alcohols used as the acyl acceptor. In non-continuous batch operation, the optimal oil/alcohol ratio and temperature were 1:4 and 40℃-50℃; however, during the continuous batch operation, the optimal oil/alcohol ratio and temperature were 1:1 and 30℃ respectively; 95% of enzymatic activity remained after 10 batches when iso-propanol adopted to remove by-product glycerol during repeated use of the lipase.

Effect of glycerol

Enzymatic transesterification of renewable oil with short chain alcohols as acyl acceptor for biodiesel production has been studied extensively in recent years. However, with these short chain alcohols as the acyl acceptor, glycerol, as one of the major by-products, has been demonstrated to have some serious negative effect on enzymatic activity. During the repeated use, lipase lost its activity dramatically which mainly due to the negative effect of glycerol.

Some hydrophilic organic (propanol, iso-propanol, butanol, tert-butanol) have been tried to remove glycerol during the repeated use of lipase and iso-propanol has been found to be the most effective for glycerol removal.

Operational stability with glycerol removal by iso-propanol

The operational stability of lipase with glycerol removal by iso-propanol has been studied further in this paper and lipase expressed good operational stability. There was no observable loss of lipase activity after 10 batches of continuous operation.

Effect of molar ratio of methanol / oil

It is well known that excessive short-chain alcohols such as methanol might inactivate lipase seriously. However, at least three molar equivalents of methanol are required for the complete conversion of the oil to its corresponding ME and effect of molar ratio of oil/methanol has been studied comparatively during batch and continuous batch operation.

In batch operation the highest ME yield (92 %) could be obtained at methanol/oil molar ratio 4:1. Either higher methanol concentration (5:1) or lower methanol concentration (3:1) would decrease ME yield to some degree.

However, it has been demonstrated that during the continuous process, lipase lost its activity dramatically at methanol/oil molar ratio 4:1 and effect of methanol/oil ratio on enzymatic activity was studied further in continuous batch operation. The optimal molar ratio of methanol/oil was 1:1 in continuous batch operation, at which lipase remained relatively high activity.

Effect of temperature

Effect of temperature on enzymatic transesterification of soybean oil was examined at the range from 30℃ to 50℃ in batch operation and high temperature resulted in relatively high ester yield. However, it has also been found that when temperature is above 50℃, enzyme loses its activity dramatically. So in batch process, 40-50℃ is optimal for enzymatic biodiesel production.

However, in continuous batch operation, it has been demonstrated that higher temperature resulted in larger loss of lipase activity and 30℃ is optimal by taking into lipase stability and activity into consideration.

It has been demonstrated that temperature, methanol/oil molar ratio and glycerol have varied effect on lipase-catalyzed transesterification of soybean oil during batch and continuous batch operation of biodiesel production. Within the optimized conditions, lipase remained high activity after continuous batch operation which demonstrates that enzymatic transesterification of renewable oil is very promising for large-scale production of biodiesel.

ENZYMATIC CONVERSION OF WASTE OIL TO BIODIESEL IN A SOLVENT-FREE SYSTEM

Hong Wu, Min-hua Zong, Qian Luo, and Hua-chang Wu*

Biotechnology Department, South China University of Technology, Guangzhou 510640, P. R. China
*****Author for correspondence (Fax: 86-20-87112979; E-mail: btmhzong@scut.edu.cn)

Introduction

Production of biodiesel from vegetable oil and animal fats has drawn more and more attention because of the increasing awareness of environmental pollution and short supply of fossil fuels. Presently, the industrial-scale production of biodiesel is performed chemically, using alkali as catalyst. However, there are several problems with this process, such as excessive methanol requirement, high energy demanding, difficulties in glycerol recovery, disposal of fatty acid alkaline salts (soaps) creating other environmental concerns. Thus enzymatic alcoholysis of triacylglycerols (TAG) seems to be a promising alternative because of its mild reaction conditions, easy recovery of glycerol and being free of chemical wastes.

Several studies on lipase-catalyzed alcoholysis of vegetable oils and animal fats with primary and secondary alcohols in a solvent or a solvent-free system have been reported.[1-3] Owing to the toxicity and flammability of organic solvents, and the easiness of product recovery, enzymatic alcoholysis in a solvent-free system is preferable.

Immobilized *Candida Antarctica* lipase was found to be the most effective for the methanolysis of oil and fats.[4,5] However, its cost is prohibitively high for this purpose. In this paper, some efforts have been made to explore the possibility to use a relatively cheap lipase from *Thermomyces lanuginosus*, commercially called Lipozyme TL IM for biodiesel production.

Experimental

Materials. Waste oil was provided by restaurant in South China University of Technology, CRL (lipase from *Candida Rugosa*), myristic acid methyl ester, palmitic acid methyl ester, steric acid methyl ester, oleic acid methyl ester, linoleic acid methyl ester, linolenic acid methyl ester and heptadecanoic acid methyl ester were purchased from Sigma (USA), Novozym 435 (lipase from *Candida Antarctica*), Lipozyme TL IM (lipase from *Thermomyces lanuginosus*) and Lipozyme RM IM (lipase from *Rhizomucor miehei*) were kindly donated by Novo Nordisk Co. (Denmark). All other chemicals were obtained commercially and of analytical grade.

Reaction. The methanolysis of waste oil was carried out at 35℃, 130rpm using 10% immobilized lipase based on oil weight. The four-step reaction was conducted as follows. The mixture of the first-step reaction contained 10g of oil and 1:1 molar equivalent of methanol. The second-, third- and fourth-step reactions were initiated by adding 0.8:1 molar equivalent of methanol upon 90% conversion of methanol to methyl esters.

Analysis. The methyl ester (ME) content in the reaction mixture was assayed with a HP4890 gas chromatography equipped with a HP-5 capillary column (0.53mm×15m) using heptadecanoic acid methyl ester as an internal standard. The column temperature was hold at 180℃ for 1 min, raised to 186℃ at 0.8℃/min and kept for 1 min, then upgraded to 280℃ at the rate of 20℃/min.

Results and Discussion

As shown in **Table 1,** Novozym 435, Lipozyme TL IM and Lipozyme RM IM could all catalyze the reaction effectively. Lipozyme TL IM is the cheapest among them and was used for further study.

Table 1 Effect of different lipases on methanolysis of waste oil

Enzyme	ME content(%)	Methanol conversion(%)
Lipozyme TL IM	32.2	96.7
Lipozyme RM IM	32.4	97.3
Novozym 435	33.1	99.4
CRL	1.2	3.5

10g waste oil, methanol/oil molar ratio1:1, 10% lipase based on oil weight, 130rpm, 40℃, 24h.

As can be seen in **Figure 1**, the conversion dropped sharply when more than 1.5 molar equivalents of methanol were present initially in the oil mixture, suggesting the severe inactivation of the enzyme. The lipase has been proved to be irreversibly inactivated by transferring it into the fresh substrates (methanol/oil 1:1,mol/mol) and following the methanolysis course, which was in good agreement with Shimada's report.[6]

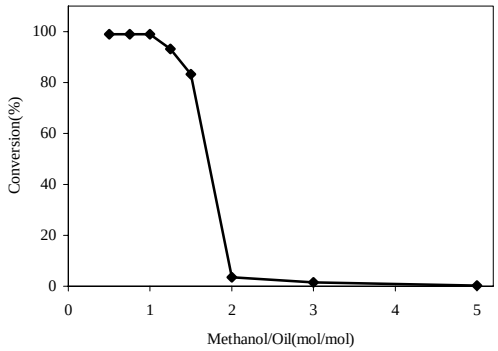

Figure 1. Effect of methanol/oil molar ratio on methanolysis of waste oil. 10g waste oil, 10% Lipozyme TL IM based on oil weight, 130rpm, 40℃, 30h. The conversion was expressed as the percentage of methanol consumed for the formation of ester (when the molar ratio of methanol /oil was less than 3), and as the ratio of methyl ester to the oil (when the molar ratio of methanol /oil was more than 3).

The influence of enzyme quantity on the methanolysis of waste oil was presented in **Figure 2**. It has been found that ME content was increased by increasing lipase quantity up to 10% based on oil weight. The conversion reached 24.7% after 12h reaction with 10% of the lipase. Interestingly, only 22.7% of waste oil was converted to its corresponding methyl esters in 12h in spite of the highest initial reaction rate with 12% enzyme. This may be explained by the observable aggregation of the immobilized enzyme at high concentration (>10% based on oil weight), which led to a lower enzymatic activity due to a higher mass transfer limitation.

Figure 3 shows temperature effect on the reaction. When the temperature was below 40℃, the reaction could be improved by raising temperature. Further increase in temperature, however, resulted in a lower ME content in the reaction mixture, indicating the inactivation of the enzyme by high temperature, which was confirmed by the low conversion of waste oil to methyl ester in the case of reusing the enzyme for the conversion of fresh substrates (methanol/oil 0.75:1, mol/mol) at 35℃.

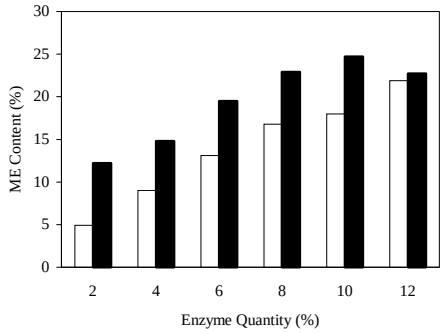

Figure 2. Effect of enzyme quantity on methanolysis of waste oil. 10g waste oil, methanol/oil molar ratio 0.75:1, 130rpm, 40℃. □, ester content upon 1h incubation; ■, ester content upon 12h incubation.

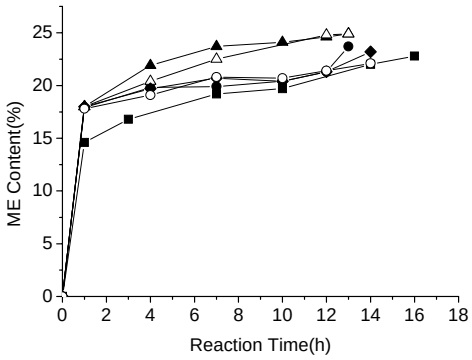

Figure 3. Effect of temperature on methanolysis of waste oil. 10g waste oil, methanol/oil molar ratio 0.75:1, 10% Lipozyme TL IM based on oil weight, 130rpm. ■,25℃;●,30℃;▲,35℃;△,40℃;◆,45℃;○,50℃.

Enzymatic methanolysis of waste oil at different shaking speed ranging from 100 to 220rpm was performed and the result showed that there was no observable difference in ME content and methanol was nearly completely converted to esters in 12h over the range from 130 to 180rpm. However, above 180rpm, little increase in reaction rate was observed with further increase in shake speed, but less ME was formed (only 22.1% in 12h at 220rpm). This was due to enzyme inactivation by higher shearing stress as indicated by the low ME content when the enzyme was reused for the methanolysis of fresh substrates (methanol/oil 0.75:1, mol/mol) at 130rpm.

At least 3 molar equivalents of methanol are required for the complete conversion of waste oil to its corresponding ME. The lipase, however, will be significantly inactivated in a mixture with more than 1 molar equivalent of methanol. Hence, a stepwise adding of methanol is necessary. The optimum substrate molar ratio (methanol/oil) was found to be 3.4:1(data not shown). The typical reaction time course was shown in **Figure 4** (with total methanol/oil molar ratio being 3.4:1). For the first-step reaction, 12h incubation (methanol/oil 1:1, mol/mol) gave a 31.9% ME content. The second step was initiated by adding methanol (with methanol/oil molar ratio being 0.8:1) into the reaction system when the incubation has lasted for 24h. The ME content reached 52.4% in 12h (total 36h). Then followed by the addition of the third batch of methanol (with methanol/oil molar ratio being 0.8:1) at the end of the second step which proceeded for 24h. The ME content reached 71.1% after incubation for another 14h (total 62h). The fourth batch of methanol (with methanol/oil molar ratio being 0.8:1) was added 10h later. The conversion of waste oil to its corresponding ME was as high as 90.2% when the incubation went on for 96h, demonstrating the effectiveness of Lipozyme TL IM, a lipase with 1,3-specificity, for biodiesel production. Acyl migration from *sn*-2 to *sn*-1 or *sn*-3 position might account for this. The similar phenomenon has also been observed by some other researchers.[7] To shorten the reaction time, the four-step procedure was modified as follows: the reaction was initiated by adding 10% immobilized enzyme (based on oil weight) into a mixture of methanol and oil (1:1, mol/mol), followed by feeding methanol three times (methanol/oil 0.8:1, mol/mol) at 12h, 24h and 38h, respectively. This four-step process converted more than 90% of the oil to its corresponding methyl esters.

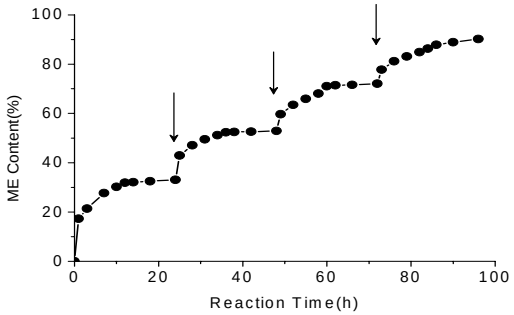

Figure 4. Reaction time course for methanolysis of waste oil. 10g waste oil, 0.38g methanol (methanol/oil molar ratio 1:1), 10% Lipozyme TL IM based on oil weight, 130rpm, 35℃. Methanol was fed three times (0.30g each) upon incubation for 24, 48 and 72h as indicated with arrows.

Conclusion

Immobilized enzyme from *Thermomyces lanuginosus*, commercially called Lipozyme TL IM showed high activity in methanolysis of waste oil. A four-step process with stepwise feeding of methanol was efficient for the conversion of waste oil to its corresponding methyl esters and so are potential for biodiesel production from waste oil.

References

1. Steinke, G.; Kirchhoff, R.; Muknerjee, K. D., *J. Am. Oil Chem. Soc.*, **2000**, *77*, 361-366
2. Watanabe, Y.; Shimada, Y.; Sugihara, A.; Tominaga, Y., *J. Am. Oil Chem. Soc.*, **2001**, *78*, 703-707
3. Watanabe, Y.; Shimada, Y.; Sugihara, A.; Noda, H.; Fukuda, H.; Tominaga, Y., *J. Am. Oil Chem. Soc.*, **2000**, *77*, 355-360
4. Shimada, Y.; Watanabe, Y.; Sugihara, A.; Tominaga, Y., J. *Mol. Catal. B: Enzym.*, 2002, *17*, 133-142
5. Köse, Ö.; Tüter, M.; Aksoy, H. A., *Bioresour. Technol.*, 2002, *83*, 125-129
6. Shimada, Y.; Watanabe, Y.; Samukawa, T.; Sugihara, A.; Noda, H.; Fukuda, H.; Tominaga, Y., *J. Am. Oil Chem. Soc.*, **1999**, *76*, 789-792
7. Kaieda, M.; Samukaw, T.; Matsumoto, T.; Ban, K.; Kondo, A.; Shimada, Y.; Noda, H.; Nomoto, F.; Ohtsuka, K.; Izumoto, E.; Fukuda, H., *J. Biosci. Bioeng.*, 1999, *88*, 627-631

COULD SIMULATION BE VALUABLE CRITERIA FOR EVALUATION OF STERICAL COAL STRUCTURE?

Masakatsu Nomura[1], Satoru Murata[1], Tiaoling Dong[1], Koh Kidena[1], Takenao Ohkawa[2], and Hisanori Komoda[2]

[1] Department of Applied Chemistry, Faculty of Engineering, Osaka University, 2-1 Yamada-oka, Suita Osaka 565-0871, Japan
[2] Graduate School of Information Science and Technology, Osaka University, 2-1 Yamada-oka, Suita Osaka 565-0871, Japan

Introduction

Recently Mathews *et al*. proposed the model structures for Upper Freeport and Lewiston-Stockton coals (Argonne premium coal), where dimethylene bridge bonds prevail as bond connecting aromatic clusters [1]. This seems not to be true for the authors because ruthenium ion catalyzed oxidation (RICO) showed the distribution of bridge bonds clearly [2], however, their evaluation for this is not to reflect the results of RICO in a precise way. Evaluation of physical density of model structures using computer simulation is now considered a valuable means to justify the models. For example, the very sophisticated model of oil sand bitumen derived asphaltene proposed by Strausz *et al*. [3] should be fragmented into several parts based on evaluation of its density by simulation. Therefore, the calculation of density of models is a very facile method to justify the model. Carlson [4], Takanohashi [5], and the authors [6-9] have been involved in studying this objective. Another point as for coal chemical structures two phase model and uniphase model such as association structure are proposed by many researchers to fail in getting a conclusion. The authors would like to consider the possibility, in the present paper, concerning whether the simulation method could be the means to discriminate above two concepts for coal structures.

Method

Evaluation of density of coal model. The calculation of physical density of the model molecules was conducted by using the computer-aided molecular design software, Cerius[2] (Molecular Simulations, Inc.) on a Silicon Graphics workstation. The method for the calculation was also essentially the same with the published procedure [6-8]. The procedure is briefly described. At first, a model molecule is input and the calculation of molecular mechanics together with charge modification is carried out to optimize its potential energy until the root-mean-square (rms) gradient becomes less than 1.0. The model is then subjected to the combined calculations of molecular dynamics and mechanics. Among the conformers examined during the calculation, one with the lowest potential energy is extracted. Subsequent molecular mechanics treatment until the rms gradient becomes less than 1.0 gives the optimized single isolated model molecule. It is then enclosed in a cell and its molecular mechanics treatment is carried out under periodic boundary conditions until the rms gradient reaches less than 1.0. Under the conditions the model molecule is surrounded by the identical cells. The molecule can extend to other cells. If a segment of it exits from one surface of the cell, the same segment of another molecule enters from the opposite surface. Thus, in this approach intermolecular interactions and void volume can be taken into consideration. During the treatment, the size of the cell is gradually decreased. After that, the combined calculations of molecular dynamics and mechanics for 10 ps are performed to afford a temporally best conformer, which is again subjected to the molecular mechanics calculation as above. After several repetitions of these calculations, the final best conformer is obtained together with the optimized density.

New method to construct structural model of coal (Density-oriented construction). The authors propose a density-oriented method to construct coal molecular models using a computer. In this method, basically, a partial model is at first constructed incrementally by connecting an aromatic fragment (a cluster) with other one (first iteration) or a further model (second or later iteration) one by one using bridge bonds, and finally a whole model of coal molecular structure is derived. In order to generate a reasonable model with an approximate value of the measured density, an aromatic fragment is connected in such a way as the empty space of the partial model is filled with this aromatic fragment, because till now MM and MD methods using a polymeric coal structure seems to fail in getting a reasonable value of its physical density. MM and MD methods seem not to be proper in obtaining the density value close to its observed value. The method proposed here is one of approaches to overcome this shortcoming of the methodology studied so far. In order to detect such empty spaces efficiently, the lattice model is introduced. Figure 1 shows the general flow of the coal-structural-model construction suing the lattice model. The aromatic fragment that can be boxed in the empty lattice space is located and connected to the partial model.

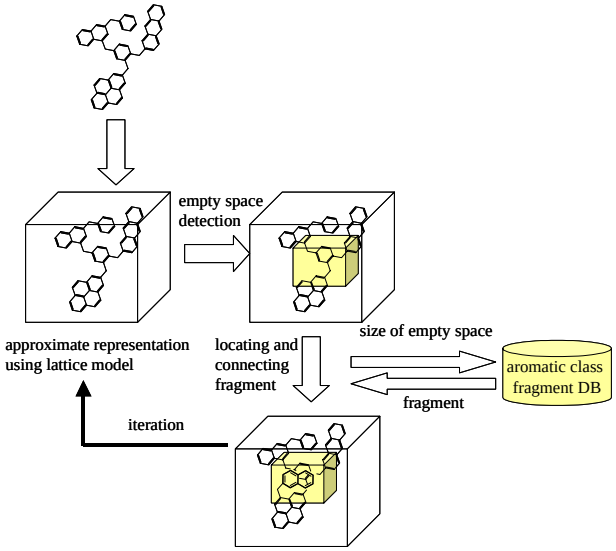

Figure 1. General flow of coal structure model construction using the lattice model.

Results and Discussion

Preference of uniphase model for density calculation. The authors have been studying coal model structures based on very many valuable data about coal organic materials. Solvent refined coal (SRC) is a very appropriate sample for analyzing its chemical constituents so that at our early stage of these studies the authors focused on the pyrolytic technique and solid state ^{13}C-NMR measurements of solubles because SRC showed very high solubility toward conventional solvent such as hexane and benzene, this indicating the fragments are relatively small due to heat treatment. In 1992 the authors proposed the fragments of Akabira coal (typical Japanese bituminous coal) and without the detailed information about the bridge bonds the authors proposed a possible coal model structure [10]. Conclusively this model lacked the quantitativeness about the ratio of aliphatic carbons to aromatic carbons because at that time NMR measurements gave only qualitative data. According to the

recent quantitative data, researchers can propose very adequate data about the above ratio [11]. Following new method proposed here is going to handle these data for the evaluation of the density of the model structure later.

As for the calculation of the density, Takanohashi *et al*. succeeded in giving very proper value of density for Zao Zhuang coal [5], where the aromatic clusters stack each other so effectively. This can be done by considering relatively small fragments of coal. Their method is the same means the authors employed because the authors have been collaborated each other so far. The details are already described at *Experimental section*.

In this method the smaller the fractions become the closer the calculated density become to the observed value. In the course of studying the calculation of the density of models the authors found that fragments can be so closely arranged when they are smaller to results in higher density. Density obtained according to the calculation can not exceed the observed value.

Density-oriented construction of coal model. The method described here was developed with the collaboration with Ohkawa and Komoda of Graduate School of Information Science and Technology of Osaka University. This method is very unique in attaining as higher density as possible. The fragments of coal should be at first determined so that the authors employed fragments proposed for Akabira coal [10], however, this fragments are not quantitative in terms of the ratio of aliphatic carbon and aromatic carbon. Less amounts of aliphatic carbons are recommended, however, the use of fragments in original paper seems not to be so serious because this method is based on the following concept: In order to attain the higher density, the fragments should be packed as closely as possible. The method is to put the fragment in a space of similar volume to that of fragment and this process is repeated to connect each fragment by adequate bridge bonding. The result was shown in Table 1. The authors finally reached the value of 1.27 g/cm^3. This value is very similar to the observed value of original coal. In this case the fragments can be connected each other to form high molecular weight. This means that the present method can not discriminate the difference between the two phase model and uniphase model. Simulation model at first was expected to give a possible means to discriminate two structural models, however, it was found that new method the authors developed was found not to become the means to solve the issue concerning associative structure of coal or two phase model structure.

Conclusion

Association structure of coal has been proposed by several researchers and a solvent system such as *N*-methyl-2-pyrrolidinone/carbon disulfide gave very high extraction yields for several coals. On the other hand, even this active binary solvent can give only very low values of extraction yield with other many coals. For these latter coals, the proposed density-oriented construction of coal model could be valuable to show reasonable density values. For a limited number of coals with high solvent extraction yield the concept of association structure of coal seems to be prevailing, however, even with these coals RICO reaction strongly indicated the presence of bridge bonds in a similar amount to other coals, where solvent extraction yields are very small. This tendency concerning bridge bonds between the former coals (high extraction yield) and the latter coals (low extraction yield) are considered to be a kind of contradiction, because bridge bonds are considered to be less with the former coals. From the combination viewpoints of density simulation of coal and the distribution of bridge bonds two phase structure concept still seems to be able to clarify the contradiction above mentioned in a reasonable way. The former coal is the extreme case of this concept and the later coal is the other extreme case.

Table 1. Evaluation of method.

Method	Density (g/cm^3)	Calculation time (min)
Measured value	1.28	-
Comics	0.97	180
Proposed method	1.27	7

References

(1) Mathews, J. P.; Hatcher, P. G.; Scaroni, A. W. *Energy Fuels* **2001**, *15*, 863.
(2) Nomura, M.; Kidena, K.; Matsumoto, K.; Murata, S.; *Proceedings of the 19th Annual Pittsburgh Coal Conference*, Sep. 23-27, **2002**, Pitsburgh, PA, USA.
(3) Mojelsky, T. W.; Ignasiak, T. M.; Frakman, Z.; McIntyre, D. D.; Lown, E. M.; Montgomery, D. S.; Strausz, O. P. *Energy Fuels* **1992**, *6*, 83.
(4) Carlson, G. A. *Energy Fuels* **1992**, *6*, 771.
(5) Nakamura, K.; Takanohashi, T.; Iino, M.; Kumagai, H.; Sato, M.; Yokoyama, S.; Sanada, Y. *Energy Fuels* **1995**, *9*, 1003.
(6) Nakamura, K.; Murata, S.; Nomura, M. *Energy Fuels* **1993**, *7*, 347.
(7) Murata, S.; Nomura, M.; Nakamura, K.; Kumagai, H.; Sanada, Y. *Energy Fuels* **1993**, *7*, 472.
(8) Dong, T.; Murata, S.; Miura, M.; Nomura, M.; Nakamura, K. *Energy Fue*ls **1993**, *7*, 1123.
(9) Ohkawa, T.; Sasai, T.; Komoda, N.; Murata, S.; Nomura, M. *Energy Fuels* **1997**, *11*, 937.
(10) Nomura, M.; Matsubayashi, K.; Ida, T.; Murata, S. *Fuel Process. Technol*. **1992**, *31*, 169.
(11) Love, G. D.; Law, R. V.; Snape, C. E. *Energy Fuels* **1993**, *7*, 639.

INTEGRATED KINETIC MODELING C KMT AND ITS APPLICATIONS

M. T. Klein, and Wei Wei

Chemical & Biochemical Engineering Department,
Rutgers University
98 Brett road c252, Piscataway, NJ 08854
Fax: 732-445-5724, weiw@rci.rutgers.edu,
mtklein@email.eng.rutgers.edu

A chemical engineering approach for the rigorous construction, solution and optimization of detailed kinetic models is described. This approach is based on the Kinetic Modeler's Toolbox (KMT) software package. Many important modeling functionalities and features are implemented in the KMT, including the Equation Building and Editing, Model Calibration, Target Estimation, Catalyst Deactivation, and Catalyst Activity Promotion.

The spreadsheet-based user interface provides a step-by-step model building strategy under a rigorous engineering framework and can help the user develop full-featured kinetic models from only a set of reaction pathways. This tool thus allows scientists and engineers to focus on the fundamental chemistry and underlying kinetics while shifting the bookkeeping and coding burden to the software.

The KMT package has by now been used successfully to develop many kinetic models, including examples in the broad categories of biological-environmental reactions, hydrocarbon reforming, dehydrogenation and oxidation processes, and thermal and catalytic cracking reaction systems. This work focuses on the kinetic modeling of Naphtha Reforming process using the KMT NetGen was used to automatically construct the reaction network for reforming reactions. CodeGen was used to generate the final mathematical equations for the model.

Important functionalities, including model calibration, target evaluation, catalyst deactivation due to coking, were also automatically implemented into the model. The Linear Free Energy Relationship (LFER) concept was used to organize and evaluate the kinetic parameters. Other models for the selective oxidation of hydrocarbons, refinery unit process models and biology-based toxicology kinetic models were also developed using the KMT approach. The simulation results are shown to compare favorably with literature data.

ChemNet™ CFD POST-PROCESSING FOR P. F. FLAME STRUCTURE AND EMSSIONS

Stephen Niksa and Guisu Liu

Niksa Energy Associates, 1745 Terrace Drive, Belmont, CA 94002, neasteve@pacbell.net

Introduction

Since the mid-1980's, simulations of coal-fired utility furnaces based on computational fluid dynamics (CFD) have been used to troubleshoot operational problems, forecast emissions, and expedite design changes such as retrofitting with low-NO_X burners and overfire air injection[1]. Simulations are now routinely tuned-in to measured exhaust NO_X emissions for any furnace firing configuration with low-NO_X or circular burners. The best case studies satisfy evaluations with measurements from various power stations firing an assortment of coals[2].

The rudimentary chemistry in CFD furnace simulations has proven to be adequate for predicting exhaust NO_X emissions across the normal operating range of utility boilers, which is limited. But it is too simple to connect to any fuel properties so a multitude of model parameters must be adjusted for every new fuel to forecast emissions in fuel switching or co-firing scenarios. One obvious remedy would be to incorporate more chemistry into the CFD reaction submodels, but the progress in this direction during the past decade has been almost imperceptible. The current benchmark on chemical complexity in CFD furnace simulations is the reduced mechanism of seven reactions among six species used to represent thermal De-NO_X in the upper elevations of a pilot-scale furnace[3], which pales in comparison to the tens of species and hundreds of reactions that are actually involved in coal-nitrogen conversion in pulverized fuel (p. f.) flames. Fact is, it is not possible to incorporate elementary reaction mechanisms with even the most rudimentary turbulent mixing and dispersion submodels, and this situation is not expected to change in the foreseeable future.

The means to exploit the advantage of realistic reaction mechanisms in coal combustor simulations are now evident in the literature[4-7]: Ignore the turbulence/chemistry interactions and use equivalent networks of idealized reactor elements to depict only the bulk flow patterns. This single premise enables the most advanced coal reaction submodels and elementary reaction mechanisms to be incorporated into furnace simulations, without approximation. One immediate advantage is that almost all reaction rate parameters can be specified from the coal properties or independently assigned from fundamental kinetics work. So fuel quality impacts will be apparent in the simulations. This aspect is emphasized here with performance evaluations with test data from lab-, pilot-, and full-scale pulverized fuel (p. f.) flames.

Computer Simulations

Overview of CNPP. Our "ChemNet™ Post-Processing (CNPP)" method first generates an equivalent network of idealized reactor elements from a conventional CFD simulation. The reactor network is a computational environment that accommodates realistic chemical reaction mechanisms; indeed, mechanisms with a few thousand elementary chemical reactions can now be simulated on ordinary personal computers, provided that the flow structures are restricted to the limiting cases of plug flow or perfectly stirred tanks. The network is "equivalent" to the CFD flowfield in so far as it represents the bulk flow patterns in the flow. Such equivalence is actually implemented in terms of the following set of operating conditions: The residence time distributions (RTDs) in the major flow structures are the same in the CFD flowfield and in the section of the reactor network that represents the flow region under consideration. Mean gas temperature histories and the effective ambient temperature for radiant heat transfer are also the same. The entrainment rates of surrounding fluid into a particular flow region are evaluated directly from the CFD simulation. To the extent that the RTD, thermal history, and entrainment rates are similar in the CFD flowfield and reactor network, the chemical kinetics evaluated in the network represents the chemistry in the CFD flowfield.

The information flow is sketched and compared with conventional CFD post-processing in Fig. 1. In conventional CFD post-processing, a radically reduced set of chemical species is used with rudimentary reaction mechanisms to predict the heat release and its impact on the flowfield. Then the converged solutions for the flowfield, temperature field, and major species concentration fields are re-analyzed with additional species and more global reaction processes to predict emissions. In contrast, CNPP utilizes the flow and temperature fields in the CFD simulations but not the species concentration fields, because these were determined with the rudimentary reaction submodels. In addition, CNPP uses fields of the turbulent diffusivity and selected conserved scalar variables, which are always computed in CFD but not normally reported to the user. The CNPP method then specifies an equivalent reactor network directly from the CFD flow and temperature fields. Finally, legitimate elementary reaction mechanisms are used to determine the concentrations of all major and various minor species across the reactor network, including any emissions of particular interest.

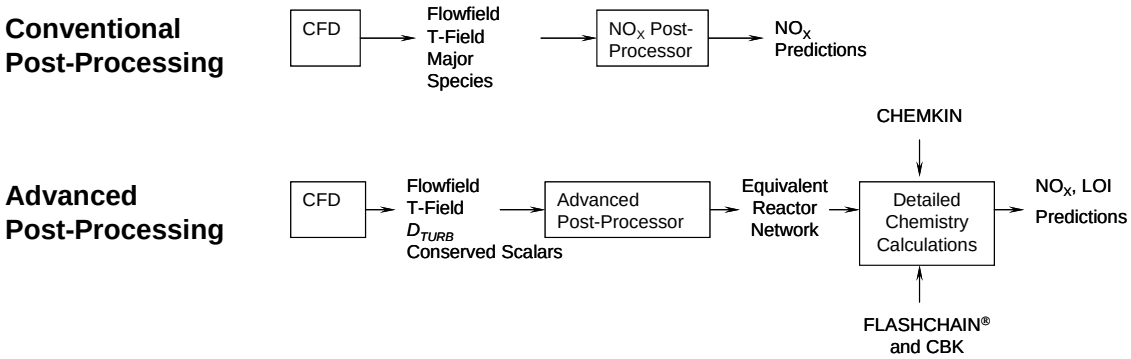

Figure 1. Schematic of the information flow in conventional and ChemNet™ post-processing.

From a practical perspective, it is only possible to implement CNPP after the CFD flowfield has first been subdivided into regions. The regions are the rudimental elements of the chemical structure of the flowfield. As such, each region sustains a collection of chemical reaction mechanisms that are distinctive. Regions are usually much more extensive than any specific flow structures. For example, the core formed by the primary jet within a dual register burner is a region, because the very high loadings of particles and soot in this region will significantly perturb the chemical reaction rates in the gas phase, especially the N-conversion mechanisms. Mixing layers formed by simultaneous entrainment of fuel-rich fluid into secondary or tertiary air streams are also regions, because the temperature profiles along the direction of mixing exhibit similar maximum values across the entire layer. The portion of an OFA jet remaining to be mixed with a process stream is another region, because the absence of fuel essentially eliminates all chemistry.

CFD Simulations. CNPP does not incorporate unusual aspects of a CFD simulation or entail any additional computational burden. The field variables obtained from the CFD simulation are gas density; gas temperature; the mass fractions of all gas species; effective mass diffusivities of all gas species; 3-components of gas velocity; wall temperature; and the dry-ash-free (daf) mass concentration of particles. Information on the particle trajectories is also required, including the 3-component position of each particle as a function of residence time, and the temperature, mass, and size of each particle.

Steps in Developing an Equivalent Reactor Network. The definition of an equivalent reactor network proceeds through the following sequence of steps:

1) The CFD flowfield is delineated into regions whose chemistry is distinctive. The actual basis for the delineation may be the local mass fractions of combustibles, especially soot and fuel particles, or a temperature field that can specify a meaningful average thermal history, or by an abundance of oxidizer and no fuel, which essentially suppresses the chemistry.

2) The RTDs of each region are determined from the CFD simulations by fluid element tracking. Each RTD is then assigned a sequence of reactors, usually by fitting the analytical RTD for a CSTR-series to specify the number of CSTRs for the RTD under consideration.

3) An average gas temperature history for each region is evaluated from the CFD gas temperature field by fluid particle tracking. The average history is then implemented in discrete form across the CSTR-series under consideration.

4) An effective ambient (wall) temperature for radiation transfer is evaluated as an average over the surrounding sections around the region under consideration. It is also implemented in discrete form across the CSTR-series.

5) If the region is a fuel injector, an average particle temperature history is assigned as the average of the thermal histories over all particle trajectories from the injector, so that the fuel's devolatilization behavior can be evaluated. The predicted volatiles yields are implemented as discrete injections into all CSTRs whose residence times include a portion of the predicted devolatilization period.

6) Entrainment rates into all regions are evaluated as functions of the nominal time coordinate through the region under consideration. These rates are specified from the definition of the total mass flux into the boundary of the region, for simple shapes, or from fluid particle tracking from the surroundings into the region, in the more general situation.

The extents of fuel-rich regions near fuel injectors are delineated with a threshold value for the combustibles mass fraction, which is the sum of all organic carbon, hydrogen, oxygen, nitrogen, and sulfur in the fuel, regardless of their appearance in reactants, intermediates or products. The local value of this conserved scalar is determined only by convective and diffusive transport, without sources or sinks. Oxygen concentrations are used to determine the extents of regions around air injection ports.

The regions in two coal flames appear in Fig. 2. The lab-scale flame is 2-D, axisymmetric in laminar flow with only two regions. The boundary to the core is the locus of positions where the combustibles mass fraction has a value of 0.5, the ultimate value after complete mixing of the core and sheath flows. Upstream of the flame front, it overlaps the boundary of all particle trajectories, and downstream it is only slightly larger, because radial transport in this laminar flowfield is relatively slow. Immediately downstream of the inlet, the core contracts while particles are forced into the centerline by the developing momentum boundary layer, and the combustibles mass fraction more-than-doubles. The core flow expands downstream of the volatiles flame front, initially, due to devolatilization, then, due to the thermal expansion of the core flow by the heat release from volatiles, soot, and char combustion, and ultimately, due to diffusion of products into the sheath and the cooling of the sheath flow near the reactor outlet.

The 1.0 MW_t pilot-scale flame in the bottom panel of Fig. 2 consists of a core, mixing layer, external recirculation zone (ERZ), OFA-region and burnout region. The mixing layer between the core and secondary air streams gradually expands until it contacts the furnace wall midway to the OFA ports. An ERZ forms in the corner bounded by the outer boundary of the secondary air stream, but is too weak to entrain particles or appreciable amounts of air or fuel compounds. As the fuel compounds in the flame core contact the secondary air stream, they mix and burn in an expanding mixing layer. This layer completely surrounds the core near the burner inlet, and fills the entire furnace downstream of the core. The most distinctive feature of the mixing layer is that the temperature profile across the layer in the normal direction passes through a maximum value which is essentially the same around the entire circumference of the core. The four air jets from the OFA ports do not penetrate onto the centerline. They also do not fill the entire flow cross section. Downstream of the OFA ports, the flow relaxes to a plug flow pattern that carries ash and exhaust into an exhaust system.

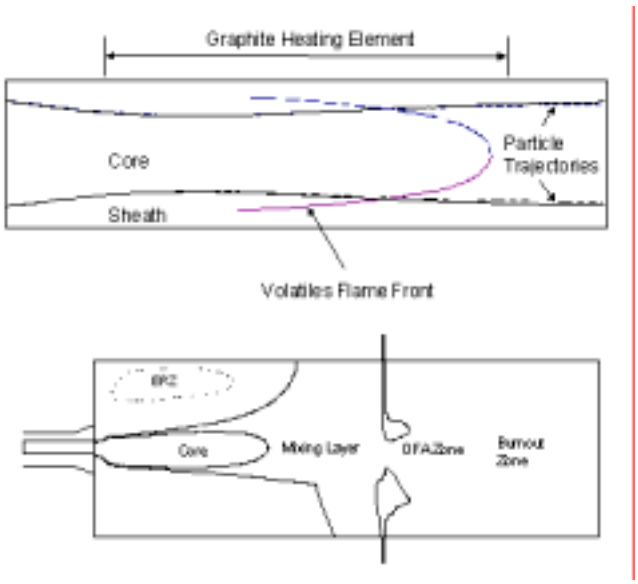

Figure 2. CNPP regions in the flowfields for (Top) a lab-scale, 2-D, axisymmetric coal flame; and (Bottom) a 1.0 MW_t weakly swirled coal flame.

Equivalent Reactor Network. An equivalent reactor network for the 1.0 MW_t pilot-scale flame appears in Fig. 3. In the network, the flame core has been subdivided into two regions. The devolatilization zone covers the upstream portion of the core in which volatiles are being released from the fuel suspension and burned with primary air. Since the primary stream is extremely reducing, no residual O_2 leaves the devolatilization zone. The NO_X reduction zone covers the downstream portion of the core in which only the N-species are converted under the influence of water gas shifting, due to the absence of O_2. The CSTR-series for the mixing layer and the SOFA zone represent the mixing of secondary and tertiary air streams, respectively. But there are no additional flows into the CSTR-series for the BO zone.

The RTD for this particular core was deconvoluted into one component with 16 CSTRs-in-series and another for plug flow with respective mean residence times of 138 and 193 ms. The CSTR-numbers were assigned by least-squares fitting to match the RTD for a series of CSTRs to the CFD-based RTD. The plug flow component represents the near-axial fluid motion under the influence of particle drag, and the CSTR-component represents flow with significant radial velocities. The RTD for the mixing layer was matched with a series of 19 CSTRs, and that for the OFA zone was represented by 6 CSTRs-in-series. The burnout zone is essentially in plug flow, which can be represented by the longest CSTR-series in the calculations.

Gas and wall temperature histories were assigned by fluid element tracking through each region to compile a population of discrete histories. Then the average of the population was assigned for the entire region, and rendered into discrete increments for each of the CSTRs in the series for the region under consideration. Since a large number of CSTRs appear in each series, there is little uncertainty introduced by the discrete representation. Similarly, entrainment histories were determined for each region on the same time scale, either by evaluating fluxes across regional boundaries or with fluid element tracking.

Entrainment into the various CSTR-series is represented as a series of discrete additions over several reactors in the series. Volatiles are entrained into the series for the first part of the flame core; secondary air is entrained into the series mixing layer; and tertiary air is entrained into the series for the OFA zone. The addition rates of volatiles were specified from the stand-alone devolatilization simulation with the average thermal histories of particles from the CFD simulation. The specific addition rates of the air streams were specified from the continuous entrainment profiles evaluated from the CFD simulation.

Reaction Mechanisms. The devolatilization submodel, called FLASHCHAIN®, determines the complete distribution of volatile compounds from almost any p. f., and also predicts the yield and elemental composition of char[8]. When combined with a swelling factor correlation and a correlation for the initial carbon density in char, it specifies all the necessary char properties for a char oxidation simulation. Hence, the complete distribution of volatiles, including gaseous fuels and soot, and all char properties are completely determined from only the fuel's proximate and ultimate analyses.

The reaction mechanism for chemistry in the gas phase contains 444 elementary reactions among 66 species, including all relevant radicals and N-species[9]. All rate parameters were assigned independently, so there are also no adjustable parameters in the submodel for gas phase chemistry. The soot chemistry submodel depicts several important effects. As soot burns, it directly competes for the available O_2 and also consumes O-atoms and OH that would otherwise sustain homogeneous chemistry. Soot also promotes recombinations of H-atoms and OH that could also sustain NO homogeneous chemistry[4]And soot reduces NO directly into N_2.

Char burning rates are determined by thermal annealing, ash encapsulation (of low-rank chars), and a transition to chemical kinetic control. The Char Burnout Kinetics (CBK) Model includes all these effects, and depicts the impact of variation in gas temperature, O_2 level, and char particle size within useful quantitative tolerances[10] However, it is not yet possible to specify the initial char reactivity within useful tolerances from the standard coal properties. We must calibrate this value with LOI predictions or some other suitable index on combustion efficiency. The submodel for char-N conversion is subject to a similar calibration requirement (with NO emissions), compounded by its simplistic mechanistic premise; viz., that a fixed fraction of char-N is converted into NO at the overall burning rate throughout all stages of char oxidation.

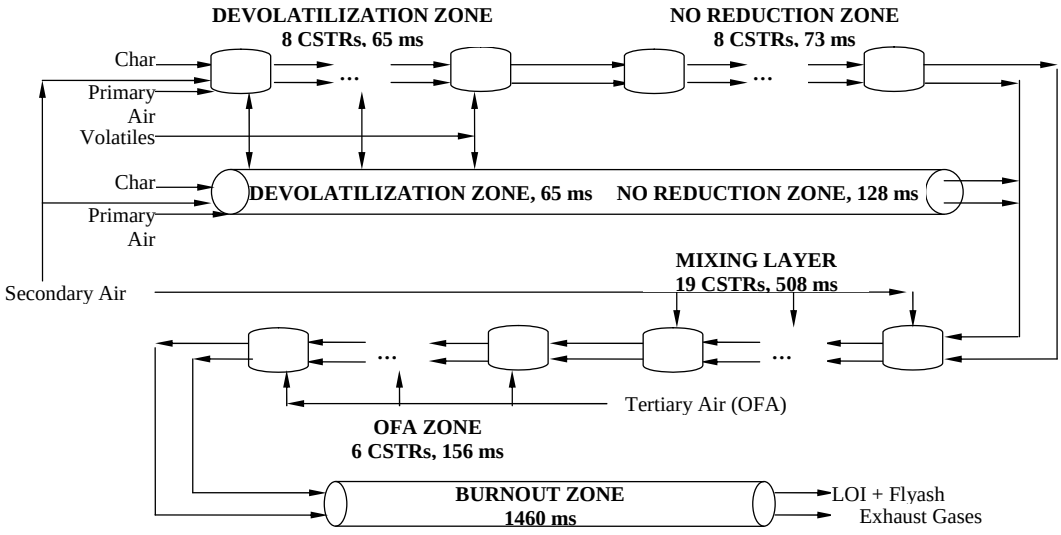

Figure 3. Equivalent reactor network for a weakly swirled, 1.0 MW_t coal flame.

To summarize, the initial char reactivity and the fraction of char-N converted to NO can only be specified from calibration procedures, whereby these parameters are adjusted to match the predicted LOI and NO_X emissions to reported values for a single set of operating conditions. Then the same values should be imposed for all other operating conditions. Except for these two parameters, all other model parameters can be assigned from the fuel's proximate and ultimate analyses within useful quantitative tolerances, or directly adopted from literature.

Applications

The discussion is this section moves through three applications at progressively larger scales.

2-D Axisymmetric Coal Flame. This test facility simulated the thermal and chemical environments in the primary zone of a pulverized coal flame without the complications of two-phase turbulent mixing. As explained elsewhere in detail[6,11], the coal burner was a two-dimensional, axisymmetric flow reactor that imposed uniform radial heat fluxes comparable to those in utility burners. An intense external radiant field stabilized the reaction fronts so that the burner could operate with any inlet O_2 level, including none at all in cases that determined the distributions of secondary pyrolysis products. As suspensions moved along the flow tube, they heated at rates exceeding 10^4°C/s to the onset temperature for primary devolatilization, released their volatiles, and burned. At any particular operating condition, O_2 depletion eventually "quenched" the chemistry at an intermediate stage determined by the proportions of coal and O_2 at the inlet. Inlet O_2 levels were progressively increased in successive cases to move the process chemistry through oxidative volatiles pyrolysis, volatiles combustion, soot combustion, and char oxidation.

Predicted distributions of the major combustion products are evaluated with the data for all three coals in Fig. 4 in terms of total weight loss, soot, CO_2, and H_2O, all expressed on a daf coal weight basis. As the O_2 level was increased from 3% to 14.6 % with the hv bituminous, the weight loss increased from 53 to 72 wt. %, due entirely to char combustion. The predicted weight loss is within experimental uncertainty throughout. The aerosol yields fell from 21 to 4 wt. % over the same range, indicating that soot oxidation was incomplete. The predicted soot yields are higher than the reported levels for O_2 levels below 7 %, but within experimental uncertainty for higher levels. Carbon dioxide yields increased monotonically with increasing O_2 levels. The H_2O yields seem to approach an asymptote because only the very small amounts of hydrogen in soot and char were available to produce H_2O once the noncondensible fuels were consumed. The predicted levels of CO_2 and H_2O are too high for intermediate O2 levels, because the predicted burning rates of the gaseous fuel compounds are too fast. Whereas the H_2O level with 14.6 % O_2 is accurately predicted, the ultimate CO_2 level is overestimated. This discrepancy is probably due to measurement difficulties for high CO_2 concentrations, because there was a substantial breach in the reported C-balance for this test.

Product distributions from the subbituminous coal also appear in Fig. 4, including the one for secondary volatiles pyrolysis (no O_2). The observed weight loss for secondary pyrolysis was 60 daf wt. %, in close agreement with the predicted value although the predicted soot yield is too high. As the O_2 level was increased from 2 % to 14.6 %, the weight loss increased as the char burned from 56 to 85 wt. % and soot yields were halved by combustion from 16 to 8 wt. %. The predicted yields are within experimental uncertainty for the entire range of O_2 levels for weight loss, and for O_2 levels over 7 % for the soot yields. Nearly all the increase in CO_2 as O_2 levels were raised from 2 to 5 % can be attributed to char oxidation, in contrast to the smaller contribution from hv bituminous char in this operating regime. The predicted levels are generally in better agreement than for the hv bituminous coal; once again, the large discrepancy in the predicted CO_2 level for 14.6 % O_2 is associated with a large breach in the C-balance for this test.

When the O_2 level was increased from 0 % to 14.6 % with the lv bituminous, the weight loss increased by only 2 wt. %, while the soot yields fell from 19 to 8 wt. %. The corresponding predictions were within experimental uncertainty throughout. Likewise, the CO_2 and H_2O levels were accurately predicted except at the lower O_2 levels.

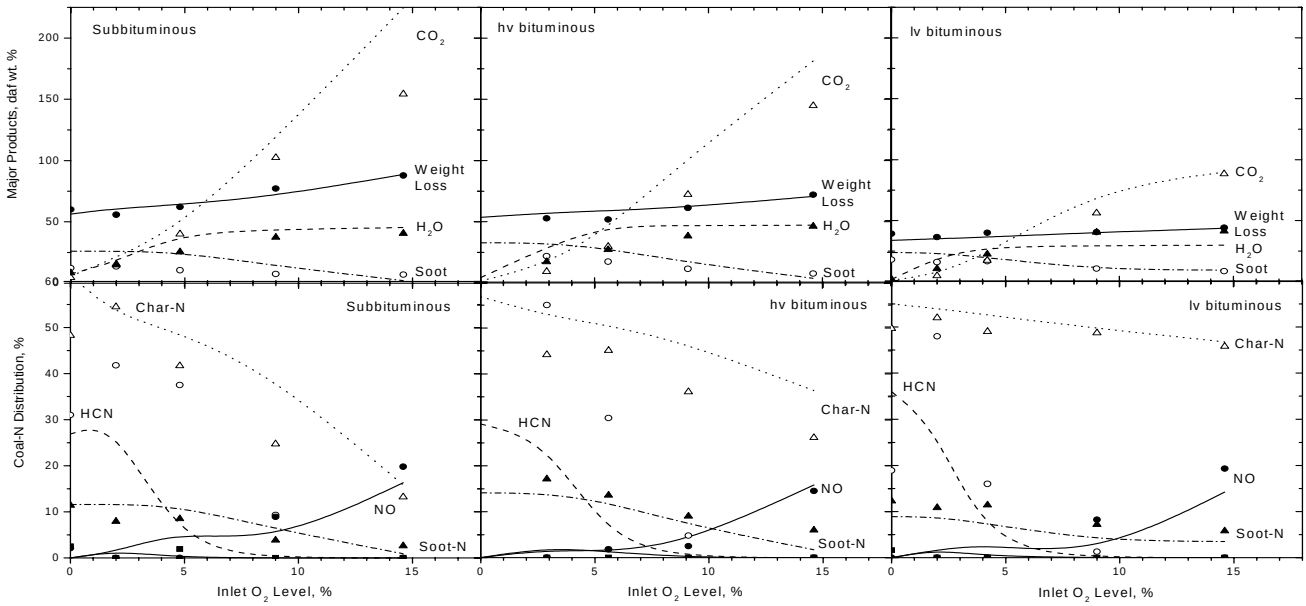

Figure 4. Evaluation of predicted distributions of major products (Top row of panels) and distributions of N-species as percentages of the coal-N (Bottom row of panels) with reported values from the subbituminous (left), hv bituminous (middle), and lv bituminous (right) coals.

The N-species distributions in Fig. 4 are resolved into char-N, soot-N, HCN, NH_3, and NO, all expressed as percentages of the coal-N. For all three coals, the predicted N-species distributions depict the observed shift in the fixed-N species from HCN with minor amounts of NH_3 but no NO for the lower two O_2 levels, through an abrupt transition to only NO (and N_2) at the highest O_2 level. The levels of char- and soot-N fall continuously for progressively higher O_2 levels, while these carbonaceous fuels burn away. For the hv bituminous coal, the predicted levels of soot-N, NH_3, and NO are within experimental uncertainty across the entire range of O_2 level. Char-N levels are slightly overpredicted, but HCN levels are too low by a factor of two or more. However, there is a breach of more than 15 % in the reported N-balance for the case with 2 % O_2, so it is difficult to pinpoint the source of these discrepancies.

With the other coals, the predicted N-species distributions are generally more accurate although, here again, HCN levels are underestimated for low O_2 levels and char-N levels are over predicted at intermediate O_2 levels. It is interesting that the reaction mechanism predicts almost 5 % N_2O and 3 % HNCO when the lv bituminous is burned in 4.2 % O_2, although these species were not monitored in the tests.

1.0 MW_t Pilot-Scale Flame. A database on emissions from biomass cofired flames was compiled in Southern Research Institute's (SoRI) Combustion Research Facility (CRF)[12,13]. The CRF consists of fuel handling and feeding systems, a vertical refractory lined furnace with a single up-fired burner, a horizontal convective pass, heat exchangers and conventional exhaust cleaning devices. Emissions from this system have been qualified against those from full-scale, tangential-fired furnaces for the operating conditions imposed in this work[14]. The 8.5 m by 1.07 m (i.d.) cylindrical furnace handles gas velocities from 3 to 6 m/s, and residence times from 1.3 to 2.5 s. The nominal firing rate is 1.0 MW_t, which was fixed for all cases in this work. A single burner generates a core of pulverized fuel and primary air surrounded by weakly swirled secondary air. For all cases in this paper, the biomass was co-milled with the coal and the mixture was directly fed into the burner. Overfire air (OFA) was injected through 4 off-radius ports located 4.6 m down the furnace. All datasets include cases with 0 (unstaged) and 15 % OFA. In the unstaged series, the OFA was combined with secondary air. Air feedrates were varied to produce exhaust (wet) O_2 levels between 2.5 and 5 %. Fuel quality was varied by firing four coals representing ranks from subbituminous through low volatile bituminous with sawdust and switchgrass at loadings of 10 and 25 % by weight.

The parity plot in Fig. 5 evaluates the predicted NO_X emissions for all the tested fuel combinations at standardized operating conditions of 3.5 % exhaust O_2 with 15 % OFA. The measured NO_X emissions increase from 140 ppm through 450 ppm while the coals were switched from the subbituminous, through two high volatile bituminous samples, through the low volatile bituminous. Each of these coals was cofired at two or three levels of sawdust and switchgrass, which generally reduced NO_X by up to 30 %. The dataset in Fig. 5 contains four baseline, coal-only cases which were used to assign various parameters in the CNPP simulations. The other twenty-one cases were predicted with no parameter adjustments whatsoever. The fuels' proximate and ultimate analyses were used to predict the compositions of all volatile and residual fuel compounds, which were then processed through full chemical reaction mechanisms in the gas phase and on soot to describe the conversion of fuel-N. Across the complete range of fuel quality, the predicted NO_X emissions are within experimental uncertainty of the measured values, except for the overprediction by 75 ppm for the measured value of 360 ppm.

The detailed flame structures from the CNPP analyses showed that two factors are primarily responsible for the significant NO_X reduction observed for CRF flames with biomass cofiring. First, there is more volatile matter from biomass and it contains a much smaller contribution from soot. Consequently, the near-burner S. R. values for the gas phase are significantly richer than in coal-only flames. Under richer conditions, near-burner NO will be reduced away and a greater proportion of the fixed-N species will be converted into N_2. CRF flames provide sufficient residence times in the flame cores for NO reduction and fixed-N conversion to N_2. Second, a significantly lower percentage of the total fuel-N will remain in the char beyond the near-burner zone, where its partial conversion to NO is inevitable. If the biomass contains nitrogen, it releases all of it in the near-burner zone. If the biomass contains no nitrogen, then the inventory of char-N beyond the flame core is reduced in proportion to the biomass loading. In either case, there is less char-N beyond the point where NO can be reduced by chemistry in the gas phase.

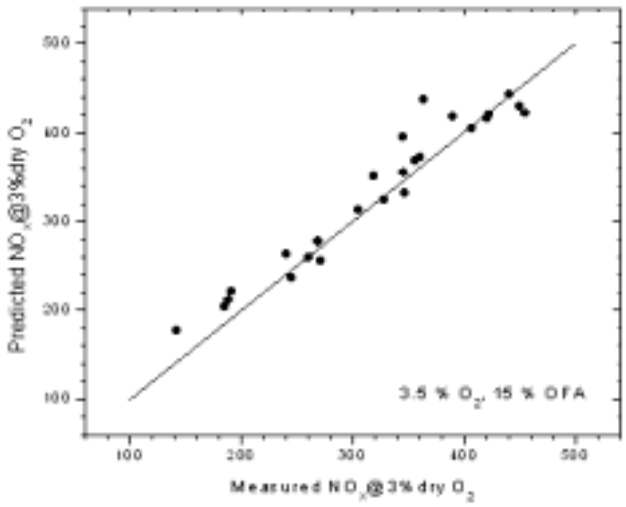

Figure 5. Evaluation of predicted NO_X emissions from 1.0 MW_t flames of 2 forms of biomass co-milled with 4 diverse coals.

Full-Scale T-fired Furnace. CNPP was successfully applied to a full-scale, tangential-fired utility furnace fired with subbituminous coal. The coal was injected into the lower furnace through tens of independent fuel injectors that were arranged with multiple close-coupled OFA ports as well as two layers of OFA at the furnace midsection. Whereas the exhaust NO_X emissions could be closely matched to reported values, this application is particularly interesting for its resolution of the total NO_X emissions into contributions from each fuel injector. The key to this capability is a deconvolution of the extremely complex RTDs for the flow from each fuel injector.

Each fuel jet generates a flow of gases that moves along the walls. This stream is regarded as a mixing layer that constitutes a separate region in the flowfield, because it contains a very high level of gaseous fuel compounds and soot. Each ribbon is surrounded above and below by air jets which, in turn, are surrounded above and below by two auxiliary air streams. These various air streams gradually mix with the ribbon flow, burning out the volatile fuels, and also with each other. Fluid tracking showed that the ribbon from each primary jet moves in a helix from the core of its parent fuel jet to the top of the fuel injection zone. The air flows between the ribbons from different fuel jets tend to isolate each ribbon, and little interaction was seen among the ribbons from primary jets at different

corners and elevations, although some ribbons were bisected by the ribbons from neighboring jets. The various collisions and deflections among these flows are responsible for the complex RTD in Fig. 6. Almost all the ribbon RTDs were too complicated to represent with a single CSTR-series. Most of the RTDs were bimodal and some were trimodal. Nevertheless, the RTDs could still be deconvoluted into multiple CSTR-series, as seen in Fig. 6. These two component RTDs are essentially independent, and their mean residence times differ by more than a factor of four, suggesting that part of the flow actually short-circuited the primary flow path. For this particular ribbon, two CSTRs represented the first component, and 20 represented the second, which approaches the limiting behavior of a single CSTR in parallel with a plug flow reactor. There are other cases like this, but most of the multimode RTDs had components in plug flow.

Due to the disparate residence times in the component RTDs for each fuel jet, the compositions of the flows into the upper furnace were significantly affected by the complexity in the RTDs. RTD-components with the shortest residence times tended to have much higher concentrations of HCN and NH_3 as they moved into the upper furnace. When these variations in composition were ultimately processed through the reaction mechanism that partitions the intermediate species into NO or N_2, they were responsible for very large differences in the NO_X levels contributed by individual fuel injectors. Indeed, the extreme values differed by a factor of ten, so that substantial portions of the exhaust NO_X could be associated with a handful of fuel injectors.

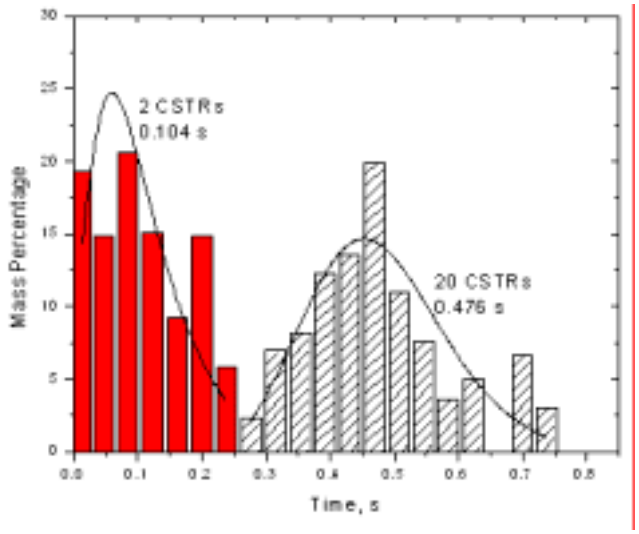

Figure 6. CFD-based RTDs (histograms) and their analytical fits (curves) for the flow from an individual fuel injector in a T-fired utility furnace.

Discussion

The CNPP method provides an alternative to conventional CFD post-processing whereby rudimentary N- conversion schemes are applied to the primary CFD temperature and concentration fields to estimate exhaust NO_X emissions. One key difference is that in CNPP, CFD simulations only specify temperature histories and mixing rates, not the species concentration fields that directly reflect the rudimentary reaction schemes. Another key difference is that the furnace is subdivided into regions that delineate the structure of p. f. flames, as in gaseous flames. The combustibles mass fraction used to delineate the regions near fuel injectors explicitly accounts for the impact of aerosol and particulate combustibles on the burning rates of gaseous fuel compounds and, especially, on the NO production rates. This aspect is responsible for the accurate predictions of NO_X emissions from the biomass cofired flames, in which volatiles chemistry determined how much of the near-burner NO was expelled into the downstream flame zones and, ultimately, into the exhaust. It also enabled the exhaust emissions from the full-scale utility furnace to be resolved into contributions from individual fuel injectors, which were surprisingly variable.

Simulations based on detailed reaction mechanisms require far fewer parameter adjustments than conventional CFD simulations whenever different fuels are considered. To depict the reported distributions in Fig. 4 of the major fuel intermediates and combustion products, but not the N-species, with CFD simulations[6], the following reactivity parameters were adjusted: 2 parameters for the devolatilization rate plus the ultimate volatiles yield; 3 parameters in the combustion rate for gaseous fuels; 3 parameters in a global rate for soot oxidation; and 4 parameters in the intrinsic char oxidation rate. In principle, there are 13 adjustable parameters in the CFD chemistry submodels. In practice, the compositions of soot and char hardly change for different coal types, so there are actually 11 effective adjustable parameters. To reproduce the product distributions in Fig. 2, all these parameters were adjusted for different coals, except for the activation energies for soot and gas combustion and the reaction order for char oxidation. Hence, 8 parameters were adjusted 3 times for a total of 24 parameter adjustments to represent the datasets on these 3 coals.

In contrast, in the detailed chemistry simulations, the rate constant for soot oxidation was adjusted to match one case with the lv bituminous coal, and the rate constant for NO reduction on soot was adjusted to match one case with the hv bituminous coal. In addition to these 2 adjustments, we generally expect to adjust the initial reactivity in CBK and the fraction of char-N converted to NO for each coal type (although the same char-N fraction was specified for all 3 coal samples in this study). Hence, 8 parameters could have been adjusted for these 3 coals, which is many fewer than 24, even without an allowance for the omission of nitrogen chemistry in the CFD simulations. This is the main practical benefit of the mechanistic complexity in the detailed chemistry simulations.

Whereas all the applications in this paper featured NO_X emissions from flames, the method is generally applicable to any set of species of particular interest. It has already been used to interpret test data on NO_X reduction with direct radical injection from dielectric barrier discharges and mercury transformations in utility exhaust systems. The method will be especially suitable for gasification systems where the chemical kinetics control the overall conversion rates, and the mixing limited analyses in conventional CFD furnace simulations no longer apply.

References

(1) Niksa, S. *Coal Combustor Modeling*, **1996**, No. 31 IEA Perspectives Series, IEA Coal Research, London.
(2) Visona, S. P.; and Stanmore, B. R. Chem. Engr. Sci., **1998**, 53(11), 2013-2027.
(3) Brower, J.; Heap, M. P.; Pershing, D. W.; and Smith, P. J., Proc. Comb. Inst., **1996**, 26, 2117-2124.
(4) Pedersen, L. S.; Glarborg, P.; et al. *Combust. Sci. Technol.*, **1998**, 132, 251-314.
(5) Benedetto, D.; Pasini, S.; Falcitelli, M.; La Marca, C.; and Tognotti, L. Combust. Sci. and Technol., **2000**, 153, 279-294.
(6) Niksa, S.; and Liu G.-S., *Fuel*, **2002**, 81(18), 2371-85.
(7) Falcitelli, M.; Tognotti, L.; and Pasini, S. Combust. Sci. Technol., **2002**, 174(11-12), 27.
(8) Niksa, S. *Combust. Flame*, **1995**, 100, 384-394.
(9) Glarborg, P.; Alzueta, M. U.; Dam-Johansen, K.; and Miller, J. A. *Combust. Flame*, **1998**, 115, 1-27.

(10) Hurt, R. H.; Sun J.-K.; and Lunden, M. *Combust. Flame*, **1997**, 113(1/2), 181.
(11) Niksa, S.; and Liu, G.-S. *Proc. Comb. Inst.*, **2002**, 29, to appear.
(12) Niksa, S.; Liu, G.-S.; Felix, L. G.; and Bush, P. V. Paper No. IJPGC2002-26136, Int. Joint Power Gen. Conf., ASME, Phoenix, AZ, June 25, **2002**.
(13) Niksa, S.; Liu, G.-S.; Felix, L. G.; Bush, P. V.; and Boylan, D. M. "Predicting NO_X Emissions from Biomass Cofiring," 28th Int. Technical Conf. on Coal Utilization and Fuel Systems, **2003**, Coal Technology Assoc., Clearwater, Fl, March.
(14) Monroe, L. S. et al., 1995, EPRI/EPA 1995 Joint Symp. On Stationary Combustion NO_X Control, Book 3, EPRI, Palo Alto, CA.

A TIME-SCALE PROBLEM FOR THE FORMATION OF SOOT PRECURSORS IN PREMIXED FLAMES

Angela Violi[1], Gregory A. Voth[2], Adel F. Sarofim[1]

[1] Department of Chemical and Fuels Engineering
[2] Henry Eyring Center for Theoretical Chemistry, Department of Chemistry

University of Utah
Salt Lake City, UT 84112

Introduction

This paper applies a previously developed tool to study the molecular transformations that occur in combustion conditions during the transition from gas phase precursors to soot particles.[1-2] To help resolve issues such as identification of pathways leading to soot formation, it is important to characterize the soot precursors, in terms of chemical structure/components. Questions like structure-pathways and structure-property relationships may lead to a deeper understanding of soot growth mechanisms. We want to address these questions theoretically by studying the growth of molecules in combustion environments, using Kinetic Monte Carlo (KMC) and Molecular Dynamics (MD) methodologies.

The processes involved in soot precursor formation exhibit a wide range of time scales, spanning pico- or nanoseconds for intramolecular processes that can occur on a particle surface to milliseconds for the formation of the first soot precursors. In order to accurately describe the soot formation process, we need to model the reactions happening at different time scales. The coupling of KMC and MD methodologies allows us to do so. The code, named KMC/MD, combines the strengths of KMC for long-time sampling, and MD for relaxation processes is based on that developed at LLNL.[2]. The time-duration between Monte Carlo events can be arbitrarily long (depending on the kinetics, model. etc), while in Molecular Dynamics, we require time steps which are a small fraction of a vibrational period. So the combination of the two techniques spans two time- and equilibrium scales. The reaction rates among the compounds present in the system are calculated using electronic configuration methods, and they are specified as probabilities.

This approach is designed to preserve atomistic scale structure: a single particle evolves in time with real three-dimensional structure (bonds, bond-angles, dihedral angles). Some preliminary results have been reported in an earlier publication for the simulation of the evolution of soot precursors in an ethylene premixed laminar flame.[1,3] In this paper the KMC/MD code is used to study the growth of aromatic structures to a nano-size range in the soot inception zone of aromatic and aliphatic laminar flames. The aromatic growth process strongly depends on the specific local regime, which is characterized by several experimental factors such as temperature, concentration of hydrogen, PAH, etc., and it is interesting to understand the influence of different environments on structural properties of the compounds formed. The use of this approach enables the investigation on the physical as well as chemical properties of the carbonaceous nanoparticles formed, such as H/C ratio, and particle morphology. After summarizing in the following section the methodological details of the computations performed, the results of hydrocarbon compounds growth are discussed in two different environments represented by low pressure aromatic and aliphatic flames.

Methodology

Molecular Dynamics, in which one chooses an appropriate interatomic potential to describe the forces between atoms and then integrates the classical equation of motion, is the most direct approach among atomistic simulations. However, the limitation in the accessible simulation time represents a substantial obstacle in making useful predictions with MD. Resolving individual atomic vibrations requires a time step of approximately femtoseconds in the integration of the equations of motion, so that reaching times of even microseconds is very difficult. In order to solve this time scale problem, MD methodology has been coupled to KMC to allow the extension of the accessible time scale by orders of magnitude relative to direct MD, while retaining full atomistic detail. During the KMC module[4-6] one escape path is chosen randomly from a list of possible transition events, weighted by the rate constant, and the system is advanced to that new state. The clock is then incremented in a way that is consistent with the average time for escape from that state, which can be determined easily from the rate constants for the possible escape paths in the list. The two methods differ in their ability to explore phase space. The ability of the KMC method to make non-physical moves can significantly enhance its capacity to explore phase space in appropriate cases. Its capability to generate states directly has many advantages, including bypassing configurations which may be difficult to escape dynamically. And so the method can be used to study the configurations of systems which may be expensive or impossible to access via MD.

Molecular Dynamics may not be able to cross the barriers between the conformations sufficiently often to ensure that each conformation is sampled according to the correct statistical weight. MD can be very useful for exploration of the local phase space whereas the KMC method may be more effective for conformational changes which jump to a completely different area of phase space.

The time-step for a single KMC iteration is a "real time," determined by the kinetics system. The reaction rates among the compounds present in the system are specified as probabilities and the surface configuration over time is then given by a master equation, describing the time evolution of the probability distribution of system configurations.

A more detailed description of the methodology is reported elsewhere.[1-3]

Conditions analyzed

Below we report the computational results obtained for the growth of aromatics in two premixed laminar flames of aliphatic and aromatic fuels in order to determine the influence of different environments, and hence reaction pathways, on the structures of particles. A low-pressure benzene-oxygen flame C/O=0.8 with an unburned velocity of 42 cm s^{-1}, p= 2.66 kPa,[7] and an acetylene/oxygen flame at a pressure of 2.67 kPa[8] have been experimentally studied by Homann and co-workers, who measured PAH and PAH radicals for these flames by mean of resonant (REMPI) and nonresonant multiphoton ionization with a frequency-doubled, pulsed dye laser and separation with a time-of-flight mass spectrometer, equipped with an ion reflector. These experimental data are used to validate the code in terms of structure properties, such as H/C ratio.

The two major inputs to the KMC/MD code are represented by the number and concentration profiles of the species that characterize the gas phase and that can contribute to the growth process and by the reaction rates that describe the velocity with which the gas-phase species are added to the growing seed. Acetylene, H, naphthalene, and acenapthylene species are considered in this work as key contributors to the PAH growth process and used as input to the

KMC/MD code. The choice of the input PAH is due to their presence in high concentrations in the PAH inventory, and to the importance that PAH with peripherally fused five-membered rings (CP-PAH), which include acenaphthylene, have in the flame formation chemistry of soot[9-101112131415] and fullerenes.[16] Acetylene is the most abundant building block[17] and contributes to the HACA mechanism. The concentration profiles have been calculated using the CHEMKIN package[18] together with a kinetic model previously developed.[19]

In using these concentrations in the atomistic model, no allowance was made in the calculated hydrocarbons and H profiles for species depletion or temperature change. A detailed description of the gas-phase species involved, and the reactions that can occur in the system, together with their rates is reported elsewhere.[20]

Results and Discussion

Homann and co-workers reported the molecular formulas of PAH in a C/H diagram for the two flames, where each point corresponds to a certain compound C_xH_y. The experimental data have been re-plotted in **Figure 1** as diamond points for the aromatic[7] *(1a)* and aliphatic[8] flames *(1b)*.

The totality of points represent the ensemble of PAH and PAH radicals with different molecular formulae. The formulae of six-ring PAH with most peri-condensed ring structures like coronene, ovalene, etc. lie on the dotted line in the diagrams. The points above the line represent PAH that are H-rich and those below that are H-poor with respect to these most condensed 6-ring structures. The authors also emphasized that large H-rich PAH play an important role in reactions, both with respect to growth and consumption, irrespective of whether they are molecules or radicals.[7] As most of the PAH are pericondensed, enriched hydrogen in their structure means 4C bays or larger coves at which reactions could take place preferentially. The results obtained through the use of KMC/MD code are plotted as filled circles on the same figure. The use of the KMC/MD methodology allows us to follow the evolution of structures in a chemically specific way. The computed data are in good agreement with the experimental results in terms of H/C ratio, and show the formation of H rich compounds corresponding to open elongated PAH with bays and coves. PAH formation does not follow a narrow path in the C-H diagram but a broad band due to the variance in H content for the same number of C atoms; the molecular formulas of the PAH form a band that widens toward larger PAH. This observation indicates that with an increase in the number of C atoms, the bandwidth for the H content becomes larger. This behavior becomes more pronounced when the fuel is changed from acetylene to benzene. The KMC/MD method is able to reproduce this trend too and this is due to the different contribution of the reaction pathways to the growth of the aromatic compounds. Having a diverse molecular base and not only the reaction sequence of hydrogen abstraction and addition of acetylene molecules to the radical site previously formed may lead to a network of aromatic-aliphatic linked structures.

The results reported in **Figure 1** are both relative to two conditions within the oxidation zone of the flames. We did that in order to emphasize the influence that the two environments have on the structures of the compounds formed. The relative contribution of the different types of growth reactions seems to depend on the fuel. In the case of aromatic fuels polymerization reactions can occur early since aromatics are in relatively large concentrations in the fuel, whereas in the case of aliphatic fuels such as acetylene, ethylene or methane the first aromatic ring must be formed from fuel decomposition products by a sequence of elementary reactions and therefore the concentrations of aromatic soot precursors are in lower concentrations than in the aromatic flames.

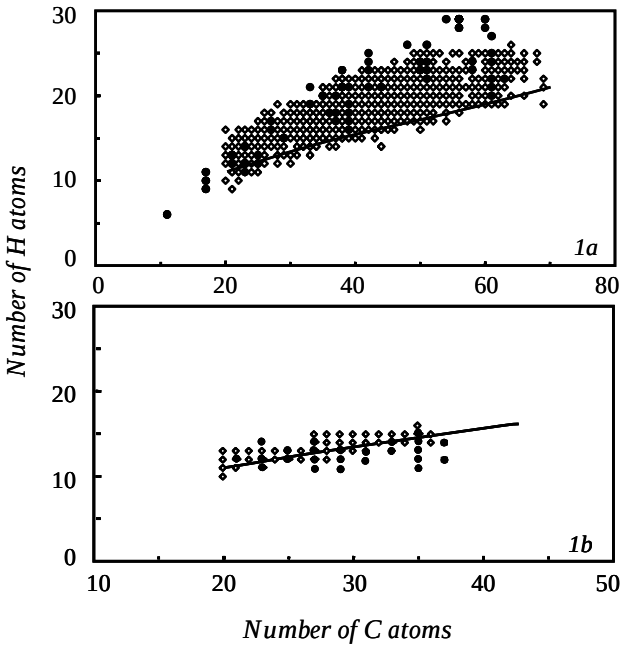

Figure 1. Hydrogen and carbon content for the aromatic (a) and aliphatic (b) flames.

In benzene flames, PAH are formed in concentrations about 100 times those found in aliphatic fuel flames of the same C/O ratio.[21] Their maximum concentrations occur within the oxidation zone and decrease at the end of it where most of the carbon is formed. Polyacetylenes arise in the oxidation zone but their concentration does not decrease as rapidly in the region where molecular oxygen has been consumed. An important difference consists in unsaturated hydrocarbons present in the oxidation zone, i.e. C_2H_2 in acetylene flames, and benzene and PAH in benzene flames. During the combustion of benzene, the benzene molecule itself is an important reactant for the formation of higher molecular weight PAH. In contrast to acetylene, benzene is completely consumed, even before the end of the oxidation zone. In the vicinity of the temperature maximum benzene is no longer available as a building block for larger molecules or particles. Within a benzene flame C_2H_2 is formed as the temperature increases. At the end of the oxidation zone, C_2H_2 is present in nearly the same concentrations as those found in acetylene flames.

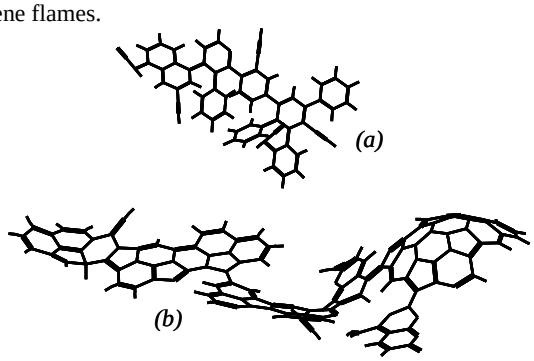

Figure 2. Intermediate compounds formed in aliphatic (a) and aromatic (b) flames.

Figure 2 reports the structures of two intermediate compounds formed in the aliphatic *(2a)* and aromatic flame *(2b)*. In the first case

the compound formed is still mainly planar and the contribution of acetylene is significant. In the lower part of the figure, the structure formed in the aromatic flame shows already three-dimensional characteristics and the contribution of aromatic hydrocarbons, such as benzene, naphthalene is prevalent.

Another important characteristic of these particles is their morphology. Ellipticity parameters are often used to characterize particle shape.[22] In order to characterize ellipticity, the aspect ratio AR is computed

$$AR = a/b$$

where a and b are the axes of the ellipse that has as its center the object's centroid.

A series of diameters of the particles are sampled. The average of these diameters is used as the spherical diameter r_s of the configurations, and an average of the longer diameters is used as "a", and an average of the shortest ones is used as "b". A better evaluation of *a* and *b* can be obtained using the Legendre ellipse that has the same geometrical moments up to the second order as the original object area. The Legendre ellipse is often used instead of the original object. The aspect ratio of the particle, defined as a/b, is reported in **Figure 3** as a function of the diameter (ED) calculated for an equivolume spherical particle.

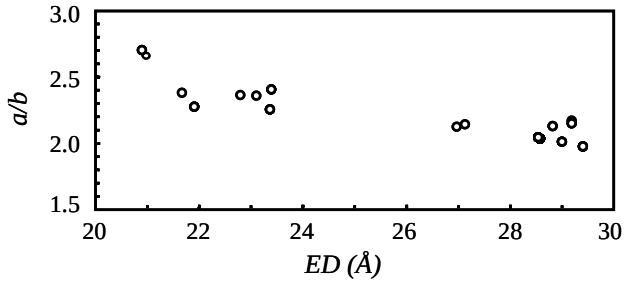

Figure 3. The aspect ratio of soot precursor molecules as a function of equivalent spherical diameter in acetylene flame (in Angstroms).

The aspect ratio of a circle is one and of an ellipse with the ratio of axes 2:1 is equal to two. The aspect ratio for the ellipse increases with an increase in the ratio of the major and secondary axes. The aspect ratio is seen to increase with increasing particle size.

The elongated shapes exhibited by the young nanoparticles is supported by "in situ" measurements on soot evolution in flames. Light scattered by nanoparticles is more depolarized than that scattered by soot particles and the depolarization ratio increases as the particle deviate from the spherical shape.[23]

Concluding Comments

The paper presents the application of Kinetic Monte Carlo and Molecular Dynamic to study soot inception in aliphatic and aromatic flames. Formation of carbonaceous nanoparticles can be followed in a chemically specific way. Properties of the particles, such as H/C ratio and morphology have been computed, showing the presence of elongated shapes for young nanoparticles. The influence of two different environments, an aromatic and aliphatic flame, is assessed in terms of structures of the particles formed. The use of this approach will enable the investigation on the physical (e.g., porosity, density, sphericity) as well as chemical (e.g., H/C, aromatic moieties, number of cross-links) properties.

Acknowledgments

This research is funded by the University of Utah Center for the Simulation of Accidental Fires and Explosions (C-SAFE), funded by the Department of Energy, Lawrence Livermore National Laboratory, under subcontract B341493. The calculations presented in this paper were carried out at the Utah Center for High Performance Computing, University of Utah that is acknowledged for computer time support. The code used is one based on the LLNL code (2).

References

1. Violi, A., Kubota, A., Pitz, W.J., Westbrook, C.K., Sarofim, A.F., *Proc. Combust. Inst.*, **2002**, in press.
2. Westbrook C. K., Kubota A., Pitz W. J., "Computational Chemistry of Plasma Polymerization," LLNL Laboratory Directed Research and Development- FY 1999, LLNL Annual Report, **1999**.
3. Violi, A., Kubota, A., Pitz, W.J., Westbrook, C.K., Sarofim, A.F., *Preprints of Symposia – American Chemical Society, Division of Fuel Chemistry*, **2002**, 47(2), 771.
4. Bortz, A. B, Kalos, M.H., Lebowitz, J.L., *J. Comp. Phys.*, **1975**, 17, 10.
5. Voter, A.F. *Phys. Rev. B*, **1986**, 34, 6819.
6. Fichthorn, K.A., Weinberg, W.H., *J. Chem. Phys.*, **1991**, 95, 1090.
7. Keller, A., Kovacs, R., Homann, K.-H., *Phys. Chem. Chem. Phys.* **2000**, 2, 1667.
8. Weilmunster P., Keller A., Homann K.-H., *Combust. Flame*, **1999**, 116, 62.
9. Frenklach, M., Clary, D.W., Gardiner, W. C., and Stein, S. E., *Proc. Comb. Inst.* 20:887, **1985**.
10. Benish, T.G., Lafleu,r A.L., Taghizadeh, K., Howard, J.B., *Proc. Comb. Inst.* 26:2319, **1996**.
11. McEnally, C. S., Pfefferle, L. D., *Combust. Sci. Tech.*, **1998**, 131: 323,.
12. Frenklach, M., Ebert L.B., *J. Phys. Chem.*, **1988**, 92: 561,.
13. Frenklach, M., Moriarty, N.W., Brown, N.J., *Proc. Combust. Inst.*, **1998**, 27,1655.
14. Frenklach, M., *Proc. Comb. Inst.*, **1996**, 26, 2285.
15. Mulholland, J.A., Lu, M., Kim, D-H., *Proc. Combust. Inst.* **2000**, 28, 2593.
16. Lafleur, A. L., Howard, J. B., Taghizadeh, K., Plummer, E. F., Scott, L.T., Necula, A., Swallow, K. C., *J. Phys. Chem.*, **1996**, 100, 17421.
17. Frenklach, M., *Phys. Chem. Chem. Phys.*, **2002**, 4(11), 2028.
18. Kee, R.J., Rupley, F.M., and Miller, J.A., **1989**, "Chemkin II: A Fortran Chemical Kinetics Package for the analysis of gas phase chemical kinetics", Sandia National Laboratories Report No. SAND 89-8009B.
19. Violi, A., D'Anna, A., D'Alessio, A., *Envir. Comb. Tech.*, in press, **2003**.
20. Violi, A., Xie H., Voth G.A., Sarofim A.F., in preparation, **2003**.
21. Richter H., Howard J.B., *Progr. Energ. Combust. Sci.*, **2000**, 26, 565.
22. Mikli, V., Kaerdi, H., Kulu, P., Besterci, M., *Proc. Estonian Acad. Sci. Eng.*, **2001**, 7(1), 22.
23. D'Alessio, A., D'Anna, A., D'orsi, A., Minutolo, P., Barbella, R., Ciajolo, A., *Proc. Combust. Inst.*, **1992**, 24, 973.

ACTIVE SITES AND ACTIVITY IN HDS CATALYSIS: THE EFFECT OF H_2 AND H_2S PARTIAL PRESSURE

*Bas M. Vogelaar, Narinobu Kagami[1], A. Dick van Langeveld[*2], Sonja Eijsbouts[3] and Jacob A. Moulijn*

Reactor & Catalysis Engineering Group, Faculty of Applied Sciences, Delft University of Technology, Julianalaan 136, 2628 BL Delft, The Netherlands.
[1]Idemitzu Kosan Co. Ltd. 26 Anesakikaigan Ichihara-city, Chiba, 229-0107, Japan.
[2]Particle Optics Group, Faculty of Applied Sciences, Delft University of Technology, Lorentzweg 1, 2628 CJ Delft, The Netherlands.
[3]Akzo Nobel Chemicals B.V., P.O. Box 37650, 1030 BE Amsterdam, The Netherlands.

Introduction

We recently reported some extraordinary results in the hydrodesulfurization of a light gas oil (LGO) [1]: At low conversion (around 50% sulfur removal) the catalyst activity appeared to be independent of the H_2 pressure. This is very uncommon, as most studies in fixed bed systems at high conversion (>95%) or in autoclave reactors report a first order dependency between activity and H_2 pressure. To understand the behavior at low conversion we must realize that in a flow reactor, the partial pressure of gas-phase inhibitors (like H_2S) scales linearly with the total pressure according to Eq. 1. Here, V_m is the molar volume at standard conditions (0.024 m^3/mol), M_S the molar mass of sulfur (0.032 kg/mol), p the total pressure, *HTO* the hydrogen-to-oil ratio, ρ_L the liquid feed density (kg/m^3), $[S_0]$ the mass fraction of sulfur in the feed, and X the level of sulfur conversion.

$$p_{H2S} = \frac{V_m}{M_S}\frac{p}{HTO}\rho_L [S_0] X \qquad \text{(Eq. 1)}$$

This means that when the total pressure in the trickle bed reactor is increased and the conversion level remains the same (as in the LGO case) the H_2S partial pressure increases correspondingly. When the inhibiting effect of H_2S is of the same magnitude as the accelerating effect of the H_2 pressure, both effects will cancel out, and the reaction rate does not change. Obviously the temperature has no effect as both total pressure and "dilution rate" (HTO) do not change.

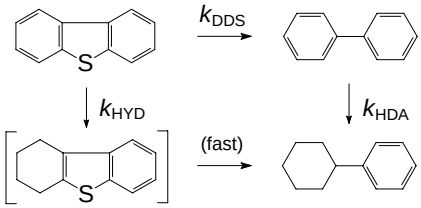

Figure 1. Simplified reaction network for the hydrodesulfurization of dibenzothiophene, adapted from [2].

The question remains why this strong H_2S inhibition only manifests itself at low conversion. A logical explanation may be found in the composition of the LGO feed: It contains a relatively high amount of sulfur (8445 ppmw), of which a large fraction consists of dibenzothiophene (DBT) and its mono-substituted analogues. These components exhibit low steric hindrance and are easily converted, mainly by the direct desulfurization route (DDS, see Fig. 1). At high conversion levels (>95%) the rate is fully controlled by the desulfurization of di-substituted DBTs [3]. These compounds are essentially converted by the prehydrogenation route (HYD), as the DDS route is retarded due to steric hindrance. The fact that H_2S inhibits the DDS route much stronger than the HYD route completes our hypothesis for the LGO HDS pressure independence at low conversion. In order to test this hypothesis we have performed several DBT HDS experiments under various process conditions upon different catalyst pretreatments.

Experimental

A model NiMo catalyst supported on γ-Al_2O_3 containing 10 wt% MoO_3 and 2.5 wt% NiO was prepared by pore volume impregnation. The catalyst was calcined, then crushed and sieved before testing. Steady state experiments were performed in a microflow trickle bed reactor using 4 grams of catalyst (250 – 500 μm) diluted with SiC particles (200 μm) to ensure proper hydrodynamic behavior. The catalyst was sulfided *in-situ* in the gas phase using 10 vol% H_2S in H_2 at 60 ml/min, 400°C and 1 atm. during 2 hours. The feed consisted of 0.2 wt% DBT and 0.2 wt% n-C_{18} (internal standard) in n-C_{16}. Samples were taken after 5 hours stabilization time and one hour later (as duplo). Batch experiments were done in a 200 ml swinging-capillary autoclave reactor using 200 mg of catalyst (150 – 250 μm). The same sulfiding procedure and feed composition as in the flow reactor was used. In one experiment 700 mg of copper powder was added as H_2S scavenger. This is a proven method to remove all H_2S produced during the reaction [2]. A blank run (without catalyst) confirmed that copper alone had negligible catalytic activity. Samples were analyzed using a GC with FID detector.

Results and Discussion

The effect of H_2 pressure on the DBT HDS activity is shown in Figure 2. The overall HDS rate constant shows a very weak dependency on H_2 pressure, just like in the LGO case we reported previously. Moreover, when we decompose the total activity into the specific rate constants for the DDS and HYD route (assuming constant selectivity, *i.e.* $k_{HDA} \approx 0$) we clearly see that the DDS rate is zero-order in pressure, whereas the HYD rate is perfectly first order. This implies that the DDS route is strongly inhibited by self-produced H_2S, and the HYD route shows no measurable inhibition.

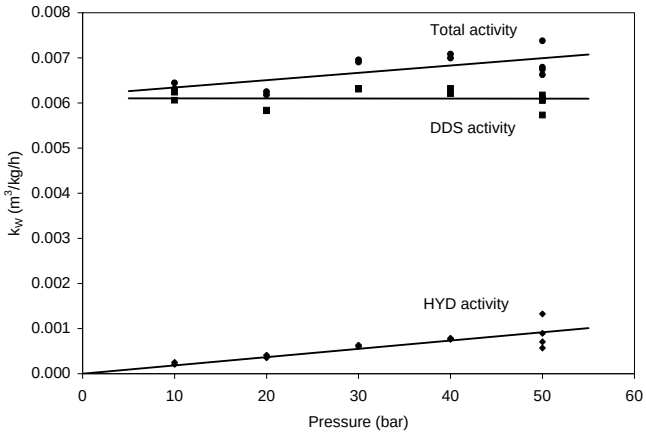

Figure 2. Effect of H_2 pressure on DBT HDS (microflow reactor, 225°C, LHSV = 2.4 h^{-1}, HTO = 588 nl/l).

At a constant H_2S partial pressure (0.2 bar) the picture changes dramatically (Fig. 3). The DDS route now shows a perfect first order fit, as well as the HYD route. Both rates are lower due to inhibition

* Corresponding author, email: A.D.vanLangeveld@tnw.tudelft.nl

by H_2S. Taking into account that this experiment was conducted at a 50°C higher temperature and the activation energy was found to be about 75 kJ/mol, the DDS rate constant at 30 bar decreased by a factor of 10 and the HYD rate constant by a factor of 2. This proves that indeed the DDS route is much more sensitive to H_2S inhibition than the HYD route.

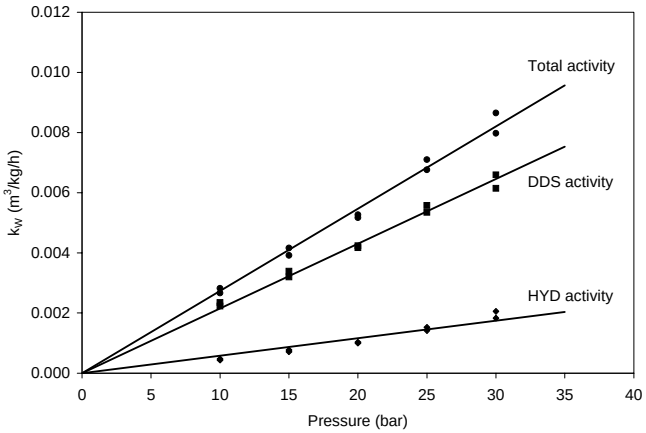

Figure 3. Effect of H_2 pressure on DBT HDS at constant (0.2 bar) H_2S partial pressure (microflow reactor, 275°C, LHSV = 2.4 h^{-1}, HTO = 588 nl/l).

In a previous paper [4] we have shown that during the HDS of thiophene in the gas phase, the state of the catalyst active phase, *viz.* the number of exposed Mo or Ni atoms (;sulfur vacancies;) changes as a result of the different conditions during presulfiding and reaction. When we look at the effect of catalyst pretreatment on the liquid phase DBT HDS (Fig. 4) we see that the total HDS activity (k_{DDS} + k_{HYD}) does not change, but the selectivity (HYD to DDS) does change. Apparently a H_2 treatment before reaction reduces the number of HYD sites and evenly increases the number of DDS sites. This can be explained when a H_2 treatment, analogous to gas phase thiophene HDS, creates sulfur vacancies on the catalyst active surface by removing sulfur and/or SH groups. These acidic groups are involved in the HYD reaction pathway, and the sulfur vacancies are responsible for the direct sulfur abstraction (DDS).

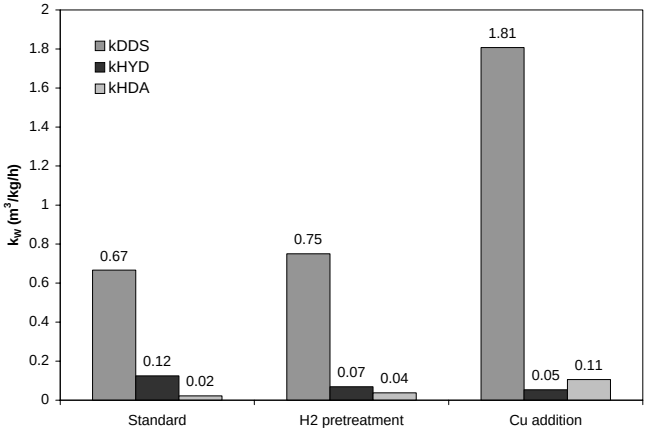

Figure 4. Effect of H_2 pretreatment and H_2S removal on the DBT HDS rate constants (batch autoclave, 350°C, 50 bar).

When all self-produced H_2S is removed from the system by copper powder, we observe a tremendous increase in DDS activity. This again proves the high sensitivity of the DDS sites to sulfur inhibition. The rate of HDA increases accordingly, so it appears that the same type of sites catalyzes the HDA reaction. The reactants and H_2S are competitive adsorbents on the vacant sites, which can also explain the perfect first-order fit in DBT conversion when self-produced H_2S is not removed. Apparently the adsorption effects normally observed (Langmuir-Hinshelwood kinetics) cancel out. Based on our observations we propose the following rate equation for the DDS route (Eq. 2).

$$r_{DDS} = \frac{k_{HDS} C_{DBT} p_{H2}}{1 + K_{DBT} C_{DBT} + K_{H2S} p_{H2S} + K_{H2} p_{H2}} \qquad \text{(Eq. 2)}$$

Here we assume that H_2 dissociation occurs on the same sites as the DDS reaction, which is not unlikely as these sites (vacant Mo or Ni atoms) apparently catalyze the HDA reaction as well. When the adsorption constants K_{DBT} and K_{H2S} are approximately equal, the number of vacant sites does not change during reaction and pseudo first-order kinetics are observed. When H_2S is removed, the adsorption of DBT becomes significant and the reaction rate will deviate from the first order model (as was the case in the experiment with Cu addition). Furthermore, when K_{H2} is small compared to K_{DBT} and K_{H2S} the reaction also becomes first order in hydrogen pressure, as was observed in our microflow experiments. Also the apparent order in p_{H2S} becomes –1, which cancels out against the first order in p_{H2} in a flow reactor (without H_2S addition), in full agreement with our DBT and LGO HDS results. The HYD route shows very little inhibition, which implies the role of H_2S as competitive adsorbent is small. Possibly, at high H_2S concentrations, the HDS of the prehydrogenated DBT molecules becomes a limiting factor.

Conclusions

In the hydrodesulfurization of high sulfur-containing oil streams (*e.g.* LGO) inhibition by self-produced H_2S plays an important role. The major fraction of sulfur compounds in these streams consists of dibenzothiophene and its mono-substituted analogues, which are mainly converted by the direct desulfurization (DDS) route. At low conversion this leads to a zero-order behavior in hydrogen pressure, because in a flow reactor the partial pressure of gaseous reaction products (in particular H_2S) scales linearly with the total pressure, and the DDS route exhibits a very strong inhibition by H_2S.

The effect of H_2S partial pressure on the catalytic performance is two-fold: The H_2S/H_2 ratio may alter the balance between DDS sites (sulfur vacancies) and HYD sites (SH groups) on the catalyst active phase. Secondly, H_2S competes very strongly with reactants for adsorption on vacant sites, thus inhibiting the DDS reaction. The effect on HYD activity is much smaller, and may be due to inhibition of the second step in this pathway; the HDS of prehydrogenated species. All experimental observations can be explained by a Langmuir-Hinshelwood kinetic model in which $K_{H2} << K_{DBT} \approx K_{H2S}$.

Acknowledgement. AKZO Nobel Chemicals, the Netherlands, and the Dutch Organization for Scientific Research (NWO) are gratefully acknowledged for financial support.

References

[1] Vogelaar, B.M.; Gast, J.; van Langeveld, A.D.; Eijsbouts, S.; and Moulijn, J.A. Prepr. Pap. - *Am. Chem. Soc., Div. Petr. Chem.*, **2002**, *47* (1).

[2] Farag, H.; Mochida, I.; and Sakanishi, K. *Appl. Catal. A - Gen.*, **2000**, *194-195*, 147-157.

[3] Vradman, L.; Landau, M.V.; and Herskowitz, M. *Catal. Today* **1999**, *48*, 41-48.

[4] Vogelaar, B.M.; Steiner, P.; van Langeveld, A.D.; Eijsbouts, S.; and Moulijn, J.A. Prepr. Pap. - *Am. Chem. Soc., Div. Petr. Chem.*, **2002**, *47* (1).

INHIBITING EFFECTS OF BASIC NITROGEN ON DEEP HYDRODESULFURIZATION OF DIESEL

*Uday T. Turaga, Gang Wang, Xiaoliang Ma, and Chunshan Song**

Clean Fuels and Catalysis Program, The Energy Institute and
Department of Energy and Geo-Environmental Engineering,
The Pennsylvania State University, University Park, PA 16802
*Corresponding author. E-Mail: csong@psu.edu

Introduction

The subject of inhibition of hydrodesulfurization (HDS) activity has been studied extensively [1] and some of the key inhibitors include aromatics, nitrogen-containing compounds, hydrogen sulfide, saturated hydrocarbon solvents, ammonia, and even water. Of these, nitrogen-containing compounds were identified as having the most severe inhibiting effect [2]. Atmospheric gas oil, which is frequently used as a diesel feedstock, typically, contains nitrogen compounds 70% of which are non-basic (e.g., carbazole type) while the rest are basic (e.g., quinoline type). Light cycle oil, a feedstock used for diesel and thermally stable naphthenic jet fuels [3, 4], contains much higher nitrogen, predominantly non-basic in nature [5]. Diesel and some jet fuel feedstocks, therefore, have enough nitrogen species to significantly influence deep HDS.

Nitrogen's effects on HDS catalytic activity could become all the more important because the U.S. Environmental Protection Agency requires that diesel in 2006 have sulfur content no more than 15 wppm [6]. Sulfur removal to such depths will require knowledge of the influence of non-sulfur diesel fuel components on deep hydrodesulfurization. Furthermore, the reactivity of nitrogen-containing heterocompounds is much lower than those of polyaromatic sulfur compounds (PASCs) [7]. Therefore, nitrogen compounds will be present in appreciable quantities even at very low sulfur levels and could significantly influence the deep HDS of PASCs.

Several researchers have clearly established the inhibiting effect of basic nitrogen compounds on the HDS of thiophene and dibenzothiophene (DBT) [8, 9]. However, there is little literature on the effects of quinoline and tetrahydroquinoline (THQ) specifically on the HDS of DBT and 4,6-dimethyldibenzothiophene (4,6-DMDBT). The present work evaluates the inhibiting effects of THQ and quinoline on a commercial Co-Mo/γ–Al_2O_3 hydrodesulfurization catalyst. This extends our previously reported studies on novel HDS catalysts [3, 10-13].

Experimental

All catalysts were evaluated in a laboratory-scale fixed-bed flow reactor which has been described elsewhere [12]. The catalyst evaluation conditions used in this project are summarized in Table 1. All catalysts were sulfided *in situ* at uniform conditions. A typical model compound feedstock contained 1500-2000 wppm of sulfur in the form of 4,6-DMDBT and DBT dissolved in hydrocarbon solvents such as *n*-dodecane (*n*-C_{12}) or *n*-tridecane (*n*-C_{13}). These feeds were spiked with either quinoline or THQ in amounts such that the total nitrogen content was 250 ppm. The liquid reaction products were characterized using a Hewlett Packard 5890 Series II gas chromatograph coupled with flame ionization (FID) and flame photometric detectors (FPD).

A Co-Mo/γ-Al_2O_3 commercial catalyst supplied by Criterion Catalyst Corporation, Houston, TX, was used for this study. This catalyst is referred to in this study by its trade name, C-344. A typical catalyst evaluation experiment used 1 g of the catalyst. All catalysts evaluated in the flow reactor were particles of 0.5-1.0 mm in diameter.

Table 1. Flow Reactor Experimental Conditions.

Catalyst Sulfidation	
Temperature	350 °C
10% H_2S in H_2 (vol.%) flow rate	200 ml/min
Time	4 hours
Deep HDS Reaction	
Temperature	240-350 °C
Pressure	660 psi
Weight Hourly Space Velocity	1-8 h-1
Hydrogen/Hydrocarbon	300 ml/ml
Catalyst particle size	0.5-1.0 mm (18-35 mesh)
Catalyst weight	1 g

Results and Discussion

Figure 1 shows the conversion of 4,6-DMDBT with and without the presence of quinoline and THQ. Similarly, Figure 2 presents conversion data for DBT. It is clear in both cases that the conversion of the PASCs is inhibited by both quinoline and THQ. However, inhibition by THQ is significantly more in comparison to that by quinoline. At higher temperatures, the inhibiting effects of quinoline on the HDS of 4,6-DMDBT are magnified. Nevertheless, quinoline continues to be weaker inhibitor in comparison to THQ.

A potential explanation for the differences in inhibiting effects shown by quinoline and THQ lies in their basicities. The aqueous phase pKa values of quinoline and THQ are 4.9 and 5.0, respectively [13]. The pKa values provide an indicator of the proton affinity tendencies of these molecules. Clearly, THQ has a marginally higher proton affinity than quinoline. Therefore, THQ could be expected to have a stronger tendency to adsorb and deactivate adsorption sites on the commercial catalyst surface. Although it is recognized that under the conditions in which HDS occurs, the molecules might be in gas phase, it is instructive in evaluating the aqueous phase to draw preliminary trends.

Determining the influence of quinoline and THQ on the HDS of PASCs is an important problem because of the characteristics of the hydrodenitrogenation of quinoline, which might be present in significant quantities at the low sulfur levels required by new specifications. The hydrodenitrogenation of quinoline takes place through one of two pathways. The first produces decahydroquinoline and propylcyclohexylamine as intermediates, while the second results in THQ and *o*-propylaniline. Both pathways lead to propylcyclohexane, which is the main product of the hydrodenitrogenation of quinoline.

Earlier studies on quinoline hydrodenitrogenation had suggested that the pathway forming THQ and *o*-propylaniline was negligible [13]. However, over phosphided Ni-Mo catalysts, Jian and Prins [14] have shown that this is not the case. They found that in the temperature range of 350-370 °C, about 35-40% of the hydrodenitrogenation of quinoline occurs through the pathway forming THQ and *o*-propylaniline as intermediates.

The results of the present paper suggest that if more of quinoline is converted through the pathway producing THQ as an intermediate, the THQ formed as an intermediate might further magnify the

inhibition of the overall HDS reaction. Therefore, the results presented in this paper quantifying the extent and difference of inhibition caused by quinoline and THQ are an important step towards further understanding of the inhibiting effects of nitrogen on deep hydrodesulfurization of diesel feedstocks. (9 pt)

Conclusions

The inhibiting effects of quinoline and THQ were evaluated for the HDS of PASCs, namely DBT and 4,6-DMDBT. Both forms of basic nitrogen were found to inhibit the HDS of both PASCs. THQ, however, had a larger inhibiting effect in comparison to quinoline. The origin of this higher inhibiting effect is tentatively attributed to the former's marginally higher proton affinity. The effect of nitrogen-containing compounds on the deep HDS of diesel feedstocks is a critical problem because with ultra-low sulfur specifications, the concentration of nitrogen will become high enough to influence the overall HDS reaction. Therefore, a better understanding of nitrogen compounds and the intermediates formed during their decomposition (e.g., THQ which is formed during the hydrodenitrogenation of quinoline) on HDS is required, towards which this paper makes an important contribution.

Acknowledgements. The authors are grateful to Professor Harold H. Schobert for useful discussions. The United States Air Force Office of Scientific Research and the United States Department of Energy supported this work.

References

1. Girgis, M. J. and Gates, B. C. *Ind. Eng. Chem. Res.* **1991**, *30*, 2021-2058..
2. Schulz, H.; Bohringer, W.; Waller, P.; Ousmanov, F. *Catal. Today*, **1999**, *49*, 87.
3. Turaga, U.T. and Song, C. *Am. Chem. Soc. Div. Pet. Chem. Prepr.*, **2002**, *47*, 97.
4. Song, C. In *Chemistry of diesel fuels* Song, C.; Hsu, C.S.; and Mochida, I. Eds. Taylor & Francis: New York, **2000**, pp 1-60.
5. Dorbon, M. and Bernasconi, C. *Fuel* **1989**, *68*, 1067.
6. EPA. *Federal Register* **1999**, *64*, 26142.
7. Zeuthen, P.; Knudsen, K.G.; Whitehurst, D.D. *Catal. Today* **2001**, *65*, 307-314.
8. Satterfield, C.N., M. Modell, and J.F. Mayer, "Interactions between catalytic hydrodesulfurization of thiophene and hydrodenitrogenation of pyridine." *AIChE Journal*, 1975. **21**: p. 1100-1197.
9. Satterfield, C.N.; Modell, M; Wilkens, J.A. *Ind. Eng. Chem. Proc. Des. Dev.* **1980**, *19*, 154.
10. Turaga, U.T. and Song, C. *Proc.16th Ann. Intl. Pitt. Coal Conf.* **1999,** Paper No. 20-25.
11. Turaga, U.T. and Song, C. *Am. Chem. Soc. Div. Pet. Chem. Prepr.*, **2001**, *46*, 275.
12. Turaga, U.T. and C. Song, "MCM-41-Supported Co-Mo catalysts for deep hydrodesulfurization of light cycle oil." *Submitted*, 2003.
13. Ho, T.C. *Catal. Rev.—Sci. & Eng.*, **1988**, *30*, 117.
14. Jian, M.; Prins, R. *J. Catal.*, **1998**, *179*, 18.

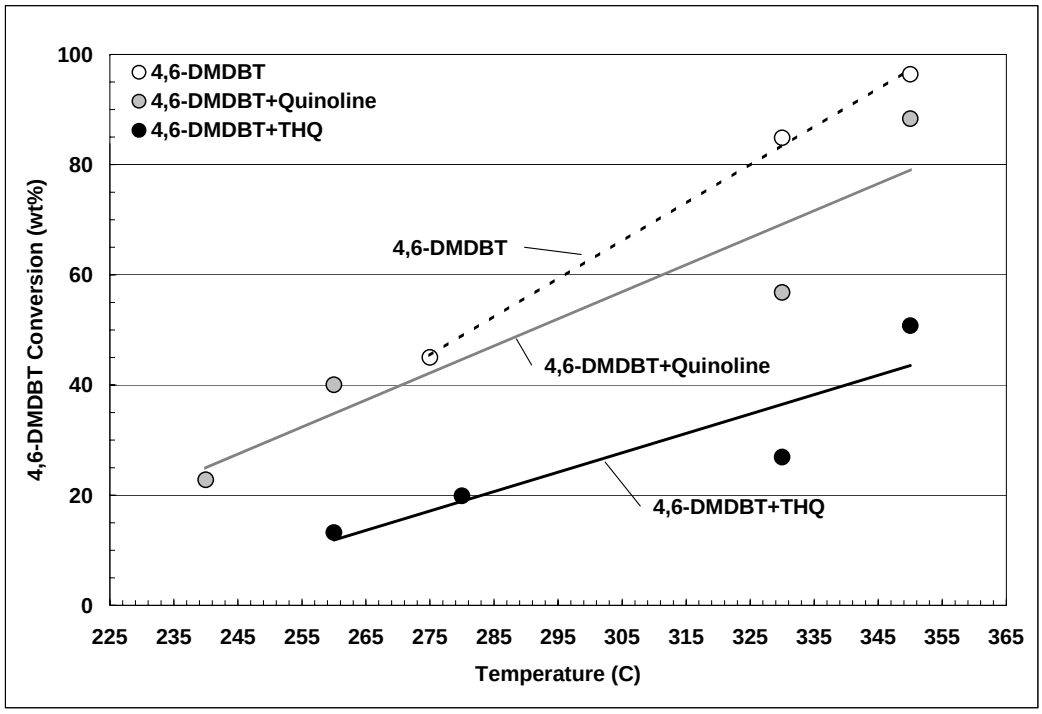

Figure 1. HDS of 4,6-DMDBT with and without basic nitrogen compounds.

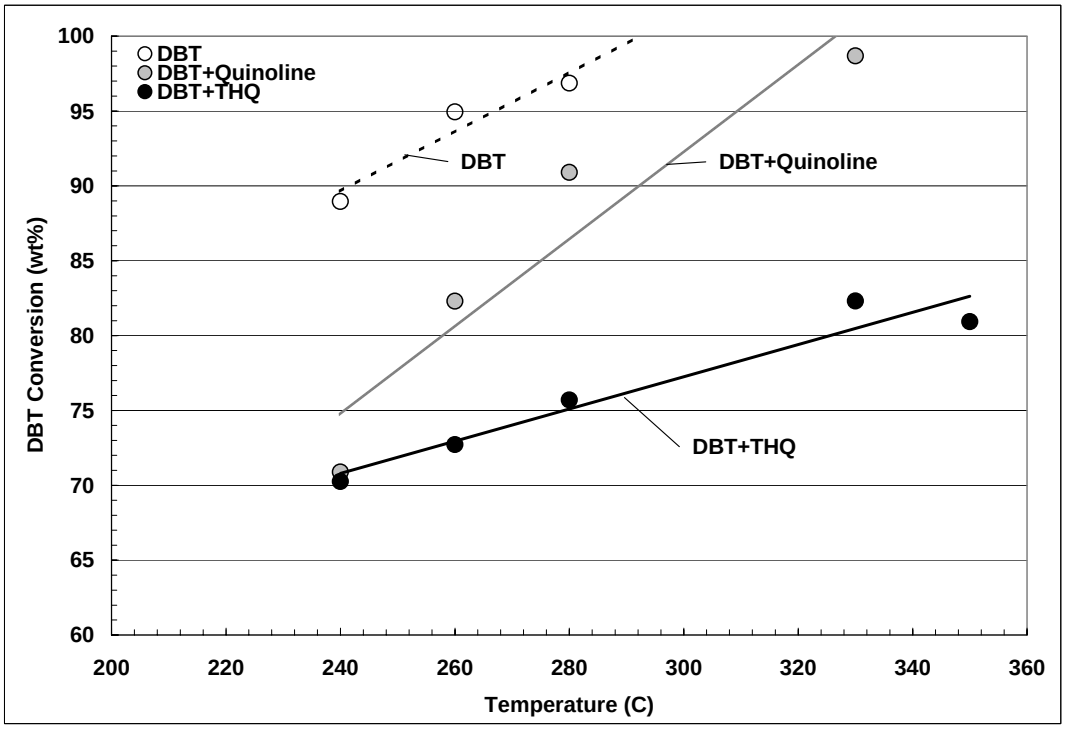

Figure 2. HDS of DBT with and without basic nitrogen compounds.

KINETIC STUDY OF EFFECTS OF AROMATIC COMPOUNDS ON DEEP HYDRODESULFURIZATION OF 4,6-DIMETHYLDIBENZOTHIOPHENE

*Jae Hyung Kim, Xiaoliang Ma and Chunshan Song**

Clean Fuels and Catalysis Program, The Energy Institute and Department of Energy and Geo-Environmental Engineering, The Pennsylvania State University, 209 Academic Projects Building, University Park, PA 16802
*E-mail: csong@psu.edu

Introduction

Deep hydrodesulfurization (HDS) of diesel fuel is an important research area due to increasingly stringent environmental regulations for the sulfur content in fuel (1). The sulfur level in diesel fuel will have to be reduced from the present 500 ppmw to 15 ppmw by 2006. Therefore, the studies on deep hydrodesulfurization of diesel fuels are being conducted by many research groups with various methods (1-4).

Sulfur compounds remaining in the current commercial diesel fuel are alkyl dibenzothiophenes (DBTs), especially those with one or two alkyl groups at the 4- and 6-positions. These alkyl DBTs have been reported to be the refractory sulfur compounds in diesel fuel (2,3), in which 4,6-dimethyl-dibenzothiophene (4,6-DMDBT) is a typical refractory sulfur compound. HDS of DBTs generally proceeds through two reaction pathways, hydrogenation and hydrogenolysis pathways (4,5). In our previous study (6), we found that hydrogenation pathway was much more dominant than hydrogenolysis pathway in HDS of 4,6-DMDBT, and the reaction pathways of 4,6-DMDBT can be described as shown in Figure 1.

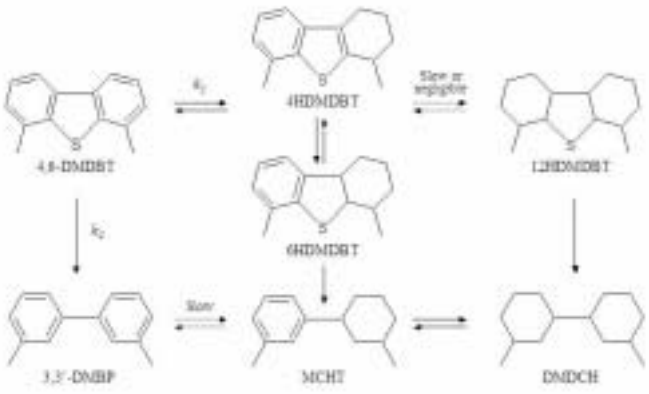

Figure 1. Schematic diagram of 4,6-DMDBT reaction pathways.

Diesel fuel and gas oil contain considerable amounts of aromatic and nitrogen compounds, which may affect the hydrodesulfurization reaction rate. The reported studies on effect of aromatic compounds on the reaction pathways of 4,6-DMDBT were limited in the literature and some privous results are still debated. Some researchers reported that the addition of aromatic compounds led to a significant negative effect on the rate of HDS, though others showed a slight inhibition of aromatics toward HDS (7). In this study, effect of aromatic compounds on HDS of 4,6-DMDBT were examined kinetically using the method that was developed in our previous study (6).

Experimental

4,6-DMDBT was used as the model sulfur compounds in the present study was used. The feed for each run contained 0.05g of 4.6-DMDBT and 4.00g of decalin as solvent. In order to examine the effect of aromatic compounds on HDS of 4,6-DMDBT, an equimolar amount of 1-methylnaphthalene (1-MN) and 4,6-DMDBT (or 0.74 mol of fluorene and 1.00 mol of 4,6-DMDBT) were added into the feed. The reactions were carried out in 25-mL, horizontal micro-reactor agitated at 200 strokes/min in a fluidized sand bath at the reaction condition of 300°C and 300psi H_2 pressure. Gas chromatography with a FID detector was used for quantitative analysis of products. GC-MS and some standard samples were used for identification of products.

Two commercial catalysts from Criterion, Cr344 ($CoMo/Al_2O_3$) and Cr424 ($NiMo/Al_2O_3$), were used after presulfidation with 10 vol % H_2S in H_2 at a flow rate of 200 ml/min, 350˚C for 4 h. After presulfidation, the catalysts were stored in decalin before use in order to minimize oxidation.

Results and Discussion

In order to get better kinetic data, the conversion of 4,6-DMDBT was kept below 20%. The main products from 4,6-DMDBT HDS were HDMDBT (hydrodimethyldibenzothiophene), MCHT (methyl cyclohexyltoluene). In addition, DMDCH (dimethyldicyclohexyl) was also detected at high conversion. During HDS of 4,6-DMDBT, the main products from 1-methylnaphthalene (1-MN) hydrogenation were 1-methylteralin (1-methyltetrahydronaphthalene) and 5-methylteralin (5-methyltetrahydronaphthalene). Hexahydrofluorene was a dominant product from hydrogenation of fluorine.

In general, HDS of individual sulfur compound follows the pseudo-first-order kinetics, thus:

$$\ln(C_{DMDBT} / C_{DMDBT0}) = -(k_1 + k_2)\cdot t \qquad (1)$$

where k_1 is the pseudo first-order rate constant for the hydrogenation pathway, and k_2 is the pseudo first-order rate constant for the hydrogenolysis pathway. The value of (k_1+k_2), the overall rate constant, can be calculated from experimental data. Figure 2 and 3 show the pseudo first order kinetic profiles of 4,6-DMDBT HDS in the presence and absence of aromatic compounds over CoMo and NiMo sulfide catalysts. The overall rate constants calculated on the basis of the experimental data are shown in Table 1.

Based on the results, the presence of 1-MN reduces significantly the HDS rate of 4,6-DMDBT. For the CoMo sulfide catalyst, the overall rate constant of 4,6-DMDBT decreases from 44.15×10^{-5} $s^{-1}g\cdot cat^{-1}$ in the absence of 1-MN to 33.90×10^{-5} $s^{-1}g\cdot cat^{-1}$ in the presence of 1-MN, and for NiMo sulfide catalyst, from 117.21×10^{-5} $s^{-1}g\cdot cat^{-1}$ to 76.22×10^{-5} $s^{-1}g\cdot cat^{-1}$. It was found that fluorene shows a much stronger effect on the overall rate constant than 1-MN. The overall rate constant in the presence of fluorene is 21.59×10^{-5} and 56.71×10^{-5} $s^{-1}g\cdot cat^{-1}$ for the CoMo catalyst and the NiMo catalysts, respectively. Koltai and coworkers reported the effects of aromatic compounds, including anthracene, phenanthrene and fluorine, on 4,6-DMDBT over NiMo sulfide catalyst at 300°C and 725 psi (7), They reported that there is no significant effect of the coexisting anthracene and dihydroanthracene on HDS of 4,6-DMDBT, even the concentration of anthracene and dihydroanthracene is 7 times higher than that of 4,6-DMDBT, while there is significant effect of the coexisting phenanthrene and fluorine on HDS of 4,6-DMDBT. Our result about the effect of fluorine is consistent with the result from Koltai and coworkers.

In this study, the individual rate constants for each reaction pathway were calculated by using the method suggested in our previous work (6). In this method, the ratio of k_1/k_2 was calculated by

the ratio of the initial selectivity of primary products, as shown below:

$$\frac{k_1}{k_2} = \frac{[\text{Initial Selectivity of HDMDBT}]}{[\text{Initial Selectivity of DMBP}]} \qquad (2)$$

Individual rate constants were calculated in combination of k_1/k_2 and (k_1+k_2) values. Table 1 lists the calculated rate constants for each reaction pathway with and without the presence of aromatic compounds. For the CoMo catalyst, the presence of the aromatic compounds degrades the rates for both hydrogenation pathway and hydrogenolysis pathway. For the NiMo catalyst, the presence of the aromatic compounds degrades slightly the rate for hydrogenolysis pathway, but degrades strongly the rate for hydrogenation pathway. The decrease of k_1/k_2 in the presence of the aromatic compounds was observed, indicating that these aromatic compounds have more effect on hydrogenation pathway than on hydrogenolysis pathway. The different effects of the aromatic compounds on the two pathways, especially over the NiMo catalyst, imply that the hydrogenation and hydrogenolysis might occur at different active sides, and the decrease of the catalytic activity of the NiMo catalyst by the aromatic compounds is probably due to a competitive adsorption between the aromatic compounds and 4,6-DMDBT for the active sites of hydrogenation.

Conclusions

In this study, effects of the aromatic compounds on HDS of 4,6-DMDBT were investigated kinetically. The presence of 1-MN and fluorene affects significantly on HDS of 4,6-DMDMBT at the reaction conditions of 300°C and 300 psi. The change in the ratio of k_1/k_2 indicates that the aromatic compounds have more negative impact on the hydrogenation pathway than on hydrogenolysis pathway. From a comparison of the two aromatic compounds, fluorene is a stronger inhibitor than 1-MN.

Acknowledgement. This work was supported in part by New Energy and Industrial Technology Development Organization, Japan, and by US Department of Energy, National Energy Technology Laboratory.

References

(1) Song, C.; Ma, X. *Appl. Catal. B: Environ.*, **2003**, *41*, 207.
(2) Ma, X.; Sakanishi, K.; Mochida, I. *Ind. Eng. Chem, Res.*, **1994**, 33, 218.
(3) Gates, B. C.; Topsoe, H. *Polyhedron*, **1997**, 16, 3213.
(4) Broderick, D. H.; Gates, B. C. *AIChE J.*, **1981**, 27, 663.
(5) Sakanishi, K.; Nagamatsu, T.; Mochida, I.; Whitehurst, D. *J. Mol. Cat. A*, **2000**, 155, 101.
(6) Kim, J, H; Ma, X.; Song, C.; Oyama, T.; Lee, Y. K. Prepr. Pap. – *Am. Chem. Soc., Div. Fuel Chem.*, **2003**, 48 (1) 40.
(7) Koltai, T.; Macaud, M.; Guevara, A.; Schulz, E., Lemaire, M.; Bacaud, R.; Vrinat, M. *Appl. Catal. A*, **2002**, *231*, 253.

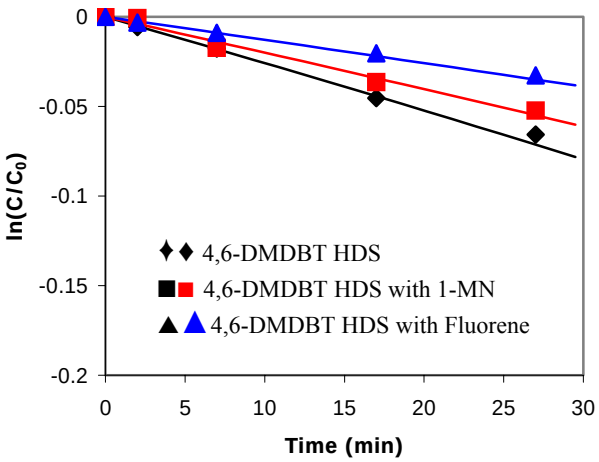

Figure 1. The effect of aromatic compounds on HDS of 4,6-DMDBT over CoMo sulfide catalyst.

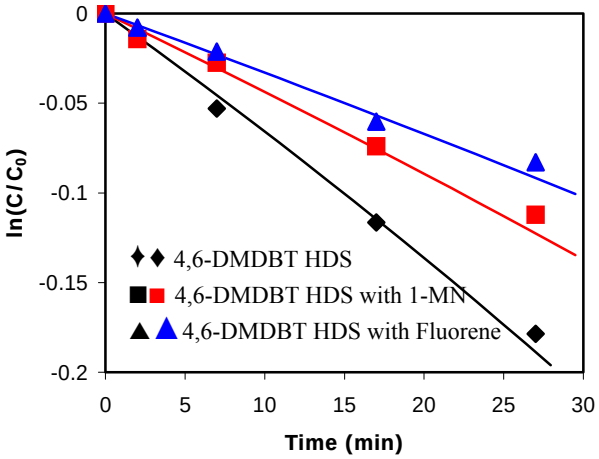

Figure 2. The effect of aromatic compounds on HDS of 4,6-DMDBT over NiMo sulfide catalyst.

Table 1. Kinetic Results for the Effect of Aromatic Compounds on Hydrodesulfurization of 4,6-DMDBT

		Rate constant (10^{-5} s^{-1} $g{\cdot}cat^{-1}$)		
Inhibitor		None	1-MN	Fluorene
CoMo Sulfide	k_1+k_2	44.15	33.90	21.59
	k_1/k_2[a]	2.26	2.22	1.79
	k_1	30.60	23.38	13.85
	k_2	13.55	10.50	7.73
NiMo Sulfide	k_1+k_2	117.21	76.22	56.71
	k_1/k_2[1]	5.36	3.66	2.65
	k_1	98.77	59.85	41.17
	k_2	18.44	16.37	15.54

[a] k_1/k_2 = [Initial selectivity of HDMDBT]/[Initial selectivity of DMBP]

APPLICATION OF DATAMINING METHOD (ID3) TO CORRELATION OF FEED PROPERTIES AND REACTIVITY FOR HDS OF DIESEL FUEL

Narinobu Kagami, Ryuichiro Iwamoto, Masaru Amano, and Tetsuji Tani

Manufacturing Deparment, Idemitsu Kosan Co., Ltd.
26 Anesakikaigan Ichihara-city Chiba, 299-0107, Japan

Introduction

In recent years, much attention has been focused on the deep hydrodesulfurisation (HDS) of diesel fuel oil because environmental legislation has become more and more strict. Then it becomes more important to estimate the reaction temperature correctly to meet the target of sulfur at various conditions using various feedstocks. Because too deep desulfurisation makes the catalyst life shorter than producing correct target sulfur diesel[1)], determining the accurate corrected WAT (weight average temperature) is very important for the management of the diesel production and the catalyst life span.

It is well known that corrected WAT is used to evaluate the catalyst life. And WAT is a function of the operation condition factors such as temperature, LHSV, Hydrogen pressure, Hydrogen-oil ratio and of the feed properties. Operation condition factors can be normalized from the formula based on n-order (pseudo) reaction and Ahrrenius plots through tuning the constant. These operation factors can be changed independently using pilot tests, however, it is almost impossible with a real feed to vary just one property independently. Therefore, the suitable selection of key factors of feed properties might be difficult using real feed.

The formula of the corrected WAT normalized to the standard from various feed properties was made by trial and error method somehow, using the factors chosen by the information of literature[2)]. However, we still need a convenient way to evaluate the validity of the chosen factors.

Recently, datamining methods tend to be used more commonly in data processing field. Datamining is one of the technologies for building knowledge-based systems by inductive inference from examples. Therefore, it can also be the method to search the valuable information from large data sets. In dataming methods, the classification analysis called ID3 (Iterative dichotomiser) is applicable.

ID3 algorithm was suggested by J.R Quinlan[3)] and extended to deal with numerical values[4)]. Using entropy of information that shows the degree of chaotic state, ID3 establishes the importance of the factor automatically.

Then ID3 was applied to evaluate the validity of the chosen factors from various feed properties for the corrected WAT normalized to the standard.

Experimental

Catalyst and Pretreatment. 100cc of commercial catalyst of CoMo type catalyst was filled in a high-pressure micro-flow reactor. Before the evaluation of SRLGO, the catalyst was presulfided in situ at 250 °C for 2h and then 300 °C for 2h in stream of a dimethyl-disulfide/SRLGO/hydrogen mixture (sulfur content, adjusted as 2.5wt%).

Pilot Test. Pilot tests were carried out using high-pressure micro-flow reactor. The temperature of the catalyst bed was kept constant to avoid temperature difference over the catalyst bed by heater blocks. Thermocouples were located in the center of the catalyst beds. In these range of the operation conditions, the results of sulfur content of the product were from 500 to 5 ppm.

Analysis of feeds and products. Six kinds of straight run light gas oils (SRLGO) from Middle East crude were tested in high pressure flow reactor. The various properties of feedstocks were measured as shown in Table 1.

The sulfur content of product was also measured. The product oils were stripped by nitrogen to get rid of the H_2S in the liquid before the measurement.

ID3 data analysis. ID3 software package were used for the analysis of the data of pilot tests (XpertRule (Lascombe and Company, Ltd.)). Figure.1 shows the algorithm of ID3. A classification rule was expressed as a decision tree. The relationship between object Item A and attribute Items X, Y, Z were examined using the entropy of information. As step 0 shows, the entropy of the object item (I) was calculated. Next object item is divided according to the attribute items, and each entropy (E (X, Y, Z)) was calculated as step 1 shows. Then the subtract values of I – E (X, Y, Z) were information gains. And the largest information gain means that the information becomes less chaotic. Then, Item X was selected as first attribute and this routine was reiterated. In this way, ID3 can select the simplest decision tree.

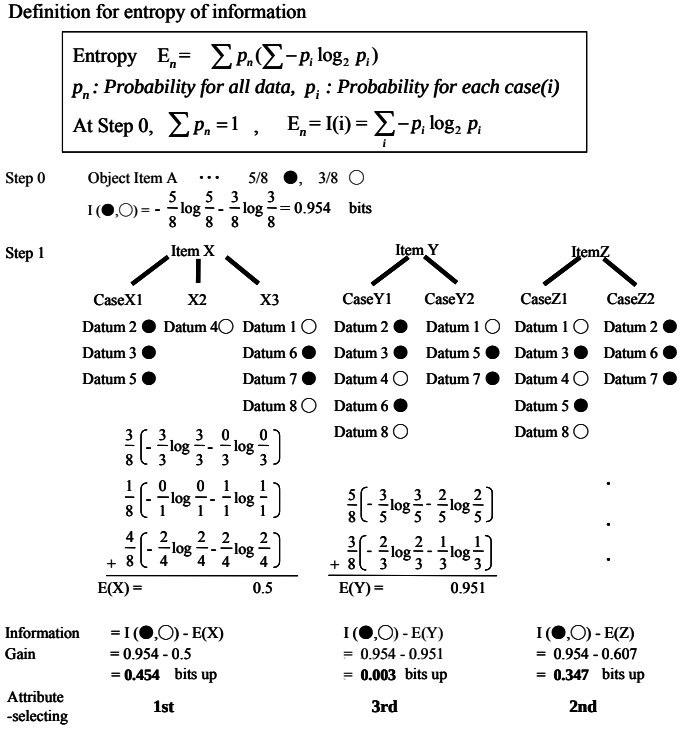

Figure 1. Outline algorithm of ID3(Iterative Dichotomiser).

Results and Discussion

Operation condition factors can be corrected independently, because each operation factor can be changed independently using the same feed stocks. It is well known that corrected WAT is used to evaluate the catalyst activity and its deactivation rate. The reaction temperature under the normalized conditions can be calculated as follows (Ahrrenius eq.1, n-order reaction eq.2, hydrogen-oil ratio eq.3, hydrogen pressure eq.4).

$$\ln k = \ln A - \frac{Ea}{RT}, \ln k'' = \ln A - \frac{Ea}{RT''} \qquad (eq.1)$$

$$k = \frac{LHSV}{n-1} \times \left(\frac{1}{S_p^{n-1}} - \frac{1}{S_f^{n-1}} \right) \qquad (eq.2)$$

$$k' = k \times \left(\frac{Hoil\text{-}Ratio_P}{Hoil\text{-}Ratio_S} \right)^{\alpha} \qquad (eq.3)$$

$$k'' = \exp(\ln k') \times \left(\frac{HP_P}{HP_S} \right)^{\beta} \qquad (eq.4)$$

In Fig.2, the actual WAT and corrected WAT standardized at a certain operation condition were shown. After the normalization of operation condition factors, the data scattering range becomes small. However, the scattering is still above 15 °C difference, depending on the properties on the kind of feed.

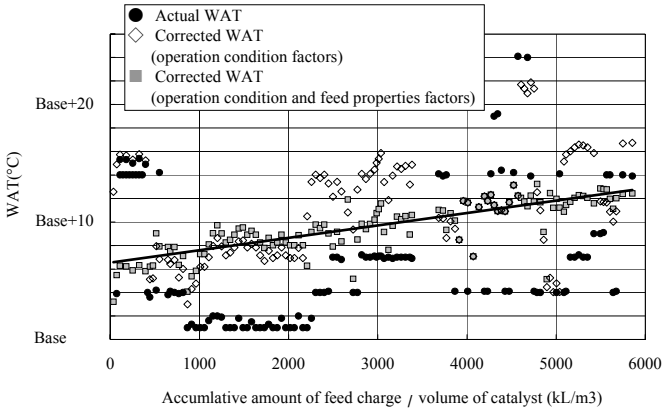

Figure 2. Actual and Corrected WAT for HDS reaction.

The WAT during the deep desulfurisation of the gas oil could be regarded to increase linearly with time on stream as shown in some literature[5]. When LHSVs were changed, accumulative amount of feed throughput per catalyst volume should be better to use instead of time on stream, to evaluate the deactivation pattern of catalyst.

Recently the inhibition of HDS reaction by nitrogen compounds was evaluated[6]. Especially the basic nitrogen compounds are thought to have the strongest effects to HDS reaction.

Moreover, it is well known that the heavier sulfur compounds (Dibenzothiophene (DBT) type sulfur compounds, especially 4,6-substituted DBT) has a lower activity than lighter sulfur compound such as benzothiophene type sulfur compounds.

Therefore, the following factors of feed properties were chosen for WAT normalized feed properties as eq.5 shows. "SpGr" is density of feed stocks and it is also used for reside hydrodesulfurization reaction. "Base N" is the content of basic nitrogen (Potentiometric titration). And "T90" is the temperature of 90% distillation (ASTM D-86), which means how heavy the feed is.

Then the trial and error method was used to determine the constant value of a, b, c (eq.5).

$$\ln A' = \ln A + a \cdot \ln\left(\frac{SpGr'}{SpGr}\right) + b \cdot \ln\left(\frac{BaseN'}{BaseN}\right) + c \cdot \ln\left(\frac{T90'}{T90}\right) \qquad (eq.5)$$

As deactivation pattern was regarded to be linear line, the least square method was applied and the standard deviation of all data was minimized changing each constant values. In this way, the values of constants were determined, and the results of normalization of feed properties are shown in Fig.2 Then, the difference from the linear line calculated by the least square became around 4 °C and much smaller than the one normalized only operation condition factors.

As described above, corrected WAT for feed properties was obtained. However, there is still the question whether the factors of feed properties chosen for normalization of the WAT are the best or not. To evaluate the validity of the chosen factors, ID3 method was used. Each difference between the data of corrected WAT normalized operation condition factors and the calculated deactivation line was examined.

Therefore, the data of subtraction from the diamond plot (◊) to the line in Fig.2 is the object item "A" and, "A" is examined by the feed properties factors, items "X, Y, Z …….. ". Operation factors are also used to convince that the normalization of them is. The one applied method is ID3, and the other is the correlation coefficient for the analysis. However, object item "A" should not be continuum but step number for the ID3 analysis. Then subtraction was classified per 2 °C.

Table 1 shows the results of the analysis. The effective factors for classification were arranged in order of increasing entropy (Class I to XII), using ID3 method. Clearly, the smaller the entropy, the more effective the factor is. However, in order to select the valid factors, they should be independent of each other. Therefore, the correlation coefficient analysis was also used, and the factors which have a coefficient above 0.8 are shown as the same pattern-code.

Table 1. The Results of ID3 and Correlation Coefficient.

Ranking of entropy (step 1, E(X,Y...))	Effective factor for classification					
I	Type of feed	.	.	.	.	.
II	**Density**	Nitrogen	**Basic nitroger**	.	.	.
III	**Saturate**	1-ring Aroma.	T50VOL%.	T60VOL%.	T70VOL%.	Viscosity
IV	Feed Sulfur	T80VOL%..	**T90VOL%...**	T95VOL%..	EP.	.
:	:	:	:	:	:	:
VII	Accumulative amount of feed	.	.	.	.	.
VIII	WAT	.	.	.	.	.
IX	LHSV	.	.	.	.	.
X	Product Sulfur	.	.	.	.	.
XI	H2/Oil	.	.	.	.	.
XII	H2 Press.	.	.	.	.	.

The most effective factor is type of feed, and it means that the feed properties factors normalization should be done. The second ranking factors are density, and nitrogen, and basic nitrogen. The correlation coefficient of nitrogen and basic nitrogen is higher, then it means that they had a monotonic relation. Therefore, only the basic nitrogen was selected considering the information described above. The third effective ranking is saturate. It was examined in the same way (eq.5) to minimize the standard deviation. However, it has almost no effect to reduce the standard deviation. The forth are Feed sulfur, T90 vol%, T95vol%, and EP, then the feed sulfur has already been used to calculate the reaction rate constant. T90 vol%, T95vol%, and EP could be considered to be the same factor, then, T90vol% should be taken.

As described above, the factors determined by trial and error method are shown in the bold type, and these are validated by ID3 and correlation coefficient analysis.

Acknowledgment. We thank Prof. Jacob A. Moulijn for generous support to publish this work.

References

(1) Knudsen, K. G.; Cooper, B. H.; Topsoe, H. *Applied Catalysis A-General,* **1999**, *189*, 205.
(2) Laredo, G. C.; los Reyes, J. A.; Cano, J. L.; Castillo, J. J. *Applied Catalysis A-General,* **2001**, *207*, 103.
(3) Quinlan, J. R. *Machine Learning*, **1986**, *1(1)*, 81.
(4) Araki, Kojima *Jinkou Chinou Gakkaishi*, **1992**, *7(6)*, 992.
(5) Gerritsen, L. A.; Vogt , K.; Huismans, A. Quinlan, *Summary At the ERTC in Berlin,* in November **1998**.
(6) Whitehurst, D. D.; Knudsen, K.; Nielsen, I. V.; Wiwel, P.; Zeuthen, P. *Abstracts of Papers of the American Chemical Society,* **2000**, *219*, 23-PETR.

FISCHER-TROPSCH PRINCIPLES OF CO-HYDROGENATION ON IRON CATALYSTS

Hans Schulz

University of Karlsruhe
Engler-Bunte-Institute
76131 Karlsruhe, Germany

Introduction

The products of Fischer-Tropsch synthesis on iron catalysts can be composed very similarly as those obtained on cobalt catalysts. This similarity requires a common principle of their formation. But amazingly, FT-synthesis on iron catalysts differs in many regards when compared with FT-synthesis on cobalt:

(1) With cobalt increasing the reaction temperature from e.g. 210 to 350 °C, changes the selectivity to methane as for being the dominant product (e.g. 90 C %). With iron even at 350 °C the methane selectivity can remain low (e.g. 7 C %): The FT-regime is stable over a wide range of temperature.

(2) Increasing the H_2/CO-ratio, respectively reducing the CO partial pressure, changes the FT-selectivity to almost pure methane (at low CO partial) whereas with iron, even when reducing the CO-partial pressure to very low values, the selectivity is merely effected. This means that the FT-regime with cobalt can only exist at sufficiently high CO-partial pressure as in contrast to iron.

(3) Increasing H_2O-partial pressure does positively affect FT-synthesis on cobalt; lowering methane selectivity, increasing chain growth probability, increasing syngas conversion (at some circumstances high H_2O-partial pressure can deactivate the catalyst). With iron, H_2O does inhibit the FT-reaction and restricts the degree of conversion.

(4) Alkali is a very efficient and essential promotor for FT-synthesis on iron, having strong effects on reaction rate and selectivity. With cobalt, no or only minor effects of alkali are noticed.

(5) The water-gas-shift reaction and its reverse generally perform fast on (alkalized) iron catalysts but are not (or only poorly) observed with cobalt catalysts.

(6) The byproducts of FT-synthesis, respectively the minor reactions performing additionally to the main stream of non-trivial surface polymerization, are significantly different with iron- as compared with cobalt catalysts. With cobalt, in contrast to iron, secondary olefin reactions of hydrogenation, isomerization and incorporation occur. Also relations to organic complex catalysis (olefin-hydroformylation, olefin-polymerization and carbene reactions) are noticed in contrast to the performance on iron catalysts.

(7) With both the catalyst metals, processes of self-organization and restructuring of the catalyst occur but they are different in principle with iron and with cobalt. With cobalt the interaction of the cobalt metal with the reactants concerns segregation of the surface. With iron it concerns reaction with carbon, being formed from CO-dissociation to produce iron carbide phases and structured or amorphous carbon phases in addition to further compositional catalyst changes.

In this paper, specifically, the processes of self-organization of the Fischer-Tropsch regime with (alkalized) iron as the catalyst are regarded, as in contrast to the behavior of cobalt catalysts.

Results and Discussion

It is seen in Fig. 1 that the Fischer-Tropsch activity - a measure hereof is the yield of FT-products (Y_{FT}) - initially ($t_{exp.}$ ca. 10 min) is about zero in all the three cases. The precipitated catalysts had been reduced with hydrogen and - generalizing - about half of the iron was in the state of metallic iron and the other half in the state of magnetide in the beginning. So it is concluded that iron in its metallic form exhibits "no" Fischer-Tropsch activity. This is in contrast to e.g. cobalt or ruthenium where essentially the metal is the active phase for FT-synthesis.

The catalyst activity develops with time in about 5 episodes, respectively, kinetic regimes. Episode I relates to the very first contact of the synthesis gas with the catalyst when it replaces the inert gas in the reactor and chromatographic effects and reactor residence-time-behavior overlap with the conversion of reactants.

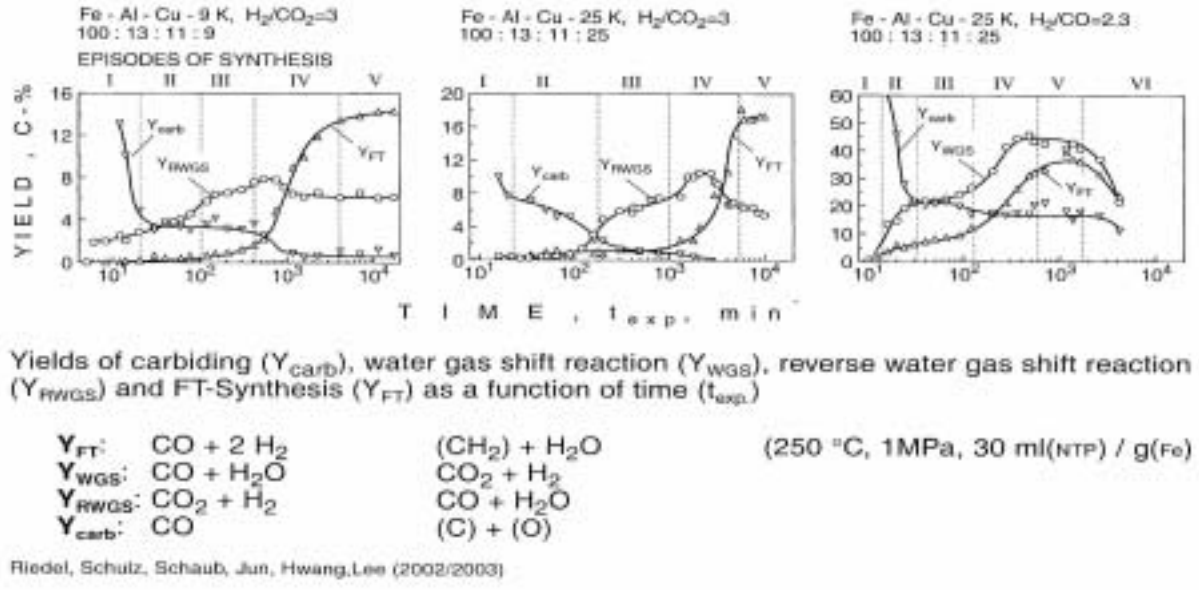

Figure 1. Initial episodes of FT-synthesis with iron as the catalyst.

In Episode II, the main process is the deposition of carbon (Y_{carb}) on the iron catalyst. The carbon yield increases to about 20 C % with the (H_2/CO = 2,3)-syngas (Fig. 1, right). With the (H_2/CO_2 = 3)-syngas the carbon yield is less excessive - e.g. 4-6 C % in Episode II (see Fig. 1, middle and left). Here with no CO but only CO_2 in the syngas, the carbon can only be formed as much as CO has been formed by the reverse water-gas-shift reaction. It is seen that also the water-gas-shift activity develops in-situ, prior to FT-activity. But even when in Episode III more CO has been formed from CO_2 plus H_2 (Y_{RWGS}), only marginal FT-activity is noticed (Fig. 1, left and middle). Then, in Episode IV after a number of hours on stream, the Fischer-Tropsch reaction sets in. Obviously, a distinct extent of iron carbiding is necessary for the catalyst to exhibit FT-activity. With the $3H_2/CO_2$-syngas this process of carbiding is slower as compared with the $2H_2/CO$-syngas.

Episode V is the steady-state of FT-synthesis. With the ($2H_2/CO$)-syngas a deactivation in Episode VI is noticed as caused by ongoing carbon formation due to high catalyst alkalization which is favorable at very low CO-partial pressure but too high for a CO-rich syngas.

In Fig. 2 the chain prolongation probability as a function of carbon number is presented for different times on stream and for the same three experiments as in Fig. 1. The result is very remarkable (and in complete contrast to what would be observed with cobalt catalysts). In dependence of time-on-stream only for the initial episodes (up to Episode III) when FT-yields are very low, the curve of growth probability is markedly affected. But during Episode IV when the FT-regime is being established as the FT-yield increases substantially, the curve shape changes only marginally. And even when comparing the steady-state curves for the three experiments the differences are small.

The surprising conclusion is that the FT-chemistry remains much the same, during establishing the FT-regime and even with both the synthesis gases $3H_2/CO_2$ and $2{,}3H_2/CO$.

It follows that increasing FT-activity here means an increase of the number of active sites, however, their nature being the same. And as the chemistry (selectivity) is invariant against the partial pressures, specifically of CO, that the sites are not dynamic in nature (in contrast to FT with cobalt).

When now searching for the common FT-principle with iron and cobalt catalysts, it should be a kinetic law, defined more by the sort of involved species than the catalyst composition (iron or cobalt). It is proposed to concern the frustration of the desorption reactions (for paraffins and olefins) thus allowing for the alternative reaction of adding C_1-species to the adsorbed chain.

In a complementary study of catalyst composition (and structure) as a function of time by XRD, Moessbauer spectroscopy, XPS it was observed that the FT-activity started to develop in correlation to the conversion of the alpha-iron-phase to a Fe_5C_2-carbide-phase. The carbide-phase is therefore regarded to possess the FT-active sites under reaction conditions and these sites appear to be very stable entities.

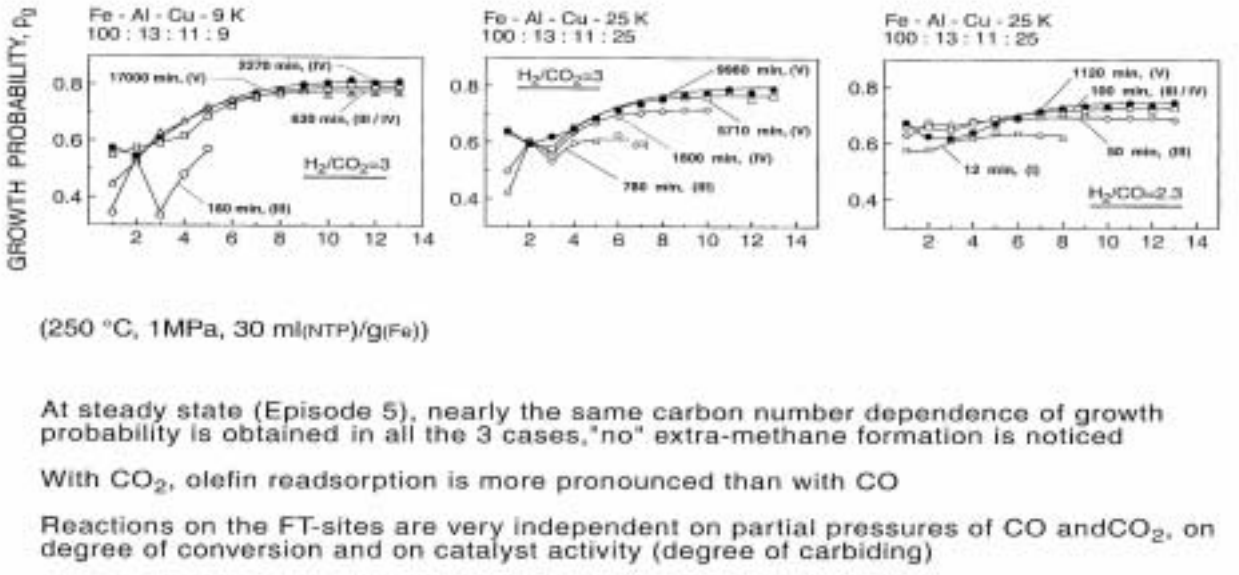

Figure 2. Chain growth as a function of time ($t_{exp.}$)

STUDY ON THE PRODUCT OF FISCHER-TROPSCH SYNTHESIS OVER SKELETON IRON METAL CATALYSTS

Yijun Lu, Peizheng Zhou

R& D Center
Hydrocarbon Technologies, Inc.
1501 New York Ave.
Trenton, NJ 08648

Introduction

Fischer-Tropsch (FT) synthesis can be used to produce either a light syncrude and light olefins or to produce heavy wax hydrocarbons. With its noticeable development of the industrial employed catalysts in SASOL, the iron-based catalysts have been widely studied as commercial FT process catalysts. For the recommended slurry bubble column reactor applied to this process, there exists one critical challenge of difficult solid/wax separation. Skeleton iron (Raney type) catalysts have been initiated years ago and well developed to match this problem solution. This novel iron catalyst has been proved superior CO hydrogenation activity and HC selectivity comparable to conventional precipitated Fe. In the work of optimizing the skeleton catalysts, we realized that the catalysts generation conditions dramatically influence catalyst physical properties and FT synthesis performance. This presentation is to show the effect on FT objective products.

In terms of the synthesis products, Anderson has provided us the thermodynamics reactions of products description in detail[1]. Water is a principal primary product. Primary alcohols and /or alpha olefins may also be primary synthesis products. Some researchers have proposed the possible mechanism steps of olefins and oxygenates formation. By far the oxygenates are believed by most people as primary products and sequentially being converted to hydrocarbons[2]. While some authors would accept the point that oxygenates, including normal alcohols, are formed via side reactions. The majority of the oxygenated products are linear with terminal functionality. The amounts and types are highly dependent on the catalyst properties and the reaction conditions. It is reported typically on iron based catalyst and ethanol is the principle oxygenate formed. This presentation provides a chart of the product distribution from novel skeleton iron catalyst, and outlines a rough relationship between the catalyst parameters and product selectivity. Particularly, the significant oxygenates product is addressed and discussed.

Experimental

Making up of skeleton iron catalyst. The patent catalysts were prepared in house and detail procedures can be found elsewhere[3,4,5]. Several typical catalyst samples were selected for presentation based on following variables.

Table 1. Description of typical skeleton iron catalyst samples

Samples	Components	Alloying (solidification)
1#	Fe/Al	**Q**uenching
2#	Fe/Al/Mn	**Q**
3#	Fe/Al/Cu	**Q**
4#	Fe/Al/Zn	**Q**
5#	Fe/Al	**S**low cooling

All catalysts were characterized by X-ray diffraction and demonstrate major phase of metal iron with trace oxides.

Slurry F-T synthesis. The synthesis was conducted in a 1NL continuous stirred tank reactor. Detail operational procedures were reported elsewhere. All above catalyst samples were tested at conditions of : 230-270^{o}C, 2.5 MPa, 2.0 NL/gcat/h, 15wt% catalyst loading. All products samples were collected and only those produced after initial period (~150hours) were analyzed as characteristic data.

Product analysis. HP 6890N series and G1530A GC were used for gas and liquid products analysis. MS-GC was the supplement instrument for verifying plausible components. In respect of the liquid analysis by capillary column, oxygenates were calculated by separated method. Perkin-Elmer CHN element analyzer was applied to ensure the accuracy of oxygenated percent in the liquid.

Results and Discussion

Figure 1 is the XRD data of the as prepared six samples, it indicates that any trace additive element, Zn, Mn, Cu (<5% in the alloy) or the residual Al is not apparently detected by X-ray diffraction. The oxides (Fe_3O_4) were thought formed during the transferring from storage regent to the instrument monitor.

Brady and Pettit firstly proposed the alkyl mechanism for the Fischer-Tropsch reaction and applied it to explain the similar hydrocarbon product distribution over catalysts such as Ni, Pd, Fe, Co, Ru or Co[2]. Furthermore, almost all researchers accept the conclusion that ethylene as the primary product. Nevertheless, these active FT catalyst components make obvious difference in product composition and distribution. Even for iron base catalysts, there are

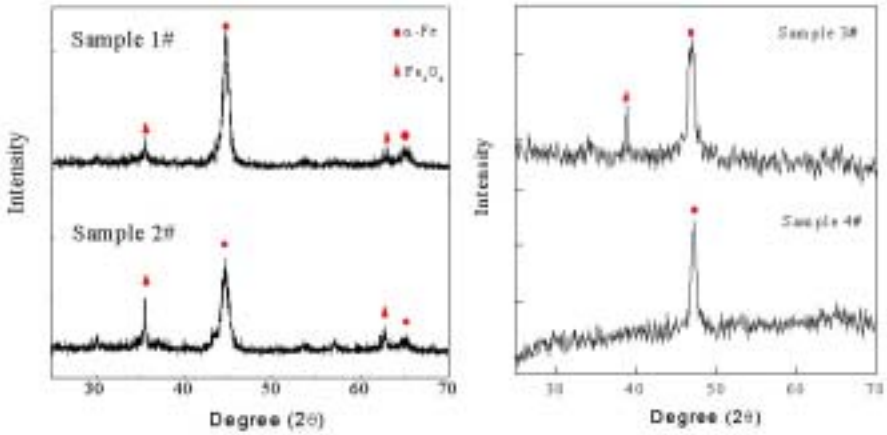

Figure 1. X-ray diffraction spectra of as prepared skeleton iron catalysts

several types catalysts resulted from different precursor material and generation routes (fuse iron, supported iron, precipitated Fe, ultra-fine iron oxide, sinter iron, ferrous alloy etc.).Thus many factors such as active component phase, granule size and combination degree with other components/supports inevitably affect the products quality. And, for each one type of iron base catalysts, say precipitated Fe catalyst, there exists a group of possible active phase comprising α-Fe, Fe_2O_3, Fe_3O_4 and Fe_xC, which complicated enough to bring up unclear characteristic product distribution[1]. Hence the catalytic polymerization mechanism study that extensively concerned by scientists may encounter a potential problem, the complex reaction system gives rise to much similar products over different catalysts (synergetic effect) and hence simplifies the mechanism (acceptable or plausible based on empirical evidence).

This demonstration is purposing on the relationship between lightly altered parameters and FT synthesis products distribution.

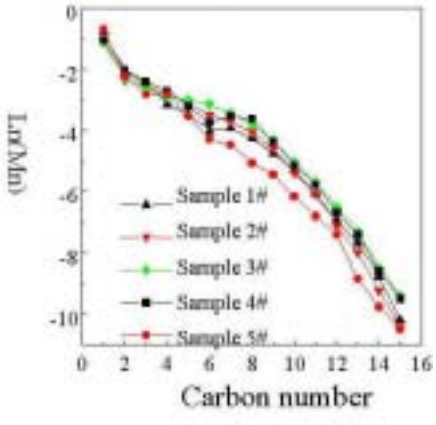

Figure 2. Characteristic carbon number distribution of iron catalysts (skeleton iron here is named as Raney Fe) tested in same reactor

Apparently, the carbon number distribution of HC products (excluded wax) synthesized over skeleton iron catalysts are not severely influenced by trace additives modifying the base catalyst. The exception is the 5# sample, which was characteristic of not-quenching solidification method in the precursor generation, shows a lower chain growth probability (α=~0.63). To explain this, the metallurgic theory should be referred. Quenching of molten alloy generally results in metal clusters exampled by $Fe_{14}Al_{44}$ (so called frozen eutectic alloy)[3]. While the slow-cooling way is subjected to yield a simple intermetallic compound such as $FeAl_3$. The later one eventually forms to small pores skeleton catalyst (average pore diameter is 15nm, in comparison with the one from former alloy, 22nm).

For all skeleton iron catalyst samples, the related FT products (liquid HC fraction) were almost exclusively linear olefins, alkanes and oxygenates, and methyl-branched was only as minor components of the product distribution. Figure 3 is a typical MS-GC spectrum (from C5 to C13), it is interesting that the normal alcohol is much significant (3rd big peak). It has been stated that the main objective of the synol process was the production of straight chain terminal alcohols of boiling range as high as C_{20}. Thus the skeleton iron catalyst may provide a shortcut to reach this objective. In some case, the amounts of normal alcohols approach 20wt% in the hydrocarbon products. While aqueous product contains about 10% of oxygenates, predominantly methanol and ethanol.

Olefins from the sample catalysts are found in amounts exceeding 50% in each carbon number ($<C_{18}$). Carbon chains in alcohols are similar to those found in hydrocarbons, and appears similar carbon number distribution trend. Yields of alcohols on a molar basis are maximal at C_2 and decreasing monotonically with increasing carbon number.

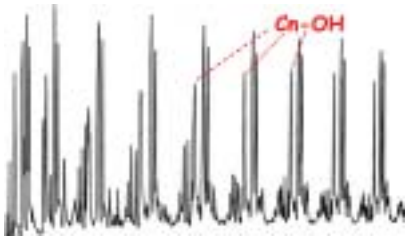

Figure 3. The typical MS-GC spectrum of F-T synthesis products from skeleton iron metal catalyst (Sample 5#)

Some experts offered the explanation that alcohols are the primary products when the synthesis is carried out at low temperatures. They are dehydrated to olefins in a second step. This assumption may find some basis in the fact that the sum total of alcohol plus olefin in synol operation is fairly constant over a wide temperature range. For the skeleton iron catalyst, it was found even at its maximum temperature (280 ^oC), the oxygenates selectivity did not decrease.

Table 2. Comparison of oxygenates amount in the HC product from different skeleton iron catalysts

Wt.%	Carbon Range			
Sample	1-2	3-5	6-9	10+
1#	5.11	2.84	2.74	1.86
2#	2.46	1.51	2.04	1.70
3#	8.17	3.12	4.90	2.40
4#	6.60	2.37	3.71	1.73
5#	8.12	3.06	4.48	2.03

From Table 2, we knew that copper and zinc added as promoters favored more oxygenates yield than manganese. It must be acknowledged that the aluminum in the skeleton iron catalyst made somehow contribution to the oxygenates formation (aluminum, copper, zinc are the conventional elements for alcohol synthesis catalyst). Nevertheless, as the digesting reaction in the course of alloy leaching step is rigorous and aluminum metal could hardly remain on skeleton surface (except the trace amount of alumna deposition), there is less possibility for aluminum acting as synol synthesis active site. But, it may attribute to any re-crystallization or active sites transfer occurred in the high temperature CO hydrogenation process.

Summary

This paper is to share a viewpoint that FT synthesis products formation mechanism, especially on iron base catalyst, may require study on the isolated active phase. Skeleton iron here exhibits an to some extent ability to produce products without other active phases disturbance.

Acknowledgment. Catalyst characterization work was executed at Material Science Lab, New Jersey Institute of Technology.

References

1. Anderson, Robert Bernard, The Fischer-Tropsch Synthesis, Academic Press, Inc., 1984, Orlando, Florida
2. Mattew J. Overett, R. Oliver Hill, John R. Moss, Coordination Chemistry Reviews, 206-207 (2000) 581-605
3. P.Zhou, L.Lee, J.Zhou and Y.Lu, US Patent 6,277,895 B1, Aug. 21,2001, Appl. No. 09/399,852.
4. Y. Lu, P.Zhou and T.Lee, Fuel Chem. Div. Prep., 46(2) (2001) 500-504.
5. Y. Lu and P. Zhou, Proceedings of 18th Annu. Intern. Pitts. Coal Conf., Dec. 3-7,2001, Newcastle, Austrialia
6. Devinder Mahajan, P. Vijayaraghavan, Fuel 78(1999) 93-100

DIRECT PARTIAL OXIDATION OF METHANE TO METHANOL: EFFECT OF REACTOR MATERIALS AND CATALYST

Qijian Zhang [1,2], Dehua He [1*], Qiming Zhu [1]

[1]State Key Lab of C1 Chemistry and Technology, Department of Chemistry, Tsinghua University, Beijing 100084, China
[2]Department of Material and Chemical Engineering, Liaoning Institute of Technology, Jinzhou Liaoning 121001, China

Introduction

Direct partial oxidation of methane to methanol (DPOM) is one of the most attractive pathways for the optimization utilization of the abundant natural gas reserves. A great deal of effort have been made on it especially since the promising results reported by Gesser et al. [1] and Lunsford et al. [2], respectively, in the early 1980s. Some important results have been obtained, e.g. high pressures and high CH_4/O_2 ratios favor methanol selectivity while high temperatures favor the deep oxidation. However, methanol yield of more than 8% has not been reproducibly achieved till now. Most of the reported methanol yields were about 3~5% and so on. And different researchers always gave different results, and even opposite ones. The discrepancies were attributed to the temperature/heat transfer effects, localized flow patterns in the reactor et al. by Brown and Parkyns [3] and Srivastava [4]. In our recent report [5], methanol yield of ca. 7~8% was obtained in a specially designed quartz lined reactor and the high yield was attributed to the isolation of the reaction mixture from metal surface. And it is believed that the discrepancy in the reported results was due to the difference of such isolation.

In the present work, the effect of the reactor material was further investigated. And the effect of catalysts was also discussed.

Experimental

The experiments of homogeneous partial oxidation of methane were carried out at 380-500℃ and 5.0 MPa in a specially designed quartz lined tubular reactor. A quartz line was tightly fixed in a stainless steel line. A Viton O-ring pressed by a locking nut was used to prevent the gas from leaking into the ringed gap between the quartz line and the SS line so as to eliminate the influence of the metal wall. The reactor structure was detailedly described in literature 5.

Catalyst of Mo-V-Cr-Bi-Ox/SiO_2 was prepared by co-precipitation as described in literature 6. The catalytic reaction was performed with 1g catalyst loaded into the reactor.

Results and Discussion

Effect of Reactor Material. The reactor materials have great effect on the performance of the direct partial oxidation of methane to methanol. Three kinds of reactor materials were used for the investigation (see the caption of Figure 1).

In the quartz lined reactor, the methane conversion of ca. 13% and methanol selectivity of more than 60% were obtained (Figure 1, Case-I). The methanol selectivity (Case-I) was the highest among the four cases considered here. The selectivity of completed oxidation product, CO2, was limited no higher than 5%. And the result obtained in the glass lined reactor (Case-II) was quite similar to the quartz lined reactor; the methanol yield of more than 7% could also be achieved except that the selectivity of CO_2 was a little higher than that in Case-I. And they were both higher than those in the other two cases (Case-III and Case-IV), which indicated that the quartz or glass lined reactor are more favorable for the direct partial oxidation of methane to methanol, especially the quartz lined reactor.

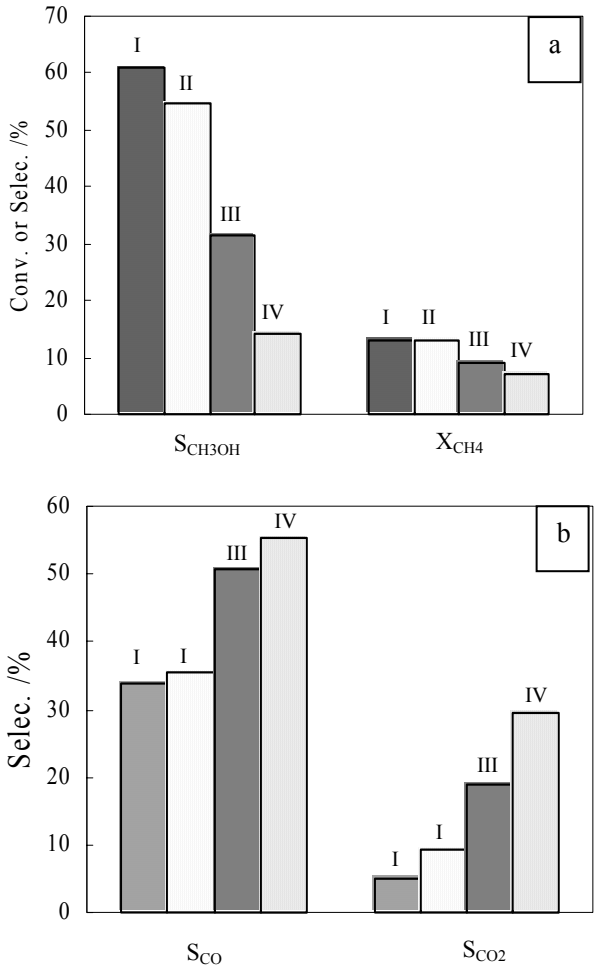

Figure 1. Effect of reactor materials on the homogeneous partial oxidation of methane to methanol
P=5.0MPa, T=440°C, $CH_4/O_2/N_2$=100/10/10(ml/min)
Case-I: Quartz lined reactor
Case-II: Glass lined reactor
Case-III:Quartz lined reactor without O-ring
Case-IV:Stainless steel reactor

In the stainless steel reactor (Case-IV), methanol selectivity was less than 15%, only about 25% of that in Case-I (Figure 1). But the deep oxidation products, CO and CO_2 were much higher; the selectivity of CO_2 was even raised to 30%. Such results indicated that the SS reactor was not suitable for the direct partial oxidation of methane to methanol because it is too easily to result in the deep oxidation.

It is well known that the iron oxide and other metal oxides are always used as the oxidation or combustion catalysts, because the oxygen in the oxides is very active. But in the direct partial oxidation of methane to methanol, the required product, methanol, is more unstable than methane, and methanol is more easily adsorbed and activated on surface of metals or metal oxides because it is a polar molecular (its dipole moment is 1.70Debyes). Therefore, the surface of metals or metal oxides is not expected to expose under the reaction conditions to cause the deep oxidation of methanol. In other words, it

is necessary to prevent the reaction mixture from contacting the surface of SS reactor during reaction.

The result of Case-III was better than that of Case-IV, but worse than those of Case-I and Case-II, which implied that part of the reactant mixture flow through the inner quartz tube, which did not contact the surface of SS reactor and give higher methanol selectivity, and part of it leaked into the ringed gap between the quartz tube and the SS tube and gave poor methanol selectivity. The methanol selectivity in the effluence was the mean result of the above two parts. It is worth to note that the methane conversion and methanol selectivity were quite similar to those reported in most of the literatures. Researchers have found that the metal surface might cause the deep oxidation of methanol and decrease methanol selectivity. Quartz or Pyrex lined reactors were recommended to be adopted in the direct partial oxidation of methane to methanol. Then how to insure the reactant not to leak into the ringed gap between the inner line and SS tube became a determinant factor, and it might be one of promising explanations for the discrepancy in the reported results .

Effect of catalyst. It is expected that the participation of catalyst could increase methanol selectivity and methane conversion. The catalytic oxidation of methane was investigated over a Mo-V-Cr-Bi-Ox/SiO_2 catalyst.

The increase of oxygen conversion with temperature in catalytic oxidation was not as abrupt as that in homogeneous oxidation, which indicated that the participant of catalyst did take some effect on the reaction. It is worth to note that when temperature was increased above 430^{o}C, the oxygen in the reactants was depleted already. But in the catalytic oxidation, the temperature when oxygen was depleted was higher than 460^{o}C. This result could be attributed to the inhibition of the free radical reaction of the homogeneous oxidation by the catalyst. The participant of catalyst could control the oxidation of methane to some extent.

However, the methanol selectivity in the catalytic oxidation was always less than 50%, which was lower than that in the homogeneous oxidation. And the CO_2 selectivity also increased higher than 10%. The participant of catalyst did not increase the methanol selectivity, but promoted the deep oxidation of methanol. This was mainly because the metal oxides catalyst is very active, and the polar molecular, such as methanol, CO et al. is very easily absorbed on them and activated. The effect of catalyst was to some extent similar to that of the metal reactor surface.

Conclusions

The existence of the metal surface of SS reactor would cause deep oxidation of methanol under the reaction condition, and decrease its selectivity. The reactor should be equipped with the metal-free material, such as quartz or Pyrex glass. And in the quartz (or Pyrex glass) lined tubular reactor, it is important to prevent the reactant mixture from leaking into the ringed gap between the inner tube and the outer SS tube.

Participant of catalyst did affect the homogeneous oxidation, but did not improve the methanol selectivity because it easily causes deep oxidation of methanol.

Acknowledgement. We acknowledge the financial support from the National Key Fundamental Research Project Foundation of the Ministry of Science and Technology of China (G199902240-06) and the Research Foundation of Tsinghua University.

References

(1) Gesser, H.D., *International Chemical Congress of Pacific Basin Societies*, **1984**, Honololu, Paper 03002.
(2) Liu, H.F.; Liu R.S.; Lunsford, J.H, *J. Am. Chem. Soc*., **1984**, 106, 4117.
(3) Brown, M.J.; Parkyns, N.D., *Catal. Today*, **1991**, 8, 305.
(4) Srivastava, R.D.; Zhou, P.; Stiegel, G.J.; Rao, V.U.S.; Cinquegrane, G., *Catalysis*, **1992**, 9,183
(5) Qijian, Zhang; Dehua, He; Jinlu, Li et al. *Appl. Catal. A: General*, **2002**, *224(1-2)*, 201
(6) Zhansheng, Han *Ph.D. thesis*, Department of Chemistry, Tsinghua University, China, **1999**

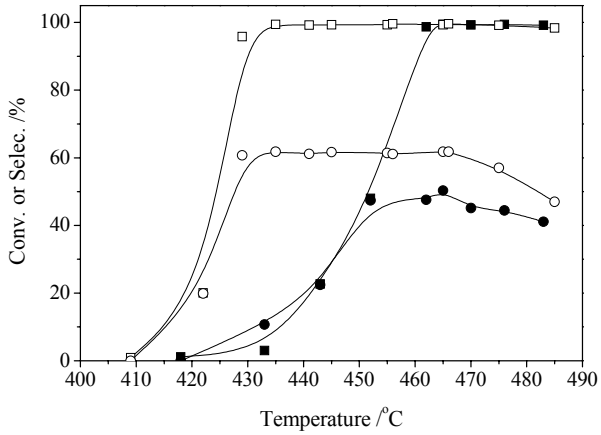

Figure 2. Comparison of homogeneous and catalytic oxidation of methane to methanol.
P=5.0MPa, $CH_4/O_2/N_2$=100/10/10(ml/min)
■-Catalytic oxygen conversion,
□-Homogeneous oxygen conversion
●-Catalytic methanol selectivity
○-Homogeneous methanol selectivity

CROSS-LINKING REACTIONS BETWEEN PHENOLS AND BENZOIC ACID: THE ROLE OF ARYL ESTERS

Phillip F. Britt, A. C. Buchanan, III, Michelle K. Kidder, and J. Todd Skeen

Chemical Sciences Division, Oak Ridge National Laboratory, P. O. Box 2008, Oak Ridge, TN 37831-6197

Introduction

It has been proposed that oxygen functional groups (i.e., carboxylic acids and their salts, phenols, and ethers), prevalent in low rank coals, are responsible for cross-linking reactions that inhibit the efficient conversion of low-rank coals to liquid fuels and chemicals.[1,2] In the pyrolysis and liquefaction of low-rank coals, cross-linking has been correlated with evolution of CO_2 and H_2O.[1] To determine if decarboxylation leads to cross-linking, the thermal decomposition of aromatic carboxylic acids was investigated.[3] It was determined that carboxylic acids predominately undergo decarboxylation by an acid promoted ionic pathway at 400 °C, but depending on the reaction conditions, small amounts (<5 mol%) of cross-linked products (i.e., arylated products) could be formed by formation and radical induced decomposition of anhydrides. Anhydride formation and cross-linking reactions were enhanced by incorporating the aromatic carboxylic acids in a polymer (poly(*m*-xylylene)-*co*-(5-carboxy-*m*-xylylene) at concentrations similar to those found in low rank coal (ca. 2.4 carboxyls per 100 carbons).[4] Since these condensation reactions readily occur at temperatures found in the thermal processing of coal (350-425 °C), additional types of cross-linking reactions, such as the condensation of carboxylic acids and phenols to make aryl esters, might be possible. Since phenols are 2-5 times more concentrated than carboxylic acids in low rank coal, aryl esters could form from condensation reactions. Aryl esters are predicted to be thermally stable up to temperatures of 650 °C based on the Arrhenius parameters reported for the C-O homolysis of phenyl acetate (log k (s^{-1}) = 15.3 – 72.3 kcal mol^{-1} / 2.303RT).[5] Pyrolysis of phenyl benzoate at 700 °C produced 90% conversion, and produced phenol, biphenyl, benzene, and dibenzofuran as the major products, but the mass balance was poor (<60%).[6] Thus, aryl esters could act as low temperature cross-links in low rank coal. However, there is little data on the formation and pyrolysis of aryl esters at temperatures relevant to those found in the thermal processing of coal (350-425 °C). In this study, we have investigated the pyrolysis benzoic acid in the presence of excess *m*-phenylphenol to study the formation and decomposition of aryl esters, and we have investigated the pyrolysis of phenyl benzoate at 400 °C to determine if aryl esters act as a thermally stable low-temperature cross-link.

Experimental

m-Phenylphenol, which contained 10% *p*-phenylphenol, was recrystallized from benzene/hexanes and dried in a vacuum desiccator over P_2O_5. Benzoic acid was purchased from Mallinckrodt, and no further purification was needed. Phenyl benzoate was purified by recrystallization from hexane/ethyl acetate (1:1) and dried in a vacuum desiccator over P_2O_5. Naphthalene was purified by sublimation. Cumene was fractionally distilled (2x). 2,5-Dimethylphenol was recrystallized in EtOH/ether. Acetone (Omni-Solv) was used with no further purification. Benzyl phenyl ether was purchased from Aldrich and used as received.

Pyrolysis of the compounds was performed in heavy walled Pyrex tubes (8 mm o.d x 12.5 cm) that were thoroughly cleaned, oven dried and cooled under argon. The desired amount of substrate (typically 20-100 mg) was weighed into the tube, and three freeze-pump-thaw cycles were performed prior to sealing the tube at ca 10^{-5} Torr. Tube volumes were kept to a minimum with the solid filling roughly one-half of the sealed pyrolysis tube. The pyrolyses were performed in a Carbolite tube furnace, which maintained the temperature to ± 1 °C. All samples were run in duplicate. After the pyrolysis, the samples were removed from the furnace and cooled in liquid N_2. The tubes were opened, and the solid products were dissolved in high purity acetone. Internal standards, 2,5-dimethylphenol, benzyl phenyl ether and cumene, were added. The products were analyzed by gas chromatography using a Hewlett-Packard 5890 Series II gas chromtograph equipped with a J&W Scientific 30 m x 0.25mm id, 0.25 μm film thickness DB-5 column and a flame ionization detector. Mass spectra were obtained at 70 eV on a Hewlett-Packard 5972 GC-MS equipped with a capillary column identical with that used for GC analysis. The products were quantitated by injection onto the GC using a HP 7673 autosampler, and the data was averaged using the GC-FID output relative to the internal standards. Response factors were measured with authentic samples or estimated from measured response factors for structurally related compounds or based on carbon number relative to the internal standards. Mass balances were calculated by comparing the recovered starting material and product equivalents to the initial charge of starting material.

Results and Discussion

The formation of aryl esters was investigated by the pyrolysis of mixtures of *m*-phenylphenol and benzoic acid. The phenyl substituted phenol was chosen instead of phenol to reduce the pressure inside the pyrolysis tubes, since pyrolysis of mixtures of phenol and benzoic acid tended to break the heavy walled glass tubes. The meta-isomer was chosen to reduce any substituent effect in the reaction, but the purified meta-isomer contained 10% of the para-isomer. Pyrolysis of a 3.1:1 mixture of *m*-phenylphenol and benzoic acid at 400 °C for 60 min produced a 69.7 ± 1.3 % yield of *m*-phenylphenyl benzoate. When the ratio of *m*-phenylphenol to benzoic acid was reduced to 1.9:1, the yield

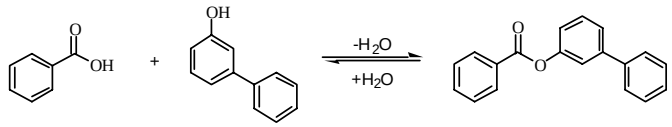

1.0 equiv 3.1 equiv

of *m*-phenylphenyl benzoate decreased to 53.6% showing that the concentration of phenol impacts the rate of condensation. The high efficiency of aryl ester formation in the sealed tube pyrolysis was surprising. It was initially thought that hydrolysis would be competitive with condensation and only a small quantity of aryl ester would be formed.

To determine the effect of temperature on aryl ester formation, a 3:1 mixture of *m*-phenylphenol and benzoic acid was heated for 60 min at 200, 250, and 300 °C. At 200 °C, only a small amount of ester (0.65%) was observed with no additional products. As the temperature was increased to 250 and 300 °C, the yield of *m*-phenylphenyl benzoate increased to 6.3% and 32.3%, respectively, but no other products were observed. At 400 °C, *m*-phenylphenyl benzoate was found in 69.7 % yield along with a small amount of other products (see Figure 1). As the reaction time increased from one to four hours, the yield of *m*-phenylphenyl benzoate decreased while the yield of the other products increased. The majority of the products appear to arise from the decomposition of benzoic acid. For example, benzene could arise from the acid catalyzed decarboxylation of benzoic acid, while the arylated products, such as diphenylphenol, terphenyl, and diphenylphenyl benzoate, suggest that benzoic acid might be decomposing by a radical pathway to

form aryl radicals.[3] The phenol coupling products could also be formed by a radical pathway.[7]

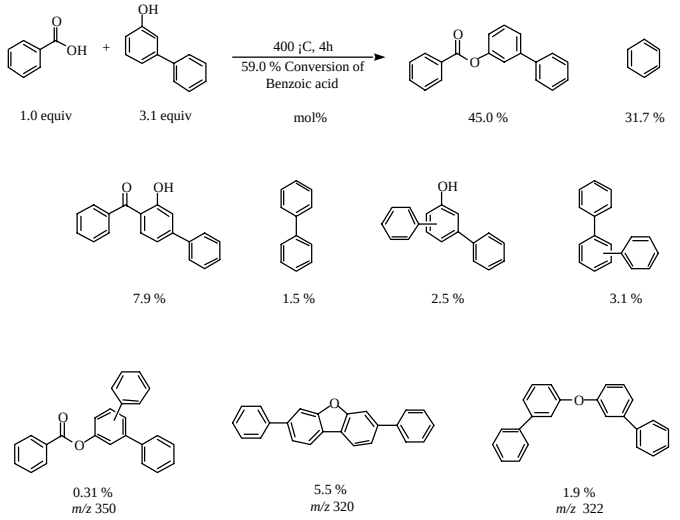

Figure 1. Products from the 400 °C pyrolysis *m*-phenylphenol and benzoic acid.

Pyrolysis of *m*-phenylphenol and benzoic acid in a 10-fold excess of naphthalene (relative to benzoic acid) at 400 °C produced the aryl ester as the dominant product. However, 1- and 2-phenylnaphthalene were the dominant arylated products rather than diphenylphenol, terphenyl, and diphenylphenyl benzoate. These results indicate that aryl radicals are possibly forming from the decomposition of benzoic acid and not from the decomposition of the phenol since no biphenylated naphthalene was observed. Aryl radicals could be formed from the formation and decomposition of benzoic anhydride as previously discussed.[3] However, benzoic anhydride was not found as a product. Thus, the formation pathways for the arylated products are still under investigation.

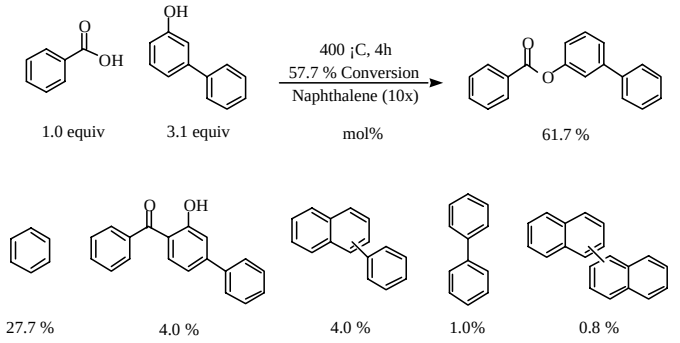

Figure 2. Products from the 400 °C pyrolysis *m*-phenylphenol and benzoic acid in naphthalene.

The pyrolysis of phenyl benzoate was studied at 400 °C to determine the thermal stability of the aryl ester. The major products (shown in Figure 3) are similar to those found in the pyrolysis of benzoic acid and *m*-phenylphenol. Surprisingly, significant amounts of phenol and benzoic acid were observed at short reaction times. As the reaction time increased, the yield of benzoic acid decreased and the yield of benzene increased. This is most likely due to the ionic decarboxylation of the benzoic acid. The formation of phenol and benzoic acid could arise from the simple hydrolysis of the phenyl benzoate by residual water in the reagents or reaction vessel, although this was thought to be unlikely since the reagents were stored over P_2O_5 before use, the reaction tubes were oven dried, and the samples were sealed under vacuum. However, since the reactions were typically run with 35 mg phenyl benzoate (177 μmol), one microliter of water (55 μmol) in the reaction tube could cause 31 % conversion to phenol and benzoic acid. Thus, residual water could be responsible for most of the conversion followed by benzoic acid chemistry, but the mechanistic details of product formation are currently under investigation.

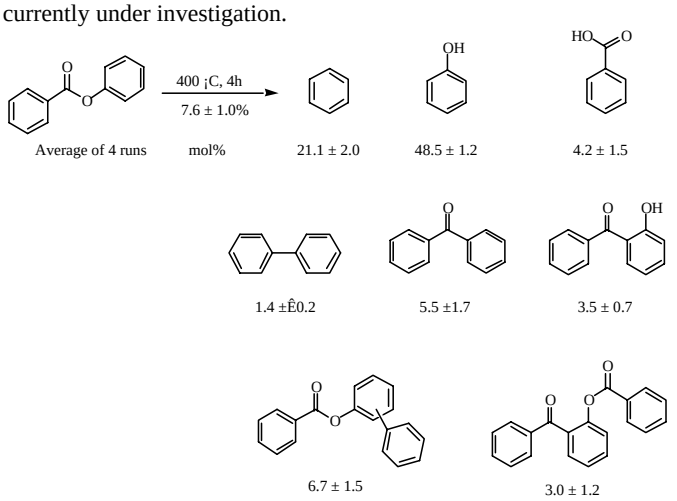

Figure 3. Products from the pyrolysis of phenyl benzoate.

Conclusions

The pyrolysis of mixtures of *m*-phenylphenol and benzoic acid were investigated at 400 °C to determine if condensation reactions could occur to form aryl esters, which could be low temperature cross-links. It was determined that aryl esters could slowly form at temperatures as low as 200 °C, but the efficiency of the reaction increased with temperature. Only *m*-phenylphenyl benzoate was found at temperatures up to 300 °C, but at 400 °C, other pyrolysis products were found which appear to arise from benzoic acid decomposition. The thermal stability of aryl esters was investigated through the pyrolysis of phenyl benzoate at 400 °C. As predicted, the aryl ester appeared to be thermally stable but hydrolytically unstable. In general, formation of aryl esters could be a low temperature pathway for the cross-linking of low rank coals. The reaction pathways for the formation of the arylated products found in the pyrolysis mixture at 400 °C are currently under investigation.

Acknowledgement. This research was sponsored by the Division of Chemical Sciences, Geosciences, and Biosciences, Office of Basic Energy Sciences, U.S. Department of Energy under contract DE-AC05-00OR22725 with Oak Ridge National Laboratory, managed and operated by UT-Battelle, LLC.

References

(1) (a) Suuberg, E. M.; Unger, P. E.; Larsen, J. W. *Energy Fuels* **1987**, *1*, 305. (b) Solomon, P. R.; Serio, M. A.; Despande, G. V.; Kroo, E. *Energy Fuels* **1990**, *4*, 42.
(2) Eskay, T. P; Britt, P. F.; Buchanan, A. C. III *Energy Fuels* **1996**, *10*, 1257.
(3) Eskay, T. P.; Britt, P. F.; Buchanan, A. C. III *Energy Fuels* **1997**, *11*, 1279.
(4) Britt, P. F.; Mungall, W. S.; Buchanan, A. C. III *Energy Fuels* **1998**, *12*, 660.
(5) Ghibaudi, E.; Colussi, A. J. *J. Chem. Soc., Chem. Comm.* **1984**, 433.
(6) Patterson, J. M.; Shiue, C. Y.; Smith, W. T., Jr. *J. Org. Chem.* **1973**, *38*, 387.
(7) Poutsma, M. L., Dyer, C. W. *J. Org. Chem.* **1982**, *47*, 3367.

PYROLYSIS OF AROMATIC CARBOXYLIC ACID SALTS: DOES DECARBOXYLATION PLAY A ROLE IN CROSS-LINKING REACTIONS?

Reza Dabestani, Phillip F. Britt, and A. C. Buchanan III*

Chemical Sciences Division, Oak Ridge National Laboratory,
P. O. Box 2008, MS-6197, Oak Ridge, TN 37831-06197

Introduction

Oxygen functional groups (i.e. carboxylic acids and their salts, phenols, and ethers) present in low-rank coals have been implicated as major contributors to retrograde reactions that inhibit efficient thermochemical conversion of low-rank coals to liquid fuels. Although low temperature ($T \leq 400$ °C) cross-linking reactions have been correlated with the loss of carboxyl groups and the evolution of CO_2 and water, [1, 2a-c, 3] the role of decarboxylation leading to cross-linked products has been questioned.[4] Thus, we have undertaken a systematic study to determine whether or not decarboxylation leads to cross-linking.[5] Our initial studies on the pyrolysis of free carboxylic acids have revealed that decarboxylation proceeds primarily by an acid-promoted cationic pathway.[5a] However, under certain reaction conditions, anhydrides, which are low temperature cross-links, can be formed by condensation of aromatic carboxylic acids.[5b,5c] Anhydrides can also decompose by a radical induced decomposition pathway to produce aryl radicals, which can lead to additional cross-linked products. Since many of the carboxylic acids in coal are ion-exchanged as alkali and alkaline earth metal salts, we recently investigated the pyrolysis of the salts of aromatic carboxylic acids by thermogravimetric analysis coupled with mass spectrometric analysis of the evolved gases (TG-MS). These studies have shown that the salts decompose at higher temperature than the corresponding acids and that the products are different.[6] Furthermore, our results indicate that divalent salts (e.g. calcium) decompose by a different pathway than the monovalent salts such as sodium and potassium. Hites and Biemann[7] have reported that pyrolysis of calcium benzoate at 500°C proceeds by a free radical mechanism to produce mainly benzene and benzophenone (in equal amounts) and small amounts of biphenyl and 9-fluorenone. Artok and Schobert [8] have reported that sodium benzoate undergoes an inefficient decomposition reaction at 450 °C to produce benzene, toluene, benzaldehyde, and biphenyl but no mechanistic details were provided for product formation. Thus, we have undertaken a systematic study of the pyrolysis of alkali and alkaline earth metal salts of benzoic acid in an attempt to provide mechanistic insights into the pathways of product formation to determine if decarboxylation leads to cross-linking.

Experimental

Sodium benzoate (Aldrich, 99%), benzene (EM Science), acetone (EMD, spectral grade), ethyl acetate (Fisher), methylene chloride (EM Science), and D_2O (99.8%, MSD Isotopes) were all used as received. Biphenyl (Aldrich, 99%), diphenylmethane (Aldrich, 99%), benzophenone (Aldrich, 99%), triphenylmethane (Aldrich, 99%), diphenylmethanol (Aldrich, 99%), triphenylmethanol (Aldrich, 98%), fluorenone (Aldrich, 99%), benzoic acid (Mallinckrodt), phthalic acid (Aldrich, 99%), 4-phenylbenzoic acid (Aldrich, 95%), 2-methylnaphthalene (Aldrich, 99%), and *p*-toluic acid (Aldrich, 98%) were all recrystallized at least once before use. Gas chromatography analysis was performed on a Hewlett-Packard 5890 Series II gas chromatograph equipped with a J&W Scientific 30 m x 0.25 mm i.d., 0.25 um film thickness DB-5 column and a flame ionization detector. Mass spectra were obtained at 70 eV on a Hewlett-Packard 5972 GC/MS equipped with a capillary column identical to that employed for GC analysis.

Pyrolysis of the compounds was carried out by loading small Pyrex tubes with the 20-50 mg of substrate and performing five freeze-pump-thaw cycles prior to flame sealing the tube at ca. 10^{-5} Torr. Tube volumes were kept to a minimum (total volume < 1 mL). The pyrolyses were conducted in a Carbolite tube furnace maintained at a temperature of 450 $\pm$ 1 °C. After the pyrolysis, the tubes were immediately removed from the furnace, cooled to room temperature and then immersed in liquid nitrogen. The tubes were cracked open and the products were removed by washing the tube with acetone ($\leq$ 1 mL). The internal standard (2-methylnaphthalene) was then added to the acetone wash, and the mixture was analyzed by GC and GC-MS. The solid residue was weighed first and then acidified with HCl to convert the salts to the corresponding acid(s). The organics were extracted with ethyl acetate, an internal standard (*p*-toluic acid) was added, and the mixture was analyzed by GC and GC-MS, and quantitated by GC.

Results and Discussion

The pyrolysis of sodium benzoate under deaerated conditions at 450 °C produced benzene, biphenyl, benzophenone, diphenylmethane, triphenylmethane, and 9-phenylfluorene (Scheme I) in good agreement with our earlier data obtained by TG-MS.[6]

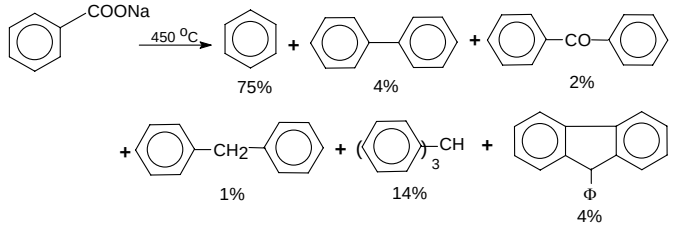

Scheme I

Phthalic acid (major) and phenylbenzoic acid (minor) have also been identified from acidification of the solid residue (see experimental). It has been difficult to quantitate the phthalate as a consequence of its poor solubility in the extraction solvent and direct silylation of the salts (to the trimethylsilyl ester) has not been quantitative. Currently, good mass balances (> 90%) have been obtained based on the weight of the acetone insoluble solids and the GC yields of the acetone soluble products (i.e., hydrocarbons).

The fact that we observe benzene and phthalic acid in the reaction products suggests that they are most likely formed by a uncatalyzed Henckel type reaction where initial decarboxylation of sodium benzoate leads to the formation of the benzene anion which can abstract a hydrogen from another molecule of sodium benzoate to form benzene and an aryl anion that can react with the carbon dioxide to form sodium phthalate (Scheme II).

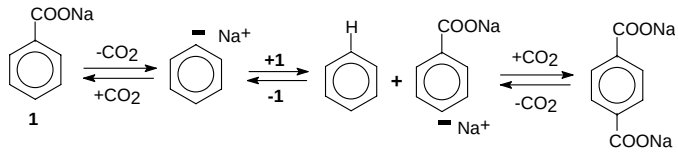

Scheme II

The remaining products could also be formed by an anionic reaction involving the benzene anion. Since the reaction tubes are sealed under vacuum, the reaction of the benzene anion with CO_2 will be slow. Thus, the anion could react with a sodium benzoate to

form benzophenone and sodium oxide as shown in Scheme III. Benzophenone could undergo additional reaction with a benzene anion to produce the sodium salt of triphenylmethanol. However, triphenylmethanol was not found as a product. Nevertheless, independent pyrolysis of triphenylmethanol produced triphenylmethane and 9-phenylfluorene in addition to carbonaceous solids. To test the intermediacy of benzophenone in the formation of these products, a sample of sodium benzoate and sodium benzoate containing 5 mole% benzophenone (co-mixed) were pyrolyzed side-by-side under identical conditions. Comparison of the pyrolysis products revealed that in the sample that contained benzophenone, the yield of triphenylmethane and 9-phenylfluorene was 2-3 times higher and the yield of benzene was about 30% lower than for the sample of sodium benzoate. These results suggest that benzophenone is an intermediate to the formation of triphenylmethane and 9-phenylfluorene via triphenylmethanol route. It was also shown that benzophenone was stable at 450 ^{o}C under the pyrolysis conditions.

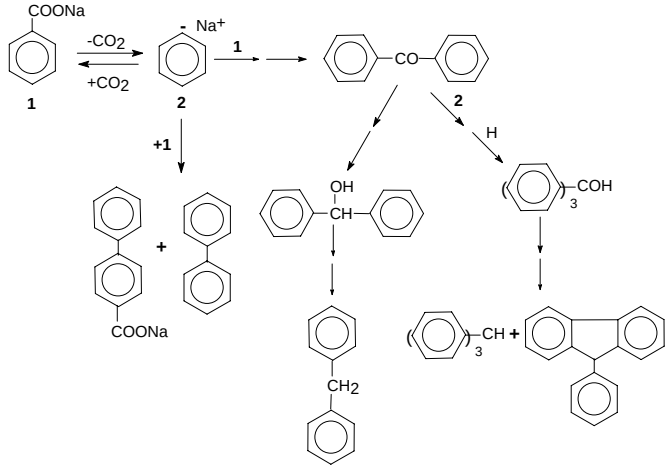

Scheme III

When the pyrolysis of sodium benzoate was carried out in the presence of water (30 mole%), benzene accounted for $\geq$ 99% of the products with biphenyl, diphenylmethane, and benzophenone accounting for the remaining 1%. There was no evidence of any triphenylmethane and/or 9-phenylfluorene. The rate of benzene formation was about three times faster than that observed in the absence of water. Thus, water could be reacting with the salt to form benzoic acid which is decomposing by an electrophilic pathway and/or the water is protonating the anion before other reactions can occur. Based on the these findings, it appears that pyrolysis of sodium benzoate proceeds by an anionic mechanism involving both a Henckel type reaction that leads to the formation of benzene and phthalic acid (Scheme II) and a second pathway (e.g. Scheme III) leading to benzophenone, biphenyl, diphenylmethane, phenylbenzoate, triphenylmethane, and 9-phenylfluorene.

Conclusions

Pyrolysis of sodium benzoate at 450 ^{o}C produces benzene, triphenylmethane, and phthalic acid (after acidification) as the major products. Biphenyl, diphenylmethane, benzophenone, phenylbenozic acid (after acidification), and 9-phenylfluorene have also been identified as the minor products in the pyrolysis. Products are consistent with an anionic decarboxylation reaction to produce the benzene anion as the key intermediate. We are currently gathering more quantitative data on the products from the pyrolysis of the monovalent salts, and we are studying the pyrolysis of calcium benzoate to determine whether or not a similar mechanism operates for the divalent cation.

Acknowledgements. This research was sponsored by the Division of Chemical Sciences, Geosciences, and Biosciences, Office of Basic Energy Sciences, U. S. Department of Energy under contract DE-AC05-960OR22464 with Oak Ridge National Laboratory, managed by UT-Battelle for the Department of Energy.

References

(1) Derbyshire, F.; Davis, A.; Lin, R. *Energy Fuels* **1989**, 3, 431.
(2) (a) Solomon, P. R.; Serio, M. A.; Despande, G. V.; Kroo, E. *Energy Fuels* **1990**, 4, 42 and references therein. (b) Serio, M. A.; Kroo, E.; Chapernay, S.; Solomon, P. R. *Prep. Pap.-Am. Chem. Soc., Div. Fuel Chem.* **1993**, 38 (3), 1021. (c) Suuberg, E. M.; Lee, D.; Larsen, J. W. *Fuel* **1985**, 64, 1668. (d) Joseph, T. J.; Forrai, T. R. *Fuel* **1992**, 71, 75.
(3) Ibarra, J. V.; Moliner, R.; Gavilan, M. P. *Fuel* **1991**, 70, 408.
(4) Manion, J. A.; McMillen, D. F.; Malhorta, R. *Energy Fuels* **1996**, 10, 776.
(5) (a) Eskay, T. P.; Britt, P. F.; Buchanan, A. C., III. *Energy Fuels* **1996**, 10, 1257. (b) Eskay, T. P.; Britt, P. F.; Buchanan, A. C., III. *Energy Fuels* **1997**, 11, 1278. (c) Britt, P. F.; Mungall, W. S.; Buchanan, A. C. III *Energy Fuels* **1998**, *12***,** 660.
(6) Clayton, T. W.; Jr., Britt, P. F.; Buchanan, A. C., III. *Prep. Pap.-Am. Chem. Soc., Div. Fuel Chem.* **2001**, 46 (1), 228.
(7) Hites, R. A.; Biemann, K. *J. Am. Chem. Soc*. **1972**, 94, 5772.
(8) Artok, L.; Schobert, H. H. *J. Anal. & Appl. Pyrolysis* **2000**, 54, 215.

CO-PYROLYSIS OF α-AMINO ACIDS WITH GLUCOSE

Ramesh K. Sharma, W. Geoffrey Chan and Mohammad R. Hajaligol

Philip Morris USA, Research Center
P. O. Box 26583
Richmond, VA 23261

Introduction

The amino acid/sugar reactions have been studied extensively in the literature due to their importance to the food industry.[1-5] According to Hodge[1], amino acid and sugar undergo a reversible condensation in aqueous mixtures. The condensation involves opening of the ring form of the sugar and addition of the amine to the carbonyl group to form the N-substituted glycosylamine. The latter may undergo condensation to form pyrazines. Spingarn et al.[2] observed that the amino acid/sugar reactions led to many products belonging to a wide variety of chemical classes. While the literature provides an insight into the reactions of amino acids with sugars, it does not give any information on the products formed in an inert environment and at conditions typical of those in a lit cigarette, i.e. high temperatures and short residence times. In this work, binary mixtures of proline, tryptophan, asparagine, aspartic acid, glutamic acid and glutamine with glucose were pyrolyzed in an inert atmosphere at different temperatures and amino acid/glucose ratios. The product tars were also pyrolyzed further in a two-zone reactor to study their secondary reactions. The extent of interaction between amino acid and glucose was determined by comparing the yields and compositions of chars and tars from the co-pyrolysis to those calculated from the separate pyrolyses of the corresponding amino acid and glucose, reported elsewhere.[6]

Experimental

Different experimental designs were used to study the co-pyrolysis and amino acid with glucose. A 30 cm long, 31 mm in diameter, quartz tube heated by a 15 cm long metal-block furnace was used as a reactor. A 200-mg sample of an equimolar binary mixture of each amino acid with glucose was pyrolyzed under helium at 300 ^{o}C to collect a low temperature tar (LTT) and a low temperature char (LTC). The LTC was then pyrolyzed further at 625 ^{o}C and a high temperature tar (HTT) and a high temperature char (HTC), were collected. The LTC and HTC were analyzed for their elemental composition. The LTT and HTT were each collected over a Cambridge pad, which was extracted with 10 mL of methanol. The extract was analyzed by gas chromatography/mass spectrometry (GC/MS). The GC/MS was also equipped with a nitrogen phosphorus detector (NPD) to help identify nitrogen compounds. Further details of the experimental procedures are given elsewhere.[6] Since the product compositions were generally complex, attention was focussed on the major components having a characteristic mass spectrum. Compound identification was achieved by matching the experimental mass spectra with the reference spectra from a commercially available reference library (NIST98), as well as by matching the chromatographic retention times with those for the available authentic samples. In the absence of authentic standards, the relative yield of a component was calculated from the total ion current and the tar yield and reported in counts/g of mixture. Such components are indicated in the table by an asterisk. Only a general form of a compound is usually given.

Results and Discussion

Only the results from the co-pyrolysis of equimolar binary mixtures of proline, tryptophan and asparagine with glucose, in the absence of secondary reactions, are presented below.

Overall Product Distribution. The pyrolysis of proline/glucose mixture was particularly interesting since proline does not form any char at 300 ^{o}C or above and the predominant condensable product is a diketopiperazine, with pyrrole and pyrroline being the minor components of the tar.[6] The overall product distributions obtained from the co-pyrolysis of proline/glucose mixture are presented in Table 1. The various yields were compared to the calculated values (not shown). It was found that the yields of LTC and HTC were nearly twice the yields calculated from the separate pyrolysis of proline and glucose. The yield of LTT was about half the calculated value. The results from the tryptophan/glucose mixture were similar although the difference between the observed and calculated yields of LTC was relatively smaller. However, for the asparagine/glucose mixture, the observed and calculated yields of the chars were essentially similar, indicating that the interactions between asparagine and glucose were comparatively small.

Table 1. Overall Product Yields from the Co-Pyrolysis of Amino Acid/Glucose Mixtures (wt.% of Mixture)

	25-300 ^{o}C			300-625 ^{o}C		
Substrate	LTC	LTT	Gaseous product	HTC	HTT	Gaseous product
Proline	27.9	24.9	47.2	8.7	4	15.2
Tryptophan	43.9	6.6	49.5	24	4.8	15.1
Asparagine	43.3	4.8	51.9	19.2	3.2	20.9

The compositions of chars from the proline/glucose mixture are presented in **Figure 1**. The point with the highest O/C ratio represents the unpyrolyzed mixture. The H/C and O/C ratios of the chars are lower than the ratio for the unpyrolyzed mixture, which is expected since the hydrogen and oxygen were likely lost as water and oxides of carbon during the pyrolysis. Interestingly, the N/C ratio of LTC is similar to the corresponding ratio for the unpyrolyzed mixture. Since proline alone does not form any char on pyrolysis the LTC and HTC from the co-pyrolysis of proline and glucose would not be expected to contain any nitrogen if the two components pyrolyzed without any interactions. The presence of nitrogen in chars confirmed strong interactions between proline and glucose. The sharp decrease in the H/C ratio for HTC was not observed with the amino acids in the absence of glucose. The chars from the

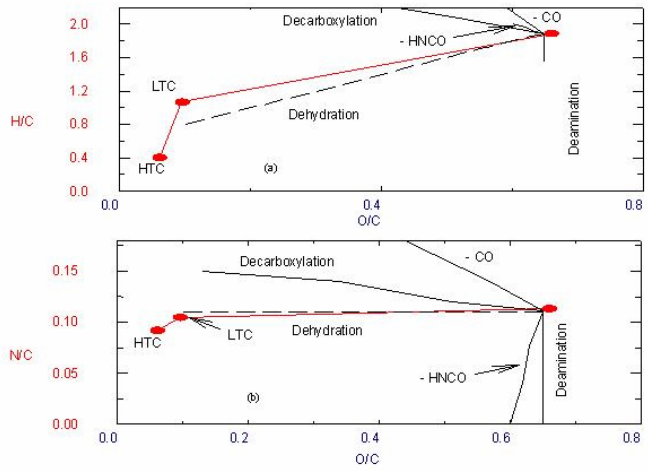

Figure 1. Composition of char from the co-pyrolysis of proline and glucose.

tryptophan/glucose mixture showed similar results. The H/C and O/C ratios decreased dramatically but the N/C ratio decreased only slightly above 300 °C. The results from asparagine/glucose mixture were somewhat different. All the three elemental ratios showed a gradual decrease as the mixture was pyrolyzed to LTC and HTC. Thus, only small interactions between the two components were indicated for the asparagine/glucose mixture. It should also be noted that the HTC from the co-pyrolysis of asparagine and glucose was as aromatic as the HTC from proline/glucose or tryptophan/glucose mixtures although asparagine and glucose have aliphatic structures.

Compositions of LTT and HTT. The compositions of LTT and HTT from the proline/glucose pyrolysis are presented in Table 2. The LTT consisted mainly of diketopiperazine, ethyldimethyl pyrazine, acetylpyrrolidine, methanolpyrrolidine and spartein. Other pyrrolidine and piperidine derivatives were also observed. Among the products, the yield of diketopiperazine was highest. The pyrazines might have been formed by self-condensation of glucosamine and fructosamine, as suggested by Hodge.[1] The HTT consisted of indole, methylindole, dimethylindole and diketopiperazine. Substituted pyrrole, imidazole and indolizines were observed in relatively low yields. The components of LTT are different than those from the pyrolysis of proline which was mainly diketopiperazine. Proline did not form any HTT. Thus, most of the nitrogenous products in co-pyrolysis were formed by interactions between proline and glucose or their decomposition products. A few of these compounds have also been reported earlier in the amino acid/sugar reactions.[3-5]

Table 2. Major Components of LTT and HTT from the Co-Pyrolysis of Proline/ Glucose Mixture (mg/g of mixture).

COMPOUND	LTT	HTT
Ethyldimethylpyrazine	11.4	
2,5-diketopiperazine	126	2.2
Indole		1.5
Methylindole		4.6
Dimethylindole		4.7
Acetylpyrrolidine*	7.2	
Methanolpyrrolidine*	5	
Pyrrolidinecarboxaldehyde*	3.7	
Cyclohexenylpiperidine*	5.2	
Hexahydrobenzocycloheptenone*	6.7	
Spartein*	16.7	

*identification based on spectral matching only, yields in counts/g of mixture.

The LTT and HTT from the pyrolysis of tryptophan/glucose mixture consisted only of nitrogen-containing compounds, many of which were polycyclic aromatic compounds (N-PACs). The major components of LTT were indole, methylindole, norharman, harman, acetylnorharman and trimethylbenzonitrile. The HTT contained mainly diketopiperazine, norharman, harman, carbazole, methylcarbazole and dimethylcarbazole. Ethylpyridylindole, dimethylphenanthroline, dimethyl β–carboline, and aminocarbazole were also observed. Some of the above components were not observed in the pyrolysis of tryptophan in the absence of glucose. Since all the above components are nitrogenous, glucose and its decomposition products either reacted completely with the nitrogenous intermediates from tryptophan or were lost to char and the gaseous product.

The LTT from the co-pyrolysis of asparagine/glucose mixture consisted mainly of succinimide, maleimide, aminohydroxypyrimidine and indole, with yields of 20.2,14.9, 1.2 and 1.1 mg/g of mixture. Dihydrodihydroxymethylpyranone aminomethyl pyrimidinone and hydroxymethyldihydrofuranone were also observed. Succinimide was also the largest component of HTT, with a yield of 23 mg/g, followed by maleimide and indole. Derivatives of indole and succinimide, such as isoindoledione and ethylendienesuccinimide, were also found in HTT. Pyrolysis of asparagine alone, in the absence of glucose, gave a negligible yield of LTT at 300 °C and the HTT consisted of succinimide, maleimide and succinimidosuccinimide, in yields of 48, 8, and 40 mg/g of asparagine.[6] Thus, the addition of glucose resulted in the formation of new products that were not observed from asparagine. For the components that were observed from both the mixture and asparagine alone, the yields from the mixture were lower. The non-nitrogenous components of the product likely originated from glucose. Substituted indoles and dihydromethylfuranone have also been observed by Coleman and Chung[3] in the pyrolysis of asparagine/sugar Amadori compounds.

The above results were also compared to those from the other aliphatic amino acids, aspartic acid, glutamic acid and glutamine. The results from the aspartic acid/glucose co-pyrolysis were essentially similar to those from asparagine/glucose and indicated a relatively small extent of interaction. On the other hand, the results from glutamine/glucose and glutamic acid/glucose pyrolysis suggested strong interactions, as in the case of proline. It should be added that asparagine and aspartic acid, when pyrolyzed without glucose, yielded negligible tar at 300 °C whereas the other amino acids gave significant yields of tars. In addition, unlike other amino acids and glucose, asparagine and aspartic acid do not undergo melting at 300 °C. These results suggest that the product distributions from the co-pyrolysis are determined by both the physical and chemical interactions between the amino acid and glucose as well as by their decomposition products.

Conclusions

Strong interactions between the components were observed in the co-pyrolysis of amino acids with glucose. The magnitude of interaction was dependent on the amino acid and the pyrolysis conditions, i.e. temperature, amino acid/glucose ratio. The co-pyrolysis generally increased the char yield at the expense of tar yield, particularly at high temperatures. Significant yield of nitrogenous char was obtained from proline co-pyrolysis although, in the absence of glucose, proline was completely converted to volatile products at and above 300 °C. Many new products were formed in co-pyrolysis that were not observed from the separate pyrolyses of amino acids and glucose.

Acknowledgements. The authors are grateful to the Philip Morris USA management for the support of this research and to Dr. Jeffrey Seeman, SaddlePoint Frontiers, for providing insights into the reaction chemistry.

References

(1) Hodge, J.E. *J. Agric. Food Chem.* **1953**, *1(15)*, 928.
(2) Spingarn, N.E.; Garvie-Gould, C. T.; Slocum, L.A. *J. Agric. Food Chem.* **1983**, *31*, 301.
(3) Coleman, III, W,M.; Chung, H.L. *J. Anal. Appl. Pyrol.* **2002**, *63*, 349.
(4) Despointes, A.H.; Yaylayan, V.A.; Keyhani, A. J. Agric. Food Chem. **1994**, *42*, 2519.
(5) Shibamoto, T.; Bernhard, R.A. J. Agric. Biol. Chem. **1977**, *41*, 143.
(6) Sharma, R.K.; Chan, W.G.; Seeman, J.I.; Hajaligol, M.R. *J. Anal. Appl. Pyrol.* **2003**, *66*, 97.

FORMATION MECHANISMS OF NITROGENOUS CHAR AND NO DURING BIOMASS COMBUSTION

Hoongsun Im, Firooz Rasouli, Mohammad Hajaligol

Philip Morris USA, Research Center
P.O. Box 26583, Richmond, VA 23261-6583, U.S.A.

Introduction

During the pyrolysis of solid fuels such as coal and biomass, the nitrogen present in the solid is evolved in part as volatile nitrogen, such as HCN and NH_3, and the remainder is retained in char [1]. The nitrogen retained in char is then emitted as nitrogen oxides (NO_x) during the subsequent combustion processes [2].

In a recent study [3], we investigated the source of NO formation during biomass combustion using various model compound mixtures. When amino acids or proteins were mixed with a particular carbohydrate such as pectin, mixtures produced NO upon combustion. Other biomass model compounds (cellulose, xylan, and lignin) did not produce NO. During the pyrolysis process, amino acids and/or proteins interact with pectin to fix nitrogen in char to make a char-N complex. Subsequently, char-N is oxidized in an oxygen-containing environment to form NO. However, the formation pathways of char-N deserve further investigation.

The present work focuses on the nitrogen fixation in char during co-pyrolysis of biomass/amino acid mixtures, and formation kinetics of NO during subsequent oxidation of char-N complex.

Experiments

Experiments were carried out in a quartz flow tube reactor with a length of 50 cm and an ID of 9.0 mm. A 100mg sample was loosely packed in the middle of the tube sandwiched by two pieces of quartz wool. The sample was heated from room temperature up to a maximum of 700 °C at the heating rate of ~12 °C/min. The sample temperature was accurately monitored by a K-type thermocouple inserted inside the sample bed. The gas flow into the reactor was controlled at 1000 ml/min by a Hastings digital flow controller. The concentration of NO in the effluent gases was continuously monitored and analyzed using an on-line NLT2000 multi-gas analyzer. The char samples from the mixtures were prepared by heating them to a given temperature and holding for 30 minutes. Nitrogen content of char was determined by elemental analysis. To estimate the formation kinetics of NO, a mixture of pectin and proline was first heated in helium to different temperatures and then heated isothermally in a gas mixture containing 0.75% oxygen. Evolved NO was monitored as a function of time until no more NO was detected.

Materials for this work were purchased from different sources as follow: Cellulose (Avicel) from FMC Corporation; pectin, rutin and glucose from ACROS; xylan and polygalactronic acid from Sigma; lignin from Aldrich; chrologenic acid from Fisher Scientific; all the amino acids (proline, asparagine, phenylalanine), and a protein (zein; a prolamine) from ACROS; and, all of the alkaloids, such as nicotine, cotinine, and myosmine used in this study were purchased from Sigma.

The mixtures of biomass model compounds (cellulose, pectin, xylan, and lignin) and other model compounds (rutin, glucose, chlorogenic acid, and polygalactronic acid) with nitrogenous organic compounds (amino acids, a protein, and alkaloids) were prepared by physical mixing. The weights of the mixtures are presented in weight percent (Wt%).

Results and Discussion

When a biomass such as peanut shell or tobacco is slowly heated in an oxidizing atmosphere, NO is primarily produced in the temperatures of 425 – 525 °C [3]. The pyrolysis of biomass does not produce any NO in this temperature range. The oxidation studies were conducted using the individual amino acids chosen above, a protein, and alkaloids mixed with each of four biomass model compounds (cellulose, pectin, xylan, and lignin). Most amino acids decompose in the temperature range of 250 °C to 350 °C producing no NO upon oxidation. However, as shown in Figure 1, the oxidation of the mixtures of proline with some biomass model compounds could produce NO. This result clearly indicates that only pectin

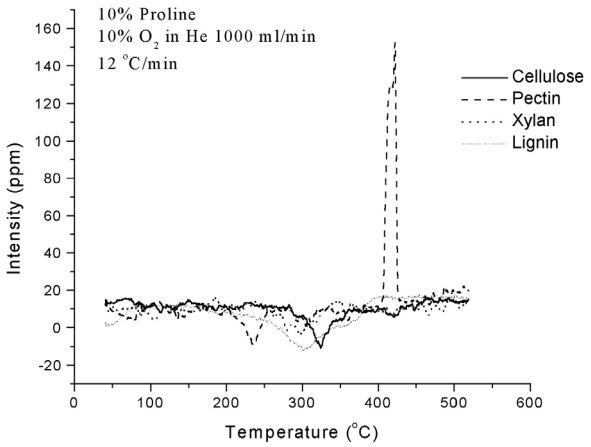

Figure 1. NO formation study from the mixtures of proline and each biomass model compound (cellulose, pectin, xylan, and lignin).

mixed with proline produced NO. When zein, a protein in a solid form, was mixed with the biomass model compounds and heated in an oxidizing atmosphere, again only its mixture with pectin produced NO. Unlike amino acids, the oxidation of pure zein produced NO (See Fig. 2). However, the pattern and the temperature range for NO

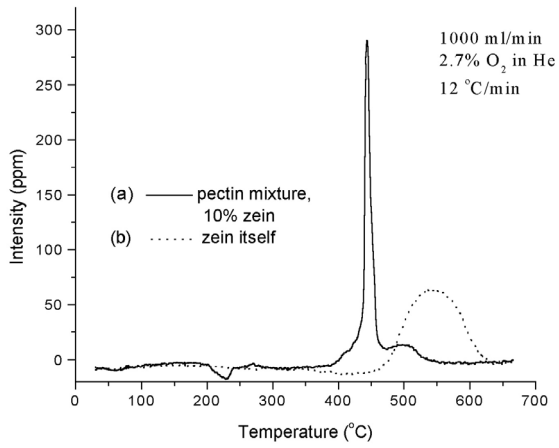

Figure 2. NO formation study from the mixtures of zein and pectin (solid line) and zein itself (dotted line) during the oxidation

formation of pure zein was quite different from its mixture with pectin. This observation indicates that proteins could also interact with pectin to produce NO. On the other hand, the mixtures of alkaloids with the biomass model compounds did not produce NO. This is expected, because the alkaloids evaporate before an interaction between them and the biomass compounds take place.

When amino acids are mixed with pectin, the mixtures produce char between 250 °C and 350 °C, and this char gives NO upon oxidation [3]. Therefore, the study of char is important to shed light on the mechanism of NO formation during biomass combustion. Two char samples of pectin and 10% proline were prepared by heating the mixture in a flow tube reactor to 350 °C where the temperature was held for 30 min. One char was produced under pyrolysis conditions while the other one was produced under a partially oxidative condition (3% oxygen). NO formation has been observed from both types of char during oxidation at the high temperature range. This observation indicated that the oxygen is not essential for preparing char-N from the biomass mixture. The chars prepared from the mixtures with cellulose under a similar condition did not produce NO. As shown in Table 1, the nitrogen content in the char from the pectin mixture is much higher than that from the cellulose mixture. This result clearly indicates that pectin and amino acids strongly interact and retain nitrogen in the char structure.

Table 1. Nitrogen contents in char from the pectin and cellulose mixtures. (unit : wt%)

Biomass	Room Temp.	250 °C	300 °C	350 °C
Pectin	1.49	0.73	0.52	0.46
Cellulose	1.13	0.09	0.10	0.08

Comparing the structures of the biomass model compounds tested in this work, only pectin contains carboxylic acid functional groups in the structure. (See Figure 3) Others have either aliphatic (sugar, cellulose, xylan) or aromatic (lignin) hydroxyl groups. Amino acids have amine functional groups in the structure. It is conceivable from these facts to assume that the amine functional groups in amino acid and the carboxylate functional groups in pectin interact to fix nitrogen in the char.

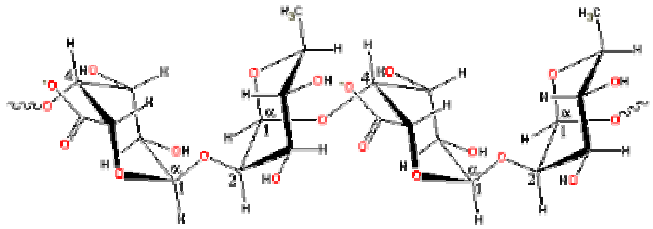

Figure 3. The structure of Pectin

To further verify this thought, a few compounds with known molecular weights and structures were chosen; ploygalactronic acid, a polymer with the subunit of pectin; chlorogenic acid, a phenolic compound with a sacharide unit; and, rutin, a phenolic compound with no sacharide unit. The first two compounds have the carboxylic acid functional group but rutin does not contain any acid group. The mixture of each acid and 10% proline produced NO at the high temperature range during the oxidation; but the mixture of rutin and 10% proline produced no NO at all. These results would further confirm our hypothesis that the condensation reaction between the carboxylic acid functional groups in biomass and the amine functional groups in amino acids would lead to the fixation of nitrogen in char.

A simple chemical reaction for the NO formation from char-N can be written as follows:

$$\text{Char-N} + O_2 \rightarrow \text{NO}$$

When the concentration of oxygen is kept constant during the reaction, the above reaction can be treated as a first order reaction with respect to the yield to be produced NO. The product yield, based on a first order reaction model for NO formation, can be expressed as:

$$\ln([NO]/[NO]_\infty) = kt; \text{ where } k \text{ is Arrhenius rate constant}$$

Under steady state conditions, the instantaneous amount of NO, $[NO]_t$ and ultimate yields of NO, $[NO]_\infty$ can be calculated from the data collected for NO at any given temperature. The $[NO]_t/[NO]_\infty$ is calculated for a few temperature reactions. Then, the activation energy and pre-exponential coefficient can be derived from the plot of $\ln([NO]_t/[NO]_\infty)$ versus the inverse of temperature (1/T). Table 2 summarizes the results based on the yields measured for NO at different temperatures.

Table 2. NO yields with respect to the reaction temperatures

T (°K)	$k = [NO]_t/[NO]_\infty$ (min^{-1})	1/T (1000 $°K^{-1}$)	ln k
762	0.048	1.312	-3.034
783	0.065	1.277	-2.734
804	0.085	1.244	-2.462
825	0.110	1.212	-2.208

From the Arrhenius plot (Fig. 4), the activation energy for NO formation reaction was estimated to be 16.3 kcal/mol with a pre-exponential coefficient of 2.39 x 10^3 min^{-1}.

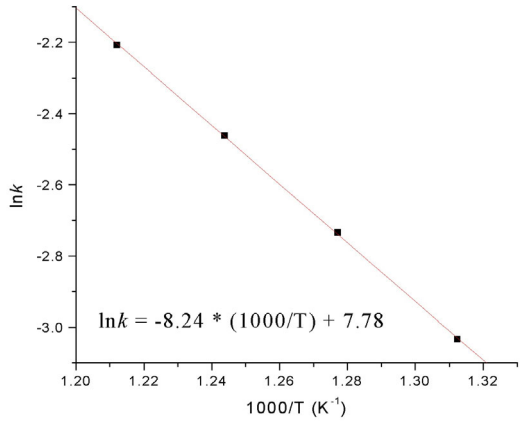

Figure 4 Arrhenius plot of NO formation from Char-N

Acknowledgment

The authors thank Dr. Robert Fenner and Dr. Donald Miser for helpful discussions. The authors also acknowledge Philip Morris USA management for their support and encouragement of basic research.

References

1. Chen, J.C., Castagnoli, C., Niksa, S., *Energy Fuels*, **1992**, 6, 264.
2. Wojtowicz, M.A., Pels, J.R., Moulijin, J.A., *Fuel Process Technol*, **1993**, 34, 1.
3. Im, H.S., Rasouli, F., Hajaligol, M. preparing for publication.
4. Sakuma, H., Matsushima, S., Munakata, S., *Agric. Biol. Chem*., 1982, 46(5), 1311.

BEHAVIOUR OF MODEL SUBSTRATES IN CATALYTIC HYDROPYROLYSIS TO INVESTIGATE PRESERVATION OF BIOMARKERS RELEASED FROM KEROGENS AND ASPHALTENES

Will Meredith[1]***, Colin E. Snape***[1]*, Gordon D. Love*[2]*, Allan McGinn*[3] *and Okan Sirkecioglu*[4]

[1]Nottingham Fuel & Energy Centre,
School of Chemical, Environmental and Mining Engineering (SChEME), University of Nottingham, University Park, Nottingham NG7 2RD, United Kingdom, Colin.snape@nottingham.ac.uk

[2]School of Civil Engineering and Geosciences, University of Newcastle, Drummond Building, Newcastle upon Tyne, NE1 7RU, United Kingdom

[3]University of Strathclyde, Dept. of Pure & Applied Chemistry, Thomas Graham Building, 295 Cathedral St., Glasgow G1 1XL, United Kingdom

[4]Dept. of Chemistry, Istanbul Technical University, 80626, Istanbul, Turkey

Introduction

The use of hydropyrolysis (commonly abbreviated to *hypy*), which refers to pyrolysis assisted by high hydrogen gas pressures (>10 MPa) in the presence of a dispersed catalyst, as an analytical pyrolysis method for liberating covalently-bound biomarker hydrocarbon structures from kerogen was first reported by Love *et al.*[(1)]. This and other subsequent studies have demonstrated the unique capability of the fixed-bed catalytic hydropyrolysis procedure to release much higher yields of aliphatic biomarker hydrocarbons (including *n*-hydrocarbons, hopanes and steranes) from immature kerogens compared to mild catalytic hydrogenation and traditional pyrolysis methods[(1-5)]. .A combination of slow heating (<20^{o}C min^{-1}), high hydrogen pressure (15 MPa) and use of a dispersed sulphided molybdenum catalyst represents the most effective regime for achieving high conversions to DCM-soluble products whilst minimising the structural rearrangement of biomarker species [(3)].

Kerogen-bound hopanes and steranes undergo the same epimerization reaction pathways as their free counterparts in the bitumen, but they are generally considerably less mature in terms of isomerisation at both ring and side-chain chiral centres. As a consequence, the biomarker profiles can be used to assess the maturity of source rocks with greater precision than using the free hydrocarbons and the successful application of hydropyrolysis to a contaminated core has been demonstrated[(5)]. Further, hydropyrolysis tests on asphaltenes isolated from a biodegraded oil seep have shown that biomarker structures sequestered in heavy oil fractions are exceptionally well preserved against microbial alteration and that interpretable biomarker profiles can be generated[(6)].

Recent work has also suggested that the bound biomarkers from the adsorbed oil phase (polars plus asphaltenes) on core rocks have the potential to provide novel information on basin filling. In essence, the adsorbed phase on a particular section of core rock is representative primarily of the first oil charge to contact the rock. Thus, while the free oil may be homogenized, mapping the maturity of the biomarkers bound to the adsorbed phase can potentially yield valuable information on the filling history for basin modelling. Other recent applications of hydropyrolysis include following the incorporation of hopanoids[(7)] into recent sediments (see Figure 1 as an example) and characterizing bound aromatic hydrocarbons from late Archean and Mesoproterozoic kerogens[(8)], the first time that a pyrolysis technique has been able to release PAHs from such highly thermally mature kerogens.

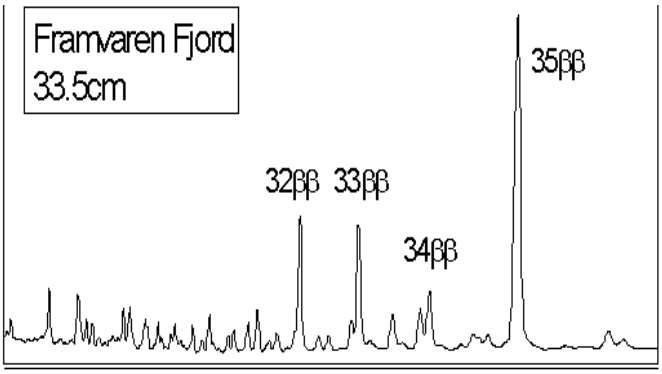

Figure 1. Hopane distribution (m/z 191 single ion chromatogram) showing the hopanes released from a high S sediment (from Framvaren Fjord, Norway) via hydropyrolysis.[(8)]

As well as providing excellent biomarker profiles for kerogens, it has been established that hydropyrolysis oils have similar bulk carbon skeletal parameters as the parent kerogens, again as a result of the high oil yields and minimal structural alteration for the hydrocarbon moieties[(9)]. In view of the potential of hydropyrolysis for a number of applications in oil exploration and as a general characterisation technique for geomacromolecules, there is a need to consider both the extent of heteroatom (C-O and C-S) bond cleavage in hydropyrolysis and the impact this might have in terms of isomerisation and cracking on the resultant biomarker distributions.

Two-stage hydropyrolysis in which the primary oil vapors pass through a bed of hydrotreating catalyst can result in the release of significantly higher concentrations of alkane biomarkers than its single stage counterpart due to a greater extent of C-O and C-S bond cleavage occurrung[(10)]. However, the aliphatic biomarker profiles are generally quite similar and, therefore, single stage hydropyrolysis is perfectly satisfactory for giving representative distributions of bound biomarkers. To investigate the extent of cracking and isomerisation undergone by *n*-alkanes and steranes upon formation from specific functionalities, a series of hydropyrolysis tests have been conducted on stearic acid, oleic acid and 5-β cholanic acid, together with cholesterol bound to a phenolic group via an ether link.

Experimental

Stearic acid, oleic acid and 5-β cholanic acid were purchased from Aldrich. 4-hydroxybenzyl cholestanyl ether was synthesized from sodium cholestanate and $C_6H_5COOC_6H_4CH_2Br$ (1:1 mole ratio) and also via the general synthetic route depicted in appendix 1 for preparing both ether and sulphide linked sterane moieties. Attempts were made to incorporate 4-hydroxybenzyl cholestanyl ether into a phenolic resole by reacting it with phenol and formaldehyde (total phenol to formaldehyde mole ratio of 2.5:1, mole ratio of phenol to 4-hydroxybenzyl cholestanyl ether of 3:1) to place the cholestane moiety in a macromolecular structure.

Single stage hydropyrolysis tests were conducted at 520^{o}C and 15 MPa as described previously[(1-5)] on the carboxylic acids and the resin by adsorbing the former on either silica or an active carbon and mixing the latter with sand before adding the dispersed Mo catalyst in the usual manner (3% /w/w Mo loading). Samples were heated resistively from 50°C to 250°C at 300°C min^{-1}, and then from 250°C to 500°C at 8°C min^{-1}, under a hydrogen pressure of 15 MPa. A

hydrogen sweep gas flow of 10 dm^3 min^{-1}, measured at ambient temperature and pressure ensured that the products were quickly removed from the reactor vessel. Products were trapped on silica as previously described and then analysed by GC-MS.

Results and Discussion

Carboxylic acids Figures 2 and 3 show the gas chromatograms of the products at different temperatures from stearic and oleic acids adsorbed on active carbon. The yields of recovered hydrocarbons from stearic and oleic acids adsorbed on silica and active carbon are listed in Table 1.

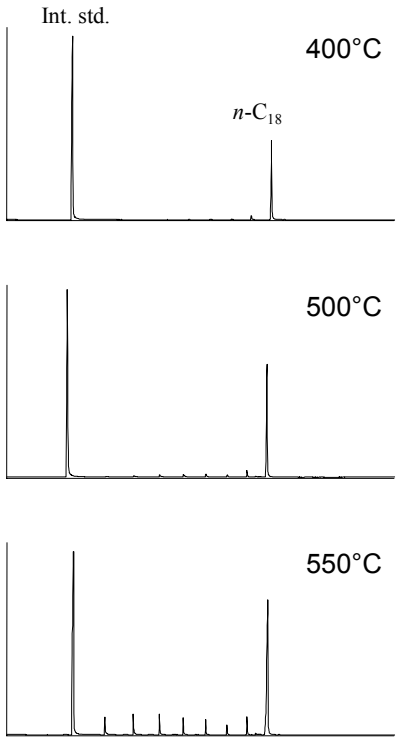

Figure 2. Gas chromatograms of hydropyrolysis products from steric acid adsorbed on active carbon.

Table 1. Product yields from stearic and oleic acids adsorbed on silica and carbon determined by GC

Yield,	Stearic acid			Oleic acid		
mg/g carbon	400	500	550	400	500	550
Carbon	219	554	695	284	640	681
Silica	445	612	906	448	630	897

Table 1 indicates that for both adsorbents the yields increase with temperature, but are higher for silica than for the active carbon. Only at 550°C is a significant degree of hydrocracking evident from Figure 2 for stearic acid to give lower boiling *n*-alkanes than *n*-octadecane. At the lower temperatures, the selectivities for hydrogenating stearic acid are >90%. Lower selectivities to *n*-octadecane are observed for oleic acid at 500 and 550°C than at 400°C. A high selectivity (>90%) was also achieved for 5-β cholanic acid to 5-β cholane but the yields were slightly lower than for stearic and oleic acids, only reaching 500 mg/g of initial carbon by 550°C. Bearing in mind that 500°C is usually a sufficiently high enough temperature to achieve maximum conversions for relatively immature kerogens, this suggests that surface O complexes are formed as the carboxylic acids are reduced to predominately C_{18} hydrocarbons.

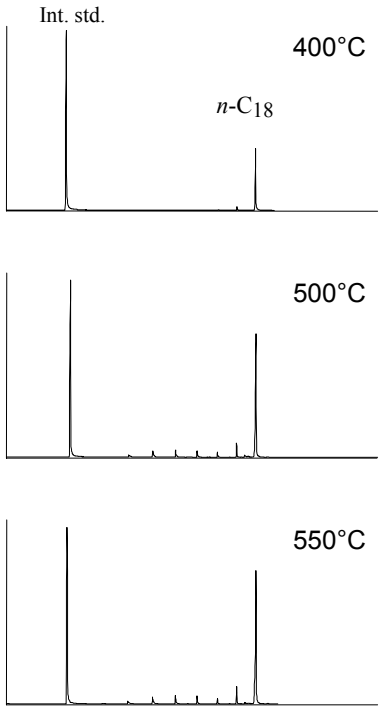

Figure 3. Gas chromatograms of hydropyrolysis products from oleic acid adsorbed on active carbon.

It is interesting to note also that, when adsorbed on silica, asphaltenes typically only give conversions of 300-400 mg/g of C compared to over 900 mg/g of C for immature kerogens. Although interactions among relatively large aromatic clusters could contribute to high char yields, complex formation between asphaltenes and surface oxygen functional groups may again be a contributory factor to suppressing yields.

Onset of ether bond cleavage A series of experiments at different temperatures were conducted on the 4-hydroxybenzyl cholestanyl ether-containing resin to establish the onset temperature for C-O bond cleavage. The yields are presented in Figure 4, which shows above 350°C the yield increases sharply. Comparable yields of cholestane and cholestanol were obtained indicating the fairly random cleavage of the C-O bond. Thus, this result verifies that any hopanoids released below 350°C from sulfur-rich sediments must be due solely to cleaving sulfide bonds.

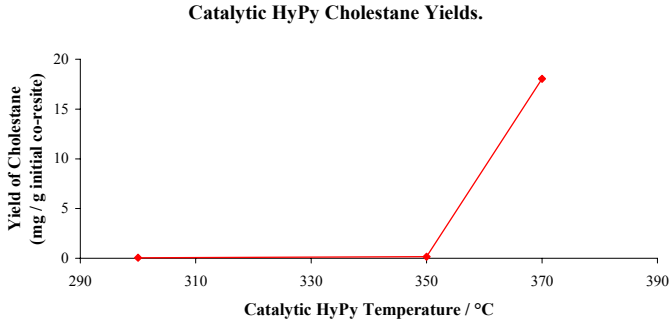

Figure 4. Yield of cholestane as a function of hydropyrolysis temperature from the 4-hydroxybenzyl cholestanyl ether co-resole.

Hopanoids – side chain cleavage Figure 1 shows the hopane profile (m/z 191 single ion chromatogram) for the recent high S sediment where the profile is dominated by the biologically-inherited C_{35} β,β hopane which is a reflection of the hopanoid skeleton being bound into the kerogen predominately via weak sulphided bonds (average of 5 bonds per chain). Indeed, hydropyrolysis at 350°C (see above) of the Framvaren sediment shows that 70%+ of the total hopanes released are still linked by one or more C-O covalent bonds. Since the strengths of C-O (ether) and C-C bonds are comparable, more cracking of the hopane side chain should accompany increasing proportions of C-O bonding for the hopanes. Further, C-C bond cleavage will also result as higher temperatures (>400°C) are experienced by the hopanoid moieties before they exit the reactor. The C_{32} β,β hopane and lighter hopanes could be diagenetic products and, consequently, the ratio of the C_{33}-C_{34} β,β hopanes to C_{35} β,β hopane is probably the best indicator of the proportion of hopanoid side chain (C-C) cracking that occurs in hydropyrolysis. This ratio is *ca*. 0.6:1.0 for the high S sediment and this is probably a reflection of the fact that one or more C-O bonds still have to be cleaved to released the majority of the hopanes. Although side chain cleavage does occur to an appreciable extent, the ring stereochemistry is not markedly affected with the β,β epimers dominating. As found previously for Göynük oil shale[1], normal pyrolysis results in virtually complete cracking of the hopane side chain with no hopanes beyond C_{32} being evident.

Conclusions

Selectivities for hydrogenating aliphatic carboxylic acids to the corresponding alkanes are extremely high with >90% being achieved for stearic acid 5-β cholanic acid. No isomerisation was evident for the cholestane-containing resin. Hydrocracking and isomerisation would thus appear to be negligible for single functionalised steranes. However, complex formation with surface oxygen functional groups for both the carboxylic acids and asphaltenes is a contributory factor to not achieving higher conversions until temperatures in excess of 500 °C. Ether bonds do not start to cleave until 350 °C indicating that biomarkers released at lower temperatures from S-rich kerogens arise from cleaving sulphides only.

Acknowledgement. The authors thank the National Environmental Research Council (NERC) for financial support (Ocean Margins LINK grants, nos. NER/T/S/2000/01366 and 2001/01153).

References

(1) Love, G.D., Snape, C.E., Carr, A.D., Houghton, R.C., 1995. *Organic Geochemistry,* **1995**, *23*, 981. (2) Love, G.D., Snape, C.E., Carr, A.D., Houghton, R.C., *Energy & Fuels*, **1996**, *10*, 149.
(3) Love, G.D., McAulay, A., Snape, C.E., Bishop, A.N., *Energy & Fuels,* **1997**, *11*, 522.
(4) Bishop, A.N., Love, G.D., Snape, C.E., Farrimond, P., *Organic Geochemistry*, **1998**, *29*, 989.
(5) Murray, I.P., Love, G.D., Snape, C.E., Bailey, N.J.L., *Organic Geochemistry,* **1998**, *29*, 1487.
(6) Murray, I.P.; Snape, C.E.; Love, G.D.; and Bailey, N.J.L. *Abs. for 19th Int. Meeting on Organic Geochemistry*, Istanbul, 6-10 September 1999, Part 1, No. PB10, pp 341-342.
(7) Farrimond, P., Bishop, A.N., Innes, H.E., Watson, D.F., Love G.D. and Snape, C.E., *Geochim Cosmochim Acta*, **2003**, *67*, 1383.
(8) Brocks, J.J., Love, G.D., Snape, C.E., Logan, G.A., Summons R.E. and Buick, R., *Geochim Cosmochim Acta*, **2003**, *67*, 1521.
(9) Maroto-Valer, M.M.; Love, G.D.; and Snape, C.E. *Energy Fuels* **1997**, *11*, 539.
(10) Snape, C.E, Love, G.D. and Murray, I.P., *Prepr. Am. Chem. Soc. Div. Fuel Chem.,* **2001**, *46(1),* 204.
(11) Snape, C.E., Meredith, W., Russell, C.A., Cooper, M., Love, G.D. and Fabbri, D., *Prepr. Am. Chem. Soc. Div. Fuel Chem.,* **2003**, *48(1),* 16.

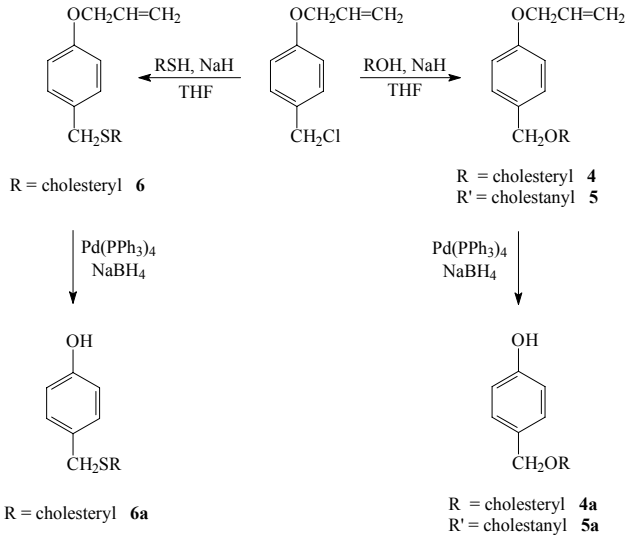

Appendix 1 General synthetic route for ether and sulphide liked steranes

PETROLEOMICS: ESI FT-ICR MS IDENTIFICATION OF HYDROTREATMENT - RESISTANT NEUTRAL AND ACIDIC NITROGEN SPECIES IN CRUDE OIL

Ryan P. Rodgers[2], Geoffrey C. Klein[1], Vince Nowlan[3], and Alan G. Marshall[2]

[1.] Department of Chemistry and Biochemistry, Florida State University, Tallahassee, Florida 32306.
[2.] Ion Cyclotron Resonance Program, National High Magnetic Field Laboratory, Florida State University, 1800 E Paul Dirac Drive, Tallahassee, Florida 32310.
[3.] Syncrude Canada Ltd., Edmonton, Alberta, T6N 1H4

Introduction

ESI FT-ICR MS analysis of complex mixtures, such as crude oil, achieves high mass resolving power ($m/\Delta m_{50\%} > 300{,}000$, in which $\Delta m_{50\%}$ denotes mass spectral peak full width at half height) and high mass accuracy (< 1 ppm).[1] Selective ionization of polar NSO compounds by ESI FT-ICR MS is of great interest in the refining of crude oils, because the nitrogen-containing compounds are known to play a key role in catalyst deactivation through coke formation on the catalyst surface. The removal of nitrogen compounds from refined fuels is also necessary to prevent the formation of gums and solid precipitates during storage. Here we apply ESI FT-ICR MS to two narrow distillation cuts that have undergone hydrotreatment for the removal of nitrogen species in crude oil. Compositional analyses of both samples before and after hydrotreatment identify species resistant to the chosen reaction conditions and helps establish removal efficiencies / reactivity of all identified species.

Experimental

Crude Oil Samples. Two narrow distillation cuts, 483-504 ˚C and 504-524 ˚C, of a crude oil were subjected to hydrotreatment for the removal of nitrogen compounds. Retention chromatography was performed to produce nitrogen concentrates for ESI FT-ICR MS analysis. 20 mg of each sample was dissolved in 10 mL of toluene and then diluted with 10 mL of methanol to a final volume of 20 mL. The samples were further diluted to a final concentration of 0.1 mg of crude/mL of solvent. One mL of the final solution was spiked with 30 μL of ammonium hydroxide to facilitate deprotonation for the ESI FT-ICR mass spectral analysis.

Mass Analysis. The crude oils were analyzed at the National High Magnetic Field Laboratory (NHMFL) with a homebuilt 9.4 Tesla Fourier transform mass spectrometer. Ions were generated externally by a micro-electrospray source and samples were delivered by a syringe pump at a rate of 300 nL/min. Approximately 2.2 kV was applied between the capillary needle and ion entrance (heated metal capillary). The externally generated ions were accumulated in a short (15 cm) rf-only octopole for 10-30 s and then transferred via a 200 cm rf-only octopole ion guide to a Penning trap. Ions were excited by frequency-sweep (100-725 kHz @ 150 Hz/μs at an amplitude of 200 Vp-p across a 10-cm diameter open cylindrical cell). The time-domain ICR signal was sampled at 1.28 Msample/s for 3.27 s to yield 4 Mword time-domain data. Ten to two hundred data sets were co-added, zero-filled once, Hanning apodized, and fast Fourier transformed with magnitude computation. A continuous wave 40 W CO_2 laser (Synrad E48-2-115, Bothell, WA) was used to investigate the presence / dissociate non-covalent ion complexes. Mass spectra were internally calibrated with respect to the most abundant heteroatom containing series over the full mass range. Homologous series were separated and grouped by nominal Kendrick mass and Kendrick mass defect to facilitate rapid identification, as described elsewhere.[2]

Results and Discussion

Variations in heteroaromatic content of two distillation cuts of a heavy crude oil both before and after hydrotreatment were first investigated by comparison of the negative ion ESI FT-ICR mass spectra of crude oil nitrogen concentrates. Figure 1 shows the broadband mass spectrum of the unprocessed nitrogen oil concentrate that represents the 483-504 ºC distillation cut. The mass spectrum is composed of ~8,000 peaks with as many as 20 peaks at a single nominal mass. Mass resolving power exceeds 300,000 for all spectra presented. Figure 2 shows a similar broadband mass spectrum of the same distillation cut after hyrdotreatment. The processed oil mass spectrum is markedly less complex with fewer peaks over a similar mass range. As evident from the comparison of Figures 1 and 2, the hydrotreatment process had little effect on the molecular weight distribution of the nitrogen concentrate analyzed.

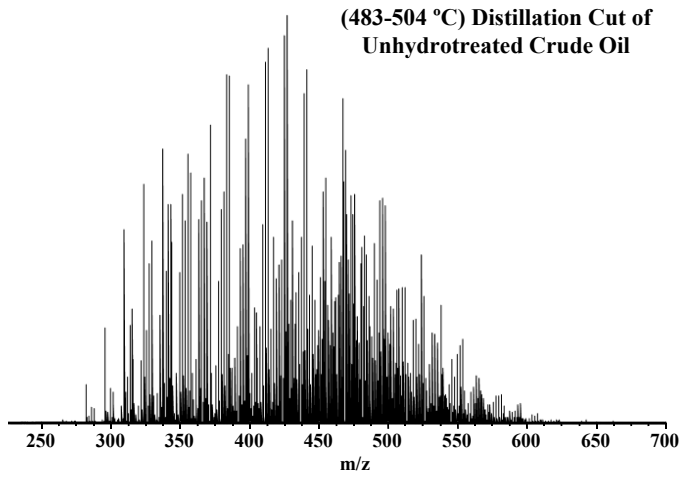

Figure 1. Broadband mass spectrum of a nitrogen concentrate isolated from narrow distillation cut of unprocessed crude oil.

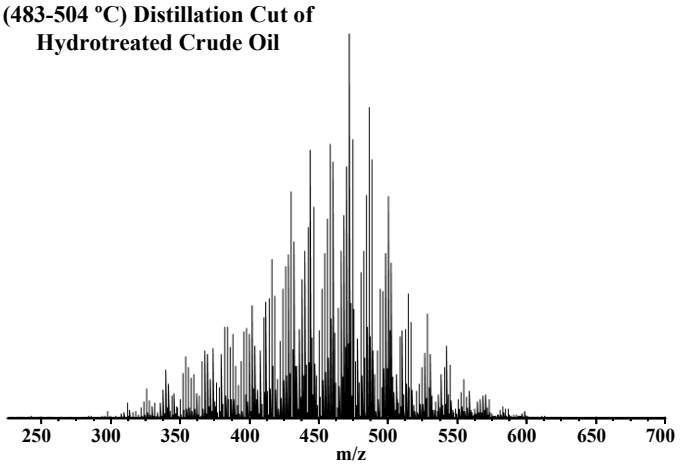

Figure 2. Broadband mass spectrum of a nitrogen concentrate isolated from narrow distillation cut of hydrotreated crude oil.

Detailed compositional differences are visually provided by comparison of the two broadband mass spectra at a single nominal mass. Figure 3 shows such a comparison at m/z = 414. Note, detailed compositional information is also provided at every other nominal mass over the entire mass range.

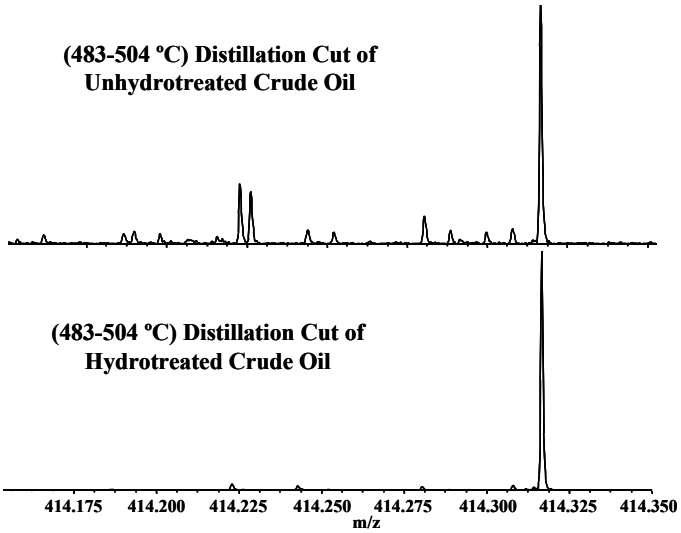

Figure 3. Zoom mass inset of both the unprocessed (top) and hydrotreated (bottom) mass spectra at m/z = 414. As with the broadband mass spectra, the hydrotreated nitrogen concentrate is far less complex than the unprocessed with fewer peaks per nominal mass.

Exact mass measurement (less than 1ppm) provided by FT-ICR allows for the assignment of elemental compositions for all observed peaks in the mass spectrum. This compositional information allows for direct comparisons of the difference classes of compounds identified in each of the crudes both before and after hydrotreatment. The comparison allows for the determination of persistent or unreactive species in the hydrotreatment process. Figure 4 shows a bar graph that lists the most abundant classes identified in the unprocessed oil nitrogen concentrate.

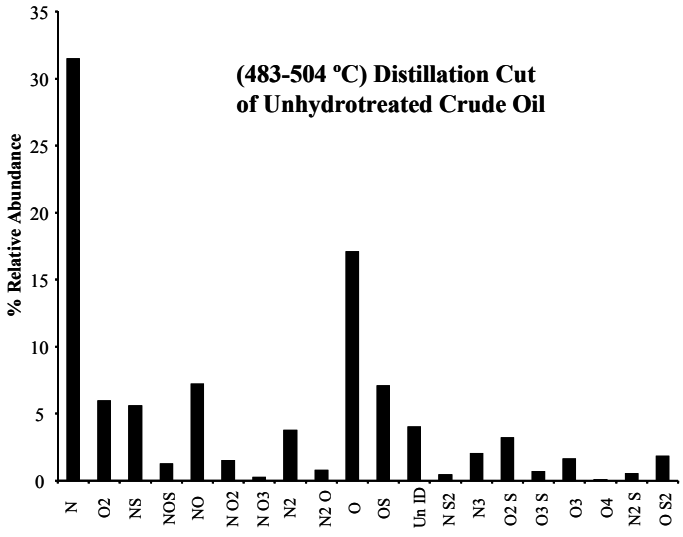

Figure 4. Bar graph that lists the most abundant classes identified in the unprocessed oil nitrogen concentrate.

Figure 5 shows a similar bar graph for the hydrotreated oil nitrogen concentrate. Comparison of the two bar graphs identifies persistent species under the chosen hydrotreatment conditions.

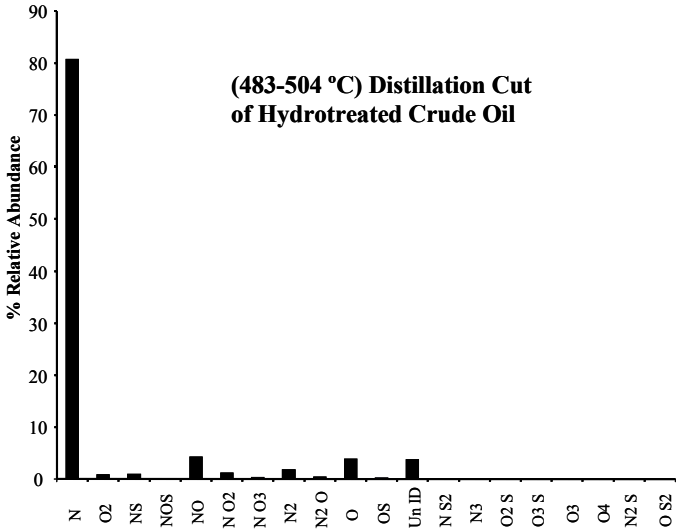

Figure 5. Bar graph that lists the most abundant classes identified in the hydrotreated oil nitrogen concentrate.

The hydrotreatment clearly has an effect on the classes of compounds observed in the ESI FT-ICR mass spectrum. However, many nitrogen species are present after hydrotreatment and appear to have relatively low reactivity under the chosen conditions. This provides insight into the reactivity of these classes under hydrotreatment conditions. Data for another distillation cut of the same oil, under the same hydrotreatment conditions show similar results. Future work will concentrate on various hydrotreating conditions in an attempt to better understand the reactivity of the N-containing heteroaromatic species present in crude oil.

Acknowledgment

This work was supported by NSF CHE-99-09502, Florida State University, and the National High Magnetic Field Laboratory in Tallahassee, FL.

References

1. Qian, K; Robbins, W. K.; Hughey, C. A.; Cooper, H. J.; Rodgers, R. P.; Marshall, A. G., *Energy and Fuels,* **2001**, 1505-1511
2. Hsu, C. S.; Qian, K.; Chen, Y. C., *Analytica Chimica Acta,* **1992**, 79-89.

A COMPARISON OF THE MAILLARD REACTIVITY OF AMINO ACIDS USING PYROLYSIS-MOLECULAR BEAM MASS SPECTROMETRY

Mark N. Nimlos, Luc Moens, Michael J. Looker,and Robert J. Evans

National Bioenergy Center
National Renewable Energy Laboratory
Golden, Colorado 80401

Introduction

The thermal decomposition amino acids and proteins in biomass plays an important role in the formation nitrogen-containing aromatic compounds during combustion[1]. The routes to the formation of nitrogen containing aromatic compounds needs to be understood as these recalcitrant, thermally stable compounds present operational problems in biomass gasification and may be of concern in other thermal processes involving biomass.

An important consideration in the thermal chemistry of amino acids and proteins is the polymer matrix that surrounds these species in biomass. Carbohydrates such as cellulose and hemicellulose exist in high concentrations in biomass and the carbonyl groups contained in these materials are susceptible to attack from the amino groups in proteins or free amino acids. This has been studied in detail as part of an effort to understand the chemistry responsible for the formation of flavor components during cooking and is often called Maillard or browning chemistry[2].

We have investigated the interaction of amino acids with glucose by pyrolyzing mixtures of these materials and measuring the gas-phase species using a Molecular Beam Mass Spectrometer (MBMS). The amino acid/glucose mixtures are a model system for Maillard chemistry occurring during the pyrolysis of biomass. We find that the amino acid proline (**6**) reacts much more rapidly than other amino acids and we believe that this is due to the unique catalytic activity of proline [3-5]

Experimental

This study used an MBMS to sample products from a heated tubular flow reactor. Solid samples contained in a quartz boat were slid into the hot zone of the reactor. During a typical experiment, the sample (200 to 300 mg) were pushed from a room temperature zone, located outside the furnace, into the furnace until the desired temperature was measured with a thermocouple attached to the sample. The sample was held at this temperature for about 5 min. or until most of the volatile components were driven off as seen with the MBMS. Multiple, sequential temperature ramps were obtained by continuing to slide the sample further into the tube furnace. Flowing helium sweeps the gas phase products into the orifice of the MBMS where they are analyzed using the mass spectrometer [6, 7].

Results and Discussion

In this study, we compared the pyrolysis behavior of eight common amino acids, glycine (**1**), alanine (**2**), aspartic acid (**3**), asparagine (**4**), 2-azetidinecarboxylic acid (**5**), proline (**6**), pipecolinic acid (**7**), and tryptophan (**8**).

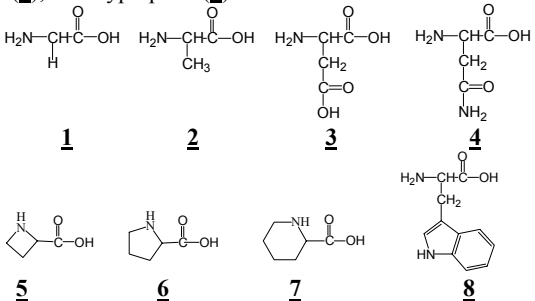

1 **2** **3** **4**

5 **6** **7** **8**

Amino acids **1**-**4**, **6**, and **8** occur naturally in biomass, while **5** and **6** serve as model compounds of secondary cyclic amines that can be compared to proline (**6**), Each of these compounds was pyrolyzed individually and in 50:50 mixtures with glucose. The gas phase products obtained during a two-staged temperature ramp (T1 = 170 °C, T2 = 325 °C) were sampled using the MBMS. The reactivities of these amino acids with glucose were compared by measuring the yields of products.

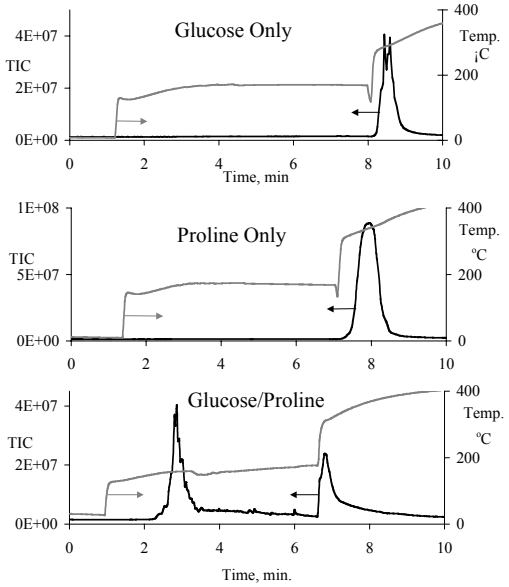

Figure 2. Evolution of products from neat glucose (top), neat proline (center), and a 50:50 glucose/proline mixture (bottom) as measured using the MBMS. The black curves are the TIC measured by mass spectrometer (axis on the left) and the grey curves are the temperature of the solid as measured with a thermocouple placed near the sample (axis on the right).

As an example, the plots in **Figure 1** show the total ion current (TIC) of products evolved from neat glucose, neat proline and a 50:50 mixture of glucose and proline. With neat proline and glucose little reaction occurs at 170 °C as evident by the low TIC signal and observation of little change in the solid. At 325 °C all of the neat samples are volatilized or reacted, there are large TIC signals and little char left. With the 50:50 mixture a vigorous reaction occurred at 170 °C. As the TIC curve at the bottom of **Figure 1** shows, this reaction was accompanied by a substantial emission of products. Less product was evolved at 325 °C but a black char remained after 5 min that comprised about ~20 % by weight of the starting material. For the proline/glucose mixture, the TIC curves in **Figure 1** clearly show that the amount of gaseous products evolved at T1 is greater than the cumulative sum of products from glucose and proline alone, which indicates that these compounds are reacting at this low temperature.

Similar experiments were conducted for the other seven amino acids shown above. To varying degrees, these amino acids also showed some reactivity with glucose at T1. In order to compare the pyrolysis of these compounds, we integrated the TIC curves during each temperature ramp and collected them in **Table I**. The first data column in this table shows the integrated TIC at T1, the second the integrated TIC at T2 and the third the ratio of the TIC at T1 to that at T2. This third column provides a comparison of the reactivity of the amino acids, *i.e.* the higher the ratio, the more reactive the amino acid. As can be seen, of the naturally occurring amino acids, proline

has the largest ratio and the greatest reactivity towards carbohydrates. This is consistent with the known catalytic properties of proline [3-5, 8].

Table I Integrated Total Ion Current [(TIC)[a] × 10^4 cnts] for amino acids mixed with glucose (50:50 mixtures)

species	Temperature ramp T1 170 °C	T2 325 °C	T1/T2
Naturally Occurring Amino Acids			
proline (**6**)	4.2	2.9	1.4
Alanine (**2**)	1.1	2.8	0.39
aspartic acid (**3**)	1.2	1.8	0.71
asparagine (**4**)	0.51	1.1	0.48
glycine (**1**)	0.77	2.6	0.29
Tryptophan (**8**)	0.86	5.9	0.15
Other Secondary Amino Acids			
pipecolinic acid (**7**)	2.0	4.5	0.44
2-azetidinecarboxylic acid (**5**)	1.3	1.2	1.10

[a]Areas are normalized to mass (mg) of starting material

Typical mass spectra obtained during these temperature ramps are shown in **Figures 2**. At T1 the neat glucose spectrum is dominated by fragmentation (both thermal and ionization), dehydration products (144 and 126) and cracking. The neat proline spectrum is dominated by fragmentation of proline and the diketopiperazine (m/z = 194 and 70), a common product of amino acid pyrolysis[9].

The mass spectrum of the 50:50 mixture at 170 °C contains some of the same peaks from the neat compounds (with greater intensity) as well as other peaks indicative of Maillard chemistry. The two prominent peaks are m/z =44 and 84 are likely due to carbon dioxide and fragment ions from **9** (1-(1'-pyrrolidinyl)-2-propanone) and **10** (2-hydroxy-1-(1'-pyrrolidinyl)-1-buten-3-one [10, 11].

9 **10**

In addition to these peaks, there are a large number of weak features that are collected in groups spaced roughly 14 amu apart. These features become more pronounced at 325 °C as is shown in the spectrum at the bottom of **Figure 2**. The spacing of these peaks is suggestive of a homologous series of compounds with increasing numbers of methyl groups. These compounds likely result from thermal cracking of the primary Maillard chemistry products such as **9** and **10**. Many of these products are probably similar to the secondary products identified elsewhere [10, 11]. In this complex suite of compounds there are nitrogen containing ring compounds including aromatic compounds.

The enhanced reactivity of proline towards glucose as indicated by **Table I** is most likely due to properties which proline a good catalyst for aldol reactions [3-5, 12]. Proline is known to be a more effective catalyst compared to primary amino acids, noncyclic secondary amino acids and cyclic amino acids with 6-membered rings [4, 5]. Interestingly, 4-membered ring amino acids were shown to have catalytic activity similar to proline. As mentioned above, we compared the reactivity of cyclic amino acids with a 4-membered ring (**5**) and a 6-membered ring (**7**) to proline. The 6-membered ring amino acid (**7**) was not as reactive as proline, while the 4-membered ring amino acid (**5**) was. This suggests that the molecular structure of proline enhances the catalytic activity for aldol reactions for the same reason that it enhances its reactivity in Maillard chemistry. The similarity of Maillar chemistry and aldol catalysis is also found in the proposed mechanisms.

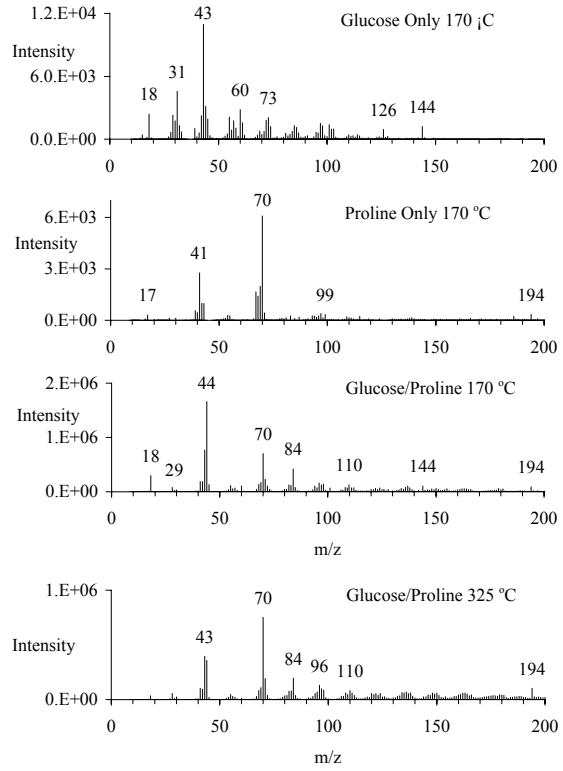

Figure 2. Averaged mass spectra of products from T1 in **Figure 1** and T2 for the glucose/proline mixture. Notice that many of the peaks in the mixture correspond to the peaks in the individual components. However, there are peaks that are unique to the mixture, most prominently at m/z = 84 and 44.

Acknowledgment

The authors gratefully acknowledge the financial support from Phillip Morris, USA Inc. and stimulating discussions with Geoffrey Chan and Mohammad R. Hajaligol.

References

1. Brink, A., P. Kilpinen, and M. Hupa, Energy Fuels, 2001. 15(5): 1094.
2. T. P. Labuza, G.A.R., V. M. Monnier, J. O'Brien, J. W. Baynes, ed. *Maillard Reactions in Chemistry, Food and Health*. 1994, Royal Society of Chemistry: Cambridge.
3. Movassaghi, M. and E.N. Jacobsen, Science, 2002. 298(5600): 1904.
4. Sakthivel, K., W. Notz, T. Bui, and C.F. Barbas, J. Am. Chem. Soc., 2001. 123(22):5260.
5. List, B., R.A. Lerner, and C.F. Barbas, J. Am. Chem. Soc., 2000. 122(10): 2395.
6. Evans, R.J. and T.A. Milne, Energy Fuels, 1987. 1(2): p. 123-137.
7. Shin, E.J., M.R. Nimlos, and R.J. Evans, Fuel, 2001. 80(12): 1697.
8. List, B., Tetrahedron, 2002. 58(28): 5573.
9. Ratcliff, M.A., E.E. Medley, and P.G. Simmonds, J. Org. Chem., 1974. 39(11): 1481.
10. Tressl, R., B. Helak, E. Kersten, and D. Rewicki, J. Agric. Food Chem., 1993. 41(4): 547.
11. HuyghuesDespointes, A. and V.A. Yaylayan, J. Agric. Food Chem., 1996. 44(3): 672
12. Rankin, K.N., J.W. Gauld, and R.J. Boyd, J. Phys. Chem. A, 2002. 106(20): 5155.

Co-Treatment for Chlorinated Organic Waste Solvents and Volatile Organic Compounds in a Laboratory Scale Spouted Bed Incineration System

Chieh Lin,Yi Hung Tseng, Ming Kuei Hsieh, Ming Da Chen and Yen Fen Li

Environmental Engineering and Science Department
National Ping-Tung University of Science and Technology (NPUST)
Nei Pu,Ping-Tung,,91201,Taiwan,R.O.C.

Introduction

Chlorinated organic waste solvents and volatile organic compounds are the by-products from most of the industrial processes for examples petroleum, chemistry, medical, electric and so on. These chlorinated compounds in the waste stream may cause some adverse effects on human health and environmental impact. One of the major treatment technology applied for these waste is incineration. In order to avoid the secondary pollution comes from incineration, evaluating the products of incomplete combustion (PICs) out of the incineration system will help to identify the better combination of the combustor and APCD operation parameters. Based on the capacity, efficiency and safety issues of treatment, incineration is recognized as one of the most popular ways to deal with the waste stream. In order to avoid the emissions of the hazardous air pollutants (HAPs) from an incinerator, it is essential to continuously monitor the operating conditions and the composition of the exhaust gas. Graham et al.,[1] conducted thermal decomposition laboratory study for a mixture of chlorinated organic compounds and found the number and complexity of thermal reaction products increased with decreasing oxygen concentration. The PICs ranged from simple chlorinated aliphatics to complex polynuclear aromatics. Staley et al., [2] and Dellinger et al.,[3] showed later there is no direct relationship between the combustion efficiency and the PICs while measurements are conducted on full-scale hazardous waste incinerator. The results suggested chemical reaction kinetics controlled the relative emission rates of the surrogate compounds during incineration tests. Taylor et al.,[4] used a detailed reaction mechanism to present molecular growth up to the formation of C8Cl6(cy) and C8Cl8(cy) under the pyrolysis of trichloroethene and conclude the important radical-molecule addition reactions leading to molecular growth.. Senkan et al.,[5,7] and Huang et al.,[6] estimated the reaction rate coefficient for the abstraction of hydrogen atoms from organic compounds by chlorine radical attack and observe trace byproducts including PAHs in the chlorinated hydrocarbon and methane flames. Lemieux et. al,[8] also indicated that combustion of dichloromethane (CH2Cl2) produces higher levels of PICs than combustion of carbon tetrachloride (CCl4). Wheatley et al.,[9] investigated the effects of both the flame and the postflame conditions on the PAH emission levels for burning plastic polymers. A clear trend in the emissions of unburned hydrocarbons is found and destruction of organic compounds is enhanced with increasing postflame residence time and temperature. Kanters et al., [10] observed with an (up to 8-fold) increase of the PVC load in the MSW , only a slight increase of chlorophenol emission level by using a micromodel combustion reactor. Van Dell et al.,[11] obtained data from burning dichlorobenzene and developed a global kinetic model to describe the fromation and destruction of PICs. Their results showed that reformation might be a dominant pathway to cause the appearance and subsequent disappearance of the same PICs as temperature and/or spatial location is varied. A laboratory scale incineration system has the ability to create the reproducible and stable experimental conditions under the designed operating criteria. These advantages stimulate the application of a laboratory scale combustor to investigate the key operating parameters related to the treatment performance in terms of the CE, the DRE of POHCs as well as the PICs. Tia et al., [12,13] studied the devolatilization and volatile combustion of a single coal particle and a batch of carbon particles in a laboratory scale spouted bed combustor. Comparison of the model prediction and the experimental data showed heat transfer controls the devolatilization rate. Wongvicha et al., [14] further developed a simulation model to predict continuous lignite char combustion in a spouted bed. In a spouted bed, about 60-65% of combustion of fuel takes place in the annulus region. Formation of the aromatic hydrocarbon products for combustion of chlorinated organic compounds in a laboratory scale spouted bed incinerator will be reported in this contribution. The goal is to identify trends in PICs emission levels with combustion parameters.

Experimental Section

A laboratory scale spouted bed incineration system is employed to simulate the hazardous air pollutants behaviors in the post-combustion region. By inducing the secondary auxiliary air after the flame, the effect on PICs formation is reported. The purpose of the post-combustion chamber is to have more space and residence time for unburned waste or fuel to proceed the complete reaction. Those hydrodynamic phenomenon and the reaction kinetic parameters will affect directly or indirectly to the chemical formation and destruction. The significant impact was introduced by the temperature quench and the particulate matter surface catalysis. Some pyrolysis pockets in the combustion zone may both inhibit the reaction and enhance the PICs formation. Toluene and heptane were chosen as the primary fuel mixing with some chlorinated aromatics hydrocarbons for combustion. The vortex auxiliary air is introduced from the radial direction alone the wall of the reactor. Temperature, flowrate and the oxygen content of the secondary auxiliary air can be controlled. Chlorinated aromatic PICs (i.e. CBz, CPz, PCB, PCN, PCDD/F) are monitored. The spouted bed is characterized as a special type of fluidized bed. Since the circulating bed medium can act as a mobile heat exchanger between the reactants and products, the spouted bed combustor is especially attractive for the incineration of low heat value fuel. The preliminary studies show the influence of the bed medium types and the packed bed high on the destruction efficiency in the spouted bed. The heterogeneous effect is also reported by applying a chemical kinetic model. The final goal of this study is to develop a numerical model to simulate the spouted bed reactor. The discrepancy between the experimental results and the model predictions will be discussed further.

The experimental system for this study basically consists of three sections: air/fuel preheater and mixer, spouted bed combustor and sampling train. The primary aspects of this study is to investigate the flue gas quenching effect and the oxygen contents on PICs formation in the downstream of flame regime. Spouted bed is characterized as a special type of fluidized bed. Since circulating bed medium can act as a mobile heat exchanger between products and reactants, the spouted bed combustor is especially attractive for the incineration of low heat value fuel in laboratory research. The combustor employed in this study is a cone-shape all quartz 60 cm length spouted bed reactor, with a 1 mm inlet diameter and 5.5 cm column diameter. The reactor was uninsulated so as to facilitate visual observation of flame stability and particle circulation. Under Combustion condition the bed height was always kept at 70mm. The bed medium is a nature silica sand with ~1.0 mm diameter. A mixing fluid of air and gasified model fuel (i.e. n-heptane and toluene) was injected through the single inlet aperture from the conical base of the spouted bed combustor. While the velocity of fluid beyond a certain minimum value, a stream of bed particles were raised rapidly in a hollowed central core (the “spout”) forming a fountain of variable

height above the bed level. The particles rain back onto the annular region between the spout and the wall and thereafter travel slowly downward in a particle dense phase with countercurrent percolation of fluid. In order to take samples from combustor and measure temperature inside bed region, three sampling probes were built at the side of the reactor. Two sampling cross, consisting of four ball joint ports which enable the insertion of probes and simultaneously sampling from different radial locations, were constructed in the freeboard region of the spouted bed reactor. All temperature reading was continuously monitored through a data acquisition on-line system. PICs, normally trace amount, were sampled by using a semivolatile/volatile organic compounds sampling train. The sampling train consists a fiber filter (1.6 □ m mean cut size), an impinger, a flow meter and a vacuum pump. Recovery solvent was placed in the impinger to trap organic compounds. The collected sample including the filter and the trap was subjected to Soxhlet extraction with dichloromethane. Analyses for DRE and PICs are performed on a HP 5890 gas chromatograph coupled to a HP 5972 mass selective detector (GC/MSD). To avoid the variation of hydrodynamic aspects in the spouted bed, the oxidizing air flow rate is fixed at the constant flow rate. The fuel lean regime is conducted to simulate the normal incineration cases. The sampling probes C, D, E are located above the bed surface 15cm, 35cm, and 55cm, respectively. The same volume of bed medium is packed in the spouted bed reactor for each experimental run. After the auxiliary fuel was ignited and the flame steady located at the bed surface, the sampling train was attached to the designed position to collect the flue gas sample. Normally, the sampling flow rate was adjusted to meet the isokinetic sampling condition and the sample was taken for hours to get enough volume for analysis.

Results and Discussion

The bed temperature is a function of the equivalence ratio as no separate temperature control is provided to the bed. Temperature contour profile in the spouted bed combustor was shown in Figure 1. The temperature difference between the center and the wall of the reactor was enlarged between Cc and Cw. This result presents the combustion reaction is still active in the post combustion region. The effluent gas was channeled to the sampling train continuously measure emission of the residues of model fuel, subsequently these values were converted to the DRE.

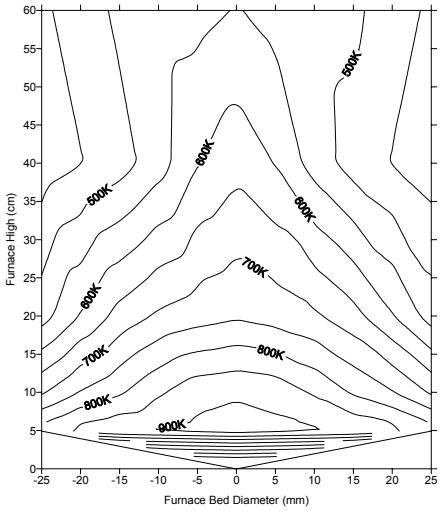

Figure 1. Temperature contour profile in the spouted bed combustor.

Figure 2 and Table 1 show the proposed pathways and the key reactions about toluene and n-heptane combustion. Since the DRE values were determined based on the residual model fuel in this study for comparison, the results only demonstrated the passive resistance of fuel decomposition during the effluent passing through the post combustion region.

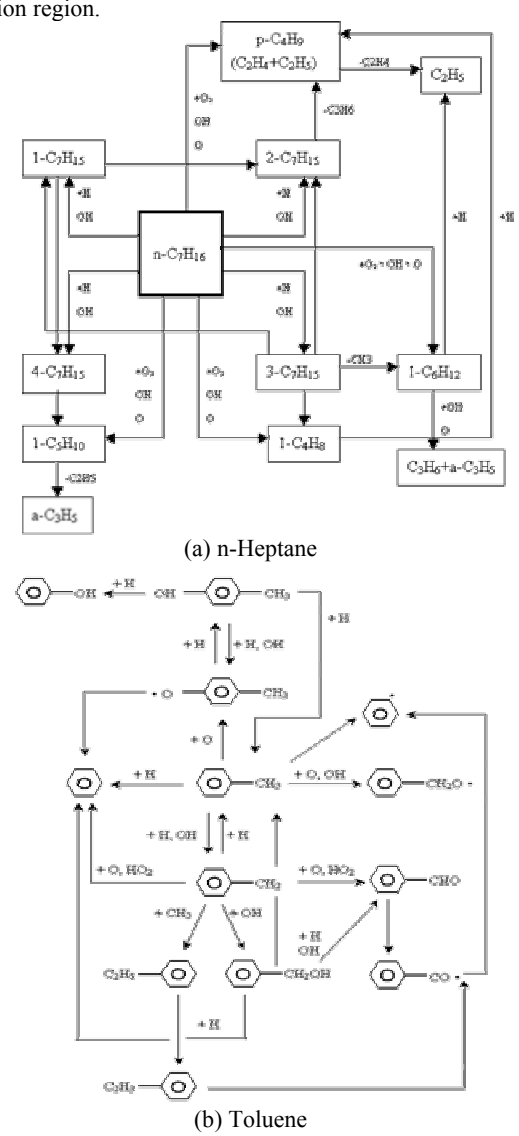

(a) n-Heptane

(b) Toluene

Figure 2. Reaction pathways of toluene and n-heptane.

Table 1. Mechanism sensitivity analysis for toluene and n-heptane.

Chemical Reaction Mechanism	Coefficient
n-Heptane	
$C_7H_{16}+O_2=HO_2+C_3H_6+C_2H_4+C_2H_5$	-8.34E-02
$C_7H_{16}+O_2=HO_2+1\text{-}C_4H8+C_2H_4+CH_3$	-6.67E-02
$C_7H_{16}+O_2=HO_2+1\text{-}C_5H_{10}+C_2H_5$	-3.48E-02
$C_7H_{16}+O_2=HO_2+1\text{-}C_6H_{12}+CH_3$	-1.41E-02
$C_7H_{16}+OH=H_2O+1\text{-}C_4H_8+C_2H_4+CH_3$	-1.83E-06
Toluene	
$C_6H_5CH_2+H = C_6H_5CH_3$	-1.19E-02
$C_6H_5CH_3+OH = C_6H_5CH_2+H_2O$	-3.75E-04
$C_6H_5CH_3+C_6H_5 = C_6H_6+C_6H_5CH_2$	-1.96E-05
$C_6H_5CH_3+H = C_6H_5CH_2+H_2$	-2.63E-07

From the results (Figure 3 & Figure 4), it was found that DRE decreased with increasing the distance from the spouted bed surface. The similar PICs distribution was demonstrated between the experimental results and model prediction. This reflected the effluent gases possible remix through the freeboard region. Nevertheless, the model fuel compound was possible reformed in the post-flame zone. In the case of chlorinated hydrocarbon combustion, the thermal degradation was happened in the bed and post-combustion region. Cl radical from the dehalogenation of chlorinated precursors can inhibit the oxidation of CO to CO2, but the abstraction of hydrogen from the methyl of toluene by chlorine radical attack can cause the increase of DRE. There is a debate in the literature on whether CE and unburned fuel emissions (i.e. DRE) correlated or not. Some studies reported satisfactory correlations while others did not reveal correlations. Our investigation may face some uncertainties because experiments were conducted in the fuel lean region, where ideally there are no significant CO and the residual fuel. In such a case PICs emissions probably resulted from fluctuations in mixing and localized quenching of the flame. In our experiments where reactor without insulated and only single flow inlet, emissions of substantial quantities of PICs were seen. Figure 5 shows the chloride effects on the yields of PICs for model fuel.

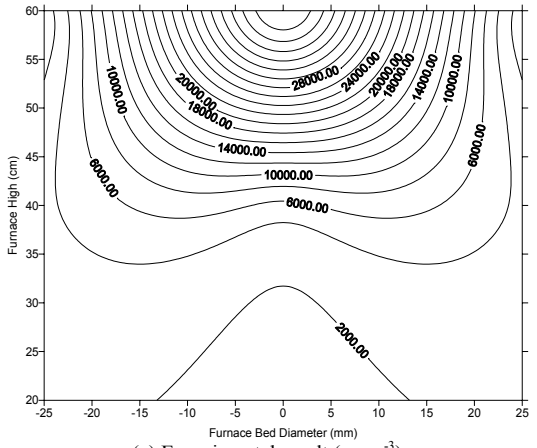

(a) Experimental result (μg m^{-3})

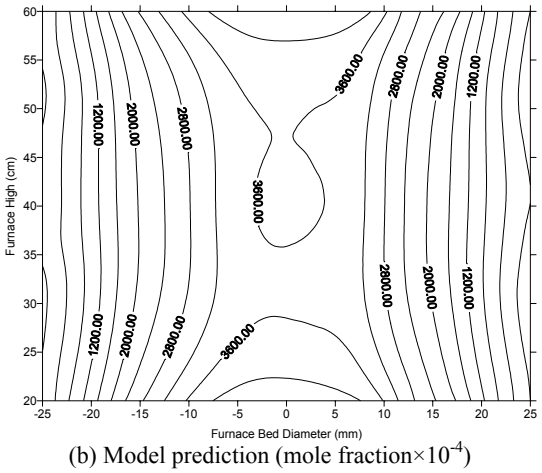

(b) Model prediction (mole fraction×10^{-4})

Figure 3. Toluene concentration in the Spouted Bed post-combustion region.

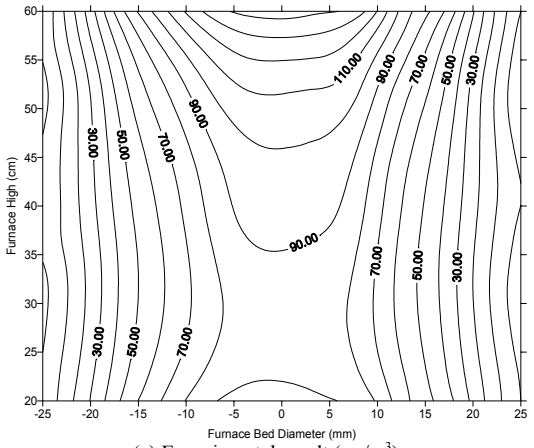

(a) Experimental result (μg/m^3)

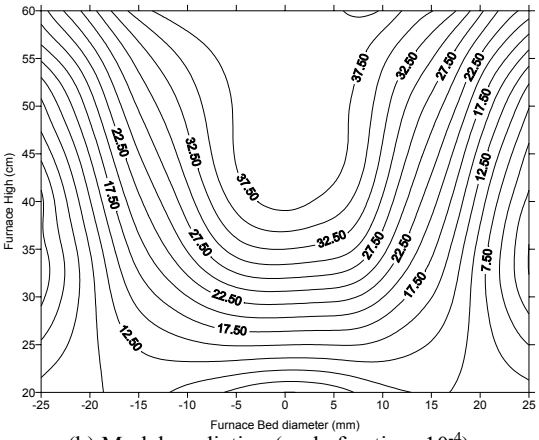

(b) Model prediction (mole fraction×10^{-4})

Figure 4. n-Heptane concentration in the Spouted Bed post-combustion region.

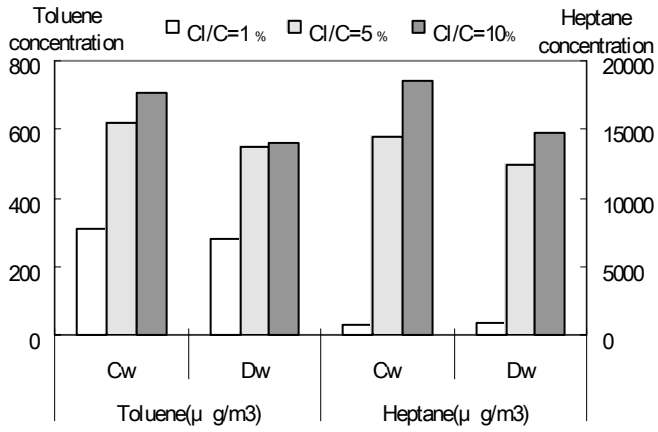

Figure 5. Toluene and n-heptane mixed with chlorinated hydrocarbon combustion.

Acknowledgement. The authors would like to thank the National Science Council of Taiwan for their financial support in this project.

References

(1) Graham, J. L., Hall, D. L., & Dellinger, B., *Environ. Sci. Technol.,* **1986,** Vol. 20, pp703-710.
(2) Staley, L. J.; Richards, M. K.; & Huffman, G. L.; *JAPCA,* **1989,** Vol. 39, pp321-327.
(3) Dellinger, B.; Taylor, P. H.; & Lee, C. C.; *J. Air Waste Manage. Assoc.,* **1993,** Vol. 43, pp203-207.
(4) Taylor, P. H.; Tirey, D. A.; Rubey, W. A.; & Dellinger, B.; *Combust. Sci. and Tech.,* **1994,** Vol.101, pp75-102.
(5) Senkan, S. M.; & Quam, D.; *J. Phys. Chem.,* **1992,** Vol. 96, pp10837-10842.
(6) Hung, J.; Onal, I.; & Senkan, S. M.; *Environ. Sci. Technol.,* **1997,** Vol. 31, pp1372-1381.
(7) Senkan S. M.; & Castldi, M.; *Combustion and Flame,* **1996,** Vol. 107, pp141-150.
(8) Lemieux, P. M.; Ryan, J. V.; Bass, C.; & Barat, R.; *J. Air & Waste Manage. Assoc.,* **1996,** Vol: 46, pp309-316.
(9) Wheatley, L.; Levendls, Y. A.; & Vouros P.; *Environ. Sci. Technol.,* **1993,** Vol.27, pp2885-2895.
(10) Kanters, M. J.; Nispen, V.; Louw, R.; & Mulder, P.; *Environ. Sci. Technol.,* **1996,** Vol. 30, pp2121-2126.
(11) Vandell, R. D.; & Smith, J. D.; *Combust. Sci. and Tech.,* **1994,** Vol. 100, pp225-243.
(12) Tia, S.; Bhattacharya, S. C.; & Wibulswas P.; *International Journal of Energy Research*, **1991,** Vol. 15, pp185-201.
(13) Tia, S.; Bhattacharya, S. C.; & Wibulswas P.; *International Journal of Energy Research,* **1991,** Vol. 15, pp203-221.
(14) Bhattacharya, S. C.; & Wibulswas P.; *International Journal of Energy Research,* **1994**, Vol. 18, pp21-47.

BIOMASS RESOURCES TO SUPPORT A LOW CARBON FUTURE

Ralph P. Overend

National Renewable Energy Laboratory
1617 Cole Boulevard, Golden, Colorado, USA

Introduction

The growing acceptance of biomass as the only renewable source of carbon for the future requires that a realistic appraisal of its potential be undertaken. While solar energy captured by wind, PV or high temperature concentrating solar systems, have very high energy supply potentials—far exceeding today's total primary energy supply of approximately 417 EJ (IEA,TPES data for 2000)—it will be delivered in the form of electricity and potentially hydrogen. However, before a purely hydrogen and electrical economy can arrive, during the 21st century the world has to undergo a carbon usage transition from directly emitting fossil carbon dioxide into the atmosphere to one in which fossil carbon is captured and sequestered, and biomass becomes the sole form of the earth's carbon resource that can be emitted directly to the atmosphere due to its short term photosynthetic cycle in the biosphere.

Unlike fossil fuels for which exploration, discovery and assessment of resources and reserves is a well known science, renewable energy accounting introduces a flow concept to describe the size and availability of the resource. Biomass is rather unusual; it exists somewhere between the intermittent, flux–only resources such as solar and wind, and the traditional fossil fuel stock perspective. This is because of its annual and perennial storage capability, allowing dispersed and captured solar energy to be concentrated and converted into useful, energy and products on a continuous basis at centralized facilities according to normal demand patterns. Thus, the photosynthesis process of solar collection, crop harvest, and transport of biomass fuels will define the availability of biomass for energy and materials purposes.

As with fossil resources, the energy conversion technologies play a huge role in enabling the solar resources by dictating the efficiency, and the utility of renewables with respect to society and the environment—in sum, their sustainability. However, this presentation will concentrate on the biomass system only up to the conversion plant gate.

Biomass resources in the USA

The renewable energy cycle for biomass starts with photosynthesis, which captures the fraction of light between 400 nm and 700 nm in the solar spectrum to provide the energy to fix carbon dioxide and split water molecules, producing raw photosynthate according to the equation:

$$CO_2 + H_2O + \text{sunlight} \rightarrow CH_2O + O_2$$

The photosynthate formula, CH_2O, is essentially the same as sugar, starch, or cellulose, the latter being the most common natural polymer on earth. Energy is obtained from biomass by means of combustion with oxygen as in a fire, or through metabolic processes, e.g., respiration to provide chemical energy for muscles and other processes:

$$CH_2O\ (\text{Biomass}) + O_2 \rightarrow CO_2 + H_2O$$

Either way, the net result is a closed cycle in which carbon dioxide and water vapor are returned to the atmosphere. This solar-energy powered closed-loop supports all life on earth, providing food for humanity, feed for animals, fibers for clothing, and materials for buildings and consumer products, in addition to fuel.

A theoretical estimate of the efficiency of photosynthesis is about 5.5%. The energy received from the sun at any given location varies with latitude and season; and the annual photosynthetic capture is a function of the water and nutrient availability and the seasonal climate variations. As a result actual crops achieve much less than this. The variation is very large ranging from the annual accumulation of less than 1 t ha^{-1} y^{-1} of dry biomass in a mature boreal forest, to approximately 50 t ha^{-1} y^{-1} of total biomass for a record corn yield (in Iowa, in 1999) of 408.2 bushels of corn per acre. This is calculated by accounting for the stalk and other above ground biomass components by means of the harvest index, which has a value of 0.5 applied to the 25.6 t ha^{-1} y^{-1} of corn kernels.

Sources of bioenergy

The primary biomass sources are natural forests, planted trees and shrubs, and agricultural crops. However, much of today's bioenergy is derived from secondary, tertiary, and post-consumer residues derived from these primary resources. Secondary residues are mainly harvesting residues and include: forest slash; crop residues such as straw and stover from cereal production; as well as minor sources such as orchard, rights of way, and vineyard prunings. Tertiary sources are usually process residues and include: black liquor produced in kraft pulping; sawdust and bark from solid wood processing; and sugar cane bagasse. Food processing tertiary residues include: orange and potato peelings; and large quantities of water containing various amounts of proteins, starches, and sugars. Animal operations that produce dairy products, eggs, and meat generate a large stream of residues (at ever increasing scales) from large feedlot operations. These are becoming regulated as concentrated animal feed operations (CAFO)s. These tertiary residues are usually high moisture and most often are treated by a process of anaerobic digestion to produce biogas, a mixture of methane and carbon dioxide, as fuel.

Much of the post consumer residues are in fact biomass: paper, packaging, crates, pallets, demolition lumber, food scraps, and sewage treatment residues. These are more and more often entering the bioenergy, biofuels, and bioproducts stream as society practices resource conservation and use. The Environmental Protection Agency's (EPA) preferred method is source reduction, which includes reuse, followed by recycling and composting, and, lastly, disposal in combustion facilities and landfills.

These primary, secondary, tertiary, and post consumer pathways are significant when compared with the US TPES of about 100 EJ. The total forest harvest is on the order of 203 M tonnes of air–dried round wood equivalents per year, which corresponds to > 3.5 EJ of primary energy equivalent. In recent years the annual corn harvest of almost 10 billion bushels (254 Mt) corresponds to over 4 EJ of primary energy equivalent produced on 3,000 km^2 (about 75 million acres, or about half of the arable crop area of the USA). Though corn stover is partly required to remain on the land to maintain fertility and reduce soil erosion, the quantity available is similar to the amount of crop and represents the largest agricultural residue potential.

Effect of Transportation on Cost

The key determinant of the feasibility of biomass is the cost of the biomass that contains the stored "free" solar energy. As the cost varies with the transportation distance from the process plant to the field or forest, as well as the opportunity cost of the feedstock, the cost is usually obtained from a supply curve. There are many factors that go into deriving the supply curve for the resource. Due to the bulk of biomass, its transportation over long distances by road is not economical, though with low cost transportation by rail, the distance can be increased. While an 80 km collection is often cited, this is only an order of magnitude. In each case, the actual collection radius will be a function of the biomass density per unit area, the nature of the terrain, road network density, and the condition and type of transportation available.

Density Relationship

One of the highest biomass densities is, in fact, the post consumer residue production of the urban areas. Cities draw upon the resources of vast areas and concentrate them in a small area resulting in a "footprint" that is much greater than the physical urban area. A useful number is a *per capita* urban residue energy generation rate of about 22 MJ *caput*$^{-1}$ d^{-1} (1.86 kg d^{-1} of residue with 11.6 MJ kg^{-1} heat of combustion, 1990). Major metropolitan areas have population densities of greater than 2000 person km^{-2}. For this population density, the thermal energy equivalent in their residues is about 4.4 GWh km^{-2}. If a short rotation woody crop was grown at yields of 15 tonne ha^{-1} y^{-1}, it would produce about 7.8 GWh km^{-2}.

Conclusion

The predicted 2020 potential of biomass costing less than 4 $ GJ^{-1} is about 8 EJ. The sources and constraints on the biomass resources contributing to this total will be discussed.

BIOMASS PYROLYSIS FOR DISTRIBUTED ENERGY GENERATION

Michael A. Serio, Erik Kroo, and Marek A. Wójtowicz

Advanced Fuel Research, Inc.,
87 Church Street, East Hartford, CT 06108 USA

Introduction

Renewable sources of energy can include solar, wind, ocean tides or temperature gradients, and biomass. However, biomass is the only renewable energy source that is capable of displacing significant amounts of solid, liquid, and gaseous fossil fuels. The historical energy consumption patterns in the U.S. indicate that wood was the dominant energy source for most of the 1800's, followed by coal in the late 1800's and early 1900's and oil and gas in the latter part of the 1900's [1]. In the future, it is likely that the dominance of fossil fuels will gradually diminish in favor of renewable sources of energy, including biomass.

Examples of candidate biomass feedstocks include wood residues and byproducts (e.g., wood chips, sawdust, tree prunings), agricultural residues and byproducts (e.g., corn stover, bagasse, rice husks) or dedicated energy crops (e.g., fast-growing trees, shrubs and grasses) [2]. An important potential source of biomass feedstocks, that is often overlooked, are the livestock and poultry manures, which are generated in significant quantities in the U.S. [2-5].

Besides landfill disposal, many different processes have been considered for utilizing biomass wastes: combustion (incineration), aerobic and anaerobic biodigestion, wet oxidation, supercritical oxidation, steam reforming, etc. [3]. However, all of these approaches have disadvantages which have prevented their widespread use. For example, combustion produces undesirable byproducts such as oxides of sulfur and nitrogen. A staged pyrolysis process has several advantages when compared to other possible approaches: 1) it can be used for all types of solid products and can be more easily adapted to changes in feedstock composition than alternative approaches; 2) the technology is relatively simple and can be made compact and low cost; 3) it can produce several usable products from solid waste streams (e.g., H_2, CH_4, CO, liquid fuels, fertilizers, activated carbon, etc.); 4) the technology is environmentally friendly (low net emissions of CH_4, CO_2, SO_2, NO_x , HAP's, VOC's); 5) it can be integrated into microturbine, fuel cell or thermophotovoltaic (TPV) systems for power generation. The main disadvantage of pyrolysis processing is that the product stream is more complex than for many of the alternative treatments. While many pyrolysis studies have been done on biomass materials, most of these have focused on production of liquid fuels, chemicals, or hydrogen [6-8], and not fuel gas mixtures (H_2, CO, CH_4).

Pyrolysis Processing of Waste Materials

The word *pyrolysis* has its roots in Greek, πυρ meaning fire, and λυσισ meaning to loosen or untie. Pyrolysis is, therefore, a process of thermal decomposition to produce gases, liquids (tar) and char (solid residue). Pyrolysis is usually understood to be thermal decomposition which occurs in an oxygen-free atmosphere, but oxidative pyrolysis is nearly always an inherent part of combustion processes. Gaseous, liquid and solid pyrolysis products can all be used as fuels, with or without prior upgrading, or they can be utilized as feedstocks for chemical or material industries. The types of materials which are candidates for pyrolysis processes include plant biomass, human and animal wastes, food scraps, crop residues, prunings, paper, cardboard, plastics, rubber [9-11]. These products are primarily polymeric in nature and pyrolysis represents a method of processing all of these materials into useful products. In the case of plant biomass, human and animal wastes, food scraps, paper and cardboard, pyrolysis can be used to produce fuels or chemicals in gaseous and/or liquid form. In the case of plastics and rubber, pyrolysis can sometimes be used for "recycling" previously manufactured materials back to monomers. Of course, pyrolysis has been used for over 100 years in the processing of coal in coke ovens [9]. Before the large oil discoveries in the Middle East, the chemical industry was largely based on byproducts from the coking process. Advanced Fuel Research, Inc. (AFR) recently completed a study which indicated that pyrolysis of used tires could be an economical way to dispose of this troublesome solid waste stream and, at the same time, produce valuable products [11]. There are several excellent reviews of the biomass pyrolysis literature [1,12-19]. Commercial processes for pyrolysis of plastics and biomass have been developed [1,6-8,9-10]. Most of these have focused on the production of liquid fuels, chemicals, or hydrogen, and not fuel gas mixtures, which are usually considered less valuable.

A recently proposed AFR scheme [20-22] for the pyrolysis processing of spacecraft wastes is shown in Figure 1. In many respects, this scheme is analogous to a "solid waste refinery" and a similar approach could be used for most types of biomass waste in terrestrial applications. The waste stream is heated in the absence of oxygen to temperatures between 673 and 873 K. Thermal decomposition occurs, producing a mixture of liquids (0-50%), gases (30-80%), and a solid residue (20-35%). The initial pyrolysis products are primarily liquids, but these liquids are easily cracked to gases (and small amounts of carbon) as the temperature is raised an additional 100-200 K. The major gas products are H_2, CO, H_2O, CO_2, CH_4. Other gas products, present in much smaller amounts, will include N_2, NH_3 and H_2S, since nitrogen and/or sulfur compounds are present in most solid wastes. The liquids will initially include a large yield of a complex mixtures of chemicals, including levoglucosan and glycoaldehyde for cellulosic wastes. This characteristic of the pyrolysis of waste streams allows for the possibility of staging the pyrolysis process. The initial stage will convert the solids to liquids and will significantly reduce the volume of the waste. In the second stage, the liquids are cracked almost completely to gases. Subsequently, the char residue can be gasified or combusted and the minerals can be recovered for later disposal or use as fertilizer or blended with concrete. The char residue will typically be less than 20% of the initial mass of the solid waste, unless there is a high inorganic content, in which case it could be as high as 35%. The gas stream will need to be cleaned to remove NH_3 and/or H_2S and then the gas can be sent to an energy conversion device (e.g., microturbine, incinerator, TPV or a fuel cell).

A significant advantage of pyrolysis processing is that these stages can be separated in time by minutes, days, or weeks, depending on the demand for the products that are being recovered from the waste. For example, adjusting the pyrolysis conditions to produce primarily liquids will significantly reduce the waste storage volume without significantly increasing the volume of gases that must be used, stored, or discarded. The char residue can also be saved for disposal rather than gasified to simplify the system operation, which may be desirable in certain installations. Alternatively, two systems can be operated in tandem, one in pyrolysis mode and one in gasification mode and the resultant gas streams can be blended to give a more constant off-gas composition. Another possibility would be to use a continuous flow reactor system such as a moving bed, fluidized-bed, or transport reactor. Direct combustion does not allow such a fine degree of control of the outcome and will convert all of the nitrogen to NO_x, an undesirable

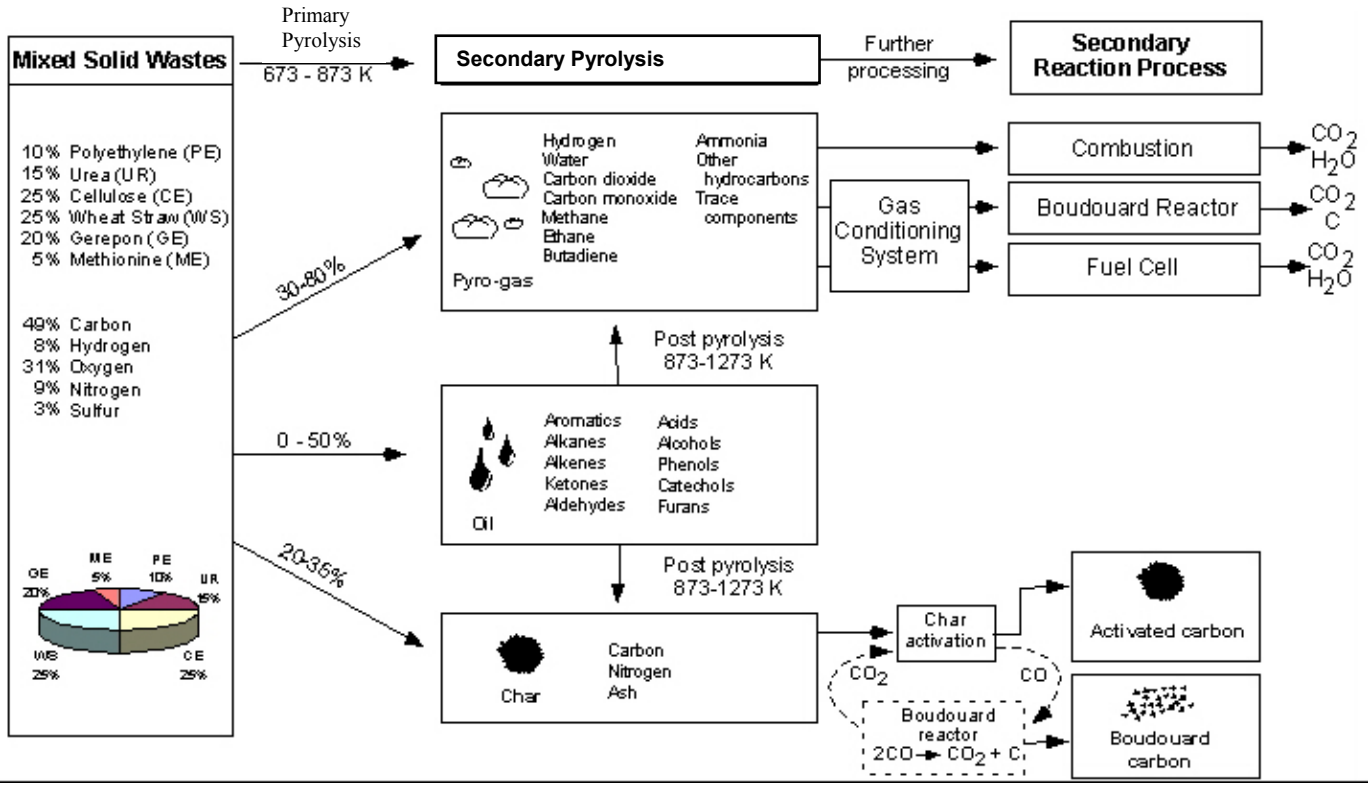

Figure 1. Pyrolysis processing scheme for Controlled Ecological Life Support System (CELSS).

product. In addition, most direct combustion systems will be adversely affected by the high mineral matter contents in many biomass materials. Direct gasification of the biomass wastes will produce a fuel gas with a lower heating value, since the hydrocarbons like CH_4 will be lost.

Experimental Methods

An extensive set of pyrolysis experimental studies at AFR has utilized a TG-FTIR instrument (thermogravimetric analysis combined with FT-IR analysis of evolved products). The application of TG-FTIR to coal analysis at AFR has been described in several publications [23-27]. By using a range of heating rates, kinetic rate constants for volatiles evolution have been obtained [26]. TG-FTIR analysis has also been used at AFR to characterize other hydrocarbon materials such as modified coal samples, [28] coal liquefaction resids [29], petroleum source rocks, [30] lubricants, [31] biomass, [32-35] waste tires, [36] and polymers [37]. This section will briefly review the use of the TG-FTIR technique at AFR for the study of biomass pyrolysis.

Details of the TG-FTIR method can be found in reference [23]. The apparatus consists of a sample suspended from a balance in a gas stream within a furnace. As the sample is heated, the evolving volatile products are carried out of the furnace directly into a 5 cm diameter gas cell (heated to 150 °C) for analysis by FT-IR. In a typical analysis procedure, a 35 mg sample is taken on a 30 °C/min temperature excursion in helium, first to 80 °C to dry, then to 900 °C for pyrolysis. After cooling, a small flow of O_2 is added to the furnace, and the temperature is ramped to 700 °C (or higher) for oxidation (or gasification). During this excursion, infrared spectra are obtained once every forty-one seconds. The spectra show absorption bands for several gases, including CO, CO_2, CH_4, H_2O, C_2H_4, HCl, NH_3, and HCN. The spectra above 300 °C also show aliphatic, aromatic, hydroxyl, carbonyl and ether bands from tar (heavy liquid products). The evolution of gases and tars derived from the IR absorbance spectra are obtained by a quantitative analysis program.

The TG-FTIR method provides a detailed characterization of the gas and liquid compositions and kinetic evolution rates from pyrolysis of materials under a standard condition (usually 30 °C/min). While the heating rates are slower than what will be experienced in most practical processes, it is a useful way of benchmarking materials. The ultimate analysis data for several biomass materials that have been studied using the TG-FTIR approach are given in Table 1. The typical TG-FTIR results from pyrolysis at 30 °C/min for these materials are given in Table 2. AFR has developed kinetic models based primarily on TG-FTIR data which can be extrapolated over a wide range of conditions. The TG-FTIR apparatus can also be used to study the reactivity of the pyrolysis residue (char) by introducing appropriate gases. Finally, a secondary reaction zone can be added to examine secondary pyrolysis of the volatile products. These secondary reactions are important in order to maximize the fuel gas production from biomass materials. Additional details can be found in Refs. 32-35.

In recent work, AFR has been involved in building and testing larger scale pyrolysis reactors with NASA support that could be used for solid waste resource recovery in space [20-22]. That project is studying the pyrolysis of mixed solid waste streams, including paper, soap, plastic, and inedible plant biomass, which are relevant to long term space travel.

A schematic of the NASA prototype reactor system is shown in Figure 2. During the initial processing step, the first stage is the primary pyrolysis zone, for thermal decomposition of the sample into gases, liquids and a char residue, while the second stage contains a catalyst bed for decomposition of the liquids. Each of these stages are heated independently (~673-873 K for the first stage, 873-1273 K for

the second stage). During the second-processing step, the purge gas is switched to CO_2 (or H_2O) and gasification of the char can occur in the first stage (if desirable) while gasification of the carbon deposits from the cracked oils will occur in the second stage. Alternatively, the conditions in the first stage can be adjusted to provide activation of the char or no reaction at all, in which case the char can be removed and used for some other purpose. A picture of the current prototype the reactor is shown in Figure 3. It is anticipated that a suitably modified system could be used in terrestrial applications to produce fuel gases for distributed power generation.

.

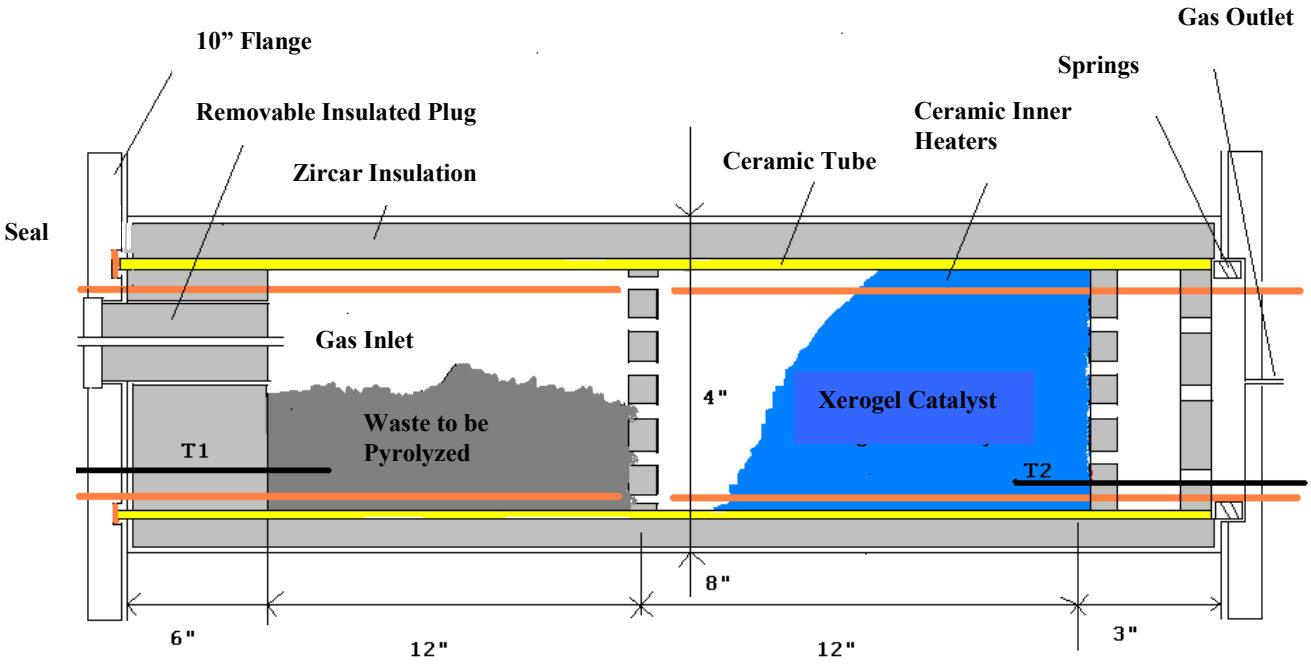

Figure 2. Schematic of First Generation Unit (FGU) two-stage pyrolysis reactor system.

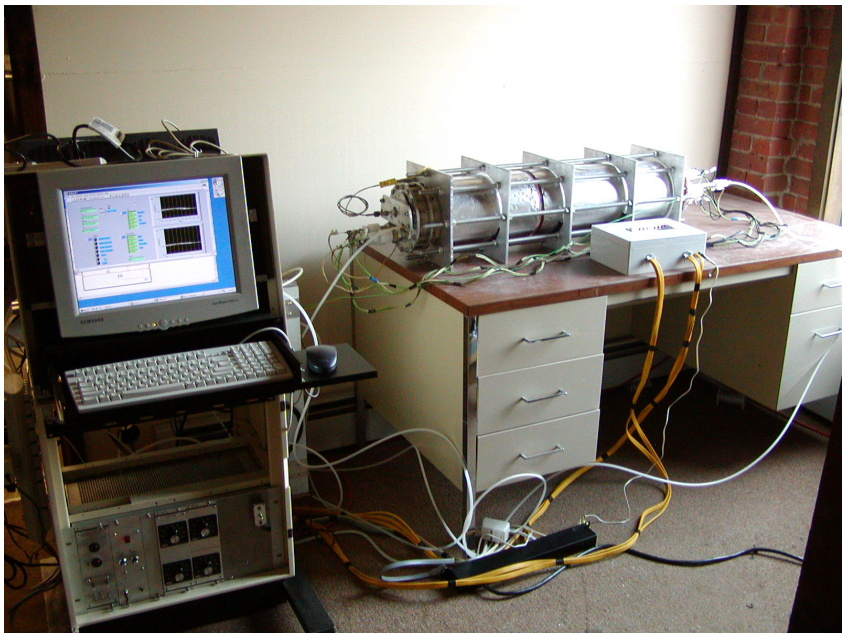

Figure 3. Picture of AFR Prototype Pyrolyzer and Control Console

Table 1. - Ultimate analysis of biomass samples

Sample	Chicken Manure[a]		Lignin[b]		Wheat Straw[c]		Miscanthus Giganteus[d]		Cellulose[e]		Xylan[f]		Wood Pellets [g]	
	AR	DAF	AR	DAF	AR	DAF	AR	DAF	AR	DAF	AR	DAF	AR	DAF
Moisture	11.4		1.9		7.9		8.7		5.0		11.0		8.2	
Ash	20.0		0.0		8.3		2.5		0.0		3.6		0.3	
C		47.4		67.4		48.0		49.4		44.0		45.0		52.1
H		6.5		6.2		6.2		5.5		6.2		6.0		5.2
O		39.5		26.2		44.9		44.0		49.8		48.9		42.2
S		1.0		0.0		0.2		0.2		0.0		0.0		0.1
N		5.6		0.2		0.7		0.6		0.0		0.0		0.3

Notes: AR = As-received; D=Dry; DAF=Dry, Ash Free
a-Plant Right (Purdy, MO); b- ALCELL Technologies, Inc., (Valley Forge, PA (ADI/L952)); c- NIST, (Gaithersburg, MD); d-Delft University of Technology; e- Avicel (pH-102/Lot 2822); f – Philip Morris USA; g – Labee Company, the Netherlands.

Table 2. Results from TG-FTIR experiments at 30 °C/min for various biomass samples

Sample	Chicken Manure	Lignin	Wheat Straw	Miscanthus Giganteus	Cellulose	Xylan	Wood Pellets
Moisture	11.2	1.9	7.5	2.5	12.4	9.5	6.3
Ash	18.3	0.0	7.9	3.8	0.0	2.0	0.0
Volatile Matter	59.1	69.5	68.0	74.4	85.3	67.6	80.8
Fixed Carbon	11.4	29.2	16.6	19.3	2.3	21.0	12.9
Tars	28.5	39.5	35.1	21.9	81.5	13.3	38.8
CH4	0.98	2.40	1.20	1.14	0.13	0.87	1.3
H2O (pyr)	18.7	7.6	21.8	18.4	5.1	24.2	16.0
CO2	14.3	1.9	14.5	9.4	2.0	15.9	5.1
CO	6.37	6.50	9.26	7.15	1.49	9.64	6.77
C2H4	0.25	0.22	0.26	0.27		0.42	0.23
SO2	0.08		0.36	0.00		0.12	0.12
COS	0.61		0.23	0.16			0.11
NH3	1.91		0.18	0.10			0.02
HCN	1.21	0.04	0.25	0.14	0.03	0.15	0.09
Formic Acid	0.72		1.61	1.66	0.34	1.75	1.73
Acetic Acid	1.63		5.52	3.59	0.57	2.65	2.37
CH3OH	0.10	2.20	1.21	1.12	0.75	1.72	0.74
Formaldehyde	0.00	0.22	0.92	1.12	1.23	0.45	2.93
Acetaldehyde	6.31	1.55	8.62	9.02			8.11
Acetone	1.04	3.91	2.38	1.86			2.15

Notes: Yields are given on wt.% dry, ash-free basis except for moisture, ash, volatile matter, and fixed carbon which are given on an as-received basis.

Application to Distributed Power Generation

In the past few years, the level of commercial interest in distributed power generation has increased dramatically. According to recent data, the amount of venture capital investment in "micropower" technology has increased from $100 million in 1996 to $200 million in 1998 and an estimated $800 million for 2000 [38]. Fuel cell systems that are currently commercial operate at relatively low temperatures and use pure hydrogen as a fuel [39]. Examples are the phosphoric acid system and the polymer electrolyte membrane (PEM) systems. In order to use these cells with a fuel gas which contains CH_4, CO, and H_2, a reformer and shift converter must be used. However, also under development are high temperature fuel cells (HTFC) which have molten carbonate (MCFC) or solid oxide electrolytes (SOFC). The latter fuel cells are especially interesting for combination with a biomass pyrolysis process, since these can tolerate a mixture of CO, CH_4, and H_2, and operate at temperatures ranging from 650 °C to 1000 °C. This high temperature heat could be used to help drive the pyrolysis and char gasification reactors and/or provide heat for building operations. Some of these HTFC systems have been successfully operated on landfill gas and digester gas,

which produce similar gas streams to the fuel gas that is produced from biomass pyrolysis.

Thermophotovoltaic (TPV) systems are also of interest because they can operate on fuel gases which contain mixtures of H_2, CH_4, and CO. These systems involve using the radiant energy from a flame to produce electricity from specially designed photovoltaic cells. TPV systems are also lower in cost and closer to commercialization than the HTFC's. A company in the Pacific Northwest (JXCrystals) is marketing TPV generation equipment for residential and mobile uses [40]. The military is also sponsoring the development of TPV systems for mobile power generation units.

A third possibility, which has near term potential, is to couple the pyrolysis process with a microturbine, such as those produced by Capstone Turbine Corp (Chatsworth, CA). These systems are much cheaper when compared to fuel cell and TPV systems and are already available in significant quantities at appropriate power generation rates. Approximately the size of a large refrigerator, Capstone's Model 330 Microturbine generates approximately 30 kilowatts of electrical power which is enough power to power a convenience store, and approximately 300,000 kilojoules per hour of heat, enough energy to heat 20 gallons of water per minute with a 20 degree heat rise. The Capstone Microturbine can operate connected to the electric utility grid or on a stand-alone basis. It remains to be seen how well microturbines can operate on hydrogen-rich fuel gas streams.

Summary

The conversion of fuel gases from biomass pyrolysis to power using either a fuel cell, TPV or microturbine system would provide numerous technical, economic, and social benefits:

- It would remove biomass from landfills where they take up valuable space and decompose to produce CH_4 and CO_2, both greenhouse gases.
- It would provide a means of generating power in remote agricultural areas, a benefit from an economic and quality-of-life standpoint to both farms in the U.S. and in underdeveloped nations.
- It would provide a means of generating off-grid power in business and residential applications where significant quantities of biomass wastes (e.g., paper, food residues) are readily available.
- The power generated would most likely replace power produced at central power stations and diesel generators from fossil fuels, thus providing a net reduction in CO_2, NO_x, and SO_2.

The technology would contribute to and benefit from the expected growth in the emerging distributed power generation industries over the next several years. Challenges remain in reducing the costs of the next generation power generation equipment and in economical production of clean fuel gases from biomass pyrolysis. It is likely that early demonstration projects will require tax incentives in order to compete with conventional power generation equipment utilizing fossil fuels.

Acknowledgements.

AFR has received support for biomass pyrolysis R&D from the NASA-Ames Research Center under contracts NAS2-99001 and NAS2-00007, which is gratefully acknowledged. The COTR was John Fisher. AFR has also received support for biomass pyrolysis studies from the University of Florida Environmental Systems Commercial Space Technology Center (William Sheehan, Project Director) and Philip Morris USA (Mohammad Hajaligol, Project Director). In addition, we would like to acknowledge support from the U.S. DOE under contract DE-FG02-00ER82936 for the pyrolysis experiments with chicken manure. Prof. Eric Suuberg of Brown University has been a consultant or collaborator on many of AFR's biomass pyrolysis projects.

References

1 Klass, D.L., "Biomass for Renewable Energy, Fuels, and Chemicals," Academic Press (1998).
2 Barrier, T.W., and Bulls, M.M., "Feedstock Availability of Biomass and Wastes," Chapter 23, in ACS Symposium Series No. 476, ACS Washington, DC pp. 410-421.
3 Chartier, P., Ferrero, G.L., Henius, V.M., Hultberg, S., Sachau, J., Wiinblad, M., "Biomass for Energy and the Environment," Pergamon, New York (1997).
4 Stanford Research Institute, "An Evaluation of the Use of Agricultural Residues as an Energy Feedstock," Vol. 1, NSF Grant No. AER74-18615 A03 (1976).
5 Gerwig, B.K., Hegg, R.D., "Assessment and Characterization of Manure in the Southeaster U.S.," Proceedings of Bioenergy '96, pp. 501-507, Sept. 15-20, 1995.
6 Rowell, R.M., Schultz, T.P., Narayan, R., "Emerging Technologies for Materials and Chemicals from Biomass," ACS Symp. Series No. 476, ACS Books, Washington, DC (1992).
7 Dayton, D.C., Chum, H.L., "Symposium on Biomass Fuels: The Introduction," Energy & Fuels, 10 (2), 267 (1996).
8 Wang, D., Czernik, S., Montané, D., Mann, M., Chornet, E., Ind. Eng. Chem. Res., 36, 1507 (1997).
9 Serio, M.A., Wójtowicz, M.A. and Charpenay, S., "Pyrolysis," In Encyclopedia of Energy Technology and The Environment, (A. Bisio and S.G. Boots), John Wiley & Sons, New York, NY, 2281-2308 (1995).
10 Bridgewater, A.V., Biomass, 22, (1-4), 279 (1990).
11 Wójtowicz, M.A. and Serio, M.A., Chemtech, 26, (10), 48-53 (1996).
12 Antal, M.J., Jr., in Adv. in Solar Energy (Boer, K.W., Duffie, J.W., Eds.), American Solar Energy Society, Boulder, CO, 1, 61 (1984); 2, 175 (1985).
13 Soltes, E.J., in Biomass Energy Development, W.H. Smith, Ed., Plenum Press, New York, 321 (1986).
14 Shafizadeh, F., in The Chemistry of Solid Wood (R. M. Rowell, Ed.), Advances in Chemistry Series No. 207, American Chemical Society, Washington, DC (1984).
15 Bridgwater, A.V., and Cottam, M.-L., Energy and Fuels, 6, (2), 113 (1992).
16 Elliott, D.C., Beckman, D., Bridgwater, A.V., Diebold, J., Severt, S.B., and Solantusta, Y., Energy and Fuels, 5, 399 (1991).
17 Overend, R. P. Milne, T. A., and Mudge, L.K., Eds., Fundamentals of Thermochemical Biomass Conversion, Elsevier, (1985).
18 Soltes, E.J., and Milne, T.A., Eds., Pyrolysis Oils from Biomass: Producing, Analyzing and Upgrading, ACS Symposium Series No. 376, American Chemical Society, Washington, DC (1988).
19 Bridgwater, A.V., Kuester, J.L., (Eds.), Research in Thermochemical Biomass Conversion, Elsevier Applied Science, London (1988).
20 Serio, M.A., Chen, Y., Wójtowicz, M.A. and Suuberg, E., "Pyrolysis Processing for Solid Waste Resource Recovery in Space," 30th International Conference on Environmental Systems, Toulouse, France July 10-13, 2000. SAE Paper No. 2000-01-2286.
21 Serio, MA., Kroo, E., Bassilakis, R., Wójtowicz, M.A., and Suuberg, E.M., "A Prototype Pyrolyzer for Solid Waste

Resource Recovery in Space," 31st International Conference on Environmental Systems, Orlando, FL, July 9-12, 2001, SAE paper No. 2001-01-2349.
22 Serio, M.A., Kroo, E., Wójtowicz, Suuberg, E., and Filburn, T., "An Improved Pyrolyzer for Solid Waste Resource Recovery in Space," 32rd International Conference on Environmental Systems, San Antonio, Texas, July 15-18, 2002, SAE Paper No. 2002-01-2402.
23 Carangelo, R.M., Solomon, P.R., and Gerson, D.G., Fuel, 66, 960 (1987).
24 Solomon, P.R., Serio, M.A., Carangelo, R.M., Bassilakis, R., Gravel, D., Baillargeon, M., Baudais, F., and Vail, G., Energy & Fuels, 4, (3), 319 (1990).
25 Solomon, P.R., Serio, M.A., Carangelo, R.M., Bassilakis, R., Yu, Z.Z., Charpenay, S., and Whelan, J., Journal of Analytical and Applied Pyrolysis, 19, 1 (1991).
26 Solomon, P.R., Hamblen, D.G., Serio, M.A., Yu, Z.Z., and Charpenay, S., Fuel, 72, (4), 489 (1993).
27 Bassilakis, R., Zhao, Y., Solomon, P.R. and Serio, M.A., Energy & Fuels, 7, 710 (1993).
28 Charpenay, S., Serio, M.A., Bassilakis, R., and Solomon, P.R., Energy & Fuels, 10, 19 (1986).
29 Teng, H., Serio, M.A., Bassilakis, R., Knight, K.S., Bates, S.C., and Solomon, P.R., ACS Fuel Chem. Preprints, 37, (4), 1903 (1992).
30 Whelan, J.K., Solomon, P.R., Deshpande, G.V., and Carangelo, R.M., Energy and Fuels, 2, 65 (1988).
31 Bonanno, A.S., Bassilakis, R., and Serio, M.A., ACS Fuel Chem. Preprints, 41(1), 62 (1996).
32 Serio, M.A., Kroo, E., Bassilakis, R., Solomon, P.R., and Malhotra, R., ACS Fuel Chem. Preprints, 36, (3), 1110 (1991).
33 Serio, M.A., Charpenay, S., Bassilakis, R., and Solomon, P.R., Biomass & Bioenergy, 7, (1-6), 104 (1994).
34 Bassilakis, R., Carangelo, R.M., and Wójtowicz, M.A., "TG-FTIR Analysis of Biomass Pyrolysis," Fuel, 80, 1765-1786 (2001).
35 de Jong, W., Pirone, A., and Wójtowicz, M.A., "Pyrolysis of Miscanthus Giganteus and Wood Pellets: TG-FTIR analysis and reaction kinetics," Fuel, 82, 1139-1147 (2003).
36 Teng, H., Serio, M.A., Wójtowicz, M.A., Bassilakis, R., and Solomon, P.R., Industrial & Engineering Chemistry Research, 34, 3102 (1995).
37 Serio, M.A., Charpenay, S., Bassilakis, R., and Solomon, P.R., ACS Div. of Fuel Chem. Preprints, 36, (2), 664 (1991).
38 "The Dawn of MicroPower," Economist, pp. 75-77, August 5, 2000.
39 Appleby, T., "Fuel Cells" in the Wiley Encyclopedia of Energy and the Environment, Wiley, New York, pp. 783-796 (1997).
40 Cougs, T.J., Fitzgerald, M.C., "Thermophotovoltaics," Scientific American, pp. 90-95 (Sept. 1998).

BIOMASS TORREFACTION STUDIES WITH A MOLECULAR BEAM MASS SPECTROMETER

Mark N. Nimlos, Emily Brooking. Michael J. Looker, and Robert J. Evans

National Bioenergy Center
National Renewable Energy Laboratory
Golden, Colorado 80401

Introduction

An important drawback to using biomass as fuel source is the fact that its energy density is much lower than that of traditional energy resources such as fossil fuels. This low density makes biomass fuel more expensive to transport, store and utilize than fossil fuel. This problem is compounded by the hydrophilic nature of the material. The absorption of moisture causes the biomass to decrease in energy density even further and make its use even more expensive and less feasible on a massive scale.

Torrefaction[1-6] is a technique to improve the energy content of biomass, which involves the heating of biomass to moderate temperatures (200-300 °C). At these temperatures, chemically bound water can be released from the biomass, increasing the carbon content and the heat of combustion. There is also the benefit that the biomass becomes more hydrophobic after torrefaction. This can be particularly important for energy densification or pellet making. Finally, there is the possibility that torrefaction could be used to increase the density of biomass pellets.

We have conducted torrefaction experiments with hardwood sawdust to measure the increase in energy content and to investigate the effect upon pellet making. We have torrefied the wood at a variety of temperatures (175–295 °C) and residence times (5–30 min.). Weight loss and heat of combustion of the resulting powder were measured. We also used a pyrolysis mass spectrometer and factor analysis to identify changes in the wood. Finally, we have used a high pressure press to prepare of pellets from torrefied wood.

Experimental

The sample material used in this research was Vermont hardwood sawdust which was prepared by grinding pellets. Small samples (100 – 200 mg) of the sawdust were placed in 5 cm ceramic boats and slid into a heated tubular reactor held at the desired temperature by a tube furnace. A small flow of nitrogen gas (0.5-1.5 L/min.) was provided to remove liberated species from the reactor. Under these conditions heat transfer effects were minimized as evidenced by the uniformity of color of the torrified wood. The temperature of torrefaction was controled using a thermocouple placed next to the samples in the furnace.

Pelletization was accomplished with a hydraulic laboratory press (Carver) with heated platens. The dies used in pelletization were Carver hardened stainless steel dies rated up to a 18,000 lb load with a .5 inch interior diameter. A 10,000 lb load was applied to each pellet.

In order to investigate the change in chemical composition, pyrolysis mass spectra of the torrefied samples were collected. The pyrolysis products from these samples were measured using a molecular beam mass spectrometer[7, 8] (MBMS). Small samples (~20 mg of the torrefied wood were inserted into a flow of hot (550°C) helium and the products were carried to the sampling orifice of the MBMS.

Finally, heats of combustion of the samples were measured (Hazen Research, Inc) using bomb calorimetry.

Results and Discussion

Weight loss

During torrefaction, the wood samples change color from a light brown (without heating) to a dark brown at the higher temperatures. **Figure 1** shows a contour plot of the measured weight loss as a function of temperature and residence time in the oven. As can be seen, temperature has a more profound effect upon the weight loss than residence time.

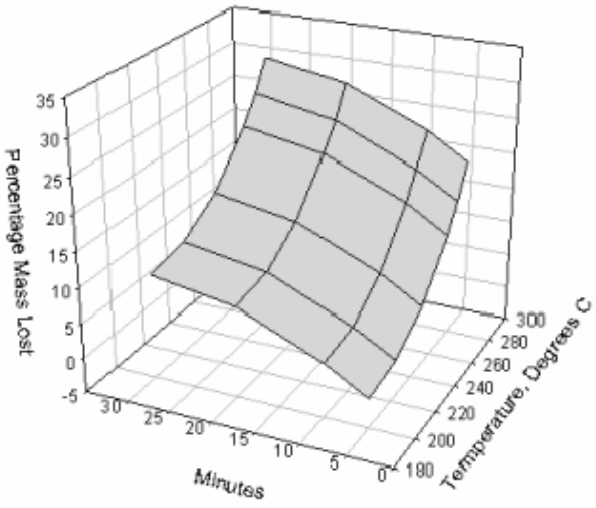

Figure 1. A contour plot of the measured weight loss *versus* the temperature and residence time of torrefaction.

Pellet density

Pellets made from the untreated and torrefied wood were often somewhat flaky though the pellets made from torrefied wood were typically less so. We made three pellets of each sample and compared the density. Within the uncertainty of our measurements, we found no change in the density of the pellets with torrefaction. When the platens of the press where heated, we typically form more dense pellets with less flaking. Because of experimental limitations, we did not systematically study this effect.

MBMS analysis

Pyrolysis MBMS data was collected for all of the torrefied samples as well as untreated sawdust. Typical mass spectra obtained freom these experiments is shown in **Figure 2**. The pyrolysis mass spectra for the untreated sawdust contains peaks for lignin's primary pyrolysis components (m/z = 210, 194 and 180) and hemicellulose pyrolysis components (m/z = 114 and 85). The spectra from the most severe condition studied (295 °C, 30 min. residence time) shows peaks for secondary lignin products (m/z = 168 and 154) and products from cellulose pyrolysis (m/z =126 and 110).

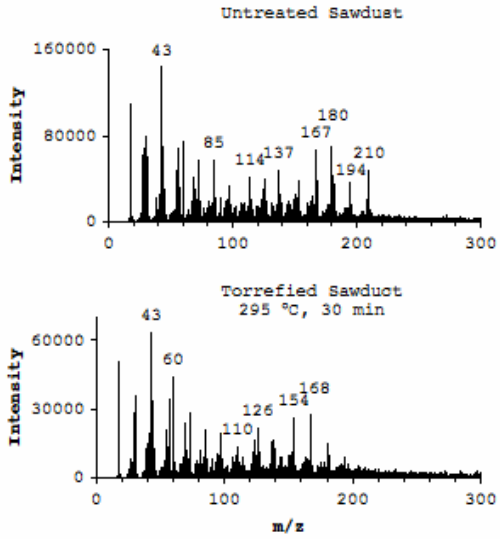

Figure 2. Pyrolysis mass spectra of untreated sawdust and sawdust torrefied at 295 °C for 30 min.

Factor analysis allows one to extract important trends from the complicated mass spectra obtained during biomass pyrolysis. This analysis was conducted using pyrolysis mass spectra obtained for the entire data set (200–295 °C, 5–30 min) and a clear trend was identified, particularly at higher temperatures. **Figures 3 and 4** show some of the results. We were able to extract two components (or factors) from our analysis. The mass spectra of the components are shown in **Fgure 3**. Factor 1 is the primary lignin products and the hemicellulose products and Factor 2 is the secondary lignin products and products from cellulose.

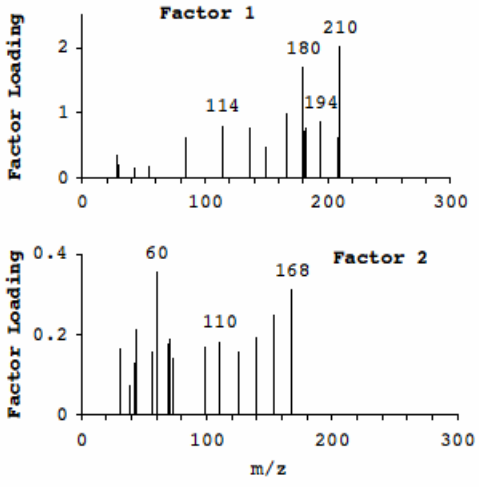

Figure 3. Spectra of correlated products from pyrolysis MBMS experiments of torrefied sawdust samples.

Figure 4 Shows the scores for these factors as a function of residence time of torrefaction at 295 °C. The plot clearly shows that with increasing residence time, factor 1 decreases and factor 2 increases. The decrease in Factor 1 with residence time is accompanied by an increase in weight loss (**Figure 1**). This may be an indication that these components are driven off of the biomass, or it could be that the thermal reactions that lead to volatile products also causes the Factor 1 components to crosslink.

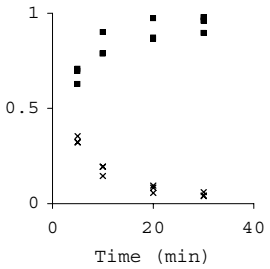

Figure 4 A plot of the scores for factor 1 and factor 2 as a function of the time of torrefication at 295 °C.

Calorimetery

Table I shows the measure heat of combustion of the torrefied sawdust samples. The measured uncertainty in our measurements is about 200 BTU/lb. The heat of combustion for the untreated sawdust was measured to be 8439 BTU/lb. As can be seen there is not a significant change in the heat as a function of temperature at the lowest residence time (5 min). At the longest residence time (30 min) there is a significant change in heat as the temperature increases.

Table I. Heat of combustion (BTU/lb) of torrefied sawdust on a dry basis

	Temperature (°C)					
Time (min)	200	225	250	275	285	295
5	8521	8546	8512	8496	8609	8397
10	8452	8574	8485	8646	8583	8931
20	8448	8285	8589	8728	9181	8728
30	8741	8669	8780	8716	9308	9494

Acknowledgment

We would like to thank the Department of Energy's Office of Science and NREL's Education Office for making this study possible.

References

1. Bourgeois, J.P.D.J., *Torrefied Wood from Temperate and Tropical Species, Advantages and Prospects*, in *Bioenergy 84*, A.E. H. Egnens, Editor. 1985, Elsevier Applied Science: London. p. 153-159.

2. F. Fonseca Felfli, C.A.L., P. Beaton, J. A. Suarez. *Efficiency test for bench unit torrefaction and characterization of torrefied biomass*. in *Biomass, Proc. Biomass Conf. Am. 4th*. 1999: Elsevier Science.

3. Pentananunt, R., A. Rahman, and S.C. Bhattacharya, Energy, 1990. 15(12): p. 1175-1179.

4. Bourgois, J. and R. Guyonnet, Wood Sci. Technol., 1988. 22(2): p. 143-155.

5. Bourgois, J., M.C. Bartholin, and R. Guyonnet, Wood Sci. Technol., 1989. 23(4): p. 303-310.

6. Lipinsky, E.S., J.R. Arcate, and T.B. Reed, Abstr. Pap. Am. Chem. Soc., 2002. 223: p. 171-FUEL.

7. Evans, R.J. and T.A. Milne, Energy Fuels, 1987. 1(2): p. 123-137.

8. Shin, E.J., M.R. Nimlos, and R.J. Evans, Fuel, 2001. 80(12): p. 1697-1709.

HYDROGEN PRODUCTION BY STEAM REFORMING OF WASTE VEGETABLE OILS

Richard J. French, and Stefan Czernik

National Bioenergy Center
National Renewable Energy Laboratory
1617 Cole Boulevard
Golden, CO 80401

Introduction

Commercially, most hydrogen is produced by steam reforming natural gas, LPG, or naphtha or by partial oxidation of heavy oil fractions. Life-cycle analysis of natural gas steam reforming shows that the amount of fossil CO_2-equivalent released into the atmosphere to produce 100 kg of hydrogen gas is 1374.5 kg.[1] An environmentally preferable alternative is to produce hydrogen from renewable resources, for example via thermal conversion of biomass[2]. In this case the CO_2 released into the atmosphere during thermo-chemical conversion is offset by the uptake of CO_2 during biomass growth. However, direct gasification of lignocellulosic biomass yields less hydrogen than steam reforming of natural gas and so cannot compete with this well-developed technology.[3] Therefore, we have studied ways to improve the profitability of hydrogen from biomass by the integrating valuable co-products into the process.[4]

Vegetable oils are derived from biomass and are potentially better hydrogen producers than lignocellulosic materials because the oils contain much less oxygen and more carbon. Sunflower oil, when converted by catalytic steam reforming, yields 25-31 g hydrogen (72% to 87% of the stoichiometric potential (complete conversion to CO_2 and H_2)).[5] Although the high cost of vegetable oil makes the process economics unfavorable low-cost waste oils, such as "trap grease", are available throughout the country. This grease is recovered from traps in the sewage lines of restaurants and food processing plants and from wastewater treatment plants. Although the bio-diesel industry considers it a potential feedstock, at present trap grease is mostly disposed of. Grease-trap-pumping companies in the Boston area pay tipping fees of 11¢/gallon.

The estimated average amount of recovered waste grease is 13 lbs/person/year.[6] The U.S.'s trap grease could produce 1 billion pounds of hydrogen annually (0.5 Mtonnes/year). Dewatered grease is available for 2-4 ¢/lb. At this cost, the feedstock contributes only 1-2 $/GJ to the total cost of hydrogen. With current market prices for hydrogen at 6-9 $/GJ range, trap grease offers an attractive opportunity for competitive production of hydrogen from renewable resources.

Preliminary reforming tests showed promising results, yielding 30 g of hydrogen from 100 g of grease (81% of the stoichiometric potential) during 17 hours of operation.[4] Hence, further investigation was warranted. The objective of the work described below was to determine the long-term catalyst efficiency under different operating conditions, as well as identify and suggest solutions to potential problems in the use of waste grease to produce hydrogen.

Experimental

Feedstock. Trap grease was obtained from the DOE Biodiesel Program for whom Pacific Biodiesel collected over 40 samples from different sites in the United States. These contained both saturated and unsaturated C_{16} and C_{18} fatty acids, fats, and small amounts of solids (University of Toronto analysis). We selected samples with a high content of free fatty acids (>70%) and low ash (<1%). These were dark colored viscous liquids at room temperature. A batch of 20 kg of such grease was homogenized by heating to 60ºC and stirring.

Initial tests were carried out using trap grease as received. However, because of difficulties with feeding (plugging the nozzle), the batch used in the long-duration experiment was washed with hot water and filtered to remove particles. Elemental analysis of this batch showed 75.7%C, 11.9%H, and 13.3%O with 0.05% ash.

Fluidized bed system. The steam reforming experiments were carried out using a bench-scale fluidized bed reactor system. The tubular two-inch-diameter inconel reactor was supplied with a perforated gas distribution plate and was externally heated electrically. The reactor contained 250-280g of commercial nickel-based catalyst (C11-NK) developed by United Catalysts for reforming moderately heavy petroleum fractions. The catalyst had been ground to a particle size of 300-500µ. Before reforming, the catalyst was activated in H_2/N_2 at the process temperature for approximately 2 hours. The reduction of NiO to Ni gave a weight loss of about 7%. The catalyst was then fluidized using superheated steam (750˚C), which is also a reactant in the reforming process. The trap grease was continuously weighed and was pumped into the reactor through a temperature-controlled injection nozzle at 60-80˚C to provide suitable viscosity. The product collection line included a cyclone and a hot-gas filter to capture fine catalyst particles and, possibly, char generated in the reactor. It also contained two heat exchangers to condense excess steam. The condensate weight was continuously monitored. The outlet gas flow rate was measured *via* a mass flow meter and a dry test meter. The concentrations of H_2, CO_2, CO, and CH_4, C_2H_4, and N_2 in the reformed gas were monitored by infrared (NDIR Model 300 from California Analytical Instruments) thermal conductivity (TCM4 from Gerhard Wagner, Germany) and an MTI micro GC. Temperatures and flows were recorded and controlled by an OPTO22 system.

Results and Discussion

At high temperatures vegetables oils undergo extensive thermal cracking leading to the formation of hydrocarbons. To minimize the extent of the competing thermal decomposition reactions Marquevich *et al*.[7] carried out catalytic reforming of those oils at 500-650˚C. However, complete conversion of the oils to gases was not achieved. In this work on "trap grease" we studied the effect of temperature in the range of 600-850˚C. The molar steam-to-carbon ratio (S/C) varied from 2.75 to 5 and the methane-equivalent gas space velocity (G_{C1}VHSV) was in the range of 950-1400 h^{-1}.

At 600˚C after 1 hour the concentration of hydrogen in the product gas from "trap grease" reforming started decreasing while that of methane and ethylene rapidly increased rapidly indicating that hydrocarbons were no longer being efficiently converted to hydrogen and carbon oxides. The yield of hydrogen was 70% at the beginning but decreased to 40% of the stoichiometric potential after only 70 minutes of operation. Also conversion of carbon to gas was less than 70%. The remaining 30% probably formed carbon deposits on the catalyst, thus reducing its activity, and larger molecular weight compounds recovered in the condensate.

At higher temperatures and S/C and lower space velocity the catalyst performed much better. At 750˚C the carbon to gas conversion was higher than 96% and the yield of hydrogen was above 70% of the stoichiometric potential for 16 hours of operation. At 850˚C, S/C=3.5, and G_{C1}VHSV of 1300 h^{-1} the yield of hydrogen was greater than 80% of the stoichiometric potential and carbon to gas conversion was greater than 99% for six hours.

A long-duration reforming test of washed and filtered "trap grease" was carried out at 850˚C, S/C=5, and at the initial G_{C1}VHSV of 970 h^{-1} (effective space velocity increased during the test due to the progressive catalyst losses from the reactor). Also, similarly to the reforming natural gas, a small amount of hydrogen (<10% of the hydrogen produced) was introduced with the steam to prevent

oxidation of the catalyst. After modest changes during the first 15 hours the gas concentrations remained stable for 120 hours as shown in Figure 1.

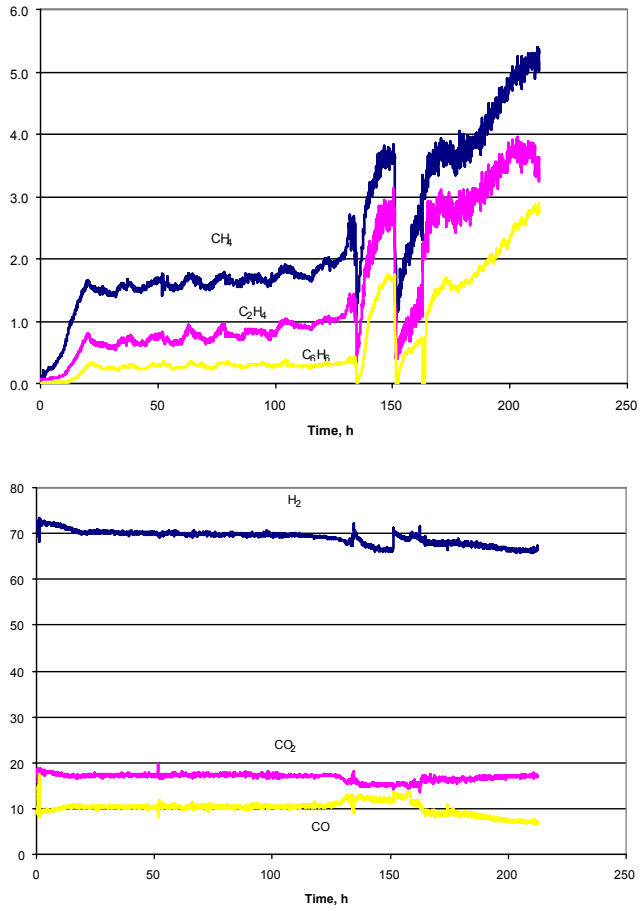

Figure 1. Composition of product gas from reforming of "trap grease," %v/v; t=850˚C, S/C=5, G_{C1}VHSV=970 h^{-1}.

At 135 hours an upset in feeding interrupted the operation. When the test was restarted a continuous decrease in hydrogen and increase in hydrocarbons was observed during the next 15 hours. We attempted to regenerate the catalyst by steam and hydrogen treatment then continued operation for the combined total of 213 hours. However, performance continuously decreased.

For 135 hours the hydrogen yield was 25 g/100 g grease and could have exceeded 28 g/100 g with the addition of water-gas shift. At the end, this yield decreased to 16.4 g/100 g grease (48% of the stoichiometric potential) as shown in Figure 3. However, throughout the whole experiment the conversion of carbon from grease to gas was 100% with the overall mass balance closure almost 100%. No carbon deposits, nickel sintering, sulfur or other poisons were detected by preliminary thermo-emission electron microscopy (TEM) and ICP analyses on the catalyst, though these remain possibilities.

The main reason for the unsatisfactory performance in the last part of the test was probably the loss of catalyst from the reactor. Out of 280 g of the C11-NK catalyst at the beginning of the experiment (260 g reduced) 65 g remained in the reactor at the end and 165 g of fine material were recovered from the cyclone and filter (30 g missing). Therefore, at the end of the experiment the space velocity was four times greater than initially, overloading the catalyst. The catalyst losses seemed to intensify after 135 hours on stream, possibly because of flow upsets and weakening of the particles during regeneration.

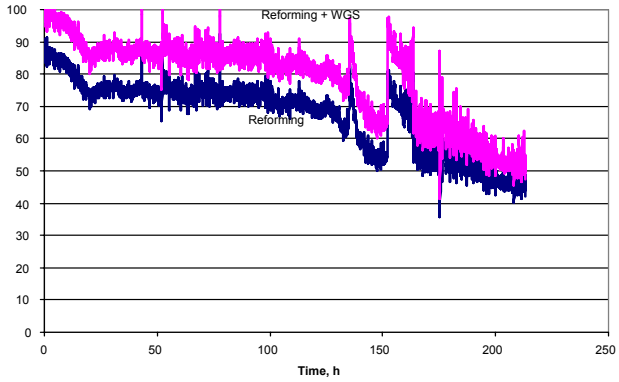

Figure 2. Yield of hydrogen produced by reforming "trap grease," % of ideal stoichiometry; t=850˚C, S/C=5, G_{C1}VHSV=970 h^{-1}.

Since these catalyst losses are not acceptable, more robust fluidisable catalysts are being produced.[8] Alternatively, a circulating fluidized bed reactor that would use easier-to-produce smaller (80 μ) catalyst particles is being considered.

Conclusions

We demonstrated fluidized bed catalytic steam reforming can produce hydrogen from "trap grease", at conditions similar to methane reforming.

The hydrogen yield was about 25 g per 100 g grease (74% of ideal for 135 hours and could be increase to 28 g by water-gas shift of the remaining CO.

Performance deteriorated after 135 hours, probably due to catalyst loss. Therefore, fluidisable attrition-resistant catalysts are being produced and a circulating bed is being considered.

Acknowledgement. We thank Shaine Tyson, manager of the NREL Biodiesel Program for providing the samples of "trap grease" and the grease analysis.

References

(1) Spath, P. L.; Mann, M. K. Life Cycle Assessment of Hydrogen Production via Natural Gas Steam Reforming. National Renewable Energy Laboratory (NREL), Golden, CO, 2000, TP-570-27637

(2) Wang, D.; Czernik, S.; Montané, D.; Mann, M.; and Chornet, E. *Ind. Eng. Chem. Res.* **1997**, *36,* 1507.

(3) Spath, P.; Lane, J.; Mann. M.; Amos, W. Update of Hydrogen from Biomass – Determination of the Delivered Cost of Hydrogen. NREL Process Analysis Task Milestone Report, April 2000.

(4) Czernik, S.; French, R.; Feik, C.; Chornet, E. *Ind. Eng. Chem. Res.* **2002,** *41,* 4209.

(5) Marquevich, M.; Coll, R.; Montané, D. *Ind. Eng. Chem. Res.* **2000**, *39,* 2140.

(6) Wiltsee, G. Urban Waste Grease Resource Assessment, 1998 Report prepared by Appel Consultants, Inc., for NREL, subcontract No. ACG-7-17090-01.

(7) Marquevich, M.; Medina,F.; Montané, D. *Catalysis Communications* **2001,** 2, 119.

(8) French, R., Magrini-Bair, K., Czernik, S., Parent, Y., Ritland, M., Chornet, E. *Prepr. Pap.-Am. Chem. Soc., Div. Fuel Chem.* **2002**, *47(2),* 759.

RENEWABLE HYDROGEN PRODUCTION BY CATALYTIC STEAM REFORMING OF PEANUT SHELLS PYROLYSIS PRODUCTS

Robert J. Evans[1]*, Esteban Chornet*[1]*, Stefan Czernik*[1]*, Calvin Feik*[1]*, Richard French*[1]*, Steven Phillips*[1]*, Yaw D. Yeboah*[2]*, Danny Day*[3] *Shivayam Ellis*[3]*, Dennis McGee*[4]*, and Matthew J. Realff*[5]

[1]National Renewable Energy Laboratory,
1617 Cole Blvd, Golden, CO 80401

[2]Clark Atlanta University
Atlanta Ga 30314
M
[3]Scientific Carbons Inc
Blakely GA 31723

[4]Enviro-Tech Enterprises Inc
Matthews NC 28105

[5]Georgia Institute of Technology
Atlanta GA 30332

Introduction

The goal of this work is the production of renewable hydrogen from agricultural residues, in the near-term time frame and at a comparable cost to existing methane-reforming technologies. Near term production of renewable hydrogen from biomass requires a co-product strategy to compete with conventional production of hydrogen from the steam reforming of natural gas.[1,2] The production of hydrogen by the processing of pyrolysis products that are produced as a by-product of activated carbon is one path that is possible to demonstrate the co-product strategy.

The original concept was that the pyrolysis oil could be fractionated into two fractions based on water solubility. The water-soluble fraction is to be used for hydrogen production and the water insoluble fraction could be used in adhesive formulations.[3] The bio-oil can be stored and shipped to a centralized facility where it is converted to hydrogen via catalytic steam reforming and shift conversion. Catalytic steam reforming of Bio-oil at 750-850ºC over a nickel-based catalyst is a two-step process that includes the shift reaction:

$$\text{Bio-oil} + H_2O \rightarrow CO + H_2$$
$$CO + H_2O \rightarrow CO_2 + H_2$$

The overall stoichiometry gives a maximum yield of 17.2 g H/100 g bio-oil (11.2 wt.% based on wood):

$$CH_{1.9}O_{0.7} + 1.26\ H_2O \rightarrow CO_2 + 2.21\ H_2$$

The process has been demonstrated at the bench scale using model compounds and the carbohydrate-derived fraction of bio-oil.[1,4] Regional networks of pyrolysis plants could be established to provide oil to a central steam reforming facility. The process is adaptable to other organic waste streams such as aqueous-steam fractionation processes used for ethanol production and trap grease. Recent laboratory work has demonstrated the feedstock flexibility with the processing of pyrolysis oil fractions from different feedstocks as well as other biomass-derived streams such as glycerine from biodiesel production, trap grease, and wood hydrolysis effluents.[5]

Although the adhesive byproduct option remains viable, commercial deployment opportunities are still not near term. Hence, other opportunities had to be developed based on the co-product strategy. The conversion of biomass to activated carbon is an alterative route to hydrogen with a valuable co-product as outlined in Figure 1. Slow pyrolysis is used in the first step of the activated carbon process to optimize the yield of charcoal and organic vapors. Southwest Georgia was identified as an excellent opportunity because of the importance of agriculture, the forest product industry, and the need for zero emission transportation fuels in the Atlanta area. Scientific Carbons Inc. in Blakely GA uses pelletized peanut shells as the feed material for the production of activated carbon. They feed the densified peanut shells to a two-stage process producing activated carbon. The vapor by-products from the first stage, pyrolysis, are currently used as fuel for steam generator.

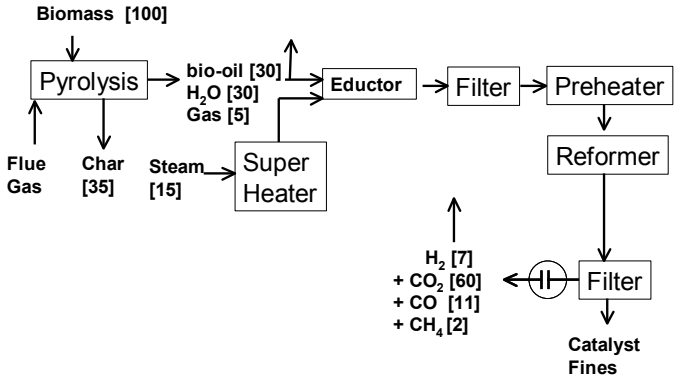

Figure 1. Mass Balance and Unit Operations in the Pyrolysis of Biomass to Activated Carbon and Steam Reforming of vapors to Hydrogen

Work at the bench scale at NREL has is promising with run times in a two-inch fluid bed reactor of over 100 hours. Systematic studies of variation in catalyst composition have shown that commercial steam reforming catalysts perform optimally for the conversion.[6] However, physical attrition is a problem since these catalysts are not manufactured for fluid bed operation.[4]

This paper reports on the first performance of the scaled-up catalytic steam-reforming reactor and on the initial tests for conversion of whole biomass pyrolysis vapors to hydrogen.

Experimental

Pelletized peanut shells were fed to a cross-draft, moving-bed pyrolysis reactor heated by propane combustion gases. Superheated steam was used to educt a fraction of the vapors through a bag house to remove char fines and then to a preheater before the reformer. 50 kg/hour of pelletized peanut shells were fed to the pyrolysis reactor that was controlled so the exit gas temperature was 500 ^{o}C. Using a helium tracer it was determined that 20% of the gaseous products were educted in the steam flow to the reformer. The steam/vapor stream then enters a preheater that raises its temperature to 650-700°C.

The catalytic fluid bed reformer was fed 5 kg/h of pyrolysis vapor. The maximum allowable operating temperature and pressure are 900 ^{o}C and 140 kPa, respectively. The reformer is equipped with internal and external cyclones for disengaging catalyst particles, instrumentation, data acquisition, and safety features (alarms, etc.). Commercial nickel-based catalyst grounded to particle size of 300-500 μ is being used in the reactor. The catalyst is fluidized using superheated steam, which is also a reactant in the reforming process. The cyclones capture both fine catalyst particles and solid carbon generated by gas phase pyrolysis of the vapors that may occur in competition with the catalytic steam reforming. The Inconel reactor with a porous material distribution plate is placed inside a three zone electric furnace to maintain the reactor at the desired temperature during the endothermic steam reforming operation. The reformed

products flow through the spray scrubbers and a cold wall condenser before passing through a coalescing filter to remove aerosols.

Results and Discussion

The purpose of the run was to reform the whole pyrolysis vapors (for the first time) in the 5 cm catalytic steam reforming fluid bed reactor. The more chemically stable, lignin-derived phenolics may be more likely to coke on the nickel catalyst. Prior runs in the 5 cm reformer have used only the aqueous carbohydrate-derived fraction of pyrolysis oil.

Gas composition at the outlet of the reformer was monitored during the operation and is shown in Figure 2. The composition of the gas indicates that the yield of hydrogen from this agricultural residue feedstock is approximately 90% of maximum. Additional optimization of process conditions should result in somewhat higher yields (note that, in a commercial operation, the remaining CO would be converted to additional hydrogen using conventional water-gas shift processing). Initial performance was variable due to unstable conditions in the reformer. A period of stable operations was then achieved until a pressure drop across the hot gas filter led to unstable operation. In these tests, the gas product stream was flared. No breakthrough of pyrolysis products was noted and the methane level, which is a sensitive indicator of catalyst activity, did not increase. The significant finding here is that the lignin-derived pyrolysis products were reformed completely. The changes in product gases were due to a systematic decrease in mass flow to the bed due to an increase in pressure drop across the hot gas filter. This build up of particulates was unexpected, but the change in product gas composition indicates better performance with an increase in hydrogen yield and decrease in relative yield of both CO and CH4 by effectively decreasing the weight hourly space velocity and increasing the steam to carbon ratio, we achieved a higher rate of conversion most likely by allowing more time for carbon gasification from the catalyst surface.

Summary and Future Work

The steam reforming of biomass pyrolysis oil, when integrated with the production of high value products, is a promising near-term approach to the production of renewable hydrogen. The application in Georgia is at a plant that makes activated carbon from peanut shells and has pyrolysis by-products available for conversion. The key technical goals for the run are to obtain preliminary performance data on the catalyst, especially physical attrition and deactivation.

In the next phase, the reactor will be run for 1000 hours with additional gas stream processing included. The hydrogen that is produced will be purified by separating hydrogen from CO and CO_2 using pressure swing adsorption. The purified hydrogen will be mixed with natural gas and used in engine demonstrations. Other agricultural residues and deployment logistics are being evaluated for cost and co-product potential.[7,8]

The hydrogen produced in the next phase of the project will be blended with CNG and used in a transportation demo. This integrated strategy will demonstrate the potential impact of hydrogen and bioenergy on the economic development and diversification of rural areas.

Acknowledgement. The authors gratefully acknowledge the support of the DOE Hydrogen Program

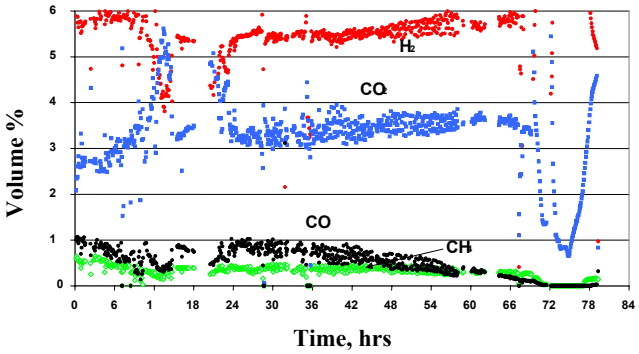

Figure 2. Gas composition from reforming peanut-shell pyrolysis vapors

References

1. Chornet, E.; Czernik, S.; Wang, D.; Gregoire, C.; Mann, M., In *Proceedings of the 1994 DOE/NREL Hydrogen Program Review,* Livermore, California, NREL/CP-470-6431; CONF-9404194, **1994**, pp. 407-432.
2. Spath, P.L.; Mann. M.K., In *Hydrogen Energy Progress XII. Proceedings of the 12th World Hydrogen Energy Conference,* Buenos Aires, Argentina, Bolcich, J. C. and Veziroglu, T. N., Eds. Vol. 3, **1998**, pp. 2057-2067.
3. Kelley, S.S.; Wang, X.-M.; Myers, M. D.; Johnson, D. K.; Scahill, J. W., In *Developments in Thermochemical Biomass Conversion,* Bridgwater, A. V. and Boocock, D. G. B., Eds., London: Blackie Academic & Professional, **1997,** pp. 557-572.
4. Chornet, E.; Czernik, S.; Feik, C.; French, R., In *Proceedings of the 2001 DOE/NREL Hydrogen Program Review,* Baltimore, MD., **2001**.
5. Czernik, S., French, R.; Feik, C.; Chornet,E., In *Progress in Thermochemical Biomass Conversion,* Bridgwater, A. V., Ed. London: Blackwell Science Ltd., **2001**, pp. 1577-1585.
6. Garcia,L., French, R.; Czernik, S.; Chornet, E., Applied Catalysis A: General, **2000**, *201*, 225-239.
7. Abedi, J.; Yeboah, Y. D.; Realff, M.; McGee, D.; Howard, J.; Bota, K.B. In *Proceedings of the 2001 DOE/NREL Hydrogen Program Review,* Baltimore, MD., **2001**.
8. Ozyurt, B. D., Realff, M. J., In *AIChE National Meeting Special Symposium*, Dallas, TX., **1999**.

Steam Gasification of Cellulose by Continuous Cross-Flow Moving Bed Type Differential Reactor

Yohsuke Yamaguchi, Chihiro Fushimi, Takeshi Furusawa
Atsushi Tsutsumi

Department of Chemical System Engineering
The University of Tokyo
7-3-1 Hongo, Bunkyo-ku, Tokyo 113-8656 Japan

Introduction

Steam gasification is a promising technology for thermochemical hydrogen production from biomass. However, a large amount of tar is produced in the biomass gasification process. This reduces thermal efficiency and causes tar troubles such as pipeline plugging and defluidization. Thus, it is very important to investigate the reaction mechanism of tar production in gasification for improvement in controllability and thermal efficiency of biomass gasifiers.

Several researchers have investigated the products and reaction mechanism of cellulose pyrolysis.[1-6] The generally accepted mechanism for cellulose pyrolysis (Broid-Shafinzadeh model[1]) consists of three coupled first order steps. There is an initial step, involving no weight loss that leads to activated cellulose the nature of which is not well understood. This is followed by a pair of competing reactions, which produces either volatiles or char and gases. Both of the two reactions lead to weight loss.[1-4] Antal *et al.* reported that the presence of steam in the pyrolysis medium had no measurable effect on cellulose pyrolysis kinetics.[7]

In the conventional methods, it is impossible to investigate the time profile of tar production in steam gasification of biomass with rapid heating in continuous feeding condition. Thus, in this study, we have developed a continuous cross-flow moving bed type differential reactor and investigated the time profile of tar evolution and char production in gasification of biomass.

Experimental

Figure 1 shows the schematic diagram of experimental apparatus. Sample was continuously fed into a preheated quartz glass reactor and conveyed by a belt through the reactor. The reactor was divided into six compartments (W90 mm×D80 mm×H40 mm) whose gas flows were independent. Steam was fed with Ar carrier gas. Gas and tar can be collected separately in accordance with the evolving time. Char was collected at the end of the reactor.

Cellulose (< 160 μm), which is major component of biomass, was used as a sample. The gaseous products (H_2, CO, CO_2, CH_4, C_2H_4 and C_2H_6) were analyzed by a micro GC. The compositions of tar and char were analyzed by a Total Organic Carbon (TOC) analyzer, a CHNS elemental analyzer and FT-IR. Molecular weight of tar was also analyzed by a Gel Filtration Chromatograph (GFC). The experiments were carried out at 673 K

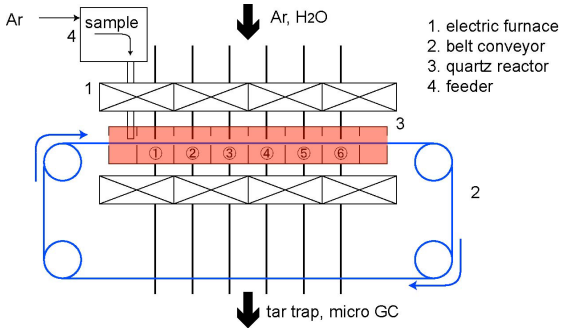

Figure 1. Schematic diagram of experimental apparatus

Results and Discussion

Analysis of gas and tar. Figure 2 shows time profile of gas evolution rate and temperature of each compartment. The initial time (0 s) was defined as the sample was fed into the reactor. The X-axis represents the time when the sample went through the middle point of the each compartment. Evolution of CO_2 and CO was dominant and that of other gases was negligible at this temperature. It is considered that CO_2 production was dominant because of the equilibrium of water-gas-shift reaction. The major product was tar at this temperature (not shown).

Table 1 shows elemental composition of produced tar. The amount of oxygen was calculated by difference. The elemental composition of tar was quite similar to that of original cellulose. **Figure 3** shows the molecular weight distribution of tar measured by GFC. The components with lower molecular weight are detected with increasing retention time. The molecular weight of the three peaks was 210, 326 and 486. Since the molecular weight of unit cellulose ($C_6H_{10}O_5$) is 162, the three peaks can be assigned to monomer (levoglucosan), dimer (cellobiosan) and trimer (cellotriosan) of cellulose. It was found that evolved tar in steam gasification was cellulose with low degree of polymerization and that the major components are levoglucosan and cellobiosan.

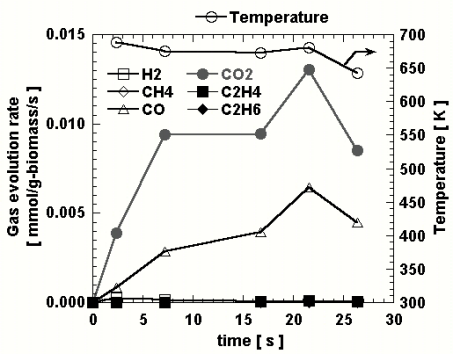

Figure 2. Time profile of gas evolution

Table 1. Elemental composition of produced tar

time [s]	C	H	O (diff.)
0 (cellulose)	44.4	6.2	49.4
2.4	45.3	5.5	48.4
7.2	46.8	5.1	47.4
16.8	48.8	5.8	44.7
21.6	47.8	5.9	45.6
26.4	47.2	5.9	46.1

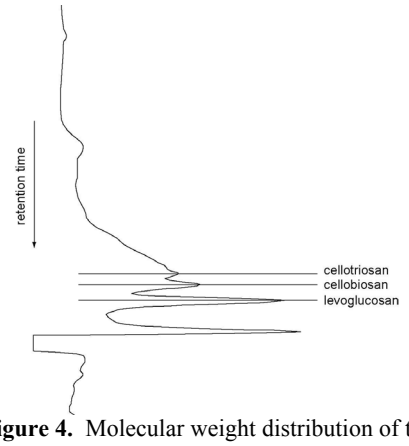

Figure 4. Molecular weight distribution of tar

Analysis of char. Char was collected by changing velocity of the belt (residence time=14.4, 28.8, 57.6 and 115.2 s) and analyzed. **Figure 4** shows time profile of conversion to volatile matter calculated from the weight reduction of char. It can be seen that the weight reduction of cellulose started about 20 s and was completed in 57.6 s. **Table 2** shows the elemental composition of char. It can be seen from this table that the elemental composition of char was quite similar to that of cellulose until 57.6 s. However, the elemental composition of char was significantly changed at 115.2 s although the weight of char was not changed in this period. In order to investigate the reaction in this period, the atomic ratios H/C and O/C were calculated and plotted on Krevelen's coal band (**Figure 5)**. It was found that dehydration of char occurs after volatile release is completed. **Figure 6** shows FT-IR spectra. It was observed that the spectra of char were similar to that of cellulose up to 57.6 s. However, the peak at 3400-3000 cm^{-1} (OH groups) was weaker and those of 1700 cm^{-1} (C=O bond) and 1600 cm^{-1} (C=C bond) were stronger at 115.2 s. This also indicates the occurrence of dehydration of char.

Figure 7 shows reaction mechanism of steam gasification of cellulose. When cellulose is heated, at first depolymerization of cellulose takes place. Then evolution of tar with low degree of polymerization takes place. The major components of tar are levoglucosan and cellobiosan. After the tar evolution is completed, dehydration of char takes place.

Conclusions

Steam gasification of cellulose was studied using a continuous cross-flow moving bed type differential reactor. The following conclusions are drawn.

(1) Depolymerization of cellulose takes place before volatiles are evolved. This does not lead weight decrease in the initial stage of gasification.
(2) The evolved tar is cellulose with low degree of polymerization. Most of them are levoglucosan and cellobiosan.
(3) Dehydration of cellulose char occurs after the evolution of tar is completed.

Acknowledgement. This study was financially supported by "Core Research for Evolutional Science and Technology" grant from Japan Science and Technology Corporation (JST). The authors appreciate this financial support.

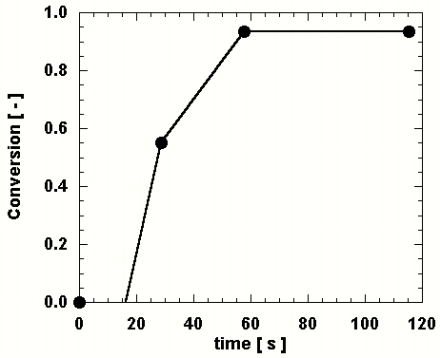

Figure 4. Time profile of conversion to volatile matter calculated from the weight of char

Table 2. Elemental composition of char

time [s]	C	H	O (diff.)
0 (cellulose)	44.4	6.2	49.4
14.4	44.7	6.2	48.2
28.8	45.5	6.2	47.5
57.6	46.6	6.0	46.7
115.2	64.5	4.0	30.9

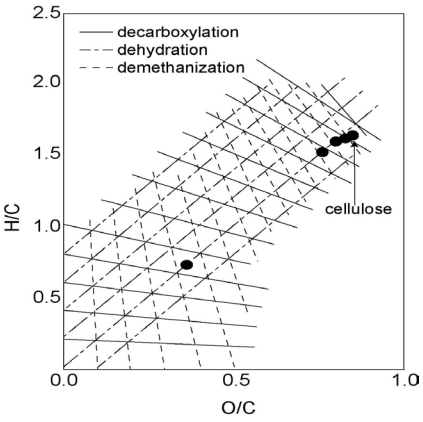

Figure 5. Krevelen's coal band

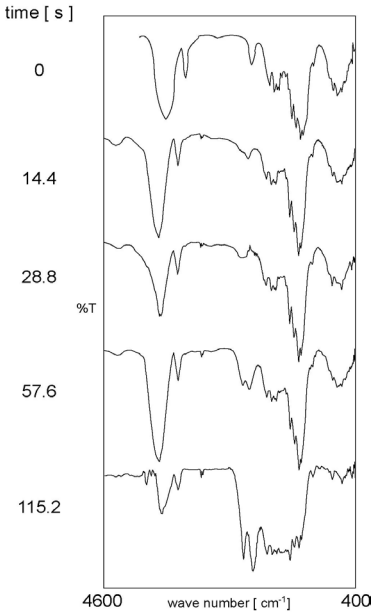

Figure 6. IR spectra of char

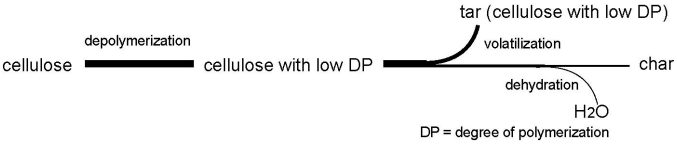

Figure 7. Reaction mechanism of steam gasification of cellulose

References

(1) Bradbury, A. G. W.; Sakai, Y.; Shafizadeh, F. *J. Applied Polymer Science*, **1979**, *23*, 3271.
(2) Banyasz, J. L.; Li, S.; Lyons-Hart, J.; Shafer, K. H. *J. Anal. Appl. Pyrolysis*, **2001**, *57*, 223.
(3) Banyasz, J. L.; Li, S.; Lyons-Hart, J.; Shafer, K. H. *Fuel*, **2001**, *80*, 1757.
(4) Li, S.; Lyons-Hart, J; Banyasz, J.; Shafer, K. H. *Fuel*, **2001**, *80*, 1809.
(5) Alves, S. S.; Figueiredo, J. L. *J. Anal. Appl. Pyrolysis* **1989**, *17*, 37.
(6) Pouwels, A. D.; Eijkel, G. B.; Boon, J. J. *J. Anal. Appl. Pyrolysis*, **1989**, *14*, 237.
(7) Antal, M. J.; Friedman, H. L.; Robers, F. E. *Combustion Science Technology,* **1980**, *21*, 141.

Plasma Gasification of Biomass in a Downflow Reactor

Zengli Zhao Haibin Li Chuangzhi WU Yong Chen
（Guangzhou Institute of Energy Conversion, CAS，Guangzhou 510070）

Abstract：The experiments of biomass gasification have been carried out using a plasma reactor, which has high temperature and high enthalpy. The product includes solid char and gas. No tar was detected. Synthesis gas (H_2+CO) is the main gas product. With the steam flow increasing, H_2/CO molar ratio ranges from 0.90 to 1.15. The gas yield is about 2L per g of biomass and the combined volume of H_2 and CO was 96%.The gas conversion of carbon was very high.

Keywords：Biomass, Plasma, Gasification

PREPARATION AND APPLICATION OF Co-Mo MODEL SULFIDE CATALYSTS FOR HYDRODESULFURIZATION

Yasuaki Okamoto

Department of Material Science, Shimane University, Matsue 690-8504, Japan

Introduction

Hydrotreatings of petroleum feedstocks have recently become more and more crucial not only to protecting the environment but also to efficient utilization of limited natural resources. Development of highly active and selective hydrotreating catalysts, in particular hydrodesulfurization (HDS) catalysts, is one of the most urgent problems in petroleum industries. Sulfided Co-Mo or Ni-Mo(W) based catalysts have been used in industry for HDS reactions. Supported Co(Ni)-Mo sulfide catalysts have been extensively studied to understand the structure and reactivity of catalytically active sites, the microscopic reaction mechanisms of HDS and hydrogenation, the effects of the support and additives and so on.[1,2] A so-called CoMoS model originally proposed by Topsøe *et al*.[1] for a catalytically active phase, in which Co locates on the edges of highly dispersed MoS_2 clusters, attracts increasing attention to explain many aspects of catalytic and spectroscopic properties. Better characterization and understanding of the nature of Co(Ni)-Mo sulfide catalyst systems in a molecular scale are of great importance to a rational design of highly active HDS catalysts.

One of the promising approaches for these purposes is to utilize model catalysts, such as homogeneous metal sulfide clusters and metal sulfide clusters on a flat surface. In the model catalyst approach for better characterization of hydrotreating catalysts, we tried to fabricate more practical model catalysts than the model catalysts constructed by means of surface science techniques and intrazeolite and homogeneous metal sulfide clusters. In the present study, model catalysts are defined as the catalysts in which all the Co atoms are present as CoMoS phases.

Experimental

Catalyst Prepation. Sulfided MoS_2/Al_2O_3 was exposed to a vapor of $Co(CO)_3NO$ at rt for 5 min (CVD technique), followed by evacuation at rt. $Co(CO)_3NO/MoS_2/Al_2O_3$ was subsequently sulfided again at 673 K to prepare a $Co\text{-}Mo/Al_2O_3$ catalyst. The resulting catalyst is designated CVD-$Co/MoS_2/Al_2O_3$. Other supports, TiO_2, ZrO_2 and SiO_2, were also examined.

Characterization and reaction. The amount of NO adsorption was measured by means of a pulse technique. The HDS of thiophene was carried out by using a closed circulation system at 623 K and 20 kPa to evaluate the initial activity of sulfided catalysts.

Results and Discussion

Preparation of Model Catalysts. The addition of Co to MoS_2/Al_2O_3 by means of the CVD technique greatly enhanced the HDS activity of MoS_2/Al_2O_3, irrespective of the Mo loading. In order to examine the location of the Co atoms deposited by the CVD technique, the Co/Mo ratio of CVD-$Co/MoS_2/Al_2O_3$ was plotted against the NO/Mo ratio of MoS_2/Al_2O_3. When the Mo loading was larger than 9 wt.% (monolayer loading), the Co/Mo ratio was proportional to the NO/Mo ratio. It has been established that NO molecules adsorb on the edge sites of MoS_2 particles rather than on the basal plane. Hence, the linear correlation between the Co/Mo and NO/Mo ratios strongly suggests that Co is located on the edge sites of MoS_2 particles at > 9 wt.% Mo. The Co $2p_{3/2}$ XPS binding energy for CVD-Co/Al_2O_3 was close to that of Co_9S_8, indicating that Co sulfide clusters form as expected. However, in the presence of MoS_2 particles, the Co $2p_{3/2}$ binding energy increased by 0.8 eV, clearly demonstrating that Co species chemically interact with the edges of MoS_2 particles.

When CVD-$Co/MoS_2/Al_2O_3$ was exposed again to a vapor of $Co(CO)_3NO$ and resulfided, the HDS activity of CVD-$Co/MoS_2/Al_2O_3$ hardly changed in spite of the increase of the Co content by a factor of 1.7. It is concluded that applying CVD once fills the edge sites of MoS_2 particles with Co atoms, constituting CoMoS phases, and that $Co(CO)_3NO$ molecules adsorbed on the edge sites of Co-MoS_2 particles are transformed into separate Co sulfide clusters. This was also supported by the FTIR spectra of NO adsorption on CVD-$Co/MoS_2/Al_2O_3$, showing that essentially all the edge sites of MoS_2 particles, that are accessible to NO adsorption, are covered by Co atoms, constituting CoMoS phases.

Evaluation of the Maximum Potential HDS Activity. Figure 1 shows the HDS activity of CVD-$Co/Co\text{-}Mo/Al_2O_3$, which was prepared by exposing sulfided $Co\text{-}Mo/Al_2O_3$ to a vapor of $Co(CO)_3NO$ and subsequent sulfidation, as a function of Co content in $Co\text{-}Mo/Al_2O_3$ impregnation catalysts. The HDS activity of $Co\text{-}Mo/Al_2O_3$ was increased, over the whole range of Co content, by the addition of Co by means of the CVD technique. It is worthy of note that CVD-$Co/Co\text{-}Mo/Al_2O_3$ shows the identical activity with CVD-$Co/MoS_2/Al_2O_3$, when Co content is lower than 2 wt.% and that the activity of CVD-$Co/Co\text{-}Mo/Al_2O_3$ gradually decreases with increasing Co content at > 2 wt.%. Taking into consideration the fact that the HDS activity of CVD-$Co/MoS_2/Al_2O_3$ is not changed by the further addition of Co and the FTIR of NO adsorption, it is concluded that the activity increase in Figure 1 results from the increase in the amount of CoMoS phases by the addition of $Co(CO)_3NO$ and that the HDS activity of CVD-$Co/MoS_2/Al_2O_3$ provides the maximum potential HDS activity for a series of $Co\text{-}Mo/Al_2O_3$ catalysts, as long as the dispersion of MoS_2 particles are not modified by the impregnation of Co.

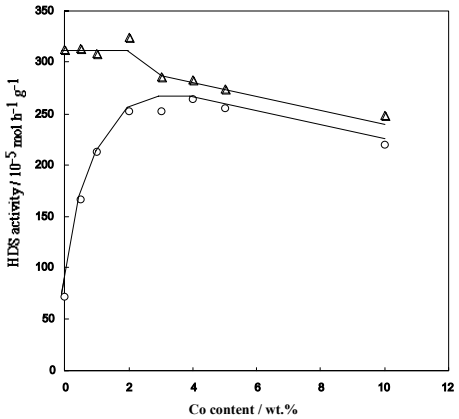

Figure 1. HDS activity of CVD-$Co/Co\text{-}Mo/Al_2O_3$ (triangle) and $Co\text{-}Mo/Al_2O_3$ (circle) as a function of the Co content in $Co\text{-}Mo/Al_2O_3$.

In conjunction with NO adsorption, the decrease in the activity of CVD-$Co/Co\text{-}Mo/Al_2O_3$ (>2 wt.% Co) was ascribed to an increasing extent of blockings of the edges of MoS_2 particles by Co sulfide particles concomitantly formed during the sulfidation of the $Co\text{-}Mo/Al_2O_3$ impregnation catalysts. The maximum HDS activity of $Co\text{-}Mo/Al_2O_3$ attained at 3 wt.% Co was lower than the activity of CVD-$Co/MoS_2/Al_2O_3$ or CVD-$Co/Co\text{-}Mo/Al_2O_3$ (< 2 wt.% Co). This is obviously caused by the blocking of the edges of MoS_2 particles by Co sulfide particles before the completion of a full coverage of the edges of the MoS_2 particles by Co. It was also shown that the CVD technique can be applied to Ni-Mo catalysts to evaluate the

maximum potential HDS activity as well as Co-Mo catalysts. The evaluation of the maximum potential HDS activity provides a promising guide line for improving catalyst performances.

Effects of the Support. We examined the effect of the support on Co-Mo sulfide catalysts by preparing the catalysts in the same way as the model catalysts. The supports and Mo contents used in the present study were SiO_2 (347 m^2 g^{-1}, 6.7 and 13 wt.% Mo), ZrO_2 (25 m^2 g^{-1}, 2.0 wt.%), TiO_2 (50 m^2 g^{-1}, 4.0 wt.%) and Al_2O_3 (177 m^2 g^{-1}, 8.7 and 13 wt.%). The Mo content of the catalyst was fixed approximately at or over its monolayer loading. The dispersion of MoS_2 particles was measured by means of NO adsorption.

The supported MoS_2 catalysts were exposed to a vapor of $Co(CO)_3NO$ to prepare CVD-Co/MoS_2/support. The Co $2p_{3/2}$ binding energies were 779.3±0.1 eV, regardless of the support. These results clearly demonstrate that the Co atoms, introduced by means of the CVD technique, interact with MoS_2 particles on the support.

Figure 2 shows the Co/Mo ratio of CVD-Co/MoS_2/support as a function of the NO/Mo ratio of the MoS_2/support samples. The Co/Mo ratio was proportional to the NO/Mo ratio, showing that Co sulfide species are located on the edge sites of MoS_2 particles. In consequence, we conclude that the Co sulfide species prepared in this way is characteristic of the CoMoS phase proposed by Topsøe *et al*.[1] and that the CoMoS phase is preferentially formed when the CVD technique is applied, irrespective of the support. It is concluded that a Co-Mo model catalyst can be prepared, when the Mo content corresponds to or exceeds a monolayer loading in MoS_2/support.

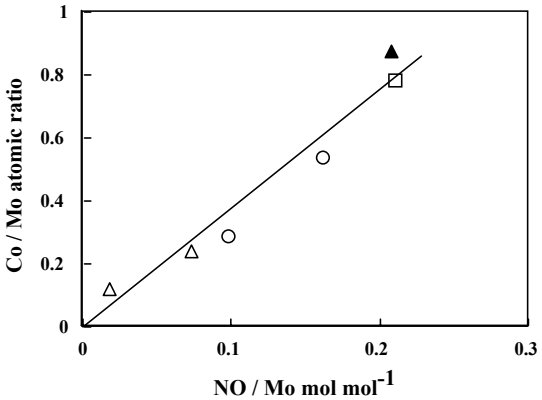

Figure 2. Correlation between the Co/Mo atomic ratio and the NO/Mo ratio for supported CVD-Co/MoS_2/support catalysts. Open triangle: SiO_2, Circle: Al_2O_3, Square: TiO_2 and Closed triangle: ZrO_2.

Figure 3 shows the catalytic activity of CVD-Co/MoS_2/support in the HDS of thiophene as a function of Co loading. A good proportional correlation was obtained for Al_2O_3-, TiO_2- and ZrO_2-supported Co-Mo model catalysts, regardless of the support and the pretreatment (pre-reduced before exposure to $Co(CO)_3NO$ or thermally decomposed after exposure). Since the straight line in Figure 3 passes through the origin, the activity is ascribed to the Co species interacting with MoS_2 or the CoMoS phase and that there are very few unpromoted Mo sites, if any, after the single adsorption of $Co(CO)_3NO$ in agreement with the FTIR of NO adsorption of CVD-Co/MoS_2/Al_2O_3. The TOF of the CoMoS phase (the slope of the line) of the Al_2O_3-, TiO_2- and ZrO_2-supported catalysts are identical. We conclude, therefore, that the support has no significant effects on these catalyst systems. The HDS activity of Co-Mo/Al_2O_3, prepared by an impregnation, was somewhat lower than that of CVD-Co/MoS_2/Al_2O_3 with similar Co and Mo loadings (Figure 3). This is obviously due to the formation of less active Co species such as Co_9S_8 clusters and Co^{2+} in the Al_2O_3 sublayer in addition to the CoMoS phases, in line with the Co 2p XPS results.

Figure 3 shows that the specific activity of the Co species supported on SiO_2 is 1.7 times higher than the activity on the other supports. Taking into account the difference in activity between CoMoS Type I and Type II, CoMoS Type I probably forms on the Al_2O_3, TiO_2 and ZrO_2 supports under the present sulfidation conditions (673 K, atmospheric H_2S/H_2), while CoMoS Type II on SiO_2. The difference is attributed to the difference in the stacking number of MoS_2 particles on the basis of the TEM observations, in agreement with others.

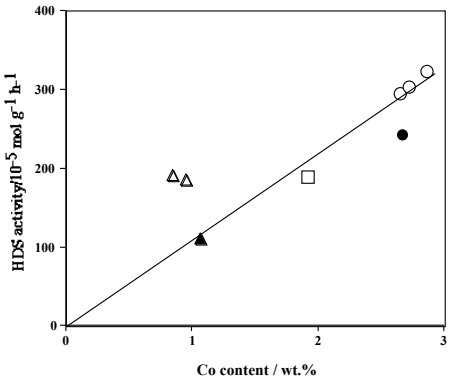

Figure 3. Correlation between thiophene HDS activity and the Co loading of supported CVD-Co/MoS_2 catalysts**.** See the captions in Fig.2 for the symbols. Closed circle: a Co-Mo/Al_2O_3 impregnation catalyst.

Conclusions

It has been found that the selective preparation of CoMoS phases supported on refractory oxides provides promising model catalysts to understand the nature of practical HDS catalysts. Effects of the support were understood in terms of the TOF of the CoMoS phases. Furthermore, the information on the maximum potential HDS activity of Co(Ni)-Mo(W) catalysts is very unique and will be helpful in the design of highly active HDS catalysts. It is shown in our study that the model catalyst approaches provide important information on the effects of the catalyst preparation and additives, the catalyst structure and the fundamental aspects of HDS catalysts such as microscopic reaction mechanisms and structure-reactivity relationships.

Acknowledgement. The present author expresses his gratitude to Dr. Takeshi Kubota (Shimane University) for useful discussions. This work has been entrusted by the New Energy and Industrial Technology Development Organization under a subsidy of the Ministry of Economy, Trade and Industry.

References

(1) Topsøe, H., Clausen, B.S., Massoth, F.E., *Catalysis Science and Technology*, eds. Anderson, J.R., Boudard, M., Springer, Berlin, 1996, Vol.11.

(2) Whitehurst, D.D., Isoda, T., Mochida, I., *Adv. Catal*., **42**, 345 (1998).Ed.; Plenum Press: New York, 1992; pp. 255-274.

RELATIONSHIP BETWEEN CATALYST STRUCTURE AND HDS REACTION MECHANISM

Narinobu Kagami[1], Bas M. Vogelaar, A. Dick van Langeveld[2], and Jacob A. Moulijn[*]

Reactor & Catalysis Engineering Group, Faculty of Applied Sciences, Delft University of Technology, Julianalaan 136, 2628 BL Delft, The Netherlands

[1]Manufacturing Deparment, Idemitsu Kosan Co., Ltd. 26,Anesakikaigan Ichihara-city, Chiba, 299-0107, Japan

[2] Particle Optics Group, Faculty of Applied Sciences, Delft University of Technology, Lorentzweg 1, 2628CJ Delft, The Netherlands

Introduction

The hydrodesulfurization (HDS) process is receiving more and more attention, because the legislative requirements on transportation fuels are becoming more severe. Therefore, it is very important to elucidate the effect on the relationship between catalyst structure and reaction mechanism of the sulfur compounds.

$CoMo/Al_2O_3$ and $NiMo/Al_2O_3$ catalysts are the work-horses in HDS processes. The so-called type II CoMoS phase has a higher activity for thiophene HDS than the so-called type I. For catalyst design such a conclusion is of crucial importance. However, this has not been unequivocally proven to hold for dibenzothiophene (DBT) HDS[1)]. It should be noted that DBT is a better model compound than thiophene to represent diesel fuel liquid phase HDS.

It is widely accepted that DBT desulfurizes via both direct desulfurization (DDS) and hydrogenation followed by desulfurization (HG-HDS) of benzene ring. This work focuses on the structure type I and type II catalyst structure and the possible relationship with the different routes of DBT HDS.

Experimental

Catalysts

$NiO\text{-}MoO_3/Al_2O_3$ catalysts (type I and type II) were prepared via liquid phase pore volume impregnation. A high purity $\gamma\text{-}Al_2O_3$ in the form of 1.5 mm cylindrical extrudates was impregnated using aqueous solutions containing the required amounts of Ni and Mo, according to the literature[2)].

Activity measurement

The activity for liquid-phase DBT HDS was determined in a batch reactor. Details on the experimental procedure can be found in the literature[1)]. Before the reaction catalysts, they were presulfided at 370 °C. Subsequently, the activity tests were carried out at 350 °C and 5 MPa hydrogen pressure. The feed consisted of 0.2wt% DBT in hexadecane (n-C_{16}).

The inhibiting effect of H_2S is quite large on DBT HDS[3)]. In order to mimic the realistic conditions of the commercial reactor bottom, dimethyldisulfide (DMDS) was added to adjust the H_2S partial pressure to 1.4bar.

Results and Discussion

In Fig. 1 a simplified reaction scheme for DBT HDS is shown. Under the applied reaction conditions the main products are cyclohexylbenzene (CHB) and biphenyl (BP). From the yields of these two products between the direct HDS (DDS) and the hydrogenation route can be discriminated.

In all cases, the time dependency of the DBT concentration followed first order kinetics.

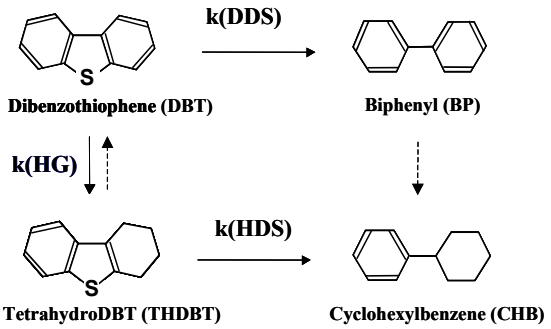

Figure 1. Simplified reaction scheme for DBT HDS

In Fig. 2, the effect of active metals loading on the DBT HDS activity for both NiMo type I and type II catalysts is shown. At increasing loading, type I catalyst did not show higher activity, probably due to formation of MoO_3 crystals, in agreement with literature. Diaz and Bussell reported that at a metal loading above 4.2 atoms Mo per nm^2, three-dimensional MoO_3 particles are formed[4)]. In contrast, type II catalyst showed higher activity at increasing loading.

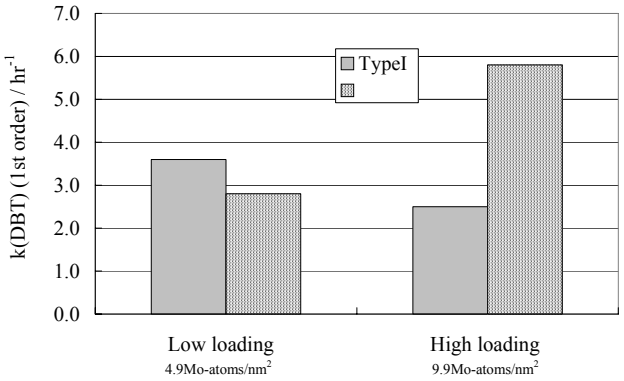

Figure 2. The effect of metal loading for DBT HDS

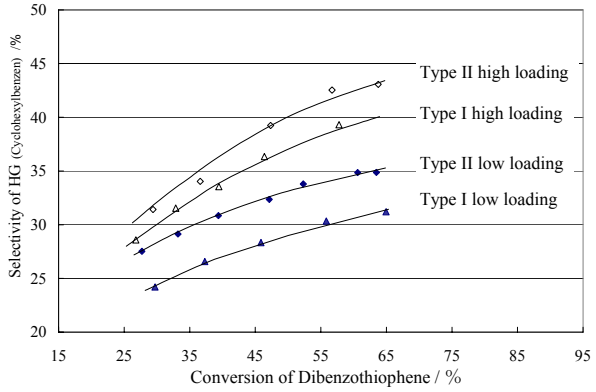

Figure 3. The effect of metal loading for hydrogenation selectivity

[*] Corresponding author, email: J.A.Moulijn@tnw.tudelft.nl

In Fig.3, the selectivity of cyclohexylbenzene, representative for the hydrogenated route is shown. Note that type II catalysts have a higher selectivity for cyclohexylbenzene. Therefore, it can be concluded that the reaction rate of hydrogenated route on type II catalyst is higher than on type I. Moreover, the higher loading catalysts show higher selectivity for cyclohexylbenzene.

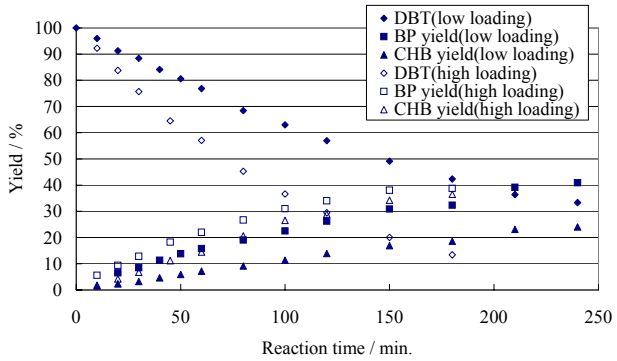

Figure 4. The yield of products HDS DBT on type II NiMo catalysts

In Fig.4, the yields of the products of high and low loading type II catalysts are shown. Time yields of cyclohexylbenzene and biphenyl became higher at increasing loading, but the former increased most. Therefore, the higher HDS activity of type II high loading catalysts is mostly dependent on an acceleration of the hydrogenation route.

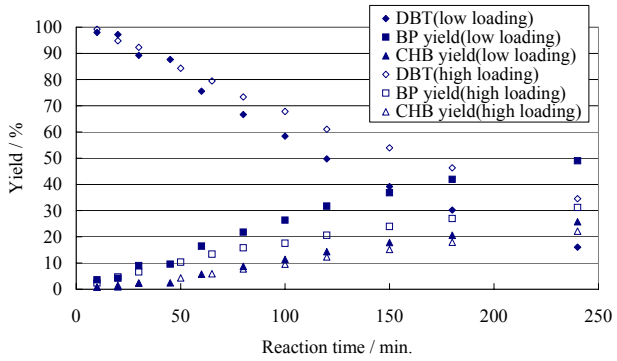

Figure 5. The yield of products HDS DBT over type I NiMo catalysts

In Fig.5, the yields of the products of high and low loading type I catalysts are shown. Time yields of cyclohexylbenzene and biphenyl decrease with increasing loading, but the former becomes much lower. Therefore, it is concluded that due to the formation of MoO_3 crystals, the direct desulfurization reaction rate decreases while hydrogenation route does not change significantly.

To unravel the reaction scheme described in Fig.1, the rate constant of each step was determined numerically by fitting the data to the kinetic model. The inverse reaction of THDBT to DBT, and the hydrogenation reaction of BP to CHB could be neglected because the rate constants were very low.

Table 1. The Rate Constants of Each Reaction Step

	kDBT	k(DDS)	k(HG)	k(HDS)	k(HG) /k(DDS)	k(HDS) /k(DDS)
TypeI Low loading	3.6	2.2	1.4	14.0	0.65	6.5
TypeI High loading	2.5	1.3	1.2	10.9	0.91	8.4
TypeII Low loading	2.9	1.7	1.2	15.9	0.69	9.4
TypeII High loading	5.9	3.0	2.9	27.5	0.99	9.3

In Table 1, the rate constants of each reaction step are given. All data show higher k (HDS) than k (DDS). Therefore, THDBT is supposed to desulfurize easier than DBT. Moreover, type II high loading had a higher k (HG)/ k (DDS) than type II low loading. Therefore, the higher HDS activity of type II high loading catalysts mainly originates from the acceleration of hydrogenation route activity.

These results can contribute to a more rational catalyst design in hydrodesulfurization. Work in that direction is in progress.

Conclusions

The various DBT HDS routes significantly depend on the catalyst structure (type I, type II). The higher HDS activity of the high loading type II catalysts mainly originates from the increased hydrogenation activity.

Acknowledgement.

We thank Dr. S. Eijsbouts (Akzo-Nobel,P.O.Box 37650,1030 BE Amsterdam, The Netherlands) for the stimulating discussions.

References

(1) Reinhoudt, H.R.; Boons, C.H.; Van Langeveld, A.D.; Van Veen, J.A.R.; Sie, S.T.; and Moulijn, J.A., *Appl. Catal. A*. **2001**, *207*, 25.

(2) Van Veen, J.A.R.; Gerkema, E.; Van der Kraan, A.M.; and Knoester, A. *J. Chem. Soc., Chem. Commun*. **1987**, 1684.

(3) Kabe, T.; Aoyama,Y.; Wang, D.; Ishihara, A.; Qian, W.; Hosoya, M.; and Zhang, Q., *Appl. Catal. A*. **2001**, *209*, 237.

(4) Diaz, A.L.; and Bussell, M.E.; *J. Phys. Chem.* **1993**,97, 470.

INTRINSIC KINETICS OF THIOPHENE HDS OVER A NiMo/SiO2 MODEL CATALYST

A. Borgna, E.J.M. Hensen, J.A.R. van Veen and J.W. Niemantsverdriet

Schuit Institute of Catalysis, Eindhoven University of Technology, PO Box 513, 5600 MB Eindhoven, The Netherlands

Introduction

Supported mixed transition metal sulfide catalysts play a pivotal role in refineries for the production of clean motor fuels. They are employed not only to hydrotreat the final products like gasoline and diesel, but also to pretreat fluid catalytic cracking or reformer feed [1]. Furthermore, they provide the hydrogenation functionality in most hydrocracking catalysts that upgrade vacuum residue to more valuable products. Two major drivers for the development of more active hydrotreating catalysts are (i) dwindling oil supplies forcing refiners to use heavier feedstock and (ii) ever-tightening motor fuel specifications (for instance, the EU Auto Oil programme II [2]). Noteworthy is that mostly the use of an improved catalyst is more economic than modifications to the process.

While research on hydrotreating catalysts has been extensive over the last 50 years [3-5], it has proven very difficult to relate catalyst structure to catalyst activity and selectivity on the molecular level. In recent years, we have employed the model catalyst approach to heterogeneous catalysis. The essential point is to prepare planar model catalysts by spin-coating which mimics the industrial pore volume impregnation method. In this way, realistic models can be obtained which are easily amenable to high-resolution spectroscopic studies. We have shown before [6,7] that the strong tandem-mix of characterization and reactivity evaluation enables detailed insight into the influence of active phase formation on the activity. Here, we will show how these well-defined models can be used to obtain intrinsic kinetics of thiophene hydrodesulfurization.

Experimental

Model catalyst preparation $NiMo/SiO_2$ planar model catalysts consisting of a Si(100) wafer covered by a thin layer of SiO_2 as support were prepared by spin-coating as extensively described before [6,7]. Planar SiO_2 model supports were prepared by oxidizing a Si(100) single-crystal wafer in air at 1023 K for 24h. After calcination the wafers were cleaned in a H_2O_2/NH_4OH solution at 338 K. Subsequently, the surface was hydroxylated in boiling water for 20-30 min. As a typical example, we describe here the preparation of $NiMo/SiO_2$. A model silica support was spin-coated in nitrogen atmosphere at 2800 rpm with an aqueous solution containing $Ni(NO_3)_2.6H_2O$ (Merck, p.a.) and $(NH_4)_6Mo_7O_{24}.4H_2O$ (Merck, purity >97%) with an atomic ratio of 1:3, respectively. The concentration of the precursor solution was adjusted to result in the required metal loadings (2 Ni at/nm^2 and 6 Mo at/nm^2). Prior to characterization or catalytic testing, a model catalyst was sulfided at a rate of 5 K/min to 673 K + 1 h in a mixture of 10 vol.% H_2S in H_2.

Reactivity evaluation. Atmospheric thiophene HDS reactions were carried out in a batch-type reactor. After sulfidation, the reactor was flushed with the reactant mixture for 5 min at the desired reaction temperature. The reaction was then carried out in batch mode by closing the reactor inlet and outlet. This was marked as zero reaction time. After a reaction time of 1 h a gas-phase sample was taken from the reactor using a precision sampling gas syringe which was injected on a DB-1 column to analyze the main products: 1-butene, n-butane, trans-2-butene, cis-2-butene, thiophene and small amounts of C_1-C_3 hydrocarbons. The HDS activities are expressed as thiophene conversion after 1 h of reaction time and per 5 cm^2 of model catalyst. These values were corrected for blank thiophene conversion measured using an empty reactor. Between two experiments the catalyst was resulfided at 673 K for 1 h.

Results and Discussion

Because diffusion limitations are absent, the use of planar model catalysts offers great advantages in kinetic studies. Catalytic data were obtained at different temperatures varying the partial pressures of hydrogen, thiophene and H_2S, respectively. The kinetic data were analyzed considering both power-law and Langmuir-Hinshelwood (L-H) kinetics Between 573 and 673 K, positive orders in thiophene and hydrogen and moderately negative orders in H_2S were obtained. Moreover, while the reaction order in thiophene significantly decreased as the reaction temperature decreases, the order in hydrogen was nearly constant and close to 1. The lower reaction order of thiophene as compared to the reaction order in hydrogen clearly indicates that thiophene adsorbs much stronger than hydrogen. The negative order in H_2S indicates that the HDS reaction is inhibited by H_2S, probably due to competition with thiophene for sulfur-defect sites. The trends in the reaction orders are in agreement with the literature [8,9]. Heats of adsorption and activation energies can be derived once a kinetic model has been adopted. Several mechanisms and associated kinetic models for the hydrodesulfurization of thiophene have been proposed in the literature [10-14].

Although the precise mechanism of thiophene HDS reaction is still under debate, we have chosen an often-used simplified reaction network consisting of elementary steps, in which thiophene exclusively adsorbs on sulfur vacancies and H_2 adsorbs dissociatively on different sites to form butadiene (B) and H_2S. Assuming that the surface reaction between adsorbed thiophene and H_2 is the rate-limiting step and the H_2S adsorption takes place on sulfur vacancies exclusively, in competition with thiophene adsorption, the following Langmuir-Hinshelwood rate expression can be obtained:

$$r = \frac{k\ K_T\ K_{H_2}\ p_T\ p_{H_2}}{(1 + K_T\ p_T + K_{H_2S}\ p_{H_2S}/p_{H_2})\ (1 + K_{H_2}^{1/2}\ p_{H_2}^{1/2})^2}$$

where k is the rate constant of the rate-determining step and K_T, K_{H2} K_{H2S} are the adsorption constants of thiophene, H_2 and H_2S, respectively. **Figure 1** shows that the experimental data measured at constant thiophene and H_2S partial pressures and varying the H_2 partial pressure can be satisfactorily fitted using the L-H equation, giving an estimation of the adsorption equilibrium constants of hydrogen at different temperatures. The optimized values indicate that the adsorption equilibrium constant is statistically non-different from zero under our experimental conditions. Therefore, the hydrogen adsorption term in the denominator can be ignored. The optimized values for the adsorption equilibrium constants at 673 K of thiophene and H_2S are 3.5 ± 0.7 bar^{-1} and 28.9 ± 1.8, respectively. The intrinsic kinetic parameters, the activation energy of the rate determining step and the heat of adsorptions, can be derived by fitting the kinetic data measured at different temperatures using non-linear multivariable fittings. **Figure 2** shows the quality of this fitting and the intrinsic parameters are summarized in **Table 1**.

The estimated value for the heat of adsorption of thiophene and H_2S are –57.8 ± 10.9 kJ/mol and –117.1 ± 11.3 kJ/mol, respectively. A broad range of values for the heats of adsorption of both thiophene and H_2S have been reported in the literature [11,12]. Theoretical values vary between -62 and -137 kJ/mol, whereas the values for the heat of adsorption of H_2S vary between –75 and –93 kJ/mol [15].

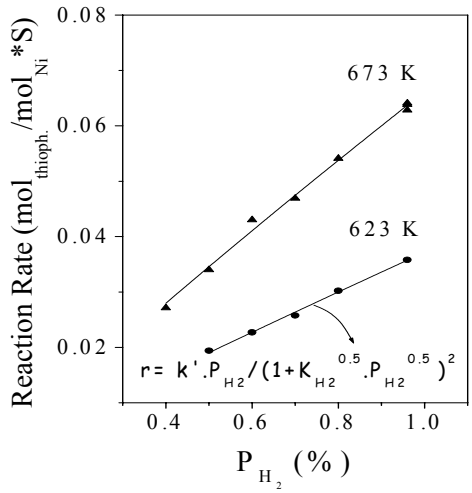

Figure 1. Dependence of the rate of thiophene HDS on the partial pressure of H_2 at different temperatures, along with data fit according to the *L-H* kinetic model. $P_{thioph.}$= 4 vol% and P_{H2S}= 0 vol%.

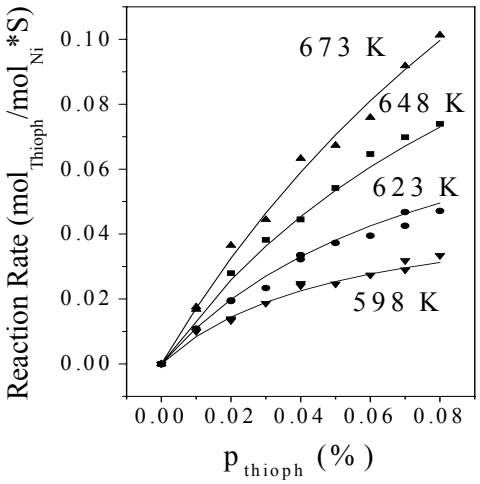

Figure 2. Dependence of the rate of thiophene HDS on the thiophene partial pressure along with a non-linear multi-variable fitting according to the L-H model. P_{H2}= 90 vol% and P_{H2S}= 0 vol%.

To summarize, the values of the heat of adsorption reported in this contribution indicate a relatively strong adsorption of both thiophene and H_2S.

The activation energy is about 85 kJ/mol, in line with theoretical calculations [15], which predict overall reaction enthalpies for C-S scission and sulfur removal of 70 kJ/mol and 73 kJ/mol, respectively. It is important to mention that much lower activation energies, usually obtained from Arrhenius plots, have been reported in the literature [16-18]. However, the activation energy derived from Arrhenius plots represents the apparent activation energy and not the real activation energy of the rate-determining step. Moreover, a decrease in apparent activation energy with increasing temperature has been frequently observed [16-18]. Such a decrease of the apparent activation energy has been often attributed to a decrease of the surface coverage of the reactants as temperature increases [17, 18]. The relation between apparent and real activation energy is:

$$E_{act}^{app} = E_{act}^{rds} + (1-\Theta_T^{\#})\cdot\Delta H_{ads}^{T} + (1-\Theta_H^{*})\cdot\Delta H_{ads}^{H_2} - \Theta_{H_2S}^{\#}.\Delta H_{ads}^{H_2S}$$

Table 1: **Intrinsic kinetic parameters obtained from non-linear multivariable fittings on a sulfided $NiMo/SiO_2$ model catalyst.**

Parameter	Value
k^0 ***(mol_{thioph}/mol_{Ni}*S)***	***0.0967***
E_{act}^{rds} ***(kJ/mol)***	***83.5***
K_{thioph}^{0} ***(bar^{-1})***	***8.7***
$-\Delta H_{ads}^{thioph}$ ***(kJ/mol)***	***-57.8***
$K_{H_2S}^{0}$ ***(bar^{-1})***	***138.9***
$-\Delta H_{ads}^{H_2S}$ ***(kJ/mol)***	***-117.1***

At high temperatures, the coverages become lower and in the limit of an empty surface, we find

$$E_{act}^{app} = E_{act}^{rds} + \Delta H_{ads}^{T} + \Delta H_{ads}^{H_2}$$

Therefore, a negative apparent activation energy may be obtained when the adsorption energies of thiophene and hydrogen are large enough. This then explains the *Volcano*-type curve recently reported by Borgna et al. [18].

Conclusion

Planar model catalysts can be applied to obtain intrinsic kinetic parameters for the relatively simple thiophene hydrodesulfurization reaction, offering an excellent opportunity to study reaction mechanism and kinetics without under diffusion-free conditions.

References

1. Gosselink, W., *CatTech*, **1998**, 4, 127.
2. Auto-Oil II Programme, Com. EU, Com 626, **2000**.
3. Prins, R., De Beer, V.H.J., Somorjai, G.A., *Catal. Rev. Sci. Eng.,* **1989**, 31, 1.
4. Topsøe, H., Clausen, B.S. Massoth, F.E., Hydrotreating catalysis, Springer, Berlin, **1996**.
5. Eijsbouts, S., *Appl. Catal. A,* **1997***,* 158, 53.
6. Kishan, G, Coulier, L., de Beer, V.H.J, van Veen, J.A.R., Niemantsverdriet, J.W, *J. Catal.,* **2000**, 196, 180.
7. Coulier, L., de Beer, V.H.J, van Veen, J.A.R., Niemantsverdriet, J.W, *J. Catal.,* **2001**, 197, 26.
8. Hensen, E.J.M., Brans, H.J.A., Lardinois, G.M.H.J., de Beer, V.H.J., van Veen J.A.R., van Santen, R.A., *J. Catal.,* **2000**, 192, 98.
9. Leliveld, R.G., van Dillen, A.J., Geus J.W, Koningsberger, D.C., *J. Catal.,* **1998**, 175, 108.
10. Massoth F.E., Chung, K.S., Proc. 7th ICC, Tokyo, **1980**, p. 629.
11. Satterfield, C.N., Roberts, G.W., *AIChE Journal,* **1968**, 14, 159.
12. H.C. Lee, Butt, J.B., *J. Catal.,* **1977**, 49, 320.
13. Vrinat, M.L., *Appl. Catal*., **1983**, 6, 137.
14. Girgis, M.J., Gates, B.C., *Ind. Eng. Chem. Res*., **1991**, 30, 2021.
15. Neurock, M., Van Santen, R.A., *J. Am. Chem. Soc.*, **1994**, 116, 4427.
16. Leglise, J., van Gestel J., Duchet, J.C., Symp. Adv. Hydrotreating Catalysts, ACS, Washington, 533, **1994**.
17. Hensen, E.J.M., Vissenberg, M.J., de Beer, V.H.J., van Veen J.A.R., Van Santen, R.A., *J. Catal.,* **1996**, 163, 429.
18. Borgna, A., Hensen, E.J.M., Coulier, L., de Croon, M.H.J.M., Schouten, J.C., van Veen, J.A.R. Niemantsverdriet, J.W., Submitted to *Cat. Lett.* (2003).

THIOPHENE HYDRODESULFURIZATION ACTIVITIES AND MICROSTRUCTURE OF SULFIDED NiW/ ɣ -Al_2O_3 CATALYSTS

Jinye Wang, Dadong Li, Hong Nie, Yahua Shi,

Zeming Jin, Xiaohong Kang

Research Institute of Petroleum Processing, SINOPEC

No. 18 Xueyuan Road, Beijing, China

Postal Code 100083

Introduction

From the recent environmental point of view, hydrotreatment of petroleum fractions to produce clean and high quality transportation fuels is becoming more and more important. Alumina supported Mo (W) catalysts, promoted by Co(Ni), are widely used in the oil industry for these purposes. There is growing need for improvements in the performance of these catalysts. There is a general agreement that the active Co–Mo–S phase is MoS_2 slab with Co atoms decorating the edge plane. The studies of the Ni–W system show that the structure of the Ni–W–S active phase is similar to that of Co–Mo–S phase[1]. It is well established that WS_2 is layered compound consisting of stacks of S–W–S layers held together by van der Waals interactions[1]. For bulk WS_2 compound, it is known that it has two kinds of structure, i.e. 2H-WS_2 and 3R-WS_2. Whether the tiny WS_2-like crystallite on the surface of sulfided NiW/ ɣ -Al_2O_3 catalyst is of 2H-WS_2 structure or 3R-WS_2 is unclear. For promoted catalysts, the atomic ratio of Ni/(Ni+W) is an important factor that affects the hydrodesulfurization(HDS) activity of NiW/ ɣ -Al_2O_3 catalyst. However, the optimal ratio is different in the literature. In this presentation we offer an evidence that the tiny WS_2-like crystallite is of 3R-WS_2 type structure. The reason is given for the explanation why the optimal ratio is 0.23 for catalysts sulfided at higher temperature.

Experimental

Catalyst preparation. ɣ -Al_2O_3 were used as support. Catalysts were prepared by wetness impregnation of support with an aqueous solution containing nickel nitrate and ammonium tungstate, followed by drying at 120 ℃ for 4 h and at 500 ℃ for 4 h. All the catalysts contained 0.19 mole atom per 100 gram of support with different Ni/(Ni+W) ratio. Catalysts were sulfided at 400 ℃ for 4 h in a flow of 15 % H_2S+H_2 before reaction and characterization. The bulk WS_2 were prepared by the sufidation of ammonium tungstate at the same conditions.

Catalytic activity. The activities of catalysts for thiophene hydrodesulfurization were measured by using a continuous flow reactor with on-line gas chromatography system. 1 gram of catalyst with 1 gram of silicon carbide particles were packed in the reactor. Catalysts were sulfided, and then feed with 25% thiophene+hexane at LHSV=6 h^{-1}, 275 ℃ and 310 ℃, a hydrogen pressure of 4.14 MPa, and H_2/oil ratio of 2000 v/v. Reaction rate constant *k* were calculated according to first-order kinetics[2].

Catalyst characterization. XRD patterns were collected on a Simens diffractometer D5005(Cu-K ɑ radiation). Extended X-ray adsorption fine structure(EXAFS) spectra of catalysts were recorded at Beijing Synchrotron Radiation Laboratory, Institute of High Energy Physics, Chinese Academy of Scienes. laser Raman spectra(LRS) were measured on Brucker RFS－100 instrument.

Results and Discussion

Preparation parameters, such as: metal loading; atomic Ni/(Ni+W) ratio; impregnation procedure; calcination temperature; activation procedure, may strongly affect the HDS activity of supported NiW/ ɣ -Al_2O_3 catalysts. At the general preparation conditions, atomic Ni/(Ni+W) ratio is one of the most important factors, since the addition of nickel has been one of the main routes to prepare improved catalysts. The ratio determines the amounts of active sites, promotion behaviors, and catalyst cost. The optimal Ni/(Ni+W) ratio for alumina supported Ni-W catalysts varied in the wide range from 0.375 to 0.6, and is much higher than the well-known optimal ratio of 0.23 ~0.33 for Co-Mo and Ni-Mo hydrotreating catalysts[3]. The results obtained in this work are arranged in figure 1, which gives the reaction rate constant of thiophene HDS vs the composition of NiW/ ɣ -Al_2O_3 catalysts.

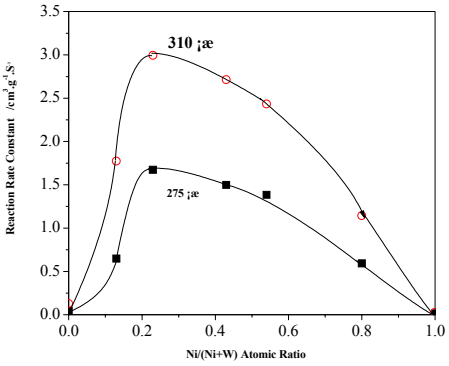

Figure 1. Thiophene HDS reactivity over sulfided NiW/ ɣ -Al_2O_3 catalysts.

The feature of the results is the marked increase in the catalytic activity with addition of of nickel atoms, the acitity increases significantly and pass through a maximum at Ni/(Ni+W) ratio of 0.23.

EXAFS was carried out to explain the above results. Figure 2 shows the Fourier transforms of tungsten EXAFS spectra for prepared WS_2 and the sulfided NiW/ ɣ -Al_2O_3 catalysts.

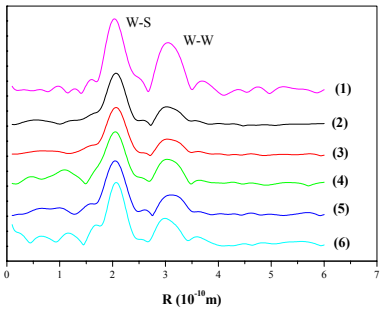

Figure 2. Fourier transforms of tungsten EXAFS spectra for sulfided NiW/ ɣ -Al_2O_3 catalysts. (1) prepared WS_2;(2) NiW-0.13*; (3) NiW-0.23; (4) NiW-0.43; (5) NiW-0.54; (6) NiW-0.80. *: the number denotes the atomic Ni/(Ni+W) ratio.

For each of the catalysts, there are two main peaks, which correspond to the first W-S and W-W coordinations in WS_2 crysallites, respectively. The highest intensities of the W-S and W-W

peaks were for the prepared WS_2, since the bulk WS_2 compound is complete cystal. EXAFS patterns of sulfided NiW/ ɣ -Al_2O_3 catalysts is very similar to the parrern of the prepared WS_2, which means that the state of W existence is WS_2-like crysallite.

The structural parameters resulting from the fit of the EXAFS data of sulfided catalysts are listed in table 1.

Table 1. Structural parameters of the W-S and W-W coordinations for sulfided NiW/ ɣ -Al_2O_3 catalysts.

Catalyst	W-S		W-W	
	N_{W-S}	R_{W-S} (nm)	N_{W-W}	R_{W-W} (nm)
NiW-0.13	4.90	0.241	1.97	0.315
NiW-0.23	4.58	0.241	1.72	0.315
NiW-0.43	5.95	0.241	2.43	0.315
NiW-0.54	5.62	0.241	2.02	0.315
NiW-0.80	4.79	0.241	2.45	0.315

As discussed afterwards, W-S coordinations of bulk WS_2 compound is 6.0. W-S coordinations of all sulfided NiW/ ɣ -Al_2O_3 catalyst are smaller than 6.0, which means that the WS_2 crystallite on the surface of catalysts is not complete one. The W-S and W-W coordinations of sulfided NiW-0.23 catalyst are the smallest of all sulfided NiW/ ɣ -Al_2O_3 catalyst, which implies that the size of WS_2-like crystallite is the smallest.

Being similar to Co-Mo-S model, Ni-W-S phase is WS_2-like structures with the Ni atoms located at edges(or corners) of WS_2-like crystallite.The smaller the WS_2-like crystallite, the more the edges(or corners) of WS_2-like crystallite for Ni atoms to occupy. The smaller WS_2-like crystallites on the surface of Catalysts is benefical to the formation of Ni-W-S phases. Thus, the sulfided NiW-0.23 catalyst with smaller WS_2-like crystallite, has higher HDS activity.

The loadings used in industrial applications are usually governed by the desire to achieve as a high activity as possible with as small amounts of the expensive metals as possible[1]. The tungsten loading used is typically in the range of 15~23 wt% W. This corresponds to approximately a monolayer coverage for an alumina support with a typical surface area of about 230 m^2/g. The tungsten loadings in this work is all less than a monolayer coverage. Thus, tiny WS_2-like crystallite on the surface of sulfided NiW/ ɣ -Al_2O_3 can not be detected by XRD method, as only bulk compound of crystallite can be detected by the method. laser Raman spectroscopy can be used for the investigation of bulk compound as well as dispersed phases[4]. By combination of these two methods, the microstructure of WS_2-like crystallite on the surface of sulfided NiW/ ɣ -Al_2O_3 can also be identified. The Raman spectra of commercial WS_2、prepared WS_2 and sulfided NiW/ ɣ -Al_2O_3 catalyst were shown in figure 3.

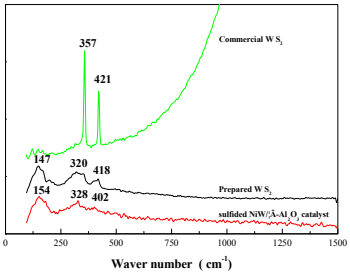

Figure 3. Raman spectra of the sulfided NiW/ ɣ -Al_2O_3 catalyst and bulk WS_2.

For bulk commercial WS_2, two peaks at 357 and 421 cm^{-1} attribute to the typical peaks of 2H-WS_2. Thus, commercial WS_2 exists as 2H-WS_2 structure. 2H-WS_2 is an example of a six-fold coordinated layer structure in which the coordination is not octahedral[5]. The crystal is hexagonal with the elongated bimolecular units: a_0=0.318 nm, c_0=1.25 nm.

The sulfur atoms around the metallic atom are at the corners of right equilateral trigonal prisms which share vertical edges with one another to build up WS_2 layers normal to the c_0 axis. The crystal is built up by repeating these complete layers one above another according to the alternating requirements of hexagonal close-packing. Parallel to c_0 axis, the sulfur anion repeats in the order of AA, BB, AA……. Because the spectra of commercial WS_2 is different from others, prepared WS_2 and sulfided NiW/ ɣ -Al_2O_3. catalyst are not of 2H-WS_2 structure.

The structure of prepared bulk WS_2 can be identified by XRD. Its XRD pattern was given in figure 4.

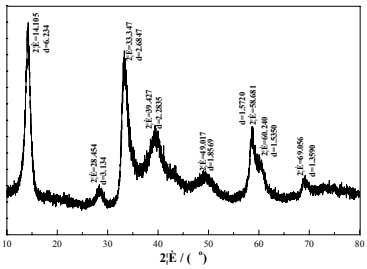

Figure 4. XRD patterns of prepared WS_2.

It is found that prepared WS_2 is mainly in the state of 3R-WS_2 structure by compared data shown in figure 2 with data from the card 35-651 and card 8-237 of JCPDS(the Joint Committee on Powder Diffraction Standards). The form of 3R-WS_2 is rhombohedral and bears the same kind of relation to hexagonal MoS_2. However, the sulfur anion repeats in the order of AA, BB, CC, AA ……. Its trimolecular hexagonal cell has the dimensions[5]:

$$a_0' = 0318 \text{ nm}, \quad c_0' = 1.875 \text{ nm}.$$

As shown in figure 1, the Raman spctra of prepared WS_2 is very similar to that of sulfided NiW/ ɣ -Al_2O_3 catalyst. It is inferred that tiny WS_2-like crystallite on the surface of sulfided NiW/ ɣ -Al_2O_3 catalyst is also mainly in the state of 3R-WS_2 structure, as the two samples sulfided at the same conditions. The tiny WS_2-like crystallite on the surface is incomplete crystal, for it just contains several units.

Acknowledgment. This work was supported by the Key Basic Research Program of Science and Technology of China(Grant No. G2000048003).

References

1. Topsøe H, Clausen B S, and Massoth F E. Hydrotreating Catalysis, eds. Anderson J R and Boudart M, Springer, Berlin, **1996**
2. Choong Hyon Kim, Wang Lae Yoon, In Chul lee et al. *Appl Catal A: General*, **1996**, *144*, 159
3. Vradman L and Landau M V. *Catal lett*, **2001**, *77*, 47
4 Payen E, Kasztelan S, Grimblot J, et al. *Catal Today,* **1988**, *4*, 57
5 Wyckoff Ralph W G. Crystal Structures, Second Edition, Volume I. a Division of John Wiley, New York, London, Sydney, **1963**

ELUCIDATION OF SULFUR BEHAVIOR FOR MOLYBDENUM SULFIDE CATALYSTS SUPPORTED ON TITANIA USING ^{35}S TRACER METHODS

Atsushi Ishihara, Dahong Wang, Weihua Qian, Toshiaki Kabe

Tokyo University of Agriculture and Technology
2-24-16 Nakacho, Koganei, Tokyo 184-8588, Japan

Introduction

The need for better hydrodesulfurization catalysts to fulfill the more strict environmental restrictions imposed on the sulfur content of transport fuels has prompted the researchers in the field to look for more active and selective catalyst formulations.[1] Several studies suggested that changing the support into titania[2] or alumina-titania mixed oxides[3] would show promising results. However, despite all the previous studies, no explanation for the substantial difference in HDS activity between alumina- and titania-supported catalysts has yet been elucidated.

In the previous work, the authors showed that the sulfidation states and behavior of sulfur on working hydrodesulfurization catalysts could be determined using ^{35}S tracer methods.[4-8] The object of the present work is to determine the sulfur behavior for TiO_2-supproted molybdenum catalysts using ^{35}S tracer methods. A ^{35}S radioisotope pulse tracer method using ^{35}S-labeled H_2S, which can exactly determine the sulfidation state of the catalyst,[4,7] was used to investigate the sulfidation and reduction states of Mo/TiO_2 catalyst. Moreover, a ^{35}S radioisotope tracer method using ^{35}S-labeled dibenzothiophene ([^{35}S]DBT), which can give information about the behavior of sulfur on the working catalyst,[4-8] was used to elucidate the sulfur mobility on the sulfided Mo/TiO_2 catalyst under the reaction conditions.

Experimental

Catalysts. TiO_2 support used in this study is a reference catalyst with a surface area of 70 m^2/g supplied from the Catalysis Society of Japan. The Mo/TiO_2 catalysts were prepared by the incipient wetness impregnation of TiO_2 support with an aqueous solution of ammonium heptamolybdate as required. This was followed by drying at 120℃ for 3h and calcination in air at 500℃ for 3h. The catalysts were denoted as MT(2), MT(3.5), MT(5), MT(6), and MT(12) where the values in parenthses represent MoO_3 contents, corresponding to 2.0, 3.5, 5.0, 6.0, 12.3 wt% MoO_3, respectively.

Sulfidation of Mo/TiO_2 catalyst using ^{35}S-labeled H_2S. A ^{35}S-radioisotope pulse sulfiding method was developed to investigate the sulfidation process. The pulse tracer apparatus is reported elsewhere.[7] A pulse of 30 vol% [^{35}S]H_2S in hydrogen was introduced in the fixed-bed reactor with a gas sampler (2.46 ml) every 10 min under N_2 carrier gas (0.5 MPa, 40 ml min^{-1}). The radioactivity of unreacted [^{35}S]H_2S absorbed by a commercially available basic scintillation solvent every 10 min was measured by a liquid scintillation counter (LSC).

HDS of [^{35}S]DBT. The HDS experiments were carried out with a fixed-bed reactor. The cata1yst was presulfided with a mixture of 5 vol% H_2S in H_2 flowing at 5 l h^{-1}, 0.1 MPa. After presulfiding, the reactor was cooled to room temperature and then pressurized with hydrogen. A decalin solution of [^{32}S]DBT was fed into the reactor at the reaction temperature by a high-pressure liquid pump. Typical reaction conditions were as follows: H_2 flow rate 25 1 h^{-1}, WHSV 28 h^{-1}, reaction pressure 5 MPa, concentration of DBT in decalin 1.0 wt%. The liquid products were collected every 15 min and analyzed by gas chromatography with an FID detector and a commercial capi11ary column. The radioactivity was measured by LSC. The feed was changed from [^{32}S]DBT to [^{35}S]DBT, neat decalin, [^{32}S]DBT successively after a reaction in each period reached a steady state. A typical operation procedure using [^{35}S]DBT radioisotope tracer method has been described in detail elsewhere.[4-8]

Results and Discussion

Sulfidation of Mo/TiO_2 catalyst using ^{35}S-labeled H_2S. **Figure 1** shows the change in radioactivity of [^{35}S]H_2S eluted during the sulfidation of MT(2) and MT(6) catalysts at various temperatures. For each catalyst, the radioactivity of unreacted [^{35}S]H_2S at 100 and 200℃ approached a constant value, equal to the radioactivity of the pulse introduced, while at 300 and 400℃, [^{35}S]H_2S seemed to accumulate on the catalysts slowly; thus the radioactivity of unreacted [^{35}S]H_2S found it difficult to approach the radioactivity in the introduced pulse. The amount of sulfur incorporated into the catalyst could be calculated by subtracting the radioactivity of released [^{35}S]H_2S from the total radioactivity introduced (the shaded area).[7] For MT(2) and MT(6) catalysts, the total sulfur were calculated to be 9.7 and 29.1 mg-S/g-cat respectively when all MoO_3 species were present as MoS_2. It is reported in our previous study[7] that MoO_3 supported on Al_2O_3 can be almost sulfided to MoS_2 at 400℃. Therefore, it is supposed here that at 400℃ all MoO_3 species on TiO_2 support were present as MoS_2, and that a part of TiO_2 support could still be sulfided when MoO_3 was supported on it. Such results suggested that the sulfide TiS_2 should play an important role on the HDS activity under the reaction conditions.

Behavior of sulfur on the sulfided Mo/TiO_2 catalyst. HDS of [^{35}S]DBT was performed to investigate the behavior of sulfur on MT(6) catalyst in the steady state. **Figure 2** shows a typical operation procedure of ^{35}S tracer method. The HDS reaction of [^{35}S]DBT was carried out on a sulfided MT(6) catalyst at 360℃. Initially, a decalin solution of 1wt% [^{32}S]DBT was pumped into the reactor until the conversion of DBT became constant. A decalin solution of 1wt% [^{35}S]DBT was then substituted for the [^{32}S]DBT and reacted until the formation amount of [^{35}S]H_2S became constant. After [^{35}S]DBT was introduced, the radioactivity of unreacted [^{35}S]DBT in the liquid product increased and approached a steady state immediately. However, it took ca. 75 min to achieve a steady state in the radioactivity of [^{35}S]H_2S produced. In order to determine the behaviour of sulfur more accurately, the [^{35}S]DBT solution was subsequently replaced by decalin solvent. It was observed that a portion of ^{35}S, which is represented by the shaded area A in **Figure 2**,

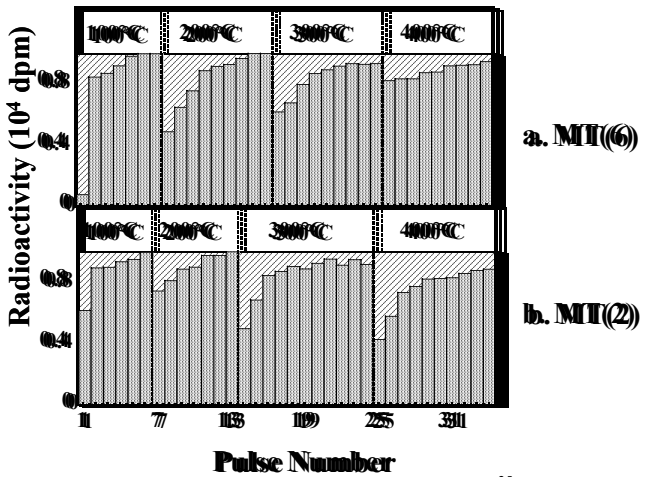

Figure 1 Sulfidation of 6%MoO_3/TiO_2 catalyst with [^{35}S]H_2S pulse at various temperatures.

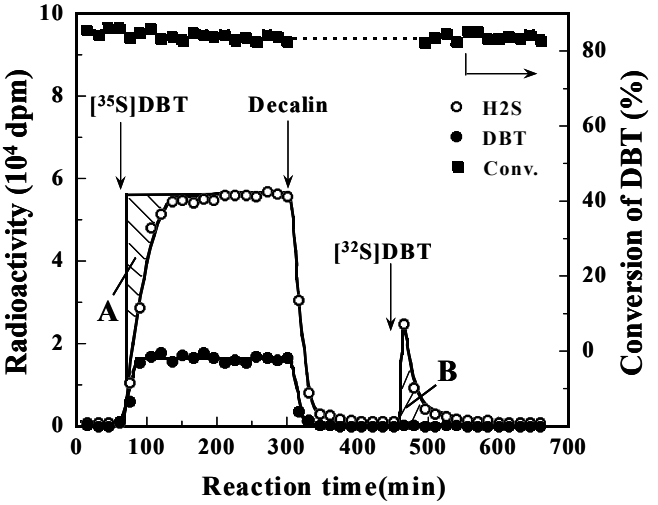

Figure 2. Changes in Radioactivities of Unreacted [^{35}S]DBT and Formed [^{35}S]H_2S and DBT Conversion with Reaction Time (360℃)

Table 1. **Amount of sulfur, release constant of [^{35}S]H_2S and HDS activity on MT(6), MA(6) catalysts and TiO_2 support**

Catalyst	Temp. (℃)	Conv. (%)	S_{CHB} (%)	S_0 (mg g-cat^{-1})	k_{RE} (10^{-2} min^{-1})	r_{HDS} (mg min^{-1} g-cat^{-1})
MT(6)	360	83.2	44.4	6.51	8.93	0.68
MA(6)	360	36.9	10.6	5.98	4.61	0.30
TiO_2	390	19.6	43.7	0.52	—	0.16

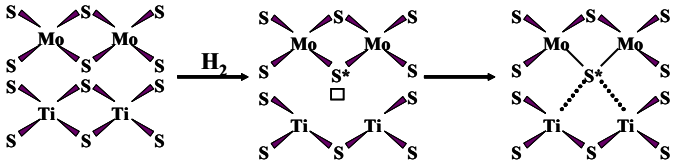

Figure 3. TiMoS phase structure for a Mo/TiO_2 catalyst

remained on the catalyst. When decalin and H_2 were used to purge the catalyst, less release of [^{35}S]H_2S was detected. When the reactant solution was replaced by [^{32}S]DBT again, a portion of ^{35}S can be released again as [^{35}S]H_2S, as shown in **Figure 2** (shaded area B). This portion of ^{35}S was approximately equal to shaded area A, which represented the total amount of labile sulfur on the catalyst under this reaction condition. According to a method reported in reference 17, the amount of labile sulfur can be calculated from the total radioactivity of the [^{35}S]H_2S released after [^{32}S]DBT was reintroduced, *i.e.*, shaded area B. To discuss the release process of [^{35}S]H_2S more accurately, the rate constant of [^{35}S]H_2S release from ^{35}S-labeled catalyst was determined. As reported previously,[8] the release of [^{35}S]H_2S in the range of area B shown in **Figure 2** can be explained with respect to a first-order reaction and the rate constant of [^{35}S]H_2S release, k_{RE} was determined.

In order to understand the promoting effect of TiO_2 support on Mo species under reaction conditions, the amount of labile sulfur (S_0) and the rate constant of H_2S release (k_{RE}) for 6% MoO_3/TiO_2, 6% MoO_3/Al_2O_3[8] and TiO_2 support[4] are given in **Table 1**. TiO_2 support presents less labile sulfur, although it was active in HDS of DBT, which clearly indicates that the HDS mechanism on TiO_2 support is different from that on Mo-based catalyst. It is suggested that the sulfur vacancies on the reduced sulfided TiO_2 support would act as the active sites for HDS reaction without sulfur accumulation.[4] Compared with the Mo/Al_2O_3 catalyst, the Mo/TiO_2 catalyst shows a little higher amount of labile sulfur (S_o); it is most important that about 2 times higher rate constant of H_2S release (k_{RE}) is obtained on the Mo/TiO_2 catalyst. The amount of labile sulfur (S_o) represents the number of active sites and the rate constant of H_2S release (k_{RE}) represents the mobility of active sites on the surface of the catalyst. Therefore, the results indicate that the presence of TiO_2 makes the sulfur on the sulfided Mo/TiO_2 catalyst more mobile rather than increasing the number of the active sites. In a recent study, we have proposed that the promoting effect of cobalt for molybdenum catalyst was due to increased mobility of the sulfur in the so-called "CoMoS" phase where the strength of the Mo-S bond was considered to be weakened.[1] Similarly, the promoting effect of TiO_2 on Mo catalyst is supposed to bring about the decrease in the strength of Mo-S bond, since the sulfur mobility on the catalyst is dependent on the bond strength of the metal sulfide. The strength of the Mo-S bond on TiO_2-supported catalyst is assumed to be weaker than that on Al_2O_3-supported catalyst. As shown in **Figure 3**, under H_2 atmosphere the sulfided Ti species can be reduced to Ti^{3+} and sulfur vacancies with electrons trapped in are formed. Sulfur in MoS_2 coordinates the sulfur vacancies in the sulfided Ti species and the so-called "TiMoS" pahse is generated. The injection of electrons from Ti to Mo through sulfur will decrease the Mo-S bond energy. Therefore, it is suggested that the role of TiO_2 in Mo catalyst is not only to act as a conventional support but also to act as an electronic promoter of the molybdenum sulfide phase.

Conclusions

When MoO_3 were supported on TiO_2 support, the sulfidation of TiO_2 support would also occur. Compared with Mo/Al_2O_3 catalyst, Mo/TiO_2 catalyst shows a little higher amount of labile sulfur (S_o) and about 2 times higher release rate constant of H_2S (k_{RE}). It was suggested that TiMoS phase structure generated for a Mo/TiO_2 catalyst weakens Mo-S bond to increase the rate of H_2S release and the HDS activity.

Acknowledgement

This work has been entrusted by the New Energy and Industrial Technology Development Organization under a subsidy of the Ministry of Economy, Trade and Industry.

References

1. Kabe, T.; Ishihara, A.; W. Qian, Hydrodesulfurization and Hydrodenitrogenation, Kodansha, Tokyo, and Wiley-VCH, New York, 1999.

2) Ramirez, J.; Fuentes, S.; Diaz, G.; Vrinat, M.; Breysse, M.; Lacroix, M. *Appl. Catal.,* **1989**, *52*, 211.

3) Yoshinaka, S.; Segawa, K., *Catal. Today*, **1998**, *45*, 293.

4) D. H. Wang, W. Qian, A. Ishihara, T. Kabe, *J. Catal.*, **2001**, *203*, 322-328.

5) Ishihara, A.; Lee, J.; Franck, D.; Higashi, R.; Wang, A.; Qian, W.; Kabe, T., *J. Catal.,* **2003** in press.

6) Kabe, T. ; Qian, W. ; Ishihara, A. , *J. Phys. Chem.,* **1994**, *98*, 912.

7) Kabe, T.; Qian, W.; Tanihata, K. ; Ishihara, A. ; Godo, M., *J. Chem. Soc. Faraday Trans.,* **1997**, *93*, 3709.

8) Qian, W. ; Zhang, Q. ; Okoshi, Y. ; Ishihara, A.; Kabe, T., *J. Chem. Soc. Faraday Trans.*, **1997**, *93*, 1821.

LOW-TEMPERATURE HYDROGENATION OF AROMATICS OVER NOBLE METAL CATALYSTS IN THE PRESENCE OF SULFUR COMPOUND

J.Abe[1,2] , *X.Ma*[1], *C.Song*[1*]
(1) Clean Fuels and Catalysis Program, The Energy Institute, and Department of Energy and Geo-Environmental Engineering Pennsylvania State University, 209 Academic Projects Building, University Park, PA, 16802
*E-mail: csong@psu.edu
(2) JGC Corporation, Technology Development Department 2205 Narita-cho, Oarai-machi, Ibaraki Pref. 311-1313, Japan
E-mail: abe.jun@jgc.co.jp

Introduction

In recent years, there is a growing interest in the demand of high quality transportation fuels with lower contents of sulfur and aromatics. In order to reduce the aromatics and to raise the cetane number of diesel fuel, deep hydrogenation of diesel fuel may become necessary in the future. Deep hydrogenation of jet fuel feedstock is also important for producing advanced thermally stable jet fuels.

Typical conventional hydroprocessing for diesel is operated at 330-360 □, and typical catalysts are Co-Mo and Ni-Mo supported on alumina. Since the hydrogenation of aromatics is highly exothermic, there is an equilibrium limitation for the hydrogenation at high temperature. On the other hand, conventional Co-Mo and Ni-Mo catalysts have to be used at higher temperature due to relatively low activity of them at low temperature. Noble metal catalysts are potential candidates for deep hydrogenation of diesel fuel at low temperature because of their high hydrogenation activity. However, it is well known that the noble metal catalysts are easily deactivated by sulfur compounds. Therefore, a two-stage hydroprocessing is adopted for deep hydrogenation. At the first stage, sulfur content is reduced to less than 5 ppmw by ultra deep hydrodesulfurization, and after hydrogen sulfide stripping, deep hydrogenation of aromatics is conducted in the second stage by using noble metal catalysts. The reduction of the sulfur contents in diesel fuel to less than 5 ppmw by hydrodesulfurization process is difficult and requires large investment.[1]

Some approaches to developing sulfur-resistant hydrogenation catalysts have been reported.[2-5] At Penn State, we have been exploring the noble metal catalysts with higher sulfur-resistance.[6-13] We reported Pd catalysts supported on zeolites tend to show higher tolerance in the batch tests. In the present study, a continuous flow fixed-bed reactor was used for the hydrogenation of tetralin to decalins in the presence of benzothiophene as a model reaction for saturation of aromatics in diesel and jet fuel feedstock. As noble metal catalysts, Pd and Pt supported on alumina, titania and some zeolites were prepared and examined.

Experimental

Preparation of catalysts. Pt supported on alumina and Y zeolite (HY) catalysts were prepared by incipient wetness impregnation of an aqueous solution of $H_2PtCl_6 \cdot xH_2O$ (Aldrich) with a nominal metal concentration of 2 wt %. Pd catalysts were prepared by incipient wetness impregnation of either $PdCl_2$ (Aldrich) dissolved in dilute hydrochloric acid (sufficient to form soluble $PdCl_4^{2-}$) or $(CH_3CO_2)_2Pd$ (Aldrich) dissolved in acetone with a nominal metal concentration of 2wt %. The details for metal salts and type of supports are listed in Table 1.

After drying, the catalysts were calcined in air at 450 □ for 3 hrs. Before use, the catalysts were reduced in a continuous flow reactor at 350□□ under H_2 flow at atmospheric pressure for 1 hr.

Reaction system and procedure. Catalytic reaction tests were conducted at 220□ and 1,000 psig (7 MPa) hydrogen pressure in a continuous-flow fixed-bed stainless steel tubular reactor. In the fixed bed, 3.3 ml of catalysts (2.0 - 0.5mm particles) were loaded, and α-alumina was loaded over and under the catalyst.

Feed used in the present study is 20 wt % tetralin (1,2,3,4-tetrahydronaphthalene, Aldrich 99%) in hexadecane (Aldrich, 99+%, anhydrous) in the absence or in the presence of benzothiophene (BT, Aldrich, 99%) with 500 ppmw based on sulfur. The liquid feed space velocity LHSV = 2.0 hr^{-1}, and H_2/oil ratio is 800 Nml-gas/ml-liquid. The liquid product samples were collected periodically and analyzed quantitatively by GC-FID (HP 5890).

Results and Discussion

Table 2 and Figure 1 show the results for the hydrogenation of tetralin over various supported Pd and Pt catalysts in the presence of BT. The hydrogenation activity of Pt catalysts supported on alumina and Y zeolite was drastically decreased in the first three hours. The activity of Pd catalyst supported on alumina also declined. However, through comparison of these catalysts, Pd catalysts supported on titania and zeolites appear to be relatively more resistant to sulfur poisoning and more stable than the other catalysts after sulfur poisoning.

However, as can be seen from Table 2, the loading density of Pd supported on titania is higher than that of other catalysts. The advantages of zeolite-supported Pd catalysts are more apparent in terms of higher conversion event at lower catalyst loading compared to the case with alumina-supported Pd catalyst.

Table 1. Properties of supports and the supported Pd and Pt catalysts

Catalyst	Support Type	Support Code	Surface Area m^2/g	SiO_2/Al_2O_3 Molar ratio	Precursor Metal Salt	Metal Loading Wt%
Pd/HY(5)	Y zeolite	CBV600	660	5.2	$(CH_3CO_2)_2Pd$	2.0
Pd/HY(46)	Y zeolite	CBV740	840	46	$(CH_3CO_2)_2Pd$	2.0
Pd/HM	Mordenite	CBV30A	512	37.5	$(CH_3CO_2)_2Pd$	2.0
Pd/MCM-41	Al-MCM-41	Al-MCM41(50)	1289	50	$PdCl_2$	2.0
Pd/Al_2O_3	γ-Alumina	LaRoche	155	Not applicable	$(CH_3CO_2)_2Pd$	2.0
Pd/TiO_2	Titania	Degussa P25	71	Not applicable	$PdCl_2$	2.0
Pt/HY(5)	Y zeolite	CBV600	660	5.2	$H_2PtCl_6 \cdot xH_2O$	2.0
Pt/Al_2O_3	γ-Alumina	LaRoche	155	Not applicable	$H_2PtCl_6 \cdot xH_2O$	2.0

Table 2. Hydrogenation of tetalin over supported Pt and Pd catalysts at 220 °C in a flow reactor

Catalysts	Pt/Al_2O_3				Pt/HY(5)			Pd/Al_2O_3			Pd/HY(5)		
Loading density, g/ml	0.550				0.486			0.520			0.474		
Sulfur content, ppmw	0	500			0	500		0	500		500		
Reaction time, hrs	4	2	4	6	4	2	4	4	2	4	2	4	6
S / Metal, by atom	n/a	0.89	1.78	2.67	n/a	1.01	2.02	n/a	0.51	1.03	0.56	1.13	1.69
Conversion, %	98.2	88.5	30.5	5.7	99.4	52.7	5.3	94.7	78.7	5.3	75.7	55.5	48.3

Catalysts	Pd/HY(46)			Pd/TiO2				Pd/MCM-41			Pd/HM		
Loading density, g/ml	0.363			1.010				0.345			0.473		
Sulfur content, ppmw	500			500				500			500		
Reaction time, hrs	2	4	6	2	4	6	7	2	4	6	2	4	6
S / Metal, by atom	0.736	1.47	2.21	0.26	0.53	0.79	0.93	0.78	1.55	2.33	0.57	1.13	1.70
Conversion, %	67.4	45.2	46.4	91.3	88.9	36.4	20.7	39.9	19.5	19.1	59.4	54.2	42.6

Reactions were conducted at 220 and 1,000psig hydrogen pressure in a continuous fixed bed stainless steel tubular reactor.

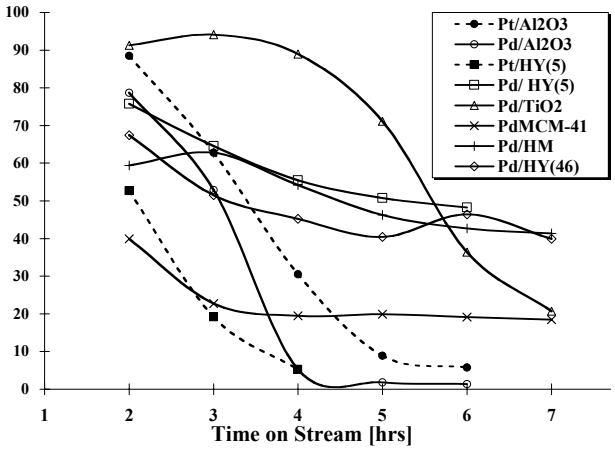

Figure 1. Hydrogenation of tetralin over noble metal catalysts at 220 and 1,000 psig of hydrogen pressure in the presence of 500 ppm sulfur.

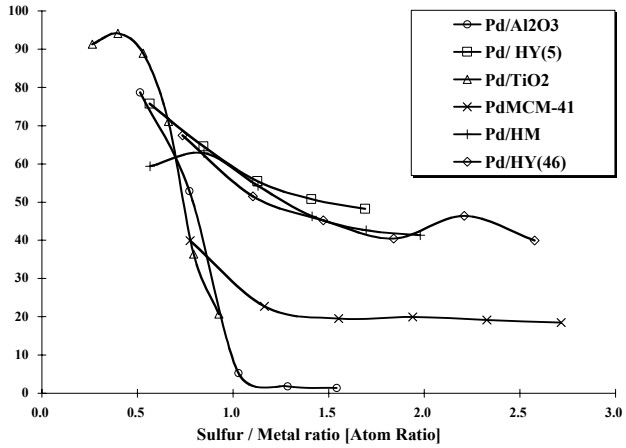

Figure 2. The hydrogenation activity over Pd catalysts as a function of the atomic ratio of sulfur and metal.

Figure 2 compares the hydrogenation activity versus the atomic ratio of sulfur to metal loading on the support. Pd catalysts supported on Y zeolites, Mordenite and MCM-41 are more sulfur-resistant and stable than other Pd catalysts when the sulfur-to-metal ratio is higher than 1.0.

Addition of BT into the feed decreased the hydrogenation activity of all the noble metal catalysts. However, it appears that zeolite supporters improve significantly the sulfur resistance of Pd catalysts. In other words, zeolite-supported Pd catalysts are clearly superior to zeolite-supported Pt catalysts under the conditions used.

For the Pd catalysts supported on zeolites, the difference between Y zeolite and mordenite supported cases in Figure 2 is not very large. However, they both are superior to the mesoporous aluminosilicate molecular sieve Al-MCM-41.

After the hydrogenation conversion decreased to 50% on for Y zeolite supported Pd catalyst, when the feed with sulfur was changed to the feed without sulfur it was observed that the hydrogenation conversion was recovered in a few hours, indicating the deactivation of the Y zeolite supported Pd catalyst by sulfur poison is reversible and recoverable.

These flow-reactor results support our proposed design concept[9,10] of sulfur-resistant noble-metal catalysts, which is based on shape selective exclusion with molecular sieve structure, hydrogen spillover and two types of sulfur resistance that was developed based on our earlier batch tests.[6-8]

Conclusions

On the basis of the hydrogenation of tetralin over different catalysts in the presence of benzothiophene, 1) Pd catalysts show less sensitive to sulfur compounds than Pt catalysts; 2) Pd and Pt supported on zeolites are superior to Pd and Pt supported on alumina and titania in their sulfur-resistant performance; 3) The deactivation

of Pd catalysts supported on zeolites by the sulfur compound is not permanent, but reversible.

Acknowledgment

We thank our colleagues in the Clean Fuels and Catalysis Program of Energy Institute at PSU (particularly Dr. Xiaochun Xu, Dr. S. Velu, Dr. Jian Zheng) for providing support samples and for assistance in the laboratory. CS is grateful to US AFOSR for providing partial financial support to CS for project work in this area, and to Prof. Harold Schobert for helpful discussions on aromatics hydrogenation related to jet fuel research.

References

(1) B. H. Cooper, B. B.L. Donnis, *Appl. Catal. A*, **1996***, 137,* 203.
(2) A. Corma, A. Martinez, V.M. Soria, *J of Catal,* **1997**, 169, 480.
(3) Y.Yoshimura, H. Yasuda, T. Sato, N. Kijima, T. Kameoka *Applied Catalysis,* **2001**, 207, 303.
(4) V.L. Barrio, P.L. Arias, J.F. Cambra, M.B. Guemez, B. Pawelec, J.L.G. Fierro, *Fuel,* **2003**, 82, 501.
(5) K.C. Park, D.J. Yim, S.K. Ihm, *Catalysis Today,* **2002**, 74, 281.
(6) S. D. Lin, C. Song, *Catalysis Today,* **1996**, 31, 93.
(7) K. M. Reddy, C. Song, *Catalysis Today,* **1996**, 31, 137.
(8) C. Song, A.D. Schmitz, *Energy & Fuel,* **1997**, 11 (3), 657.
(9) C. Song, *Chemtech,* **1999**, 29 (3), 26
(10) C. Song, *Am. Chem. Soc. Symp. Ser.,* **2000**. 738, 381.
(11) J. Zheng, M. Sprague, C. Song . *Am. Chem. Soc. Div. Petrol. Chem. Prep.,* **2002**, 47 (2), 100.
(12) M. Sprague, J. Zheng,, and C. Song. Am. Chem. Soc. Div. Petrol. Chem. Prep., **2002**, 47 (2), 103.
(13) C. Song and X. Ma. *Applied Catalysis B: Environmental*, **2003**, 41 (1-2), 207.

PERCEPTION ON THE NATURE OF THE PERFORMANCE OF NI-BASED CATALYST FOR DIESEL CLEANING

Qi Sun, Wayne Turbeville, Jurgen R. Ladebeck

Süd-Chemie Inc, P. O. Box 32370, Louisville, KY 40232, USA, e-mail: qsun@sud-chemieinc.com

Introduction

Catalytic deep hydrogenation of aromatics and desulfurization of diesel is playing a more and more important role in providing environment-friendly fuels. Supported noble metal catalysts on various supports have been proved being superior catalysts for low-temperature hydrogenation of aromatic [1,2] and hydro-desulfurization at high temperatures [3]. However, they are sensitive to sulfur. A trace of them can poison the catalysts. High content Ni/SiO_2 or Ni/Al_2O_3 are practical catalysts to hydrogenate aromatic and remove tough sulfur species from diesel and other fuel oils. In the present work, the performances of different Ni-based catalysts were described and the nature of hydrogenation of aromatic and desulfurization was investigated.

Experimental

Catalyst: Ni/SiO_2 and Ni/Al_2O_3 catalyst with Ni content of 60% were prepared by co-precipitation method, followed by calcinations and extrusion.

Catalytic test: The catalytic performance of Ni/SiO_2 and Ni/Al_2O_3 catalysts for aromatic hydrogenation and desulfurizastion were tested on a pressurized fixed-bed continuous flowing stainless steel reactor (i.d. 1") packed with extruded catalyst (diameter of 1/16'). The test condition simulated industrial operating process: LHSV of $3h^{-1}$; pressure of 450psig and temperature of 190°C. An excess of H_2 was co-supplied to the reactor with diesel feedstock, which consists of 25.5% of aromatic, 4.2% of poly-aromatic and 55ppm of sulfur organic (benzothiophene, dibenzothiophene etc sulfur poly-aromatic).

Product analysis: The quantitative analysis of aromatic and sulfur in the products were carried out using an aromatic analyzer with FID detector and sulfur analyzer (ANTEK 7400), respectively. A HP 6890 GC with FID detector was used to detect cracking hydrocarbon product in the gas phase.

Results and Discussion

Ni/SiO_2 and Ni/Al_2O_3 show excellent activity for aromatic hydrogenation using a sulfur-free feed. 100% aromatic conversion can be achieved on these two catalysts at desired temperatures. However, the S-containing feed leads to the deactivation of the catalysts because the sulfur compounds may deposit on the catalyst surface and poison the active sites. With the time on stream, aromatic conversion decreases (or aromatic leakage increases) and sulfur leakage in the liquid product increases.

Hydrogenation activity relates to the Ni particle size, but sulfur tolerance depends on several different factors. High Ni specific area in the Ni/Al_2O_3 and Ni/SiO_2 catalysts is crucial for a high performance catalyst. For the same type Ni-based catalyst, sulfur tolerance increases with the increase of Ni specific surface area. A linear relationship between Ni specific surface area and sulfur tolerance was observed, as shown in Figure 1. However, the linear relationships for different Ni-based catalyst, i.e. Ni/SiO_2 and Ni/Al_2O_3, show significant difference. It is not the same type of linear relationship between sulfur tolerance and Ni surface area of different type catalysts (Ni/SiO_2 and Ni/Al_2O_3), indicating different intrinsic catalytic capacity per unit Ni surface on Ni/SiO_2 and Ni/Al_2O_3 catalysts. The results strongly demonstrate that, except for Ni surface area, the support has significant effect on the performance of aromatic hydrogenation and sulfur tolerance.

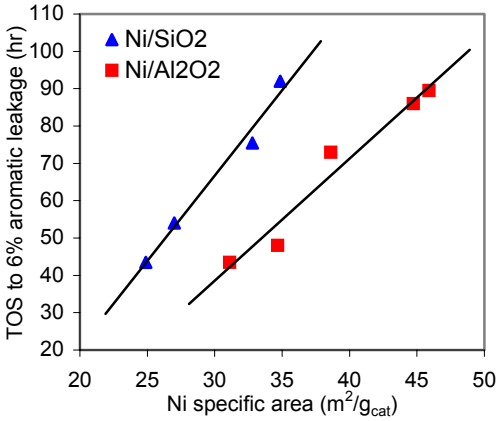

Figure.1: Correlation between sulfur tolerance and Ni specific surface area of different Ni-based catalysts.

Figure 2 illustrates the difference of the performance of Ni/SiO_2 and Ni/Al_2O_3 catalysts for aromatic hydrogenation and sulfur tolerance. Their deactivation behaviors are very different. Although Ni surface area of Ni/SiO_2 is lower than Ni/Al_2O_3, the deactivation rate at beginning hours on Ni/SiO_2 is much lower than that on Ni/Al_2O_3; after 48hours' run on Ni/SiO_2, aromatic shows up in the product and the deactivation rate increases and becomes higher than that on Ni/Al_2O_3. In another word, Ni/SiO_2 catalyst exhibits two different deactivation rates.

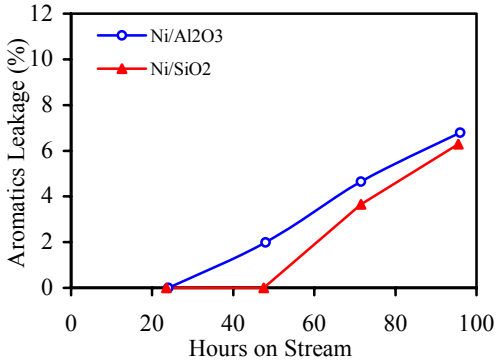

Figure 2: Comparison of the performance of Ni/SiO_2 and Ni/Al_2O_3 catalysts for aromatic hydrogenation and sulfur tolerance. Ni surface area, Ni/SiO_2 : $34.9 m^2/g_{cat}$, Ni/Al_2O_3 : $42.0 m^2/g_{cat}$.

The results indicate the pore structures of Ni/Al_2O_3 and Ni/SiO2 catalysts play an important role. As shown in Figure 3, the mean maximum pore diameter of Ni/Al_2O_3 catalyst is much bigger than that of Ni/SiO_2 and there is almost no small pore (<20 Å). Ni/SiO_2 catalyst shows a bi-model pore structure. The smaller pore size is between 6~25Å and bigger pore diameter is in a very narrow range of 30~40Å. Since the sizes of sulfur compound in the diesel fuel might be bigger than the smaller pores in Ni/SiO_2, the diffusion adsorption of sulfur species on the active Ni sites in small-pore would be prohibited by the pore size. Aromatic/poly-aromatic and benzothiophene/ ploy-ditheophene molecules would easily enter into those big pores and are hydrogenated or deposited on active Ni surface in big pores, resulting in the deactivation. However, H_2

molecules can readily diffuse into both big and small pores and dissociatively adsorb on the active Ni surface. Those dissociatively adsorbed hydrogen might migrate from small pore to big pore by surface diffusion or spillover, which is much faster and more efficient than direct gas molecule transportation in pore channels. The spillover hydrogen has extra-high reactivity and could partially re-generate the poisoned metallic active sites by surface hydrogenation of organic sulfur compound to H_2S. H_2S can be purged away by the stream; or some of them can further bond with metallic Ni to form NiS_n clusters, resulting in the second deactivation. Since the small pore could not stop the diffusion of H_2S to small pore, the active Ni sites in the small pore would be finally poisoned by H_2S. As a result, the deactivation behavior of Ni/SiO_2 would become similar to that of NI/Al_2O_3. Since the Ni surface area of Ni/Al_2O_3 is higher than that of Ni/SiO_2, the deactivation rate of Ni/SiO_2 after 48hours's run becomes higher than that of Ni/Al_2O_3. If the Ni surface areas if Ni/SiO_2 and Ni/Al_2O_3 are the same or similar, it is found that the deactivation rate of Ni/SiO_2 after 48hours' run is slightly lower than that of Ni/Al_2O_3 (the results not shown).

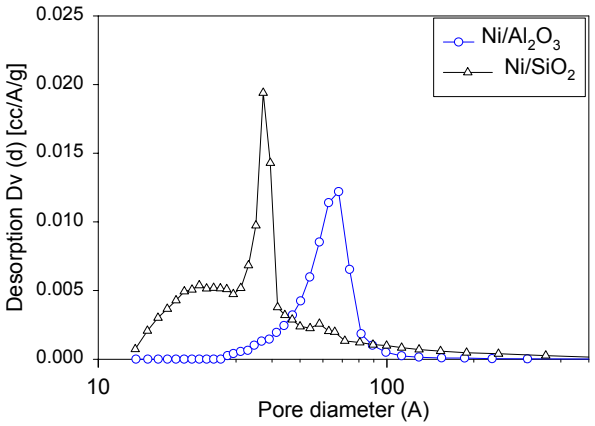

Figure 3: Pore diameter distribution of Ni/SiO_2 and Ni/Al_2O_3 catalysts

Therefore, the combination of bi-model pore structure makes the Ni metal sites exhibit higher sulfur resistance than that on the Ni in single-model pore channels. As a result, it shows higher intrinsic catalytic capacity for deep aromatic hydrogenation and desulfurization. The deactivation of the catalyst, however, cannot be overcome by this combination because H_2S can also diffuse into small pores, poison the metallic Ni sites and leads further deactivation. This observation and conclusion are in agreement with the results on zeolites [4].

Conclusion

High Ni specific area is crucial for hydrogenation and sulfur tolerance. Activity and sulfur tolerance increase with increasing Ni surface area. A linear relationship exists between Ni surface area and hydrogenation and sulfur tolerance performance. Ni/SiO_2 and Ni/Al_2O_3 show significant difference in aromatic hydrogenation and sulfur tolerance; Ni/SiO_2 has higher intrinsic activity than Ni/Al_2O_3 due to *'combination effect'*. Shape selectivity and hydrogen spillover (surface diffusion) significantly promote catalyst performance for deep aromatic hydrogenation and sulfur tolerance.

References

1. C. Song, CHEMTECH, 29(1997) 26
2. J. Barbier, E. Lamy-Pitara, P. Marecot, et al., Adv. Catal., 37 (1990) 279
3. D. Huang, P. Jerus and W. Faris, U. S. patent, 06462244
4. C. Song, in " Shape-Selective Catalysis: Chemicals Synthesis and Hydrocarbon Processing",(C. Song, J. M. Garces and Y. Sugi Ed.), ACS Sym. series 738, p383

SYNTHESIS OF POROUS CARBON MATERIALS BY CARBONIZATION IN NATURAL ZEOLITE NANOCHANNELS

Billur Sakintuna[1], Zeki Aktaş[2] and Yuda Yürüm[1]

[1]Faculty of Engineering and Natural Sciences
Sabanci University
Tuzla, 34956 Istanbul, Turkey
[2]Department of Chemical Engineering
Ankara University
Tandoğan, 06100 Ankara, Turkey

Introduction

Porous carbons are commonly used as catalysis and adsorbents and catalyst supports. Because of the presence of the three-dimensional channels, zeolites have molecular-sieve property used in adsorption and catalytic purposes. The zeolite-templated carbons has large surface areas and micropore volumes, without activation that is required to open new accessible microporous structures [1-2].It should be noted that macropores, mesopores and micropores are defined here as pores of the width above 50 nm, between, 2 and 50 nm, and below 2 nm, respectively[3].

Carbon framework formed in narrow pores of zeolites retained to templated carbon particles exhibited the morphology of the zeolite template particles. On the basis of this concept, there were few studies on the carbon formation in the zeolite nanoscale pores. Poly furfuryl alcohol[1] and polyacrylonitrile[4] was carbonized in the zeolite channels and then the resultant carbon was obtained by washing with HF. In addition to zeolite frames, mesoporous silica molecular sieves[5,6] were also used.

In the present study new porous carbon materials were synthesized by using a natural Turkish zeolite as template. The structure and morphology of zeolite-carbon composite and resulted carbon material was characterized by several means.

Experimental

Zeolite Samples as a Template

Zeolite samples were obtained from Enli Mining Company, Gördes, Manisa, Turkey. The major mineral present in the samples were reported to be clinoptilolite. Four different particle sizes of the zeolite sample (-30 μm, -0.1, -0.5 and -1.0 mm) were used in this study. Their BET surface areas, (m^2/g), pore volume and pore diameters were given in Table 1.

Synthesis Procedure

The zeolite templates was impregnated with aqueous solution of sucrose containing sulfuric acid as described in a previous study[6]. 1 g of zeolite was added to a solution obtained by dissolving 1.25 g of sucrose and 0.14 g of H_2SO_4 in 5 g of H_2O. the mixture was dried at 100 °C, 6 hours and at 160°C additional 6 hours. After adding again sucrose and H_2SO_4, the same procedure was repeated. The carbonization was carried out at different temperatures, 700, 800 and 900 °C. The zeolite-carbon composite material was then washed with concentrated HF for removing the silica template.

The replication of zeolite using phenol-formaldehyde resin was also studied. The zeolites were ion exchanged with excess 1M NH_4Cl for a total of 3 days. The zeolite samples dried under vacuum at 125°C for 5 hours. Solid phenol was added to the flask and incubated with the zeolite at 65 °C under reduced pressure overnight. Excess formaldehyde was heated to 120 °C to liberate its monomer to produce zeolite-phenol-formaldehyde-resin composite. The samples were heated to 125 °C at 1 °C/min for 5 hours and carbonized at 700, 800 and 900°C for 14 hours in inert atmosphere[2]. Figure 1 illustrates the polymerization of phenol-formaldehyde resin.

Table 1. BET surface area, pore volume and pore diameter of zeolites templates.

Zeolite Type	BET surface area, m^2/g	BJH method cumulative desorption pore volume, cc/g	BJH method desorption pore diameter, Å
- 30 μm	59.44	0.1323	39.39
-0.1 mm	50.18	0.1126	39.37
-0.5 mm	51.20	0.1125	39.33
-1.0 mm	47.15	0.1027	39.24

FTIR Analysis

FT-IR spectra of carbonized and activated samples were measured with a Bruker EQUINOX 55 FT-IR spectrometer. Coal samples were dried under a nitrogen atmosphere at 110ºC for 24 hours. KBr pellets were prepared by grinding 2.5 mg of dry coal sample with 200 mg of dried KBr. Spectra were obtained with 200 scans at a resolution 2 cm^{-1}.

Surface Analysis

Surface areas of activated carbons were determined by a Quantachrome NOVA 2200 Series volumetric gas adsorption instrument. Surface area of the samples were determined by using BET equation in the relative pressure range of 0.05 to 0.30, over five adsorption points.

X-Ray Diffraction Measurements

X-ray diffractograms of the samples of carbonized and activated products were measured with a Bruker axs advance powder diffractometer fitted with a Siemens X-ray gun and equipped with Bruker axs Diffrac PLUS software. The sample was rotated (15 rpm) and swept from 2q = 10º through to 90º using default parameters of the program. The X-ray generator was set to 40kV at 40 mA.

Furthermore, after carbonization of the samples 57% weight loss was also examined via thermogravimetric analysis (TGA). TGA using a Netzsch STA 449C instrument were undertaken upon both the zeolite-carbon complexes and carbon, which was obtained after tereatment with HF.

NMR Measurements

Samples were probed further by ^{13}C CPMAS, ^{29}Si CPMAS and ^{27}Al MAS NMR using an Inova 500MHz Varian system.^{13}C CPMAS, ^{29}Si CPMAS and ^{27}Al MAS NMR spectra were acquired at 125 MHz, 100 MHz and 130 MHz fields respectively, using Si_3N_4 rotors set to 6 Hz. Pulses were separated by a 1s delay in the case of carbon, 2s delay in the case of silicon and 0.25s delay in the case of aluminum.

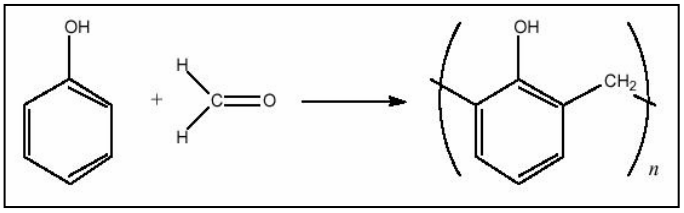

Figure1. Schematic representation of the phenol-formaldehyde resin.

Results and Discussion

BET sureface area and adsorption-desorption analysis of zeolite templates were perfomed and represented in Figure 2 and 3. As expected with increasing particle diameter, surface area was decreased.

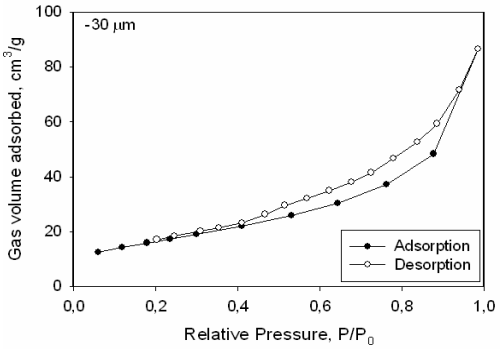

Figure 2. Gas adsorption/desorption isotherms of N_2 at 77K for the zeolite template of the -30 μm size fraction

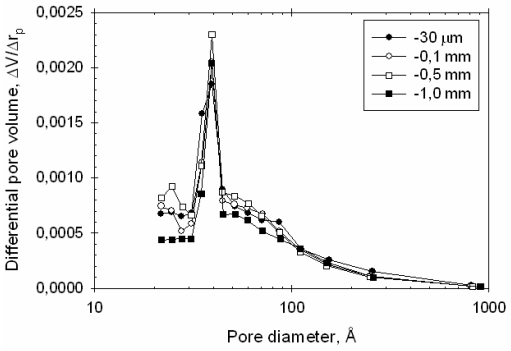

Figure 3. Pore size distributions for the samples (according to the BJH method[8])

In the nitrogen adsorption there is initially uptake, followed by a rapid approach to equilibrium, and so the most reasonable explanation for this behavior is that there is significant adsorption capacity and very high diffusion resistance within the nanopores. The nanopore surface equilibrates rapidly in the first instances. This is followed by diffusion into the micropores. The adsorption isotherms of resultant carbon materials were also analysed. The surface areas and volumes of replicas produced by HF etching of zeolites were showed that almost all pores of the zeolite templates were filled with carbon material.

Nitrogen adsorption isotherms of the zeolite-carbon composites and carbon provide the confirmation that the resulted carbons were nanoporous. Because of the zeolite templates have nanoscale pore size, all zeolite-carbon samples showed low-pressure hysteresis. This suggest that the nanopores may have constrictions of the width comparable to the size of the nitrogen molecule. And also there is a possibility that not all the pores are in the exterior region [7].In the adsorption isotherms of the zeolite-carbon composites, no steps were observed as in the previous studies [7], which indicates that the almost all pores were deposited with carbon. BET areas of resulted carbons have large surface areas.

The percentage of carbon in the zeolite-carbon composites was estimated from the termogravimetric weight loss in air between 100 and 800 °C. Major weight loss was observed between 700 and 800 °C for both sucrose and resin case, indicating that carbon was burned in this range.

Zeolite-sucrose and zeolite-resin carbonized samples have distinct diffraction patterns consisting of narrow Bragg peaks. The zeolite-carbon composites have the almost the same XRD patterns with the zeolite template used for their preparations with lower intensities. After removing the silica template by washing with HF, carbon structure was examined in the XRD. Broad diffraction features were observed at 25 ° and 41° 2θ which was represented of (002) and (10) reflections of graphitized carbon, corresponding to the stacking of carbon sheets, that found in turbostratic structure of carbon. FTIR studies of synthesized carbons also showed that porous carbon material have characteristic bands near 3500 cm^{-1}, and 1450 cm^{-1} are due to OH stretching and aromatic C-H absorption due to the aromatic structure of resultant carbon. Further evidence of the presence of the zeolite-polymer composite was obtained. by FTIR spectroscopy. Characteristic bands for poly (phenol-formaldehyde) resin at. 3500 cm^{-1} were assigned to OH stretching modes and several sharp bands at 1500 cm^{-1} were attributed to C-O, C-C groups similar to those found for the bulk poly (phenolformaldehyde).

Further work is being carried out to give an explanation the mechanism of formation of carbon materials and affects of synthesis conditions to the resultant porous carbon properties.

References

1. Kyotani, T., Nagai, T.,Inoue, S., Tmita, A., *Chem. Mater*, **1997,** 9,609-615.
2. Johnson, S.A., Brigham, E:S., Ollivier, P.J., Mallouk, T.E., *Chem. Mater***, 1997**, 9, 2448-2458.
3. Sing, K.S.W., Everett, D.H., Haul, R.A.W., Moscou, L., Pierotti, R.A., Rouquerol, J., Siemieniewska, T., *Pure Appl. Chem*, **1985**, 57, 603.
4. Enzel, P., Bein,T., *Chem Mater*, **1992**, 4, 819.
5. Jun, S., Joo, S.H., Ryoo, R., Kruk., M., Jaroniec, M., Liu Z., Ohsuna, T., Terasaki, O., *J. Am. Chem., Soc*., **2000**, 122, 10712-10713.
6. Ryoo, R., Joo, S.H., Jun, S., *J. Phys. Chem. B*., **1999,** 103, 37, 7743-7746.
7. Kruk, M., Jaroniec, M., Ryoo, R., Joo, S.H., *J. Phys. Chem. B***., 2000**, 104, 7960-7968.
8. BJH* method : Barrett, E.P., Joyner, L.G., Halenda, P.H., **1951**, *Journal of American Chemical Society*, 73, 373-380.

THERMAL REACTION OF CATECHOL OVER NANO-PARTICLE IRON OXIDE AND QUARTZ

Eun-Jae Shin, Mohammad Hajaligol and Firooz Rasouli

Philip Morris USA, P.O.Box 26583, Richmond
VA 23261-6583,
Tel: 804-274-6112, Fax: 803-274-1994
E-mail: EunJae.Shin@pmusa.com

Introduction

The phenolic compounds in the tars derived from coal liquid and/or coal and biomass pyrolysis and gasification have been recognized to cause operational and health related problems [1]. Substituted phenols have also been identified in cigarette smoke [2]. We selected catechol ($C_6H_4(OH)_2$) as a phenolic model compound because it is a representative structure in coal as well as in lignin, a major biomass constituent, and also an abundant phenolic compound in cigarette smoke.

The cracking of catechol vapor over nano-particle iron oxide/quartz mixture and quartz under partially to fully oxidative conditions is presented in this work. Conversion of catechol and product distribution over the iron oxide and quartz were compared. Temperature dependence of the reaction was presented in terms of an activation energy. The effects of catechol concentration and oxygen were also considered.

Experimental

The details of experimental set up and procedure are given elsewhere [3, 4]; only a brief description is given here. All reactions were carried out under atmospheric pressure and partially to fully oxidative conditions in a quartz tube reactor. The quartz reactor consists of inner and outer tubes, with reactions occurring in the inner tube, coupled to a Molecular Beam Mass Spectrometer (MBMS) for product detection. An electric furnace was set with two temperature zones.

The first zone was varied in the range from 180°C to 220°C for slow volatilization of the starting material so that steady state could be obtained. The vapor concentration of catechol was varied in the range of $6x10^{-3}$ to $18x10^{-3}$ mmol/min by varying the temperature in 10°C intervals. The second zone was varied in the range from 260°C to 480°C with 20°C intervals to study its effect on iron oxide versus quartz performance. The bed of the iron oxide (2.5mg)/quartz (1g) mixtures or quartz (1g) was preheated to a given reaction temperature before any reactant is passed through the bed. 10 ml/min of argon was used as an internal standard to get semi-quantitative data. 3% of oxygen was added in helium as a typical oxygen concentration and its effect on the reaction was evaluated by varying it in the range of 3-21% in He. A bed of nano-particle iron-oxide/quartz mixture, or of quartz was placed at the rear end of the inner tube between two pieces of clean quartz wool.

Catechol was purchased from Acros (>99% pure) and used as received. A sample of catechol was loaded in a quartz holder called "boat" which is inserted into the first heated zone with a preheated flowing helium carrier gas. The vapors formed in this zone pass through the bed of the iron oxide and the final products exiting the reactor (inner tube) are diluted with the neat carrier gas in the outer tube and, before condensing, sampled into the orifice of the MBMS. Finally, factor analysis was used to deconvolute the complex chemistry of the catechol conversion.

Results and Discussion

The total conversion of catechol over the nano-particle iron oxide and quartz beds is shown in Fig. 1. In this work, the conversion is defined as the difference between the total amount of catechol fed to the system (measured under the conditions with no significant conversion) and the amount that exited the system, divided by the total amount fed. The estimate of un-reacted catechol is done by monitoring a single ion (m/z 110) as a function of evolution time by MBMS. The monitoring is done in such a way that the integrated area of the steady-state evolution of the single ion resulting from various reaction conditions was subtracted from that resulting from controlled condition where no reaction was observed.

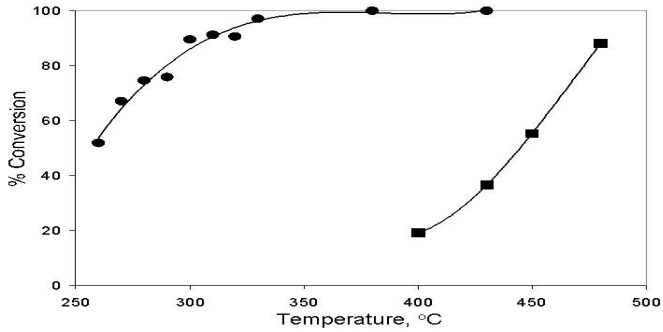

Fig. 1: Total conversion from catechol cracking over nano-particle iron oxide/quartz mixture (●) and quartz (■) as a function of temperature with $6x10^{-3}$ mmol catechol/min and 3% of oxygen.

Each data point in Fig. 1 represents the averaged result of more than two experiments under the same conditions and a fresh catalyst was used for each new experiment. The presence of nano-particle iron oxide lowered the temperature for a given conversion by about 180°C. About 50 % of catechol converted at a temperature as low as 260°C over iron oxide, whereas comparable conversion of catechol was observed at a temperature above 400°C over quartz. Comparison in product distribution over nano-particle iron oxide/quartz mixture and quartz was done with 3% of oxygen and a catechol concentration of $18x10^{-3}$ mmol/min at reaction temperatures that resulted in a comparable conversion of catechol for both cases. Fig. 2 shows the average spectra of the products obtained from two cases for about 50% catechol conversion.

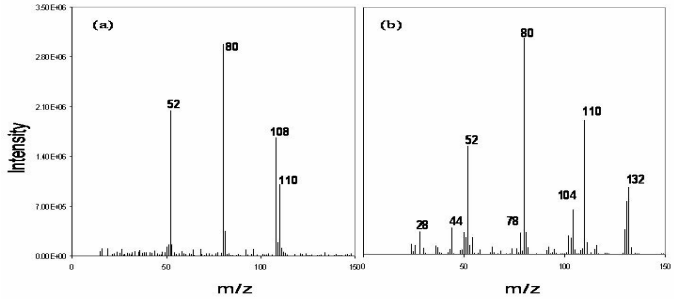

Fig. 2: Average spectra of products (with background correction) detected by MBMS resulting from catechol cracking over (a) iron oxide/quartz mixture at 260°C and (b) quartz at 450°C with 3% oxygen.

For the cracking reaction over the iron oxide as shown in Fig. 2 (a), the peak at m/z 110 and its fragment ions at m/z 54, 64, 82, and 92, that are too small to be seen, belong to catechol. The major products from catalytic cracking of catechol were found at m/z 52 (C_4H_4, i.e., vinyl acetylene), m/z 80 (C_5H_4O, i.e., cyclopentadienone) and m/z 108 (C_7H_8O, i.e., cresols or $C_6H_4O_2$, i.e., o-benzoquinone). The cracking of catechol over nano-particle iron oxide is a complete cracking at temperatures above 380°C. At 430°C temperature,

catechol is totally converted to only carbon dioxide (m/z 44) and a small amount of possibly carbon monoxide (m/z 28) with 3% oxygen in the gas flow. Product distribution of catechol cracking at 450°C temperature over quartz is shown in Fig. 2 (b) where products observed comprise the same as those seen in the iron oxide case as well as a new group of products especially some aromatic compounds that were newly formed over quartz. Possible identities of the aromatic compounds are benzene (m/z 78), styrene (m/z 104), indene (m/z 116) and indanone (m/z 132). It is surprising to observe this level of reactivity with quartz at this temperature since catechol thermally begins to decompose at temperatures above 500°C [5]. This could be attributed to the surface effect induced by quartz, which must have lead to limited reactions to produce more aromatic compounds.

To uncover the underlying changes in chemistry as a function of process parameters, factor analysis was applied on the MBMS mass spectra obtained under various reaction conditions. The factor analysis extracted four classes of products that were correlated with the reaction conditions. These four classes of products were used to qualitatively and quantitatively observe trends of conversion and product distributions in the heterogeneous cracking of catechol. Fig. 3 reveals the four classes of products derived from the factor analysis.

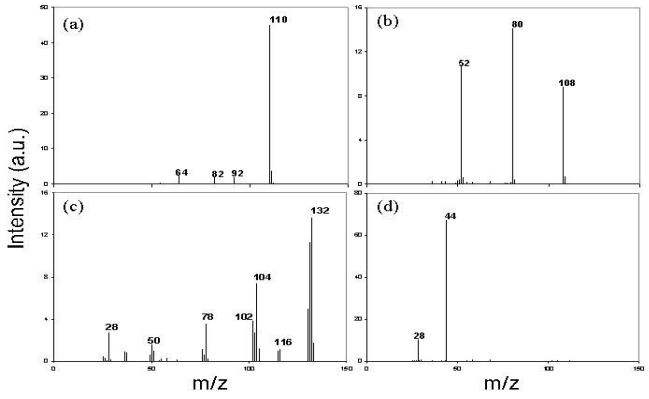

Fig. 3: Four classes of products, (a) primary, (b) secondary I, (c) secondary II, and (d) tertiary products that are derived from factor analysis.

Fig. 3(a) represents a spectrum that belongs to the pure catechol without any contribution from cracking products that is called primary products. As catechol undergoes cracking with partial oxidation, a few major products are formed as shown in Fig. 3(b). A group of aromatic compounds is presented in Fig. 3(c). These products shown in Fig. 3(b) and (c), must have been derived from the cracking of catechol and subsequent reactions of cracking products so that this class of products would be called secondary products I and II given in Figs 3(b) and 3(c), respectively. Lastly, thermally stable products, carbon dioxide and carbon monoxide, are contained in Fig. 3(d) and they could be derived from further cracking and oxidation of the secondary products and they are called tertiary products. Water (m/z 18) must have formed but it was not included in our scan range because of the uncertainty resulting from background water from the MBMS. The conversion and product distribution in catechol cracking over the iron oxide/quartz mixture and quartz, determined by the factor analysis, are given in Fig. 4 where the variation of conversion and the formation of classes of products as a function of temperature for a constant catechol ($18x10^{-3}$mmol/min) and oxygen (3%) concentrations are exhibited. This clearly shows the trend of the formation of each class of products.

The effect of temperature can be effectively described in terms of a global activation energy. Based on the assumption of a pseudo-first order reaction, kinetic parameters resulted from two different conditions are compared in Table 1. The activation energy over nano-particle iron oxide mixed with quartz was a factor of about 2 lower than for quartz, suggesting a strong effect of the presence of nano-particle iron oxide on the cracking reactions.

The effect of oxygen concentration on the cracking of catechol over nano-particle iron oxide was studied at 280°C and 330°C temperatures and a feed rate of $18x10^{-3}$ mmol/min. At 280°C, the conversion of catechol was slightly promoted with the increase in oxygen concentration but product distribution was not affected, i.e. major products were the secondary products (Fig. 3(b)). The effect of oxygen concentration was even less at 330°C, where the catechol conversion was almost 100% with the secondary products I as major products under 3% of oxygen.

The effect of catechol concentration on the cracking reaction over nano-particle iron oxide was studied at 280°C with 3% of oxygen. Again, product distribution was not affected by varying the concentration of catechol at this condition, i.e., the secondary products I remained the major products, but the conversion of catechol was promoted with a decrease in catechol concentration.

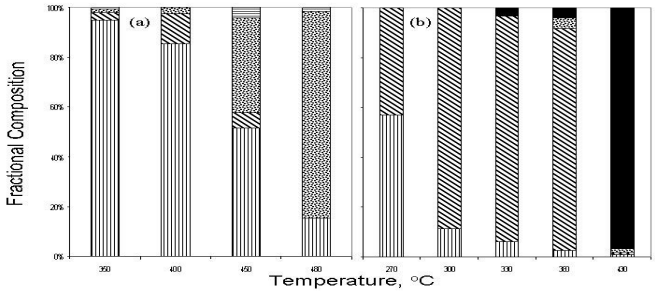

Fig. 4: Fractional concentration of four classes of products resulted from factor analysis as a function of temperature over (a) quartz and (b) iron oxide; (vertical line) primary, (hatched) secondary I, (dots) secondary II and (solid) tertiary products: catechol feed=$18x10^{-3}$ mmol/min, O_2=3%.

Table 1: Arrhenius parameters for catechol cracking over iron oxide and quartz assuming first-order kinetics.

	E_a (kcal/mol)	A (s^{-1})	Correlat. Coeff.
Quartz	30.2	3.3×10^{10}	0.99
Iron Oxide	15.5	3.6×10^{7}	0.96

Conclusions

Nano-particle iron oxide promotes the vapor phase cracking of catechol at a temperature as low as 260°C. Derived kinetic data indicates a strong catalytic effect of iron oxide on the catechol cracking. Reaction products were distinctively classified into four groups and exhibited changes as a function of reaction conditions. The effects of oxygen and catechol concentrations were insignificant in the range of the conditions tested.

Acknowledgement. The authors thank Felecia Logan for experimental work. We also acknowledge Philip Morris USA management for their support and encouragement of basic research.

References

(1) Lai, C.S.; Chen, P.; Longwell, J.P. ; Peters, W.A. *Fuel*, **1987**, *66*, 525.
(2) Sharma, R.K.; Fisher, T.S.; Hajaligol, M.R. *J. Anal. Appl. Pyrolysis*, **2002**, *62*, 281.
(3) Shin, E.J.; Hajaligol, M.R.; Rasouli, F. *Fuel*, submitted.
(4) Evans, R.J.; Milne, T.A. *Energy & Fuel*, **1987**, *1*, 123.
(5) Wornat, M.J.; Ledesma, E.B.; Marsh, N.D. *Fuel*, **2001**, *80*, 1711.

IMPACT OF ORIENTED HYDROGEN TRANSFERS ON THE PYROLYSIS OF HYDROCARBONS UNDER RESTRICTED DIFFUSION

A. C. Buchanan, III, Michelle K. Kidder, Phillip F. Britt

Oak Ridge National Laboratory
Chemical Sciences Division
Bethel Valley Road
P. O. Box 2008, MS-6197
Oak Ridge, Tennessee 37831-6197

Introduction

The kinetics, conversion efficiency and product quality during thermal processing of fossil and renewable energy resources into fuels or chemicals can be impacted by restricted mass transport for these cross-linked, macromolecular materials. We have been interested in understanding how these macroscopic effects might be rooted in alterations in the underlying reaction pathways (radical, ionic, catalytic, etc.). We have developed model systems that address restricted diffusion effects by immobilizing fuel model compounds onto silica surfaces.[1-5] The Si-O-C_{aryl} linkage that forms from the condensation of the phenolic precursor with the surface silanols of a high purity, nonporous, fumed silica is thermally robust, up to ca. 550°C, but is readily hydrolyzed in aqueous base such that surface-attached products can be recovered for analysis.[1-5]

Previous studies of surface-immobilized hydrocarbons revealed that thermal decomposition reaction rates and product selectivities can be significantly different than that of analogous liquid and vapor phase reactions.[2] Our recent research has been focusing on two-component systems that explore the effects of hydrogen donor and non-donor spacers on the surface. In the decomposition of surface-immobilized 1, 3-diphenylpropane (≈DPP) at 375 °C (Figure 1a), we found that spacer molecules bearing reactive benzylic C-H bonds (e.g. diphenylmethane) could dramatically accelerate the pyrolysis rate for ≈DPP compared with surfaces containing inert spacers (e.g. biphenyl).[1] This phenomenon is unique to the surface and attributable to the diffusional constraints, since the pyrolysis rate of DPP in solution does not depend on the structure of the diluent.[6,7] Experiments with a deuterium labeled spacer provided additional evidence for a process involving a series of rapid hydrogen transfer steps with free radical intermediates on the surface.[1] This process provides a mechanism for radical centers to rapidly relocate in a diffusionally constrained environment without the need for physical movement as shown in Figure 1b. We have now expanded this research to investigate the possible impact of molecular orientation on the rate of the hydrogen transfer, radical relay process by examining isomeric hydrogen donor spacer molecules based on the hydroaromatics, fluorene, tetralin, and 9,10-dihydrophenanthrene as shown in Figure 2.

Experimental

GC analysis was performed on a Hewlett Packard 5890 Series II gas chromatograph employing a J & W Scientific 30 m x 0.25 mm DB-5 column (0.25 μM film thickness) and flame ionization detection. Detector response factors were determined relative to cumene (hydrocarbon products) or 2, 5-dimethylphenol and *p*-hydroxybiphenyl, *p*-HOBP, (phenolic products) as internal standards. Mass spectra were obtained at 70 eV with a Hewlett Packard 5972A/5890 Series II GC-MS equipped with a capillary column matched to that used for GC analyses.

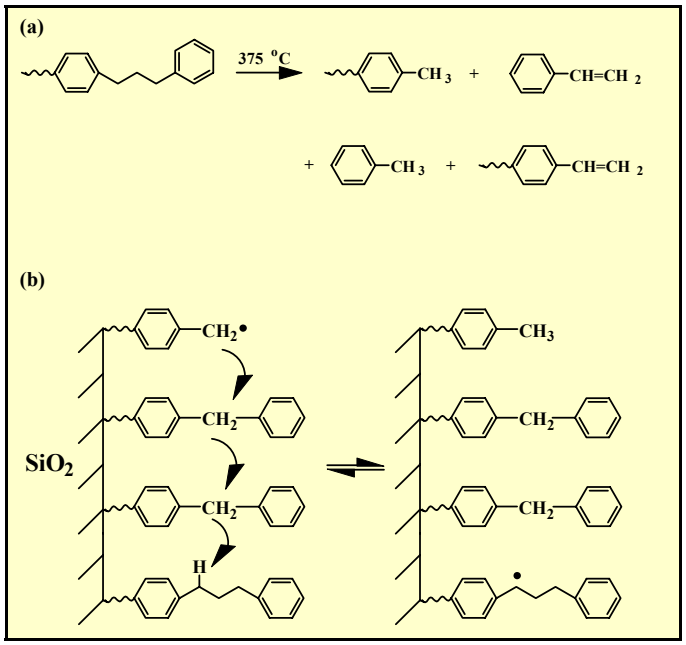

Figure 1. (a) Major products formed from the pyrolysis of silica-immobilized 1,3-diphenylpropane via a radical chain mechanism. (b) Hydrogen transfer, radical relay pathway in the presence of diphenylmethane spacer.

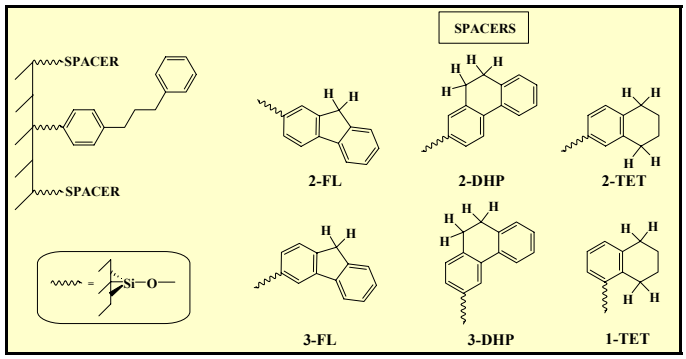

Figure 2. Silica-immobilized substrates under investigation.

Materials. Cabosil M-5 silica from Cabot Corp. (200 m^2/g; ca. 4.5 SiOH/nm^2 or 1.5 mmol SiOH/g) was dried at 200 °C for 4 hours, and cooled in a desiccator before use. Benzene was distilled from sodium. High purity acetone and dichloromethane were commercially available and used as received. Cumene was fractionally distilled (2x) and 2,5-dimethylphenol was recrystallized from ethanol. *p*-Hydroxybiphenyl, 5,6,7,8- tetrahydro-2-naphthol (2-hydroxytetralin, or 2-HOTET) and 5,6,7,8-tetrahydro-1-naphthol (or 1-hydroxy tetralin, 1-HOTET) were commercially available and purified by repeated recrystallizations from benzene/hexane. The synthesis of *p*-(3-phenylpropyl)phenol (HODPP)[5] and 2-hydroxyfluorene (2-HOFl)[1] were previously described. The multi-step synthesis of the 3-hydroxyfluorene (3-HOFl), 2-hydroxy-9, 10-dihydrophenenathrene (2-HODHP), and 3-hydroxy-9, 10-dihydrophenanthrene (3-HODHP) precursors will be reported elsewhere.

Preparation of Surface-Attached Materials. Procedures for the preparation of the two component surfaces have been described previously.[1] In general, HODPP and the desired spacer phenol were dissolved in benzene in the appropriate mol ratios, and then were added to a benzene slurry containing Cabosil. The benzene was evaporated and the phenolic material was attached to the surface through heating at 225 °C for 1 h in an evacuated (2 x 10^{-6} torr) sealed Pyrex tube. Unattached phenols where removed via sublimation at 225-275 °C for 1 h under dynamic vacuum (5 x 10^{-3} torr). Surface coverage analysis was performed as described previously[1] using *p*-HOBP as the internal standard.

Pyrolysis Procedure. The pyrolysis apparatus and procedure have been described.[1-5] In brief, a weighed amount of sample was placed in a T-shaped Pyrex tube, evacuated and sealed at ca. 2 x 10^{-6} torr. The sample was pyrolyzed in a pre-heated calibrated Carbolite three-zone tube furnace, and the gas phase products were trapped in the tube arm placed in a liquid nitrogen bath. The volatile products collected in the trap were dissolved in acetone (50-150 μL) containing the internal standards, and the solution was analyzed via GC and GC-MS. Surface-attached pyrolysis products were hydrolyzed from the silica with 1N NaOH. The internal standards, 2, 5-dimethylphenol and *p*-HOBP were prepared in NaOH and added to the solution. The solution was acidified and extracted with CH_2Cl_2, evaporated, then silylated with a mixture of *N, O*-bis(trimethylsilyl)-trifluoroacetamide (BSTFA)/pyridine 1:2 (ca. 300 μL) and analyzed via GC and GC-MS.

Results and Discussion

The two-component surfaces under investigation are shown in Figure 2. Two-component surfaces involving the fluorene (FL) and tetralin (TET) spacers have been prepared to date by the co-condensation of the phenolic spacer with HODPP in a single step as described above. The initial stoichiometries were adjusted to prepare surfaces at saturation coverage with similar spacer:DPP mol ratios (approximately 3:1).

Thermolyses were conducted at 375 °C in vacuum sealed Pyrex tubes. The major products (ca. 98 % at low ≈DPP conversions) formed from the free-radical induced chain decomposition are gas-phase and surface-attached toluene and styrene as shown above in Figure 1a. These products are formed in similar amounts at low conversions indicating that there is little regioselectivity in the pyrolysis reaction as found previously for ≈DPP in other two-component surfaces.[1] Small amounts of surface-attached $PhCH_2CH_3$ (0.1-3.0 mol %) are also observed, as well as trace amounts of gas-phase $PhCH_2CH_3$ (0.05-0.1 mol %). In the case of the fluorene spacers, addition of surface-attached fluorenyl radical to the surface-attached styrene is also detected and can account for several mol % of the products. Mass balances are typically 99.6 ± 2.5 % indicating that all significant products are accounted for.

The free radical chain mechanism for the decomposition of DPP on the surface or in fluid phases has been discussed in detail elsewhere.[1, 5-9] For surface-attached DPP, initiation by a small amount of C-C homolysis (74 kcal/mol) forms chain carrying gas-phase and surface-attached benzyl radicals. The reaction is then propagated through hydrogen abstraction at the two regiochemically distinct benzylic carbons of ≈DPP to form the gas-phase and surface-attached toluene products, as well as benzylic radicals that undergo β-scission to produce the surface-attached and gas-phase styrene products. Termination occurs through coupling of the benzyl radical. The overall rate of decomposition of ≈DPP is governed by the rates of hydrogen transfer steps, which are particularly sensitive to the surface coverage and the structure of intervening spacer molecules. As noted above, in the presence of spacer molecules possessing benzylic C-H bonds, a hydrogen transfer, radical relay process provides an effective means for overcoming the impact of the restricted translational diffusion on the surface (Figure 1).

The initial reaction rates for ≈DPP at 375 °C in the presence of the hydroaromatic spacer molecules were obtained from the slopes of linear regressions of ≈DPP conversion versus reaction times as shown in Figure 3 for the two isomeric fluorene spacers. The measured ≈DPP pyrolysis rates are presented in Table 1. As expected, the ≈DPP decomposition rates increased dramatically in

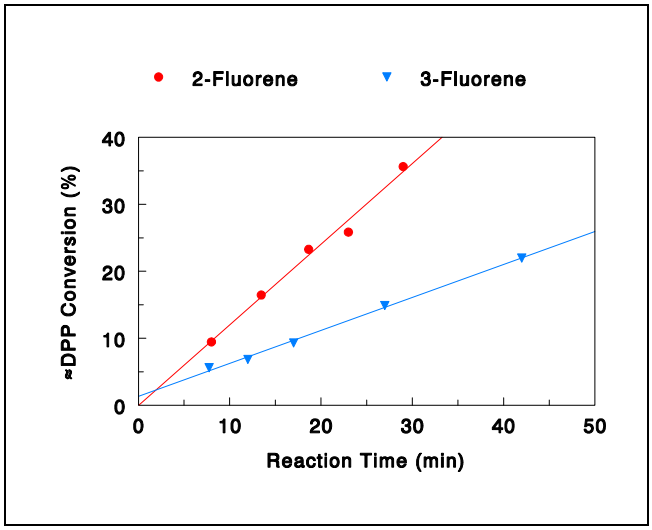

Figure 3. Comparison of rate of ≈DPP conversion at 375°C in the presence of the 2-fluorene and 3-fluorene spacers.

the presence of the hydrogen donor spacers relative to surfaces of -≈DPP at similar surface coverages without hydrogen donating spacers (ca. 0.4 %/h). However, it is clear that the rates are sensitive to the orientation of the spacer molecule on the surface. For example, the rate of ≈DPP pyrolysis with the 2-FL spacer is 2.4-times faster than that with the 3-FL. Furthermore, the ≈DPP conversion rate for the 2-TET spacer is 3-times faster than for 1-TET (Table 1).

Table 1. Impact of Hydroaromatic Spacer Orientation on ≈DPP Pyrolysis Rate at 375 °C.

Surface	*Coverage (mmol/g)*	*Rate (%/h)*
≈DPP/≈2-FL	0.16 / 0.43	72.2
≈DPP/≈3-FL	0.12 / 0.33	29.6
≈DPP/≈2-TET	0.11 / 0.45	15.1
≈DPP/≈1-TET	0.085 / 0.28	5.0

The results suggest that a *meta*-orientation for the surface linkage, with respect to the reactive benzylic hydrogens, is the most efficient geometry for promoting the hydrogen transfer, radical relay process on the surface. This will be tested further with the two dihydrophenanthrene spacer molecules shown in Figure 2. Based on the results presented above, the prediction would be that the 2-DHP spacer will produce a faster ≈DPP pyrolysis rate than the 3-DHP isomer. Additional studies will probe the generality of this orientation effect at higher ≈DPP surface dilution (ca. 7:1 mol ratio

of spacer: ≈DPP). Molecular modeling studies will also be employed to understand the origin of these orientation effects.

Conclusions

These pyrolysis studies clearly show that geometric constraints can play a large role in the rates of hydrogen transfer steps for high temperature, free-radical reactions under restricted diffusion. These new insights suggest that the local structure of hydrocarbon resources may play a role in the efficient utilization of native hydrogen during thermochemical processing.

Acknowledgment. This research was sponsored by the Division of Chemical Sciences, Geosciences, and Biosciences, Office of Basic Energy Sciences, U.S. Department of Energy under contract DE-AC05-00OR22725 with Oak Ridge National Laboratory, managed and operated by UT-Battelle, LLC.

References

(1) Buchanan, A. C., III; Britt, P. F.; Thomas, K. B.; Biggs, C. A. *J. Am. Chem. Soc.* **1996**, *118*, 2182.
(2) Buchanan, A. C., III; Britt, P. F. *J. Anal. Appl. Pyrolysis* **2000**, *54*, 127.
(3) Britt, P. F.; Buchanan, A. C., III; Malcolm, E. A. *Energy Fuels* **2000**, *14*, 1314.
(4) Buchanan, A. C., III; Britt, P.F.; Skeen, J. T.; Struss, J. A.; Elam, C. L. *J. Org. Chem*. **1998**, *63*, 9895.
(5) Buchanan, A. C., III; Biggs, C. A. *J. Org. Chem*. **1989**, *54*, 517.
(6) Poutsma, M. L.; Dyer, C. W. *J. Org. Chem*. **1982**, *47*, 4903.
(7) Gilbert, K. E. ;Gajewski, J. J. *J. Org. Chem*. **1982**, *47*, 4899.
(8) Sweeting, J. W.; Wilshire, J. F. *Aust. J. Chem***. 1962**, *15*, 9.
(9) King, H.-H.; Stock, L. M. *Fuel* **1982**, *61*, 1172.

A DENSITY FUNCTIONAL THEORETICAL STUDY OF S-H BOND STRENGTHS IN ORGANIC THIOLS AND A MODEL MoS CLUSTER

James A. Franz, Michel Dupuis, and Donald M. Camaioni and Jerome Birnbaum

Pacific Northwest National Laboratory, 902 Battelle Boulevard, MS K2-57, Richland, WA 99352

Introduction

Hydrosulfurization (HDS) is carried out by exposure of a substrate fuel source to a regime of hydrogen pressure and high temperatures in the presence of Co/MoS or Ni/MoS catalysts on γ-Al_2O_3 supports [Topsoe et al., 1996]. At temperatures of HDS, and in the presence of organosulfur structures, thermal free radical chemistry will accompany or even dominate many pathways of organic structure transformation. Hydrogenation and dehydrogenation of organic structure will be particularly sensitive to the nature of organosulfur intermediates. A major pathway of hydrogenolysis and hydrogenation is initiated by the transfer of hydrogen atom from a closed shell molecule to an acceptor [Rüchardt et al. 1997]. This reaction is the starting point for hydrogenation of unsaturated organic structure. The reaction is the reverse of the disproportionation reaction of two free radicals, and depends on the enthalpy change of the forward reaction. To predict the rate of reaction in eq 1, key information required is the bond strength of

$$RH + RHC{=}CH_2 \underset{}{\overset{\Delta H^o \sim \Delta H^{\ddagger}}{\rightleftharpoons}} R\bullet + \dot{R}CH\text{-}CH_3 \quad (1)$$

the participating organic or catalyst function (R-H, eq 1). In this paper, we present results of a density functional theory investigation of bond strengths of a series of thiols, and of the HDS prototype model, CpMo[(μ-S)$_2$(μ-SH)$_2$]MoCp, **1**, Cp = η^5-C_5H_5 [Rakowski DuBois, 1998]. This system is representative of a class of MoS cluster systems that are models of exfoliated MoS_2 catalysts [Curtiss, et al. 1996]. The level of theory for prediction of accurate (ca. 1-2 kcal/mol error) S-H bonds is explored. The reactivity of the prototype MoSH functionality in initiating homolytic hydrogenation steps is provided by the computational predictions.

Electronic Structure Calculations

Electronic structure calculations were carried out using the Gaussian 98 [Frisch, M.J., et al.] set of programs. Geometries were optimized using the LANL2DZ basis set {Hay et al. 1985] and effective core potentials within the B3LYP hybrid DFT formalism [Lee et al, 1998, Becke, et al 1993]. Vibrational calculations were carried out to verify ground states and to identify low frequency internal torsional modes for correction of electronic energies to enthalpies at 298 K. Vibrational frequencies were scaled by 0.9806 for zero point energy corrections and by 0.9989 for internal energy corrections. [see DiLabio et al. 1999] The electronic energy of H atom was set to -0.5 hartree. Bond strengths were calculated by two methods, direct dissociation (eq 2), and using isodesmic calculations (eq 3), with the bond strength of H_2S, 91.2 kcal/mol, as a reference. The substrates examined were H_2S,PhSH,

$$RS\text{-}H \rightarrow RS\bullet + H\bullet \quad (2)$$

$$RS\text{-}H + HS\bullet \rightarrow RS\bullet + H_2S \quad (3)$$

2-mercaptonaphthalene (Nap-2-SH), and methyl mercaptan. Using B3LYP/LANL2DZ geometries, three basis sets were examined for single point energy calculations, LANL2DZ, LANL2DZdp, and a basis set using the LANL2DZ basis set for Mo and the 6-311++G(2d,2p) basis set for C, S, and H, denoted LANLMo63.

Results and Discussion

Direct calculations of bond dissociation enthalpies (eq 2) typically underestimate bond strengths, at modest levels of theory, with improvement with basis set. This trend is shown for thiols examined here, for which the calculate BDEs have increased to within 0.5 kcal/mol of experiment with the use of the extended basis set on C, H, and S atoms. Under favorable circumstances, isodesmic calculations (eq. 3) converge to experimental values at more modest levels of theory than required for eq. 2. In cases examined here, use of increasingly larger basis sets leads to convergence from values of BDE higher in all cases than experiment to within 0.5 kcal/mol of experiment for CH_3SH, PhSH, and Nap-2-SH. Taking the values of eq. 3 (isodesmic) values, bond strengths for CH_3SH, PhSH, and Nap-2-SH are predicted to be 87.7, 79.3, and 78.1 kcal/mol, compared to experiment, 87.3, 78.9, and 77.9 kcal/mol, respectively. The calculations predict (by eq. 3) an S-H bond strength of 73.2 kcal/mol for the MoS model cluster, **1**(eq 4).

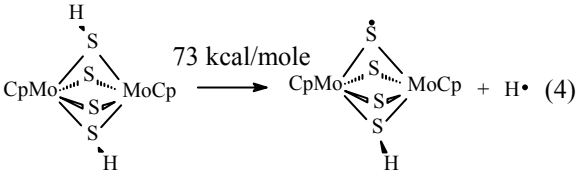

(4)

1

Thus, the μ_2-SH bond, a functional group suggested to be present in heterogeneous MoS catalysts, is *much more reactive* than conventional thiols in radical-forming reactions. Thus, for example the key radical initiating step leading to hydrogenation/ dehydrogenation of olefinic structure, hydrogen transfer to an olefin, which is controlled by the S-H bond strength, will occur several orders of magnitude faster than with simple organic thiols (eqs 5,6):

$$Mo_2SH + CH_2{=}CH_2 \rightarrow Mo_2S\bullet + CH_3\text{-}CH_2\bullet \quad (5)$$

$$CH_3\text{-}CH_2\bullet + Mo_2SH \rightarrow CH_3CH_3 \quad (6)$$

Conclusions

Density functional theory calculations suggest that the SH functional group in MoS clusters should exhibit substantially enhanced homolytic reactivity compared to conventional thiols, leading to enhanced rates of hydrogenation and other radical pathways. The accuracy of the prediction of the S-H bond strength of **1** awaits experimental determination of the S-H bond strength.

Acknowledgement. This work was supported by the Office of Science, Office of Basic Energy Sciences, U.S. Department of Energy under contract DE-ACO6-76RLO 1830.

References

(1) Topsoe, H.; Clausen, B.S.;Massoth, F.E. Hydrotreating Catalysis. Science and Technology. Springer-Verlag, Berlin, 1996, 310pp.

(2) Rüchardt, C.; Gerst, M.; Ebenhoch, J. *Angew. Chem. Intl. Ed. Engl.* **1997**, *36*, 1406.

(3) Rakowski DuBois, M. *Catalysis by Sulfido Bridged Dimolybdenum Complexes*, in Catalysis by Di-and Polynuclear Metal Cluster Complexes, Richard D. Adams and F. Albert Cotton Eds., Wiley-VCH Inc., New York, **1998**, p. 127-143, and references therein.

(4) Curtis, M. D. *Hydrodesulfurization Catalysis and Catalyst Models Based on Mo-Co-S Clusters and Exfoliated MoS_2*, in Transition Metal-Sulfur Chemistry ACS Symposium Series 653, Stiefel, E. I.; Matsumoto, K. Eds. **1996**, p. 154-175, and references therein.

(5) Frisch, M.J. et al. Gaussian 98, Gaussian, Inc., Pittsburgh PA, 2001

(6) Hay, P.J. and Wadt, W.R. J. Chem. Phys. **1985**, *82*, 270,284, 299.

(7) (a) Lee, C.; Yang, W.; Parr, R.G. *Phys. Rev. B* **1988**, *37*, 785. (b) Becke, A.D. *J. Chem. Phys.* **1993**, *98*, 5648.

(8) DiLabio, G.A.; Pratt, D.A.; LoFaro, A.D.; and Wright, J.S. *J. Phys. Chem A* **1999**, *103*, 1653-1661.

Table 1. S-H Bond Dissociation Enthalpies (kcal/mol, 298K) for CpMo[(μ-S)$_2$(μSH)$_2$]MoCp (1), H_2S, CH_3SH, PhSH, and Naphthalene-2-thiol

Level of Theory	H_2S (expt 91.2)	**1**		PhSH (expt 79.1)		Nap-2-SH (expt 77.9)		CH_3SH (expt 87.3)	
	Eq 2	Eq 2	Eq. 3	Eq2	Eq 3	Eq 2	Eq 3	Eq 2	eq 3
LANL2DZ	78.7	63.3	76.6	67.8	81.1	66.9	80.3	75.3	88.7
LANL2DZdp	88.0	70.6	74.7	76.6	80.6	75.5	79.6	84.3	88.4
LANLMo63	90.4	72.5	73.2	78.5	79.3	77.4	78.1	86.9	87.7

PYROLYSIS RATE ENHANCEMENT FOR 1,3-DIPHENYLPROPANE CONFINED IN MESOPOROUS SILICAS

Michelle K. Kidder, A. C. Buchanan, III, Phillip F. Britt, Zongtao Zhang, and Sheng Dai

Oak Ridge National Laboratory
Chemical Sciences Division
Bethel Valley Road
P.O. Box 2008, MS-6197
Oak Ridge, Tennessee 37831-6197

Introduction

Our research on the effects of restricted mass transport on the pyrolysis kinetics and mechanisms of fuel model compounds has employed molecules chemically attached to the surface of fumed silica particles.[1,2] These silica nanoparticles are nonporous and derive their moderately high surface areas (200 m^2 g^{-1}) from the small particle size (12 nm). Hence, the molecules are all attached on the external surface of the relatively flat, low fractal dimension (2.08) silica in essentially a two-dimensional confinement. Organic energy resources such as coal are porous solids, and mass transport limitations in the processing of non-softening coals have been attributed to hindered tar transport between pores.[1] Hence, we are now extending our fundamental pyrolysis studies to investigate the effects of pore confinement on pyrolysis mechanisms. Our initial studies focus on mesoporous silica-immobilized 1,3-diphenylpropane bound to the pore walls via a Si-O-C_{aryl} linkage.

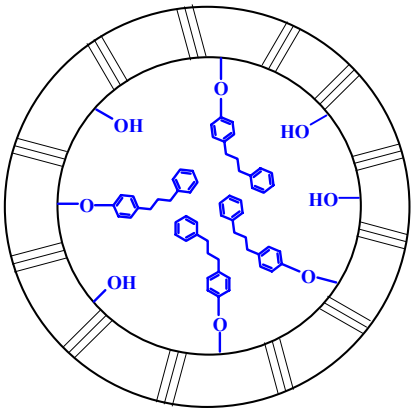

Experimental

Materials. Benzene was distilled from sodium before use. High purity acetone, dichloromethane, 1,1,3,3-tetramethyldisilazane and water were commercially available and used as received. Cumene was fractionally distilled (2x), and 2, 5-dimethylphenol and *p*-phenylphenol were recrystallized (3x) from hexanes and benzene/hexanes, respectively, prior to use. Cabosil was commercially available (Cabot Corp.). The mesoporous silica, SBA-15, was prepared following standard procedures employing the $EO_{20}PO_{70}EO_{20}$ amphiphilic triblock copolymer as template and reaction temperatures of 35 °C for 20 hours and then 80 °C for 48 hours.[3] MCM-41 was synthesized by standard methods using hexadecyltrimethylammonium bromide as the template.[4] Resulting pore sizes and surface areas are given in Table 1.

Surface Attachment. Surface attachment procedures followed a previously established method,[1,2] and only highlights are given below. Excess *p*-(3-phenylpropyl)phenol (HODPP) is adsorbed onto the surface of the dried silica by solvent evaporation from a benzene slurry. The attachment reaction was performed at 225 °C for 1 h, in a fluidized sand bath on a thoroughly degassed, evacuated (< 10^{-5} Torr), sealed sample. The sample was then transferred to another tube, connected to a vacuum at 5 x 10^{-3} Torr, and heated in a tube furnace from 225 to 275 °C at a rate of 10 °C/ min and held at 275 °C for 10 min, to remove unattached HODPP. The samples were stored in a desiccator under vacuum. Surface coverage analysis was determined via the base hydrolysis procedure described below, and by carbon elemental analysis (Galbraith Laboratories).

Silylation of Cabosil, SBA-15 and MCM-41. The silylation reactions were performed according to the procedure of Anwander, et. al.[5] The silica was dried at 200 °C for 4 h and cooled in a desiccator. Approximately 0.1 – 0.2 g of the dried material was suspended in ca. 10 mL of *n*-hexane. 1,1,3,3-Tetramethyldisilazane (5 mmol) diluted in 5 mL *n*-hexane, was added to the silica slurry and stirred at ambient temperature for 24 h. The unreacted disilazane was separated by filtration on a 30 mL fine fritted filter (30F), followed by several additional washings with *n*-hexane. The solid material was dried under vacuum for 5 h at room temperature, then heated to 250 °C for 3 h under high vacuum. Surface coverage analysis was performed by carbon elemental analysis.

Surface and pore analysis. The surface analysis based on the nitrogen adsorption and desorption isotherm at 77 K was performed on a Quantachrome AUTOSORB-1 system. The BET specific surface area was obtained from the nitrogen adsorption data in the relative pressure range from 0.05 to 0.35. The pore size data was analyzed by the BJH (Barrett-Joyner-Halenda) method from an analysis of the desorption branch of the isotherm.

Thermolysis Procedure. A weighed amount of sample (0.03-0.09 g) was placed in one end of a thoroughly cleaned T-shaped Pyrex tube, evacuated, and sealed at ca. 2 x 10^{-6} Torr. The sample was inserted into a preheated temperature-controlled tube furnace (±1°C) fitted with a copper sample holder, and the other end was placed in a liquid nitrogen bath. The products that evolved were collected in the cold trap and dissolved in acetone (0.1-0.2 mL) along with 0.1 mL each of a solution of the internal standards, cumene, and 2, 5-dimethylphenol, and *p*-phenylphenol. These products were analyzed by GC on a Hewlett-Packard 5890 Series II gas chromatograph employing a J & W Scientific 30 m x 0.25 mm i.d., 0.25 µm film thickness DB-5 column and a flame-ionization detector. Mass spectra were obtained at 70 eV with a Hewlett-Packard 5972A GC-MS equipped with a capillary column matched to that used for GC analyses. The surface–attached products were analyzed through base hydrolysis of the solid residue in 1N NaOH, addition of 2,5-dimethylphenol (0.1 mL) and *p*-phenylphenol (1.0 mL) as internal standards, acidification of the solution with HCl, and extraction with dichloromethane. The solvent was evaporated and the residue was silylated with BSTFA:pyridine (1:2) and analyzed via GC and GC-MS.

Results and Discussion

Surface Chemistry. Semi-crystalline, mesoporous silicas MCM-41 and SBA-15 contain hexagonally arranged mesopores of controllable size that can be readily functionalized with organic and organometallic moieties.[6] Applications range from chemical separations to catalysis. Most surface derivatization schemes involve the reaction of a silane coupling agent (R_3Si-Cl, R_3Si-OR', R_3Si-NH-SiR_3) with the surface silanols to give a siloxane linkage (≡Si-O-SiR_3) to the surface. The disilazane, Me_2HSi-N-$SiHMe_2$, has been used to report the density of accessible silanol sites for MCM-41.[5] In Table 1, quantitative silylation results for this reagent reacting with Cabosil, SBA-15 (5.6 nm), and MCM-41 (2.9 nm) are compared. Our value for the density of accessible surface silanols for MCM-41 (1.99 nm^{-2}) compares favorably with that obtained by Anwander for a MCM-41 with a slightly higher surface area of 1139 m^2/g (1.85 nm^{-2}). Note that similar densities of surface silanols are obtained for silylated Cabosil and SBA-15.

In our studies of the pyrolysis of immobilized fuel model compounds on the surface of Cabosil, we have employed a different surface derivatization method that does not employ silane coupling reagents.[1] The reaction of the surface silanols with a phenolic precursor results in a Si-O-C_{aryl} linkage to the surface. We have found this linkage to be thermally robust to ca. 550 °C, which permits the study of pyrolysis reactions under surface confinement. However, the linkage is easily cleaved with aqueous base permitting the recovery of reaction products from the surface. It is anticipated that the maximum surface densities of the larger DPP moieties will be less than for the smaller silane derivative. The three silicas were reacted with excess *p*-HOPh$(CH_2)_3$Ph and analyzed by both chemical analysis (*vide supra*) and carbon elemental analysis (combustion). The surface coverages for these two methods (Table 1) are in agreement for all three silicas within ± 5% indicating that the DPP molecules can be completely recovered from the mesoporous silicas by the chemical method. As expected, the DPP surface densities are lower than the $SiHMe_2$ densities. However, it is interesting that the magnitude of this effect is larger for the mesoporous solids suggesting a more crowded environment than on the exterior surface of the nonporous Cabosil particles. These hybrid materials are being further characterized by BET surface analysis, FTIR, and NMR relaxation measurements.

Table 1. Surface Derivatization of Silicas with $(Me_2HSi)_2NH$ and *p*-HOPh$(CH_2)_3$Ph

Surface Analysis	Cabosil (200 m^2/g)	SBA-15 (543 m^2/g; 5.6 nm pore)	MCM-41 (1088 m^2/g; 2.9 nm pore)
---SiH$(CH_3)_2$			
Coverage (mmol/g)[a]	0.68	1.45	2.97
Density (nm^{-2})[c]	**2.12**	**1.77**	**1.99**
---Ph$(CH_2)_3$Ph			
Coverage (mmol/g)[a]	0.55	0.94	1.62
Coverage (mmol/g)[b]	0.53	0.99	1.71
Density (nm^{-2})[c]	**1.78**	**1.37**	**1.43**

[a] From elemental analysis (carbon) on a per g of derivatized silica basis. [b] From chemical analysis on a per g of derivatized silica basis. [c] Surface density calculated on a per g of silica basis.

Pyrolysis Results. Surface-attached 1,3-diphenylpropane (≈DPP) undergoes a free radical chain decomposition reaction at 375°C to produce surface-attached toluene and gas-phase styrene plus the complementary product pair, gas-phase toluene and surface-attached styrene.[2,7] The free radical chain mechanism (chain length in excess of 200) involves hydrogen abstraction by surface-attached

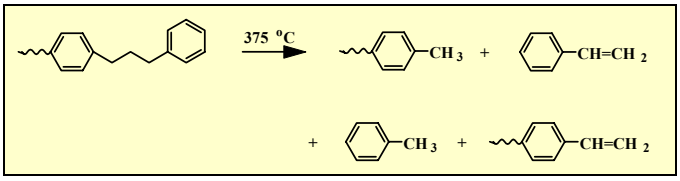

Figure 1. Products from pyrolysis of mesoporous silica-attached DPP. The jagged line represents position of attachment.

and gas-phase benzyl radicals from the benzylic positions of ≈DPP to give regiochemically distinct benzylic radicals, which undergo facile β-scission to produce the surface-attached and gas-phase styrene products, as well as regenerating the chain carrying benzyl radicals. Reaction rates and selectivity in product formation are highly dependent on surface coverage (proximity of neighboring molecules and radicals involved in hydrogen transfer propagation steps). The ≈DPP pyrolysis rate at saturation surface coverages is comparable to that for DPP in fluid phases, but the rate decreases dramatically with decreasing surface coverage. As can be seen from the data in Table 2, ≈DPP pyrolysis rates at saturation surface coverage for the mesoporous silicas, despite the lower density of derivatized sites, are somewhat faster than that for the Cabosil and appear to be faster for the smaller pore size. This suggests that there is a pore-size dependence for the pyrolysis rate, which likely arises from faster hydrogen atom transfer steps on the surface, for the smaller, more highly curved pores. Additional studies of smaller pore size MCM-41 materials (1.7-2.4 nm) are in progress. Since the size of a DPP molecule is approximately 1.2 nm, these pores could become quite crowded and lead to interesting pyrolysis behavior.

Selectivity in product formation, measured by the ratio of styrene to toluene yields in the gas phase also appears to be slightly larger for pore-confined DPP compared with the Cabosil suggesting an unexpected selectivity in the rates of hydrogen abstraction at the two benzylic carbons.[7] This phenomenon is also under current investigation.

Table 2. Pyrolysis Rates for Surface-Immobilized 1,3-Diphenylpropane (≈DPP) at Saturation Surface Coverage.

Silica	Pore Size (nm)	≈DPP Surface Coverage (mmol/g)	≈DPP Density (nm^{-2})	≈DPP Rate at 375°C[a] (%/h)
Cabosil	NA	0.53	1.8	8.4
SBA-15	5.6	0.99	1.4	11.3
MCM-41	2.9	1.71	1.4	14.4

[a] Rates are obtained from the slopes of plots of ≈DPP conversion versus time, and have a typical accuracy of ± 10%.

Conclusions

Mesoporous silicas, SBA-15 and MCM-41, can be derivatized with phenols to give novel hybrid materials possessing thermally robust Si-O-C_{aryl} linkages. Initial pyrolysis results for the surface-attached DPP probe molecule suggest that pore confinement can lead to larger reaction rates and alterations in product selectivity that may correlate with pore size. Additional experiments with smaller pore size MCM-41 silicas are in progress.

Acknowledgment. This research was sponsored by the Division of Chemical Sciences, Geosciences, and Biosciences, Office of Basic Energy Sciences, U.S. Department of Energy under contract DE-AC05-00OR22725 with Oak Ridge National Laboratory, managed and operated by UT-Battelle, LLC.

References

(1) Buchanan, A. C., III; Britt, P. F. *J. Anal. Appl. Pyrolysis* **2000**, *54*, 129; and references therein.
(2) Buchanan, A. C., III; Britt, P. F.; Thomas, K. B.; Biggs, C. A. *J. Am. Chem. Soc.* **1996**, *118*, 2182.
(3) Zhao, D.; Feng, J.; Huo, Q.; Melosh, N.; Fredrickson, G. H.; Chmelka, B. F.; Stucky, G. D. *Science* **1998**, *279*, 548.
(4) Beck, J. S.; Vartuli, J. C.; Roth, W. J.; Leonowicz, M. E.; Kresge, C. T.; Schmitt, K. D.; Chu, C. T-W.; Olson, D. H.; Sheppard, E. W.; McCullen, S. B.; Higgins, J. B.; Schlenker, J. L. *J. Am. Chem. Soc.* **1992**, *114*, 10834.
(5) Anwander, R.; Nagl, I.; Widenmeyer, M.; Engelhardt, G.; Groeger, O.; Palm, C.; Roser, T. *J. Phys. Chem. B* **2000**, *104*, 3532.
(6) Anwander, A. *Chem. Mater.* **2001**, *13*, 4419.
(7) Buchanan, A. C., III; Biggs, C. A. *J. Org. Chem*. **1989**, *54*, 517.

THE EFFECTS OF NANOPARTICLE IRON OXIDE ON CO AND NO REMOVAL IN BIOMASS PYROLYSIS AND OXIDATION PROCESSES

Ping Li, Firooz Rasouli, and Mohammad R. Hajaligol

Research Center, Philip Morris USA
4201 Commerce Road
Richmond, VA 23234

Introduction

Nanoparticle iron oxide such as NANOCAT® Superfine Fe_2O_3 (referred as NANOCAT® hereafter) by Mach I, Inc. was evaluated as a potential catalyst for Direct Coal Liquefaction (DCL) process shortly after it became available.[1] Recently, it was found that the material, which has an average particle size of 3 nm, was an efficient CO catalyst with a performance far better than other supported or un-supported iron oxide.[2] It is also known that the reduced form of Fe_2O_3 such as Fe_3O_4 is the effective catalytic component for CO + NO reaction.[3] Therefore, NANOCAT® could potentially be used as a catalyst for the simultaneous CO and NO removal in biomass pyrolysis and combustion, for example, in cigarette.[4]

The kinetics of NANOCAT® as a CO catalyst in the well-controlled gaseous environments of CO and O_2 has been presented elsewhere.[2,5] However, the performance of a CO/NO catalyst in a clean, contaminant-free gaseous environment is not necessarily transferable to the application of biomass pyrolysis and combustion since a lot of other pyrolytic products could potentially deactivate the catalyst. In this study, biomass was pre-mixed with NANOCAT® prior to pyrolysis and oxidation. The mixed NANOCAT® went through the pyrolysis and the oxidation processes with biomass and its effect on CO and NO removal was then evaluated. The experimental results on biomass were compared to those obtained in the controlled gaseous environment and the possible difference in the catalytic mechanism under two different conditions was discussed.

Experimental

Materials. The NANOCAT® sample was purchased from MACH I, Inc. (King of Prussia, PA.). The sample was a free flow, brownish color powder with a bulk density of only 0.05 g/cm^3. The average particle size was 3 nm and the BET surface area was 250 m^2/g, according to the manufacturer. The biomass sample used in the experiment was a mixture of tobacco powders including Bright, Burley, and Oriental. Sample also contained 7% moisture. The powder was sieved through a 200-mesh screen. The CO (4%), NO (5000 ppm), and O_2 (21%) gases, all balanced with Helium, and mixtures of 3.44% CO with 20.6% O_2, also balanced with helium, were purchased from BOC Gases with certified analysis.

Flow tube reactor system. The experiments with biomass were carried out in a flow tube reactor system. 500 mg of biomass powder was used as a control sample. 500 mg of biomass + 50 mg of NANOCAT®, mixed thoroughly, was used as the test sample. The samples were then placed in a quartz flow tube (length: 50 cm, I.D: 2.0 cm) and sandwiched by two clean pieces of quartz wool in the center of the flow tube. The flow tube was then placed inside a Thermcraft furnace controlled by a temperature programmer. The sample temperature was monitored by an Omega K-type thermocouple inserted into the sample. Another thermocouple was placed in the middle of the furnace, outside the flow tube, to monitor the furnace temperature. An in house Labview-based program recorded the temperature data. The temperatures of the sample were used in all plots except indicated otherwise. The inlet gases to the flow tube were controlled by a Hastings digital flow meter. The effluents first passed through an ultra fine fiber glass filter pad to collect the room temperature condensables. The gases were then analyzed by an online NGA2000-MLT multi-gas analyzer from Rosemount Analytical. The analyzer used non-dispersive near infrared detectors for CO, NO and CO_2, and a paramagnetic detector for oxygen. The rate of data acquisition was one measurement for all gases per second.

A two-step experiment of pyrolysis and oxidation was carried out for both pure biomass and biomass mixed with NANOCAT®. In the first step, sample was heated at about 12 ^{o}C/min. heating rate to 350 ^{o}C with a hold time of 20 minutes under 500 mL/min. flow of helium. After the sample was completely cooled down to the ambient temperature, the second step, the oxidation of the freshly formed char was performed. In this step, the inlet gas containing 21% O_2, was flown at 500 mL/min., and the temperature was raised from ambient to 750 ^{o}C at about 12 ^{o}C/min. heating rate. CO, NO, and CO_2 production in both steps, and O_2 consumption in the second step were measured. The condensate collected in the pyrolysis step was also gravimetrically measured.

The catalytic performance of NANOCAT® for CO + O_2 and CO + NO reactions in the well-controlled gaseous environments were evaluated in the same setup but with a narrower quartz tube (I.D.: 0.8 cm). The total gas flow rate was fixed at 1000 mL/min. and the NANOCAT® used in each test was 50 mg.

Results and Discussion

Under the well-controlled gaseous condition, NANOCAT® was an efficient catalyst for the $2CO + O_2 = 2CO_2$ reaction, as shown in **Figure 1**. The performance of NANOCAT® was significantly better compared to the other forms of iron oxide such as α-Fe_2O_3. The onset temperature was at least 100 ^{o}C lower and the CO conversion efficiency was almost ten times higher.[2] The dramatic improvement was attributed to the small particle size and the existence of the FeOOH phase in NANOCAT®. In the absence of O_2, NANOCAT® was reduced by CO to form Fe_3O_4, FeO, and Fe, which were catalysts for the $2CO + 2NO = 2CO_2 + N_2$ reaction, also shown in **Figure 1**.

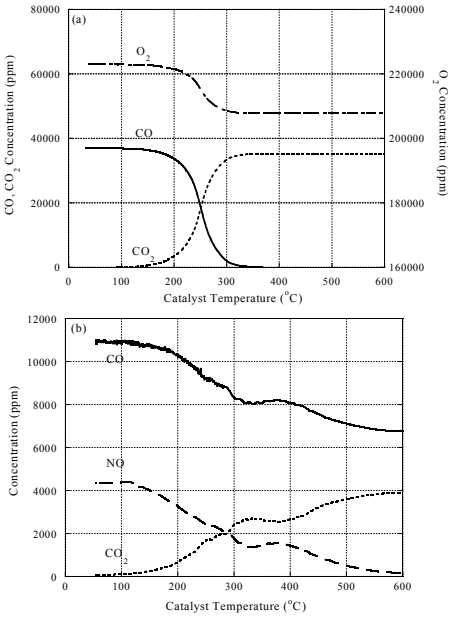

Figure 1. Flow tube test of NANOCAT® as the catalyst for (a) CO + O_2 reaction, (b) CO + NO reaction.

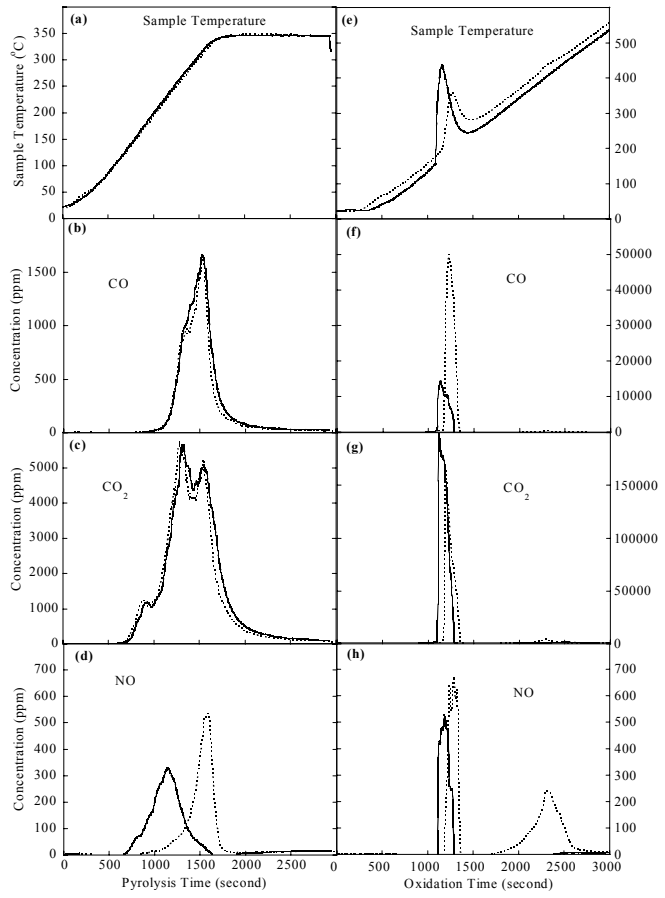

Figure 2. Temperature profile and CO, CO_2, and NO production during pyrolysis ((a) – (d)) and oxidation ((e) – (h)) processes. Solid line: test sample with biomass powder and NANOCAT®. Dashed line: control sample with biomass powder only.

The pyrolysis and oxidation of mixture of biomass and NANOCAT® constitute a much more difficult chemical environment for CO and NO catalysts to be effective. Many products evolved during the pyrolysis of biomass could potentially deactivate the catalysts. Thus, it is important to investigate the performance of NANOCAT® in an environment controlled by the biomass pyrolysis and oxidation processes. The tests were carried out by mixing biomass and NANOCAT® together and the mixtures then underwent the pyrolysis and the subsequent char oxidation process, as the control biomass sample. The results are shown in **Figure 2** and the integrated data are summarized in **Table 1**. It can be clearly seen that the effects of NANOCAT® on CO, CO_2, and NO evolution during the pyrolysis were minimal. The only notable change was that with NANOCAT®, NO evolved at lower temperature. However, significant changes were observed in the subsequent char oxidation process of the sample with NANOCAT®. CO production was reduced by 67%, from 1.89 to 0.63 mmol, and NO was also reduced by 57%, from 0.060 to 0.026 mmol. Since the CO oxidation is highly exothermic, a bigger temperature rise was observed for the sample with NANOCAT®, as shown in **Figure 2 (e)**. One interesting observation was that the increase of CO_2 (8.37 - 5.93 = 2.44 mmol) was more than the decrease of CO (1.89 – 0.63 = 1.26 mmol), suggesting that the oxidation of other compounds also contributed to the total CO_2 production. A lower amount of condensate was collected in the filter pad for the biomass sample mixed with NANOCAT®, 50.6 mg versus 64.3 mg for the control biomass sample because some of the condensable components were adsorbed by NANOCAT® during the pyrolysis step. These adsorbed components were then catalytically oxidized to CO_2 during the oxidation step. Higher O_2 consumption for the char sample with NANOCAT® (8.96 vs. 7.02 mmol) also confirmed this mechanism.

Table 1. Summary of the Pyrolysis and Oxidation Results (mmol)

		CO	CO_2	NO	O_2
Pyrolysis	Control	0.18	1.11	0.049	
	Test	0.21	1.17	0.047	
Char Oxidation	Control	1.89	5.93	0.060	7.02
	Test	0.63	8.37	0.026	8.96

In addition to the CO + NO reaction, NO + char reaction could also contribute to the total removal of NO.[6] This is clearly another possible mechanism to explain the decrease of NO production in the oxidation step of the biomass mixed with NANOCAT®. Additional tests were carried out to verify if the existence of NANOCAT® would promote the NO + char reaction. The experiments were done by simply switching 21 % O_2 to 1500 ppm of NO in the oxidation steps. As shown in **Figure 3**, the onset temperature of NO + char reaction was reduced in the biomass char sample with NANOCAT® and the complete NO removal was achieved at a temperature less than 400 ^oC, which was more than 200 ^oC lower compared to the control sample.

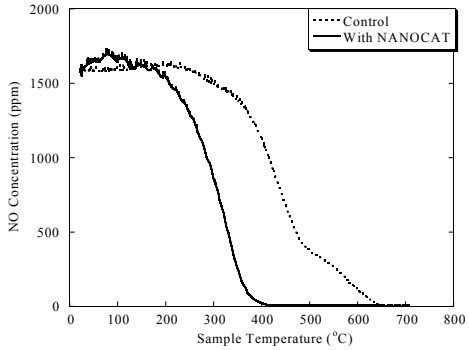

Figure 3. The effect of NANOCAT® on NO + char reaction.

Acknowledgment

The support of Philip Morris USA management on fundamental science research is gratefully acknowledged.

References

1. Huffman, G. P., Ganguly, B., Zhao, J., Rao, K. R. P. M., Shah, N., Feng, Z., Huggins, F. E., Taghiei, M. M., Lu, F., Wender, I., Pradhan, V. R., Tierney, J. W., Seehra, M. M., Ibrahim, M. M., Shabtai, J., Eyring, E. M., *Energy Fuels*, **1993**, *7*, 285.
2. Li, P., Miser, D. E., Rabiei, S., Yadav, R. T., Hajaligol, M. R., *Appl. Catal. B,* **2003**, in press.
3. Randall, H., Doepper, R., Renken, A., *Appl. Catal. B*, **1998**, *17*, 357.
4. Li, P., Rasouli, F., Hajaligol, M. R., *Beiträge zur Tabakforschung International*, **2003**, submitted.
5. Li, P., Shin, E., Miser, D. E., Rasouli, F., Hajaligol, M. R., to be published in *Nanotechnology in Catalysis*; Zhou, B., Hermans, S., Somorjai, G. A., Ed., Kluwer Academic/Plenum, **2003**.
6. Aarna, I., Suuberg, E. M., *Fuel*, **1997**, *76*, 475.

STUDIES ON CHEMICAL MECHANISM OF 1-HEPTENE ACID-CATALYZED REACTIONS

Zheng Li, Jian-Fang Zhang, Chao-He Yang, Hong-Hong Shan

State Key Laboratory of Heavy Oil Processing, University of Petroleum, Dongying, Shandong, 257061, P. R. China

Introduction

There have been a few disputes about the mechanisms of alkenes reactions on solid acidic catalysts for over half a century since Greensfelder and Thomas proposed their carbenium ion theory in 1949. It is generally accepted that the active centers in those reactions are protic acidic centers (Brønsted Acid Centers) on the catalyst surface and that the reactive intermediates are carbenium ions. Most researchers agreed that the cracking of carbenium ions happens via the β-C-C-bond scission mechanism. That theory is still being quoted in most literatures on catalytic cracking for it did explain some features of catalytic cracking and forecast the product distribution of some reactions successfully. Nevertheless, large quantities of experimental data have shown that its simple description of catalytic cracking process was not accurate enough. The carbenium ions also undergo skeletal isomerization via the protonated cyclopropane mechanism[1]. That course is demonstrated

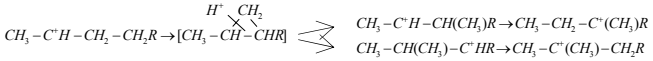

Fig 1. Protonated Cyclopropane Mechanism

by Fig 1. Reactions of alkenes over acidic catalysts are often accompanied by the formation of alkanes. However, such reactions are not yet known in detail.

Experiment

In this paper, pulsating reaction system (Fig 2) and a mini reactor with 1.5 mm i.d. were employed to investigate the fast reactions of alkenes. 1-heptene was chosen as substrate due to its limited number of reaction pathways and products. The most commonly used types of zeolite on FCC unit, USY and HZSM-5, were introduced to the experiments.

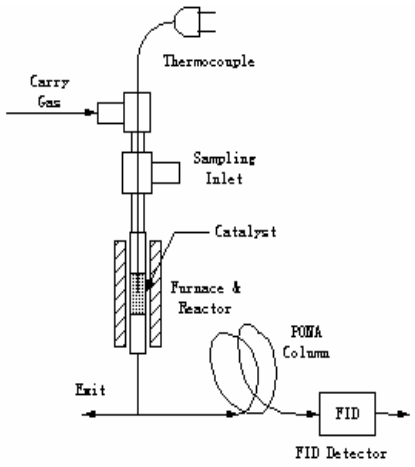

Fig 2. Flowchart of Pulsating Reaction System

Results and Discussion

Cracking Products of 1-Heptene. According to the β-scission mechanism, the primary cracking products, butene, of 1-heptene should be linear. However, experimental data showed that product was skeletally isomerized to a large degree (Seen in Table 1). For instance, in the cracking products of 1-heptene over USY and HZSM-5 at 500 ºC, the iso/normal ratios of butene were 0.561 and 0.822 respectively, which are higher than thermodynamic equilibrium value (0.46[2]). Although the possibility of skeletal isomerization of primary products after cracking can not be taken out of consideration, it is obviously unreasonable that the degree of isomerization always exceeds the thermodynamic equilibrium value. The same result had been shown by 1-heptene's cracking over HZSM-5 at 510 ºC in Buchanan's research[3], in which the iso/normal ratio of butene was 0.742, whereas the equilibrium ratio under that condition is 0.458[2]. It proves that at least some of the isobutene is primary product of the cracking and not a result of post-isomerization. Thus, the excess isobutene in 1-heptene cracking may be understood if skeletal isomerization of carbenium ions is a prerequisite for cracking.

Table 1. Cracking Products of 1-Heptene at 500 ºC

Catalyst	Conv. wt%	Yield wt%					i-$C_4^=$/ $C_4^=$
		$C_3^=$	i-$C_4^=$	t-2-$C_4^=$	c-2-$C_4^=$	1-$C_4^=$	
USY	97.36	19.568	15.286	5.809	5.038	1.115	0.561
HZSM-5	96.57	13.024	14.653	1.394	1.080	0.703	0.822

Saturated Products of 1-Heptene. Notable amounts of dimethyl-substituted alkanes with the same carbon number as the substrate were found in catalytic conversion products of 1-heptene (Seen in Table 2). For examples, over USY and HZSM-5 at 500 ºC, the yields of 2,3-dimethyl pentane are 2.808 wt% and 2.887 wt% respectively in the products. According to traditional carbenium ion mechanisms, those iso-alkanes must be secondary products. They are produced through substrate's isomerization and then hydrogen transfer (Route A) or hydrogen transfer then isomerization (Route B). It is a fact that hydrogen transfer reactions are reversible reactions and their reaction rates are fairly low under common catalytic cracking temperature. If those iso-alkanes are produced through Route A, there must be some corresponding iso-alkenes in the products. Unfortunately, those corresponding iso-alkenes are totally absent in the products (Seen in Table 3). If those iso-alkanes are produced through Route B, the iso/normal ratios must be less than the thermodynamic equilibrium value of isomerization reactions. However, the experimental data are 3.7 and 0.45, and the equilibrium value is 0.21[4]. Consequently, traditional carbenium ion mechanism cannot rationalize those excess iso-alkanes. At least some of the iso-alkanes are primary products and it is reasonable that extensive skeletal isomerization of the carbenium ions may precede hydrogen transfer.

Table 2. Saturated C_7 Products of 1-Heptene at 500 ºC

Yield wt%	Catalyst Type	
	USY	HZSM-5
n-C_7^0	0.758	6.401
2,4-DM-C_5^0	0.122	-
3,3-DM-C_5^0	0.151	0.906
2-M-C_6^0	3.050	4.027
2,3-DM-C_5^0	2.808	2.887
3-M-C_6^0	1.413	1.418
3-E-C_5^0	1.877	3.226

Those excess branching of cracking products and hydrogen transfer products are therefore intrinsic features rather than incidental occurrences, and traditional carbenium ion mechanisms cannot explain them.

In addition, observable quantities of ethyl-substituted alkanes and alkenes with the same carbon number as the substrate were detected in the products. Moreover, those ethyl-substituted products bore some characteristics of primary products for they stood out when the substrate conversion was fairly low. Obviously, those phenomena can not be rationalized by protonated cyclopropane mechanism.

Table 3. Isomerized C_7 Alkenes of 1-Heptene at 500 ºC

Yield wt%	Catalyst Type	
	USY	HZSM-5
2-$C_7^=$	6.468	8.856
3-$C_7^=$	7.437	14.424
2,4-DM-2-$C_5^=$	0.551	0.612
2-M-2-$C_6^=$	1.833	2.386
3,4-DM-2-$C_5^=$	1.305	1.400
3-M-2-$C_6^=$	8.255	9.529
3-M-3-$C_6^=$	2.130	3.071
3-E-2-$C_5^=$	2.206	1.158

Proposition of CTS Mechanism. On the basis of the above analysis, we put forward a new mechanism to explain the catalytic transformation of 1-heptene, in which the Cyclo-Transition State (CTS) postulated earlier for isomerization of carbenium ions were applied as a starting point for the carbenium ions fission and hydrogen transfer steps. The CTS mechanism introduced protonated dialkylcyclopropane and dialkylcyclobutane, which are thermodynamically favorable in its formation by quantum-mechanical calculations[5][6][7], as transition states. Then, rings on those three-membered or four-membered ringed ions opened at different position, which lead to the formation of branched carbenium ions. Finally, those branched carbenium ions proceeded β-C-C-bond scission, hydrogen transfer and desorption (isomerization), if possible. The CTS mechanism could be represented as Fig 3.

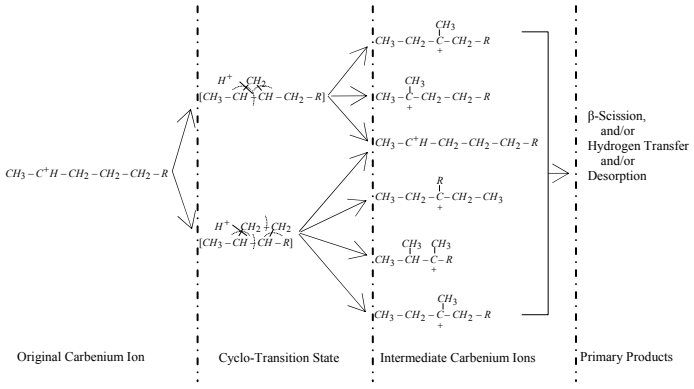

Fig 3. CTS Mechanism

It can be inferred from Fig 3 that the overall reaction depicted by CTS mechanism is the transformation of a secondary carbenium ion to a tertiary one or a secondary one. From the viewpoint of energy, there is a positive driving force for the reaction. Thus, the proposed mechanism is practicable since the reaction pathway doesn't involve a high energy barrier.

Product Predictions of CTS Mechanism. According to CTS mechanism, there are five types of intermediate carbenium ions produced with different skeleton altogether. Those intermediate carbenium ions and their following reactions are shown in Fig 4. In order to simplify the analysis, we only discuss the reactions of the most thermodynamically stable carbenium ions of each type, that is, tertiary or secondary carbenium ions, for those reactions happen more easily than others.

Some assumptions are soundly made in the design of reaction pathways of those intermediate carbenium ions. Two kinds of β-scission reactions, which will lead to the formation of methyl carbenium ion or ethyl carbenium ion, will not happen. The reason is that the formations of those primary carbenium ions are strong endothermic reactions and they are highly energetically unfavorable under common FCC temperature. During the course of desorption of carbenium ions from catalyst surface, an H atom will be donated by a carbenium ion to the acid center. The abstraction of H atom from methyl groups is considered as an impossible reaction because such abstraction from other kind of carbon atoms proceeds more facilely [1].

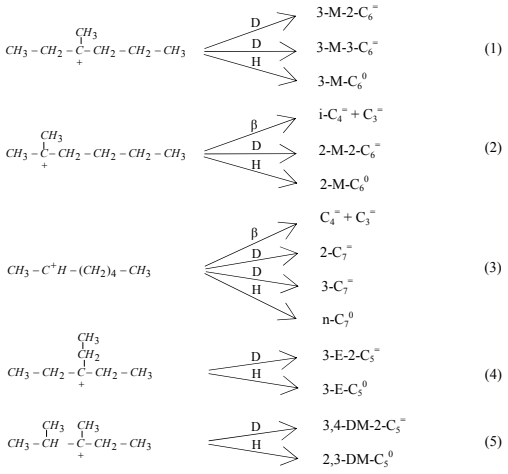

Fig 4. Reaction Pathways of Intermediate Carbenium Ions
NOTE: D, H and β in Fig 4 mean desorption, hydrogen transfer and β-Scission respectively,

There is one point should be noted in Fig 4. It seems that 2,3-dimethylpentene would be produced through carbenium ions' desorption in reaction (5). However, that reaction doesn't happen at all since the electron donating effect of methyl groups strengthen the C-H bond on the tertiary C atom.

Conclusions

Generally speaking, the predictive primary products of cracking, isomerization and hydrogen transfer of 1-heptene by this new mechanism are perfectly consistent with the experimental results shown in Table 1, 2 and 3. Furthermore, with this new mechanism, the excess iso-hydrocarbons in the products of 1-heptene over solid acid catalyst could be well understood.

In a word, the CTS mechanism not only inherits all the advantages of β-scission mechanism and isomerization mechanism, but also it is capable of providing a logical explanation for experimental facts which can not be explained by those traditional mechanisms in a satisfactory way. This new mechanism casts a new

light on the relation among catalytic cracking, isomerization and hydrogen transfer of alkenes.

Acknowledgement. We greatly appreciate the financial support given by the Ministry of Education, PetroChina, and SINOPEC to the research of this subject.

References

(1) Yury V. Kissin; *Catalysis Review,* **2001**, 43(1&2), 85-146.
(2) Chen Junwu; Cao Hanchang; *Catalytic Cracking Technology and Engineering*; Sinopec Press: Beijing, **1995**; pp. 112-155
(3) J. S. Buchanan; J. G. Santiesteban; W. O. Haag; *Journal of Catalysis*, **1996,** 158, 279–287.
(4) Huang Guoxiong; Li Chenglie; Liu Fan; *Hydrocarbon Isomerization*; Sinopec Press: Beijing, **1992**; pp.15-25.
(5) S. Tiong Sie; *Ind. Eng. Chem. Res.* **1992**; 31, 1881-1889.
(6) Wu Feng; Erik Vynckier; Gilbert F. Froment; *Ind. Eng. Chem. Res.* **1993**, 32, 2997-3005.
(7) Zhao Liuzhou; Zhou Han; Shi Zhicheng; *Acta Petrolei Sinica (Petroleum Processing Section)*, **2002**, 18 (4), 90-94.

CONVERSION CO_2 TO FORMATE BY FORMATE DEHYDROGENASE IMMOBILIZED IN SILICATE MATRIX

Hong Wu , Zhong-yi Jiang , Song-wei Xu*

School of Chemical Engineering and Technology, Tianjin University ,Tianjin 300072, China.

Introduction

The efficient utilization of CO_2 will not only help to alleviate greenhouse effect, but also to obtain useful chemicals and materials as well. Unlike traditional CO_2 conversion reaction such as heterogeneous catalysis, photocatalysis and electrocatalysis, a novel bio-pathway has been explored, by which CO_2 is converted to formate, an important organic compound and a clean fuel. Herein, formate dehydrogenaes ($F_{ate}DH$) was employed as the biocatalyst while reduced nicotinamide adenine dinucleotide (NADH) as a terminal electron donor. Sol-gel technology was introduced to encapsulate $F_{ate}DH$. $NaHCO_3$ was used as reactant instead of CO_2 as substrate since the whole reaction was conducted in aqueous solution and HCO_3^- is the main form of CO_2 dissolved in water. In addition, liquid-solid two-phase reaction system is much easier to manipulate than gas-liquid-solid three-phase reaction system. The $F_{ate}DH$-containing silicate matrix was characterized by UV spectrum and TEM. Base on the ordered reaction mechanism, kinetic parameters of both the free and immobilized enzymatic reactions were determined.

Enzyme immobilization by sol-gel process

The initial sol was prepared by mixing 2.60g of tetraethyl orthosilane (TEOS), the precursor, and 0.55g of 1.5% HCl, the acid catalyst. The mixture was oscillated for 3 min to form homogeneous solution, and then 1.05 g of 1% NaOH was dropwised to adjust the pH to 7.0. $F_{ate}DH$ solution (0.2 μM phosphate buffer at pH 7.0) was added in the sol. Enzyme-contained silicate gel was formed within 50~60sec and then was aged for 7days at 4 $^\circ C$.

Characterization of the gel

No leakage of $F_{ate}DH$ from the gel after long time soaking in the buffer was detected by UV-3010 Spectrometer (Hicathi, Japan), and the maximum absorption of the free $F_{ate}DH$ and immobilized $F_{ate}DH$ was both at 280nm. TEM (100CX-II, JEOL) picture showed that enzyme dispersed uniformly in the gel.

Bioconversion reaction and kinetic parameters

$NaHCO_3$ can be catalyzed to formate by $F_{ate}DH$ when NADH acts as an electron donor. The initial-rates of free and immobilized $F_{ate}DH$ catalytic reaction at 25 $^\circ C$ and pH7.0 were determined by the decrease of NADH concentraton which was measured by a UV spectrometer at 340nm. The concentration of $F_{ate}DH$ was fixed at 0.2 μM, while NADH concentration (denoted by A) varied from 0.05 to 0.5mM and that of $NaHCO_3$ (denoted by B) varied from 0.8 to 5.0mM.

According to the ordered enzymatic reaction mechanism proposed by Dalziel (Equation 1)[1,2], kinetic parameters were fitted out. A series of initial rate measurements having been made under a constant initial concentration of A and different concentrations of B, a plot of $\frac{[E_0]}{v_0}$ versus $\frac{1}{[B_0]}$ gave a straight line, with both slope and intercept as the linear functions of $\frac{1}{[A_0]}$. Varying the concentration of A, the slopes and intercepts of the primary plots may be plotted against $\frac{1}{[A_0]}$, and the 4 kinetic parameters ($\phi_0, \phi_A, \phi_B, \phi_{AB}$) can be determined as the function of slopes and intercepts.

$$\frac{[E_0]}{v_0} = \phi_0 + \frac{\phi_A}{[A_0]} + \frac{\phi_B}{[B_0]} + \frac{\phi_{AB}}{[A_0][B_0]} \qquad (1)$$

Kinetic parameters of both free enzyme reaction and immobilized enzyme reaction are listed in Table 1.

Table 1. Kinetic parameters of both free and immobilized $F_{ate}DH$ catalyzed reactions

	Freed $F_{ate}DH$	Immobilized $F_{ate}DH$
ϕ_0	$3854s$	$3928s$
ϕ_A	$213s \cdot mM$	$243s \cdot mM$
ϕ_B	$5699s \cdot mM$	$10301s \cdot mM$
ϕ_{AB}	$329(mM)^2 \cdot s$	$1011(mM)^2 \cdot s$
K_{mA}	$55\mu M$	$63\mu M$
K_{mB}	$1.5mM$	$2.6mM$
K_{SA}	$58\mu M$	$98\mu M$

Experimental results showed that both the free and immobilized $F_{ate}DH$ enzymatic reactions obey the ordered mechanism. The larger Michaelis-Menten kinetic constants of immobilized $F_{ate}DH$ compared with free $F_{ate}DH$ reaction indicate that the binding force between the substrate and the immobilized enzyme is weaker. This may be due to the diffusion hindrance of the substrate from bulk solution to the gel and the accessibility hindrance of the immobilized enzyme in the three-dimensional silicate network.

Conclusions

The conversion of CO_2 to formate by formate dehydrogenase was explored using $NaHCO_3$ as reactant instead of CO_2 itself. Kinetic parameters of both free and immobilized enzymatic reactions were determined based on the ordered mechanism.

Acknowledgement. The financial support from the National Natural Science Foundation of China (No.20176039) was greatly acknowledged.

References

(1) Dalziel, K. *Nature,* **1963**,*197* (2), 462.
(2) Dalziel K. *The Journal of Biological Chemistry,* **1963**, *238* (8), 2850.

CRACKING AND CRACKING SELECTIVITY OF ALKANE AND ALKYL AROMATICS: EFFECTS OF DISPERSED CATALYSTS AND HYDROGEN DONORS

Bin Shi * *GuoHe Que*

State key laboratory of heavy oil processing, University of Petroleum, Dongying, ShanDong, 257061, China

Introduction

The synergism between dispersed catalysts and hydrogen donors were important for the systems of the traditional coal catalytic liquefaction and hydrocracking processing of heavy oil **(1**~3**)**. Some studies show the synergism was helpful to effective inhibition the regression reaction in the liquefaction of coal and the formation of coke and asphaltene in heavy oil hydrocracking**(1**~3**)**. However, the effects of dispersed catalysts and hydrogen donors on the selectivity of cracking reaction of coal and heavy oil molecular were unclear.

It is known that there are some long-chain hydrocarbons in the paraffin of residue oil. Meanwhile, there exist some poly-ring aromatic in the aromatics, resin and asphaltene of residue oil, which have alkyl side-chain"•—" or alkyl bridge-chain"•—•". This work aimed to investigate the effects of dispersed catalyst and hydrogen donor on the cracking and cracking selectivity of these characteristic structures in heavy oil. Some model compounds have been chosen to simulate the cracking of residue oil. Normal eicosane, as model compound for paraffin, butyl benzene and 1,6-diphenylheptane, as model compounds for aromatics, resin and asphaltene in residue oil, were introduced to investigate the effects of dispersed catalyst and hydrogen donor on the cracking and cracking selectivity of these model compounds in the systems of thermal-, hydrothermal and catalytic hydrocracking of the model compounds in high temperature 440^{o}C.

Experimental

About 0.1000~0.2000g reactant including 0.1000g normal eicosane (Aldrich purity is 99%), butyl benzene (Aldrich purity is 99%) and 1,6-diphenylheptane, (self-made, purity is about 90%, impurity mainly is ph-CO-$(CH_2)_5$-ph) and some additives including H-donor tetralin (THN, purity is 99.3%) or aromatic solvent 1-methylnaphthelene(MN, purity is 97%), whose amount generally is 100%wt of model compound, or oil-soluble dispersed catalysts MoDTC, metal of whose amount generally is 1%wt of model compound, was charged into a quartz tube and placed in a 40ml non-stirred high pressure micro- reactor, washed with nitrogen or hydrogen, pressurized nitrogen or hydrogen to 7.0Mpa. Then the micro- reactor was preheated in 300^{o}C liquid tin bath for 15 minutes, and inserted into another tin bath whose reaction temperature was desired. During the reaction, the pressure was about 15.5Mpa. The micro-reactor was cooled with ice water quickly when defined reaction time was achieved. Recovered with about 25mL chloroform or dichrolmathane, the cracking products were analyzed by GC-MS and GC. Some conversion was emphasized as follows:

Cracking of model compound = a certain recovered cracking product wt%×100/ recovered model compound wt%;

Conversion of THN = the recovered naphthalene wt%×100/(the recovered naphthalene wt% + recovered THN wt%).

Conversion of MN = the recovered Methyl tetralin wt%×100/(the recovered Methyl tetralin wt% + recovered MN wt%)

Results and Discussion

Normal Eicosane. It is known that long chain hydrocarbons are rich in the paraffin of residue oil (4). N-eicosane was chosen by reason of the same structure as paraffin of residue oil. Thermal, hydrothermal, catalytic hydrocracking of n-C_{20} could be performed, while thermal, hydrothermal, catalytic hydrocracking of the binary system of n-C_{20}/tetralin and the binary system of n-C_{20}/MN were also carried out, respectively. The detailed studies have been reported in literature (5,6). It seems that distribution in carbonic number of the products in the four cracking reaction has not changed and the catalytic hydrocracking of n-C yielded more cracking products than hydro thermal and thermal cracking of n-C_{20} did. On the other hand, it is clear that H-donor or aromatic solvent, especially H- donor, inhibited cracking of n-C_{20} in hydrogen donor or aromatic solvent. What is different was that the ratio of n-alkanes to α–olefins in thermal cracking and thermal-cracking with aromatic solvent was about 1:1, and that in thermal–cracking in H-donor decreased to about 1:0.5. The proportion of α–olefins in hydrothermal of n-C_{20} remained about 15~10% and hydrothermal of n-C_{20} with H-donor hardly gave α–olefins. It is obvious that hydrogen-in-gas and hydrogen provided from H-donor could have hydrogenated the olefins resulted from cracking of n-C_{20} and the former could enhance cracking of n-C_{20} and the latter could inhibit cracking. Based on the fact that there were no clear iso-alkanes and iso-alkenes in the cracking products of n-C_{20}, it is obvious that the cracking reaction of n-C_{20} manifests the character of radical reaction pathway in the thermal, hydrothermal, catalytic hydrocracking system of n-C_{20} and in the thermal, hydrothermal, catalytic hydrocracking system of the binary system of n-C_{20} and tetralin.

Butyl Benzene. It is known that there are some poly-ring aromatic hydrocarbons, which have alkyl side-chain"•—", in the aromatics, resin and asphaltene in residue oil (7). Butyl benzene was chosen because of the same structure as the aromatic of residue oil. Thermal, hydrothermal, catalytic hydrocracking of butyl benzene have been performed, while thermal, hydrothermal, catalytic hydrocracking of the binary system of butyl benzene / tetralin or the binary system of butyl benzene/MN were also carried out as comparison. Different products from different process gave out as listed in Table 1:

No benzene was produced in the thermal cracking. The thermal-cracking products of butyl benzene were mainly composed of ethyl benzene and toluene and the former was more than the latter. It is resulted from that butyl benzene in the system of thermal-cracking mainly were γ- bond scission and β- bond scission, in which α- bond scissions did not happen.

Molecular hydrogen enhanced the cracking of butyl benzene. In the hydro cracking, the cracking products of butyl benzene were mainly composed of benzene and toluene, but the amount of benzene was more than that of toluene. It is clear that butyl benzene in the system of hydrothermal mainly is α-bond scission and β- bond scission, in which little γ-bond scissions experience.

The effect of THN or MN was inhibition of cracking reaction in the non-catalyzed systems, however the effect of the former was more outstanding than that of the latter. Compared with the degree of inhibition of β- bond scission, more γ-bond scissions could be inhibited by hydrogen donor according to the distribution of cracking products.

Dispersed catalysts enhanced α-bond scission and β- bond scission of butyl benzene in the catalytic hydrocracking, especially α-bond scission. It is clear that molecular hydrogen activated by catalysts mainly attacked the α-bond in Ar-CH_2-CH_2-CH_2-CH_3 and subsequently experience α-bond scissions.

The effect of THN was not clear to the catalytic cracking selectivity of butyl benzene, although the catalytic cracking of butyl benzene was decreased by THN. Compared with the effect of H-

donor on the catalytic cracking selectivity, the effect of dispersed catalysts was dominant in the catalytic cracking of butyl benzene.

In the catalytic hydro cracking of 1,6-diphenylheptane, solvent 1-methyl naphthalene can be hydrogenated into methyl tetralin and then could play similar part in the system as tetralin. However, the effect of mixture of 1-methyl naphthalene and methyl tetralin was weaker than that of tetralin.

1,6-Diphenylheptane. There are some poly ring aromatics hydrocarbons, which have alkyl bridge-chain"•—•", in the aromatics, resin and asphaltene in residue oil (7). The similar cracking experiments of 1,6-diphenylheptane as butyl benzene have been done. From Table 2 and Table 3, the cracking character of 1, 6-diphenylheptane in different systems could be found:

Thermal-cracking products of 1, 6-diphenylheptane were mainly composed of toluene, benzene and propyl benzene, since ethyl benzene and styrene were not main products in the thermal cracking. It is clear that of 1,6-diphenylheptane in thermal cracking underwent four kinds of cracking ways, which were α-,β-, γ-bond scission and homolysis.

In the hydrothermal cracking, molecular hydrogen enhanced the four cracking ways of 1,6-diphenylheptane and the products of 1,6-diphenylheptane were mainly composed of benzene and toluene, however, the amount of benzene was more than that of toluene. It is deduced that butyl benzene in the system of hydrothermal mainly were α-bond scission and β- bond scission, in which little γ-bond scissions and homolysis underwent.

In the catalytic hydrocracking system, dispersed catalysts enhanced the α-bond scission and β- bond-scission in the four cracking ways of 1,6-diphenylheptane, especially α-bond scission. It is concluded that polar catalyst was absorbed by aromatic ring and hydrogen activated by catalysts preferentially and mainly attacked the α-bond in ph$CH_2CH_2CH_2CH_2CH_2CH_2$ph and subsequently experienced α-bond scissions. On the other hand, the primary products such as phenyl pentane and phenyl butane also underwent similar α-bond scissions and β- bond scission into secondary products benzene and toluene as butyl benzene in catalytic hydrocracking system.

For cracking selectivity, thermal and hydrothermal cracking were the basis of other processes, dispersed catalysts affected the cracking selectivity of alkyl aromatics on a relatively clear extent, while hydrogen donor had influence on a certain extent on the cracking selectivity on the basis of the thermal, hydrothermal and catalytic hydrocracking systems of 1,6-diphenyl heptane, although the cracking was decreased by THN.

Compared with the effect of H-donor on the catalytic cracking selectivity, the effect of dispersed catalysts was dominant in the catalytic cracking of 1,6-diphenyl heptane.

Since iso-products did not be found in the thermal cracking, hydrothermal and catalytic hydro cracking of 1,6-diphenylheptane, it seems that the compound experienced the radical reaction in the systems.

In the catalytic hydro cracking system, 1-methyl naphthalene can be hydrogenated into methyl tetralin and then could play similar part in the system as tetralin. However, the effect of mixture of 1-methyl naphthalene and methyl tetralin was weaker than that of tetralin.

Conclusions

(1) Model compounds including n-eicosane, butyl benzene and 1,6-diphenylheptane experienced the radical reaction in the single system of model compound and the binary system of model compound and tetralin in thermal, hydrothermal, catalytic hydrocracking system.

(2) Molecular hydrogen enhanced the cracking of model compounds, while H-donor decreased the cracking of model compounds. On the other hand, dispersed catalyst greatly enhanced the cracking of model compounds.

(3) For cracking selectivity of the three compounds, thermal and hydrothermal cracking were the basis of other processes, dispersed catalysts affected the cracking selectivity of alkyl aromatics on a relatively clear extent, and hydrogen donor had influence on a certain extent on the cracking selectivity on the basis of the thermal, hydrothermal and catalytic hydrocracking systems.

References

(1) ShuChai.Guo. Chemistry and Chemical Engineering of Coal [M] Chemistry Industry Press(China) **1991**, 274-285.

(2) Bin Shi, D.L.Lin,L.Q.Wang, G.H.Que. Synergism between Hydrogen Donors and Dispersed Catalysts in LHVR Hydrocracking Preprints, American Chemistry Society, Petroleum Chemistry Division. **2001,**46(4), 325-328.

(3) Bin Shi, Guohe Que Effects of H-Donors and dispersed catalysts on Catalytic hydrocracking of residue Preprints American Chemistry Society Petroleum Chemistry Division. **2002,** 47(2), 113-116.

(4) WenJie Liang. Petroleum Chemistry [M]. Press of University of Petroleum (China), **1993**.

(5) Bin Shi, Guohe Que Thermal-cracking and catalytic hydrocracking reaction of tetralin and normal eicosane with steady isotope. Preprints, Div. Fuel Chem., ACS, **2002**, 47(1), 251-254.

(6) Bin Shi, L.Q.Wang, D.L.Lin, G.H.Que.Hydrogen-transfer between hydrogen donors and model compounds with steady isotope Preprints American Chemistry Society Petroleum Division. **2001**, 46(4), 325-329.

(7) Wang Zi Jun. Study on molecular structure of vacuum residue by ruthenium ions catalyzed oxidation [Doctoral Dissertation] University of Petroleum, China, **1996.**

Table1 Effect of dispersed catalysts, H-donor and aromatic solvent on the cracking of butyl benzene in different systems.

		N_2			H_2			H_2		
Additives (100%wt)		--	THN	MN	--	THN	MN	--	THN	MN
Catalyst (1%wt)		--	--	--	--	--	--	Mo	Mo	Mo
Cracking products	Benzene	0	0	0	14.9	8.2	10.1	30.0	13.0	22.0
	Toluene	7.8	3.6	5.6	27.9	18.6	23.7	32.9	15.1	25.5
	Ethyl Benzene	15.7	2.3	11.8	2.1	0.50	1.1	0.9	0.23	0.51
Conversion of additive (%)		--	10.7		--	--	--	--	14.1	34.9

Table2 Effect of catalysts , H-donor and aromatic solvent on the cracking of 1,6-diphenylheptane in different systems.

		N_2			H_2			H_2		
Additives(100%wt)		--	THN	MN	--	THN	MN	--	THN	MN
Catalyst (1%wt)		--	--	--	--	--	--	Mo	Mo	Mo
Cracking products	Benzene	67.4	33.5	46.3	96.2	61.7	85.3	223.3	121.7	157.2
	Toluene	60.0	27.5	48.3	82.8	54.3	73.2	154.7	82.9	99.1
	Ethyl benzene *	15.6	4.8	7.5	20.0	11.1	23.1	30.9	11.4	26.5
	Propyl benzene	24.5	13.1	17.6	39.5	36.7	35.2	73.2	50.3	60.2
	Butyl benzene	4.9	4.1	4.0	26.2	14.6	22.6	34.8	13.8	26.5
	Pentyl benzene	3.1	3.5	5.2	12.6	1.9	10.3	34.8	11.3	20.6
	Hexyls benzene	5.5	2.1	4.8	3.6	3.3	4.0	5.5	1.3	4.9
Conversion of additive (%)		--	10.3	--	--	22.6	--	--	12.9	29.1

Table3 Effect of catalysts and H-donor on the cracking selectivity of 1,6-diphenylheptane in different systems.

	N_2			H_2			H_2		
Additives(100%wt)	--	THN	MN	--	THN	MN	--	THN	MN
Catalyst (1%wt)	--	--	--	--	--	--	Mo	Mo	Mo
α-bond scissions	100	100	95.5	100	100	100	100	100	100
β- bond scission	86.6	87.1	100	95.6	86.5	93.5	82.8	76.6	73.8
γ- bond scission	28.1	25.0	21.3	46.3	39.5	51.2	28.7	20.5	80.7
homolysis.	33.6	36.8	32.9	39.6	56.5	39.4	32.0	68.7	82.2

FUEL FORMULATION EFFECTS ON DIESEL PARTICULATE FILTER REGENERATION

André Boehman, Juhun Song, Mahabubul Alam and Vince Zello

The Energy Institute
The Pennsylvania State University
405 Academic Activities Building
University Park, PA 16802

Kirk Miller

ConocoPhillips
600 N. Dairy Ashford
Houston, TX 77252

Introduction

Diesel particulate emissions pose a significant potential health hazard. Control of diesel particulate emissions is an issue requiring the attention of the fuels, engine and aftertreatment industries. To achieve the reductions in particulate emissions mandated by the US Environmental Protection Agency in 2007, use of diesel particulate filters (DPF) will be a necessity [1]. To enable the implementation of particulate and NOx control technologies, the US EPA has mandated that ultra low sulfur fuels be available to enable advanced aftertreatment strategies, which can be highly sulfur sensitive [2]. A critical requirement for implementation of diesel particulate filters on diesel-powered vehicles is having a low "break even temperature," defined as the temperature at which particulate deposition on the filter is balanced by particulate oxidation on the filter. This balance point needs to occur at sufficiently low temperatures to fit within the exhaust temperature range of a typical diesel vehicle duty cycle. Catalytic coating on the diesel particulate filter, use of a fuel borne catalyst and oxidation catalysts placed upstream of the particulate filter can all reduce this balance point temperature. Another important factor in lowering the balance point temperature is fuel sulfur content, because the sulfur dioxide generated during combustion can poison catalyst activity [1,2].

Modification of diesel fuel composition, for example, by blending with oxygenated fuels, can contribute to reducing emissions. Addition of biomass-derived fuels and synthetic fuels to diesel fuel basestocks is a means of producing a cleaner burning diesel fuel. Blending with oxygenated or zero sulfur fuels can lead to particulate emissions reductions by interfering with the soot formation process and by decreasing the formation of sulfates. However, in the case of biodiesel fueling (e.g., "B20", a blend of 20vol.% methyl soyate in diesel fuel) there is a well documented increase of 2-4% in NOx emissions [3]. As shown by Van Gerpen and co-workers [4,5] and Szybist, et al. [6], the NOx increase with biodiesel fueling is attributable to an inadvertent advance of fuel injection timing. The advance in injection timing is due to the higher bulk modulus of compressibility, or speed of sound, in the fuel blend, which leads to a more rapid transferal of the pressure wave from the fuel pump to the injector needle and an earlier needle lift.

In this paper we present comparative study of the impact of sulfur content and biodiesel blending on particulate trap operation. The means of comparison is analysis of the impact of fuel composition on the break even temperature.

Experimental

Tests were performed with a Cummins ISB 5.9L turbodiesel engine (MY2000, 235 HP max output) connected to a 250 HP capacity, eddy current absorbing dynamometer. The engine has been heavily instrumented, with a 0.1 crank angle resolution crank shaft encoder, a cylinder pressure sensor, a needle lift sensor and in-cylinder visualization using an AVL 513D Engine Videoscope. The engine and dynamometer are operated through an automated control system. Connected to the engine exhaust is a catalyzed diesel particulate filter. Exhaust samples are pulled upstream and downstream of the DPF, while exhaust temperature, filter temperature and pressure drop across the DPF are monitored.

Test Procedure. Prior to a break even temperature (BET) test, the filter is cleaned of particulate via operation at elevated temperature. Then, the exhaust temperature is reduced while the filter is filled with particulate matter until the pressure drop across the filter reaches 20 inches of H_2O. Then, exhaust temperature is increased in steps by increasing the load on the engine. Four fuel formulations were considered, a low sulfur diesel fuel (LSD, 325 ppm sulfur), ultra low sulfur diesel fuel (ULSD, 15 ppm sulfur), a 20 vol.% blend of biodiesel ("B20") with LSD (LSD/B20) and a B20 blend with ULSD (ULSD/B20).

Particulate mass measurements are obtained with a Sierra Instruments BG-1 Micro Dilution Test Stand by sampling onto Pallflex 90 mm filters. Measurement of the soluble organic fraction (SOF) of the particulate matter is performed by weighing the sample filter before and after solvent extraction using dichloromethane (DCM). Gaseous emissions were obtained with an AVL CEB II raw diesel emissions bench.

Results and Discussion

As shown recently by Szybist and Boehman [7], fuel injection timing advances of 0.3 crank angle (CA degrees) and 1 CA degree are observed in "pump-line-nozzle" configuration fuel systems, for B20 and B100 respectively. This injection timing advance in a purely mechanical fuel injection system may not be as likely in an electronically controlled fuel injection system. In the Cummins ISB engine, the Bosch fuel system is electronically controlled which potentially complicates the interpretation of fuel effects on injection timing. The engine controller itself may shift injection timing due to differences in throttle position required to meet the required load because of differences in the calorific value of the test fuels.

Figure 1 shows the particulate composition during the filter loading period and indicates that there are some modest differences in the rate and composition of the particulate that is depositing on the DPF.

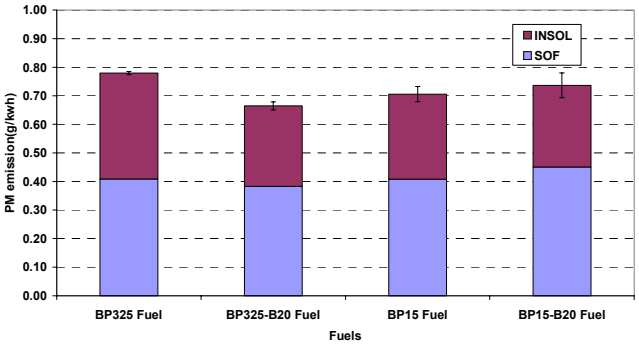

Figure 1. Particulate composition during the filter loading process for the various test fuels.

Figure 2 shows the variation of engine-out NOx emissions during the filter regeneration process, caused by the differences in fuel composition and the presence of biodiesel fuel. Figure 3 shows the extent of conversion of engine-out NO to NO_2 across the

catalyzed DPF due to oxidation. Figure 4 indicates the variation in break even temperature with test fuel composition. The BET is determined by following the slope in the variation of pressure drop as exhaust temperature increases.

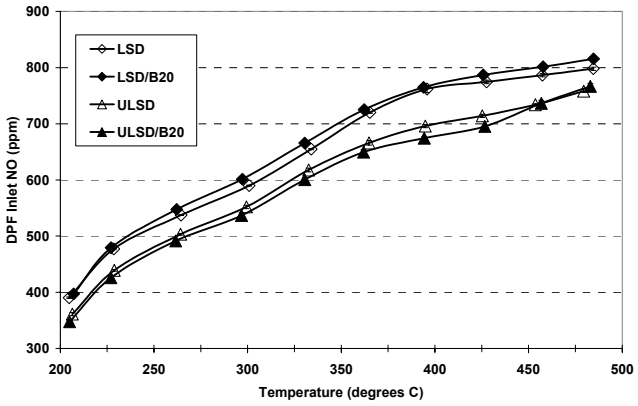

Figure 2. Variation in engine-out NOx emissions during the filter regeneration process for the various test fuels.

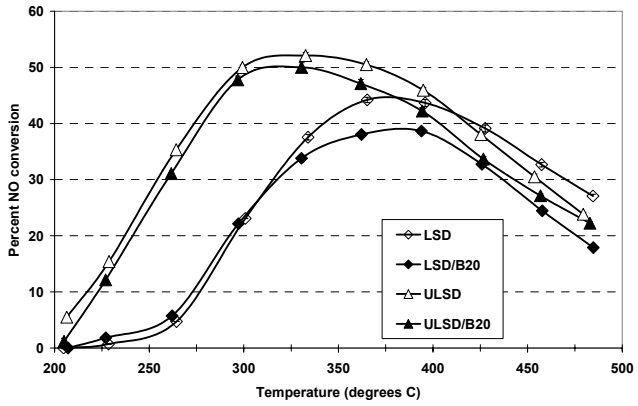

Figure 3. Variation in NO conversion to NOx across the DPF during the filter regeneration process for the various test fuels.

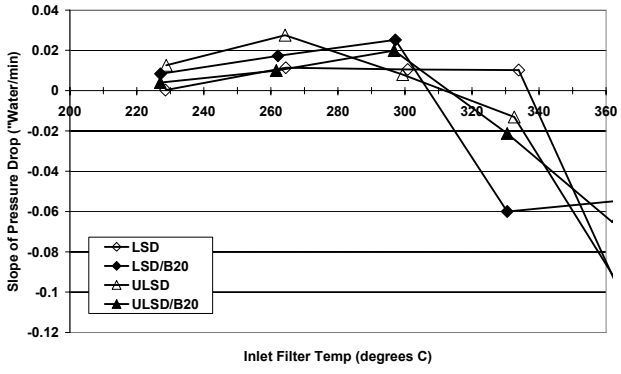

Figure 4. Filter temperature versus slope of the pressure drop, indicating the break even temperature for the various test fuels.

The results in Figures 1-4 show that although there is modest variation in the composition and mass emissions rate of particulate matter from the engine between the test fuels, there are differences in engine-out NOx and, as a consequence, NO conversion across the catalyzed DPF. For both base fuels, the LSD and ULSD, there is an engine-out increase in NOx, which is comprised mostly of NO. Subsequently, the engine-out NO is oxidized to NO_2 over the catalyst that is impregnated into the DPF. The NO_2 assists in the oxidation of the particulate matter on the DPF, because NO_2 is a more aggressive oxidizer of diesel particulate matter than O_2 [1]. However, the conversion of NO to NO_2 is inhibited by the presence of SO_2 in the exhaust, which is 20 times higher for the LSD than for the ULSD. So, the NO conversion to NO_2 is lower and requires an additional 100°C exhaust temperature to become significant for the LSD due to its higher sulfur content.

Of great interest is that the net effect of the higher engine-out NOx emissions for the LSD/B20 fuel leads to the lowest break even temperature, 308°C. Consistent with one's expectations, the LSD has the highest BET. However, the ULSD and ULSD/B20 fuels yield the same BET. This difference in BET may be explained by the generally lower NOx emissions for the ULSD and ULSD/B20 fuels relative to the LSD and LSD/B20 fuels. There is more NOx with the LSD and LSD/B20 fuels to serve to oxidize the particulate matter on the DPF after conversion of NO to NO_2, but for the LSD the NO conversion is inhibited and the particulate oxidation is inhibited by the higher sulfur content.

Conclusions

While there is ample evidence in the literature of the deleterious effects of sulfur on aftertreatment devices, the results presented here show that other fuel related phenomena can have just as significant an effect on the performance of an aftertreatment device. In this specific case, the lowest break even temperature for a catalyzed DPF was observed with biodiesel blended into a low sulfur fuel.

Acknowledgement The authors wish to thank ConocoPhillips for its support of this work and Keith Lawson and Etop Esen of ConocoPhillips for their technical guidance.

This paper was written with support of the U.S. Department of Energy under Cooperative Agreement No. DE-FC26-01NT41098. The Government reserves for itself and others acting on its behalf a royalty-free, nonexclusive, irrevocable, worldwide license for Governmental purposes to publish, distribute, translate, duplicate, exhibit, and perform this copyrighted paper.

References

(1) Allansson, R., et al., "Optimising the Low Temperature Performance and Regeneration Efficiency of the Continuously Regenerating Diesel Particulate Filter (CR-DPF) System," SAE paper 2002-01-0428, 2002.

(2) Schmidt, D., et al., "Review and assessment of fuel effects and research needs in clean diesel technology," ASME ICE-Vol 36-1, 2001, p. 23-36.

(3) Graboski, M.S. and R.L. McCormick, "Combustion of fat and vegetable oil derived fuels in diesel engines." *Progress in Energy and Combustion Science*, 1998, **24**(2): p. 125-164.

(4) Monyem, A., J.H. Van Gerpen, and M. Canakci, "The effect of timing and oxidation on emissions from biodiesel- fueled engines". *Transactions of the ASAE*, 2001, **44**(1): p. 35-42.

(5) Tat, M.E., et al., "The speed of sound and isentropic bulk modulus of biodiesel at 21 degrees C from atmospheric pressure to 35 MPa." *Journal of the American Oil Chemists Society*, 2000, **77**(3): p. 285-289.

(6) Szybist, J.P., et al., "Diesel fuel formulation effects on injection timing and emissions," Prepr. Pap. - *Am. Chem. Soc., Div. Fuel Chem.*, **2003**, *48(1), 428*.

(7) Szybist, J.P. and A.L. Boehman, "Behavior of a diesel injection system with biodiesel fuel," Society of Automotive Engineers Technical Paper No. 2003-01-1039, 2003.

BIODIESEL PRODUCTION BY A CONTINUOUS PROCESS USING A HETEROGENEOUS CATALYST.

Gerard Hillion [(1)], Bruno Delfort [(1)], Dominique le Pennec [(1)], Laurent Bournay [(1)], Jean-Alain Chodorge [(2)]

[(1)] Institut Français du Pétrole (IFP), 1&4 av de Bois Préau, 92852 Rueil-Malmaison Cedex - France
[(2)] Axens, IFP Group Technologies, 89 bd F. Roosevelt, 92508 Rueil-Malmaison Cedex - France

Introduction

The reactions for direct transformation of vegetable oils into methyl esters and glycerol have been known for more than a century. The reactions of interest today, mainly those producing methyl esters from rapeseed, soybean and sunflower oils, have been studied and optimized in order to manufacture the high quality diesel fuel known as biodiesel.

With over ten years of development and commercial use in Europe, biodiesel has now proved its value as a fuel for diesel engines [**1-3**]. The product is free of sulfur and aromatics, and, as it is obtained from renewable sources, it reduces the lifecycle of carbon dioxide emissions by almost 70% compared to conventional diesel fuel. Moreover, recent European regulations have restricted sulfur content in diesel fuel to no more than 50 ppm in year 2005. Sulfur is known to provide diesel fuels with a lubricity that will disappear as the regulations take effect. Biodiesel addition at levels of one to two per cent in diesel blends has the beneficial impact of restoring lubricity through an antiwear action on engine injection systems [**4-5**].

Several commercial processes to produce fatty acid methyl esters from vegetable oils have been developed and are available today. These processes consume basic catalysts such as caustic soda or sodium methylate which form unrecyclable waste products. This paper provides a general description of a new process using a heterogeneous catalytic system.

Biodiesel Production Processes

The transesterification of triglycerides to methyl esters with methanol is a balanced and catalyzed reaction as illustrated in Figure 1. An excess of methanol is required to obtain a high degree of conversion.

Rapeseed and soybean oils are among the main vegetable oil candidates for biodiesel uses. Their compositions are summarized in Table 1.

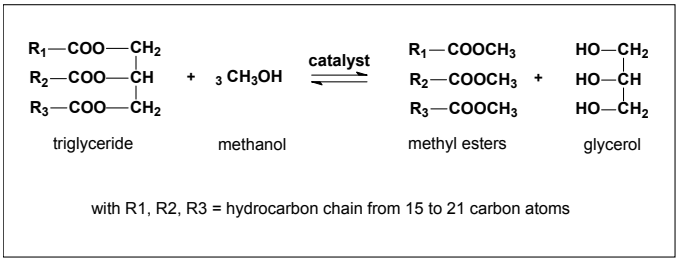

Figure 1. Overall reactions for vegetable oil methanolysis

The conventional catalysts in natural oil transesterification processes are selected among bases such as alkaline or alkaline earth hydroxides or alkoxides [**6**]. However, transesterification could also be performed using acid catalysts, such as hydrochloric, sulfuric and sulfonic acid, or using metallic base catalysts such as titanium alcoholates or oxides of tin, magnesium, or zinc. All these catalysts act as homogeneous catalysts and need to be removed from the products after the methanolysis step.

Table 1. Fatty Acid Compositions for Rapeseed Oil and Soya Oil (weight %)

Fatty Acid Chain		Rapeseed Oil	Soybean Oil
Palmitic	C16:0	5	10
Palmitoleic	C16:1	< 0.5	
Stearic	C18:0	2	4
Oleic	C18:1	59	23
Linoleic	C18:2	21	53
Linolenic	C18:3	9	8
Arachidic	C20:0	< 0.5	< 0.5
Gadoleic	C20:1	1	< 0.5
Behenic	C22:0	< 0.5	< 0.5
Erucic	C22:1	< 1	

Conventional Homogeneous Catalyzed Processes. In conventional industrial biodiesel processes, the methanol transesterification of vegetable oils is achieved using a homogeneous catalyst system operated in either batch or continuous mode.

In most cases the catalyst is sodium hydroxide or sodium methylate. It is recovered after the transesterification reaction as sodium glycerate, sodium methylate and sodium soaps in the glycerol phase. An acidic neutralization step with, for example, aqueous hydrochloric acid is required to neutralize these salts. In that case glycerol is obtained as an aqueous solution containing sodium chloride. Depending on the process, the final glycerol purity is about 80% to 95%.

When sodium hydroxide is used as catalyst, side reactions forming sodium soaps generally occur. This type of reaction is also observed when sodium methylate is employed and traces of water are present. The sodium soaps are soluble in the glycerol phase and must be isolated after neutralization by decantation as fatty acids. The loss of esters converted to fatty acids can reach as high as 1% of the biodiesel production. These operations are illustrated in Figure 2.

Heterogeneous Catalyzed Process. To avoid catalyst removal operations and soap formation, much effort has been expended on the search for solid acid or basic catalysts that could be used in a heterogeneous catalyzed process [7-10]. Some solid metal oxides such as those of tin, magnesium, and zinc are known catalysts but they actually act according to a homogeneous mechanism and end up as metal soaps or metal glycerates.

In this paper a new continuous process is described, where the transesterfication reaction is promoted by a completely heterogeneous catalyst. This catalyst consists of a mixed oxide of zinc and aluminium which promotes the transesterification reaction without catalyst loss. The reaction is performed at a higher temperature than homogeneous catalysis processes, with an excess of methanol. This excess is removed by vaporization and recycled to the process with fresh methanol.

The desired chemical conversion is reached with two successive stages of reaction and glycerol separation to displace the equilibrium reaction. The flow sheet for this process appears in Figure 3.

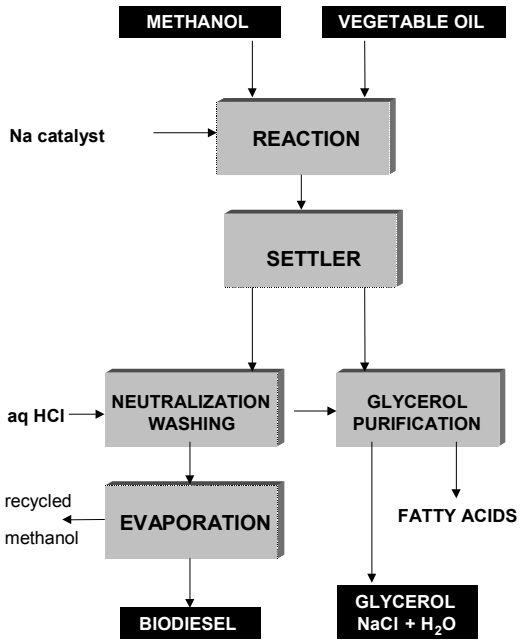

Figure 2. Global scheme for a typical continuous homogeneous catalyzed process.

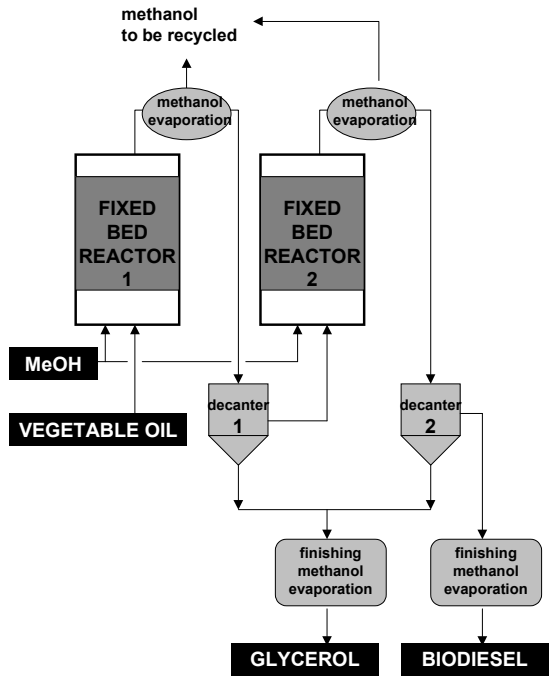

Figure 3. General scheme for a continuous heterogeneous catalyzed process

The catalyst section includes two fixed bed reactors that are fed by oil and methanol at a given ratio. Excess methanol is removed after each of the two reactors by a partial flash. Esters and glycerol are then separated in a settler. Glycerol phases are joined and the last traces of methanol are removed by vaporization. Biodiesel is recovered after final recovery of methanol by vaporization under vacuum and then purified to remove the last traces of glycerol. Typical characteristics of biodiesel obtained from rapeseed oil and soybean oil in pilot plant operations are reported in Table 2.

Table 2. Main Characteristics of the Biodiesel Fuels Obtained from Rapeseed Oiland Soybean Oil with Heterogeneous Catalyzed Process.

Characteristics of Biodiesel		From Rapeseed Oil	From Soybean Oil	Required European Specifications
Methyl esters	*wt - %*	> 99.0	> 99.0	96.5
Monoglycerides	*wt - %*	0.5	0.5	0.8
Diglycerides	*wt - %*	0.02	0.02	0.2
Triglycerides	*wt - %*	0.01	0.01	0.2
Free glycerol	*wt - %*	< 0.02	< 0.02	0.02
Total glycerol	*wt - %*	0.15	0.15	0.25
Acid number	*mg KOH /kg*	< 0.3	< 0.3	0.5 max
Water content	*mg/kg*	200	200	500 max
Metal content	*mg/kg*	< 3	< 3	-
Phosphorus	*mg/kg*	< 10	< 10	< 10

General conditions : methanol/vegetable oil ratio : 1; temperature : 200°C; LHSV : $0.5h^{-1}$

In this heterogeneous process, the catalyst is very stable with no metal leaching. There is no formation of either glycerate salts or metal soaps which affords the following advantages : no neutralization step is required, there is no introduction of water, and there is no salt formation; this accounts for an exceptional glycerol purity. In addition, there is no waste production of low-value fatty acids.

The purity of methyl esters exceeds 99% with yields close to 100% of the theoretical. Glycerol treatment is much easier than in homogeneous catalyzed processes. A simple elimination of methanol by vaporization suffices and no chemicals are required. The glycerol produced is neutral, clear and exempt from any salt, with purities above 98%. This valuable product could be used in many chemical applications without further treatment. If required, pharmaceutical grade can easily be reached.

The process feeds are limited to vegetable oils and methanol and the only products are biodiesel and a high-purity glycerol that is free of water and salt. With all its features, the process can be considered as a green process.

Experiments on methanolysis with acid-containing vegetable oils have also been conducted with no special acid removal treatment of the raw material. Methanolysis of a blend of 5% oleic acid in rapeseed oil leads to an ester product composition compatible with biodiesel requirements. In that case, esterification and transesterification reactions occur simultaneously. Results are summarized Table 3.

Table 3. Compositions of Ester Phases Obtained from Two Successive Fixed Bed Reactors (weight %). Neutralized Or Acidic Oil.

Feedstock Composition			Reactor 1		Reactor 2	
Rapeseed Oil (wt %)	Oleic Acid (wt %)	Acid Index	Methyl Esters (wt %)	Acid Index	Methyl Esters (wt %)	Acid Index
100	0	< 1	94.5	0.15	99.0	0.15
95	5	11	86.8	2.1	98.3	0.4

General conditions : methanol/vegetable oil ratio : 1; temperature : 200°C; LHSV : $0.5h^{-1}$

Conclusions

Increasing biodiesel consumption requires optimized production processes that are compatible with high production capacities and that feature simplified operations, high yields, and the absence of special chemical requirements and waste streams. The high quality of the glycerol by-product obtained is also a very important economic parameter. A heterogeneous catalyzed continuous process allows all these objectives to be attained.

References

1. Wilson, E.K., *Chemical & Engineering News*, **2002,** May 27,
2. Biodiesel - A Success Story, *Report of the International Energy Agency*, February **2002**.
3. Vermeersch, G., *Oléagineux. Corps gras. Lipides.,* **2001,** *8*, pp.33.
4. Montagne, X., *2nd European Motor Biofuels Forum,* Graz, September **1996**.
5. G. Hillion, X. Montagne, P. Marchand, *Oléagineux. Corps gras. Lipides.,* **1999,** , 6, pp.435.
6. Kreutzer, U., *J. Am. Oil. Chem. Soc.,* **1984,** *61* , pp.343.
7. Stern, R.; Hillion, G.; Rouxel, J. J.; Leporq, S. US Patent 5,908,946 (**1999**)
8. Stern, R.; Hillion, G.; Rouxel, J. J. US Patent 6,147,196 (**2000**)
9. Vogel, R. F.; Rennard, R. J.; Tabacek, J. A. US patent 4,490,479 (**1984**)
10. Gelbard, G.; Brès, O.; Vielfaure-Joly, F. *J. Am. Oil. Chem. Soc.,**1995,** 72, pp1*

Eliminating the NO_x Emissions Increase Associated with Biodiesel

Elana Chapman, Mike Hile, Mike Pague, Juhun Song, André Boehman

Department of Energy and Geo-Environmental Engineering
Pennsylvania State University

Abstract

Implementing greater biodiesel use is inhibited in part because of the observed increase in NO_x emissions as compared to conventional petroleum diesel fuel. A relation between the saturation of the fuel with NO_x emissions has been established in the literature. This research explored two approaches of achieving a more saturated biodiesel fuel and observing its effects on NO_x emissions blended as B20. The first option explored is blending of the biodiesel fuel with short-chained, saturated methyl esters. The second is the hydrogenation of soybean oil prior to transesterification. A 60% capylic/40% capric blend was mixed with B100 as a means of increasing the fuel's saturation. Another fuel containing a high percentage of oleic acid methyl ester was observed as an ideal hydrogenated fuel. Emissions testing revealed expected percentage decreased NO_x levels for the caprylic/capric blend, but the high oleic "hydrogenated" blend revealed a smaller NO_x emissions decrease than was expected.

Introduction

Biodiesel is an alternative diesel fuel created by the conversion of oils, fats and fatty acids to methyl and ethyl esters via esterification processes [1]. A variety of vegetable oils, typically soybean oil in the United States, and animal fats provide the source of the triglyceride fats and oils [2]. Continuous feedstock growth and livestock production provide a constant supply of source material allowing biodiesel to be a renewable source of fuel, which can be created domestically.

Additionally, biodiesel is miscible with petroleum-based diesel and works in any diesel engine with little or no modifications as pure biodiesel or as a blend with any other diesel fuel. It fact, biodiesel contains a higher oxygen content resulting in a more complete combustion of the fuel. Moreover, it is a cleaner burning fuel and reduces most harmful emissions such as particulate matter, unburned hydrocarbons and carbon monoxide.

However, a few issues need to be resolved before biodiesel fuels can be a prominent alternative fuel. The economics of providing an appropriate source material and of producing an affordable final product to create acceptable biodiesel fuels must be feasible. Moreover, engine emissions using biodiesel fuels typically increase emissions of oxides of nitrogen [3].

One approach appears to be increasing the degree of saturation of the ester molecules contained in the biodiesel. This report will investigate two potential options that may be used to achieve a higher degree of saturation: hydrogenation of the biodiesel fuel and the blending of the biodiesel fuel with a saturated methyl ester. Also presented are the results of calculations and experiments that were performed as a means of establishing these approaches as viable options to reduce NO_x emissions.

Biodiesel Processing

Vegetable oils are generally water-insoluble and consist of one mole of glycerol and three of fatty acids. They are more commonly referred to as triglycerides. The fatty acids contained in the oil vary in the length of the carbon chains, as well as the number of unsaturated (double) bonds [4]. In order to be used as a diesel substitute the vegetable oil triglycerides must be converted to methyl esters. This is accomplished through the process of transesterification [4].

Experimental

The intent of the project is to decrease the NO_x emissions from biodiesel combustion through the saturation of the biodiesel methyl esters, specifically methyl esters made from soybean oil.

Blending Approach. The first option to achieve a higher saturation level in biodiesel fuel is to add an appropriate amount of a saturated methyl ester to the biodiesel. This was determined based on research by McCormick and coworkers, who determined the relationship between NO_x emissions and iodine value, as shown in Figure 1[5]. Additionally, it has been found that increasing the degree of saturation, increasing the length of the hydrocarbon chain and decreasing the degree of branching all affect the freezing points of organic molecules directly producing poor cold flow properties of biodiesel fuels [1, 6, 7]. Therefore, a blend of 60% capryllic acid methyl ester and 40% capric acid methyl ester (the "additive"), donated by Stepan Company, was chosen so that its short hydrocarbon chain length would help offset the adverse effect of saturation on cold flow properties.

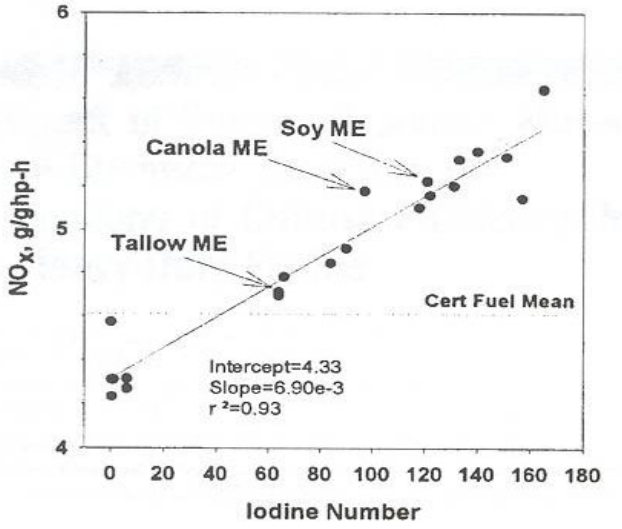

Figure 1. Iodine Number vs. NO_x [5].

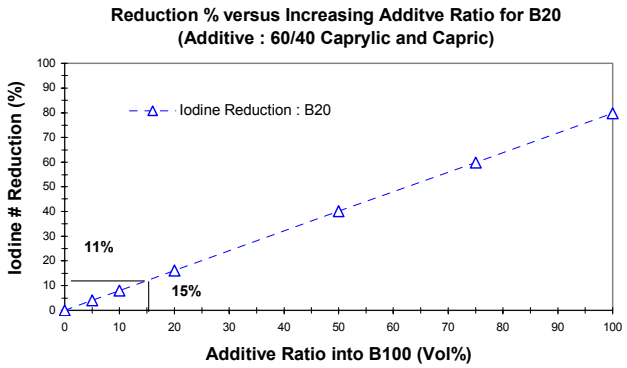

Figure 2. Reduction % versus increasing additive ratio for B20.

Hydrogenation Approach. The second option explored to this end was to use the industrial process of hydrogenation. Hydrogenation is, "the addition of hydrogen to a double or triple bond to yield a saturated product." [8] This option of saturation of

the molecules is particularly attractive as the process of hydrogenation is already being conducted on an industrial scale and is a well established technology. For this project, hydrogenated soy methyl ester was not available, so a substitute material was used which closely resembled the ideal iodine value, but did not adequately emulate the chemical composition.

Results and Discussion

It was observed that both options could reduce the NO_x emission by 1.5~3% relative to B20 fuel. Based on mode averaged NO_x reduction, caprylate/caprate blending generated around 2.8 % NO_x reduction over all the modes that is expected as summarized in the right side of Figure 3, confirming that iodine and NO_x correlation holds still valid for B20 blends. The raw data is compared in Figure 4.

As hydrogenated B20 has a little lower iodine number and density than caprate added B20, it was expected that NO_x reduction of this will be greater than other if other properties change remains constant for NO_x. But this was less effective to reduce NO_x than blending as seen in the same plot.

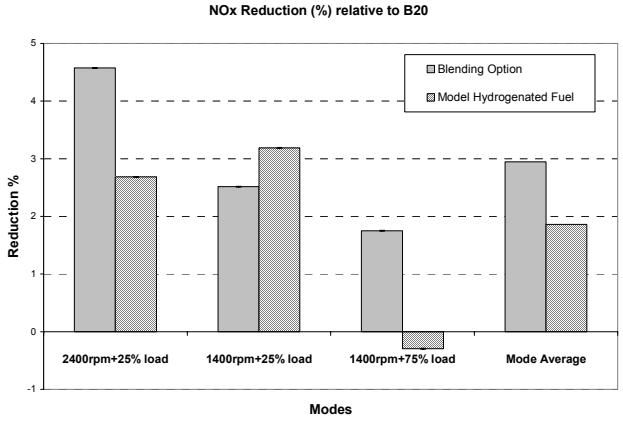

Figure 3. Percent NOx emissions reduction relative to B20 blend.

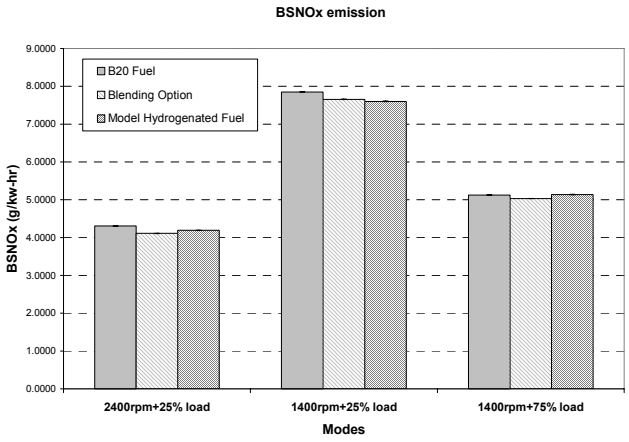

Figure 4. Brake specific NO_x emissions ($BSNO_x$) comparision.

Conclusions

From a review of literature, it was determined to focus the project investigation on the reduction of NO_x through the saturation of biodiesel methyl esters. Two approaches were taken to achieve this goal: blending and hydrogenation.

The blending approach involved the blending of short-chained, saturated methyl esters with biodiesel fuel. This approach was found to produce the desired reduction in NO_x emissions and improve the cold flow property. The NO_x reductions found in practice were in good agreement with predicted values. Unfortunately, while this option produced the desired results, the high cost of the saturated methyl esters makes this process economically unfeasible.

The second approach is the hydrogenation of soybean oil prior to transesterification. A second literature review was conducted to examine the process and process parameters of hydrogenation. Upon completion of this literature review, it was determined that hydrogenation is a viable option to increase the saturation of the biodiesel fuel methyl esters. To produce a blend that will reduce NO_x while not increasing the cloud point a high selectivity must be achieved during hydrogenation. Further research should be conducted to determine exact conditions for hydrogenation including temperature, catalyst type and loading, and pressure to produce the desired fatty acid chains. The experiments conducted on a fuel representing a hydrogenated product did show a reduction in NO_x emissions, but not to the extent predicted by calculations. This may be due to the fact that the fuel was lacking in stearic and plamitic acids. Another possible reason is that the engine used has an electronic controlled injection. This injection is very sensitive to fuel property such as heating value and density. As our "hydrogenated" fuel did not exactly match what a true hydrogenated biodiesel fuel would contain this test was not truly representative. If high selectivity is possible, hydrogenation is a viable solution to solve this problem as it is already in practice in the food industry.

Finally, increasing the saturation of biodiesel fuel is a way to reduce the emission of oxides of nitrogen. There are several methods to achieve this increase in saturation, two of which have been discussed here. Further research into hydrogenation or other methods of increasing saturation is suggested.

Acknowledgement. We would like to thank Dr. Robert McCormick of NREL,Dr. Michael Adewumi and Dr. André Boehman of Penn State, and Dr. Haas of the USDA Philadelphia Office. Additionally, we appreciate the support of P&G Chemicals and Stepan for their generous donation of the chemical supplies.

References

1. Graboski, M.S., and McCormick,R.L., "Combustion of Fat and Vegetable Oil Derived Fuels in Diesel Engines." Prog. Energy and Combust. Sci., 1998. **24**(2): p. 125-164.
2. Suppes, G., Rui, Y., Regehr, E., "Hydrophilic Diesel Fuels- Ignition Delay Times of Several DIfferent Fuel Blends." Society of Automotive Engineers, 1997 (971686).
3. EPA, A Comprehensive Analysis of Biodiesel Impacts on Exhaust Emissions (EPA420-P-02-001). 2002, United States Environmental Protection Agency.
4. Ma, F., Hanna, M., "Biodiesel production: a review." Bioresources Technology, 1999. **70**: p. 1-15.
5. McCormick, R., Graboski, M., Alleman, T., Herring, A., Tyson, S., "Impact of Biodiesel Source Material and Chemical Structure on Emissions of Criteria Pollutants from a Heavy-Duty Engine." Environ. Sci. Tech., 2001. **35**(9): p. 1742-1747.
6. Gomez, M., Gonzalez, E., Howard-Hildige, R., Leahy, J., Rice, B., "Winterisation of Waste cooking oil methyl ester to improve cold temperatures fuel properties." Fuel, 2002. **81**(1): p. 33-39.
7. Knothe, G., "Cetane number of branched and striaght-chained fatty esters determined in an ignition quality tester." Fuel, 2002. **Article in Press.**
8. McMurry, J., Organic Chemistry, 4th ed. 1995, Pacific Grove, CA: Brooks/Cole Publishing Company.

EFFECTS OF BIOMASS BLENDING ON COMBUSTION ASH

Christopher J. Zygarlicke and Bruce C. Folkedahl

Energy & Environmental Research Center (EERC)
University of North Dakota
Box 9018
Grand Forks, ND 58202-9018

Introduction

Cofiring biomass and coal in stoker-fired combustion systems may create some technical challenges. The diversity of the inorganic content of various biomass types coupled with the already known diversity of coal compositions makes it difficult to predict with great certainty the combustion performance of biomass–coal combinations. Recent work shows that intense characterization of biomass inorganics and controlled combustion experiments may aid in determining the behavior of combustion ash materials, including the interaction of biomass-derived alkali such as potassium with coal silicates. Mechanisms of ash deposit and fly ash particulate formation, including the role of fine silica, alkali, and alkaline-earth elements, and chlorine in biomass are being investigated (1–5). Stoker-fired boilers are popular for biomass cofiring because of the ease of fuel feeding, but even with these systems, issues such as production of different concentrations and quantities of fine particulate or aerosols, ash deposition rates, and the strength of ash deposits do arise. (6). In this paper, fundamental mechanisms of ash formation and deposition associated with biomass cofiring with coal were tested in a pilot-scale stoker-fired combustion system at the Energy & Environmental Research Center (EERC).

Experimental

Coal and Biomass Analysis. One representative coal (Cordero Rojo subbituminous) sample and two biomass fuels (wood chips and sunflower hulls) were selected for analysis and combustion testing. The coal and biomass fuels were selected for availability and either current use or the likelihood of future use in commercial applications. All fuels were analyzed for heating value, proximate–ultimate analysis, chlorine, major ash chemistry (i.e., SiO_2, Fe_2O_3, etc.), organically associated elements using chemical fractionation analysis, and mineral content using computer-controlled scanning electron microscopy (CCSEM).

Combustion Testing. The EERC's combustion test facility was modified to simulate a grate-fired system, called the combustion test stoker (CTS). The CTS is an upfired reactor (approximately 32 kg/hr, or 70 lb coal/hr) that contains an existing fouling probe bank to simulate convective surfaces and an electrostatic precipitator (ESP) for particulate control and ash capture. Three single-day combustion tests were completed including a baseline coal test and tests of 40 wt% blends of wood chips and sunflower hulls with the baseline coal. Firing rate was controlled to achieve a minimum furnace exit temperature of 983°C (1800°F) at nominally 20% excess air on a volume basis. Data comparisons included grate ash properties, fly ash properties, and flue gas properties as they pertain to fuel combustion efficiency. Fly ash collected in the ESP was analyzed for carbon content and particle size using a Malvern sizing instrument. Ash deposits were collected from the fouling probe bank and analyzed using scanning electron microscopy and major ash chemistry.

Results and Discussion

Table 1 lists the analysis data for the test fuels. The Cordero Rojo coal is typical of many Powder River Basin (PRB) coals in its analysis. The sample fired here was drier (20 wt% moisture) than the as-received fuel from the mine (typically 26 wt%). Inorganics were present at the 5.14 wt% level and consisted primarily of silica (31 wt%), alumina (19 wt%), and calcium (25 wt%) on an as-received basis. Sodium was present at about 1 wt%. Chloride content of the coal was measured at 21.3 µg/g.

Table 1. **Coal and Biomass Analysis Data**

Fuel Description	Cordero Rojo Coal	Wood Chips	Sunflower Hulls
	As-Fired	As-Fired	As-Fired
Proximate Analysis, wt%			
Moisture	20	5.2	11.4
Volatile Matter	37.61	78.54	72.21
Fixed Carbon	37.25	15.71	13.53
Ash	5.14	0.55	2.85
Ultimate Analysis, wt%			
Hydrogen	5.87	6.28	7
Carbon	53.37	46.46	46.35
Nitrogen	0.67	0.01	1.39
Sulfur	0.23	0.36	0.52
Oxygen	34.72	46.34	41.89
Ash	5.14	0.55	2.85
Heating Value, Btu/lb	9325	7764	7754
Chloride, µg/g	21.3	71.9	
Fuel Size, cm	1.905 × .635	1.27 × 0	.635 × 0
Ash Analysis, wt%	As-Fired	As-Fired	As-Fired
SiO_2	31.2	7.52	2.95
Al_2O_3	18.6	1.75	0.83
Fe_2O_3	4.57	8.76	0.71
TiO_2	1.65	0.41	0.06
P_2O_5	1.24	2.39	14.2
CaO	24.5	33.4	13.6
MgO	5.28	5.48	14
Na_2O	0.9	0.88	0.05
K_2O	0.42	37	47.2
SO_3	11.7	2.42	6.38
Select Mineral Phases, wt%			
Quartz	25	2	0
Kaolinite	19	0	0
Mixed Clays	16	12	0
Iron Oxide	1	2	2
Phosphate Mineral	4	0	0
Pyrite	2	2	0
Gypsum	2	35	0
Unclassifiable	11	43	95

The as-fired wood chips were low in moisture (5.2 wt%) and ash (0.55 wt%) and contained a high-volatile-matter component. They were milled to an average size of about 1.3 cm × 0. Because of the low moisture content, the as-fired wood chips had a fairly high heating. The low ash content was dominated by calcium (33 wt%) and potassium (37 wt%). Chloride content was measured at 71.9 µg/g.

Sunflower hulls were fired as received with no additional preparation. They contained a moderate level of moisture at 11.4 wt% and a fairly low ash content of 2.85 wt%. Heating value and volatile matter were similar to the wood. The inorganic portion of the hulls comprised mainly alkali and alkaline-earth elements: 47 wt% potassium, 14 wt% magnesium, and 14 wt% calcium. Phosphorus

and chloride contents were high relative to the other fuels at 14 wt% and 601 µg/g, respectively.

Chemical fractionation indicated that nearly all of the alkali–alkaline-earth elements in the biomass fuels are organically associated, showing extractions of 90% or more from water and ammonium acetate. About 25% of the calcium in the sunflower hulls is extracted in the HCl extraction stage and may be bound as a carbonate. A portion of the calcium (about 40 wt%) and potassium (65 wt%) in the Cordero Rojo coal is tied up with clay materials.

CCSEM analyses indicate quartz (25 wt%), kaolinite (19 wt%), and other mixed clays (16 wt%) as the major mineral phases present in the Cordero Rojo coal. The major mineral phases present in the wood sample were gypsum at 35 wt%, mixed clays at 12 wt%, and high concentrations of unclassifiable minerals (43 wt%), which were either very fine calcium carbonate or "bright" spots of organically bound potassium and calcium. Minor amounts of quartz, iron oxide, mixed clays, and pyrite were present in the wood. The sunflower hulls show little if any discernable mineral matter with the electron microscope except for some iron oxide. Unclassifiable minerals total 95%, which are primarily very fine carbonate or silica structures or "bright" potassium spots in the sunflower organic matrix that are excited by the rastering electron beam and are identified by CCSEM as small particles with a mixed elemental analysis consisting of 50%–95% potassium and an array of other elements. This type of analysis is characteristic of high concentrations of organically bound inorganics with little in discernable mineral particles.

Ash deposition on convective surfaces was minimal for all tests, baseline coal as well as the coal–biomass cofiring tests. Only a few grams of ash were sticking to the ash deposition probe, and the material was mostly calcium and potassium sulfates. The resulting deposition observed would not significantly reduce the capability of a boiler to produce steam. The highest deposit growth rate was observed for the baseline coal. This deposit, however, had the lowest strength of any of the deposits generated. The highest-strength deposit was observed for the 60–40 Cordero Rojo–sunflower hull blend, which also had the lowest growth rate. Analysis of the 60–40 coal–sunflower hull blend deposit showed a potassium–calcium–aluminosilicate bonding matrix essentially "gluing" the deposit together. The high concentration of potassium in the sunflower hulls reacted with the abundant calcium–aluminosilicates derived from the coal, which led to lower-melting-point phases of lower viscosity which tend to increase strength development in ash deposits. Analysis of the 60–40 coal–wood chip blend deposit showed a calcium–iron–aluminosilicate bonding matrix with iron crystallizing out of the melt. The crystallization of the iron can decrease the strength of the melt by creating areas that fracture more readily. The low ash content of the wood chips also contributed to a lower ash deposition rate and strength.

Furnace exit gas temperatures (FEGTs) during the pilot-scale tests ranged from 1021° to 1065°C (1870° to 1948°F). Slightly higher (56°C [100°F]) FEGTs could trigger more severe fouling. Also, the quantity of fly ash generated during these tests was lower than considered typical for stoker-fired applications. Therefore, these observations may have been influenced by some minor grate clinker formation. In summary, the dynamics of the stoker system create cooler burning and flame temperatures, resulting in lower FEGTs, which diminish fouling propensity.

Figure 1 shows that fly ash particle-size distribution decreased when biomass was blended with the coal. This was expected because of the fine size of the fuel minerals in the biomass and the preponderance of organically associated alkali metals and alkaline-earth components. In terms of fly ash generation, the alkalies can be expected to form fine particulates in the form of potassium sulfate, potassium phosphate, chlorides, and calcium sulfate, among other fine species. The shift to a finer fly ash particle size as a result of biomass cofiring could be problematic for units with small ESPs or, in some cases, old stokers still using multicyclones for particulate control. It is recommended that units lacking adequate ESP surface or using multicyclones consider ESP upgrades or installation of fabric filters for collection of fine particulate to meet emissions standards.

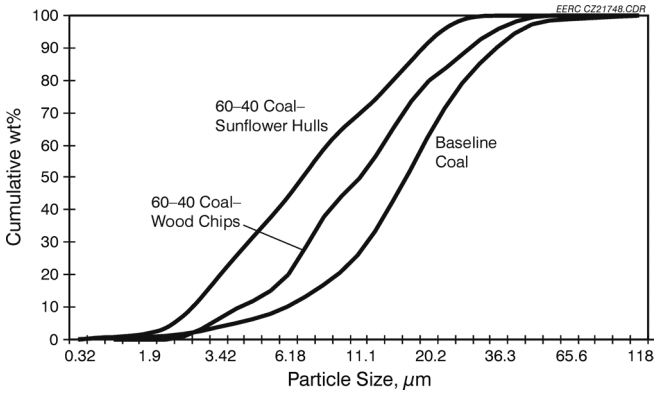

Figure 1. Fly ash-size distribution by Malvern analysis – 60–40 Cordero Rojo–wood chips

Acknowledgment. This work was supported by the United States Department of Energy National Energy Technology Center under Cooperative Agreement No. DE-FC26-00NT41014. The EERC acknowledges NETL Performance Monitor Philip M. Goldberg for his supervision.

References

1. Folkedahl, B.C.; Zygarlicke, C.J. Cofiring Wood Residue and Sunflower Hulls with Coal. In *Proceedings of the 27th International Technical Conference on Coal Utilization & Fuel Systems*; Clearwater, FL, March 4–7, 2002; Vol 1, pp 515–526.
2. Folkedahl, B.C.; Zygarlicke, C.J.; Strege, J. Influence of Biomass Cofiring on $PM_{2.5}$ Ash Produced in a 7-kW Coal Combustion System. Presented at the NETL $PM_{2.5}$ Conference, Pittsburgh, PA, April 9–10, 2002.
3. Folkedahl, B.C.; Zygarlicke, C.J.; Hutton, P.N.; McCollor, D.P. Biomass for Energy – Characterization and Combustion Ash Behavior. In *Proceedings of Power Production in the 21st Century: Impacts of Fuel Quality and Operations*; Harding, N.S.; Baxter, L.L.; Wigley, F.; Frandsen, F., Eds.; Snowbird, UT, Oct 28 – Nov 2, 2001.
4. Sondreal, E.A.; Benson, S.A.; Hurley, J.P.; Mann, M.D.; Pavlish, J.H.; Swanson, M.L.; Weber, G.F.; Zygarlicke, C.J. Review of Advances in Combustion Technology and Biomass Firing. *Fuel Process. Technol*. **2001**, *71* (1–3), 7–38.
5. Zygarlicke, C.J.; McCollor, D.P.; Toman, D.L.; Dahl, J. Ash Interactions During the Cofiring of Biomass with Fossil Fuels. In *Proceedings of the 26th International Technical Conference of Coal Utilization, and Fuel Systems*; Clearwater, FL, March 5–8, 2001; pp 237–248.
6. Frandsen, F.J.; Nielsen, H.P.; Jensen, P.A.; Hansen, L.A.; Livbjerg, H.; Dam-Johansen, K.; Sorensen, H.S.; Larsen, O.H.; Sander, B.; Henriksen, N.; Simonsen, P. Deposition and Corrosion in Straw- and Coal-Straw Co-Fired Utility Boilers. In *Proceedings of the Engineering Foundation Conference on the Impact of Mineral Impurities in Solid Fuel Combustion*; Kona, HI, Nov 2–7, 1997; Wall, T.F.; Baxter, L.L., Eds.; 1997; 14 p.

PREDICTING NO_X EMISSIONS FROM BIOMASS COFIRING

Stephen Niksa[a], Guisu Liu[a], Larry Felix[b], P. Vann Bush[b], and Douglas M. Boylan[c]

[a]Niksa Energy Associates, 1745 Terrace Drive, Belmont, CA 94002, neasteve@pacbell.net
[b]Southern Research Institute, P. O. Box 55305, Birmingham, AL, 35255-5305
[c]Southern Company Services, Inc., P. O. Box 2641, Birmingham, AL, 35291-8195

Introduction

In theory, biomass cofiring should reduce NO_X emissions simply because most forms of biomass contain less fuel-N than the coals they displace. The yields of volatiles are generally much higher from biomass than from coal, and volatiles contain many compounds that can effectively reduce NO in fuel-rich flame zones. Biomass also decomposes faster than coal, which tends to steepen near-burner temperature profiles and enhance the ignition characteristics. These factors are expected to improve NO_X emissions by more than the displacement of coal-N. But the database from pilot- and full-scale testing exhibits mixed results, including substantial representation for no effect, for less reduction than the displacement of fuel-N, and for enhanced reduction over the displacement of fuel-N.

The premise for our work is that uncontrolled variables are responsible for the ambiguities in the existing database. A testing campaign was staged to characterize the most likely parameters, including the biomass form, coal type, biomass injection configuration, burner staging, and furnace stoichiometry. The database from the testing campaign was then interpreted with simulations based on full chemistry for fuel decomposition, volatiles combustion including fuel-N conversion, soot conversion, and char burnout. Once the model predictions were demonstrated to be accurate, the simulation results were interrogated to determine how the biomass affected NO_X emissions. We find that two factors determine whether biomass cofiring will reduce NO_X emissions: (1) Does the abundance of gaseous volatiles, not soot, from biomass reduce away the NO formed near the burner; and, (2) Is significantly less char-N released into downstream flame zones by the addition of biomass. This paper emphasizes the interpretation of the database with detailed chemical reaction mechanisms. More thorough descriptions of the simulation methodology are available[1,2].

Testing Program

All tests were conducted in Southern Research Institute's (SoRI) Combustion Research Facility (CRF). The CRF consists of fuel handling and feeding systems, a vertical refractory lined furnace with a single up-fired burner, a horizontal convective pass, heat exchangers and conventional exhaust cleaning devices. Emissions from this system have been qualified against those from full-scale, tangential-fired furnaces for the operating conditions imposed in this work[3]. The 8.5 m by 1.07 m (i.d.) cylindrical furnace handles gas velocities from 3 to 6 m/s, and residence times from 1.3 to 2.5 s. The nominal firing rate is 1.0 MW_t, which was fixed for all cases in this work. A single burner generates a core of pulverized fuel and primary air surrounded by weakly swirled secondary air. For all cases in this paper, the biomass was co-milled with the coal and the mixture was directly fed into the burner. Overfire air (OFA) was injected through 4 off-radius ports located 4.6 m down the furnace. All datasets include cases with 0 (unstaged) and 15 % OFA. In the unstaged series, the OFA was combined with secondary air. Air feedrates were varied to produce exhaust (wet) O_2 levels between 2.5 and 5 %.

Table 1. Fuel Properties

	SD	SG	JR	GL	PR	JW
Proximate, as rec'd						
Moisture	9.5	15.2	19.3	5.8	1.9	0.8
Ash	0.4	29.5	5.4	6.6	15.1	14.6
Volatiles	78.1	47.6	39.6	33.7	33.2	20.0
Carbon	11.9	7.7	35.7	54.0	49.9	64.6
Ultimate, daf wt. %						
C	49.8	56.1	74.9	81.8	83.4	89.5
H	6.1	5.4	4.9	5.0	5.5	4.6
O	43.9	35.7	18.8	10.0	7.5	3.3
N	0.2	2.4	0.9	2.0	1.8	1.7
S	0.0	0.4	0.4	1.1	1.8	0.9
$<d_P>$, μm	163	173	29	53	48	34

Fuel quality was varied by firing four diverse coals with two forms of biomass. Nominal properties of the six primary fuels appear in Table 1 in order of increasing rank, from left to right. Moisture levels are highest for the low-rank fuels, especially switchgrass (SG) and subbituminous coal (JR). Ash levels are widely variable and especially high for biomass SG and for the hv bituminous (PR) and low volatile bituminous (JW) coals. Whereas it appears that the volatility of sawdust (SD) is much higher than SG's, on a dry-ash-free (daf) basis, their volatiles yields are almost identical. The daf-volatiles contents of the coals fall by more than a factor of two over this suite of samples, which will definitely affect the conversion of coal-N into NO_X. Carbon contents increase and oxygen contents decrease for fuels of progressively higher rank. The pair of biomass samples represents most of the range of elemental compositions seen for diverse forms of biomass. The represented range of coal rank, from subbituminous through lv bituminous, is similarly broad. The hydrogen, nitrogen, and sulfur levels are not rank-dependent. Whereas almost all biomass contains little nitrogen and sulfur, sample SG contained the most nitrogen of any of the fuels, due to its decomposition before firing. The particle size distributions (PSDs) are typical utility grinds for the coals, except for the much finer grind of JR, whereas the biomass grinds are much coarser, as expected.

Computer Simulations

It is not currently possible to incorporate detailed chemical reaction mechanisms into conventional CFD simulations of pulverized fuel (p. f.) flames. Since chemistry in the gas phase, especially volatile-N conversion chemistry, was suspected to play a dominant role in NO_X production during biomass cofiring, Niksa Energy Associates developed a new computational approach for this application based on our "ChemNet™ Post-Processing (CNPP)" method. The CNPP method first generates an equivalent network of idealized reactor elements from a conventional CFD simulation. The reactor network is a computational environment that accommodates realistic chemical reaction mechanisms; indeed, mechanisms with a few thousand elementary chemical reactions can now be simulated on ordinary personal computers, provided that the flow structures are

restricted to the limiting cases of plug flow or perfectly stirred tanks. The network is "equivalent" to the CFD flowfield in so far as it represents the bulk flow patterns in the flow. Such equivalence is actually implemented in terms of the following set of operating conditions: The residence time distributions (RTDs) in the major flow structures are the same in the CFD flowfield and in the section of the reactor network that represents the flow region under consideration. Mean gas temperature histories and the effective ambient temperature for radiant heat transfer are also the same. The entrainment rates of surrounding fluid into a particular flow region are evaluated directly from the CFD simulation. To the extent that the RTD, thermal history, and entrainment rates are similar in the CFD flowfield and reactor network, the chemical kinetics evaluated in the network represents the chemistry in the CFD flowfield. Whereas this paper emphasizes the application to biomass cofiring, separate publications explain the simulation methodology in greater detail[1,2,4].

CFD Simulations

CFD simulations of the CRF were performed by Reaction Engineering International (REI) for all tests with PR coal and various biomass. Cases with JR and JW were performed at SoRI, using REI's Configurable Fireside Simulator (CFS) for the CRF. The CFS imposes a fixed computational grid on the calculations, and is therefore suitable for parametric case studies with the same firing configurations. No CFD were available for cases with the second hv bituminous coal (GL) because these flame structures were expected to be very similar to the PR flames.

The most surprising feature in the CFD simulations is that all fuel particles remained on the furnace axis throughout this furnace. Neither mixing in the near-burner zone nor radial OFA injection disperses the particles off their original trajectories. Near the burner, the primary air stream was significantly expanded by the release of volatiles from the fuel suspension and by thermal expansion. This expansion zone delineates a fuel-rich core from the outer, annular flow of secondary air. Nominal residence times in the core range from 120 to 170 ms. The expansion of the primary flow promotes entrainment of secondary air into the core, because some of the secondary flow penetrates the expansion boundary. In addition, a portion of secondary air is entrained into the core as soon as it passes the edge of its delivery tube in the fuel injector. Together, these entrainment mechanisms almost instantaneously mix about 20 % of the secondary air into the primary flow.

The mixing layer between the core and secondary air streams gradually expands until it contacts the furnace wall midway to the OFA ports. An external recirculation zone (ERZ) forms in the corner bounded by the outer boundary of the secondary air stream, but is too weak to entrain particles or appreciable amounts of air or fuel compounds. As the fuel compounds in the flame core contact the secondary air stream, they mix and burn in an expanding mixing layer. This layer completely surrounds the core near the burner inlet, and fills the entire furnace downstream of the core. The most distinctive feature of the mixing layer is that the temperature profile across the layer in the normal direction passes through a maximum value which is essentially the same around the entire circumference of the core. Maximum gas temperatures approach 1700°C in cases where fuels of the highest heating values were fired without OFA, and 1600°C in cases with 15 % OFA. Residence times in the mixing layer to the OFA location vary from 500 to 600 ms. The four air jets from the OFA ports do not penetrate onto the centerline. They also do not fill the entire flow cross section. Downstream of the OFA ports, the flow relaxes to a plug flow pattern that carries ash and exhaust into an exhaust system. The total residence time from the burner to the furnace exit is approximately 2.5 s.

Equivalent Reactor Network

As seen in Fig. 1, the bulk flow patterns are delineated in the regions assigned by CNPP from the CFD simulation. The baseline PR flame consists of a core, mixing layer, ERZ (which is inconsequential), OFA-region and burnout (BO) region. All other flames have the same regions. The CSTR network from the CNPP analysis of the baseline PR flame also appears in Fig. 1. The networks for all other CRF flames have similar branches and feedstreams but appreciably different quantitative specifications. In the network, the flame core has been subdivided into two regions. The devolatilization zone covers the upstream portion of the core in which volatiles are being released from the fuel suspension and burned with primary air. Since the primary stream is extremely reducing, no residual O_2 leaves the devolatilization zone. The NO_X reduction zone covers the downstream portion of the core in which only the N-species are converted under the influence of water gas shifting, due to the absence of O_2. The CSTR-series for the mixing layer and the OFA zone represent the mixing of secondary and tertiary air streams, respectively. But there are no additional flows into the CSTR-series for the BO zone.

The RTD for this particular core was deconvoluted into one component for 16 CSTRs-in-series and another for plug flow with respective mean residence times of 138 and 193 ms. The plug flow component represents the near-axial fluid motion under the influence of particle drag, and the CSTR-component represents flow with significant radial velocities. The networks for other fuels usually have only one flow channel for the entire core, and the bulk flow pattern is plug flow. The RTD for the mixing layer was matched with a series of 19 CSTRs, and that for the OFA zone was represented by 6 CSTRs-in-series. The BO zone is essentially in plug flow.

Note that entrainment into the various CSTR-series is represented as a series of discrete additions over several reactors in the series. Volatiles are entrained into the series for the first part of the flame core; secondary air is entrained into the series mixing layer; and tertiary air is entrained into the series for the OFA zone. The addition rates of volatiles were specified from the stand-alone devolatilization simulation with the thermal histories of particles from the CFD simulation. The specific addition rates of the air streams were specified from the continuous entrainment profiles evaluated from the CFD simulation.

Reaction Mechanisms

The devolatilization submodel, called FLASHCHAIN®, determines the complete distribution of volatile compounds from almost any p. f., and also predicts the yield and elemental composition of char[5]. When combined with a swelling factor correlation and a correlation for the initial carbon density in char, it specifies all the necessary char properties for a char oxidation simulation. Hence, the complete distribution of volatiles, including gaseous fuels and soot, and all char properties are completely determined from only the fuel's proximate and ultimate analyses.

The reaction mechanism for chemistry in the gas phase contains 444 elementary reactions among 66 species, including all relevant radicals and N-species[6]. All rate parameters were assigned independently, so there are also no adjustable parameters in the submodel for gas phase chemistry. The soot chemistry submodel depicts several important effects. As soot burns, it directly competes for the available O_2 and also consumes O-atoms and OH that would otherwise sustain homogeneous chemistry. Soot also promotes recombinations of H-atoms and OH that could also sustain NO homogeneous chemistry[7]. And soot reduces NO directly into N_2.

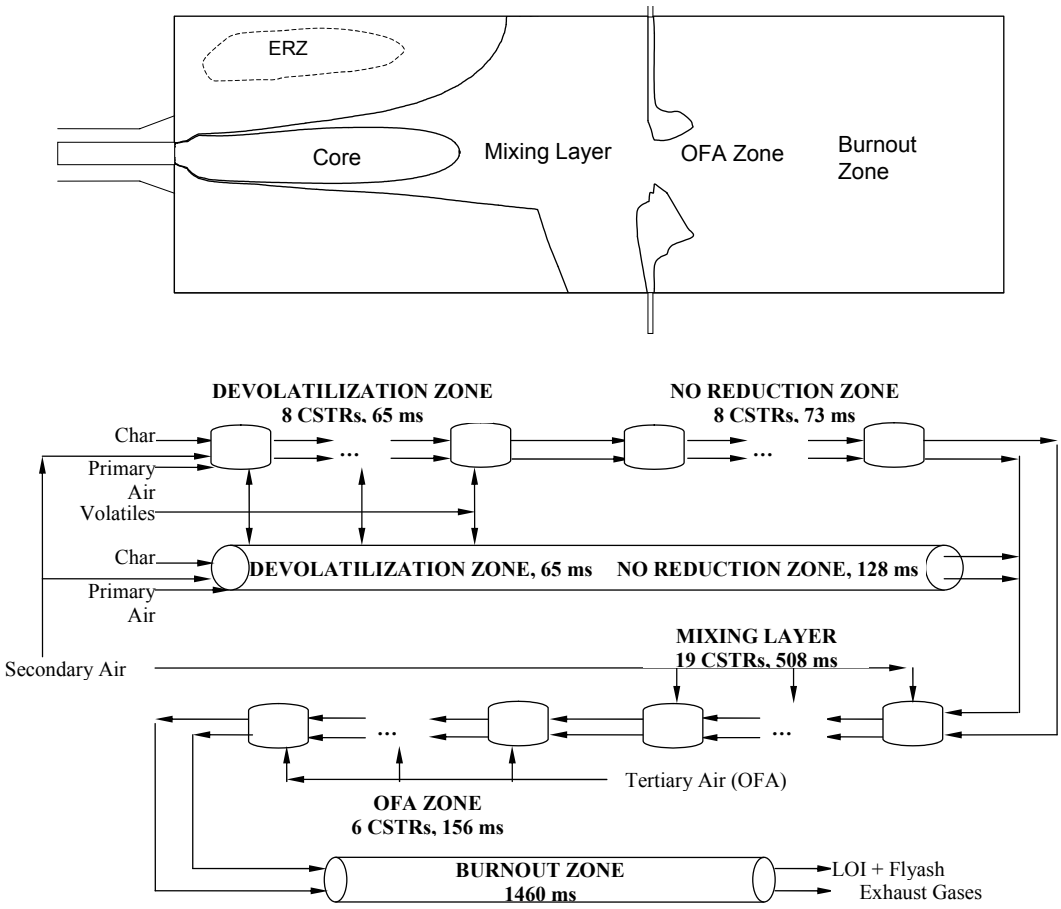

Figure 1. (Top) CNPP regions delineated from the CFD simulation for the baseline PR flame, and (Bottom) equivalent reactor network.

Char burning rates are determined by thermal annealing, ash encapsulation (of low-rank chars), and a transition to chemical kinetic control. The Char Burnout Kinetics (CBK) Model includes all these effects, and depicts the impact of variation in gas temperature, O_2 level, and char particle size within useful quantitative tolerances[8]. However, it is not yet possible to specify the initial char reactivity within useful tolerances from the standard coal properties. We must calibrate this value with LOI predictions or some other suitable index on combustion efficiency. The submodel for char-N conversion is subject to a similar calibration requirement (with NO emissions), compounded by its simplistic mechanistic premise; viz., that a fixed fraction of char-N is converted into NO at the overall burning rate throughout all stages of char oxidation.

To summarize, the initial char reactivity and the fraction of char-N converted to NO can only be specified from calibration procedures, whereby these parameters are adjusted to match the predicted LOI and NO_X emissions to reported values for a single set of operating conditions. Then the same values should be imposed for all other operating conditions. Except for these two parameters, all other model parameters can be assigned from the fuel's proximate and ultimate analyses within useful quantitative tolerances, or directly adopted from literature.

Calibration and Extrapolation Procedures

The fraction of char-N converted to NO during char oxidation was assigned to fit the NO_X emissions from the coal-only baseline flames for each coal sample. These same values were applied in all cofiring simulations. Values for biomass were unnecessary because biomass chars contain no nitrogen.

Only 13 CFD simulations were developed for the CRF under this project, yet almost 300 tests were simulated with detailed reaction mechanisms. All but one of the cases with CFD simulations had 15 % OFA, and were for the coal-only baselines or the high loading of biomass. Extrapolations to operating conditions without CFD were based on perturbations to the flame temperature profiles and air entrainment rates. All these procedures were established for the coal-only baseline flames to describe the reported impact of furnace stoichiometry and staging level on the NO_X emissions. Once established, the same extrapolation procedures were then applied without adjustment to the cofiring cases.

Results

The discussion in this section moves through the mechanistic basis for NO_X reduction via biomass cofiring, beginning with the distinctive devolatilization behavior of the various fuels in the testingprogram. Then the NO_X predictions are evaluated in comparisons with data, followed by our interpretations for the major trends based on the detailed flame structure of CRF flames.

Table 2. Distributions of Secondary Pyrolysis Products and Char Properties.

	SD	SG	JR	GL	PR	JW
Volatiles, daf wt. %						
Wt. Loss	86.1	86.0	65.2	56.5	59.8	39.7
Soot	4.3	13.4	30.1	33.7	37.9	26.8
CH_4	7.1	7.4	0.7	0.4	0.5	0.3
C_2H_2	2.2	1.3	1.5	1.0	1.3	2.3
C_2H_4	1.4	1.5	0.0	0.0	0.0	0.0
H_2	2.1	1.7	3.4	3.6	4.0	3.5
CO	48.4	41.5	12.9	7.2	6.1	1.7
CO_2	8.2	8.0	6.4	2.2	1.7	1.0
H_2O	12.1	7.7	7.6	4.9	4.3	1.8
HCN	0.0	0.0	1.26	2.47	2.24	1.52
NH_3	0.24	2.90	0.0	0.0	0.0	0.0
H_2S	0.0	0.44	0.42	1.17	1.91	0.96
Char Comp., daf wt. %						
C	94.7	97.1	98.9	98.4	98.5	98.2
H	3.4	2.5	0.5	0.5	0.4	0.5
O	1.9	0.4	0.0	0.0	0.0	0.0
N	0.0	0.0	0.4	1.1	1.0	1.26
S	0.0	0.0	0.1	0.1	0.1	0.0
Char ash, wt.%	2.5	75.7	15.9	14.2	30.9	21.8
Char size, μm	97.6	103.6	29.9	59.1	54.1	41.7

Predicted Devolatilization Behavior. Since the heating rate of primary air in the CRF is very fast, the primary devolatilization products are instantaneously converted into secondary volatiles pyrolysis products. The predominant transformation during secondary pyrolysis is the conversion of tar into soot, with simultaneous release of tar-O as CO, tar-H as H_2, and most of the tar-N as HCN. In addition, all aliphatic hydrocarbons are converted into CH_4 and C_2H_2, which can add to the soot phase during the latest stages. The predicted distributions of secondary pyrolysis products are collected in Table 2. Total volatiles yields are the same for both forms of biomass and, at 86 daf wt. %, much higher than the yields from any of the coals. The biomass product distributions are dominated by CO, with substantial amounts of hydrocarbons, especially CH_4, and CO_2 and H_2O. H_2 is another major fuel compound from biomass. But there is surprisingly little soot, considering that tar, the soot precursor, is 25 to 45 % of the daf fuel mass released during primary devolatilization. The reason is the abundance of tar-O, which approaches 40 % of the tar mass. This oxygen converts most of the tar into CO rather than soot during secondary pyrolysis. Essentially all the fuel-N is released as NH_3 during secondary pyrolysis. The abundance of NH_3 with SG, and its higher soot yield and lower CO yield, are the major difference between the two biomass forms.

In contrast, the secondary pyrolysis products from all the coals are dominated by soot which is, by far, the most abundant product. The total hydrocarbon yields are comparable from all coals, but less than a fourth of the hydrocarbon yields from the biomass. Hydrogen yields are also comparable, and double those from biomass. The yields of the oxygenated gases diminish with coals of progressively higher rank, in accord with the trend in the coal-O levels. But even the highest CO yield from JR coal is only about one-quarter the CO yield from the biomass. The only N-species is HCN although, in actuality, a minor amount of NH_3 may have been released from JR coal (but none of the others). The N-species yields are directly proportional to the coal-N levels, as expected.

Char compositions are very similar among all six fuels, except that the most abundant heteroatoms in biomass chars are H and O. versus H and N in the coal-derived chars. The char-N levels are negligible in biomass chars. They are comparable but lower for the coal-derived chars and certainly not negligible. Perhaps the most significant variation in char properties is among the char-ash levels. The values for SG and PR are definitely high enough to inhibit char oxidation during the latest stages of burnout, according to the ash inhibition mechanism in CBK. The mean char sizes are disparate for the biomass and coal chars, but more similar than the whole coal values because biomass shrinks and the coals swell during devolatilization, especially the bituminous coals

Table 3. Evaluation of Predicted NO_X for 3.5 % O_2 with 15 % OFA.

Series	Fuel	NO_X, ppm @ 3 % dry O_2	
		Pred.	Mes'd
1	PR hv bit	325	328
	PR/10%SD	255	271
	PR/20%SD	236	245
	PR/15%SG	277	269
	PR/20%SG	258	260
5	GL hv bit	372	360
	GL/10%SD	365	273
	GL/20%SD	318	327
6	GL hv bit	368	356
	GL/10%SG	399	340
	GL/20%SG	349	336
7	JR subbit	263	240
	JR/10%SG	203	185
	JR/20%SG	177	142
	JR/10%SD	221	191
	JR/20%SD	212	189
12	JW lv bit	419	422
	JW/5%SD	416	420
	JW/10%SD	417	389
	JW/20%SD	436	364
13	JW lv bit	429	450
	JW/5%SG	422	455
	JW/10%SG	442	440
	JW/20%SG	404	407

Evaluation of Predicted NO_X Emissions. The reported impact of fuel quality on NO_X emissions is extremely complex. It depends on which coal is fired, which biomass is cofired, which cofiring level is imposed, and which injection configuration is used. Table 3 presents the measured and predicted NO_X emissions for all cases with co-milled fuel injection and 15 % OFA that had 3.5 % exhaust O_2. Cofiring with 10 % SD always reduced NO_X, except with JR coal (and with GL coal with 0 % OFA). With the same injection, cofiring with 20 % SD reduced NO_X with JR and GL but not with JW. With PR/20 % SD, NO_X was reduced with 15 % OFA (but not with 0 % OFA). Cofiring with 20 % SG was effective on PR and JW, but notwith GL and JR. With 10 % SG, cofiring was effective with JR, but not with GL and JW; PR was not tested at this condition.

As seen in Table 3, the predicted emissions for PR hv bit coal (Ser. 1) are within experimental uncertainty for all biomass cofiring combinations. They correctly depict the more-than-20 % reduction in NO_X with the highest loadings of both biomass forms, and a proportional decrease in NO_X for progressively higher biomass loadings. No discrepancy exceeds 16 ppm. Similarly, the predictions for JR subbit. (Ser. 7) depict the proportional reductions in NO_X with higher biomass loadings, and the greater effectiveness of SD compared to SG. In this series no discrepancy exceeds 35 ppm. Cases with the JW lv bit. coal are within experimental uncertainty for SG co-firing (Ser. 13), which did not reduce NO_X at either of the lower switchgrass loadings. The predicted NO_X reduction with 20 % SG (Ser. 12) was under 10 %, in accord with the measured value. But with SD cofiring on JW coal (Ser. 12), the predictions show no significant NO_X reduction for any SD loading, at

odds with the reported reductions up to 11 % for loadings of 10 and 20 %.

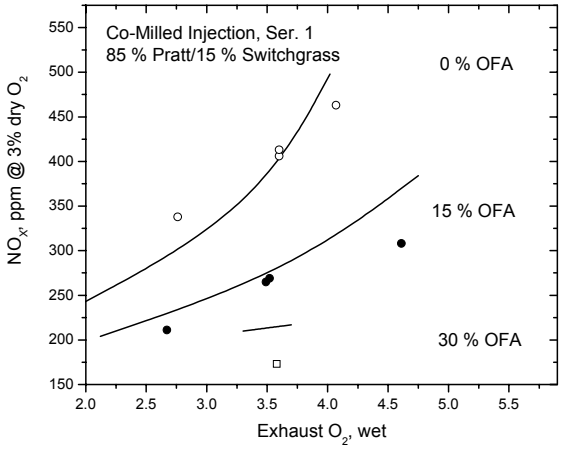

Figure 2. Predicted (Curves) and measured (data points) NO_X emissions for 3 staging levels and a range of exhaust O_2 levels for PR/15 % SG flames.

Predicted NO_X emissions with GL coal (Ser. 5 and 6) are not as accurate as all others, and the reported behavior is more complex. With SD cofiring, the reported extent of NO_X reduction is significantly greater for a 10 % loading than for 20 %. With SG cofiring, the same extent of NO_X reduction was reported for both loadings. But the predicted NO_X emissions are actually higher than the coal-only baselines with both biomass forms. Unfortunately, no CFD simulations were available for any of the GL test cases, so the specifications for PR-coal were applied in all GL-cases. A breakdown in this extrapolation procedure may be responsible for the discrepancies in the predictions, although they may also reflect a flaw in the mechanisms for this particular chemical environment.

The accuracy of the extrapolation procedures for furnace stoichiometry and staging level are apparent in Fig. 2. This set of predictions covers the full ranges of furnace stoichiometry (which determines exhaust O_2 level) and degree of air staging in the test program. The predictions are based on the procedures developed to fit the NO_X emissions for the coal-only baseline tests over the same domain of conditions, starting with only a single CFD simulation for 3.5 % O_2 and 15 % OFA. The same procedures were then applied without modification to the biomass cofiring cases, such as the 15 % SG on PR in Fig. 2. The predictions are within experimental uncertainty except, perhaps, for the highest O_2 level with 15 % OFA. Notwithstanding, it is evident that these extrapolations did not introduce intolerable uncertainties into the predictions, and CNPP can be successfully applied with many fewer CFD simulations than test conditions.

Discussion

The predicted structure of the flame core for the PR/20%SD flame appears in Fig. 3. In contrast to SG, SD has almost no fuel-N. This cofired flame still generates 25% less NO_X than the PR-only baseline flame, which is slightly more than the reduction expected for the removal of fuel-N alone. The time scale in Fig. 3 depicts the core as well as the first quarter of the mixing layer. For this particular test, devolatilization is completed within 80 ms, and the flow leaves the core at 118 ms. The total residence time in the mixing layer is 476 ms, but only the first 150 ms are shown in Fig. 3. The S. R. value for the gas phase falls sharply while volatiles are released into the flow, making it more reducing. It then relaxes to an ultimate value 0.864, which is significantly more reducing than both the PR-only baseline and the PR/20%SG flame. Although SD and SG have identical volatiles yields, the gas phase in the SD-core becomes more reducing because more CO and less soot are produced by the primary volatiles from SD.

Initially, the CO concentration surges during the ignition period, then increases more gradually during the oxidation of char and soot. Its ultimate value and the persistence of H_2 reflect water gas shifting once all O_2 has been consumed. The maximum CO concentration is double that in the PR/20%SG flame. The H_2 mass fraction persists at roughly 1000-2000 ppmw across the entire core. Moreover, hydrocarbons, especially C_2H_2 (not shown), persist at 1000 ppmw or more across the entire devolatilization zone. This is the only flame core with an appreciable amount of hydrocarbons in the presence of NO, although their concentration is still much lower than those of CO and H_2.

As for the other flames, almost half the char burns out in the core, but hardly any soot burns out in this particular core. The more reducing character of the gas phase in this core imparts several distinctive features to the N-species conversion chemistry. The N-speciation is dominated by HCN and NO, as for the PR-only baseline flame. The NH_3 released by the SD is rapidly converted to HCN and NO within 40 ms. But NO does not accumulate at the expense of HCN, as in both of the other flame cores. Instead, the HCN concentration surges while NO accumulates. Some prompt N-fixation mechanisms involving N_2 in air must be responsible because the total maximum amount of fixed-N species is double the maximum value in the PR/20%SG flame, and the SG-cofired flame has significantly more volatile-N. NO reduction begins at 75 ms but by the exit of the core, there is still 1390 ppmw HCN and 465 ppmw NO, which are both much higher than in either of the other flames. Early in the mixing layer, NO reduction accelerates while the HCN concentration plummets. The NH_3 concentration reaches 92 ppm before vanishing with the HCN concentration. The ultimate NO concentration after both other fixed-N species have been eliminated is only 143 ppmw, which is 25 ppm lower than the analogous level in the PR/20%SG flame. Even though there was a higher concentration of fixed-N species in the core, the greater reducing potential yielded a lower NO concentration in the mixing layer, after chemistry in the gas phase was exhausted. Since the extents of char burnout at this point are comparable for the PR/20%SG and PR/20%SD flames, the 20 ppmw reduction for the PR/20%SD flame persists in the exhaust emissions.

A surge in the extent of soot burnout coincides with the entrainment of secondary air. Due to the high maximum temperatures in the mixing layer, the extent of soot oxidation eventually overtakes the extent of char oxidation at 220 ms. The soot burns out in the mixing layer, whereas char is carried over into the OFA and BO regions.

The structures of the coal-only and the biomass cofired flames in the CRF are qualitatively similar: All exhibit a very rapid surge in the NO level immediately after injection, due to the ignition of volatiles under the very lean conditions associated with the primary streams during the initial stages of devolatilization. But as more volatiles are released, the gas phase becomes progressively more reducing, which enables the early NO to be reduced into HCN and NH_3. The extent of reduction is determined by the S. R. value among the gaseous species only and the residence time available before the core fluid is exposed to secondary air in the mixing layer. All fixed-N species are rapidly converted into NO and N_2 at the beginning of the mixing layer, which then sustains the oxidation of soot and char.

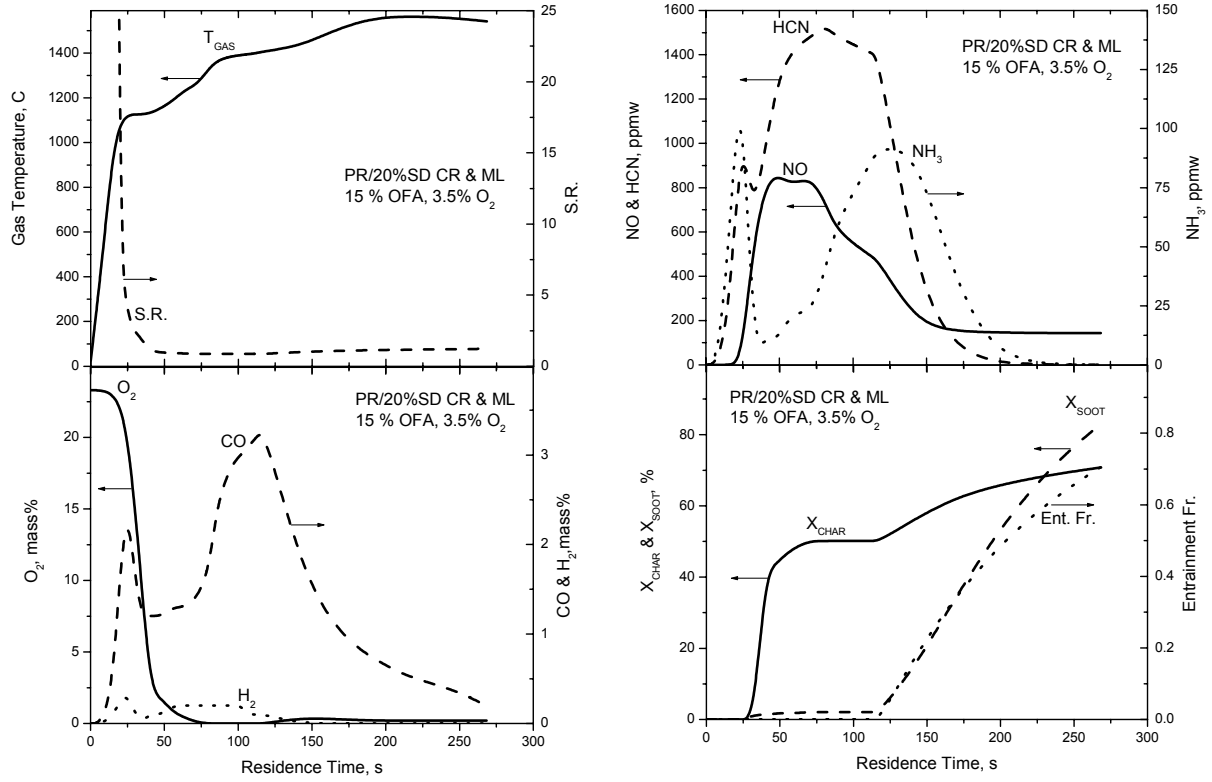

Figure 3. Structure of the core of the PR/20%SD flame showing, in counterclockwise order from the upper left, the operating conditions, major species, char and soot burnout, and N-species.

From this point onward, chemistry in the gas phase is inconsequential, and the conversion of some of the char-N into NO supplements the NO_X inventory.

Two factors are primarily responsible for the significant NO_X reduction observed for CRF flames with biomass cofiring. First, there is more volatile matter from biomass and it contains a much smaller contribution from soot. Consequently, the near-burner S. R. values for the gas phase are significantly richer than in coal-only flames. Under richer conditions, near-burner NO will be reduced away and a greater proportion of the fixed-N species will be converted into N_2. CRF flames provide sufficient residence times in the flame cores for NO reduction and fixed-N conversion to N_2. Second, a significantly lower percentage of the total fuel-N will remain in the char beyond the near-burner zone, where its partial conversion to NO is inevitable. If the biomass contains nitrogen, it releases all of it in the near-burner zone. If the biomass contains no nitrogen, then the inventory of char-N beyond the flame core is reduced in proportion to the biomass loading. In either case, there is less char-N beyond the point where NO can be reduced by chemistry in the gas phase.

The first factor is especially sensitive to fuel quality. Indeed, even the NO_X emissions from the four coal-only flames are ordered according to the volatiles yields and contributions from soot. While the volatiles yields decrease and the soot contributions increase for coals JR, PR, GL, and JW (cf. Table 2), the baseline NO_X emissions in the staged flames increased from 240 to 338 to 358 to 436 ppm (cf. Table 3). Biomass cofiring mitigated these differences by enhancing volatiles yields and by reducing the soot contributions. The net effect was significant NO_X reduction for the cofired flames, even when the biomass supplements the inventory of fuel-N. The extent of reduction was directly proportional to the biomass loading with both forms of biomass on JR and PR coals. But it was only proportional to the SG loading in flames cofired with JW coal; cofiring JW with sawdust was ineffective at all but the highest loadings. Cofiring GL coal reduced NO_X, but the magnitude was disproportionate at 10 % loadings with both biomass forms.

Acknowledgement. This work was partially sponsored by an award (DE-FC26-00NT40895) under the Biomass Cofiring Opportunities Program administered by the National Energy Technology Laboratory.

References

(1) Niksa, S.; and Liu G.-S., *Fuel*, **2002**, 81(18),2371-85.
(2) Niksa, S.; and Liu, G.-S., "Advanced CFD Post-Processing for P. F. Flame Structure and Emissions," 28th Int. Technical Conf. on Coal Utilization and Fuel Systems, **2003**, Coal Technology Assoc., Clearwater, Fl, March.
(3) Monroe, L. S. et al., 1995, EPRI/EPA 1995 Joint Symp. On Stationary Combustion NO_X Control, Book 3, EPRI, Palo Alto, CA.
(4) Niksa, S.; and Liu, G.-S. *Proc. Comb. Inst.*, **2002**, 29, to appear.
(5) Niksa, S. *Combust. Flame*, **1995**, 100, 384-394.
(6) Glarborg, P.; Alzueta, M. U.; Dam-Johansen, K.; and Miller, J. A. *Combust. Flame*, **1998**, 115, 1-27.
(7) Pedersen, L. S.; Glarborg, P.; et al. *Combust. Sci. Technol.*, **1998**, 132, 251-314.
(8) Hurt, R. H.; Sun J.-K.; and Lunden, M. *Combust. Flame*, **1997**, 113(1/2), 181.

STUDY ON THE MECHANISM OF NO_X FORMATION FOR CO-COMBUSTION OF PULVERIZED COAL AND BIOMASS

Xiaoqian Ma[1], Shiyun Su[1] , Zengli Zhao[2] , Xiaobing Zhang[1,3] Yong Chen[2]

[1]College of Electric Engineering, South China University of Technology, Guangzhou, 510640, China

[2]Guangzhou Institute of Energy Conversion, Chinese Academy of Sciences, Guangzhou,510070, China

[3]City College and Graduate School of The City University of New York, New York, 10031, U.S.

Introduction

A problem of much concern about coal combustion is the contaminations of NO_x, among which ~ 95% is NO.[1] People have been studying the co-combustion of coal powder and biomass for the following reasons.[2-4] 1. Since the heat value of biomass (pulverized wood and rice hull are studied in the paper) is usually lower than coal, substituting coal with a proper amount of biomass can decrease the burning temperature, especially at the rear part of the furnace where most NO_x is produced. 2. The coke produced in biomass combustion can reduce NO so that less NO is released. 3. The co-combustion of coal powder and biomass helps utilize the non-recycable source. In the paper, using the burning temperature data of coal powder in one dimension furnace, we numerically calculate the amounts of produced NO when the coal powder is and is not mixed with biomass. Also calculated are the amounts of reduced NO by HCN and by coke which are produced in co-combustion when the effects of the biomass on temperature is and is not taken into consideration. We shall find out capability of different biomasses to reduce NO_x.

Computing Model

The simplifications which the calculation is based on are as followings: 1. The axial length of the one dimension furnace meets the requirement of large space jet; 2. The heat loss by radiation, the body force and the effects on flow by the chemical reactions are negligible so that the combustion can be approximated as adiabatic; 3. The properties do not change with temperature or composition. Shown in Table 1 are the known parameters of the jet.[5,6] in which b_0 is the half width of the jet exit, a the jet flow constant, u_0 initial velocity of the jet flow, Y_0 the initial partial mass concentration, and Y_∞ the ambient partial mass concentration.

Table 1. Known parameters of the jet

b_0	a	u_0	Y_0			Y_∞		
mm	/	m/s	O_2	N_2	HCN	O_2	N_2	HCN
7	0.105	29.4	0.188	0.7	6.04×10^{-5}	0.21	0.78	0

Listed below are the formulae used to compute the co-combustion reaction rate of pulverized coal and biomass.

$$R_{HCN\to NO} = 10^{11}\rho_g Y_{HCN}\left(Y_{O_2}\right)^c \exp\left(-33700/T_g\right) \quad (1)$$

$$R_{NO-N_2} = 3\times10^{12}\rho_g Y_{HCN} Y_{NO} \exp\left(-33700/T_g\right) \quad (2)$$

$$R_{N_2-NO} = 3\times10^{14}\rho_g{}^{1.5} Y_{N_2} Y_{O_2}{}^{0.5} e^{\frac{-65300}{T_g}} \frac{M_{NO}}{M_{N_2} M_{O_2}{}^{0.5}} \quad (3)$$

$$R_{NO-N_2} = 4.24\times10^4 \frac{A_E m_{char}}{VOL} P Y_{NO_{SUP}} e^{-\frac{1.465\times10^8}{RT_g}} M_{NO} \quad (4)$$

in which $R_{\alpha\text{-}\beta}$ is the rate at which α is converted to β in kg/m^3/s, ρ_g the mixed gas density in kg/m^3, Y_α the partial mass concentration of composition α, c the reation coefficient whose value is set to be 0.4 here, T_g the gas temperature in K, VOL the coke volume in m^3, M_α the molar mass of α in g/mol, A_E the particle surface area of coke, which is set at 0.7 m^2/g, m_{char} the coke mass rate in g/s, P the total pressure in atm, Y_{NOsup} the partial NO mass concentration on coke surface, and R the gas constant in kJ/kg/K.

Results

The results we obtain are shown in the following figures. A variable B is defined to indicate the ratio of the mass flow rates of biomass and coal powder. The parameters used to run the calculation can be obtained by writing to the correspondence author Ma, Xiaoqian at epxqma@scut.edn.cn.

(1) Temperature distribution without the effects of biomass

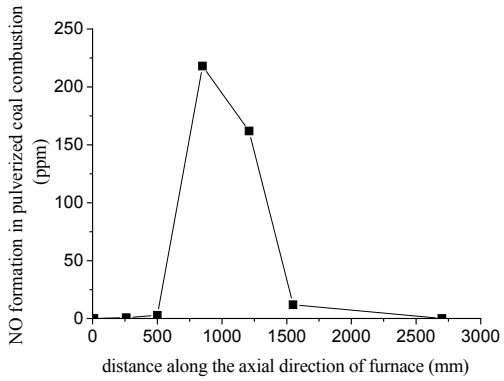

Figure 1. NO formation distribution in pulverized coal combustion without the effects of biomass on temperature.

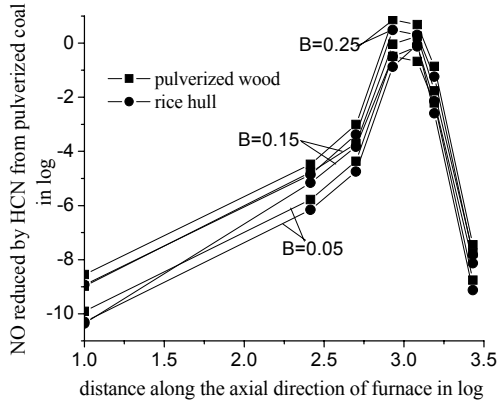

Figure 2. Distribution of reduced NO by HCN from pulverized coal in co-combustion without the effects of biomass on temperature.

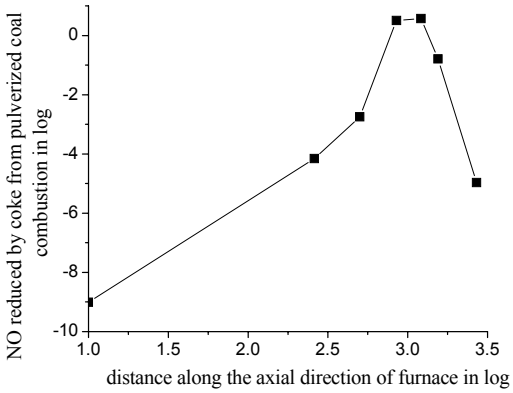

Figure 3. Distribution of reduced NO by coke from pulverized coal in co-combustion without the effects of biomass on temperature.

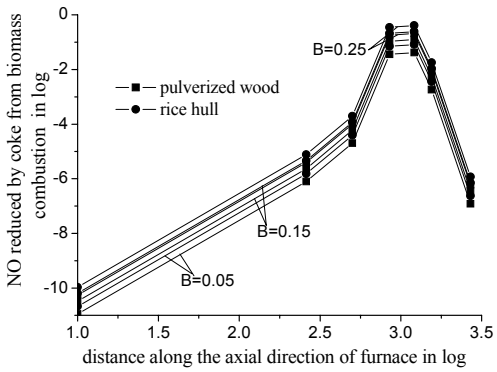

Figure 4. Distribution of reduced NO by coke from biomass in co-combustion without the effects of biomass on temperature.

(2) Temperature distribution with the effects of biomass combustion by means of energy balance

Equations (1)-(4) can be used to analyze the reduction capability.

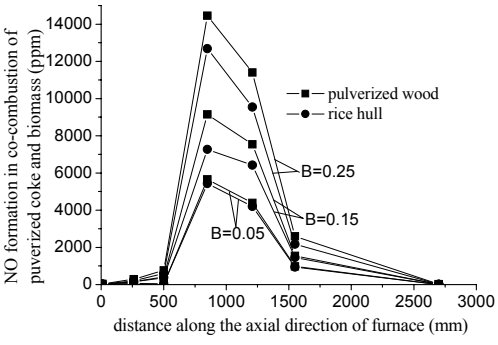

Figure 5. NO formation distribution in co-combustion with the effects of biomass on temperature.

Discussion and Conclusions

Temperature is a factor of importance on NO formation. Due to the limited space available here, we would like to skip this point and emphasize on the NO reduction by HCN and coke produced in the combustion. Figures 2-4 show that in co-combustion when the effects of biomass on temperature are neglected, the reduced NO by HCN, and by the coke in the pulverized coal combustion and in the co-combustion of coal powder and biomass, are in the same order, all of

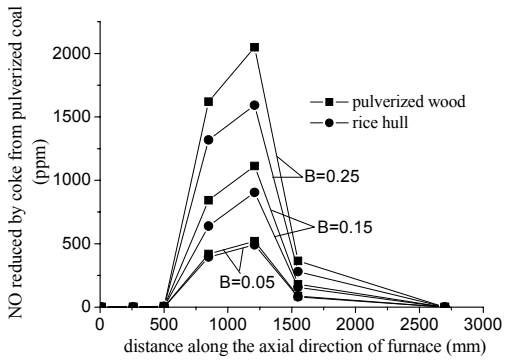

Figure 6. Distribution of reduced NO by coke from pulverized coal in co-combustion with the effects of biomass on temperature

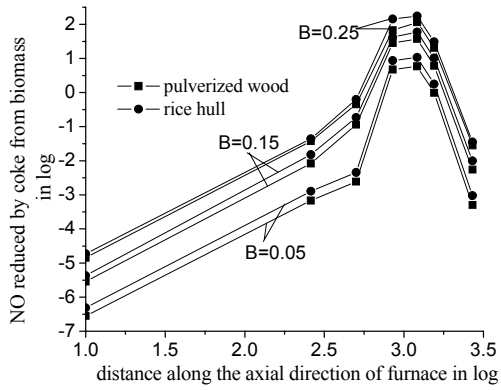

Figure 7. Distribution of reduced NO by coke from biomass in co-combustion with the effects of biomass on temperature

which are vanishingly little compared with the total amount of the produced NO. With the effects of biomass on temperature, the coke from pulverized coal elevates the amount of reduced NO, as indicated in Figure 6. The elevation is enhanced with increasing B, and more when pulverized wood is co-combusted than when rice hull is. Showed in Figure 7 is the distribution of reduced NO by coke from biomass at different B in co-combustion. The increment in amount of reduced NO with growing B increases by orders of magnitude, and the increment rate is far larger than that of the NO formation (see Figure 5), and that of the NO reduction by coke from pulverized coal (see Figure 6).

References

1. Zhao, J. In *Emission Contamination and Noise of Thermal Power Equipments* [C]; Science Press: Beijing, 1995.
2. Purvis, M. R. I.; Tadulan, E. I.; and Tariq, A. S. *Int. J. Energy Res.*, 2000, **24**: 917-933.
3. Skreiberg, O.; Glarborg, P.; Jensen, A.; and Dam-Johnansen, K. *Fuel*, 1997, **76**(7): 671-682.
4. Brink, A.; Bostrom, S.; Kilpinen, P.; and Hupa, M. *IFRF Combust. J.*, 2001. NO. 200107.
5. Han, C.; Xu, M.; Zhou, H.; and Qiu, J. In *Coal Combustion* [C], Science Press: Beijing, 2001.
6. Li, C.; and Tan, L. *Fuel*, 2000, 79(15): 1899-1906.

HRTEM, Synchrotron, and Simulation Techniques Applied to Activity and Selectivity Correlation in Hydrodesulfurization Catalysts

Russell R. Chianelli[1], Gilles Berhault[2], Miguel José Yácaman[3], Apurva Mehta[4], Sergio Fuentes[5], Gabriel Alonso[6], and Myriam De la Rosa[1].

(1) Materials Research and Technology Institute, University of Texas at El Paso, Burges Hall Room 321, El Paso, TX 79968-0685,
(2) LACCO-CNRS, Poitier, France.
(3) Chemical Engineering, University of Texas at Austin,
(4) Stanford Synchrotron Radiation Laboratory, Menlo Park, California.
(5) Centro de Ciencias de la Material Condensada, Enseñada, Mexico.
(6) CIMAV, Chihuahua, Chihauhau, Mexico.

Introduction

Faced with heavier crudes and increasingly strict regulations regarding sulfur content of fuels, better HDS, HDN and HDM catalysts are sought requiring a deeper understanding of the structure and function of transition metal sulfide based catalysts. Basic functions that describe catalyst activity such as the role of promoters (Co, Ni) and the role of carbon are becoming better understood[1]. However, the disordered state of the catalytically stable active phases has hindered complete understanding and "idealized catalysts" that yield specific information do not exist under reactor conditions. In this report small angle scattering (SAXS), wide-angle scattering (WAXS), high resolution transmission electron microscopy (HRTEM) and simulation techniques using CERIUS[2] software (ACCELRYS Corp.) are applied to commercial alumina supported and unsupported CoMo catalysts stabilized in real feeds. Through application of these multiple techniques new information regarding structure/function relations in these catalysts are reported.

Background

The first report of the periodic effect in catalysis by TMS (transition metal sulfides) emphasized the importance of determining the "stable catalytic state"[2]. The SCS (stable catalytic state) is the solid-state phase that is stable in the catalytic environment. For example the SCS for Mo under standard HDS (hydrodesulfurization) conditions is MoS_2 and for Ru is RuS_2. Much of the literature that purports to describe the fundamental origin of catalytic effects ignores the importance of the SCS and report results on catalyst precursors that change under catalytic conditions.

The Role of Carbon

Further work after the original paper describing the SCS discusses periodic relations between the SCS and their ability to catalyze the HDS and other reactions. However, these papers only describe the relation between the bulk crystalline SCS and their catalytic properties. Recent results indicate that the surfaces of the SCS contain carbon directly bonded to the catalytic metals[3]. Thus, the TMS catalysts are properly described as sulfide supported transition metal carbides (SSTMC). Therefore, the complete SCS for Mo is $MoS_{2-x}C_x$ and for Ru is $RuS_{2-x}C_x$. A similar situation exists for Mo and W catalysts that are promoted with Co or Ni. A description of TMS catalysts that fails to take into account the important role of carbon in stabilized HDS catalyst cannot give an accurate description of the fundamental origin of catalytic properties in these catalysts. It is also true that promotion must be described as a symmetrical synergism rather than promotion of one phase by another in order to understand the true nature of the effect; for example promotion of Mo by Co and symmetrically promotion of Co by Mo[4].

Although the role of carbon in TMS catalytic materials has been largely ignored due to the difficulty in characterizing carbon on stabilized catalysts, refinery operators have for many years recognized the existence of "hard carbon" (carbide carbon) and "soft carbon" (coke) in hydrotreating catalysts. In this paper the importance of carbon in understanding the fundamental origins of catalytic behavior in TMS is discussed. Recent evidence for the TMS to form stable carbide surface phases is shown in figure 1. Figure 1 shows the carbon edge Auger electron yield for a tested HDS MoS_2 catalyst compared with Mo_2C. Since the Auger electrons only come from very close to the surface it is concluded that both surfaces are identical and that the Mo in both cases is bound to carbon.

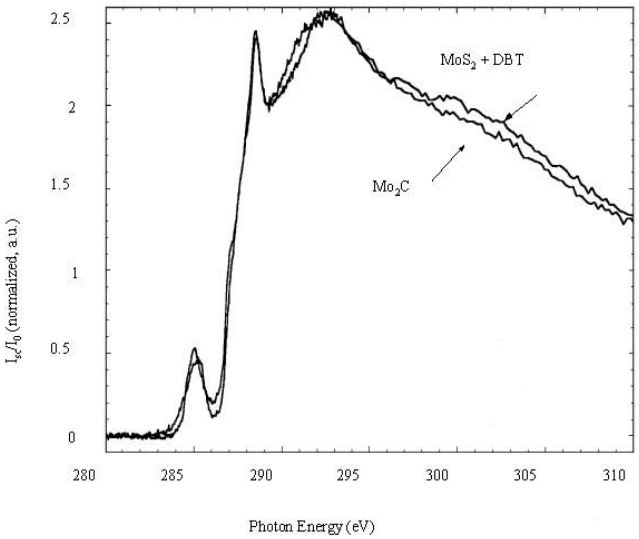

Figure 1: Auger Spectra of Carbon on Catalysts

These studies refer to catalysts that have been pretreated and then exposed to the catalytic feed. These catalysts become the sulfide supported carbides (SCS) described above. However, carbon can be incorporated into the catalyst before pretreatment and this leads to highly active catalysts with unusual pore distributions[5]. For example some catalysts with surface areas greater than 250 m^2/gm had most of the surface area in the 40 - 45Å region. We have termed these catalysts "*amorphous zeolitic sulfides*" because pore distributions can be very narrow around 4nm. They also have an unusual "sponge-like" appearance as shown in Figure 2. This may lead to a fractal description of these catalysts in the future. Associated with these properties are unusual selectivity properties.

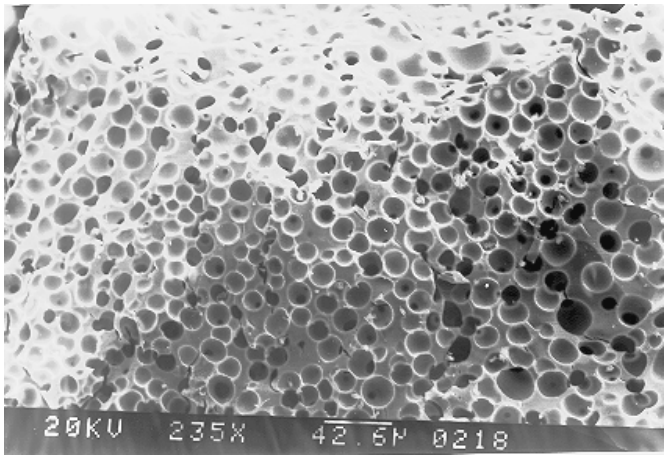

Figure 2: SEM of Amorphous Zeolitic MoS_2 Catalyst

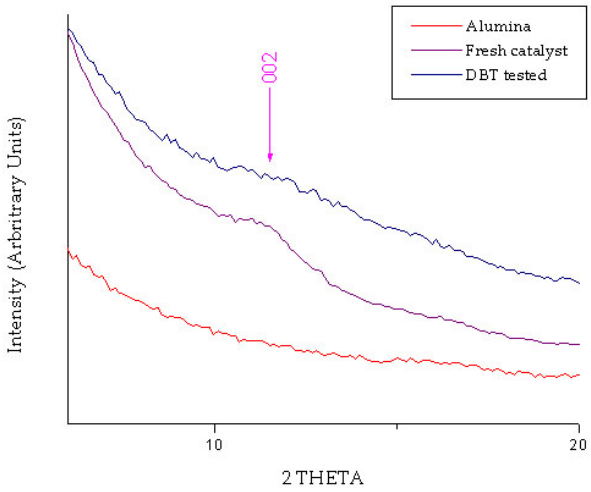

Figure 3: Low angle scattering region for supported catalysts.

Supported Commercial Catalysts:

The fundamental advances described above have been made on unsupported pure catalytic phase such as MoS_2 and promoted MoS_2. Although unsupported catalysts are finding new commercial application because of their high volumetric activity, working commercial catalysts are still predominately alumina supported of the type $Co(Ni)MoAl_2O_3$. Although catalytic functions measured on unsupported catalysts generally extrapolate to supported catalysts, direct structural information has been hard to obtain due to the disordered state of the active phases.

In the later part of this report SAXS, WAXS, HRTEM and simulation techniques using CERIUS[2] software are applied to commercial alumina supported CoMo catalysts that have been tested on real feeds and to non-commercial alumina and silica supported CoMo catalysts. By combining this data with HRTEM and simulation data the following conclusions are reported:

- Scattering from the active phases is easily obtained by subtraction of the alumina support.
- Analysis of the active phase scattering indicates that the catalyst consists of mainly single layers of MoS_2 in contrast to HRTEM studies that "see" only stacked layers (See figure 3).
- Catalysts that have been run for long periods of time under high-pressure conditions tend to "destack".

In addition scattering results from catalyst run for extended periods in high pressure real feed reactors showed the presence of three phases: $MoS_{2-x}C_x$, $Co_9S_8$and Co metal. This result is surprising in view of the accepted theories of Co promotion and underlines the necessity of determining the SCS for operating catalysts as a basis for understanding activity and selectivity correlations.

References

[1] Chianelli, R.R., Daage, M., and Ledoux, M. J., "Fundamental Studies of Transition Metal Sulfide Catalytic Materials", *Advances in Catalysis*, **1994**, 40**,** 177.

[2] T. A. Pecoraro and R. R. Chianelli, "Hydrodesulfurization Catalysis by Transition Metals", *J. Catal.* **1981**, 67(2), 430.

[3] Gilles Berhault, Apurva Mehta, Alexandru Pavel, Jianzhong Yang, Luis Rendon, Miguel Jose Yacaman, Leonel Cota Araiza, Alberto Moller, and Russell R. Chianelli, "The Role of Structural Carbon in Transition Metal sulfide Hydrotreating Catalysts" *J. Catalysis*, **2001**, 198, 9.

[4] Gilles Berhault, Leonel Cota Araiza, Alberto Duarte Moller, Apurva Mehta, Russell R. Chianelli, "Modifications of Unpromoted and Cobalt-promoted MoS_2 during thermal treatment by Dimethysulfide", *Catalysis Letters*, **2002**, 78, 81.

[5] Characterization and HDS Activity of Mesoporous MoS2 Catalysts Prepared by in situ Activation of Tetraalkylammonium Thiomolybdates. G. Alonso, G. Berhault, A. Aguilar, V. Collins, C. Ornelas, S. Fuentes and R. R. Chianelli. *Journal of Catalysis* **2002**, 208, 359.

POSSIBLE WAYS TO ACHIEVE DEEP HDS OF LIGHT CYCLE OIL

Ki-Hyouk Choi, Yozo Korai, Isao Mochida

Institute of Material Chemistry and Engineering, Kyushu University
Kasuga-Koen, Kasuga, Fukuoka 816-8580 JAPAN

INTRODUCTION

It has been known that light cycle oil(LCO) from fluid catalytic cracker(FCC) is hard to be desulfurized due to its much higher aromatic content than straight run gas oil. Aromatic species in LCO inhibit HDS by occupying the active site for hydrogenation with their higher adsorption energy than sulfur species. Removal of aromatic species prior to HDS by hydrogenation looks not practical because of high hydrogen consumption and presence of strong inhibitor, sulfur and nitrogen species. Furthermore, hydrogenation of aromatic species prefer the low reaction temperature due to equilibrium limitation, meaning the low reaction rate.

We presented already the effect of aromatic and nitrogen contents on the HDS of LCO to indicate that the aromatic inhibition is more distinct in HDS of refractory sulfur species, such as 4,6-DMDBT and such inhibition can not be avoided by using very acidic catalyst which contains zeolite and higher reaction temperature(360 ^{o}C)[1].

In the present study, we examined possible ways to achieve deep desulfurization of LCO, such as

- splitting of LCO and desulfurization of each fractions.
- lowering the cut point of LCO below boiling point of 4,6-DMDBT
- blending the low boiling point LCO into LGO

As indicated in the previous presentation, 4,6-DMDBT and other di- and tri-alky DBT suffer strong inhibition by aromatic species. Hence, LCO containing the least amount of 4,6-DMDBT and other alky DBT having higher BP than 4,6-DMDBT is anticipated to achieve deep desulfurization even with abundant aromatic species in itself. LGO can be postulated to dilute LCO to reduce the inhibition by aromatic species. But the beneficial effect may depend on the characteristics of LCO and its blending ratio. Such points are studied by using conventional catalysts and reaction conditions.

EXPERIMENTS

LCO, HCO, fractionated LCO were used as feed oil. As-distilled straight run gas oil, LGO was also used. The basic properties of feed oils are listed in **Table 1**. Cut point of the fractionated LCO was not clear as shown in carbon and sulfur chromatograms in **Fig. 1**.

Commercially available CoMo/alumina and NiMo/alumina were used after grinding and sieving with 380 mesh nylon sieve. NiMo catalyst was characterized to have higher acidity than CoMo catalyst by NH3 TPD. Hydrodesulfurization experiments were conducted by using autoclave-type reactor(100 ml internal volume) at 340 or 360 ^{o}C. Initial hydrogen pressure was adjusted to 50 kg/cm^2. 10 g of feed oil and 1 g of pre-sulfided catalyst at 360 ^{o}C for 2 hours under 5% H_2S/H_2 stream, were charged into the reactor. Reaction time was 2 hour. Feed and products were analyzed by GC-AED(HP5890Plus and G2350A).

RESULTS AND DISCUSSION

LCO 300- didn't contain 4-MDBT, 4,6-DMDBT and other alkylated DBTs. In contrast, LCO 340- contains small amount of those species as shown in Fig. 1. After 2 hour reaction at 360 ^{o}C over NiMo catalyst, HDS of LCO 300- was nearly completed to give less than 5 ppmS. LCO 340- gave also the very low level of sulfur, less than 5 ppmS. However, LCO 300+ and LCO 340+, which contained larger amount of 4-MDBT, 4,6-DMDBT and other alkylated DBTs, provided 109 and 278 ppmS in HDS product, which were 4.1 and 17.4 % of total sulfur content of feed oils, respectively. Reaction temperature was higher(360 ^{o}C) than conventional HDS condition(340 ^{o}C). These observations indicated the possible way to achieve deep desulfurization of LCO feed by fractionation followed by conventional HDS of low boiling point fraction.

LGO blended with small amount of LCO(1 wt% and 10 wt%) was examined at 340 ^{o}C for 2 hour reaction as shown in **Table 2** in order to examine the possibility of diluting LCO with LGO for improvement of HDS reactivity of LCO. Inhibition of aromatic compounds on HDS was anticipated to be alleviated by diluting it in LGO, which had less amount of aromatic compounds.

However, blended LGOs showed higher remaining total sulfur contents than both of LCO and LGO over both of CoMo and NiMo catalysts. Remaining content of 4-MDBT and 4,6-DMDBT were also slightly higher than those of LCO and LGO. Over CoMo catalyst, LGO containing 10% LCO was less active than that containing 1% LCO. In contrast, NiMo showed reverse reactivity order, LGO-1%LCO was less active than LGO-10%LCO over NiMo catalyst. NiMo catalyst was suggested to have higher activity in HDS of LGO in the presence of LCO due to its higher hydrogenation activity and acidity than CoMo catalyst. Remaining content of 4-MDBT and 4,6-DMDBT followed the same trends with those of remaining total sulfur contents. The above observation means that HDS of LGO was strongly inhibited by adding small amount of LCO, even 1%, while LCO could be much more easily desulfurized than LGO. LCO can be noted by its higher aromatic content than LGO. Hence, small amount of aromatic compounds could strongly inhibit HDS of LGO.

LCO and HCO, which had different FBP, 322 and 463 ^{o}C, respectively, were compared by hydrotreating at 340 ^{o}C over CoMo and NiMo catalysts. Carbon and sulfur chromatograms are plotted in **Fig. 2**. Feed LCO contained 41 ppmS 4,6-DMDBT, which was 0.84% of total sulfur species in LCO. In contrast, Feed HCO contained 162 ppmS 4,6-DMDBT, 1.26% of total sulfur species in HCO. HDS results on those feed oils were listed in **Table. 2**. LCO leaved only 1.5 - 1.8% of total sulfur content after HDS, while HDS product of HCO contained 21.5 - 27.5 % of original sulfur content. Such difference between LCO and HCO was more distinct in remaining content of 4,6-DMDBT. 12.8 - 21.3% and 79.0 - 81.3% of 4,6-DMDBT contained in feed oil were remained after HDS of LCO and HCO, respectively. These findings indicated again the importance of cutting point of LCO to attain deep desulfurization.

NiMo catalyst was more active than CoMo one in HDS of LCO. 4,6-DMDBT in LCO was also more removed over NiMo catalyst than CoMo catalyst. In contrast CoMo catalyst showed better activity in HDS of HCO than NiMo catalyst, while the latter catalyst provided slightly lower content of 4,6-DMDBT in HDS product than the former catalyst. Superiority of NiMo catalyst in HDS of LCO is believed to be from its higher hydrogenation activity and acidity, which is effective to remove the strongly adsorbed aromatic species and refractory sulfur species. However, such activity was disappeared in HDS of HCO, suggested to be due to inhibition of high boiling point aromatics compounds and more refractory sulfur species. The extent of desulfurization was limited by such inhibitors and, hence remaining sulfur content was decided by the content of reactive sulfur species, resulting higher activity over CoMo catalyst, which has been believed to be more active in HDS of reactive sulfur species than NiMo catalyst, although CoMo catalyst also suffered inhibition by aromatic and refractory sulfur species.

CONCLUSIONS

First of all, deep desulfurization of LCO could be achieved by splitting LCO and followed HDS of lower boiling point fraction over conventional catalyst. LCOs fractionated under 300 ^{o}C and 340 ^{o}C were successfully desulfurized to less than 5 ppmS. However, high boiling point fraction(300 ^{o}C+ and 340 ^{o}C+) showed very limited HDS reactivity.

Blending of LCO into LGO retarded HDS even with small amount, in particular over CoMo catalyst. NiMo catalyst showed better activity in HDS of LGO, LCO and blended LGO than CoMo catalyst. HDS of HCO was much difficult compared with LGO and LCO. CoMo provided higher sulfur removal than NiMo catalyst in HDS of HCO.

Acknowledgement. This work was supported by the New Energy and Industrial Technology Development Organization (NEDO) through Petroleum Energy Center(PEC) under a subsidy from the Ministry of Economy, Trade and Industry.

REFERENCES

(1) Choi, K.-H.; Korai Y.; Mochida, I. *Prepr. Am. Chem. Soc., Div. Fuel Chem.* , 2003, 48(1), 101.

Table 1. Basic Properties of LCOs

Name	IBP(^{o}C)	FBP(^{o}C)	Sulfur Content(ppm)
LGO	-	-	13800
HCO	134	463	12900
LCO	168.5	322.0	4800
LCO 300+	LCO Cut fraction over 300 ^{o}C		2640
LCO 300-	LCO Cut fraction under 300 ^{o}C		450
LCO 340+	LCO Cut fraction over 340 ^{o}C		1596
LCO 340-	LCO Cut fraction under 340 ^{o}C		301

Table 2. Remaining content(ppmS) of sulfur species in HDS products.

Over CoMo Catalyst

	Total Sulfur	DBT	4-MDBT	4,6-DMDBT
LGO	523(3.8%)	0(0.0%)	11(10.2%)	19(51.3%)
LCO-1[*1]	688(5.0%)	1(0.5%)	14(12.9%)	20(51.5%)
LCO-10[*2]	669(5.2%)	1(0.4%)	13(12.2%)	20(52.6%)
LCO	86(1.8%)	0(0.0%)	4(4.0%)	9(23.1%)
HCO	2776(21.5%)	2(0.8%)	143(35.8%)	132(81.3%)

Over NiMo Catalyst

	Total Sulfur	DBT	4-MDBT	4,6-DMDBT
LGO	444(3.2%)	1(1.0%)	14(12.5%)	11(29.7%)
LCO-1[*1]	462(3.4%)	1(1.0%)	14(12.5%)	13(33.4%)
LCO-10[*2]	367(2.8%)	1(0.7%)	12(10.9%)	11(28.9%)
LCO	72(1.5%)	0(0.0%)	4(4.1%)	5(12.8%)
HCO	3551(27.5%)	21(7.6%)	21(52.7%)	128(79.0%)

*1 : 1 wt% LCO blended LGO, *2 : 10 wt% LCO blended LGO

* Values in parenthesis are ratio of remaining content and original content.

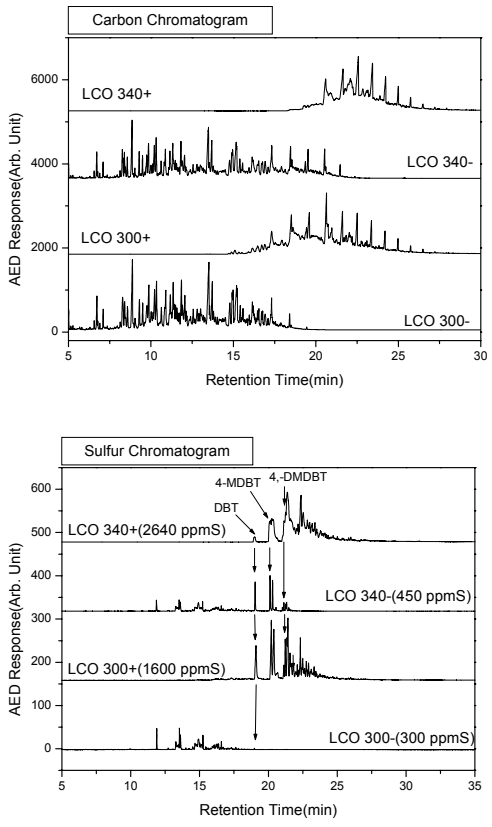

Fig. 1. Carbon and sulfur-specific chromatograms of fractionated LCOs.

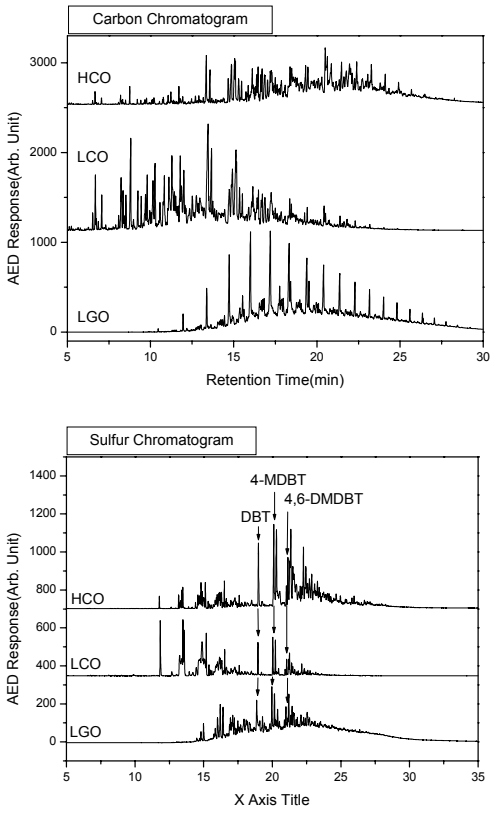

Fig. 2. Carbon and sulfur-specific chromatograms of LGO, LCO, HCO.

Effect of Feed Quality on Deep Desulfurization of Diesel

A. Stanislaus, A. Al-Barood and H. Qabazard

Petroleum Refining Department,
Petroleum Research and Studies Center,
Kuwait Institute for Scientific Research,
P. O. Box 24885, Safat, Kuwait.

INTRODUCTION

The specifications and demand of petroleum based fuels have been changing continuously in the international fuels market. During the 1990s a series of regulations on the specifications of gasoline and diesel were introduced in many countries to reduce harmful emissions from transportation vehicles. For example, in the USA and Europe sulfur content of diesel was first reduced from 2000 ppm to 500 ppm and it is currently set at 350 ppm. Further reductions in sulfur limits to 50 ppm have been proposed in Europe with tighter specifications on other properties such as density, poly aromatic hydrocarbons, cetane number, etc. Germany has introduced 10 ppm sulfur limit for diesel from January 1, 2003, and the U.S. will impose a 15 ppm sulfur cap in 2006. Similar low sulfur specifications are also targeted in many other countries, and most probably will be predominant worldwide during the next decade.

Although the new environmental regulations that limit the sulfur levels of diesel and other transportation fuels to very low levels are beneficial from environmental point of view, meeting the required stringent specifications represent a major operational and economic challenge for the petroleum refining industry. The tightening of sulfur specifications of diesel fuel to very low levels requires deep desulfurization of diesel feedstocks. The shift from normal to deep desulfurization is a very complicated technical problem. Many factors such as the catalysts, process parameters, and the nature of sulfur compounds present in the feed can have a significant influence on the degree of desulfurization of diesel feeds[1-3]. Among these, the feedstock quality plays an important role on deep desulfurization since the types of sulfur, nitrogen and aromatic compounds and their concentrations in different feedstocks are different. In the present work, a comparative study of the degree of desulfurization of two different feedstocks, namely coker gas oil (CGO) and straight run gas oil (SRGO) and their blends under different operating severities was made. The kinetics of desulfurization of both feeds under deep desulfurization conditions were also studied.

EXPERIMENTAL

Two feedstocks, namely, SRGO (density@15 ^{o}C, 0.846 g/ml; sulfur, 1.47 wt%; Nitrogen, 60 ppm; aromatics, 27 wt%; T_{95} = 368 ^{o}C) and CGO (density@15 ^{o}C, 0.876 g/ml; sulfur, 0. 76 wt%; Nitrogen, 1020 ppm; aromatics, 46 wt%; T_{95} = 380 ^{o}C) were used in the present studies. Hydrotreating experiments were conducted in a fixed bed reactor unit using a commercial Co-Mo/Al_2O_3 catalyst (surface area = 200 m^2/g; pore volume = 0.6ml/g). 75 ml of the catalyst diluted with an equal volume of carborundum was charged into the reactor in such a way that the catalyst section was in the middle section of the reactor. Coarse carborundum and inert alumina balls were loaded above and below the catalyst bed. After the catalyst was loaded, the reactor was placed in position inside a vertical electrically heated furnace. Five thermocouples into a thermowell at the center of the reactor tube were used to monitor the reactor temperature at various points. Before the introduction of the feed, the catalyst was presulfided with 3 wt% dimethyl disulfide in straight run gas oil using a standard procedure [4]. When presulfiding was completed, the gas oil feed was introduced and the reactor temperature and other conditions were adjusted to the desired levels. During the run, the temperature was changed in the sequence 320 → 340 → 360 → 380 ^{o}C and back to 320 ^{o}C. After maintaining each temperature condition stabilized for 24 hours, three samples were collected at each temperature at 8 h intervals. The sulfur contents of the feed and hydrotreated products were determined using a Coulamax sulfur analyzer. Before sulfur analysis, the hydrotreated product was stripped with nitrogen gas in an ultrasonic water bath to remove the residual H_2S from the product oil. The individual sulfur compound distributions in the feed and product oils were determined with a high resolution gas chromatograph equipped with a 30m x 0.32mm x 0.4µ SPD-1 capillary column and a sulfur chemiluminescence detector (SCD).

RESULTS AND DISCUSSION

Fig. 1 shows the residual sulfur content in the hydrotreated products as function of the operating temperature for the SRGO feed at two different LHSVs. It is seen that the total sulfur in the hydrotreated product steadily decreases with increasing reactor temperature. The LHSV also has a remarkable effect on the degree of desulfurization. The results indicate that the LHSV has to be reduced to 2 and the reactor temperature has to be increased to 365 ^{o}C to achieve the desired 350 ppm sulfur in the product oil. In the case of CGO feed, a higher temperature (377 ^{o}C) is required to reach the same sulfur target indicating that CGO is more resistant to desulfurization than SRGO (Fig. 2).

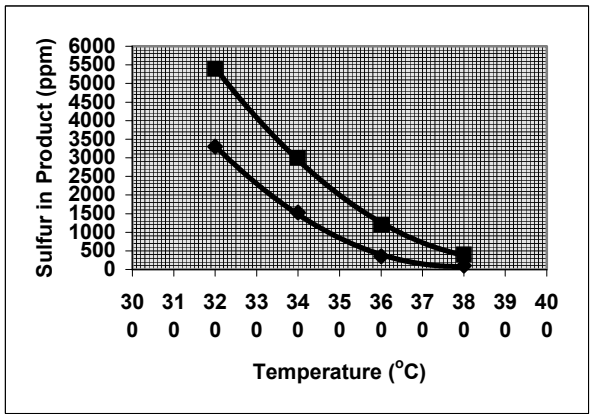

Fig 1. Sulfur in Product vs. Reactor Temperature for SRGO.

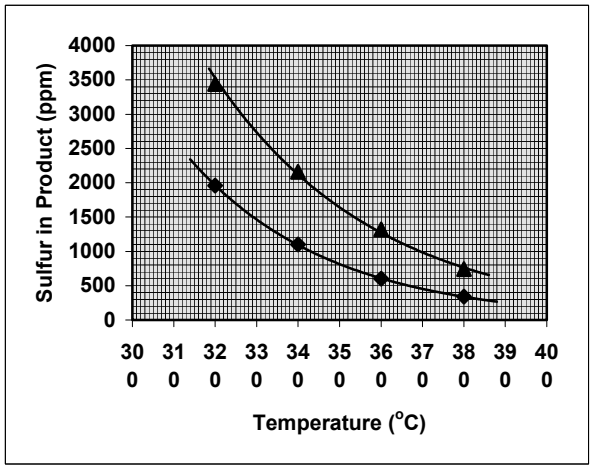

Fig 2. Sulfur in Product vs. Reactor Temperature for CGO.

Blends of SRGO and CGO were evaluated for deep HDS and the results showed that inclusion of CGO in the SRGO feedstock required higher severity operation to obtain the desired low sulfur level in the product (Fig. 3).

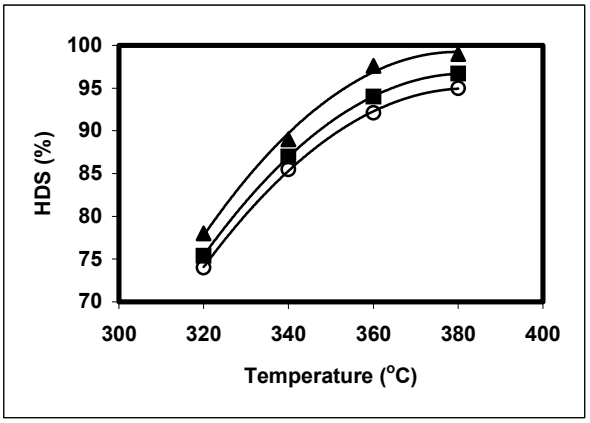

Fig 3. Effect of Blending CGO with SRGO on the degree of desulphurization.

With a view to understand the low reactivity of CGO compared with SRGO, the types of sulfur compounds and their distribution in both feeds were analyzed by a high resolution gas chromatograph equipped with a 30m x 0.32mm x 0.4µ SPD-1 capillary column and a sulfur chemiluminescence detector. Fig. 4 shows the sulfur compounds distribution in CGO and SRGO

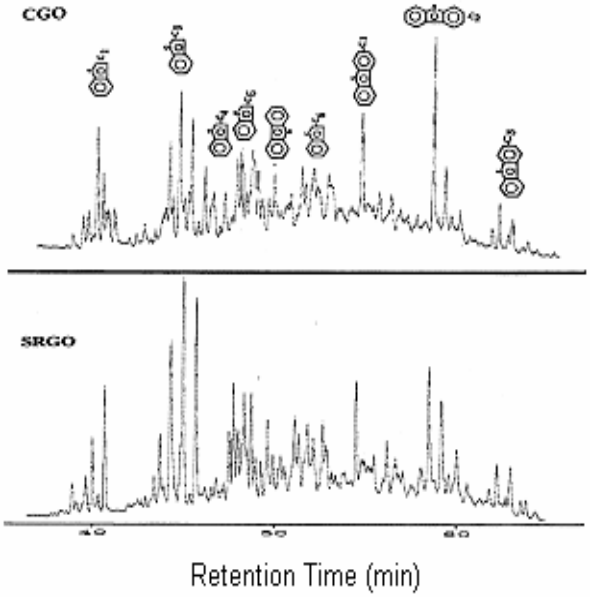

Fig 4. Sulfur Compounds distribution in CGO and SRGO

It is seen that both feeds contain a complex mixture of sulfur compounds that can be classified into two major groups: (i) alkyl benzothiophenes (BT); (ii) dibenzothiophene (DBT) and its alkyl DBTs. The HDS reactivities of these sulfur containing species are considerably different. Benzothiophene and its alkyl derivatives are more easily desulfurized than dibenzothiophene and its alkyl derivatives. Studies have shown that dibenzothiophene with alkyl substituents at 4 or 6 or 4 & 6 positions are more resistant to desulfurization under normal hydrotreating conditions [5-7]. Steric hinderance by the alkyl groups restricts the access of the sulfur atom to the active sites of the catalyst.

The results presented in Fig. 4 show that the concentration of the refractory sulfur compounds are slightly higher in the CGO feed. The low reactivity of the sulfur compounds could be partly attributed to this. However, this may not be the only reason for the low reactivity of CGO. A closer examination of the composition of the two feedstocks shows that the nitrogen content of the CGO is 17 times higher than that of SRGO. The aromatic content of the CGO is also substantially larger than that of SRGO. Model compound studies conducted in this laboratories on the inhibiting effects of nitrogen and poly nuclear aromatic (PNA) compounds showed that nitrogen compounds are stronger inhibitors of HDS than the PNAs. In a recent study, Knudsen et al., [8] found that nitrogen containing molecules and in particular basic nitrogen compounds strongly inhibited the HDS reaction. The inhibition by nitrogen compounds could be a major cause for the lower HDS of CGO compared with SRGO.

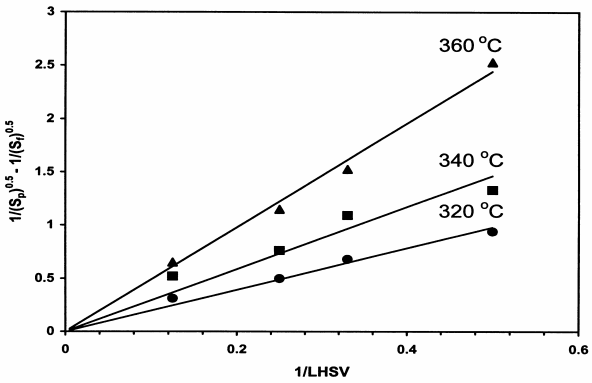

Fig 5. 1.5 order plot of kinetic data for HDS of CGO

Tests conducted at various LHSVs were used to for kinetic data analysis and for determining the apparent order for deep HDS of both types of gas oils. The results presented in Fig. 5 clearly show that a reaction order of 1.5 fits the kinetic data even under deep desulfurization conditions. Reaction orders varying between 1.4 and 2 have been reported in the literature for gas oil desulfurization (9-11). The activation energies calculated from the Arrhenius plots (Fig. 6) were 24 kcal/mole and 30 kcal/mole for SRGO and CGO feeds, respectively.

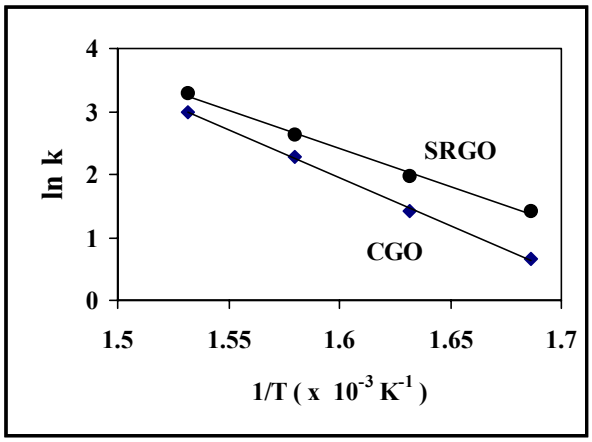

Fig. 6. Arrhenius plots for sulfur removal from straight run and coker gas oils

The higher activation energy observed for deep HDS of CGO is consistent with the key role played by the nitrogen species in inhibiting HDS reaction. The adsorption of nitrogen species on the active sites and their poisoning effect usually decreases with increasing temperature leading to a higher temperature sensitivity for HDS reaction and thereby resulting in higher activation energy for the nitrogen-rich CGO feed.

REFERENCES

1. Song, C., and Ma, X., Applied Catalysis B: Environmental, 41, 207 (2003).
2. Whitehurst, D. D., Isoda, T., and Mochida, T., Advances in Catalysis, 42, 345 (1998).
3. Landau, M. V., Catalysis Today, 36, 393 (1996).
4. Qabazard, H., Abu-Seedo, F., Stanislaus, A., Andari, M., Absi-Halabi,M., Fuel Science and Technology International, 13, 1135 (1995).
5. Knudsen, K.G ., Cooper, B. H., and Topsoe, H., Applied Catalysis A:General, 189, 205 (1999).
6. Houalla, M., Broderik, D. H., Spare, A. V., Nag, N.K., De Beer, V. H. J., Gates, B. C., and Kwart, H., Journal of Catalysis, 61, 523 (1980).
7. Machaud, P., Lamberton, J, L., Perot, G., Applied catalysis A:General, 169, 343 (1998).
8. Knudsen, K.G., Whitehurst, D.D., and Zeuthen, P., A detailed understanding of the inhibition effect of organic nitrogen compounds for ultra deep HDS and the consequences for choice of catalyst., Presented at the 3rd International Conference on Refinery Processing., AIChE Spring National Meeting , Atlanta GA, March 5-9 (2000).
9. Sie, S.T., Fuel Processing Technology, 61, 273(1999).
10. Bej, S.K., Dalai, A.K., and Adjaye, J., Petroleum Science and Technology, 20, 887 (2002).
11. Shiflett, W.K., A Users Guide to the Chemistry, Kinetics and Basic Reactor Engineering of Hydro Processing, Presented at the 5th International Conference on Refinery Processing., AIChE Spring National Meeting , New Orleans, March 11-14 (2002).

Selection and Further Activation of Activated Carbons for Removal of Nitrogen Species in Gas Oil as a Pre-Treatment for Deep Desulfurization

YOSUKE SANO, KI-HYOUK CHOI, YOZO KORAI and ISAO MOCHIDA

Institute of Material Chemistry and Engineering,
Kyushu University, Kasuga, Fukuoka 816-8580, Japan

INTRODUCTION

World refining industry is facing new and stricter challenges on the heteroatom content in their major products, such as diesel fuel and gasoline. The sulfur content of diesel fuel must be lowered to 15 ppmS from current 500 ppmS and even further regulations may be implemented with accelerated concerns on the atmospheric pollution[1]. Several kinds of new ideas have been proposed and some of them were practically examined to achieve the ultra deep desulfurization. However, more efficient and economic process is still required in spite of various efforts,. Critical barriers in obtaining ultra deep desulfurization are refractory sulfur species, which have very low reactivity under conventional hydrotreating conditions, and are strongly inhibited by H_2S, NH_3 and nitrogen species. The inhibitors retard the desulfurization reaction, very markedly in ultra deep region [2, 3]. In our previous study, we intended to improve the HDS-reactivity by reducing the nitrogen and sulfur species in the feed oil. Sulfur and nitrogen species were adsorptively removed by activated carbon. Activated carbon and activated carbon fiber have been recognized to be versatile absorbents of gaseous and liquid molecules. Its surface and properties can be easily controlled.

In spite of various advantages in such technology, material cost may limit its practical application. Hence, more adsorption capacity and low cost are still wanted with activated carbon.

In the previous study, we examined a number of adsorbents to find the best one and their reasons.

We attempted to improve the performance of activated carbon and carbon fiber by modifying its surface property and discovered the functional groups that are effective for the adsorption.

EXPERIMENTAL

I Activated carbon materials

The activated carbon was treated by HNO_3, H_2SO_4 and H_2O_2 and dried at respective appropriate temperature. The activated carbon was analyzed by TPD to measure its functional groups

II. Adsorption

Straight run gas oil (11,780 ppmS and 260 ppmN) used in this study was provided by a Japanese commercial refinery. Carbon materials (activated carbons and activated carbon fibers), which were dried at 110 ^oC under vacuum oven prior to adsorption experiment, were packed into the stainless steel tube of 50mm length and 6 mm diameter. Key properties of carbon materials were listed in Table 1. SRGO was fed into the tube by a HPLC pump at the rate of 0.1 ml/min and at the pressure of 20psi. The temperature of the adsorption reactor was maintained at 10～40℃ by water bath. The eluted oil was sampled at every 60min for 30 sec and analyzed by GC-AED (Atomic Emission Detector, HP5890P, and G2350A).

Results and Discussion

Fig.1 showed the breakthrough profiles of nitrogen species over various adsorbents. The activated carbons had larger adsorption capacity than silica gel which practically treated in the refinery. In this figure, MAXSORB-II of largest surface area and highest oxygen content showed the best adsorption capacity. And, MAXSORB-III showed much lower adsorption capacity than that of MAXSORB-II. However, heating at 600^oC under H_2 atmosphere reduced adsorption capacity of nitrogen species of MAXSORB-II.

Fig.2 compared the TPD profiles of MAXSORB-II and MAXSORB-III. The activated carbon produced CO_2 at 200-400^oC and CO at 600-800^oC. MAXSORB-II showed a particular large CO desorption while another did smaller desorption.

Fig.3 and Fig.4 showed the nitrogen breakthrough profiles by treated MGC-B and OG-20A series. H_2O_2-, H_2SO_4, HNO_3-treated activated carbons, which dried at 180^oC, 400^oC and 600^oC respectively, showed better adsorption than those of as received ones. However, HNO_3-treated, which dried at 350^oC, showed worse adsorption than those of as received.

Fig.5 and Fig.6 showed the TPD spectrums of these activated carbons. As you can see, activated carbon of larger adsorption capacity for nitrogen species has distinct CO peak at 600-800^oC. MGC-HNO_3, of low adsorption capacity for nitrogen species showed CO_2-peak at 200-400^oC. After heated at 600^oC and these functional group was removed, the breakthrough profile showed better one.

These findings indicated that surface species responsible for CO evolution during TPD is more effective than those for CO_2. The latter groups may inhibit for the Nitrogen adsorption.

The present study clarified that CO producing functional groups are responsible for adsorptive removal of nitrogen species. Hence introduction of such group through the surface oxidation appeared to be very effective to enlarge the adsorption. Basic nature of C=O may be responsible to adsorb the acidic and neutral –NH- groups. Carboxyl group on the surface of activated carbon appeared to reduce the adsorption of nitrogen species, probably through with COO groups.

Conclusion

Adsorption capacity of carbon materials depended on the textural and surface properties of them.

The most important functional group of activated carbon is C=O group and carbonyl group maybe inhibit the Nitrogen species adsorption.

References

1. T. R. Halbert, G. B. Brignac, R. A. Demmin, and E. M. Roundtree, *Hydrocarbon Engineering*, June, (2000)2.
2. D. D. Whitehurst, T. Isoda, and I. Mochida, *Adv. Catal*., **42**(1998)345.
3. D. D. Whitehurst, H. Farag, T. Nagamatsu, K. Sakanishi, and I. Mochida, *Catal. Today*, **45** (1998)299.

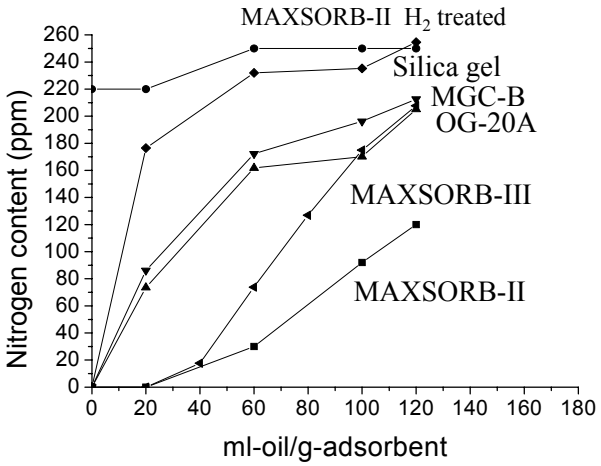

Figure 1. Breakthrough profiles of various materials

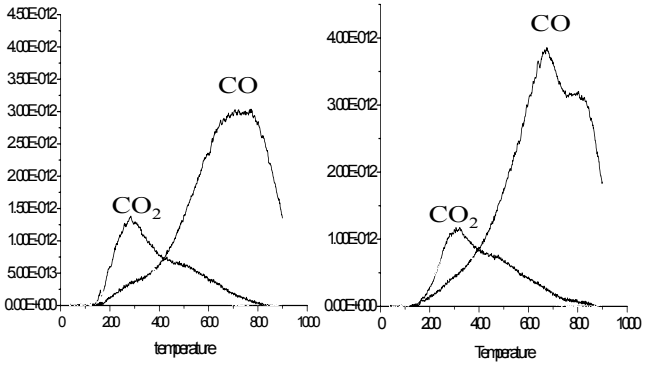

Figure.2 TPD results of MAXSORB-II and MASORB-III

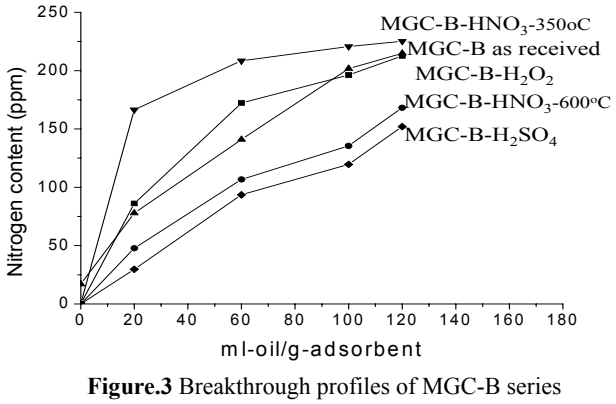

Figure.3 Breakthrough profiles of MGC-B series

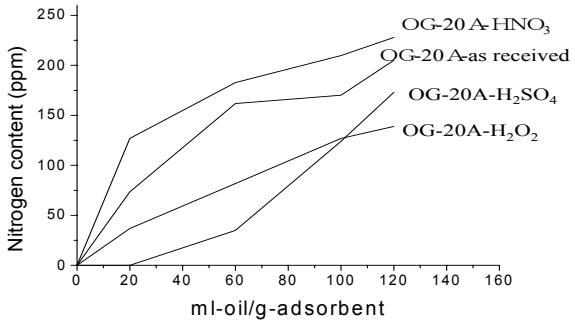

Figure 4 Breakthrough profiles of OG-20A series

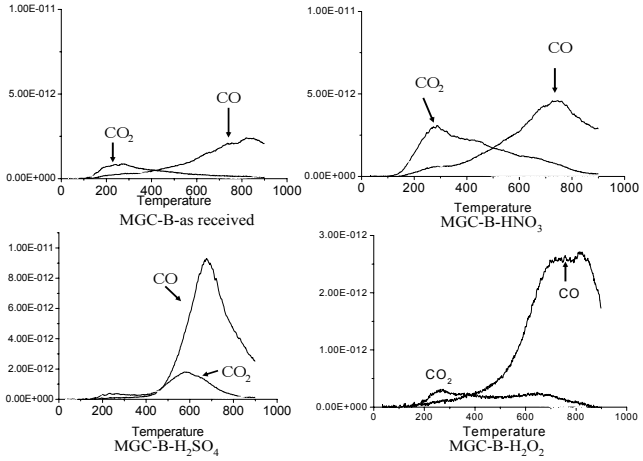

Figure.5 TPD results of MGC-B series

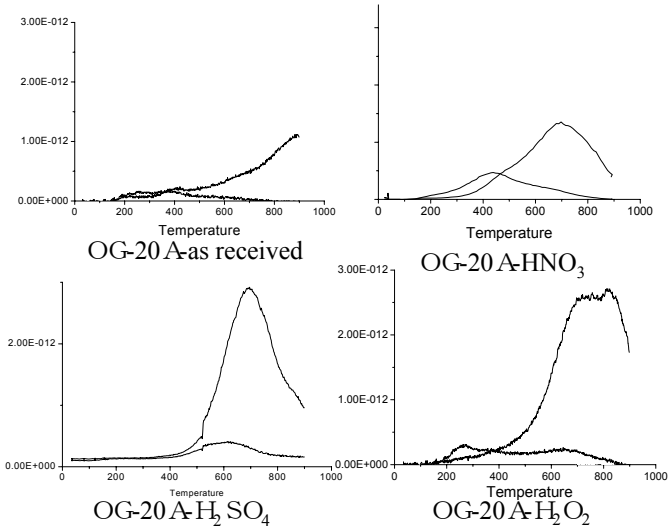

Figure.6 TPD results of OG-20A series

STATISTICAL MODEL FOR BENZENE PREDICTION IN CATALYTIC REFORMING

Qamar Zafar, Börje Gevert[2] and Margareta von Sivers*[1]*

Materials and Surface Chemistry, Chalmers University of Technology, Göteborg, S-412 96, Sweden *[1]Scanraff, s-453 81 Lysekil. *[2]Corresponding and presenting author
gevert@surfchem.chalmers.se

Introduction

The maximum limit of benzene content in gasoline is set or will be 1 % in many areas. Scanraff is producing gasoline with 1 % benzene content according to the specifications. Major contributor to the gasoline pool is reformate (more than 80 %). So benzene reduction in the reformate has a major effect in meeting the specification imposed. Due to this reason Scanraff interested in a model, which can predict and control benzene in the reformate. There has been some interest in predicting benzene production in catalytic reforming in the recent years (1-3). The reactions can be studied with kinetic modeling when the content of different molecule types are known in the feed. The objective of this paper is to present a statistical model which will be able to predict benzene in the reformate. Multivariate data analysis (MVDA) was used to develop this prediction model (4). The study was done as a Master of Science thesis between Chalmers and Scanraff (5)

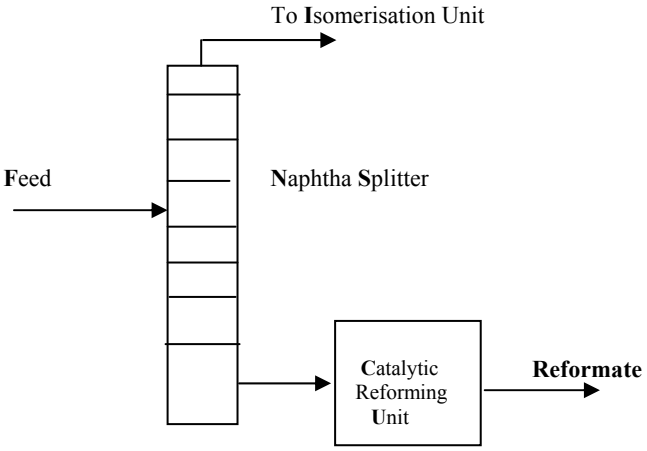

Figure 1. Blockdiagram of the reformer

Straight run naphtha is mixed with naphtha from conversion processes and the mixture is hydrodesulfurised (Figure 1). After this the naphtha is split into two streams, the light part to the isomerisation plant and the heavier part to the Platformer. The feed to the Platformer is preheated before it enters the first fired heater followed by the first reactor. The volume in the first reactor is 20 % of the total reactor volume, the volume in the second rector is 30 % and the volume in the last reactor is 50 %. Since the reactions are endothermic, the stream leaving the first reactor has to be heated up before it enters the second reactor, and so on. The aim of the Platformer is to produce aromatic hydrocarbons from the naphtha by catalytic reforming. The naphthens are easily converted to aromatics but the paraffins are more difficult to convert. There is a need for hydrogen for the reactions, which is added before the first reactor. Hydrogen is produced in the reactions and a compressor circulates the hydrogen. A low level of hydrogen increases the formation of coke. The catalyst in the reactors is circulated continuously through the CCR (Continuous Catalyst Regeneration) where the coke on the catalyst is combusted at low oxygen level. By this procedure, the catalyst activity and thereby the yield is kept constant in the reactor. The reformate is pumped to a stabilizer column where the LPG is stripped. The product quality of the reformate varies depending on which gasoline blend Scanraff wishes to sell at the moment. The normal parameters (that the operators are able to control) are:

MON	90-91	(controlled by the feed rate and the temperature in the Platformer)
Benzene	1.4-1.5% by volume	(controlled by the separation in the naphtha splitter)
Vapor pressure	15-30 kPa in the reformate	(controlled by the separation stabilizer)

Collection of data

A set of 16 process variables was identified as potential importance. The available collection of data was also important for the selection. As a response variable the benzene content in the stabilized reformate was chosen. From the process computer the 8000 sets of values on process parameters and online analysis result were loaded to the statistical program, see Table 1. The computer software used was Simpca 8, Umetrics (www.umetrics.com).

Table 1. Used Process Parameters

No.	Explanation	Abbr.	Units
1	Feed to the naphtha splitter	Feed	m^3/hr
2	Feed to the catalytic reformer	Capacity	m^3/hr
3	Pressure at top of naphtha splitter	Top Pres.	bar (g)
4	Temp. at top of naphtha splitter	Top Temp.	°C
5	Reflux ratio in naphtha splitter	Reflux ratio	ratio
6	Steam fed in to naphtha splitter	Steam	m^3/hr
7	Temperature in catalytic reformer	WAIT	°C
8	Pressure in catalytic reformer	Pressure	bar (g)
9	H_2 to hydrocarbon ratio in reformer	H2/HC	m^3/m^3
10	Temperature diff. through 1st reactor in reforming unit	DT1	°C
11	C6-naphthene in the feed to the reformer	*C6-naphth.*	Vol. %
12	C7-parafins in the feed to the reformer	C7-paraf.	Vol. %
13	Density of the feed to reformer	Density	kg / m^3
14	C7-aromatics in the feed to the reformer	C7-aroma.	Vol. %
15	Naphthenes in the feed to the reformer	Naphthenes	Vol. %
16	Aromatics in the feed to the reformer	Aromatic	Vol. %

Results and Discussion

PLS analysis results in model coefficients for the variables called PLS weights. In PLS loading plot (Figure 2), the weights for the X-variables (variables with black color in fig 2) denoted W indicates the importance of these variables in the modeling of Y (Benzene). Here we have an indication which variables from table 1 that are important. It can be seen that the C6-naphtenes lies far from the center in the same side of plot, where benzene lies so we can say that C6-naphtenes is highly positively correlated with benzene. In other words, higher C6-naphtenes content in the feed, higher will be the benzene in the product. Aromatic lies in opposite direction of benzene that is why it is negatively correlated with benzene in the product, higher the aromatics content in the feed lower will be the benzene in the product. So we can interpret that variables lying on right side of vertical line in the plot are positively correlated with benzene and variables lying on left of side are negatively correlated with benzene in the product Due to the holdup time in the distillation

towers, furnaces, pipes and in the catalytic reformer there is a time lag between the different parameters and the final benzene in the reformate. An adjustment for this is included in the calculation.

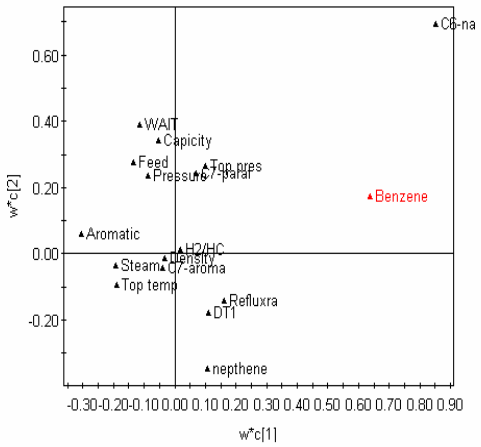

Figure 2. PLS loading plot

The Model

The model was based on refined large set of observation. Outliers of were taken away. Many of them were taken during process offset which occurs when the crude oil were changed. Aromatics, Top temperature and Steam have negative effect on benzene in the product. So with increasing Aromatics content in the feed to the Catalytic Reformer, increasing temperature the top of naphtha splitter and increasing steam fed to naphtha splitter, benzene in the product will decrease and vice versa. Top pressure in naphtha splitter has positive effect so increasing top pressure in the splitter will increase benzene in the product and by decreasing top pressure benzene will be decreased in the product. C7-paraffins content in the feed to the Reformer has positive effect, so this content should be decreased if we want less benzene in the product. From the plot in fig 2 it can be seen that both feed and capacity have no significant effect on benzene in the product. Reformer operates at the full capacity or at lower capacity. But it could affect other properties of the product. WAIT, Pressure, H2/HC and DT1 have also non-significant effect on benzene in the product. Finally we have five important factors through which benzene can be controlled in the product.

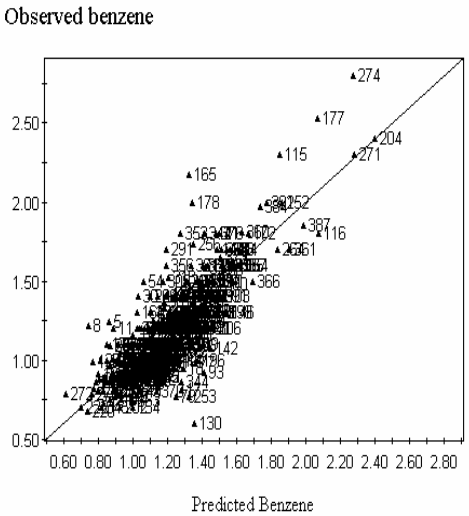

Figure3. Observed vs predicted benzene in reformate

Predicted benzene = (-0.000977702) Feed + (0.000918617) Capacity + (0.236916) Top pressure +(-0.0148667) Top temperature +(0.0884271) Reflux ratio + (-0.0252994) Steam + (-0.000715595) WAIT +(-0.0243255) Pressure + (0.0184419) H2/HC +(0.00125487) DT1 +(0.399348) C6-naphtenes +(0.00895488) C7-paraffins + (-0.00137813) Density +(-0.0144831) C7-aromatics + (0.000417643) Naphthenes + (-0.0420511) Aromatics + 4.49877.

The units of these factors are presented in table 1. The model cannot be transferred directly to other refiners instead the collection of data has to be done and followed with a new calculation. The model was tested with actual data used to develop the model, which is presented in Figure 3. In Figure 4 the model was instead tested with a complete new set of data collected in a later time than the data used for developing the model. It can be seen that the model agree well with predicting the benzene content in reformate.

Conclusions

The most important parameters for Benzene in the product are:

1. C6-naphthenes content in the feed to the Catalytic Reformer has dominating positive effect in the model.
2. Other significant factors in the model are Aromatics, Steam, Top pressure and Top temperature.
3. Operating parameters for Catalytic Reformer has no effect, in formation of benzene in the product.
4. We have three process variables in naphtha splitter namely
   - Steam fed to the naphtha splitter.
   - Top pressure in the naphtha splitter.
   - Top temperature in the naphtha splitter.

Acknowledgement. Financial support from Preem environmental fond is appreciated

References

(1) L.E Turpin, ‘‘Predicting Component Yields in a Commercial Catalytic Reformer Using a Kinetic Model’’ ACS- Meeting 222, Petroleum Division, August 2001.

(2) W. Wei, M.T. Klein, G. Hou, S.Y. Nandoliya, L.J. Broadbelt, “Kinetic modeling software tools for catalytic reforming”, ACS-Meeting 223, Petroleum Division, paper 63. April 2002.

(3) H. C. Kim, H.S. Yoon, L. Turpin, A. Lakshmanan, N. S. Park, “A Reformer Model For A Petrochemicals Complex”, Spring 2001 edition of Petroleum Technology Quarterly.

(4) N. Kettaneh-Wold and S. Wold, ‘’Multi- and Megavariate Data Analysis’’, Umetrics Academy.

(5) Qamar Zafar, M.Sc. thesis, Department of Applied Surface Chemistry, Chalmers University of Technology, 2002.

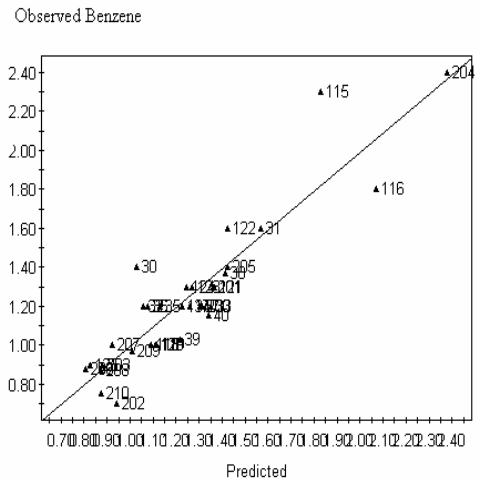

Figure 4. Benzene, new sets of data

HYDRODESULFURIZATION OF FLUID CATALYTIC CRACKED NAPHTHA OVER BIFUNCTIONAL Ni-Mo/HZSM-5 CATALYST

Changlong Yin, Ruiyu Zhao and Chenguang Liu

Key Laboratory of Catalysis, CNPC
State Key Laboratory of Heavy Oil Processing,
College of Chemistry & Chemical Engineering
University of Petroleum, Dongying, Shandong 257061, China

Introduction

Fluid catalytic cracked (FCC) naphtha currently contributes 80~85% of the total gasoline product pool in China, and it provides more than 95% of the sulfur in the gasoline. In order to comply with product specifications or to ensure compliance with environmental regulations, the sulfur compounds may require removal, which are expected to become more stringent in the future. Combined with sulfur reduction in fuel, the content of olefin in gasoline is limited to as low as 10% in the near future. It is well known that olefinic components account for about 40% in the cracked naphtha, which contribute a relatively high octane number for the cracked naphtha.

An obvious approach is isomerization of paraffins in naphtha to offset the loss of olefin, but the octane value of isomerized paraffin is less than that of equivalent olefin, octane number loss is still distinct in practice operation. Alternatively, another way is to increase the content of other components with high octane value, such as aromatics. At present, the content of aromatics in FCC naphtha is 15~20% and the maximum content in gasoline pool is limited to 35%, so there is quite big space to increase of aromatics. It would be desirable to develop an efficient process, with which can not only remove sulfur, but also aromatize paraffin and olefin to minimizes loss of octane value from olefin containing naphtha feedstock. This can be implemented by using a bifunctional catalyst with an inexpensive procedure.

It has been shown that HZSM-5 zeolite can be modified by incorporation of metal or metal oxides in order to obtain catalysts for selective hydrocarbon conversions (1-3). Activity, selectivity and stability of the catalysts for those shape selective reactions depend not only on the porous structure of the zeolite but also on the density of acid sites and their strength distribution, as well as on metal sites distribution and metal support interaction(4). The catalyst systems prepared in this way operate bifunctionally. Nickel on HZSM-5 has been found to be active in the aromatization, hydrocracking and isomerization of hydrocarbon(5-7).

In the present paper, a series of zeolite supported Ni-Mo catalysts were prepared by impregnation method, the activities of hydrogenation and aromatization of the catalysts as well as hydrodesulfurization were investigated.

Experimental

Preparation of catalyst. The mixture of commercially available NaZSM-5 (Si/Al atomic ratio=35) and alumina (zsm-5/alumina mass ratio = 50) were mixed with dilute nitric acid and extruded into diameter 1.5mm sticks. The sample was dried in air at 110 ºC for 20h, and the supports containing ZSM-5 were obtained by calcination of above dry sticks at 500 ºC for 6h. For sodium removal, the supports were treated with a solution of 1.0 M ammonium nitrate and then calcined at 500 ºC for 4h. The ZSM-5 supported Ni-Mo catalysts were prepared using incipient wet impregnation method. The precursors of the active components Ni-Mo were nickel nitrate and ammonium molybdate. All catalysts were dried at 110 ºC overnight, and then were calcined at 500 ºC for 4 hr.

Characterization of the catalysts. X-ray powder diffraction analysis was carried out with a Rigaku D/max-□A diffractometer using a graphite-filter CuKα radiation at a scan rate of 2 degrees per minute. BET sorption was used for measuring surface of the catalysts. The final Na content in the catalyst after ammonium nitrate treatment and the Ni and Mo contents in the catalysts were determined with atomic absorption spectrometry method.

Catalyst activity. Catalytic activity measurements were carried out in a high pressure micro-reactor unit of 24 mm I.D., 100cm in length. 100 ml of the catalyst extrudates were loaded in the reactor. Presulfiding is carried out before the reaction at 200 ºC for 1 hour, and 300 ºC for 2 hours and 360 ºC for 3 hours with a liquid stream containing 3w% CS_2 in cyclohexane. FCC naphtha is then admitted at test temperature. The H_2/feed ratio is 150 and LHSV is $3h^{-1}$. The reaction product was cooled and separated into gaseous and liquid products in a high-pressure separator. The average hydrodesulfurization activity was calculated as the % conversion of total sulfur in feed and in units of % HDS. The PIONA composition of the feed and hydrotreated naphtha was analyzed by gas chromatography, using a Varian 3800 chromatograph and a 100m PONA capillary column. Two kinds of FCC naphtha produced from two refineries of China were used as the feedstock. The main characteristics of the feed naphthas were shown in table 1. Aromatization activity and hydrogenation activity were measured as the percentages in the increase of aromatics and the decrease of olefin in the hydrotreated naphtha compared with the feed naphtha. Research octane number of the samples was calculated from PIONA composition.

Results and Discussion

Physico-chemical properties

The X-ray diffraction patterns of the supports with different content of HZSM-5 (50%) are completely matched with that of the pure HZSM-5, the Ni-Mo/HZSM-5 catalysts' XRD patterns exhibit almost identical intensity of the peaks with HZSM-5 except some NiO and MoO_3 peaks occurring in the latter's. The BET surface area and metal content of the catalysts were shown in table 2. The decrease in surface area after metal loading may be due to the channel occupation of nickel and molybdenum.

Table 1. Characteristics of the Feed Naphtha.

	Feed 1	Feed 2
Total sulfur, ppm	719.6	1235.6
RON	94.18	92.37
Composition (wt%)		
Aromatics	21.02	16.31
Isoparaffin	29.81	30.54
Naphthene	11.55	11.50
Olefin	26.90	31.52
Paraffin	5.26	4.38
Unidentified	5.46	5.74

Table 2. BET Area and Metal Contents in Catalysts.

	HZSM-5	Ni-Mo (a)	Ni-Mo (b)
BET area, m^2/g	313.8	246.4	274.2
Na content, %	0.066	0.081	0.086
Ni content, %	--	2.1	1.1
Mo content, %	--	7.6	3.6

Effect of reaction pressure on the catalyst's activity. Figure 1 shows the effect of reaction pressure on the liquid yield, HDS and the RON of the hydrotreated products over Ni-Mo/HZSM-5(a) and table 3 lists the detailed composition of the products. The liquid yield and HDS% of the products increase with the enhancement of reaction pressure, while the RON of the products decreases with the raising of pressure. From the composition of the hydrotreated products over Ni-Mo/HZSM-5(a) it can be found that at low pressure the content of aromatics in the product increased, while at high pressure aromatics is hydrogenated, which contributes to the increase of naphthene. We can find from figure 1 that the HDS% of the product is very sensitive to the reaction pressure, especially at 0.5~1.0MPa. The low liquid yield at low reaction pressure reveals that cracking of the naphtha was carried out on the catalyst because of the acidity of the HZSM-5. Figure 2 shows the effect of reaction pressure on the liquid yield, HDS and the RON of the hydrotreated products over Ni-Mo/HZSM-5(b). The similar trends of the liquid yield, HDS and the RON of the hydrotreated products were obtained.

Table 3. Composition of the hydrotreated products over Ni-Mo/HZSM-5(a) (wt%).

Pressure, MPa	0.5	1.0	2.0
Aromatics	21.89	20.96	18.33
Isoparaffin	32.11	37.57	40.18
Naphthene	12.03	12.72	15.99
Olefin	23.01	14.24	8.84
Paraffin	8.54	12.83	15.45
Unidentified	2.41	1.62	1.44

Feed 1, reaction temperature, 360ºC.

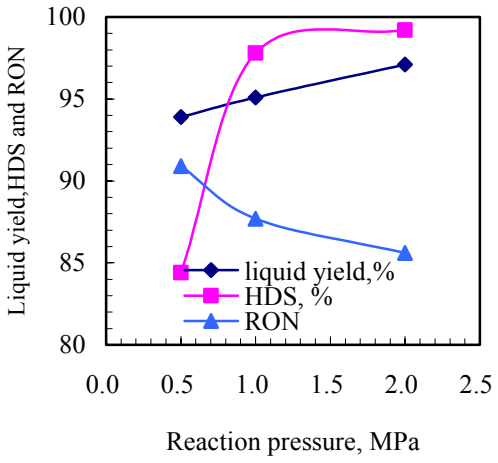

Figure 1. Effect of reaction pressure on the liquid yield, HDS and the RON of the hydrotreated products over Ni-Mo/HZSM-5(a). Temperature, 360ºC.

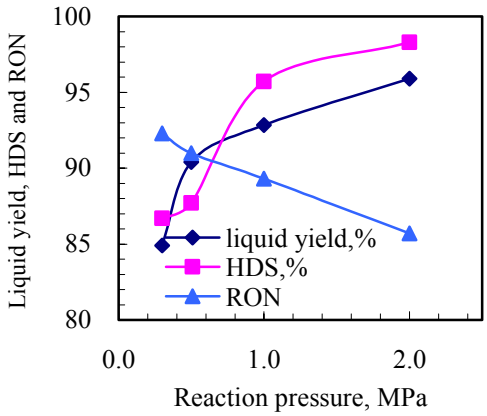

Figure 2. Effect of reaction pressure on the liquid yield, HDS and the RON of the hydrotreated products over Ni-Mo/HZSM-5(b). Temperature, 400ºC

Effect of Reaction Temperature. Effect of reaction temperature on the liquid yield, HDS and the RON of the hydrotreated products over Ni-Mo/HZSM-5(a) at 2.0MPa was shown in figure 3. It is well known that temperature enhancement can favor the hydrogenation and HDS reactions in the process of naphtha hydrotreatment, which can be testified with the results shown in table 4. The decrease of the liquid yield must be the result of more cracking occurring over the catalyst with the increase of the temperature. About 25 percent of aromatics in feed were hydrogenated at 380ºC, which led to the RON fall of the product. A little of the naphtha was probably aromatized at 400ºC according to the data in table 4, but the adding of the aromatics can't offset the part that was hydrogenated, so the content of aromatics in the product was still depressed. Figure 4 gives the effect of reaction temperature on the liquid yield, HDS and the RON of the hydrotreated products over Ni-Mo/HZSM-5(b) at 0.5MPa and table 5 lists the composition of the hydrotreated products. The increase of HDS% and the decrease of the liquid yield maybe due to the same reasons as before, while the gain of RON in the hydrotreated products does owe to the raising in aromatics content. It can be concluded from the above results that at high pressure the main reactions in the process of naphtha hydrotreatment are hydrogenation of olefin and aromatics, and the hydrogenation degree increase with the enhancement of the temperature; while aromatization is dominated at low pressure, and the aromatization degree increases with the temperature enhancement, which contributes to the increase of RON.

Table 4. Composition of the Hydrotreated Products over Ni-Mo/HZSM-5(a) (wt%).

Reaction Temp. ºC	360	380	400
Aromatics	19.81	15.67	18.72
Isoparaffin	40.77	42.26	40.75
Naphthene	14.08	15.55	15.22
Olefin	8.93	8.78	8.80
Paraffin	14.89	15.25	13.69
Unidentified	1.46	2.48	2.79

Feed 1, pressure, 2.0MPa.

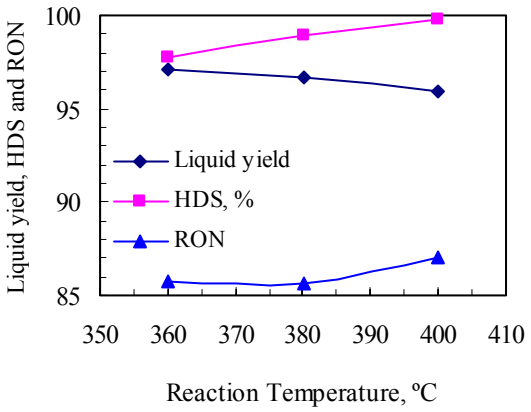

Figure 3. Effect of reaction temperature on the liquid yield, HDS and the RON of the hydrotreated products over Ni-Mo/HZSM-5(a). Feed 1, pressure, 2.0MPa.

Table 5. Composition of the Hydrotreated Products over Ni-Mo/HZSM-5(b) (wt%).

Reaction Temp. ºC	280	380	400
Aromatics	17.35	20.71	24.61
Isoparaffin	32.66	34.82	32.15
Naphthene	12.06	13.59	13.10
Olefin	28.15	17.68	16.42
Paraffin	6.93	9.40	8.35
Unidentified	2.83	3.79	5.32

Feed 2, pressure, 0.5MPa.

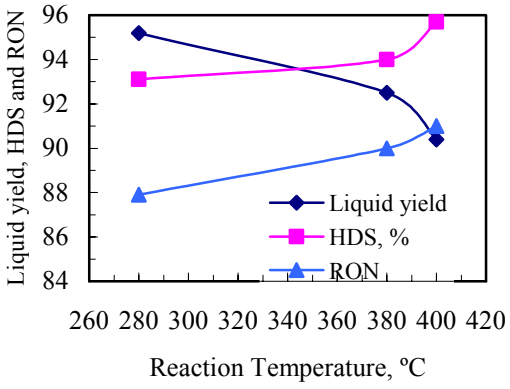

Figure 4. Effect of reaction temperature on the liquid yield, HDS and the RON of the hydrotreated products over Ni-Mo/HZSM-5(b). Feed 2, pressure, 0.5MPa.

Conclusions

Experimental results show that Ni-Mo/HZSM-5 bifunctional catalyst has excellent HDS and hydrogenation properties. The liquid yield and HDS% of the products increase with the enhancement of reaction pressure, while the RON of the products decreases with the raising of pressure. Elevation of reaction temperature can promote the HDS and the aromatization process, but leads to the loss of liquid yield at the same time. The main reactions at high reaction pressure in the process of naphtha hydrotreatment are hydrogenation of olefin and aromatics, and the hydrogenation degree increase with the enhancement of the temperature; while at low pressure aromatization is dominated in the process, and the degree increases with the temperature enhancement, which contributes to the increase of RON in the products.

Acknowledgement. Financial support from PetroChina Corporation Limited is greatly appreciated.

References

(1) D. Seddon, *Catal. Today* **1990**, *6(3),* 351
(2) Y. Ono, *Catal. Rev. –Sci. Eng.* **1992**, *34(3),* 179
(3) M. Guisnet; N. S. Gnep; F. Alario. *Appl. Catal. A* **1992**, *89*, 1
(4) S. Uemiya; I. Koike; E. Kikuchi, *Appl. Catal.* **1990**, *65*, 143
(5) D. Sun; Z. Zhao, *Ind. Eng. Chem. Res*. **1991**, *76*, 171
(6) C.V.V. Satyanarayana; D. K. Chakrabarty, *Appl. Catal*, **1990**, *66,* 1
(7) T. Inui; Y. Makino; F. Okazumi; S. Nagano; A. Miyamoto, *Ind. Eng. Chem. Res.* **1987**, *26,*647

A STUDY ON REMOVAL OF HYDROGEN SULFIDE FROM LIGHT OIL WITH SOLID BASE

Yongfeng Duan Yuzhi Xiang Daohong Xia

(College of Chemistry & Chemical Engineering, University of Petroleum, Dongying, 257061, China)

Abstract: For removal hydrogen sulfide from light oils, a novel solid base, with activated carbon as supporter and alkali or earth-alkali compound as active component, has excellent adsorption capacity for hydrogen sulfide and advantages of simple preparation and inexpensive cost of raw material has been developed . In addition, an additive can promote significantly the removal of hydrogen sulfide by the solid base was also studied.

Keywords: hydrogen sulfide, solid base, removal, adsorption, additive

1、INTRODUCTION

Sulfur compounds exist in various light oils made from petroleum. Such as mercaptan, hydrogen sulfide, which cause foul odors and deteriorate the finished products. In addition, due to their acidity, they are corrosive to metals, which is harmful for storage and usage of oil products. Therefore, it is necessary to remove them.

In the refining industry, an aqueous base such as sodium hydroxide or ammonia is employed fulfilling the purpose. Although its effectiveness and the low cost of fresh caustic are the reasons for its widespread use, the aqueous base especially sodium hydroxide always causes some problems. Such as spending many caustic materials, and discarding lots of hazardous waste. So environmental agencies around the world have tightened the regulations aimed at controlling its disposal. Solid bases merge as an ideal alternative to the aqueous bases to overcome the environmental and economic problems. The report concerning solid base is mostly concentrate in mercaptan oxidation, these solid bases selected from the group consisting of magnesium, nickel, zinc, copper, aluminum, iron oxides and mixtures thereof[1-4]. However the report concerning solid base on removal of hydrogen sulfide was hardly consulted.

This paper reports the effect of factors of preparation for the solid base on removal of hydrogen sulfide at ambient temperature. Thus selecting the optimum factor of preparation for the solid base on the removal of hydrogen sulfide in light oil.

2、EXPERIMENTAL

2.1 Preparation of solid base

Activated carbon marked by DV-01was used as supporter in this study. Physical properties of the activated carbon is listed in Table 1.

Table 1 physical property of activated carbon

BET surface area /$m^2.g^{-1}$	945.8
Bulk density /$g.mL^{-1}$	0.519
Intensity, %	95.0
Pore volume /$mL.g^{-1}$	0.72
Particle size/mesh	6－16

The activated carbon was calcined at high temperature for 6h, then impregnated with a aqueous solution of some alkalic materials at ambient temperature. The saturated activated carbon was filtrated in vacuum for period of time, then dried period of time at special temperature.

2.2 Experimental Oil

Petroleum ether(boiling point 90—120℃) was used as experimental oil with 800—1000μg/g hydrogen sulfide concentration.

2.3 Capability test of solid base for the removal of hydrogen sulfide

1g solid base was loaded in a 200ml flask, to this flask 100ml experimental oil was added, then the solution was electromagnetism stirred at ambient temperature with protection of nitrogen, the stirred speed was 350rpm. The hydrogen sulfide concentration in light oil was analyzed with period by the method of GB/T1792-88.

2.4 Materials calculation

The adsorption quantity of solid base for hydrogen sulfide as follows: $X_g = (C_0-C_t)\bullet\rho V\bullet 10^{-3}/M$

where

X_g: the adsorption quantity of the solid base for hydrogen sulfide mg/g

C_0: Preliminary concentration of hydrogen sulfide μg/g

C_t: concentration of hydrogen sulfide at t hour μg/g

ρ、V: density, vol. of oil g/ml, ml

M: the quality of the used solid base g

3、RESULTS AND DISCUSSION

3.1 The effect of different chemical components of solid base on the removal of H_2S

With different alkalic materials, six kinds of solid base were prepared and the removal capacities for H_2S were tested. The results are shown in Fig.1.

As can be seen from Fig.1, the SB15 solid base for absorption of hydrogen sulfide has the highest capacity.

The solid base adsorption for hydrogen sulfide has a competitive between physical adsorption and chemical adsorption. The removal capacity for hydrogen sulfide of the solid base was the sum of physical adsorption and chemical adsorption. Different solid base has different surface area and chemical center, so the capacity for hydrogen sulfide removal is alternatively. SB15 has the best chemical components.

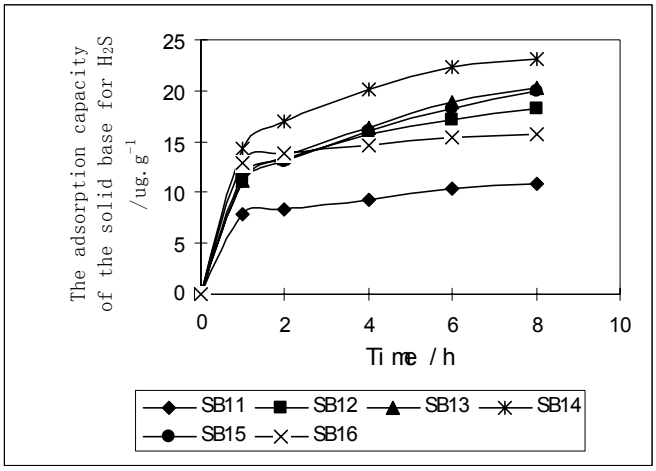

Fig.1 The adsorption capacity of different solid base

3.2 The effect of solid base vacuum filtration time on the removal of H_2S

Experiments examine the effect of time of vacuum filtration during preparation of the solid base for the removal of hydrogen sulfide. The activated carbon was impregnated with the optimum concentration of aqueous, then the loaded activated carbon was vacuum filtrated by different time, thereby making A series of solid bases. The removal of hydrogen sulfide were tested and the results are demonstrated in Fig.2.

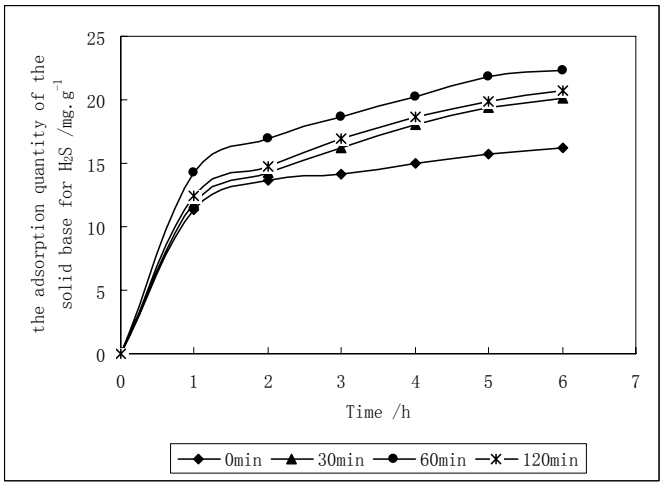

Fig.2 The adsorption capacity of the solid base by different time of vacuum filtration

Fig.2 shows that the adsorption capacity of the solid base for hydrogen sulfide firstly increased and then decreased with the increase of the vacuum filtration time during the preparation of the solid base. As a result, the time of vacuum filtration is a major factor for the solid base on removal of hydrogen sulfide, the optimum time of vacuum filtration should be 60 min.

3.3 The effect of solid base drying time on the removal of H_2S

A series of solid bases were made with different time of drying from short to long. And the removal of hydrogen sulfide of these solid bases were examined. The experimental results are shown in Fig.3.

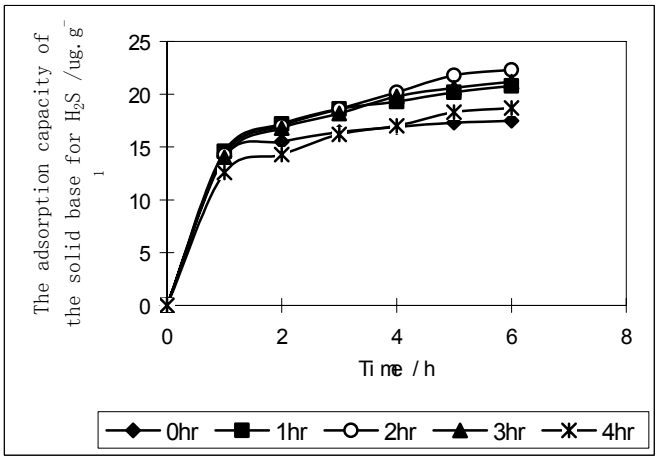

Fig.3 The adsorption capacity of the solid base by different time of drying

Fig.3 shows the adsorption quantity of the solid base for hydrogen sulfide firstly increased then decreased with the time of drying prolonged in the preparation of the solid base. The shorter the time of drying is, the higher the water content of the solid base is, the higher water content of the solid base reduced the physical adsorption of the solid base for hydrogen sulfide. With the further drying, the water is so less in the solid base that can not provide the polar environment for the chemical adsorption. consequently the chemical adsorption quantity of hydrogen sulfide in the solid base was decreased greatly.

It was found that the optimum time of drying for the solid base with good properties should be 2 hr.

3.4 The effect of additive on the removal of H_2S

It is believed that the function of polar compound is to serve as a proton transfer medium in the chemical reaction. Specially the compounds are selected from the group consisting of water, alcohols, esters, ketones, diols and mixtures thereof[5]. A group of polar compounds was chosen as the additive for the solid base for removal of H_2S. Experiments were carried out for measuring the adsorption capacity of the solid base with different quantity of the additive.

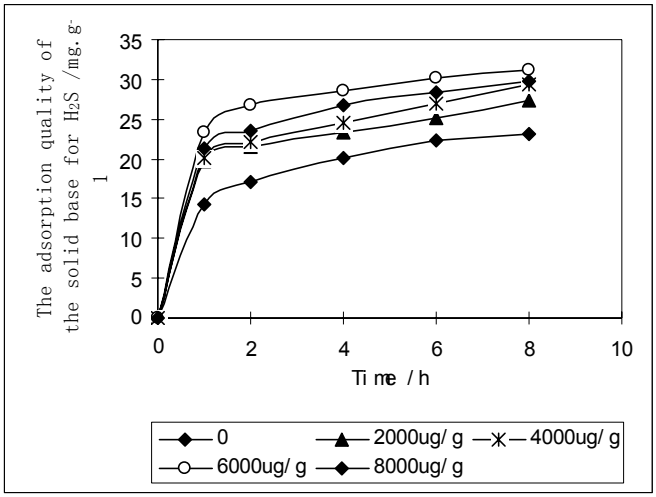

Fig.4 The adsorption capacity of the solid base for H_2S with different amount of additive

Fig.4 shows the adsorption capacity of the solid base for hydrogen sulfide has greatly increased after the additive was added. The adsorption ability of the solid base for hydrogen sulfide firstly increased and then decreased with the increase of the quantity of additive. The adsorption capacity of the solid base was enhanced after the additive was added, thus the adsorption of the solid base for hydrogen sulfide has greatly increased.

4、CONCLUSIONS

1、Preparation factors of the solid base play an important role for the solid base on removal of hydrogen sulfide. The preparation factors include the components of solid base, the time of vacuum filtration and the time of drying.

2、The adsorption capacity of the solid base for hydrogen sulfide was the sum of physical adsorption and chemical adsorption.

3、Adding a group of polar compounds can promote significantly the removal of hydrogen sulfide by the solid base. The optimum quantity of the additive is 6000 μg/g.

REFERENCES

1. F. Cavani, F. Trifiro, *Catalysis Today.* 1991,11:173
2. P. Ansquer, J. M. Orgebin, US Patent 5,382,354(1995).
3. J. J. Alcaraz, B. J. Arena, R. D. Gillespie, et al. *Catalysis Today*. 1998, 43(1-2):89-99.
4. Jiang De-en, Pan G, Zhao B, et al. *Applied Catalysis A:General.* 2000,201(2):169-176.
5. Arena, J. Blaise, Holmgren, et al. US Patent 5,232,887(1993).

HIGH CONVERSION SLURRY BED HYDROCRACKING PROCESS FOR PRODUCING HIGH OCTANE GASOLINE AND HIGH CETANE DIESEL SIMULTANEOUSLY FROM VACUUM GAS OIL

Jiashun Zhou

College of Chemistry and Chemical Engineering, University of Petroleum, Dongying, Shandong, P.R. China 257061

Introduction

Fluid catalytic cracking process (FCC) is one of the most important processes for producing high octane gasoline. Thermal cracking and isomerization reactions were the main reactions in FCC process. As more isomerized fractions, olefins and aromatic fractions contained in liquid products, the octane number RON of FCC gasoline is generally higher than 90, and the cetane number of diesel is about 30. The percentage of liquid yields in FCC process was usually within the range from 75% to 80%.

High cetane diesel was usually obtained from fixed-bed hydrocracking process. In the process, surfer and nitrogen contained in feed, olefins generated while cracking reaction tacking place and part of the aromatic fractions were hydrogenated. As a result, the octane number RON of gasoline fraction was only about 70, and the cetane number of diesel was usually more than 50.

We could get high octane gasoline from FCC process, and we also could get high cetane diesel from fixed-bed hydrocracking process. It is hard to obtain both of them from a single process up to now.

Slurry bed hydrocracking process is a kind of thermal cracking process in the presence of hydrogen and dispersed catalyst. In this process there were less isomerization and less hydrogenation. The so called dispersed catalyst were such substance as powder of natural ore, powder of coal, water or oil soluble salt which might contain Co, Mo, Ni, Fe, W, Mn, etc. [1-2] The characteristics of the liquid yields of the process were that the octane number of gasoline was not too low, usually in the range of 70 to 80; the cetane number of diesel was usually over 40. If same measure was applied to raise the octane number of gasoline fraction from 70 to 90, we could obtain high octane gasoline and high cetane diesel from slurry bed hydrocracking process simultaneously.

Methanol can react with olefins and produce oxygen containing compounds, which have a higher than 110 octane number. These kind compounds usually used as the additives to raise the octane number of gasoline. When the feedstock was blend with methanol, hydrogen, dispersed catalyst, the above reactions take place accompany with cracking reactions and hydrogenation reactions. In some cases if the dispersed catalyst can solve in methanol, the mixing procedure of feed with catalyst was simplify and the catalyst become more active and efficient, and as a result, more feed was converted to gasoline and diesel. This was what we dealt with, the high conversion slurry bed hydrocracking process for producing high octane gasoline and high cetane diesel simultaneously from vacuum gas oil. We named this process as HHH process[3].

Experimental

The Catalyst. The dispersed catalyst used in slurry process was normally the metal elements of Mo, Ni, Fe, Co etc., which were usually used in fixed-bed hydrocracking process. These kinds of catalyst can be used in mild slurry bed hydrocracking process also, whereas less free radical occurs in the reaction environment. If used in critical process, such as with a temperature 440 to 480°C, whereas more thermal cracking reaction occurs, the radical cracking reaction would be restrained. The macro behavior was that once the catalyst was added, the conversion of the feed lowered down.

The catalyst used in HHH process differed much from the most commonly used catalyst in slurry bed hydrocracking process as shown above. It was the solution of copper nitrate solved in methanol. Since methanol contained in it, when the catalyst was dispersed in the feed and used to promote the cracking and hydrogenation reactions, methanol acted as a king of reactant and reacted with the olefins yielded while hydrocarbon cracking. Thus, oxygen containing hydrocarbons were produced. As we know, these hydrocarbons have high octane number, which was usually more the 110(RON). When the boil point of these compounds fit the ranges of gasoline, it could raise the octane number of gasoline fraction. While used as a diesel fraction, it can increase the oxygen containing of diesel, and as a result, decrease the discharge of particulates from the engines.

Pilot Plant Experiments. The pilot plant has a capacity of 2.8L/hour of liquid feed. The feed and catalyst mixed in a preheating unit, and hydrocracked in a slurry reactor, and then separated into gasoline, diesel and bottom oil using a distilling unit. The average temperature of the reactor was controlled at 430°C, 440°C and 450°C. System pressure was 11MPa and the volume space hour velocity was $0.6h^{-1}$.

Feed Composition. The feed of pilot plant was consisted of 97.42% of vacuum gas oil of Xinjiang crude oil and 2.58% of the dispersed catalyst. The properties of the vacuum gas oil were presented in Table 1. The dispersed catalyst was the methanol solution of copper nitrate. In the catalyst, there were about 3m% to 4m% of copper, 10m% of water and 5m% of carbon disulphide.

Table 1. The Properties of Feed Vacuum Gas Oil

Boil Point Range, °C	360~520
Specific gravity, g/cm^3	0.9182
H/C Atomic Ratio	1.73
Sulfur, m%	0.079
Saturate, m%	75.8
Aromatic, m%	17.1
Resin, m%	7.1

Results and Discussion

Products Distribution. Pilot plant experiments results were illustrated in Table 2. All the date listed was excluded the quantity of methanol added as the solvent of dispersed catalyst. When the reaction temperature was 450°C, the conversion of the feed vacuum gas oil was over 95%. In which, more then 90% was gasoline and diesel.

Table 2. Production Distribution

Reaction Temperature, °C	430	440	450
Gas(C_1~C_4), m%	5.63	5.90	5.95
Gasoline(C_5~180°C), m%	20.45	27.31	31.73
Diesel(180~350°C), m%	46.46	53.11	58.57
Bottom Oil(>350°C), m%	27.91	14.14	4.23
Conversion of Feed, m%	71.35	85.49	95.66

Properties of Gasoline and Diesel. As illustrated in Table 3. The gasoline fraction contains less aromatics, less olefin, more paraffin, more isoparaffin, and more oxygen containing compounds. The octane number (RON) was 89. It was just a little below than the FCC process. And also, the sulfur containing of the gasoline fraction was only 0.0181m%. The total sulfur contained in gasoline fraction occupied 7.5m% of the total sulfur contained in feed gas oil. This

kind of gasoline can be simply used as clean gasoline. If blending with other high octane fraction and raising the RON to 95~97, more profit could be obtained from this HHH process.

The properties of diesel fraction were presented in Table 4. The obvious characteristics of diesel were low sulfur containing (0.0135m%), low condensation point (-38°C), and a much higher cetane index than the FCC diesel. The total sulfur contained in diesel occupied 10.3m% of the total sulfur contained in feed. Like the gasoline fraction, this kind of diesel can be used as clean diesel also. It would get better effect if blend it with the diesel from fixed-bed hydrocracking process, and raise the cetane number to 45.

Table 3. Properties of Gasoline

Aromatics, m%	17.6
Paraffin, m%	15.4
Isoparaffin, m%	19.5
Cyclane, m%	11.8
Olefin, m%	14.3
Methanol, m%	0.024
Oxygen Containing Compounds, m%	10.0
Octane Number, RON	89
Sulfur, m%	0.0181

Table 4. Properties of Diesel

Specipic Gravity, g·cm^{-3}	0.8824
Aniline Point, °C	55
Sulfur, m%	0.0135
Cetane Index	41
Condensation Point, °C	-38

Characteristics of Catalyst. The concentration of dispersed catalyst copper in reaction system was only 800~1000ppm. As shown above, the HHH process had high conversion and high liquid recovery ratio. One of the reasons was that the catalyst was very finely dispersed in the gas oil. And as a result, the catalyst had high activity to prompt the cracking, hydrogenation and etherification reactions. Figure 1 showed the relative percentage of catalyst particle number and volume of different diameter. These particles were separated from the bottom oil. In the preheating unit or reaction unit, the particles should be much fine. Although the total volume of the catalyst particle, which had less than 1μm diameter, was only about 17%, the number of them was over 80%. Another reason might be the formal electronic configuration of copper. At high temperature copper(I) was the most stable state. It has a $3d^{10}4S^0$ outer electron, and low valence state. The copper(I) might be hydrogenated to copper(0), and copper(0) might react with hydrogen sulfide changing the formal oxidation state to 2. Copper(II) changed to copper(I) again. During the changing of oxidation state, the free radical reaction might be accelerated.

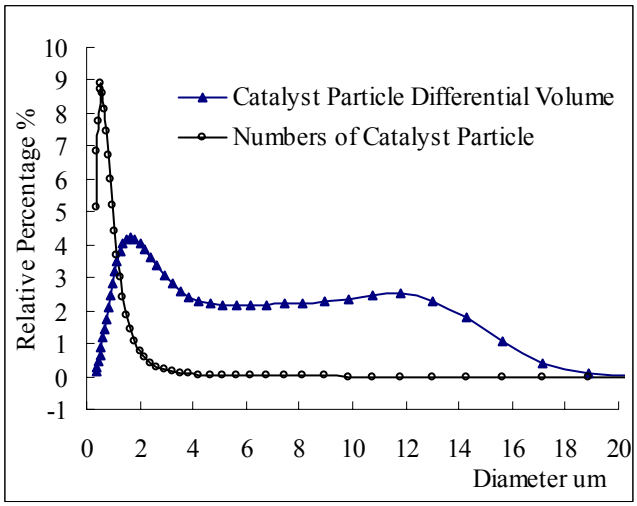

Figure 1. Distribution of Catalyst Particle

Conclusions

By using slurry bed hydrocracking process and using the copper-based methanol solution as dispersed catalyst, high octane number gasoline and high cetane number diesel can be obtained simultaneously from vacuum gas oil. At 450°C, the conversion of the feed gas oil was over 95%, in which, more than 90% was gasoline and diesel. The octane and cetane number of gasoline and diesel were 89 and 41.

References

(1) Cooke, W.S. et al.; *Prepr. Pap. –Am. Chem. Soc., Div. Fuel Chem.* **1995**, *40(3)*, 599-603.

(2) Strausz, O.P. et al.; *Prepr. Pap. –Am. Chem. Soc., Div. Pet. Chem.* **1995**, *40(4)*, 741-742.

(3) Zhou, J. et al.; *CN Patent 031120997.*

CONSIDERATION ON CHEMICAL STRUCTURES AND THERMAL PROPERTIES OF COKING COAL
(1) STRUCTURAL FACTORS FOR COAL PLASTICITY

Masakatsu Nomura, Masataka Hiro, Misa Katsuyama, Koh Kidena, and Satoru Murata

Department of Applied Chemistry, Faculty of Engineering, Osaka University, Suita, Osaka 565-0871, JAPAN

Introduction

Thermoplastic properties of coal are necessary for making a high quality metallurgical coke. In order to develop the effective procedure for coke-making, factors and mechanisms for coal plasticity had been investigated so far[1]. However, the plastic properties were so complicated that clear explanation was not established yet. In this paper, two coals, a strongly coking coal and a slightly coking coal were analyzed in a chemical view in detail to discuss differences in chemical structure and thermal properties concerning coal plasticity.

Experimental

Goonyella (GNY) and Witbank (WIT) coals were provided by the Iron and Steel Institute of Japan. Table 1 summarized the analytical results of these coals. GNY is a strongly coking coal, while WIT is a slightly coking coal. All ^{13}C NMR spectra were recorded on a Chemagnetics CMX-300 spectrometer with a ^{13}C frequency of 75.55 MHz. The measurement conditions and the method for treatments of spectra were described elsewhere[2]. Ruthenium ion catalyzed oxidation (RICO) reaction of the coal samples was performed under the reaction conditions reported previously[3]. Heat treatment of the coals was conducted using a tubular electric furnace. Three grams of coal were placed at the center of a quartz tube, this tube being set up on the furnace. After being purged with nitrogen flow, the tube was heated up to the determined temperature at 3 K/min of heating rate. When reaching the determined temperature, the coal sample was cooled down under nitrogen at ambient temperature. The yields of char, tar, gaseous products were determined by their weights, the remaining portion being assigned as light fraction that are escaped from the system during the procedure for recovering gases.

Table 1. Properties of the sample coals

coal	C content (wt%, daf.)	MF (log(ddpm))	Gieseler temperatures (°C)		
			ST	MFT	RT
GNY	87.3	2.99	397	456	498
WIT	82.5	0.60	412	432	446

MF=Gieseler maximum fluidity, ST=softening temperature, MFT=maximum fluidity temperature, RT=resolidification temperature

Results and Discussion

Structural features of the two coals. Carbon distribution in the coals was evaluated from the NMR data. GNY coal could be characterized by greater amount of aromatic carbon and larger size of aromatic rings compared with WIT coal. On the other hand, oxygen-substituted aromatic carbon was richer in WIT coal than in GNY coal. As for the size of aromatic rings, the average number of aromatic carbons per a cluster was 15 for WIT and 18 for GNY. RICO reaction can give information concerning aliphatic moieties in coal according to the formation of carboxylic acids. Figure 1 shows the distribution of aliphatic monocarboxylic acids, which are derived from alkyl side chains in coal. GNY and WIT coals have rather similar distribution of alkyl side chains ranging from C1 to C7. However, as the carbon number increases, WIT coal has a tendency to have longer alkyl side chains than GNY coal. The distribution of dicarboxylic acids, which correspond to the alkylene bridge structure, also indicated similar results. These structural differences should lead to the differences in themoplastic properties of the coals.

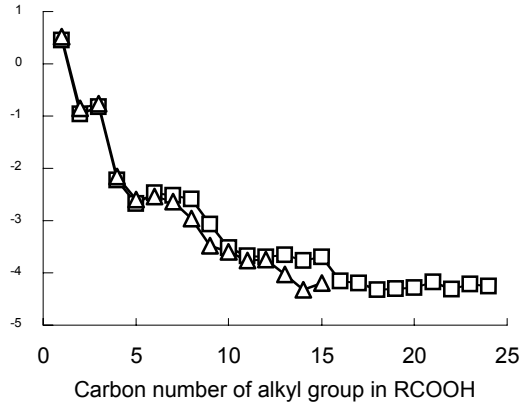

Figure 1. The distribution of aliphatic monocarboxylic acid (RCOOH) obtained from RICO reaction products of GNY and WIT coals.

Heat treatment of the coals. In order to observe thermal behavior of the coals concerning the formation of volatile materials, the coal samples were heat treated under inert atmosphere. The target temperatures for the heat treatments were softening temperature and resolidification temperature, which are shown in Table 1. Table 2 summarized the yields of tar fraction during the heat treatment. The results strongly indicated that WIT coal tended to be pyrolyzed earlier than GNY coal. The fact that WIT coal is rich in aliphatic structure would lead to this tendency. GNY keeps a greater amount of tar in the plastic range (the temperature range between ST and RT), the tar acting as metaplast at the plastic state. It can be concluded that an appropriate size of aromatic rings and the presence of metaplast materials promote the plasticity of coal.

Table 2. The yields of tar after heat treatment of the coals

coal	tar yield (wt%) in the heat treatment at	
	softening temp.	resolidification temp.
GNY	1.6	6.0
WIT	6.0	8.0

softening and resolidification temperatures were shown in Table 1.

Conclusions

Based on the chemical structural data, the differences between a strongly coking coal and a slightly coking coal were estimated. Clear structural differences, the distribution of aliphatic chains and bridges and the size of aromatic rings, were observed.

Acknowledgement. This work was partially supported by a Grant-in-aid provided by the Iron and Steel Institute of Japan.

References

(1) For example, Fitzgerald, D. *Fuel*, **1956**, *35*, 178.
(2) Nomura,M.; Kidena,K.; Hiro,M.; Murata,S. *Energy Fuels*,**2000**,*14*,904.
(3) Artok,L.; Murata,S.; Nomura,M.; Satoh,T. *Energy Fuels*, **1998**, *12*, 391.

CONSIDERATION ON CHEMICAL STRUCTURES AND THERMAL PROPERTIES OF COKING COAL (2) DIFFERENCES AMONG MACERAL CONCENTRATES

Koh Kidena, Masataka Hiro, Misa Katsuyama, Satoru Murata, and Masakatsu Nomura

Department of Applied Chemistry, Faculty of Engineering, Osaka University, Suita, Osaka 565-0871, JAPAN

Introduction

Thermoplastic properties must be caused by various factors. The authors have investigated coal plasticity in chemical structural viewpoint. A preceded paper[1] discussed on the structural differences between the two coals. The differences of chemical structures and properties among various maceral types were focused here, in order to verify the relationship between chemical structural features and plasticity of the samples.

Experimental

The maceral concentrates obtained from two kinds of coal, Goonyella (GNY) and Witbank (WIT) coals, were employed. Each coal was separated into six fractions by float-sink separation method. Two of six fractions were used, those properties being shown in Table 1. The fraction with higher density contains 50% of inertinite and is low fluidity, while that with lower density corresponds to vitrinite-rich fraction and the fluidity is high. The former fraction is called as "A" sample, and the latter "B" sample. The methods for the ^{13}C-NMR measurements and ruthenium ion catalyzed oxidation (RICO) reaction were shown in the preceded paper[1]. Additionally, the amount of transferable hydrogen in coal was evaluated by the reaction of coal with anthracene at 420^{o}C for 5 min.[2]

Table 1. Properties of the samples

	density	C content	MF	maceral composition, vol%		
sample	g/cm^3	wt%, daf.	ddpm	V	E	I
WIT-A	1.35-1.40	83.2	3	47.5	2.7	49.8
WIT-B	1.28-1.29	81.7	62	86.8	3.2	10.0
GNY-A	1.35-1.40	87.1	1	50.2	2.5	47.3
GNY-B	-1.26	86.9	9741	94.1	1.2	4.7

MF=Gieseler maximum fluidity; V=vitrinite, E=exinite, I=inertinite

Results and Discussion

Structural features of maceral concentrates. Distribution of carbon functional groups in the samples determined by solid-state ^{13}C-NMR measurement is shown in Table 2. "A" fractions, the inertinite-rich fractions, have much more aromatic carbon than the "B" samples, the vitrinite-rich fractions. H/C values and FTIR spectra for each sample also implied that aromaticities of the "A" samples are higher than those of the "B" samples. Another interesting feature of carbon distribution data shown in Table 2 is the fact that the "B" samples have much more carbon for Ar-O, Ar-C, -OCH_n-, CH_2 and CH_3 than the "A" samples. The preceding two parameters, Ar-O and Ar-C, indicate oxygen- and carbon-substituted aromatic carbon, respectively, while the latter three indicate carbon in chain structures. Therefore, the "B" samples have more aliphatic carbons with more substituted aromatic carbons and oxygen adjacent aliphatic carbons than the "A" samples. The results from RICO reactions of the samples supported such the structural features, but the distribution of acids with straight chains was not so different between GNY-A and GNY-B. Therefore, it could be assumed that the difference between them observed in ^{13}C-NMR data can be attributed to the quantity of branched-alkyl and -alkylene groups: GNY-B seems to have many branched ones. Actually, the observation of aliphatic polycarboxylic acids in RICO products strongly supported that the quantities of branched bridge structures are larger with GNY-B than with GNY-A.

Table 2. Distribution of carbon functional groups of the samples by solid-state ^{13}C-NMR

carbon type	WIT-A	WIT-B	GNY-A	GNY-B
C=O, COOH, COOR	3	<1	<1	<1
Ar-O	9	9	3	5
Ar-C	14	15	12	17
bridgehead, Ar-H	57	50	68	56
aliphatic-O	1	2	2	3
CH_2	11	16	8	11
CH_3	5	7	6	7
f_a (carbon aromaticity)	0.80	0.74	0.83	0.78

Hydrogen transferability. The amounts of transferable hydrogen in the samples are given in Table 3. A prior study[2] indicated that amounts of transferable hydrogen correlated with the values of Gieseler fluidity. Transferable hydrogen is effectively consumed in stabilizing fragments (radicals) generated by heating. As to the comparison of the amount, the "B" samples had larger amounts of transferable hydrogen as expected, this being correlated well with the high fluidity of the "B" samples. Besides, it was found that the "B" samples had a relatively greater branched aliphatic portion, as mentioned above. Such a portion might contribute to high fluidity because it chemically cleaves easily to afford a small molecular weight fraction during this period. So, the presence of an appropriate amount of aliphatic moieties is also one of the factors for the appearance of plasticity.

Table 3. The amount of transferable hydrogen of the samples

sample	amounts of transferable hydrogen (mg/g-daf. coal)
WIT-A	0.65
WIT-B	0.72
GNY-A	0.63
GNY-B	1.0

More detailed data from RICO reaction products and themogravimetric analyses of the samples gave a lot of valuable information when the plastic properties of the maceral concentrates were discussed.

Conclusions

Vitrinite-rich "B" samples which have higher fluidity and lower physical density contained relatively greater amount of long aliphatic chains and bridges with WIT coal and greater amount of branched aliphatic moieties with GNY coal. Both "B" samples had much substituent on the aromatic rings and their structures were constructed from relatively small aromatic clusters connected by aliphatic moieties and alicyclic parts. The amount of transferable hydrogen well correlated with the fluidity of the samples.

Acknowledgement. The maceral concentrates were provided by Sumitomo Metal Industries, Ltd. This work was partially supported by a Grant-in-aid provided by the Iron and Steel Institute of Japan.

References

(1) Part 1 "consideration on chemical structures and thermal properties of coking coal (1) structural factors for coal plasticity"
(2) Kidena K.; Murata, S.; Nomura, M. *Energy Fuels*, **1996**, *10*, 872.

PROMOTING EFFECT OF WATER ON COAL HYDROGENATION USING AMMONIUM TETRATHIOMOLYBDATE AS A DISPERSED CATALYST

Yoshiharu Yoneyama, Kazuaki Tanaka, Noritatsu Tsubaki

Department of Material Science and Life Science, Faculty of Engimeering, Toyama University,
3190 Gofuku, Toyama 930-8555, Japan

Chunshan Song

Fuel Science, Department of Energy & Geo-Enviromental Engineering, The Pennsylvania State University
206 Hosler Building, University Park, PA 16802-5000

Introduction

Water has a promoting effect on hydrogenation of Wyodak coal using ammonium tetrathiomolybdate (ATTM) as a dispersed MoS_2 catalyst.[1] The conversion of Wyodak coal increased from 29.5 to 66.5 wt% under hydrogenation conditions using ATTM with water addition at 350 °C. In order to clarify this effect we conducted hydrogenation of model compounds such as 2,2'-dinaphthyl ether or 4-(1-naphthylmethyl)bibenzyl using ATTM with and without water addition.[2,3] It was found that the promoting effect of water on coal conversion is principally due to the formation of highly active MoS_2 catalyst from ATTM with water addition. However it was also found that water addition promotes the formation of CO_2,[1] and the conversion of coals and model compounds were the largest at 375 °C.[2,4]

In the present study, in order to clarify the effect of water on coal hydrogenation using ATTM, the hydrogenation of various coals from low rank and high rank coal was carried out. Usually it is considered that coal structures are changed with increasing coal rank: aromatic moieties become larger and the strength of the linkages connecting aromatic moieties becomes stronger. We have already found that water addition promote the cleavage of C-O and C-C linkages under hydrogenation conditions using ATTM.[2,3] It is interesting to determine the effectiveness of water addition for the hydrogenation of various rank coals using ATTM.

Experimental

Basic properties of coals are listed in Table 1. The coals were dried under vacuum over 24 h before use. ATTM was dispersed as a catalyst precursor onto coal (1 wt% Mo on dmmf basis) by incipient wetness impregnation from its aqueous solution. The impregnated or the raw coal samples were freeze-dried for 6h, and then dried in a vacuum oven at 60 °C for 24 h before use.

For the experiments with added water, the weight ratio of water was kept at 0.46. Hydrogenation was carried out using 2 g of the coal samples with or without added water in a 25 ml tube bomb reactor at 350, 375 and 400 °C for 30 min under an initial hydrogen pressure of 6.9 MPa. All the reactions were carried out without any organic solvents. The products were separated into gases, oil (hexane soluble), asphaltene (toluene soluble), and preasphaltene (tetrahydrofuan soluble). The conversions were calculated by the sum of gases, oil, asphaltene, and preasphaltene yields. The gaseous products were analyzed by GC.

Table 1. Elemental Analysis of Coals (%, daf)

Coal	C	H	N	O[a]	Ash[b]
Beulah-Zap	72.9	4.8	1.1	21.2	9.7
Wandoan	73.4	6.4	1.2	14.9	9.9
Taiheiyo	73.4	7.1	1.6	18.1	10.1
Wyodak	75.0	5.4	1.1	18.5	8.8
Illinois #6	77.6	5.0	1.4	16.0	15.4
Pittsburgh #8	83.2	5.3	1.6	9.8	9.3
Yubari	84.0	5.9	2.1	7.9	3.4
Upper Freeport	85.5	4.7	1.6	8.2	13.1

[a] By difference [b] wt% dry base

Results and Discussion

Figure 1 shows the effect of water addition on the conversion of various coals at 350, 375, 400 °C. At 350 °C, the effect of water addition was significant: the conversions of coals except for Yubari and Upper Freeport coal increased dramatically. For example, the conversion of Illinois #6 coal increased from 29.6 to 61 wt%. However, at 375 °C, the promoting effect of water addition was dependent on coal types. For some coals such as

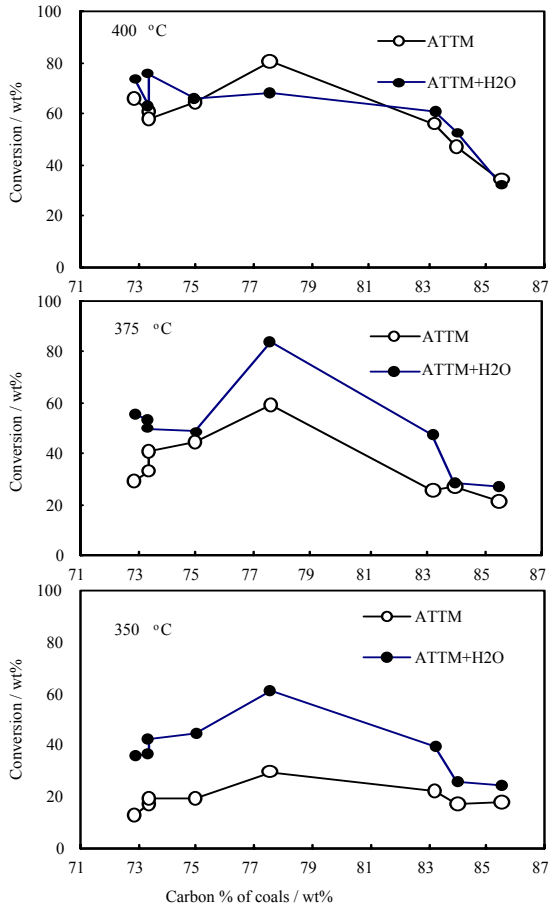

Figure 1. Effect of water addition on catalytic hydrogenation of various coals at 350, 375 and 400 °C for 30 min.

Beulah-Zap lignite, Illinois #6 and Pittsburgh #8 coals, water addition increased the conversion, however for other coals the promoting effect of water was not obvious. At 400 °C promoting effect of water addition was very low. For Illinois #6 coal, water addition had negative effect on coal conversion. We observed similar negative effect of water addition on the conversion of Wyodak coal and coal model compounds under hydrogenation conditions.[1,2] However in this study the negative effect of water addition on hydrogenation of Wyodak coal was not observed. It is known that ATTM decomposes to yield MoS_2 under hydrogenation conditions.[1] Because the MoS_2 catalyst generated from ATTM with water addition has much more larger surface area than that without water addition,[5] the MoS_2 catalyst from ATTM with water addition is much more active. Thus the coal conversion with water addition seems to be large.

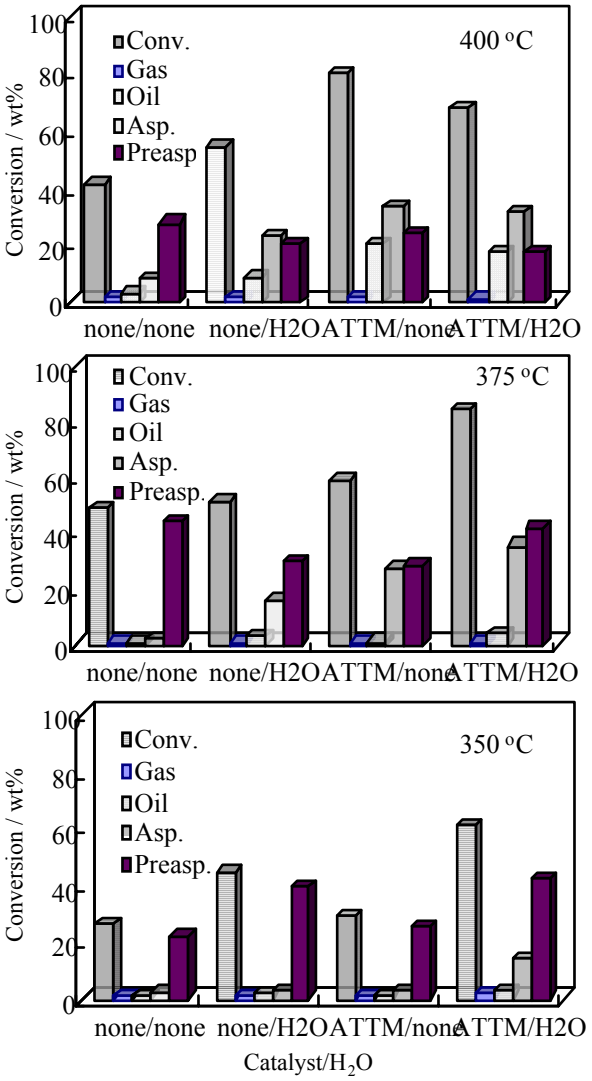

Figure 2. Effect of water addition on catalytic liquefaction of Illinois #6 under 6.9MPa H_2 for 30 min.

In this study, the conversion of Illinois #6 was the largest. Thus the effectiveness of water addition for coal liquefaction was seemed to become clear to analyze the products from the liquefaction of Illinois #6 coal. The effect of water addition on liquefaction of Illinois #6 coal is shown in Figure 2. For catalytic liquefaction conditions, the increase in the conversions was due to the increase in asp. and preasp. yield at 350 and 375 °C. The decrease in the conversion was due to the decrease in preasp. yield at 400 °C. This result is compatible with our previous result of coal and coal model compound, as mentioned avove.[1,2] Gas and oil yields were also enhanced with water addition, but these yields were not high. In gaseous products, CO_2 was principal, and water addition promoted the formation of CO_2. For other coals CO_2 was also the principal gas, and water addition enhanced CO_2 yields under both catalytic and noncatalytic hydrogenation conditions. It seemed that water addition promoted that decarboxylation reactions of coals.[1,6] It was found from the results above that water addition promoted the depolymerization of coal under hydrogenation conditions, but did not depolymerize coals to increase oil yields. For noncatalytic hydrogenation, water addition also increased the conversion and this was due to the increase in oil yield. Since it was found that the combination of water added and pyrite has a promoting effect on coal hydrogenation, the oil yield increased at 400 °C under the catalytic conditions.[6]

Conclusions

In order to clarify the effect of water on coal hydrogenation using ATTM as a dispersed MoS_2 catalyst, several coals were hydrogenated at 350, 375, 400 °C for 30 min. Water addition promoted the all coal conversions at 350 °C significantly. However this promoting effect became weaker with increase in temperature. The effect of water addition on the coal conversions at 375 °C was dependent on coal used. The conversion of most coals did not change so much at 400 °C, even though water was added. In addition Illinois #6 coal decreased with water addition at 400 °C. We have found that promoting effect of water on coal hydrogenation was significant at lower temperature.

References

(1) Song, C.; Saini, A. K. *Energy Fuels* **1995**, *9*, 188.
(2) Yoneyama, Y.; Song, C.; Reddy, K. M. *Catalysis Today* **50**, 19.
(3) Yoneyama, Y.; Song, C. *Energy Fuels* **2002**, 16, 767.
(4) Song, C.; Saini, A. K.; Yoneyama, Y. *Fuel*, **2000**, 79, 249.
(5) Yoneyama, Y.; Song, C. Prepr. Pap.-*Am. Chem. Soc. Div. Fuel Chem*., **1997**, 42, 52.
(6) Yoneyama, Y.; Okamura, M.; Morinaga, K.; Tsubaki N. *Energy Fuels* **2002**, 16, 48.

LOW TEMPERATURE OXIDATION OF COAL – EVALUATION OF TRANSFERABLE HYDROGEN

Koh Kidena, Masanori Murakami, Satoru Murata, and Masakatsu Nomura

Department of Applied Chemistry, Faculty of Engineering, Osaka University, Suita, Osaka 565-0871, JAPAN

Introduction

Oxidation of coal is known to affect coal reactivity in liquefaction or carbonization[1]. Even at temperature lower than 100°C, oxidation gives serious effects as seen in weathering phenomena. In general, it is considered that oxidation induces chemical structural changes such as the conversion of methylene carbon into carbonyl or carboxyl group. Such changes were supported by various sources of analytical results, mainly FT-IR spectra. If the structural changes could be clarified qualitatively and quantitatively, the authors could consider the amount of transferable hydrogen with the assumption that transferable hydrogen would be lost easily during oxidation.

The authors reported[2] the reaction of coal with polynuclear aromatic hydrocarbon compounds as a measure to evaluate the amount of transferable hydrogen, which was another access of mobile hydrogen, by referring to the previous report by Yokono and Sanada *et al*.[3]. Although the values derived from this method could indicate the hydrogen donatability under thermal conditions, it seems not to give the intrinsic amount of mobile hydrogen since the reaction of coal with polynuclear aromatic hydrocarbon was performed at high temperature such as 420°C. Various types of complex reactions are expected during the heating to such the high temperature. In order to obtain the information on mobile hydrogen or transferable hydrogen, what sorts of reactions occurred on active sites should be clarified as possible as one can. This paper focused on the low temperature oxidation of coal. The detailed observation of oxidation reaction could be a plausible method for evaluating reactive hydrogen in coal molecule.

Table 1. Properties of the sample coals

Coal	C content wt%, daf.	H/C	Ash	VM	FC
			wt%, db.		
Luscar (LS)	88.3	0.63	9.5	23.5	67.0
Goonyella (GO)	88.1	0.69	9.8	23.4	66.8
Pittstone-MV (PM)	85.7	0.77	7.3	34.3	58.4
Workworth (WW)	84.7	0.84	13.8	34.2	52.0
Witbank (WB)	82.5	0.72	8.0	32.9	59.1
K-Prima (KP)	81.2	0.87	3.8	43.4	52.8

Experimental

Six coal samples of bituminous range with variety of carbon content were used. These coals were supplied by the Iron and Steel Institute, Japan, and originally mined at various sites. Table 1 lists the sample coals used in this study. Oxidation treatment of pulverized sample was performed at 100-200°C under the flow of pure oxygen in a heating chamber that was installed in FT-IR spectrometer, and in an electric furnace of a themobalance, respectively. These experiments allow us to accomplish in-situ monitoring of both diffuse reflectance FT-IR spectra and sample weight.

The oxidized coal samples were separately prepared in an electric furnace under the flow of pure oxygen at determined temperature. Chemical analyses of oxygen functional groups such as hydroxyl and carboxyl groups were performed with conventional titration methods on the oxidized samples.

Results and Discussion

In-situ FT-IR measurement during oxidation. Low temperature oxidation of coals was performed at 100-200°C for 3 hours. As is generally known, in-situ measurement has a great advantage for the quantitative analysis of the changes during any treatments. Peaks at 1674-1759 cm^{-1} and 2920-2950 cm^{-1}, which are assigned as C=O stretching and aliphatic C-H stretching vibrations, respectively, were focused on since they must change during oxidation treatment. In order to give the quantitative discussion, the obtained spectra were converted with Kubelka-Munk function, which is available to the IR spectra with diffuse reflectance method. Since the changes in C-H peak were small, the increment of carbonyl peak during oxidation treatment was evaluated by the peak heights on the basis of those in untreated coal. The results at various temperatures for Goonyella coal were shown in **Figure 1**. This figure showed that the oxidation rate, slope in this figure, declined with time. The authors are assuming that reactive methylene groups would react preferentially against oxidation when the rate was relatively high. Such the active ones could be converted into carbonyl group in the beginning of the treatment or even at low temperature. In this paper, the amount of hydrogen at active methylene groups was evaluated by the results at 140°C as discussed below.

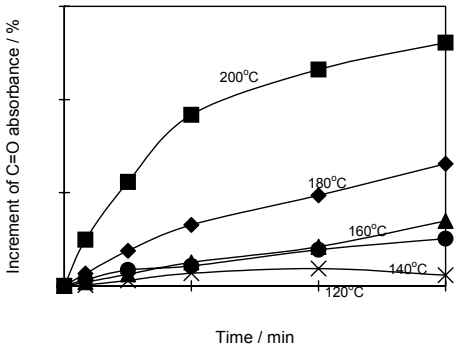

Figure 1. The increment of C=O stretching region in in-situ FT-IR spectra of Goonyella coal during the oxidation treatment.

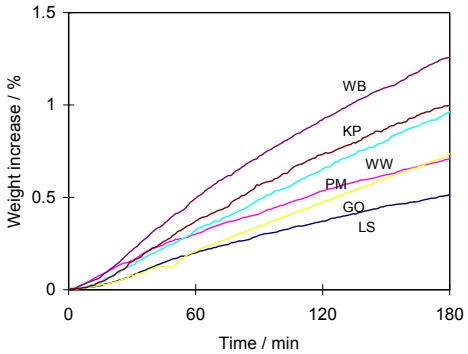

Figure 2. Weight increase during the oxidation treatment at 140°C.

Weight increase during oxidation. Weight increase was also observed in the oxidation treatment of the coals at 120°C or higher. Since weight of the sample was constant under argon flow at 100-200°C, the observed weight increase should be originated by oxygen uptake. Weight increase during oxidation treatment depended largely on the temperature. Higher temperature resulted in a greater degree

of weight increase. The weight increase of various coals at 140°C was plotted in **Figure 2**. Apparently, the increment was different from coal to coal. However, as shown in **Figure 3**, the increment of C=O peak intensity during oxidation treatment at 140°C correlated well with weight increase during similar treatment. Interestingly, this correlation did not depend on the coal type. On the other hand, when the similar plots were made from the data at higher temperature than 140°C, the correlation depended on the coal type. Therefore, rather simple reactions are expected to occur during oxidation at lower temperature such as 140°C up to 3 h.

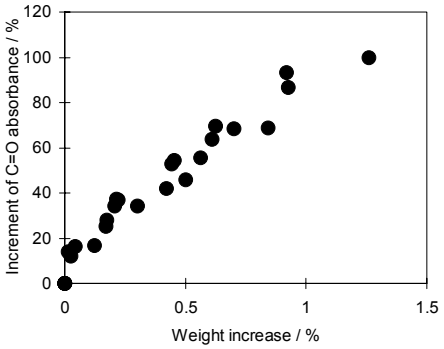

Figure 3. Correlation between the increment of C=O stretching peak intensity and weight increase during the course of oxidation treatment at 140°C for 3 h.

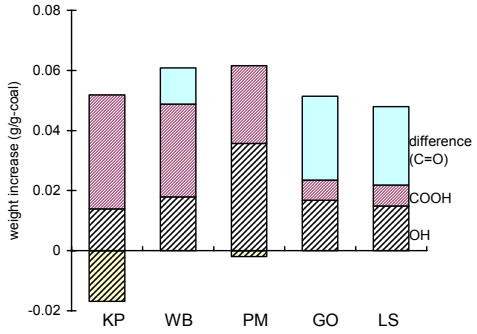

Figure 4. The increment of oxygen functional groups in regard to weight increase during the oxidation treatment at 200°C.

Functional group analysis of oxidized coal samples. Hydroxyl group and carboxyl group were analyzed according to chemical methods to elucidate chemical structural changes during oxidation. The original coals have minor amount of these functional groups because the sample coals are bituminous coals. At 140°C, the change of functional groups could not be observed quantitatively, while there observed significant changes for the samples treated at 200°C under oxygen. For each coal, both hydroxyl and carboxyl groups were increased by oxidation treatment at 200°C. Carbonyl carbon also must be increased, however, there are no methods to quantify it. Oxygen forms other than hydroxyl and carboxyl groups were carbonyl and ether. There is no need for considering the formation of etheric oxygen during the oxidation treatment, so the increase of the carbonyl group could be calculated by subtracting [hydroxyl and carboxyl] from whole increment of oxygen atoms during oxidation. The increments of the oxygen functional groups during oxidation at 200°C were summarized in **Figure 4.**

Evaluation of transferable hydrogen. During the oxidation at 140°C, both hydroxyl and carboxyl groups were not changed so that the formation of carbonyl group could be a main candidate for structural change during oxidation. In order to evaluate the amount of transferable hydrogen, the authors assumed rather simple reaction at this temperature: active methylene groups are converted into carbonyl groups such as quinone structure via peroxy type intermediate. As the active sites with higher reactivity, partially hydrogenated polyaromatic hydrocarbon structure could be proposed instead of simple methylene group in diarylmethane. In this reaction, the formation of carbonyl group gave 8 units of increase per 1 unit of decrease of molecular weight (CH_2 -> C=O). One of two hydrogen atoms on methylene carbon could act as mobile hydrogen so that one hydrogen should be counted for one methylene group. Therefore, the amount of transferable hydrogen could be calculated as [weight increase]/7/2, where weight increase should be corrected with ash content to give the values on dry ash free basis. Thus, the amount of transferable hydrogen was evaluated for each coal, then, the results were compared with the similar values obtained by the other reactions: the reaction with anthracene at 420°C for 5 min in a sealed tube[2], and the one with sulfur at 180°C for 24 h in dichlorobenzene[4].

Data at 200°C were also applied for evaluating the amount of transferable hydrogen with several assumptions of structural changes during oxidation treatment.

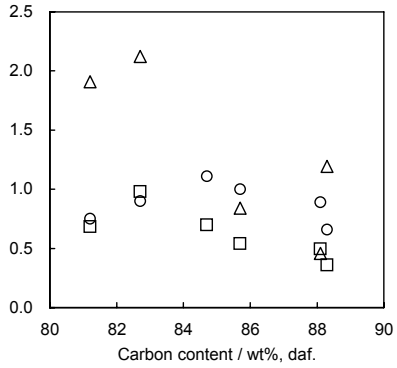

Figure 5. The amount of transferable hydrogen evaluated by weight increase during oxidation at 140°C for 3 h (square), by the reaction with anthracene (circle), and by the reaction with sulfur (triangle).

Conclusions

Low temperature oxidation of coal was performed under the flow of pure oxygen. The spectral and weight changes during the oxidation treatment were monitored by FT-IR and thermobalance, respectively. Besides, the oxidized samples were analyzed by chemical titration methods to observe the increase of oxygen functional groups. Based on these data, the amounts of transferable hydrogen were evaluated with the assumption of reactions during the oxidation treatment. The results were significantly different from the values obtained by other methods: the reaction with anthracene, or the reaction with sulfur.

Acknowledgement. Coal samples employed in this study were provided by the Iron and Steel Institute, Japan (ISIJ). A part of this work was performed with assistance of ISIJ. The authors thank ISIJ for useful discussion.

References

(1) For example, Neavel, R. C. *Fuel*, **1976**, *55*, 237; Crelling, J. C; Schrader, R. H.; Benedict, L. G., *Fuel* **1979**, *58*, 542.
(2) Kidena, K.; Murata, S.; Nomura, M. *Energy Fuels* **1996**, *10*, 872.
(3) Yokono, T.; March, H.; Yokono, M. *Fuel*, **1981**, *60*, 607.; Yokono, T.; Takahashi, N.; Sanada, Y. *Energy Fuels*, **1987**, *1*, 360.
(4) Larsen, J. W.; Azik, M.; Lapucha, A.; Li, S.; Kidena, K.; Nomura, M. *Energy Fuels*, **2001**, *15*, 801.

NEW, COMPUTER-DISCOVERED PATHWAYS FOR METHANE AND ETHANE PYROLYSIS

David M. Matheu[a], Jeffrey M. Grenda[b], Mark Saeys[c], William H. Green, Jr.[d]

[a]National Institute of Standards and Technology Div. 8380
Gaithersburg, MD 20899
[b]ExxonMobil Research and Engineering
Annandale, NJ 08801
[c]Universiteit Gent, Petrochemical Technology Lab
Ghent, Belgium, B-9000
[d]Dept. of Chemical Engineering, Massachusetts Institute of Technology
Cambridge, MA 02139

Introduction

Our further understanding of fuel-rich combustion and oxidation processes (as well as process improvement in the multi-billion-dollar light hydrocarbon cracking industry) depends in part on the development of accurate, detailed chemical kinetic mechanisms for hydrocarbon pyrolysis. These models can be large, with thousands of reactions and species, reflecting the real complexity of the gas-phase chemistry. Unfortunately, such complexity makes by-hand construction of pyrolysis mechanisms exceedingly difficult – the building of mechanisms by-hand is especially prone to the inadvertent omission of important chemical pathways, and the inclusion of unimportant ones. As a step toward systematically-developed, elementary-step-based alkane pyrolysis mechanisms for arbitrary conditions, this work examines methane pyrolysis, using a new software algorithm to construct an appropriate mechanism automatically. A preliminary examination of ethane pyrolysis, using the same tool, is also presented.

Autocatalysis in Methane Pyrolysis. Methane pyrolysis has been extensively studied for many decades, both for its potential to convert methane to more valuable hydrocarbons, and its importance within larger combustion and pyrolysis processes. Beginning in the 1970's, Chen and coworkers performed numerous experiments on methane pyrolysis at lower temperatures and moderate pressures (below 1100 K and 0.5-1.0 atm) [1-3], and discovered a sharp autocatalysis at very low methane conversion (< 1%), which neither surface reactions nor the then-current gas-phase chemical kinetics models could account for. Indeed, they found autocatalysis a general but inexplicable feature of lower-temperature (< 1100 K) methane pyrolysis. This system's autocatalytic behavior defied explanation until the 1990 work of Dean[4].

Dean proposed the importance of cyclopentadiene, formed via the pressure-dependent pathways of Equation (1):

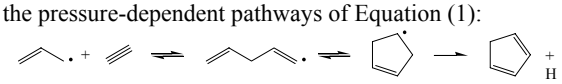

(1)

Cyclopentadiene, once formed, may function as a chain-brancher by dissociating into the resonantly stabilized cyclopentadienyl radical, and a hydrogen atom:

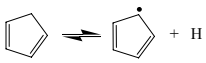

(2)

Both the cyclopentadienyl radical and the hydrogen atom abstract hydrogens from CH_4 under the experimental conditions:

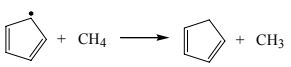

(3)

The cyclopentadiene product can dissociate to cause chain branching once again. With these reactions Dean provided the first plausible explanation for the autocatalytic upturn measured by Chen et al.

However, recent experimental and theoretical data on the enthalpy and entropy of formation for cyclopentadienyl[5;6] indicate that reactions (1)-(3) alone are not sufficient to explain autocatalytic behavior. Dean used a cyclopentadienyl enthalpy of formation close to the 1982 value of McMillen and Golden ($\Delta H_f(298)$ = 242 kJ/mol) [7], whereas more recent values from various research groups are about 18 kJ/mol higher (clustered around 260 kJ/mol). With the new thermochemical parameters for cyclopentadienyl, reaction (2) no longer proceeds rapidly enough to drive autocatalysis to the extent observed. Figure 1 below shows how the predictions of Dean's 1990 mechanism change when more recent data for cyclopentadienyl radical are used. That mechanism is now clearly unable to explain the strong autocatalysis in methane pyrolysis, and a new mechanism is needed.

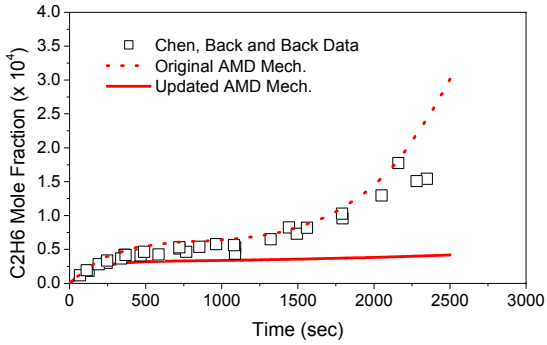

Figure 1. Attempts to explain autocatalysis in methane pyrolysis at 1038 K and 0.58 atm for very low conversions of methane. Open symbols represents experimental data sets from Chen and coworkers. The dotted line represents the prediction of the mechanism of Dean in 1990. The solid line illustrates the Dean mechanism once again, but this time with updated kinetic parameters, most importantly improved thermodynamic data for cyclopentadienyl radical.

Minor-Product Yields in Ethane Pyrolysis. Due to its industrial importance, ethane pyrolysis has been studied extensively. Most ethane cracking models used in industry are proprietary, and employ extensive parameter fitting, lumping, and tuning that allow optimization of industrial ethane cracking. These models also assume high-pressure-limit conditions for almost all reactions. Such models are extremely useful to chemical engineers, but further understanding of ethane pyrolysis under industrial conditions may need explicit, elementary-step-based mechanisms that incorporate pressure-dependence.

Computational Method: Mechanism Generation with Integrated Pressure-Dependence

This work uses a new software algorithm, called "XMG-PDep", to systematically construct the appropriate reaction mechanisms for methane and ethane pyrolysis, "from scratch", for a specified temperature, pressure, and set of initial species concentrations[8;9]. A full description of this tool can be found in Matheu[8].

Results for Methane and Ethane Pyrolysis

Figure 2 below shows the generated model's prediction of ethane concentration with the experimental data of Chen, Back, and Back[1-3]. The autocatalytic upturn in ethane concentration is clearly captured; no mechanism parameters were manipulated or adjusted to

fit any data. A CHEMKIN-compatible version of the mechanism is available from the authors.

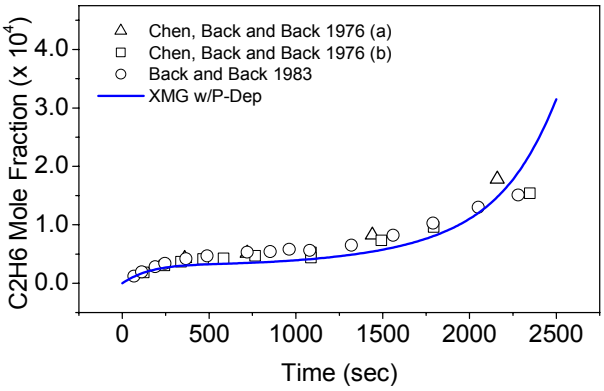

Figure 2. XMG-PDep predicted ethane concentration at 1038 K and 0.58 bar, compared with three data sets from Chen and coworkers.

Radical production analysis in Figure 3 below shows a selection of the top net-radical-producing reactions – these reactions function as chain-branchers which can give rise to the observed autocatalysis. The dissociation of cyclopentadiene, noted by Dean, is still an important pathway, but a collection of reverse disproportionation reactions are also critical to explaining the autocatalytic behavior in this model. In addition, cyclopentadienyl radical now arises not via allyl addition to acetylene to form cyclopentadiene (1), but by propargyl addition to acetylene to form the radical directly.

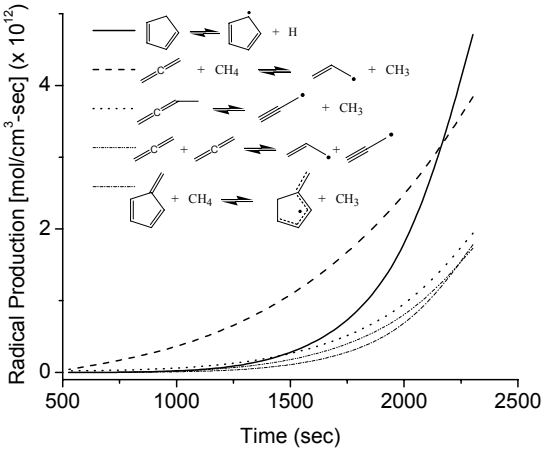

Figure 3. Main radical production routes for autocatalysis in methane pyrolysis. Each curve represents a *net* rate of radical production, for which the reverse direction has been taken into account.

Preliminary Results for Ethane Pyrolysis. We have found our generated mechanism to agree well with the high-conversion neat ethane pyrolysis experiments of Glasier and Pacey[10], in particular for butadiene and acetylene concentration. In addition, early results suggest that key reactions for the formation of these minor products during industrial ethane pyrolysis are likely to be pressure-dependent, contrary to prevailing understanding. Table 1 presents ratios of the rate constant *k(T,P)* over the high-pressure-limit rate constant for a dilute ethane pyrolysis example, at 1100 K and 100 bar Ar. Table 1 does not imply industrial ethane pyrolysis, as a whole, is strongly pressure-dependent, but it suggests that even at very high pressure, incorporation of pressure-dependence could be needed to describe the formation of important minor products like acetylene.

Table 1. Selected Ratios of k/k(inf) at 1100 K and 100 bar Ar, Dilute Ethane Pyrolysis.

Reaction	k/k_{inf}
C2H6 → C2H5 + H	0.45
C2H3 → C2H2 + H	0.28
C3H7 → C2H4 + CH3	0.67

Conclusions

We have used a new software tool to build chemical kinetic models for methane and ethane pyrolysis, automatically, with systematic criteria and with full incorporation of pressure-dependent effects. The methane mechanism yields surprising new pathways that can explain the mystery of experimentally-observed, low-conversion autocatalysis. The ethane mechanism suggests that some important pathways will be pressure-dependent, in spite of the common claim that industrial ethane pyrolysis occurs entirely within the high-pressure limit.

Acknowledgement. The authors thank Dr. A. M. Dean for much assistance and participation in this work. This work was financially supported by the Division of Chemical Sciences, Office of Basic Energy Services, Office of Energy Research, U.S. Department of Energy, through grant DE-FG02-98ER14914, as well as the EPA Center for Airborne Organics, and an NSF CAREER award to WHG (CTS-9875335), and a postdoctoral research associateship award to DMM from the National Research Council (U. S.).

References

(1) Back M. H.; Back, R. A., in *Pyrolysis: Theory and Industrial Practice*; Albright, L. F., Crynes, B. L., and Corcoran, W. H., ed.; Academic Press: New York, 1983; pp. 1-24.
(2) Chen, C. J.; Back, M. H.; Back, R. A. *Can. J. Chem.* **1975**, *53*, 3580.
(3) Chen, C. J.; Back, M. H.; Back, R. A. *Can. J. Chem.* **1976**, *54*, 3175-3184.
(4) Dean, A. M. *J. Phys. Chem.* **1990**, *94*, 1432-1439.
(5) Kiefer, J. H.; Tranter, R. S.; Wang, H.; Wagner, A. F. *Int. J. Chem. Kin.* **2001**, *33*, 834-845.
(6) Roy, K.; Braun-Unkhoff, M.; Frank, P.; Just, Th. *Int. J. Chem. Kin.* **2001**, *33*, 821-833.
(7) McMillen, D. F.; Golden, D. M. *Ann. Rev. Phys. Chem.* **1982**, *33*, 493-532.
(8) Matheu, D. M. Ph.D. Thesis, Massachusetts Institute of Technology, **2002**.
(9) Matheu, D. M. , Dean, A. M., Grenda, J. M., and Green, W. H. Jr. *J. Phys. Chem A*., submitted for publication.
(10) Glasier, G. F.; Pacey, P. D. *Carbon* **2001**, *39*, 15-23.

THE WATER-GAS-SHIFT REACTION: A REACTION NETWORK ANALYSIS OF THE MICROKINETIC MODEL

Caitlin Callaghan, Ilie Fishtik and Ravindra Datta

Fuel Cell Center and Department of Chemical Engineering,
Worcester Polytechnic Institute
Worcester, MA 01609

Introduction

The De Donder formula that relates the rate of an elementary reaction to its thermodynamic affinity has proved to be useful in the analysis of reaction kinetics and mechanisms. The affinity is considered as the driving force for a chemical reaction, determining both its direction and magnitude. Further, the affinity is a state function and follows the same linear combination rules as chemical reactions in a reaction network. In particular, the affinity of the elementary reactions is linearly related to the affinity of the overall reaction. An alternate form of the De Donder relation for an elementary reaction, given here, provides an insightful approach to the analysis of elementary reactions as well as sequences of series and parallel reaction schemes.

In this work, we present a new rate-affinity formalism for reaction networks and use it to systematically study the microkinetics of the water-gas-shift (WGS) on a copper catalyst [1]. The first step in our analysis is the development of a detailed microkinetic model of WGS reaction comprising 13 elementary reactions. We next utilize a new reaction network analysis in terms of Kirchhoff's Laws and an alternate form of the De Donder equation. This new approach provides a deeper understanding of the relationship between the rates of the elementary and overall reactions, and allows rational simplification of reaction networks and kinetic analysis.

Microkinetic Model

The mechanism of the WGS reaction is assumed to proceed via a set of elementary reactions (ERs) comprising of active sites on the surface of the catalyst (S), surface intermediates, and terminal species. Our starting point in the development of the microkinetic model is the experimental evidence according to which the WGS reaction normally proceed via the following set of eight surface intermediates: H_2OS, COS, CO_2S, H_2S, HS, OHS, OS, and HCOOS. From these surface species, a plausible set of ERs may be generated using an appropriate chemical reaction generator. The stoichiometry of the ERs is further dictated by the application of the UBI-QEP method used to calculate the energetic characteristics of each of the ERs. The ERs are limited to the three types of reactions for which the UBI-QEP method may be applied:

1. AB(g) + S ⇆ ABS
2. AB(g) + S ⇆ AS + BS
3. AS + BCS ⇆ ABS + CS

The set of ERs selected under the above stoichiometric constraints is given the Table 1. The UBI-QEP method was applied next to calculate the activation energies and enthalpies of each ER [1]. Further, the pre-exponential factors were estimated using the conventional transition state theory. In accordance with Waugh [2], an immobile transition state without rotation for all of the species is assumed. A pre-exponential factor of 10^1 $Pa^{-1}s^{-1}$ results for the adsorption/desorption reactions while 10^{13} s^{-1} results for surface reactions. Some of the pre-exponential factors were adjusted slightly to conform to the known WGS thermodynamics.

Table 1. A Microkinetic Model for the WGSR

s_1:	$H_2O + S \leftrightarrows H_2OS$
s_2:	$CO + S \leftrightarrows COS$
s_3:	$CO_2S \leftrightarrows CO_2 + S$
s_4:	$HS + HS \leftrightarrows H_2S + S$
s_5:	$H_2S \leftrightarrows H_2 + S$
s_6:	$H_2OS + S \leftrightarrows OHS + HS$
s_7:	$COS + OS \leftrightarrows CO_2S + S$
s_8:	$COS + OHS \leftrightarrows HCOOS + S$
s_9:	$OHS + S \leftrightarrows OS + HS$
s_{10}:	$COS + OHS \leftrightarrows CO_2S + HS$
s_{11}:	$HCOOS + S \leftrightarrows CO_2S + HS$
s_{12}:	$HCOOS + OS \leftrightarrows CO_2S + OHS$
s_{13}:	$H_2OS + OS \leftrightarrows 2OHS$

Elementary Reactions

According to the thermodynamic transition state theory (TTST), the rate, or turn-over frequency (TOF), of the forward and reverse reactions are defined as:

$$\overrightarrow{r}_\rho = \overrightarrow{k}_\rho \prod_{i=1}^{r} a_i^{-\nu_{\rho i}} \quad \text{where} \quad \overrightarrow{k}_\rho = \kappa \frac{k_B T}{h} \exp\left(-\frac{\Delta \vec{G}_\rho^{\pm o}}{RT}\right)$$

$$\overleftarrow{r}_\rho = \overleftarrow{k}_\rho \prod_{i=r+1}^{n} a_i^{\nu_{\rho i}} \quad \text{where} \quad \overleftarrow{k}_\rho = \kappa \frac{k_B T}{h} \exp\left(-\frac{\Delta \overleftarrow{G}_\rho^{\pm o}}{RT}\right)$$

The ratio of the reverse and forward steps illustrates the interrelation of the forward and reverse reactions through the affinity of the reaction. Thus, the net rate is:

$$r_\rho = \overrightarrow{r}_\rho \left(1 - \frac{\overleftarrow{r}_\rho}{\overrightarrow{r}_\rho}\right) = \overrightarrow{r}_\rho \left\{1 - \exp\left(-\frac{A_\rho}{RT}\right)\right\}$$

which constitutes the conventional De Donder relation. The degree of reversibility and the direction of the reaction flux are determined by the sign and magnitude of the affinity. The affinity is calculated for each elementary reaction based on the following expression:

$$-\frac{A_\rho}{RT} = \sum_{i=1}^{n} \nu_{\rho i} \mu_i = -\ln K_\rho + \alpha_{\rho o} \ln \theta_o + \sum_{k=1}^{q} \alpha_{\rho k} \ln \theta_k + \sum_{i=1}^{n} \beta_{\rho i} \ln P_i$$

For $A_\rho > 0$, the net rate is positive, i.e., the reaction proceeds in the forward direction while the reaction proceeds in the reverse direction for $A_\rho < 0$. When $A_\rho = 0$, the net rate $r_\rho = 0$. As the affinity approaches zero, the forward and reverse rates approach a common value, the exchange rate, $r_{\rho,0}$. The formal definition of exchange rate is [3]:

$$r_{\rho,0} \equiv \left| \frac{\partial r_\rho}{\partial (A_\rho / RT)} \right|_{A_\rho \to 0}$$

Furthermore, we assume the linear free energy relation

$$\beta_\rho = \frac{d\left(\Delta \vec{G}_\rho^{\pm o}\right)}{d\left(\Delta G_\rho^{o}\right)}$$

where β_ρ is a constant, called the symmetry factor, that takes on a value between zero and one[4]. The symmetry factor represents the fractional change of the standard Gibbs free energy of reaction and is frequently assumed to be ½ for elementary reactions [5].

Application of the linear free energy relation to the rate of an ER yields:

$$r_\rho = r_{\rho,0}\left[\exp\left\{\beta_\rho \left(\frac{A_\rho}{RT}\right)\right\} - \exp\left\{(\beta_\rho - 1)\left(\frac{A_\rho}{RT}\right)\right\}\right]$$

where the exchange rate is $r_{\rho,0} = \left(\vec{r}_\rho\right)^{\beta_\rho} \left(\overleftarrow{r}_\rho\right)^{1-\beta_\rho}$.

Further, for the special case of $\beta_\rho = ½$, the expression reduces to

$$r_\rho = 2r_{\rho,0}\sinh\left(\frac{A_\rho}{2RT}\right)$$

For the limiting case when the reaction is in the vicinity of equilibrium ($A_\rho \to 0$) expansion of the exp function in the locality of zero and truncating after the first term yields:

$$r_\rho \approx r_{\rho,0}\left(\frac{A_\rho}{RT}\right)$$

which, in the spirit of irreversible thermodynamics, is a linear equation in terms of the driving force [2,6]. For large values of affinity ($A_\rho \to \infty$), the rates of the ERs can be written as

$$r_\rho \approx r_{\rho,0}\exp\left(\frac{\beta_\rho A_\rho}{RT}\right)$$

Reaction Network Analysis

A reaction route (RR) is defined as a linear combination of p ERs s_ρ ($\rho = 1,2,\ldots,p$), [1]

$$RR = \sum_{\rho=1}^{p}\sigma_\rho s_\rho$$

where σ_ρ are the stoichiometric numbers chosen so as to eliminate all the intermediates in the case of an overall RR, or all intermediates except one specified intermediate in the case of an intermediate RR

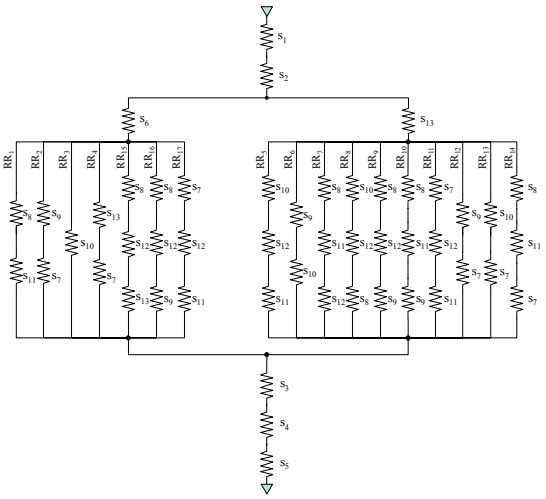

Figure 1. Reaction network for the 13-step WGSR microkinetic model.

(IRR). Here we are concerned only with a system comprising a single overall reaction (OR) and multiple overall RRs. The k^{th} RR is defined by

$$RR^{(k)} = \sum_{\rho=1}^{p}\sigma_\rho^{(k)} s_\rho$$

where k = 1,2,…,N. Thermodynamics provides the affinity expression for the given OR or IR

$$A_T^{(k)} = \sum_{\rho=1}^{p}\sigma_\rho^{(k)} A_\rho$$

with the affinity of the OR or IR remaining invariant for all RRs. This invariance requires that [8]

$$\sum_{k=1}^{N}\nu^{(k)}A^{(k)} = \sum_{\rho=1}^{p} r_\rho A_\rho$$

where $\nu^{(k)}$ represents the flux of the reaction through the k^{th} RR. When the definition of affinity is applied, the following results

$$r_\rho = \sum_{k=1}^{N}\sigma_\rho^{(k)}\nu^{(k)}$$

In other words, if an ER is involved in more than one RR, its rate is equal to the sum of its stoiciometric number for the RR times the flux of the k^{th} RR.

In the electrical analogy of reaction networks, each ER is viewed as a resistance of value $r_{\rho,0}^{-1}$. The affinity is considered equivalent to voltage and the RR flux $\nu^{(k)}$ is viewed as the current through a branch. Application of electrical theory and Kirchhoff's Laws to the reaction network gives the following relationship for series and parallel fluxes along a single RR, respectively. For the linear, series case, we see that the effective resistance $1/\nu_0^{(k)}$

$$\frac{1}{\nu_0^{(k)}} = \frac{(\sigma_\rho^{(k)})^2}{r_{\rho,0}}$$

in direct analogy with the overall resistance being a sum of resistances in series. For effective resistances in parallel

$$\nu_{T,0} = \sum_{k=1}^{N}\nu_0^{(k)}$$

which is analogous to the inverse total resistance being equal to the sum of inverse resistances for a parallel network.

Table 2. Affinities, Rates, and Exchange Rates for a 13-step WGSR Microkinetic Model (T = 150°C, Feed: 0.1 H_2O, 0.1 CO, 0.8 N_2)

Step	A_r	r_ρ	$r_{\rho,0}$	$r_{\rho,0}^{-1}$
s_1	5.25E-08	3.79E-03	6.07E+07	1.65E-08
s_2	5.25E-08	3.79E-03	6.07E+07	1.65E-08
s_3	1.45E-07	3.79E-03	2.20E+07	4.55E-08
s_4	5.23E-04	3.79E-03	6.10E+03	1.64E-04
s_5	1.45E-07	3.79E-03	2.20E+07	4.55E-08
s_6	1.10E+00	3.79E-03	2.89E+00	3.46E-01
s_7	2.89E+00	2.04E-06	5.92E-04	1.69E+03
s_8	7.98E+00	1.89E-03	2.00E-01	5.01E+00
s_9	5.09E+00	1.58E-08	2.61E-06	3.82E+05
s_{10}	7.98E+00	1.89E-03	2.00E-01	5.01E+00
s_{11}	4.46E-07	1.90E-03	3.58E+06	2.80E-07
s_{12}	-5.09E+00	-2.02E-06	3.33E-04	3.00E+03
s_{13}	-3.99E+00	-2.69E-13	5.66E-11	1.77E+10

Results

The reaction network involving a complete list of RRs [1] is presented in Figure 1. From the affinities, rates and exchange rates of the ERs (Table 2) it may be deduced that the dominating RRs will be found in the left hand set of RRs in Figure 1. This conclusion is based on the magnitudes of the inverse exchange rates for ERs 6 and 13. As can be seen, the resistance ($r_{\rho,0}^{-1}$) via ER 6 is much smaller than that via ER 13. As a result, the contributions coming from the

Table 3. Calculated Fluxes for RR with lower resistance (i.e. s_6) (T = 150°C, Feed: 0.1 H_2O, 0.1 CO, 0.8 N_2)

RR	$(\nu_{,o}^{(k)})^{-1}$
RR_1	5.36E+00
RR_2	3.84E+05
RR_3	5.36E+00
RR_4	1.77E+10
RR_{15}	1.77E+10
RR_{16}	3.85E+05
$\boldsymbol{RR_{17}}$	4.69E+03

RRs involving the ER 13 are negligible as compared with the contributions coming from the RRs in which the ER 13 is not involved. These are just the RRs on the left hand side in Figure one, i.e., RRs $_1$, RR$_3$, etc.

These results are in complete agreement with our previous numerical analysis based on the evaluation of individual contributions coming from single RRs (Figure 2).

When the effective resistances of the parallel pathways in the remaining RRs are compared (Table 3) and from the numerical results of Figure 2, it becomes clear that RR_1 and RR_3 are dominant, except at temperatures above 300^{o}C, when RR_2 also contributes. This analysis confirms that the formate and the associative routes are dominant in the WGS reaction, although the redox route contributes at higher temperatures [8].

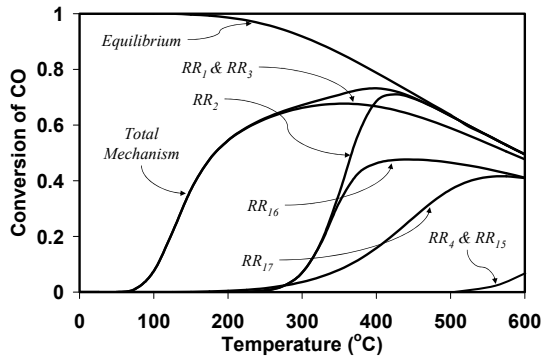

Figure 2. Simulation of CO conversion vs. temperature for Cu(111) along RRs including s_6.

Conclusions

The reaction network analysis based on an alternate form of the De Donder relation is a useful tool for reduction, simplification and rationalization of the microkinetic model. This approach also provides an interesting analogy between a reaction and electrical network thus allowing the description of a chemical reaction network in terms of Kirchhoff's Laws. Application of the proposed formalism to the analysis of the WGS reaction mechanism validated the reduced model developed earlier based solely on a numerical RR analysis [1].

References

(1) Fishtik, I.; Datta, R. *Surf. Sci.*, **2002**, *512*, 229.
(2) Waugh, K. C., *Catalysis Today*, **1999***, 53*, 161.
(3) Wagner, C. *Advan. Catal. Relat. Subj.* **1970**, *21*, 323.
(4) Bokris, J.; Reddy, A.; Gamboa-Aldeco, M. *Modern Electrochemistry 2A*. *Fundamentals of Electrodics*, 2nd ed.; Kluwer/Academic/Plenum: New York, 2000.
(5) Connors, K. A. *Chemical Kinetics. The Study of Reaction Rates in Solution*; VCH Publishers: New York, 1990.
(6) Haase, R. *Thermodynamics or Irreversible Processes*; Dover Publications, Inc.: New York, 1990.
(7) Haase, R. *Z. Phys. Chem. Neue Folge*, **1982**, *132*, 1.
(8) Shustorovich, E.; Bell, A. *Surf. Sci.*, **1991**, *253*, 385.

ANALYSIS AND KINETIC MODELING IN ULSD HYDROTREATING

C. López-García, M. Roy-Auberger, T. Chapus, F. Baco

Institut Français du Pétrole, CEDI "René Navarre", BP3, 69390 Vernaison, France

Introduction

Production of ultra low sulfur diesel (ULSD) is an essential problem for refiners, as this objective requires a comprehensive knowledge in the matter of crude oil reactivity. A kinetic model was developed in order to estimate the most accurate operating conditions necessary to achieve sulfur levels as low as 10 ppm. The quantification of refractory or inhibiting compounds contained in feedstocks and effluents is obtained by accurate analytical methods and taken into account in the kinetic model. This paper presents these results.

Experimental

Feed and hydrotreating experiments. Hydrotreating experiments were carried out on a pilot plant unit[1] with an upflow fixed bed reactor, loaded with a commercial $NiMo/Al_2O_3$ catalyst from Axens. Pressure and temperature ranges were chosen according to standard industrial conditions (320-360°C, 2-9 MPa). Liquid hourly space velocity (LHSV) was varied between 0.5 and 4 h^{-1}. Experiments were performed with several feedstocks from different refinery units: straight run, LCO and mixtures.

Analytical techniques. Feedstocks and effluents were characterized mainly in order to determine the content of aromatics, saturates, nitrogen and sulfur. Sulfur speciation was also carried out. The analysis of aromatics and saturates[2] is based on a mass spectrometry analysis. This method allows quantification of 8 aromatic families $C_nH_{2n-6,-8,-10\ldots-16,-18}$ and polyaromatics; saturates are detailed as paraffins, and 2 naphthenic families.

Total sulfur content is determined by X-Fluorescence according the ASTM D2622 method on a PW 2510 from Philips. Total nitrogen content is analyzed by chemiluminescence (IFP internal method). Speciation sulfur analysis was carried out on a GC HP 5890 Series II equipped with a sulfur chemiluminescence detector Sievers model 355 B. GC-SCD has an excellent selectivity, sensitivity and has an equimolar sulfur response. A SPB1 sulfur column from SUPELCO (30 m, 0.32 mm I.D., 4 µm) was used in this study. The GC conditions were as follows: 3 ml/min He as carrier gas; column temperature: 60°C (0 min) to 280°C (40 min) at a rate of 5°C/min with on-column injection. The FID detector: 350 ml/min of air, 31 ml/min of H_2. Burner: 800°C, 4 ml/min of air, 97 ml/min H_2. Reaction cell: ~8 torr. Ozone generator: 60 ml/min at 60 psig and 25°C. The injection volume was 0.5µl of sample diluted to obtain about 200 ppm of total sulfur.

Results and Discussion

Analysis. It is well known that the dibenzothiophene family (DBT's) contains the most refractory sulfur compounds in diesel cuts.[3,4] Relative reactivities reported in literature indicate that the refractory nature increases when alkyl substituents are adjacent to the sulfur atom. Hence, reactivity to hydrodesulfurization (HDS) is as follows: DBT > 4-methyldibenzothiophene > 4,6-dimethyldibenzothiophene. The refractory nature of 4,6-dialkylDBT's is due to steric hindrance (two alkyl groups block access of hydrogen to the sulfur atoms) and/or electronic effects.[5]

In order to improve the detailed kinetic study of hydrotreating of sulfur compounds, a GC-SCD technique was used to develop a detailed identification of DBT compounds and their quantification. Identification work is comprehensively described elsewhere.[6] Quantification accuracy has been evaluated with addition of thiophene as internal standard (99.1% purity, Sigma Aldrich) and a LCO doping with DBT, 4-methylDBT and 4,6-dimethylDBT (4,6-DiMeDBT). Additionally, an injection of a weighed thiophene, benzothiophene and dibenzothiophene (Sigma Aldrich) mixture was systematically analyzed in the beginning, halfway and at the end of a series of analysis in order to verify the quantitative results.

The sulfur content (%w/w) of the samples was in the range of 0.03% to 2.6% in feedstocks and 0.0005% to 0.1% in hydrotreated products. Figure 1 shows an example the chromatogram obtained for a LCO gasoil and its effluent at 99.4 % HDS. The LCO feed is constituted of benzothiophenes and dibenzothiophenes; the product contains only some dibenzothiophenes. The analysis method allows for the identification of 32 alkyl-dibenzothiophene compounds among which various 4,6-alkylDBT's (such as 4,6-DiMeDBT, 4-methyl, 6-ethylDBT, 2,4,6-TrimethylDBT, 1,4,6-TrimethylDBT, 4,6-diethylDBT and 3,4,6-TrimethylDBT) corresponding to the most refractory sulfur compounds as identified in Figure 1.

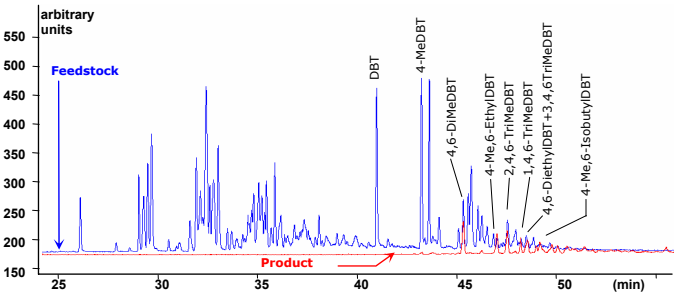

Figure 1. Sulfur profile of a 0.33% S feedstock and its 0.0021% S hydrotreated product.

Reactivity of refractory sulfur species. Achieving ultra low sulfur levels implies converting the most refractory compounds contained in diesel cuts such as 4,6-dimethydibenzothiophene and other substituted DBT with alkyl groups in 4,6 position. Moreover, this refractory nature is associated to a preferred reaction pathway.[4] DBT compounds substituted in 4,6 position are preferably hydrogenated, whereas non-substituted DBT preferably undergo direct desulfurization (Figure 2).

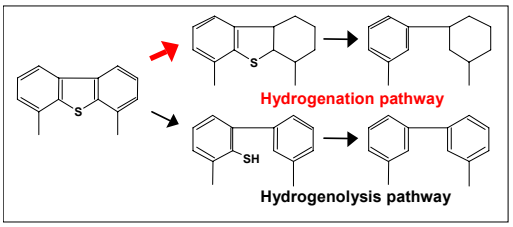

Figure 2. Preferred reaction pathway for 4,6-DiMeDBT

The quantification of each DBT compound was determined by GC-SCD analysis of feedstocks and products. The reactivity of DBT compounds has been calculated assuming a first order kinetic law. Ten feedstocks and their hydrotreated products were used for this purpose. Results for a LCO at 3 different LSHV are presented in Figure 3.

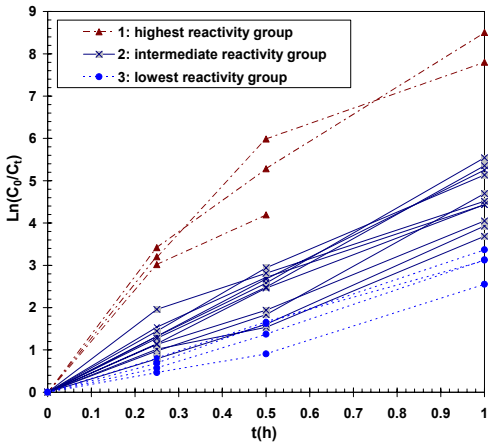

Figure 3. DBT's 1st order kinetic constants for a LCO feedstock.

This study allowed to distinguish 3 reactivity groups:

- DBT's easy to convert, with a reactivity close to the unsubstituted DBT.
- An intermediate reactivity group with a reactivity similar to 4-MeDBT.
- DBT's very difficult to convert, with a reactivity close to that of 4,6 dimethylDBT.

Table 1 presents the average ratio k_{DBT}/k_i for the 3 groups previously defined; k_{DBT} is the first order constant of DBT, k_i is the average first order constant of the considered substituted DBT. These ratios were compared to calculated average values reported by Ma et al.[7] and our results are in good agreement with those reported in literature.

Table 1. Ratio k_{DBT}/k_i of 1st order rate constants for the 3 groups

Group	This work	Ma et al.[7]
1	1.32	1.12
2	4.03	3.03
3	6.92	7.89

Kinetic Modeling. With these various results, a Langmuir-Hinshelwood lumped kinetic model was developed taking into account:

- the differences of reactivities of DBT compounds.
- the two reaction pathways for desulfurization: hydrogenation and direct hydrodesulfurization.
- the inhibiting effect of the various compounds in industrial feedstocks, especially aromatics and nitrogen compounds.

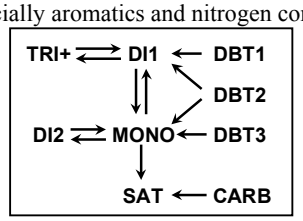

Figure 4. General kinetic scheme for diesel hydrotreating.

The kinetic scheme presented in Figure 4 is based on lumping of chemical species, as detailed in Table 2. Inhibitor effects are taken into account through competitive reaction of hydrogenation of aromatics and through competitive adsorption of H_2S, NH_3 and other species on the active sites. Through this model, HDS performances can be predicted for any diesel feedstock (straight-run, LCO and mixtures) taking into account their chemical composition. Aromatic conversion and hydrogen consumption are also predicted.

Table 2. Lumps considered in the kinetic model

Name	Description
DBT1	DBT group 1 easy to convert by direct desulfurization
DBT2	DBT group 2 with intermediate reactivity, can react through direct HDS or hydrogenation
DBT3	DBT group 3 containing the most refractory compounds, reacting through hydrogenation
S	very reactive sulfur compounds directly converted in H_2S
TRI+	polyaromatics
DI1	conjugated diaromatics
DI2	non conjugated diaromatics
MONO	monoaromatics
N	nitrogen group 1 containing very reactive nitrogen compounds directly converted in NH_3
CARB	nitrogen group 2 as carbazoles reacting by hydrogenation
SAT	saturated compounds

Figure 5 presents a parity plot between results from pilot plant experimentation and from reactor simulation, of straight run gasoil, LCO gasoil and mixtures. For all feedstocks, model prediction is close to experimental results.

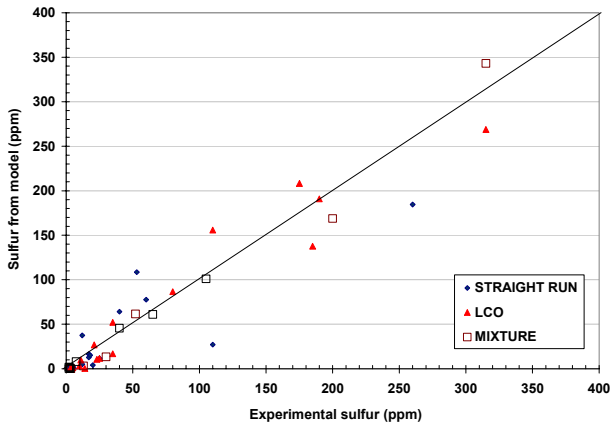

Figure 5. Sulfur prediction parity plot for different type of diesels.

Conclusions

An accurate analysis method for sulfur speciation was developed and allowed to elaborate a kinetic hydrotreating model adapted to ULSD prediction for industrial feedstocks. This model is based on a lumped reaction scheme distinguishing three refractory sulfur families thanks to the identification. The Langmuir-Hinshelwood representation takes into account the inhibiting effect of aromatics and nitrogen species on HDS. A good agreement between most experimental and predicted sulfur content was obtained. The effect of nitrogen species will be subject to further study in order to improve the HDS predictions.

References

(1) Burkhardt T., Verstraete J., Galtier P., Kraume M. *Chemical Engineering Science*. **2002**, *57*, 1859-1866.
(2) Castex H., Boulet R., Juguin J., Lepinasse A. *Revue de l'Institut Français du Pétrole*. **1983**, *38*(4), 523-532.
(3) Houalla M, Broderick D.H., Sapre A.V., Nag N.K., De Beer V.H.J., Gates B.C., Kwart H. *Journal of Catalysis*. **1980**, *61*, 523-527.
(4) Whitehurst D.D., Isoda T., Mochida I. *Advances in Catalysis*. **1998**, *42*, 345-471.
(5) Meille V., Schulz E., Lemaire M., Vrinat M. *Applied Catalysis A: General*. **1999**, *187*, 179-186.
(6) C. López García, M. Becchi, M.F. Grenier-Loustalot, O. Païsse, R. Szymanski. *Anal. Chem.* **2002**, *74*, 3849-3857.
(7) Ma X., Sakanishi K., Mochida I. *Ind. Eng. Chem. Res*. **1994**, *33*, 218-222.

FLAMMABILITY CHARACTERISTICS OF PURE HYDROCARBONS

Tareq A. Albahri

Chemical Engineering Dept. - Kuwait University
P.O.Box 5969 - Safat 13060, Kuwait

Introduction

The flammability characteristics of chemical substances are very important for safety considerations in storage, processing, and handling. These characteristics which include the flash point temperature (FPT), the auto ignition temperature (AIT), and the upper and lower flammability limits (UFL, LFL) are some of the most important safety specifications that must be considered in assessing the overall flammability hazard potential of a chemical substance, defined as the degree of susceptibility to ignition or release of energy under varying environmental conditions. Experimental values of these properties are always desirable, however, they are scars and expensive to obtain. When experimental values are not available and determining them by experimental means is not practical, a prediction method which is desirably convenient and fast must be used to estimate them.

Technical Development

When the flammability characteristics cannot be determined experimentally, empirical equations for their determination are available. However, these methods available in the literature for estimation of the flash point[1,2,3,4,5,6], the autoignition temperature[7], the upper and lower flammability limits[1,8,9,10, 11] are not very accurate and sometimes produce serious errors. Here we develop a structural group contribution (SGC) method[12] to predict the FPT, AIT, UFL, and LFL of pure hydrocarbons with higher accuracy than the above methods that can be applied with less difficulty using only the molecular structure of the compound. The method is notable for the absence of any theoretical procedure which has previously been used to estimate the AIT of pure substances from only their molecular structure.

The structural groups derived from the Joback group contribution approach[12], with some modification, and their contribution values are shown in Table 1 for calculating the flash point as an example. Other structural groups and their contribution values have been developed for the AIT, LFL, and UFL. The target property are calculated using the following non-linear equation[13],

$$\Phi = \left[a + b\left(\sum_i (\Phi)_i \right) + c\left(\sum_i (\Phi)_i \right)^2 + d\left(\sum_i (\Phi)_i \right)^3 + e\left(\sum_i (\Phi)_i \right)^4 \right] \quad (1)$$

where Φ is FPT, AIT, UFL, or LFL, ∑(Φ)i is the sum of the molecular structure group contributions for FPT (Table 1), AIT, UFL, or LFL (not shown), and a, b, c, d, and e are constants from Table 2.

The data on the flammability properties of more than 500 pure substances were obtained from the property databanks of the AIChE-DIPPR[14] on the AIT and the API-TDB[15] on the FPT, UFL, and LFL. An optimization algorithm based on the least square method was used to probe the structural groups and calculate their contribution values to the target property. The nonlinear regression algorithm minimizes the sum of the difference between the calculated and experimental values of the target properties using the solver function in Microsoft Excel. Convergence was always achieved in less than one minute on a Pentium IV-1.7GHz PC. The average deviations in the predicted properties for all types of hydrocarbons are shown in Table 3. The accuracy of the model predictions are shown in Figures 1 and 2 as examples.

Table 3. SGC values for estimation of the flash point temperature.

HC type	Serial no.	Group	$(FPT)_i$
Paraffins	1	$-CH_3$	0.4832
	2	$>CH_2$	0.5603
	3	α- >CH−	0.5275
	4	β- >CH−	0.5499
	5	g- >CH−	0.4778
	6	δ- >CH−	0.4543
	7	α- >C<	0.4008
	8	β- >C<	0.5281
	9	$-C_2H_5$ (branch)	1.0370
Olefins	10	$=CH_2$	0.4078
	11	=CH−	0.6037
	12	=CH− (cis)	0.5913
	13	=CH− (trans)	0.6216
	14	α- >C=	0.7135
	15	β- >C=	0.6550
	16	=C=	0.8659
	17	≡CH	0.4475
	18	≡C−	0.8387
Cyclic	19	$>CH_2$	0.6080
	20	>CH−	0.4217
	21	α- >CH− (cis)	0.7148
	22	α- >CH− (trans)	0.6986
	23	β- >CH− (cis)	0.6518
	24	β- >CH− (trans)	0.4601
	25	g- >CH− (cis)	0.7167
	26	g- >CH− (trans)	0.5899
	27	>C<	0.1847
	28	=CH−	0.5287
Aromatics	29	=CH−	0.6205
	30	$>CH_2$	1.5159
	31	>C= (fused)	0.8898
	32	>C=	0.6150
	33	>C= (ortho)	0.7535
	34	>C= (meta)	0.7384
	35	>C= (para)	0.7675

Groups 32 through 35 are all non-fused. In non-cyclic compounds, α-, β-, g-, and δ- refer to the second, third, fourth, and fifth positions along the HC chain, respectively. In cyclic compounds, α-, β-, and g- refer to the second, third, and fourth position along the cyclic ring with respect to group 20, respectively.

Table 2. Coefficients for Equation (1).

Property	a	b	c	d	e
FPT	84.65	64.18	-5.6345	0.360	-0.0101
AIT	780.42	26.78	-2.5887	-0.3195	-0.007825
UFL	18.14	3.4135	0.3587	0.01747	3.403E-04
LFL	4.174	0.8093	0.0689	0.00265	3.76E-05

Table 3. Statistical analysis for the flammability predictions of Equation (1)

Property	No. of data points	Property Range	R^2	Average deviation
FPT	287	165 - 511 K	0.99	1.68 % [a]
AIT	131	473 - 828 K	0.92	4.20 % [a]
UFL	464	4 - 100 V%	0.96	1.25 V% [b]
LFL	454	0.11 - 6 V%	0.93	0.04 V% [b]

[a] Ave. % error, [b] Difference between experimental and calculated values.

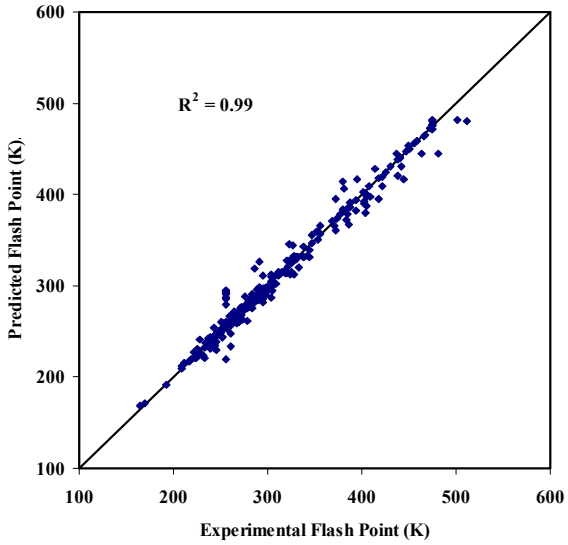

Figure 1. Parity plot for the flash point temperature of 299 pure hydrocarbon liquids using SGC values from Table (1).

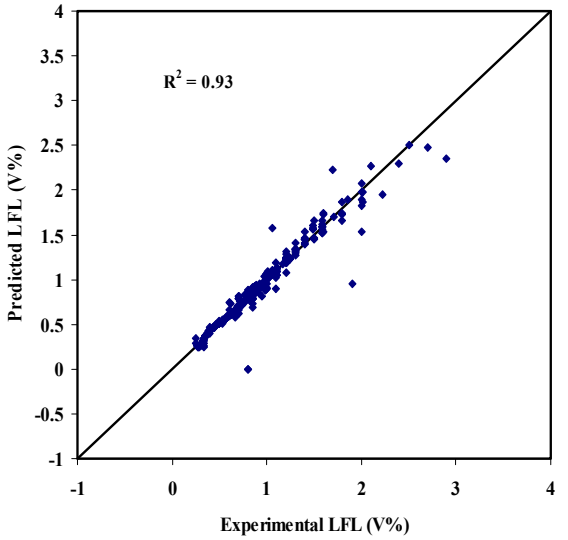

Figure 2. Parity plot for the LFL of 472 pure hydrocarbon liquids using the SGC method.

Discussion

The model predictions were in excellent agreement of the experimental data for all the properties investigated as shown in Table 3. The correlation of the predictions of the proposed model shows the superiority of the SGC method over the other methods in the literature. The maximum errors and deviations for all the predicted properties are also satisfactory. The structure-based group contribution technique proves to be a powerful tool for predicting the flammability characteristics of pure hydrocarbon liquids. The clear advantage of the method is its ability to estimate the FPT, AIT, UFL, and LFL of a hydrocarbon substance provided that the chemical structure is known. Another advantage is the ability of the method to probe the structural groups that have significant contribution to the overall flammability property of pure components.

This work demonstrates that the complex flammability properties can be modeled by a simple SGC method using non-linear-regression optimization models. Considering the difficulty and complexity of developing a first principles model of the flammability characteristics involving the kinetics and dynamics of combustion on the molecular level, the SGC method can be an effective alternative. The SGC predictive models can learn about inherent relationships among various structural groups and their contribution to the overall flammability property of the molecule such as group interactions, structural orientation, skew, hindrance, steric, resonance, inductive, and chiral effects that are usually unknown. Furthermore, the method is based on the molecule's structural data which is always known. Once properly developed, SGCs offer predictions quickly and accurately on a personal computer using a spreadsheet. The SGC method can also be used for synthesizing molecules (i.e. choosing a molecule with a desired property). This can be done by invoking the inverse property of the model; what is the best combination of inputs that lead to certain outputs.

The SGC method is especially useful for the automatic generation and reliable estimation of AIT, FPT, UFL, and LFL of pure component for which no data exists. The method may be used in predictive models to estimate the flammability characteristics for light petroleum fuels such as naphtha and gasoline, using proper mixing rules and interaction parameters, when the molecular composition is known[16]. Finally, the method is notable for the absence of any group contribution method which has previously been used to estimate the AIT of pure hydrocarbon liquids from only their structure.

Acknowledgment. This work is part of a project on the simulation of light petroleum fractions supported by Kuwait University research grant no. EC 04/01.

References

(1) Bodhurtha, F. P. Industrial Explosion Prevention and Protection, Mc-Graw-Hill, New York, 1980.
(2) Riazi, M. R. and Daubert, T. E. Hydrocarbon Processing. 56, 81-83, 1987.
(3) Patil, G. S. Fire and Materials, 12, 127-131, 1988.
(4) Satyanarayana, K. and Kakati, M. C. Fire and Materials, vol. 15, pp. 97-100, 1991.
(5) Jones, J. C. Journal of FIRE SCIENCES, vol. 16, pp. 222-229, May/June 1998.
(6) Suzuki, T.; Ohtaguchi, K.; Koide, K. J. of Chem. Eng. of Japan, 1991, 24 (2), 258-261.
(7) Suzuki, T. Fire & Materials. 1994, 18, 81-88.
(8) Crowl, D. A. and Louvar, J. F. Chemical Process Safety, Fundamentals with Applications, Prentice Hall, Englewood Cliffs, 1990.
(9) Santamaría-Ramiro, J. M. and Braña-Aísa, P. A. Risk Analysis and Reduction in the chemical Process Industry, Chapman & Hall, New York, 1998, p.64.
(10) Martin S. High, Ronald P. Danner, Ind. Eng. Chem. Res. 1987, 26, 1395-1399.
(11) William H. Seaton, J. of Hazardous Materials, 1991, 27, 169-185.
(12) Reid, R.C.; Prausnitz, J.M.; Polling B.E.; The properties of gases and liquids, Hill: N.Y., 1987.
(13) Albahri, T. A. Ind. and Eng. Chem. Res., in press.
(14) American Institute of Chemical Engineers, DIPPR Project 801Pure Component Data in DIPPRO, public version, January 31, 1996.
(15) The American Petroleum Institute and EPCON international, API Technical Database V2.1.1, 2000.
(16) Neurock, M; Nigam, A.; Trauth, D.; Klein, M.T, Chemical Engineering Science, 1994, 49(24A), 4153-4177.

CATALYSTS FOR THE HYDROGEN ECONOMY

ROBERT J. FARRAUTO

ENGELHARD CORPORATION,
101 WOOD AVENUE, ISELIN, NJ 08830

Pollution emissions from mobile sources have been controlled for the last 30 years by monolithic catalysts in the exhaust system. The catalysts enhance the rate of conversion of unburned CO, HC and NO_x to harmless products. Throughout the world emission standards are becoming ever more stringent, thus demanding more from the catalyst and engineering design of the power source. Furthermore, fossil fuel combustion generates large quantities of green house gases such as CO_2. The widespread use of fuel efficient lean burn vehicles (diesel) is hindered by lack of an adequate technology for NO_x reduction. Although progress has been made with NO_x -storage systems, especially in Japan, the presence of sulfur and complicated regeneration requirements have hindered their application. As diesel engines gain in popularity due to their fuel efficiencies the problem of dry particulate removal from the exhaust must be managed. Although all of these problems are being addressed we must continue to be aware of the negative consequences of not having alternative technologies for energy and power generation.

The problem of limited energy supply, generation of primary pollutants and green house gases is raising the importance of a hydrogen economy and the need to investigate alternative means of power generation from reliable and ideally renewable- sources of fuel. The fuel cell is a critical technology for the future.

The fuel cell generates power by direct conversion of chemical energy, i.e. H_2 and O_2, to electrical energy avoiding the traditional combustion processes that generate pollutants (Appleby 1999; St Pierre and Wilkinson 2001). Furthermore, the system power efficiency is no longer limited by the Carnot cycle in which chemicals must be first combusted to produce mechanical energy. Greater efficiency translates to energy conservation and lower emissions of CO_2 depending on the source of hydrogen necessary to operate the fuel cell. For this reason there has been tremendous research in attempting to develop fuel cells as an alternative to conventional combustion systems used for power generation. Ideally one can envision a system whereby natural sources of energy such as solar, wind, geothermal, hydroelectric, etc. can be used to extract hydrogen from water producing an essentially inexhaustible source of energy needed to operate a fuel cell. Natural gas is the logical fuel to convert to hydrogen during the transition to renewable sources.

There are four basic fuel cells systems, solid polymer electrolyte or the proton exchange membrane (PEM) with efficiency close to 40%, phosphoric acid (PAFC) at 45%, molten carbonate (MCFC) and solid oxide (SOFC) both between 60-70%. Each has its own particular application in diverse markets (Heck et al 2002). Alkaline fuel cells continue to be used for space applications but these require ultra clean pure hydrogen and oxygen and hence are not considered feasible for more earthly applications. Phosphoric acid fuel cells are operating throughout the world powering large buildings (> 250Kw) but are not considered cost effective for lower power applications.

The most highly visible fuel cell applications are for vehicles. Toyota and Honda have produced a few PEM powered fuel cell vehicles currently being demonstrated in the US and Japan but it is now widely accepted that the market will not be realized until at the earliest 2010 mass production. Most automobile companies have abandoned the concept of generating hydrogen on-board from gasoline in favor of hydrogen storage. The later technology is critical for the implementation of fuel cell vehicles (Dagini 2002). The most feasible concept is to develop a hydrogen infrastructure where your local service station provides hydrogen generated from natural gas that is then stored on-board the vehicle as a liquid, gas or solid hydride.

An early market for PEM fuel cells will be residential or distributed power for homes. The concept is to reform natural gas or LPG in the home to provide H_2 for the anode of the PEM fuel cell. A common thread in all applications is the safe and compact generation of the H_2 by catalytic reforming of the liquid or gaseous fuel (Katikaneni and Song 2002).

Today's lecture will briefly describe the principles of the PEM fuel cell and the unit operations for the catalytic generation of hydrogen from fossil fuels.

References:

Appleby, A. "The electrochemical engine for vehicles" Scientific American 281 (1) 1999

Dagini, R. "Tempest in a tiny tube" Chemical Engineering News, January 14, 25, 2002

Heck, R., Farrauto, R. with Gulati, S. "Catalytic air pollution control: commercial technology" second edition, Wiley and Sons, NY. 2002

Katikaneni, S. and Song, C. " Fuel processing for fuel cells" Catalysis Today 77 (1,2) 2002

St. Pierre, J. and D. Wilkinson, "Fuel cells a new, efficient and cleaner power source" AIChE Journal 47, 1482 (2001)

DESULFURIZATION BY ADSORPTION AND CATALYTIC STEAM REFORMING OF DIESEL FOR FUEL CELL APPLICATIONS

Shaker Haji, Joanna Ziemlewski, and Can Erkey

Department of Chemical Engineering
Environmental Engineering Program
University of Connecticut
Storrs, CT 06269-3222

Introduction

Hydrogen is the ideal fuel for PEM Fuel Cells in terms of system integration. The lack of an infrastructure for distribution of hydrogen necessitates the development of technologies for production of hydrogen from other sources such as methanol, gasoline and diesel. Liquid fuels can be converted to H_2 by a series of steps which include oxidation or steam reforming, high temperature shift conversion, low temperature shift conversion and preferential oxidation.[1,2,3,4]

An important consideration in reforming of hydrocarbon fuels is that they contain significant amounts of sulfur containing compounds such as thiophenes, benzothiophenes and dibenzothiophenes. Currently sulfur levels in diesel and gasoline are around 500 and 300 parts per million by weight (ppmw), respectively. The presence of such compounds at such concentrations has a detrimental effect on the performance of catalysts used in reforming, water gas shift reactors, and the fuel cell stacks. For example, the presence of 100 ppm thiophene in a simulated gasoline mixture caused the hydrogen content of the effluent from the fuel processing unit to drop from 60 to 40 % over a 25 hours reaction time.[3] It is generally agreed that hydrocarbon fuels need to be desulfurizered to concentrations less than 0.1 ppm sulfur which necessitate incorporation of desulfurization technologies into the fuel processor.[5]

The use of diesel as a source of hydrogen for PEM fuel cells is advantageous since:

1. diesel has a much higher energy density than other fuels (42.5 MJ/kg, LHV for diesel vs. 20.0 MJ/kg LHV for methanol),
2. diesel fuel infrastructure is already in place.

However, reforming of diesel fuel is complicated and requires high temperatures.

In this article, we report our results on the use of carbon aerogels as an adsorbent for desulfurization of diesel. In addition, various precious metal commercial catalysts for steam reforming of diesel were tested and compared to a catalyst synthesized in house. Hexadecane was used as a model for diesel fuel while dibenzothiophene (DBT) was used as a model of sulfur compound. DBT is chosen for it is a refractory polyaromatic sulfur compound and is present in diesel in appreciable amount. The carbon aerogels were synthesized and characterized in our lab. Two different CAs with two different average pore diameters were studied. Both adsorption isotherms and approach to adsorption equilibrium curves are discussed here.

A laboratory scale reactor system was designed and constructed to investigate steam reforming of diesel for fuel cell applications. Using n-hexadecane as a surrogate diesel fuel, catalytic steam reforming was investigated at various conditions to maximize production of hydrogen.

Experimental

Carbon Aerogel. The resorcinol-formaldehyde (RF) aerogels were synthesized by the reaction of resorcinol with formaldehyde in aqueous solution in the presence of a catalyst. Two formulations were made using different catalyst amount and composition. After several days of curing the mixture, a monolith was formed and it was immersed in acetone overnight. Subsequently, acetone was extracted with liquid and supercritical carbon dioxide. Then the RF aerogels were converted to carbon aerogels by pyrolysis in an inert nitrogen atmosphere at 1085^{o}C. The carbon aerogel was characterized using nitrogen adsorption.

Sulfur Adsorption. The carbon aerogel (CA) monoliths were crushed to pass through sieves with Tyler mesh number of 14 then vacuumed for 45 min at room temperature before it was used in the adsorption experiments. The adsorption data were obtained using batch technique. A series of vials containing 160 mg CA and 7.5 g of DBT solution in n-hexadecane solution along with a stirring bar were sealed and stirred at room temperature. Stirring was continued until equilibrium was reached for determination of adsorption isotherm curves or until a specified time to follow the kinetics of adsorption. Subsequently, the solution was filtered and analyzed by gas chromatography with FID detector.

Reforming Catalysts. Several commercially available catalysts were studied, including 0.5 wt.% Pt/Al_2O_3, 0.5 wt.% Rh/Al_2O_3, and 0.5 wt.% Pd/Al_2O_3. Additionally, 1 wt.% Pt/CeO_2-ZrO_2 was synthesized via the sol-gel method using $Zr(OC_3H_7)_4$ and $Ce(NO_3)_3{\cdot}6H2O$. Platinum was incorporated into the porous support using the supercritical deposition method. The catalysts were characterized by hydrogen chemisorption, BET and XRD.

Steam Reforming. The catalyst was inserted in a 1.27 cm OD tubular reactor within a tube furnace. Fuel and water were mixed and vaporized before the entrance and fed into the reactor. The steam-to-carbon ratio was set at one and conversion of the fuel was measured in the temperature range 500 – 1000 K. The steam-to-carbon ratio was then increased to two and again conversion was measured over the same temperature range. The product stream was analyzed with a gas chromatograph equipped with a thermal conductivity detector.

Results and Discussion

Carbon aerogels (CAs) were studied as adsorbents for the desulfurization of liquid hydrocarbon fuels for fuel cell applications. The properties of CA synthesized were found to depend on the resorcinol/catalyst and resorcinol/water mole ratios. This change in properties also affected the sulfur adsorption behavior and capacity as will be shown later. Table 1 summarizes the properties of the two different CAs obtained using the two different formulations.

Table 1. Properties of the prepared carbon aerogels.

Formulation	S_{tot} (m^2/g)	D (nm)		V_{tot} (cm^3/g)	V_{mic} (cm^3/g)	S_{mic} (m^2/g)	V_{mic}/V_{tot} (%)
	BET	BET	BJH		t-plot		
F1	741	4.1	4.3	0.78	0.12	252	15.4
F2	670	21.1	22.2	3.63	0.12	233	3.3

S_{tot}: BET total surface area. D: average pore diameter. V_{tot}: total pore volume. V_{mic}: micropore volume. S_{mic}: micropore surface area.

First, an approach to equilibrium data was obtained to study the behavior of the sulfur-compound (DBT) adsorption onto CA. This was tested with a solution of 250 ppmw of DBT (43.5 ppmw S content) in n-HD. It took around 8 days for the adsorption process to reach to equilibrium. That could be explained by the presence of micropores in the CAs, which slows down the DBT adsorption process. The 4 nm CA adsorbed 93% of the sulfur initially present in the solution, while the 22 nm CA adsorbed 98.5% of it. Though the 4 nm CA has larger surface area, the 22 nm CA adsorbed more DBT than the earlier one. Figure 3 shows the first 24 hours of the adsorption process. The observation in the difference in the adsorption rate, with the two different CAs, may be attributed to the difference in the pore diameter.

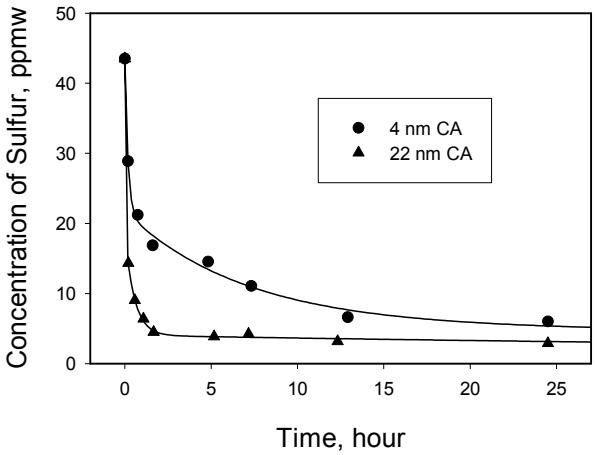

Figure 1. The approach to equilibrium curves for the adsorption of DBT on CA.

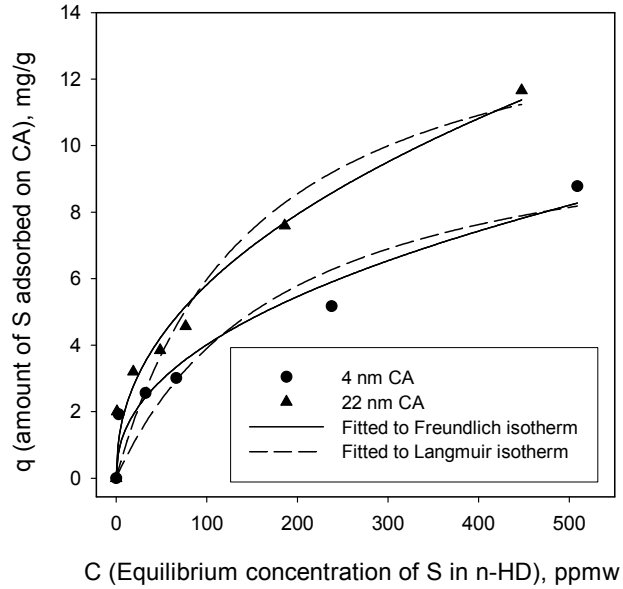

Figure 2. Adsorption isotherms for DBT at room temperature on CA. The experimental data is fitted to the equations of Freundlich and Langmuir isotherms.

Figure 2 illustrates the adsorption isotherms for DBT on the two different pore size CAs at room temperature and atmospheric pressure. As the initial concentration of sulfur in the solution increased, the amount of DBT adsorbed on CA increased. Up to the range of the initial sulfur concentration in these sets of experiments (4000 ppmw DBT = 696 ppmw S), the loading of DBT on CA is far from saturation. The trend of the adsorption isotherms shows that the 22 nm CA has higher sulfur adsorption capacity than the 4 nm CA. For a given sulfur concentration in the solution, the equilibrium adsorbed amount of DBT on the 22 nm CA is higher than that on the 4 nm CA. It was expected that the 4 nm CA would adsorb more amount of the sulfur compound (DBT) than the 22 nm CA, since the former has higher surface area. However, this was not the case. This demonstrates that changing the initial concentrations of the reactants and the catalyst not only changes the pore size, but also changes the chemical structure and the physical/chemical properties of the surface of the carbon aerogel. The adsorption isotherms for the adsorption of DBT on both carbon aerogels were fitted to both Freundlich and Langmuir isotherms, as shown in Figure 2. The Langmuir model corroborates what was mentioned earlier that the 22 nm CA has higher sulfur adsorption capacity than the 4 nm CA, giving an adsorption capacity different by 35%.

When DBT and NA are equally present in the solution (1.04 mM each), both carbon aerogels showed selectivity in adsorption for DBT. Both CAs have similar selectivity, 1.61 and 1.47 moles DBT adsorbed/moles NA adsorbed for 4 nm and 22 nm CA, respectively. However, the presence of NA in n-HD reduced the amount of DBT adsorbed onto both CA by around 6 %. This means that if the diesel fuel contains high concentration of aromatic compounds that are similar in structure with sulfur compounds, then the capacity of the carbon aerogel will be reduced.

For steam reforming of diesel, the product stream included H_2, CO, CO_2, ethane, ethylene, and methane. Conversion of both the hexadecane and water increased with increasing temperature for each type of catalyst. The higher temperatures also resulted in little amounts of ethane and ethylene. However, the CO_2:CO ratio decreased, due to reverse water gas shift at higher temperatures. Additionally, raising the steam-to-carbon ratio increased the CO_2:CO ratio. The effluent gas compositions were close to the values calculated from equilibrium calculations using Gibbs Free Energy Minimization. Furthermore, it was found that CeO_2-ZrO_2 as a support was more active than Al_2O_3.

Acknowledgment. This work was supported by the U.S. Army.

References

1. Brown, L.F., Int. J. Hydrogen Energy, 2001, 26, 381-397.
2. Joensen, F., Rostrup-Nielsen, J. R., J. Power Sources 2002, 105(2), 195-201.
3. Moon, D.J., Sreekumar, K., Lee, S.D., Lee, B.G., Kim, H.S., Appl.Catal. A: Gen., 2001, 215(1-2), 1-9.
4. Yanhui, W.; Diyong, W., Int. J. Hydrogen Energy, 2001, 26(8), 795-800.
5. Larminie, J., Dicks, A., Fuel Cell Systems Explained; John Wiley & Sons: England, 2002.

ADSORPTIVE DESULFURIZATION OF JP-8 JET FUEL AND ITS LIGHT FRACTION OVER NICKEL-BASED ADSORBENTS FOR FUEL CELL APPLICATIONS

*Xiaoliang Ma, Subramani Velu, Lu Sun, and Chunshan Song**

Clean Fuels and Catalysis Program, The Energy Institute and Department of Energy and Geo-Environmental Engineering, Pennsylvania State University, University Park, PA 16802
*E-mail: csong@psu.edu
Mehdi Namazian, and Siva Sethuraman

Altex Technologies Corporation, 650 Nuttman Road, Santa Clara, CA 95054

Introduction

Fuel cell is one of the most promising and convenient energy conversion devices for generating electricity for mobile vehicles, portable power and stationary power plants. For the automotive fuel cells and micro-fuel cells, liquid hydrocarbon fuels are promising candidate fuels due to their higher energy density, availability, and safety (1). For the military fuel cells applications, jet fuel (JP-8) is a widely used logistic fuel. However, the sulfur level in JP-8 can be as high as 3000 ppm, as per the fuel spec, but in practice ranges from 400 to 1600 ppmw (2). The major sulfur compounds in JP-8 are alkyl sulfur compounds, especially 2,3-dimethylbenzo-thiophene (2,3-DMBT) and 2,3,7-trimethyl-benzothiophene (2,3,7-TMBT) (3,4). The sulfur compounds in the fuel, and the resulting H_2S, produced during reforming process, are poisonous to the catalysts used in the reformer and the subsequent water-gas-shift system, and also to the electrode catalysts in fuel cell stack (1). Thus, the sulfur compounds in the liquid hydrocarbons have to be reduced to less than 0.1 ppmw for polymer electrolyte membrane fuel cell (PEMFC) and at least less than 30 ppmw for the solid oxide fuel cell (SOFC). The conventional hydrodesulfurization processes operate at high temperature (300-400˚C) and require high-pressure hydrogen (30-80 kg/cm^2) and are not able to achieve such a low sulfur level economically (5). Consequently, the current hydrotreating technology is not suitable for meeting the need of ultra-clean liquid hydrocarbon fuels for the fuel cell applications.

Development of new deep desulfurization processes of the liquid hydrocarbon fuels has become one of the major challenges in developing the hydrocarbon processor for fuel cell applications. In our previous work, we proposed a process at Penn State University based on selective adsorption for removing sulfur (PSU-SARS) for on-board and on-site desulfurization (4-10). We have prepared, synthesized and tested many potential adsorbents, including metal complex, metal ions exchanged zeolites, carbon materials, reduced metals, metal halides, metal sulfides, and metal oxides with and without supports. In this paper, we report our current approaches in the adsorptive desulfurization of real jet fuels and fractionated fuels over nickel-based adsorbents.

Experimental

The JP-8 jet fuel used in the present study was provided by US Air Force Wright Laboratory. From total sulfur analysis, the sulfur concentration in this jet fuel is 736 ppmw. A light fraction (light JP-8) of JP-8 with sulfur concentration of 380 ppmw was obtained from this JP-8 fuel by fractionation to cut off about 30 wt % of the fuel (heavy fraction). The adsorbents (Adsorbent-2 and Adsorbent-5) used in the present study are nickel-based materials. Adsorbent-2 has a surface area around 90 m^2/g without any support, while Adsorbent-5 has a surface area around 150 m^2/g with alumina support. The adsorption experiments were performed under ambient pressure in a fixed-bed adsorption device, which was described in detail in one of our previous papers (8). The fuel was fed into the adsorption column through a LC pump and flowed down through the adsorption bed. Analysis of sulfur compounds in the JP-8 fuels and treated fuels was performed by using GC with a capillary column, XTI-5 (Restek) 30 m x 0.25 mm x 0.25 micrometer, and a pulsed flame photometric detector (PFPD). The method for identifying the sulfur compounds in the fuel was described in a previous paper (4). An Antek 9000 Series Sulfur Analyzer (detection limit 0.5 ppmw) was used for the determination of total sulfur in the fresh fuels and treated fuels.

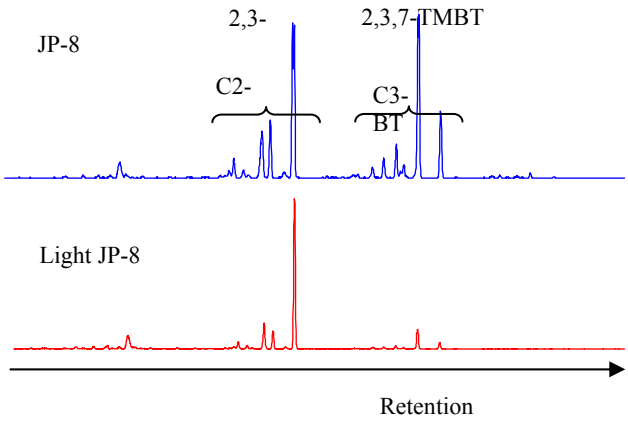

Figure 1. GC-PFPD chromatogram of JP-8 and light JP-8.

Results and Discussion

The major sulfur compounds in the JP-8 and in the light fraction of JP-8 are the alkyl benzothiophenes with two to three carbon atoms in the alkyl group(s), as shown in Figure 1.

The breakthrough curves for adsorptive desulfurization of the light JP-8 over Adsorbent-2 at 27 ˚C and 200 ˚C are shown in Figure 2. It is clear that at the operating temperature of 27 ˚C, the sulfur concentration in the treated light JP-8 is less than 1 ppmw before the effluent amount increases to 8 g/g (gram of the treated light JP-8 per gram of the adsorbent), indicating that almost all sulfur in the JP-8 is removed by the selective adsorption. After 8 g/g of effluent amount, the sulfur concentration increases sharply with increasing elution fuel volume. At the operating temperature of 200 ºC, the breakthrough curve is similar to that at 27 ºC before 8 g/g of effluent amount, but after this point, the sulfur concentration increases slowly with further increasing elution volume, being only 60 ppmw at 56 g/g of effluent amount. This result implies that the increase in temperature results in better desulfurization performance of Adsorbent-2.

From comparison of adsorptive desulfurization of the two fuels over Adsorbent-2 at 200 ºC, as shown in Figure 2, the breakthrough point for the whole JP-8 fuel at a sulfur level of 1 ppmw is 2 g/g, and then, the sulfur concentration in effluent increases much more quickly than that for the light JP-8. One of the reasons is that the total sulfur concentration in the initial JP-8 is about two times higher than that of the initial light JP-8.

Among the two adsorbents (Adsorbent-2 and Adsorbent-5) for desulfurization of the JP-8 at 200 ºC, the breakthrough curve for Adsorbent-5 is below that for Adsorbent-2, indicating that Adsorbent-5 has better performance for adsorptive desulfurization than Adsorbent-2, probably because Adsorbent-5 has higher surface area than that of Adsorbent-2.

Figure 3 shows the adsorptive capacity as a function of outlet sulfur concentration. The adsorptive capacities were calculated by integration of the Figure 2 curves. From comparison between

Adsorbent-2 and Adsorbent-5 for adsorptive desulfurization of the JP-8 at 200 ºC, the breakthrough capacity of the former at 30 ppmw sulfur level is 11.5 mg/g, while the latter is 5.0 mg/g, indicating again that Adsorbent-5 is significantly better than Adsorbent-2. The highest adsorptive capacity in the four cases shown in Figure 3 is 16 mg/g (milligram of sulfur per gram of adsorbent) at a breakthrough sulfur level of 30 ppmw for the light JP-8 over Adssorbent-2 at 200 ˚C, 4.8 h^{-1} of LHSV. It is more than 3 times higher than that for the light JP-8 over Adsorbent-2 at 27 ˚C, 24 h^{-1} of LHSV.

In comparison between the light JP-8 and the JP-8 over Adsorbent-2 at the same operating conditions, it is of interest to note that the breakthrough capacity for the light JP-8 is about 3 times higher than that for the JP-8. The results indicate that the adsorptive capacity is not only dependent on the adsorbent but also dependent on the operating conditions and the fuel composition.

Analysis of the effluent by GC-PFPD shows that the first breakthrough sulfur compounds in the adsorptive desulfurization of the JP-8 is 2,3,7-TMBT, indicating that the adsorbent has lower selectivity for 2,3,7-TMBT than for 2,3-DMBT. This result implies that at least a part of adsorption sites on the surface have only weak interaction with 2,3,7-TMBT, probably due to the steric hindrance of the methyl group at the 7-position of benzothiothene. As shown in Figure 1, the concentration of 2,3,7-TMBT in the JP-8 is much higher than that in the light JP-8. This is probably the main reason why the breakthrough capacity of the adsorbent for the whole JP-8 fuel is lower than that for the light JP-8. Another reason is that the heavy aromatics coexisting in the JP-8 might affect the adsorptive capacity of the adsorbent.

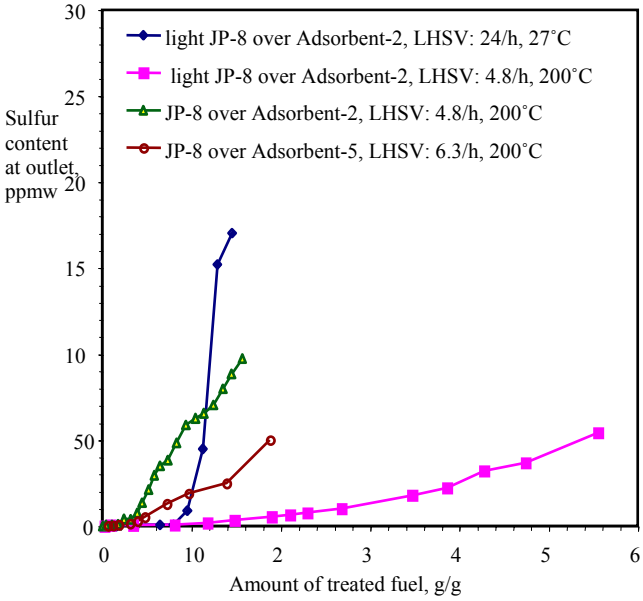

Figure 2 Breakthrough curves for adsorptive desulfurization.

Conclusions

The results presented here indicate that the nickel-based adsorbents show higher adsorptive capacity and selectivity for removing sulfur from real JP-8 fuels. The adsorptive capacity is not only dependent on the adsorbent but also dependent on the operating conditions and the fuel composition. The breakthrough capacity of Adsorbent-2 for desulfurization of the light JP-8 at 200 ˚C corresponding to 30 ppmw sulfur level is 16 mg/g. The alkyl group at the 7-position of benzothiophene appears to inhibit the approach of the alkyl benzothiophene to the adsorptive sites through the steric hindrance, resulting in the low adsorptive selectivity for such sulfur compounds.

Acknowledgments. This work was supported in part by US Department of Defense (DARPA Palm Power Program) and in part by US Department of Energy (National Energy Technology Laboratory). We are grateful to the DARPA Palm Power Program management team and DOE/NETL project management for helpful discussions, and for permission to publish this work.

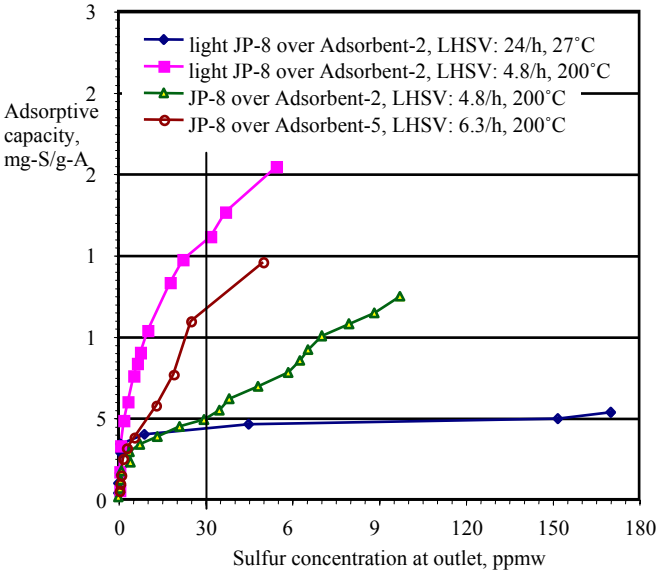

Figure 3 Adsorptive capacity as a function of sulfur concentration at outlet

References

(1) Song, C., *Catalysis Today*, 77 (1), 17-50 (2002).
(2) Edwards, T., *Am. Chem. Soc. Div. Petrol. Chem. Prepr.,* 45, 436-439 (2000).
(3) Ma, X., Sprague, M., Sun, L., and Song, C., *Prepr., Div. Pet. Chem., Am. Chem. Soc*., 47, 48-49 (2002).
(4) Ma, X, Sun, L., and Song, C., *Catal. Today*, 77, 107-116 (2002).
(5) Song, C., Ma, X., *Appl. Catal. B.,* 41, 207-238 (2003).
(6) Velu, S., Ma, X., and Song, C., *Am. Chem. Soc. Div. Petr. Chem. Prepr.,* 48, 58-59 (2003).
(7) Velu, S., Watanabe, S., Ma, X., and Song, C., *Am. Chem. Soc. Div. Petr. Chem. Prepr.,* 48, 56-57 (2003).
(8) Ma, X., Sprague, M., Sun, L., and Song, C., *Am. Chem. Soc. Div. Fuel Chem. Prep.,* 47, 452 (2002).
(9) Velu, S., Ma, X., and Song, C., *Am. Chem. Soc. Div. Fuel Chem. Prep.,* 47, 457 (2002).
(10) Ma, X., Sun, L., Yin, Z. and Song, C., *Am. Chem. Soc. Div. Fuel Chem. Prep.,* 46, 648-649 (2001).

ADSORPTION/OXIDATION OF METHYL MERCAPTAN ON ACTIVATED CARBONS

Svetlana Bashkova[2], Andrey Bagreev[1] and Teresa J. Bandosz[1]

[1]Department of Chemistry, the City College of New York and the [2]Graduate School of the City University of New York, 138th street and Convent Ave, New York, NY 10031; e-mail: tbandosz@ccny.cuny.edu

Introduction

The process of removal of mercaptans is of great scientific and practical importance.

Mercaptans (thiols) are highly reactive sulfur-containing species well known for their disagreeable odors. The most volatile of thiols is methyl mercaptan (CH_3SH), which is one of the natural sources of sulfur emitted into the atmosphere. It is a colorless gas with a smell like rotten cabbage. Methyl mercaptan has very low odor threshold (one part in 5 x 10^{10} parts of air) [1] and therefore is added at low concentrations to natural gas to detect the leak if it develops. Occupational exposure limit for CH_3SH is 0.5 ppm or 0.9 mg/m^3. At a higher concentrations methyl mercaptan becomes very toxic and may cause harmful health effects.

Taking into account the chemical and physical features of methyl mercaptan molecule [2], it can be adsorbed at room temperature and presence of air on the activated carbon surface in small pores via dispersive interactions. On the surface of the carbons methyl mercaptan is converted to dimethyl disulfide (DMDS) the adsorption of which at room temperature is much stronger then that of methyl mercaptan (MM) [2].

An objective of this paper is to describe the adsorption/oxidation of methyl mercaptan from wet air streams on commercial activated carbons, to identify the reaction products and to study the influence of the carbon surface and structural parameters on the removal/oxidation of methyl mercaptan.

Experimental

Materials. Adsorption of methyl mercaptan was performed on four samples of activated carbons of various origins. Among the carbons studied were BAX-1500 (wood based -Westvaco), S208 (coconut shell - Waterlink Barnabey and Sutcliffe), BPL (bituminous coal - Calgon) and PCB (coconut shell-Calgon).

The as received materials were studied as adsorbents for methyl mercaptan in the dynamic tests described below. After this test and purging with air the samples are considered as exhausted and they are designated with an additional letter "E".

Methods. To evaluate the capacity of carbon adsorbents for CH_3SH removal under wet conditions dynamic tests were carried out at room temperature. Adsorbent samples were ground and packed into a glass column (length 370 mm, internal diameter 9 mm, bed volume 6 cm^3) and prehumidified with moist air (relative humidity 80 % at 25 ºC) for one hour. The amount of water adsorbed was then estimated from the increase in the sample weight. Moist air containing 0.3 % (3,000 ppm) CH_3SH in nitrogen was then be passed through the column of adsorbent at 0.5 L/min. The breakthrough of CH_3SH was monitored using a MicroMax monitoring system (Lumidor) with an electrochemical sensor. The adsorption capacities of each sorbent in terms of mg of CH_3SH per g of carbon can be calculated by integration of the area above the breakthrough curve and from the CH_3SH concentration in the inlet gas, flow rate, breakthrough time, and mass of sorbent. The amount of weakly adsorbed CH_3SH was evaluated by purging the adsorbent column with air immediately after the breakthrough experiment.

Nitrogen adsorption isotherms were measured using an ASAP 2010 analyzer (Micromeritics, Norcross, GA, USA) at 77K. Before the experiment the samples were degassed at 393K to constant pressure of 10^{-5} torr. The isotherms were used to calculate the specific surface area, S_{N2}; micropore volume, V_{mic} and total pore volume, V_t. All the parameters were determined using Density Functional Theory (DFT) [3,4,12].

To evaluate the surface pH a 0.4 g sample of dry adsorbent was added to 20 mL of deionized water and the suspension stirred overnight to reach equilibrium. The pH of the suspension was measured using an Accumet Basic pH meter (Fisher Scientific, Springfield, NJ, USA).

Thermal analysis was carried out using TA Instruments Thermal Analyzer (New Castle, DE, USA). The heating rate was 10 deg/min in a nitrogen atmosphere at 100 mL/min flow rate.

To get information about the oxidation products GC/MS study was done using Shimadzu Gas Chromatograph/Mass Spectrometer model QP 5050. In this case the separation was done on Shimadzu XTI –5 column (bonded 5 % phenyl) 30 m long, 0.25 mm internal diameter. Temperature programming was set to ensure the complete separation of the reaction products. The samples for analysis were received by extraction with methanol and some heating.

The surface chemistry wase evaluated using the Boehm titration method [5]. In this approach one gram of carbon sample was placed in 50 ml of the following 0.05 N solutions: sodium hydroxide, sodium carbonate, sodium bicarbonate and hydrochloric acid. The vials were sealed and shaken for 24 h and then 10 ml of each filtrate was pipetted and the excess of base or acid was titrated with HCl or NaOH.

Results and Discussion

From the breakthrough tests, methyl mercaptan breakthrough curves are obtained and collected in **Figure 1**. The results show the highest breakthrough capacity for the BPL carbon, the capacity of S208 carbon is a little smaller after that goes PCB and the smallest capacity is obtained for the BAX. According to the **Table 1**, all the carbons have approximately the same pH around 7, so the differences in their performance must lie in their structural and surface parameters.

The adsorption of MM on the carbon surface can be physical or chemical. For instance, for the BAX carbon, the amount of MM desorbed during air purging is relatively high (more than 10 %). For the other three carbons only traces of methyl mercaptan are desorbed suggesting strong adsorption of the CH_3SH and/or oxidation products.

In order to link the behavior of carbons as methyl mercaptan adsorbents to specific features of materials, the chemical analysis of the surface was done using Boehm titration [5]. The results are presented in **Table 2**. The total amount of groups can be linked to the adsorption capacities of the carbons studied (**Table 1**) for the three of our samples. Despite the highest amount of total groups for the BAX carbon, its amount of basic groups and pH (**Table 1**) may be to small for the efficient removal of CH_3SH.

To explain the dependence of the capacity on the surface pH the possible mechanism of adsorption/oxidation process is taken into consideration. It is supposed that adsorbed MM reacts with oxygen and than it is stored in the pore system in the form of DMDS [6-8].

$O_2 \rightarrow O_{2\,L}$ (1)

$O_{2\,L} \rightarrow 2\,O_{ads\text{-}L}$ (2)

$CH_3SH_{\,g} \rightarrow CH_3SH_{\,L}$ (3)

$CH_3SH_{\,L} \rightarrow CH_3S^-_{\,L} + H^+$ (4)

$CH_3S^-_{\,L} \rightarrow CH_3S^-_{\,ads\text{-}L}$ (5)

$2\,CH_3S^-_{\,ads\text{-}L} + O_{ads\text{-}L} \rightarrow CH_3SSCH_{3\,ads\text{-}L} + O^{2-}$ (6)

$O^{2-} + 2\,H^+ \rightarrow H_2O$ (7)

where subscripts g, ads, and ads-L correspond to the species in gas, adsorbed, and liquid phases, respectively; O_{ads} is dissociatively adsorbed oxygen.

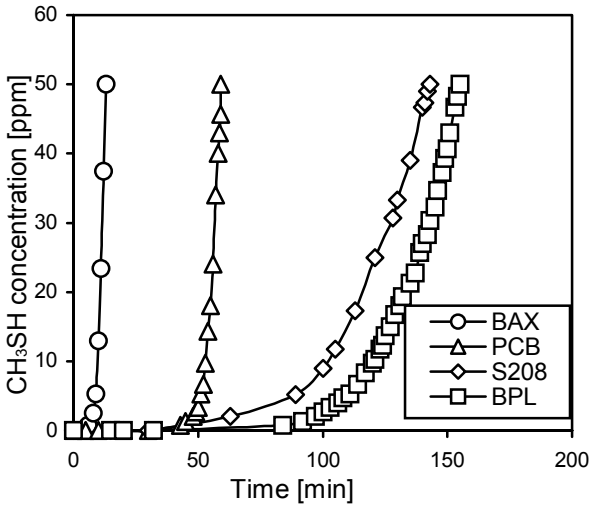

Figure 1. CH_3SH breakthrough curves.

Table 1. pH of the surface, amount of water preadsorbed, breakthrough time and CH_3SH breakthrough capacities for the materials studied.

Sample	pH	pHE	Amount of water [mg/g]	Brthr.time [min]	CH_3SH capacity [mg/g]	CH_3SH desorbed [mg/g]
BAX	7.20	6.78	163.4	13	28.2	0.48
BPL	7.41	3.82	89.9	155	216.8	0.03
S208	7.47	5.94	92.6	143	162.2	0.04
PCB	7.57	5.34	78.2	59	68.2	0.11

Table 2. Results of Boehm titration [mmol/g].

Sample	Carboxylic groups	Lactonic groups	Phenolic groups	Basic groups	Acidic groups	Total groups
BPL	0.00	0.05	0.45	0.40	0.50	0.90
S208	0.00	0.05	0.31	0.40	0.36	0.81
BAX	0.20	0.21	0.49	0.35	0.90	1.25
PCB	0.00	0.00	0.25	0.45	0.25	0.70

By solving a set of equations, describing the steps of MM dissociation and adsorption/oxidation [8], it was found that the pH where the transition in capacity may occur is about 7.5. It suggests that for all carbons with the average surface pH greater than 7.5 concentration of CH_3S^- in the adsorbed state will be equal to CH_3SH in a gas phase (100% dissociation + adsorption), which is required for effective CH_3SH removal. It is about 2.7 pH unit less than for simple dissociation in water. These results support the significance of the activated carbon surface and its effect on physicochemical processes taking place in the pore system.

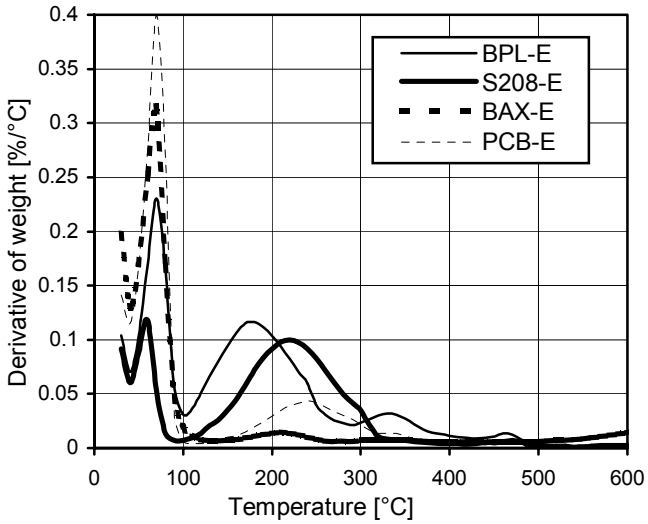

Figure 2. DTG curves in nitrogen for exhausted samples.

To study the reaction products, the GC/MS analysis was carried out [7]. Received chromatograms indicated two peaks for most of the samples: DMDS as a first peak and methyl methane thiosulfonate (MMTS) as a second peak..Intensity of the first peak is 10-50 times bigger than that of the second peak indicating formation of DMDS as a main reaction product.

Another way to investigate surface reaction products is to perform thermal analysis (TA) [6-11]. The curves received for our carbons from differential thermogravimetric analysis (DTG) are presented in **Figure 2**. DTG gives the weight derivative as a function of temperature. For all of the curves there are two major peaks present. First, centered at about 80 ºC represents desorption of water [6-7] and second, centered between 100 ºC and 300 ºC (depending on the sample) is assigned to desorption of DMDS. Methyl mercaptan physically adsorbed is very unstable, boiling temperature of CH_3SH is 4.4 – 7.5 ºC [1]. From **Figure 2** it is seen that for BPL and BAX samples DTG curves are shifted to the lower temperatures of desorption suggesting weaker adsorption of DMDS than in the case of S208 and PCB carbons which may be caused by the differences in the structural parameters between these samples. For most of the samples there is a shoulder centered at about 300 ºC, which may correspond to MMTS. This shoulder is more pronounced for BPL and S208 carbons and indeed there is more MMTS detected using GC-MS for these two samples. The formation of MMTS as one of the reaction products may partially explain the decrease in pH for our carbons (**Table 1**). Another reason for a pH decrease can be the formation of sulfonic acid adsorbed strongly adsorbed inside the carbon pores from where it cannot be easily extracted. Sulfonic acid

may also react with the carbon surface to form some derivatives strongly bonded to the carbon matrix.

From the analysis of the structural parameters [6,7], BAX and BPL are the most heterogeneous ones with the wide range of pores mostly in the mesoporous region. S208 and PCB, on the other hand, are very homogeneous with all the pores smaller than 20 Å. This may explain the weaker adsorption forces for dimethyl disulfide on BPL and BAX demonstrated by a shift of the second DTG peak to a lower temperature of desorption. Another reason for the low capacity of the BAX carbon is, even though it structurally resembles BPL, it has a small volume of the pores smaller than 10 Å [7], which should be active in the process of CH_3SH adsorption/oxidation.

Acknowledgment

This work was supported by the donors of the Petroleum Research Fund, administered by the ACS (Grant # ACS-PRF#35449-AC5).

Rferences

1. Karchmer, J.H. Wiley, New York**,** 1970, 1, 466**.**
2. Tanada, S.; Boki, K.; Matsumoto, K. *Chem. Pharm. Bull*. 1978, 26, 1527.
3. Lastoskie, C.M., Gubbins, K.E.; Quirke, N. *J. Phys. Chem*. 1993, 97, 4786.
4. Olivier, J.P. *J. Porous Materials*, 1995, 2, 9.
5. Boehm, H.P. *Carbon* 1994, 32, 759.
6. Bashkova, S.; Bagreev, A.; Bandosz. T.J. *Environ. Sci. Technol*., 2002, 36, 2777.
7. Bashkova, S.; Bagreev, A.; Bandosz. T.J. *Ind.Eng.Chem..Res*., 2002, 41, 4346.
8. Bagreev, A.; Bashkova, S.; Bandosz. T.J. *Langmuir,* 2002, 18, 8553.
9. Adib, F.; Bagreev, A.; Bandosz, T.J. *Environ. Sci. Technol***.** 2000, *34*, 686.
10. Adib, F.; Bagreev, A.; Bandosz, T.J. *J. Coll. Interface Sci*. 1999, 214, 407.
11. Adib, F.; Bagreev, A.; Bandosz, T.J. *J. Coll. Interface Sci*. 1999**,** 216, 360.
12. Gregg, S.J.; Sing, K.S.W. Academic press, New York, 1982.

MECHANISTIC INVESTIGATIONS ON THE ADSORPTION OF ORGANIC SULFUR COMPOUNDS OVER SOLID ADSORBENTS IN THE ADSORPTIVE DESULFURIZATION OF TRANSPORTATION FUELS

*S.Velu, Xiaoliang Ma and Chunshan Song**

Clean Fuels and Catalysis Program, The Energy Institute, and
Department of Energy and Geo-Environmental Engineering,
The Pennsylvania State University,
209 Academic Projects Building, University Park, PA 16802
E-mail: csong@psu.edu

Introduction

The deep removal of organic sulfur compounds from gasoline, diesel and jet fuel to produce ultra-clean transportation fuels, particularly for fuel cell applications, is becoming a paramount issue in recent years because the sulfur content in the fuel needs to be reduced to < 1 ppmw. Adsorptive desulfurization is a promising approach to produce fuel cell grade gasoline and diesel at relatively low temperature and low pressure without using hydrogen gas, and advantageous compared to the conventional hydrodesulfurization method that uses high temperature and high hydrogen pressure.[1]

Adsorptive desulfurization is based on the ability of a solid adsorbent to selectively adsorb organic sulfur compounds from liquid transportation fuels. Since these fuels consist of various thiophenic sulfur compounds together with considerable amount of aromatics and olefins, the selective removal of sulfur compounds is challenging. A new concept developed at Penn State University known as selective adsorption for removing sulfur (PSU-SARS) is being explored in our laboratory with a variety of adsorbents based on various materials such as zeolites, metal compounds, and mixed metal oxides.[1-3]

In order to develop a selective adsorbent for removing sulfur compounds, it is necessary to understand the nature of interaction between sulfur compounds and adsorbents. Thiophene has two pairs of electrons on S atom. One pair of electrons is in the six-electron π system and the other lies in the plane of the ring. Consequently, thiophene can act as either an n-type donor by donating the lone pair of electrons of the sulfur atom to the metal (direct S—M bond) or as a π-type donor by utilizing the delocalized electrons of the aromatic ring to form a π-complex with the metal or metal ion. At least eight different coordination geometries of thiophene are known in organometallic complexes and they include direct S—M bond, π-complex formation and geometries involving both direct S—M bond and π-complexes.[1,4] This indicates that thiophenic sulfur compounds can be removed from the transportation fuels either by the formation of direct S—M bonds or by π-complexation. However, in the later, aromatics and olefins in the fuel may compete and this would decrease the selectivity for the adsorption of sulfur compounds.

The objective of the present study is to investigate if the direct S—M interaction or π-complex formation is involved in the adsorption of thiophenic sulfur compounds on the given adsorbent. And also to understand which type of interaction (direct S—M interaction or π-complex formation) is favorable for the selective adsorption of only sulfur compounds without adsorbing aromatics and olefins present in the fuel. For this purpose, a model fuel containing thiophene (aromatic sulfur compound), tetrahydrothiophene (non-aromatic sulfur compound), benzene (non-sulfur aromatic) and 1,5-hexadiene (non-sulfur olefin) as shown in Scheme-1 has been prepared and used as a feed. Adsorbents based on zeolites, mixed metal oxides, supported metal compounds, etc have been tested. Since Ag-exchanged zeolite is known to form π-complexes with aromatics and olefins,[5] it is considered as representative for adsorption of sulfur by π-complexation. The observed results are corroborated with electron density on S atom and C—C bond order of the sulfur compounds, aromatic and olefin derived from computer simulation. Understanding the mechanism of sulfur adsorption in this study will be very useful to develop selective adsorbents for removing sulfur from transportation fuels for refinery and fuel cell applications.

Thiophene

Tetrahydrothiophene

Benzene

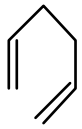

1,5-hexadiene

Scheme 1. Adsorbates added to n-decane solvent in the preparation of a model fuel

Experimental

Zeolites containing various metal ions were prepared either by ion exchange or impregnation of NH_4Y-zeolite with a SiO_2/Al_2O_3 molar ratio = 5 as described earlier.[3] Mixed metal oxide and supported metal adsorbents were prepared by co-precipitation and impregnation, respectively. The model fuel containing thiophene, tetrahydrothiophene as sulfur compounds, each 270 ppmw on the sulfur basis, in n-decane was prepared. About 270 ppmw of benzene and 270 ppmw of 1,5-hexadiene were also added to the fuel. The adsorptive desulfurization was performed using a flow apparatus as described elsewhere.[1-3] Analysis of treated fuel was performed using an Antek 9000 Series Sulfur Analyzer as well as a GC equipped with a flame ionization detector. Computer-aided molecular orbital calculations were performed using CAChe and MOPAC as described earlier.[6]

Results and Discussion

Figure 1 shows the breakthrough curves for the adsorptive desulfurization of the model fuel used in the present study over Ag-exchanged Y-zeolite. As can be seen, all the compounds, namely thiophene, tetrahydrothiophene, benzene and 1,5-hexadiene are completely adsorbed. The breakthrough points for the adsorption of benzene, thiophene and 1,5-hexadiene are about 22, 28, and 50 g, respectively. Tetrahydrothiophene was not detected in the treated fuel even after 50 g of fuel treatment. These results indicate that Ag-exchanged Y-zeolite forms π-complexes with benzene, 1,5-hexadiene and thiophene and that the π-complexation with 1,5-hexadiene being stronger than that with benzene and thiophene. The absence of tetrahydrothiophene in the treated fuel indicates that Ag-exchanged zeolite also makes direct S—M bond and this is even more stronger compared to the π-complexation with 1,5-hexadiene or thiophene. Since thiophene has a pair of electrons in the plane of the ring, it could form a direct S—M bond and π-complexation simultaneously.[1, 2] In such case, the adsorption of thiophene could be much more stronger than that of tetrahydrothiophene because of the simultaneous involvement of both types of bonding interactions. However, the observed results indicate that thiophene involves mainly π-complexation using delocalized electrons of the aromatic ring rather

than a direct S—M bond with Ag-exchanged zeolite. This is because the electron density on S atom of the thiophene is only 5.696 compared 6.042 in tetrahydrothiophene as calculated from computer simulation, implying that the S—M bond between the adsorption site and thiophene is much weaker than that between the adsorption site and tetrahydrothiophene.

The initial concentration of benzene was around 270 ppmw. However, its concentration in the outlet reached up to 700 ppmw after reaching the saturation value. This indicates that benzene initially adsorbed is desorbed during the course of the adsorption under the present experimental conditions. Similar result has also been observed in the adsorption of thiophene and this further substantiates that probably only π-type interaction exists between thiophene and Ag-exchanged zeolite.

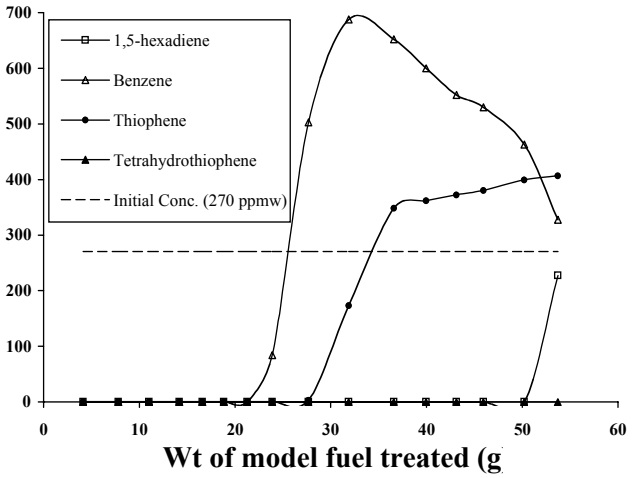

Figure 1. Breakthrough curves for the adsorption of thiophene, tetrahydrothiophene, benzene and 1,5-hexadiene in n-decane over Ag-exchanged Y-zeolite at 80˚C. Wt of adsorbent: 3.5 g; LHSV = 12 h^{-1}. The outlet conc. of thiophene and tetrahydrothiophene are on the sulfur basis.

The adsorption of aromatics and olefins along with sulfur compounds by π-complexation would deteriorate the quality of transportation fuels. The competitive adsorption of aromatics and olefins with sulfur compounds would also decrease the selectivity and adsorption capacity. In fact, it has been found from our earlier experiments that the presence of about 10 wt % of toluene in a model gasoline fuel decreases the adsorption capacity of Ag-exchanged zeolite by about 20 times.[7] Similarly, the presence of olefin decreases the capacity by about 6 times.

Figure 2 shows the breakthrough curves for the adsorptive desulfurization of the model fuel over a Ni-based supported metal adsorbent. Unlike that observed over Ag-exchanged Y-zeolites, only sulfur compounds (thiophene and tetrahydrothiophene) are removed over this adsorbent. The outlet concentrations of benzene and 1,5-hexadiene are very close to that present in the feed, indicating that they are not adsorbed at all. These results suggest that sulfur compounds are adsorbed by the direct S—M bond formation rather than by π-complexation over the Ni-based supported metal adsorbent. It is also interesting to note that the breakthrough curve of thiophene coincides with that of the tetrahydrothiophene and this indicates that these two compounds interact with the adsorbent to the same extent although there is a considerable difference in the electron density on S atom between these two sulfur compounds.

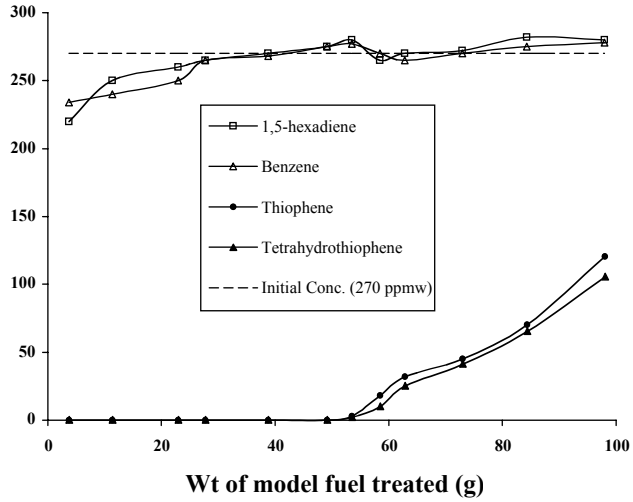

Figure 2. Breakthrough curves for the adsorption of thiophene, tetrahydrothiophene, benzene and 1,5-hexadiene in n-decane over Ni-based supported metal adsorbent at 80˚C. Wt of adsorbent: 4.5 g; LHSV = 12 h^{-1}. The outlet conc. of thiophene and tetrahydrothiophene are on the sulfur basis.

Various other adsorbents such as such as mixed oxides derived from hydrotalcite-like anionic clays, transition metals supported on mesoporous materials, etc have also been tested in the present study. Based on the results obtained, better adsorbents selective for removing only sulfur compounds have been selected for the adsorptive desulfurization of real gasoline, diesel and jet fuel.

Conclusions

Depending on the nature of adsorbent used, thiophenic sulfur compounds form either π-complexes using delocalized electrons of the aromatic ring or a direct S—M bond using the lone pair of electrons of the sulfur atom present in the plane of the ring. While thiophene is removed by π-complexation over adsorbents such as Ag-exchanged zeolites, it is removed by the direct S—M interaction over Ni-based supported metal adsorbent.

Sulfur removal by π-complexation is less selective due to the competitive adsorption of aromatics and olefins present in the transportation fuels. On the other hand, sulfur compounds can be selectively removed by the direct S—M interaction.

Acknowledgements. This work was supported in part by the US department of Energy and in part by the US department of Defense.

References

(1) Song, C.; Ma, X. *Applied Catalysis B: Environmental*, **2003**, 41, 207.
(2) (a) Ma, X.: Sun, L.; Song, C. *Catal.Today*, **2002**, 77, 107; (b) Song, C. *Catal.Today*, **2002**, 77, 17.
(3) Velu, S.; Ma, X.; Song, C. *Submitted for publication*.
(4) Reynolds, M.A.; Guzei, A.; Angelici, R.J. *J.Am.Chem.Soc*. **2002**, 124, 1689.
(5) Takahashi, A.; Yang, R.T.; Munson, C.L.; Chinn, D. *Langmuir*, **2001**, 17, 8405.
(6) Song, C.; Ma, X.; Schmitz, A.D.; Schobert, H.H. *Appl.Catal. A*, **1999**, 182, 175.
(7) Velu, S.; Watanabe, S. Ma, X.; Song, C. *Preprints-Am.Chem.Soc., Division of Petroleum Chemistry*, **2003**, 48, 56.

NEW CERIA-BASED SELECTIVE ADSORBENTS FOR REMOVING SULFUR FROM GASOLINE FOR FUEL CELL APPLICATIONS

*Shingo Watanabe, S. Velu, Xiaoliang Ma and Chunshan Song**

Clean Fuels and Catalysis Program, The Energy Institute and
Department of Energy and Geo-Environmental Engineering
The Pennsylvania State University
209 Academic Project Building, University Park, PA 16802
*E-mail: csong@psu.edu

Introduction

In order to improve the air quality, the federal governments in various countries have announced new regulations to reduce the sulfur contents in transportation fuels. The U.S. Environmental Protection Agency (EPA), for example, has recently announced a new regulation that mandates refineries to reduce the sulfur content in gasoline to below 30 ppmw from the current average of 300 ppmw and in diesel to below 15 ppmw from the current level of 500 ppmw by 2006. The interest in the desulfurization of transportation fuels is further motivated by the development of fuel cells to power automobiles, because fuel cell powered vehicles do not emit noxious gases such as SOx, NOx, CO, etc. However, for fuel cell applications, the sulfur content in the transportation fuels need to be further reduced to <1 ppm.

Catalytic hydrodesulfurization (HDS) is the conventional method that is being employed by the refineries to produce clean transportation fuels.[1] Although HDS process can remove sulfur compounds from gasoline close to 30 ppmw, it is highly inconvenient and very expensive process to produce fuel cell grade gasoline. Several alternative methods such as adsorption, alkylation, oxidation, extraction, etc. have been developed in recent years. Among them adsorption is considered to be more promising because adsorption can be accomplished at low temperature and pressure. Since gasoline contains significant amount of olefins and aromatics, the adsorbent should be selective to remove only organic sulfur compounds without co-adsorbing the olefins and aromatics.

A new concept is being developed in our laboratory at Penn State University known as "Selective adsorption for removing sulfur (PSU-SARS)" for the selective removal of organic sulfur compounds from gasoline, diesel and jet fuel. Several new adsorbents based on zeolites, mixed oxides, supported metal compounds, activated carbons, etc, are being developed and some of them exhibit excellent adsorption capacity for the desulfurization of gasoline and jet fuels.[2-4]

Owing to its high oxygen storage capacity, redox properties and good metal-support interactions, CeO_2 has been known as an excellent support for base and noble metals in variety of catalytic process, including auto exhaust three-way catalyst.[5] It also enhances the reducibility of base and noble metals supported on it. CeO_2-based adsorbents have also been developed in recent years for the removal of H_2S and SOx from flue gas, natural gas and coal-derived gas.[6] CeO_2 has been evaluated as a high temperature regenerable desulfurization sorbent, which yields elemental sulfur upon regeneration. Our recent work on the desulfurization of jet fuel indicated that Ce loaded zeolites exhibit fairly good adsorption properties.[7]

Taking into account the interesting properties of the CeO_2, the present study aimed at developing CeO_2-based regenerable adsorbents for the removal of thiophenic sulfur compounds present in the gasoline. Various metal-loaded high-surface-area CeO_2 mixed oxides synthesized by coprecipitation and impregnation methods have been used as adsorbents for the desulfurization of a model gasoline containing 265 ppmw of sulfur in the form of thiophene in a batch reactor at ambient temperature and pressure. The best adsorbents screened have been used to test in the dynamic adsorption study for the desulfurization of model and real gasoline.

Experimental

All the adsorbents were prepared using metal nitrates (Aldrich Chem. Co.) by urea gelation/co-precipitation method.[6] 10 atomic % metal containing CeO_2 adsorbents had metal/Ce=1/9 mole ratio. 20 at.% and 40at.% correspond to metal/Ce=2/8 and 4/6 mole ratio, respectively. Precipitates were dried at 110°C over night, and calcined at 450°C for 6 hrs in air employing a temperature ramp of 2°C/min. Model gasoline feed containing thiophene (sulfur concentration 265ppmw) in isooctane was used for studying the sulfur removal capacity.

The adsorptive desulfurization was performed using 25mL bottle (I.D.=2.4cm) with cap as a batch reactor and a flow apparatus. In the batch reaction 0.1 g of adsorbent was stirred well with 5 g of fuels under ambient temperature and pressure for 10 min. For flow system desulfurization the adsorbents were packed in a stainless steel column with an internal diameter of 4.6 mm and length of 75 mm. The adsorbent bed volume was about 1.25 cc. The model gasoline was fed into the column using HPLC pump. The feed flow rate was 0.05 cc/min. Antek 9000 Series Sulfur Analyzer (detection limit 0.5 wppm) determined the total sulfur concentration of the treated. The breakthrough volume and capacity were calculated from the breakthrough curves considering the sulfur content at the breakthrough point was below 1 wppm.

Result and Discussion

The study on sulfur removal capacity and the amount of sulfur removed are shown in Figure 1 and Table 1, respectively. Doping metal into ceria improved the adsorption capacity for removing thiophene. The adsorption capacity of CeO_2 is only about 2 mg/g of adsorbent and the capacity increases up to about 9 mg/g when 10 atomic % Y, La, Zn, Ni, Sr and Ag doped on to CeO_2. Y-CeO_2 and La-CeO_2 show sulfur adsorption capacity almost 4.5 times larger compared to the capacity of CeO_2 alone.

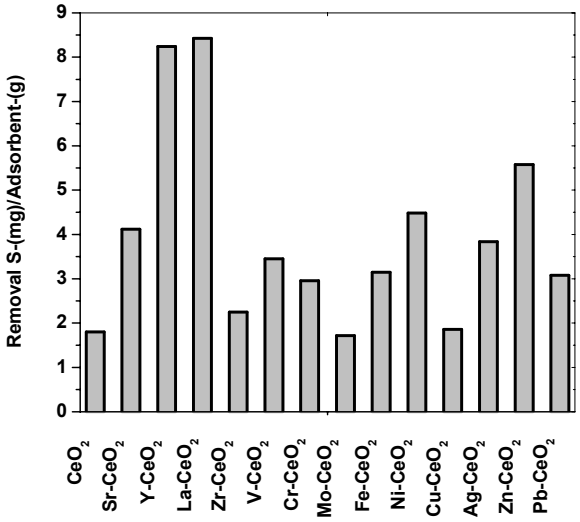

Figure 1. Adsorptive desulfurization of CeO_2-based adsorbents

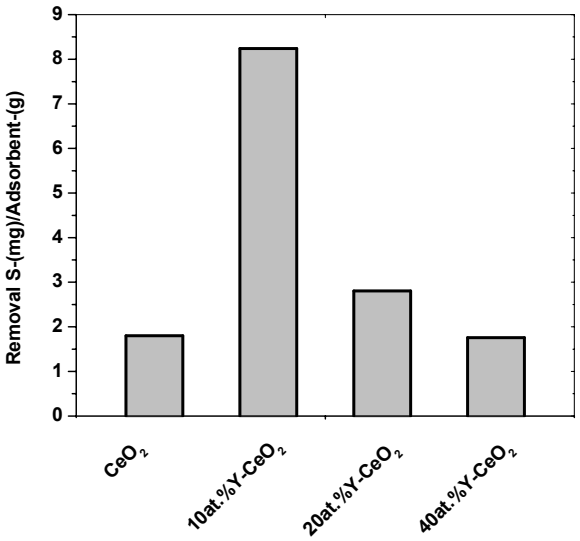

Figure 2. Comparison of various mole ratio of Y doped CeO_2 of adsorptive desulfurization

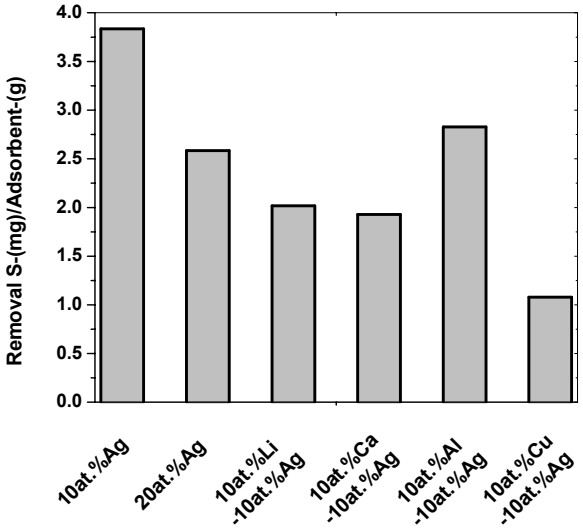

Figure 3. Comparison of modified Ag-CeO_2 of adsorptive desulfurization

The 10at.% of Y-CeO_2 has been compared with different concentration of Y-CeO_2. As can be seen from figure 2, the 10at.% Y doped CeO_2 adsorbent has higher sulfur removal capacity than 20 and 40 at.% Y-CeO_2 adsorbents. Therefore, 10 atomic % of Y is the optimum amount for doping with CeO_2 for the adsorptive desulfurization of gasoline of the present study.

Table 1. Amount of Sulfur Adsorbed by CeO_2 based Adsorbents, Initial Fuel/Adsorbent=50,wt

Adsorbents	Amount of Sulfur Adsorbed (%)
CeO_2	12.6
Sr/CeO_2	30.1
Y/CeO_2	60.3
La/CeO_2	58.5
Zr/CeO_2	15.6
V/CeO_2	22.1
Cr/CeO_2	20.4
Mo/CeO_2	11.9
Fe/CeO_2	20.9
Ni/CeO_2	31.8
Cu/CeO_2	13.6
Ag/CeO_2	27.4
Zn/CeO_2	40.1
Pb/CeO_2	22.4

Ag doped CeO_2 adsorbents were modified by additional 10 atomic % metals. Additional metals offer significant improvement on sulfur adsorption performance as seen in figure 3. A 10 at.% Ag-CeO_2 exhibit higher capacity compared to 20 at.% Ag-CeO_2. Increasing Ag concentration showed similar trend on Y-CeO_2 adsorbents results. Addition of Cu dramatically decreases the capacity compare to the addition of other metals under the present experimental conditions.

Further modifications of adsorbents are currently underway in order to increase the sulfur adsorption capacity. Since the adsorbents, in the present study have been used without any reduction treatment, these adsorbents will be able to regenerate easily for the subsequent desulfurization.

Summary

A new series of high-surface-area CeO_2-based mixed oxides have been tested as adsorbents in the desulfurization of a model gasoline containing 265 ppmw of sulfur at ambient temperature. The results indicated that a 10 at.% of Y and La doped into CeO_2 exhibit higher desulfurization capacity of about 9 mg of sulfur per g of adsorbent at room temperature just in 10 min stirring. Effect of Y loading on the adsorption performance indicated that the 10 at % loading is the optimum for the adsorptive desulfurization of thiophenic sulfur compounds under the present study.

The study on selectivity between thiophenic sulfur compounds, olefins and aromatics over these CeO_2-based mixed oxide adsorbents under the batch as well as dynamic adsorption is currently underway and the detailed results will be reported.

Acknowledgments. This work was supported in part by the US department of Energy and in part by the US department of Defense.

References

(1) C. Song and X. Ma, Applied Catalysis B Environmental, **2003,** *41(1-2)* 207-238; C. Song, *Catalysis Today*, **2002**, 77, 17-49.
(2) X. Ma, L. Sun, Z. Yin and C. Song, *Preprint Paper – American Chemical Society,* Division Fuel Chemistry, **2001***, 46(2),* 648-649.
(3) X. Ma, M. Sprague, L. Sun and C. Song, *Preprint Paper – American Chemical Society,* Division Fuel Chemistry **2002***, 47(2),* 452-453.
(4) S. Velu, S. Watanabe, X. Ma, L. Sun and C. Song, *Preprint Paper – American Chemical Society,* Division Petroleum Chemistry **2003***, 48(2),* 56-57.
(5) A.B. Hungria, A. Iglesias-Juez; Martinez-Arias, A.; M. Fernandez-Garcia,; J.A. Anderson; J.C. Conesa; J. Soria, *Journal of Catalysis*, **2002**, 206, 281.
(6) M. Kobayashi,; M. Flytzani-Stephanopoulos, *Industrial and Engineering Chemistry Research,* **2002**, 41, 3115.
(7) S. Velu, X. Ma and C. Song, *Preprint Paper – American Chemical Society,* Division Fuel Chemistry **2002***, 47(2),* 447-448.

ON-BOARD HYDROCARBON FUEL PROCESSORS FOR FUEL CELL VEHICLES: PERFORMANCE AND SYSTEM INTERACTIONS

Sitaram Ramaswamy, Robert Moore, Meena Sundaresan, Claudia Villa-Diniz

Fuel Cell Vehicle Modeling Program
ITS, University of California, Davis
One Shields Ave.
Davis, CA 95616

Introduction

Fuel cell vehicles have received considerable attention over the last six years. The promise of having cleaner electrical propulsion technology using hydrogen and oxygen, with water being the only product, is indeed alluring. However, the lack of an established hydrogen infrastructure presents a significant barrier that has to be overcome in the long term. Meanwhile, for the near term, a number of different approaches exist as possible workarounds to this lack of hydrogen infrastructure. On board fuel processors that would generate hydrogen from liquid hydrocarbon fuels have been proposed as possible near term solutions under the assumptions that, existing liquid fuel infrastructure can be used, the technical challenges related to fuel processing can be solved and that the increased local emissions & efficiency hits can be kept small. Given the complex nature of fuel processors, the fuel cell stack and water & thermal management systems the answers are not very straightforward and any analysis of the fuel processor system for vehicles has to be done in the context of the overall system.

The Fuel Cell Vehicle Modeling Program at the Institute of Transportation Studies at UC Davis, has been engaged in studying different fuel cell vehicle technologies via models and simulations. Currently, there exist models for a Direct Hydrogen (DH) fuel cell vehicle, Indirect-Methanol (IM) fuel cell vehicle and Indirect Hydrocarbon (IH) fuel cell vehicle. The salient feature of these models is the ability to characterize the performance of the vehicles under different drive cycles and to capture the impact of system dynamics on the performance of the vehicles and sub-systems.

We have developed a detailed model of a fuel processor system (FPS) and analyze the steady and dynamic characteristics of a fuel processor system for fuel cell vehicles. These impacts will be illustrated via specific examples based on model simulations.

Model Description

FPS model: **Figure 1** shows the IH fuel processor's main subsystems, which include a fuel, steam and air pre-heater/mixer, autothermal reformer, CO cleanup unit (high and low temperature shift reactors and PROX), steam generator and burner. The details of the different components of the FPS system are as described below.

Fuel, steam and air pre-heater/mixer: The fuel pre-heater unit accepts liquid fuel streams from the gasoline tank and mixes with steam provided by the steam generator. The mixture combines with air before being sent to the ATR, and the burner supplies the heat required for this process.

Autothermal Reformer: The autothermal reaction can be expressed as

$$C_nH_mO_p + x(O_2+3.76N_2) + (2n-2x-p)H_2O = nCO_2 + (2n-2x-p+m/2)H_2 + 3.76xN_2$$

where x is the oxygen-to-fuel molar ratio. The autothermal reactor should be operated in a manner that the overall reaction is exothermic, but at a low value of oxygen to fuel ratio where the higher hydrogen yields and concentrations are favored. The partial oxidation process of the ATR is a fast reaction and provides the necessary endothermic energy for the steam reformation process. The ATR is a thermodynamic model using parameters from Chan and Wang[1] and for the purposes of this study the fuel used was iso-octane.

CO cleanup: As in the IM fuel processor, the IH processor consists of shift and PROX units; however, an additional high temperature shift reactor is necessary due to the higher levels of CO emitted by the ATR fuel processor. The HTS and LTS models used here are detailed models incorporating kinetics (based on Podolski and Kim[2] 1974 for the HTS and Amadeo and LaBorde[3] 1995 for the LTS), mass transfer and heat transfer. These models also assume a decreasing (currently fixed) temperature profile that helps ensure better CO cleanup. They are thermally integrated with the steam generator in a counterflow arrangement. Provisions are also made for water/steam injection into the reformate stream prior to its entry into the HTS and LTS units. This helps maintain the requisite S/C ratios that were determined to be the optimal values based on stand-alone testing of the HTS and LTS units. The selectivity in the PROX unit is based on Kahlich[4] (1997).

Airbleed: Air bleed is used to meet the requirements of CO tolerance in the stack. The airflow is set at 3% of the dry reformate flow exiting the PROX based on an estimated concentration of 100 ppm of CO in the H2 exit flow.

Steam Generator: The steam generator uses heat from the anode exhaust burner and shift reactor units to generate steam used in the steam reformation process of the autothermal reaction. The steam generator is the slow step in the fuel processor system, relative to the air compressor, which is assumed to respond instantaneously. Currently, the steam generator is assigned a time-constant of 0.01s which is a fairly aggressive number but can be adjusted based on the specific steam generator specifications.

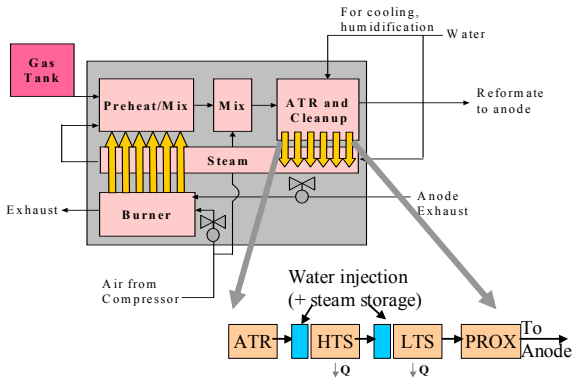

Figure 1: FPS sub-system overview; the ATR, HTS and LTS units are modeled as specific unit ops.

Results and Discussion

The primary focus of ths section is on the issues of energy efficiency and transient response of the fuel processor. In the fuel processor analysis, the FP Overall Efficiency is defined as the fuel processor efficiency over the drive-cycle, and includes H2 utilization and air bleed losses. This definition allocates the losses due to incomplete utilization of the hydrogen in the fuel cell stack to the fuel processor. Additionally the losses due to the O2 (air) bleed into the anode are also associated with the fuel processor.

$$\text{FPS efficiency} = \frac{(\text{H2_consumed@stack} * \text{LHV_H2})}{(\text{Fuel_into_fuel_processor} * \text{LHV_fuel})}$$

This enables comparison of the IH fuel supply system with the direct hydrogen fuel supply system (where utilization is ~99% and air-bleed losses are zero). The one caveat here is that the parasitic losses due to the ATR (and burner) compressor is not included in the FPS efficiency but is treated as a fuel cell system loss. The IH fuel processor overall efficiency was found to be in the range 67-64 % for 10-100% power (Note: this included 85 % utilization efficiency and 97 % air bleed efficiency).

The dynamic response of the fuel processor is influenced by a number of factors. One is the steam generation rate, which is in turn related to the anode exhaust energy content (the primary source of heat for the steam generator). Under transient conditions, during up-transients, there is not much energy available in the anode stream. On the other hand, during down transients, there is excess energy available in the anode stream. The other factors are associated with the control scheme adopted to manage fuel/air/steam flows.

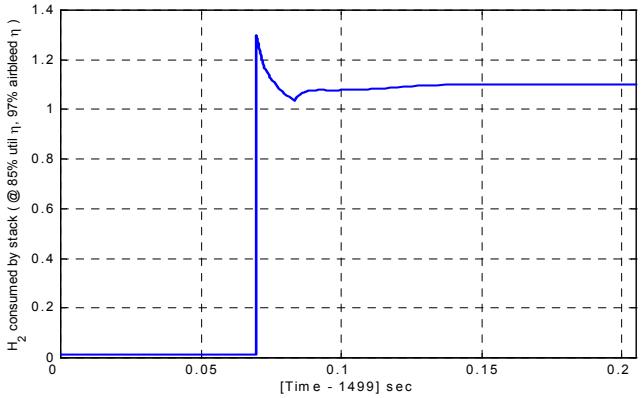

Figure 2: Transient response of the FPS unit from idle to 100% power; quick response a consequence of internal volumes and assumptions related to fast air & steam supply.

The control scheme slaves the fuel and air-flow rates to the steam generation rates while trying to maintain proper O/C levels in the ATR. Additionally the optimized HTS and LTS units are sensitive to any departures from the design inlet flow temperatures. During our preliminary investigations, we found that under transient conditions there were phase lags in the supply of steam during ramp-up and ramp-downs caused by interactions with the stack subsystem. As a consequence, it was difficult to limit CO at levels below 1% at the PROX entry if we did not have water injection AND steam storage (buffer) prior to the HTS & LTS. Once the water injection and steam storage (<2 liters volume) systems were introduced prior to the shift units, we were able to demonstrate the transient performance seen in Figure 2

Dynamic operation also has an impact on the overall efficiency over the drive cycle. Since the vehicle velocity profile over different drive-cycles can be quite different, the efficiency also depends on the drive-cycle considered for the analysis. Table 1 shows the impact of drive cycles on the fuel processor efficiency, with the corresponding vehicle efficiency (based on *[work done by vehicle against drag/friction forces]/[fuel energy supplied]*). The main impact on the fuel processor efficiency is due to the varying degrees of stack H2 utilization under dynamic conditions.

Table 1: Efficiency variation with drive cycle, comparison of the FUDS, HIWAY and US06 drive cycles

	IH FUDS	IH HIWAY	IH US06
FP overall eff (%)	56	66	65
• *FP efficiency*	*82*	*82*	*81*
• *H2 airbleed eff*	*97*	*97*	*97*
• *H2 utilization eff*	*70*	*83*	*82*
Vehicle Efficiency (%)	20	27	25

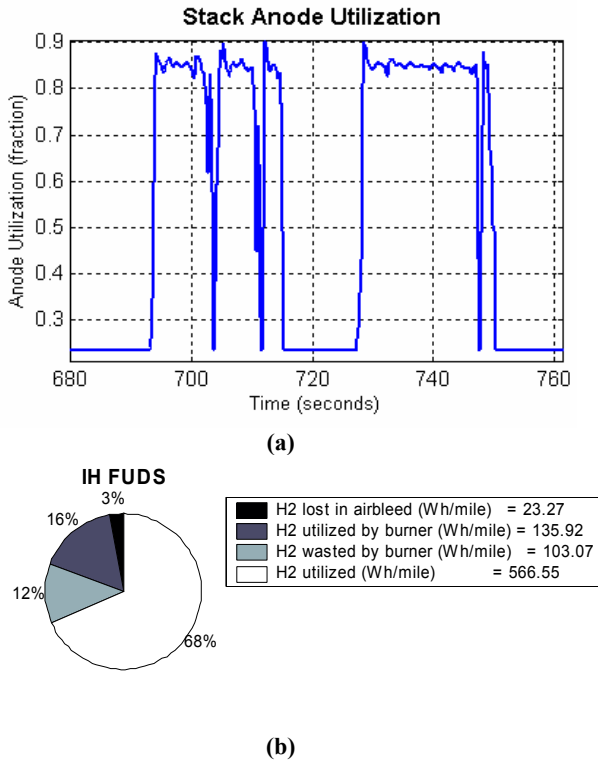

Figure 3: (a) Stack Anode Hydrogen utilization - snapshot over the FUDS cycle. (b) Hydrogen utilization and losses in Wh/mile – total Hydrogen production – 829 Wh/mile

Figure 3a shows a snapshot of the hydrogen utilization in the stack over the FUDS drive cycle – a cycle characterized not so much by high average power but more by the number of up-down transients encountered. As mentioned before, despite a fairly fast fuel processor, the nature of the interaction between the fuel-processor and the fuel cell stack, can cause variations in the H_2 utilization, thus impacting overall efficiency. The low utilizations occur during turn-downs; this results in high energy availability at the burner, not all which can be used for generating steam (since the steam is available at a point when the FP is also ramping down). Figure 3b shows the breakdown of where the hydrogen produced ends up and highlights the fact that 12% of the hydrogen produced effectively ends up being flared. This indicates that in order to improve the efficiency of the process, alternative approaches (hybridization, hydrogen buffering,

different control approaches, recycle loop) may need to be investigated. However, the authors believe that these approaches have their own set of problems and will have to be carefully analyzed taking both system dynamics and interactions into account.

In summary, on-board fuel processor design & controls present formidable challenges and our dynamic models have helped highlight some of them. Additionally, we have presented some of the issues that can come up when integrating the fuel processor with the rest of the fuel cell system. Alternative approaches both in the design and control space need to be explored further.

Acknowledgment. This work was supported by Fuel Cell Vehicle Modeling consortium at ITS, University of California at Davis [http://fcv.ucdavis.edu].

References

1. Chan, S.H. and Wang, H.M., International Journal of Hydrogen Energy, **2000,** v. 25, pp. 441-449,
2. Podolski, Walter F. and Young, G. Kim, Ind. Eng. Chem., Process Des. Develop. , **1974** v.13, No. 4, pp. 415-421
3. Amadeo, N.E. and Laborde, M.A., International Journal of Hydrogen Energy, **1995**, v. 20, no. 12, pp. 949-956
4. Kahlich, M.J., Gasteiger, H.A., Behm, R.J., Journal of Catalysis, **1997** v. 171, pp. 93-105,

EFFECT OF WATER ON PERFORMANCE AND SIZING OF FUEL-PROCESSING REACTORS

Marco J. Castald, Rene LaPierre, Maxim Lyubovski, William Pfefferle and Subir Roychoudhury

Precision Combustion, Inc., 410 Sackett Point, North Haven, CT 06473

Introduction

Current fuel processor design analyses, that comprise autothermal reformers (ATR), water-gas-shift (WGS) and preferential oxidation (PROX) reactors, either focus on individual reactor performance or on overall system integration and efficiency. This has led to a significant level of understanding of the requirements for a fuel processor system. For individual reactors, the analyses have indicated that fast start-up, transient response, size and weight are very important. On the other hand, the overall system analyses have highlighted the importance of heat management and the necessity to recycle as much water as possible, while maintaining its demand to a minimum. To date, connection has mainly been made on the effect of water on ATR performance and its impact on overall fuel processor design. However, a connection between the effect of water on CO clean-up reactors, i.e the WGS and PROX, and, in turn, the effect on overall system efficiency, has been lacking. While it is recognized that water will directly impact the WGS reactor, as water is a reactant in that system, the full extent has not been explored. Recent kinetic data coupled with a reactor design model sheds light on the impact water has on WGS reactor sizing and performance, where its impact on the overall system efficiency can be quantified. Moreover, water is generally considered an inert in the PROX reactor, yet recent experimentation on those reactors indicate that water has a significant impact on the multiplicity of steady-state operation and can impact the performance in terms of a synergistic effect with oxygen.

To identify the issues that need to be considered when designing a fuel processor system for optimized efficiency a preliminary process flow diagram (PFD) has been generated. The PFD was then simulated in ASPEN to calculate the amount of heat removal or addition that would be needed to ensure efficient operation of the system. The feed rate of the fuel, water and air led to a steam-to-carbon (S/C) ratio of 2.0 and an oxygen-to-carbon (O/C) ratio of 1.0. The intent of the simulation was to determine the critical issues that need to be investigated when designing a fuel processor system. To that extent, only major components were incorporated and the ancillary components such as blowers, pumps and vaporizers were not included because they are considered secondary in terms of system design for maximum efficiency. It is recognized that those components add some complexity but for a first cut analysis they are considered less important.

Results and Discussion

The results of the simulation of the preliminary PFD identified some issues that should be a focus for proper design and layout of all the components of the fuel processor. One main issue that was revealed during the simulation was the possible integration of various streams into components that would not have been expected from an overall system analysis. For example, analyses have been done to determine the effect of water input and recycle on overall efficiency without much regard given to the impact on reactor performance. A viable solution often proposed is the use of a condensing heat exchanger where the water recovered could be recycled into the ATR and lessen the demand of the water feed rate.

Water gas shift reactor analysis.

Tests were done to generate input data for ASPEN and to explore the impact of water on reactor performance. Those tests varied the steam to carbon (H2O/C) ratio entering an autothermal reactor (ATR) from 1.5 to 2.0, while keeping O/C ratio constant at 0.9. The WGS reactor was initially investigated in order to determine needed space velocities in the WGSR to achieve 90% or higher of equilibrium CO conversion. The experiments were done to evaluate the effectiveness of the LTS reactor at high space velocities with different water concentrations. The test results show that a higher water concentration in the ATR stage allows smaller WGS stages. In general, a slight increase in water addition to the ATR inlet results in a significant decrease in WGS reactor size and consequently pressure drop. In fact, if the water supplied to the ATR is at a steam to carbon ratio of 2.0, PCI's water gas shift reactor can reduce the CO, in a single stage, to below 1%, which is where a PROX reactor could be used. Experiments and calculations indicate that for every 1% increase in H2O to the ATR, there is almost a 10% decrease in water-gas shift reactor size when using conditions approximately similar to those tested.

From the experiments and modeling, it is clear that ATR H2O/C ratio greater than 1.5 would allow efficient WGS reactor design. To determine the optimal steam content entering the ATR, a system level calculation must be done to couple the effects of additional steam on fuel processor efficiency in light of a single stage WGS. The calculation must include parameters such as pressure drop, reactor size and weight, heat exchanger size and weight and dynamic interaction between the various components comprising the fuel processor.

Preferential oxidation reactor analysis:

To complete the effect of water on the co cleanup train reactors, investigation into PROX performance was done for various water concentrations. Those tests resulted in two significant findings that impact the design of PROX reactors and consequently system design. Dual steady state nature of the Reactor was the first finding from those tests. Generally a reactor in which a single, exothermic reaction is occurring will operate in one of two stable steady states. Additionally an unstable steady state solution to the mass and energy balance will be present. However, when multiple reactions are occurring in a reactor, there is the possibility of more than three possible steady state solutions. This arises from the fact that each reaction has a unique mole balance curve that superimposes upon each other. The energy balance line can then intersect each mole balance curve more than once adding up to four or more stable steady state conditions where the mole and energy balances are satisfied[1]. This phenomena is seen with the PROX reactor being developed, particularly at dry feed concentrations. Selective oxidation of CO in hydrogen over different catalysts has been extensively examined. In general, different precious metal catalysts have been found to be highly selective for the PROX reaction.

A general understanding of these systems is that at temperatures before the onset of the CO lightoff the surface is covered with adsorbed CO. As the temperature is increased the fraction of the surface covered with CO decreases, and this opens up sites for oxygen adsorption and subsequent reaction. Above a certain temperature the fraction of CO occupying the surface decreases even further and hydrogen chemisorbs and reacts on the surface in competition with CO, reducing the selectivity towards CO oxidation. Therefore, a common feature of all these systems is that there exists a window of operation in temperature between the lightoff curves for CO and H2, the object being to operate at a catalyst temperature sufficient for high activity of CO oxidation (for reduced size of catalytic reactor), but below that for significant consumption of the

hydrogen. This results in different temperature windows and optimum catalyst temperatures, which need to be identified for different catalyst formulations.

We observed the dual steady state behavior of the reactor only at dry feed conditions. However, when the water content is above 15% in the feed, the reactor consistently gives high CO conversion with nearly 45% selectivity. In addition, oxygen is detected in the product stream at varying levels, depending on the conditions tested. In comparison to monolith or pellet beds, we suspect that short contact time substrates should allow PROX reactors to operate at significantly lower water concentrations before the onset of the hydrogen oxidation reaction, i.e. the high temperature steady state. Initial analysis indicates that heat removal at the catalyst surface is a very important parameter in avoiding dual steady state operation because heat generated from the CO oxidation reaction is quickly transferred into the gas phase, thus moderating the surface temperature.

Table 1 displays representative results from experiments that show the dual steady state nature of the selective CO oxidation reactor. The first row provides the results of the reactor operating in the preferred steady state. The CO conversion was 22% with oxygen conversion at 30%, which results in a selectivity of slightly above 40% with a commensurate temperature rise. The second row shows for the exact same inlet compositions and temperature, the reactor was operating in another, high temperature, and undesired steady state. The data indicate that this state was one in which high hydrogen consumption occurred. The evidence for that was seen in the complete conversion of oxygen, without a change in CO conversion and the higher surface temperature as compared to the previous state. Since hydrogen was considered the fuel in this case, this state must be avoided to ensure the efficiency of the reactor system remains high.

Table 1: Results of dual steady state behavior of the PROX reactor.

------- Inlet Concentrations -------					-Reactor Temperature-		---Conversion ---	
O_2	H_2	CO	CO_2	H_2O	Inlet	Surface	O_2	CO
1.69	43.46	1.41	18.08	7.30	91.8	160.1	30.12	22.15
1.68	44.40	1.41	18.10	7.30	90.0	253.5	101.34	23.01

Additional experiments have been conducted that varied it from 0.7 to 3.0 holding all other feed conditions constant. Dual steady state operation was observed for the entire range tested providing more evidence that the water amount in the feed composition is probably the dominant factor. This type of experiment was repeated for a different CO feed concentration and nearly the same behavior was recorded. This dual steady state nature persists for a wide range of lambda, which points to the fact that dual steady state is more influenced by feed composition and more specifically by water amount. Since water has high heat capacity this may temper the heat rise and delay the onset of H_2 oxidation reaction.

The second significant result from the PROX testing with various water concentrations was evidence of a water-oxygen synergy within the Reactor. Table 2 comprises representative conditions and results from repeat experiments that indicated a water oxygen synergistic reaction occurring. The objective of the three experiments were to determine the contribution of oxygen and water separately toward oxidation of CO and consumption of hydrogen. The first row of the table provides the conditions and results of a baseline experiment, where the system was operating at its targeted steady state position. Here the conversion is as expected, greater than 90% with 50% selectivity. The temperature rise from the inlet to the outlet is consistent with the amount of reaction. The surface temperature rise also tracks with the gas phase temperature rise; recall this reactor substrate operates close to the gas phase due to high transport properties. The second row has the results of the condition where the water is not included in the influent. The third row shows the results of an experiment where the water influent was resumed and the oxygen was turned off. Each time a reactant was turned off, nitrogen was adjusted to compensate for that loss to maintain a constant GHSV. Inspection of the CO conversion shows that the sum of the CO conversions from the individual reactants does not add up to the conversion when they are both present. In fact, the water alone shows nearly zero reaction which is expected because that condition represents a water gas shift reaction of which the kinetics are very slow at that temperature. It is clear, however, that it is not only the oxygen that is converting the CO since its conversion is only 26% as compared to a 92% conversion when water is present. It is evident that water somehow initiates or promotes the CO oxidation reaction.

Table 2: Evidence for a water-oxygen synergy within the PROX reactor.

------- Inlet Concentrations -------					--Reactor Temperature---			---Conversion ---		
O_2	H_2	CO	CO_2	H_2O	Inlet	Surface	Outlet	O_2	CO	lamba
0.65	31.79	0.55	13.90	32.88	101.2	194.3	192.2	73.33	92.36	2.36
0.65	31.74	0.55	13.91	--	109.6	136.0	135.5	6.15	26.23	2.36
--	31.86	0.55	13.91	32.88	110.4	112.4	109.9	--	-0.50	--

Other researchers have observed similar water enhanced reactions. For example there was a study that showed a hydrogen water synergy[2] and a carbon dioxide water synergy[3]. Both studies indicated that water addition increased the amount of CO oxidation more than expected or predicted. The current experiments, shown in the table, add another piece of evidence to the water assisted or water enhance CO oxidation observations. These results point toward water acting as a catalyst or promoter for the selective CO oxidation on alumina supported platinum based catalysts. It is known that water has a high heat capacity, thus its temperature controlling, or heat absorbing, capability is recognized as one way to control reactions that liberate heat. In the case of the selective oxidation of CO this is very important, as discussed above, so as not to activate or light-off the hydrogen oxidation reaction. Yet water plays a significant role as a promoter in this reaction sequence.

One possible explanation for why water promotes this type of reaction is that water is conjectured to absorb and become activated by the stabilized alumina support while the CO is preferentially absorbed and activated by the catalyst metal. The CO can now be oxidized by the activated water or incoming oxygen. That leaves behind a hydrogen molecule from the water and an oxygen radical. The oxygen radical probably reacts with gas phase hydrogen more readily than gas phase CO purely because of the abundance of hydrogen. However, the hydrogen molecule left behind from the water may desorb or become displaced by another incoming CO molecule and enter the gas phase. This may help explain why we see a water oxygen synergy and a high selectivity toward CO oxidation when the hydrogen concentration is nearly 60 times greater.

Acknowledgement. The authors are appreciative of the experimental support from Brian Nentwick and also acknowledge the National Science Foundation's support in conducting a significant portion of this research. Opinions, findings, and conclusions or recommendations are those of the authors and do not necessarily reflect the views of the National Science Foundation.

References

(1) Fogler H.S. In *Elements of Chemical Reaction Engineering*; Second Ed.; Prentice Hall: Englewood Cliffs, N.J., 1990; pp. 383-485.
(2) Kahlich, M.J., Gasteiger, H.A., Behm, R.J., *J. New Mat. Electrochem. Systems*. **1997**, 171, 93.
(3) Avgouropoulos, G., Ioannides, T., Matralis, H.K., Bastista, J., Hocevar, S., *Catal. Today*, 2002*, 75*, 157.

Progress of FCC Technology in Improving Product Distribution and Quality

Chao-He Yang, Hong-Hong Shan, Jun-Sheng Zheng, Gen-Lin Niu, Jian-Fang Zhang

State Key Laboratory of Heavy Oil Processing,
University of Petroleum,
271 North 2nd road, Dongying, Shandong 257061, P.R. China

Introduction

In China, the fluid catalytic cracking (FCC) process is one of the most important refining processes, it affords about 80% of gasoline and 30% of diesel oil in market, but now it is faced with a baptism to satisfy the need for producing environmentally-cleaner gasoline and diesel fuels. During the recent decade, almost all the FCC processes became the RFCC (residue fluid catalytic cracking) processes by revamping for processing the heavier feedstock, and RFCC technology got great development around the reaction system, including the feeding atomization, quick separation of oil vapor and spent catalyst, steam stripping of high efficiency, temperature control of reaction, as well as the innovation of riser reactor [1-3].

In order to improve the product distribution, as well as reduce the olefin content and increase the octane number of FCC gasoline, and raise the cetane number of FCC diesel fuel, many technology innovations were proposed and tested in China. In this article, four new processes, including Maximizing Iso-Paraffins technology, Two-Stage Riser FCC technology, Flexible-Double Function FCC technology and Assistant Gasoline Riser Technology were introduced from their principles of technology and results of experiment or industrial test.

The shortage of the traditional RFCC riser

Although the feedstock of RFCC is different from that of distillate FCC because of its high boiling point, high resin and asphaltene content, and high contaminant concentration, the reactor, riser, is the same for RFCC and FCC process yet. In general, the distillate FCC is thought to be a gas-solid catalytic reaction, but gas, liquid, and solid exist simultaneously in reactor for RFCC. The studies on product distribution along the riser of RFCC show that the main conversion of feedstock to gasoline and diesel distillates is completed in the front stage of riser [4]. Figure 1 gives the variation of product distribution along the riser length of RFCC unit in a Sinopec Petrochemical Factory. It means that the riser is too long to result in an ideal product distribution at the exit of riser [5-6].

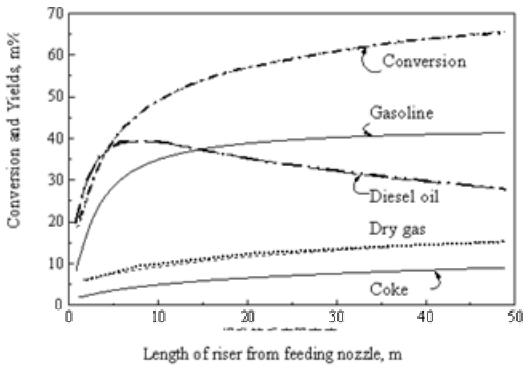

Figure 1. Conversion of feedstock and yields of products versus the length of riser (Simulated result of commercial RFCC unit)

The high olefin content of RFCC gasoline is another problem, it may be close to 60% for residual feedstock from paraffin crude. Although the many special catalysts were developed to reduce the olefin content, it is difficult to seek for a good compromise of operation conditions with the traditional RFCC for improving product quality as well as the product distribution. Therefore, the new reaction technologies of RFCC were proposed.

Maximizing Iso-Paraffins technology (MIP)

The MIP technology [7] was developed by the Research Institute of Petroleum Processing (RIPP), Sinopec, and was put into commercial use in Gaoqiao refinery. Its advantage is able to respectively create the favorable reaction conditions for heavy feedstock cracking into intermediate products and for upgrading the desired products. The theoretical foundation is that the high temperature and short reaction time is favorable to heavy feedstock cracking, but the isomerization and hydrogen transfer for improving product quality requires low temperature and long reaction time. As shown in figure 2 the most important innovation in MIP is the revamp for the traditional riser.

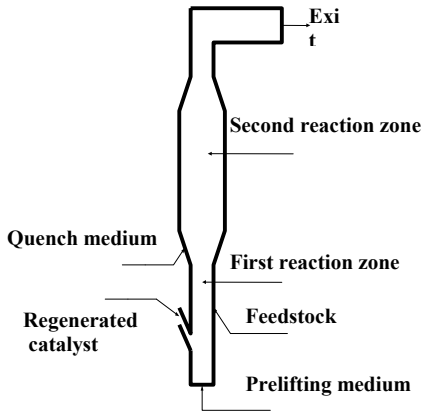

Figure 2. The riser reactor of MIP

The riser was classified into two reaction zones, and varies in diameter for different zones. The first reaction zone with a small diameter at the initial stage of riser is responsible for the cracking of heavy feedstock. This zone can provide the high temperature and short reaction time by controlling the catalyst recycle and the proper design. The second reaction zone with a larger diameter at the downstream section of riser is responsible for the completion of hydrogen transfer and isomerization. A quench medium, such as raw gasoline, LCO, water, or spent catalyst, is introduced into the starting section of this zone to decrease the temperature of the fluid come from the first zone. It is thought that the gasoline produced in the first zone were upgraded by improving the hydrogen transfer and isomerization and restraining the secondary cracking. The observation in pilot unit obviously shows that the conversion of feedstock was increased and the olefin content of gasoline decreased. Under the similar conversions, the yields of dry gas and coke for MIP is similar with the traditional FCC technology, the yield of gasoline increases by 1.37 percents (from 43.07% of traditional FCC to 45.07% of MIP), the yield of diesel oil has a slight increase too. The olefin content of FCC gasoline is 27.2% for MIP, compared with the traditional FCC technology, it drops by 12.4 percents, the aromatic content increases by 6.4 percents, MON increases by 1.3 units and RON has no obvious change. In addition, the sulfur content of gasoline has a notable decrease.

Two-Stage Riser FCC technology (TSRFCC)

In 1994, the TSRFCC technology [8-10] was proposed by the State Key Laboratory of Heavy Oil Processing, University of Petroleum (East China), and was put into industrial test in 2002 at a revamped unit of 10 thousand ton/year capacity. This year there are four RFCC units to be modified by the TSRFCC technology in China. The TSRFCC aiming at the disadvantage that the activity of catalyst and the selectivity to ideal products fall greatly at the anaphase of reaction in the traditional one-stage riser FCC (OSRFCC) replaces the present single riser reactor by two riser reactors, has two catalyst cycling system. A series of TSRFCC technologies have been developed for various product schemes. TSRFCC-I technology is suitable for enhancing the yield of light oil, especially the ratio of diesel to gasoline. Figure 3 shows the flowsheet of TSRFCC-I technology.

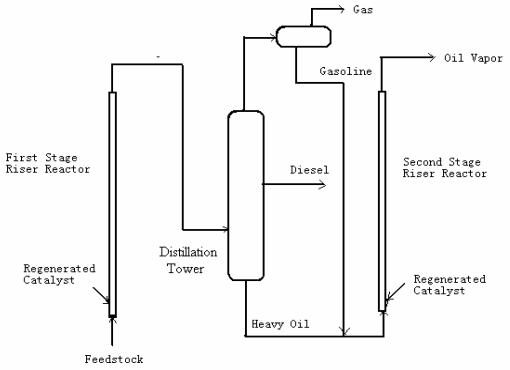

Figure 3. flowsheet of TSRFCC-I technology.

After the first stage cracking reaction to a proper extent, diesel distillate as a part of the final product is separated, while heavy oil (or heavy oil and gasoline when olefin reduction of gasoline is needed) enters the second stage riser reactor, contacts with the regenerated catalysts and reacts simultaneously. Therefore, diesel is well protected from non-desired second cracking since it does not take part in the reaction in the second stage after the separation, which increases the yield of diesel. On the other hand, the partial pressure of diesel at the second stage is effectively lowered, so it is optimal for the large molecules of heavy oil breaking down to generate more light oil. The two risers in TSRFCC-I technology are designed to keep the total reaction time less than 2 seconds, this affords a favorable condition for high temperature and short time operation. Compared with the recycle oil, the residue is easier to cracking, but more difficult to atomize, vaporize, and diffuse into the pores of catalyst, so the recycle oil will firstly vaporize and diffuse into the pores of catalyst and cover the active sites when both together enters the riser at the same time, this does affect the effective conversion of residue. The residue and recycle oil entering the two different risers respectively is reasonable for improving the product distribution.

The industrial test shows that the TSRFCC can enhance the conversion of feedstock and ameliorate product distribution greatly. Light oil and liquid product yields increase by 4 percents and 3 percents respectively, the ratio of diesel to gasoline rises obviously, and yield of dry gas and coke decreases by 2 percents, the capacity of FCC unit raises by 20%~30%. The olefin content of FCC gasoline was reduced by 6-8 percents without recycle of FCC naphtha. When the FCC naphtha is partly recycled to the second riser, the olefin content of FCC gasoline could be dropped by 15-20 percents without the deteriorating of product distribution relative to the traditional RFCC technology.

FDFCC and Assistant Gasoline Riser Technology

Flexible-Double Function FCC technology [11-12] (FDFCC) was developed by Luoyang Petrochemical Engineering Corporation, Sinopec. Assistant Gasoline Riser Technology [13] was proposed by University of Petroleum (Beijing). These two technologies are mainly used in the FCC gasoline upgrading, especially the reduction of olefin content. In these two technologies, another riser reactor is added to process the FCC gasoline based on the traditional RFCC technology. For Assistant Gasoline Riser Technology, the gasoline reactor consists of a riser and a reaction bed followed, it assures to afford the low temperature and long reaction time for hydrogen transfer and isomerization.

The industrial test for FDFCC was completed in 2002, it can reduce the olefin content of FCC gasoline by 20-30 percents, raise the RON by 1-2 units, lower sulfur content 15-20%, and increase the ratio of diesel oil to gasoline. But the yield of dry gas and coke increases obviously for FDFCC technology. As to the Assistant Gasoline Riser Technology, observation in pilot unit shown that the olefin content of gasoline was reduced by 15-20 percents, the conversion of olefin in gasoline is close to 60%, only about 1.5% of gasoline was converted into dry gas and coke, and RON of gasoline has a slight increase.

Conclusion

In China, the key problem of RFCC process is to reduce the olefin content of gasoline and to keep the product distribution and gasoline octane number from dropping at least. Based on the different understandings to the chemical mechanism of isomerization, hydrogen transfer, and cracking of olefin component, as well as their relationship, many new RFCC technologies were developed, but the TSRFCC technology gives a better result.

References

(1) Hou Fusheng. *Petroleum Processing and Petrochemicals*. **2001**, 32(1):1-6
(2) Miao Yi, Guan Minghua, Luo Yibin. *Petroleum Processing and Petrochemicals*. **2000**, 31(8):1-7
(3) Xie Chaogang, Zhong Xiaoxiang, and Yang Yinan. *Petroleum Processing and Petrochemicals*. **2001**, 32(1):26-30
(4) Niu Genlin, Yang Chaohe. *Journal of Fuel Chemistry and Technology*. **2002**, 30(3):249-253
(5) Dong Wei. *Doctoral thesis, University of Petroleum.* **2001**
(6) Dong Wei, Xu Chunming, Gao JInsen. *Journal of the University of Petroleum, China.* **2000**, 24(6):4-7
(7) Xu Youhao, Zhang Jiushun, and Long Jun. *Petroleum Processing and Petrochemicals*. **2001**, 32(8):1-5
(8) Zhang Jianfang, Shan Honghong, and Yang Chaohe. *US Patent,* **2002**, Application Number: 0108887A1
(9) Zhang Jianfang, Shan Honghong, and Yang Chaohe. *Chinese Patent,* **2002**, Application Number: 00134054.9
(10) Zhang Jianfang, Shan Honghong, and Yang Chaohe. Ninth Annual Conference of Catalytic Cracking. **2002.11**, Guangzhou
(11) Zhang Fuyi, Zhang Lixin, Li Zhanbao. *Chinese Patent,* **CN96212360.9**
(12) Tang Haitao, Wang Longyan, Wei Jialu. Ninth Annual Conference of Catalytic Cracking. **2002.11**, Guangzhou
(13) Gao JInsen, Xu Chunming, Bai Yaohua. Ninth Annual Conference of Catalytic Cracking. **2002.11**, Guangzhou

Study on Product Distribution along the Riser Reactor in RFCC Unit

Jun-Sheng Zheng, Chao-He Yang, Gen-Lin Niu, Feng Du, Hong-Hong Shan, and Jian-Fang Zhang

State Key Laboratory of Heavy Oil Processing, University of Petroleum, 271 North Second Road, Dongying 257061 China

Introduction

In China, nearly 70% of gasoline pool and 30% of diesel oil are produced by the fluidized catalytic cracking processing (FCC) which is one of the most important processes for converting heavy distillates into light fuels. But the FCC feedstock becomes heavier and heavier for the reason that the decrease of the conventional crude and the increase of demand for light fuels. Since the residuum have a high content of resin, asphaltene, high contaminant concentration and high boiling point, the residuum fluidized catalytic cracking (RFCC) technology has been got a great development in technology scheme, such as catalyst, feed nozzle type, etc[1-2]. But the key of the RFCC process, the riser reactor, is the same for RFCC and FCC process yet, and the study on the product distribution and composition changes of products along the commercial RFCC riser is very important, but quite scarce. The present paper gives a primary but detail understanding on the product distribution and composition changes of products along the riser reactor of a commercial RFCC unit.

Experimental

In order to make out the true reaction behavior, product distribution and composition changes of products along the riser in RFCC process, a new sampling system which can gain satisfied samples from commercial RFCC riser was developed by the State Key Laboratory of Heavy Oil Processing. Details about this sampling system refer to the previously published papers [3-4]. With the modified sampling system, the gases, the oil samples and the oily catalyst were obtained at the different positions along the commercial riser in the RFCC unit, Qingdao Petrochemical Factory, SINOPEC. Figure 1 described the sampling position distribution in the commercial riser.

The gaseous products, the PIONA and the RON/MON of gasoline were analyzed by a HP5890II GC with an UP-3000 workstation, developed by the Analysis Centre of University of Petroleum. In order to remove the absorbed oil, the oily catalysts were first extracted with n-C_5H_{12} as solvent in Soxhlet apparatus, and then stripped by steam at 515°C for 20min, finally analyzed with a combustion-GC method to determine the coke yield. The boiling point distribution of the liquid products and the dissolved oil were determined by a Simulated Distillation GC. The sulfur content of the gasoline distillated from the liquid product was measured by the Micro-Coulomb method.

The RFCC feedstock in Qingdao Petrochemical Factory is the atmospheric residuum of the mix of Shengli, Cabinda and Far East crude. The sulfur, carbon residue, saturate, aromatics, resin, and asphaltene contents of the feedstock is 3400*u*g/g, 4.29wt%, 52.06wt%, 24.08wt%, 22.60wt%, and 1.26wt% respectively.

Whether the representative samples were got from commercial riser is the key for the present work to be successful. From the obtained samples including gas, liquid and oily catalyst, the material balance can be made at each sampling point. In order to verify the veracity of the data, comparison was made between the sampling point and the product distribution of RFCC unit. The yields of gasoline and diesel oil of the RFCC unit are 42m% and 23m%, respectively. The ratio of recycle is 0.137 in commercial production,

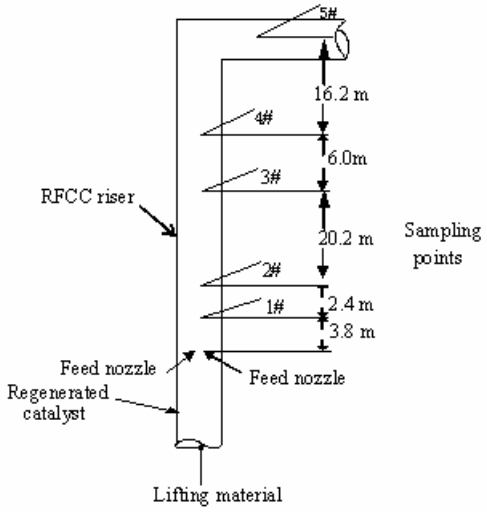

Figure 1. Illustration of sampling points on RFCC riser

so the single-through yields of gasoline and diesel oil is 42×(100-13.7) m% and 23×(100-13.7) m%, that is, 36.3 m% and 19.8m%,respectively, which is similar with the gasoline and diesel oil yield from material balance at the 4# sampling point. And also, the quality of gasoline at 5# sampling point close to the exit of riser, such as sulfur content, olefin content, is similar with the raw gasoline of the commercial RFCC unit.

Results and Discussion

Product distribution along commercial riser. The total amount in every sampling point for making material balance is the sum of gases and liquid products collected in sampling process, as well as the oil absorbed in oily catalysts. The product weight and yield are calculated as follows:

- Coke yield = coke in catalyst × the ratio of catalyst to oil;
- The weight of gas and oil =the weight of gases + the weight of liquid products + the weight of oil absorbed in oily catalyst;
- Gasoline yield = (the weight of gasoline in liquid products + the weight of C_5^+ in gases + the weight of gasoline in oily catalyst)/the weight of gas and oil × (100-coke yield);
- Diesel oil yield = (the weight of diesel oil in liquid products + the weight of diesel oil in oily catalyst)/the weight of gas and oil × (100-coke yield);
- Heavy oil yield = (the weight of heavy oil in liquid products + the weight of heavy oil in oily catalyst)/the weight of gas and oil × (100-coke yield);

Analysis and calculated results for gaseous composition and product distribution from different sampling positions were listed in table 1 and table 2 respectively.

Table 1. Analysis Result of Gases along RFCC Riser

Sample No.	1#	2#	3#	4#	5#
C_1+C_2, m%	18.55	11.48	8.52	12.39	18.55
C_3+C_4, m%	57.37	59.21	62.83	63.22	65.38
$C_3^=+C_4^=$, m%	45.75	48.51	49.42	49.22	49.99
$(C_1+C_2)/(C_3+C_4)$	0.32	0.19	0.14	0.20	0.28
$(C_3^=+C_4^=)/(C_3+C_4)$	0.80	0.82	0.79	0.79	0.77

Table 2. Product Distribution along RFCC Riser

Sample No.	1#	2#	3#	4#
Gasoline, m%	25.92	34.93	38.23	38.21
Diesel Oil, m%	21.00	19.65	19.18	19.62
Heavy Oil, m%	28.56	21.65	20.35	17.19

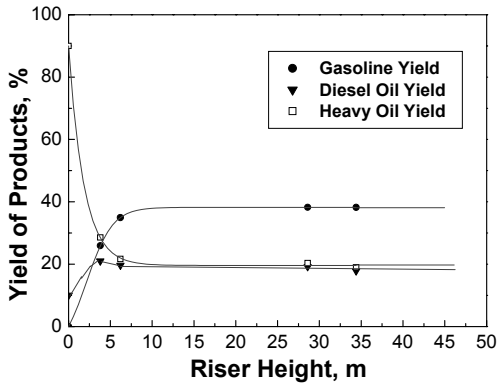

Figure 2. Product yields Vs. riser height

It is shown from table 1 that the ratio of (C_1+C_2) to (C_3+C_4), which means the relative capacity of thermal cracking and catalytic cracking, gets its minimum value in the middle of the riser and then increases. This phenomenon is consistent to the change of catalyst activity along the RFCC riser [5]. At the mix zone of catalyst and feedstock close to the position of feedstock nozzles, the higher contact temperature of oil gas and catalyst (560°C) and the adsorption of high-boiling point components on catalyst surface make the thermal cracking reactions take a more important role relative to catalytic reaction. At the tail of riser, the obvious formation of catalytic coke on the catalyst leads to the same result. Although the content of (C_3+C_4) and $(C_3^{=}+C_4^{=})$ in gases increase along the riser, the ratio of $(C_3^{=}+C_4^{=})$ to (C_3+C_4), which is the hydro-transfer behavior index of catalytic catalyst, arrives at its top point at the middle of riser and then decreases. This means that the hydro-transfer behavior of catalyst depends on the activity of catalyst and the effective reaction time.

Table 2 and figure 2 described the change of product yield along the RFCC riser. The gasoline yield reaches its maximum point at the middle of riser, but the yield of diesel oil reaches its maximum point at the initial stage of riser. The yield of heavy oil (>350°C) deceased along the riser, but the trend of diminution shrinks quickly; there is no notable change at the later half of riser. In another words, the change of product distribution is drastic in the initial stage of riser and tempered at the later half of riser. In the initial stage of riser, the heavy oil yield decreases from 90m% in feedstock to 28.9m% at the first sampling point, and nearly 60m% of feedstock are converted into gasoline, diesel oil, gaseous product and coke. This points again that the initial stage play a very important role in RFCC processing, and improving the contacting situation of feedstock with regenerated catalyst is a key method to get satisfied product distribution and maximum refinery profit.

Composition and Properties Changes in Gasoline. Table 3 lists the composition and properties in gasoline at different sampling points. The naphthene content in gasoline has no notable change for the reason that the naphthene is relative stable in FCC process [6]. The olefin content of gasoline first increases to its maximum at the middle of riser and then decreases. Based on the change analysis of catalyst activity along the riser [5], the thermal cracking plays a more important role in the conversion of feedstock to gasoline and diesel distillates, the olefin content of gasoline increases firstly with its rapid formation in the initial stage of RFCC riser. At the top of olefin content in gasoline, the yield of gasoline reaches a stable number, and then the olefin in gasoline will be reduced gradually with the reaction proceeding in the later section of RFCC riser. There is no significant change in RON, MON and anti-knock index of gasoline. This may be explained by the corresponding increase of aromatics with the decrease of olefin in gasoline.

Table 3. Properties of Gasoline along Commercial Riser

Sample No.	1#	2#	3#	4#	5#
Paraffin , m%	32.6	27.0	29.2	30.0	29.9
Naphthene , m%	9.4	8.5	9.0	9.5	9.7
Aromatics , m%	19.9	18.1	14.7	16.8	22.2
Olefin , m%	37.8	46.2	47.0	43.5	37.9
RON	92.6	92.3	93.0	92.6	92.3
MON	79.4	79.2	79.8	79.4	79.2
Anti-knock index	86.0	85.8	86.4	86.0	85.8
Sulfur content, μg/g	430	382	264	251	230

The sulfur content of gasoline decreases along the riser, but the tendency of decrease shrinks quickly. The sulfide is one type of L-bases, and the cracking of sulfide should first be absorbed in catalyst and then be cracked to H_2S or other sulfides [7]. At the rear of riser, the cracking centre of catalyst was covered with coke, and the cracking activity decreasing, so the tendency of sulfur content decreasing become slowly.

Conclusions

This work gives the changes of product distribution and properties of products along riser in commercial RFCC unit. The present studies will be favorable to the progress of RFCC technology.

Acknowledgement. This work was supported by the PetroChina, the Ministry of Education and the Qingdao Petrochemical Factory, SINOPEC. Thanks Guo-qing Fu and Tong-peng Mo for their help in sampling process and Zhong-xiang Han, Jin-you Wang, Bin Luo and Jian-wen Wang for their work in analysis of products.

References

(1) Yan Ran-zhao. *Oil and gas processing.* **1997***, 7(3)*, 40-44.
(2) Hou Fu-sheng. *Petroleum processing and petrochemicals.* **2001**, *31(1)*, 1-6.
(3) Xu Chun-ming, Lin Shi-xiong, Lu Liang-gong. *Petroleum refinery engineering.* **1997**, *27(3)*, 39-42.
(4) Xu Chun-ming, Lu Liang-gong, Lin Shi-xiong. *Journal of the University of Petroleum, China.* **1997**, *21(2)*, 72-75.
(5) Shan Honghong, Yang Chaohe, Niu Genlin. Preprints, Division of Petroleum Chemistry, ACS. **2002,** 47(3):321-322
(6) Chen Junwu, Cao Hanchang, Catalytic Cracking Technology and Engineering, China Petrochemical Press: Beijing, 1995; pp.130-132.
(7) *Zheng JunSheng, Li ChunYi, Yuan Q-Min, Li Min, Yang ChaoHe Shan HongHong, Zhang JianFang, Journal of the University of Petroleum, China. **2002**, 26(1), 88-90.*

Studies on the Interactions between ZnO and USY

Qimin Yuan,Chunyi Li,Hongyan Yang,Honghong Shan, Chaohe Yang,and Jianfang Zhang

State Key Laboratory of Heavy Oil Processing, College of Chemistry and Chemical Engineering, University of Petroleum, Dongying, Shandong Province, P.R. China 257061

Introduction

USY/ZnO/Al_2O_3 additive has excellent sulfur removal activity for FCC gasoline [1,2]. However, it deactivates very quickly under hydrothermal conditions at 800°C. In the additive USY and Al_2O_3 are two main components and the deactivation is impossible to be caused by the interaction between the two conponents. So, the destruction can only be due to ZnO. In the paper, XRD technique was used to investigate the interactions between USY and ZnO.

Experimental

The impregnation method was used to prepare the USY/ZnO samples with various ratios. These samples were calcined at different temperatures and then measured by a D/MAX-IIIA X-ray diffractometer.

Results and Discussion

Effect of ZnO contents and preparation The XRD patterns of the samples calcined for 6 hours at 500°C were shown in figure 1. When ZnO content is 40%, the characteristic peaks of ZnO(2θ=31.8,34.5,and 36.2°) are stronger, of which 36.2° is the strongest peak, and 34.5° is the weakest; the peaks of USY also can be detected though they are very faint. However, the order of the peak intensities change with the decrease of ZnO content. For 30% ZnO, the order is still 31.8°> 36.2°>34.5 °, while, for 20% ZnO it is 31.8 °>34.5 °> 36.2° and the peak at 36.2° is very weak. When the ZnO content decreases to 10%, the peaks of 31.8 ° and 34.5 ° can also be detected clearly, but the one at 36.2° almost disappears.

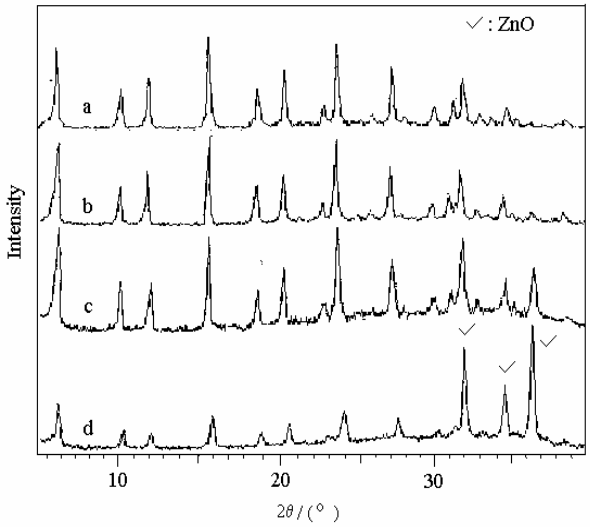

Figure 1. XRD patterns of USY/ZnO with different ratios. The contents of ZnO: a, 10%(wt); b, 20%(wt); c, 30%(wt); d, 40%(wt).

It is well known that the diffraction intensity mainly depends on the kind, number and arrangement of the atoms forming the crystal cells. In X-ray diffraction of polycrystalline, the relative peak intensity may vary with crystal surface orientation[3]. If we mixed USY and ZnO with the ratio of 9/1(wt), the sequence of the characteristic peak intensity of ZnO also changes after being calcined (**Fig.2**). The peak intensities of 31.8° and 36.2° are very similar in the XRD pattern of sample before being calcined; however, after being calcined, the peak at 36.2° is lower than the one at 31.8°. Obviously, it is unreasonable to attribute the change to the crystal surface orientation. In our opinion, this may be caused by the strong interaction between USY and ZnO.

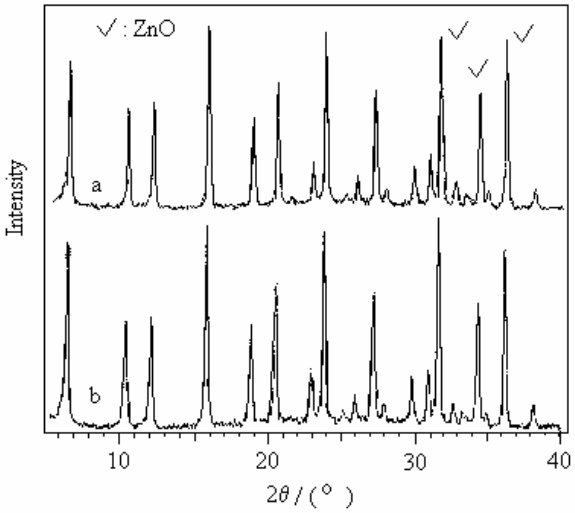

Figure 2. XRD patterns of USY/ZnO (9/1, wt.): a, mixed directly; b, sample further calcined at 500°C for 6h.

For those prepared by impregnation method, ZnO can dispersed uniformly on the USY surface, that is to say they can contact intimately. So the diffraction peaks of ZnO affected by USY seriously. At low ZnO content, there may be no large crystal particles of ZnO. Therefore, the characteristic peaks of ZnO are not the same as that of pure ZnO.

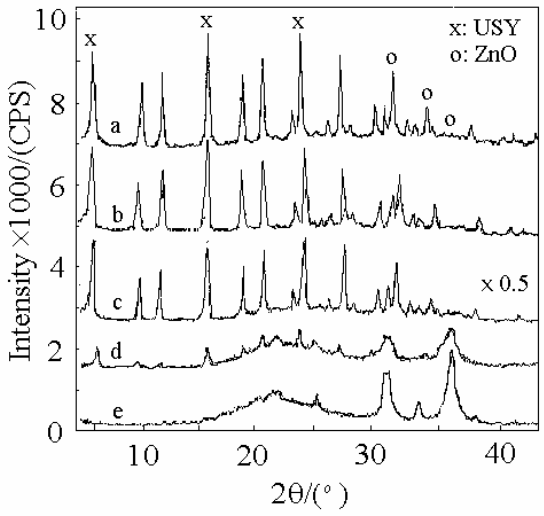

Figure 3. XRD patterns of USY/ZnO (ZnO content: 15wt%) calcined at various temperatures: a: 400°C, b: 600°C, c: 700°C, 750°C, and 800°C.

Effect of calcining temperature The XRD patterns of the ZnO/USY samples contained 15%（wt） ZnO calcined for 6 h at various temperatures were shown in **Figure.3.** Zn in the samples calcined at 400 and 600°C is present as ZnO. The characteristic peaks of ZnO weaken with temperature, and disappears completely with those of USY together in the one calcined at 800°C. This shows that some reactions between USY and ZnO take place, otherwise the crystal structure of USY is impossible to be destroyed and converts to amorphous state. We plot the peak intensities of USY (15.7°) and ZnO (31.6°) vs. calcining temperature and obtain fig.4, from which we see that USY and ZnO change according to the same trend with temperature. This proves again that the destruction of USY is caused by ZnO. In fig.4 we can also find that ZnO can not destroy USY significantly when the temperature is lower than 600°C. However, when it is higher than 650°C, the destructive effect gets more and more serious. When the temperature rises to 800°C, the peak intensity of both USY and ZnO drops to zero.

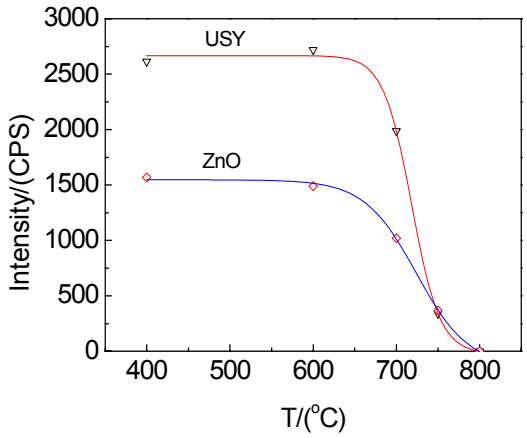

Figure 4. Trends of peak intensity of USY (2θ=15.7°) and ZnO (2 θ =31.6°) with temperature.

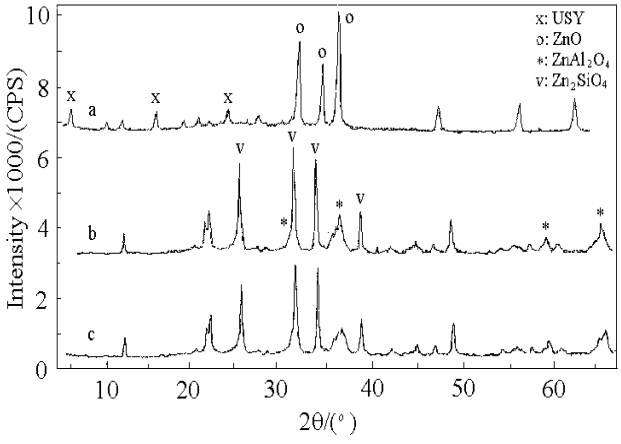

Figure 5. XRD patterns of 3/2 (wt) USY/ZnO samples. a: calcined at 700°C for 6 h, b: sample "a" further calcined at 800°C for 4 h, c: sample "a" further treated in 100% steam at 800°C for 4 h.

Destruction of ZnO to USY How ZnO to destroy the USY crystal structure has two possibilities. One is that a kind of solid-melting material forms between USY and ZnO, just like the destruction of V_2O_5 to USY under high temperature; another is that ZnO can react with Si and/or Al of USY framework via solid phase reactions, and thus destroys the USY crystal structure. Unlike V_2O_5, However, the melting-point of ZnO is far more 1000°C, so the possibility of form solid-melting material is very small. Thus, the destruction of ZnO to USY can only attribute to solid phase reactions between ZnO and USY.

Formation of $ZnAl_2O_4$ spinel and Zn_2SiO_4 willemite The XRD patterns of the 3/2(wt) ZnO/USY samples calcined for 6 h at various temperatures were shown in **Figure.5.** The XRD patterns of sample "a" shows USY crystal structure is not seriously destroyed under 700°C. However, sample "b " shows the characteristic peaks of USY and ZnO have been replaced by the strong peaks of Zn_2SiO_4 willemite (2θ=25.3,31.5,34°) and the weak peaks of $ZnAl_2O_4$ spinel （2θ=31.2,37.0,59.2°）. In **Figure.5,** the broad peak at 31° , and the two weak peaks at 25.2° and 34° correspond to the characteristic peaks of Zn_2SiO_4 willemite; while the two broad peaks at 31° and 36.5° correspond to the characteristic peaks of $ZnAl_2O_4$ spinel, which shows that the structures of Zn_2SiO_4 willemiteand $ZnAl_2O_4$ spinel. have been formed in the samples calcined at 750 °C and 800°C. However the samples were calcined at 750 °C or 800°C, the peak intensity of $ZnAl_2O_4$ spinel at 36.5° is always stronger than the one of Zn_2SiO_4 willemite at 31°. Meanwhile,the peak of Zn_2SiO_4 willemite at 34° is very weak. Thus, it can be concluded that ZnO reacts preferentially with the framework Al of USY to form $ZnAl_2O_4$ spinel, and cause the collapse of the USY crystal structure. For the Si/Al ratio of USY is very high, the peak intensities of Zn_2SiO_4 willemiteand are stronger than that of $ZnAl_2O_4$ spinel. Furthermore, the XRD patterns of the samples calcined and treated with steam at 800°C are all almost the same, so the interactions between ZnO and USY have no relations with the steam.

In addition, XPS results show that ZnO can react with surface of HZSM-5 zeolite, and then form $[ZnOH]^+$ [4,5,6]. The mechanism of the interaction between ZnO and USY maybe similar to that , ie. ZnO firstly reacts with the oxygen of Bronsted acid of USY, and formed $[ZnOH]^+$. Through the dehydration between $[ZnOH]^+$ and adjoining aluminum hydroxy at high temperature, Zn and Al can be connected by oxygen to form spinel structure. Certainly, this is just a guess, and the detailed explanations need further research.

Conclusions

Temperature is the determined factor and steam does not play a great role in the destruction of ZnO to USY. The results shows that in the USY/ZnO ZnO can capture the framework Al of USY at high temperature to form $ZnAl_2O_4$ spinel to cause the collapse of the framework of the USY zeolite, and the USY then converts to amorphous state. The alumina and silica can further react with ZnO, if it is enough, to form $ZnAl_2O_4$ spinel and Zn_2SiO_4 willemite.

Acknowledgement. The project is supported by China Petroleum and Natural Gas Stock Corporation(Contract No: 01030206)

References

(1) Chun,Y.Li;Hong,H.S;Bo,Y.Zhao;Chao,H.Y;Jian,F.Z. *Acta Physico Chimica Sinica*,**2001**,17(7),641.
(2) Hong,H.S;Chun,Y.Li;Qi,M.Y;Jun,S.Z;Chao,H.Y;Jian,F.Z. *Chinese J. catal*.,**2002**,accepted.
(3) Wan,J.Z. *Petrochemical Technology,* **2001,** 30(7),571.
(4) Erndt,H; Lietz,G; Volter, J. *Appl. Catal. A*, **1996,** 146(2),351.
(5) Erndt, H;Lietz,G; Volter,J. *Appl. Catal. A*, **1996,** 146(2),365.
(6) Jun,C;Fu,X.D.*Chinese J. Catal*, **2001,**22(3): 229.

Evaluation of Sulfur Removal Additive for FCC Gasoline in a Recycling Fluidized-Bed Apparatus

Li Chun-Yi, Du Feng, Yuan Qi-Min, Shan Hong-Hong, Yang Chao-He, Zhang Jian-Fang

State Key Laborotary Heavy Oil Processing, College of Chemistry and Chemical Engineering, University of Petroleum, Dongying, Shandong Province, 257061 P.R. China

Intruduction

SO_x is one of the most important pollutants of air. With the increase of automobile number, its pollution is more and more serious. So the developed countries promulgated rules to limit the sulfur content of gasoline stringently. In China, the sulfur content of gasoline must be equal to or less than 800 μg/g, and will be reduced greatly in the near future. Therefore, developing effective and cheap sulfur removal technologies is a very important thing.

FCC is the leading process for transforming heavy oil to light fuels. In China about 80% commercial gasoline is from FCC. Because most of FCC feeds are not pretreated, the sulfur content of FCC gasoline is far higher than catalytic reforming, isomerization and alkylation gasoline components. That is to say, the sulfur in commercial gasoline is mainly from FCC gasoline. Therefore, almost all the sulfur removal routines of gasoline, such as hydrotreating of FCC feed, hydrodesulfurization of FCC gasoline, adsorption desulfurization, etc. are aiming at FCC gasoline. In these technologies, hydrotreating of FCC feed, which operates under high temperature and pressure, is a very effective way to desulfurize, but it is also very costive; hydrodesulfurization of FCC gasoline can operate under relatively mild conditions, however, how to avoid the decrease of octane number is a difficult problem; the process of adsorption desulfurization is quite complex, and H_2 is needed to restrain coke formation in sulfide adsorption step and to regenerate the adsorbent [1-3].

In fact, if the sulfur content of FCC gasoline can be reduced *in situ* FCC process, it is no doubt that this will be the most convenient and cheapest technology for sulfur removal. Wormsbecher and Kim [4-6] invented the additive for sulfur reduction of FCC gasoline which can be added into the reaction-regeneration system of FCC expediently based on the real situation to promote the cracking of sulfur compounds in the gasoline range. The maximum of sulfur reduction is about 40% compared to the sulfur content of gasoline produced without adding the additive if the additive is combined with the specially developed FCC catalyst [7]. Although the sulfur reduction percent is quite high, the highest absolute amount of sulfur removed is only about 200μg/g. In China, the sulfur content of FCC gasoline is often higher than 1000μg/g. Obviously, if only less than 200μg/g sulfur can be reduced, then the technology seems useless. Therefore, we aim at the situation in China to develop the technology of sulfur removal additive of FCC gasoline.

In our previous work, we have designed the additive which includes selective adsorption site of sulfides and sulfide cracking site [8]. According to the idea we prepared USY/ZnO/Al_2O_3 additive and evaluated it in a confined fluidized bed unit for catalytic cracking experiments with VGO as the feed. The results show that the additive has excellent sulfur removal performance, and no marked effect on the product distribution was observed except for a little increase in coke yield [9]. In the paper, we will introduce the evaluation results of the additive in recycling fluidized bed reactor.

Experimental

The VGO feed was provided by Shenghua refinery. The properties of the feed have been introduced somewhere[9].

The FCC catalyst used in the experiments is Vector 60 SL regenerated catalyst. The USY/ZnO/Al_2O_3 additive was prepared with semi-synthesis method. Firstly we mixed the $Zn(NO_3)_2$ and $Al(NO_3)_3$ solutions together, and then dripped $NH_3 \cdot H_2O$ solution into the mixed solution with continuous stirring till to all the solution to be deposit. After filtration and washing, we dried the deposit at 120°C for 10 h, and then calcined it in a muffle at 700°C for 6 h. Crashing and screening the solid, we obtained the additive with the size 0.078~0.18mm. The BET area was determined by Nitrogen adsorption-desorption on an ASAP 2010 surface area analyzer and is 206 m^2/g.

The evaluation of the additive was conducted in the recycling fluidized-bed apparatus for catalytic cracking experiments (fig. 1). The pure FCC catalyst or the mixed catalyst (the FCC catalyst/the sulfur removal additive = 7/3 (wt./wt.)) is firstly added into the system before experiments. When the temperatures of all the controlled points reach the set values and the catalyst impelled by steam can recycle normally, the steam is switched to heated feed. Thus, the catalytic cracking of the feed takes place in the riser and the coked catalyst is regenerated in the regenerator by air. In our experiments, the feeding rate was 4kg/h; the temperatures at the outlet of the riser and the regenerator were 500°C and 680°C, respectively; the catalyst/oil ratio was controlled at 5.9.

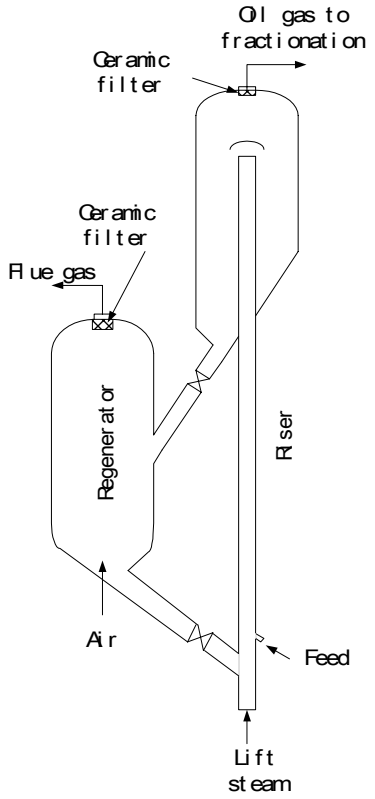

Figure 1. Schematic of FCC apparatus for experiments.

When the reaction proceeded stably, we collected the gas, liquid and flue gas for 1 h to calculate the material balance, analyze the coke, dry gas, and C3+C4 yields by chromatography. Gasoline and diesel are separated from the liquid product by distillation. The sulfur

content of the gasoline was determined by Micro-Coulomb method. Hydrocarbon composition and octane number of the gasoline were analyzed by HP5890.

Results and discussion

The USY/ZnO/Al_2O_3 additive was evaluated in a recycling fluidized-bed apparatus for catalytic cracking experiments with the catalyst/oil ratio of 5.9 at 500°C. The results adding 30% the additive and using pure FCC catalyst under the same conditions are listed in table 1. From the table we can see that the conversion adding 30% the additive is about 8 percent points higher than that using pure FCC catalyst because the additive is more active than the FCC catalyst, however, the sulfur content of the gasoline adding the additive is 784.3 μg/g, nearly 32% lower than that using pure FCC catalyst. Compared to the situation using the pure FCC catalyst, adding the additive can improve the yields of C3+C4, gasoline and diesel with almost the same dry gas yield, especially the yield of gasoline increases by more than 5 percent points with almost the same selectivity; the negative effect is that the yield of coke increases by 2.25 percent points.

Table 1. Comparisons of the experimental results in Riser

		30% Additive	FCC Catalyst
Condition	Temperature, °C	500	500
	Catalyst/Oil	5.9	5.9
	Residence time, s	0.90	0.91
Yield wt%	H_2	0.48	0.26
	Dry gas	2.31	2.21
	C3+C4	14.33	13.95
	Gasoline	44.93	39.51
	Diesel	19.16	18.10
	Coke	7.25	5.01
Conversion, %		68.82	60.68
Yield of light oil, wt%		64.09	57.61
Selectivity %	Dry gas	3.36	3.64
	C3+C4	20.82	22.99
	Gasoline	65.29	65.11
	Diesel	27.84	29.82
	Light Oil	93.13	94.94
	Coke	10.53	8.26
Sulfur content μg/g	Gasoline	784.3	1150
	Coked catalyst	99.81	97.85
Sulfur reduction of gasoline, %		31.8	-

Our previous work shows that in FCC gasoline about 80% sulfides are thiophene and thiophenes with different or different number alkyls [10], and the others are mercaptans, thioethers and di-sulfides. Mercaptans, thioethers and di-sulfides are easier to crack to H_2S and hydrocarbons, thiophenes, however, are relatively more difficult to desulfurize by cracking because of their stable conjugation structure. Thus, to remove thiophenes effectively, the additive must have higher activity besides its selective adsorption ability to sulfides. So that the conversion and the light oil yield are higher is what we have expected.

Moreover, all the sulfides in FCC gasoline can form coke or sulfur contained coke during cracking [11], however, thiophenes are easier to form coke because of their lower H/C ratio. The experiments using pure thiophene as the feed show that thiophene can cracking to hydrocarbons and H_2S, meanwhile coke is unavoidable because the formations of hydrocarbons and H_2S need hydrogen which is from thiophene directly or indirectly [12]. Benzothiophenes are even easier to form coke than thiophene for its even lower H/C ratio [11]. Since the sulfur removal additive we prepared can adsorb and crack sulfides selectively, that the coke yield is higher is not abnormal.

Table 2. Comparisons to the hydrocarbon composition and octane number of the gasoline produced using pure FCC catalyst and adding 30% the additive.

Catalyst	Adding 30% USY/ZnO/Al_2O_3	FCC Catalyst
Alkane, %	25.47	25.62
Naphthene, %	8.20	7.07
Aromatic, %	30.27	29.85
Alkene, %	35.99	37.47
RON	95.9	96.1
MON	82.2	82.4

The hydrocarbon compositions and octane numbers of the gasoline are listed in table 2. Adding the additive, we can see that in the gasoline naphthene and aromatic increase a small amounts and alkene decreases about 1.5 percent points. Obviously, the additive can not change the gasoline composition significantly. Consequently, both the RONs and MONs are almost the same in the two situations of adding and not adding the additive.

Conclusions

The USY/ZnO/Al_2O_3 sulfur removal additive for FCC gasoline has excellent sulfur removal activity. At 500°C and the catalyst/oil ratio of 5.9, the sulfur content of gasoline can be reduced more than 30% when 30% the additive is added compared to the situation using pure FCC regenerated catalyst, and adding the additive can improve the yields of C3+C4, gasoline and diesel except for about 2 percent point increase in coke yield.

Acknowledgment. This work was supported by PetroChina. The issue number is 010302-06.

References

1. Oil & Gas J., Sept. 10, 2001: 8.
2. Irvine R L, Benson B A, and Varraveto D M. *NPRA Annual Meeting*, Texas, **1999**. AM-99-42.
3. Greenwood G J, Kidd D, and Reed L. *NPRA Annual Meeting*, Texas, **2000**. AM-00-12.
4. Wormsbecher R. F., Kim G. US Patent: *5,376,608* (**1994**).
5. Wormsbecher R. F., Kim G. US Patent: *5,525,210* (**1996**).
6. Cheng W.C., Kim G., Peters A.W., Zhao X., and Rajagopalan K. *Catal. Rev.-Sci. Eng.*, **1998**, **40**(1&2): 39.
7. Balko J., Podratz D., Olesen J. *NPRA Meeting*, March 26-28, Texas, **2000**. AM-00-14.
8. Li C. Y., Shan H. H., Zhao B. Y., Yang C. H., Zhang J. F.. *Acta Physico Chimica Sinica*), **2001**, **17**(7): 641.
9. Shan H. H., Li C. Y., Yuan Q. M., Zheng J. S., Yang C. H., Zhang J. F. *Chinese J. Catal.*, **2002**, **23**(3): 245.
10. Shan H. H., Li C. Y., Zhao B.Y., Du F., Yang C.H., Zhang J.F. *J. Uni. Petro.*, **2001**, **25**(6): 78.
11. Pang X.M., Li C.Y., Shan H.H., Zheng J.S., Yang C.H., Zhang J.F., Li S.B. *J. Uni. Petro.*, **2002**, accepted.
12. Shan H.H., Li C.Y., Zhao H., Yang C.H., Zhang J.F. *J. of Fuel Chemistry*, **2001**, **29**(6): 481.

Maximum FCC diesel yield with TSRFCC technology

Hong-Hong Shan, Wei Zhao, Chang-Zheng He, JianFang Zhang, and Chao-He Yang.

State Key Lab of Heavy Oil Processing, University of Petroleum, 271 North Second Road, Dongying
257061 P.R. China

Introduction

After a quite long time exploration, steadily heavier crude oil is becoming one of the toughest frontiers in fluid catalytic cracking (FCC) process. Almost at the same time, stringent environmental constraints also put a big pressure on FCC process to readjust its product distribution and improve its product quality.

In recent years, many upgrades and modification have been done for RFCC units. In terms of process technology, MSCC[1], Down-Flow FCC[2], Double-Riser FCC[3] and Two-Stage Riser FCC[4,5] (TSRFCC) were developed one by one. Another term is advanced by FCC equipment enhancement such as novel feed nozzle[6], fast separating system at riser outlet[7], high-efficiency regenerator, multi-step reactor strippers, and riser terminations, etc. Among these technologies and studies, obviously, most are merely peripheral modification around the FCC riser reactor; quite few touched the very course of FCC reaction except that MSCC and Down-Flow FCC are on the way to real industrialization.

Riser reactor, commonly applied by worldwide FCC (One-Stage Riser, OSRFCC) process, was proved that, in the second half of riser, the activity and selectivity of the catalyst drop dramatically and over-cracking of intermediate products occurs[8], which deteriorate markedly the product distribution and final products properties. Based on this fact, a novel FCC process named TSRFCC had been invented successfully in china. The features of this new process are attributed to catalyst in relay, subsection reaction, high catalyst/oil (C/O) ratio and short residence time, through which the average activity and selectivity of the catalyst are enhanced and undesirable secondary reaction and thermal reaction are suppressed efficiently. Some former studies proved that TSRFCC process open a fairly good way to maximize gasoline yield. But under the atmosphere of insufficient supply of diesel in the worldwide market, especially in China, how to maximize diesel/gasoline ratio is a very important and urgent task. TESRFCC-I technology, a modified TSRFCC process had been studied on this paper to fulfill the task.

The Configuration and Theory of TSRFCC-I

The primary difference between TSRFCC and TSRFCC-I is that in the latter process the diesel cut produced by the first stage riser is removed from the internal products, then the rest parts of gasoline and heavy oil being injected into the second stage riser instead of overall internal products in series in the original TSRFCC process. Figure 1 shows the principle flow chart of both OSRFCC and TSRFCC processes. In the modification of commercial plants, the internal fractionating tower will be a new one or the former one.

Firstly, TSRFCC-I inherits the original features of catalyst in relay and subsection reaction to ensure oil vapor contact regenerated catalyst in both stages. Secondly, removing internal diesel produced by the first stage avoids its over-cracking in the second stage, thus maximum diesel yield can be achieved. Thirdly, removing internal diesel enhances the heavy oil conversion to light oil in the second stage, llustrated by chemical balance of catalytic cracking reaction.

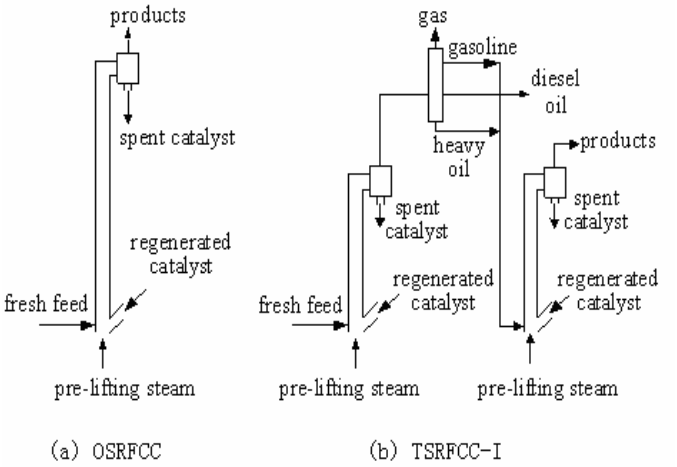

Figure 1 Comparison between OSRFCC and TSRFCC-I

Experimental

The performance of TSRFCC-I was evaluated in a pilot FCC plant[4]. One mixture of 65wt%VR + 35wt%VGO was employed as feedstock, the properties in Table 1. Catalyst used is commercial equilibrium catalyst ZC-7300, the microactivity is 60. Gaseous products were analyzed in HP5890II and Varian GC-3800C, and liquefied products in HP5880A.

Table 1 Property and composition of FCC feedstock

Density(20°C, g/ml)		0.9205	CCR (wt%)	4.62	
Group components (wt%)	saturated	52.37	Metal Content (ppm)	Fe	2.52
	aromatics	30.08		Ni	4.90
	resin	17.47		Cu	/
	asphaltene	0.076		V	0.095
element components (wt%)	H	12.67	Distillation range(°C)	0%	331
	C	85.91		10%	467
	N	0.31		20%	491
	S	0.16		30%	518

The main reaction conditions include temperature 490~520°C, the ratio of catalyst to feedstock 6, and residence time 1.5~2.2 s.

Results and Discussion

Yield Distribution Table 2 shows the product distributions of two different technologies. Compared with OSRFCC, at high conversion, TSRFCC-I showed a 6-7 percent point increase in diesel yield, accompanied by a 1.5-2 percent point increase in light oil while maintaining the same level of liquid product yield. Moreover, a 2 percent point decrease of dry gas yield was achieved. Obviously, reduced effect of thermal cracking had been confirmed as well as the yield distribution of TSRFCC-I had been markedly improved.

Table 2 Product structure of OSRFCC and TSRFCC-I

Pro. Distri. (wt%)	OSRFCC		TSRFCC	
hydrogen	0.19	0.14	0.11	0.15
dry gas	4.27	4.42	2.3	2.68
LPG	19.72	17.84	17.73	18.27
gasoline	50.07	50.47	45.11	44.86
diesel	15.15	14.13	23.44	21.87
heavy oil	4.41	5.84	3.24	3.75
light oil	65.23	64.6	68.56	66.73
coke	6.38	7.30	8.17	8.57
liquid product yield*	84.94	82.44	86.29	85
Conversion**	95.59	94.16	96.75	96.25

* Liquid product yield = LPG + gasoline + diesel
** Conversion = (100 – heavy oil)%

It is commonly believed that dry gas is produced by thermal cracking abiding by free radical mechanism. In the second half of conventional riser with 3 second above residence time, oil vapor can't fully contact acid sites due to deposited coke on the catalyst, so high temperature increases thermal cracking dramatically and quickly, as a result, increasing dry gas yield appears. In the course of TSRFCC-I, at the outlet of first stage riser oil vapor is separated with the deactivation catalyst in time before impending increasing thermal cracking, then injected into the second stage to contact with the regenerated catalyst exhibiting great accessibility of active sites. Consequently, thermal cracking was reduced radically and dry gas yield was minimized accordingly.

In the term of diesel, TSRFCC-I showed a 6-8 percent point increase compared with OSRFCC at similar conversion. It can be explained by two reasons. Firstly, removing internal diesel as final product prevent it from over-cracking in the second stage. Secondly, a great amount of active sites on the catalyst in the second stage cater for the heavy oil cracking well, which make speed of diesel producing surpass cracking. Diesel yield and diesel/gasoline ratio can therefore be maximized, which satisfies the changing trend of marketing structure.

Light oil yield in TSRFCC-I is 1-2 percent point higher than that in OSRFCC at highly extended conversion while keeping sound yield structure. Even though gasoline yield is relatively low in TSRFCC-I via cracking twice, the increase of diesel yield compensate the decrease of light oil for the loss of gasoline yield excessively.

As far as coke is concerned, the relatively high yield may be related to the hydrocarbons entrapped in the pores of the catalyst and carried through the inefficient stripping. This situation will be improved in FCC commercial unit.

To fully utilize TSRFCC-I technology, an optimum internal conversion must be controlled. Inappropriate internal conversion will definitely break the balance of two stages and deteriorate the course of reaction in whichever stage unavoidably, so the overall product structure is doomed to get worse. Numerous experiments proved that an optimum internal conversion must be chosen at the point where the high yield and selectivity of light oil in first stage was obtained and catalysis of catalyst dropped evidently. Only by doing so, two stages can run effectively and intimately.

Product Properties Data concerning the composition of LPG are shown in Table 3. The total yields of propylene and butylenes in TSRFCC-I are 85wt% above, versus 81wt% below in OSRFCC, higher 4 percent point. Higher light olefin yield in FCC unit is compatible with the trend of increasing demand of petrochemical feedstock.

Table 3 C_3 and C_4 olefins contents (wt%)in LPG

Olefin	OSRFCC		TSRFCC	
C_3	33.56	34.56	40.15	37.70
C_4	47.27	40.83	47.23	47.49
Total olefin	80.84	75.39	87.38	85.20

Used feedstock, a kind of paraffin-rich oil, is potentially efficient to produce smaller olefins by catalytic cracking leading to higher olefin content in FCC gasoline. This explains why gasoline produced by paraffin-based crude is generally unqualified for the environmental regulations. At the same conversion, gasoline in TSRFCC-I, compared with OSRFCC, gives a similar content of n-paraffins, an increase of i-paraffins, a considerably deduction of olefins as well as an increase of octane number. The composition data of gasoline are present in Table 4.

Table 4 Gasoline composition of OSRFCC and TSRFCC-I (wt%)

Items	OSR1	TSR1	OSR2	TSR2	OSR3
Conversion	80	96.56	76.27	96.75	95.78
n-paraffin	5.58	5.40	5.36	5.42	5.11
i-paraffin	23.65	28.12	25.79	29.90	24.00
naphthene	7.79	8.07	8.00	7.65	6.34
aromatic	18.86	25.45	16.82	18.75	19.02
olefin	44.31	33.13	44.09	38.29	45.47
RON	90.9	94.2	90.9	93.2	93.2
MON	78.0	80.8	78	80.0	80.0
Anti-knock index	84.4	87.5	84.4	86.6	86.6

The feed is nearly converted completely in the present of catalyst via two stages. Employing regenerated catalyst and higher C/O ratio brought by subsection reaction in the second stage increase the amount of accessible active sites, which would lead to more hydrogen transfer, so more gasoline olefins would be saturated, otherwise, the probabilities of isomerization and aromatization also increased, as a result, the gasoline olefinicity went down significantly. Higher octane numbers of increased aromatics and i-paraffins than decreased olefins account for the little enhancement of gasoline octane numbers.

Conclusions

The novel TSRFCC-I process (vs. TSRFCC) has a great impact on yield structure, conversion and products properties. Removing diesel cut from internal products boosts overall conversion, maximizes the production of diesel and diesel/oil ratio, minimizes the content of olefins in gasoline, and improves the qualities of LPG and gasoline. Due to the unique configuration of TSRFCC-I process, maximizing the profitability of FCC units will become possible in the near future.

Acknowledgement. This work was Supported by the PetroChina.

References

(1) Chang, T., Louisiana Refinery Revamp Takes Advantage of Heavy Sour Margins. Oil & Gas J., 96(45), 68-72(1998).
(2) Ren-sheng Deng, Teng-fei Liu, Fei Wei, Yong Jin, Composition of the Process in Riser and Downer Reactors, Chemical Reaction Engineering and Technology, 17(3), 238-243(2001).
(3) Hai-tao Tang, Research and Development of Flexible Multi-Functional FCC process, Petroleum Refinery Engineering, 31(6), 8-10(2001).
(4) Jian-fang Zhang, Hong-hong Shan, Zheng Li, Gen-lin Niu, Yu-dong Sun, New Development of FCC Through Two-staged Riser in Series. I. The Reactor of Two-staged Riser, ACTA PETROLEI SINICA(PETROLEUM PROCESS SECTION), 16(5), 66-69(2000).
(5) Zheng Li, Jianfang Zhang, Honghong Shan, Zhongxiang Han, Feng Du, Development of Two-stage Riser FCC Technology II. Increase of The Light Fraction Yield and Decrease of The Olefins Content in Gasoline, ACTA PETROLEI SINICA(PETROLEUM PROCESS SECTION), 17(5), 26-29(2001).
(6) Zhouping Lai, High-efficiency Feed Nozzle for RFCC unit, Petro-chemical Equipment Technology, 17(5), 15-18(1996).
(7) Zhanyou Cao, Votex Type Fast Separation System at FCCU Riser Outlet, Petroleum Refinery Engineering, 28(3), 14-18(1999).
(8) Jun-wu Chen and Han-chang Cao, Catalytic Cracking Technology and Engineering, SINOPEC Press, 1991.
(9) Xiang-yu Li, Market Analysis and Forecast to Diesel, Shanghai Chemical Industry, (1), 31-34(2001).

Cracking behavior of MCM-22, ZSM-5 and Beta as FCC catalyst additives

Liu Zhongqing, Fu Jun, He Mingyuan and Li Minggang

Research Institute of Petroleum Processing,
Beijing, China, 100083

1 Introduction

To meet the production of the different commercial and increasingly stringent environmental demands, FCC as an important gasoline producing unit will point to decreased sulfur, to maximize the octane barrel while keeping a good output, and to be flexible enough to increase the production of valuable C_3~C_5 olefins and isobutene, which are desired for producing oxygenates and alkylated gasoline. It is difficult to accomplish all these goals with a simple catalyst formulation, and one may oversee the possibilities of using, besides Y, other zeolites, either as the main active components or as catalyst additives. In order to explore good FCC catalytic materials, other than ZSM-5 and Y, researchers have investigated zeolites, such as, Beta and Omega[1,2,3] as FCC catalyst additives. MCM-22 zeolite, with nonconnected 10 and 12 member ring channels, may play an important role in the multi-function of FCC catalyst.

It was reported in the open literature[4,5] that the behavior of MCM-22 in catalytic cracking of pure paraffins is between 10 member ring zeolites, such as ZSM-5, and 12 member ring zeolites, such as Beta. Corma et al[6] compared the behavior of MCM-22 zeolite with that of ZSM-5 zeolite as FCC catalyst additives. It is found that MCM-22 produces less total gases, as well as less dry gases, with a lower loss of gasoline than ZSM-5, in the line of the claims in Mobil patents[7,8].

In the present work we have studied the catalytic cracking of a FCC feedstock on a FCC catalyst with MCM-22 as an additive, and the results are compared with those obtained on ZSM-5 and Beta additives respectively. The influence of pore geomertry on cracking parameters such as the hydrogen transfer coefficient (HTC), and the cracking mechanism ratio (CMR) is also discussed.

2 Experimental

2.1 Materials

The zeolites used were Beta, ZSM-5 and MCM-22. The former two were provided by RIPP (Research Institute of Petroleum Processing), and the latter was synthesized in the lab[9]. The parent zeolites were subject to steam treatment at 1 atmosphere of steam and 800^{0}C for 4h. The characteristics of the zeolites used in this work are given in Table 1.

The base FCC catalyst used was CC-16, which used USY as the main active craking component, and did not contain an additive, a commercial FCC catalyst produced by Changling Catalyst Corporation. The base catalyst was also steamed at 1 atmosphere of steam and 800^{0}C for 4h, then mixed with the steamed zeolites Beta, ZSM-5 and MCM-22, respectively. The percentage of the zeolite over the total catalyst was 8wt%. All catalysts were palletized, crushed, and sieved, a 0.59 to0.84 mm diameter fraction was taken.

2.2 Reaction procedure

The feedstock, a vacuum gasoil mixed with a vacuum resid by 30wt%, whose characteristics were given in Table 2, has been cracked in a down flow MAT unit, which has been designed to accomplish the ASTM D-3907 standard. Catalyst loading was always 5 grams. All reactions were carried out at 500 ^{0}C, and a time-on-stream of 60 seconds. In order to get different conversion levels, different catalyst-to-oil ratios were obtained by changing the amount of feedstock. The liquid products were collected in a glass receiver located at the exit of the reactor, which was refrigerated in a water-ice bath. Meanwhile, the gaseous products were collected in a gas buret by water displacement. Coke was determined in-situ by combustion in an air stream at 600^{0}C for 1h and monitoring the CO_2 formed by means of an IR cell. Gases were analyzed by GC. Liquid products were analyzed by simulated distillation.

3 Results and Discussion

In Fig1 the total conversion and selectivities are given for different catalyst-to-oil ratios and therefore, for different conversion levels, at 500 ^{0}C of reaction temperature and 8wt% of steamed additive over the total catalyst. The results (Fig1a) show that, at the same catalyst-to-oil ratios, the catalyst with MCM-22 additive has the lowest activity among all the catalysts, and even lower than the base catalyst which does not contain an additive. The data in Table 1 indicate that MCM-22 is a hydrothermal stable zeolite both in the case of structure and acidity, so the lower activity may be attributed to the limitations of diffusion of the large molecules in the feedstock through the two-dimensional 10 member ring windows in MCM-22 crystal. In Fig1, the results also show that MCM-22 additive yields more gasoline, LCO and coke, less gases comparing with ZSM-5, and less gasoline and LCO, more coke and gases comparing with Beta, in accordance with the open literature[6,7,8]. These indicate that the cracking behavior of MCM-22, which contains both10 and 12 member ring channels, is between that of ZSM-5, which only contains 10 member ring channels, and Beta, which only has 12 member ring channels.

The ratio of $C_4^0/C_4^=$ observed in the gas products were defined as the hydrogen transfer coefficient (HTC), which reflects the hydrogen transfer activity of a catalyst[10]. In Fig2a, the results show that the HTC for MCM-22 is the largest, then, Beta, and ZSM-5 is the smallest among the three zeolites. These indicate that the hydrogen transfer activity of the three zeolites is: MCM-22>Beta>ZSM-5. In addition, the olefinicity of the gas products also can reflect the hydrogen transfer activity of a zeolite. In Fig2b, the $C_3^=$ /Total C_3 ratio is in the following order: ZSM-5>Beta>MCM-22, in agreement with the conclusion reached from the analysis of the HTC, that is, the hydrogen transfer activity of MCM-22 is even higher than Beta, which has 12 member ring channels. The reason may be that it is ease to occur hydrogen transfer reaction of the molecules of products in the 12 member ring super cages of MCM-22, which have 10 member ring apertures, since the molecules of cracking products are difficult to diffuse through the 10 member ring windows. The results we got are in agreement with that in the Mobil patents[7,8], but Corma[6] et al found that the $C_3^=/C_3^0$, $C_4^=/C_4^0$ ratios are higher for MCM-22 than for ZSM-5, and they suggested the reason may be that there is a relatively low amount of framework Al content in the super cages of MCM-22.

The cracking mechanism ratio (CMR), which is defined as the ratio of dry gases (methane, ethane, and ethylene) to isobutane in the gas products, is used to measure the ratio of monomolecular to bimolecular types of cracking, since C_1 and C_2 are typical products from protolytic cracking, while iC_4 is a typical product formed by β-scission of branched products[11,12]. The results from Fig2c show that the CMR is largest for ZSM-5 among the three additives, the CMR for MCM-22 is little larger than that of Beta, and far smaller than that of ZSM-5. These indicate the ratio of protolytic to β-scission cracking occur on zeolites in the following order:

ZSM-5>MCM-22>Beta, and also indicate that the 12 member ring cavities, which, is half of the supercages of MCM-22, opened to the exterior, at the end of the crystal platelets of MCM-22, play a more important role in the catalytic cracking reaction than the 10 member ring channels of MCM-22.

4 Conclusions

When MCM-22, ZSM-5, and MCM-22 use as FCC catalyst additive respectively, in agreement with their structure, MCM-22 yields more gasoline, LCO and coke, less gases comparing with ZSM-5, and less gasoline and LCO, more coke and gases comparing with Beta. The hydrogen transfer activity of MCM-22 is higher than that of ZSM-5 and Beta; while the cracking mechanism ratio (CMR) of MCM-22 is much lower than that of ZSM-5, little larger than that of Beta, which means that the 12 member ring cavities on the crystal surface of MCM-22 play an important role in the catalytic cracking reaction. The performance of MCM-22 in catalytic cracking reaction is between that of ZSM-5 and Beta, and close to that of Beta.

Table 1 Physicochemical Characteristics of the Zeolites

Zeolites		S_{BET} / m^2/g	SiO_2/ Al_2O_3	V_{micro}/ ml/g	NH_3-TPD acidity / mmol/g	Pyridine adsorbed acidity (200°C) / μmol/g		
						Brönsted	Lewis	B+L
Fresh Samples	MCM-22	572	27	0.202	1.092	61.0	9.5	70.5
	ZSM-5	397	32	0.162	1.074	91.5	7.1	98.6
	Beta	610	30	0.229	1.220	54.2	20.2	74.4
Steamed Samples	MCM-22(S)	486	27	0.161	0.207	37.3	7.1	44.4
	ZSM-5(S)	350	32	0.150	0.166	13.6	33.3	46.9
	Beta(S)	440	30	0.166	0.120	33.9	57.1	91.0

Table 2 Characteristics of the Feedstock

Density (20°C) /g/cm^3	0.8731	Refractive Index (70°C)	1.4682
Distillation Curve / °C		ν(80°C) /mm^2/s	17.56
IBP	189	Acid Number /mgKOH/g	0.07
5%	398	Conradson Carbon/wt%	0.7
10%	418	Ash Content/wt%	0.05
30%	457	Slufur /wt%	0.12
50%	497	Nitrogen/wt%	0.11
70%	549	Carbon/wt%	86.43
90%	73.5%, 560°C	Hydrogen/wt%	13.53

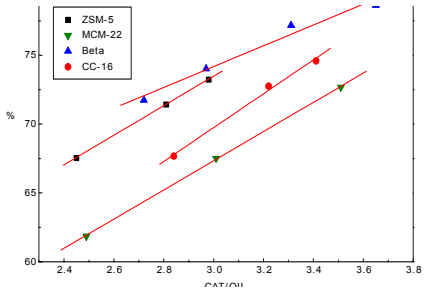

Fig 1a Conversion

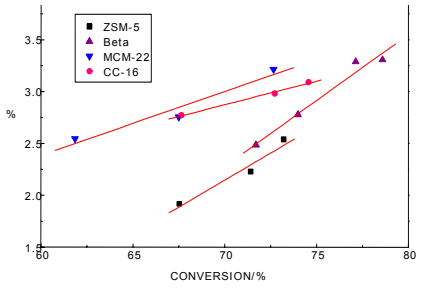

Fig1b Coke

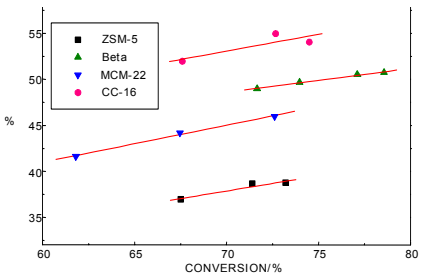

Fig1c Gasoline

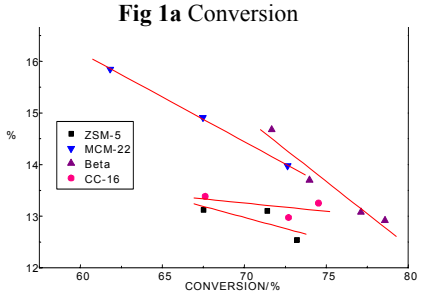

Fig1d LCO

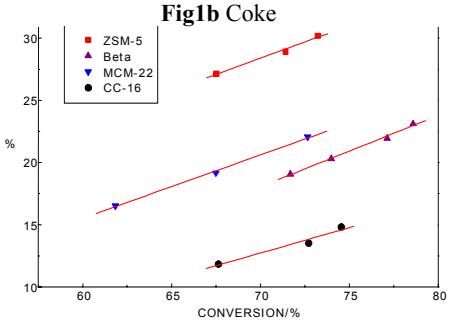

Fig1e LPG

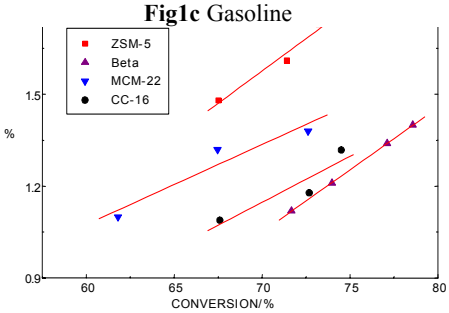

Fig1f Dry gases

Fig 1 Total conversion and Selectivities of products in the catalytic cracking of feedstock at T=500^{0}C, TOS=60s, and 8wt% of steamed additive

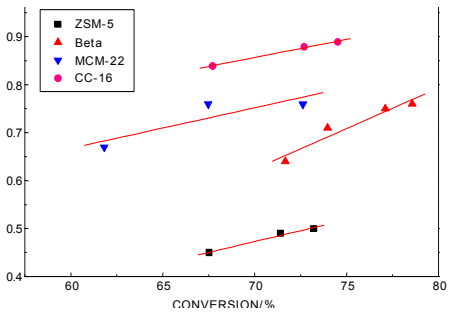

Fig2a HTC

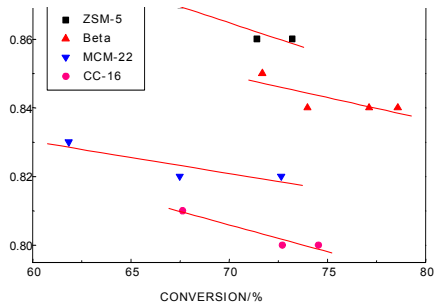

Fig2b $C_3^=$/ Total C_3

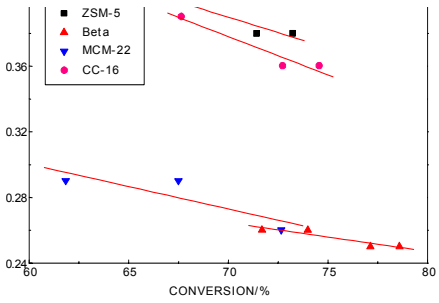

Fig2c CMR

Fig 2 Ratios of interest in the catalytic cracking of feedstock at T=500^{0}C, TOS=60s, and 8wt% of steamed additive

5 References

1. Jacquinot, E. J., Raatz, F., and Macedo, A., et al., *Stud. Surf. Sci. Catal.*, 1989, 46, 115.
2. Bonetto, L., Corma, A., and Cambior, M., et al., *Appl. Catal.*,**1992**, *82*, 37.
3. Bonetto, L., Corma, A., and Herrero, E., In Proceedings 9th International Zeolite Conference,. Higgins, J. B., and Treacy, M. M. J., eds., Montreal, 1992; Vol 2. pp. 369.
4. Corma, A., Davis, M., Fornes, V., et al., *J. Catal.*, **1997**, *167*, 438.
5. Corma, A., Alfaro, V. G., Orchilles, A. V., *Appl. Catal. A*, **1995**, *129*, 203.
6. Corma, A., Triguero, J. M., *J. Catal.*, **1997**, *65*, 102.
7. Absil, R. P. L., Angevine, P. J., Bundens, R. G., et al., *US 4983276*, 1990.
8. Absil, R. P. L., Angevine, P. J., Bundens, R. G., et al., *US 5039640*, 1990.
9. Liu, Z. Q., Wang, Y. M., Fu, J., He, M. Y., *Chin. J. Catal.*, **2002**, *23(5)*, 439.
10. Zhu, H. Y., A Dissertation for Ph. D. of RIPP, Beijing, 2001.
11. Wielers A F H, Vaarkamp M, Post M F M, *J. Catal*, **1991**, *127*, 51.
12. Yan, L. J., A Dissertation for Ph. D. of RIPP, Beijing, 1999.

TRANSFORMATION OF N-HEPTANE OVER HZSM-5 AND METAL/HZSM-5 CATALYSTS

Changlong Yin, Jingbing Wang, Wenyu Deng and Chenguang Liu

Key Laboratory of Catalysis, CNPC,
State Key Laboratory of Heavy Oil Processing
College of Chemistry & Chemical Engineering
University of Petroleum, Dongying, Shandong 257061, China

Introduction

Light alkanes aromatization over zeolite based catalysts is well known (1,2). It has been shown that HZSM-5 zeolite can be modified by incorporation of metal or metal oxides in order to obtain catalysts for selective hydrocarbon conversions (3-5). Activity, selectivity and stability of the catalysts for those shape selective reactions depend not only on the porous structure of the zeolite but also on the density of acid sites and their strength distribution, as well as on metal sites distribution and metal support interaction (6). The catalyst systems prepared in this way operate bifunctionally. Among the Group VIII metals, platinum and palladium supported on HZSM-5 have been widely and thoroughly investigated (7). Nickel on HZSM-5 has been found to be active in the aromatization, hydrocracking and isomerization of hydrocarbon (8-10).

In the present paper, a series of zeolite supported metal catalysts were prepared by impregnation method, the transformation of n-heptane over the catalysts was investigated

Experimental

Preparation of catalyst. A certain ratio (50:50 in this paper) of commercially available NaZSM-5 (Zhoucun, China, Si/Al atomic ratio=35) and alumina were mixed with dilute nitric acid, the mixture was then extruded into diameter 1.5mm sticks. The sample was dried in air at 110 ºC for 20h, and the supports containing ZSM-5 were obtained by calcination of above dry sticks at 500ºC for 6h. For sodium removal, the supports were treated with a solution of 1.0 M ammonium nitrate and then calcined at 500 ºC for 4h. The ZSM-5 supported nickel catalysts were prepared using incipient wet impregnation method. A series of Ni/HZSM-5, Mo/HZSM-5 and Ni-Mo/HZSM-5 catalysts were prepared according to this method. The active components NiO and MoO_3 were deduced from nickel nitrate and ammonium molybdate, respectively. All catalysts were dried at 110 ºC overnight, and then were calcined at 500 ºC for 4 hr.

Characterization of the catalysts. X-ray powder diffraction analysis was carried out with a Rigaku D/max-□A diffractometer using a graphite-filter CuKα radiation at a scan rate of 2 degrees per minute. Temperature programmed desorption (TPD) experiments were conducted on a self-installed TPD/TPR combined apparatus. About 0.1g of sample was placed in a stainless tubular reactor with inner diameter of 6mm. The sample was treated in a flow of ultra-pure nitrogen at a flow rate of 30ml/min at 150ºC for 2h to remove the impurity absorbed on the surface of samples. The reactor was cooled down to 50ºC and then NH_3 was pulsed into the system until the saturation of adsorption of NH_3 was reached at this temperature. The flow of nitrogen was kept for another 2h at 50ºC in order to obtain a high quality base line. Then the reactor was heated from 50ºC to 540ºC at a rate of 8ºC/min, holding at 540ºC for 60min. The gas evolved during each TPD run was detected with a thermal conductivity detector (TCD) and recorded by computer. The final Na content in the catalyst after ammonium nitrate treatment and the Ni and Mo contents in the catalysts were determined with atomic absorption spectrometry method.

Catalyst activity. Catalytic activity measurements were carried out in a high pressure micro-reactor unit of 10 mm I.D., 40cm in length. 10 ml of the catalyst extrudates were loaded in the reactor. For reduction process, the catalyst is reduced in H_2 atmosphere for 3 hours at 360ºC (for Ni/HZSM-5) or 500ºC (for Mo/HZSM-5 and Ni-Mo/HZSM-5). Pure n-heptane is then fed at test temperature. The reaction conditions are reaction pressure, 0.2~1.0MPa, H_2/feed ratio, 150, and LHSV, $2h^{-1}$. The reaction product was cooled and separated into gaseous and liquid products in a high-pressure separator. The gaseous products in this test were not analyzed, and the PIONA compositions of the liquid products were analyzed using a Varian 3800 gas chromatography equipped with a FID detector and a 100m-quartzose PIONA column.

Results and Discussion

Catalysts Characterization. The X-ray diffraction pattern of the support with 50% HZSM-5 content was completely matched with that of the pure HZSM-5, the Ni/HZSM-5, Mo/HZSM-5 and Ni-Mo/HZSM-5 catalysts' XRD patterns exhibit almost identical intensity of the peaks with HZSM-5 except some NiO and MoO_3 peaks occurring in the latter's. The final Na contents in the 50% HZSM-5 support is 0.066%; the Ni content in Ni/HZSM-5 catalyst is 7.1%; the content of Mo in Mo/HZSM-5 is 6.8%; the contents of Ni and Mo in Ni-Mo/HZSM-5 are 7.6% and 2.1%, respectively.

The spectrums of NH_3-TPD from HZSM-5(50%), Mo/HZSM-5 and Ni-Mo/HZSM-5 were shown in figure 1.It was reported (11) that according to the desorption temperature on NH_3-TPD profile, the acid cites were classified as weak (<300ºC), medium (300~450ºC) and strong (450~550ºC). It was indicated from the results that the acid sites distribution of the Mo/HZSM-5 and Ni-Mo/HZSM-5 changed after the metal incorporation in HZSM-5, the medium and strong acid sites in the catalysts weakened due to the effect of Ni and Mo.

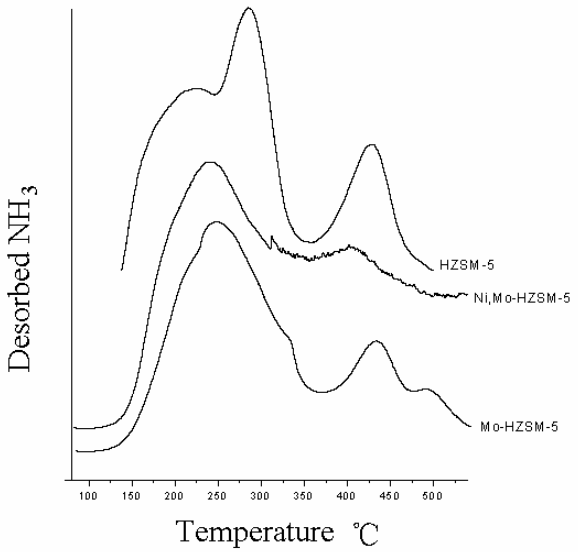

Figure 1. Temperature-programmed desorption spectrums of NH_3 from HZSM-5, Mo/HZSM-5 and Ni-Mo/HZSM-5

Effect of hydrogen pressure and reaction temperature. Effect of hydrogen pressure on the conversion of n-heptane and aromatics selectivity over Ni/HZSM-5 catalyst was shown in figure 2. The conversion of n-heptane increases with the enhancement of the hydrogen pressure, but the aromatics selectivity of the product decreases with the raising of the hydrogen pressure, which indicating that low hydrogen pressure can promote the production of aromatics. It is well known that low hydrogen pressure is in favor of dehydrogenation, while the dehydrogenation of n-heptane produces the aromatics. Figure 3 illustrates the effect ofreaction temperature on the aromatics selectivity over Mo/HZSM-5 and Ni-Mo/HZSM-5 catalysts. Aromatics selectivities of the two catalysts increase with the elevation of the reaction temperature, but Ni-Mo/HZSM-5 catalyst shows higher aromatics selectivity than that of Mo/HZSM-5 at 380~400ºC. There is a general acceptance (12) that the major role of the metal in the catalyst is to accelerate the combination of surface hydrogen, which formed from the dehydrogenation and dehydrocyclization process involved as key steps in the conversion of alkanes to aromatics via alkenic intermediates. The Ni-Mo may have a more marked tendency to accelerate the combination of surface hydrogen than the Mo in the catalyst, so the aromatics selectivity of the Ni-Mo/HZSM-5 catalyst is higher than that of Mo/HZSM-5. The relatively less medium and strong acid sites in Ni-Mo/HZSM-5 than in Mo/HZSM-5 is potentially related to the higher aromatization activity of the former.

Effect of metal component. The detailed products selectivity from n-heptane over HZSM-5, Mo/HZSM-5, Ni/HZSM-5 and Ni-Mo/HZSM-5 catalysts was summarized in Table 1. Under the same reaction conditions, Mo/HZSM-5 and Ni-Mo/HZSM-5 show higher conversion of n-heptane than the rest two catalysts. The aromatics selectivity increases with the order of HZSM-5, Mo/HZSM-5, Ni/HZSM-5 and Ni-Mo/HZSM-5. The Ni-Mo catalyst gives the highest aromatics selectivity 54.89, while the aromatics selectivity of the HZSM-5 is only up to 25.53. The relatively high percent ratios of paraffin and iso-paraffin in the products achieved from n-heptane over above four catalysts indicates that cracking of n-heptane occurring in the reactions. From the results it can be found that about 60% of n-heptane was cracked over HZSM-5 and only 20% of the feed was changed into aromatics. While only 30% of n-heptane was cracked over Ni-Mo/HZSM-5 and above 50% of the feed was changed into aromatics. The cracking of alkanes is related to the acidic sites on the catalyst; the incorporation of Ni-Mo on the HZSM-5 has weakened the medium and strong acidic sites on the HZSM-5, which depressed the cracking of n-heptane over the catalyst. The cracking of n-heptane over Mo/HZSM-5 and Ni/HZSM-5 was also restrained and the aromatics selectivity of the two catalysts was higher than that of HZSM-5 but lower than that of Ni-Mo/HZSM-5. The group components of the products from n-heptane over Ni-Mo/HZSM-5 with the reaction temperature were illustrated in figure 4. The results reveal that nheptane was mainly cracked over Ni-Mo/HZSM-5 at low reaction temperature (<300ºC), and at high temperature n-heptane was mainly aromatization over the catalyst. A few of olefin and naphthene were detected in the products of n-heptane over above tested catalysts, which can be thought of reasonably as the intermediate products of the dehydrogenation and dehydrocyclization processes.

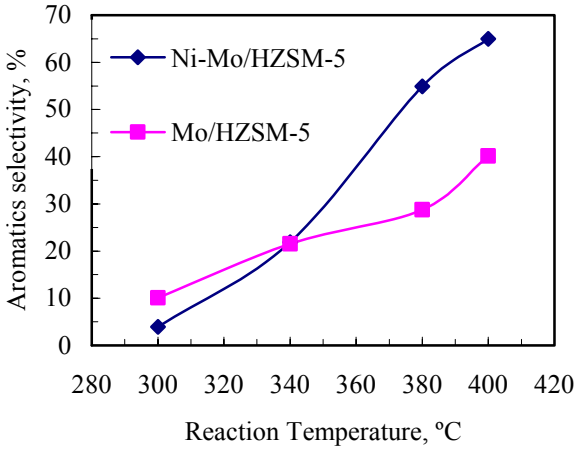

Figure 3. Effect of reaction temperature on the aromatics selectivity over Mo/HZSM-5 and Ni-Mo/HZSM-5 catalysts. Hydrogen pressure, 0.2MPa, H_2/feed ratio, 150, and LHSV, $2h^{-1}$.

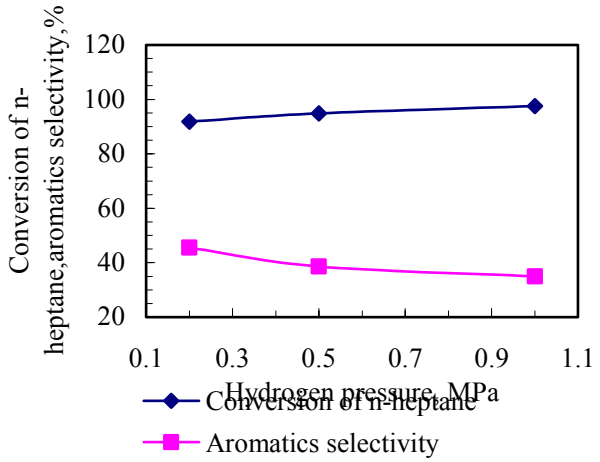

Figure 2. Effect of hydrogen pressure on the conversion of n-heptane and aromatics selectivity over Ni/HZSM-5 catalyst. Temperature 380ºC, H_2/feed ratio, 150, and LHSV, $2h^{-1}$.

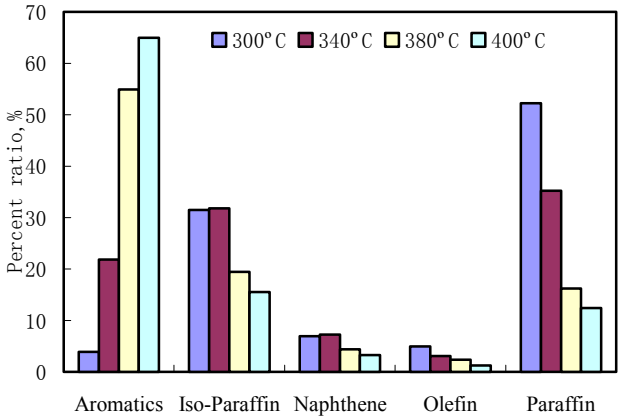

Figure 4. Products distribution from n-heptane over Ni-Mo/HZSM-5 with different reaction temperature. Hydrogen pressure, 0.2MPa, H_2/feed ratio, 150, LHSV, $2h^{-1}$

Table 1. Products Selectivity from n-heptane over Different Catalysts

Catalysts	HZSM-5	Mo	Ni	Ni-Mo
Conversion,%	**90.2**	**95.7**	**91.8**	**96.4**
Selectivity,%				
Aromatics	**25.53**	**28.71**	**45.51**	**54.89**
C6	2.44	2.20	4.50	3.88
C7	9.19	10.66	17.67	22.10
C8	9.73	11.30	17.20	21.60
C9	3.50	4.02	4.37	5.55
C10+	0.66	0.54	1.77	1.76
Iso-paraffin	**37.22**	**36.41**	**27.78**	**19.43**
C4	11.56	6.30	6.33	3.75
C5	17.13	15.05	11.18	7.10
C6	6.23	8.69	5.33	4.63
C7+	2.3	6.38	4.96	3.95
Naphthene	**2.67**	**2.49**	**2.39**	**4.39**
C6	0.62	0.10	0.40	0.88
C7	1.55	2.19	1.36	2.70
C8	0.12	0.05	0.11	0.24
C9	0.00	0.00	0.00	0.04
C10+	0.38	0.15	0.52	0.53
Olefin	**1.23**	**0.78**	**1.18**	**2.39**
C4	0.19	0.41	0.09	0.19
C5	0.24	0.32	0.18	0.39
C6	0.34	0.05	0.32	0.85
C7+	0.47	0	0.59	0.97
Paraffin	**33.13**	**29.54**	**20.15**	**16.20**
C3	2.71	1.39	3.00	2.23
C4	20.63	12.55	10.68	6.91
C5	8.07	12.87	4.89	5.40
C6	1.72	2.73	1.58	1.57
C7+	0.00	0.00	0.00	0.10
Unidentified	**0.22**	**2.06**	**2.99**	**2.70**

Hydrogen pressure, 0.2MPa, H_2/feed ratio, 150, and LHSV, $2h^{-1}$

Conclusions

The reaction of n-heptane over Ni/HZSM-5, Mo/HZSM-5 and Ni-Mo/HZSM-5 bifunctional catalysts was mainly Low hydrogen pressure can reduce the conversion of n-heptane but at the same time accelerate the production of aromatics. Experimental results show that the aromatization activity of the catalysts increases with the elevation of the reaction temperature and the incorporation of metal in HZSM-5 decreases the cracking reaction on the catalysts, while at the same time increases the reactions that may result in the production of aromatics, i.e. dehydrogenation and dehydrocyclization.

Acknowledgement. Financial support from PetroChina Corporation Limited is greatly appreciated.

References

(1) C. P. Nicolaides; N. P. Sincadu; M. S. Scurrell. *Catal. Today.* **2001**, 71, 429
(2) J. A. Biscardi; E. Iglesia. *J. Catal.* **1999**,182, 117
(3) D. Seddon, *Catal. Today* **1990**, *6(3),* 351
(4) Y. Ono, *Catal. Rev. –Sci. Eng*. **1992**, *34(3),* 179
(5) M. Guisnet; N. S. Gnep; F. Alario. *Appl. Catal. A* **1992**, *89*, 1
(6) R. J. Taylor; R. H. Petty, *Appl. Catal*. **1994**, *119*, 121
(7) S. Uemiya; I. Koike; E. Kikuchi, *Appl. Catal.* **1990**, *65*, 143
(8) D. Sun; Z. Zhao, *Ind. Eng. Chem. Res*. **1991**, *76*, 171
(9) C.V.V. Satyanarayana; D. K. Chakrabarty, *Appl. Catal*. **1990**, *66,* 1
(10) T. Inui; Y. Makino; F. Okazumi; S. Nagano; A. Miyamoto. *Ind. Eng. Chem. Res.* **1987**, *26,* 647
(11) J. R. Grzechowiak; J. Rynkowski, *Catal. Today*. **2001**, 65, 225-231
(12) J. A. Biscardi; G. D. Meitzner; E. Iglesia. *J. Catal*. **1998**, 179, 192

CHEMICAL STRUCTURE CHANGE OF RECYCLING VACUUM BOTTOM RESIDUE FROM SLURRY-BED HYDROCRACKING OF KARAMAY ATMOSPHERIC RESIDUE IN THE PILOT PLANT

Bin Shi, Guohe Que

State Key Laboratory of Heavy Oil Processing, College of Chemistry & Chemical Engineering, University of Petroleum, Dongying, Shandong 257061, China, shibin@hdpu.edu.cn

INTRODUCTION

Since the early 1980s, slurry-bed hydrocracking of residue has been developed for upgrading poor-quality residue, which may be high content of sulfur, metal and Conrason carbon residue, to produce distillate product(1). Conventionally slurry bed hydrocracking of residue is achieved by once-through heating residue in a high-pressure hydrogen atmosphere in the presence of a dispersed and disposable catalyst (2). However, once-through hydrocracking mode dependent on different reaction conditions can give 60%~80 % conversion (<524^{o}C). To achieve higher conversion of residue and keep coke formation low and the operation successful at the same time, some hydrocracking modes can be adopted such as cracked vacuum residue recycling, cracked atmospheric residue recycling and cracked vacuum gas oil recycling. Generally cracked atmospheric residue recycling model can achieve higher conversion and get more distillate products than the other three models at the same reaction conditions. The objective of this study is to investigate chemical structure change of cracked atmospheric residue recycling from slurry-bed hydrocracking and to evaluate the subfractions change in the cracked atmospheric residue recycling.

EXPERIMENTAL

The feed was chosen as Karamay atmospheric residue and obtained from Karamay Petrochemical Complex, Xingjiang, China. The property of Karamay atmospheric residue (>360^{o}C) and its vacuum residue (>500^{o}C) was presented in Table 1. Keeping the total VSHL is 1h^{-1}, Karamay atmospheric residue was hydrocracked in the presence of about 1000 ppm multi-metal dispersed catalyst, under 10MPa H_2, 445 ^{o}C,in an pilot plant of 120 kg/d and the products were fractionated into gases, naphtha (C_5~180^{o}C), AGO (180~360 ^{o}C) and atmospheric bottom residue (>360^{o}C). Some atmospheric bottom residue (about 5wt%) was thrown off, and the other atmospheric bottom residue was pumped back intermittently and mixed with the fresh feed for recycled hydrocracking (the ratio is 1:1). Thus we can obtain non-recycled atmospheric bottom residue, which is the once-through atmospheric bottom residue (ABR#), the first-time recycled atmospheric bottom residue (first-ABR), the second-time recycled atmospheric bottom residue (Sec-ABR), the third-time recycled atmospheric bottom residue (Third-ABR). The atmospheric bottom residues(>360^{o}C) were distillated into the corresponding vacuum bottom residues(>500^{o}C), which include fresh VBR(VBR), the once-through vacuum bottom residue (VBR#), the first-time recycled vacuum bottom residue(first-VBR), the second -time recycled vacuum bottom residue(Sec-VBR), the third-time recycled vacuum bottom residue(Third-VBR) and these VBRs were precipitated using n-pentane. The pentane-solubles were separated into fraction 1 (mixture of saturates, light and middle aromatics), fraction 2 (heavy aromatics), fraction 3(light resins), fraction 4 (middle resins) and fraction 5 (heavy resins) by the alumina chromatography column with 5% water. The separation scheme is shown in Figure1. The contents of H, C and average molecular weights of all subfractions were determined by Shimazsu Element Analyzer and Knauer analyzer by VPO, respectively. Structural parameters of fractions for all VBRs were calculated based on Density Method and the calculation program was shown in the appendix (2).

Table 1. Properties of Karamay atmospheric residue and Karamay Vacuum Residue

Sample	AR	VR
Density, d_4^{20}	0.9442	0.9613
Viscosity (100°C), mm^2·s^{-1}	109	1115
Molecular weight (VPO)	470	950
CCR, wt%	7.0	11.0
C, wt%	86.6	87.1
H, wt%	12.5	11.9
H/C atomic Ratio	1.73	1.62
N, wt%	0.13	0.63
S, wt%	0.13	0.24
Ni, ug·g^{-1}	11.8	21.6
V, ug·g^{-1}	0.35	0.65
Ca, ug·g^{-1}	346	460
Fe, ug·g^{-1}	10.2	20.4
Saturate wt%	50.4	35.3
Aromatic	22.2	25.6
Resin	27.2	38.3
n-C_7 Insoluble	0.2	0.8

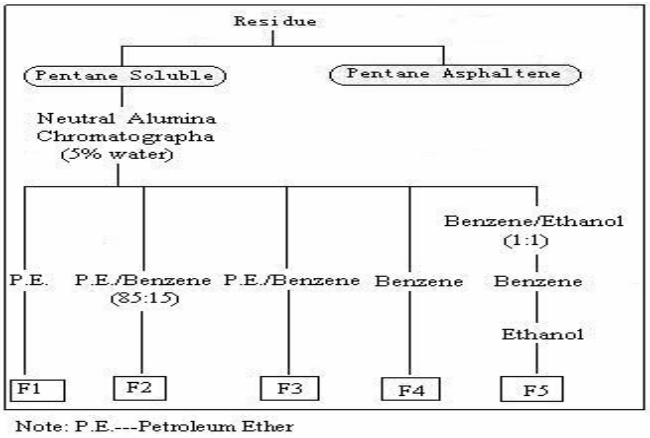

Figure1 Separation of six subfractions in residue

RESULTS AND DISCUSSION

Change of Six Fraction Yields. From Table2, it is clear that the VGO and vacuum bottom residue yields of AR have been greatly changed after slurry-bed hydrocracking. Before reaction, VGO and VBR in Karamay atmospheric residue were 41.02%, 58.98% and after hydrocracking, they were 61.77%, 38.23%. When cracked atmospheric residue was recycled from slurry bed hydrocracking(recycling ratio 1:1) , the decrease of VGO in AR and the increase of VBRs depended on different recycling times. The more recycling times were, the less yields of VGO were and the more yield of VBRs were. It shows that the recycled AR is the more refractory with the recycling times.

Tables 2 yields for different recycle times of VGO and vacuum bottom residue

	VGO(*W*/%)	VBR(*W*/%)
ABR	41.02	58.98
ABR#	61.77	38.23
First- recycled ABR	58.31	41.69
Second- recycled ABR	55.71	44.29
Third- recycled ABR	31.92	68.08

Tables 3 Subfractions yields for feed and different times recycled VBRs

	VBR	VBR#	First-VBR	Sec-VBR	Third-VBR
F1(*W*/%)	54.53	42.58	42.09	41.84	41.47
F2(*W*/%)	9.98	9.27	9.64	9.10	8.77
F3(*W*/%)	13.28	13.27	13.76	13.83	12.80
F4(*W*/%)	7.26	6.13	6.40	7.20	7.29
F5(*W*/%)	8.42	6.65	5.98	6.95	6.18
F6(*W*/%)	6.53	22.11	22.12	21.08	18.88
Coke(*W*/%)	0	1.80	2.45	2.89	4.57
F1+F2(*W*/%)	61.51	51.85	51.67	50.94	50.24
F3+F4+F5(*W*/%)	28.96	26.05	26.14	27.98	26.27

From Table3, it is clear that the yields of six sub fractions in fresh vacuum residue and residues from once-through operation and the recycling-operation have been changed, although F1+F2 (saturates and aromatics) was the main fraction of fresh VBR and hydrocracked VBRs. Among six sub fractions, F1 and F6 have considerably changed after slurry-bed hydrocracking, On the one hand, F1 in VBR decreased sharply, while F6 and coke increased sharply. On the other hand, with recycling-operation times increasing, the yields of six fractions in recycled VBRs have changed smooth. It is clear that the biggest change happened in the once-through hydrocracking operation. It is shown that it is in the first time hydrocracking process (the once-through hydrocracking process) that the cracking and condensation reaction of fresh feed was the most obvious in all processes. Although the increasing cracking yields could be achieved through recycling operation of cracked atmospheric residue, increasing degree of that was limited since cracking reaction of ABR had almost been finished. On the contrary, the degree of increasing of condensation reaction was very clear depended on the recycling-operation times.

H/C and average molecular weight of six fraction. From Table 4, H/C of six subfractions for feed and different times recycled VBR show different change. H/C of F1 hardly changed and the H/C of F2, F3, F4 and F5 decreased a little. However, H/C of F6 decreased sharply. Tables 5 give out the average molecular weight (VPO) of six subfractions for feed and different times recycled vacuum bottom residue. It is obvious that average molecular weight of all six subfractions decreased after once-through hydrocracking and different ABR recycling times hydrocracking. Among six subfractions, the decreasing trends of F6, F5 and F4 were very clear, especially for F6. It is shown that in the hydrocracking and different cracked ABR recycling hydrocracking, the moleculars of six subfractions have experienced different degree cracking reactions. On the other hand, the more complex molecular (F6, F5 and F4) have gone through the more considerable cracking reactions. In addition, the de-aggregation reaction of C_5-asphaltene can be important in the hydrocracking based on the three-time sharp change of average molecular weight before and after once -through reaction.

Tables 4 H/C of fractions for feed and different times recycled VBRs

H/C	VBR	VBR#	First-VBR	Sec-VBR	Third-VBR
F1	1.76	1.75	1.72	1.73	1.76
F2	1.51	1.43	1.31	1.31	1.35
F3	1.49	1.27	1.16	1.17	1.19
F4	1.44	1.28	1.23	1.17	1.19
F5	1.41	1.43	1.34	1.32	1.28
F6	1.38	0.88	0.84	0.83	0.86

Tables 5 Average molecular weight (VPO) of fractions for VBR and different-time recycled VBRs

	VBR	VBR#	First-VBR	Sec-VBR	Third-VBR
F1	730	682	637	614	608
F2	880	718	549	518	550
F3	1160	871	781	708	704
F4	1485	988	894	695	699
F5	1484	791	733	798	909
F6	7879	2545	2247	2330	1684

Structural parameters of subfractions for VBR and different-time recycled VBRs. From Table 6-9**,** Structural parameters of fractions for VBR and different-time recycled VBR have different degree change in the once-through hydrocracking and recycled hydrocracking process. After once-through hydrocracking, structural parameters including Condesation Index, aromaticty, C_T, C_A, R_A, R_T of six fractions have changed greatly compared to the corresponding of feed. Then after ABR recycling hydrocracking, structural parameters of six fractions have changed smooth deepened on the recycling times and the changing trend show Condesation Index, aromaticty, C_T, C_A, R_A, R_T of six fractions have more change to a smooth limit while more recycling times go on. It is shown that the substantial chemical structure change happened in the first hydrocracking. For F_6, F_5 and F_4, the important change can be more obvious

CONCLUSION:

1. Saturates and aromatics were the main subfractions of fresh VBR and all hydrocracked VBRs
2. Structural parameters of six fractions after once-through hydrocracking have changed greatly compared to the corresponding of feed. It is shown that the substantial chemical structure change happened in the first-time hydrocracking.
3. Structural parameters of six fractions have changed smooth deepened on the recycling times. After different times recycling hydrocracking, the average molecular weights of six subfractions decrease and the content of saturates decreases obviously, while asphaltene and resins increase sharply, C/H, aromaticity and Condensation Index of the asphaltene increase.

REFERENCES:

[1] Alberto Del Bianco,Nicoletta Panariti and Mario Marchionna , Upgrading heavy oil using slurry processes [J]. Chemtech, 1995,25.(11):35-43

[2] Wen Jie Liang Petroleum Chemistry [M]. Press of University of Petroleum (China), 1993

Tables 6 Structural parameters of fractions for VBR and different-time recycled VBRs

		F1	F2	F3	F4	F5	F6
VBR	Conden. Index	0.136	0.217	0.223	0.240	0.242	0.245
	C_T	47.0	63.7	84.4	107.0	104.7	528.6
	C_A	4. 9	17.4	24.2	34.5	36.2	198.0
	R_T	4.2	7.9	10	14	14	65.8
	R_A	0.7	3.9	5.6	8.1	8.5	49.0
	R_N	3.5	4.0	4.8	5.5	5.1	16.8
VBR#	Conden. Index	0.140	0.242	0.281	0.278	0.229	0.360
	C_T	49.0	52.8	64.3	71.9	51.7	184.8
	C_A	5.6	17.6	28.6	31.8	17.4	141.1
	R_T	4.4	7.4	10.0	11.0	6.9	34.3
	R_A	0.9	3.9	6.7	7.4	3.8	34.8
	R_N	3.6	3.5	3.4	3.6	3.1	-0.5
First-times recycled VBR	Conden. Index	0.149	0.271	0.308	0.288	0.259	0.371
	C_T	46.0	40.5	57.9	64.7	50.7	166.5
	C_A	6.0	16.8	30.8	30.8	20.5	132
	R_T	4.4	6.5	9.9	10	7.6	31.9
	R_A	1.0	3.7	7.2	7.2	4.6	32.5
	R_N	3.4	2.8	2.7	3.1	2.9	-0.7
Second-times recycled VBR	Conden. Index	0.146	0.273	0.306	0.302	0.265	0.372
	C_T	44.4	38.2	52.6	50.32	56.0	172.3
	C_A	5.5	16.1	27.5	26.4	23. 4	138.0
	R_T	4.2	6.2	9.0	8.6	8.4	33.0
	R_A	0.9	3.5	6.4	6.1	5.3	34.0
	R_N	3.4	2.7	2.7	2.5	3.1	-1.0
Third-times recycled VBR	Conden. Index	0.136	0.263	0.302	0.300	0.275	0.368
	C_T	43.7	40.6	52.3	51.1	64.3	125.1
	C_A	4. 6	15.8	26.6	26.2	28.6	97.1
	R_T	4.0	6.3	8.9	8.7	9.8	24.0
	R_A	0.6	3.5	6.2	6.0	6.6	23.8
	R_N	3.3	2.9	2.7	2.6	3.2	0.2

Tables 7 Aromacity of subfractions for VBR and different-time recycled VBRs

f_a (%)	VBR	VBR#	First-VBR	Sec-VBR	Third-VBR
F1	10.37	11.28	12.96	12.41	10.51
F2	27.33	33.34	41.5	42.12	38.97
F3	28.69	44.51	53.24	52.32	50.87
F4	32.19	44.19	47.7	52.6	51.23
F5	34.56	33.6	40.42	41.74	44.56
F6	37.45	76.36	79.34	80.13	77.61

Tables8 R_T of subfractions for VBR and different-time recycled VBRs

R_T	VBR	VBR#	First-VBR	Sec-VBR	Third-VBR
F1	4.2	4.4	4.4	4.2	4.0
F2	7.9	7.4	6.5	6.2	6.3
F3	10.0	10.0	9.9	9.0	8.9
F4	14.0	11.0	10	8.6	8.7
F5	14.0	6.9	7.6	8.4	9.8
F6	65.8	34.3	31.9	33.0	24.0

Tables9 R_A of subfractions for VBR and different-time recycled VBRs

R_A	VBR	VBR#	First-VBR	Sec-VBR	Third-VBR
F1	0.7	0.9	1.0	0.9	0.6
F2	3.9	3.9	3.7	3.5	3.5
F3	5.6	6.7	7.2	6.4	6.2
F4	8.1	7.4	7.2	6.1	6.0
F5	8.5	3.8	4.6	5.3	6.6
F6	49.0	34.8	32.5	34.0	23.8

Appendix:

Density Method for calculating structural parameters of subfractions in residue is as follows:

1.Relative density: $D_4^{20}=1.4673-0.04.31\times H\%$

2.Ratio of H/C atom: $H/C =11.92\times H\%/C\%$

3.Mc/d: $Mc/d=Mc/(D_4^{20} \times C\%)$

4.Corrected Mc/d: $(Mc/d)c= Mc/d-6.0(1- C\% - H\%)/ C\%$

5.Aromaticity in an average molecular: $fa=0.09(Mc/d)c-1.15\ H/C +0.77$

6.Condesation Index in an average molecular: $C.I=2-H/C-fa$

7.Total carbon atom in an average molecular: $C_T=(C\%\times M)/12.01$

8.Aromatic carbon atom in an average molecular: $C_a= C_T \times fa$

9.Total rings in an average molecular: $R_T=[C_a\times(C.I)/2]+1$

10.Aromatic rings in an average molecular: $R_A=(C_a -2)/4$

11.naphthenic rings in an average molecular: $R_N=R_T-R_A$

Note: M refers to average molecular weight

Hydrocracking of LiaoHe Vacuum Residue with Oil-Soluble Co-Ni Bimetallic Catalysts and Hydrogen Donor

Bin Shi * *Guohe Que*

State key laboratory of heavy oil processing University of Petroleum, Dongying, ShanDong, 257061, PRC
E-mail:shibin@hdpu.edu.cn

INTRODUCTION

The use of oil-soluble metal compounds to enhance the distillate yield and to reduce coke formation has been studied extensively in the hydrocracking of poor-quality heavy residue, which often have high contents of sulfur, nitrogen, metal, asphaltene and CCR (1). Such compounds are based on the transition metals, like Mo, Ni, Co, W, Cr, V, Fe, Cu, Zn and so on. It is clear and important that the corresponding metal sulfide, such as MoS_2, Ni_8S_9, CoS, Fe_{1-X} S and so on can be the activation catalysts in the slurry-bed hydrocracking of heavy oil (2). On the other hand, it is well known and of great industrial importance that the addition of a second transition metal Co or Ni to a binary sulfide such as MoS_2 or WS_2 can produce an enhancement of HDS activity (3). Some researchers also transplanted the promoters of Co, Ni or Fe into the dispersed Mo catalytic hydrocracking system of poor-quality heavy residue considering the addition of promoter can decrease the cost of the disposable catalysts and they found that Ni-Mo, Co-Mo and Fe-Mo show very clear enhancement of hydrocracking activity compared to monometallic dispersed catalyst (4-6). The reason is attributed to the better dispersion effect or synergism effect like the supported catalysts such as Mo-Ni (Fe)/Al_2O_3 in the slurry-phase hydrocracking system. As the promoters, we are very interested in the performance of bimetallic catalysts of Co and Ni in the hydrocracking system.

Hydrogen donor in petroleum chemistry can be classified into three kinds in a broad sense. That is the hydrogen donors can produce anionic hydrogen, radical hydrogen and molecular hydrogen, which include complex hydride (such as $LiAlH_4$ and $NaBH_4$), poly-ring hydroaromatics and gaseous hydrogen and water gas ($CO+H_2+CO_2+H_2O$). In a narrow sense, hydrogen donor indicates those poly-ring hydroaromatics that have incompact C-H bondage and the typical hydrogen donors are tetralin, dihydroanthrancene and so on. Since these compounds can provide radical hydrogen reacted with hydrogen-acceptors, when heated together with them, thus hydrogen donors have often been applied into coal liquefaction, petroleum residue conversion, transportation fuel and other petroleum chemicals as hydrogen shuttle, hydrogen-transferor and radical scavenger based on their important roles (7).

In the paper we investigated and evaluated the application of bimetallic oil-soluble catalysts and the combination of bimetallic oil-soluble catalysts and hydrogen donors in the slurry-phase catalytic hydrocracking of LiaoHe vacuum residue.

EXPERINENTAL

The naphthenic-base LiaoHe vacuum residue (LHVR) was upgraded and the main properties were reported in Table 1. The experiments were carried out in a 100ml FDW-01 magnetic-stirred autoclave and LiaoHe vacuum residue was upgraded with two kinds of oil-soluble monometallic catalysts cobalt naphthenic and nickel naphthenic as hydrocracking dispersed catalyst, and tetralin (THN) as hydrogen donor. The experimental procedure was as follows: 34g residue blended with 200μg/g Co-naph or Ni-naph or their mixture of the Co-naph and Ni-naph and 3.4g tetralin (THN) was placed in the autoclave, pressurized hydrogen to 7.0Mpa, heated to reaction temperature 436 ^oC and then maintain it smoothly. The autoclave was cooled with water quickly when defined reaction time 1h was achieved. After reaction, the products were recovered with toluene. The toluene-insoluble (TI or coke) was separated from the reaction product by centrifugation. The toluene-soluble was treated to remove toluene and the products were distillated into AGO (160~350 ^oC), VGO (350 ~450^oC) and reacted residue (>450^oC). The amounts of naphthalene and tetrahydronaphthalene were analysed by GC.

RESULTS AND DISCUSSION

Comparison of hydrothermal, catalytic hydrocrcking system and hydrothermal system with hydrogen donors. In order to make a comparison of catalytic activities between the Ni-based oil-soluble monometallic catalyst and Co-based oil-soluble monometallic catalyst used in LiaoHe vacuum residue hydrocracking processes, the same concentrations of these two kinds of catalysts were separately used in the hydrocracking experients, while the hydrothermal and hydrothermal in the presence of 10%wt tetrlin based on feed were also conducted as comparison, the results are listed in Table 2.Both of the monometallic catalysts and tetralin could suppress coke formation and cracking reations in comparison with hydrothermal cracking system without adding catalysts and H-donor and the effects of the two oil-soluble catalysts were more clear than that of tetralin. However, the Co-based oil-soluble catalyst gave lower total conversion yield than the Ni-based oil-soluble catalyst did. The former produced higher conversion per unit coke than the latter did. The conversion per unit coke was 23.60% for the Co-based oil-soluble catalyst, 18.02%for Ni-based oil-soluble catalyst and 9.11% for tetralin, 6.66% for hydrothermal cracking.

Table 1 Composition and properties of LHVR

Molecular weight, (VPO)	870	V, μg/g	2.9
Density/g/cm^3 (20^oC)	0.9976	Ni, μg/g	123
Saturates	17.4	C,m%	86.9
Aromatics	30.3	H,m%	11.0
Resins	50.2	N,μg/g	10800
C_7-asphaltene	2.1	S,μg/g	4300
Total metal content,μg/g	259	CCR, %	14.4

Catalytic hydrocracking of LHVR by using oil-soluble Ni- Co bimetallic catalysts. As shown in Table 3, the combined employment of Ni-based oil-soluble catalyst and Co-based oil-soluble catalyst seems to produce slight synergetic effect on the coke inhibition. With 200μg/g Co-based oil-soluble catalyst and 200 μg/g Ni-based oil-soluble catalyst, the coke yield was 2.39% and 3.34%, respectively; and conversion was 56.40% and 60.21%, respectively. With 100 μg/g Co and 100 μg/g Ni bimetallic catalysts, the coke yield and conversion were 2.71% and 59.00%, which were nearly simple mathematical addition of corresponding yields.

As the promoters of a second transition metal Co or Ni to a binary sulfide such as MoS_2 or WS_2 of HDS catalyst, the addition of the promoters can produce a great enhancement of HDS(3). As the promoters of Co, Ni or Fe in the dispersed Mo catalytic hydrocracking system of residue, the improvement is also considerable(4-6). But the combination effect between Ni and Co was very slight so that it is reasonable that the combination of Ni-Co oil-soluble bimetallic catalysts could produce simple

mathematical addition effect on the coke inhibition, residue conversion and conversion per unit coke in the upgrading residue, which was different from the clear and traditional synergism between Mo and Co or Mo and Ni in the HDS systems.

Catalytic hydrocracking of LHVR by using oil-soluble Ni-Co bimetallic catalysts and Tetralin. The authors have studied the synergism between hydrogen donors and Mo, Ni, Co and Fe dispersed monometallic catalysts in the literature (8,9). The activities of the four pure oil-soluble catalysts were improved based on conversion per unit coke, especially the activity of Mo gave a large leap with a combinatin with tetralin, however the order of catalyst activities did not changed. The combination of monometallic catalysts and tetralin could effectively inhibit coke formation and yield a good upgrading of LHVR (8,9).

The upgrading results of catalytic hydrocracking of LHVR with oil-soluble Ni-Co bimetallic catalysts and tetralin were listed in Table 4, in which the upgrading results with pure Ni-Co bimetallic catalysts or pure tetralin were also listed as comparison. Table 4 shows more coke generated in the cracking of residue with pure H-donor or pure dispersed Ni-Co bimetallic catalysts. However, H-donor combined with dispersed bimetallic catalyst could improve upgrading results of LHVR than with pure H-donor or pure Ni-Co bimetallic catalysts. The synergism between hydrogen donor and dispersed Ni-Co bimetallic catalyst in hydrocracking conversion of LHVR was the same clear as that between dispersed monometallic catalysts and H-donors according to the value of conversion per unit coke. It is clear that synergism between hydrogen donor and dispersed Ni-Co bimetallic catalysts was important to upgrading of heavy residue.

CONCLUSION

1. Compared with hydrothermal cracking, the addition of dispersed monometallic catalysts or hydrogen donor can improve upgrading of vacuum residue.
2. The combination of Ni-Co oil-soluble bimetallic catalysts produces simple mathematical addition effect on the coke inhibition and residue conversion in the upgrading residue, which was different from the clear and traditional synergism Mo and Co or Mo and Ni in the HDS systems.
3. It is clear that there is synergism between dispersed Ni-Co bimetallic catalyst and hydrogen donor in LHVR cracking conversion and the synergism helped to effectively inhibit coke

Acknowledgment. The authors thank Mr.Bin Huang for his helpful and aborative experimental work.

REFERENCES:

1. Alberto Del Bianco and Nicoleta Panariti. Thermocalalytic hydro conversion of heavy petroleum cuts with dispersed catalyst [J] Appl.Catal, 1993,(94):1-16
2. Chengguang Liu. Hydrocracking of Gudao vacuum residue in the presence of dispersed catalysts [D] University of petroleum: 1991
3. Petroleum Chemistry [M] edited by WenJie Liang. Press of University of Petroleum (China), 1993
4. Ruihua Sheng Hydrocracking of LHVR with bimetallic oil-soluble catalysts [D] University of petroleum: 1997.
5. Zongxian Wang,Hongyu Zhang,Aijun Guo, Guohe Que Catalytic hydrocracking of petroleum vacuum residue by using a combination of molybdenum based oil-soluble and iron-based water-soluble catalysts Preprints, Div. Fuel Chem. ACS. 1998.43. (2). 486-489..
6. Pradhan V.R., Herrick D.E., Tierney J.W. et al. Finely dispersed iron, iron-molybdenum and sulfated iron oxides as catalysts for coprocessing reactions [J] Energy & Fuels, 1991, 5: 712
7. Bin Shi, Guohe Que. Hydrogen Donor (personal communication to Dr.Oona Schmid and Dr.J.G.Speight).
8. Bin Shi, Guohe Que Effects of additives and H-donors on catalytic hydrocracking of residue Preprints American Chemistry Society Petroleum Division. 2002.47(2). 113-116
9. Bin Shi, D.L.Lin,L.Q.Wang, G.H.Que. Synergism between hydrogen donors and dispersed catalysts in LHVR hydrocracking. Preprints American Chemistry Society Petroleum Division. 2001.46.(4).325-328

Table 2 Hydrocracking of LHVR with oil-soluble monometallic catalysts or tetralin

Reaction system	Product distribution /wt%				Conversion wt%	Conversion per unit coke
	<350°C	350~450°C	>450°C	coke		
Blank	45.77	19.43	25.61	9.79	65.20	6.66
THN (10%wt)	41.54	22.36	29.06	7.02	63.92	9.11
Ninaph (200μg/g)	35.25	25.96	35.45	3.34	60.21	18.02
Conaph (200μg/g)	26.70	29.70	41.21	2.39	56.40	23.60

Table 3 Catalytic hydrocracking of LHVR by using oil-soluble Ni-Co bimetallic catalysts

Catalysts, μg/g		Product distribution/wt%				Conversion wt%	Conversion per unit coke
Conaph	Ninaph	<350°C	350~450°C	>450°C	coke		
200	0	26.70	29.70	41.21	2.39	56.40	23.60
180	20	28.36	28.94	40.50	2.40	57.30	23.87
160	40	30.95	27.25	39.29	2.51	58.20	23.19
100	100	32.80	26.21	38.09	2.71	59.00	22.60
40	160	33.18	26.32	37.51	2.99	59.50	19.90
0	200	35.25	25.96	35.45	3.34	60.21	18.02

Table 4 Catalytic hydrocracking of LHVR by using oil-soluble Ni-Co bimetallic catalysts and tetralin

Catalysts, μg/g		Tetralin	Coke /wt%	Conversion /wt%	Conversion per unit coke	Donating yield of tetralin /wt%
Conaph	Ninaph					
0	0	0	9.79	65.20	6.66	---
		10	7.02	63.92	9.11	84.23
200	0	0	2.39	56.40	23.60	--
		10	1.39	54.98	39.55	25.32
160	40	0	2.51	58.20	23.19	--
		10	1.59	56.00	35.22	27.10
100	100	0	2.61	59.00	22.61	--
		10	1.73	57.42	33.19	29.33
40	160	0	2.99	59.50	19.90	--
		10	1.93	57.91	30.00	32.00
0	200	0	3.34	61.21	18.33	--
		10	2.29	59.35	25.92	34.86

Steps in the Development of the GTL Process

R. L. Espinoza, D. S. Jack, H. A. Wright, J. D. Allison and S. R. Landis

Ponca City Technology Center, ConocoPhillips, PO Box 1267, Ponca City, OK 74602

1. Introduction

A commercial GTL process requires the synthesis of several different technologies with the core ones being those closely related to the generation of synthesis gas (CO + H2), Fischer-Tropsch synthesis and refining the F-T products. The methodology for the development of these technologies is similar, although some components (eg catalysis, reactor, modeling, etc) may be present in a higher degree in any given one, depending upon the stage of development. In this paper, and based on our experience, we will summarize the main technical development areas and the degree of detail necessary as a function of the project stages.

2. First Phase: Definition of the basic technology components

The full development of a GTL technology is an expensive process that may require an investment of a few hundred million dollars. Even this first definition stage, or exploratory stage, may require a considerable investment. There should therefore already be some basic ideas and/or preliminary experimental results that justify this first phase. Typical activities at this stage are:

- Catalyst screening. It is desirable to concentrate on a pre-selected main catalysis system (e.g., Fe or Co for FT, noble metal or standard refinery type FT wax hydrocracking catalyst for products upgrading), although work should include other systems to maximize chances for significant innovation. Normally this stage is characterized by a large amount of short experimental tests in micro reactors, with full characterization on only selected samples. There is an important input from the open literature (to avoid re-inventing the wheel) and a high creativity component. Catalyst deactivation studies are mostly confined to the identification of deactivation mechanism(s). Different catalyst supports and preparation techniques are studied at this stage.

- Selection of the reactor system. This should proceed in close coordination with the catalyst development due to the strong interdependence between these two elements. Micro reactors are commonly used, predominantly fixed bed and CSTR type reactors. This stage is characterized by the identification of the main advantages and disadvantages of the various reactor types and technical challenges for reliable commercial application.

- Preliminary modeling. Development of global kinetic equations, preliminary selectivity correlations, preliminary reactor(s) models based mainly on literature data for hydrodynamics, heat and mass transfer, solubilities, diffusion effects, etc

- Process integration. It is important to begin full time process engineering activities to understand how the emerging technologies fit into a commercial flow scheme. This activity also provides guidance to the technology team regarding the most important areas of research focus to ensure commercial success. Early process optimization proposals are developed.

3. Second Phase: Pilot Plants and definition of choice technology

In this stage, the type of reactors to be further developed has been identified, as well as the catalysts families and final desired products spectra. This phase is characterized by a period of focusing for the various developmental activities. Final products are produced in larger amounts and their properties are expected to be similar to those expected in commercial plant.

- Catalysis. This is a period of consolidation for the accuracy of predictive versus observed behavior. Efforts now concentrate on characterization, support design, stability, selectivity, costs and beginning of scale-up efforts. Design must be adapted to the characteristics of the selected reactor(s) and their effect on catalyst performance.

- Reactors. Depending upon the type selected, some hydrodynamic data are now available from smaller reactors and proposed solutions to their characteristic shortcomings are preliminarily tested and designs improved. A period of deeper technological understanding begins.

- Modeling. New data are used to improve existing models. Accuracy is improving and they can be used for preliminary commercial design. More sophisticated tools (like CFD) can now be developed.

- Process Integration. Optimum current technology configuration of the GTL process is now proposed, although it may still be subject to further improvement during the next phase. These results will help to focus the technical development even further.

4. Third Phase: Demonstration Plant

At this point, the main components of the GTL technology have been developed and will be put to the test. No major changes should occur, although an incremental improvement on the technology is expected. Final products are fully representative of commercial ones.

- Catalysis. The scale-up of the catalysts preparation to commercial size batches is completed well ahead of the plant start-up. Efforts now concentrate on the demonstration of all the elements of catalyst performance, and some "polishing up" is still expected. These elements have been considered in the design of the system, including requirements for efficient process integration.

- Reactors. The design and construction have concentrated not only on economic factors but also on
reliability. Catalyst development results have played an important role.

- Modeling. Data from the larger reactor size should only result in minor improvements. Models are consolidated for commercial design.

- Process Integration. Desired plant configuration is defined. Reactor and catalysts characteristics have been taken into account.

Figures 1 and 2 illustrate the catalyst development process. Figure 1 is a typical example of industrial catalyst development. During the first or exploratory stage, the selected catalyst family do not perform optimally and the increase in performance – in this case catalyst intrinsic activity – is not high. The reason is that the chosen catalyst family must also fulfill other requirements like physical properties, selectivity, deactivation behavior and be adequate to the characteristics of the most probable reactor to be selected. At the onset of the second or consolidation stage, where the contribution of surface characterization increases and as the understanding of the catalyst system increases, there is a better match between predicted and expected catalyst behavior. This facilitates the design of improved versions of the same family of catalysts. The goal in this stage is to improve the performance of the chosen catalyst family in a fast manner, getting as close to the optimum as possible. During the later part of this phase, resources allocated to the identification of improved catalyst systems – probably a different catalyst family - should increase to avoid stagnation.

Figure 2 is an example of one of the constraints that are frequently encountered in industry during the catalyst development process. In this case, the methane selectivity was another parameter that had to be improved, while at the same time increasing the catalyst activity. Notice that as the understanding of the catalyst behavior increased, it was possible to keep lowering the selectivity towards the undesired methane production. This continuous improvement began to stagnate towards the later part of the second stage, probably indicating that we are reaching the optimum limits for the current catalyst family, when the catalyst is operated in the desired reactor and at the optimum range of operating conditions, as identified in the overall plant optimization studies.

This paper will include more examples to illustrate the typical activities during the different development stages of a GTL technology, like characterization activities, catalyst batch sizes, reactor sizes, model evolution, carbon efficiency, product generation, and reactor development tools (e.g. cold flow models).

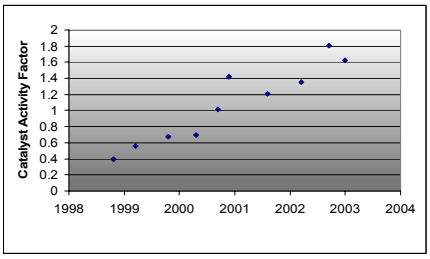

Figure 1. Typical improvement in catalyst activity as system understanding improves.

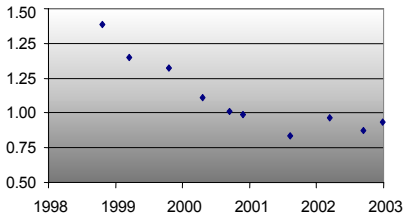

Figure 2. Relative Methane selectivity vs time. Reaching catalyst family limits?

SPRAY DRIED IRON CATALYSTS FOR SLURRY PHASE FISCHER-TROPSCH SYNTHESIS

Dragomir B. Bukur [(a)], Wen-Ping Ma [(a)], Victor H. Carreto Vazquez [(a)], Lech Nowicki [(a)] and Adeyinka A. Adeyiga [(b)]

[(a)] Department of Chemical Engineering, Texas A&M University, College Station, TX 77843
[(b)] Department of Chemical Engineering, Hampton University, Hampton, VA. 23688

Introduction

Recent developments in Fischer-Tropsch (F-T) technology have been directed towards the use of slurry bubble column reactors and maximization of production of high molecular weight hydrocarbons (wax). A critical issue in this reactor type is the ability to separate catalyst particles from the wax, which accumulates in the reactor. Catalysts with high attrition resistance are needed for this purpose.[1]

Researchers at Hampton University and University of Pittsburgh have studied attrition properties of iron F-T catalysts prepared by spray drying of Fe/Cu/K/SiO_2 precursors.[2-5] Attrition properties were evaluated using several types of tests: ultrasonic irradiation, fluidized bed and jet-cup method. Activity and selectivity of some of these catalysts were evaluated in a fixed bed reactor and were found to be comparable to that of the Ruhrchemie catalyst prepared by conventional precipitation.

The above studies of attrition properties provide information on relative attrition strength of different catalysts. However, test conditions employed are not representative of conditions encountered in a slurry bubble column reactor (SBCR) or a stirred tank slurry reactor (STSR).

The present study has been undertaken to investigate attrition properties of two iron F-T catalysts, synthesized at Hampton University, by following changes in particle size distribution (PSD) during F-T synthesis in a STSR, and to provide information on activity and selectivity of these catalysts in a slurry reactor.

Experimental

Catalyst Synthesis. Details of catalyst preparation procedure can be found elsewhere.[2-3] Briefly, the catalyst containing binder silica was prepared by co-precipitation of iron and copper nitrates, followed by washing and addition of aqueous potassium carbonate and silica binder. The resulting slurry was spray dried at 250°C in a bench scale Niro spray dryer. The catalyst containing precipitated silica was prepared by simultaneous precipitation of Fe/Cu/SiO_2 precursor. Aqueous tetraethylorthosilicate (TEOS) was used as a source of silica.

Characterization Methods. Slurry samples withdrawn from the STSR were first washed with a commercial solvent to remove residual liquid medium. After drying the catalyst samples were analyzed by SEM (morphological properties) and their particle size distribution (PSD) was determined by a Coulter Counter Multisizer. SEM specimens were observed at different magnifications using a JEOL JSM-6400 Scanning Electron Microscope at 10 mA for 8 minutes.

Slurry Reactor. Catalysts were tested in a one-liter STSR (Autoclave Engineers). Details of reactor set-up, operating procedures and product quantification can be found elsewhere. [6-7]

Results and Discussion

Morphological Properties. SEM micrographs of as received (no sieving or calcination) spray-dried catalysts prepared at Hampton University are shown in Figures 1 and 2. Particle size distribution of 100 Fe/5 Cu/4.2 K/11 (P) SiO_2 (P = precipitated silica) catalyst (HU2061) is broad and most of the particles are irregularly shaped with some of them having plate-like morphologies (Fig.1). Smaller particles (5-10 μm) are nearly spherical, but with rough surfaces. The observed morphology (large number of irregularly shaped) is not expected to result in high attrition strength. Majority of particles of 100 Fe/5 Cu/4.2 K/1.1 (B) SiO_2 (B = binder silica) catalyst (HU3471) are spherical (Fig. 2), but their external surfaces are relatively rough. Particle size distribution for this catalyst is also rather broad.

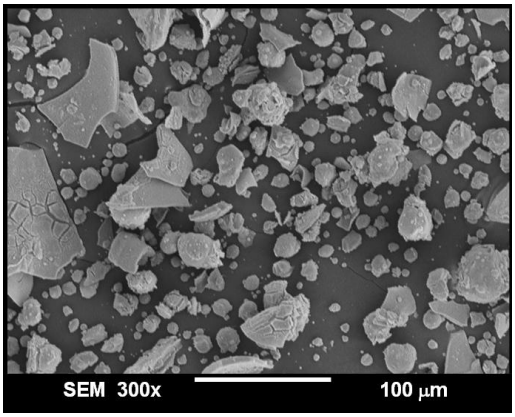

Figure 1. SEM image of 100 Fe/5 Cu/4.2 K/11 (P) SiO_2 catalyst.

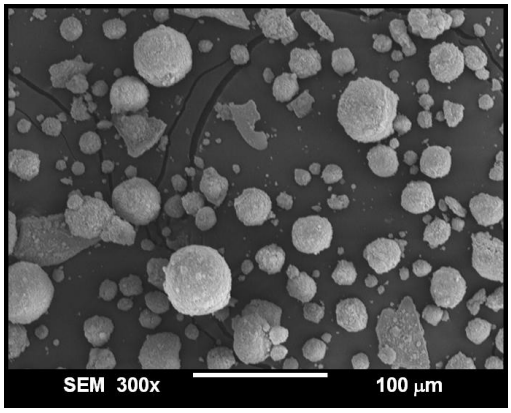

Figure 2. SEM image of 100 Fe/5 Cu/4.2 K/1.1 (B) SiO_2 catalyst.

Catalyst Activity and Selectivity. As received catalysts (14-15 g) and 320-350 g of Durasyn 164 oil (a hydrogenated 1-decene homopolymer, ~ C_{30} obtained from Albemarle Co.) were loaded into the STSR. The catalysts were pretreated in CO at 280°C, 0.8 MPa, 3 Nl/g-cat/h for 12 hours. Slurry samples were withdrawn from the reactor before the pretreatment and at the end of the run for particle size distribution measurements. After the pretreatment, the catalysts were tested at 260°C, 2.1 MPa, H_2/CO = 0.67 and gas space

velocities of either 3.1 Nl/g-Fe/h (run SB-20601) or 3.3 Nl/g-Fe/h (run SB-34701).

Changes in synthesis gas conversion with time are shown in **Figure 3**. During the first 50-80 hours of testing the syngas conversion increased with time reaching 85-87%. After reaching the maximum conversion, the catalysts started to deactivate, and at 200 hours on stream the syngas conversion was about 76%. Both catalysts were tested up to 384 h (SB-20601) and 449 h (SB-34701) on stream under different process conditions (results not shown) and then the slurry samples were withdrawn for PSD measurements.

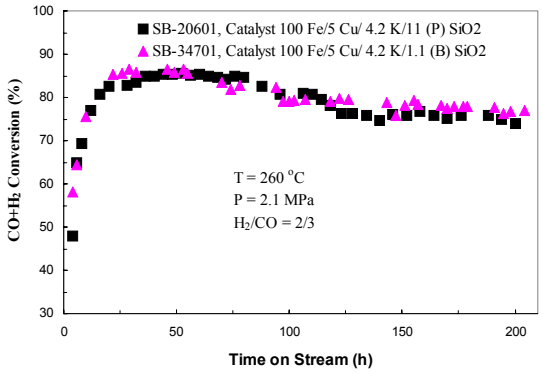

Figure 3. Change in syngas conversion with time-on-stream.

Hydrocarbon selectivities (CH_4 and C_5^+) were similar in both tests. Methane selectivity (**Figure 4**) decreased during the first 150 h of testing, reaching a stable value of 2.0±0.2% (carbon atom basis). Selectivity of C_5^+ hydrocarbons (liquids and wax) was high in both tests. It increased to 84-86% during the first 130 hours of testing, and then remained fairly stable. Methane and C_5^+ selectivities were independent of conversion level and/or process conditions.

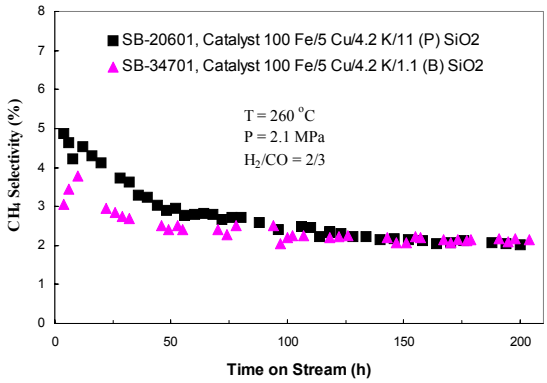

Figure 4. Change in CH_4 selectivity with time-on-stream.

Attrition Properties. Attrition behavior of catalysts tested in this study was evaluated on the basis of observed changes in morphological properties (via SEM), and changes in particle size distribution (PSD) after STSR testing. From PSD results, one can obtain several parameters that can be used to quantify attrition. These are: changes in Sauter mean diameter ($d_{3,2}$), and change in fraction of fine particles (particles < 10 μm in diameter) during testing in the STSR. Generation of fine particles (fines) is important in assessing attrition behavior of iron F-T catalysts, since fine particles cause separation problems during SBCRs' operation. Results from PSD measurements are summarized in **Table 1**.

Table 1. Summary of PSD Results Obtained Using the Coulter® Counter Multisizer (From Volume Distributions)

Run ID	t*, h	% Change after t* hours in the STSR	Change in fraction of fines
		$\Delta d_{3,2}$	< 10 μm
SB-20601	380	87	62.5
SB-34701	449	39.9	3.7

Attrition results show that HU2061 catalyst used in run SB-20601 had much lower attrition resistance relative to HU3471 catalyst (run SB-34701). This catalyst experienced large reduction in Sauter mean diameters (87%) after 380 h of testing in the STSR. The inferior attrition strength of this catalyst is also reflected in considerable generation of fine particles during the STSR test (62.5 %). HU 34701 catalyst had experienced a modest reduction in Sauter mean diameter (over a longer period of testing) and generation of fine particles was small. The attrition properties of this catalyst are satisfactory for use in a SBCR.

Concluding Remarks

Spray-dried catalysts with compositions 100 Fe/5 Cu/4.2 K/11 (P) SiO_2 and 100 Fe/5 Cu/4.2 K/1.1 (B) SiO_2 have excellent selectivity characteristics (low methane and high C_5^+ yields), but their productivity and stability (deactivation rate) need to be improved. Mechanical integrity (attrition strength) of these two catalysts was markedly dependent upon their morphological features. The attrition strength of the catalyst made out of largely spherical particles (1.1 (B) SiO_2) was considerably higher than that of the catalyst consisting of irregularly shaped particles (11 (P) SiO_2). Improvements in spray drying operating parameters resulting in narrower PSD and higher sphericity could lead to further improvements in the attrition strength.

Acknowledgement

This study was supported in part by the U. S. Department of Energy Grant DE-FG26-00NT40822.

References

1. Jager, B.; Espinoza, R. *Catal. Today*, **1995**, 23, 17.
2. Jothimurugesan, K.; Goodwin, J. G., Jr.; Santosh, S. K.; Spivey, J. J. *Catal. Today* **2000**, 58, 335.
3. Jothimurugesan, K.; Spivey, J. J.; Gangwal, S. K.; Goodwin, J. G., Jr. in "Natural Gas Conversion V", *Stud. Surf. Sci. Catal.* **1998**, 119, 215.
4. Zhao, R.; Goodwin, J. G., Jr.; Jothimurugesan, K.; Gangwal, S. K.; Spivey, J. J. *Ind. Eng. Chem. Res.* **2001**, 40, 1065.
5. Sudsakorn, K.; Goodwin, J. G., Jr.; Jothimurugesan, K.; Adeyiga, A. A. *Ind. Eng. Chem. Res.* **2001**, 40, 4478.
6. Bukur, D. B.; Patel, S. A.; Lang, X. *Appl. Catal.* **1990**, 186, 329.
7. Bukur, D. B.; Nowicki, L.; Lang, X. *Chem. Eng. Sci.* **1994**, 49, 4615.

MIXED IRON-MANGANESE OXIDE NANOPARTICLES

Jr-iuan Lai,[1,5] Kurikka V. P. M. Shafi,[1,5,] Abraham Ulman,[1,5] Nan-Loh Yang,[2,5] Min-Hui Cui,[2,5] Thomas Vogt,[3] Claude Estournès,[4]*

[1]Department of Chemical Eng., Chemistry & Material Science, Polytechnic University, 6 Metrotech Center Brooklyn, NY 11201.
[2]Department of Chemistry, CUNY at Staten Island, 2800 Victory Boulevard,Staten Island.
[3]Physics Department, Brookhaven National Laboratory, P.O. Box 5000, Upton, NY 11973-5000
[4]Institut de Physique et Chimie des Matériaux de Strasbourg Cedex, France
[5]The NSF MRSEC for Polymers at Engineered Interfaces

Introduction

Magnetic nanoparticles have applications in information storage,[1] color imaging,[2] magnetic refrigeration,[3] medical diagnosis,[4] controlled drug delivery,[5] and as ferrofluids.[6] Thus, developing a new synthetic route for magnetic nanoparticles and the investigation of their properties are of great importance.[7]Nanocrystal materials are also known to have superior mechanical properties due to the extremely fine grain size[8]. However, it has not been well established that alloy and alloy-oxide composite coatings with nanocrystal grains have unique properties at high temperatures. Nanocrystal structures promote selective oxidation, forming protective oxidation scales with superior adhesion to the substrate.[9]

Ferrites, the transition metal oxides having a spinel structure, are technologically important because of their interesting magnetic and electrical properties. They are used in magnetic inks and magnetic fluids, and for the fabrication of magnetic cores of read/write heads for high-speed digital tapes or for disc recording.[10] One important example is manganese oxide, which has the desirable properties of low cost and low toxicity. As with other electrically conductive metal oxides, manganese oxide stores electrical charge by a double insertion of electrons and cations into the solid state. Maghemite (γ-Fe_2O_3, the ferrimagnetic cubic form of iron(III) oxide) is also technologically important, as it is being used widely for the production of magnetic materials and catalysts. Because of the small coercivity of Fe_2O_3 nanoparticles, which arises from a negligible barrier in the hysteresis of the magnetization loop, they can be used as magneto-optical devices. Magneto-optic media can be made by depositing magnetic and optically transparent materials, and maghemite particles satisfy this condition, since they can be easily incorporated in to ultrathin polymer films. In this paper, we discuss the sonochemical synthesis and characterization of nanosized manganese iron oxide powder

Experimental

Synthesis. Samples of α-Fe_2O_3, γ-Fe_2O_3, and manganese iron mixed oxide nanoparticles with varied Mn:Fe ratios, as well as Mn_2O_3 were synthesized using ultrasonication. Manganese iron mixed oxides were prepared by irradiating mixtures of different ratios of amorphous Fe_2O_3 nanoparticles (5-10 nm in diameter) and $Mn_2(CO)_{10}$ with a high intensity ultrasonic horn, under air, for 2 hours. Due to the high cavitational rate ($>10^9$ K s^{-1}) in the ultrasonication process, the synthesized products are amorphous nanoparticles. Elemental analysis of the amorphous nanoparticles was obtained by atomic absorption. The amorphous nanoparticles were crystallized using an annealing process, at temperatures. determined by DSC measurements. Pure γ-Fe_2O_3 nanoparticle samples were prepared by heating amorphous Fe_2O_3 nanoparticles at 300°C for 3 hours, while α-Fe_2O_3, Mn_2O_3 and manganese iron mixed oxides are prepared by heating the corresponding amorphous nanoparticle samples at 500°C for 3 hours.

Characterization Powder XRD was performed by using a Philips X-ray diffractometer (Cu K_α radiation, λ = 1.5418 Å). Synchrotron Powder X-ray Diffraction experiments were preformed at the beamline X7A of the National Synchrotron Light Source (NSLS) at Brookhaven National Laboratory with a linear position-sensitive detector gating electronically on the Kr-escape peak. Nanocrystal size and morphology were estimated by using a Phillips CM-12 Transmission Electron Microscope (100 KeV) Element analysis was performed by using Perkin-Elmer flame and graphite furnace atomic absorption spectroscopy. Magnetic data of the solid samples were obtained with a Princeton Applied Research vibrating sample magnetometer Model 155 (VSM) and a Quantum Design SQUID MPMS-XL (AC and DC modes and maximum static field of ± 5 T). X-band EPR spectra were recorded on a Bruker ESP380E spectrometer equipped with a HP 5361 frequency counter. The unpaired spin density was evaluated by comparison with a diphenylpycrilhydrazyl (DPPH) as an internal standard marker calibrated against Mn^{2+}/CaO with known spin number.

Results and Discussion

Figure 1(shown left) presents a TEM image of crystalline manganese iron mixed oxide with 32.08% Mn_2O_3 content. The bright field image shows aggregation due to sintering. This is a common phenomenon when amorphous nanoparticles are heated. The diffraction pattern reveals that these nanoparticles are highly crystallized. The XRD patterns for γ-Fe_2O_3, mixed γ-Fe_2O_3-Mn_2O_3 oxide nanoparticle samples with Mn_2O_3 concentration from 8.49% to 32.08%, where *a* is the index of γ--Fe_2O_3 and *b* is the XRD pattern of synthesized Fe_2O_3. The XRD pattern of synthesized Fe_2O_3 matches well the γ--Fe_2O_3 index. Patterns *c~f* show the XRD for manganese iron mixed oxide with Mn_2O_3 concentrations from 8.49% to 32.08%. The comparison of patterns *c~f* to *a* reveals that the positions and relative intensities of the strong peaks match those of γ-Fe_2O_3, which is spinel structure.

In Figure 2, *a* is the index of $Mn_{2-x}Fe_xO_3$ and *e* is the synthesized Mn_2O_3. Patterns *b~d* are for manganese iron mixed oxides with Mn concentrations from 60.38% to 68.87%. As is apparent from Figure 3,4, the index of $Mn_{2-x}Fe_xO_3$ is almost the same as that of Mn_2O_3, and hence *a* was used as index of both $Mn_{2-x}Fe_xO_3$ and Mn_2O_3. The XRD pattern of the synthesized Mn_2O_3 matches the index of Mn_2O_3. By comparing b~d to *a*, it was found that the positions and relative intensities of the strong peaks in these patterns match to $Mn_{2-x}Fe_xO_3$ which is bixbyite structure. Figure 3 shows the synchrotron powder X-ray diffraction of the sample with ≤ 5% Mn(III). The crystal structure of this sample is γ-Fe_2O_3. This suggests that when the Mn(III) concentration is ≤5% it does not prevent the crystal from adopting the stable α-Fe_2O_3 structure. We have not investigated the concentration window between 5% and 8.49% Mn(III), and hence the exact concentration where the transition from γ- to α-Fe_20_3 occurs is still unknown.

X-ray studies reveal another interesting behavior of samples with low Mn(III) content. The annealing at 500°C should crystallize the pure amorphous iron oxide to the α-Fe_2O_3 form, which is a hexagonal structure. Indeed, when the Mn(III) concentration was ≤5%, the α-Fe_2O_3 structure was maintained. Thereafter, in nanoparticle samples with Mn(III) concentration between 8.49% and 32.08% the transition from spinel (γ-Fe_2O_3 obtained at 300°C) to

hematite(α-Fe_2O_3 obtained at 500°C) was suppressed. That the mixed oxide samples crystallized as γ-Fe_2O_3 suggests single-phase

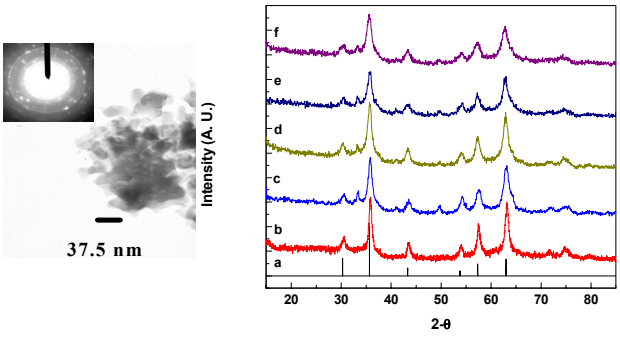

Figure 1 XRD patterns: a. index of γ-Fe_2O_3; b. Fe_2O_3; c. 8.49% Mn(III); d. 18.87% Mn(III); e. 27.83% Mn(III); f. 32.08% Mn(III). TEM image of manganese iron mixed oxide with 32.08% Mn(III). is shown on left

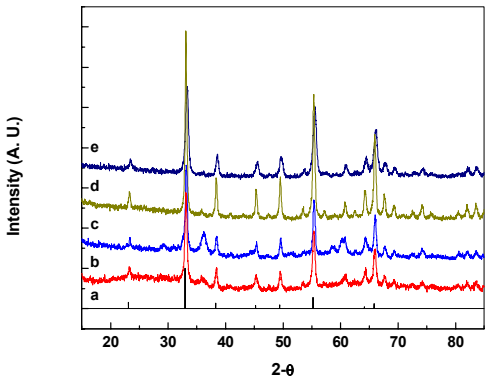

Figure 2. XRD patterns: a. index of $Mn_{2-x}Fe_xO_3$; b. 65.09% Mn(III); c. 60.38% Mn(III); d. 68.87% Mn(III); e. Mn_2O_3

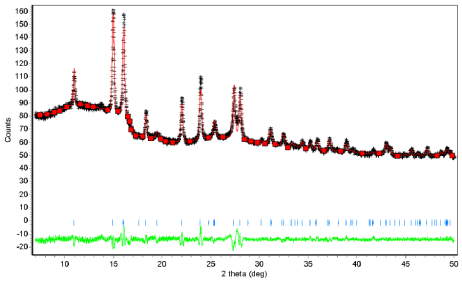

Figure 3. Synchrotron powder x-ray diffraction of ≤ 5% Mn sample

compounds and not mixtures. If the latter was the case, the XRD patterns should have peaks of both α-Fe_2O_3 and Mn_2O_3, which was not observed in any of our samples. We observed that even pre-annealed samples require temperatures as high as 600°C to completely convert to the α-phase, indicating high activation energy for this process. We believe that the suppression of the γ- (cubic) to α-Fe_2O_3 (hexagonal) transition is due to the fact that while Mn(III) has a cubic spinel phase (with more free volume) it does not transform into a hexagonal one, and therefore doping Fe_2O_3 with Mn(III) increases the activation energy for the transition to the more compact α-phase, which requires lattice contraction. Thus, above a critical concentration (between 5 and 8.5%) the transition needs temperatures higher than 600°C to complete. Figures 4 presents the magnetization curves of γ-Fe_2O_3, manganese iron mixed oxide and Mn_2O_3 at 5K. When the magnetization measurements were carried out at room temperature, no coercivity could be observed. Bulk γ-Fe_2O_3 is ferrimagnetic. However, due to their small dimensions, γ-Fe_2O_3 nanoparticles are superparamagnetic. Mn_2O_3 nanoparticles, on the other hand, show antiferromagnetic behavior, similar to the bulk material. The magnetization curves of crystalline Fe-Mn mixed oxide nanoparticles with Mn(III) concentrations from 8.49% to 38.68% show superparamagnetic behavior where as the samples with Mn(III) from 54.72% to 68.87% are linear with small positive susceptibility, which is in agreement with antiferromagnetic behavior. These results show that as the crystal structure transforms from spinel to bixbyite, the magnetic properties transform from superparamagnetic to antiferromagnetic. Taken together the results show that the maximum of the magnetization decreases with the increasing Mn(III) concentration.

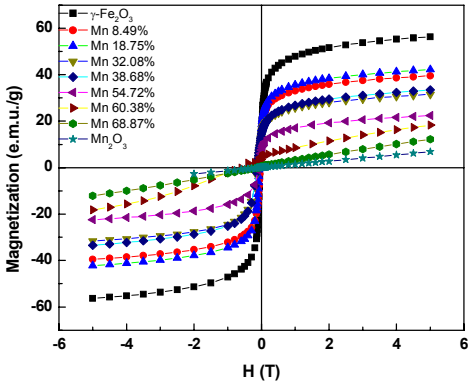

Figure 4. Magnetization curves at 5K.

EPR studies (not shown) also reveal that the spin densities (per gram of Fe_2O_3 and per gram of sample) of Mn(III) doped Fe_2O_3 nanoparticles decrease markedly with increasing Mn(III) The normalized spin density of the sample with 68.9% Mn(III) is 6 x 10^{21} spins/g Fe_2O_3, one order of magnitude lower than that of sample with 8.5% Mn(III) (8.5 x 10^{22} spins/g Fe_2O_3). Such a reduction in the normalized spin density can be attributed to antiferromagnetic coupling of Fe with Mn.

Conclusions

All physical measurements support compete mixing of the Fe(III) and Mn(III) ions in the mixed oxide amorphous samples. According to XRD, the crystal structures of manganese iron mixed oxides change from spinel to bixbyite crystal structures with increasing of Mn(III) content. The γ-Fe_2O_3 crystal structure of samples with low Mn(III) content shows that the samples are single-phase compounds. This might due to the replacement of Fe(III) atoms with Mn(III) atoms as supported by EPR data of efficient antiferromagnetic coupling due to the presence Mn(III).

References

1.Audram, A. G.; Huguenard, A. P. In *U.S. Patent*: U.S., 1981.
2.Ziolo, R. F. In *U.S. Patent*, 1984.
3. McMichael etal *J. Magn. Magn. Mater.* **1992**, *111*, 29.
4.Josephson, L. et al *Bioconjugate Chem.* **1999**, *10*, 186.
5.Bhatnagar,S.P.; Rosensweig, R.E. *J.Magn. Magn.Mater.* **1995**, *149*.
6.Rosensweig,R.E.*Ferrohydrodynamics*;MIT Press:Cambridge, 1985.
7. Shafi, K. V. P. M.et al *Chem. Mater.* **2002**, *14*, 1778.
8.Morris, D. *Mechanical Behaviour of Nanostructured Materials*; Trans Tech Publications Ltd., 1998.
9.Gao, W.; Liu, Z.; Li, Z.; Li, S. S.; Gong, H. *International Journal of Modern Physics B* **2002**, *16*, 128.
10.Charles, S. W.; Popplewell, J. *Ferromagnetic Materials*; North-Holland: Amsterdam, 1980; Vol. 2.

ACETYLENES AS PROBES IN THE FISCHER-TROPSCH REACTION

Yulong Zhang, Li Hou, John W. Tierney and Irving Wender

Department of Chemical and Petroleum Engineering
University of Pittsburgh
Pittsburgh, PA 15261

Introduction

Present worldwide interest in the Fischer-Tropsch (FT) synthesis is centered on the conversion of natural gas to synthesis gas which is then converted to diesel and jet fuels over a cobalt catalyst.

Incorporation of probe molecules has been used widely in elucidating the mechanism of FT reactions. Several C1 probes such as methyl chlorides $CHxCl_{4-x}$[1], and nitromethane CH_3NO_2[2] in FT reactions have been studied. The results suggested that C1 species derived from decomposition of these C1 molecules can be incorporated into FT and serve as monomers for chain growth. Surface C1 species were captured using cyclohexene as a probe on ruthenium catalysts.[3] In this paper, acetylenic compounds have been used as probes.

Experimental

Catalyst Preparation. Cobalt catalysts were prepared by an incipient wetness impregnation technique. Vista B alumina with grain particle sizes of 70-140 mesh was calcined at 500° C for 10 h before impregnation. Cobalt nitrate was dissolved with suitable amounts of deionized water, and then impregnated on calcined alumina. The catalyst was dried at 110° C overnight, and calcined at 300° C for 2 h. An iron catalyst with a composition of 100Fe/1.25K/4.4Si was obtained from the University of Kentucky.

Incorporation of Probes. FT reactions were carried out in a stainless-steel tubular microreactor of 3/8 in (0.95cm) diameter. Probe molecules were added into the FT reaction continuously by a syringe pump. A thermocouple was inserted into the middle of the catalyst bed. 0.5 g of cobalt or 1.0 g of iron catalysts were mixed with 1 g of quartz sands and loaded in the reactor. The catalyst then was activated by H_2 at a rate of 50 ml/min, with a temperature program ramping from room temperature to 350° C at 1° C/min, holding at 350° C for 10 hours. After reduction, the temperature of the reactor was lowered to the reaction temperature in H_2. The gas stream then was switched to Ar. The FT reaction was started by gradually increasing the CO and H_2 flow rates and, at the same time, decreasing the Ar flow rate in 2 h to avoid the temperature surge due to highly active sites present in the fresh catalyst. Wax products were collected by a hot trap at about 200° C. Liquid products were collected by a cold trap in an ice-water bath. A stream of effluent gas was split out between hot and cold traps and went through three sampling valves and analyzed by two GCs (HP6890, HP5890) controlled by HP Chemstation equipped with three GC columns (HP-5 capilary column, Porapak Q packed column, and Carbonsphere packed column) for online analysis of whole products except for heavy waxes. Transfer lines before sampling valves are kept at 230° C to avoid condensation of heavier products. Liquid products collected in the cold trap were analyzed by HP GC-MS with a HP-5 capillary column to identify components of the FT products.

Probe incorporations were carried out at 100 psi (0.7MPa), The probe molecules were added in pentane (10% in volume) with a total flow rate of 2ml/h. Other conditions varied with the catalyst: iron catalyst, WHSV=3.6NL/g/h, CO/H_2=3/2, 170° C and 260° C; cobalt catalyst, WHSV=7.2NL/g/h, CO/H_2=1/2, 150 ° C, 180° C and 220° C.

The pump and the transfer lines of the reaction system were washed with pentane after each experiment to reduce possible interference by remaining probes and condensations of previous runs. Conversions were kept below 5% to ease the condensation of the heavier hydrocarbons at transfer lines.

Results and Discussion

1-Hexyne, 2-hexyne, phenylacetylene, 4-phenyl-1-butyne and 1-phenyl-1-propyne were used as probe molecules. 1-Hexyne, phenylacetylene and 4-phenyl-1-butyne have terminal carbon-carbon triple bonds. 2-Hexyne and 1-phenyl-1-propyne have internal carbon-carbon triple bonds. 1-Hexene was added for comparison purposes.

Incorporation on Cobalt Catalyst. Incorporation of alkynes is much more effective than incorporation of olefins. At 150° C, FT on cobalt catalyst is essentially inactive. Incorporation of 1-hexene is negligible at this temperature. However, 1-hexyne is readily incorporated and $C7^+$ products are formed under such conditions. It could be postulated that all the products obtained at 150° C originate from 1-hexyne. 1-Hexyne initiates chain growth and the hydrocarbon chain grows by stepwise addition of C1 monomers.

Since products of incorporation of 1-hexyne overlap normal FT products, it is difficult to distinguish the alkyne initiated products from normal FT products. Several phenylacetylenes were used as probe molecules. With the phenyl group as a marker, the products from normal FT and from alkyne initiated FT were easily distinguished by GC and GC-MS.

Figure 1 shows the GC-MS results of incorporation of 4-phenyl-1-butyne. It is apparent that normal FT products (labeled underneath) and 4-phenyl-1-butyne initiated FT products (labeled with a benzene ring) are formed.

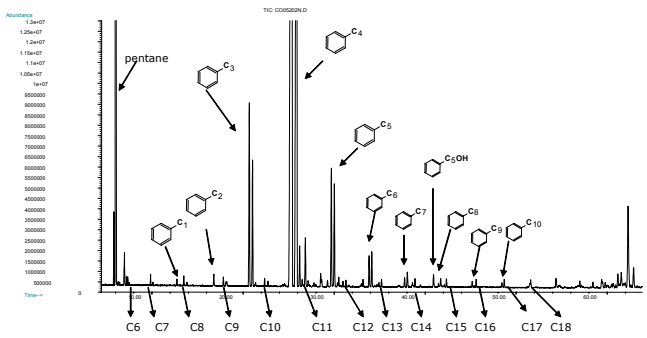

Figure 1. GC-MS analysis of FT liquid products with 4-phenyl-1-butyne addition at 180° C, CO/H_2=3/2, 0.7 MPa, cobalt catalyst.

With incorporation of terminal alkynes, the chain grows from the end of the carbon-carbon triple bond and produces a series of products with α-olefins as the main product. This behavior is very similar to normal FT reactions, suggesting that the intermediates formed from adsorption of terminal alkynes are similar to the intermediates in normal FT.

Incorporation of internal alkynes behaves differently from incorporation of terminal alkynes. Branched hydrocarbon chains are formed with incorporation of 2-hexyne. The activity for incorporation of internal alkynes is lower than incorporation of terminal alkynes. Unlike terminal alkynes, from which dimerization always occurs, internal alkynes do not dimerize.

Except for phenylacetylene, incorporation of above alkynes produces aldehydes and alcohols with one added carbon. 1-Heptanal

and 1-heptanol are formed with addition of 1-hexyne. 5-phenyl-1-pentanal and 5-phenyl-1-pentanol are obtained with incorporation of 4-phenyl-1-butyne. Incorporation of the internal alkynes leads to branched aldehydes and alcohols. In any case, only oxygenates with one carbon more than the probes are formed on cobalt. This is reminiscent of the hydroformylation reaction. To test the mechanism of oxygenate formation, thiophene was injected. It is well-known that sulfur poisons FT activity but hydroformylation is resistant to sulfur. Results show that hydrocarbon products from normal FT and probe initiated FT diminish with injected thiophene, but oxygenate formation is much less affected. This suggests that the oxygenates are formed by hydroformylation. It is recognized that the FT reaction occurs at conditions just below those at which carbonyls are formed.[4] Shultz[5] has shown that hydroformylation occurs on incorporation of olefins into FT on cobalt catalysts.

Incorporations on Iron Catalysts. Incorporation of the probes on an iron catalyst was carried out at 170° C and 260° C. At 170° C, normal FT activity on iron catalyst is negligible and the observed products originate only from incorporation of probe molecules. At 260° C, both normal FT and the initiation by the probe molecule are observed. **Figure 2** shows the GC-MS analysis of liquid products of FT with phenylacetylene addition.

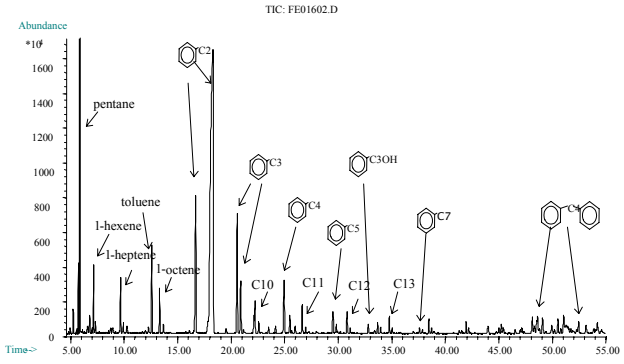

Figure 2. GC-MS analysis of FT liquid products with phenylacetylene addition at 260° C, CO/H_2=3/2, 0.7 MPa, iron catalyst.

It is clear that two types of chain growth mechanisms take place with incorporation of phenylalkynes at 260° C. In addition to the normal FT products, phenylacetylene initiated products are superimposed.

Oxygenates originating from phenylalkynes are observed. With addition of phenylacetylene at 170° C, about half of the C^{9+} products are oxygenates, mainly aromatic aldehydes and alcohols. Oxygenates decrease with increase in temperature to 260° C and aldehydes are hydrogenated to alcohols.

In 1970s, a group of Russian researchers[6] explored synthesis of alcohols with fused iron catalysts. It was found that acetylene can initiate chain growth for higher oxygenate formation at high pressure (above 10MPa) and 170-190° C in CO hydrogenation. Their aim was to produce higher alcohols. Our experiments were conducted under 0.7 MPa on a precipitated iron catalyst, which is close to normal FT conditions on iron catalysts. Our results show that incorporation of probes enhances oxygenate selectivity and overall activity at 170° C.

Mechanisms of Incorporation and FT. Chain growth in FT is believed to be stepwise polymerization of monomers with one carbon and product distribution follows Schultz-Flory kinetics. This distribution is generally true except for much lower C2 and higher CH_4 yields than predicted. Lower C2 yields may indicate a deviation from the standard stepwise polymerization mechanism. It has been explained as the result of readsorption and incorporation into the FT product. However, chain growth may start from C2 rather than the C1 monomer. Carbon-carbon coupling of the C1 species into C2 is slower than subsequent chain growth. Adsorption of acetylene forms C2 intermediates which initiate chain growth[6]. Higher yield of alkyne probe initiated FT products than the normal FT products at lower temperature provides an evidence for this mechanism. Much easier incorporation of alkynes than olefins suggests that that the initiating entity of chain growth may be more unsaturated than an alkyl.

Conclusions

Phenylalkynes are incorporated into FT on both cobalt and iron catalysts and function as a chain growth initiator to the position of carbon-carbon triple bond. Incorporation of terminal phenylalkynes, such as phenylacetylene and 4-phenyl-1-butyne produces straight chain phenylalkenes and phenylalkanes. Incorporation of an internal alkyne, such as 1-phenyl-1-propyne, yields branched phenylalkenes and phenylalkanes. At low temperatures, almost all of the products originate from phenylalkyne incorporation; at such conditions normal FT activity is very low. At normal temperatures, alkyne originated and normal FT products are superimposed. Oxygenates are also produced and vary with catalyst and reaction temperature. Iron catalysts produce oxygenates of various chain lengths. Cobalt catalysts produce oxygenates only with one carbon more than the probe molecules, which resembles hydroformylation. At low temperatures, the primary oxygenates are aldehydes; with increase in temperature the aldehydes are hydrogenated to alcohols.

It is tempting to suggest that there is an energy barrier to formation of the initial carbon-carbon bond in the FT reaction. This is overcome by laydown of two carbons from an acetylenic molecule. As to formation of hydroformylation products, initial adsorption of an acetylenic molecule "leaves" a double bond in the adsorbed probe; this may undergo a hydroformylation reaction.

Acknowledgements. We thank Dr. Davis of CAER for providing the iron catalyst and the U. S. Department of Energy for financial support (Grant No. DE-FC26-99FT40540).

References

(1) Van Barneveld, W. A. A.; Ponec, V. In *J. Catal.*, 1984; Vol. 88, pp 382-387.
(2) Cavalcanti, F. A. P.; Oukaci, R.; Wender, I.; Blackmond, D. G. *J. Catal.* **1990**, *123*, 270-274.
(3) Ekerdt, J. G.; Bell, A. T. *J. Catal.* **1980**, *62*, 19-25.
(4) Pichler, H. *Adv. Catal.* **1952**, *4*, 271-342.
(5) Schulz, H.; Claeys, M. *Appl. Catal. a-Gen.* **1999**, *186*, 71-90.
(6) Loktev, S. M. *J. Catal.* **1982**, *17*, 255-230.

EFFECT OF CALCINATION TEMPERATURE ON THE PERFORMANCE OF Co/ZrO_2 CATALYSTS FOR FISCHER-TROPSCH SYNTHESIS

Hongxia Zhao, Jiangang Chen, Yuhan Sun

State Key Laboratory of Coal Conversion,
Institute of Coal Chemistry, Chinese Academy
of Sciences, P.O.Box 165, Taiyuan 030001, P.R. China

Introduction

Cobalt has been one of the most commonly used metals for Fischer-Tropsch catalysts since the 1930s because of its high activity [1]. It has become well established that the performance of a heterogeneous catalyst not only depends on the intrinsic catalytic activity of the components but also on its texture and stability. One of the most important factors in controlling the texture and strength of a catalyst involves the correct choice of a support and the preparation of the support in the appropriate form.

Zirconium oxide has attracted considerable attention recently as a catalyst support because of its high thermal stability and the amphoteric character of its surface hydroxyl groups [2-3]. Extensive studies have been made of the effect of temperature on the development of the porous texture or structure in samples of zirconia [4]. The majority of the textural studies have, however, been confined to low calcination temperature (<500℃). More important, to the best of our knowledge few investigators have studied the development of the acidity of the support surface with the increasing temperature.

In this study, the effect of the calcination temperature of the zirconia support on the physico-chemical properties of supported cobalt catalysts will be investigated. Furthermore, the performance of the impregnated catalysts in the Fischer-Tropsch synthesis will be investigated.

Experimentle

Preparation. Samples of zirconia were made by precipitation at room temperature. A solution of zirconyl chloride was added dropwise, concurrently with a solution of ammonia. Followed by washing and drying, calcination was carried out in a muffle furnace at various temperatures up to 800℃.

Samples of catalysts were prepared by the incipient wetness impregnation method.

Characterization. The surface areas, total volumes and pore size distribution of the samples were measured with ASAP-2000 Micromeritics instrument. XRD was recorded in Rigaku D/max-γA with Cu target at 40 kV and 100 mA. NH_3-TPD was carried out in a flow apparatus. The sample (100 mg) was pretreated at 600℃ in Ar for 2 h and saturated with NH_3 at 100℃. After removing the physically adsorbed ammonia, the sample was heated to 650℃ at 10 ℃/min in a Ar flow of 50ml/min.

Catalyst activity evaluation The performance of the catalysts in the Fischer-Tropsch synthesis was tested at 2 Mpa, $1000h^{-1}$ and a H_2/CO ratio of 2 in a fixed bed reactor of i.d.10mm. Following reduction in a flow of hydrogen at 400℃for 6 h, the samples were switched to syngas. Mass balances were commenced after the reaction was on-line for 24 h. The CO, H_2, CH_4 and CO_2 products were analyzed on the TCD and the gas hydrocarbons were detected by the FID. Liquid and solid products were collected in a cold trap and a hot trap respectively and then were offline analyzed by the FID.

Results and Discussion

From the results summarized in **Table 1**, it is evident that the porous texture of the zirconia supports is different. With the increasing of calcination temperature, the surface area decreased and the average pore diameter increased. Once they were loaded by cobalt, an interesting phenomenon was observed. All catalysts had smaller surface area compared to their counterpart supports. It should be noted that the pore diameter of CoZr120 and CoZr400 was larger than their counterpart supports Zr120 and Zr400. Under this condition cobalt crystallite blocked smaller pores, thus the average pore diameter increased. On the other hand, Zr600 and Zr800 had a larger pore, so cobalt could fit in the pore and adsorbed on the inner wall, hence the average pore diameter of CoZr600 and CoZr800 decreased.

Table 1. Textural Properties of Samples

Samples	BET/$m^2 \cdot g^{-1}$	Pore diameter/nm
Zr120	349	3.1
Zr400	101	6.6
Zr600	32	17.6
Zr800	15	25.5
CoZr120	133	4.8
CoZr400	68	6.7
CoZr600	26	14.7
CoZr800	13	22.5

The X-ray spectra (**Figure 1** , **Figure 2**) of Zr120 showed only two very broad bands in the range of 2θ from 18 to 40° and from 40 to 70°, this being indicative of a very low degree of crystallinity. The profiles of other zirconia supports showed that it consisted of mixtures of the stable monoclinic phase and the metastable tetragonal phase. The content of monoclinic phase increased with increasing calcination temperature. There were no Co_3O_4 diffraction peaks and tetragonal phase appeared in the profile of CoZr120 indicated that cobalt was highly dispersed and the loading of cobalt promoted the transformation from amorphous-phase zirconia to tetragonal-phase zirconia. Co_3O_4 diffraction peaks appeared on others suggests larger cobalt particle formed and the particle size of cobalt increased with the calcination temperature of the support increased.

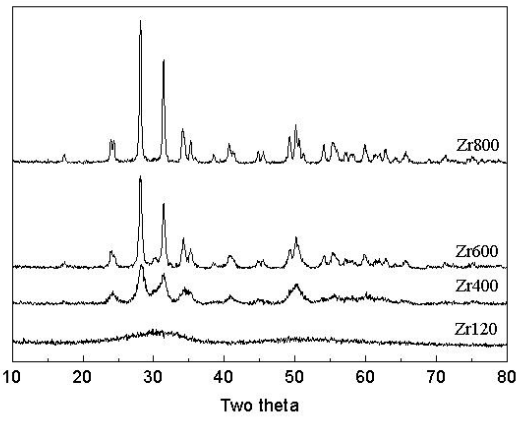

Figure 1 XRD profiles of ZrO_2 supports

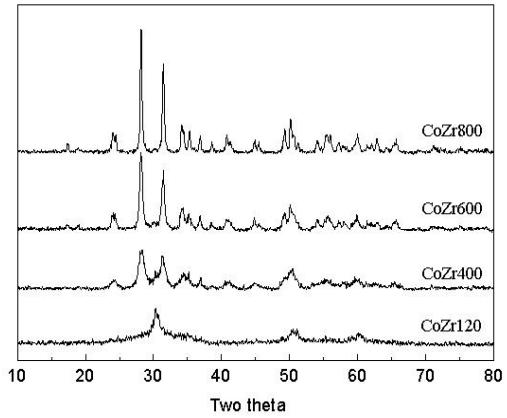

Figure 2 XRD profiles of Co/ZrO_2 catalysts

NH_3-TPD (**Figure 3**) results indicated that the acidity of the zirconia supports decreased with the increasing calcination temperature. Sample Zr120 had the strongest acidity and Zr800 had the weakest acidity. On the surface of Zr120, several kinds of acid centers existed. However, on the surface of Zr800 only weaker acid centers appeared and the stronger acid centers disappeared. This means that stronger acid centers on the surface of the support disappeared with the increasing calcination temperature.

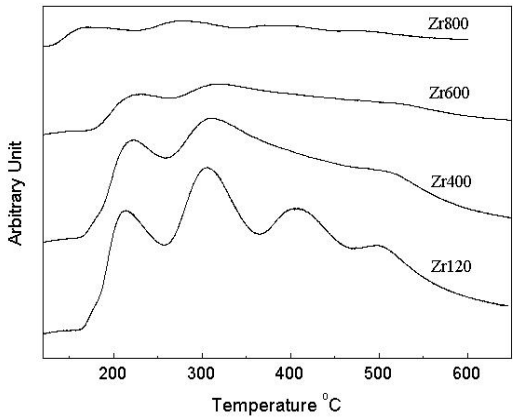

Figure 3 NH_3-TPD profiles of ZrO_2 supports

The catalytic activity and selectivity of Co/ZrO_2 catalysts were shown in **Table 2**. CO conversion and products selectivity were strongly depended on the calcination temperature of the supports. With the calcination temperature of the supports increased, the catalytic activity and selectivity increased and catalyst CoZr600 which support was calcined at 600℃ had the optimal catalytic properties. The catalytic performance of CoZr800 depressed to a certain degree compared to CoZr600 due to the reduce of the surface area of Zr800 for sintering at higher calcination temperature.

Table 2 Properties of F-T Synthesis of Co/ZrO_2 Catalysts

Catalysts	θ /℃	Conversion/%	CH_4./%	C_{5+}/%
CoZr120	210	2.7	35.4	34.7
	220	16.3	34.7	36.6
CoZr400	210	21.4	32.1	43.4
	220	53.2	15.5	75.4
CoZr600	210	82.3	4.5	92.2
	220	94.2	3.7	93.0
CoZr800	210	66.9	8.9	86.0
	220	90.4	8.5	83.3

Conclusions

The texture, crystallite phase and acidity of zirconia are greatly influenced by the calcination temperature of the support. Accompanying phase transformation and crystallite growth, the surface area of the support lost rapidly on calcination. Calcination may have a great influence on the surface acidity of zirconia and consequently affect the catalytic performance of the catalysts.

Acknowledgment

This work was supported by the financial support of State Key Foundation Program for Development and Research of China. (Contact No.G1999022402)

References

1 E. Iglesia, Appl. Catal. A., 1997, 161: 59-78
2 M. Valigi, D. Gazzoli, I.Pettiti, G.Mattei, S.Colonna, S.De Rossi, G. Ferraris. Appl. Catal. A., 2002, 231: 159-172
3 P.D.L.Mercera,J.G.Vanommen, E.B.M.Doesburg, A.J.Burggraaf, and J.R.H.Ross. Appl. Catal. A., 1990, 57: 127-148
4 V.G.Milt, E.A.Lombardo, M.A.Ulla. Appl. Catal.B:Environmental 2002, 37:63-73

Effect of Pretreatment on Reduction and Activity of the Boron-Modified Co/TiO_2 Fischer-Tropsch Catalyst

Jinlin Li[1] and Neil J. Coville[2]

1. College of Chemistry and Life Science, South Central University for Nationalities, Wuhan 430074, P.R. China
2.Department of Chemistry, University of the Witwatersrand, Johannesburg, Wits 2050, South Africa

Introduction

Supported cobalt catalysts have been widely employed for Fischer-Tropsch (F-T) synthesis of long chain hydrocarbons from Syngas [1]. Cobalt has certain advantages over iron or ruthenium as a catalyst, such as longer catalytic life time, less water-gas-shift activity and production of a modified product. As with many supported transition metal catalysts, the structure and catalytic properties of supported cobalt catalysts can be affected by cobalt loading, support, preparation method and pretreatment conditions. Numerous studies have focused on the pretreatment effects on the supported cobalt catalysts [2-10]. Calleja et al. [7] investigated the pretreatment effects on the Fischer-Tropsch reaction over a Co/HZSM-5 catalyst, and found that the calcination and reduction temperatures did not have an effect on the catalyst activity. The results obtained by Rathousky et al.[9], however, revealed that the pretreatment conditions had a significant effect on the catalytic properties of Co/Al_2O_3 and Co/SiO_2 catalysts. Turnover frequency (TOF) for the F-T reaction decreased with increasing calcination temperature for both Co/Al_2O_3 and Co/SiO_2. However, the total reaction rate increased for Co/Al_2O_3 while it decreased for Co/SiO_2 [8-10]. Belambe et al. [11] studied the pretreatment effects on the activity of a Ru-promoted Co/Al_2O_3 catalyst for F-T reaction. The calcination temperature was found to have a pronounced effect on the overall activity of the catalyst, but not on TOF. The reduction temperature had only a negligible effect on the overall activty and TOF.

The pretreatment effects on cobalt supported on titania have not prevously been reported in the literature. A previous investigation into the effect of boron on Co/TiO_2 catalysts indicated that boron decreases the reducibility of a Co/TiO_2 catalyst [12]. In parallel, the total CO hydrogenation rate was decreased by the addition of boron. TOF, however, was not affected by boron. In this study, the pretreatment effects on the catalytic properties of the boron-modified Co/TiO_2 catalyst were investigated. TPR, H_2 chemisorption and O_2 titration have also been used to check the pretreatment effects on the reducibility and dispersion of the catalyst.

Experimental

Catalyst preparation and pre-treatment. From the previous investigation, we found that the 10 wt% cobalt supported on the titania modified by 0.1 wt% boron catalyst had good activity for the F-T reaction [12]. This catalyst also showed good resistance for the sulfur poisoning [13]. This catalyst was thus used in this study. The titania modified by 0.1 wt% boron was prepared by pore volume impregnation of titania (Degussa P25, BET surface area: $50 m^2/g$; pore volume: 0.51ml/g) with a boric acid solution. The sample was dried at 120°C for 16 h then calcined at 400°C for 6 h. Cobalt (10 wt%) was deposited on the boron-modified titania by pore volume impregnation with cobalt nitrate solution. The sample was redried at 120°C for 16 h before calcination. The catalyst was calcined at different temperatures (200-400°C) using flowing air (GHSV = 2000 h^{-1}) for 16 h. After calcination, the catalyst was cooled down to room temperature and stored in a dry atmosphere. Before carrying out the F-T reaction, the catalysts were reduced for 16 hours at various temperatures (200-450°C) under flowing hydrogen (GHSV = 2000 h^{-1}).

Characterization techniques. Temperature Programmed Reduction (TPR), H_2 chemisorption and O_2 titration were used to characterize the catalysts. The methods used have previously been described [12, 13].

Reactor study. The catalysts, calcined and reduced at various temperatures, were tested for their activity and selectivity in the Fischer-Tropsch reaction in a fixed-bed flow reactor. The procedure has been described early [12,13]. The catalyst amount (~ 2 g) used for various experiments was kept constant. Fischer-Tropsch reaction was carried out at a pressure of 8 bar; a temperature of 230°C; GHSV of 350 h^{-1}(of CO) and a CO/H_2 1:2 ratio for more than 400 h. Mass balances were carried out after the catalysts were on line for > 80 h. An on line GC , two off line GCs were used to analyse the composition of the product spectrum.

Results

TPR. The TPR spectra of the catalysts calcined at various temperatures are shown in Figure 1. Three reduction peaks can be observed for the catalyst calcined at 200 °C. The first peak, ranging from 180-200°C, was attributed to the reduction of the NO_X group from $Co(NO_3)_2$. This peak became smaller when the catalyst was calcined at 300 °C and it disappeared after calcination at 400 °C due to the complete decomposition of nitrate[9]. Two peaks between 250-550°C were assigned to the reduction of Co_3O_4 supported on titania. The reduction of Co_3O_4 supported on titania proceeded in two stages [14], namely a primary reduction of Co_3O_4 to CoO and a subsequent reduction of CoO to Co metal. It is apparent that the Co_3O_4 reduction peaks shift to higher temperature and the area of reduction peaks decreases with increasing calcination temperature, suggesting that calcination decreases the reducibility of the catalyst.

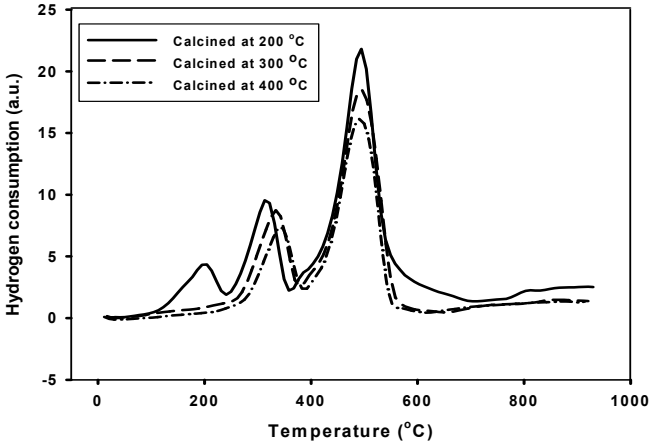

Figure 1. TPR profiles of the catalyst calcined at different temperature.

H_2 chemisorption and O_2 titration. The effects of pretreatment conditions on the percentage dispersion (% exposure) and percentage reduction of the catalysts were measured by H_2 chemisorption and O_2 titration. The results are shown in Tables 1, 2. With the exception of the dried catalyst, the percentage dispersion and percentage reduction of catalysts were found to decrease with increasing calcination temperature. As the reduction temperature was increased the % reduction did increase up to 300 °C after which there was little further effect.

The percentage dispersion increased initially and then decreased on increasing the reduction temperature. The maximum dispersion occurred in the catalyst reduced at 300 ^{o}C.

Fischer-Tropsch synthesis. The effect of calcination on the catalytic properties of the catalyst are shown in Table 1. The initial CO conversions were measured after about 30 min of reaction, while the steady-state CO conversions and the CO hydrogenation rates were measured after 80 h of reaction when the CO conversions are constant. The steady-state CO conversions decreased by about 25% from the initial conversions for all the calcination temperatures. Increasing calcination temperature was found to cause a linear decrease of both the steady-state CO conversion and total reaction rate for the F-T reaction. When the calcination temperature was increased from 200^{o}C to 400^{o}C, the reaction rate decreased by 30%. The product selectivity and α value were not affected by the lower temperature calcination. The higher temperature calcination shifted the product spectrum to the lower weight hydrocarbons. CO_2 was also found to be produced at the higher calcination temperatures. Turnover Frequency (TOF) was constant and independent of the calcination temperature. Table 2 shows the F-T reaction results obtained with the catalyst calcined at 300^{o}C, but reduced at various temperatures. At this calcination temperature, the reduction temperatures have a significant effect on the F-T reaction rate. When the reduction temparature was increased up to 350 ^{o}C, the total reaction rate almost kept constant. Further increasing reduction temperature (400 and 450 ^{o}C) resulted in a clear decrease in CO conversion. The reduction temperature, however, did not have effect on TOF and product selectivity.

Discussion

Effect of pretreatment on the extent of reduction and dispersion of Co/B/TiO_2. The TPR and O_2 titration results revealed that the reducibility of the catalyst decreased with increasing calcination temperature. This may be due to (i) the smaller Co_3O_4 crystallite size (from XRD result, not shown) or (ii) the formation of surface cobalt compounds through metal-support interactions at higher calcination temperature [2]. Ho et al. [15] found a surface $CoTiO_3$-like phase in Co/TiO_2 catalysts, in addition to the Co_3O_4 phase, after calcination at 400^{o}C. The amount of surface compound was dependent on the cobalt loading and calcination temperature. The "surface compounds" formation has been reported by others for non-promoted Co/SiO_2, Co/Al_2O_3 [2,3] and Ru-promoted Co/Al_2O_3 catalysts [11]. Our results revealed that the extent of reduction of the catalyst was not changed at the lower reduction temperatures (from 250 to 350 ^{o}C) but that the higher reduction temperatures (400, 450 ^{o}C) increased the extent of the reduction of the catalyst. This may be because the higher temperature causes the partial reduction of titania support resulting in a increase in the total reduction content, which was measured by total O_2 consumption [15].

The results shown in Table 1 reveals that the dispersion (% exposure) of the catalyst decreases with increasing calcination temperature. Hydrogen chemisorption has been reported to be suppressed for the catalysts which are poorly reduced [4-6]. Ho et al. [16] observed a decrease in chemisorption values with increasing calcination temperature for a Co/SiO_2 catalyst. Belambe et al. [11] also found the same effect for a Ru-promoted Co/Al_2O_3 catalyst. The results indicate that the higher reduction temperature gives a catalyst with a lower dispersion of catalyst, probably due to the strong metal-support interaction (SMSI). TiO_2 is a typical SMSI support. The higher temperatures can reduce TiO_2 to TiO_X which blocks the surface metal cobalt sites and can cause loss of dispersion [17].

Effect of pretreatment on Fischer-Tropsch reaction of Co/B/TiO_2 catalyst. The data in Table 1 shows that the total CO hydrogenation rate decreases, and TOF is almost constant with increasing calcination temperature. This suggests that the decrease in total rate is the result of a decrease in the number of cobalt active sites due to the lower reducibility of the catalyst at the higher calcination temperature. This is consistent with the results obtained by other researchers for the SiO_2, and Al_2O_3 supported cobalt catalysts. Ho et al.[16] studied the effect of calcination temperature on the surface characteristics and CO hydrogenation activity of a Co/SiO_2 catalyst. They did not observe any change in TOF with calcination temperature. Belambe et al. [11] studied the effect of pretreatment on the activity of Ru-promoted Co/Al_2O_3 F-T catalyst. Their results indicated that the F-T reaction activity decreased with increasing calcination temperature. TOF was constant and was independent of the calcination temperature and the extent of reduction of catalyst. In contrast, the results obtained by Rathousky et al. [9] exhibited an increase in total CO hydrogenation activity for a Co/Al_2O_3 catalyst at higher calcination temperatures. They indicated that cobalt-aluminium oxides formed due to high calcination temperature which favored the increased yield of hydrocarbons.

Selectivity data and α value data revealed that the higher calcination temperature favored the lower weight hydrocarbons. Poorly-reduced catalysts contain a large fraction of stable surface oxide phases which are highly inactive for CO hydrogenation, but active for water-gas-shift reaction [18]. A higher H_2/CO ratio at the surface caused by the WGS reaction would promote the formation of lower weight hydrocarbons. The reduction temperature did not have a significant effect on the selectivity of the catalyst. This suggests that there is no change in the chemical properties of the active cobalt sites [11]. Calleja et al. [7] (for Co/HZSM-5 catalyst) and Fu and Bartholomew [6] (for Co/Al_2O_3 catalyst) also obtained similar results.

Conclusions

Pretreatment conditions were found to have a significant effect on the reducibility and activity of 10 wt% cobalt supported on titania catalyst modified by 0.1 wt% boron. The percentage reduction and percentage dispersion decreased with increasing calcination temperature. The higher calcination temperatures decreased the total CO hydrogenation activity, but did not affect the turnover frequency. The decrease in CO hydrogenation rate with increasing calcination temperature is attributed to a decrease in the number of surface active sites. The higher reduction temperature also decreased the total activity. This is the result of the loss of dispersion due to the TiO_X blocking the surface active sites at the higher reduction temperatures. The higher calcination temperature shifted the product spectrum to the lower weight hydrocarbons, however, the reduction temperature did not affect the product selectivity.

Acknowledgements. The authors gratefully acknowledge (i) financial support from Sasol and the S.A. FRD , (ii) the technical assistance of Mr. B. Chassoulas.

References

(1) Anderson, R. B. Fischer-Tropsch Synthesis, Academic Press: New York, 1984.
(2) Chung, K. S.; Massoth, F. E. *J. Catal*. **1980,** 64, 320.
(3) Chin, R. L.; and Hercules, D. M. *J. Phys. Chem*. **1982,** 86, 360.
(4) Yoon, K. E.; Moon, S. H. *Appl. Catal.* **1985,** 16, 289.
(5) Ihm, S.; Lee, D.; Lee, J. *J. Catal*. **1988**, 133, 544.
(6) Fu, L.; Bartholomew, C. H. *J. Catal.* **1985,** 92, 376.
(7) Calleja, G.; Lucas, A.; Grieken, R. V. *Appl. Catal.* **1991**, 68, 65.

(8) Lapidus, A.; Krylova, A.; Rathousky, J. *Appl. Catal.* **1991**, 73, 65.
(9) Rathousky, J.; Krylova, A. Zukal, A. *Appl. Catal.* **1991**, 79,167.
(10) Lapidus, A.; Krylova, A.; Rathousky, J.; Jancakova, M. *Appl. Catal.* **1992,** 80, 1.
(11) Belambe, A. R.; Onkaci, R.; Goodwin, Jr. J. D. *J. Catal.* **1997**, 166, 8.
(12) Li, J.; Coville, N. J. *Appl. Catal. A:* **1999,** 181, 201.
(13) Li, J.; Coville, N. J. *Appl. Catal. A:* **2001**, 208, 177.
(14) Martens, J. H.; van't Blik, H. F. J. *J. Catal.* **1986**, 97, 200.
(15) Ho, S. W.; Cruz, J. M.; Houalla, M.; Hercules, D. M. *J. Catal*. **1992,** 135, 173.
(16) Ho, S. W.; Houalla, M.; Hercules, D. M. *J. Phys. Chem.* **1990,** 94, 6396.
(17) van de Loosdrecht, J.; van der Kraan, A. M.; van Dillen, A. J. *Catal. Lett.* **1996,** 41, 27.
(18) Reuel, R. C.; Bartholomew, C. H. *J. Catal.* **1984,** 85, 78.

Table 1. Effect of Calcination Temperature on the Catalyst

Tc (°C)	Uncalcined	200	300	350	400
Dispersion (% exposure)	0.9	1.95	1.71	1.69	1.42
Reduction(%)	40.5	51	42.5	40.9	37.6
CO Conversion (mol%)					
Intial[a]	32	65	58	54	47
Steady state[b]	28.5	49	43	39	35
Reaction rate (S-S)					
(μmole/g cat./s)	0.46	0.79	0.69	0.63	0.58
TOF ($10^3.s^{-1}$)[c]	24.5	25.9	24.2	24.9	26
Selectivity (%, by mass)					
C_1	15.6	11.2	11.5	13.2	19
C_2-C_4	14.2	12.7	9.4	11.5	15
C_5-C_{11}	48.7	47.6	52.3	49	46
C_{12}-C_{18}	16.3	17.5	19	18.5	15.5
C_{18+}	5.4	10.5	8.8	7.3	4.5
CO_2 selectivity (%, by mass)	0	0	0	0.8	1.5
α value	0.69	0.8	0.79	0.75	0.54

[a] Reduction temperature: 300°C; reaction conditions: T=230°C, P=8 bar, H_2/CO=2:1,measured after about 30min of reaction; [b] Measured after 80 h of reaction; [c] Based on total H_2 chemisorption.

Table 2. Effect of Reduction Temperature on the Catalyst

Tr (°C)	250	300	350	400	450
Dispersion (%, exposure)	1.5	1.71	1.65	1.41	1.2
Reduction (%)	35	42.5	40.9	43.3	45.6
CO Conversion (mol%)[a]					
Initial	53	58	57.2	40	35
Steady state	39	43	42.5	33	29
Reaction rate (S-S)					
(μmole/gcat./s)	0.65	0.69	0.68	0.57	0.47
TOF ($10^3.s^{-1}$)	26	24.2	24.6	25.6	24.5
Selectivity (%, by mass)					
C_1	12	11.5	13	14.9	12
C_2-C_4	8.9	9.4	11	10.6	10.4
C_5-C_{11}	49	52.3	53	50	51
C_{12}-C_{18}	21	18.5	16	17	17.9
C_{18+}	9	8.8	7	6.9	8.6
α value	0.73	0.79	0.75	0.69	0.76

[a] Calcination temperature: 300°C; reaction conditions: T=230°C, P=8 bar, H_2/CO=2:1.

INFLUENCES OF REACTION CONDITIONS ON STREAM REFORMING OF METHANE OVER Ni/ZrO_2 CATALYST

Jie HU[1,2], Dehua HE[1], Yingwei LI [1], Hui WANG[1], Xin ZHANG[1]*

[1] State Key Laboratory of C_1 Chemistry and Technology, Department of Chemistry, Tsinghua University, Beijing 100084, P.R. China
[2] Henan Textile College, Zhengzhou, 450007, P.R. China

Introduction

The stream reforming of methane is a major process for producing hydrogen rich syngas in industry. Recently, the hydrogen production from the stream reforming of methane has attracted researchers' much attention in the world owing to the development of hydrogen fuel cell.[1-3] It has become a new hotspot to develop an efficient catalytic process for producing highly pure hydrogen gas.

Ni based catalysts have been mostly used in the stream reforming of methane in industry. In order to decrease the carbon deposit on the surface of Ni catalyst, a high H_2O/CH_4 ratio has been usually adopted. Furthermore, high reaction temperatures are required for the stream reforming of methane because it is a highly endothermic reaction. Therefore, highly thermostable and carbon deposit-resisting catalysts are desired in the stream reforming of methane. The selection of a suitable support may be an effective way for improving the thermo-stability and carbon deposit-resisting ability of the Ni based catalysts.

Recently, ZrO_2 has been widely investigated as a support in the carbon dioxide reforming of CH_4 to syngas and showed a quite positive effects on the catalytic performance.[4-6] ZrO_2 possesses both acidic and basic properties and shows a relatively high thermo-stability in catalytic reactions. Ni/ZrO_2 showed relatively high carbon deposit-resisting ability and stability in the carbon dioxide reforming of CH_4 to syngas. [7-8] Recently, we have investigated the performance of Ni/ZrO_2 catalyst in the stream reforming of methane. Here, we report the influences of reaction conditions and preparation conditions of the catalyst on the catalytic performance of Ni/ZrO_2.

Experimental

Preparation of samples. ZrO_2 was prepared by a precipitation method. A solution of $ZrOCl_2 \bullet 8H_2O$ was slowly added to a well-stirred ammonium solution at room temperature with controlling pH value at 10 during the precipitation. The obtained white precipitate was aged in the mother liquor for 2.5 h, filtered and washed with deionized water until no detectable Cl^-. The resultant paste was dried at 110 ^oC overnight and calcined at 650 ^oC for 5 h. Ni/ZrO_2 Catalyst was prepared by a wet impregnation method. An aqueous solution of $Ni(NO_3)_2 \bullet 6H_2O$ was added to ZrO_2 powder for the impregnation. After being evaporated and dried at 110 ^oC overnight, the sample was calcined at 650 ^oC for 3 h.

Reaction Procedure. The stream reforming of methane was carried out in a fixed-bed flow type quartz tube reactor (i.d. 8 mm). The catalyst (0.2 - 0.5g) was packed in the reactor and pretreated in a stream of 9%H_2-N_2 (120 ml/min) at 650 ^oC for 3 h. After reduction, the feed gas of stream, CH_4 and N_2 ($H_2O/CH_4/N_2$=2/1/2.67, 170ml/min) was introduced into the reactor and the reaction went on from 550 to 850 ^oC at atmospheric pressure. The reactor effluent was introduced into a condenser to condense the liquid components and then the dry effluent gas was analyzed by on-line gas chromatographs (TDX-01 column, TCD detector).

Characterization of catalysts. The crystal phases of ZrO_2 were determined by XRD (BrÜker, D8 Advance powder diffractometer) with CuKα radiation with a nickel filter. The crystal size of ZrO_2 was calculated from the half-width of the reflection of monoclinic phase determined by XRD. The specific surface area of ZrO_2 was measured by BET method on Micromeritics ASAP-2010C adsorptionmeter using N_2 as adsorption gas.

Results and Discussion

Under the reaction conditions of 650^oC, $H_2O/CH_4/N_2$=2/1/2.67 and SV=$1.98\times10^4h^{-1}$, 85% CH_4 conversion and 70% CO selectivity were obtained over 10%Ni/ZrO_2 catalyst in the stream reforming of methane. The influence of the reaction temperatures on the catalytic performance is shown in Fig. 1. In the temperature range of 650 ^oC~ 800 ^oC, the conversion of methane increased with the increase of temperatures and researched 100% at 800 ^oC. CO selectivity also increased monotonously with the increase of temperatures from 650 ^oC to 800 ^oC.

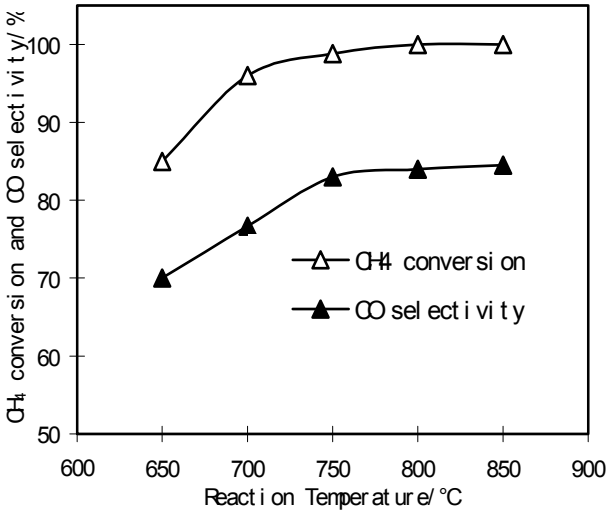

Figure 1. Catalytic performance of 10%Ni/ZrO_2 and effect of reaction temperatures. ($H_2O/CH_4/N_2$=2/1/2.67 and SV=$1.98\times10^4h^{-1}$)

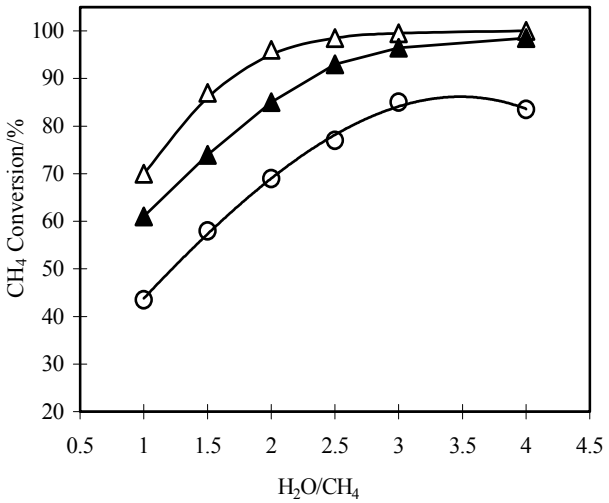

Figure 2. Influence of H_2O/CH_4 ratios on catalytic activity (10%Ni/ZrO_2, $T_{reduction}$ = 650^oC, SV=$1.98\times10^4h^{-1}$) Reaction temp.: Δ 700^oC; ▲ 650 ^oC; ○ 600^oC.

The effect of the ratios of H_2O/CH_4 on the stream reforming of methane was investigated in the range of H_2O/CH_4 ratio from 1/1 to 4/1 under the conditions of 600~700 °C and $1.98\times10^4 h^{-1}$SV. The conversion of methane increased monotonously with the increase of H_2O/CH_4 ratios at all tested temperatures in the ratio of H_2O/CH_4 = 1/1~3/1 (Fig. 2). When the H_2O/CH_4 ratio was over 3.5, the conversion of methane kept constant at all tested temperatures. The effect of H_2O/CH_4 ratios on CO selectivity is shown in Fig. 3. The selectivity of CO decreased with the increase of H_2O/CH_4 ratios at all tested temperatures and dropped dramatically down to 12% at 600 °C when H_2O/CH_4 ratios researched 4/1.

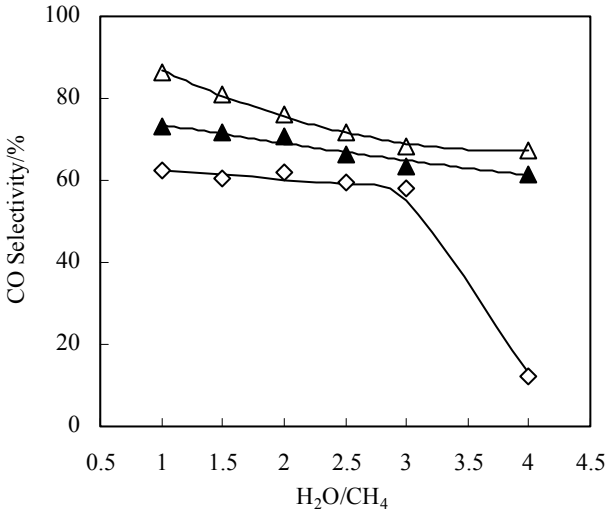

Figure 3. Influence of H_2O/CH_4 ratios on CO selectivity
(10%Ni/ZrO_2, $T_{reduction}$ = 650°C, SV=$1.98\times10^4 h^{-1}$)
Reaction temp.: Δ 700°C; ▲ 650 °C; ◇ 600°C.

The influence of SV on the catalytic activity is shown in Fig. 4. Both methane conversion and CO selectivity decreased with the increase of SV in the range of $1.98\times10^4 h^{-1}$ ~ $9.74\times10^4 h^{-1}$ at 550 ~ 850 °C. The increase of space velocity would result in short contact time of the reactants with the surface of catalyst, which will be unfavorable for the adsorption and activation of the reactants and leads to the decrease of CH_4 conversion. It was reported that CO and CO_2 would be formed in parallel in the stream reforming of methane[9] and our experiment results of the influent of SV on CO selectivity seem to support this supposition.

The support ZrO_2 was calcined at 550~850 °C before impregnation with the solution of $Ni(NO_3)_2\bullet6H_2O$. The characterization of the support showed the specific surface area of ZrO_2 decreased evidently and its crystal size increased in some sort with the increase of calcination temperature. Influence of calcination temperatures of the support ZrO_2 on the catalytic performance at the reaction temperatures of 650 °C and 800°C is shown in Table 1. Changing the calcination temperatures of the support ZrO_2 showed no evident influence on the conversion of methane and CO selectivity. The effect of the reduction temperatures of Ni/ZrO_2 catalyst on the catalytic performance was also examined in the reduction temperature range of 450~750°C. Under the reaction temperature of 650 °C, the catalyst reduced at 550°C showed a higher CH_4 conversion than at other reduction temperatures. But no influence was found on CO selectivity when changing the reduction temperature of Ni/ZrO_2 catalyst.

The stability of Ni/ZrO_2 was also examined under the reaction conditions of 650 °C, H_2O/CH_4 =1.5/1 and 5.1×10^4 mL/g-cat▪h for 30 hours. Although the tested times (30 hours) was not enough for check the stability of the catalyst, both CH_4 conversion and CO selectivity did not decrease and kept constant during the tested period.

Acknowledgment. We acknowledge the financial support from the Research Foundation of Tsinghua University.

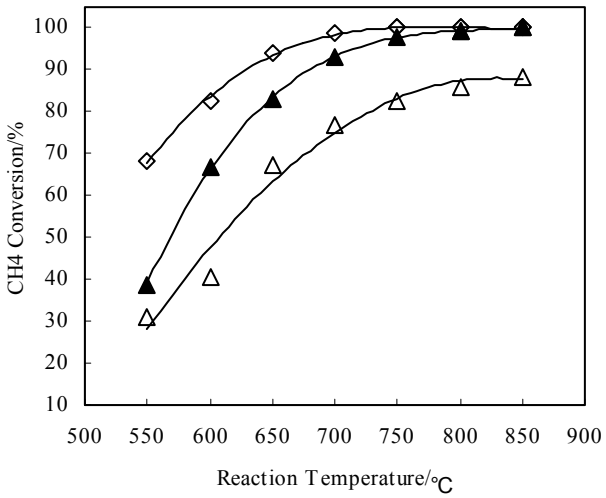

Figure 4. Influence of space velocities on catalytic activity
(10%Ni/ZrO_2, $T_{reduction}$ = 650°C, $H_2O/CH_4/N_2$=2/1/2.67)
◇ : SV=$1.98\times10^4 h^{-1}$; ▲: SV=$4.87\times10^4 h^{-1}$; Δ: SV=$9.74\times10^4 h^{-1}$.

Table 1 Influence of calcination temperatures of support

Calcination temperature / °C	Reaction temperature / °C			
	650 °C		800 °C	
	CH_4 Conv. /%	CO Sele. /%	CH_4 Conv. /%	CO Sele. /%
550	65.8	61.0	94.3	82.3
650	69.8	60.7	96.3	82.1
750	65.4	63.2	95.8	82.3
850	65.6	62.6	96.0	83.3

References

1 Solh T. E., Jarosch, K., de Lasa, H. I, Appl. Catal. A: General. **2001**, *210*, 315-324
2 Dong W.S., Roh H.S., Jun K.W., Park, S.E., Oh, Y.S., Appl. Catal. A: General, **2002**, *226 (1-2)*, 63-72
3 S.Hegarty M.E., O'Connor A.M., Ross J.R.H., Catal. Today, **1998**, *42*, 225-232
4 Bitter J.H., Seshan K., Lercher J. A., J. Catal., **1999**, *183*, 336
5 Wei J.M., Xu B.Q., Li J.L., Cheng Z.X., Zhu Q.M., Appl. Catal. A, **2000**,*196*, L167-172
6 Wei J.M., Xu B.Q., Cheng Z.X., Li J.L., Zhu Q. M.**,** Stud. Surf. Sci. Catal., **2000**, *30*, 3687-3692
7 Wei J.M., Xu B.Q., Sun K.Q., Li J.L., Zhu Q. M., Chem. J. Chin. Univ., **2002**, *23*, 2196
8 Xu B.Q., Wei J.M., Yu Y.T., Li J.L., Zhu Q. M., Top. Catal., **2003**, *22 (1/2)*, 77
9 Ho K., Hughes R., Chemical Engineering Journal, **2001**, *82(1-3)*, 311-328

Hydrocarbon Fuel Composition Effects on Fuel Cell Reformer Performance and Light-off

Rod Borup, Michael A. Inbody, José I. Tafoya, Will J. Vigil and Dennis Guidry

Los Alamos National Laboratory
MST-11, MS J579
P.O. Box 1663
Los Alamos, NM 87545

Introduction

Fuel cells have high efficiency for conversion of fuel to electricity. However, most types of fuel cells do not have high power density and efficiency operating directly from the hydrocarbon fuels currently widely available for transportation applications (gasoline and diesel), thus require fuel reforming. The choice of fuel for fuel cells is likely to be different for differing fuel cell applications, and debates exist about what the future fuels for fuel cell transportation applications will be. Potential on-board vehicle applications for fuel cells include both prime mobility power and auxiliary power production, and the fuel requirements will vary depending upon the power production application.

The start-up of fuel processors for transportation applications is one challenging area requiring development for commercialization. The light-off of the fuel processor is examined with different fuel components to examine the fuel composition effect during start-up. Chemical equilibrium favoring carbon formation may be impossible to avoid during a fuel rich start-up of a fuel processor.

Hydrogen production from the catalytic oxidation and steam reforming (ATR) of liquid hydrocarbon fuels is examined to determine fuel composition effects on the partial oxidation and reforming aspects of the fuels. Fuel processing performance of individual fuel components is compared with the fuel processing performance of blended fuel components and the reformulated gasoline to examine synergistic or detrimental effects the fuel components have in a real fuel blend.

Experimental

To examine the effect of the fuel on hydrogen production devices, various fuel components and real fuels have been tested in fuel auto-thermal reformers (ATR) and fuel reforming systems. Fuel reforming has been conducted by catalytic partial oxidation and reforming using air as oxidant. Typical ATR catalysts which are noble metal based (such as platinum and rhodium) have been employed in this work. The catalysts are supported onto a high surface area substrate, either a monolith honeycomb, or a reticulated foam. For gasoline reforming, the gasoline, or gasoline component is vaporized, then mixed in vapor phase with steam. The fuel/water mixture is then mixed with air, preheated and introduced to the reforming catalyst. Carbon formation during light-off was measured by monitoring carbon via *in situ* laser absorption and scattering measurements. The oxidation catalyst is preheated to a temperature of about 250 – 300 ^{o}C so that fuel light-off occurs when the fuel/air mixture is introduced.

The analysis of the fuel effect on the product composition stream is conducted by various analytical techniques, specifically laser scattering and laser fluorescence, gas chromatography, FTIR (Fourier transform infrared), NDIR (non-dispersive infrared), paramagnetic oxygen and GC/MS (gas chromatography/mass spectrometry).

Various fuel compositions and components have been measured in these reactor systems. Main components include aliphatic (straight-chained and branched chained), aromatic, napthenic, olefinic. Hydrotreated naptha, reformulated gasoline, kerosene, de-odorized kerosene, low sulfur diesel, diesel fuel and bio-diesels are some of the fuels which have been used.. Additives examined include anti-oxidant No. 29 (2,6-Di-Tert-Butyl-4-methylphenol), anti-oxidant No. 22 (N, N'-Di-Sec-Butyl-P-Phenylenediamine) and DMA-548.

Results and Discussion

The start-up of the fuel processor for transportation applications is a key challenge for commercialization. Some of the challenges in starting the fuel processor system include: the speed of start-up to limit on-board energy storage, start-up without stored water onboard the vehicle, limiting the energy consumed during the start-up, and limiting the fuel processor durability by the formation of carbon. These start-up challenges can be affected by the fuel composition used for the reformer. Hydrocarbon components and fuel blends were measured for their propensity for light-off. The light-off of a reformer, especially under rich conditions and without use of steam, makes it difficult to avoid regimes in which carbon formation is not favored by chemical equilibrium.

The reformer light-off was measured by introducing fuel/air/steam mixture to the reformer at a O/C = 0.9, S/C = 1.0, then ramping the temperature of the catalyst bed in the reformer. The outlet composition was measured in real time by a mass spectrometer to observed when oxygen consumption started, and hydrogen, carbon monoxide and carbon dioxide were generated. An example light-off for iso-octane with 20% pentane is shown in figure 1.

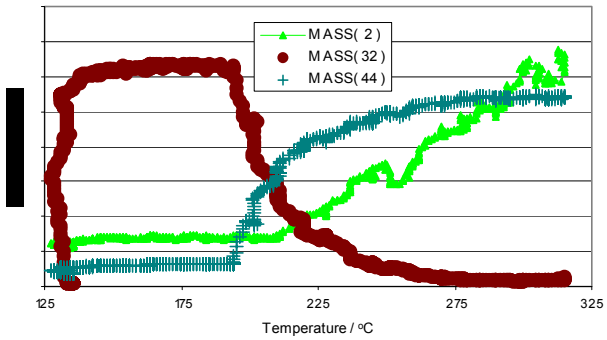

Figure 1. Reformer light-off with iso-octane and 20% pentane at O/C = 0.9 and S/C = 1.0.

Monitoring the light-off temperature of the reformer as a function of fuel helps determine the relative fuel effect on the reformer start-up. Iso-octane is typically used as a gasoline fuel simulant, and is thus used in all measurements for comparison purposes. Figure 2 shows the light-off of various straight-chained hydrocarbons, from n-pentane to n-decane, iso-octane and mixtures of iso-octane and pentane and hexane at 80% iso-octane. As the carbon length of the straight chained molecules is increased, the light-off temperature of the reformer increases. However, the light-off temperature of all of the straight-chained hydrocarbons are lower than the light-off temperature of iso-octane. As iso-octane is mixed with the straight-chained hydrocarbons, the light-off temperature is reduced.

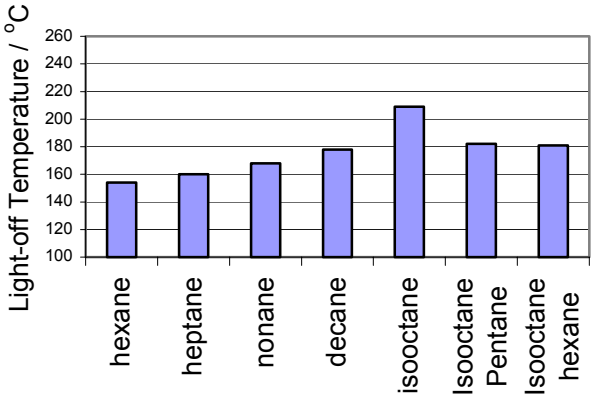

Figure 2. Reformer light-off with various aliphatic hydrocarbons (n-hexane, n-heptane, n-nonane, n-decane, iso-octane, iso-octane + 20 % n-pentane and iso-octane + 20 % n-hexane).

A ubiquitous impurity in hydrocarbon fuels tends to be sulfur, in various compounds, and has been shown to be detrimental to the reforming of hydrocarbons.[1] To examine the effect of sulfur and sulfur compounds on the light-off of reformers, thiophene and dibenzothiophene were added to iso-octane at levels of 100 ppm and 1000 ppm. These results are shown in figure 3. The sulfur at levels of 100 ppm for both thiophene and dibenzothiophene are not detrimental to the light-off of the reformer, in fact decrease the light-off temperature of the catalyst by 10 to 15 °C. However, when the compounds are added at a concentration of 1000 ppm, favorable effect disappears with thiophene, and dibenzothiophene increases the light-off temperature by over 30 °C.

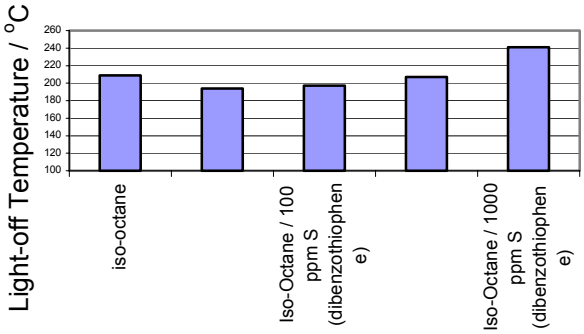

Figure 3. Reformer light-off with iso-octane and iso-octane with 100 ppm thiophene, 100 ppm dibenzothiophene, 1000 ppm thiophene and 1000 ppm dibenzothiophene (ppm by weight of S).

The current fuel infrastructure for transportation applications consists mainly of gasoline and diesel fuel. These fuels have many constituents, including generally relatively high content of aromatic components (~ 20 %). Aromatic components have been shown to slow the reforming kinetics and to increase carbon formation.[2] Figure 4 shows the light-off measurements of iso-octane, and iso-octane mixed with various aromatic compounds found in gasoline (xylene) and diesel fuel (anthracene, naphthalene). In addition, reformulated gasoline (RFG), kerosene, low sulfur diesel fuel and a commercial diesel fuel were measured for their light-off.

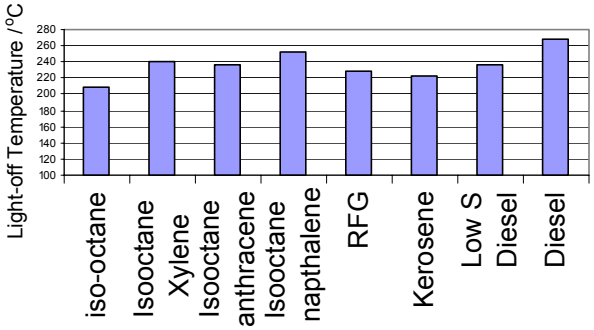

Figure 4. Reformer light-off with various aromatic hydrocarbons and fuels (iso-octane, iso-octane + 20 % xylene, iso-octane + 5 % anthracene, iso-octane + 5 % naphthalene, RFG – reformulated gasoline, kerosene, Low sulfur diesel fuel, and commercial diesel fuel).

The addition of aromatic compounds all increased the light-off temperature of iso-octane. The fuel blends all showed higher light-off temperatures than did iso-octane.

The steady-state relative rates for catalytic partial oxidation for different fuels has also been measured for various operating conditions after reformer light-off has occurred. Figure 5 shows relative reaction rate for various fuel components, mixtures and a Phillips Petroleum Hydrotreated Naptha stream at a S/C of 1.0. The relative reaction rates vary as the O/C ratio varies due to temperature changes. At lower O/C ratios, the adiabatic temperature rise is lower, thus the overall reaction rate is lower. The reaction rate for all components is higher at higher O/C, and subsequently, higher temperatures. The oxidation rates for O/C's of 0.7 and 0.8 are fastest for iso-octane. The addition of aromatics such as xylene slows the oxidation rate and conversion. Real fuel composition mixtures such as the Phillips Naptha and reformulated gasoline show a faster oxidation rate than that of iso-octane/xylene mixtures even though the relative aromatic concentration is approximately the same. At high O/C ratios (O/C = 1.0), the real fuel mixtures show an equal or faster oxidation rate compared with pure iso-octane. The resulting decrease in the oxidation rate due to the presences of aromatic hydrocarbons indicates that the fuel composition will have an affect on the required size (and cost due to catalyst loading) of the fuel processor. If it is possible to make a non-aromatic containing fuel available, the fuel processing size and cost would be positively affected.

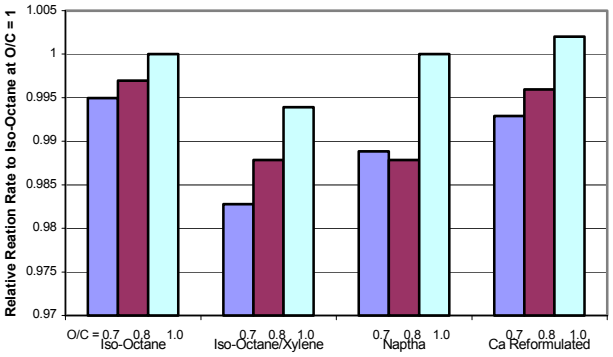

Figure 5. Relative oxidation rates of iso-octane, iso-octane/20% xylene, naptha and reformulated gasoline.

Conclusions

Fuel composition is important to reforming of fuel for transportation fuel cell systems. The fuel composition can affect the reformer light-off and start-up, the oxidation and reforming kinetics. Aliphatic hydrocarbons tend to have favorable light-off and reforming characteristics compared with aromatic components.

Acknowledgment

This work was supported by the Department of Energy Hydrogen, Fuel Cells and Infrastructure Technologies Program.

References

(1) Paul Berlowitz et al. 2003 Spring AIChE Meeting, New Orleans, March 30 – April 3.

(2) Borup et al. Fuel Composition Effects on Fuel Processor Dynamics, Office of Advanced Automotive Technologies Transportation Fuel Cell Power Systems FY 2000 Accomplishments Report.

CeO_2-Al_2O_3-SUPPORTED NOBLE METAL CATALYSTS FOR STEAM REFORMING OF HYDROCARBONS FOR FUEL CELLS

*Jian Zheng, James Jon Strohm, Chunshan Song**

Clean Fuels and Catalysis Program, The Energy Institute, and Department of Energy & Geo-Environmental Engineering, Pennsylvania State University, 209 Academic Projects Building, University Park, PA 16802
*Email: csong@psu.edu; Tel: 814-863-4466; Fax: 814-865-3248

Introduction

Recently, increasing attention has been paid on exploring compact fuel processors for fuel cell applications around the world[1,2]. We are exploring a fuel-cell fuel processor using logistic fuel (such as JP-8 jet fuel) for portable fuel cell application. As mentioned in our recent papers[3,4], our approach to solving the potential problem of carbon formation during reforming of higher hydrocarbon fuels is to conduct catalytic fuel reformation in two stages, with a pre-reformer (oxygen-assisted if necessary) to break-down most C_8-C_{13} hydrocarbons to C_1 to C_2 molecules plus CO and H_2, followed by steam reforming (possibly also oxygen-assisted) in main reformer to produce reformats (H_2, CO, CO_2).

Most industrial steam reforming of light hydrocarbons (C_1-C_4) uses a supported Ni catalyst. While the studies on steam reforming using noble-metal catalysts are limited, there are evidences indicating that these materials can be more active and more resistant to carbon formation than conventional Ni catalysts[3-10]. However, the metal activity over various supported materials for steam reforming under different conditions results in some contradictory trends in the literature. The specific activities of metals supported on alumina or magnesia have generally been found to be[5]: Rh ~ Ru > Ni ~ Pd ~ Pt > Re > Co. Turnover numbers have also been reported for steam reforming of methane and ethane on noble metals relative to Ni. For silica-supported catalysts used for methane steam reforming, the relative activities are[6]: Rh (1.6) > Ru (1.4) > Ni (1) > Pd (0.6) > Pt (0.5), whereas for alumina-supported systems with ethane[7, 8]: Rh (13) > Ru (9.5) > Pd (1.0) ~ Ni (1.0) > Pt (0.9). For the steam reforming of propane/propene mixtures, the order of activity is[9]: Rh ~ Ir > Pt > Co > Ru > Ni ~ Re. While the order of activity per metal site (on the base 100 for Rh) for the toluene steam reforming is[10]: Rh (100) > Pd (29) > Pt (19) > Ni (17) > Ir (13). It seems that rhodium has been generally found to be the most active metal, whereas no common agreement and knowledge has been achieved on the activity of iridium as catalyst for steam reforming of hydrocarbons.

With the need for on-board reforming for fuel cell applications, there has been renewed interest in developing more active catalysts that can operate under more demanding conditions at lower steam-to-carbon ratios for reforming of hydrocarbons. Instead of using Al_2O_3 as support, some new materials, such as those having unique features for stabilizing noble metal dispersion and for improving the oxygen storage (e.g., CeO_2, ZrO_2, etc.), have been examined[11-14]. Catalytic properties of CeO_2 and CeO_2-containing materials have been studied extensively[13]. Noble metal based catalysts (Pt, Pd and Rh) deposited on various support such as Al_2O_3, CeO_2 and ZrO_2, have been tested in various reforming processes, and they provide good catalytic activity in methane, propane or n-butane steam reforming reactions[11, 14]. The presence of CeO_2 as a promoter has also been found to confer high catalytic activity to the alumina-supported Pd catalyst for methane steam reforming[11]. Furthermore, the catalytic activity and the synergetic effect for the Pd/CeO_2/Al_2O_3 catalysts are strongly dependent on the crystallinity, dispersion and stoichiometry of the CeO_2 promoter deposited. Highly crystalline CeO_2 increases the catalytic activity of a Pd-supported catalyst when used in methane steam reforming[11].

In the present work, various noble metals have been supported on CeO_2 modified Al_2O_3 for the steam reforming of jet fuel via a two-step process (i.e. pre-reforming under low temperature and main reforming at high temperature). Ce has been found to improve both the activity and coke-resistance of Rh and Ir supported Al_2O_3 catalysts.

Experimental

CeO_2-Al_2O_3 (containing 20wt% CeO_2) support was prepared by wet impregnation of γ-Al_2O_3 (UOP LaRoche VGL-15) with $Ce(NO_3)_3{\cdot}6H_2O$ (Aldrich) followed by calcinations at 800˚C in air for 3 hours.

$RhCl_2$ (Aldrich) has been supported on both γ-Al_2O_3 and CeO_2•Al_2O_3 by wet impregnation, with nominal metal content of 2wt%. In both cases, the obtained $RhCl_2$ supported material was soaked into NH_4OH solution for several hours, followed by filtration and calcinations to remove NH_3, Cl^{-1}, and other impurities.

Various noble metals (such as Pt, Pd, Ru, Rh, Ir) have also been supported on Al_2O_3 and CeO_2.Al_2O_3 by wet impregnation, with nominal metal content fixed at 1 wt% for main reforming.

Jet fuel formulation. A readily available NORPAR-13 (consisting mainly normal paraffin, with average carbon number of 13) has been chosen as an important type of jet fuel. Since there is no much sulfur in NORPAR-13 (the sulfur content of NORPAR-13 is 4ppmw as analyzed by us using Antek 9000ES total sulfur analyzer), it can actually be regarded as a near sulfur-free clean jet fuel that can be utilized in large amount and directly for steam reforming in fuel processor for fuel cell application.

Simulated gas mixture. As described previously[4], SGM-2 (47.5% CH_4, 35.5% H_2, 7.0% CO_2, 9.0% C_2H_6, and 1.0% C_3H_8) has been chosen as an extreme example for the reformats from incomplete pre-reforming, since there is a significant concentration of higher hydrocarbons (C_2H_6 and C_3H_8).

Reaction conditions. A given amount of catalyst sample (1g for pre-reforming, 0.1 g for main reforming) was loaded in the middle of the stainless steel reactor tube (Inconel 800H alloy, with 0.54" O.D. X 0.375" I.D. and 24" long), with the remaining tube filled with α-Al_2O_3 beads.

For pre-reforming, NORPAR-13 jet fuel was introduced with one of the two HPLC pumps through the pre-heater into the reactor with a volumetric flow rate of 1.38 ml/hr. The water flow is kept at 4.02 ml/hr with a steam to carbon ratio of 3:1. The fuel flow is to simulate the real conditions defined by the calculations for a 20 watts solid-oxide fuel cell

For main reforming, CH_4 feed flow rate in the SGM-2 was chosen to be 13.7 ml/min, which also simulates the energy requirement for a 20 watts solid-oxide fuel cell.

Before starting the reforming, water was introduced for 30 minutes before pumping/flowing the reactant oil/gases. Catalyst screening is then performed in a laboratory continuous-down-flow tubular reactor (as described in our previous papers[3,4]) at atmospheric pressure in the temperature range of 514˚C (for pre-reforming) and 600-800°C (for main reforming), respectively.

During the pre-reforming reaction, the liquid products are collected every several hours by a liquid condenser with volume measured for the calculation of total conversion. For the main reforming, the gas products after condensing of remaining steam are analyzed on-line by a multi-gas analyzer GC-TCD for the calculation of conversion and product distributions.

Results and Discussion

Figure 1 shows a 10-hour pre-reforming run of the NORPAR-13 (4ppm S) at 514˚C using the modified 2%Rh/CeO_2•Al_2O_3 catalyst.

It can be found that the conversion is always near 100%. In the products, hydrogen is near 55%, the content of CO is only 5%, while the CO_2 and CH_4 are the dominant carbon-containing products with similar contents (both around 20%). There is almost no higher hydrocarbon such as ethane in the product gases.

In order to understand the effect of Ce on the Rh/CeO_2•Al_2O_3 catalyst for pre-reforming of jet fuels, we also prepared a comparative 2%Rh/Al_2O_3 followed by same NH_3-H_2O treatment.

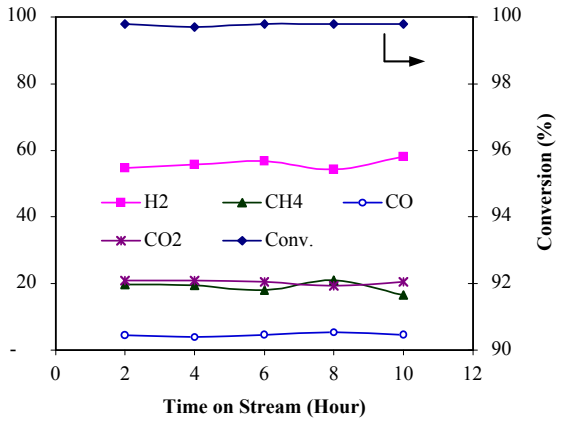

Figure 1. Pre-reforming of NORPAR-13 over modified 2% Rh/CeO_2•Al_2O_3 catalyst at 514˚C, S/C=3, atm.

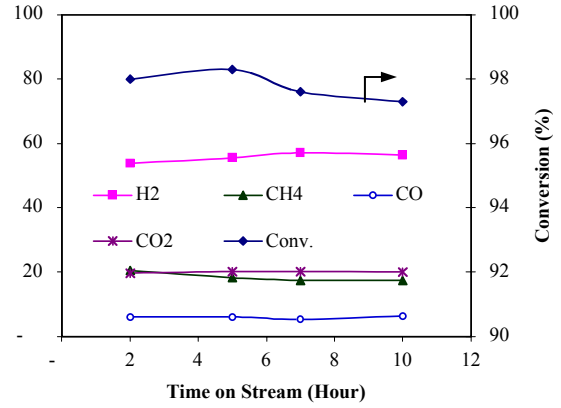

Figure 2. Pre-reforming of NORPAR-13 at 514˚C over modified 2%Rh/Al_2O_3 catalyst (S/C=3, atm).

Figure 2 shows another 10-hour pre-reforming run of the NORPAR-13 (4ppm S) at 514˚C using the modified 2%Rh/Al_2O_3 catalyst under exactly same reaction conditions as in **Figure 1**.

It can be seen that with the absence of Ce, the modified 2%Rh/Al_2O_3 catalyst shows lower activity: the conversion is around 97%-98% and there is a trend of deactivation with time on stream, which indicates that Ce in the modified Rh/CeO_2•Al_2O_3 catalyst is important for the improved catalytic activity. The composition of the gas products is similar to previous 10-hour run, with hydrogen around 56%, CO at 6%, CO_2 around 20%, and methane around 18%, which are close to the equilibrium pre-reformate composition[15].

Figure 3 shows the TPO-IR results of used catalysts Rh/CeO_2•Al_2O_3 (a) and Rh/Al_2O_3 (b), after 10-hour pre-reforming of NORPAR-13 at 514˚C. Peaks at 200-400˚C can be attributed to either the desorption of CO_2 or the oxidation of highly amorphous carbon while any peak at 400˚C-600˚C is the oxidation of carbon filament on the used catalysts[16, 17].

It can be seen that there is an obvious high temperature peak at 400-600˚C in the case of Rh/Al_2O_3, indicating that the presence of Ce is important to prevent carbon formation during pre-reforming of jet fuel.

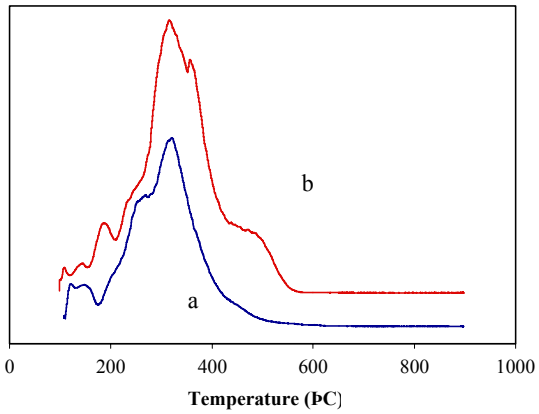

Figure 3. TPO-IR of used catalysts 2%Rh/CeO_2•Al_2O_3 (a) and 2%Rh/Al_2O_3 (b), after 10-hour pre-reforming of NORPAR-13 at 514˚C, S/C=3, atm.

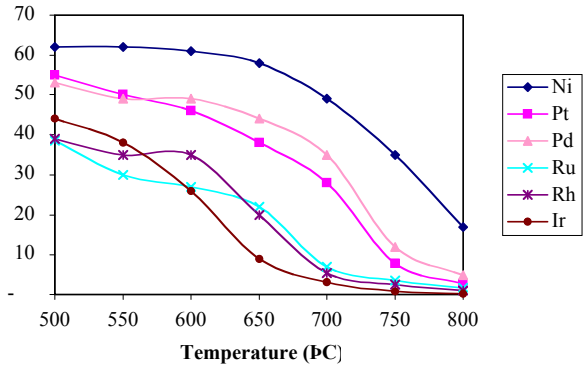

Figure 4. Steam reforming of SGM-2 on 1wt% noble metal supported on CeO_2-Al_2O_3 (GHSV=21500h^{-1}, S/C=1.5, atm)

As studied previously[4], we found that different metal shows different activity for steam reforming of methane at high temperature (800˚C). The understanding of this metal activity trend is important that can serve as a guide for the selection of good catalyst composition for steam reforming of hydrocarbons. We have carried more systematic studies on the activitity trend for different transition metal supported on same CeO_2•Al_2O_3 for the steam reforming of SGM-2 (contains not only methane, but also ethane and propane) under various reaction temperatures.

Figure 4 shows the steam reforming of SGM-2 at 500˚C-800˚C of 1wt% metals on the same CeO_2•Al_2O_3 support. The y-axis of **Figure 4** is the CH_4 content in the product gases. The lower of this value means the less un-reacted CH_4 (thus the higher conversion of

CH_4). It can be seen that at higher temperature (e.g. 800˚C), Ir is the most active among all the metals, which show following trend:

Ir > Rh ~ Ru > Pt ~ Pd > Ni.

However, at lower temperature (e.g. 500˚C), Ir loses its superiority to Rh and Ru, showing the following trend:

Rh ~ Ru > Ir > Pd ~ Pt > Ni.

This actually indicates that in the case of pre-reforming (usually working at around 500˚C), the most active metal could be Rh rather than Ir, which has already been verified by our previous pre-reforming work[3].

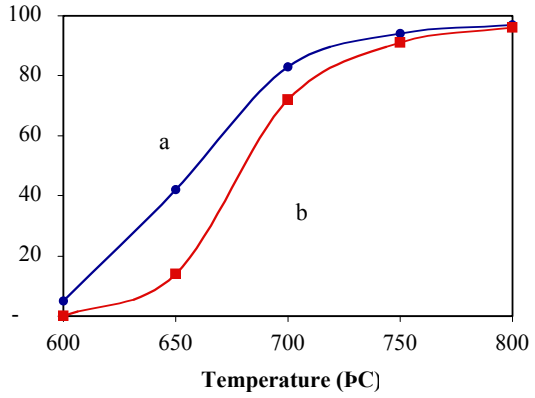

Figure 5. Steam reforming of SGM-2 on 1wt% Ir supported on CeO_2-Al_2O_3 (a) and Al_2O_3 (b) (GHSV=21500h^{-1}, S/C=1.5, atm)

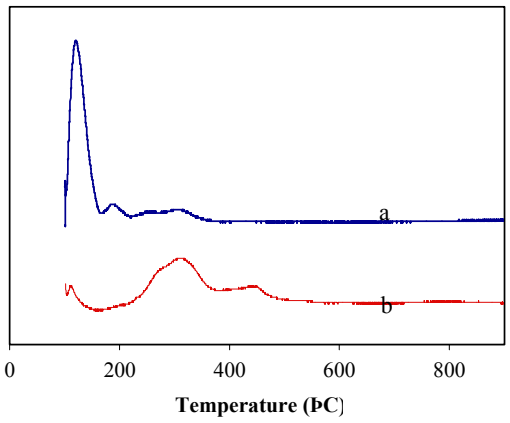

Figure 6. TPO-IR of used catalysts 1%Ir/CeO_2•Al_2O_3 (a) and 1%Ir/Al_2O_3 (b), after 10-hour main reforming of SGM-2 at 800˚C, S/C=1.5, atm.

Figure 5 shows the steam reforming results of SGM-2 over Ir supported on CeO_2-Al_2O_3 and Al_2O_3 under same steam/carbon ratio with changing temperature. It is clear that in the presence of Ce, the Ir/CeO_2-Al_2O_3 catalyst is more reactive, especially at lower temperature, than the Ir supported on Al_2O_3 alone. This indicates that Ce helps promote the steam reforming of hydrocarbons.

Figure 6 shows the TPO-IR results of used catalysts Ir/CeO_2•Al_2O_3 (a) and Ir/Al_2O_3 (b), after 10-hour main reforming of SGM-2 at 800˚C. Peaks at 200-400˚C can be attributed to either the desorption of CO_2 or the oxidation of highly amorphous carbon, while any peak at 400˚C-600˚C is the oxidation of carbon filament on the used catalysts[16, 17].

It can be seen that, similar to the results shown in **Figure 3**, there is an obvious high temperature peak at 400-600˚C in the case of un-promoted Ir/Al_2O_3, indicating that the presence of Ce is important to prevent carbon formation during steam reforming of lower hydrocarbons at 800˚C due to enhanced oxidative property.

Conclusions

Various metals (Rh, Ru, Ir, Pt, Pd, Ni) supported on CeO_2 promoted Al_2O_3 have been studied for steam reforming of liquid hydrocarbons (such as jet fuel). At higher temperature (such as 800˚C), Ir/CeO_2-Al_2O_3 catalyst shows the highest activity for steam reforming of lower hydrocarbons among all the CeO_2-Al_2O_3 supported noble metal catalysts. However, at lower temperature as in the case of pre-reforming (at around 500˚C), Ir loses its superiority to Rh and Ru. Ce helps promote the steam reforming of hydrocarbons by improving both the activity and coke-resistance of Rh and Ir supported catalysts.

Acknowledgement. We are grateful to the DoD/DARPA Palm Power Program management for supporting this work under sub-contract to Altex Technologies Inc. We also wish to thank Dr. Mehdi Namazian of Altex for helpful discussions on fuel reforming, and UOP for providing LaRoche γ-Al_2O_3 samples. Thanks also go to Dr. Jian-Ping Shen, Dr. Altin Orhan, Mr. Ronald Copenhaver and Ms. Lu Sun of PSU for their assistance.

References

(1) Song, C. *Catalysis Today*, **2002**,77, 17-49.
(2) Trimm, D.L.; Onsan, Z.I. *Catal. Rev.*, **2001**, *43 (1,2)*, 31-84; Larminie, J.; Dicks, A. In *Fuel cell Systems Explained;* John Wiley: New York, **2000**, pp.308.
(3) Zheng, J.; Shen, J.P.; Song, C.; Pan, W.; Strohm, J.J. *Prepr. Pap. - Am. Chem. Soc., Div. Fuel. Chem.*, **2003**, *48 (1)*, 374.
(4) Zheng, J.; Song, C. *Prepr. Pap. - Am. Chem. Soc., Div. Fuel. Chem.*, **2003**, *48 (1)*, 378.
(5) Kikuchi, E.; Tanaka, E.; Yamazaki, Y.; Morita, Y. *Bull. Japan Petrol. Inst.*, **1974**, *16*, 95.
(6) Rostrup Nielsen, J.R. In *Catalysis Science and Technology*; Andersen, J.R.; Boudart, M., Ed.; Springer-Verlag, New York, **1984**; Vol. 4, pp.34.
(7) Grenoble, D.C. *J. Catal.* **1973**, *51*, 203.
(8) Gandhi, H.S.; Piken, A.G.; Stepien, H.K.; Shelef, M.; Delosh, R.G.; Heyde, M.E. *SAE Techn. Pap. Ser. No. 770166*, in SAE Automotive Engineering Congress, Detroit, **1977**.
(9) Duprez, D.; Pereira, P.; Grand, M.; Maurel, R. *J. Catal.*, **1982**, *75*, 151.
(10) Igarashi, A.; Ohtaka, T.; Motoki, S. *Catal. Lett.*, **1991**, *13*, 189-194.
(11) Craciun, R.; Daniell, W.; Knozinger, H. *Appl. Catal. A: Gen.*, **2002**, in press.
(12) Hofstad, K.H.; Rokstad, O.A.; Holman, A. *Catal. Lett.*, **1996**, *36*, 25.
(13) Barbier, J.Jr.; Duprez, D. *Appl. Catal. B: Environ.* **1993**, *4*, 105.
(14) Kikuchi, E.; Nemoro, Y.; Kajiwara, M.; Uemiya, S.; Kojima, T. *Catal. Today*, **2000**, *56*, 75.
(15) Wei, P.; Song, C. Unpublished data.
(16) Zheng, J.; Song, C.; Pan, W.; Sun, Lu; Armor, J.; Nataraj, S.: Wilhelm, F. *Prepr. Pap. - Am. Chem. Soc., Div. Fuel. Chem.*, **2003**, *48 (2)*, to be accepted.
(17) Strohm, J.J.; Zheng, J.; Song, C. *Prepr. Pap. - Am. Chem. Soc., Div. Fuel. Chem.*, **2003**, *48 (2)*, to be accepted.

AN INNOVATIVE EFFICIENT COMBINED CYCLE FOSSIL AND BIOMASS FUEL POWER GENERATION AND HYDROGEN PRODUCTION PLANT WITH ZERO CO_2 EMISSION

Meyer Steinberg, Consultant

Energy Resources Division
Brookhaven National Laboratory
Upton, NY 11973-5000

Introduction

An advanced combined cycle for fossil and biomass fuel power generation and hydrogen production is described. An electric arc hydrogen plasma black reactor (HPBR)[(1)] decomposes the carbonaceous fuel (natural gas, oil, coal and biomass) to elemental carbon and hydrogen. When coal and biomass feedstocks are used, the contained oxygen converts to carbon monoxide. Any ash and sulfur present are separated and removed. The elemental carbon is fed to a molten carbonate direct carbon fuel cell (DCFC)[(2)] to produce electrical power, part of, which is fed back to the HPBR to power the hydrogen plasma. The hydrogen is used in a solid oxide fuel (SOFC) cell for power generation. The remaining high temperature energy in the gases from the fuel cells are used in a back-end steam rankine cycle (SRC) for generating additional power. The CO formed is converted to hydrogen using a water gas shift reactor (WGS). The plasma reactor is 60% process efficient, the direct carbon fuel cell is up to 90% thermal efficient, the solid oxide fuel cell is 56% efficient and the steam reaction cycle is 38% efficient. Depending on the feedstock, the combined cycles have efficiencies ranging from over 70% to exceeding 80% based on the higher heating value of the feedstock and are thus twice as high as conventional steam plants which are 38% efficient. The CO_2 emissions are proportionately reduced. Since the CO_2 from the direct carbon fuel cell and the water gas shift is highly concentrated, the CO_2 can be sequestered to reduce emission to zero with much less energy loss than occurs in conventional plants. Alternatively, these combined cycle plants can produce hydrogen for the freedomCAR program in combination with electrical power production at total thermal efficiencies much greater than obtained with fossil fuel reforming and gasification plants producing hydrogen alone.

Figure 1 presents a flow diagram of the combined cycle plant based on coal and biomass feedstock and indicates the functions of each of the units and the stoichiometric reactions taking place. A thermodynamic evaluation of the combined cycle system is given in Table 1. The mass balance, the energy distribution and the thermal efficiency of the entire system are given for a range of fossil and biomass fuels and includes the corresponding CO_2 emissions. The conclusion of this study is that for a wide variety of fossil fuels and biomass (wood), this combined cycle system results in efficiencies for electrical power production that are more than twice as high as conventional steam plants. The CO_2 emissions are thus cut in half. When the system is configured to produce hydrogen in addition to electrical power, the SOFC is eliminated and only the direct carbon fuel cell (DCFC) generates power, in which case, the total thermal efficiency can exceed 90%. This shows how integrated the hydrogen plasma black reactor (HPBR) functions with the direct carbon fuel cell (DCFC) in a combined system. The HPBR supplies the carbon fuel for the DCFC, which in turn supplies the power to the HPBR.

References

1. Sequin, L., The Karbomont Production Plant, Montreal, Canada, Private Presentation, 2002.
2. Cooper, J. F., Turning Carbon Directly into Electricity, Science and Technology Review, Lawrence Livermore National Laboratory, CA, 2001, 4-12.

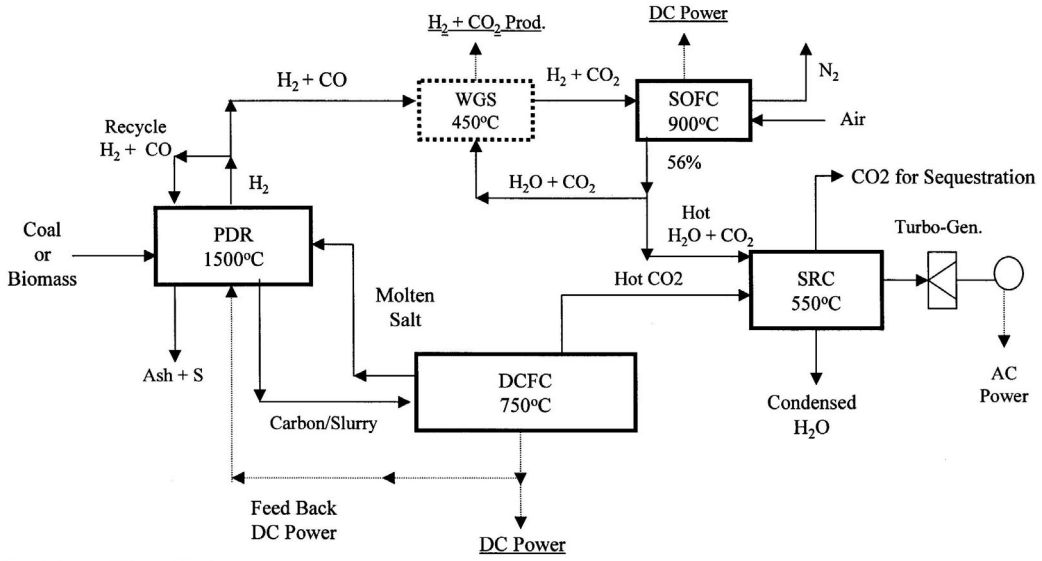

HPBR - Hydrogen Plasma Black Reactor
Lignite Coal $CH_{0.77}O_{0.24} = 0.76C + 0.24\ CO + 0.385\ H_2$
Kentucky Bit. Coal $CH_{0.81}O_{0.08} = 0.92\ C + 0.08\ CO + 0.40\ H_2$
Biomass: $CH_{1.38}O_{0.59} = 0.41\ C + 0.59\ CO + 0.69\ H_2$
WGS - Water Gas Shift
Lignite $0.24\ CO + 0.24\ H_2O = 0.24\ CO_2 + 0.24\ H_2$
Bituminous $0.08\ CO + 0.08\ H_2O = 0.08\ CO + 0.08\ H_2$
Biomass: $0.59\ CO + 0.59\ H_2O = 0.59\ CO_2 + 0.59\ H_2$
SOFC - Solid Oxide Fuel Cell
$H_2 + 1/2\ O_2 = H_2O$ (High Transport)
DCFC - Direct Carbon Fuel Cell
$C + O_2 + CO_2$ ($CO_3^=$ Ion Transport)
SRC - Steam Boiler Rankine Cycle

Figure 1. Coal or Biomass Fueled Combined Cycle Plasma Composition (PDR) with Direct Carbon Fuel Cell (DCFC), Hydrogen Solid Oxide Fuel Cell (SOFC) Backend Steam Rankine Cycle (SRC) Power Generation

Table 1
Electrical Power Production in the HPBR/DCFC/SOFC/SRC Combined Power Cycle Plant
Thermal Efficiency Evaluation and CO_2 Emission
Basis: -1 gmol of Fuel

Fuel Feedstock		Natural Gas	Crude Oil	N. Dakota Lignite Coal	Kentucky Bituminous Coal	Biomass Wood
Molar Composition (MAF)		CH_4	$CH_{1.7}$	$CH_{0.77}O_{0.24}$	$CH_{0.81}O_{0.08}$	$CH_{1.38}O_{0.59}$
Plasma Decomp. Products Mole/Mole Fuel						
C		1.0	1.0	0.76	0.92	0.41
CO		-	-	0.24	0.08	0.59
H_2		2.0	0.85	0.39	0.41	0.69
Ash, S, N (wt%)		-	~1.0	9.8	12.6	1.1
Enthalpy of Decomposition Kcal/gmol		18.0	+3.0	+3.6	+4.8	+12.7
Electrical Energy Generation All Energy Values in Kcal/gmol fuel						
Unit	Eff. %					
DCFC	90	84.6	84.6	64.3	77.8	34.7
SOFC	56	76.2	32.4	23.8	18.7	48.7
SRC	38	26.3	13.3	9.8	8.8	16.2
HPBR	60 - Consumed	-30.0	-5.0	-6.0	-8.0	-21.2
Net Electricity Generation, Kcal(e)		157.1	125.3	91.9	97.3	78.4
HHV of Fuel, Kcal(t)		212.0	149.0	110.3	119.0	112.8
Heat Exch. for Preheat* Kcal(t)		14.8	16.2	7.7	6.5	18.9
Thermal Efficiency - %		74.1	84.1	83.3	81.8	69.5
CO_2 Emission, Lbs/Kwh(e)		0.531	0.610	0.955	0.833	(0.986)**
CO_2 Reduction from conventional 38% SRC cycle - %		48.7	56.5	54.4	53.6	100.0

HPBR = Hydrogen Plasma Black Reactor
DCFC = Direct Carbon Fuel Coal
SOFC = Solid Oxide Fuel Cell
SRC = Steam Rancine Cycle

* This is the amount of heat unconverted from high temperature gas and can be used to preheat the incoming feed to reactor temperature by heat exchange.
**For biomass this is the amount of CO2 emitted from power cycle, however, because of the photosynthesis of biomass there is a zero net emission of CO_2.

Prediction of Deactivation Rates and Mechanisms of Reforming Catalysts

Aaron L. Wagner, R. Scott Osborne, Jon P. Wagner

1600 W. Hill St., Louisville, KY 40210

Introduction

As fuel cells near commercialization for industrial and residential applications, failure of the fuel processing system becomes less and less tolerable. Fuel cell system manufacturers must deliver reliable performance of both the stack and reformer for several years without significant change-out of components. One key to guaranteeing lifetime performance of the fuel processor is an accurate prediction of the deactivation of the catalytic components of the processor.

The conversion of hydrocarbons to high quality hydrogen as a feed for PEM fuel cells typically utilizes a series of reactions. These reactions include desulfurization of the hydrocarbon followed by reforming to syngas and then the CO cleanup reactions of water-gas shift and partial oxidation or partial methanation. The competing methods for converting hydrocarbons to a hydrogen rich syngas include steam reforming (SR), catalytic partial oxidation (CPOX) and autothermal reforming (ATR). Steam reforming has a high efficiency but heat transfer and mass transfer present non-trivial challenges and can significantly limit catalyst performance. CPOX generates excess heat and therefore does not require external heat input but produces a reformate with lower hydrogen content and typically exhibits higher operating temperatures. Many fuel processor developers favor ATR due to the balance of efficiency to produce hydrogen and the self-sustaining nature of the reaction at moderate temperatures.

Steam Reforming Catalysts

Traditional tubular nickel steam reforming catalysts have a typical lifetime of 3 to 5 years when employed for large-scale hydrogen production (1,000,000scf/day). Primary steam reforming catalysts contain 10-20% Ni supported on α–Al_2O_3, calcium aluminate, or Magnesium aluminate. Typically, natural gas steam reformers are operated with exit temperatures from 800°C to 870°C (but tube wall temperatures can range from 700°C up to a maximum hot spot of 920°C) at S:C ratios from 2.5 to 4.0 and at a GHSV on the order of 2,000/hr.

Catalyst failure is due to either coke formation, the presence of fouling agents such as sulfur, chlorine, or iron, or can be the result of physical breakdown due to thermal cycling and/or poor initial physical integrity. Deactivation manifests itself by an increase in tube wall temperature or an increase in pressure drop.

Determination of Coke Resistance. Since standard reforming catalysts require several months to form carbonaceous deposits under standard operating conditions, a test was designed to accelerate the coke formation reaction. Coke is usually formed when the rate of carbon deposit caused by cracking is greater than the rate of oxidation or hydrogenation. This coke grows in needle like formations underneath the active nickel sites on the catalyst.

The accelerated test consists of performing steam reforming of *n*-hexane on 300cc of 12 x 16 mesh sized catalyst particulates. The test is conducted at ~3,000/hr at an initial S:C of 6. After 24hrs on stream, the S:C ratio is lowered. The test is run until an increase in ΔP is observed between the inlet and outlet of the reactor. The increase in pressure is a result of carbon formation on the catalyst and will occur quite rapidly when conditions are conducive to coke formation. This test is useful for determining relative coking resistance between catalysts. Data from this test is used in conjunction with field data to predict operating lifetimes. As an example, in **Figure 1** an experiment was carried out at a S:C ratio of 3. A Ni-/-α–Al_2O_3 catalyst shows immediate pressure increase whereas a Ni-/-Ca aluminate catalyst promoted with potassium can operate for hundreds of hours. Decreasing the S:C ratio to 1.6 was necessary to facilitate coking of the catalyst and thereby an increase in pressure.

The acidity of a steam reforming catalyst is proportional to its propensity to form coke. By utilizing a more basic support such as calcium aluminate and by promoting with the basic K, the coking resistance of tubular steam reforming catalysts has been greatly increased. The laboratory results have been confirmed by field operation.

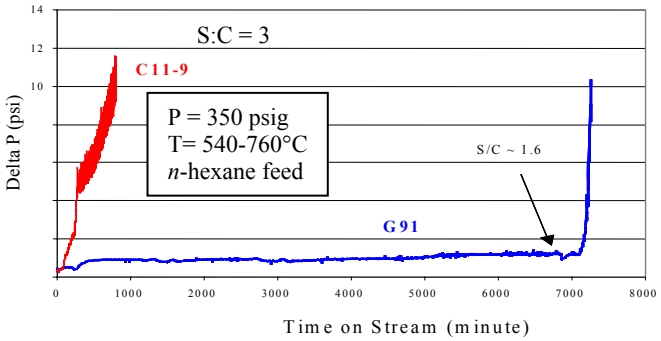

Figure 1. Change in pressure across commercial Ni / αAl_2O_3 (C11-9) and Ni/Calcium Aluminate + K (G91) catalysts as a function of time on stream.

The Effect of Sulfur. Nickel catalysts are susceptible to poisoning by sulfur by the formation of nickel sulfide on the surface of the catalyst. Sulfur by itself will not cause a catastrophic failure of the reformer, but will decrease activity of the catalyst to the point that methane conversion is no longer at acceptable levels. Due to the drop in steam reforming activity, tube wall temperatures can increase to non-optimal levels. In addition, the suppression of the reforming reaction can increase the propensity to form carbon leading to pressure drop build-up.

Sulfur poisoning can also cause coke formation necessitating more frequent coke removal steps such as steaming.

Hydrothermal Effects on the Catalyst. As Ni-/-Alumina type catalysts operate at high temperatures and in the presence of steam, nickel aluminate spinel may form on the catalyst. This inactive phase is evidenced by either discoloration of the catalyst from dark gray to light green or can be seen by XRD. Nickel spinel can be difficult to reduce resulting in decreased catalyst performance. The spinel can also add to the loss of physical integrity of the catalyst increasing the attrition of the catalyst as evidenced by increased ΔP across the bed.

A test was designed to show differences between catalysts in the presence of steam at elevated temperatures. Initial methane conversion activity was measured on a series of catalysts. The catalysts were then exposed to 100% steam for 16hrs at 870°C. Activity measurements are repeated after this treatment. Deactivation of catalysts following the steam treatment was easily explained by Ni spinel formation as detected and quantified by XRD.

Autothermal Reforming Catalysts

There are several differences between Autothermal reforming catalysts and traditional steam reforming catalysts. As a rule, ATR

catalyst must possess higher activity, stability in both oxidizing and reducing atmospheres and be supported on high geometric surface area substrates with minimal pressure drop. Sulfur tolerance and coking resistance are as essential to ATR catalysts as they are to steam reforming catalysts but since ATR catalysts are typically precious metal based, sulfur tolerance is even more crucial.

Stable substrates. The most effective ATR catalysts contain Rh supported on a stabilized alumina washcoat. The catalyst is typically washcoated on either a high cell density cordierite or metal monolith or reticulated ceramic or metal foam structures. A main constituent of cordierite is silica that has a propensity to migrate under high steam conditions at elevated temperatures. The migration of silica could be disastrous to down stream catalysts and should be avoided at all costs. In order to examine whether silica migrates from cordierite making the support unsuitable for ATR applications, monoliths coated with ATR catalysts were operated under ATR conditions for several thousand hours.[1] SEM images were made and EDAX elemental mapping conducted across the channels of the monolith (Figure 2). Silica was present in the areas where the cordierite substrate was found but no evidence of silica was found in the catalytic layers. Based upon this evidence, cordierite appears to be acceptable for ATR applications and is usually the substrate of choice based on the wide availability and reasonable cost.

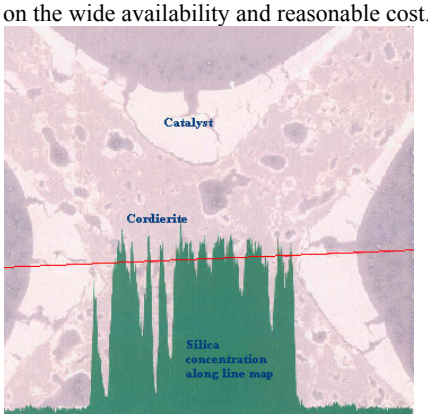

Figure 2. EDAX line map of silica concentration from Rh ATR catalyst to cordierite support.

The ATR testing apparatus. Autothermal reforming experiments are performed in a triple heated zone reactor with a separate pre-reactor vaporization vessel. Monolithic catalysts are wrapped in ceramic gauze and placed into the bottom zone of the furnace with the upper two zones used for mixing. After condensing excess water from the reactor outlet, gas flow-rates are measured with an American Meter Company® wet test meter and gas composition is determined by a Varian® CP2003 micro gas chromatograph with separations carried out in both molecular sieve and PPQ columns. Test unit gas and temperature control is handled by a Camile® PC based control system.

Designing an accelerated aging test. Typically, ATR reactors will operate at a gas hourly space velocity of ≥100,000/hr at a S:C ratios from 2 to 3 and O:C ratios from 0.7 to 1.0. The goal is to design a test that will elucidate differences between catalysts that would not manifest themselves until thousands of hours on stream are achieved. To accelerate deactivation, it was found that operation at elevated O:C ratios or decreased S:C ratios was necessary. It is possible to show differences between relatively stable catalysts under these conditions. Increasing pressure or steam does not have the same effect as it does for Ni steam reforming catalyst. Increased S:C has the effect of increasing the maximum operating temperature for the catalyst thereby increasing the rate of surface area loss due to sintering. Increased O:C appears to effect the nature of the active Rh sites more than the stabilized alumina support. Figure 3 is an example of various reactions conditions on the deactivation rate of a Rh/ stabilized alumina catalyst.

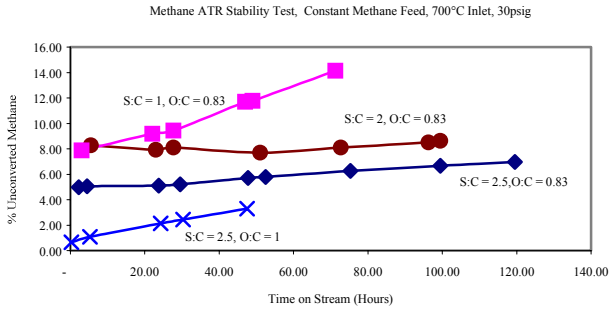

Figure 3. Unconverted methane as a function of time on stream for various reaction conditions.

Deactivation mechanisms. There are three main deactivation mechanisms that are assumed to be involved for Rh-Alumina based ATR catalysts. The first is sulfur poisoning. Due to the complexities in testing for sulfur tolerance, this issue will be addressed in future papers. The second deactivation mechanism is the loss of surface area by the support and the resulting decrease in Rh dispersion. Simple BET surface area measurements can offer evidence of this mechanism but the traditional air calcinations may not be adequate to sinter stabilized alumina supports. The presence of steam and reducing atmospheres is often necessary to reveal differences in surface area stability but may still not account for catalyst deactivation. In particular, catalysts that were tested for several hundred hours that showed ATR deactivation did not show significant decreases in surface area. As a result, the observations of Wong and McCabe[2] appear to be the most relevant to catalyst deactivation. They found that oxidation of Rh / alumina catalysts caused most of the Rh to diffuse into the bulk and resulted in a large decrease in CO oxidation activity. As a result, modifications to both the alumina as well as the addition of promoters and stabilizers to the Rh increase the stability of ATR catalysts.

Conclusions

Traditional steam reforming catalysts deactivate due to poisoning by sulfur, formation of Ni spinel and coke formation on the catalyst. Several tests have been designed to simulate these poisoning events in an effort to accelerate the deactivation of these catalysts. These accelerated deactivation tests have proven useful in the improvement of Ni steam reforming catalysts. For ATR and CPOX catalysts, surface area stability and the anchoring of precious metals such as Rh is of utmost importance for the stability of catalysts. Tests have been designed to accelerate these deactivation mechanisms in an effort to both compare catalyst formulations as well as to predict activity over 40,000 hour lifetimes.

Acknowledgement. We would like to acknowledge the contributions of Paul Steppe, Steve Spivey, Don Tackett, Wolfgang Gabriel, Dr. Yeping Cai and Dr. Jason Zhao to this work.

References

(1) Flytzani-Stephanopoluos, M.; Voecks, G.E. *Conversion of Hydrocarbons for Fuel-Cell Applications*. **1981**, JPL Publication 82-37, DOE/ET-11326, p. 77.
(2) Wong, C. and McCabe, R.W. *J of Catal* **1989**, 119, pp. 47-64.

Sulfur Resistance of Rh/CeO_2-Al_2O_3 Catalysts During Steam Reforming of Jet Fuels at Low Temperature

Jian Zheng, James Jon Strohm, Chunshan Song, Xiaoliang Ma, Lu Sun*

Clean Fuels and Catalysis Program, The Energy Institute, and Department of Energy & Geo-Environmental Engineering, Pennsylvania State University, 209 Academic Projects Building, University Park, PA 16802

*Email: csong@psu.edu; Tel: 814-863-4466; Fax: 814-865-3248

Introduction

Fuel cell has been identified as a potential device for portable power supply because it is convenient, quiet and energy efficient. The choice of liquid fuels such as jet fuel and diesel fuel as logistic fuels is an important consideration for portable fuel cells, because they are widely available and have lower volume and higher energy density. The challenges and opportunities on fuel processing for fuel cell applications have been discussed in a recent review[1].

One of the main problems in developing fuel pre-processor for micro-fuel cell application using liquid hydrocarbon fuels such as JP-8 jet fuel is how to eliminate the carbon formation from higher hydrocarbons during reforming. Our approach[2, 3] to solving this problem is to conduct catalytic fuel reformation in two stages with a pre-reformer (at temperature around 450-550˚C) to break-down most C_8-C_{13} hydrocarbons to C_1 to C_2 molecules plus CO and H_2, followed by steam reforming (at temperature of around 800˚C) in main reformer to produce final reformates (H_2, CO, CO_2). A 2wt% Rh supported CeO_2-promoted γ-Al_2O_3 catalyst with thorough removal of impurity Cl has been found to exhibit stabilized excellent activity for the steam reforming of various sulfur-clean model jet fuels at 514˚C[2].

Most of the original liquid hydrocarbon fuels contain certain amount of sulfur (ranging from several wppm to over a thousand wppm), which is a severe poison for steam reforming catalysts because sulfur compounds are strongly chemisorbed on metal surface[4, 5]. The development of sulfur-resistant reforming catalysts for fuel processor is therefore another important yet challenging task.

In order to improve the sulfur-resistance of metal supported catalysts, one must have a fundamental understanding of how sulfur interacts with the metal surfaces. Tremendous work has been done in the literature on studies of sulfur chemisorption on metal surfaces[4-10]. Ni or noble metal supported catalysts for both steam reforming at low temperature (such as pre-reforming at around 500˚C)[11-15] and oxygen-assisted reforming at high temperature (such as autothermal reforming and partial oxidation at around 800˚C)[16-23] have been reported to show certain levels of sulfur-resistance.

The adsorption equilibrium of sulfur compounds (typically H_2S) depends on mainly temperature besides factors such as the composition of gas phase (such as P_{H2S}/P_{H2} and P_{H2O}/P_{H2} etc)[4]. In general, the sulfur adsorption on metal such as Ni decreases with increasing temperature (between 500˚C-850˚C)[4]. As a consequence, higher sulfur-resistance has been reported for autothermal reforming at high temperature than that for low temperature reforming.

The present paper reports on our preliminary work on the sulfur-poisoning of noble metal supported CeO_2-Al_2O_3 catalysts for the steam reforming of sulfur-containing model jet fuel (NORPAR-13) at both low and high temperature. A bimetallic Rh-Ni/CeO_2-Al_2O_3 catalyst has been found to show excellent sulfur-resistance even at low temperature.

Experimental

CeO_2-Al_2O_3 (containing 20wt% CeO_2) support was prepared by wet impregnation of γ-Al_2O_3 (UOP LaRoche VGL-15) with $Ce(NO_3)_3 \cdot 6H_2O$ (Aldrich) followed by calcinations at 800˚C in air for 3 hours.

$RhCl_2$ (Aldrich) has been supported on both γ-Al_2O_3 and CeO_2•Al_2O_3 by wet impregnation, with nominal metal content of 2wt%. In both cases, the obtained $RhCl_2$ supported material was soaked into NH_4OH solution for several hours, followed by filtration and calcinations to remove NH_3, Cl^{-1}, and other impurities.

Jet fuel formulation. A readily available NORPAR-13 (consisting mainly normal paraffin, with average carbon number of 13) has been chosen as an important type of jet fuel. Since there is no much sulfur in NORPAR-13 (the sulfur content of NORPAR-13 is 4 wppm as analyzed by us using Antek 9000ES total sulfur analyzer), it can actually be regarded as a near sulfur-free clean jet fuel that can be utilized in large amount and directly for steam reforming in fuel processor for fuel cell application.

Reaction system. A catalyst (1.0 gram with particle size of 18~35 mesh) is placed into the middle of stainless steel reactor tube (Inconel 800H alloy, with 0.54" O.D. X 0.375" I.D. and 24" long), with the remaining tube filled with α-Al_2O_3 beads. Before introducing the fuel, the catalyst is heated up to a certain temperature (500˚C) under the hydrogen flow of 20 ml/min, which is controlled by the mass flow controller system, and kept at this temperature for several hours. Then the carrier gas is switched to nitrogen. At the same time, the pre-heater is turned up to certain temperature high enough for vaporizing of the fuel ($C_{13}H_{28}$, b.p. 234˚C) and water before entering the reactor.

To start the test, water was first introduced for 30 minutes before opening the fuel flow to ensure that there is always steam accompanying fuel flow in the reactor lines. The fuel is then introduced with one of the two HPLC pumps through the pre-heater into the reactor with a volumetric flow rate of 1.38 ml/hr. The water flow is kept at 4.02 ml/hr with a steam to carbon ratio of 3:1.

During the reaction, the liquid products are collected every hour by a liquid condenser with volume measured for the calculation of total conversion; the gas products are analyzed on-line by a multi-gas analyzer GC-TCD for the calculation of product distributions.

Results and Discussion

In general, higher temperature will result in higher conversion of the fuels, since the steam reforming alone is endothermic. However, there is also a risk for carbon formation. In order to prevent carbon formation, the pre-reforming temperature should be around 500ºC[2, 24].

Previously, we have screened various noble metal supported catalysts for pre-reforming of different model jet fuels, such as dodecane (model jet fuel MJF-1), 20wt% trimethylbenzene containing dodecane (MJF-2), and 10wt% 1,3,5-trimethylbenzene, 5wt% ethylbenzene and 5wt% butylbenzene containing dodecane (MJF-3). A modified noble metal catalyst, 2wt% Rh supported on CeO_2•Al_2O_3 followed by soaking in NH_4OH, has been found to exhibit satisfactory catalytic activity and stability for pre-reforming of these model jet fuels at 514˚C for up to 240 hours (accumulated 10 days)[2]. The same catalyst has also been utilized for pre-reforming of NORPAR-13 (containing 4ppm impurity sulfur) and shows good performaces[25].

It is important to know the sulfur resistance of such noble metal supported catalyst for a long-term pre-reforming with certain sulfur content level. We thus added 3-methylbenzo-

thiophen in pure NORPAR-13 to form NORPAR-S1 (15ppm total sulfur) and NORPAR-S2 (33ppm total sulfur).

Figure 1 shows a 34-hour pre-reforming run of the NORPAR-S2 (33ppm S) at initially 514˚C using the same modified catalyst. From **Figure 1** it can be seen that within 11 hours on stream the conversion of NORPAR-S2 (33ppm S) on the modified 2%Rh/CeO_2•Al_2O_3 catalyst is very high and close to that of pure NORPAR-13 (4ppm S)[25]. But the activity decreases gradually during 11-22 hours on stream, and dramatically down to only 72% within another 3 hours on stream. Meanwhile, the CH_4 selectivity keeps decreasing throughout the entire experiment.

By increasing the reaction temperature slightly (from 514˚C to 535˚C), the activity is recovered to some extent, but with further time on stream, it deactivates again. This indicates that sulfur poisoning of the current 2%Rh/CeO_2•Al_2O_3 catalyst is very severe even in the presence of 33ppm S.

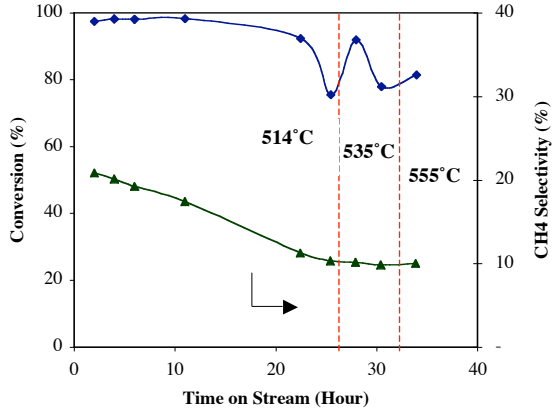

Figure 1. Pre-reforming of NORPAR-S2 (33ppm total sulfur) over modified catalyst (2% Rh/CeO_2•Al_2O_3, NH_4OH treated)

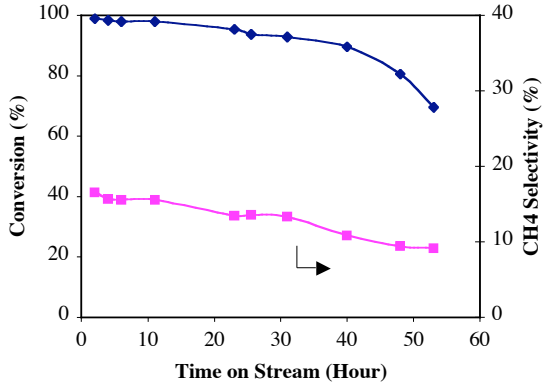

Figure 2. Pre-reforming of NORPAR-S1 (15ppm total sulfur) over modified catalyst (2% Rh/CeO_2•Al_2O_3, NH_4OH treated)

There seems certain critical point in terms of accumulated sulfur to Rh ratio which causes the dramatic poisoning and deactivation of active Rh sites: at around 20th hour on stream, the S/Rh ratio is estimated to be 0.10 as assuming all the sulfur is bond to Rh metal. So the sulfur-poisoning results from **Figure 1** indicate that when S/Rh ratio reaches around 0.10, the Rh clusters will no longer be as good catalytic active sites for pre-reforming of jet fuel as previously without sulfur poisoning.

In order to verify this, we carry out another long-term pre-reforming run using NORPAR-13 containing lower sulfur level. **Figure 2** shows a 53-hour pre-reforming run of the NORPAR-S1 (15ppm S) at 514˚C using the same modified 2%Rh/CeO_2•Al_2O_3 catalyst.

From **Figure 2** it can be seen that similarly within 11 hours on stream the conversion of NORPAR-S1 (15ppm S) on the modified 2%Rh/CeO_2•Al_2O_3 catalyst is very high and close to that of pure NORPAR-13 (4ppm S)[25]. The activity decreases gradually during 11th-40th hours on stream, with conversion at 23rd hour still around 95.5%. But then it decreased dramatically down to only 70% within another 13 hours on stream (from 40th hour to 53rd hour). There is also certain break-though point at around 40th hour on stream, at which the deactivation rate is suddenly increasing. By calculation, the S/Rh ratio at around 40th hour on stream in this pre-reforming run is also around 0.10. Therefore, it seems true that when S/Rh ratio reaches around 0.10, the Rh clusters will no longer be as good catalytic active sites for pre-reforming of jet fuel as previously without sulfur poisoning. According to Rostrup-Nielsen's pioneering study, sulfur poisoning of a steam reforming catalyst takes place as a shell poisoning due to pore diffusion restrictions and the sulfur coverage in the shell is typically 80-90% at conventional pre-reforming conditions[14]. Our results indicate that most of the shell Rh have been covered by sulfur at S/Rh break-through ratio of 0.1.

Figure 3 shows the TPO-IR results of the used 2% Rh/CeO_2•Al_2O_3 after pre-reforming of pure NORPAR-13, NORPAR-S1 and NORPAR-S2 at the conditions described above for same time-on-stream (10 hours). There are a few peaks shown in the TPO-IR temperature ranges of <400˚C, which can be attributed to desorption of CO_2 and combustion of highly amorphous carbon previously adsorbed on the used catalysts[24]. There is almost no peak appearing in the range of 400˚C-600˚C that is attributed to filament carbon, indicating no significant carbon formation on these catalysts. Furthermore, there is no much difference among the three samples within the error range, showing that the slight increase of sulfur content does not promote carbon formation problem.

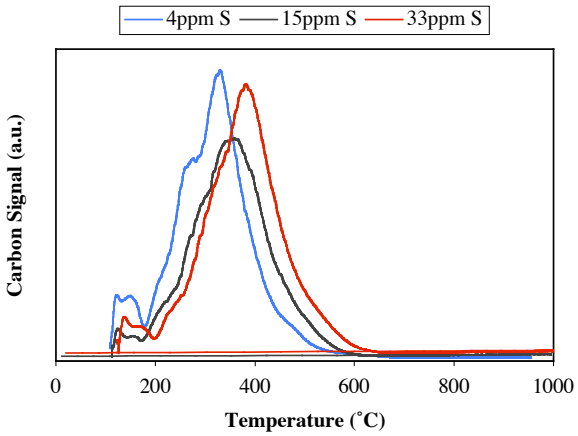

Figure 3. TPO-IR results of used 2% Rh/CeO_2•Al_2O_3 catalyst after pre-reforming of NORPAR-13, NORPAR-S1 and NORPAR-S2 at 514˚C for 10 hours.

By on-line analyzing the product gas mixtures, we do not find H_2S gas (<1 ppm); meanwhile there is only around 1ppm total sulfur in the remaining liquid products. So it is clear that almost all the sulfur goes to the catalyst and the mechanism for S-poisoning during pre-reforming seems to be purely sulfur bonding on the metal sites.

One way to solve this sulfur-poisoning problem is to carry out oxidative steam reforming at higher temperature (such as 800˚C). **Figure 4** shows a 22-hour oxidative reforming test of the NORPAR-S2 jet fuel (with total sulfur of 33ppm) at 800˚C using the same 2% $Rh/CeO_2•Al_2O_3$ catalyst that has already undergone the previous 34-hour pre-reforming at 514-555˚C (as seen in **Figure 1**).

The conversion is always 100% throughout the entire experiment, which shows that the sulfur poisoning of the Rh metal supported catalyst (in the presence of 33ppm S) is no longer a severe problem itself during oxidative steam reforming at higher temperature. The composition of the products is as follows: H_2 around 63%, CO at 23% and CO_2 around 14%, with no CH_4 remaining.

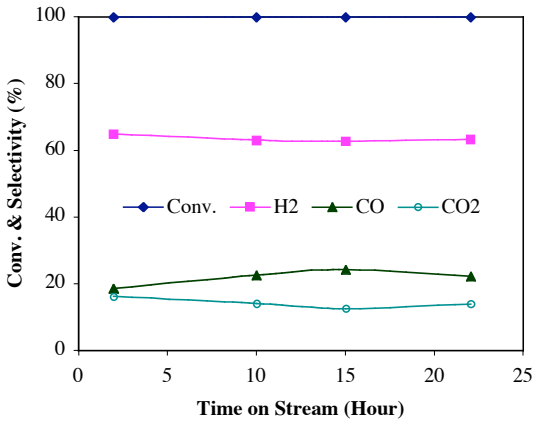

Figure 4. Oxidative Steam reforming of NORPAR-S2 (33ppm total sulfur) on modified $2\%Rh/CeO_2•Al_2O_3$ catalyst (S/C=3, O/C=0.8, 800°C, atm).

However, as measuring on-line the H_2S content from the gas products, we do observe around 3ppm H_2S, together with large amount of H_2 and CH_4 etc. This indicates that the one-step oxidative reforming of jet fuel, although shows no sign of deactivation by sulfur poisoning, still causes potential problem for the following integrated processes for utilization of fuel cell system, which also shows high sensitivity to sulfur poisoning.

Another disadvantage of the one-step oxidative reforming at high temperature is the much severe carbon formation problem, as seen in the TPO-IR of used catalyst and □-Al_2O_3 beads around the catalysts in **Figure 5**.

In **Figure 5**, the peak in the range of 400˚C-600˚C appears slightly in the case of used catalyst but very significantly on Al_2O_3 beads (noting the different y-axis). Therefore, it is challenging to have good control of reforming system due to the coke formation in not only the catalyst but also the inert material (such as Al_2O_3 beads in the current case).

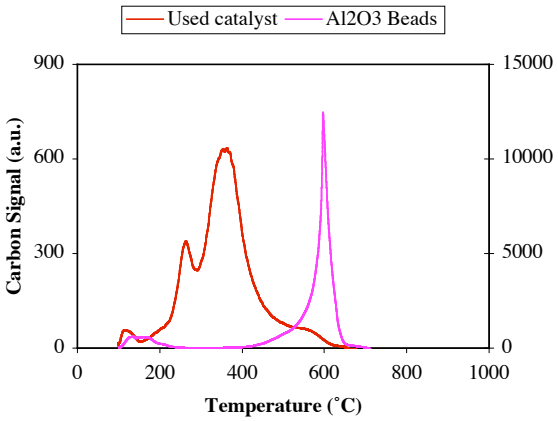

Figure 5. TPO-IR results of used $2\%Rh/CeO_2•Al_2O_3$ catalyst after oxidative steam reforming of NORPAR-S2 (containing 33ppm sulfur) at 800˚C for 22 hours.

In order to solve the sulfur-poisoning problem of the $2\%Rh/CeO_2•Al_2O_3$ catalyst during pre-reforming, the modify of the catalyst is necessary, such as introducing second metal component that can easily bond with sulfur atom so that the Rh active sites can be protected. Based on this, we prepared a bimetallic $Rh\text{-}Ni/CeO_2•Al_2O_3$ catalyst and tested it for pre-reforming of NORPAR-S2 (33ppm sulfur). **Figure 6** shows a 72-hour pre-reforming of the NORPAR-S2 jet fuel using the promoted $Rh\text{-}Ni/CeO_2•Al_2O_3$ catalyst under exactly same conditions as in **Figure 1**.

The conversion is almost 100% throughout the entire experiment, only drops to around 98% at the end of the 72-hour run, showing that the promoted bimetallic $Rh\text{-}Ni/CeO_2•Al_2O_3$ catalyst has good sulfur resistance during pre-reforming of jet fuels. The composition of the products as follows is constant throughout the test: H_2 around 58.5%, CH4 at 19.6%, CO_2 around 21.8%, and less than 1% CO. There is no H_2S (within the detection limit) in the product gas. The excellent sulfur-resistant catalyst therefore provides much more flexibility for fuel cell application.

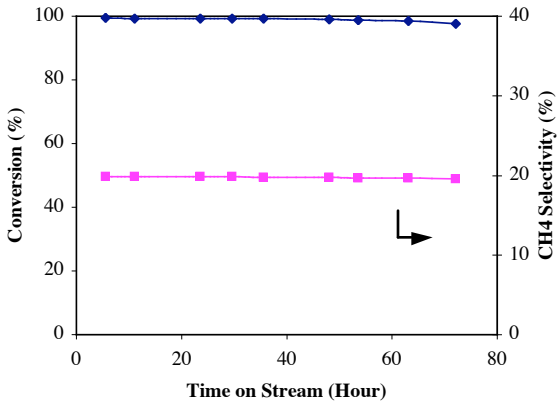

Figure 6. Pre-reforming of NORPAR-S2 (33ppm total sulfur) over promoted $Rh\text{-}Ni/CeO_2•Al_2O_3$ catalyst at 514˚C, atm.

Conclusions

An active pre-reforming catalyst, the monometallic 2%Rh/CeO_2•Al_2O_3, deactivates by sulfur poisoning during the pre-reforming of sulfur-containing jet fuels. Sulfur tends to bond with Rh metal so strongly that almost no remaining sulfur can be detected in the products, both in the liquids and the gases. A breakthrough point for faster deactivation rate is found at S/Rh coverage around 0.10. An oxidative steam reforming of the sulfur-containing jet fuels over the same monometallic catalyst avoids the sulfur poisoning problem but causes severe carbon formation on even inert Al_2O_3 beads. A promoted bimetallic Rh-Ni/CeO_2•Al_2O_3 catalyst proves to be sulfur-tolerant and shows excellent activity for the pre-reforming of jet fuel containing 33 ppm sulfur.

Acknowledgement. We are grateful to the DoD/DARPA Palm Power Program management for supporting this work under sub-contract to Altex Technologies Inc. We also wish to thank Dr. Mehdi Namazian of Altex for helpful discussions on fuel reforming, and UOP for providing LaRoche γ-Al_2O_3 samples. Thanks also go to Mr. Ronald Copenhaver of PSU for help in setting up the reactor system.

References

(1) Song, C. *Catal. Today*, **2002**,77, 17-49.
(2) Zheng, J.; Shen, J.P.; Song, C.; Pan, W.; Strohm, J.J. *Prepr. Pap. - Am. Chem. Soc., Div. Fuel. Chem.*, **2003**, *48 (1)*, 374-377.
(3) Zheng, J.; Song, C. *Prepr. Pap. - Am. Chem. Soc., Div. Fuel. Chem.*, **2003**, *48 (1)*, 378-381.
(4) Rostrup-Nielsen, J.R. in Catalysis, Science and Technology, Anderson, J.R.; Boudart, M. , Eds, **1984**, *Vol. 5*, 1-117.
(5) Bartholomew, C.H.; Agrawal, P.K. *Adv. Catal.,* **1982**, *31,* 135-242.
(6) Foord, J.S.; Reynolds, A.E. *Surf. Sci*., **1985**, *152/153*, 426-433.
(7) Foord, J.S.; Reynolds, A.E. *Surf. Sci.*, **1985**, *164*, 640-648.
(8) Rodriguiz, J.A.; Chaturvedi, S.; Jirsak, T. *Chem. Phys. Lett.*, **1998**, *296*, 421-428.
(9) Rodriguez, J.A.; Hrbek, J. *Acc. Chem. Res*., **1999**, *32*, 719-728.
(10) Zolfaghari, A.; Villiard, F.; Chayer, M.; Jerkiewicz, G. *J. Alloys Comp*., **1997**, *253/254*, 481-487.
(11) Duprez, D.; Mendez, M.; Little, J. *Appl. Catal.*, **1986**, *27*, 145-160.
(12) Delahay, G.; Duprez, D. *Appl. Catal*., **1989**, *53*, 95-105.
(13) Christiansen, L.J., Andersen, S.L. *Chem. Eng. Sci*., **1980**, *35*, 314-321.
(14) Christensen, T.S. *Appl. Catal. A: Gen*., **1996**, *138*, 285-309.
(15) Rostrup-Nielsen, J.R.; Christensen, T.S.; Dybkjaer, I. *Stud. Surf. Sci. Catal.,* **1998**, *113*, 81-95.
(16) Moon, D.J.; Sceekumar, K.; Lee, S.D.; Lee, B.G.; Kim, H.S. *Appl. Catal. A: Gen.*, **2001**, *215*, 1-9.
(17) Ming, Q.; Healey, T.; Allen, L.; Irving, P. *Catal. Today*, **2002**, *77,* 51–64.
(18) Kramarz, K.; Bloom, I.D.; Kumar, R.; Ahmed, S.; Wilkenhoener, R.; Krumpelt, M. *US Pat., No. 6,303,098*, **2001**.
(19) Kopasz, J.P.; Miller, L.E.; Ahmed, S.; Devlin, P.; Pacheco, M. *SAE Technical Paper Series*, **2002**, 2002-01-1885.
(20) Palm, C.; Cremer, P.; Peters, R.; Stolten, D. *J. Power Sources*, **2002**, *106*, 231-237.
(21) O'Connor, R.P.; Klein, E.J.; Schmidt, L.D. *Catal. Lett*., **2000**, *70*, 99-107.
(22) Krummenacher, J.J.; West, K.N.; Schmidt, L.D. *J. Catal.*, in press.
(23) Cable, T.L.; Brakas, A.B.; Ruhl, R.C.; Milliken, C.E. *US Pat., No. 6,238,816*, **2001**.
(24) Strohm, J.J.; Zheng, J.; Song, C. *Prepr. Pap. - Am. Chem. Soc., Div. Fuel. Chem.*, **2003**, *48 (2)*, to be accepted.
(25) Zheng, J.; Strohm, J.J.; Song, C. *Prepr. Pap. - Am. Chem. Soc., Div. Fuel. Chem.*, **2003**, *48 (2)*, to be accepted.

Novel CeO_2 supported Ni-Rh bimetallic catalysts for reforming of bio-ethanol to produce hydrogen for fuel cells

*Junichiro Kugai, S. Velu, Chunshan Song**

Clean Fuels and Catalysis Program, The Energy Institute, and
Department of Energy and Geo-Environmental Engineering
The Pennsylvania State University
209 Academic Projects Building, University Park, PA 16802.
*E-mail: csong@psu.edu

Introduction

Recently, there is a growing interest worldwide in the development of fuel cells for automobiles and stationary power plants because they have the potential to offer unique opportunities for significant reduction in energy use and emissions of environmental pollutants. Polymer electrolyte membrane fuel cell (PEMFC), which operates at low temperature, is considered as promising candidate for automobile applications. However, the PEMFC uses pure H_2 or H_2-rich gas as a fuel and this needs to be produced on-board a vehicle from a suitable liquid hydrocarbon fuels. Owing to the high energy density and ready availability, methanol and gasoline are considered as preferred fuels, and methods for the catalytic reforming of these fuels to H_2-rich gas has been reported.[1-4] On the other hand, bio-ethanol, which is a mixture of water and ethanol, produced from fermentation of biomass, is a renewable raw material and could be used as an alternative primary fuel for the on-board production of H_2 for fuel cells. Some of the advantages of using bio-ethanol to produce H_2 for fuel cell applications are; (i) Bio-ethanol is a renewable raw material and can be cheaply obtained from sugarcane, corn or cellulose feedstock such as wood chips. (ii) The process is CO_2 neutral as the CO_2 produced in the reforming reaction can be consumed for the biomass growth. The system therefore offers a closed carbon loop. (iii) Unlike methanol, the bio-ethanol is non-toxic, and (iv) Unlike gasoline, the bio-ethanol is sulfur-free, and this avoids the risk of sulfur poisoning on the reforming and fuel cell electrode catalysts.

Unlike methanol reforming, the catalytic methodology for ethanol reforming is not well developed, and more efficient and highly active catalysts are needed. Steam reforming of ethanol has been reported to occur relatively at high temperature, around 700˚C. In lower temperature, the reaction produces a wide range of liquid and gaseous products, including H_2, CO, CO_2, CH_4, CH_3CHO, CH_3COOH, $C_2H_5OC_2H_5$, ethylene depending on the nature of metal and support.[5-7] Oxidative steam reforming of ethanol has also been reported to be more efficient for the low temperature reforming of ethanol for H_2 production.[8]

The objective of the present study was to develop a novel highly efficient catalyst system for the on-board reforming of bio-ethanol to produce fuel cell grade H_2 gas at relatively lower temperature. A detailed literature review reveals that C—C bond cleavage is an important step in the reforming of ethanol to produce H_2 and carbon oxides[5-8]. Both Ni and Rh are known to favor the C—C bond rupture effectively.[9] In addition, since Ni has hydrogenation ability, it is expected to combine chemisorbed hydrogen to form H_2 gas. Thus, a series of Ni-Rh bimetallic catalysts with different Ni/Rh atomic ratios have been synthesized. The nature of support also plays an important role in the ethanol reforming. Acidic and basic supports are known to favor dehydrogenation / dehydration and condensation reactions. Hence, in the present study, redox supports such as CeO_2, ZrO_2 and CeO_2-ZrO_2 mixed oxides having high surface area, above 100 $m^2\ g^{-1}$ have been chosen. The effect of combination of Rh and Ni, and the nature of support on the catalytic performance in the steam reforming and oxidative steam reforming of ethanol are studied over these catalysts for the first time.

Experimental

In order to optimize the Ni/Rh atomic ratio for the better catalytic performance in the ethanol reforming, commercially available high surface area CeO_2 (BET surface area = 148 $m^2\ g^{-1}$) obtained from Rhodia Co. Three catalysts, 10wt%Ni/CeO_2, 2wt%Rh/CeO_2, and 2wt%Rh-10wt%Ni/CeO_2 were prepared by the incipient wetness impregnation method. The catalysts were calcined at 450˚C for 3 h in air, palletized, crushed and sieved to 18-35 mesh. About 0.5g of catalyst was loaded in the reactor. Steam reforming of ethanol was performed in a fixed bed stainless-steel down-flow reactor. A premixed ethanol-water mixture with a water/ethanol molar ratio of 4 was fed into the reactor through a vaporizer and the mixed with Ar carrier gas. Prior to the catalytic reaction, the catalysts were reduced in-situ in a H_2 flow (10% H_2 in Ar). Effluent of the reaction was analyzed using an on-line GC equipped with a sampling loop injector, 30 feet Hayesep DB packed column, and a TCD detector.

Results and Discussion

Steam reforming of ethanol has been performed at 335 and 395˚C over Rh-Ni/CeO_2 catalysts synthesized in the present study. Fig. 1 compares the conversion of ethanol in the steam reforming over these catalysts at 335 and 395˚C. It can be seen that at 335˚C, the Rh-Ni/CeO_2 catalyst exhibited slightly higher activity than Rh/CeO_2 catalyst. The Ni/CeO_2 catalyst is much less active compared to other two catalysts. On the other hand, all catalysts exhibited almost complete conversion, close to 100 %, at 395˚C. These results indicate that Rh is more active than Ni in the low temperature range though Ni becomes as active as Rh in the high temperature range. The high activity of Rh can be attributed to the ease of C—C bond cleavage of ethanol on Rh metal surface[9]. The support CeO_2 exhibits very poor performance under the present experimental conditions, indicating that the metals supported on the CeO_2 display active sites for the ethanol reforming.

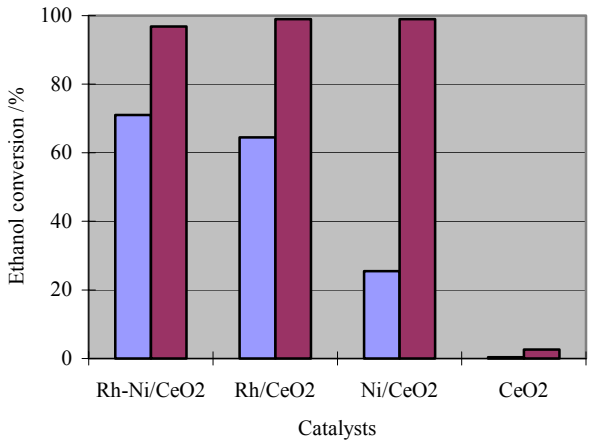

Figure 1 Comparison of ethanol conversion at 335 and 395˚C over CeO2-based Bimetallic catalysts. Left bar; 335˚C and right bar; 395˚C

H_2, CO, CO_2, CH_4, and acetaldehyde are the major products obtained in the steam reforming of ethanol in the present study. The selectivities of H_2 and carbon containing products at 335˚C and 395˚C are shown in the Table 1. Hydrogen selectivity was indicated

by molar ratio of produced hydrogen in all the products. Carbon selectivity was indicated by molar ratio of carbon included in each carbon-containing products to carbon included in all carbon-containing products. From the table, it can be seen that H_2, CO, CO_2, CH_4 are main products and acetaldehyde is only produced at 335˚C, which is insufficient temperature for complete C—C bond cleavage. Acetaldehyde can be considered to be an intermediate in the steam reforming of ethanol.[5-8] Higher selectivity of H_2 has been observed Rh/CeO_2 catalyst despite the highest ethanol conversion obtained over $Rh\text{-}Ni/CeO_2$.

Table 1 Product selectivity of ethanol reforming at 335 and 395˚C unit: %

Catalyst Temp.	H_2	CO	CO_2	CH_4	acetaldehyde	acetone
Rh-Ni						
335	33.4	21.8	34.6	30.4	13.3	0
395	34.5	8.6	55.0	33.5	2.9	0
Rh						
335	35.4	46.9	14.6	30.8	7.7	0
395	38.8	8.2	62.3	29.5	0	0
Ni						
335	29.1	14.0	40.8	6.1	23.5	10.8
395	29.7	4.9	56.0	39.0	0	0

At 335˚C, the selectivity for CO_2 decreases in the order, Ni/CeO_2 > $Rh\text{-}Ni/CeO_2$ > Rh/CeO_2. When taking the ratio of CO_2 selectivity to CO selectivity into account, it is clear that the presence of Ni causes the reaction of CO to CO_2. At 395˚C, CO_2 selectivity over all three catalysts increases and becomes closer to each other. This means under the present experimental conditions, water-gas shift reaction also takes place over these catalysts. It should be that Ni has higher water-gas shift reactivity than Rh at 335˚C, but Rh also exhibits as high water-gas shift reactivity as Ni at 395˚C. Diagne et. al.[10] reported that $Rh/CeO_2\text{-}ZrO_2$ catalyst has much higher CO_2/CO ratio than Rh/CeO_2 and Rh/ZrO_2 in the selectivity of ethanol steam reforming reaction. Therefore it is anticipated that using $CeO_2\text{-}ZrO_2$ support with Rh and Ni metals leads to further increase in CO_2/CO ratio.

Suppressing methane production is one of the interests of this work. Ni was added to promote the combination of atomic hydrogen species on the metal surface into molecular hydrogen. But Ni functioned as a promoter for water-gas shift reaction and hydrogenation of surface CHx species rather than a promoter for dehydrogenation of surface hydrogen. It is reported that ethanol is dehydrogenated to adsorbed acetaldehyde species, then further dehydrogenated to H_2, CO, and CHx(x=2,3) on Ni surface[11]. Therefore CHx species is considered to be hydrogenated easily to produce methane in the presence of molecular or adsorbed hydrogen and more methane is produced on Ni surface. On Rh surface, on the other hand, ethanol is dehydrogenated into oxametallacycle species, which is readily decomposed to H_2, CO, CHx($x \leq 2$) and suppress the production of methane[12]. Some amount of ethanol is converted via acetaldehyde intermediate according to the fact that acetaldehyde was observed on Rh/CeO_2 catalyst in low temperature in our work. This might be a cause of a lot of methane production even on Rh-containing catalysts.

Conclusions

The steam reforming of ethanol on $Rh\text{-}Ni/CeO_2$ bimetallic catalyst exhibited high ethanol conversion and CO_2 selectivity. It is concluded that Ni has higher water-gas shift activity than Rh. However its hydrogen selectivity was slightly lower than Rh/CeO_2 catalyst.

Acknowledgement

This work was supported by Nippon Shokubai Co., Ltd. and by the Pennsylvania State University.

References

(1) Song, C. *Catal.Today*, **2002**, 77, 17.
(2) Velu, S.; Suzuki, K.; Okazaki, M.; Kapoor, M.P.; Osakai, T.; Ohashi, F. *J.Catal*. **2000**, 194, 373.
(3) Ming, Q.M.; Healey, T.; Allen, L.; Irving, P. *Catal.Today*, **2002**, 77, 51.
(4) Moon, D.J.; Sreekumar, K.; Lee, S.D.; Lee, B.G.; Kim. H.S. *Appl.Catal. A General*, **2001**, 215, 1.
(5) Marino, F.; Boveri, M.; Baronetti, G.; Laborde, M. *Int. J. Hydrogen Energy*, **2001**, 26, 665.
(6) Breen, J. P., Burch, R., Coleman, H. M., *Appl. Catal. **B** Environmental*, **2002**, 39, 65.
(7) Fierro, V.; Akdim, O.; Mirodatos, C.; *Green Chemistry*, **2003**, 5, 20.
(8) Velu, S., Satoh, N., Gopinath, C. S., Suzuki, K., *Catal. Lett.*, **2002**, 82, 145.
(9) Sheng, P.-Y.; Yee, A.; Bowmaker, G.A.; Idriss, H. J.*Catal.* 2002, 208, 393.
(10) Diagne, C., Idriss, H., Kiennemann, A., *Catal. Commun*., **2002**, 3, 565.
(11) Takezawa, N., Iwasa, N., *Catal. Today*, **1997**, 36, 45.
(12) Brown, N. F., Barteau, M. A., *Langmuir*, **1992**, 8, 862.

GOLD BASED CORE-SHELL NANOPARTICLES AS FUEL CELL CATALYTS

*Mathew M. Maye, Jin Luo, Sandy Chen, Wai-Ben Chan, H. Richard Nasland, Chuan-Jian Zhong**

Department of Chemistry, State University of New York at Binghamton, Binghamton, NY 13902. * cjzhong@binghamton.edu

The ability to control the size of gold materials in the range of a few nanometers is important for the exploration of the unique catalytic properties of gold [1,2]. This presentation describes an investigation of the preparation of gold and gold alloy nanoparticles as electrocatalysts in several reactions including methanol oxidation, carbon monoxide oxidation and oxygen reduction. The goal is to explore the potential use of such nanoparticles as fuel cell catalysts. Core-shell type gold nanoparticles of 1-10 nm core size with organic monolayer encapsulation are studied for the preparation of catalysts towards the electroreduction of oxygen and the electrooxidation of carbon monoxide and methanol. The low catalytic activity, poisoning or instability of many existing platinum based metal catalysts are some of the current challenges to the development of fuel cell catalyst technology. It is thus important to develop a fundamental understanding of the correlation between the size, shape, and interparticle spatial properties and the catalytic activities.

We choose to explore monolayer-capped nanoparticles because highly monodispersed nanoparticles with 2-5 nm core sizes (± 0.3-0.7 nm) can be easily prepared by a combination of two-phase synthesis and thermal processing protocols [3,4]. We have studied the assembly of these core-shell nanoparticles on high surface area carbon materials to evaluate their catalytic properties. The catalytic activities of the nanostructured catalysts have been studied in both acidic and alkaline electrolytes. Different alloy compositions of gold with other transition metals were varied using synthetic and processing protocols. The loading of catalysts on metal oxides (e.g., TiO_2) and carbon supporting materials has been systematically investigated. The catalytic activation and fuel cell performance have also been evaluated.

Both electrochemical and thermal approaches have been used to activate the catalysts. For the electrochemically-activated gold nanoparticles assembled on glassy carbon electrodes, which involved the application of a polarization potential to ~+800 mV, an anodic wave was observed for the oxidation of methanol in alkaline electrolytes, which closely matched the potential for Au oxide formation (Figure 1) (*5*,*6*). This observation, along with the anodic current exhibiting a linear increase with methanol concentration, whereas the cathodic wave decreased with methanol concentration, is again supportive of an electrocatalytic mediation mechanism. In electrochemical quartz crystal nanobalance measurements, a mass wave was detected corresponding to this current wave, implying an initial product release followed by formation of surface oxygenated species. The surface of the activated nanocrystals was examined using x-ray photoelectron spectroscopy (XPS) (*7*), which indicated the effective removal of the capping agents and the formation of surface oxides on gold nanocrystals. In comparison with the electrochemically-activated catalysts, similar results have been observed for thermally activated gold catalysts. XPS analysis of the catalysts has revealed a complete removal of the shell components and the formation of oxides less than the electrochemical activation (*8*). Interestingly, the catalytic activity upon activation was also found to be dependant on the nature of the molecular-wire agent used to assemble the nanoparticle catalysts. We are systematically investigating several parameters that can be controlled (i.e., alloy composition, size, calcination, loading, etc.), and develop an in-depth delineation of these parameters with the catalytic activities. The results should provide important insights for the exploration of gold nanoparticles in practical fuel cell catalysis.

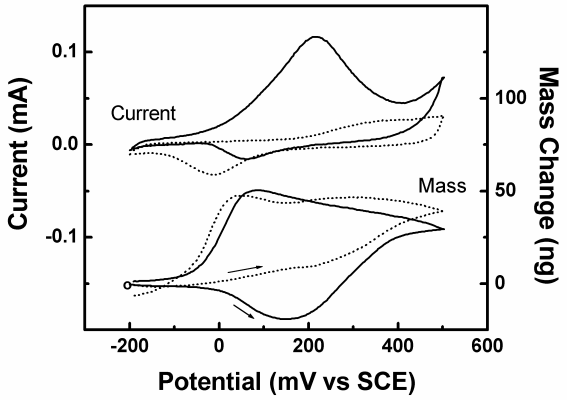

Figure 1. Current and mass responses for the electrocatalytic oxidation of methanol at activated NDT-linked $Au_{2\text{-nm}}$ on GC electrode in 0.5 M KOH with 3.0 M methanol (solid line) and without (dotted line). (Electrode geometric area: 0.2 cm^2; scan rate: 50 mV/s).

Recently, we have been investigating the catalytic properties of these nanomaterials in several fuel cell reactions. Latest results from electrochemical measurements of catalytic activities, along with XPS, XRD, HRTEM, and FTIR characterizations of structures and morphologies, have revealed that gold-based alloy nanoparticles (1-5 nm) are electrocatalytically active towards MeOH oxidation, CO oxidation, and O_2 reduction. Using carbon black and TiO_2 as supporting materials, these nanoparticles have shown high catalytic activity in both acidic and alkaline electrolytes under room temperature. Implications of the results to further refinement of the catalyst preparation in terms of composition and size will be discussed.

References:

(1) Haruta, M. *Catal. Today*, **1997,** *36*, 153.
(2) Valden, M.; Lai, X.; Goodman, D. W. *Science*, **1998**, *281*, 1647.
(3) Brust, M.; Walker, M.; Bethell, D.; Schiffrin, D. J.; Whyman, R. *J. Chem. Soc., Chem. Comm*. **1994**, 801.
(4) (a) Maye, M. M.; Zheng, W. X.; Leibowitz, F. L.; Ly, N. K.; Zhong, C. J. *Langmuir,* **2000**, *16*, 490 (b) Maye, M. M.; Zhong, C. J. *J. Mater. Chem.,* **2000**, *10*, 1895.
(5) Lou, Y.; Maye, M. M.; Han, L.; Luo, J.; Zhong, C. J. *Chem. Commun*., **2001**, 473.
(6) Luo, J.; Maye, M. M.; Lou, Y.; Han, L.; Hepel, M.; Zhong, C. J. *Catal. Today*, **2002**, *77*, 127.
(7) Maye, M. M.; Luo, J.; Lin, Y.; Engelhard, M. H.; Hepel, M.; Zhong, C. J., *Langmuir*, **2003,** *19*, 125.

Hydrodesulfurization Studies on SBA-15 Supported CoMo, NiMo Catalysts

G. Murali Dhar*, Manoj Kumar, K S Rawat, G Muthukumaran, & L D Sharma
Indian Institute of Petroleum, Dehradun – 248005
B. David Raju and K S Rama Rao
Indian Institute of Chemical Technology, Hyderabad – 500 007

ABSTRACT

Development of fuel cells is receiving increasing attention due to their high efficiency and environmental benefits. There are five types of fuel cells that attracted attention, among which proton exchange membrane fuel cell (PEMFC) is promising prospects. hydrocarbon fuels such as gasoline and diesel and useful fuels for fuel cells provided the sulfur level in fuels is brought down to few ppm. ultradeep desulfurization to bring sulfur to such a low level is a challenging task. Calculations reveal that to bring down sulfur from present level to 500 ppm to 0.1 ppm, seven times more active catalysts are needed. In quest highly active of novel catalysts for this purpose use of novel supports is a very important approach. In this communication hydrodesulfurization studies on SBA-15 supported Mo, CoMo, NiMo catalysts will be discussed with help of TPR, oxygen chemisorption etc characterization studies. The catalysts showed out standing activities for thiophene HDS. A comparison will also be made with HMS mesoporous material supported analogues of the same catalysts of comparable composition and evaluated under identical conditions.

ENVIRONMENTAL APPLICATIONS OF ESI FT-ICR MASS SPECTROMETRY: THE IDENTIFICATION OF POLAR N, S AND O CONTAINING PAH SPECIES IN CRUDE OIL AND COAL EXTRACTS

Ryan P. Rodgers[2], Geoffrey C. Klein[1], Zhigang Wu[1], and Alan G. Marshall[2]

[1.] Department of Chemistry and Biochemistry, Florida State University, Tallahassee, Florida 32306.
[2.] Ion Cyclotron Resonance Program, National High Magnetic Field Laboratory, Florida State University, 1800 E Paul Dirac Drive, Tallahassee, Florida 32310.

Introduction

The number of distinct chemical components of petroleum is already approaching tens of thousands, and is thus becoming roughly comparable to the number of genes (genome) or proteins (proteome) in a given biological species. Therefore, the inherent complexity of crude oil and its derived products has until now made environmental analysis difficult or in some cases, impossible. Once introduced to the environment, subsequent biotic and abiotic modifications of the petroleum product further complicate an already complex mixture. Traditional analytical techniques such as Liquid Chromatography (LC), Gas Chromatography (GC) and Gas Chromatography – Mass Spectrometry have inadequate chromatographic resolution for the baseline separation of all species present in most petroleum distillates above diesel fuel. As a result, combined techniques (such as GC-MS and LC-MS) are ineffective due to co-eluting species that complicate the mass spectrum and hinder component identification. Furthermore, mass spectrometers commonly employed for GC-MS and LC-MS are low resolution / low mass accuracy quadrupole mass filters or quadrupole ion trap type mass analyzers that are unable to adequately resolve complex mixtures for individual component identification. As a result, the utilization of traditional analytical techniques provides a limited amount of compositional information and is often dominated by a large unresolved "hump", commonly referred to as an unresolved complex mixture (UCM). Fourier Transform Ion Cyclotron Resonance Mass Spectrometry (FT-ICR MS) benefits from ultra-high mass resolving power (greater than one million), high mass accuracy (less than 1 ppm) and rapid analysis which make it an attractive alternative for the analysis of petroleum products that range from crude oil to diesel.

Experimental

Crude Oil Samples. Crude oil and coal samples were prepared by dissolving ~10-20 mg in 3 mL toluene, and then diluting with 17 mL MeOH. Less than 1% (vol/vol) ammonium hydroxide solution (30%) was added to facilitate deprotonation of the acids and neutral nitrogen compounds to yield [M-H]- ions. For positive ion ESI, the MeOH / toluene solution was spiked with HAc to 1% (vol/vol) to facilitate protonation of basic species to yield [M+H]+.

Mass Analysis. The crude oils were analyzed at the National High Magnetic Field Laboratory (NHMFL) with a homebuilt 9.4 Tesla Fourier transform mass spectrometer. Ions were generated externally by a micro-electrospray source and samples delivered by a syringe pump at a rate of 300 nL/min. Approximately 2.2 kV was applied between the capillary needle and ion entrance (heated metal capillary). The externally generated ions were accumulated in a short (15 cm) rf-only octopole for 10-30 s and then transferred via a 200 cm rf-only octopole ion guide to a Penning trap. Ions were excited by frequency-sweep (100-725 kHz @ 150 Hz/μs at an amplitude of 200 Vp-p across a 10-cm diameter open cylindrical cell). The time-domain ICR signal was sampled at 1.28 Msample/s for 3.27 s to yield 4 Mword time-domain data. Ten to two hundred data sets were co-added, zero-filled once, Hanning apodized, and fast Fourier transformed with magnitude computation. Data was collected and processed by a modular ICR data acquisition system (MIDAS).[1,2] Mass spectra were internally calibrated with respect to the most abundant heteroatom containing series over the full mass range. Homologous series were separated and grouped by nominal Kendrick mass and Kendrick mass defect to facilitate rapid identification, as described elsewhere.[3]

Results and Discussion

Sulfur, nitrogen and oxygen containing PAH species are of environmental concern because of their high polarity and subsequently their tendency to migrate from contaminated spill sites. The complexity of polar fractions has hindered individual component identification and largely led to their classification based on compound classes (by way of class based chromatographic separation). The high resolution and mass accuracy afforded by FT-ICR MS allows the identification of individual compound classes (as well as their corresponding type) in mixtures as complex as crude oil, without prior chromatographic separation. Figure 1 shows a broadband positive ESI FT-ICR mass spectrum of South American crude oil with more than 11,000 different species resolved and identified between 300 < m/z < 900 at an average mass resolving power of ~400,000.

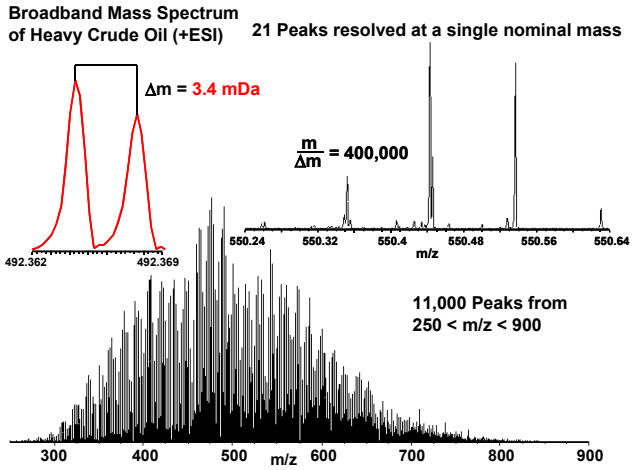

Figure 1. Broadband positive ion ESI FT-ICR mass spectrum of South American heavy crude oil composed of over 11,000 resolved species. A zoom mass inset (top, right) shows 21 peaks resolved at a single nominal mass. A second inset (top, left) shows the baseline resolution of a commonly encountered doublet (SH_4 vs C_3) in petroleum samples.

Similar information is provided from the negative ESI FT-ICR mass spectrum of the same oil. Combined, the two ionization methods allow for the compositional analysis of crude oils at an unprecedented level. Figure 2 shows the combined positive and negative ion ESI FT-ICR mass spectra of the same crude presented in Figure 1 with over 17,000 different species identified. Such detailed analysis provides a powerful tool for the composition based fingerprinting of crude oils for the purpose of contaminant identification. The two ionization methods fundamentally target different compound classes. In positive ion mode, only the basic components of the crude oil are ionized and subsequently detected by the mass spectrometer.

Conversely, in negative mode the acidic species are preferentially ionized and detected.

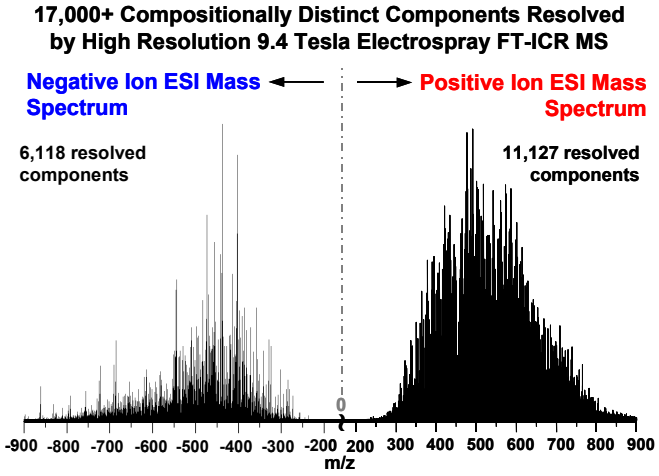

Figure 2. Combined positive (right) and negative (left) ESI FT-ICR mass spectra of a South American heavy crude oil shows over 17,000 resolved species for a single crude oil. Species identified include heteroatom containing crude acids (negative ion) and bases (positive ion) as well as slightly polar nitrogen containing compounds.

Comparisons of crude oils from different geochemical locations allows for a unique composition based fingerprint that can be used for crude oil identification. Figure 3 shows zoom mass insets at a single nominal mass of two crudes collected from different geographical locations. The compositional differences are clearly evident and correlate well with known compositional differences determined by extensive chromatographic class based separations. Similar composition based fingerprinting could conceivably be used to identify a contaminant source even after prolonged weathering. Experiments to test this hypothesis are currently underway and will be presented if completed.

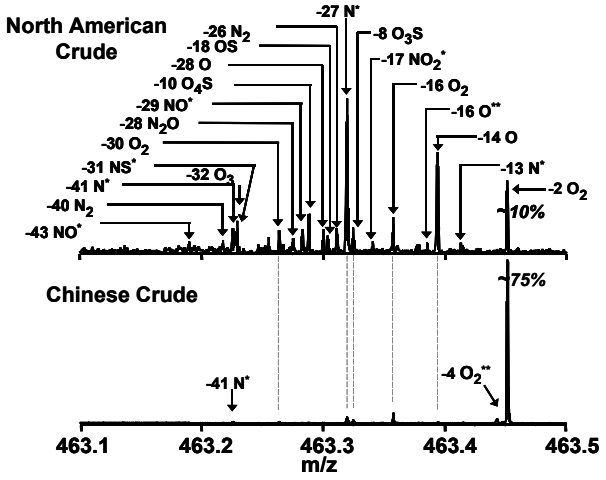

Figure 3. Zoom mass insets for the same single nominal mass of both a North American and Chinese crude oil highlight the differences in composition. The North American crude is much more complex, composed of many different heteroatom containing acidic species. Conversely, the Chinese crude is relatively simple, with carboxylic acid species dominating the majority of the species identified. FT-ICR mass spectral analysis of these two oils confirmed compositional differences discerned in a separate study that employed extensive chromatographic class based separations. The FT-ICR analysis was completed without chromatographic sample pretreatment and in less than one day.

Similar information is also available for coal derived materials. Comparison of crude oil and coal extracts shows that it is quite easy to distinguish on source from another based on the FT-ICR MS compositional analysis. Figure 4 shows the 3-D van Krevelen plots for the shared heteroaromatic classes for both a crude oil and pyridine coal extract.

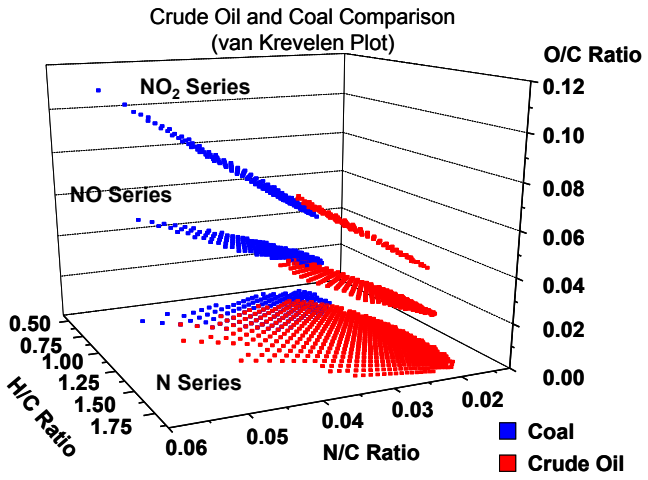

Figure 4. Visualization of the compositional differences is shown in a van Krevelen diagram for both the Coal (in Blue) and Crude Oil (in Red) for a series of shared classes (N, NO, and NO2). The coal classes clearly have a lower H/C ratio (indicative of more aromatic and less alkyl substituted material) than the crude oil asphaltenes allowing for one to be clearly differentiated from the other.

ESI FT-ICR mass spectrometry is a powerful tool for the characterization and identification (at the level of elemental composition for every resolved peak) of both crude oil and coal derived materials. Although its initial application has largely limited to process compositional and bulk characterization analyses, FT-ICR MS stands poised to make a significant impact in environmental applications that entail complex mixture analysis.

Acknowledgment

This work was supported by NSF CHE-99-09502, Florida State University, and the National High Magnetic Field Laboratory in Tallahassee, FL.

References

1. Senko, M. W.; Canterbury, J. D.; Guan, S.; Marshall, A. G. Rapid Commun. Mass. Spectrom., 1996, 10, 1839-1844.
2. Blakney, G. T.; van der Rest, G.; Johnson, J. R.; Freitas, M. A.; Drader, J. J.; Shi, S. D.-H.; Hendrickson, C. L.; Kelleher, N. L.; Marshall, A. G. In 49th ASMS Conference on Mass Spectrom. and Allied Topics: Chicago, IL, 2001.
3. Hsu, C. S.; Qian, K.; Chen, Y. C., *Analytica Chimica Acta,* **1992**, 79-89.

COMBINED USE OF COMPOUND SPECIFIC $\delta^{13}C$ AND δD STABLE ISOTOPE MEASUREMENTS TO AID THE SOURCE APPORTIONMENT OF PAHs

Chenggong Sun, Mick Cooper and Colin E. Snape

Nottingham Fuel & Energy Centre, School of Chemical, Environmental and Mining Engineering (SChEME), University of Nottingham, University Park, Nottingham NG7 2RD, United Kingdom, colin.snape@nottingham.ac.uk

Introduction

The potential of using compound-specific stable carbon isotopic analysis for the source-apportionment of environmental polycyclic aromatic hydrocarbons (PAHs) has been established by O'Malley *et al*. [1,2], Lichtfouse *et al*. [3] and the authors [4-6]. O'Malley *et al*. indicated that PAH arising from wood burning and vehicle emissions exhibited significantly different isotopic signatures [1] and the same authors have also reported the isotopic compositions of *n*-alkanes and PAH produced from combustion of C_3 and C_4 plant species [2]. Lichtfouse *et al*. [3] have reported significant anthropogenic hydrocarbon inputs into soil using a combination of biomarker, $\delta^{13}C$ and ^{14}C analyses. The authors have found that the $^{13}C/^{12}C$ isotopic ratios for PAH derived from coal and wood pyrolysis and diesel particulates vary over a range by *ca*. 8 ‰ which can provide a basis for source apportionment in a number of environments [4-6].

Variations in the carbon stable isotope ratios ($\delta^{13}C$) for PAHs from different sources typically cover a range of only a few ‰, with typically those from coal conversion being close to -24 to -25 ‰, compared to values of -28 to -29 ‰ for transport fuel particulates in the UK. The exception to this relatively narrow range being the exceedingly isotopically light PAHs ($\delta^{13}C$ values as low as –60 ‰) reported by the authors obtained from carbon black production using biogenic methane as the feedstock [7]. To improve the ability of stable isotope measurements to source apportion environmental PAHs, the hydrogen stable isotopes ($\delta^{2}H$) of PAHs from two conversion processes and from petrol and jet fuel particulates have been measured for the first time. The relatively wide range of $\delta^{2}H$ values, in conjunction with the $\delta^{13}C$ values described, potentially provides much greater degree differentiation between PAHs from different sources. We will shortly report on the impact of biodegradation on the $\delta^{2}H$ values for coal-derived PAHs will be addressed.

Experimental

Both compound-specific $\delta^{13}C$ and $\delta^{2}H$ measurements were carried out using a ThermoFinnigan Delta+XP GC-IRMS instrument. The reported carbon isotopic data, expressed in terms of the conventional δ-notation giving the permil (‰) deviation of the isotope ratio from the standard Peedee Belemnite (PDB), represent the arithmetic means of at least two duplicate analyses where variations were generally less than 0.5 ‰. Normal GC-FID and GC-MS analyses were conducted on the aromatics prior to carrying out compound-specific $\delta^{13}C$ measurements. Compound-specific $\delta^{2}H$ analyses were performed using a GC/TC (High Temperature Conversion; 1450°C) unit, interfaced to the mass spectrometer [8,9]. Reported deuterium measurements are expressed as the permil deviation of the isotope ratio from Vienna Standard Mean Ocean Water (VSMOW). Data reported are the arithmetic means of at least two duplicate analyses, where variations were generally less than 3 ‰.

Figure 1 illustrates a typical chromatogram obtained from GC-TC-IRMS analysis.

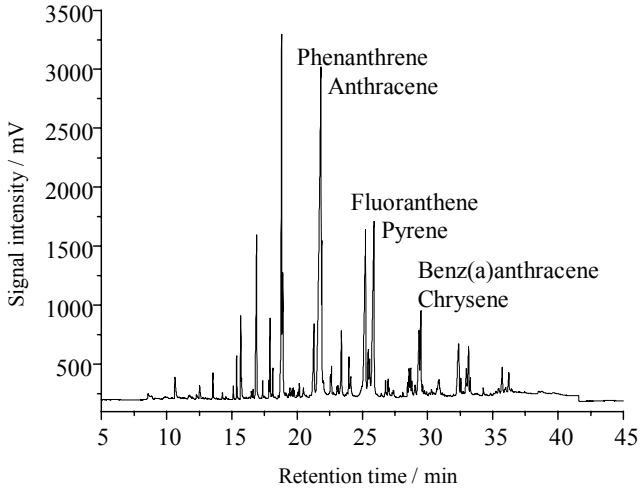

Figure 1 Chromatogram obtained from GC-TC-IRMS analysis of the Gasworks coal tar

Results and Discussion

Table 1 lists the carbon isotopic ratios of PAHs extracted from the high temperature carbonization and gas works (former Town gas plants in the UK) coal tars and the jet fuel and gasoline particulates. As expected from our earlier work, most of the PAHs have stable carbon isotopic ratios in the range of –22 to –30 ‰. Since British UK bituminous coals have bulk isotopic values close to –23 ‰, it may be concluded that, when PAHs are released as primary devolatisation products with minimal structural alteration, little in the way of isotopic fractionation occurs. However, when PAHs result from ring-growth, the smaller hydrocarbons in the primary volatiles undergo a series of complex transformations involving carbon-carbon bond formation, cyclisation and/or ring fusion. In one, or all of these processes, ^{12}C will be preferentially incorporated into the PAH where a kinetic isotope effect is operative. This could be the case for the coal tar from the Town gas plant having $\delta^{13}C$ values ranging from –27.5 to-29.5 ‰[5].

Typical carbon isotopic values of UK transport fuels have been found to be in the range –27 to –29 ‰. Again, PAHs derived from these sources reflect the carbon isotopic signature of the parent fuels to some extent (Table 1). The gasoline-derived PAHs display a trend to isotopically lighter values with increasing molecular mass. In contrast, the jet fuel-derived PAHs are isotopically heavier but display the same trend to isotopically lighter values with increasing molecular mass as for the petrol. Although detailed studies are required to understand these isotopic trends, the data in table 1 indicated that corresponding PAHs differ in isotopic composition by 2-4 ‰ for petrol and jet fuel particulates.

Li *et al*. [13] have determined $\delta^{2}H$ composition of individual alkanes in crude oils from the Western Canadian Sedimentary Basin, as a means of characterization of source organic matter, thermal maturity and migration. Comparison of individual alkanes from oils sourced from different geological provinces revealed a large range of $\delta^{2}H$ values, often of the order of *ca* 100 ‰, in addition to variations between alkanes in the same sample of *ca* 30 ‰. Also of relevance

are the δ^2H values in the range of –80 to –100 ‰ for a number of bituminous coals reported by Mastalerz et al.[11].

Table 1 $\delta^{13}C$ values for PAHs from selected coal tars and transport fuel particulates

PAH	Gasworks coal tar	HT coal tar	Jet fuel	Gasoline
Phenanthrene	-27.5	-24.8	-22.7	-26.5
Anthracene	-27.5	-24.8	-22.7	-26.5
Fluoranthene	-28.5	-24.5	-23.5	-27.1
Pyrene	-28.3	-24.5	-23.2	-26.9
Benz(a)anthracene	-28.9	-24.2	-24.1	-27
Chrysene	-28.9	-24.2	-23.5	-27
Benzo(b)fluoranthene	-28.8	-24.8	-25.7	-27.8
Benzo(k)fluoranthene	-28.8	-24.8	-25.7	-27.8
Benzo(a)pyrene	-28.9	-25.2	-25.5	-28.5
Indeno(1,2,3-cd)pyrene	-29.5	-26.4	-27.8	-29.4
Dibenz(a,h)anthracene	-29.5	-26.4	-27.8	-29.4
Benzo(ghi)perylene	-30	-26.6	-28.1	-29.6

Table 2 listed the δ^2H isotopic signatures for the PAHs derived from the samples investigated here. Of note are the large differences in $^2H/^1H$ isotopic ratio, both between samples derived from the different sources, where differences of *ca* 40‰ are observed, and between PAHs in the same sample, where variations of up to 20‰ are apparent. The jet fuel PAHs are isotopically lighter than those from petrol. Likewise, PAHs from high temperature carbonization are lighter and more nearer the isotopic values of whole coals than those in the gasworks tar. Figure 2 illustrates the correlation between δ^2H and $\delta^{13}C$ isotopic signatures of PAHs in the range phenanthrene to chrysene, indicating the very clear differentiation between the four samplesinvestigated. Thus, the advantages for source apportionment of utilizing both $\delta^{13}C$ and δ^2H isotopic values become readily apparent.

Table 2 δ^2H values for PAHs from selected coal tars and transport fuel particulates

PAH	Gasworks coal tar	HT coal tar	Jet fuel	Gasoline
Phenanthrene	-49.3	-73.2	-	-61.5
Anthracene	-49.3	-	-	-61.5
Fluoranthene	-42.2	-67.9	-74.3	-49.1
Pyrene	-40.0	-65.3	-74.1	-54.7
Benz(a)anthracene	-38.7	-72.1	-71.1	-47.1
Chrysene	-33.5	-72.6	-71.1	-47.1
Benzo(b)fluoranthene	-33.5	-81.1	-61.2	-47.0
Benzo(k)fluoranthene	-34.0	-81.1	-61.2	-47.0
Benzo(a)pyrene	-33.2	-68.3	-60.2	-51.2
Indeno(1,2,3-cd)pyrene	-33.2	-75.5	-68.9	-49.2
Dibenz(a,h)anthracene	-33.2	-	-68.9	-51.2
Benzo(ghi)perylene	-32.2	-71.6	-67.5	-54.0

Conclusions

Variations in the carbon stable isotope ratios ($\delta^{13}C$) for PAHs from different sources cover a range of only a few ‰, with typically To improve the ability of stable isotope measurements to source apportion environmental PAHs, the hydrogen stable isotopes of PAHs reported here have demonstrated the wide range of δ^2H values that exists. These have been used in conjunction with the $\delta^{13}C$ values to provide a much greater degree of differentiation between petrol and jet fuel-derived PAHs and between PAHs from different coal conversion processes than the $\delta^{13}C$ values alone.

Acknowledgement. The authors thank the European Coal & Steel Community (ECSC) for financial support and Prof. David Lee, Manchester Metropolitan University and Prof. Chris Wilson, Sheffield University with Qinetiq for providing the jet fuel particulate sample.

References

(1) O'Malley, V.P.; Abrajano Jr., T.A.; Hellou, J. *Org. Geochem.*, **1994**, *21*, 809-822.
(2) O'Malley, V.P., Burke, R.A.; Schlotzhauer, W.S. *Org. Geochem.*, **1997**, *27*, 567-581.
(3) Lichtfouse, E.; Budzinski, H.; Garringues, P.; Eglinton, T.I. *Org. Geochem.* **1997**, *26*, 353-359.
(4) McRae, C.; Love, G.D.; Murray, I.P.; Snape, C.E.; Fallick, A.E. *Anal. Commun.* **1996,** *33*, 331-333.
(5) McRae, C.; Snape, C.E.; Fallick, A.E. *Analyst*, **1998**, *123*, 1519-1523.
(6) McRae, C.; Sun, C-G; Snape, C.E.; Fallick, A.E.; Taylor, D. *Org. Geochem.* **1999**, *30*, 881-889.
(7) McRae, C.; Sun, C-G; Snape, C.E.; Fabbri, D; Tatari, D.; Trombini, C.; Fallick, A.E. *Environ. Sci. & Technol.,* 2000, **34**, 4684-4686.
(8) Burgoyne T. & Hayes J.M. *Anal. Chem*. **1998**, *70*, 5136.
(9) Hilkert A.W.; Douthitt C.B.; Schlü er H.J.; Brand W.A. *Rapid Comm. Mass. Spec*., **1999**, *13*, 1226-1230.
(10) Li M.; Huang Y.; Obermajer M.,;Jiang C.; Snowdon L.R. & Fowler M.G. *Org. Geochem*. **2001**, *32*, 1387-1399.
(11) Mastalerz M. & Schimmelmann A. *Org. Geochem*. **2002**, *33*, 921-931.

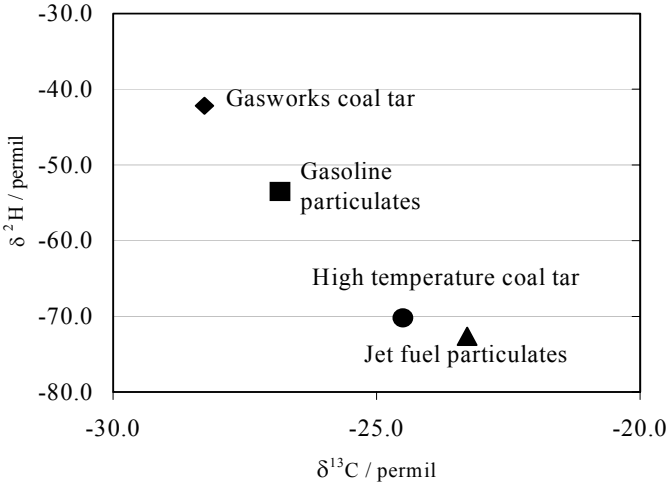

Figure 2 Correlation of $\delta^{13}C$ and δ^2H for selected PAHs generated by transport fuels and coal utilisation

NANOSTRUCTURE EFFECTS UPON SOOT OXIDATION

Randy L. Vander Wal and Aaron J. Tomasek
NCMR c/o NASA-Glenn
M.S. 110-3
21000 Brookpark Rd.
Cleveland, OH 44135

Introduction

Studies of soot oxidation have ranged from *in situ* flame studies to shock tubes to flow reactors [1]. Each of these systems possesses particular advantages and limitations related to temperature, time and chemical environments. Despite the aforementioned differences, these soot oxidation investigations share three striking features. First and foremost is the wide variation in the rates of oxidation. Reported oxidation rates vary by factors of +6 to - 20 [2] relative to the Nagle Strickland-Constable (NSC) rate for graphite oxidation [3]. Rate variations are not surprising, as the temperatures, residence times, types of oxidants and methods of oxidation differ from study to study. Nevertheless, a valid explanation for rate differences of this magnitude has yet to be presented.

Experimental

Soots possessing different nanostructures were produced by pyrolysis of acetylene, benzene or ethanol. These soots still in aerosol form were introduced into the post flame gases produced by a lean, premixed flame supported on a sintered metal burner. The soot and a portion of the post combustion gases were directed into a 1 inch outer diameter quartz chimney of 6 inches in length, placed directly above the quartz tube. With this setup, the temperature along the chimney axis was 750 +/- 30 ºC, as measured by a type K thermocouple. This variation was within the error range of the thermocouple, +/- 25 ºC, and hence it was taken as constant at 750 ºC. With a known entrance gas velocity, the residence time of the soot within the chimney is readily calculated based on buoyant acceleration as 75 +/- 5 ms.

With this configuration, oxidation was conducted well above the flame front, in the post flame gases. Burning with equivalence ratio less than one ensures that that the OH concentration within the post-flame gases is insignificant [10]. Given vastly slower rates for oxidation of carbons by H_2O or CO_2, the primary oxidant was considered to be the excess O_2 [1]. The soot stream appeared as a thin cylinder with yellow C_2 swan band emission associated with burning soot. Partially oxidized soot was collected at the chimney exit by thermophoretic sampling directly upon a lacey TEM grid.

Results and Discussion

Figure 1 plots the mass burnout rates versus free O_2 concentration for the soots derived from the different fuels. Burnout rates are calculated relative to the initial particle size before introduction into the flame environment. The mass loss rate increases with increasing O_2 concentration as expected for all soots, yet the soots derived from benzene and acetylene exhibit a dramatic difference in their oxidation rates. As observed, the acetylene soot requires a much higher ambient O_2 concentration to achieve the same level of burnout (for any given reaction duration) as the benzene derived soot. The soot derived from ethanol exhibits a very similar rate as the benzene soot. The faster burnout rate for the benzene and ethanol derived soots is also reflected in their complete oxidation at O_2 concentrations far lower than that of the acetylene derived soot, despite similarly sized primary particles for these two soots. Plotted for reference is the calculated NSC rate at each O_2 concentration at the measured post-flame gas temperature [3]. As seen in Fig. 1, the measured rates for the graphitic acetylene soot lie much closer to the NSC rates. Notably the oxidation rates of all the soots exceed the NSC rate. HRTEM images of the soot have been obtained and reported elsewhere [4]. These images form the basis for our subsequent discussion and lattice fringe analysis as follows next.

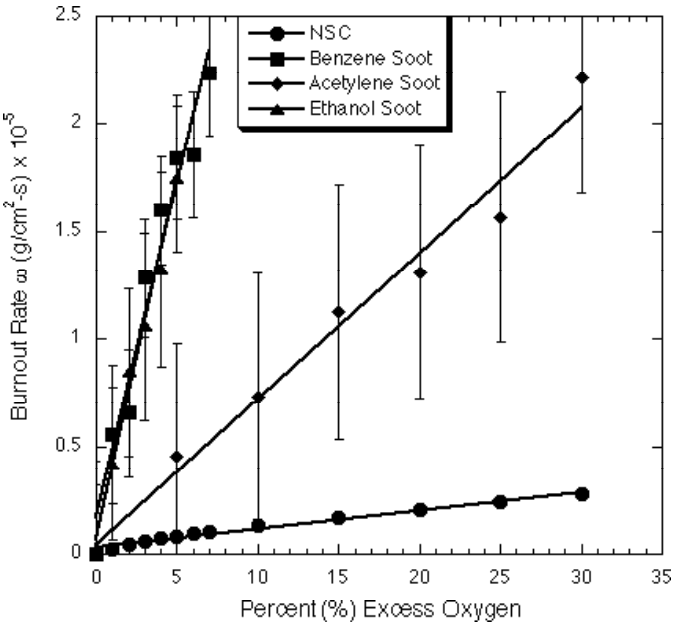

Figure 2 Dependence of soot mass burnout rate with O_2 percentage in the post-flame gases. The NSC rate is also shown for comparison.

Soot Structure. Although the relation between carbon structure and reactivity is well-known in carbon science from thermal and oxidative studies of and graphite [5]; the relation for soot remains unstudied. It is well-known that graphite oxidation proceeds anisotropically, i.e, the reactivity of basal plane carbon atoms is far lower than that of edge site carbon atoms. Measurements by Rosner and Allendorf observed a 10 - 100-fold reactivity difference between isotropic and pyrolytic graphite, intrepreted on the basis of the differerent reactivities of carbon atoms within basal plane versus edge site positions [5].

Consequently, the observed reactivity will be an average of basal versus edge site carbon atom reactivities for graphitic layer planes of finite dimensions [3]. As the layer plane size decreases, the number of edge site carbon atoms will necessarily increase in proportion to the number of basal plane carbon atoms, allowing one to expect the overall reactivity to increase. In addition to the size of the graphene segments, their relative curvature will also impact their oxidation rate. Curvature arises from 5-membered rings within the aromatic framework [6]. This curvature imposes bond strain because the orbital overlap giving rise to the electronic resonance stabilization is lessened [7]. Therein the C-C bonds are weakened and individual atoms are more exposed, i.e. they are more susceptible to oxidative attack. It is for these same reasons that fullerenes and carbon nanotubes are less resistant towards oxidation than planar graphite [7, 8].

This duality of reactive sites forms the physical basis for the NSC oxidation rate expression which takes into account both edge and basal plane carbon sites and their associated reactivities [3]. However, this semi-empirical rate is based on pyrolytic graphite, a

structure with extended basal planes and correspondingly few edge site carbon atoms. Consequently the overall oxidation rate would be expected to be relatively low compared to most other carbons possessing a less graphitic structure. Notably there is no corresponding model or rate expression that takes into account the curvature of graphitic layer planes and the associated impact upon oxidative stability.

Thus the reactivity of a soot particle towards oxidation depends upon its nanostructure, i.e. the size, orientation and organization of the graphene layer planes. Variations in the graphene layer plane dimensions, curvature, and relative orientation will greatly impact the reactivity of the individual graphene segments, and hence the overall particle reactivity. Yet as discussed, little attention has been given to soot particle nanostructure and its impact upon reactivity towards oxidation within combustion systems. To the degree to which the soot nanostructure reflects a dependence upon inception and growth conditions, so too will its oxidation rate reflect a similar dependence. Our results clearly illustrate a dependence of the burnout rate upon the soot nanostructure as governed here by both the initial fuel and soot growth conditions.

Conclusions

The work reported here illustrates a dependence of the soot particle nanostructure upon synthesis conditions; namely temperature, time and initial fuel identity. Such structural variations in the graphene layer plane dimensions necessarily alters the ratio of basal plane versus edge site carbon atoms. A corresponding variation in the overall reactivity, reflecting an average of the different reactivities associated with these specific atomic sites arises. This variation is illustrated here between a disordered soot derived from benzene and a graphitic soot derived from acetylene. Their oxidation rates differ by nearly 5-fold. Curvature of layer planes, as observed for an ethanol derived soot, is found to substantially increase oxidative reactivity. Relative to fringe length as a manifestation of graphitic structure, curvature more effectively increases reactivity towards oxidation. Larger variations in oxidation behavior may be expected, depending upon the soot synthesis conditions. Other physical properties may similarly be affected.

Acknowledgements. This work was supported by a NASA NRA 99-HEDs-01 combustion award (RVW) administered through NASA cooperative agreement NAC3-975 with The National Center for Microgravity Research on Fluids and Combustion (NCMR) at The NASA-Glenn Research Center. The authors gratefully acknowledge Gordon M. Berger for assistance with the experiments and Dr. Y. L. Chen and David R. Hull for the TEM imaging.

References

(1) Kennedy, I. M.; *Prog. Energy Combust. Sci.* **1997,** *23 ,* 95. (and references therein).
(2) Puri, R.; Santoro, R. J.; and Smyth, K. C.; *Combust. and Flame* **1994,** *97,* 125.
(3) Nagle, J. Strickland-Constable, R. F.; *Proc. of the Fifth Carbon Conf.* **1962,** *1,* pp.154-162.
(4) Vander Wal, R. L.; and Tomasek, A. J.; *Combust. and Flame* (in press).
(5) Rosner, D. E.; and Allendorf, H. D.; *AIAA Journal* **1968,** *6,* 650.
(6) Kroto, H. W.; Heath, J. R.; O'Brien, S. C.; Curl, R. F.; and Smalley, R. E.; *Nature*, **1985,** *318,* 162.
(7) Dresselhaus, M. S.; Dresselhaus, G.; and Eklund, P. C.; *Science of Fullerenes and Carbon Nanotubes,* Academic Press Inc. **1996**.
(8) "*Carbon Nanotubes, Preparation and Properties*", CRC Press Inc., (T. W. Ebbesen Ed.), **1997**.

CURRENT STATUS AND FUTURE TREND OF NITROGEN OXIDES EMISSIONS IN CHINA

Hezhong Tian, and Jiming Hao

Air Pollution Control Division
Dept. of Environ. Sci. & Eng.
Tsinghua University
Tsinghua Campus, Haidian District
Beijing, 100084, P.R. China

Introduction

In recent years, NO_X emissions produced by energy use and economic activities in China have received increasing attention from Chinese government as well as from domestic and foreign scientists, because of its implication in the chemical complexity of acid rain, photo-chemical smog and fine particulate (PM_{10}/$PM_{2.5}$) formation in air which causes a threat to human health and ecosystem. Therefore, knowing about the present status and future trend of NO_X emissions in China will play an active role in regulating NO_X control strategies.

In this study, the database of historical energy consumption in China was established, as well as the database of future energy demand between 2000 and 2030, which was deduced from energy consumption in 2000 by the means of sectoral analysis methodology. The database of NO_X emission factors specified by different economic sectors and different fuel types was constituted on the basis of field experiments and reference survey. Then, the present and future NO_X emissions in China were evaluated and analyzed.

Scope and Methodology

Scope. The regions studied cover 31 provinces/autonomous regions/municipalities on the Chinese mainland. Eight large economic sectors are taken into consideration, including thermal power generation (POW), other energy transformation (OTR), agriculture (AGR), industry (IND), transportation (TRA), construction (CON), service (SER), and residential consumption (RES). Eleven types of fossil fuels are investigated, i.e., coal, coke, crude oil, gasoline, kerosene, diesel, residual oil, LPG, refinery gas, coal gas, natural gas, and other gases [1].

The necessary energy consumption data during the period from 1980 to 2000 were derived from energy balance tables of the whole nation and/or each province in terms of economic sectors, fuel types, and provinces. While, the energy demand up to 2030 were projected by the means of sectoral analysis methodology, which were based on the relevant statistical data in China Statistical Yearbook [2,3].

Methodology. Emissions of NO_X in China was evaluated by combining energy consumption and NO_X emission factors, which can be expressed by the following hierarchical formula [1,4]:

$$Q_T^N(t) = \sum_i Q_i^N(t) \quad (1)$$

$$Q_i^N(t) = \sum_j Q_{i,j}^N(t) \quad (2)$$

$$Q_{i,j}^N(t) = \sum_f \sum_k Q_{i,j(k),f}^N(t) \quad (3)$$

$$Q_{i,j(k),f}^N(t) = (1 - P_{i,j(k),f}^N(t)) K_{i,j(k),f}^N(t) F_{i,j(k),f}(t) \times 10^{-3} \quad (4)$$

Where: Q^N=Emissions of NO_X calculated as NO_2; K^N=Emission factor of NO_X weighted as NO_2; F=Fuel consumption; P^N=Efficiency of NO_X removed by pollution control measures; T=China; t=Year; i=Province; j=Economic sector; f=Fuel type; $j(k)$=Emission source category in the economic sector j.

Emission factors of NO_X. The database of NO_X emission factors was constituted based on field experiments and literature investigation, which was specified by different economic sectors and different fuel types.

Results and Discussion

Economic growth and energy consumption. Since 1980s, China's economy has been growing rapidly. The national GDP grew from 451.78 billion Yuan in 1980 to 8944.22 billion Yuan in 2000, with an annual average growth rate of 9.7%(**Figure 1**). It also can be seen that the structure of the economy and the share of different economic sectors have changed gradually through years of economic and product restructuring. While the Secondary Industry (including industry and construction) still keeps a fairly steady share of total GDP, the Tertiary Industry, which is less energy–intensive, has gradually expanded to approximately one-third of the total GDP.

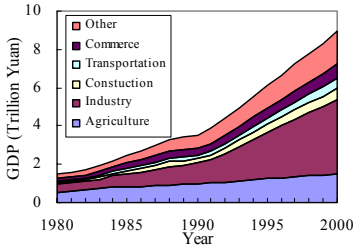

Figure 1. The structure of China's national GDP, 1980~2000.

In the same time, the total primary energy consumption has increased from 602.75Mtce to 1302.97Mtce (**Figure 2**). With the continuously rapid growth of economy, China's energy consumption experienced a steadily increase until 1996, at which primary energy consumption reached a peak value of 1389.48Mtce. However, a decline in primary energy use has occurred in the late 1990s. Contrary to all earlier expectations, the years between 1996 and 2000 witnessed a continuous decline in China's consumption of primary energy, mostly driven by the reduced use of coal--the most significant fossil fuel energy in China. From a peak value of 1447Mt in 1996, China's coal use dropped to 1245Mt in 2000, and coal's share of total primary energy consumption fell from 74.7% to 66.1%.

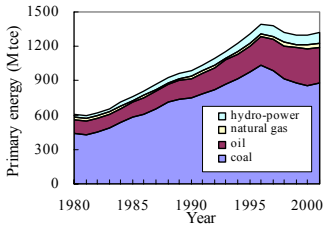

Figure 2. The primary energy consumption in China, 1980~2000.

Current status of NO_X emissions in China. Based on national and provincial energy consumption data and specific NO_X emission factors, the national gross NO_X emissions in the period of 1980 to 2000 are evaluated (see **Figure 3**). As can be seen, with the continuously rapid growth of economic activity and coal-dominated energy consumption, total emissions of NO_X in China grew steadily in the past two decades, from 4.76Mt in 1980 to a peak of about 12.03Mt in 1996, with an annual average growth rate of 6%. However, accompanying the reduction of primary energy consumption and coal use, total NO_X emissions began to decrease after 1996. NO_X emissions decreased to a low value of 11.18Mt in 1998. This reduction is contrary to all former expectations and can be

mainly explained by the change of energy consumption mix and the lower primary energy consumption, especially the reduction of coal final consumption. Since then, NO_X emissions increased slowly again up to 11.77Mt in 2000 [5].

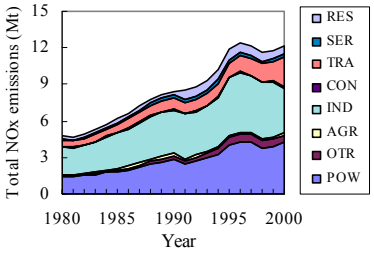

Figure 3. China's Total NO_X emissions by sectors, 1980~2000

Also, it can be seen that China's NO_X emissions is unevenly allocated in different economic sectors and fuels (see **Figure 3** and **Figure 4**). POW is the largest sources (over 1/3 of the totals), followed by IND and TRA. Similarly, Fired-Coal is the main fuel source with a share of about 63% of the totals in 2000, and followed by diesel, coke, and gasoline. In addition, China's NO_X emissions were mainly concentrated in the eastern and central provinces, accounting over 80% of the totals.

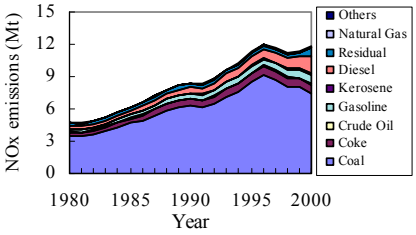

Figure 4. China's Total NO_X emissions by fuel types, 1980~2000

Trend of NO_X emissions in China. Based on different economic growth rates assumption, three scenarios of future energy demand in China were designed, which were called Low (L), Mid (M) and High (H) scenario, respectively. The assumed GDP in the future was shown in **Figure 5,** and the projected primary energy demand was shown in **Figure 6**.

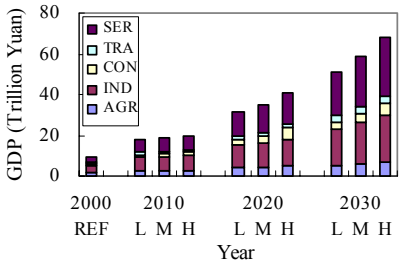

Figure 5. China's future national GDP by economic sectors

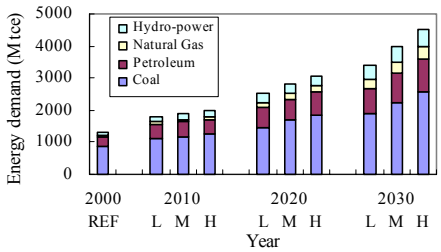

Figure 6. China's future primary energy demand by fuel types

As can be seen, the future energy demand in China will increased steadily with the rapid economic growth. By the year of 2020 and 2030, the national GDP will reach up to 31.5~50.2 trillion Yuan and 51.3~68.0 trillion Yuan, respectively. Meanwhile, the projected primary energy consumption will amount to 2528~3067Mtce and 3382~4498Mtce, respectively.

Combining the projected energy consumption with NO_X emissions factors and the assumed NO_X control efficiency, trend of NO_X emissions in China were evaluated (see **Figure 7** and **Figure 8**).

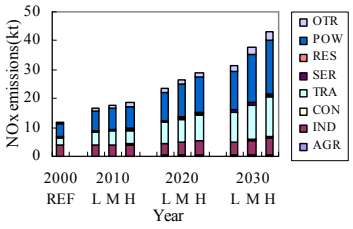

Figure 7. China's future NO_X emissions by economic sectors

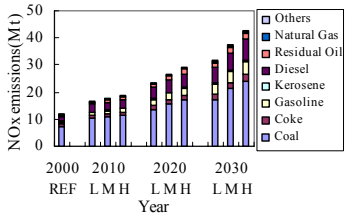

Figure 8. China's future NO_X emissions by fuel types

It can be seen that China's NO_X emissions will probably increase to about 23.6~29.1Mt in 2020 and 31.5~43.0Mt in 2030, respectively if none effective control measures were adopted. Further, China's NO_X in the future will still remain unevenly allocation among different fuels and economic sectors. By 2030, fired-coal will still be the largest fuel source, accounting for about 56% of the totals, and the share of POW, TRA and IND will be about 45%, 32% and 14%, respectively.

Conclusions

With rapid economic growth and energy consumption increase, China's NO_X emissions have reached up to a high value of 11.77Mt in 2000. If none effective control measures taken, China's total NO_X emissions will probably rise to as high as 31.5~43.0Mt in 2030, becoming the largest NO_X emission country in the world. Therefore, It is very necessary for China to regulating increasingly strict NO_X emission control standards and relevant policies as soon as possible.

Acknowledgment. This work is partially supported by the State Environmental Protection Administration (SEPA) of China under contract 98-1-01. However, the opinions expressed herein are those of the authors themselves and should not be constructed as representing the official positions of Tsinghua University, or SEPA.

References

1. Hao J.M.; Tian H.Z.; and Lu Y.Q., ES&T. **2002**, 36, 552-560
2. National Bureau of Statistics (NBS), China Statistical Yearbook 2002, China Statistical Press: Beijing, 2002.
3. NSB, China Energy Statistical Yearbook (1997-1999), China Statistical Press: Beijing, 2002.
4. Kato, N.; Akimoto, H., Atmos. Environ. **1992**, 26A, 2997-3017.
5. Streets D.G.; Waldhoff S.T., Atmos. Environ. 2000, 34, 363-374.

ADVANCED FLUE GAS TREATMNENT BY NOVEL DE-SOX TECHNOLOGY OVER ACTIVE CARBON FIBERS

*Masaaki Yoshikawa and Isao Mochida**

R & D Department, Osaka Gas Co., Ltd. 6-19-9, Torishima, Konohana-ku, Osaka554, Japan
* Institute of Advanced Material Study, Kyushu University 6-1, Kasugakoen, Kasuga-shi, Fukuoka 816, Japan

Introduction

There is a worldwide increase in the discharge of the sulfur dioxide from the use of fossil fuel. Especially in the Asia region, recent increases in the discharge are large, but environmental countermeasures have been retarded for the sake of economical efficiency. Though in the advanced nation, the limestone gypsum method is mainly used as stack gas desulphurization facility, it is the method in which both cost of equipment and operational cost are expensive.

On the other hands, it becomes obvious that SOx and NOx in flue gas can be removed at room temperature by using active carbon fibers (ACF) subjected to surface treatment such as heat treatment [1, 2]. The flue gas treatment technology using ACF is a semidry oxidation type de-SOx method that is effective even around room temperature. In addition, this technology enables by-products such as sulfuric acid, sulfates, nitric acid, and various nitrates to be recovered, and is applicable in the field of flue gas treatment to which the conventional de-SOx method, such as the limestone gypsum method, could not be applied for economical reasons.

Experimental

Characteristics of ACF catalyst

To evaluate the basic characteristics of de-SOx over ACF, comparison was made between four kinds of commercialized ACFs under the untreated condition. Table 1 shows the comparison of the properties of ACFs. Because the structures such as an external surface area, specific surface area, and pore size are unified in the manufacturing process, there is slight difference in structure of raw materials. But the compositions of raw materials significantly vary with types; phenol-type (Kuraray Chemicals Co., Ltd.) or cellulose-type (Toyobo Co., Ltd.) ACFs have high oxygen content, PAN-type (Toho tenax Co., Ltd.) ACF has high nitrogen content, and pitch-type (Adall Co., Ltd.) ACF has the largest carbon content, which indicates that the compositions of raw materials may exert great influence on the chemical properties of ACFs In order to improve the performances of desulphurization, high temperature heating treatment in the inert gas, such as nitrogen, were carried out at several conditions, described later.

Desulphurization reaction tests

Desulphurization reaction was examined in a fixed bed flow reactor at 25-50 °C , with a flow rate 400 ml/min of 1000ppm SO_2, 5% O_2, and 10-15% H_2O in N_2 over 2 g of ACF catalyst to adjust W/F (Catalyst weight by Flow rate) to 5 * 10^{-3} g min/ml. SO_2 concentration were analyzed continuously at the inlet and outlet of the reactor using Infrared SO_2 Gas Analyzer (SOA-7000, Shimadzu Co., Ltd.). Steady-state SO_2 conversion was observed when the SO_2 concentration at the outlet of the reactor became stable.

Table 1. Comparison of the properties of ACFs made of different raw materials

	Pitch type ACF	PAN type ACF	Phenol type ACF	Cellulose type ACF
Composition formula of raw materials	$[C_{124}H_{80}NO]n$	$[C_3NH_3]n$	$[C_{63}H_{55}O_{11}]n$	$[C_6H_{10}O_5]n$
Carbon content in raw material (%)	93.1	67.9	76.6	44.4
Diameter of fiber (μm)	10 to 18	7 to 15	9 to 11	15 to 19
External surface area (m^2/g)	0.2 to 0.6	0.9 to 2.0	1.0 to 1.2	0.2 to 0.7
Specific surface area (m^2/g)	700 to 2500	500 to 1500	900 to 2500	950 to 1500
Pore volume (ml/g)	0.3 to 1.6		0.22 to 1.2	
Pore diameter (nm)	to 2	2 to 4	1.8 to 4.4	1 to 1.8
Tensile strength (kg/mm^2)	10 to 20	20 to 37	30 to 40	6 to 10
Elastic modulus (kg/mm^2)	200 to 1200	7000 to 8000	1000 to 1500	1000 to 2000
Elongation (%)	1.0 to 2.8	to 2.0	2.7 to 2.8	
PH	7		7	
Ignition temperature (°C)	460 to 480	470	470	
Benzene adsorbing amount (%)	22 to 68	17 to 50	22 to 90	30 to 58
Iodine adsorbing amount (mg/g)	900 to 2200		950 to 2400	
Methylene blue decolorizing ability	to 400	to 300	to 380	

Results and Discussion

Fig.1 shows the change of de-SOx performances of commercialized four kinds of untreated ACFs with elapse of time. All the ACFs used have the same specific surface areas of about 1,000 m^2/g. The reactions were performed under the same condition that the inlet SO_2 concentration was 1000 ppm, the reaction temperature was 25°C, and water content 10%, which means super-saturated condition.

The Y-axis in the figure indicates the SO_2 breakthrough ratio (outlet SO_2 concentration / inlet SO_2 concentration). The figure shows the de-SOx activities of these four kinds of ACFs in decreasing order: pitch-type, PAN-type, phenol type, and cellulose-type ACFs. The figure also revealed that the de-SOx ratio was kept stable even after 15 hours.

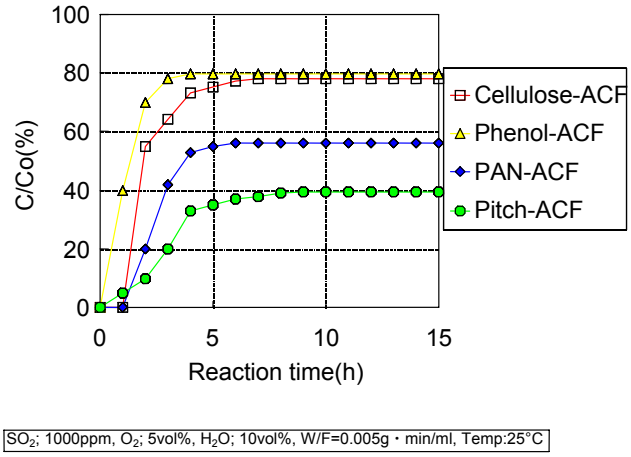

Fig. 1. Basic characteristics of de-SOx reactions over various ACFs

Like the above, the results of investigation on basic characteristics of de-SOx reaction over ACFs revealed that the pitch type ACF is most suitable for the performance. Because the four kinds of ACFs are scarcely different in structures including the specific surface area and pore size, chemical properties of them

seemed to affect the performance of de-SOx reactions. Considering that the pitch type ACF contains the largest carbon content and the least content of both oxygen and nitrogen in the raw material, and ACF with less oxygen groups may be suitable for de-SOx reactions, we investigated to achieve high perfomance of ACFs.

Therefore we devised to reduce oxygen groups of ACF as much as possible in order to accelerate this reaction. So we tried to remove the oxygen groups on the surface by carrying out high temperature heating treatment of pitch-type ACFs in the nitrogen. Fig. 2 shows the result of de-SOx when ACF with 1,060 m^2/g of specific surface area was heat treated in the temperature range from 600 to 900°C in the nitrogen. The reaction condition was nearly the same as the basic characteristics mentioned above, but the W/F (contact time) was reduced by half to 2.5 * 10^{-3} g min/ml.

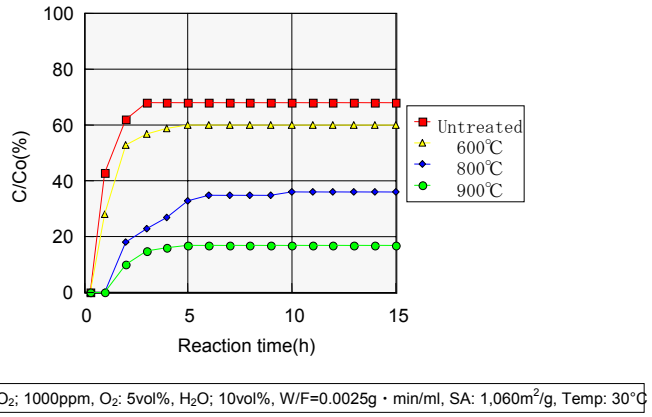

Fig. 2. Change of the de-SOx performance by heat treatment temperature

The figure clarified that the de-SOx performance was improved as the heat treatment temperature rose, and in 900°C, it reached the performance over 80%. The de-SOx performance was stable after the reaction initiation over 50 hours, and as the product material, sulfuric acid was continuously recovered. The material balance between removed SO_2 and recovered sulfuric acid agreed in the proportion over 98%.

Fig. 3 shows the summary of the result of six kinds of ACFs different in specific surface area, and the X-axis indicates the heat treatment temperature in an atmosphere of nitrogen, while the Y axis shows the de-SOx ratio. The figure revealed that de-SOx ratios of ACFs are proportional to the heat treatment temperature, and de-SOx ratio becomes higher with increasing the specific surface area. The ACF with the maximum specific surface area of 2,150 m^2/g, which was heat-treated at 900°C, showed 100% of de-SOx performance in this contact time. On the other hand, the ACF of 1000 m^2/g specific surface area stopped at 80% performance even with 900°C heat treatment temperatures.

It is considered that therefore, the performance is decided by the correlation between the improvement of the surface by the heat treatment and adsorption capacity.

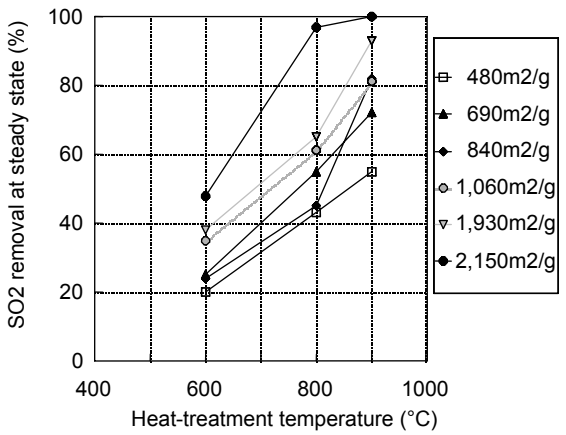

Fig. 3. Correlation between the heat treatment temperature of ACF and the de-SOx ratio

In the de-SOx over ACF, the reaction mechanism is considered like the following.

First, SO_2 is adsorbed onto the active sites on the surface of ACF, and oxidized with oxygen in flue gas into SO_3. Immediately sulfuric acid is formed by hydration of the SO_3 with water in flue gas, then, finally the sulfuric acid is absorbed in water and desorbed from the surface of ACF. In the above-mentioned reaction process, desorption of sulfric acid from the ACF surface is considered to be a rate controlling step, and therefore it is most important to increase the desorption rate. The fact that condensation of water in flue gas onto ACF doesn't inhibit adsorption of SO_2 but accelerates the reaction is the confirmation-finished by the different experiment.

On the other hand, it is also known that pore diameter and surface area of ACF do not decrease by the heat treatment at 1000°C [3]. The heat treatment increases markedly the electrical conductivity of ACF [4]. The image potential of an SO_2 molecule with the graphitic pore wall should stabilize the dipole-oriented structure in micropores of ACF, then it intensifies the catalytic activity for the SO_2 oxidation.

The oxygen function groups of ACF surface inhibits the desorption of generated sulfuric acid by its hydrogen bonding ability, and the de-SOx reaction is inhibited. Therefore, the heat treatment of pitch-type ACFs in the nitrogen removes surface oxygen functin gruops to make the hydrophobic surface, and it becomes the high activity catalyst for the desulphurization reaction.

References

1. S.Kisamori; K.Kuroda; S.Kawano; I.Mochida; Y.Matsumura; and M.Yoshikawa, Energy & Fuel, **1994**, Vol. 8, No. 6,1337
2. I.Mochida; S.Kisamori; M.Hironaka; S.Kawano; Y.Matsumura; and M.Yoshikawa, Energy & Fuel, **1994**, Vol. 8, No. 6,1341
3. T. Ohlubo; C.M.Yang; E.Raymundo-Pinero; Linares-Solano; and K.Kaneko, Chem. Phys. Letters, **2000**, 329, pp.71-75
4. M. Ruike; N.Murase; J.Imai; C.Ishii; T.Suzuki; and K.Kaneko, J. Colloid Interface Sci. **1998**, 207, pp.355

PREDICTING MERCURY SPECIATION IN COAL-DERIVED FLUE GASES

Stephen Niksa[a] and Naoki Fujiwara[b]

[a]Niksa Energy Associates, 1745 Terrace Drive, Belmont, CA 94002, neasteve@pacbell.net
[b]Coal Research Laboratory, Idemitsu Kosan Co., Ltd., Chiba 299 0267, Japan, nffish@po.iijnet.or.jp

Introduction

The coal burning utility industry is expected to mount a massive response to comply with as-yet unspecified regulations on mercury emissions from power plants that take effect in late 2007. Two Hg control technologies have already shown promise in full-scale evaluations: (1) sorbent injection with Hg recovery on particulates in ESPs or, preferably, baghouse filters; and (2) Hg recovery with the precipitated solids from wet SO_X scrubbers. Many aspects remain to be resolved, primarily because Hg control is affected by so many conditions in the power plant. Fuel quality is paramount because it determines the exhaust concentrations of acid gases (HCl, SO_2, and NO_X) and UBC, and the flyash composition – all of which affect Hg transformations. The furnace firing conditions that govern UBC emissions are the most important, whereas those that affect NO_X, moisture, and O_2 levels are secondary. The configuration of unit operations in the exhaust system determines the time-temperature history across the system, as well as when particulates are removed from the exhaust stream, as well as when the exhaust will contact catalytic agents such as SCR catalysts and filter cakes of flyash. In turn, each of these aspects affects the process chemistry. Whether or not these conditions change frequently will be determined by the operating practices of individual utility companies. Frequent coal switching accentuates the fuel quality impacts; low-NO_X retrofits accentuate the impact of furnace firing conditions; SCR installation primarily affects Hg control in systems with wet scrubbers, but would be less important for control with ESPs and baghouses.

To assist utilities sorting through the multitude of variables and equipment combinations to formulate cost-effective compliance strategies, mathematical models are being developed in parallel with the control technology. Most models rely on traditional engineering regressions of databases on Hg transformations in pilot- and full-scale testing. With the widespread dissemination of the data from 84 power plants collected under EPA's ICR program, several authors reported regressions on the effectiveness of specific unit operations for Hg control[1-4]. Unfortunately, these regressions are not statistically significant[2] (except for systems with spray dryer absorbers), due to errors and omissions in the ICR database and inadequacies in the regression functions, among many other reasons. As an example of the ambiguities, consider that, in the ICR database, the percentages of oxidized Hg at the inlets to the air pollution control devices span a range from 2 to 100 % for the most common coal-Cl levels, from 100 to 200 ppm[2]. And this excessive scatter is associated with coal-Cl, the coal property that is widely held as the determining factor on Hg transformations.

In parallel, the complexity of the Hg reaction system spawned a body of scientific observations that are now being synthesized into fundamental transformation mechanisms. These mechanisms are being expanded to describe progressively more of the interactions among exhaust species at the molecular scale. For example, the first elementary chemical reaction mechanisms for Hg oxidation were introduced in 2000[5,6]. They were then supplemented with more chemistry to quantitatively interpret the laboratory database on systems without particles in 2001, including inhibition by moisture and by NO under some, but not all, conditions[7]. In 2002, they were expanded with chemistry on UBC particles to interpret the data from coal-derived exhausts from lab-scale flames[8], and with chemistry on inorganics to generate Cl_2 from HCl[9]. They are now being expanded for the impact of sulfur species[10], and being used to predict behavior in pilot-scale coal flames, as the final prerequisite for applications in full-scale systems. The progress in developing predictive mechanisms for Hg capture on sorbents has been similarly rapid[11].

This paper surveys the development of predictive reaction mechanisms for Hg transformations in flue gases from coal-fired furnaces. Mercury oxidation is emphasized, although Hg adsorption on inherent flyash components and sorbents is recognized as an essential ingredient for any predictive capability in practical applications. Evaluations of predictions with test data are reported for progressively larger and more complex systems. To summarize the technical discussion, the reaction mechanisms are used to identify the most important fuel properties and firing practices for Hg oxidation under typical conditions in utility exhaust systems.

Mathematical Modeling

Modeling Objectives. The ultimate goal is to predict (i) the partitioning of Hg species between vapor and particulate forms and (ii) the proportions of elemental and oxidized Hg in the gas phase at the inlets to all control devices, given sets of standard coal properties, basic firing conditions, and operating conditions along the exhaust system. The partitioning onto particulates is important because adsorbed Hg can be completely collected with either ESPs or baghouses. The extent of oxidation is important because only oxidized Hg (Hg^{2+}) is water-soluble and therefore recovered in scrubbers. Also, Hg^{2+} is somewhat more difficult to collect on carbon-based sorbents. So there is a clear need for predictions (i) and (ii) at the outlets of air heaters and SCR units and the inlets to sorbent injection manifolds, ESPs, baghouses, and scrubbers. But there is less motivation to develop detailed mechanisms for SO_2 scrubbers, because full-scale testing has already established that the Hg control in scrubbers can be accurately estimated from the proportion of oxidized Hg at the inlet and the liquid-to-gas ratio of the scrubber, with secondary influence from the solution pH[4,12].

All the mercury leaving a furnace is elemental. Since the abundance of oxidized mercury expected under thermochemical equilibrium for flue gas temperatures does not materialize in actual exhaust systems, the extent of Hg oxidation from the economizer outlet through the stack inlet is determined by chemical kinetics. This oxidation primarily occurs across air heaters, while the exhaust is quenched at several hundred degrees per second, and is promoted by high concentrations of carbonaceous particles, as found in baghouse filtercakes. There is minimal Hg adsorption on particulates above 350°F, but significant recovery as temperatures are progressively reduced below this threshold. Unburned carbon is the most effective sorbent in inherent flyash, except with the flyashes from low-rank coals that contain substantial amounts of Ca. Oxidation and adsorption are not independent because UBC and high levels of Ca and Fe in flyash promote Hg oxidation, as apparent in the significant surge in the extent of oxidation across baghouse filter cakes.

Hg Oxidation Mechanism. Mercury oxidizes in three phases: in the gas phase; on particulates, especially UBC; and over SCR catalysts. The database on Hg oxidation across SCR units is just beginning to emerge and is still inadequate for mechanistic interpretations. So, in the near-term, contributions from SCRs must be estimated with correlations, which will improve as more data becomes available. But the extents of oxidation in the gas phase and over particulates can be accurately estimated with detailed mechanisms, as explained in the following two sections.

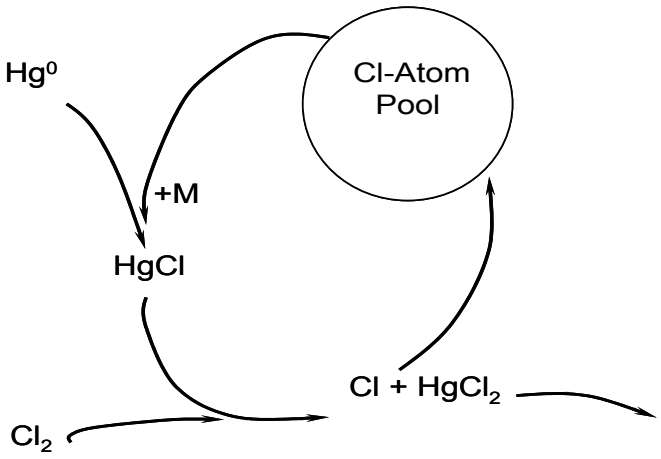

Figure 1. Cl-atom recycle during homogeneous Hg oxidation.

Homogeneous Hg Oxidation. The total amount of Hg in coal-derived exhausts is typically less than 10 ppbv. Consequently, Hg cannot possibly affect the concentrations of any of the species that participate in its own oxidation, because all are present at much higher concentrations. In other words, chemistry that does not involve Hg sets the concentrations of Cl, Cl_2, O, OH, and HO_2 that subsequently participate in the Hg oxidation. As explained elsewhere[7,8], our homogeneous mechanism includes 8 reactions for Hg oxidation that involve Hg^0, HgCl, $HgCl_2$, Cl, Cl_2, HCl, HOCl, H, and OH. This submechanism represents a Cl-atom recycle sketched in Fig. 1 whereby the Cl-atom consumed in the partial oxidation of Hg^0 into HgCl is regenerated in the subsequent oxidation of HgCl by Cl_2 into $HgCl_2$. All supporting kinetic submechanisms were taken directly from the literature and used without modification, consistent with the much higher concentrations of the species in these mechanisms. The Cl oxidation submechanism accounts for a broad range of HCl concentrations, and incorporates additional coupling of Cl chemistry and NO_X chemistry. The moist CO oxidation submechanism is an update of previous efforts by Prof. Dryer and co-workers at Princeton and describes the kinetics of moist CO oxidation at low to moderate temperatures, allowing for perturbations from NO_X conversion and interactions with NO_X and SO_X conversion chemistry. The H/N/O submechanism describes the kinetics of NO_X conversion at low to moderate temperatures. In total, 168 elementary chemical reactions are included in the homogeneous Hg^0 oxidation mechanism, without any adjustable parameters.

This mechanism alone was able to quantitatively interpret several reported datasets with synthetic flue gases without particulates[6,13-15]. As seen in Fig. 2, the mechanism accurately depicts the inhibiting effect of moisture and NO (left panel), and covers a broad range of Hg and HCl concentrations (right panel), including saturation of HCl promotion when the HCl/Hg ratio exceeds 4000.

The accuracy of these predictions notwithstanding, it soon became clear that the homogeneous mechanism alone would not be sufficient to describe Hg oxidation in utility exhaust systems. Whereas the tests behind Fig. 2 imposed gas quenching rates that were more than an order of magnitude faster than in typical air heaters, the lab tests by Mamani-Paco and Helble[15] imposed realistic quench rates. And for these conditions, the homogeneous oxidation mechanism predicted negligible extents of oxidation, in accord with the test results. More importantly, when the homogeneous Hg oxidation mechanism alone was evaluated with the measured extents of Hg oxidation for 5 coals in a lab-scale flame[16], it performed poorly, despite its success with all the available datasets with synthetic exhausts. Among these five coals, Coal D has an unusually high Cl-content and gave the most extensive Hg oxidation, as expected. In contrast, the homogeneous mechanism predicted the minimum extent of oxidation for this coal, and complete oxidation with all others. These simulations also revealed why the mechanism was failing. According to the homogeneous mechanism, Cl-atoms oxidize Hg^0 into HgCl (as seen in Fig. 1). The Cl-atom concentration develops from explosive chemistry, whereby a long induction period is needed to ignite the production of Cl-atoms at the slow quench rates in utility exhaust systems. Once this chemistry ignites, the Cl-atom concentration surges, which ultimately oxidizes most, if not all, the available Hg. This same mechanism is responsible for Hg oxidation in many of the lab-scale tests without particulates, where excessive quench rates enhanced the ignition characteristics. But it is incompatible with the moderate extents of Hg oxidation often reported for coal-derived exhausts under the operating conditions in utility exhaust systems.

Heterogeneous Chemistry. The following heterogeneous reaction subset was combined with the homogeneous mechanism to rectify the problems in the predictions for coal-derived exhausts:

$$StSA(s)+HCl \rightarrow StCl(s)+H \quad (1)$$
$$StCl(s)+Cl \rightarrow Cl_2+StSA(s) \quad (2)$$
$$StCl(s)+Hg \rightarrow StSA(s)+HgCl \quad (3)$$

There are two types of carbon sites in the mechanism: StSA(s) denotes an unoccupied site and StCl(s) denotes a chlorinated site. Unoccupied sites may be chlorinated by deposition of HCl with release of H-atoms into the gas phase, according to eq. 1. Chlorinated sites are freed either by recombination with a Cl-atom, to generate Cl_2 vapor (eq. 2), or by partial oxidation of Hg into HgCl on a chlorinated site (eq. 3). Competitive adsorption and chemistry among many other exhaust species, particularly SO_X and NO_X, were omitted for lack of kinetic information.

The proposed heterogeneous chemistry is restricted to only the carbon in the flyash. That is, in the simulations, the surface areas for heterogeneous chemistry are based on a mean size for only the suspended UBC in the entrained ash. Inorganic components of the ash do not participate. This premise would be unable to depict the distinctive Hg oxidation behavior of flyashes with elevated levels of iron oxides[17,18] or, perhaps, from subbituminous coals with high Ca levels[19]. Calcium compounds can be chlorinated by HCl adsorption[20].

As seen in Table 1, adding the heterogeneous submechanism rectified the problems in the predictions from the homogeneous mechanism alone. The improved performance reflects the much more robust activity of a chlorinated carbon surface, compared to Cl-atoms. The surface is chlorinated by HCl, the most abundant Cl-species in coal-derived exhausts, and the large storage capacity of carbon for Cl ensures that a source of Cl will be present to oxidize Hg over a broad temperature range, so initiation is not problematic.

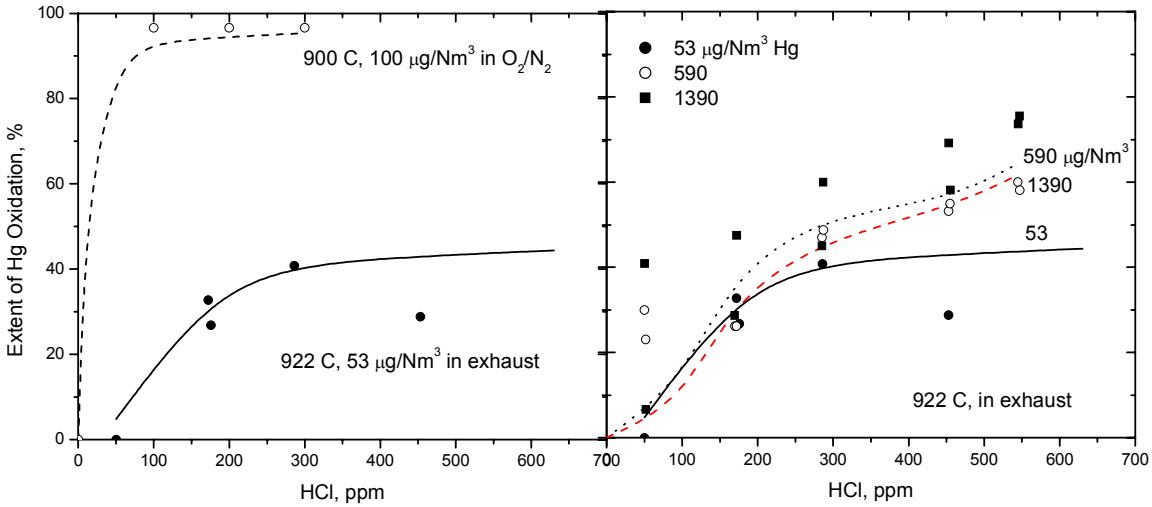

Figure 2. (Left) Comparison between extents of Hg oxidation in the absence (○) and presence (●) of water and NO; and (Right) extents of Hg oxidation for various Hg levels in exhaust prepared from natural gas combustion.

Table 1. Evaluation with flue gases from lab-scale flames.

Coal	Measured Oxidation, %	Predicted Homo/Hetero, %
A	22.8	40.2
B	48.7	42.2
C	27.5	29.6
D	93.2	71.2
E	46.5	27.6

Super-equilibrium levels of Cl-atoms are no longer necessary, so Hg is predicted to oxidize for systems with realistic quench rates. The predicted concentrations of both Cl- atoms and Cl_2were almost an order of magnitude lower than with the homogeneous mechanism only. The combined mechanism also predicted a surge in the extent of oxidation across the UBC in a final filter in the lab-scale exhaust system, consistent with the behavior in baghouse filtercakes. Most important, the predicted extents of Hg oxidation for the longest residence times were not excessive, and the complete mechanism identified the distinctive behavior of the coal with the highest Cl-content (Coal D). In addition, recent studies with x-ray absorption fine structure spectroscopy revealed Hg-Cl bonds on carbon surfaces after sorption by either Hg^0 or Hg^{2+} in synthetic flue gases that contained moisture, SO_2, and HCl[21]. Also, HCl does adsorb onto carbon at low temperatures, although the only data we found so far[22] are for activated carbon fibers with no structural similarities to UBC from a coal-fired furnace.

Input Data Requirements. The input data needed to characterize Hg oxidation in coal-derived exhausts with these mechanisms are as follows: The fuel properties consist of a proximate analysis and an ultimate analysis expanded with the Hg- and Cl-contents. The heating value is also needed whenever a furnace rating and S. R. value are used to estimate the exhaust composition leaving the economizer. Alternatively, total coal and air flowrates will also specify the moisture and CO_2 levels in the exhaust. Measured exhaust O_2 levels are much better than estimates. Complete emissions levels are required, including HCl, CO, NO_X, and SO_X. Measured values of HCl are much more reliable than estimates, due to the uncertainties on coal-Cl levels. The partitioning of flyash among bottom ash, economizer ash, and flyash is required, along with LOI data on the flyash. UBC properties (size, total surface area) are used in the analysis, but can usually be estimated from characterization data in the literature.

The essential operating conditions consist of the configuration of all unit operations in the system, and the time-temperature history from the economizer outlet to the stack. It is best to formulate a time-temperature history with temperatures at the inlet and outlet to each unit, and the nominal residence times (which can be estimated from total gas flows and unit cross sections). Finer resolution within the air heater is helpful but not usually available.

Results

Validation With a 1.0 MW_t Pilot-Scale Furnace. Mercury speciation was monitored in Southern Research Institute's Combustion Research Facility (CRF)[23]. The CRF consists of fuel handling and feeding systems, a vertical refractory lined furnace with a single up-fired burner, a horizontal convective pass, several heat exchangers in series and a baghouse filter. Emissions from this system have been qualified against those from full-scale, tangential-fired furnaces for the operating conditions imposed in this work[24]. The 8.5 m by 1.07 m (i.d.) cylindrical furnace handles gas velocities from 3 to 6 m/s, and residence times from 1.3 to 2.5 s. The nominal firing rate is 1.0 MWt, which was fixed for all cases. A single burner generates a core of pulverized fuel and primary air surrounded by weakly swirled secondary air. Overfire air (OFA) was injected through 4 off-radius ports located 4.6 m down the furnace. The gas temperature history along the exhaust system compares very well with the histories assigned from temperature profiling on full-scale systems.

Mercury speciation was monitored with a PS Analytical Hg detector using samples extracted from the flue gases with an Apogee Scientific QSIS probe. Two sampling positions were used to monitor the speciation at 163 and 280°C. In addition, all major flue gas species were measured, including HCl, SO_2, CO_2, CO, NO_X, SO_X, and O_2. Both LOI and UBC levels were determined for the flyash. LOI was used in all calculations, for consistency with the other evaluations with data completed to date. The test procedures are more completely described elsewhere[23].

Table 2. Evaluation with flue gas from a 1.0 MW_t furnace.

Coal	Coal-Cl, daf wt. %	LOI, wt. %	Hg Oxidation, %	
			Pred.	Mes'd
Bit. #1	0.010	4.8	74.8	76.0
Bit. #1/H_2O	0.010	4.8	72.0	63.0
Bit. #2	0.013	4.2	50.0	52.0
PRB	0.013	0.2	18.9	18.7
PRB	0.013	0.2	29.0	30.0

Two test series are included in the model validations. The baseline firing conditions were imposed on three coals, including two Eastern bituminous and a PRB subbituminous. Steam injection into the burner was applied with one of the bituminous coals. In the second test series with PRB, Cl_2 was injected at two concentrations where the flue gases were at 573°C, upstream of the heat exchangers. It is important to realize that the test conditions were directly imposed in all simulations, and none of the model parameters were adjusted in any of these cases. The characteristics of UBC in the simulations were specified from the reported LOI levels and characterization data in the literature. For cases with LOI levels under 1 %, the nominal UBC size was adjusted downward for consistency with char burnout predictions. Otherwise, the reported flue gas composition and exhaust thermal history were imposed without modification.

As seen in Table 2, the predictions are remarkably accurate for all three coals. Both bituminous coals have substantially higher extents of Hg oxidation than the PRB, as expected. But Bit. #1 also has significantly more oxidized Hg than Bit. #2 despite similar coal-Cl and LOI levels. Both bituminous coals had unusually low Cl-levels which were either equal or below the PRB's so, clearly, coal-Cl is not the determining factor in Hg oxidation. The mechanism depicts the large variations due to coal quality within experimental uncertainty throughout, based primarily on the substantial variations in the LOI levels. The impact of steam injection is also evident in the predictions, albeit only qualitatively.

To simulate cases with Cl_2 injection on PRB-derived flue gas, Cl_2 concentrations of 9, 17, and 69 ppm were instantaneously imposed in the simulations at the point where the exhaust temperature was 573°C. In all cases, the predicted extent of Hg oxidation at the injection position was zero. However, Hg was predicted to oxidize immediately thereafter. As seen in Fig. 3, the predicted extents of Hg oxidation are essentially within the ranges assigned from the tests (as indicated by the error bars) for the whole coal (at 0.9ppm Cl_2) and for both cases with Cl_2 injection. The slight overpredictions for both of the tested Cl_2 levels are expected from the omission of finite-rate mixing, which could easily be rectified. Insufficient data is available to validate the predicted saturation for high Cl_2 levels.

Predictions for Coal-Fired Utility Exhaust Systems. The complete Hg oxidation mechanism was used to simulate various fuel and exhaust properties under typical operating conditions. The baseline fuel is an eastern high volatile bituminous coal with 0.1 ppm Hg and 100 ppm Cl. The overall stoichiometric ratio for the furnace was 1.19. As seen in Fig. 4, variations in both coal-Cl and coal-Hg are most important for the low end of either range, then these effects saturate at the highest levels that arise in practical applications. For these particular simulation conditions, coal-Cl becomes unimportant for levels above 0.15 wt. %, which is near the upper limit on typical coal-Cl levels. Whereas the predicted extents of Hg oxidation become more sensitive for progressively lower coal-Cl levels, they

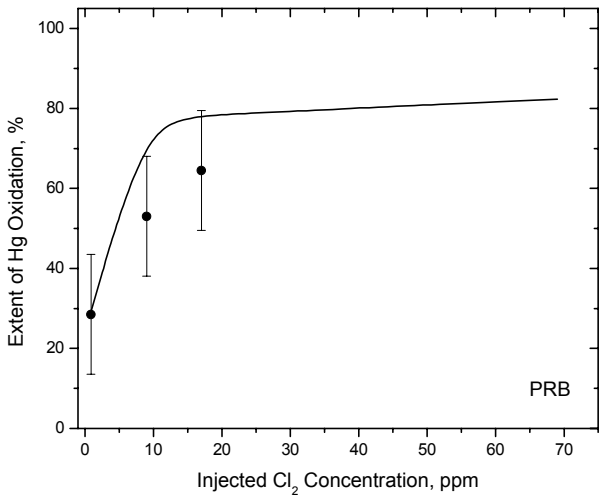

Figure 3. Evaluation of predicted extents of Hg oxidation with Cl_2 injection.

do not vanish until, strictly speaking, all Cl has been eliminated from the reaction system. Cases with 0.001, 0.005, and 0.02 % coal-Cl correspond to exhaust HCl concentrations of 0.6, 2.8, and 11.2 ppm. The predicted extents of Hg oxidation for these respective cases increase from 67 to 71 to 82 %, a net change of 15 %.

The impact of variations in coal-Hg appears to cover a similar range in Fig. 4 but, in fact, the plotted range of coal-Hg values is greater than the actual range of reported values. It is extremely unusual to find coal-Hg values greater than 0.2 ppm, or less than 0.05 ppm. Within this restricted range of coal-Hg, this parameter is a relatively weak influence on the extent of Hg oxidation.

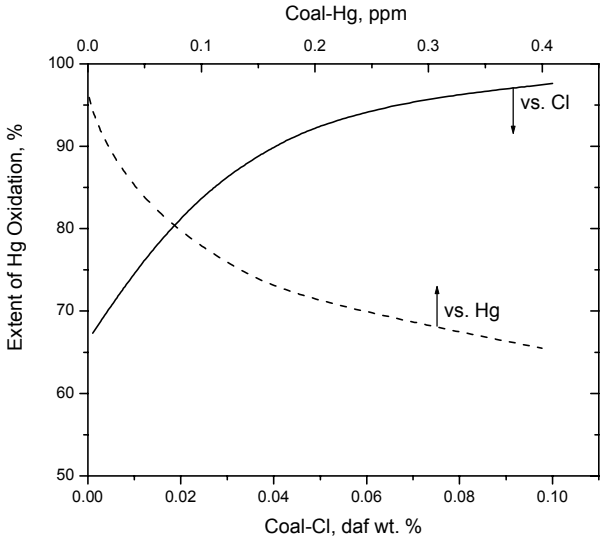

Figure 4. Predicted sensitivities to coal-Cl (solid curve) and coal-Hg (dashed curve) for baseline conditions with hv bit coal.

The strongest impact of all is seen with variations in the UBC level, which appears in Fig. 5. As the UBC was increased from 0.1 to 7 wt. %, the predicted extents of Hg oxidation increased from 5 to 90 %. Indeed, the single most important reason for the extensive Hg oxidation in the flue gases from hv bit coals is their relatively high UBC levels. The variation with the mean UBC size is due to the role

of UBC surface area in the oxidation mechanism. Based on detailed characterization studies of the characteristics of UBC from p. f. flames[25], we expect the UBC size to be significantly larger than the size of the coal feed, unless LOI is less than 1 wt. %.

The predicted impact of variations in exhaust O_2 and NO indicated that both factors are among the least important in this reaction system, provided that all else remains the same. In practice, variations in both O_2 and NO are almost always associated with substantial changes to UBC levels. But at a fixed UBC level, variations in O_2 levels are usually inconsequential, and variations in NO levels are only important for levels below 200 ppm, which are rarely encountered with large-scale flames.

Predictions for variable quench rates were prepared for ± 30 % variations around the mean quench rate. The predicted extents of Hg oxidation increase for slower quench rates in this range, from 59 % with fast quenching to 74.8 % for the baseline quench rate to 93.5 % for the slowest quench rate. So the time-temperature histories across the exhaust system must be specified within fairly close tolerances.

Summary

A heterogeneous reaction mechanism is needed to initiate Hg oxidation under utility exhaust conditions, and also to sustain the partial oxidation of Hg into HgCl. The heterogeneous Hg mechanism described here represents the chlorination of carbon in the ash by HCl, with subsequent recombination of Cl-atoms and partial oxidation of Hg into HgCl on the chlorinated sites. In conjunction with the original homogeneous reaction mechanism, it depicts the observed coal quality impacts in the exhausts from lab- and pilot-scale flames within useful quantitative tolerances without heuristic adjustments to the kinetic parameters or operating conditions.

The same homogeneous mechanism previously interpreted all the available datasets on Hg oxidation in synthetic exhausts, without particulates. But when the homogeneous reaction mechanism was applied to the conditions in the exhaust systems of coal-fired furnaces, where quench rates are much slower, several problems surfaced. Without rapid quenching, Cl-atom concentrations usually remained below the threshold for initiation of Hg oxidation. And in cases with appreciable Hg oxidation, the oxidation persisted through the lowest temperatures in the simulations, because the rate of Cl-atom recombination is slow. In the evaluation with the lab-scale coal flame data, this problem became apparent as essentially complete Hg oxidation for the longest residence times with four of the five coals, which was contradicted by the data and by the reported coal quality impacts.

Adding the heterogeneous submechanism rectified these problems by supplanting Cl-atoms with a chlorinated carbon surface. The surface is chlorinated by HCl, the most abundant Cl-species in coal-derived exhausts, and the large storage capacity of carbon for Cl ensures that a source of Cl will be present to oxidize Hg over a broad temperature range, so initiation is not problematic. Super-equilibrium levels of Cl-atoms are no longer necessary, so Hg is predicted to oxidize for systems with realistic quench rates. The predicted concentrations of both Cl-atoms and Cl_2 were almost an order of magnitude lower than with the homogeneous mechanism only.

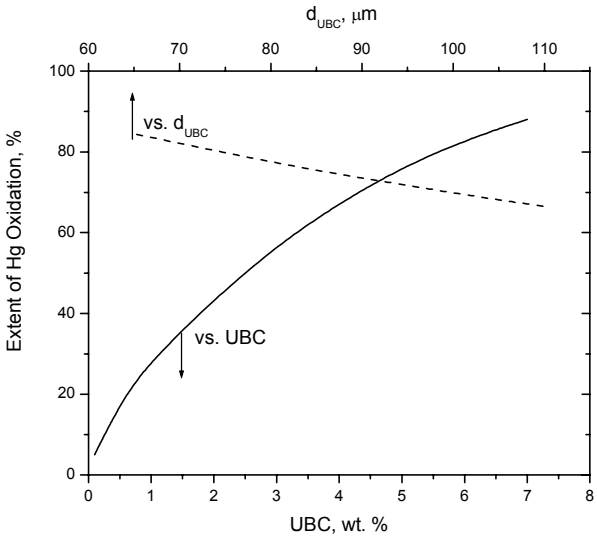

Figure 5. Predicted sensitivities to the level (solid curve) and mean size (dashed curve) of UBC for baseline conditions with hv bit coal.

Adding the heterogeneous submechanism also provides the basis for a truly predictive capability, and interprets some of the more perplexing aspects of Hg oxidation seen in full-scale test data. In the CRF datasets, the reported extents of Hg oxidation ranged from 20 to 75 % even though the coal-Cl contents were essentially uniform. Whereas this broad range is similar to the large spread seen in the ICR database for similar coal-Cl contents, it is even more compelling because strictly the same firing conditions were imposed on all coal types and all relevant operating conditions were accurately recorded. The complete mechanism depicts these variations within experimental uncertainty without any parameter adjustments, and also identifies LOI variations as their predominant underlying cause. From a practical standpoint, this finding implies that high LOI levels will compensate for low coal-Cl and vice versa. Hence, subbituminous coals exhibit the lowest extents of Hg oxidation whenever both their Cl-contents and LOI levels are very low, as with the PRB in the CRF tests. Indeed, simply spiking the PRB-derived flue gases with Cl_2 almost completely oxidized the Hg even while the LOI remained very low. Our mechanism quantitatively interpreted this behavior, which paves the way for an important supporting role for modeling in the development of more effective Hg control processes. Evaluations of the mechanism with data from full-scale tests are already underway.

Acknowledgement. This study was partially sponsored by the New Energy Development Organization's (NEDO) Clean Coal Technology Center under the Toxic Metals Project, and administered by the Coal Research Laboratory, Idemitsu Kosan Company, Ltd. Supplemental funding to interpret the CRF datasets was provided by Southern Research Institute under their EPRI-sponsored "Mercury Chemistry" project.

References

(1) Chu, P.; Behrens, G.; Laudal, D., Proc. U. S. EPA-DOE-EPRI Combined Power Plant Air Pollutant Control Symp.: The Mega Symp. and AWMA Specialty Conf. on Mercury Emissions: Fate, Effects, and Control, 2001, Chicago, IL, Aug. 21-23.

(2) Afonso, R.; Senior, C., Proc. U. S. EPA-DOE-EPRI Combined Power Plant Air Pollutant Control Symp.: The Mega Symp. and AWMA Specialty Conf. on Mercury Emissions: Fate, Effects, and Control, 2001, Chicago, IL, Aug. 21-23.

(3) Berkenpas, M. B.; Rubin, E. S.; Smith, D. N.; Gibbon, G. A.. Proc. U. S. EPA-DOE-EPRI Combined Power Plant Air Pollutant Control Symp.: The Mega Symp. and AWMA Specialty Conf. on Mercury Emissions: Fate, Effects, and Control, 2001, Chicago, IL, Aug. 21-23.

(4) Weilert, C. V.; Randall, D. W., Proc. U. S. EPA-DOE-EPRI Combined Power Plant Air Pollutant Control Symp.: The Mega Symp. and AWMA Specialty Conf. on Mercury Emissions: Fate, Effects, and Control, 2001, Chicago, IL, Aug. 21-23.

(5) Widmer, N.C.; West, J.; Cole, J.A., Proc. A&WMA Annual Conf., 2000, Salt Lake City, AWMA, Pittsburgh.

(6) Sliger, R. N.; Kramlich, J. C.; Marinov, N. M., Fuel Process. Technol. 2000, 65-66(0), 423-438.

(7) Niksa, S.; Helble, J. J.; Fujiwara, N., Environ. Sci. Technol. 2001, 35, 3701-3706.

(8) Niksa, S.; Fujiwara, N.; Fujita, Y.; Tomura, K.; Moritomi, H.; Tuji, T.; Takasu, S., J. A&WMA 2002, 52(8):894-901.

(9) Edwards, J. R.; Srivastava, R. K.; Lee, C. W.; Kilgroe, J. D.; Ghorishi, S. B., Proc. U. S. EPA-DOE-EPRI Combined Power Plant Air Pollutant Control Symp.: The Mega Symp. and AWMA Specialty Conf. on Mercury Emissions: Fate, Effects, and Control, 2001, Chicago, IL, Aug. 21-23.

(10) Qiu, J.; Helble, J. J., "Development of an Improved Model for Determining the Effects of SO_2 on Homogeneous Hg Oxidation," 28th Int. Technical Conf. on Coal Utilization and Fuel Systems, 2003, Coal Technology Assoc., Clearwater, Fl, March.

(11) Sjostrom. S.; Ebner, T.; Ley, T.; Slye, R.; Richardson, C.; Machalek, T.; Richardson, M.; Chang, R., J. A&WMA 2002, 52, 902-911.

(12) DeVito, M. S.; Rosenhoover, W. A.; Proc. A&WMA Annual Conf. 1999, St. Louis, AWMA, Pittsburgh, Paper No. 99-33.

(13) Widmer, N. C.; Cole, J. A.; Seeker, W. R.; Gaspar, J. A. Combust. Sci. Tech. 1998, 134, 315-326.

(14) Hall, B.; Schager, P.; Lindqvist, O. Water, Air, and Soil Pollution 1991, 56, 3-14.

(15) Mamani-Paco, R. M.; Helble, J. J. Proc. A&WMA Annual Conf., 2000, Salt Lake City, AWMA, Pittsburgh.

(16) Fujiwara, N.; Fujita, Y.; Tomura, K.; Moritomi, H.; Tuji, T.; Takasu, S.; Niksa, S., Fuel, 2002, 81(16):2045-52.

(17) Norton, G. A.; Yang, H.; Brown, R. C.; Laudal, D. L.; Dunham, G. E.; and Okoh, J. M., Proc. A&WMA Annual Conf. 2000, Salt Lake City, AWMA, Pittsburgh, Paper No. 00-167.

(18) Lee, C. W.; Kilgroe, J. D.; and Ghorishi, S. B., Sixth Annual Waste-to-Energy Conf. 1998, p. 221-238.

(19) Carey, T. R.; Hargrove, O. W.; Richardson, C. F.; Chang, R.; and Meserole, F. B., Proc. A&WMA Annual Conf. 1997, AWMA, Pittsburgh, Paper No. 97-WP72A.05.

(20) Ghorishi, B.; Gullett, B. K.; Jozewicz, W.; and Kozlowski, W., EPRI-DOE-EPA Combined Utility Air Pollution Control Symposium: The MEGA Symp. 1999, EPRI, p. 19-59.

(21) Huggins, F. E.; Huffman, G. P., Energy Fuels 1999, 13(1):114.

(22) Mangun, C. L.; Benak, K. R.; Economy, J.; and Foster, K. L., Carbon 2001, 39:1809-1820.

(23) Gale, T.; Cushing, K., EPRI-DOE-EPA-A&WMA Combined Utility Air Pollution Control Symposium: The MEGA Symp. 2003, EPRI, to appear.

(24) Monroe, L. S. et al., EPRI-DOE-EPA Combined Utility Air Pollution Control Symposium: The MEGA Symp. 1995, Book 3, EPRI, Palo Alto, CA.

(25) Hurt, R. H.; and Gibbins, J. R., Fuel 1995, 74(4):471-480.

Evaluation of Mercury Stability in Ontario Hydro Method Solutions for Mercury Speciation in Flue Gas Generated from Coal-Fired Stationary Sources

Jenny Q. Sun, Karen S. Uhrich and Richard L. Schulz

Energy & Environmental Research Center
University of North Dakota
PO Box 9018
Grand Forks, North Dakota 58202-9018

Abstract

In 1994, the Ontario Hydro (OH) mercury speciation sampling method began development and eventual validation. This method, initially proposed by Dr. Keith Curtis of Ontario Hydro, was shown to provide reliable mercury speciation results. As a result, a draft American Society for Testing and Materials (ASTM) method was issued in 1998(1).

The stability of mercury in the OH solutions depends on the various reagents added into solutions during the breakdown. The amount of these reagents is not stated very clearly in the method, rather it depends on experienced people performing the breakdown. This would result in the variation of the sample solution conditions and subsequently affect the mercury stability. The research presented here addresses some of these concerns.

Background

The 1990 Clean Air Act Amendments (CAAAs) required the U.S. Environmental Protection Agency (EPA) to determine whether the presence of mercury in the stack emissions from fossil fuel-fired electric utility power plants poses an unacceptable public health risk. EPA's conclusions and recommendations were presented in the *Mercury Study Report to Congress* and *Utility Air Toxics Report to Congress* (2). The first report addressed both the human health and environmental effects of anthropogenic mercury emissions, while the second addressed the risk to public health posed by the emission of mercury and other hazardous air pollutants from steam electric-generating units. Although these reports did not state that mercury controls on coal-fired electric power stations would be required, they did indicate that EPA views mercury as a potential threat to human health. Therefore, it was concluded that mercury controls at some point might be necessary. EPA also indicated that additional research information was necessary before any definitive statement could be made. In an effort to determine the amount and types of mercury being emitted into the atmosphere by coal-fired power plants, EPA issued an information collection request (ICR) in late 1998. In addition to requiring all coal-fired power plants to measure and report their coal mercury concentrations, 80 power stations were required to measure the speciated mercury concentration in the flue gas. The method chosen by EPA for measuring speciated mercury in the stack gas was the Ontario Hydro (OH) mercury speciation method.

Beginning in 1994, the Energy & Environmental Research Center (EERC), with funding from EPRI and the U.S. Department of Energy, helped to develop and eventually validate the OH mercury speciation sampling method. Initially, the method was only used by research organizations with highly trained people. However, when EPA issued the ICR a number of sampling organizations and laboratories with varying degrees of training and experience began using this method. It is clear that if this method is going to be used on a regular basis, understanding of each step of this method rather than personal experience or interpretation of the method is imperative.

The OH method (Figure 1) consists of three KCl solution impingers, one HNO_3–H_2O_2 solution impinger, three $KMnO_4$–H_2SO_4 solution impingers, and a silica gel desiccant in sequence. The coal combustion flue gas passes through KCl first, then H_2O_2, and finally $KMnO_4$. The oxidized mercury presumably will be trapped in the KCl solution, and the elemental mercury will be trapped in the $KMnO_4$ solution. The mercury trapped in the H_2O_2 solution is considered elemental mercury and will be added to the mercury portion from $KMnO_4$ in the final calculation. The saturated $KMnO_4$ (about 5%) solution was added to the KCl during the breakdown to remove SO_2 by the reaction between $KMnO_4$ and SO_2. The method states that the purple color should remain for at least 15 minutes. In the initial design of OH method, hydrochloric acid was added at the end of break-down to rinse off the KCl and $KMnO_4$ impingers preserving the mercury in sample solutions. This step released chlorine gas due to the reaction between HCl and $KMnO_4$, and chlorine is considered hazardous to the operators. A later-modified procedure calls for 10% hydroxylamine solution to replace the hydrochloric acid. This approach eliminated the chlorine gas problem; however, it also reduced the acidity of KCl solution and chloride concentration in $KMnO_4$.

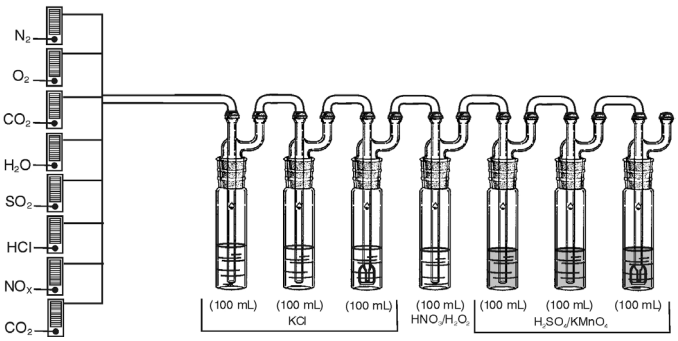

Figure 1. OH method impinger train.

The OH method results could be used directly to evaluate the mercury species at the sampling points and compare or confirm the continuous emission monitor's (CEM) performance. In either case, accurate results are crucial for the researchers to make subsequent decisions or justifications of the following work. When field crews were equipped with a cold-vapor atomic absorption (CVAA) mercury analyzer on-site, the samples could be analyzed shortly after the samples were collected. In some cases, the samples were analyzed on-site, and some duplicates had to be sent to another lab for analysis as a mean of quality assurance/quality control. When the CVAA analyzer has not been available on-site, the collected samples have to be sent to another lab for analysis. The delivery can take several days or even weeks because the samples are considered hazardous material and must be shipped on the ground. The stability of mercury in these solutions becomes a concern as the results show bias low or a faded purple color of the solution. The maximum holding time for each kind of solution has not been addressed in the method.

The following questions outline the concerns regarding the stability of mercury in OH method solutions:

- It is well known that mercury is very stable in the solutions where chloride is present and the solution is acidic. Mercury in 10% hydrochloric acid could last for years

without degrading. In general, after the breakdown, the KCl solution would have a low pH value because of the acid gases in the flue gas dissolved in the KCl solution and the additional 10% nitric acid added. The problem is that most of time the amount of 10% nitric acid was limited by the significant amount of water from the flue gas moisture during the sampling period and the amount of hose-rinsing water. Both have to be combined with the KCl solution in the final volume (500mL). To avoid overflowing, operators have to reduce the amount of 10% nitric acid. By doing so, will the stability of mercury in solution be compromised? A minimum amount of 10% nitric acid should be established to ensure mercury is maintained in the solution under any sampling process.

- According to the method, the $KMnO_4$ solution should be added to the KCl solution during the breakdown until the purple color persists for 15 minutes to neutralize any SO_2 that may be dissolved in the KCl solution. Since "purple" is not a clear-cut value for the oxidizing strength measurement, how much purple has to be provided to sustain mercury and prevent the slow reaction between SO_2 and $KMnO_4$ afterwards? If the color becomes brown or pink instead of purple, is it an indication of solution degrading and mercury disappearing?
- When samples need to be shipped after the breakdown, the samples are usually treated without further reducing the $KMnO_4$, assuming that $KMnO_4$ preserves the mercury in solution. This raises two issues: first, it costs much more for shipping and handing because $KMnO_4$ is considered an oxidizer and explosive hazardous material and, second, it is not known whether $KMnO_4$ or other components preserve the mercury. Which components in the solution are crucial for mercury preservation? In which solution is mercury more stable, in non-reduced or reduced solution*?*

Two solutions, KCl and $KMnO_4$, will be evaluated here since more than 95% of mercury is trapped in these two solutions.

Experimental

Table 1 summarizes the simulated flue gas conditions for generating OH method blank solutions for further spiking tests. Simulated flue gas component concentrations were chosen to represent high- and low-sulfur coals combusted in U.S. power plants. Moisture was not used in these tests since it is irrelevant to this study.

Table 1. Simulated flue gas component concentrations

	O_2	CO_2	SO_2	HCl	NO_2	NO
high sulfur coal	6%	12%	2500ppm	50ppm	15ppm	300ppm
low sulfur coal	6%	12%	200ppm	50ppm	15ppm	300ppm

After the simulated flue gas passed through the impingers for 1 hour, the solutions were transferred to 500-mL volumetric flasks. The mercury was spiked into the volumetric flask. The solutions were treated under controlled conditions that are summarized in Table 2.

A schematic of the bench-scale testing system and the impinger train used in this study is shown in Figure 1. All tests were sampled at a total flow rate of 30 standard cubic feet per hour (scfh) for a period of 1 hr. All of the components of the simulated flue gas were generated from a compressed cylinder. As shown in Figure 1, the gas flow was controlled by a mass flow controller and passed through a heated gas manifold to the OH method train.

All of the samples generated were analyzed by a CETAC M6000A CVAA spectrometer at wavelength 254 nm.

All of the chemical reagents used in this study were analytical grade.

Table 2. Preserving Conditions

Test for KCl portion	high sulfur				low sulfur			
	1	2	3	4	1	2	3	4
add $KMnO_4$ barely enough	x				x			
add $KMnO_4$ barerly enough+ additional 5mL						x		
add $KMnO_4$ barerly enough+ additional 10mL			x				x	
No 10% HNO_3 rinse only $KMnO_4$ -15mL				x				x

Test for $KMnO_4$ portion	high sulfur				low sulfur			
	1	2	3	4	1	2	3	4
2-3 mL of hydroxylamine chloride	x				x			
2-3 mL of hydroxylamine chloride		x				x		
2-3 mL of hydroxylamine chloride			x				x	
no hydroxylamine chloride added				x				x

Results and Discussion

To evaluate the effect of SO_2 on mercury stability in OH method solutions, simulated high- and low-sulfur coal flue gases were used for comparison. Comparing the mercury reading over the 2 weeks of low and high SO_2 under the condition of without adding any 10% HNO_3 during the breakdown, the mercury in the low-SO_2 KCl solution started to decrease after 22 hours but not in the high-SO_2 KCl solution. It indicates that the high concentration of SO_2 in flue gas might lowers the pH of the KCl solution to an adequate level to preserve mercury without additional 10% HNO_3. However, it should be pointed out that, because SO_2 in flue gas can only be estimated, the minimum quantity of 10% HNO_3 for 500 mL KCl solution should be established to sustain mercury.
50 mL of 10% nitric acid, based on the results from this experiment, can be used as a guideline.

To determine the stability of mercury in both reduced and non-reduced solutions, the samples were split into two portions after mercury had been spiked. One portion was kept as is, and the other portion was reduced 1 hr after sampling by either hydroxylamine chloride or hydroxylamine sulfate addition until the solution was colorless. The results from both high- and low-SO_2 concentration tests show that there is no mercury degradation on the reduced solution portion. This means the samples are not considered hazardous materials. This could considerably reduce the cost of shipping and make it much easier for handling the solutions as well. These tests proved that mercury could be preserved well after the $KMnO_4$ in solutions had been reduced, as long as the sample was properly treated beforehand. The other motivation for promoting the sample's reduction is that without the $KMnO_4$ in the solutions, the sample solutions do not let off chlorine gas, which is harmful for the operators.

It was noticed that there were some color changes in the KCl solutions when $KMnO_4$ was added, leaving little purple. The purple color disappeared after 1 day and a brown fluffy precipitate formed. The mercury readings for the period over 3 weeks in these bottles show no significant difference from those with more $KMnO_4$. This suggests that excess amounts of $KMnO_4$ may not be necessary during the breakdown.

Conclusions

- It should be stated clearly in the OH method that hydroxylamine chloride has to be used for $KMnO_4$–H_2SO_4 solution rather than any kind of hydroxylamine because mercury can be given off as a gas after $KMnO_4$ is reduced without the presence of chloride in solution. Even though the method calls for few drops of hydroxylamine chloride solution during the breakdown, it still provides some degree of preservation for mercury. 2–3 mL hydroxylamine chloride was used in this experiment, and the result showed this is an adequate amount for stabilizing mercury in the $KMnO_4$ solution.
- The acidity of the KCl solution is very crucial for mercury preservation, especially when low-sulfur coal is burned. Even with the $KMnO_4$ added to the solution, the amount of 10% nitric acid should be no less than 50 mL for 500 mL of KCl solution.
- When samples are treated properly during breakdown, they can be reduced to a colorless solution afterward to avoid the difficulty of storage, shipping, or handling without jeopardizing the mercury stability.

References

ASTM D 6784-02 Standard Test Method for Elemental, Oxidized, Particle-Bound and Total Mercury in Flue Gas Generated from Coal-fired Stationary Source (OH Method)

(1) Hunt, J. E.; Winans, R. E.; Ahrens, M.; and Xu, L. Prepr. Pap. - *Am. Chem. Soc., Div. Fuel Chem.*, **1999**, *44* (3), 610.

(2) Beck, J. S.; Vartuli, J. C.; Roth, W. J.; Leonowicz, M. E.; Kresge, C. T.; Schmitt, K. D.; Chu, C. T-W.; Olson, D. H.; Sheppard, E. W.; McCullen, J. B.; Higgins, J. B.; Schlenker, J. L. *J. Am. Chem. Soc*. **1992**, *114*, 10834.

(3) Winans, R. E. In *Advances in Coal Spectroscopy*; Meuzelaar, H.L.C, Ed.; Plenum Press: New York, 1992; pp. 255-274.

Mercury combustion chemistry resolved: A new mitigation approach

Keith Schofield

Materials Research Laboratory, University of California, Santa Barbara, CA 93106

Introduction

Trace levels of mercury compounds in any high temperature process volatize as elemental atomic mercury. This is unreactive in the gas phase and is largely exhausted as atoms into the atmosphere. Its emissions are difficult to control, as absorbers and other methods are not very effective at retaining the atoms of its very volatile condensed liquid phase. This behavior stems from the somewhat unique chemistry of mercury. In the gas phase it displays mainly very weakly bound molecules such as its oxide, hydroxide and monohalides. Its only stable gaseous molecule of significance in combustion is mercuric dichloride. This is exceptional having a first bond strength of about 360 kJ/mol. However, at high temperatures, although thermodynamically favored, the formation is kinetically restricted and no direct channels exist. The intermediates that would be necessary for its formation are not stable. Nevertheless, what is observed in practice is that a small fraction of the mercury in exhaust gases is present as the dichloride. This and the atomic mercury appear to constitute the elements mass balance. Extensive kinetic modeling studies have failed to satisfactorily explain this occurrence and generally have concluded that the chemistry is more complex[1,2] . Although numerous experiments have endeavored to find a correlation between this fractional degree of conversion and some operational parameter, nothing has emerged. The data are inconsistent and there is no satisfactory explanation why the ratio varies, is unpredictable, and how the conversion occurs. The very important practical aspect of such a conversion is that whereas atomic mercury emissions are difficult to control, the dichloride is readily soluble in water.

Because the chemistry of mercury starts in the high temperature gases and ends in the exhaust gas phase it has always been considered a gas phase phenomenon. Moreover, condensed phase mercury is a very volatile liquid. In the exhaust gases from coal combustors the traces of mercury are on a parts per billion by volume scale implying that conditions will always be above the dew point. Condensation of mercury would appear to be out of the question. As a result, the combustion chemistry of mercury has always been limited to considering a dominance of gas phase reactions.

In previous studies in this laboratory it was found that if sodium and sulfur are present in flame gases at very low levels (ppmv) that sodium sulfate forms very efficiently not in the flame gases themselves but on a cooled surface intercepting the flows[3,4]. The reduced dimensionality of the surface facilitates the process as well as changing the chemistry from the gas phase to the condensed phase regime. Moreover this chemistry is dominated by the surface, utilizing the gases solely as a source of ingredients and also disregards any concepts of dew point. Based on this background it was decided to run several test experiments with low levels of mercury in the burned flame gases and see if any deposition might occur on a cooled probe immersed in the exhaust. The very first experiment yielded an abundant yellowish deposit with a rate of deposition (atoms/s) essentially the same in magnitude to those collected in alkali sulfate[3,4] or carbonate deposit[5] experiments. Obviously mercury has a significant heterogeneous chemistry that has never been examined. This presentation outlines the results of this first quantitative examination of the nature of these deposits and determines the major controlling parameters in such systems.

Experimental

Flame Deposition Methods. A flat flame atmospheric pressure burner produces a one-dimensional cylindrical flame surrounded by an identical shielding flame. The inner flame is used as the experimental laminar plug flow medium containing the additives[4]. Propane, oxygen, nitrogen flames have been used over a range of fuel lean and rich equivalence ratios. Mercury is introduced into the inner flame unburned gas flow as a fine aqueous aerosol from an ultrasonic nebulizer. Solutions of mercuric nitrate or acetate at strengths of 0.008 to 0.05 N have been used and produce concentrations of atomic mercury in the burned gases of up to about 30 ppmv. Such levels produce deposition rates of several milligrams of mercury per hour. Differing flame concentrations are obtained by varying the solution strength. Small quantities of sulfur or chlorine also can be added using certified gas cylinder mixtures of 0.1% SO_2 in N_2, 514 ppmv Cl_2 in N_2, and 998 ppmv HCl in N_2. Calibrated electronic mass meters control all the gas flows.

Several cylindrical collection probes have been used. These are about 12 mm in diameter which is about the same size as the inner flame. They are of Inconel-600 stainless steel with a central channel for air or water-cooling. A thermocouple built into the wall thickness monitors surface temperature. One probe is tightly clad with a two-micron thick foil of platinum. A probe is held horizontally in the vertical flame burned gas flows and the burner raised or lowered to examine downstream location effects. Important additional experiments have utilized probes that can be internally heated. Also of Inconel stainless steel these have been useful in facilitating numerous experiments that more realistically simulate the cooler exhaust gas chemistry and also for measuring ablation rates of deposits with traces of different flowing reactive gases. The unheated probes have examined behavior at downstream times of about 5-15 ms whereas the heated probes were located at about 0.1 s downstream where the burned gases of these flames have cooled to about 200 ^oC. Probe temperatures have been in the range 55-400 ^oC.

Characterization Methods. A powerful combination of four analytical techniques has permitted an essentially total analysis of the observed deposition, erosion and conversion processes. A Nicolet Fourier Transform Raman Spectrometer has been used to obtain the Raman spectra of some deposits and their x-ray spectra also have been obtained on a Bruker High Temperature Powder X-Ray Diffractometer. Quantitative analyses have utilized a Thermo Jarrell Ash Inductively Coupled Plasma/Atomic Emission Spectrometer (ICP/AES). For this, deposits are dissolved off the probe with dilute nitric acid and can be analyzed for both their mercury and sulfur content. This provides for very accurate quantitative data. To assess the thermal stabilities of various mercury compounds, in particular mercuric oxide, sulfate and dichloride, a Mettler Thermogravimetric Analyzer has proven to be very useful.

Results

Figure 1 illustrates the Raman spectrum of the yellowish colored deposit obtained in the very first experiment on this system. It was collected 6 ms downstream in the burned gases of an oxygen rich $C_3H_8/O_2/N_2$ (0.9/5/16) flame that contained 25 ppmv Hg, 75 ppmv SO_2, and 50 ppmv Cl_2 in the unburned gas flows. The probe was cooled to 60 ^oC with water. It was collected in two hours indicating a significant collection efficiency (30%) which compares almost exactly with similar deposits of alkali sulfates and carbonates. The deposit was a uniform smooth powder layer. As seen from Figure 1 and the comparison with the spectra of purchased samples, the deposit appears to be essentially quite pure mercuric sulfate. A second identical experiment, but without the sulfur dioxide, also yielded a deposit but this time it was brown in color.

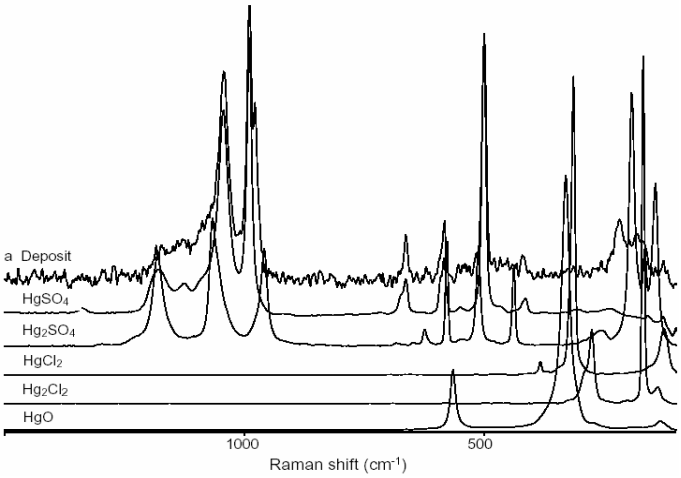

Figure 1. Raman spectrum of a flame generated deposit (a), compared to those of several purchased samples of pure anhydrous mercury compounds.

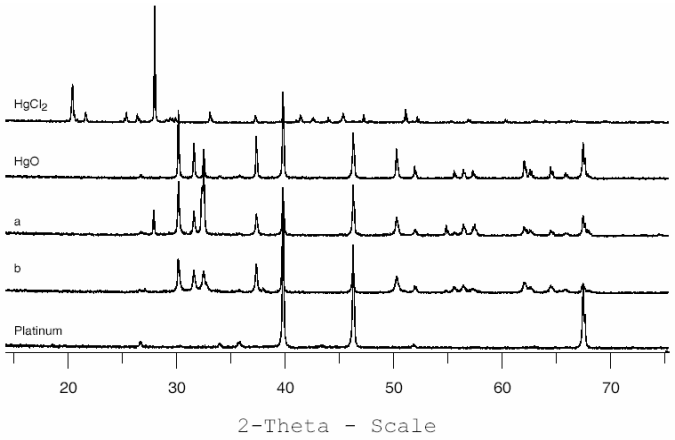

Figure 2. X-ray powder spectra of two flame deposits, (a) from a flame containing traces of mercury and chlorine, (b) from a similar flame but with no chlorine addition. These are compared to the spectra of purchased mercury compounds.

Its x-ray spectrum is indicated as trace a) in Fig. 2. A third experiment adding solely mercury to the flame gave a slightly larger also brown deposit. Its spectrum is trace b) in Fig. 2. Comparisons with other spectra clearly indicated that these deposits were mercuric oxide. However, trace a) also indicates the presence of a small contribution from mercuric dichloride. The lines of platinum present in these spectra result from scattering from the platinum strip substrate on which the samples are placed. These analyses were sufficient to indicate the heterogeneous chemistry of mercury and explain the formation mechanism of mercuric dichloride.

Consequently, as now confirmed by more than a hundred additional experiments, what happens in the exhaust gases is not as complicated as previously thought. The mercury on approaching the surface is rapidly converted to a molecular form. If sulfur is present then mercuric sulfate is produced. This is thermally stable up to about 550 ^{o}C. If the system is sulfur-free the mercury falls back to its second preference which is to form mercuric oxide. This is thermally stable to about 450 ^{o}C. Classical inorganic textbooks indicate that both of these can be vigorously attacked at temperatures above about 100 ^{o}C by chlorine and converted to mercuric dichloride. Serendipitously, solid mercuric dichloride is very volatile. It is labeled as a corrosive sublimate. Its vapor pressure is 10 torr at 180 ^{o}C, 50 at 230 ^{o}C, boiling at about 300 ^{o}C. As a result the mechanism is simple and elegant. Mercury deposits on any surface that the gases encounter, including ash particles, that have cooled sufficiently to permit the formation of the sulfate or oxide. This is then attacked in fact by hydrogen chloride that is the dominant chlorine source in burned gases. The deposit is converted to the dichloride, subliming back into the gas phase. The surface acts solely as a catalytic intermediate to facilitate the thermodynamic driving force for the formation of the very stable gaseous dichloride.

An examination of the condensed phase chemistry of molecular mercury indicates its rather limited extent. It does display two valences but consists mainly of its oxide, sulfate and halides. The carbonate, nitrates and sulfide are rather unstable and the hydride and hydroxide are not known. The results obtained herein display a preference for divalency and for sulfate over oxide. At higher temperatures there is an indication that the sulfate deposit becomes basic forming to some degree Schuetteite, $HgSO_4.2HgO$.

Deposits are obtained only under fuel lean conditions. Their rate of formation is first order in the mercury concentration and mercury is the dominant controlling species. This is evident in that sulfate and oxide deposition rates are the same. Deposition rates also are not sensitive to sulfur concentrations but do strongly depend upon the concentrations of chlorine in the flame gases. There is no evidence to support that the dichloride forms directly on the surface.

Experiments in cooler downstream locations (0.1s, 200 ^{o}C exhaust gas temperatures) have indicated, so far, a narrower formation temperature window than would be expected from the thermal stabilities of the sulfate and oxide. The lower formation threshold is about 150 ^{o}C, but the upper limit is only about 300 ^{o}C. This is being studied further but seems to result from competing reducing reactions that possibly arise from remaining trace levels of CO and/or H_2 in the exhaust gases from fuel lean combustion.

A New Emissions Mitigation Approach [6]

With this level of understanding of the emissions chemistry of mercury it now has been possible to develop a new method for its control. This is based on the concept of introducing a large surface area in the region of the cooling exhaust gases where the temperatures are optimal for mercury to deposit as the sulfate or oxide. The exhaust gases and hence mercury are made to encounter the surface numerous times during passage through this region. In this way an optimal conversion to dichloride can be achieved. The already present water scrubbers then can remove this.

Acknowledgement. This work made use of the MRL Central Facilities supported by the National Science Foundation under Award No. DMR00-80034.

References

(1) Niksa, S.; Fujiwara, N.; Fujita, Y.; Tomura, K.; Moritomi, H.; Tuji, T.; Takasu, S., *J Air &Waste Manage. Assoc.* **2002**, 52, 894- 901.
(2) Xu, M.; Qiao, Y.; Zheng, C.; Li, L.; Liu, J., *Combust Flame*, **2003**, 132, 208-218.
(3) Steinberg, M.; Schofield, K., *Twenty-Sixth Symposium (International) on Combustion,* The Combustion Institute, Pittsburgh, **1996**, 1835-1843.
(4) Schofield, K., *Combust. Flame*, **2003**,133, 147-156.
(5) Steinberg, M.; Schofield, K., *Combust. Flame*, **2002**, 129, 453-470.
(6) Schofield, K., U.S. Patent Application, May 1, 2003.

NICKEL SPECIATION OF URBAN PARTICULATE MATTER FROM DAVIE, FLORIDA

Kevin C. Galbreath,[1] Charlene R. Crocker,[1] Carolyn M. Nyberg,[1] Frank E. Huggins,[2] and Gerald P. Huffman[2]

[1]Energy & Environmental Research Center
University of North Dakota
15 North 23rd Street
Grand Forks, ND 58203

[2]CFFS/CME, University of Kentucky
105 Whalen Building
533 South Limestone Street
Lexington, KY 40506

Introduction

Nickel (Ni) from natural and anthropogenic sources pervades the environment. A significant natural source of atmospheric Ni is windborne dust particles derived from the weathering of rocks and soils and from volcanic eruptions.[1] Industrialization has increased its flux into the environment primarily through 1) combustion and incineration sources; 2) high-temperature metallurgical operations; 3) primary Ni production; and 4) chemical and catalyst manufacturing.[2, 3] The mobile source contribution to Ni emission inventories is small and derives primarily from engine wear and impurities in engine oil and fuel additives.[4] Commercial marine vessels are significant mobile sources of Ni in areas near harbors.[5]

Title III of the 1990 Clean Air Act Amendments (CAAA)[6] identifies 189 chemicals, including Ni, as potential hazardous air pollutants (HAPs). Many stationary sources have had to report Ni emissions as part of the U.S. Environmental Protection Agency's (EPA's) Toxics Release Inventory (TRI).[7] Although TRI and similar reporting provide estimates of the amounts of Ni released into the environment, they are not an indicator of toxicity because the acute, chronic, and cancer-causing effects vary significantly for the different chemical species of Ni. For example, nickel subsulfide (Ni_3S_2) is considered the most carcinogenic Ni species on the basis of available human epidemiology and animal studies.[3,8–10] The carcinogenicity of water-soluble Ni salts such as $NiSO_4 \cdot xH_2O$ and insoluble nickel oxide compounds such as Ni-containing spinels (e.g., $NiFe_2O_4$), however, is controversial.[3, 10, 11] Therefore, determining the speciation of Ni in ambient air is of the utmost importance for assessing the respiratory health risks associated with Ni.

Ni speciation analyses were conducted on urban total suspended particulate (TSP), PM_{10}, and $PM_{2.5}$ samples collected from Davie, Florida, using x-ray absorption fine structure (XAFS) spectroscopy. Automated scanning electron microscopy (ASEM) was also used to determine the number concentrations (frequency %) of Ni-containing particles in Davie, Florida, TSP and to evaluate the particle-size distributions of Ni.

Experimental

Ambient TSP, PM_{10}, and $PM_{2.5}$ samples were collected continuously during August 26–31, 2002, from an urban Broward County State and Local Air Monitoring Station (SLAMS) and National Air Monitoring System (NAMS) site located in Davie, Florida (26.08°N, 80.24°W). The locations of major PM_{10} point sources in relation to the sampling site and a wind rose diagram for the sampling period are shown in **Figure 1**. The PM_{10} emission estimates in **Figure 1** are based on 2001 statistics from the Florida Department of Environmental Protection. Point sources in the vicinity of the Davie site include residual (No. 6 fuel) oil- and gas-burning power plants, cement kiln operations, and municipal waste incineration facilities. Significant mobile sources of TSP, PM_{10}, and $PM_{2.5}$ near the Davie site include motor vehicle, aircraft, and marine vessel traffic. The wind rose diagram in **Figure 1**, created from hourly average wind speed and direction measurements from the Fort Lauderdale International Airport, indicates that winds were predominantly marine in origin and that mobile and point sources east-southeast and southeast of the Davie site probably contributed to TSP, PM_{10}, and $PM_{2.5}$ during the sampling period.

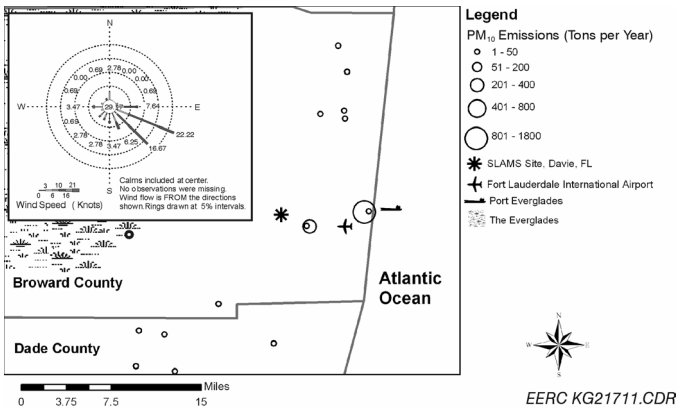

Figure 1. Davie, Florida, SLAMS/NAMS site, major PM_{10} point source, Fort Lauderdale International Airport, and Port Everglade locations and a wind rose diagram for the sampling period.

The following equipment and EPA Compendium Methods[12] were used to sample ambient TSP, PM_{10}, and $PM_{2.5}$:

- Tapered electronic oscillating microbalance (TEOM), Rupprecht & Patashnick Model 1400a (EPA Compendium Method IO-1.3).
- Automatic cartridge collection unit (ACCU), Rupprecht & Patashnick
- Sequential air sampler (SAS), Rupprecht & Patashnick Model 2025 (EPA Compendium Method IO-2.3)
- High-volume air sampler (HVAS), General Metal Works (EPA Compendium Method IO-2.1)

TSP was collected on Type A/E glass fiber filters, whereas PM_{10} and $PM_{2.5}$ were collected on GF/C glass fiber filters. Urban TSP was also collected on a moving carbon tape using a Burkard seven-day recording volumetric spore trap (BVST). Field filter blank samples were collected for quality control purposes. Ni concentrations of the field filter blanks, Davie TSP, and a National Institute for Standards and Technology (NIST) standard reference material (SRM) 1648 (urban TSP) were determined using microwave digestion followed by graphite furnace atomic absorption spectroscopy (GFAAS).

X-Ray Absorption Fine Structure Spectroscopy. Ni and S XAFS spectra were obtained at beam lines X-18B and X-19A, respectively, of the National Synchrotron Light Source (NSLS), Brookhaven National Laboratory, New York. Ni XAFS spectra were collected in fluorescence mode using a multielement Ge detector, whereas the S XAFS spectra were collected in the same mode using a Passivated Implanted Planar Silicon (PIPS) detector. Multiple scans, typically between three and five scans, were combined to produce the overall spectrum. Ni XAFS spectra were analyzed using the procedures described by Brown et al.,[13] Lee et al.,[14] and Koningsberger and Prins.[15] XANES spectra of reagent-grade Ni compounds and synthesized Ni compounds, acquired in previous

investigations,[16–18] were used essentially as "fingerprints" for identifying and quantifying Ni species. The following Ni compounds are included in this spectral database: Ni^0, NiS, NiS_2, Ni_3S_2–Ni_7S_6 mixture, NiO, $Ni(OH)_2$, $NiSO_4 \cdot xH_2O$, $C_4H_6NiO_4 \cdot 4H_2O$, $NiCO_3$, and $NiFe_2O_4$.

Automated Scanning Electron Microscopy. The ASEM method utilizes digital image analysis and electron probe microanalysis (EPMA) techniques to locate, size, and chemically analyze individual ash particles with submicron diameters as small as 0.3 μm. Particles collected on the carbon tape of the BVST were analyzed for Ni using the ZAF method which corrects x-ray intensities for differences in the atomic number (Z), absorption (A), and fluorescent (F) effects of the calibration standards relative to the sample. The chemical composition obtained in this manner is semiquantitative at best because of the short x-ray counting time employed (10 s), the use of flat mineral standards for calibration, and the fact that no matrix corrections for particle diameter, shape, or density were applied.

Results and Discussion

Sulfur K-Edge XAFS Spectroscopy Analyses. The absorption intensities for the TSP-, PM_{10}-, and $PM_{2.5}$-containing filters are significantly greater than the absorption signals for the corresponding blank filters. Hence, the sulfur absorptions are primarily caused by the PM_{10} and $PM_{2.5}$ trapped within the filters. The energy location of the sulfur peaks in sulfur XANES spectra for the SAS filter blank and the filters containing TSP, PM_{10}, and $PM_{2.5}$ are all consistent with the presence of the sulfate (SO_4) species. The XANES sulfur species detection limit is approximately 3% of the total sulfur present, thus >95% of the sulfur in Davie TSP, PM_{10}, $PM_{2.5}$, and SAS filter blank is present as SO_4-based compounds.

Nickel K-Edge XAFS Spectroscopy Analyses. Ni K-edge XAFS spectra for filter blanks and filters containing Davie TSP, PM_{10}, and $PM_{2.5}$ indicated that Ni is mostly concentrated in PM_{10}. Duplicate GFAAS analyses of Davie TSP indicated that it contains 86 ppm Ni. Ni absorption is approximately proportional to Ni concentration; thus the Davie PM_{10} sample was estimated to contain approximately 140 ppm Ni. These Davie TSP and PM_{10} Ni concentrations correspond to airborne Ni concentrations of ≈1.5 ng/m^3, which is very similar to the annual average ambient Ni concentration of 1.9 ng/m^3 estimated for Broward County by EPA.[19] These Ni concentrations are much lower in comparison to average urban ambient air Ni concentrations, which range from 5 to 50 ng/m^3 and are more representative of Ni concentrations found in remote and rural areas.[8, 9, 20, 21] The low airborne Ni concentrations at the Davie, Florida, air-monitoring site may represent the atmospheric burden of "background" Ni derived from long-range transport via the southeast and easterly North Atlantic trade winds (**Figure 1**).

The Ni K-edge absorption signals from the filters containing Davie TSP and PM_{10} were sufficiently intense to process and create XANES spectra. Spectra from the Ni XANES database were compared to the TSP and PM_{10} spectra using a least squares fitting procedure. Estimates, based on the least squares fitting, of the Ni species compositions of Davie TSP and PM_{10} are provided in **Table 1**. Davie PM_{10} contains a much greater proportion of $NiSO_4 \cdot xH_2O$ relative to TSP, probably because of the greater surface area of PM_{10} on which $NiSO_4 \cdot xH_2O$ heterogeneously condensed or adsorbed.

Table 1 XANES Ni Speciation Results for Davie TSP and PM_{10}, % of Total Ni

Ni Species	TSP	PM_{10}
$NiSO_4 \cdot xH_2O$	40	78
$NiFe_2O_4$	50	22
NiS	10	<5

ASEM. Approximately 800 to 1100 urban TSP particles were analyzed at random on portions of the BVST carbon tape using ASEM. Compared in **Figure 2** are the number concentrations of Ni-bearing particles, arbitrarily defined as containing ≥10 wt% Ni, sampled during each of four days (August 27–30, 2002). Approximately 8% of the particles sampled on August 27, 29, and 30 contained ≥10 wt% Ni, whereas on August 28 about 15% of the particles were Ni-bearing. Apparently, additional emission sources of Ni were contributing to the TSP sample collected on August 28 or the Ni emission rate for a particular source in the Davie, Florida, area increased on August 28.

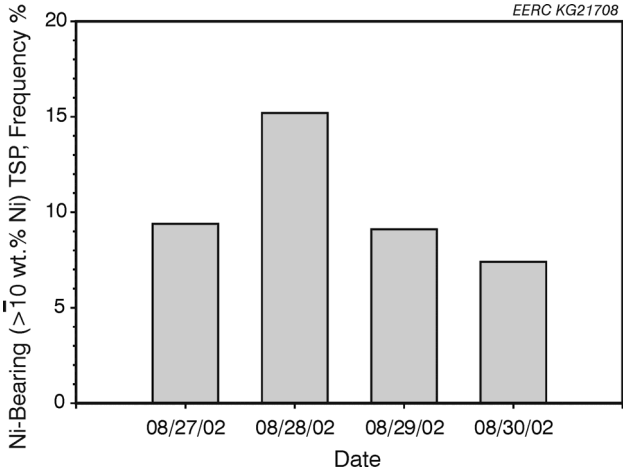

Figure 2. Number concentrations of Ni-bearing (≥10 wt %) particles in Davie TSP samples.

The particle-size distributions of Ni-bearing particles are compared in **Figure 3**. Most of the Ni-bearing particles are <10 μm in diameter, indicating that they were released from combustion sources. Ni-bearing particles sampled on August 30 were significantly coarser relative to those sampled on August 27–29.

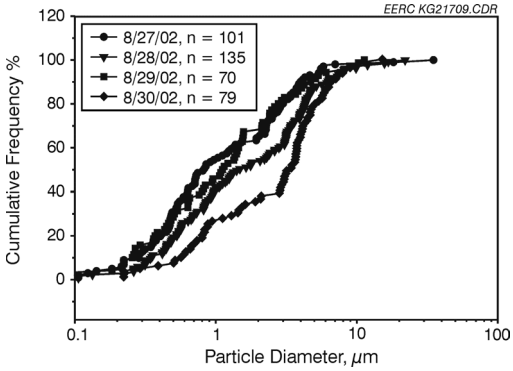

Figure 3. Particle-size distribution of Ni-bearing (≥10 wt%) particles in Davie TSP.

Conclusions

The airborne Ni concentration of .1.5 ng/m^3 measured at the Davie, Florida, SLAMS/NAMS site during August 26–31, 2002, is similar to the EPA estimated annual average ambient Ni concentration of 1.9 ng/m^3 for Broward County.[19] Approximately 8%–15% of the total number of particles sampled from the Davie, Florida, SLAMS/NAMS site contained significant Ni concentrations, ≥10 wt%. Most of these Ni-bearing particles were <10 μm in diameter. XANES results indicated that $NiSO_4 \cdot xH_2O$ and a nickel oxide compound, possibly $NiFe_rO_4$, were the dominant Ni species occurring in TSP, although a small proportion of NiS was also present. The PM_{10} fraction lacked NiS, but $NiSO_4 \cdot xH_2O$ was much more abundant in comparison to TSP, probably because of the greater surface area of PM_{10} on which $NiSO_4 \cdot xH_2O$ heterogeneously condensed or adsorbed. The quantity of the $PM_{2.5}$ fraction was insufficient to quantify Ni and perform speciation analyses. Sulfur K-edge XANES analyses indicated that >95% of the total sulfur in the TSP, PM_{10}, and $PM_{2.5}$ samples is present as SO_4.

Acknowledgment. This investigation was supported by the Nickel Producers Environmental Research Association (NiPERA) through the Energy & Environmental Research Center (EERC) Jointly Sponsored Research Program, which is supported by the U.S. Department of Energy (DOE) National Energy Technology Laboratory under Cooperative Agreement No. DE-FC26-98FT40321. We are grateful to Mr. Kenneth P. Larson of the Broward County Commission, Department of Planning and Environmental Protection, Air Quality Division, for facilitating the EERC sampling of urban particulate matter at its SLAMS/NAMS site in Davie, Florida. XAFS investigation of fossil fuel-derived particulate matter is supported in part by a National Science Foundation Collaborative Research Activities in Environmental Molecular Science grant to the University of Kentucky. We also acknowledge DOE for its support of synchrotron facilities, without which this work would have been impossible.

References

1. Nriagu, J.O. A Global Assessment of Natural Sources of Atmospheric Trace Metals, *Nature* **1989**, *338*, 47–49.
2. U.S. Environmental Protection Agency. *Locating and Estimating Air Emissions from Sources of Nickel*; Office of Air Quality Planning and Standards, Research Triangle Park, NC, March 1984, EPA-450/4-84-007f.
3. Nickel Producers Environmental Research Association (NiPERA). *Occupational Exposure Limits Criteria Document for Nickel and Nickel Compounds, Volume 1: Summary, Conclusions, and Recommendations;* Prepared for the European Commission, Directorate-General V, Public Health and Safety at Work Directorate. Prepared by NiPERA in collaboration with Eurometaux, Dec 24, 1996.
4. U.S. Environmental Protection Agency. *Documentation for the 1996 Base Year National Toxics Inventory for Onroad Sources*; Emission Factor and Inventory Group (MD-14); Emissions, Monitoring and Analysis Division, Research Triangle Park, NC, June 2000.
5. U.S. Environmental Protection Agency. *Documentation for Aircraft, Commercial Marine Vessel, Locomotive, and Other Nonroad Components of the National Emissions Inventory*; Emission Factor and Inventory Group (D205-01); Emissions, Monitoring and Analysis Division, Research Triangle Park, NC, Nov 2002.
6. *Provisions for Attainment and Maintenance of National Ambient Air Quality Standards*; U.S. Public Law, 101–549, 1990.
7. U.S. Environmental Protection Agency. *1996 Toxics Release Inventory, Public Data Release–Ten Years of Right-to-Know*; EPA 745-R-08-005, Washington, DC, May 1998.
8. Agency for Toxic Substances and Disease Registry (ATSDR). *Toxicology Profile for Nickel*; Prepared by Sciences International, Inc., under subcontract to Research Triangle Institute under Contract No. 205-93-0606, U.S. Department of Health and Human Services, Public Health Service, Atlanta, GA, Sept 1997.
9. Health Canada, Canadian Environmental Protection Act. *Priority Substances List: Supporting Documentation, Health-Related Sections, Nickel and Its Compounds*; Ottawa, Canada, 1993.
10. U.S. Environmental Protection Agency. *Study of Hazardous Air Pollutant Emissions from Electric Utility Steam Generating Units—Final Report to Congress: Volume 1*; EPA–453/R–98–004a, Washington, DC, Feb 1998.
11. Toxicology Excellence for Risk Assessment (TERA). *Toxicological Review of Soluble Nickel Salts;* Prepared for the Metal Finishing Association of Southern California, Inc., U.S. Environmental Protection Agency, and Health Canada. Prepared by TERA under subcontract in part with Science Applications International Corporation, EPA Contract No. 68-C7-0011, March 1999.
12. U.S. Environmental Protection Agency. *Compendium of Methods for the Determination of Inorganic Compounds in Ambient Air*; EPA/625/R-96/010a, Washington, DC, June 1999.
13. Brown, G.E., Jr.; Calas, G. ; Waychunas, G.A.; Petiau, J. In Hawthorne, F.C., Ed.; *Spectroscopic Methods in Mineralogy and Geology*; Rev. in Mineral. Vol. 18, Mineralogical Society of America, Washington, DC, 1988, Chapter 11, pp 431–512.
14. Lee, P.A.; Citrin, P.H.; Eisenberger, P.; Kincaid, B.M. *Rev. Mod. Phys*. **1981**, *53*, 769–808.
15. Koningsberger, D.C.; Prins, R. *X-Ray Absorption. Principles, Applications, Techniques of EXAFS, SEXAFS, and XANES*, J. Wiley & Sons: New York, 1988.
16. Galbreath, K.C.; Zygarlicke, C.J.; Toman, D.L.; Huggins, F.E.; Huffman, G.P. Nickel and Chromium Speciation of Residual Oil Combustion Ash, *Combust. Sci. Technol.* **1998**, *134* (1–6), 243–262.
17. Galbreath, K.C.; Zygarlicke, C.J.; Huggins, F.E.; Huffman, G.P.; Wong, J. Chemical Speciation of Nickel in Residual Oil Ash. *Energy Fuels* **1998**, *12*, 818–822.
18. Galbreath, K.C.; Toman, D.L.; Zygarlicke, C.J.; Huggins, F.E.; Huffman, G.P.; Wong, J. Nickel Speciation of Residual Oil Fly Ash and Ambient Particulate Matter Using X-Ray Absorption Spectroscopy. *J. Air Waste Manage. Assoc.* **2000**, *50 (11)*, 1876–1886.
19. U.S. Environmental Protection Agency. *National Air Toxics Assessment*, 1996, http://www.epa.gov/ttn/atw/nata/tablconc.html (accessed April 16, 2003).
20. Schroeder, W.H.; Dobson, M.; Kane, D.M. Toxic Trace Elements Associated with Airborne Particulate Matter: A Review, *Air Pollut. Control Assoc.* **1987**, *11*, 1267–1287.
21. Sunderman, Jr., F.W.; Oskarsson, A. *Nickel,* In *Metals and Their Compounds in the Environment: Occurrence, Analysis, and Biological Relevance*, Merian, E., Ed.; VCH: Weinheim, 1991, pp 1101–1126.

FISCHER-TROPSCH PRINCIPLES OF CO-HYDROGENATION ON COBALT CATALYSTS

Hans Schulz

University of Karlsruhe
Engler-Bunte-Institute
76131 Karlsruhe, Germany

Introduction

CO-hydrogenation on the metals Ni, Ru, Co, and others, commonly yields methane, as discovered by Sabatier and as thermodynamically to be expected. But at adequate catalyst preparation, at relatively low temperature, methane becomes a minor product and the formation of linear olefins and paraffins dominates. The conclusion has then to be "methane formation is frustrated in the Fischer-Tropsch regime", this allowing for chain growth, the intrinsic characteristic of Fischer-Tropsch synthesis. It is outlined in the lecture in more detail how **frustration of distinct basic reactions** rules the Fischer-Tropsch regime - rather than promotion of others.

A further principle of FT-synthesis with cobalt is its extreme **dynamic character** responding sensitively with its product composition (chain length, branching, olefin/paraffin-ratio, oxygenates) against changes of temperature and of the partial pressures of CO, H_2 and H_2O (most pronouncedly p_{CO}, in contrast to the behavior of iron as catalyst).

With cobalt (also Ni and Ru) it appears that the reactants and intermediates are dynamically featuring as part of the active catalytic sites, such behavior is well-known in homogeneous catalysis with transition metal complexes.

The principle of **self-organization** for attaining the steady-state conversion is a very important feature of FT-synthesis with cobalt as the catalyst. Obviously, a thermodynamically driven segregation of the cobalt surface and thereby **sites disproportionation** occurs (Fig. 1). This follows from time resolved measurements of activity and selectivity and related kinetic modeling together with surface structure imaging.

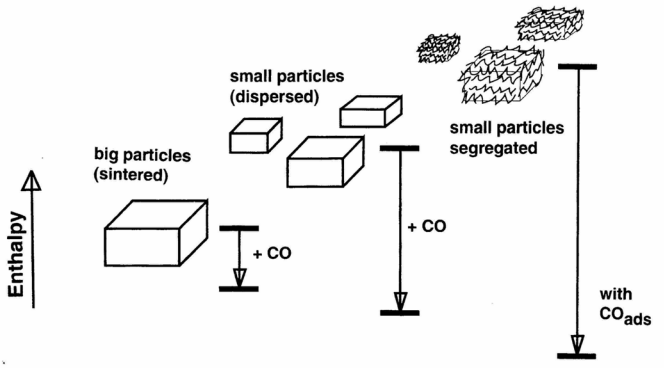

Figure 1. Thermodynamic view of cobalt surface segregation under FT-conditions: Segregation is favored against sintering and surface-annealing by CO-chemisorption. An equilibrium state of surface reconstruction is being approached.

The principle of **spatial constraints** applying to distinct basic reactions appears additionally to operate. To elaborate the influences of these principles from experimental results, the conversion is modeled as a kind of **polymerization** and the relevant influences are specified as moderating ideal polymerization.

Results and Discussion

As a function of time (duration of the experiment) it is investigated how the steady-state Fischer-Tropsch regime is established:

- The reaction rate (of CO-consumption) increases (factor of 3 to 10),
- The chain growth probability increases,
- Methane selectivity decreases,
- Secondary olefin hydrogenation and isomerization decrease,
- Branching probability decreases.

These kinetic changes are explained in conjunction with catalyst restructuring, caused by strong CO chemisorption, proceeding as segregation of the catalyst surface to increase the number of active sites and disproportionate on-plane-sites into on-top-sites and in-hole-sites, the on-top-sites exhibiting catalytic properties, resembling those of transition metal complexes and the in-hole-sites showing high activity for dissociation (of CO), whereas the common on-plane-sites are much deactivated through CO-adsorption (and methyl-coverage). Of course, such steady-state should be highly dynamic.

The preferred **monomer** for chain growth appears to be the methylene species, as concluded from the observed reversible terminal CH_2-splitting from added labeled olefins, relating the chemistry on the on-top-sites to that of transition metal carbene complexes.

Ethene to act as a monomer is also observed as a minor reaction, to relate the chemistry on the growth sites to homogeneous olefin polymerization. CO as a monomer is also possible (as related to olefin hydroformylation), however, only as a minor reaction to produce alcohols and aldehydes.

Spatial constraints at the growth sites are concluded to operate as for preferred olefin readsorption at their alpha-position, for the decline of branching with increasing size of the growing chain and for suppressed desorption after branching.

The most important principle of any FT-regime appears to be **frustration of desorption** and this to concern the reaction of associative desorption of an alkyl together with a H to desorb as a paraffin molecule. This causes the accumulation of **deactivating methyl species** on the catalyst surface (mainly on on-plane-sites) and allows for chain growth to become dominant.

In **conclusion**, the important process of surface segregation and thereby active sites generation and moderation can be influenced by promotors and the conditions of segregation in order to design catalysts for optimal technical application.

SYNTHESIS AND CHARACTERIZATION OF NANO-SIZED IRON PARTILCES ON A POLYSTYRENE SUPPORT AS POTENTIAL FISCHER-TROPSCH CATALYSTS

Amruta Desai[1], Devinder Mahajan[1,2], and Miriam Rafailovich[2]

[1]Energy Sciences & Technology Department, Brookhaven National Laboratory, Upton, NY 11973-5000, USA.
[2]Department of Materials Science & Engineering, Stony Brook University, Stony Brook, NY 11794 USA

Introduction

Iron is inexpensive that makes it the most desirable material to catalyze Fischer-Tropsch (F-T) synthesis[1]. Iron is also desirable because the hydrocarbons produced are high in olefinic content. Prior to World-War II, the commercial plants utilized Fe-based catalysts in Germany and South Africa. The Fischer-Tropsch reaction is best described by Equation 1:

$$n\,CO + 2nH_2 \rightarrow -(CH_2)_x- + n\,H_2O \quad (1)$$

$$CO + H_2O \rightarrow CO_2 + H_2 \quad (2)$$

The F-T reaction is always accompanied by the well-known water-gas-shift reaction (WGSR) (Equation 2). The WGSR reaction is facile under the temperature (260° - 280°C) and the pressure (2000 – 3000 kPa) conditions under which Fe-catalyzed F-T reaction takes place. The value of x in Equation 1 determines the product distribution that can range from methane for x = 1 to high molecular weight waxes.

One of the crucial problems associated with the F-T reaction is the following. As the F-T reaction proceeds, the volatile (low molecular weight) hydrocarbons exit the reactor by the flowing gas but the higher molecular weight waxes remain in the reactor. After certain period on-line, the waxes accumulate to a point that it encapsulates the catalyst and reduces its effectiveness. Moreover, after the F-T reaction, the catalyst/waxy product separation is problematic to regenerate the catalyst.

We recently reported[2] the use of nano-sized unsupported Fe particles in an attempt to enhance the space-time-yield (STY) during the F-T reaction. But a facile method to synthesize nano metal catalysts remains a challenge. New methods are sought to facilitate synthesis of supported nano materials for potential applications in catalysis, gas separation and storage. Polymers provide structural flexibility than well-studied inorganic frameworks such as zeolites. To this effect, there are reports of the use of polymers as a support to stabilize colloidal iron dispersions[3], synthesis of highly porous metal-organic frameworks consisting of supertetrahedron clusters when capped with monocarboxylates[4] that are stable up to 300°C and materials based on dendrimers in which metal nanopartilces are encapsulated in the dendritic framework[5]. This paper summarizes our attempt to synthesize nano-sized materials that could be used to enhance STY yield and provide a pathway to an effective catalyst/wax separation. We report herein a facile synthesis of supported Fe nano particles that are embedded in the polystyrene matrix.

Experimental

Synthesis of Nano Fe particles Supported on Polystyrene (Fe-PST). Polystyrene is a porous polymer that could provide selective porosity to gas absorption and separation. Moreover, polystyrene (PS) may be able to remain stable under reaction conditions of higher temperature (250°C - 300°C) that are required for F-T synthesis. The strategy was to attempt to simultaneously synthesize polystyrene from the styrene monomer to be used as the supporting matrix, while producing the nano-sized Fe particles at the same time. Though the polymerization process requires initiators, we used the produced nano-sized Fe particles as initiators to polymerize the monomer styrene and create its own matrix to envelope the nano Fe particles. The polymer matrix may be suited to protect the Fe particles without changing their properties.

The procedure developed to produce polymer-supported nano Fe metal particles involved thermal decomposition of $Fe(CO)_5$ in the presence of a monomer that was allowed to concurrently polymerize. The method involved mixing 50ml purified styrene monomer with 50 ml hexadecane solvent in a glass flask, adding 1.2 ml $Fe(CO)_5$ after purging with argon, stirred and heated at 100°C at ambient atmosphere. The solution turned black in a few minutes after heating was initiated indicating the formation of zero-valent Fe. The darkening of the solution was followed by gradual solidification of the solution over time indicating polymerization of styrene. The product in this case was a slightly brownish solid in which black Fe particles could be distinctly seen.

Characterization of Fe-PST. The NSF funded Garcia Center for Engineered Polymer Interfaces in the Materials Science and Engineering Department at SUNY at Stony Brook houses state-of-the-art instruments to characterize polymeric materials. Characterization of the samples included using the Transmissions Electron Microscopy (TEM), Differential Scanning Calorimeter (DSC), Fourier Transform Infrared Spectroscopy (FTIR), Gel Permeation Chromatography (GPC), Electron Paramagnetic Resonance (EPR), and measurement of magnetic properties.

Results and Discussion

The overall observed reaction can be described as follows:

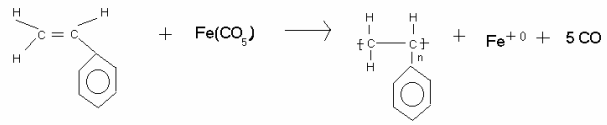

(3)

Mechanistically, the reaction sequence is better described as a combination of Reactions 4 and 5:

$$Fe(CO)_5 \overset{\Delta}{\Rightarrow} \text{“Fe”} + 5\,CO \quad (4)$$

$$\text{Styrene} \overset{\text{“Fe”}}{\Rightarrow} \text{Fe-Polystyrene} \quad (5)$$

The $Fe(CO)_5$ decomposition reaction is written first in the sequence because we recently reported[6] the rate constant for this reaction to be 3×10^{-6} s^{-1}. The reaction rate for Reaction 4 is far greater than the styrene polymerization during Reaction 5 as we observed the solution viscosity that increased slowly with time and took four days till the contents of the flask could not be further stirred. Therefore, we infer the role of Fe nano particles, initially produced during the reaction, appears to initiate polymerization of styrene. The synthesized material is best described as polystyrene containing nano particles of Fe (Fe-PST).

The synthesized material contains nano particles of Fe in polystyrene matrix. The physical appearances of the materials are as follows. As shown in Figure 1, pure polystyrene exists as a white material whereas polystyrene containing Fe (Fe-PST) becomes

colored. The freshly prepared Fe-PST material is black that slowly changes to brick red on exposure to air. The homogeneous spread of the brick red color also shows that the Fe particles do not just reside on the polystyrene surface but rather are highly dispersed throughout the matrix. The brick red color is likely due to the oxidation of zero-valent iron to iron oxide.

Figure 1: Physical appearance of: pure polystyrene (left) and thermally prepared Fe-PST material (right). Note that as shown, the brick red color in the right sample is due to oxidation that was originally black (prior to oxidation) as seen at the core of the sample.

The Fe-PST material was characterized by various techniques. The TEM of the sample is shown in Figure 2. It is evident that the Fe particles are part of the polystyrene matrix that are seen as dark spots in the TEM image shown in Figure 2. The mean particle size was calculated to be 44 nm.

Figure 2. TEM micrograph of Fe-PST material prepared by thermal treatment of a mixture containing $Fe(CO)_5$ and styrene monomer.

The average molecular weight of a polymer sample are usually expressed as number average, M_n and weight average, Mw, values. The gel permeation chromatography (GPC) was used in this work to determine the molecular weight distribution of polystyrene in the thermally synthesized Fe-PST material. The GPC chromatogram describes the relative amount of polymer molecule as a function of molecular sizes. The molecular weight is found in order to ensure that the synthesized matrix consists of reasonably large polystyrene molecules, establishing, the success of the polymer synthesis reaction and giving information of the polymerization process. For a purified polystyrene sample with EPR data, the weight average molecular weight, M_w, was found to be 59.6K and number average molecular weight, M_n, 19.3K with the highest population at M_p= 49.9K (Figure 3). The polydispersity, M_w/ M_n of this sample is about 3, which is a value higher than normal low conversion radical polymerization; this polydispersity is expected for high conversion systems. Thus the GPC and the TEM data show that the nano Fe particles of a mean size of 44 nm are formed and get well dispersed in the polystyrene polymer whose average molecular weight is 59,600.

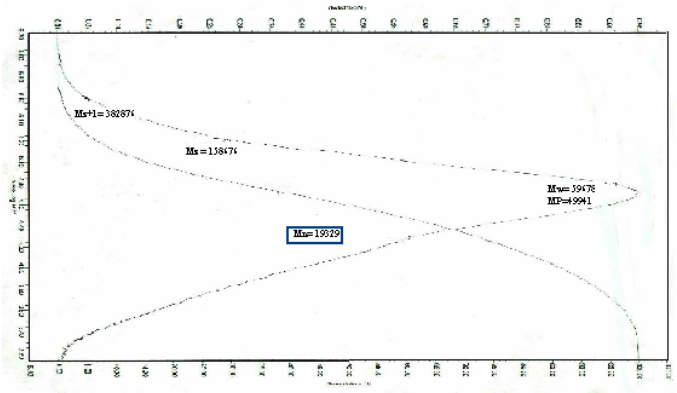

Figure 3. The chromatogram depicts the molecular weight distribution for the thermally synthesized sample. M_w = 59.6K; M_n= 19.3K and M_p= 49.9K. A curve of cumulative amount is also shown.

Conclusions

To conclude, a polymeric material containing nano particles of Fe(0) and polystyrene can be conveniently prepared by the thermal treatment of a solution containing iron pentacarbonyl and styrene monomer in hexadecane. The TEM data show that the mean particle size of synthesized Fe particles is 44 nm and the Fe particles are well dispersed throughout the polystyrene matrix. The Fe-PST material, as prepared under an inert atmosphere, contains Fe particles in zero-valent oxidation state that appear as black particles. On exposure to air, the Fe slowly starts to oxidize to a brick red material that is likely to be iron oxide.

Further characterization of these materials by Differential Scanning Calorimetry (DSC), Fourier Transform Infrared Spectroscopy (FTIR), Electron Paramagnetic Resonance (EPR), and measurement of their magnetic properties is underway to establish their morphology, rheology and other structural properties. The DSC measurement will allow us to establish thermal stability of these materials to allow us to evaluate their potential as Fischer-Tropsch catalysts.

Acknowledgment

This work was supported by the U.S. Department of Energy under Contract No. DE-AC02-98CH10886.38. A start-up grant (to DM) from the State University of New York at Stony Brook is gratefully acknowledged.

References

1. Dry, M.E. in: J.R. Anderson, M. Boudart (Eds.), Catalysis, Science and Technology, Springer-Verlag, Berlin, 1981, p. 159 and references therein.
2. Mahajan, D., Gütlich, P., Stumm, U. Catal. Commun. **4** (2003) 101-107.
3. Smith T. W., Wychick D. J. Phys. Chem., **84** (1980) 1621-1629.
4. Li, H., Eddaoudi, M., O'Keeffe, M., Yaghi, O. M. Nature, **402** (1999) 276-279.
5. Tully, D.C., Frechet, M. J. Chem. Commun., (2001) 1229-1239.
6. Mahajan, D., Papish, E.T., Pandya K. Ultrasonic Sonochem., submitted (2003).

HIGH PRESSURE CO_2 REFORMING OF CH_4 OVER NI/MGO CATALYST DERIVED FROM NANO-MgO

Yu-He Wang, Bo-Qing Xu and Qi-Ming Zhu

State Key Lab of C_1 Chemistry and Technology
Department of Chemistry, Tsinghua University
Beijing 100084, China

Introduction

There has been a general interest in recent in the more efficient use of natural gas (methane) and in the decrease of carbon dioxide in the atmosphere. The production of synthesis gas by CH_4/CO_2 reforming is one of the attractive routes for the utilization of CH_4 and CO_2. The product mixture of this reaction from a stoichiometric (1:1) feed has a high CO/H_2 ratio that is suitable for methanol and F-T synthesis, because low CO/H_2 ratios favor methanation and suppress chain growth [1]. Great efforts have been focused on the development of catalysts that shows high activity and stability.

Generally, CH_4 is preserved at high pressures in natural gas fields, and most F-T synthesis and methanol synthesis from CO/H_2 are performed at high pressures in the GTL (gas to liquid) process. Hence, from an economical point of view, the CH_4/CO_2 reforming should be carried out at high pressures in such a process [2]. In addition, in terms of the utilization of synthesis gas, the compressed synthesis gas is more convenient. It has been proposed that researchers must appreciate that the key problem is catalyst life at high pressures because customers need H_2 at >1.0 MPa and compression of large volumes of product gas is not very acceptable [3]. As it is well known that higher pressures favor coking and deactivation of catalysts in the CH_4/CO_2 reforming to synthesis gas, researches of the reforming reaction at high pressures are required. However, most of the researches were performed at atmospheric pressure, and only a few studies were conducted at high pressures [2-8]. To date no high stable Ni-based catalysts are reported in the dry reforming of methane at high pressures. Our searches have shown that Ni/MgO-AN catalyst (Ni-loading: 8.8%wt), the support of nano-MgO (named as MgO-AN) prepared by thermal processing of an alcogel of $Mg(OH)_2$, was extremely stable at 973-1123 K for CH_4/CO_2 reforming at atmospheric pressure [9]. In this paper, we have explored the catalytic performance of Ni/MgO-AN at high pressures CH_4/CO_2 reforming.

Experimental

Catalyst preparation and characterization. Magnesia support was prepared by sol-gel method with $MgCl_2 \cdot 6H_2O$ (A.R., Beijing Yili Chemical Reagent Co.) and $NH_3 \cdot H_2O$ (A.R., Beijing Yili Chemical Reagent Co.). Obtained $Mg(OH)_2$ hydrogel was changed to alcogel by washing with ethanol and then calcined at 650 ºC in flowing N_2 for 5 h, named as MgO-AN (S_{BET} = 59.3 m^2/g). Catalyst of Ni/MgO-AN (Ni-loading: 8.8%wt, S_{BET} = 48.1 m^2/g) was prepared by wet impregnation of an aqueous solution of $Ni(NO)_3 \cdot 6H_2O$ (A.R., Beijing Yili Chemical Reagent Co.) onto MgO-AN support [9]. The obtained paste was dried at 120 ºC overnight and then calcined at 650 ºC for 5 h in air. Temperature programmed oxidation (TPO) experiments of carbon species formed on catalysts were performed on a thermogravimetric analyzer (SETARAM TGA 92) in flowing air. TEM measurements were performed on a H-800 electron microscope.

Catalyst tests and product analysis. A catalytic activity test of CH_4/CO_2 reforming was carried out in a fixed-bed continuous-flow reaction system. The reactor was made of a quartz tube (7 mm i.d.) tightly fixed in a stainless steal tube. A Viton O-ring pressed by a locking nut was used to prevent the gas from leaking into the ringed gap so as to eliminate the influence of the metal wall. The reaction temperature was measured by a thermal couple, which was protected with a quartz tube (6 mm o.d.) with a dead end. The flow rate of CH_4/CO_2 = 1/1 (Huayua gas chemical & technology Ltd. Co., Beijing) was controlled by a mass flow controller (Brooks 5850E) and the pressure of the reaction system was controlled by a back-pressure regulator (Type 806, Badger Co.). The outlet gas was cooled to remove H_2O and sampled by a six-port valve and analyzed by an on-line gas chromatograph (Varian 3400 GC, Ar carrier and 2 m TDX-01 column) with a TCD detector. The catalyst bed contains 40 mg Ni/MgO-AN that was diluted with 100 mg inactive α-Al_2O_3 (Homemade by calcining the commercial Al_2O_3 to 1350 ºC). Before the reaction, the catalyst was reduced with a flowing 5.0% H_2/N_2 at 1123 K for 1 h. Blank reaction tests showed that CH_4 conversion is less than 2.0% under the current reaction conditions within 50 h.

Results and Discussion

Figure 1 shows the dependence of CH_4 conversion and CO yield on the time on stream for 8.8%Ni/MgO-AN catalyst with GHSV=1.6×10^4 ml/h·g_{cat} under 1.5 MPa at 1023 K. Results indicate that activity of the catalyst decreases with increasing the reaction time-on-steam (TOS) up to 10 h, but no further decline is observed thereafter when the reaction was continued to TOS = 50 h. Both CH_4 conversion and CO yield can reach a constant value, 23.5% and 29.6% respectively. The CH_4 conversion and CO yield can be estimated to be 39.5% and 49.5% on the basis of thermodynamic calculation in CO_2 reforming CH_4 (CH_4/CO_2 = 1/1, total pressure 1.5 MPa, reaction temperature 1023K) at equilibrium.

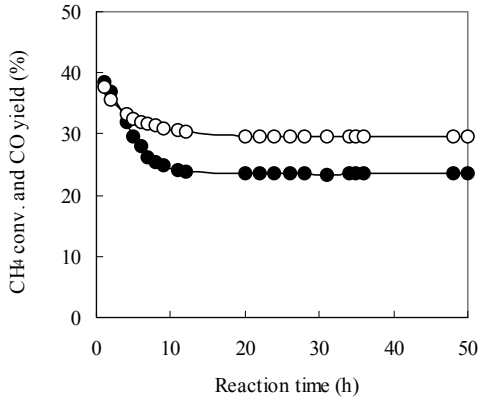

Figure 1. Stability test for 8.8%Ni/MgO-AN at 1.5MPa 1.6×10^4 ml/h·g_{cat} 1023K CH_4/CO_2=1/1. —○— CO yield —●— CH_4 conversion

Pressure and space velocity dependences studies were conducted at pressures varying from 1.0 to 2.0 MPa and at space velocity from 1.2×10^4 to 2.0×10^4 ml/h·g_{cat}. Results show that the stability in these different reaction conditions is the same with the behavior depicted in Figure 1. **Figure 2 and 3** show the effect of pressure and space velocity on CH_4 conversion and CO yield. These results show CH_4 conversion and CO yield decreased with increasing the reaction pressure as well as with increasing the reactant space velocity as expected from thermodynamics analysis. The effect of space velocity on activity implied that the reaction system had eliminated the contribution of mass-transport control.

It has been recognized that carbon deposition is the main cause of the deactivation of supported nickel catalysts in the reforming of CH_4 with CO_2 [10]. TPO measurements (**Figure 4**) show that the amount of carbon deposition on the used catalyst increases slowly with reaction time up to a constant value within 50 h. After 10 h on stream the loading of carbon deposition does not increase any more

with reaction time. The increasing tendency of carbon deposition is inverse proportion with the decreasing tendency of the CH_4 conversion and CO yield during the initial period. Although carbon was deposited on the catalyst, the activities became unchanged thereafter after 10 h on stream. The results imply that the carbon deposition did not block all active sites [5].

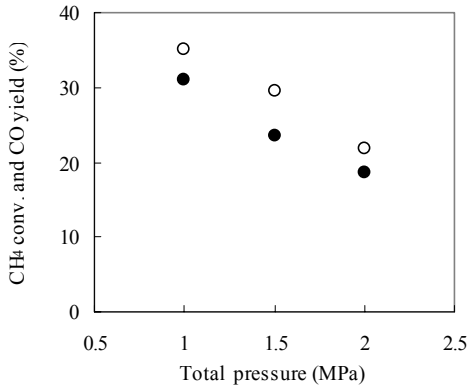

Figure 2. Dependence of activity on total pressure over 8.8%Ni/MgO-AN at 1.6×10^4 ml/h·g_{cat} 1023K CH_4/CO_2=1/1 TOS=50h. —○— CO yield —●— CH_4 conversion

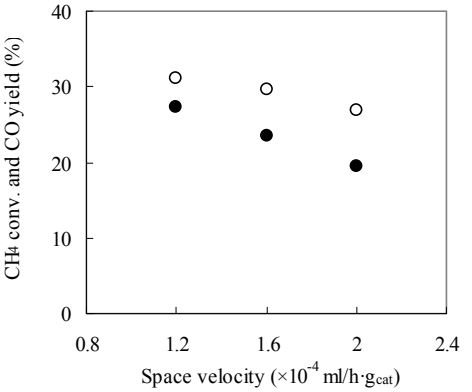

Figure 3. Dependence of activity on space velocity over 8.8%Ni/MgO-AN at 1.5MPa 1023K CH_4/CO_2=1/1 TOS=50h. —○— CO yield —●— CH_4 conversion

The sinter of nickel is another cause of deactivating catalysts in the CH_4/CO_2 reforming [10]. The TEM image of reduced catalyst shows that the metal nickel was dispersed on the magnesia supports uniformly (**Figure 5A**). In the TEM observation of used catalyst, larger nickel particle are found on the surface of catalyst **(Figure 5B)**. At the same time, TEM measurements revealed that the carbon deposits were of the filamentous types that can be removed by reaction with CO_2. The TEM image shows that the filamentous carbon grows from the larger nickel particle and some small nickel crystal stand on the tip and the middle of the filamentous carbon.

From the stable activity and unchanged amount of carbon deposition after 10 h on stream, it can be concluded that the catalyst deactivation was closely related with the amount of carbon deposits on the catalyst. The stable catalysis of Ni/MgO-AN catalyst seems to be associated with its ability to avoid formation of graphitic carbons and to maintain a dynamic equilibrium of the filamentous carbons with the reactant and product molecules at the catalyst surface.

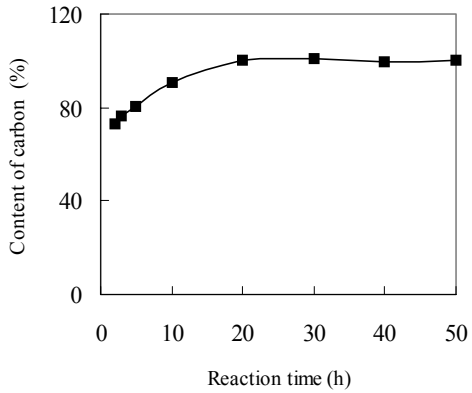

Figure 4. Dependence of the amount of carbon deposition on reaction time over 8.8%Ni/MgO-AN at 1.5MPa 1.6×10^4 ml/h·g_{cat} 1023K CH_4/CO_2=1/1. —○— CO yield —●— CH_4 conversion

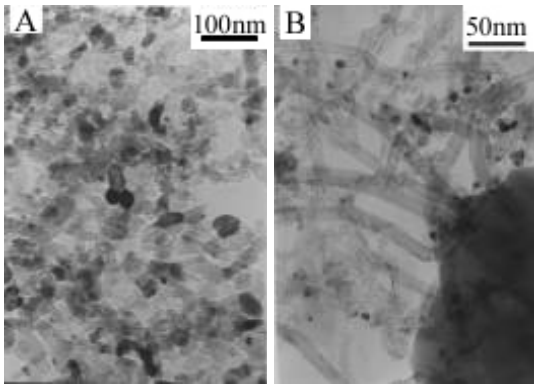

Figure 5. TEM images of fresh and used 8.8%Ni/MgO-AN
A. Reduced on flowing 5.0% H_2/N_2 for 1h at 1123K
B. After 50h on stream at 1.5MPa 1.6×10^4 ml/h·g_{cat} 1023K

References

1. Bradford, M.C.J., Vannice, M.A., *Appl. Catal*. 1996, 142, 73-96.
2. Nagaoka, K., Takanabe, K., Aika, K., *Chem. commun*., 2002, 1006–1007.
3. Tomishige, K., Himeno, Y., Matsuo, Y., Yoshinaga, Y., Fujimoto, K. *Ind. Eng. Chem. Res.*, 2000, 39, 1891-1897.
4. York, A.P. E., Claridge, J.B., Brungs, A.J., Tsang, S.C., Green, M.L.H., *Chem. Commun.*, 1997, 39-40.
5. Nagaoka, K., Okamura, M., Aika, K., *Catal. Commun.*, 2001, 2, 255-260.
6. Shamsi, A., Johnson, C.D., *Environmental Challenges and Greenhouse Gas Control for Fossil Fuel Utilization in the 21st Century*, 2002, 269-283.
7. Pan W., Song C.S.，*Abstracts of Papers of the Am. Chem. Soc.*, 219: 71-Petr. Part. 2, Mar. 26, 2000.
8. Brungs, A.J., York, A.P.E., Claridge, J.B., Márquez-Alvarez, C., Green, M.L.H., *Catal. Lett.*, 2000, 70, 117-122.
9. Xu B.Q., Wei J.M., Wang H.Y., Sun K.Q., Zhu Q.M., *Catal. Today*, 2001, 68, 217-225.
10. Tomishge, K., Chen Y.G., Fujimoto, K., *J. Catal.*, 1999, 181, 91-103.

Fischer-Tropsch Synthesis: Overview of Reactor Development and Future Potentialities

Burtron H. Davis

Center for Applied Energy Research, University of Kentucky
2540 Research Park Drive
Lexington, KY 40511

Since its discovery in the 1920s, the Fischer-Tropsch Synthesis (FTS) has undergone periods of rapid development and periods of inaction. Within ten years of the discovery, German companies were building commercial plants. The construction of these plants stopped about 1940 but existing plants continued to operate during WWII.

Two types of reactors were used in the German commercial plants: the parallel plate reactors and a variety of fixed-bed tubular reactors. For the parallel plate version, the catalyst bed was located in tubes fixed between the plates which was cooled by steam/water that passed around the tubes within the catalyst bed (figure 1). In another version, the reactor may be regarded as finned-tube in which large fins are penetrated by a large number of parallel or connected catalyst filled tubes. Various designs were utilized for the tubular fixed bed reactor with the concentrical tubes being the preferred one. This type of reactor contained catalyst in the area between the two tubes with cooling water-steam flowing through the inner tube and on the exterior of the outer tube (figure 2).

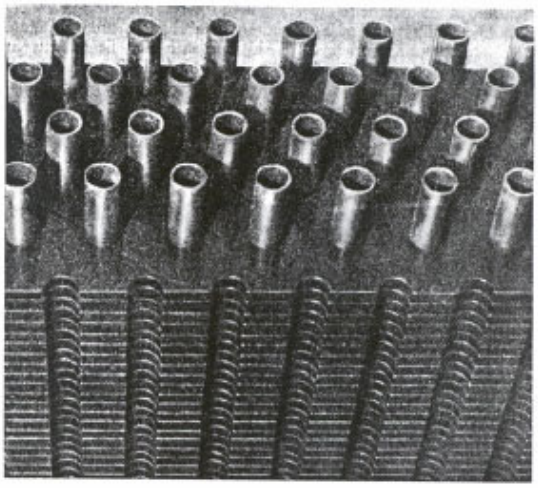

Figure 1. Parallel plate reactor.

The basic reactor designs were considered by Storch to be well defined by 1950. These were described by Kölbel as shown in figure 3 [1]. The parallel plate reactor, normally used for atmospheric pressure synthesis with the cobalt catalyst in Germany, is represented by a in figure 3. Usually fins were attached to the reactor tubes to facilitate the transfer of heat from the catalyst bed to the coolant. The arrangement of the double walled reactor (figure 2) is shown in b, figure 3. Many simple tubes filled with catalyst could be arranged in a shell (tube in shell) reactor system; a version of this type of reactor was and is still utilized by Sasol (Arge reactor) (c, figure 3).

Late 1940-early 1950 was a period of very active research and development for FTS and a variety of reactors were utilized. The circulating fluid bed reactor system had been developed during WWII by Standard Oil (NJ) for catalytic cracking (FCC process). It performed so successfully that it quickly became the dominant reactor

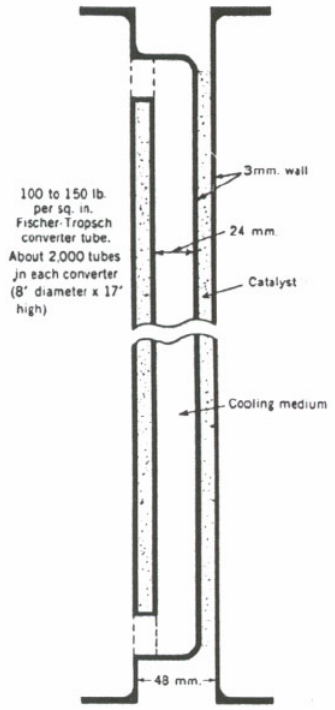

Figure 2. Section of Middle-Pressure Ruhrchemie Synthine reactor tube.

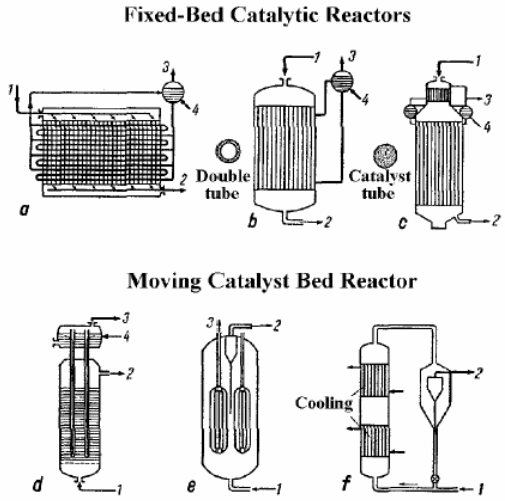

Figure 3. Reactor types (a, parallel plate, Ruhrchemie 1936; b, double tube, Ruhrchemie 1938; c, Arge tube, Ruhrchemie-Lurgi 1952; d, liquid phase, Rheinpreussen 1943; e, fixed fluid bed, Hydrocol 1948; f, circulating fluid bed, Kellogg 1958; 1, synthesis gas (gas entry and flow pater); 2, unconverted gas and products; 3, cooling vapor; 4, coolant drum).

type for catalytic cracking. Several organizations worked to develop versions of this reactor for FTS. The group headed by HRI developed the fixed fluid bed reactor for their commercial plant located in Brownsville, TX (e, figure 3). The adequate supply and low price of oil from the Middle East caused the plant to be closed just as the operating problems were being solved. Among the major problems was the degradation of the catalyst which created separation problems as well as rapid loss of catalyst from the reactor zone. The Kellogg Company

was a leader in developing a circulating fluid bed reactor for FTS and this is the version adapted by Sasol for their high temperature FTS plants (f, figure 3). In spite of many operating problems that led to Kellogg abandoning the development to Sasol, the problems were overcome and Sasol eventually operated 16 of these reactors at Secunda (producing more than 100,000 b/d) and additional smaller ones at Sasolburg. Recently all of the 16 reactors at Secunda were replaced by 8 fixed fluid bed reactors [2].

During and following WWII, Kölbel and coworkers worked on the development of a slurry phase reactor (d, figure 3). Following WWII a pilot plant was operated with an iron catalyst under conditions selected to produce gasoline range products as the dominant liquid product [3]. This plant utilized a reasonably simple design for the reactor (figure 4). While Kölbel and coworkers developed much understanding of the scientific and engineering principles for the operation of the slurry bubble column reactor, much of which is summarized in a recent book [4], the mass balance during operation of the pilot plant was not adequate or they utilized a catalyst with a selectivity that has not been duplicated since then during 50 years of work by many groups (figure 5). During and for about 10 years following WW II, the US Bureau of Mines operated a 50-70 bbl/day slurry reactor pilot plant at Louisiana, Missouri (flow diagram, figure 6; reactor schematic, figure 7). Because they used fused iron or precipitated catalysts sintered at high temperatures to provide attrition resistance, the catalyst particle density was such that catalyst dispersion was affected by both gas and liquid flow. Operation of the Bureau of Mines pilot plant was terminated after only four runs had been made but laboratory scale work has continued, with some interruptions, since that time. In the early 1990s, Sasol completed development of their slurry bubble column reactor and brought on-stream a 2,500 bbl/d, 5 meter diameter reactor and this has operated without problems for more than 10 years. For the commercial plant in Qatar, 11 meter diameter reactors will be utilized with a cobalt based catalyst.

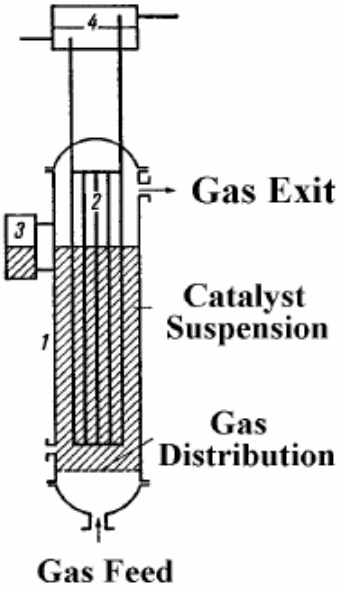

Figure 4. Reactor for synthesis in liquid phase (Rheinpreussen-Koppers) (1, cylindrical reactor; 2, cooling tubes; 3, liquid level regulator; 4, vapor-liquid chamber).

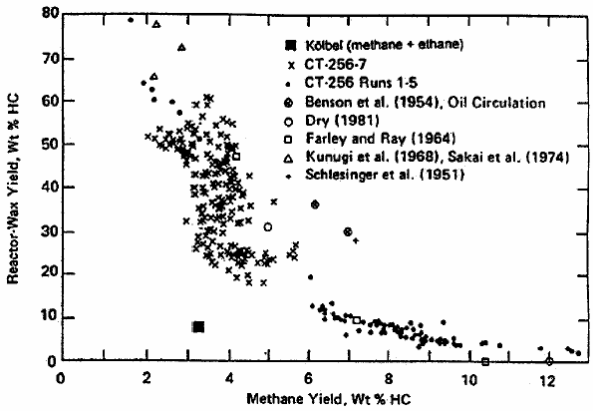

Figure 5. Reactor-wax yield vs. methane yield.

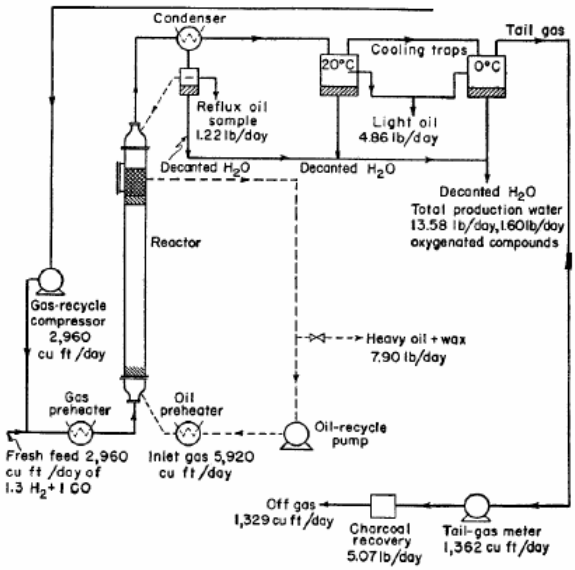

Figure 6. Typical flow diagram of U.S. Bureau of Mines oilcirculation **process.**

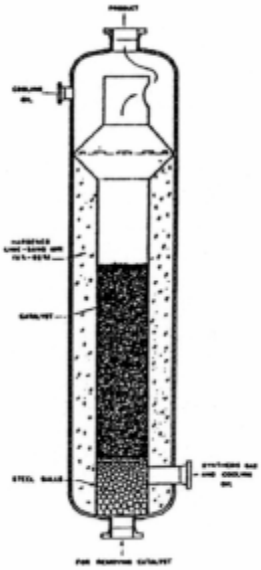

Figure 7. Slurry reactor used by U.S. Bureau of Mines.

In both Germany and the US, attempts were made to utilize a high recycle of unconverted gas (up to about 100:1 recycle:feed) to maintain temperature control in the reactor. A schematic of a multilayer reactor that utilizes cooling coils between the catalyst bed layers is illustrated in figure 8. Multilayer reactors were also used in other process schemes where the catalyst would be cooled by adding a spray of oil at the top of the reactor so that evaporation could remove much of the heat of reaction or the beds could be completely immersed in liquid or foam.

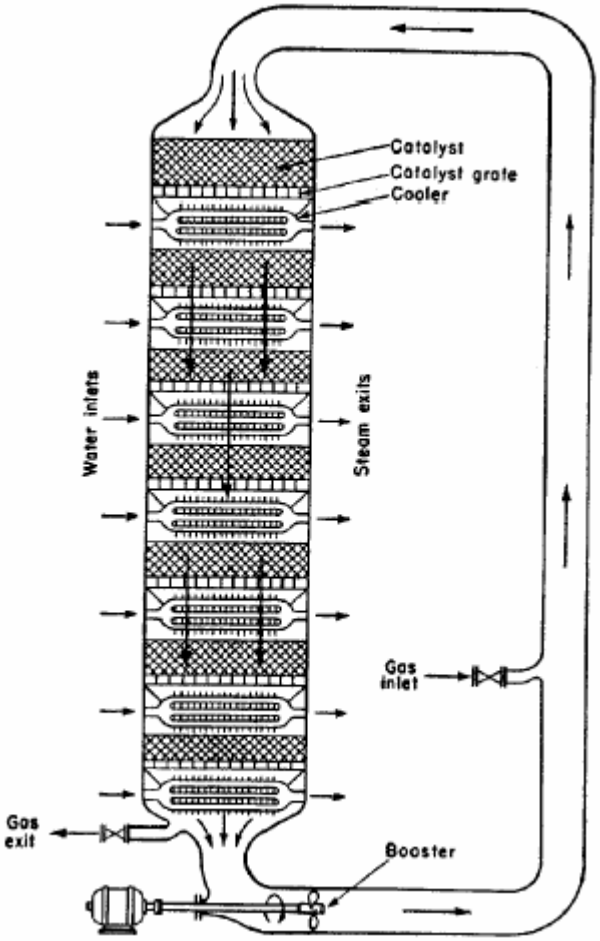

Figure 8. Multilayer converter for gas recycle, 20 atm.

For nearly 75 years, the "art" of reactor development has outpaced the "science and engineering understanding." For example, a translation of "The evaluation of converters for exothermic and endothermic catalytic reactions occurring within narrow temperature limits" was written during 1942 by a worker for I.G. Farbenindustrie A.G. at Leuna, where a major FTS commercial plant was operated[5]. The paper was translated because of interest in the US about design methods used in Germany. The translators considered that the methods were extreme simplifications of the actual physical problems and that their actual description of the phenomena that really occur were questionable. Two examples were cited: (1) the assumption that the heat generated per unit volume of catalyst is constant throughout the reactor could not represent the actual case and (2) the assumption that all of the heat generated was carried away by conduction through the catalyst bed in a direction transverse to the main gas flow to leave the reactor at the same temperature as it enters the reactor ignored the heat carried out of the reactor by the products. This provides an example of the difficulties modelers had during the pre-computer age. During the past 50 years exceptional advances have been made in reactor engineering and attention has been directed toward modeling bubble column reactors, driven in part by the potential application of these in large 30-50,000 bbl/day plants. Thus, instead of the simple concept of a reasonably uniform reactor volume, it is now recognized that the flows and the material distributions are very complex, as illustrated in the schematic in figures 9 and 10. Extensive modeling and/or experimental works are being conducted by many groups located in many countries. An example of the extent and complexity of the efforts is illustrated in the program at Washington University (located in the US) that is funded by government and industrial organizations (figure 11).

To predict the type of the next generation of reactors is fraught with danger. Today there is extensive interst in micro and this applies to reactors. Chemical companies are considering a variety of microchannel reactors with the intent of replacing one large reactor with many, many smaller reactors that provide improved control of important operating conditions. Others are looking at the adaptation monolith reactor technology that has been so successfully applied to auto catalysis to the more complex situation encountered in FTS.

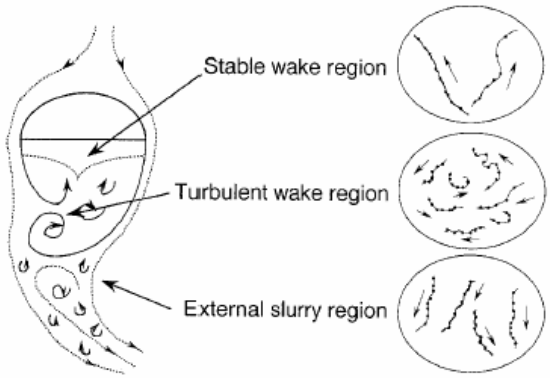

Figure 9. Typical particle trajectories within three different flow regions around a rising bubble.

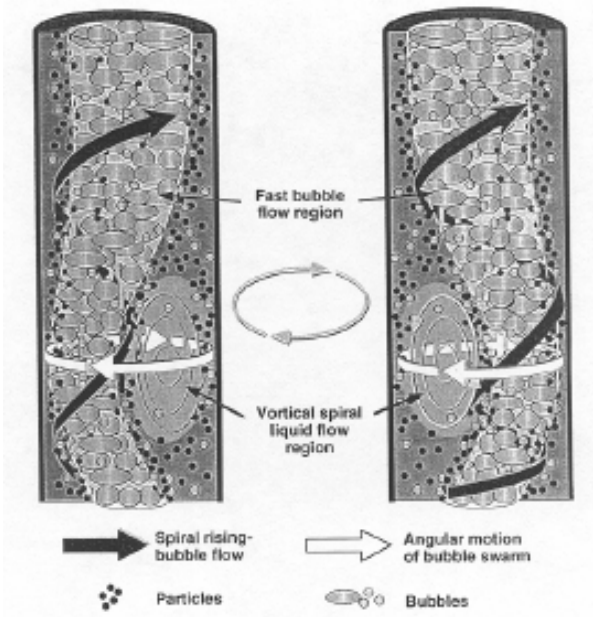

Figure 10. Model of flow scheme in the slurry bubble column.

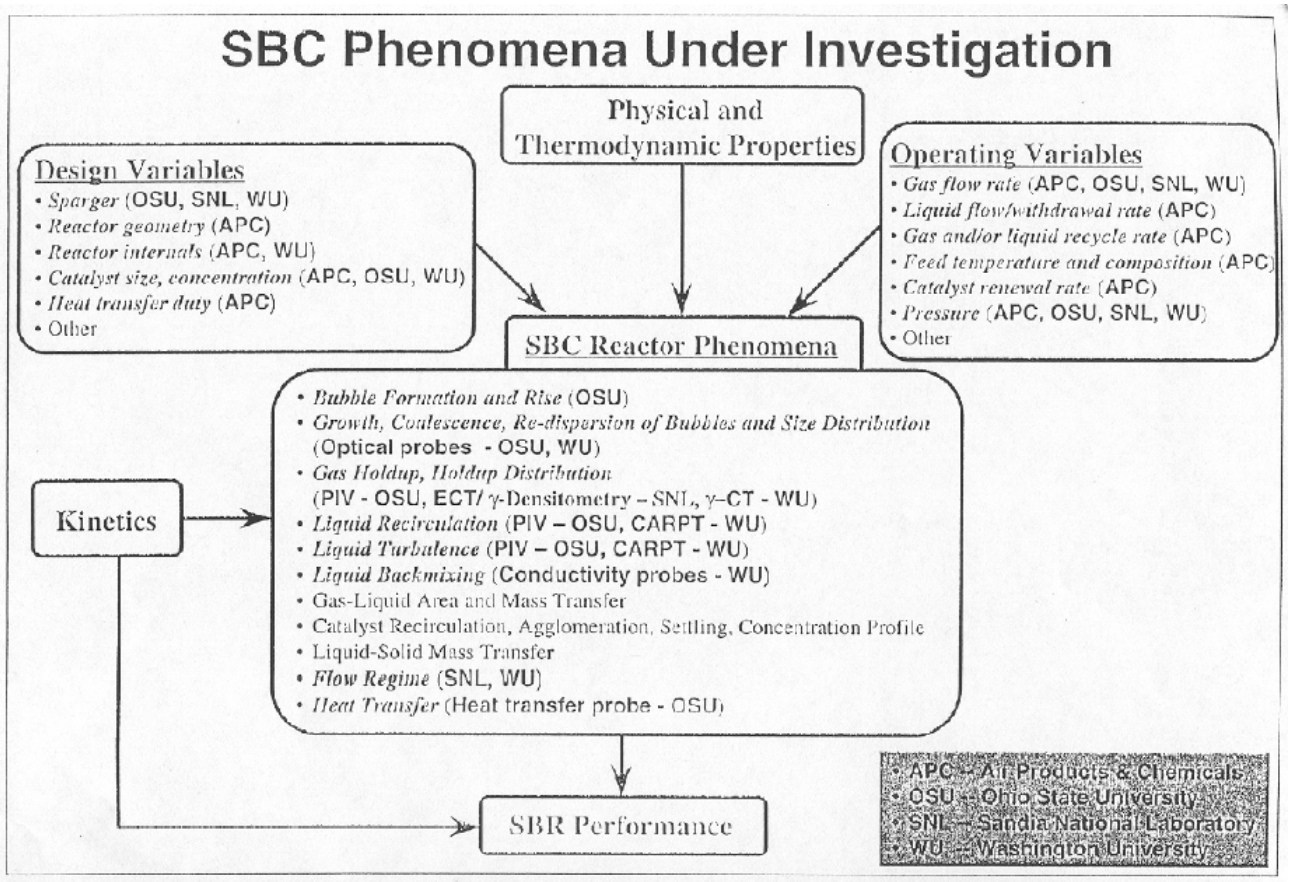

Figure 11. SBC phenomena under investigation.

While the reactor development has been slow, the changes in FT process developers have been very rapid. A comparison over a four year period (1999 vs. 2003) shows many changes with mergers and dropouts dominating the scene. This means that the "ownership" of reactor technology will become even less-well defined.

Acknowledgment. This work was supported by U.S. DOE contract number DEFC26-
98FT40308 and the Commonwealth of Kentucky.

References

1. H. Kölbel in Chimie Organique,(K. Winnacker and L. Küchler, Eds), Part 3, Editions Eyrolles, Paris, 1966, pp 627-740.
2. Jager, B., M. E. Dry, T. Shingles and A. P. Steynberg; Experience with a new type of reactor for Fischer-Tropsch synthesis; Catal. Lettr., 7, 293-302 (1990).
3. Kolbel, Herbert; M. Ralek; The FT synthesis in the liquid phase; Catal.Rev. Sci.Eng. 21 (l980) 225.
4. Deckwer, W.-D.; Bubble Column Reactors; Wiley, 1985.
5. "The evaluation of converters for exothermic and endothermic catalytic reactions occurring within narrow temperature limits," G. Wirth (R.C. Grass and H.J. Kandiner, translators, U.S. Bureau of Mines Information Circular 7587, Nov., 1950.

ConocoPhillips GTL Technology: The COPox™ Process as the SynGas Generator

H. A. Wright, J. D. Allison, D. S. Jack, G. H. Lewis; S. R. Landis

Ponca City Technology Center, ConocoPhillips, PO Box 1267, Ponca City, OK 74602

Abstract

This paper discusses the development of ConocoPhillips GTL technology specially the development of our proprietary COPox™ SynGas technology. This paper discusses what the COPox™ process is; how ConocoPhillips has developed the technology; and where ConocoPhillips is in the development of the technology. This paper will also discuss general syngas chemistry and where the COPox™ process fits into the spectrum of syngas technologies. A comparison with the leading SynGas technology shows that for an integrated GTL plant, COPox™ technology can improve the overall carbon efficiency of the GTL plant.

Introduction

ConocoPhillips has developed proprietary Gas-to-Liquids (GTL) technology to use to convert stranded natural gas to easily transportable fuels. This Gas-to-Liquids technology actually consists of at least three separate technologies that are integrated together to produce a highly efficient GTL process.

1. ConocoPhillips has developed a syngas process, catalyst, and reactor system for syngas generation called the COPox™ process.
2. ConocoPhillips has also developed a proprietary Fischer-Tropsch catalyst and reactor.
3. ConocoPhillips has also developed a proprietary Product Upgrading technology to convert the long chain hydrocarbons to useful fuel range materials.
4. ConocoPhillips has integrated these processes to enable high carbon efficiency; which results in a lower gas consumption per barrel of product produced.

What is the COPox™ Process

This paper concentrates on the COPox™ technology at ConocoPhillips. The COPox™ process is a synthesis gas generation technology. It is based on the catalytic partial oxidation of natural gas:

$$CH_4 + \tfrac{1}{2}\, O_2 \rightarrow 2\, H_2 + CO$$

This reaction is exothermic and with preheat can be run autothermally so that no additional external heat source is needed to aid in the generation of synthesis gas. We have found that successful catalytic partial oxidation should be operated with millisecond contact times with Gas Hourly Space Velocities around 500,000 hr^{-1} . The high space velocity of the COPox™ process relative to other systems means that the reactor volumes are considerably smaller leading to lower reactor and catalyst costs.

We started the development of ConocoPhillips GTL technology in 1997. We initially started working on Fischer Tropsch technology but quickly realized that if we were to get a breakthrough in this overall area we would have to tackle the syngas generation costs as well. Some studies were showing that upwards of 60% of the cost of a GTL plant could be in the syngas and related areas of the plant.[1] It was clear, that even a breakthrough in Fischer Tropsch would not make GTL economically viable without more.

In 1998, we started the development of the COPox™ process after a process economics review indicated that it could result in a lower cost, more efficient GTL process than other available technologies.

Since 1998, we have initiated a technology program for the COPox™ process as part of an overall GTL effort. Over 40 full time individuals work in the continuing development of COPox™ technology. This includes work in all areas of the technology commercialization including catalyst development, reactor process and mechanical design, reactor modeling including computational fluid dynamics; and process design engineering for scale up of our technology to the demonstration scale. Another 60 individuals work in the operations and maintenance of our new 400 BPD Demonstration Plant.

We currently have reactors of many different sizes in operation in Ponca City, OK. We learned early on in the development of the COPox™ technology, that most experiments needed to be done in high-pressure pilot reactors instead of the quartz atmospheric reactors often used in academia. We have two demonstration scale reactors that will be started up this summer that are each capable of processing enough natural gas to produce 400 BPD of liquid product out the back end of the plant. Table 1 shows the number and type of COPox™ reactors in operation in Ponca City.

Table 1. COPox™ High Pressure Reactors in Operation in Ponca City

Reactor Type	Number	FT Liquid Production
Demonstration Scale	2	400 BPD
Pilot Scale	2	>2 BPD
Catalyst Testing Scale	12	0.2 – 0.5 BPD

SynGas Chemistry

In addition to the partial oxidation reaction already mentioned, there are several other reactions that need to be accounted for in understanding the various means for syngas generation. The first is the steam methane reforming reaction $CH_4 + H_2O \rightarrow 3H_2 + CO$. The next is full combustion: $CH_4 + 2\, O_2 \rightarrow 2\, H_2O + CO_2$. The last key reaction is the water gas shift reaction $CO + H_2O \rightarrow CO_2 + H_2$

The combination of these reactions can aid in our understanding of why ConocoPhillips COPox™ technology can result in a very highly efficient GTL process. Each of the other syngas technologies use these reactions and approach thermodynamic equilibrium. Let's compare several possible syngas generators to COPox™ process for GTL plants.

1. Steam Methane Reformer (SMR)
2. Autothermal Reformer (ATR)
3. COPox™ Process
4. Non-Catalytic POX reactor (POX)

An important understanding of a natural gas feed, Cobalt FT catalyst based GTL Process is that H2 is consumed with CO in an overall ratio of 2.0 to 2.2. The closer this ratio is achieved in the syngas manufacturing step coupled with maximizing CO production, the more efficient the GTL Process will be.

There are several competitor syngas technologies used in a GTL process. Some potentially use a SMR to generate syngas. This uses the steam methane reforming reaction to make syngas with a H2/CO ratio of about 3.

An ATR makes syngas from the combustion, reforming, and water gas shift reaction. Oxygen is fed to the reactor so that the

system is autothermal. The H2/CO ratio of the syngas is dependent upon the steam to carbon ratio. Typically the steam to carbon ratio ranges from 0.6 to 1.0 or even more. This S/C ratio results in a syngas with a H2/CO ratio of 2.3 –2.5 or so. As the amount of steam declines the H2/CO ratio of the product syngas moves closer to the desired 2.0.

The COPox™ process will result in a syngas slightly below 2.0 in practice. The higher-pressure operation reduces the ratio from the ideal H2/CO ratio of 2 [2].

A non-catalytic POX reactor will result in a syngas H2/CO ratio in the 1.7-1.8 range. Figure 1 shows the H2/CO ratios of syngas produced by these various means.

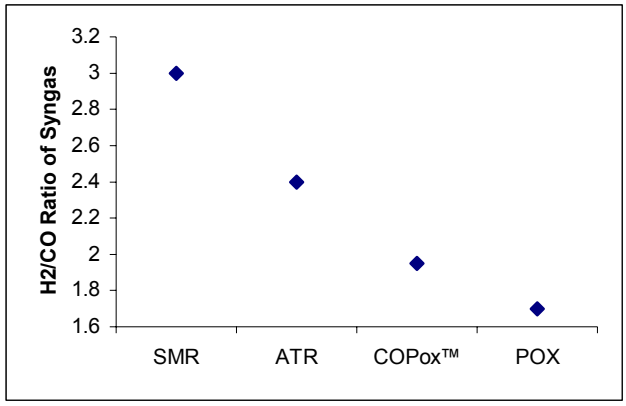

Figure 1. The Hydrogen to CO ratio of the syngas from various syngas generators determines the ultimate efficiency of the GTL process.

Clearly the farther from the Fischer Tropsch ideal ratio slightly greater than 2, then the more inefficient the overall GTL process probably is.

Another way to look at syngas generators is to look at the CO yield of the various means of producing syngas. If you pay for carbon from some natural gas source, it is clear that you want as much of it as possible to end up as CO not carbon dioxide. Figure 2 shows the single pass CO yield of the COPox™ process versus an ATR with a S/C (steam to carbon) ratio of 1.0 and 1.5 (assuming no CO2 or heavy hydrocarbon recycling). You can now see why there will be a continuing drive to lower the steam to carbon ratios in ATR's even further.

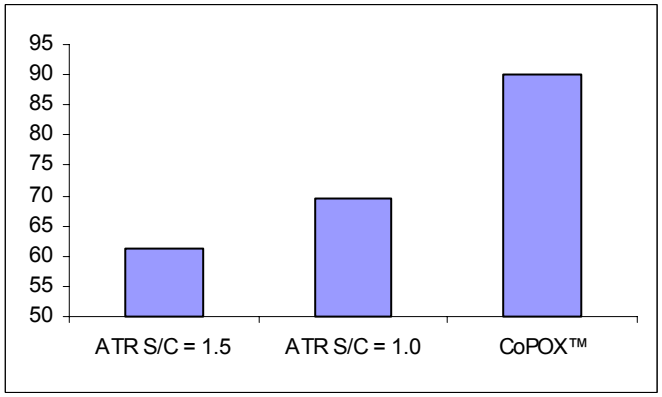

Figure 2. Carbon Monoxide yields for several ATR cases versus a COPox™ process. Assumes no recycle.

Conclusions

In conclusion, the COPox™ process provides the means to have a high efficiency and lower cost GTL facility. ConocoPhillips has spent the last 5 years developing the technology through the demonstration scale. The Demonstration Plant is in the commissioning stage and includes 2 reactors capable of producing syngas for a 400 BPD Fischer Tropsch plant.

References:

(1) Choi, G.; Kramer, S.; Tam, S.; and Fox, J; Prepr. Pap. - *Am. Chem. Soc., Div. Fuel Chem.*, **1997**, *42* (2), 667-671.

(2) Allison, J. D.; Swinney L. D.; Niu, T; Ricketson, K; Wang, D; Ramani, S.; Straguzzi, G. I.; Minahan, D. M.; Wright, H. A.; Hu, B.; U.S. Patent Application 20020115730; 2002.

Plasma Spray Coatings for Designing Next-Generation Supported Metal Catalysts for Methane Conversion into Clean Fuels

A. Kulkarni and H. Herman

Dept. of Materials Science & Engineering
Center for Thermal Spray Research
State University of New York
Stony Brook, NY 11794

Introduction

The commercial pathway to clean fuel production from methane requires an initial conversion into a mixture of synthesis gas, a mixture of carbon monoxide and hydrogen. This initial step results in more than two-thirds of the total process cost and is a target of extensive research. Ceramic systems such as membranes could play a critical role in synthesis gas production as well as hydrogen separation technologies. Plasma spray methods, in which powder particles are melt-sprayed onto a substrate, where they form a thick film, leaving an integral structure with pores, is a viable approach to fabricating membranes. Through-pores in the range from nano-sized to sub-micron are readily obtainable within such deposited microstructures. These pore systems can be employed for gas separation, operating at temperatures from ambient through over 2000^{o}C, e.g., using zirconia-based ceramics.

Experimental

Plasma spray is relatively straightforward in concept but rather complex in function. The plasma torch operates on direct current, which sustains a stable, non-transferred electric arc between a tungsten cathode and a annular water-cooled copper anode. A plasma forming gas (generally, argon or other inert gas, complemented by a few percent of an enthalpy enhancing gas, such as hydrogen) is introduced within the torch interior, the gas becoming ionized, and on exiting the anode nozzle, ionic-electron recombination occurs, relealsing consider enthalpy which is sufficient to melt and accelerate refractory ceramics to sonic velocities. The effective temperature of the plasma is in excess of 15,000K for a typical dc torch operating at 40 kW. The powder particles, approximately 40 micrometers in diameter, are accelerated and melted in the flame on their high-speed (100-300 M/sec) path to the substrate, where they impact and undergo rapid solidification. Plasma spray is used to form deposits of greater than 10 micrometers of a wide range of industrial materials, including nickel and ferrous alloys, refractory ceramics, such as aluminum oxide and zirconia-based ceramics.

Plasma spray technology has great potential in natural gas-related programs. It is clear that thermal spray can play a special role in the production of ceramic membranes for gas separation processes. In fact, thermal spray has been used for a number of years in the production of both electrodes and interconnects in solid oxide fuel cell (SOFC) manufacture. The NSF-supported Center for Thermal Spray Research, at SUNY-Stony Brook, has pioneered in the processing of controlled-porosity permeable ceramics. Part and parcel of this activity has been the capability to characterize the pore structure using a suite of experimental techniques: Mercury Porosymmetry, and working with NIST, Small-Angle Neutron Scattering (SANS) and X-Ray Computed Microtomography (XCMT).

Results and Discussion

XCMT studies have been carried out at the Advanced Photon Source/Argonne National Laboratory (APS/ANL) and the National Synchrotron Light Source/Brookhaven National Laboratory (NSLS/BNL) to characterize/visualize microstructure of thermal sprayed ceramic coatings (e.g., alumina, zirconia-based ceramics). Experiments focus on quantitative characterization of porosity and its variation with thickness. Through such studies, we wish to further our understanding on the influence of thermal exposure on relative changes in microstructural features in these coatings.

Experiments are being directed at SOFC and porous membranes. It is necessary to characterize multi-layered films of these functional energy-related functional coatings. This allows for characterization of a complete SOFC stack consisting of an interconnect, a cathode, an electrolyte and an anode. The system in case is porous nickel/YSZ cermet anode, a YSZ electrolyte and a porous (La,Sr)MnO3 cathode. While porosity plays a crucial role in operation of these SOFCs, the high operating temperatures (800^{o} – 1000^{o}C) of these structures cause microstructural changes and, thus, degradation of properties. Hence, maintenance of the porous structure is important.

Acknowledgment. This research at SUNY-Stony Brook is supported by the National Science Foundation MRSEC Program under Agreement No. DMR-9122444.

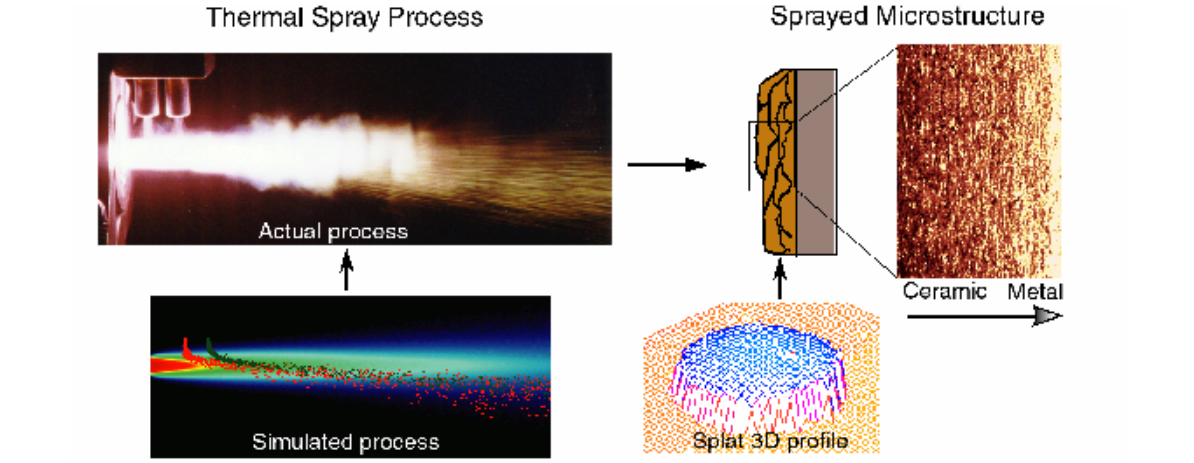

PLASMA CO_2 REFORMING OF METHANE VIA CORONA DISCHARGES

Changjun Liu, Genhui Xu

State Key Laboratory of C1 Chemistry and Technology,
School of Chemical Engineering, Tianjin University,
Tianjin 300072, China

Introduction

A lot of attentions have been recently paid to the CO_2 reforming of methane to syngas. A major reason for it is that this reaction can provide us a syngas with a 1/1 ratio of H_2 and CO, which is typically suitable for the synthesis of valuable oxygenated chemicals.[1] Among the catalysts developed, Al_2O_3 supported Ni catalysts were extensively investigated due to their relatively high activity and low cost. The major problem for the further practical application of these nickel catalysts is the deactivation of the catalyst, suffered from carbon deposition on the catalyst during reactions. Many investigators are working on the improvement in this nickel catalyst by using the addition of promoters,[2, 3] using novel reactor configurations,[4] and using different supports.[3] In this work, we attempt to use an AC corona discharge plasma for the CO_2 reforming of methane to syngas. A stable operation of plasma CO_2 reforming of methane has been achieved.

Experimental

The corona discharge dry reforming was carried out in a quartz tube reactor with an I.D. of 6.0 mm and a length of 0.6 m. The reactor system has been described previously.[5] The corona discharge reactor consists of two electrodes, a top metal wire electrode and a lower hollow electrode as the grounded one. The volume between these two stainless steel electrodes is 340 mm^3. The feed gases, CO_2, CH_4 and the dilution gas, helium, are introduced into the reactor via flow meters. The feed gas flow enters the upstream wire electrode and exits at the downstream grounded one. The gas discharge is generated between these two electrodes by an AC generator. The AC electric field operates at a frequency of 60 Hz. The AC voltage provides us with an easy way to generate the streamer corona discharge, which takes place only when the voltage reaches a sufficiently high level during each half cycle. In the discharge volume, the interaction between accelerated charged particles (i.e., electrons and ions) and other chemical species (i.e., molecules and radicals) takes place. The feed and effluent product gases are analyzed by an on line gas chromatograph with a TCD detector.

Results and Discussion

Figure 1 shows an effect of input voltage on discharge reactions with a constant CO_2/CH_4 ratio of 4:1. The conversions of CH_4 and CO_2 increase with the increasing input voltage at the beginning. The formation rates of products, syngas and a small amount of C_2 hydrocarbons, also increase with this increasing input voltage. The methane conversion increases slightly with the increasing input voltage after the input voltage reaches 5 kV, but the formation of syngas increases quickly with the increasing input voltage.

Figure 2 presents an effect of residence time on the plasma dry reforming. Evidently, the low residence time (high flow rate) is favored for the production of syngas (C_2 hydrocarbons too). This suggests that the plasma dry reforming is a quickly reaction.

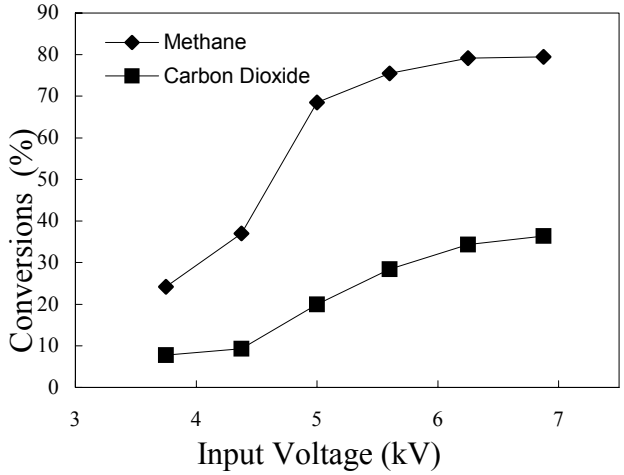

Figure 1. Effect of input voltage (gas composition: CH_4 — 5%, CO_2 — 20%, He — 75%; total gas feed: 100 cm^3/s; ac electric field frequency: 60Hz).

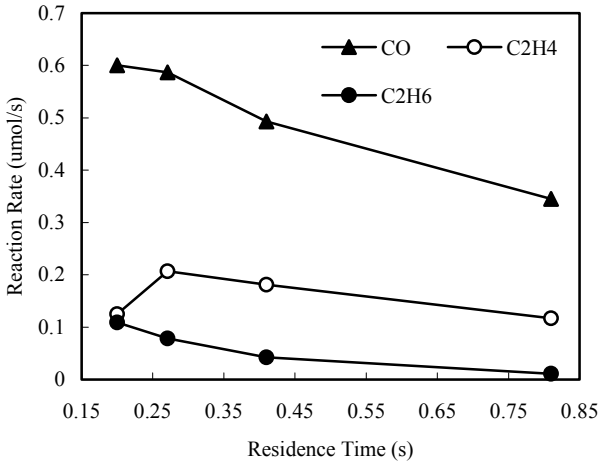

Figure 2. Effect of residence time (gas composition: CH_4 — 5%, CO_2 — 20%, He — 75%; total gas feed: 100 cm^3/s; ac electric field frequency: 60Hz).

The present investigation confirms the plasma dry reforming of methane using a simple corona reactor is effective. The major advantage of this plasma dry reforming is its high stability. The ratio of hydrogen and carbon monoxide of syngas produced is based on the feed ratio of methane and carbon dioxide. The input voltage (or the input power) and the residence time (or the feed flowrate) have also a significant effect. Further investigation is being conducted.

References

1. Lunsford J.H., *Cata. Today*, **2000**, 63, 165-174.
2. Lemonidou A. and Vasalos I.A., *Appl. Catal. A*, **2002**, 228, 227-235.
3. Chang J.-S., Park S.E, Yoo Y.W., and Park J.-N., *J. Catal.*, **2000**, 195, 1-11.
4. Wang L., Murata K., and Inaba M., *ACS Symp. Series*, 852, 57-68.
5. Liu C.-J. (1996) Oxidative synthesis of higher hydrocarbons from CO_2 and CH_4 by streamer discharges. ***Chem. Lett.***, 749.

OPPORTUNITIES AND CHALLENGES FOR FUEL CELLS IN INDIA

T.S.R. Prasada Rao[1] and Uday T. Turaga[2]

[1]Sarasijam Technologies, New Delhi 110024, India
[2]Fuel Science Program, Department of Energy and Geo-Environmental Engineering, The Pennsylvania State University, University Park, PA 16802, U.S.A.

Introduction

Recent U.S. initiatives such as Freedom CAR exemplify a growing commitment to energy conversion using fuel cells because of their efficiency and environmental advantages. The growing feasibility of fuel cells has important implications particularly for developing countries like India. Fuel cells could make available an opportunity to provide clean energy to India's population of one billion and reduce its energy supply-demand gap. Such opportunities, however, are tempered by enormous technical and economic challenges. Technical challenges include identification and development of suitable fuel cell technologies for applications often unique to the developing world. Some of the available fuels might call for modified reforming technologies to produce hydrogen. Economic challenges include the need for more stringent environmental regulations, incentives for cleaner forms of energy, infrastructure development, and a less risk-averse business climate.

Increased Capacity and Productivity of Energy Conversion and Utilization

The consulting firm, McKinsey and Co., Inc., in a recent study said that India needs economic growth of 10% every year to avoid societal conflict and satisfy the needs and aspirations of a population that is already at one billion and growing. Providing energy required to fuel such economic growth is not a trivial issue of simply producing more petroleum, natural gas, and electricity. Because of constrained resources and new environmental drivers, e.g., the Kyoto Protocol to which India is a signatory, a significant increase in the productivity of energy conversion and utilization is required.

Fuel cells, in principle, could provide that jump in both environmental and economic productivity. For example, from an environmental productivity perspective, it is estimated that a 200 kW fuel cell-based power plant will generate 60% less carbon dioxide than a coal or natural gas fired power plant. Although fuel cells for transportation are an area of intense research in the developed world and have relevance for public transportation in developing countries like India, e.g., buses and railways, this paper will highlight the role of fuel cells for power generation which will most likely be the first commercial application of fuel cells in India.

Fuel Cells for Power Generation

In 2000, the total electricity generation capacity in India was almost 100,000 MW, the bulk of which came from coal-fired power plants (see Table 1 for a distribution of power generation by fuel-type). On a per capita basis, electricity sold to consumers in India was a paltry 0.3 MWh as compared to 11 MWh in the U.S. Obviously, with development, per capita electricity consumption in India is bound to increase in the future. Although generation capacity has been growing at 5% annually, growth needs to be 15% to meet the target economic growth rate of 10%.

More substantially, there needs to be a drastic improvement in the efficiency or productivity of both electricity generation and transmission and distribution (T&D). Currently, India's productivity levels are abysmally low at 34 and 4% of those in the U.S. for the generation and T&D of electricity, respectively. While policy reforms will certainly improve these productivity levels substantially, they cannot be expected to account entirely for the growth required in electricity generation.

Fuel cells for power generation have the most near-term potential in three Indian markets. The first of these is the premium power market i.e., segments willing to pay a premium for power supply that is adequate and, more importantly, reliable. Because of shortage (exceeding 11% in 1997) and uncertainty of power supply, several segments of this market, e.g., hotels, hospitals, information technology companies, and certain manufacturing plants, have invested in some form of captive power generation. These segments that already have some form of captive power generation will evolve into niche markets for fuel cells. The Tata Energy Research Institute recently studied this niche markets and found that the key issues are cost and the availability of fuels for either direct use in fuel cells or reforming to produce hydrogen. Some results from this study are presented in Table 2. While some segments of this markets will support capital costs of $3,000-4,000/kW, extensive penetration will occur only when the costs come down to $500-1,000/kW.

The second market could comprise remote and rural areas where electricity supply is currently unavailable and difficult because of infrastructure problems. These areas would typically use locally available opportunity fuels such as biomass. It is expected that significant governmental incentives and support would create and sustain this niche market.

The final market comprises large stationary-power generation using fuel cells particularly if technologies using molten carbonate and solid-oxide fuel cells become cost-effective and commercially available. A significant problem with the Indian power industry is T&D losses of the order of 20-25% of total electricity generated, as compared to less than 2% in the U.S. Although effective policy reforms should reduce this number considerably, any continuation of this situation could result in the development of a strong distributed fuel cell-based power generation market.

It is expected that the distributed power generation market will see players besides typical power producers. These new entrants could include fuel supply and transport companies seeking growth through the fuel cell-based power generation. These markets will, however, become real only if the cost of fuel cell-based power decreases from current estimates of $3,000-5,000/kW to $800-1,000/kW or less.

Fuel Processing Issues

The availability of fuels for either direct use or reforming to produce hydrogen will be a critical issue. Hydrogen, natural gas, methanol, gasoline, and diesel are all typical fuels or hydrogen sources for fuel cells. Of these, gasoline and diesel are currently produced in surplus of demand in India. However, consumption rates for both are going to increase substantially in the near future. Further, sulfur specifications for these fuels are much higher than tolerated by reforming catalysts or the fuel cells. The remaining fuels, hydrogen, natural gas, and methanol, are all in short supply. The utilization of these fuels in fuel cells could also be limited because of safety and infrastructure considerations. For example, widespread use of compressed natural gas for public transportation was recently not found viable because of the absence of a pipeline-based distribution network.

Two other fuels, dimethyl ether (DME) and renewable biomass, could become important in the long-term for hydrogen production. Key success factors for a DME scheme are access to cost advantaged gas, proximity to market, and the presence of credible business and technology partners. DME is distinct from liquefied natural gas (LNG) because (1) DME requires cheaper receiving facilities and (2) a competitively priced fuel on a much smaller scale can be delivered.

In the late 1990s, one of this paper's authors conceptualized and spearheaded the DME Project Consortium which included British Petroleum, Indian Oil Corporation (India's largest publicly-owned oil company), Gas Authority of India (India's largest natural gas company), and the Indian Institute of Petroleum (India's premier downstream petroleum research and development organization). The project was initially established to promote DME as a clean alternative to diesel fuel. Rapid changes in market economics, however, changed the project's focus into positioning DME as a fuel for power generation. Briefly, the plan was to produce DME directly from methanol using Haldor Topsoe's proprietary technology (licensed to BP). DME from such a plant, ideally located in the Middle East, would be shipped to India via tanker and sold to power generators to produce clean electricity. Economic feasibility studies had suggested a viable rate of return for such a project. Although the project has been shelved, it remains an interesting and viable proposal.

Sixty percent of India's labor is employed in agriculture which is the cornerstone of the country's economy. Agriculture-derived biomass is a renewable feedstock that is underutilized for generating energy. Recently, several initiatives have been taken to exploit the use of agricultural biomass for power generation. There is strong governmental support for these initiatives and technologies utilizing renewable feedstocks for hydrogen production, e.g., hydrogen production using carbohydrates, should be advantageous for the fuel cells market.

Conclusions

Several economic and environmental drivers are motivating developing countries like India to evaluate fuel cells. The development of new fuel cell technology that is cost-effective, suited to local needs, and employs region-specific and opportunity fuels should be commercially successful. This paper has highlighted the Indian situation with respect to the need for fuel cells, the power generation needs, and identified specific fuel supply strategies to meet any growth in fuel cells.

Acknowledgements. The authors are grateful to Uma Parameswaran, Anju Sharma, Manoj Kumar, and Vibhuti Shekhar Mishra of Sci Tech Patent Art Limited, Hyderabad for useful inputs.

Table 1. Electricity generation in India (1998) and the U.S. (1999) by fuel type.

Fuel	Percent of electricity generated in India	Percent of electricity generated in U.S.
Coal	71	58
Natural gas	8	9
Oil	1	3
Nuclear	2	20
Hydro	18	10
Total	100	100

Table 2. A summary of issues concerning representative niche markets for stationary power generation using fuel cells in India.

Market	Power needs (MW)	Potential fuel cell (FC) types[1]	Potential FC-based electricity	Comments[2]
Hotels	0.5-5.0	PAFC, MCFC, SOFC	Multiple 0.2-0.25 MW units	Natural gas must be available
Chlor-alkali industry	5-45	MCFC, SOFC	Multiple 0.2-0.25 MW units	Hydrogen readily available; balance of plant requires heat
Pulp and paper industry	2-50	MCFC, SOFC	Multiple 0.2-0.25 MW units	Natural gas must be available; balance of plant requires heat
Dairy industry	<5	PEMFC, AFC, PAFC	One or two 10-50 kW units	Biogas reforming technologies for hydrogen will be an advantage
Telecom and IT	<5	PEMFC, AFC, PAFC	One or two 10-50 kW units	Natural gas must be available

[1]PAFC, Phosphoric acid fuel cell; MCFC, Molten carbonate fuel cell; SOFC, Solid oxide fuel cell; PEMFC, Polymer electrolyte membrane fuel cell; AFC, Alkaline fuel cell.

[2]It is trivial to state that cost is an issue common to all markets.

REFORMING CATALYSTS FOR ON-BOARD FUEL PROCESSING

Theodore Krause, Magali Ferrandon, and Cécile Rossignol

Chemical Engineering Division
Argonne National Laboratory
9700 South Cass Ave.
Argonne, IL 60439

Introduction

Fuel cell development has seen remarkable progress in the past decade because of an increasing need to improve energy efficiency as well as to address concerns about the environmental consequences of using fossil fuels for the propulsion of vehicles.[1] The lack of an infrastructure for producing and distributing H_2 has led to a research effort to develop on-board fuel processing technology for reforming hydrocarbon fuels to generate H_2.[2] The primary focus is on reforming gasoline, because a production and distribution infrastructure for gasoline already exists to supply internal combustion engines.[3]

The choice of the reaction process for on-board reforming depends on the operating characteristics (e.g., varying power demand, rapid startup, frequent shutdowns) for transportation applications. Steam reforming results in the highest concentration of H_2 but has heat transfer limitations. Autothermal reforming and partial oxidation may be self-sustaining but result in lower H_2 concentrations due to the N_2 dilution because air, and not pure oxygen, is used. Because steam reforming is heat and mass transfer limited, it does not respond rapidly to changes in the power demand (i.e., "load following"), which would be experienced frequently during a normal driving cycle. When power demand decreases rapidly, the catalyst can overheat, causing sintering, which in turn results in a loss of activity. Autothermal reforming can overcome the load following limitations of steam reforming since the heat required for the endothermic reactions is generated within the catalyst bed, a property that allows for more rapid response to changing power demands and faster startup.[4] The lower operating temperature of catalytic autothermal reforming has several advantages, including less complicated reactor design, wider choice of materials of construction, and lower fuel requirements during startup over the higher operating temperature of partial oxidation or the endothermic steam reforming processes for transportation applications.[5]

To meet the performance targets established by the Department of Energy for on-board fuel processing for transportation applications (i.e., process the feed at a gas hourly space velocity (GHSV) of 200,000 h^{-1} with a fuel conversion of >99.9% and a H_2 selectivity of >80% and have a lifetime of 5,000 h) new reforming catalysts will have to be developed that exhibit higher activity and better thermal and mechanical stability than commercial Ni-based steam reforming catalysts.

Experimental

Three different formulations of the ANL catalyst,[6] Rh, Pt or Rh-Pt dispersed on a gadolinium-doped ceria substrate and coated onto 600 cpi cordierite monoliths, were evaluated for autothermal reforming of a sulfur-free (<450 ppb S) gasoline and a low sulfur (30 ppm S) gasoline, both purchased from Chevron Phillips Chemical Company. These catalysts were tested in a microreactor system consisting of a 0.50-in. diameter stainless steel reactor tube contained in a temperature-programmable furnace. The fuel feed rate was 0.18 mL/min and the air and water feed rates were set so that O_2:C ratio ranged from 0.45–0.50 and H_2O:C ratio ranged from 1.6–1.8. The length of the monolith samples was varied so that the gas-hourly space velocity, based on the feed composition, ranged from 27,000–110,000 h^{-1}. A blank-tube experiment was conducted to determine the extent of gas-phase thermal cracking. For these experiments, the furnace was maintained at a constant temperature over the range of 500–800ºC and the temperatures at the top and the bottom of the monolith were measured using Omega K-type thermocouples. Samples of the product gas were analyzed for H_2, CO, CO_2, and C_1–C_8 hydrocarbons using either a Hewlett-Packard 5890 Series II gas chromatograph or a Wasson gas chromatograph-mass spectrometer.

Results and Discussion

The Rh-containing catalysts (Rh and the bimetallic Rh-Pt) were more active than the Pt catalysts, both producing a fuel gas containing >55% H_2 on a N_2-free, dry basis from the sulfur-free gasoline at a furnace temperature of 700ºC, as shown in **Figure 1**. For the two Rh-containing catalysts, the carbon selectivity to CO_x exceeded 90% and fuel gas contained 3–3.5% hydrocarbon by volume, with CH_4 being the primary hydrocarbon product. The Pt catalyst was less active, producing a fuel gas containing 33% H_2 on a N_2-free, dry basis. For the Pt catalyst, the carbon selectivity to CO_x was ~50% and the fuel gas contained 19% hydrocarbon by volume, consisting mainly of aromatics, such as benzene and toluene, and C_2–C_6 olefins. A blank-tube experiment showed that the gasoline can undergo gas-phase reactions, including oxidation reactions involving O_2 to produce CO and CO_2, and thermal cracking to yield a wide range of hydrocarbons, including benzene, toluene, and C_2–C_6 olefins, and some H_2. The fact that the Rh-containing catalysts performed better is not surprising, since studies have shown that Rh is more active than Pt for steam reforming.[7]

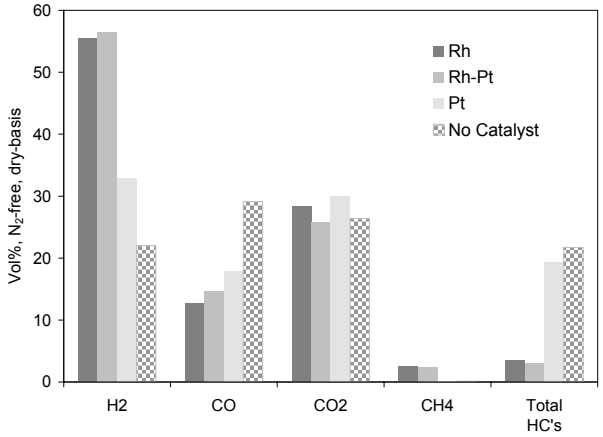

Figure 1. Primary product yield for Rh, Rh-Pt, and Pt catalysts for reforming sulfur-free gasoline at a GHSV of 27,000 h^{-1}. The O_2:C ratio was 0.5 and H_2O:C ratio was 1.8. Furnace temperature is 700ºC.

The effect of the gas-hourly space velocity (based on the feed rate) on product yield for the Rh-catalyst was investigated as shown in **Figure 2**. The H_2 concentration in the fuel gas decreased very slightly from 55% to 54% as the GHSV was increased from 27,000 to 110,000 h^{-1}. Although the H_2 concentration was relatively independent of GHSV, the CO concentration increased from 12.7 to 17.0% and the CO_2 concentration decreased from 28.4 to 23.6% as the GHSV was increased from 27,000 to 110,000 h^{-1}. The increase in the CO concentration with increasing GHSV is significant because it can increase the size of the water-gas shift reactor in the fuel processor.

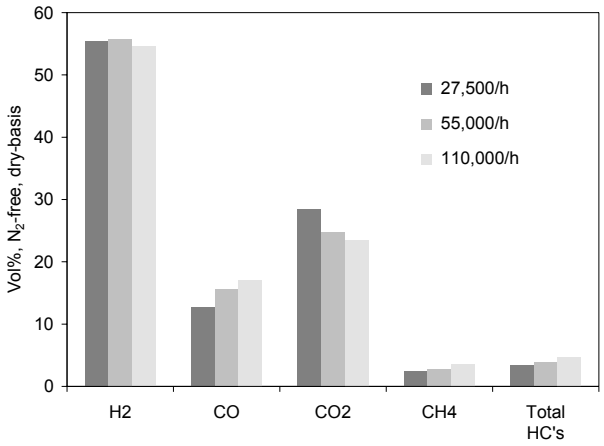

Figure 2. Primary product yield for Rh catalyst for reforming sulfur-free gasoline for GHSV from 27,000-110,000 h^{-1}. The O_2:C ratio was 0.5 and H_2O:C ratio was 1.8. Furnace temperature was 700°C.

Hydrocarbon breakthrough is a concern because it reduces the fuel efficiency and, depending on the nature of the hydrocarbon, may poison other catalysts in the fuel processor. **Figure 3** shows the yield of C_2–C_6 hydrocarbons, benzene, toluene, and xylenes, for the Rh catalyst at three different furnace temperatures. As expected, the hydrocarbon yield decreases as the furnace temperature is increased. Generally, the low carbon number (C_2–C_5) hydrocarbons are produced by the cracking of higher carbon number hydrocarbons present in gasoline. In addition to being present in gasoline, benzene and toluene can be produced by a number of reactions during reforming, including demethylation of toluene and xylenes, dehydrogenation of cyclohexane and cyclohexane derivatives,[8] and cyclic rearrangement of paraffinic molecules larger than C_6,[9] that are present in the gasoline. Aromatics are problematic because they tend to adsorb more strongly on the active metal sites and are more difficult to reduce than aliphatic hydrocarbons.[8]

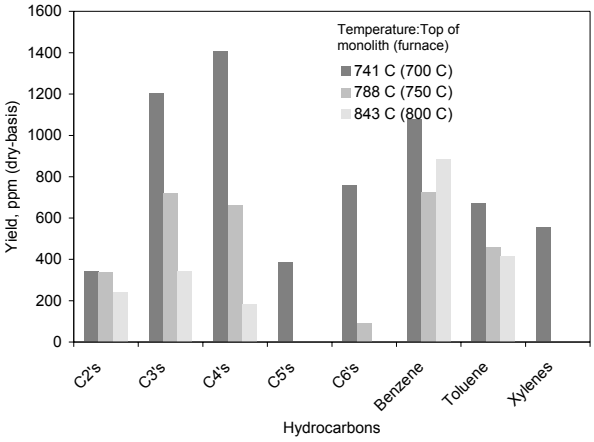

Figure 3. Selected hydrocarbon yields for Rh catalyst from reforming sulfur-free gasoline at three different furnace temperatures. GHSV, 27,000 h^{-1}; O_2:C ratio, 0.5; and H_2O:C ratio, 1.8.

A long-term test using both the no-sulfur and low sulfur gasolines was conducted to investigate the stability and sulfur tolerance of the Rh catalyst. As shown in **Figure 4**, the H_2 concentration decreased slightly from 59% to 56% in the fuel gas produced from the no sulfur gasoline during the first 48 h. When the fuel was switched to the low sulfur gasoline, the H_2 concentration decreased from 54% to 49% and the CH_4 concentration increased from 2.7% to 5 %.

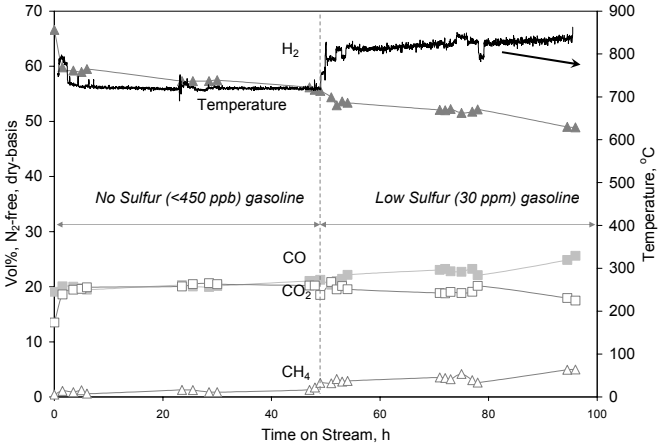

Figure 4. Primary product yields for Rh catalyst from reforming sulfur-free gasoline and a low sulfur gasoline. GHSV, 57,000 h^{-1}; O_2:C ratio, 0.45; and H_2O:C ratio, 1.6.

Conclusions

Rh, Pt, and Pt-Rh supported on a gadolinium-doped ceria substrate were evaluated for their ability to autothermally reform a no-sulfur gasoline. The Rh-containing catalysts produced a fuel gas with >55% H_2 (N_2-free, dry-basis) at a furnace temperature of 700°C and a GHSV of 27,000 h^{-1}. The H_2 concentration in the fuel gas produced by the Rh catalyst was constant at 54–55% as the GHSV was increased from 27,000 to 110,000 h^{-1}; however, the CO concentration increased as the GHSV was increased. Long-term testing of the Rh catalyst with both no sulfur and low sulfur gasolines showed that the catalyst loses activity due to deactivation and sulfur poisoning, but complete loss of reforming activity was not observed.

Acknowledgement. This work was supported by the Office of Hydrogen, Fuel Cells, and Infrastructure Technologies, U.S. Department of Energy, Office of Energy Efficiency and Renewable Energy, under Contract W-31-109-ENG-38.

References

(1) Carrette, L.; Friedrich, K. A.; Stimming, U. *Fuel Cells*, **2001**, *1(1)*, 5.
(2) Ranabm, V. *Chem. Ind,*. **1997**, 771.
(3) Arthur D. Little, Inc., Multifuel Reformers for Fuel Cells Used in Transportation - Assessment of Hydrogen Storage Technologies, U.S. Department of Energy, DOE/CE/50343-1, **1994**.
(4) Kumar, R.; Ahmed, S.; Krumpelt, M.; Myles, K. M., **1993**, U.S. Patent 5,248,566.
(5) Ahmed, S.; Krumpelt, M. *Int. J. of Hydrogen Energy*, **2001**, *26(4)*, 291.
(6) Krumpelt, M.; Ahmed, S.; Kumar, R.; Doshi, R. **2000**, U.S. Patent 6,110,861.
(7) Rostrup-Nielsen, J. R., *J. Catal*., **1973**, *31*, 173.
(8) Kopasz, J., Krause, T., "Fuel Requirements for Fuel Cell Systems," *Preprints Symposium of the Division of Fuel Chemistry of the American Chemical Society*, **2002**, *47(2*), 489.
(9) Wang, X., Gorte, R. J. Appl. Catal. A Gen., **2002**, *224*, 209.

HYDROGEN PRODUCTION FROM METHANE USING A REDUCTION-FREE NICKEL CATALYST

Richard A. Couttenye[*], *Marianela Hoz de Vila*[*], *Steven L. Suib*[+]

U-60, [+]Department of Chemistry, and [*]Department of Chemical Engineering, University of Connecticut, Storrs, Connecticut 06269

Introduction

Hydrogen (H_2) has been widely used in: a)petroleum industry, b) production of ammonia, c) hydrogenation of fats and oils, d) welding, e) production of hydrochloric acid, f) fuel for rockets, and recently for fuel cells. Worldwide, 48% of hydrogen is produced from natural gas, 30% from oil (mostly consumed in refineries), 18% from coal, and the remaining (4%) via water electrolysis. The conventional steam reforming for the production of H_2 from methane (CH_4) is a high-temperature process (>800°C) and produce carbon monoxide also. The latest publications in catalytic decomposition of methane to produce hydrogen have been reviewed by Choudhary[3] et.al. It is noticed that nickel catalysts needed to be activated prior to use (i.e. reduction with H_2 at 600°C for 2h), hence, having a reduction-free catalyst is desirable.

The present investigation involved the synthesis and characterization of a novel nickel catalyst (no activation required) for H_2 production from CH_4.

Experimental

Catalyst preparation. The cordierite ($(Mg_2Al_4Si_5O_{18}$, Corning's Celcor substrate code 9475 with 400 squares/inch^2) monolith substrate was initially dipped into a 0.5 M nickel (II) acetate tetrahydrate ($(CH_3CO_2)_2Ni.4H_2O$, CAS: 6018-89-9, Aldrich Chemical company Milwaukee, WI) solution for 24 hours at room temperature, and dried at 120°C for 5 hours. The monoliths were then calcined in air at 500°C during 2h. The final catalyst content on the monolith was 8 wt%.

X-ray Photoelectron Spectroscopy (XPS). Thermal decomposition (25-400°C) of Nickel(II) acetate, in vacuum, was followed by C 1s, O 1s, Ni 2p regions in the XPS spectra using a Leybold-Heraeus spectrometer model LHS-11.

X-ray Diffraction (XRD). X-ray diffraction (XRD) analysis was used to identify the nature of the powder material. X-ray diffraction (XRD) data were obtained with a Scintag 2000 XDS diffractometer with CuKα X-ray radiation. Powder samples were placed on aluminum slides and scanned at 4° 2θ/min. The beam voltage and beam current were 45 kV and 40 mA, respectively.

Scanning electron microscopy (SEM). The morphology of the materials, before and after reaction, was checked by scanning electron microscopy (SEM). SEM micrographs were taken in an Amray 1810 Scanning Electron Microscope. Samples were mounted on carbon tape onto aluminum sample holders for analysis.

Catalyst activity. The Nickel catalysts was tested in a quartz tube reactor operating at atmospheric pressure. A reactant mixture of 15% methane in helium was fed to the reactor at 30mL/min. Three catalytic monoliths (D= 10mm, L= 20mm) were staked in the reactor with a total catalyst load of 0.12 g. The product stream was analyzed using mass spectrometry (MS) with a MKS-UTI PPT quadrupole residual gas analyzer. The effect of flow rate (5-60mL/min) and reaction temperature (450-550°C) on hydrogen production was evaluated.

Results and Discussion

Ni (2p) regions in the XPS spectra for nickel (II) acetate decomposition in vacuum showed formation of metallic nickel on the surface at 400°C. The decrease of O (1s) line intensity also confirmed the presence of small amounts of nickel oxide.

Likewise, decomposition of nickel (II) acetate in air at 500°C for 1 hour results in the formation of a mixture of nickel oxide and metallic nickel as shown in the XRD spectrum (Figure 1)

Mass spectroscopy data showed 100% selectivity toward hydrogen in the gas phase for methane decomposition on the nickel catalyst. No detrimental effect on activity or selectivity was observed after 25 hours of continuous operation.

Figure 2 shows the effect of temperature on methane conversion. Conversion increases linearly with temperature in the 450-550°C range. The flow rate effect on hydrogen production is shown in Figure 3. For this particular system, it is confirmed that further increase in flow rate (>30mL/min), will result in only a small increase in hydrogen production.

SEM micrograph of the sample taken after 3 hours of reaction (475°C) showed carbonaceous materials deposited on the catalyst surface. This result was expected since CO and CO_2 were not generated during the reaction due to the lack of oxygen.

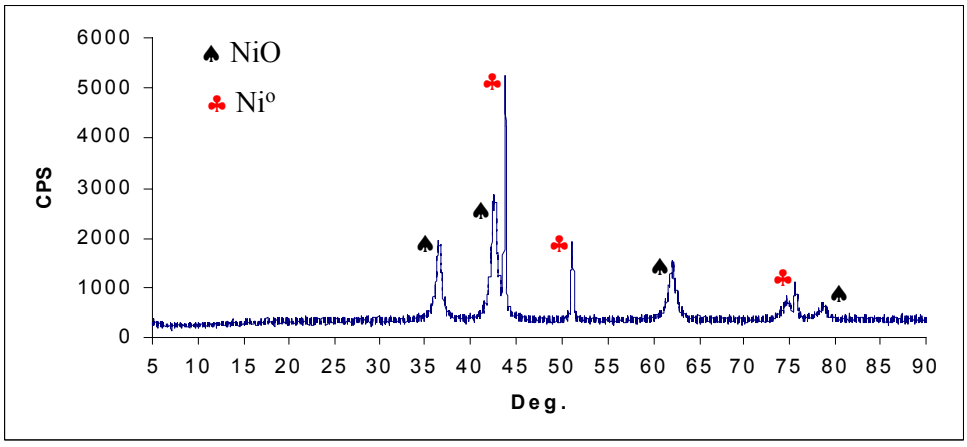

Figure 1. XRD of nickel acetate after decomposition in air at 500oC during 1hr.

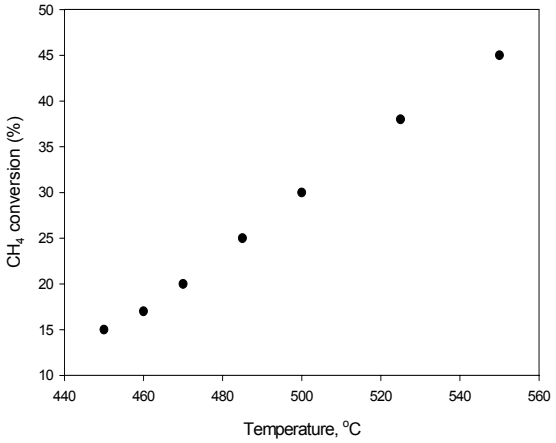

Figure 2. Effect of Temperature on the methane production conversion. Feed, 15% CH_4 in He. Flow rate, 30 ml/min

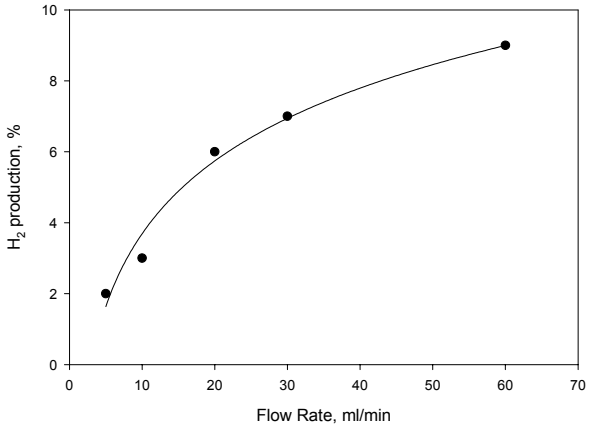

Figure 3. Effect of Flow rate on H_2 Feed, 15% CH_4 in He. Temperature: 475°C.

Conclusions

Thermal decomposition (500°C for 1h) of nickel acetate in air results in the formation of a mixture Ni^o and NiO. This mixture is catalytically active for decomposition of methane at 450°C, and reduction of the catalyst prior to the reaction, is not needed.

The active specie during the methane decomposition at 475°C seems to be Ni^o as suggested by the XRD and XPS results. Conversion of methane range from 15% (450°C) to 45% (550°C), with 100% selectivity to H_2 in the gas phase.

References

(1) Recupero, V.; Pino, L.; Di Leonardo, R.; Lagana, M.; Maggio, G. *Journal of Power Sources*., **1998**, *71*, 208.

(2) Lindström, B.; Agrell, J.; Pettersson, L.J. *Chemical Engineering Journal*., **2003**, *93*, 91.

(3) Choudhary, V.R.; Banerjee, S.; Rajput, A.M. *Applied Catalysis A: General*., **2002**, *234*, 259.

COMPARATIVE STUDY OF CARBON FORMATION ON SUPPORTED NI CATALYSTS DURING CH4 REFORMING USING TEOM, TPO-IR, TPD-IR AND TGA TECHNIQUES

Jian Zheng[a], Chunshan Song[a], Wei Pan[a], Lu Sun[a], Shankar Nataraj[b], Frederick Wilhelm[b], and John N. Armor[b]*

[a]Clean Fuels and Catalysis Program, The Energy Institute and Department of Energy & Geo-Environmental Engineering, Pennsylvania State University, University Park, PA 16802
*Contact e-mail: csong@psu.edu
Email: csong@psu.edu; Tel: 814-863-4466; Fax: 814-865-3248
[b]Air Products & Chemicals Inc., Allentown, PA 18195.

Introduction

Carbon formation is an important problem in steam reforming and CO_2 reforming of hydrocarbons on supported metal catalysts, which has been an active research subject for several decades[1-2].

Different techniques have been used to obtain quantitative information regarding the carbon deposition. Thermogravimetric analyzer (TGA) has been frequently applied for analyzing the deposited carbon. However, some concerns have been raised on the TGA method, such as incomplete contact between the reaction mixture and the catalyst, buoyancy effect, as well as different values for the flow resistance[3].

Recently, a new technique for measuring the weight changes of the sample during the process of coking or gasification has been employed, i.e. the so-called TEOM (tapered element oscillating microbalance), in which the changes in sample weight (ATM, average total weight signal) are determined from changes in the vibration frequency of the cell containing the catalyst[4-5]. It appears that this method is free from disadvantages inherent in the conventional TGA method, since TEOM determines changes in the weight of the catalyst sample that is in contact with the full reaction mixture stream[6]. The TEOM reactor can be operated up to a pressure of 6 MPa and 700˚C.

More recently, another sensitive method for measuring of carbon formation on used catalysts has been studied, i.e. the so-called TPO-IR, which combines the temperature-programmed oxidation of carbon with the infrared detection of CO_2 (highly sensitive to existence of CO_2) [7-8]. However, there has been less study on the comparison of these two new techniques (TPO-IR and TEOM) with the conventional TGA methods.

Commercial Ni/Al_2O_3 reforming catalysts with or without CaO promoters were chosen in this study for the steam reforming and CO_2 reforming of methane at different temperatures. The above-mentioned three techniques were used for the detection of carbon deposition, with emphasis on the reliability and accuracy of each method.

Experimental

Two commercial Ni/Al_2O_3 catalysts were obtained from Süd Chemie: un-promoted C11-9-09 with 1-15% NiO, 85-99% Al_2O_3 (as per the data provided by vendor), and promoted G-91 with 15-25% NiO, 45-60% Al_2O_3, 5-15% $CaAlO_2$, 5-15% CaO and 1-10% K_2O.

TEOM. CO_2 reforming of CH_4 was performed in the TEOM (1500PMA, Rupprecht & Patashnick Co.) reactor at temperature of 450˚C-650˚C at atmospheric pressure and a CO_2/CH_4 ratio of 1.0. Before each reaction, the catalyst (50mg) was reduced in a mixture of H_2 and Ar (5/15 ml/min). The temperature was increased with a rate of 10˚C/min from room temperature to 650˚C and kept for 1.5 hours. After pre-reduction process and upon reaching stabilized baseline of microbalance at reaction temperature, reactant gas containing CO_2 and CH_4 (1:1 mol ratio) was introduced into the TEOM reactor. The ATM weight change of the tapered element was monitored continuously by computerized data acquisition system.

TPO-IR, TPD-IR, TPOr-IR. LECO RC-412 multiphase carbon determinator was used for all the temperature-programmed oxidation (TPO-IR) studies, where gases evolved from the sample during the TPO (30˚C/min from 100˚C to 1000˚C) were transferred from the furnace by a purge gas (300 ml/min) into the flow cell of the infrared spectrometer. The furnace was cleaned by running the same TPO on blank quartz sample boat. The IR intensity as related to amount of CO_2 (therefore carbon) was calibrated daily by running TPO-IR using standard carbon material (containing known amount of $CaCO_3$).

For the temperature-programmed desorption, ultra-high-purity N_2, was used as the inert purge gas, which was therefore named as TPD-IR since no oxidation (besides desorption) could occur. In some cases, a TPOr-IR (r- stands for second) was carried out on the samples following a TPD-IR run.

TPO-TGA. 20 mg of used catalysts after methane reforming was put on a ceramic sample boat for TPO analysis in Mettler TG-50 instrument. By heating the sample in high flow of air (100 ml/min) from room temperature to 900˚C with 10˚C/min, the weight change was recorded as related to possible carbon burning or metal oxidation.

Results and Discussion

After steam methane reforming for 5 hours at 540-820˚C and 200-400 psi with steam/carbon ratio ranging from 1 to 3.5 on two commercial SMR catalysts (C11-9-09 and G-91), we carried out TPO-TGA experiments trying to determine the amount of carbon deposited after each SMR experiments. To our surprise initially, there was no weight loss (attributing to burning of carbon) on all the used samples. Instead, a weight gain was observed at TPO temperature range of 300˚C-600˚C. For comparison, the TPO-TGA experiments of the two catalysts after pre-reduction at different temperature (450˚C-650˚C) but without SMR reaction have also been done. A similar weight gain of the catalysts is also found with changing amount. This weight gain can therefore be attributed to the oxidation of Ni metal reduced during SMR.

It is clear that TPO-TGA alone can not discriminate carbon burn off and Ni oxidation, especially when only a trace amount of carbon was formed that needs to be detected. Therefore, the set up and reliable use of other sensitive techniques is needed specifically for carbon formation study.

TEOM was used to analyze dynamic process of carbon formation on the same commercial catalysts in terms of change of catalyst weight. Since TEOM was run on-line during methane reforming, it is therefore capable to avoid any other effects (such as the post-run oxidation of Ni, as mentioned above) besides the reforming reactions.

In order to simplify the carbon analysis, we carried out CO_2 (instead of steam) reforming of methane at 650˚C under atmospheric pressure, since carbon formation during CO_2 reforming of methane is known to occur readily and it is easier to analyze when compared with steam reforming of methane[2,9-14].

Figure 1 shows the TEOM profile of CO_2 methane reforming on G-91 (CaO-promoted) catalyst at 650˚C and atmospheric pressure. It should be noted that the time on stream is in term of seconds. It can be seen that carbon forms quickly with the catalyst as soon as the reforming is started. By changing the reaction time, it is possible for us to finely control the amount of carbon deposited on the Ni catalyst, since the ATM signal stabilized quickly after stopping of CO_2 and CH_4 flow simultaneously.

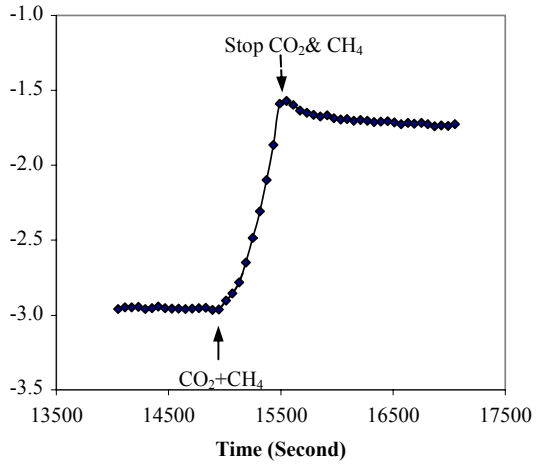

Figure 1. TEOM profile on G-91 catalysts during CO_2 reforming of CH_4 (CO_2:CH_4=1:1, 650˚C, atm)

Figure 2 shows the comparative TEOM results of CO_2 reforming of CH_4 on C11-9-09 (un-promoted) and G-91 (CaO-promoted) catalysts. Both catalysts show very quick carbon formation. However, contrary to the results by Wang and Lu[9], we find that the CaO-promoted G-91 catalyst shows more resistance to carbon formation in the initial reaction as compared with C11-9-09 in terms of the slope of the curves in **Figure 2**.

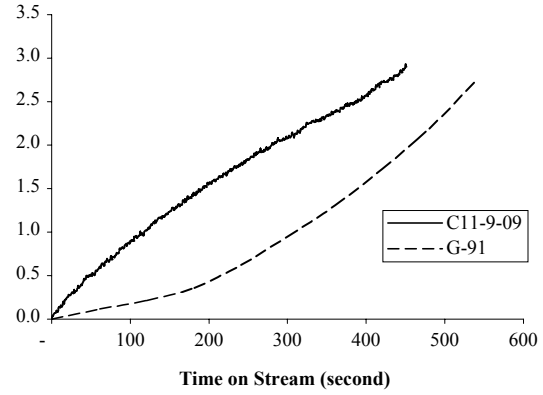

Figure 2. TEOM Results on C11-9-09 and G-91 catalysts during CO_2 reforming of CH_4 (CO_2:CH_4=1:1, 650˚C, atm)

TPO-IR experiments have also been done on the used catalysts after CO_2 reforming of methane using TEOM reactor. Previously, we found that the amount of the TPO-IR peaks at lower temperature (<400˚C) almost kept constant in all used SMR catalysts, these peaks are probably related to desorption of CO_2 chemisorbed on Ni supported catalysts during reforming reaction[7].

Figure 3 shows the TPO-IR (a), TPD-IR (b), and TPD-IR immediately followed by TPOr-IR (c) on G-91 catalyst after CO_2 reforming of CH_4. Comparing curve (a) and curve (b), the TPO-IR and TPD-IR were done with same temperature program using similar amount of sample but with different carrier gases (O_2 and N_2, respectively). It can be seen that the peaks at T<400˚C are present in both cases, which verifies that these peaks may not be related to the carbonaceous carbon deposit, but the chemically adsorbed CO_2 on either Al_2O_3 support or certain metal species. It is also worth mentioning that the TPD-IR signal tends to have higher intensity than that of TPO-IR, as also observed but not discussed by Li and Gonzalez[8]. This might be related to different interfering effects of O_2 and N_2 for IR detection. Therefore, care should be taken when trying to simply subtract the TPO-IR with TPD-IR spectra to derive the amount of carbon deposit.

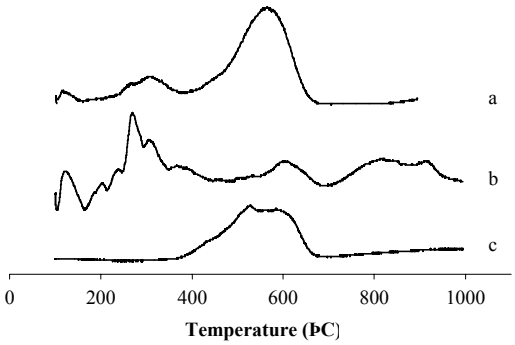

Figure 3. TPO-IR (a), TPD-IR (b), and TPD-IR immediately followed by TPOr-IR (c) on G-91 catalyst after CO_2 reforming of CH_4 (CO_2:CH_4=1:1, 650˚C, atm)

It is interesting to note that following TPD-IR of G-91, if the sample was allowed to expose to air for certain time before a subsequent TPO-IR (thus named as TPOr-IR), the peaks in this temperature range (T<400˚C) could re-appear. However, if the TPOr-IR was carried out immediately after TPD-IR, as shown in curve (c) of **Figure 3**, no such peaks is present, which verifies again the above attribution.

TPO-IR of activated carbons or other non-graphitic carbon materials shows peaks generally in the range of 400-600˚C, while that of graphite carbon shows peak in the range of 600-800˚C. None of these peaks can be seen in TPD-IR profile.

As discussed for our previous observation[7], we believe that the peak at 400˚C-600˚C in curve (a) and (c) is due to oxidation of filament carbon on G-91 catalyst. Using SEM, we actually observed the carbon filaments on the catalysts[7].

The TPD-IR of C11-9-09 (figures not shown) has no peaks at 400˚C-900˚C, therefore the TPO-IR alone gives the information of carbon formation. On the contrary, care should be taken for the samples containing CaO and other promoters (such as in the case of G-91), since it is possible for the formation of $CaCO_3$ (noting the TPD-IR peak at around 800˚C in curve b of **Figure 3**) or some other carbonate during the reforming of methane. As observed previously, the presence of CaO made the reduction of NiO much harder[7], the formation of certain carbonate from un-reduced NiOx is therefore also possible, which complicates the TPD-IR as seen in curve b of **Figure 3**.

It is interesting to make a comparison of the quantitative analytical results of TEOM and TPO-IR in terms of amount of carbon formed. Such a comparison can also be a validation to each other.

In doing so, we have carried out CO_2 reforming of methane on G-91 and C11-9-09 catalysts in the TEOM system with the amount of carbon formation controlled by changing the time on stream and determined the amount of carbon from TEOM profiles. TPO-IR was conducted on the used catalysts collected from TEOM for independently analyzing the amount of carbon deposits.

The comparison of carbon formation detected by these two methods is shown in **Figure 4**. There is a fairly good correlation between these two techniques. Furthermore, the un-promoted C11-9-09 shows a better consistence between the two methods, noting that the slope of the linear trend line is very close to 1, while G-91 shows larger amount of carbon detected by TEOM than by TPO-IR. This is possibly again related to the complication due to the existence of CaO promoters as discussed above.

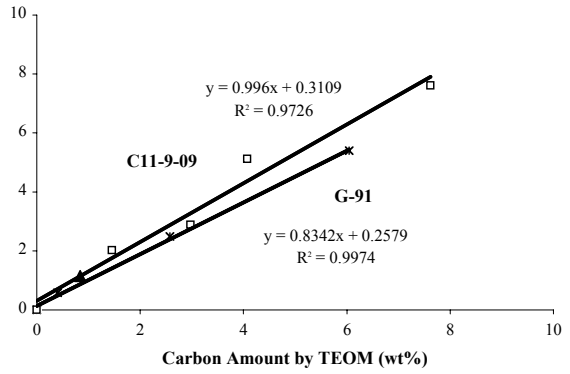

Figure 4. Comparison of carbon formation by TEOM & TPO-IR (CO_2:CH_4=1:1, 650˚C, atm)

We should point out that it is more difficult to quantify the amount of carbon deposits after steam reforming, although the results in Figure 4 show very good correlations for carbon deposits on catalysts used for CO_2 reforming.

Conclusions

Four different methods (TEOM, TPO-IR, TPD-IR, and TPO-TGA) have been used comparatively for more accurate and reliable measurements of carbon formation on used Ni/Al_2O_3 reforming catalysts with and without Ca-promotion. By changing purge gas during TPO-IR from O_2 to N_2 (thus TPD-IR), the present study distinguished the origin of each TPO-IR peaks. The accuracy of the TPO-IR analysis has been further verified by means of CO_2 reforming of methane using TEOM for dynamic characterization of carbon formation.

Acknowledgment. We are grateful to Air Products and Chemicals Inc., and the Pennsylvania State University for partial financial supports, and to the members of HYCO group of APCI and the APCI-PSU SAMCOM for their support of this collaborative project. We also wish to thank United Catalyst Inc./Süd Chemie for providing the catalyst samples. JZ would like to thank Dr. Orhan Altin of PSU for assistance with the use of TPO-IR instrument and Dr. Yinzhi Zhang of PSU for providing activated carbon samples.

References

(1) Rostrup Nielsen, J. Steam Reforming Catalysts, **1975**, Danish Technical Press, Copenhagen.
(2) Bartholomew, C. H. Catal. Rev. - Sci. Eng., **1982**, 24, 67-112.
(3) Stasinska, B.; Golebiowski, A.; Stolecki, K.; Borowiecki, T. Ads. Sci. Tech., **2001**, 19, 441-453.
(4) Fung, S.C.; Querini, C.A.; Lium, K.; Ho, T.C.; Rumschitzki, D.S. Stud. Surf. Sci. Catal., **1994**, 88, 305.
(5) Pan, W.; Srimat, S.; Song, C.S.; Armor, J. North Am. Catal. Soc. Meet., Toronto, Canada, June **2001**.
(6) Liu, K.; Fung, S.C.; Querini, C.A.; Rumschitzki, D.S.; Ho, T.C. Stud. Surf. Sci. Catal., **1997**, 111, 652.
(7) Zheng, J.; Pan, W.; Song, C.S. Prepr.- Am. Chem. Soc. Fuel Div., **2002**, 47, 245-248.
(8) Li, B.; Gonzalez, R.D. Catal. Lett., **1998**, 54, 5–8
(9) Wang, S.; Lu, G. Q. J. Chem. Tech. Biotechnol., **2000**, 75, 589-595
(10) Song C; Srimat S.T.; Murata, S.; Pan W.; Sun, L.; Scaroni, A.W.; Armor J.N. Am. Chem. Soc. Symp. Ser., **2002**, 809, 258-274.
(11) Srimat S.T.; Pan W.; Song C; Armor J.N. Am. Chem. Soc. Div. Fuel Chem. Prep., **2001**, 46 (1), 92-93.
(12) Armor J.N.; Martenak, D.J. Appl. Catal. A: Gen, **2001**, 206 (2), 231-236.
(13) Srimat S.T.; Song C. Am. Chem. Soc. Symp. Ser., **2002**, 809, 289-302.
(14) Pan W.; Song C. Am. Chem. Soc. Symp. Ser., **2002**, 809, 316-329.

HYDROGEN PRODUCTION FROM INTEGRATED METHANOL REFORMING OVER Cu-ZnO/Al_2O_3 AND Pt/Al_2O_3 CATALYSTS FOR PEM FUEL CELLS

*Weidong Gu, Jian-Ping Shen and Chunshan Song**

Clean Fuel and Catalysis Program, The Energy Institute and Department of Energy & Geo-Environmental Engineering
The Pennsylvania State University, 209 Academic Projects Building, University Park, PA 16802
*E-mail: csong@psu.edu

Abstract

The objective of this work is to design a fuel processor based on integrated oxidative steam reforming of methanol that can achieve efficient production of H_2 with minimum CO (<30ppm CO) in a single reactor for proton-exchange membrane fuel cell applications. This paper reports on hydrogen production from methanol using four different Cu-ZnO/Al_2O_3 and two different Pt/Al_2O_3 catalysts from commercial sources. For low-temperature steam reforming, Cu-ZnO/Al_2O_3 catalysts show high activity for methanol conversion. Pt/Al_2O_3 catalyst displays very low activity for methanol conversion but high activity for CO conversion. By using a combination of selected Cu-ZnO/Al_2O_3 and Pt/Al_2O_3 catalysts under tailored conditions, integrated oxidative steam reforming of methanol can achieve effective H_2 production at low temperatures (≤ 230 °C) with minimum CO (<30 ppm) which is suitable for PEM fuel cell applications.

Introduction

Fuel cells are one of the most promising energy conversion devices due to their high intrinsic efficiency and ultra low emissions.[1-3] Fuel cell vehicle based on proton-exchange membrane fuel cells can use hydrogen in an electrochemical cell to convert chemical energy directly into electricity for use with an electric motor. Of the five types of fuel cells, the proton exchange membrane fuel cell is considered to be most promising for transportation application.[1-4] While the ideal fuel is pure hydrogen, it is not yet widely available due to the lack of infrastructure coupled with higher cost of pure H_2. On-board reforming of methanol and hydrocarbon fuels to produce hydrogen is considered to be a practical solution for automotive fuel cell applications.[2-4]

Methanol is one of the promising candidate fuels[5-16] for producing hydrogen on-board due to the following advantages: mild reforming reaction conditions; no needs for desulfurization; no needs for pre-reforming; no serious carbon formation problem. Under ambient condition, liquid methanol has a high volumetric energy density. Many studies have been conducted on steam reforming of methanol.[2-16] Methanol can be produced from natural gas, coal, other fossil fuels as well as renewable resources. H_2 production from methanol may involve various reactions:

Methanol decomposition:
$CH_3OH \longrightarrow CO + 2H_2$ ($\Delta H^\circ = +92.0$ kJ/mol)

Steam reforming:
$CH_3OH + H_2O \longrightarrow CO_2 + 3H_2$ ($\Delta H^\circ = +49.4$ kJ/mol)

Water gas shift
$CO + H_2O \longrightarrow CO_2 + H_2$ ($\Delta H^\circ = -41.1$ kJ/mol)

Partial oxidation:
$CH_3OH + 0.5O_2 \longrightarrow CO_2 + 2H_2$ ($\Delta H^\circ = -192.2$ kJ/mol)
$CH_3OH + 0.25O_2 \longrightarrow 0.5CO_2 + 0.5CO + 2H_2$ ($\Delta H^\circ = -50.8$ kJ/mol)

Oxidative Steam reforming of methanol:
$CH_3OH + 0.5H_2O + 0.25O_2 \longrightarrow CO_2 + 2.5H_2$ ($\Delta H^\circ = -71.4$kJ/mol)

The objective of this work is to design a fuel processor based on integrated oxidative steam reforming of methanol that can achieve efficient production of H_2 with minimum CO (<30ppm CO) in a single reactor for proton-exchange membrane fuel cell applications. In this paper, we report our studies on the methanol reforming over four different Cu-ZnO/Al_2O_3 and two different Pt/Al_2O_3 catalysts obtained from commercial sources, with emphasis on the effects of reaction conditions and configuration of catalyst combinations to minimize CO formation and efficient CO cleanup (<30ppm), that will simplify reformer design for on-board application.

Experimental

Three Cu-ZnO/Al_2O_3 catalysts, C18HA, C18-7-01 and C18 HALM, were obtained from Sud Chemie Ltd. Another Cu-ZnO/Al_2O_3 catalyst, KATALCO 83-3, was received from Synetix, ICI. We obtained 3 different Pt/Al_2O_3 catalysts, 5%Pt/Al_2O_3 from Pressure Chemical Co. and 1% Pt/Al_2O_3 and 0.5% Pt/Al_2O_3 from Engelhard Corp. We also prepared two hybrid catalysts with C18HA and 5% Pt/Al_2O_3, C18HA and 1% Pt/Al_2O_3 (weight ratio is 3:1) as well as two layer catalysts.

The methanol reforming experiments were performed in a fixed-bed down-flow stainless steel reactor with 0.4 inch ID. The reactor temperature was maintained with a tubular electric furnace. The reactor was charged with 0.3 g of the catalyst with particle size 0.5-1 mm and borosilicate beads supported the catalyst bed. A premixed methanol and water with a H_2O to methanol mole ratio of 1.4 was pumped through the reactor using a liquid pump (ISCO Syringe Pump 500). Helium was used as carrier gas with mass flow controller from Brooks Instrument. The outlet stream of reaction products was analyzed by on-line gas chromatography (SRI8610C) equipped with thermal conductivity detector and 6'SIL GEL/3' MOL SIEVE columns. In order to detect the outlet CO concentration in ppm level, an Agilent 3000 Micro GC equipped with TCD detector, and Molecular sieve 5A and Plot Q columns was used. Prior to the reforming reaction, the catalysts were reduced in H_2 atmosphere at 350˚C for 30 min. using a temperature ramp of 2˚C/min. and then cooled down to the reaction temperature (180˚C-275˚C).

Results and Discussion

The methanol reforming reaction has been performed over four different commercial Cu/Zn/Al catalysts in the temperature range 180-275°C. The catalyst activity in terms of methanol conversion is shown in **Table 1** [Reaction condition: liquid feed (H_2O/CH_3OH=1.4 mol ratio) 3ml/h; WHSV= 8.69 h^{-1}; Catalyst loading 0.3g; Carrier gas He 80ml/min].

Table 1. Effect of temperature on catalytic activity for methanol conversion over four different CuZn-based commercial catalysts

Temperature	Methanol conversion (mol%)			
	KATALCO 83-3	C18-7-01	C18 HA	C18 HALM
180˚C	39.66	40.35	32.52	34.27
210˚C	68.4	72.84	77.79	55.34
230˚C	93.61	98.14	97.34	95.91
275˚C	100	100	100	100

When the reaction temperature is at ≥ 230 °C, all catalysts showed similar activity. For a given catalyst, the activity increases with reaction temperature. When the reaction temperature reaches 230˚C, methanol conversion over the Sud Chemie catalysts exceeds 95% and at 270˚C methanol is totally converted over all the four

Cu/Zn/Al catalysts. The more interesting aspect is that CO formation also changes as a function of reaction temperature. With the temperature decrease from 275˚C down to 180˚C, CO content decreases from around 1.5% to about 0.05%. This is due to two reasons, the low reaction temperature can suppress the methanol decomposition, which leads to CO, and water gas shift reaction is favored at low temperature, which converts CO into CO_2 and H_2.

Comparisons of methanol conversion and CO formation are shown in **Figures** 1 and 2, respectively, for tests over different Cu-ZnO/Al_2O_3 and Pt/Al_2O_3 catalysts as well as a hybrid catalyst at 230˚C after 3 hours time on stream.

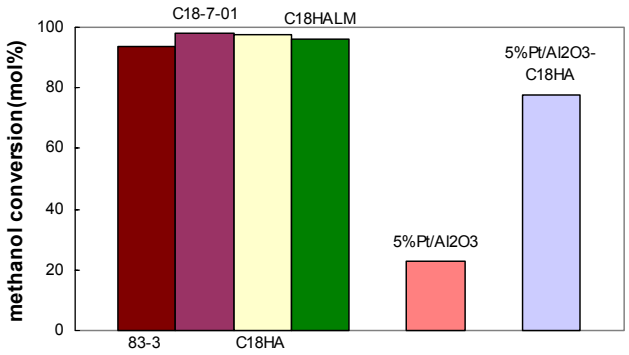

Figure 1. Conversion of methanol in steam reforming over CuZn-based and Pt-based commercial catalysts. Reaction conditions: temperature 230˚C; liquid feed (H_20/CH_3OH=1.4 mol ratio) 3ml/h; Catalyst loading 0.3g; WHSV= 8.69h^{-1}; Carrier gas He 80ml/min; time on stream 3 hr.

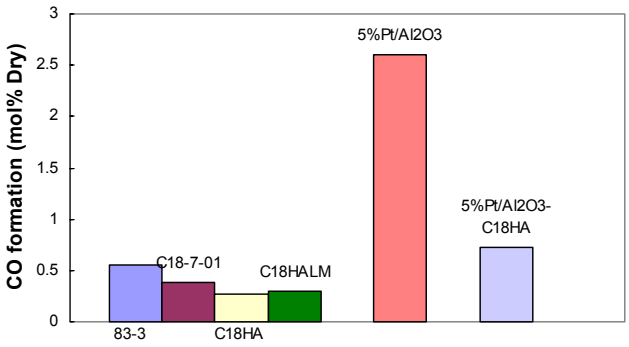

Figure 2. Yield of CO from methanol steam reforming over CuZn-based and Pt-based commercial catalysts. Reaction Conditions: temperature 230˚C; liquid feed (H_20/CH_3OH=1.4 mol ratio) 3ml/h; Catalyst loading 0.3g; WHSV= 8.69h^{-1}; Carrier gas He 80ml/min; time on stream 3 hr.

It can be seen that all the CuZn-based commercial catalysts exhibit a high methanol conversion of over 90 % under the present experimental conditions. Although the methanol conversions over these catalysts are similar at ≥ 230 °C, a considerable difference in CO yield can be noted. For instance, the C18HA offers the lowest CO yield of about 0.3 %. This is lower at least by 1000 ppm compare to the CO yield obtained over other CuZn-based catalyst. Such a difference in CO yield is significant because the CO content in the final product needs to be ≤ 30 ppm for on-board PEM fuel cell applications. On the other hand, the platinum-based catalyst has a very low activity for low-temperature methanol steam reforming. In addition, they produce relatively large amount of CO. It is likely that methanol undergoes decomposition rather reforming over these catalysts under the present operating conditions.

For oxidative steam reforming of methanol, air is a convenient oxidant for on-board application. Since the CuZn-based commercial catalyst, C18HA offered the lowest CO yield in the methanol steam reforming (see Fig. 2), this catalyst was used to evaluate the performance in the Oxidative steam reforming of methanol (OSRM) reaction. The experiments were conducted using O_2/CH_3OH mol ratio from 0 to 0.5. Carrier gas was not used in the OSRM reaction because the N_2 present in the air acted as a carrier gas. **Table 2** shows the effects of O_2/CH_3OH mol ratio on methanol conversion, H_2 yield and CO formation at 230˚C [liquid feed 1.8ml/h (H_20/CH_3OH=1.4 mol ratio); C18HA catalyst loading 0.3g; time on stream for the reaction 3hr].

Table 2. Oxidative steam reforming of methanol over C18HA catalyst at different O_2/MeOH ratios at 230˚C

O_2/CH_3OH ratio	CH_3OH conversion	CO yield (ppm)	H_2 yield (mol%)
0	60.8	848	70.4
0.1	74.6	2602	66.6
0.2	86.9	3125	69.2
0.3	97.4	3371	54.4
0.5	98.4	3642	49.4

As the O_2/CH_3OH ratio increases, the methanol conversion also increases. This increase is apparently related to oxidative conversion. However, a related fact is that as O_2/CH_3OH ratio is decreased, the carrier (inert N_2 in air) is also reduced. During the reaction process, the carrier gas also affects heat transfer, and the heat transfer speed could decrease due to lower carrier gas flow rate. Heat transfer affects the reaction due to endothermic nature of steam reforming reaction and exothermic nature of partial oxidation. Another evidence for the inert gas effect comes from a comparison between 230˚C steam reforming with 80ml/min carrier gas flow and with 15 ml/min carrier gas flow [230 °C "oxidative" steam reforming with O_2/CH_3OH =0 (carrier Ar at 15ml/min)]. The methanol conversion with 15 ml/min carrier gas flow is much lower than that with 80ml/min carrier gas flow. Therefore, the heat transfer seems to be a very important factor. CO formation increased and H_2 formation decreased with increasing O_2/CH_3OH ratio, indicating that partial oxidation is the reason.

We also examined methanol oxidative steam reforming using one hybrid catalyst (1% Pt/Al_2O_3 mechanical mixture with C18HA , weight ratio is 1:3) and two-layer catalyst bed (upper layer is 1%$PtAl_2O_3$ and lower layer C18HA, weight ratio is 1:3). Air was used as oxidant and O_2/CH_3OH ratio is 0.3. Other reaction condition is the same as above. **Figure 3** compares methanol conversion over C18HA, hybrid (1% Pt/Al_2O_3+ C18HA mix) catalyst and two-layer (1% Pt/Al_2O_3 // C18HA) catalyst. The observed catalytic activity order is C18HA > hybrid > two layers cat. This once again indicated that at 230ºC Pt activity is low and heat transfer is important during reforming process.

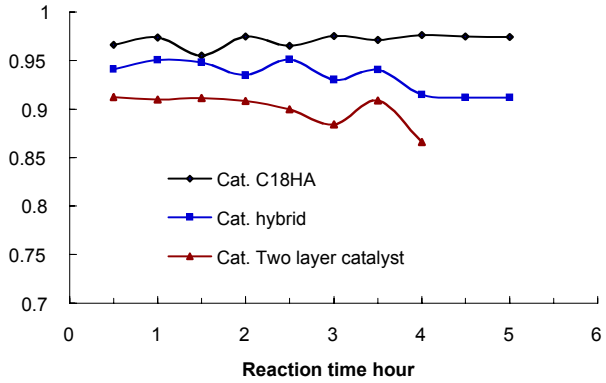

Figure 3. Comparison of catalytic activity of C18HA with hybrid and double layer commercial catalysts in the oxidative steam methanol reforming at 230 °C.

On the basis of the above results, we designed a two-zone reactor. Methanol steam reforming or oxidative steam reforming over CuZn-based commercial catalysts takes place in the first zone placed at the top while the CO conversion by preferential oxidation (PrOX) takes place over 1%Pt/Al_2O_3 catalyst in the second zone with air feed before the second zone, as shown in **Figure 4**.

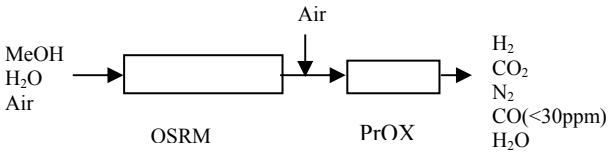

Figure 4. Scheme of integrated methanol reformer

The first zone for oxidative steam reforming (OSRM) was kept at 230˚C; liquid feed 1.8ml/h (H_20/CH_3OH=1.4 mol ratio); OSRM-O_2/MeOHmole ratio 0.3; catalyst loading (C18HA) 0.3g. The air ratio, defined as the amount of air used in the PrOX reaction in the second zone to the amount of air used in the OSRM reaction in the first zone, varied between 0.11 to 0.53. The second zone for CO oxidation was kept at 150 °C.

Table 3. Integrated MeOH OSRM and PrOX at different air ratio

Air ratio	MeOH conversion	CO yield (ppm Dry)	H_2 yield (mol % Dry)
0.11	92	1330	63.9
0.12	96.3	477	57.2
0.15	96.4	215	55.1
0.39	94.1	139	56.0
0.47	95.3	102	55.4
0.53	96.8	31.2	52.4

Table 3 Summarizes the results of integrated OSRM reaction over C18HA and PrOX reaction over 1%Pt/Al_2O_3 in a two-zone reactor after 3 h time on stream. With the increasing air ratio, the CO concentration in the outlet product gases (dry) decreases greatly, down to as low as 31 ppm. The H_2 yield changes only to a small extent as the air ratio is varied between 0.12-0.47. Thus Pt has a good selectivity and activity for CO preferential oxidation under the conditions used.

We further examined the effect of the Pt loading under the same conditions: 230˚C MeOH oxidative reforming over C18HA (0.3g), 150˚C preferential oxidation over 0.5%Pt and 1%Pt Al_2O_3. **Table 4** shows the experimental results (after 3hr time on stream) corresponding to air ratio 0.39 and 0.53**.**

Table 4. Comparison Pt loading under air ratio 0.39 and 0.53

	Air ratio 0.39		Air ratio 0.53	
	0.5% Pt Al_2O_3	1% Pt Al_2O_3	0.5% Pt Al_2O_3	1% Pt Al_2O_3
MeOH conversion (mol %)	95.1	92.4	95.8	96.8
H_2 yield (mol %)	50.4	55.5	50.2	52.4
CO yield (ppm, Dry)	122	106	10.5	31.2

It is interesting to note that CO concentration over the 0.5%Pt/Al_2O_3 with an air ratio of 0.53 is lower than that over 1%Pt/Al_2O_3 indicating that Pt loading significantly affects the CO conversion in the PrOX reactor. The results clearly demonstrate that by using a two-zone reactor design with a combination of two types of commercial catalysts, high methanol conversion and very low CO concentration (10-30 ppm) could be achieved under mild reaction conditions.

Conclusions

Our preliminary results on the steam reforming and oxidative steam reforming of methanol over different CuZn-based and Pt-based commercial catalysts indicated that the CuZn-based catalysts have high activity at low temperature of around 230˚C. Among the catalysts tested, the C18HA commercial CuZn-based catalyst offered the lowest CO yield in the steam reforming of methanol. The Pt-based catalysts are not effective for methanol reforming, but good for CO oxidation.

By designing the two-zone reactor with a combination of a selected Cu-ZnO/Al_2O_3 catalyst and a selected Pt/Al_2O_3 catalyst, a high methanol conversion (above 95 %) and very low CO concentration (10-30 ppm) could be ~~was~~ achieved under ~~at~~ mild reaction conditions (≤ 230 °C). An integrated oxidative steam reforming of methanol over C18HA Cu-ZnO/Al_2O_3 at 230˚C coupled with CO preferential oxidation over 0.5%Pt/Al_2O_3 at 150˚C produced H_2-rich gas with a CO concentration well below 30ppm suitable for on-board PEM fuel cell applications.

Acknowledgement.

This work was supported by Conoco Phillips and DOE under DOE Cooperative Agreement. Instrument No. DE-FC26-01NT41098. We wish to thank Dr. Etop Esen, Dr. Joe Allison, Dr. Steven McDonald, and Mr. Kirk Miller of Conoco Phillips, Mr. Daniel Cicero of DOE NETL, Dr. Andre' Boehman of PSU and Dr. Chao-Yang Wang of PSU for helpful discussions. We gratefully acknowledge Sud Chemie Ltd, Synetix, and Engelhard for providing various catalyst samples. We also thank Dr. S. Velu for his assistance in setting up the online micro-GC and for helpful discussions on methanol conversion, and Mr. Ronald Copenhaver for his help in setting up the flow reactor.

References

1). Larminie, J.; Dicks, A. Fuel cell Systems Explained. John Wiley, New York, **2000**, 308 pp.
2). Chalk, S.G.; Miller, J.F., Wagner, F.W. J Power Sources, **2000**, 86 (1-2), 40-51.
3). Trimm, D.L.; Onsan, Z.I. Catalysis Reviews-Science and Engineering, 2001, 43 (1-2), 31-84.
4). Song, C. *Catal. Today*, **2002, 77,** 17-49.
5). Edwards, N.; Ellis, S.R.; Frost, J.C.; Golunski, S.E.; van Keulen, A.N.J.; Lindewald, N.G.; Reinkingh, J.G. J. Power Sources, 1998, 71 (1-2), 123-128.
6). Breen, J.P.; Ross, J.R.H. Catal. Today, **1999**, 51 (3-4), 521-533.
7). Peppley, B.A.; Amphlett, J.C.; Kearns, L.M.; Mann, R.F. Appl. Catal. A: Gen., 1999, 179 (1-2), 21-29 APR 5
8). Peppley, B.A.; Amphlett, J.C.; Kearns, L.M.; Mann, R.F. Appl. Catal. A: Gen., **1999**, 179 (1-2), 31-49.
9). Wiese W, Emonts B, Peters R. J. Power Sources, **1999**, 84 (2), 187-193.
10). Peters R, Dusterwald HG, Hohlein B. J. Power Sources, **2000**, 86 (1-2), 507-514.
11). Reitz, T. L., Ahmed, S., Krumpelt, M., Kumar, R. and Kung, H. H. Stud. Surf. Sci. Catal., **2000**, 130, 3645-3650.
12). Fierro, J. L. G. Stud. Surf. Sci. Catal., **2000**, 130, 177-186.
13). Velu S, Suzuki K, Okazaki M, Kapoor M.P., Osaki T, Ohashi F. J. Catal., **2000**, 194 (2), 373-384.
14). de Wild PJ, Verhaak MJFM. Catal. Today, **2000**, 60 (1-2), 3-10.
15). Lindstrom, B. Agrell, J. Pettersson,L.J. *Chem. Eng. J,* **2002, 4053,** *1-11*
16). Shen, J.; Song, C. *Catal. Today* , **2002, 77,** *89-98*

Water-Gas Shift Catalysis on Pt Bimetallic Catalysts

Sara Yu Choung, Magali Ferrandon, and Theodore Krause

Chemical Engineering Division
Argonne National Laboratory
9700 South Cass Ave.
Argonne, IL 60439

Introduction

The water-gas shift (WGS) reaction ($CO + H_2O = CO_2 + H_2$) is of interest due to its presence in the fuel processing process for fuel cell applications. For polymer electrolyte fuel cells, the CO levels in reformate must be reduced to <100 ppm because CO poisons the Pt anode catalyst of the fuel cell. Current commercial WGS catalysts, CuZn and FeCr, have some drawbacks for use in on-board fuel processing. These catalysts require an activation step consisting of a controlled *in situ* reduction. In the reduced state, large temperature excursions are observed when they are exposed to air, resulting in loss of activity because of sintering. In addition, exposure to condensation during shutdown can cause reoxidation and poor mechanical stability. For on-board reforming, the Department of Energy has established the following performance and cost targets for new WGS catalysts: gas hourly space velocity (GHSV) ≥30,000 h^{-1}, CO conversion ≥90%, CO selectivity ≥99%, lifetime >5000 h, and cost <\$1/kW_e.

Ceria based WGS catalysts were chosen for study because they possess redox properties under WGS reaction conditions. These catalysts are reported to undergo a bifunctional redox mechanism where CO is adsorbed on a transition metal, oxygen is transferred from ceria for the oxidation of CO, and ceria is reoxidized by the dissociation of H_2O [1]. In this study, ceria was doped with zirconia due to its smaller ionic radius, which causes strain in the ceria lattice and promotes the formation of oxygen vacancies and Ce^{3+} [2]. We have found that the addition of a dopant (Zr or Gd) increases WGS activity of Pt-supported samples at temperatures above 300°C [3]. In addition, we observed that the WGS activity (per gram catalyst) increased with Pt loading (0.87–2.86 wt%) [3]. When compared on a per mole of Pt basis, the rates were similar, indicating that the WGS rates (per mole of Pt) are independent of Pt loading (0.87–2.86 wt%) [3]. In order to reduce the amount of Pt necessary to achieve higher WGS rates and enhance the activity of the Pt, different Pt bimetallic formulations were investigated for their role as possible promoters to enhance the WGS activity and stability of Pt/doped ceria catalysts. The bimetallic formulations were selected on the basis of theoretical studies of the energetics of H_2O dissociation and reactions between $CO_{ads} + OH_{ads}$ on Pt-mixed metal clusters [4].

Experimental

Doped ceria supports were prepared by coprecipitation or purchased from Rhodia. The supports were all calcined in air at 500°C before introduction of the metal(s). Tetraammineplatinum(II) nitrate [$Pt(NH_3)_4(NO_3)_2$] was used as the Pt precursor for Pt, Pt+B, and Pt+C and hydrogen hexachloroplatinate(IV) [H_2PtCl_6] was used for Pt+A and Pt+D. Metals were introduced using incipient wetness impregnation techniques. The samples were dried in air at 120°C overnight and calcined in air at 500°C for 2 h. Pt contents ranged from 0.87–1.0 wt%. The effects of the Pt precursor and the different supports on WGS rates were found to be minimal (≤20%).

The WGS activity measurements were carried out in a flow microreactor using a synthetic reformate with the following composition: 6.9% CO, 10.35% CO_2, 31.05% H_2, 31.0% H_2O, and 20.7% N_2. In order to maintain a constant bed volume, α-alumina was used as a diluent. The WGS activity of the α-alumina was found to be negligible. The total volume of catalyst and diluent loaded into the reactor was 0.5 ml. The amounts of catalyst (0.05–0.4 ml) and diluent (0.1–0.45 ml) and the gas flow rate were adjusted to maintain differential reactor conditions at the lower temperatures (conversion ≤15%) by varying the GHSV (200,000–1,500,000 h^{-1}). The samples were pretreated in 4%H_2/He at 400°C for 1 h. The WGS rate measurements were performed at a catalyst bottom bed temperature of 250–400°C. The temperatures at the top of the catalyst bed and the outside wall of the reactor were also monitored during the experiment. The CO and CO_2 concentrations in the effluent were continuously monitored using an on-line infrared gas analyzer (California Analytical Instruments, Model ZRH Infrared Analyzer). Samples were also analyzed using a gas chromatograph (Hewlett Packard 5890 Series II) equipped with thermal conductivity detectors to determine and verify the concentration of the gases and to determine whether methane formation occurs during reaction. CO_2 was separated on a J&W Scientific GS-CarbonPLOT column using He as the carrier gas. CO, H_2, N_2, and CH_4 were separated on a J&W Scientific GS-MolSieve column using Ar as the carrier gas.

Results and Discussion

The WGS activities (CO converted to CO_2) of different Pt bimetallic formulations (Pt+M) are compared to Pt on a per Pt basis in Figure 1. Pt+A and Pt+B have higher rates than when Pt is present alone, indicating that the addition of A and B is favorable for promoting the WGS reaction. Slight methane formation is observed on Pt+B with methane selectivities ≤5%. On the other hand, the addition of C and D seems to have inhibiting effects on WGS because lower rates are observed on Pt+C and Pt+D than with Pt.

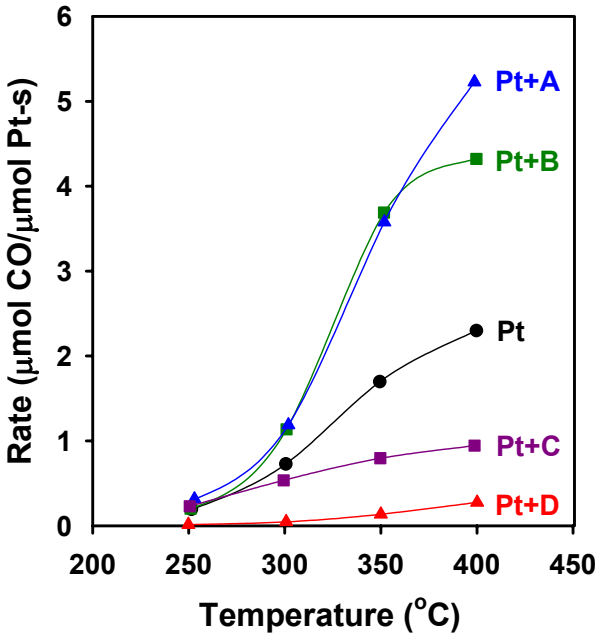

Figure 1. WGS activity of Pt and Pt+M supported on doped ceria [250–400°C, GHSV = 200,000–1,500,000 h^{-1}].

The activities of Pt+A and Pt+B are compared to Pt at 300°C with time on stream in Figure 2 in order to compare the stability of these samples during WGS. Both Pt and Pt+B deactivate rapidly initially and then deactivate more slowly after some time on stream. Pt loses half of its activity after about 40 h and Pt+B deactivates

more rapidly than Pt and loses half of its activity after about 2 h. Pt+A is more stable than Pt and maintains its initial activity over 60 h. Wang *et al.* report that the deactivation observed during WGS on Pt/ceria and Pd/ceria catalysts is caused by the loss of metal surface area [5]. The Pt+A bimetallic formulation may inhibit the sintering of Pt, resulting in the enhanced stability during WGS.

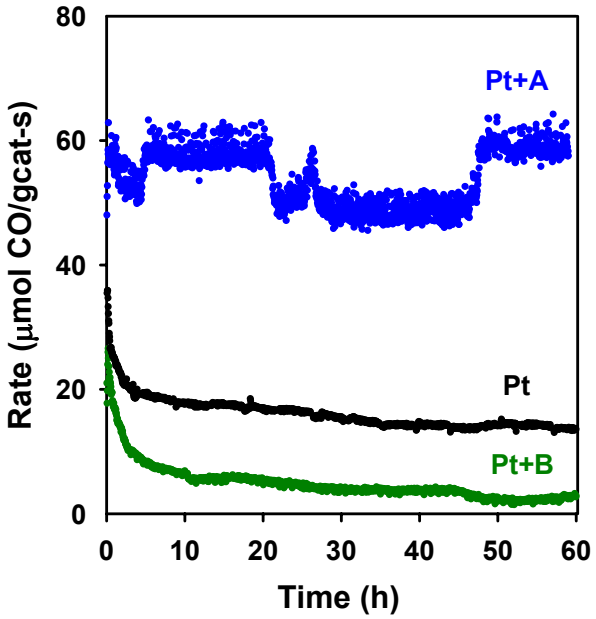

Figure 2. WGS activity of Pt, Pt+A, and Pt+B supported on doped ceria vs. time on stream [300°C, GHSV = 300,000–400,000 h^{-1}].

Conclusions

The bimetallic formulations, Pt+A and Pt+B supported on doped ceria, showed higher rates than Pt alone, demonstrating that the addition of A and B enhances WGS. Lower rates were observed on Pt+C and Pt+D, indicating that the presence of C and D inhibits WGS. The samples that showed enhanced WGS activity, Pt+A and Pt+B, were tested for their stability and compared to Pt. By itself, Pt loses half of its activity after about 40 h; Pt+B deactivates more rapidly than Pt, losing half of its activity after about 2 h. Pt+A is more stable than Pt and maintains its initial activity over at least 60 h. The WGS activity and stability of Pt were increased by the bimetallic formulation, Pt+A.

Acknowledgement. This work was supported by the Office of Hydrogen, Fuel Cells, and Infrastructure Technologies, U.S. Department of Energy, Office of Energy Efficiency and Renewable Energy. Argonne National Laboratory is operated by the University of Chicago for the Department of Energy under Contract No. W-31-109-ENG-38.

References

(1) Bunluesin, T.; Gorte, R. J.; and Graham, G.W. *Appl. Catal. B.* **1998**, *15*, 107.
(2) Trovarelli, A.; de Leitenburg, C.; and Dolcetti, G. *Chemtech* **1997**, 32.
(3) Choung, S. Y.; Krebs, J.; Ferrandon, M.; Souleimanova, R.; Myers, D.; and Krause, T. "Water-gas Shift Catalysis," presented at DOE Hydrogen, Fuel Cells, and Infrastructure Technologies 2003 Merit Review Meeting, May 19-22, 2003, Berkeley, CA.
(4) Ishikawa, Y.; Liao, M.-S.; and Cabrera, C. R. *Surf. Sci.* **2002**, *513*, 98.
(5) Wang, X.; Gorte, R. J.; and Wagner, J. P. *J. Catal.* **2002**, *212*, 225.

CERIA-SUPPORTED Cu-Pd BIMETALLIC CATALYSTS FOR OXYGEN-ASSISTED WATER-GAS-SHIFT REACTION FOR PROTON-EXCHANGE MEMBRANE FUEL CELLS

Elise S. Bickford[ab], S.Velu[a], and Chunshan Song[abc]*

[a]Clean Fuels and Catalysis Program, The Energy Institute
[b]Intercollege Graduate Program in Materials
[c]Department of Energy and Geo-Environmental Engineering
The Pennsylvania State University
209 Academic Projects, University Park, PA 16802
*Presenting author

Introduction

Proton exchange membrane (PEM) fuel cell, which operates at low temperature, is considered to be the potential candidate for on-board power generation in automobiles. The major impediment to commercialization of PEM fuel cells for automobiles is the need for a fuel processing system to convert liquid fuels such as methanol, gasoline, etc into a CO-free hydrogen-rich gas, because the presence of even traces of CO, over 10 ppm, is a poison to the platinum electro catalysts used in the PEM fuel cells. It has been shown[1] that as the CO concentration increases, the cell voltage drops and the performance of PEM fuel cell deteriorates dramatically.

Water-gas shift (WGS) reactor, which significantly reduces the CO concentration in the down stream of the reformer, is the critical component of the fuel processor. Cu/Al_2O_3 commercial catalysts have long been used in the water-gas-shift reaction.[2,3] Although the results have been positive, it is very difficult to achieve CO levels below 10 ppm with these catalysts. In addition, the catalysts are pyrophoric and consequently they degrade during operation.

CeO_2 has been known to have many beneficial properties in catalysis, such as promoting the water-gas-shift reaction in steam reforming, improving the dispersion of surface metals, and store and release oxygen.[4,5] The later property is expected to help minimizing the pyrophorocity of the copper metal supported on CeO_2.

The use of Pd as the sole active metal component in three-way catalyst (TWC) has received considerable attention on the basis of economical aspects and its remarkable activity in oxidation reactions. Many tests have been conducted on Pd/CeO_2 catalysts to understand the metal support interactions.[6,7] These tests and others have helped to fuel research on these catalysts for reforming[8], oxidation[9] and WGS reactions.[10-13] The addition of base metals such as Cu, Cr and Mn to the Pd/CeO_2 catalyst improved the performance of NO reduction reactions due to the formation of Cu-Pd alloy.[13] These properties have lead to understanding the role of ceria and precious metals in the TWC for vehicle exhausts emission conversion and the desire to harness these properties into creating newer, cheaper and more efficient catalysts for low temperature WGS reaction.

The objective of the present investigation was to develop a new CeO_2-based Cu-Pd bimetallic catalyst for low temperature WGS reaction for on-board fuel cell applications and to study in detail the role of each metal on the catalytic performance. In order to achieve a good metal dispersion, nano structured high surface area CeO_2 was prepared and used as a support. Commercial high surface area CeO_2 was used to optimize the Cu/Pd atomic ratio in the WGS reaction. The preliminary results are presented in this communication.

Experimental

$Cu-Pd/CeO_2$ optimization: A series of catalysts with 0.5-1.5 wt % Pd and 1-40 wt% Cu were prepared by depositing them on to a commercial high surface area CeO_2 support with a BET surface area of 148 $m^2\ g^{-1}$, obtained from Rhodia, using deposition precipitation (DP) method as described in the literature.[14] CeO_2 was placed in a beaker and submerged in H_2O. Appropriate solutions of $Cu(NO_3)_2$ in H_2O and $Pd(CH_3COO)_2$ in acetone were prepared. Meanwhile, the pH of the CeO_2/H_2O suspension was adjusted to ~9.2 using dilute KOH solution and then the salt solution was added drop-wise to the CeO_2/H_2O slurry. After complete addition, the pH of the solution was measured and adjusted to ~9.0. The solution was aged for one hour at room temperature and filtered and washed with distilled water until the pH of the filtrate was 7. The catalysts were dried over night at 120°C before calcination at 2°C/min to 400°C and held for 3 1/3 hours.

Water-Gas-Shift Reaction: The WGS reaction was performed at 210°C in a down-flow fixed-bed stainless steel reactor using 0.5 mL of the catalyst (particle size 1000-500μm). This temperature was chosen because the commercial $Cu-ZnO/Al_2O_3$ catalysts obtained from Sud Chemie exhibited better performance and was chosen as a base of comparison. The experimental conditions consisted of using an initial CO concentration of 2000 ppmv, and the space velocity of 12,000 h^{-1} (dry basis). The gas compositions used in the WGS reaction over the catalysts were 0.2 % CO, 10% CO_2, 40.0 % H_2O, and the balance was Ar gas. In the O_2 assisted WGS reaction, 1.0 % O_2 in the form of air was also added to the feed. The effluent of the reactor was analyzed on-line using an Agilent 3000 A MicroGC equipped with thermal conductivity detectors. The CO detection limit was well below 10 ppm. Prior to the reaction, the catalyst was reduced in situ at 250˚C for 2 h in H_2 gas (flow rate : 15mL/min).

Results and Discussion

Preliminary experiments on the optimization of Cu/Pd ratio for the WGS were performed over Cu-Pd supported on a commercial high surface area CeO_2 obtained from Rhodia. Fig. 1 shows the effect of Pd loading on the catalytic performance in the WGS reaction at 210˚C. It can be seen that, under the present experimental conditions, the 1 wt% Pd exhibits a maximum CO conversion of about 46 %. All subsequent catalysts were therefore synthesized with 1 wt% Pd by varying the Cu loading from 1 to 40 wt %.

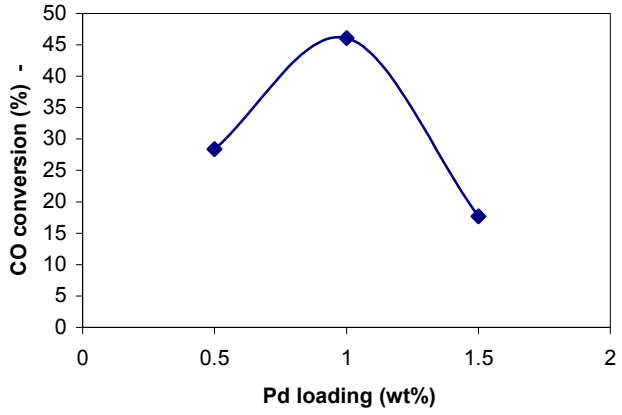

Figure 1. Effect of Pd loading on CO conversion in the WGS reaction over $Cu-Pd/CeO_2$ catalyst

The effect of Cu loading on the catalytic performance shown in Fig. 2 indicates that the CO conversion remains between 40 and 50 wt % until the Cu loading of 20 wt % and shows a maximum CO conversion close to 80 % when the Cu loading is increased to 30

wt %. The CO conversion decreases with further increase in Cu loading and this supports the previous findings[13] that in the Cu-Pd bimetallic catalysts, as the Cu concentration increases the turnover frequency of the catalyst decreases, and the CO light off temperature decreases. It also supports the findings of Kundajovic and Flytzani-Stephanopoulos[16] that Cu is present as larger CuO particles at the surface, that do not interact strongly with the support, thereby decreasing the overall activity of the catalyst at higher Cu loadings.

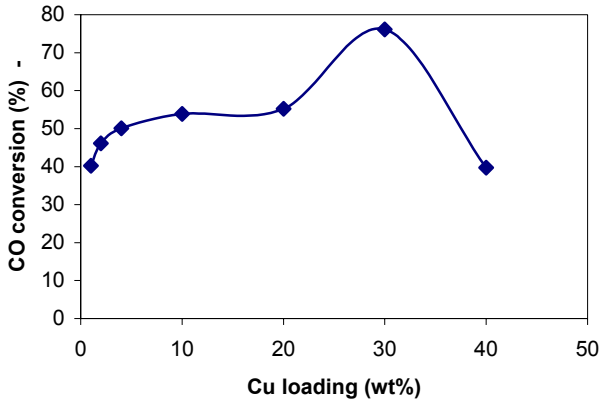

Figure 2: Effect of Cu loading on CO conversion in the WGS reaction over Cu-Pd/CeO_2 catalyst

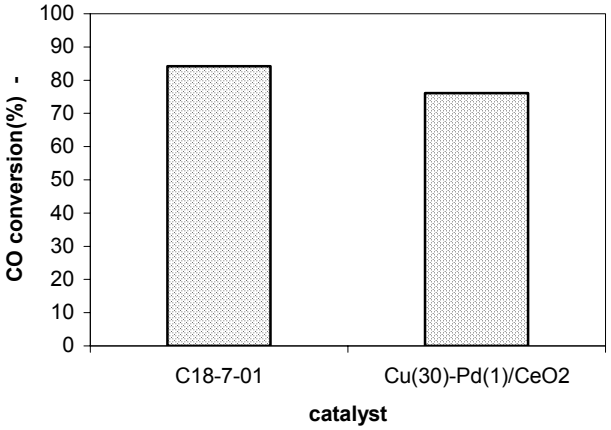

Figure 3: Comparison of commercial CuO/ZnO/Al_2O_3 catalyst with the Cu(30)-Pd(1)/CeO_2 in the WGS reaction

Figure 3 shows a comparison of the conversion results over a commercial CuO/ZnO/Al_2O_3 catalysts obtained from SudChemie (C18-7-01) and the laboratory made Cu-Pd bimetallic catalyst with 30 wt % of Cu and 1 wt % of Pd supported on commercial CeO_2. It is interesting to note that the catalytic performance of the laboratory-made Cu-Pd/CeO_2 is very close to that of commercial catalyst under the present experimental conditions. Several parameters such as catalyst composition, pre-reduction temperature, etc. are needed to be optimized in order to achieve higher CO conversion at relatively low temperature. Thus, there is a lot of scope to improve the performance of Cu-Pd/CeO_2 catalyst in the low temperature WGS reaction.

Future tests will include optimizing the conditions for this catalyst, investigating the effect of different methods of support preparation, method of metal loading, etc. Later tests will also include investigating the oxygen-assisted WGS reaction to better utilize the oxidation properties of precious metal within the bimetallic catalyst.

Conclusions

The effect of Cu and Pd loading on the catalytic performance in the WGS reaction over Cu-Pd/CeO_2 catalyst at 210˚C indicated that the catalyst with 30 wt % of Ce and 1 wt % of Pd exhibit a higher CO conversion close to 80 %. This laboratory prepared catalyst is as active as commercial CuO/ZnO/Al_2O_3 catalyst obtained from Sud Chemie. Since the composition of the Cu-Pd/CeO_2 catalyst and the pretreatment conditions are not yet optimized, it is anticipated that the catalytic performance in the low temperature WGS reaction can be further improved.

Acknowledgements. The authors wish to thank US Department of Energy for partial support of the project work.

References

(1) Springer, T. E.; Rockward, T.; Zawodzinski, T. A.; Gottesfeld, S. *Journal of The Electrochemical Society* **2001**, *148*, A11-A23.
(2) Sengupta, G.; Gupta, D. K.; Sen, S. P. *Indian Journal of Chemistry* **1978**, *16A*, 1030-1032.
(3) Utaka, T.; Sekizawa, K.; Eguchi, K. *Applied Catalysis A: General* **2000**, *194-195*, 21-26.
(4) Trovarelli, A. *Catal. Rev.-Sci. Eng.* **1996**, *38*, 439-520.
(5) Whittington, B. I.; C.J., J.; Trimm, D. L. *Catalysis Today* **1995**, *26*, 41-45.
(6) Badri, A.; Binet, C.; Lavalley, J.-C. *J.Chem.Soc.Faraday Trans.* **1996**, *92*, 1603-1608.
(7) Cordatos, H.; Gorte, R. J. *Journal of Catalysis* **1996**, *159*, 112-118.
(8) Craciun, R.; Daniell, W.; Knozinger, H. *Appl. Catal. A-Gen.* **2002**, *230*, 153-168.
(9) Sharma, S.; Hilaire, S.; Vohs, J. M.; Gorte, R. J.; Jen, H. W. *Journal of Catalysis* **2000**, *190*, 199-204.
(10) Hilaire, S.; Wang, X.; Luo, T.; Gorte, R. J.; Wagner, J. *Appl. Catal. A-Gen.* **2001**, *215*, 271-278.
(11) Wang, X.; Gorte, R. J.; Wagner, J. P. *Journal of Catalysis* **2002**, *212*, 225-230.
(12) Kang, M.; Song, M. W.; Kim, K. L. *React.Kinet.Catal.Lett.* **2002**, *75*, 177-183.
(13) Hungria, A.B.; Iglesias-Juez, A.; Martinez-Arias, A.; Anderson, J. A.; Conesca, J. C.; Soria, J. *Journal of Catalysis* **2002**, *206*, 281-294.
(14) Fu, Q.; Weber, A.; Flytzani-Stephanopoulos, M. *Catalysis Letters* **2001**, *77*, 87-95.
(15) Zhang, Y.; Andersson, S.; Muhammed, M. *Appl. Catal. B-Environ.* **1995**, *6*, 325-337.
(16) Kundakovic, L.; Flytzani-Slephanopoulos, M. *Appl. Catal. A-Gen.* **1998**, *171*, 13-29.

Synthesis of nanocrystalline catalysts for the water-gas shift reaction

Ranjan K. Pati[a], Ivan Lee[b], Deryn Chu[b] and Sheryl H. Ehrman[a]

[a]Department of Chemical Engineering, University of Maryland, College Park, MD 20742
[b]US Army Research Laboratory, 2800 Powder Mill Road, Adelphi, MD 20783

Introduction:

In recent years fuel cell technology is a promising method for generating electricity for mobile and stationary applications. Interest in fuel cells is driven by their potentially high efficiency and lower emissions [1]. A factor that draws interest to the fuel cell is that it can operate at efficiencies two to three times that of the internal combustion engine, and it requires no moving parts. Many different types of fuel cells have been developed, with the proton exchange membrane (PEM) fuel cell attracting the most interest for mobility applications. This type of fuel cell operates by electrochemical oxidation of hydrogen generating electricity, while forming water. The partial oxidation and steam reformation reactions are the two key steps for the generation of hydrogen from hydrocarbons and alcohols. In both, the products are carbon monoxide, carbon dioxide and hydrogen. The fuel cell is highly sensitive to poisoning especially by carbon monoxide, which can significantly lower the performance of the fuel cell at concentrations above 50 ppm. The water-gas shift (WGS) reaction is used to convert carbon monoxide and water to hydrogen and CO_2 products. In most of the cases, the presence of suitable catalysts in the WGS reaction can reduce the concentration of CO down to 10 ppm. In this study, the focus will be on the development of improved catalysts for the WGS reaction as it plays a potential role for generating fuel cell hydrogen.

There are various kinds of catalysts used commercially for the WGS reaction including binary CuO-ZnO and ternary CuO-ZnO-Al_2O_3 and CuO-ZnO-Cr_2O_3 mixed oxides, Au supported on Fe_2O_3, Au supported on TiO_2 etc [2]. Recently, it has been reported that pure ceria and a combination of transition metal supported ceria increases the rate of the WGS reaction as compared to the binary CuO-ZnO and ternary CuO-ZnO-Al_2O_3 and CuO-ZnO-Cr_2O_3 commercial water gas shift catalysts [2]. Ceria-based WGS catalysts have attracted increasing attention because of the high oxygen storage capacity and mobility of oxygen. Additionally the ceria based catalysts are also expected to be more stable with respect to high temperature, water and air. Various chemical methods have been reported in the literature for the preparation of ceria and ceria based catalysts including co-precipitation [3, 4], hydrothermal [5, 6], microemulsion [7, 8], surfactant assisted precipitation [9] etc. All of the above methods involve multiple, time consuming step. The objective of this study is to prepare high surface area pure and transition metal supported ceria by the flame spray pyrolysis method (FSP).

Experimental Procedure:

For this investigation, cerium acetate, cerium-triethanolamine, cerium-diethanolamine, and transition metal nitrate precursor solutions have been used as the feed. The principle of the process is the *in situ* evaporation and subsequent burning of the precursor droplets, which leads to gas-phase synthesis of the desired product. In the flame, the precursors are expected to vaporize and to react to form oxides. The liquid precursor feed was supplied by a nebulizer and atomized with compressed air resulting in a fine spray with a droplet mass. Premixed methane/oxygen/nitrogen gas was used in the burner. The resulting powder has been collected onto a water cooled substrate via thermophoresis.

Cerium (III) acetate hydrate, $Ce(CH_3CO_2)_3.xH_2O$ was dissolved in glacial acetic acid at 80°C to obtain a 0.3M Ce^{3+} solution. The solution was diluted either with acetic acid or a mixture of 80 vol% isooctane and 20 vol% isobutanol to obtain a 0.15 M Ce^{3+} solution. These precursor solutions were stable above 65°C. For making the cerium-TEA and cerium DEA solutions, a stoichiometric amount of cerium acetate was dissolved in DI water and mixed with ammonia solution to make the precipitation of cerium hydroxide and then this precipitate has been dissolved in TEA and DEA to make Ce-TEA and Ce-DEA. All these solutions were filtered before filling into the syringe.

Characterization:

Bulk chemical composition was determined by using electron microprobe analysis. Thermogravimetric analysis (TGA) was used to determine if the precursors have completely reacted to the oxides. Transmission electron microscopy (TEM) was used to determine the morphology of the powder and to quantitatively investigate dispersion. Surface area of the powder has been measured using the Brunauer, Emmett and Teller (BET) gas absorption method. To understand the chemical composition and phase relationship, Fourier transform infrared spectroscopy (FTIR) was used to determine the bonding between the transition metal and cerium species and X-ray diffraction (XRD) was used to investigate the crystal structure of the synthesized powder.

The activity of the synthesized catalysts for the WGS reaction was investigated using a small plug flow reactor. Gas chromatography is used to quantify the concentrations of products. To determine the reaction rate, measurements has been made of CO conversion as a function of the partial pressures of the reactants and products, CO, CO_2, H_2O and H_2. Catalysts performance has been determined by generating conversion profiles as a function of temperature under realistic WGS conditions. The objective here is to identify the compositions that result in the improved activity, as measured by conversion, at the expected operating temperatures (~200°C and ~400°C).

Results and Discussion

Thermogravimetric analysis (TGA) of the synthesized powder has been carried out in a Perkin Elmer TGA 7 thermal analyzer at a heating rate of 10°C/min. Fig-1 illustrates the thermogram of CeO_2 powder prepared from the cerium acetate precursor as a typical example. The synthesized powder may be considered to be composed of some carbonaceous material and the metal oxides trapped in the pyrolysed mass produced by the oxidation process during flame synthesis. There is a total of ~2.14% wt loss with two steps of wt loss is shown in the thermogram. The first wt loss is in the temperature range of ~20 - 200°C, which is associated with the loss of water absorbed by the sample from atmosphere. The major wt loss was happened at a temperature range of 300 - 500°C. This wt loss is basically due to the loss of a small amount of carbonaceous material present in the sample, which is also clear from FTIR (fig-2). After 500°C, the sample is almost carbon free.

Fourier transformed infrared (FTIR) ( ) a spectrum of the ceria powder obtained from cerium acetate precursor is shown in Fig-2. The IR absorption bands in the region of 2800-2900 cm^{-1} are the C-H stretching mode o hydrocarbons. These bands may be due to the presence of acetic acid in the product. Residual water and a hydroxyl group are detected with a large band at around 3500 cm^{-1}, corresponding to the O-H stretching frequency, and broad band at 1600 cm^{-1} due to the bending vibration of associated water. An

additional band at around 1400 cm^{-1} may be due to the presence of carboxylic acid in the sample.

The morphology of the ceria particles obtained from the cerium acetate precursor was investigated by transmission electron microscopy (TEM) (Hitachi 600AB, operated at 200kV). The bright field micrograph (Fig-3) of the synthesized powder reflected the basic powder morphology where the smallest visible particle can be identified with the crystalline and / or their aggregates. From the micrograph it is revealed that the particles are nearly spherical with the average particle size in the range of 50-60 nm.

The appearance of large particles (~150 nm) in the TEM may indicate that two particle formation mechanisms are present independently. Large particles may be formed directly from precursor droplets that do not completely evaporate. It may be presumed that the particles having size of 50nm could be formed by precursor evaporation and subsequent gas phase reaction, ceria nucleation, surface growth, coagulation and sintering.

Future work:

The addition of iso-octane, which has high combustion enthalpy and high evaporation/burning rate, increases the flame temperature enhancing precursor evaporation [10], which therefore reduces the formation of the byproduct. Similarly homogeneous ceria powders can be obtained by using large amounts of oxygen in the flame where the particles experience high temperatures and long residence times.

Conclusion:

The Flame Spray Pyrolysis method (FSP) is promising method for the synthesis of nanocrystalline ceria and metal supported ceria powder. The particle size of the synthesized ceria powder is in the range of 50-60 nm.

Acknowledgement: R. K. Pati and S. H. Ehrman acknowledge the support from the ARL under the ARL PEER program.

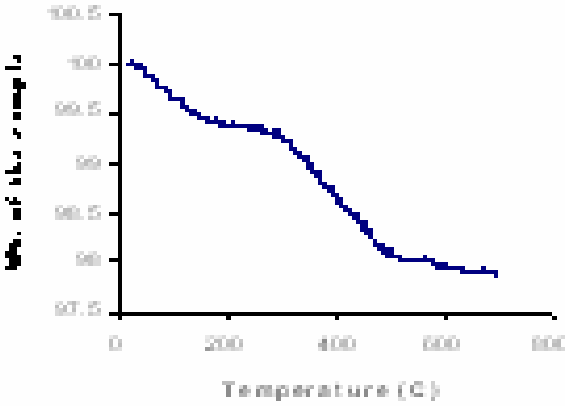

Fig-1: Thermogravimetric analysis of the ceria powder obtained from cerium acetate precursor

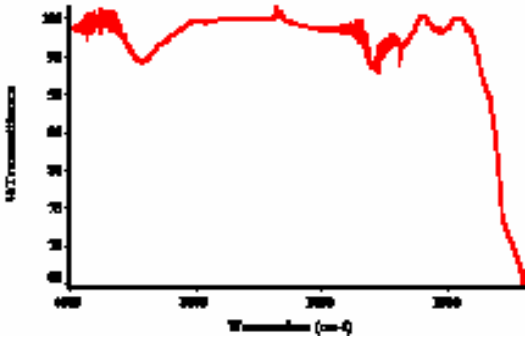

Fig-2: FTIR spectra of the ceria powder obtained from cerium acetate precursor.

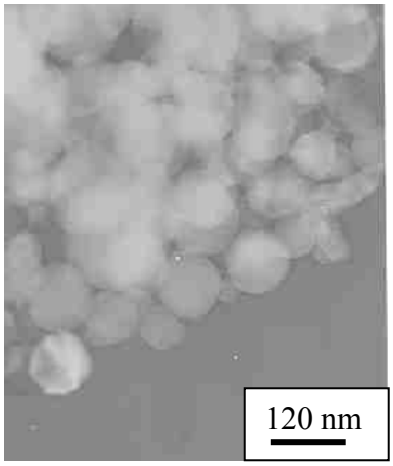

Fig- 3: Transmission electron micrograph of the ceria powder.

References:

1. Ahmed, S., Krumpelt, M., Intl. J. Hydrogen Energy, 2001. 26: p. 291
2. Li, Y., Fu, Q., Stephanopoulos, M F., Appl. Catal B: Environmental, 2000. 27: p. 179
3. Djuricic, B., Pickering, S., J. Europ. Ceram. Soc., 1999. 19: p.1925
4. Bruce, L A., Hoang, M., Hughes, A E., Turney, T W., Appl. Catal., A 1996. 134: p. 351
5. Hirano, M., Inagaki, M., J. Mater. Chem.., 2000. 10: p. 473
6. Hakuta, Y., Onai, S., Terayama, H., Adschiri, T., Arai, K., J. Mater. Sci. Lett. 1998. 17: p. 1211
7. Martinez-Arias, A., Fernandez-Garcia, M., Ballesteros, V., Salamanca L N., Conesa, J C., Otero, C., Soria, J., Langmuir, 1999. 15: p. 4796
8. Masui, T., Fujiwara, K., Peng, Y M., Sakata, T., Machida, K., Mori, H., Adachi, G., J. Alloy. Compd. 1998. 269: p. 116
9. Terrible, D., Trovarelli, A., Llorca, J., deLeitenburg, C., Dolcetti, G., J. Catal., 1998. 178: p. 299
10. Mädler, L., Stark, W J., Pratsinis, S E., J. mater. Res., 2002. 17: 1356

Low Cost Hydrogen Transport Membranes

Anthony F. Sammells, Shane E. Roark ,
Michael V. Mundschau, and Thomas F. Barton

Eltron Research Inc.
4600 Nautilus Court South
Boulder, CO 80301
www.eltronresearch.com

Introduction

Eltron Research Inc. is developing low cost, multi-phase membranes for separating hydrogen from hydrogen containing feedstreams (Figure 1). This is being addressed using metal/ceramic composites which facilitate high proton and electron conduction. Membranes are being developed for high (>750°C) and low (<425°C) temperature applications and have been successfully operated under a high pressure differential (250 psi) for extended times. Under ambient pressure, hydrogen transport rates >25mL/cm^2/min have been achieved at 400°C.

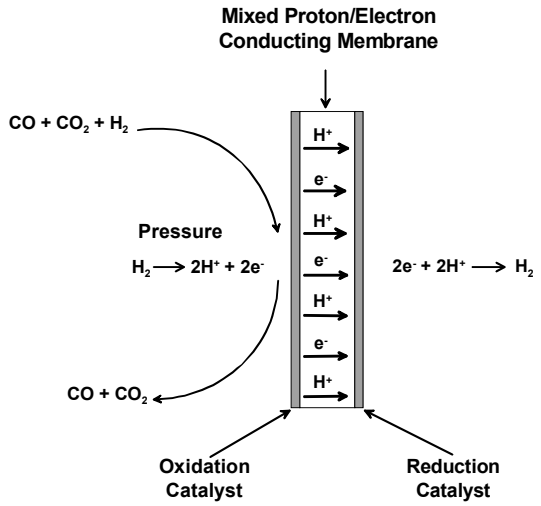

Figure 1. Schematic diagram of metal/ceramic composite membrane process for separating hydrogen from a mixture of gases.

Experimental

Doped perovskites $A_{1-x}A_x'B_{1-y}B_y'O_{3-\delta}$, where x and y are the fractions of dopants in the A and B sites, respectively, and δ is the number of oxygen vacancies,[1-3] were prepared using conventional high temperature solid state synthesis techniques. Corresponding cermets $A_{1-x}A_x'B_{1-y}B_y'O_{3-\delta}$/M were prepared by sequential pressing and sintering at elevated temperatures under controlled atmosphere conditions.

The inlet hydrogen source was initially diluted with helium. This facilitated determination of the membrane seal quality. H_2 and He fractions within inlet and sweep streams were determined by TCD-GC using a Shimadzu GC 14-A with a 12-ft. by 1/8-in. stainless steel Carbosphere column. Ultra-high purity Ar was used as the carrier gas to optimize detection limits for hydrogen and helium.

Results and Discussion

Hydrogen transport metal/ceramic composite membranes under development at Eltron consist of an adherent ceramic phase and a low cost hydrogen permeable metallic phase. The ceramic phase can either be a dense mixed proton and electron conductor or a porous non-conducting material. This latter approach is largely for providing mechanical support when thin-film metal alloys are used.

Hydrogen permeation P(mole·m^{-1}·s^{-1}·Pa$^{1/2}$) through these membranes, in the absence of surface kinetic limitations, is dependent on the membrane thickness, *t*, according to,

$$P = \frac{J \cdot t}{\sqrt{p_{H_2}, in} - \sqrt{p_{H_2}, out}}$$

where J is the hydrogen flux through the membrane in mole·m^{-2}·s^{-1}. For this class of membrane, the dependency of hydrogen flux upon thickness is shown in Figure 2 at 320°C. These membranes have been successfully operated for thousands of hours at both ambient pressure and with a 250 psi pressure differential between the hydrogen feed and permeate side.

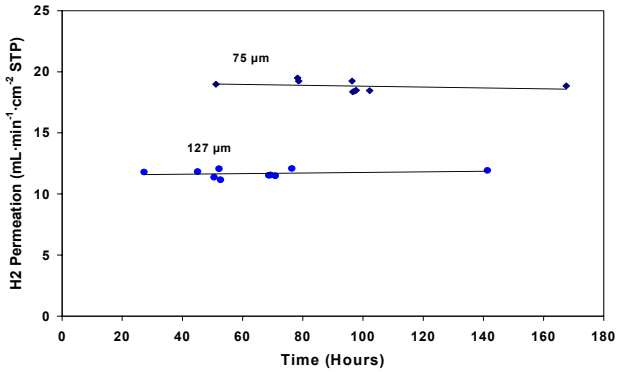

Figure 2. Hydrogen permeation as a function of time at 320°C for different membrane thicknesses. The feed gas was 80 mL/min 80/20 H_2/He and the sweep gas was approximately 250 mL/min Ar.

The performance of our low cost membranes operating under ambient pressure conditions as a function of temperature (Figure 3) and Ar sweep rate (Figure 4) on the hydrogen permeate side are shown below. As can be seen, hydrogen diffusion fluxes >25 mL/cm^2/min have been achieved at 400°C.

A simplified block diagram of a hydrogen separation unit installed in an integrated gasification combined cycle (IGCC) plant is shown in Figure 5. The diagram shows three options for installation, indicated as baseline, alternative 1, and alternative 2. The alternative 1 option assumes the membrane materials will be tolerant to sulfur and particulate material, and that the raw syngas from coal gasification can be sent directly to the unit. The baseline option also assumes sulfur tolerance, but the gas stream must be filtered prior to entering the unit. If the membrane materials are not sulfur tolerant, then alternative 2 will be necessary, and the unit will be inserted after desulfurization. This condition will require reheating the gas stream through a heat exchange prior to entering the hydrogen separation unit.

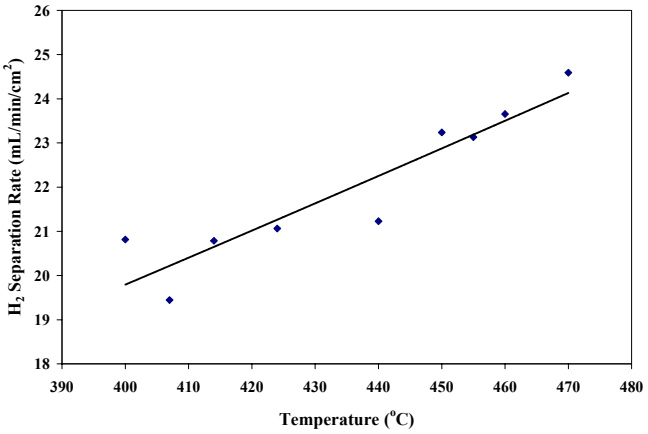

Figure 3. Hydrogen diffusion as a function of operating temperature under ambient pressure conditions. Ar sweep rate on permeate side 300 mL/min.

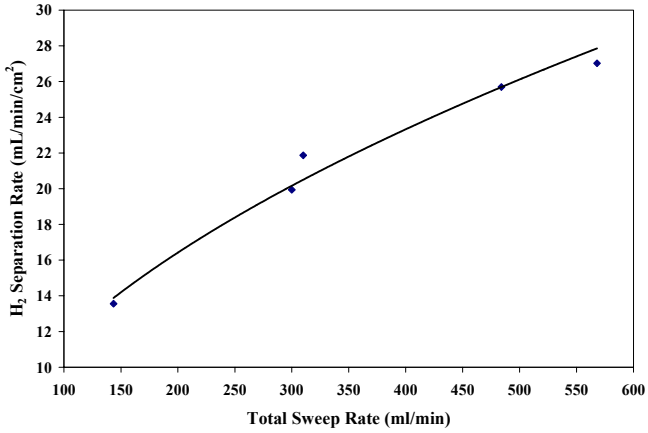

Figure 4. Hydrogen diffusion as a function of Ar sweep rate on the permeate side at 400°C. Ambient pressure conditions.

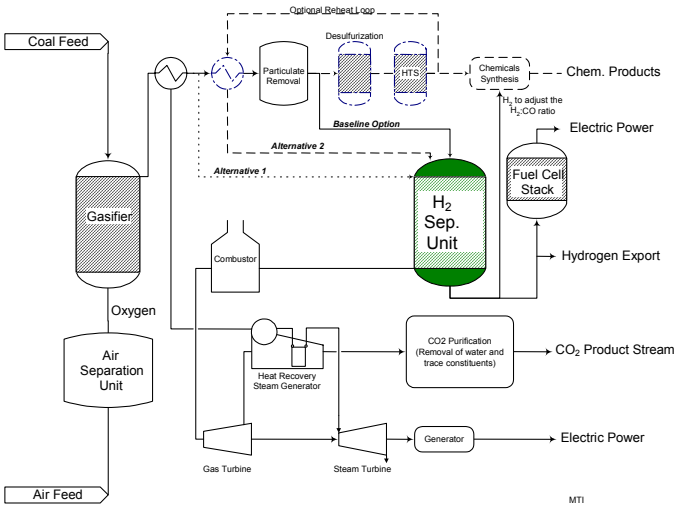

Figure 5. Diagram of an IGCC plant with three installation options for a hydrogen separation unit.

Acknowledgment

This work is supported by DOE/NETL under Contract Number DE-FC26-00NT40762.

References

(1) White, J. H.; Schwartz, M.; and Sammells, A. F. U.S. Patent 5,821,185, October 13, 1998.
(2) White, J. H.; Schwartz, M.; and Sammells, A. F. U.S. Patent 6,037,514, March 14, 2000.
(3) White, J. H.; Schwartz, M.; and Sammells, A. F. U.S. Patent 6,281,403, August 28, 2001.

PRODUCTION OF SYNTHESIS GAS FROM METHANOL WITH NONTHERMAL PLASMA

Shigeru Futamura and Hajime Kabashima

National Institute of Advanced Industrial Science and Technology
AIST Tsukuba West, 16-1 Onogawa, Tsukuba, Ibaraki, 305-8569 Japan

Introduction

Recently, application of nonthermal plasma to the processes for the production of hydrogen[1-5] and synthesis gas[6–10] has attracted much attention due to its technical merits such as quick response, low and flexible reaction temperature, and facile operations. Only batch systems are available for relatively new approaches such as photocatalysis[11,12] and mechano-catalysis.[13, 14] On the other hand, reactions can be carried out in flow systems with nonthermal plasma, and furthermore, higher energy efficiency and higher rate for hydrogen production are obtained in water splitting. Based on these findings, the system of nonthermal plasma can be extended to processes of fuel reforming at lower temperatures. It has been already reported that process load can be reduced in the steam reforming of aliphatic hydrocarbons with nonthermal plasma.[5]

It is essentially important to optimize the plasma-generating method and reaction conditions from the practical viewpoint. However, this kind of information has been sparsely documented in the literature. This paper presents the effects of reactor type and voltage waveform and frequency on the efficiencies in the production of synthesis gas from methanol.

Experimental

A ferroelectric packed-bed reactor (**FPR**) and a silent discharge reactor (**SDR**) used in this research were described in detail elsewhere.[15,16] Methanol was introduced to the reactor by passing N_2 through methanol in a small volume of water-bubbling device set in a thermostatic bath. Methanol concentrations were adjusted with the temperature at the thermostatic bath. The gas residence time varied from 8.9 to 44.3 s for **FPR** and 0.36 to 1.80 s for **SDR** at 0.50 to 0.10 L/min of gas flow rate. The both reactors employed 5-5000 Hz ac and high voltage up to 11 kV was applied to both of them. No breakdowns occurred during operations within their maximum voltages.

The values of plug-in power and applied voltage for **FPR** and **SDR** were measured with a digital powermeter and a digital wavemeter, respectively. Combination of a model of high voltage amplifier 20/20/B (Trek Japan, Co., Ltd.), a function generator (FG-2, Wavetek), and an oscilloscope (SONY TEKTRONIX TDS 3052) was used instead of a Neon transformer to estimate the power consumptions in both the reactors. In the applied voltage range of 3 kV to 11 kV, data sets were collected for power consumptions in the reactors and methanol conversions only with this amplifier. Then, the actual power consumptions without using 20/20B were calculated by comparing the methanol conversions at the same applied voltages with and without 20/20B. With this procedure, it was shown that about 10±2% and 20 %±3% of plug-in power were consumed in **FPR** and **SDR**, respectively.

The volatile byproducts were identified by GC-MS. Methanol conversion and byproduct yields were determined by FID-GC. The concentrations of CO, CO_2, N_2O, ethane, ethylene, and acetylene were determined by GC with both of TCD and FID and the combined columns of Porapak Q+N and Molecular Sieve 13X. H_2 and methane were quantified by TCD-GC with a packed column of Molecular Sieve 13X.

Results and Discussion

Definitions of RED and the yields of H_2, CO, and CO_2. As a measure of energy density for **FPR** and **SDR**, reactor energy density (RED) will be used later (1), where Power denotes the plug-in power. The yields of H_2 and COx (x = 1 and 2) are defined in (2) and (3), respectively.

$$\text{RED (kJ / L)} = \text{A X Power (kW)} / [\text{Gas flow rate (L/min)} / 60] \quad (1)$$

(A = 0.1 and 0.2 for **FPR** and **SDR**, respectively.)

$$H_2 \text{ yield (mol\%)} = 50 \text{ X } [H_2 \text{ concentration (ppm)} / \text{initial } CH_3OH \text{ concentration (ppm)}] \quad (2)$$

$$\text{COx yield (mol\%)} = 100 \text{ X } [\text{COx concentration (ppm)} / \text{initial } CH_3OH \text{ concentration (ppm)}] \quad (3)$$

Waveform Effect on the Reaction Behavior of CH_3OH. Tables 1 and 2 show the waveform effect on the reaction behavior of methanol in N_2. Applied voltages were set to obtain comparable methanol conversions for **FPR** and **SDR**.

Table 1. Effect of Voltage Waveform on Methanol Conversion

Reactor	Waveform	Applied voltage (kV)	Reactor power consumption (W)	MeOH conv. (mol%)
FPR	Triangle	6.86	0.48	26
FPR	Sine	6.84	0.22	12
FPR	Square	6.88	0.21	8
SDR	Triangle	9.20	1.99	21
SDR	Sine	9.36	1.32	18
SDR	Square	9.34	1.31	10

Voltage frequency: 50 Hz. Power consumptions in 20/20B varied in the range of 520 to 524 W. Methanol concentration 1.0 %; Q = 100 mL/min.

Table 2. Effect of Voltage Waveform on Product Distribution

Reactor	Waveform	MeOH conv. (mol%)	Product yield (mol%)		
			H_2	CO	CO_2
FPR	Triangle	26	5.3	4.9	0.9
FPR	Sine	12	2.6	2.4	0.5
FPR	Square	8	1.1	1.0	0.2
SDR	Triangle	21	4.2	3.2	0.7
SDR	Sine	18	3.1	2.1	0.4
SDR	Square	10	1.4	0.8	0.2

Voltage frequency: 50 Hz. Power consumptions in 20/20B varied in the range of 520 to 524 W. Methanol concentration 1.0 %; Q = 100 mL/min.

Table 1 clearly shows that higher applied voltages and larger reactor power consumptions are required for **SDR** than for **FPR** to attain comparable methanol conversions. Since the power consumptions for the primary power source (20/20B) do not change, irrespective of waveform and applied voltage, the energies of energetic electrons in nonthermal plasma are consumed in methanol conversion more effectively in **FPR** than in **SDR**. The catalytic effect of $BaTiO_3$ can be neglected at ambient temperature, the different performances of **FPR** and **SDR** are ascribed to the reactor-dependent populations of electron energies in nonthermal plasma.

With **FPR**, the molar ratios of H_2 to CO {[H_2] / [CO]} are ca. 2.20, irrespective of waveform and methanol conversion (Table 2).

On the other hand, $[H_2]$ / [CO] increases from 2.63 (triangle) to 3.50 (square) with **SDR**. Irrespective of the reactors, CO was obtained in ca. 5-times higher yields than CO_2. Under our reaction conditions, the step of CO oxidation to CO_2 is slow due to the absence of O_2 and H_2O. The lower ratios of H_2 to CO could be partly ascribed to higher mole fractions of CO_2.

Frequency Effect on Methanol Conversion. In use of a Neon transformer (Neon) at 50 Hz of plug-in voltage, **FPR** worked much better than **SDR** in methanol conversion. At higher frequencies, however, **SDR** was much more sensitive to frequency change than **FPR** (Figs. 1 and 2). At 500 Hz, methanol conversion was far lower than that with the Neon transformer at 50 Hz for **FPR** (Fig. 1). On the other hand, comparable conversions were obtained for **SDR** (Fig. 2). With this reactor, methanol was almost quantitatively converted at 5000 Hz. The power consumptions in 20/20B at 5000 Hz did not change with **FPR** and **SDR**.

The product distribution was not affected by frequency. The lifetime of the energetic electron is shorter than 10^{-6} s, and it does not seem that reactor type and voltage properties drastically affect the product-forming processes.

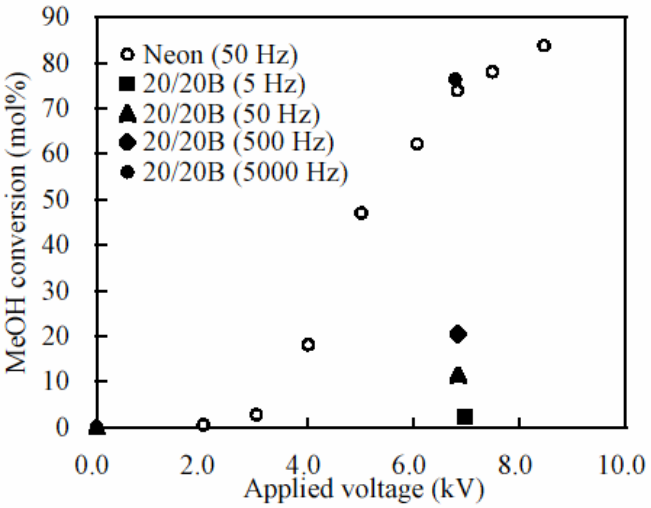

Figure 1. Effect of power source and frequency in the methanol conversion with **FPR**. Methanol concentration 1.0 %; Q = 100 mL/min.

Additive Effect of H_2O and O_2. With **FPR** at 50 Hz of plug-in voltage, additive effect of H_2O and O_2 was investigated with $[H_2O]$ / $[CH_3OH]$ up to 1.0 and $[O_2]$ / $[CH_3OH]$ up to 0.15. The general trend was that these additives improved the carbon balance in the reaction rather than promote the methanol conversion. At higher concentrations of O_2 and H_2O, abatement of the endothermicity in methanol conversion and H_2 consumption are in a trade-off relationship with each other.

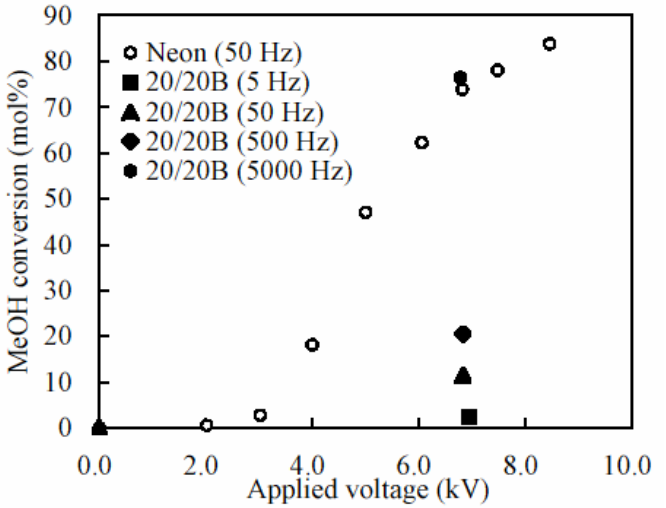

Figure 2. Effect of power source and frequency in the methanol conversion with **SDR**. Methanol concentration 1.0 %; Q = 100 mL/min.

Conclusions

It has been shown that effects of waveform and frequency are reflected in the process of methane reforming with nonthermal plasma, and that this effect depends on reactor type.

Acknowledgment. This work was partly supported by the Grants-in-Aid from New Energy and Industrial Technology Development Organization of Japan (NEDO).

References

(1) Chen, X.; Marquez, M.; Rozak, J.; Marun, C.; Luo, J.; Suib, S. L.; Hayashi, Y.; Matsumoto, H. *J. Catal*., **1998**, 178, 372.
(2) Tanabe, S.; Matsuguma, H.; Okitsu, K.; Matsumoto, H. *Chem. Lett*., **2000**. 1116.
(3) Kabashima, H.; Einaga, H.; Futamura, S. *Chem. Lett.*, **2001**, 1314.
(4) Yao, S. L.; Okumoto, M.; Nakayama, A.; Suzuki, E. *Energy Fuels*, **2001**, 15, 1295.
(5) Kabashima, H.; Einaga, H.; Futamura, S. *IEEE Trans. Ind. Appl.*, **2003**, 39, 340.
(6) Zhou, L. M.; Xue, B.; Kogelschatz, U.; Eliasson, B. *Energy Fuels*, **1998**, 12, 1191.
(7) Kado, S.; Urasaki, K.; Sekine, Y.; Fujimoto, K. *Chem. Commun*., **2001**, 415.
(8) Bromberg, L.; Cohn, D. R.; Rabinovich, A.; Alexeev, N. Prepr. Pap. – Am. Chem. Soc., *Div. Fuel Chem.,* **2001**, 46(1), 1.
(9) Kabashima, H.; Futamura, S. Prepr. Pap. – Am. Chem. Soc., *Div. Fuel Chem.,* **2002**, 47(2), 661.
(10) Kabashima, H.; Futamura, S. *Chem. Lett*., **2002**, 1108.
(11) Takata, T.; Tanaka, A.; Hara, M.; Kondo, J. N.; Domen, K. *Catal. Today*, **1998**, 44, 17.
(12) Kudo, A. *J. Ceramic Soc. Jpn*., **2001**, 109, S-81.
(13) Ohta, T. *Appl. Energy*, **2000**, 67, 181.
(14) Hara, M.; Komaba, M.; Hasei, H.; Yashima, M.; Ikeda, S.; Takata, T.; Kondo, J. N.; Domen, K. *J. Phys. Chem. B*, **2000**, 104, 780.
(15) Futamura, S.; Zhang, A.; Yamamoto, T. *IEEE Trans. Ind. Applicat*., **2000**, 36, 1507.
(16) Einaga, E.; Ibusuki, T.; Futamura, S. *IEEE Trans. Ind. Applicat*., **2001**, 37, 1476.

EFFECTS OF REDOX PROPERTIES ON ISOSYNTHESIS OVER ZrO_2 BASED CATALSYTS

Yingwei Li, Dehua He, Qiming Zhu, Boqing Xu*

State Key Lab of C_1 Chemistry and Technology
Department of Chemistry, Tsinghua University
Beijing 100084, China

Introduction

Isosynthesis refers to the reaction that selectively converts coal or natural gas derived syn-gas (CO + H_2) to i-C_4 hydrocarbons (isobutene and isobutane). Zirconium dioxide catalyst has been shown to be active for this reaction with a high selectivity to isobutene.[1] It is well known that zirconia possesses explicitly particular chemical properties; acidic and basic properties and oxidizing and reducing properties.[2] The effects of acidic and basic properties on the catalytic performance of isosynthesis have been extensively investigated over zirconia based catalysts.[3-8] However, little work has been reported on the effects of redox properties of zirconia based catalysts on the isosynthesis. The primary objective of present work is to identify the function of redox properties on isosynthesis selectivities through a systematically investigation on the effects of acid-base and redox properties upon the catalytic performances of zirconia based catalysts in the isosynthesis. The redox property was modified by doped ZrO_2 with various quantities of CeO_2 and Y_2O_3. The reduction and acid-base properties were systematically investigated using temperature programmed reduction (TPR) and desertion (TPD) study. In parallel, steady-state isosynthesis activities and selectivities were measured to relate the observed catalytic performances to the acid-base and redox properties characterized on these CeO_2 and Y_2O_3 doped ZrO_2 catalysts.

Experimental

Preparation of catalysts. Preparation of zirconia catalyst has been described in our previous work.[7] CeO_2-ZrO_2 and Y_2O_3-ZrO_2 mixed oxides were synthesized by co-precipitation of a mixed solution of $ZrOCl_2$ and various additives, cerium or yttrium nitrate salts, with ammonium solution.

Characterization of catalysts. The acid-base properties of the catalysts were measured by temperature programmed desorption (TPD) of ammonia and carbon dioxide,[7] respectively. Temperature programmed reduction (TPR) studies were carried out in a conventional system equipped with a thermal conductivity detector (TCD). The amount of catalyst used was 100 mg in all cases. TPR was carried out in a flow of 5% H_2/Ar (20 ml/min) at a heating rate of 10 K/min.

Reaction Procedure. The hydrogenation of CO was carried out in one quartz lined stainless steel tubular reactor[9] at 5.0 MPa, 673 K and 650 h^{-1}. The detailed process of pretreatment and evaluation of catalysts please refer to our previous paper.[8]

Results and Discussion

Three CeO_2 doped ZrO_2 (12, 50, 88 mol% CeO_2) and five Y_2O_3 doped ZrO_2 (2.5, 4.5, 6.2, 8.6, 12.0 mol% Y_2O_3) were prepared and tested for their isosynthesis activities. Pure ZrO_2 prepared in this study has a specific area ca. 55 m^2 g^{-1}. All the CeO_2-ZrO_2 and Y_2O_3-ZrO_2 mixed oxides have moderate specific areas in the range of ca. 80 to 130 m^2 g^{-1}. Monoclinic phase was the dominating crystal phase for pure ZrO_2 prepared in this study. However, tetragonal and cubic ZrO_2 phases were the main crystal phases for all the CeO_2 and Y_2O_3 doped ZrO_2 mixed oxides.

The reduction behaviors of CeO_2-ZrO_2 and Y_2O_3-ZrO_2 mixed oxides were investigated by means of the H_2-TPR technique. Only a small quantity of H_2 was consumed on pure ZrO_2.[10] The incorporation of CeO_2 and Y_2O_3 to ZrO_2 greatly enhanced the reduction behavior of ZrO_2. The maximum quantity of H_2 consumption for CeO_2 and Y_2O_3 doped ZrO_2 mixed oxides was obtained at 50% CeO_2 and 8.6% Y_2O_3 doped, respectively. This enhancement of H_2 consumption can be attributed to the mobility of lattice oxygen that was enhanced and then be more active to react with H_2 by the incorporation of CeO_2 or Y_2O_3 with ZrO_2.[10]

The acid and base properties of the CeO_2 and Y_2O_3 doped ZrO_2 catalysts also varied with the quantities of dopants added. The amount of acidic and basic sites for CeO_2-ZrO_2 mixed oxides both remarkably decreased with an increase in the content of CeO_2. For Y_2O_3-ZrO_2 mixed oxides, the amount of acidic sites increased slightly with more and more Y_2O_3 doped. However, the amount of basic sites decreased with an increase in the content of Y_2O_3 from 4.5% to 12%. It is not clear what caused 2.5% Y_2O_3 doped ZrO_2 catalyst to have so small quantity of basic sites (ca. 44.2 μmol g^{-1}).

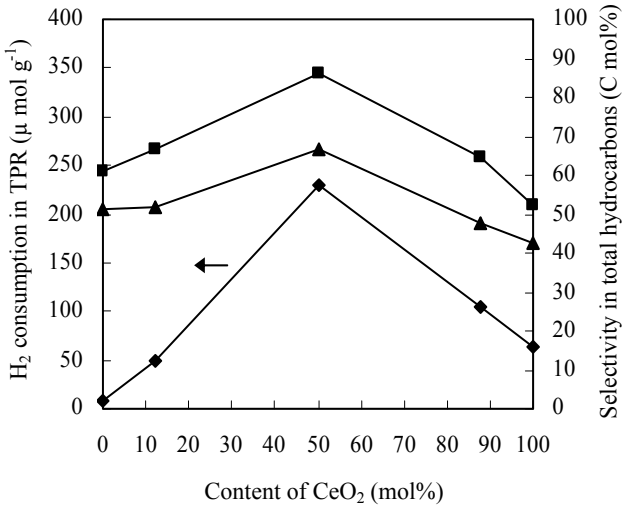

Figure 1. Quantities of H_2 consumption and selectivities to C_4 and i-C_4 in total hydrocarbons as a function of content of CeO_2 for CeO_2-ZrO_2 mixed oxide catalysts. ■ C_4 selectivity in total hydrocarbons, ▲ i-C_4 selectivity in total hydrocarbons.

The catalytic test results of the CeO_2-ZrO_2 and Y_2O_3-ZrO_2 mixed oxide catalysts in the isosynthesis are related to the redox properties of the zirconia based catalysts. Figure 1 shows the quantities of H_2 consumption in TPR measurement and selectivities to C_4 and i-C_4 in total hydrocarbons as a function of the content of CeO_2 doped in the catalysts. It can be seen that the highest selectivity to C_4 in total hydrocarbons was obtained over the catalyst which has a maximum quantity of H_2 consumption. Similar results were obtained over the Y_2O_3-ZrO_2 mixed oxide catalysts. The maximum was at 50%CeO_2 and 8.6%Y_2O_3, respectively. The selectivity to i-C_4 in total hydrocarbons also increased with increasing the quantity of H_2 consumption, as shown in Figure 1. However, the selectivity to i-C_4 in total hydrocarbons was unnecessarily achieved the maximum over the catalyst which has a maximum H_2 consumption in the TPR. For the Y_2O_3-ZrO_2 mixed oxide catalysts, the maximum H_2 consumption was at 8.6%Y_2O_3 doped. The highest selectivity to i-C_4 in total hydrocarbons was, however, obtained over the 6.2%Y_2O_3 doped ZrO_2 catalyst. No direct relationship between the amount of acidic or

basic sites and the selectivity to C_4 and i-C_4 in total hydrocarbons was observed for both CeO_2 and Y_2O_3 doped ZrO_2 catalysts, as shown in Figure 2 for CeO_2 doped ZrO_2 catalysts. Therefore, the improvement of catalytic performances over some CeO_2 and Y_2O_3 doped ZrO_2 catalysts can be attributed to the enhancement of reduction properties that are suggested to be related to the increased mobility of lattice oxygen.[10]

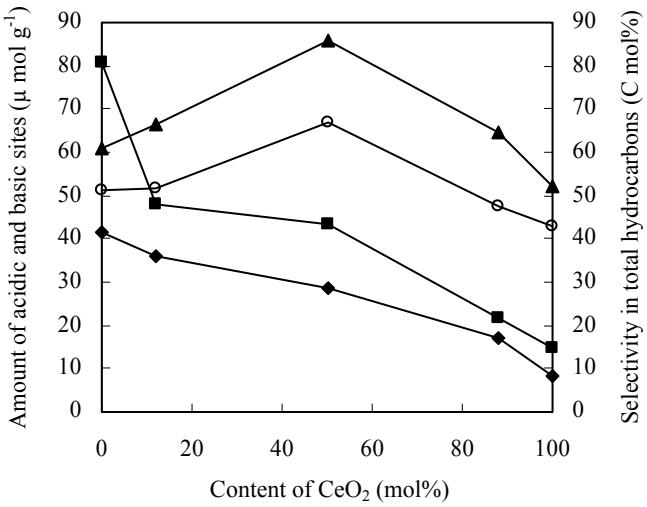

Figure 2. Amount of acidic and basic sites and selectivities of C_4 and i-C_4 in total hydrocarbons as a function of content of CeO_2 for CeO_2-ZrO_2 mixed oxide catalysts. ♦ Amount of acidic sites, ■ Amount of basic sites, ▲ C_4 selectivity in total hydrocarbons, ○ i-C_4 selectivity in total hydrocarbons.

However, the redox property can't be assigned to be the only factor in determining the catalytic performances of the catalysts. For Y_2O_3-ZrO_2 mixed oxide catalysts, the highest i-C_4 selectivity in total hydrocarbons was achieved over 6.2%Y_2O_3 doped ZrO_2 based catalyst neither 8.6%Y_2O_3 nor 12%Y_2O_3 doped catalysts which both have larger quantities of H_2 consumption. It is also found that the selectivity to C_4 and i-C_4 in total hydrocarbons showed a sharp decline with more C_1 and C_2 hydrocarbons when the content of Y_2O_3 was increased from 8.6% to 12%, although similar redox properties were obtained over these two catalysts. This would be ascribed to the large decrease of basic sites on the 12%Y_2O_3 doped ZrO_2 catalyst (ca. 45 μmol g^{-1}) since basic sites has been suggested to be significant for the formation of i-C_4 hydrocarbons.[4,6-8] The marked decrease of basic sites can also explain the lower i-C_4 selectivities in total hydrocarbons for the 88%CeO_2 and 2.5%Y_2O_3 doped ZrO_2 catalysts compared to that for pure ZrO_2 catalyst. The amount of basic sites for these two catalysts was ca. 21.5 and 44.2 μmol g^{-1}, respectively. However, it was ca. 81 μmol g^{-1} for pure ZrO_2 catalyst. Therefore, the improvement of C_4 and i-C_4 selectivities in total hydrocarbons over some CeO_2 and Y_2O_3 doped catalysts would be attributed to the enhancement of redox properties meanwhile maintaining an appropriate amount of base sites over these catalysts.

Acknowledgment

Financial support of this study is provided by the Foundation for Fundamental Research of Tsinghua University and the Analytical Foundation of Tsinghua University.

References

1. Maehashi, T.; Maruya, K.; Domen, K.; Aika, K.; Onishi, T. *Chem. Lett.*, **1984**, 747.
2. Tanabe, K. *Materials Chemistry and Physics*, **1985**, *13*, 347.
3. Maruya, K.; Maehashi, T.; Haraoka, T.; Narui, S.; Asakawa, Y.; Domen, K.; Onishi, T. *Bull. Chem. Soc. Jpn.*, **1988**, *61*, 667.
4. Feng, Z. T.; Postula, W. S.; Akgerman, A.; and Anthony, R. G. *Ind. Eng. Chem. Res.*, **1995**, *34*, 78.
5. Jackson, N. B.; and Ederkt, J. G. *J. Catal.*, **1990**, *126*, 31.
6. Su, C. L.; Li, J. R.; He, D. H.; Cheng, Z. X.; and Zhu, Q. M. *Appl. Catal.*, **2000**, *202*, 81.
7. Li, Y. W.; He, D. H.; Cheng, Z. X.; Su, C. L.; Li, J. R.; and Zhu, Q. M. *Journal of Molecular Catalysis A: Chemical*, **2001**, *175*, 267.
8. Li, Y. W.; He, D. H.; Yuan, Y. B.; Cheng, Z. X.; and Zhu, Q. M. *Energy & Fuels*, **2001**, *15* (6), 1434.
9. Li, Y. W.; He, D. H.; Zhu, Q. M. Prepr. Pap. – *Am. Chem. Soc., Div. Fuel Chem.*, **2002**, *47* (1), 168.
10. Otsuka, K.; Wang, Y.; and Nakamura, M. *Appl. Catal.*, **1999**, *183*, 317.

TOWARDS THE DEVELOPMENTS OF ROBUST WATER-GAS SHIFT REACTORS

Robert M. Enick[1], Anthony V. Cugini, Richard P. Killmeyer, Bret H. Howard, Bryan M. Morreale[2], Michael V. Ciocco[2] and Felipe Bustamante[1]

U.S. Department of Energy
National Energy Technology Laboratory
P.O. Box 10940, Pittsburgh PA 15236
(1) NETL Research Associate, University of Pittsburgh
enick@engrng.pitt.edu, (2) NETL Site Support Contractor, Parsons Project Services Inc.

Introduction

Hydrogen permeable Water-Gas Shift membrane reactors are being considered for the simultaneous production of separate hydrogen and carbon dioxide-streams from a coal gasification plant. As hydrogen permeates the membrane, the conversion of carbon monoxide and water to carbon dioxide and hydrogen in this equilibrium-limited reaction increases, resulting in the production of a high purity, low pressure hydrogen permeate and a high pressure, carbon dioxide-rich stream for sequestration[1].

The design of these membrane reactors requires models of the reaction kinetics and membrane performance at the post-gasifier conditions expected for various coal gasification plant configurations, with temperatures up to 1173 K, pressures up to 6.89 MPa, and hydrogen sulfide concentrations as high as 1000 ppm.

The first objective of this study is to describe the intrinsic kinetics of the forward Water-Gas Shift reaction at post-gasifier conditions in a high-pressure quartz reactor. In a commercial reactor, the reacting gas mixture flow would contact the reactor surfaces, the membrane, and heterogeneous catalyst particles. Because each of these solid surfaces may dramatically influence the reaction kinetics[2], the forward WGS kinetics will also be determined in a high-pressure quartz reactor packed with a material that corresponds to each of these surfaces. If a significant rate enhancement is found to be associated with the reactor material and membrane surface, the need for the introduction of the heterogeneous catalyst particles may be eliminated.

The second objective of this study is to determine the effect of temperature, pressure, alloy composition and hydrogen sulfide feed stocks on the hydrogen permeance of several Pd/Cu alloy membranes.

Experimental

Kinetic studies. Details of the reactor configuration are given elsewhere[2]. Basically, CO and water were fed premixed to the reactor through a narrow annulus with a volume less than one tenth that of the reaction zone. The gases were rapidly heated to the reaction temperature as they passed though the annulus. CO flowrate was controlled with Brooks mass flow controllers. Water was added to the CO stream by means of a syringe pump. Tubing upstream and downstream the reactor was heat-taped and insulated to avoid condensation of water. Reactor temperature was controlled with a thermocouple placed directly on the top of the reactor; pressure was controlled with a pressure controller downstream the reactor. Conversions were kept lower than 2% in the quartz reactor studies to forfeit any effect of the reverse reaction. The effluent from the reactor was analyzed with a GC equipped with a TCD detector.

Permeation studies. The hydrogen membrane test (HMT) unit, fabricated at the NETL, was designed to evaluate membrane performance at high-temperatures and pressures via steady-state hydrogen flux testing and has been described previously[3].The apparatus was designed to operate at temperatures and pressures up to 1173 K and 3 MPa, respectively.

The various compositions Pd/Cu alloy membranes of interest in this study (40, 53, 60, and 80 wt% Pd), were prepared by ACI Alloys as 100 micron thick foils, 99.9% purity, while pure palladium and copper foils were obtained by Alfa Aesar. Membranes were fabricated for testing by brazing foil disks to thick nickel alloy washers having negligible hydrogen permeability; high-purity gold powder was used as brazing material. Brazing was done in a muffle furnace at 1400 K. A porous metal support was utilized on the permeate side of the membrane foil to prevent foil distortion and possible mechanical failure at high temperatures in the presence of a pressure drop. The membrane surface contacted the porous support surface but was not bonded to it. The resulting mounted membranes had an active hydrogen permeation diameter of approximately 8.5 mm. The membrane brazing and mounting techniques were developed at the NETL.

Sulfur-tolerance studies. The hydrogen permeance in the presence of 1000 ppm hydrogen sulfide of several of the Pd/Cu membranes described previously was determined within the NETL's Hydrogen Membrane Batch (HMB) unit. The HMB unit was designed to evaluate the hydrogen permeance of possible sulfur tolerant membrane materials over a wide range of temperatures (up to 1073 K) and relatively low-pressures (up to 0.5 MPa). The hydrogen permeance of the alloys of interest in this study was determined through a transient analysis monitoring the change in hydrogen concentration of the retentate while a constant concentration was maintained on the permeate side.

Results and Discussion

Kinetic studies. An early work by Graven and Long[4] addressed the high-Temperature (>850^{o}C), ambient-pressure gas-phase forward Water-Gas Shift Reaction (FWGSR). The authors found that the chain reaction mechanism previously proposed by Bradford[5] was consistent with their experimental rate expression. For very-low conversions (i.e. <1%), the rate can be expressed as $r=k[H_2O][CO]^{1/2}$. However, the effect of high-pressure was not assessed in that study. Our results for the high-pressure (16 bar) reaction in the quartz reactor confirmed the validity of such form of the rate of reaction (not shown here). Figure 1 compares the Energy of Activation of the high-temperature, high-pressure FWGS with the high-temperature, low-pressure experimental results by Graven and Long; the figure also shows the rate constant obtained from the Bradford mechanism by using the pseudo-steady state approximation (i.e., analytical solution) or from a numerical solution of the concentration profile of each one of the species at low pressure (in both cases the rate constant for each elementary reaction were taken from the GRI kinetic database). There is good agreement between the values of the energies of activation, although the values of the rate constant differ. We are currently studying this behavior. One possible explanation of the higher results by Graven and Long is the occurrence of the Boudouard reaction ($2CO \leftrightarrow C + CO_2$), which would give an artificially higher CO conversion; in our experiment carbon was removed by overnight treatment with oxygen (we found that an induction period of more than 24hr was required for the carbon formation to affect the results). The energy of activation and pre-exponential constants for the high-pressure reaction are 69 Kcal/mol and $1.03*10^{11}$ $l^{0.5}$ $mo^{l-0.5}$ s^{-1}, respectively.

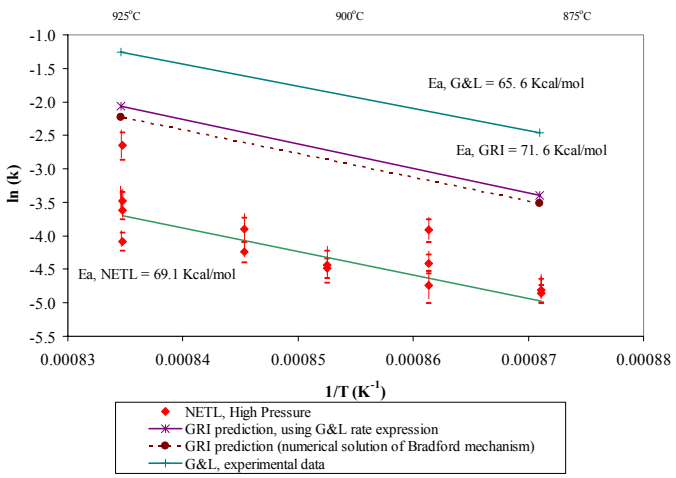

Figure 1. Energy of Activation of the high-temperature, gas-phase Forward Water-Gas Shift Reaction. NETL results: quartz reactor, 16-bar, $(y_{CO})_0 = 0.8$, $(y_{H2O})_0 = 0.2$, residence time < 4s.

A large increase in H_2O conversion was observed when the reaction was run in the Inconel reactor. Such enhancement in the reaction rate can be related to the Inconel walls; similar behavior was observed for the reverse Water-Gas Shift Reaction[2]. Equilibrium conversions are attained at relatively low temperatures, indicating that the membrane-reactor would be diffusion-limited rather than kinetic-limited. However, parallel reactions (e.g., methanation) become more noticeable under these conditions. Finally, metal dusting is a concern in using Inconel.

Permeation Studies. The hydrogen permeance results of this study are illustrated in Figure 2 as a function of temperature. With the exception of pure palladium, the hydrogen permeance of the 60 wt% Pd/Cu membrane exhibited the highest permeance of the alloy membranes studied at temperatures below 748 K while the 80 wt% Pd/Cu alloy exhibited the highest permeance at temperatures above 748 K. Both the 60 wt% Pd/Cu and 53 wt% Pd/Cu alloy membranes exhibited significant decreases in permeance with respect to temperature through their respective crystalline phase transition from bcc to fcc.

The 60 wt% Pd/Cu and 53 wt% Pd/Cu alloy membranes exhibited unique permeance responses with respect to the temperature induced phase transitions (bcc-fcc). The alloys displayed their highest permeance values at the low temperature, bcc phase. In addition, the permeance of both alloys decreased with temperature through their respective crystalline phase transition (bcc to fcc) while the fcc phases showed similar trends as the bcc phase with respect to temperature.

Decreases in hydrogen permeance greater than an order of magnitude in the presence of hydrogen sulfide were observed for the low-temperature, bcc crystalline phase of the 60 wt% Pd/Cu and 53 wt% Pd/Cu alloys. However, minimal changes were evidenced by the 80, 60, 53 and 40 wt% alloys at temperatures corresponding to the fcc crystalline phase.

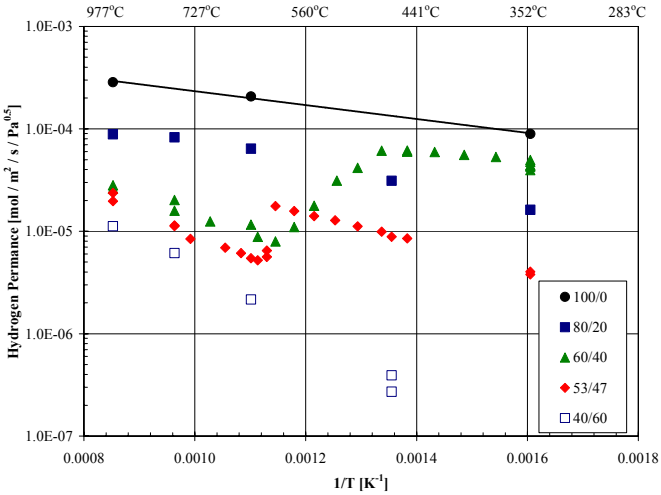

Figure 2. Hydrogen permeance results of several Pd/Cu alloys examined in this study.

Conclusions

The first experimental study of the high-pressure, high-temperature forward Water-Gas Shift reaction was conducted. Additionally the hydrogen permeance of a broad range of Pd/Cu alloy membranes was studied. The performance of the Pd/Cu membranes in the presence of sulfur was determined. Both the kinetics and permeance are required to evaluate the feasibility of a Water-Gas Shift membrane reactor at gasifier conditions. The finding of this study may be summarized as follows:

- The high-temperature, high-pressure forward Water-Gas Shift reaction appears to follow the same chain reaction mechanism than the low-pressure reaction. However, a negative influence of the high-pressure on the rate of reaction was observed. Current research efforts are underway to explain this phenomenon.
- The crystalline phase of the Pd/Cu alloys was found to have a great impact on the permeance of hydrogen both in the presence and in the absence of H_2S. Alloys with the fcc crystalline phase exhibit a higher sulfur-tolerance.

Acknowledgement. This work is supported through the "Gasification Technologies" and "Transportation Fuels and Chemicals" product lines at NETL.

References

(1) Enick, R.; Morreale, B.; Hill, J.; Rothenberger, K.; Cugini, A.; Sriwardane, R.; Poston, J.; Balachandran, U.; Lee, T.; Dorris, S.; Graham, W.; Howard, B. In: *Advances in Hydrogen*; Kluwer Academic/Plenum Publishers, New York, 2000; pp 93-100.
(2) Bustamante, F.; Enick, R.; Cugini, A.; Killmeyer, B.; Howard, B.; Rodgers, W.; Rothenberger, K.; Ciocco, M.; Morreale, B.; Shi. S. *AIChE J*, in review.
(3) Morreale, B.; Ciocco, M.; Enick, R.; Morsi, B.; Howard, B.; Cugini, A.; Rothenberger, K. *J. Membr. Sci*. **2003**, *212*, 87.
(4) Graven, W.; Long, J. *J. Am. Chem. Soc.* **1954**, *76*, 26602, 6421
(5) Bradford, B. *J. Chem. Soc.* **1933**, 1557.

AN OLD/NEW APPROACH TO THE PARTIAL OXIDATION OF ALKANES

P. C. Ford, P. Grosso, L. Laverman, I. M. Lorkovic, E. W. McFarland, D. Schaefer, J. H. Sherman, G. D. Stucky, S.Sun, M. Weiss, A.Yilmaz, G.Yilmaz, X. P. Zhou)

Departments of Chemistry and Biochemistry and of Chemical Engineering. University of California, Santa Barbara, CA 93106
GRT, Inc., 5662 Calle Real #373, Santa Barbara, CA 93117

Introduction

The transformation of natural gas feedstocks to higher value compounds continues to present an important intellectual challenge with strong economic rationales. Here we describe a new integrated, multi-step process for the selective partial oxidation of alkanes to alcohols, ethers or alkenes that provides unprecedented product control.

These transformations are carried out in a sequential zone flow reactor (SZFR) and involve bromination of alkane to alkyl bromide(s) and HBr followed by reaction of this mixture with a solid metal oxide (MO) to neutralize the HBr and generate oxygenated products (alcohols or ethers) or alkenes plus solid metal bromide and, lastly, oxygenation of the spent solid to regenerate the MO and Br_2 for reuse (Scheme 1)

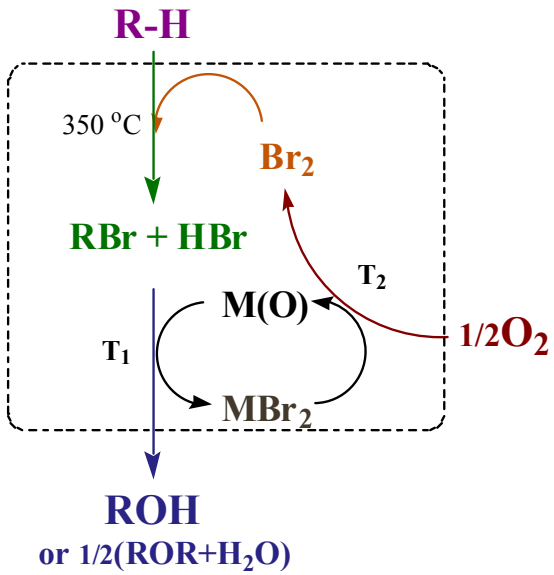

Thus, the overall transformation of alkane to alcohol, ether, or alkene utilizes dioxygen as the ultimate oxidant, for example:

$$R\text{-}H + 1/2\ O_2 \rightarrow ROH \qquad (1)$$

Results and Discussion

The key to the successful partial alkane oxidation reported here is the use of a solid transition metal oxide (or MO mixture) on a stable support to react with the alkyl bromide and effect bromide/oxide metathesis under mild conditions. While others have considered related approaches, the integration of these steps into a single scheme is unique. Furthermore, the specific MO mixture composition determines product distribution and thus provides unprecedented product control, especially with feedstocks other than methane. For example, with ethane certain MO compositions and reaction conditions give mostly alcohols or ethers (see below), while others give predominantly ethylene or acetaldehyde.

The SZFR consists of two serial fixed bed reactors. In the first, a stream of Br_2 and excess alkane (1-3 bar) reacts over glass beads (60-120 mesh) at 350 °C, and the Br_2 is fully consumed. Then the resulting alkyl bromide(s), HBr and excess alkane are directed into the second reactor containing supported metal oxide at T_1 (200-250 °C). The exiting products are identified and analyzed by ^{1}H-NMR and GC (with MS, TCD or FID detection) techniques. Longer runs demonstrate that most of the oxide equivalents can be utilized. After the metathesis capacity is largely consumed, O_2 is passed into the second reactor at T_2 (300-500 °C) to regenerate the MO and Br_2. The bromide retained on spent solids was quantitatively recovered as Br_2 (This procedure also releases CO_2 from carbon deposited during the metathesis.) Repetitive runs (> 10) cycles with regenerated MO showed no loss of activity. Material balances were established for bromine and carbon.

Examples of effective solid reactants for oxide/bromide metathesis are 50/50 CuO/ZrO_2 (MO-1) and 43/7/50 $Co_3O_4/Sm_2O_3/ZrO_2$ (MO-2). Products from these two differ considerably. MO-1 gives predominantly alcohols and more deep-oxidation to CO_2, while MO-2 gives largely ethers. For example, a 10:1 methane:Br_2 feed to a reactor containing MO-1 (3.6 g) led to 8.1% conversion with comparable amounts of CH_3OH (37%), CO_2 (35%) and unconverted CH_3Br (29%) in the product stream. A similar run with MO-2 gave CH_3OH (20%), $(CH_3)_2O$ (20%), CO_2 (5%), and unconverted CH_3Br (40%) and CH_2Br_2 (15%). Reaction of pure CH_3Br with MO-1 or MO-2 generates some CO_2 due to reduction of metal center oxidants (Cu(II) or Co(III), respectively). Larger CO_2 yields in the integrated system are attributed to reactions of polybrominated methanes, and can be addressed by improving bromination selectivity by introducing electrophilic catalysis or otherwise optimizing reaction conditions.

Experiments with ethane:Br_2 streams give less CO_2 and a richer product array. EtOH and Et_2O are the principal products, others include ethylene, acetaldehyde, vinyl bromide, ethyl acetate and butadiene, as well as unreacted EtBr. The relative yields are sensitive to MO composition and specific reaction conditions; e.g, MO-1 favors EtOH, MO-2 favors Et_2O, while other oxides and higher T_1 give very high selectivities for ethylene

Ongoing studies are focused on improving overall conversion and controlling product selectivity and include investigations of bromination catalysis and the design and optimization of metathesis solids and conditions.

Acknowledgement. This research was supported by a sponsored research agreement between GRT Inc. and UC Santa Barbara.

SYNGAS QUALITY IN GASIFICATION OF HIGH MOISTURE MUNICIPAL SOLID WASTES

Yongseung Yun, Seok Woo Chung, and Young Done Yoo

Plant Engineering Center
Institute for Advanced Engineering
633-2, Goan-ri, Baegam-myeon
Yongin, Gyeonggi-do, 449-863 Korea

Introduction

With widespread environmental concerns among non-technical people around the conventional incinerators in city areas, it becomes more and more difficult to get permission for new municipal solid wastes (MSW) treatment facilities in Korea like many other countries. Although dioxins are not a problem anymore technically because of the added SCR facility in reducing dioxins below the environmental regulations of 0.1 ng/Nm^3, residents in Korea still remain skeptical and start to insist that advanced technologies should be employed in order to build a new MSW treatment facility in their backyard. Germany and Japan are in the front of building MSW plants applying advanced technologies like pyrolysis, gasification, and melting. In applying the advanced technologies into Korean MSW that has unique features in composition like high moisture content due to waste vegetables, which in turn result in low heating value of MSW, there are great demand in proving the technology with actual Korean MSW before introducing major scale plants of 150-600 ton/day size.

During the last few years, newly enforced waste separation policy in major cities in Korea yielded an increased heating value of MSW as high as 3,000 kcal/kg. Since small cities are still in lag behind of following wastes separation policy, gasification plants in Korea should have a room to treat the low heating value waste quality at least for the introductory plants. Following the ever-increasing heating value in MSW that can be recovered as an alternative energy source, it appears that installing advanced MSW technology plants are inevitable in Korea in the next few years. In this paper, current research status of gasification using MSW of high moisture content is discussed.

Gasification Facility

Figure 1 shows the 3-D view of 2.5 ton/day-class gasification facility that was being developed for the municipal solid wastes. Maximum pressure and temperature for the operation are 1 bar and 1550^{o}C, respectively.

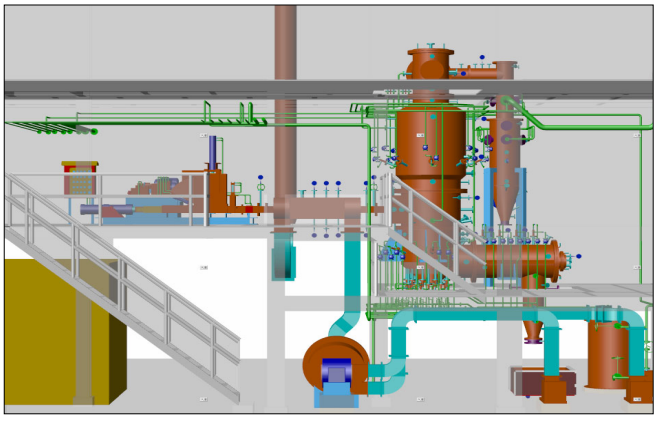

Figure 1. 3-D design view of the 2.5 ton/day MSW gasification system.

Plant consists of feed accepting apparatus, MSW compacting section, partial pyrolysis section, gasification/melting reactor part, slag homogenizing section, and quick syngas quenching section. Feed is introduced into the plant as 20 liters vinyl bags that are one way to discard MSW in Korean cities, after which MSW vinyl bags are compressed and pushed into the partial pyrolysis section in that few centimeters of surface parts are carbonized. During the compressing operation, about 10-30% of the moisture in MSW are extracted. Extracts are scavenged and pumped into the end section of the partial pyrolyzing section. Main gasification section works with LPG burners located at the bottom part of the reactor. Molten slag flows into the slag homogenizer that works to ensure the melting of all inorganic components and finally drops into the water-quenching chamber to produce slag. Gasifier temperature is maintained typically in 1,200-1,450^{o}C range while the slag homogenizer in 1,400-1,550^{o}C.

Figure 2 exhibits key components of the plant (Left: gasifier section, Right: slag homogenizer). Gasifier contains two layers of refractories with water cooling pipes and jackets around the main gasification area. Pure oxygen is provided after vaporizing and compressing from liquefied oxygen storage tanks.

High moisture-containing MSW from Y-City in Korea has an average high heating value of 2,176 kcal/kg (as-received basis) with 55.8% moisture and 6.9% ash. Components of MSW in weight were 46.8% kitchen food wastes, 27.1% paper, 5.9% textiles, 11.1% vinyls, 2.3% plastics, 6.9% glass and porcelain. Another tested MSW of medium moisture from K-City in Korea contains 50.4% moisture, and 5.5% ash with HHV of 2,686 kcal/kg. Components of K-City MSW consist of 29.6% kitchen food wastes, 33.7% paper, 9.7% textiles, 19.5% vinyls, 5.6% plastics, 1.9% foam materials.

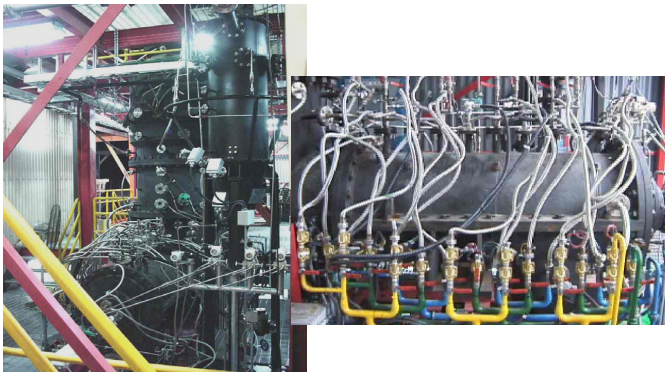

Figure 2. Gasification section (left) and the slag homogenizing section (right) of the pilot gasification facility.

Results and Discussion

Gasification results for the 55.8% moisture-containing MSW are illustrated in **Figure 3**. Syngas composition shows CO 25-30%, 20-35% hydrogen, and 22-40% CO_2.

Figure 4 demonstrates typical waste compositions and produced syngas quality from similar types of gasification plants of Italy, Japan, and Germany. Korean MSW contains highest moisture content followed by Japanese MSW near 50%. MSW from European countries exhibits less than 30% moisture, but much higher inorganic composition of reaching 25% compared to less than 8% in Korea and Japan. As expected, high moisture containing MSW yielded lower CO/H_2 and higher CO_2 contents, which result in lower heating value in syngas. Gasification of Korean MSW produces a syngas of typical 26-28% CO and hydrogen composition with a HHV 1,640 kcal/Nm^3. In this case, cold gas efficiency based upon HHV was 53%.

Figure 5 shows gasification results for the 50.4% moisture-

containing Korean MWS from the K-City where most of food wastes are separated and reusable materials are recycled. Most of moisture originated from soaked rain during storage in K-City.

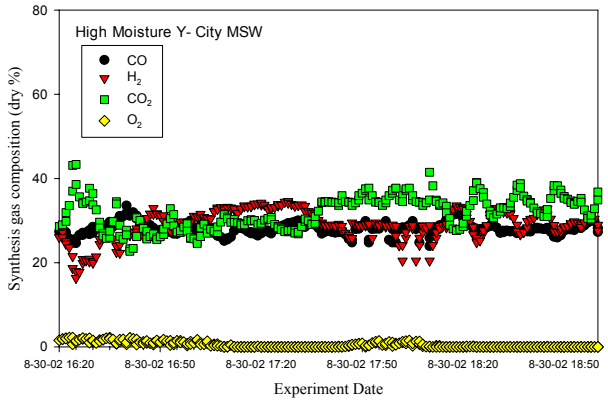

Figure 3. Syngas compositions from gasification of 55.8% moisture MSW from Y-City in Korea.

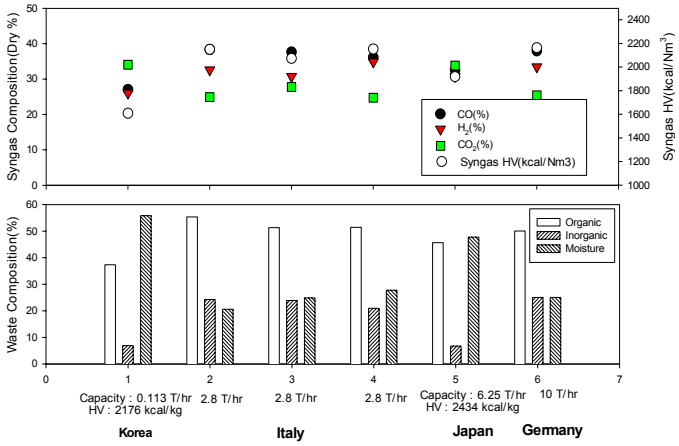

Figure 4. Comparison of syngas composition and heating value by similar types of gasification for MSW from several countries.

Moreover, the MSW in K-City contains more papers and less kitchen wastes than Y-City MSW and thus providing more organics feed for gasification at the same weight basis. Resulting syngas composition demonstrates a higher heating value in syngas as 2,125 kcal/Nm^3 with 38% CO and 32% hydrogen contents. Energy content in syngas from K-City MSW is almost as high as heating value from coal gasification. Therefore, with appropriate cleanup steps, the produced syngas can be utilized as a good alternative energy source.

Slags produced from high moisture Y-City MSW are shown in **Figure 6** in that few mm of round and sharp-edged shapes are illustrated.

To utilize slags for construction materials, they should fulfill the requirements in environmental leaching regulation. **Table 1** demonstrates that produced slags are environmentally safe in leaching tests. Please note that Korean leaching regulations are about ten times less stringent than in Japan and other developed countries. The results in Table 1 exhibit that even more stringent regulations can be met through the gasification/melting process.

Conclusions

Experience in coal gasification during the last ten years has been successfully applied for the MSW gasification/melting pilot plant. Gasification for Korean MSW of high moisture content yielded a syngas comprising of 22-40% CO and 25-38% hydrogen with a heating value equivalent of syngas from coal gasification. Since energy grade in MSW would increase above 3,000 kcal/kg in major cities, advanced gasification/melting process for MSW appears to be an inevitable choice in Korea based upon the option of producing clean energy without polluting environment as well as the people's wish for advanced technology that ensures less pollutants in their backyard.

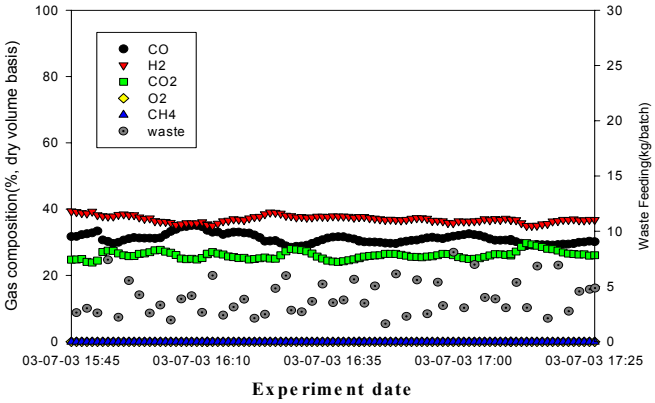

Figure 5. Syngas compositions from gasification of 50.4% moisture MSW from K-City in Korea.

Figure 6. Produced slags by gasification/melting from high moisture Y-City MSW (unit: cm).

Table 1. Leaching Test Results for Slags from Y-City MSW

Item	Unit	Result	Korean Environmental Standards
Total Hg	mg/l	n.d.	0.005
Cd	mg/l	n.d.	0.3
Pb	mg/l	0.03	3.0
Cr^{+6}	mg/l	n.d.	1.5
As	mg/l	n.d.	1.5
Se	mg/l	n.d.	-
Tota CN	mg/l	n.d.	1.0
Organo-phosphrous	mg/l	n.d.	1.0
Alkyl-mercury	mg/l	n.d.	-
PCB	mg/l	n.d.	-
Trichloroethylene	mg/l	n.d.	0.3
Tetrachloroethylene	mg/l	n.d.	0.1

Acknowledgement

This work was supported in part by KISTEP as one of National Research Lab. Projects in Korea under the contract 2000-N-NL-01-C-224.

Alkane CH Activation and Catalysis by O-Donor Ligated Ir Complexes

*Antek G. Wong-Foy, Gaurav Bhalla, Xiang Y. Liu, Roy A. Periana**

Department of Chemistry
Loker Hydrocarbon Institute
University of Southern California

Highly efficient and selective transition metal mediated methods for the functionalization of alkanes is still largely an unsolved problem that poses significant challenges to both homogeneous and heterogeneous chemists alike. One of the key reasons for this is that the C-H bonds of saturated alkanes are thermodynamically and kinetically difficult to break. However, significant advances have been made in our understanding of how C-H bonds are broken and formed by the use of well defined, homogeneous organometallic complexes.[1] These complexes generally contain either high oxidation state early transition metals or low oxidation state late transition metals. The ligands used in these systems range from C-donor, *e.g.* cyclopentadenty ligands, to mono and multi-dentate P- or N-donor ligands, to chelating NC or PC type ligands. O-donor ligands have been used to a much smaller extent with early transition metals and to our knowledge, for late transition metals, this is absent altogether.

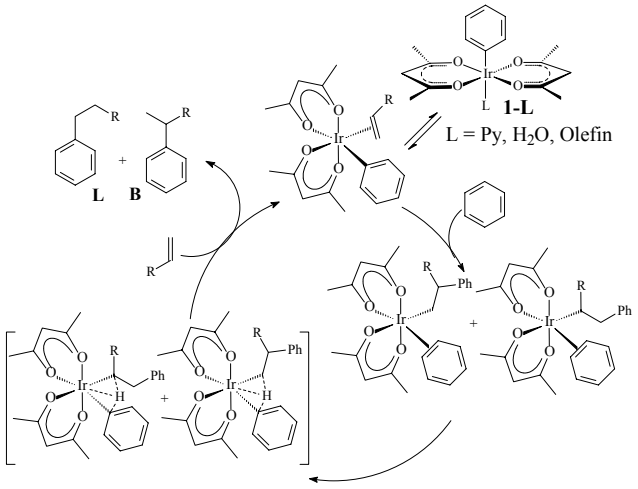

Figure 1. Proposed CH Activation Reaction Mechanism for Hydro-Arylation of Olefins by a bis-acac,O,O-Ir(III) Species.

Recently, we demonstrated that the O-donor Ir(III) complex, bis-acac-O,O-Ir(III)(Ph)(L), **1-L**, catalyzes the hydroarylation of unactivated olefins with unactivated arenes to generate alkyl benzenes with a preference for the anti-Markovnikov product.[2] Other studies have shown that related bis-acac Ir(III) complexes can also isomerize terminal alkenes to mixtures of internal ones.[2c]

Herein we report that bis-acac-O,O-Ir(III)(CH_3) complexes where the phenyl group in **1** is replaced with a methyl group react with alkanes by CH activation to generate the corresponding alkyl-Ir complexes under mild conditions. The synthesis of dinuclear Ir complex, [Ir(μ-acac-O,O,C^3)(acac-O,O)Me]$_2$, **2**, that was used in these studies was prepared as show in Scheme 1. As shown, there is a facile equilibrium between the mono-nuclear Ir complex, **2-solv**, and the dinculear complex, **2** on dissolution in CH_2Cl_2.

Scheme 1. Synthesis of (acac)$_2$Ir(CH_3) Complexes

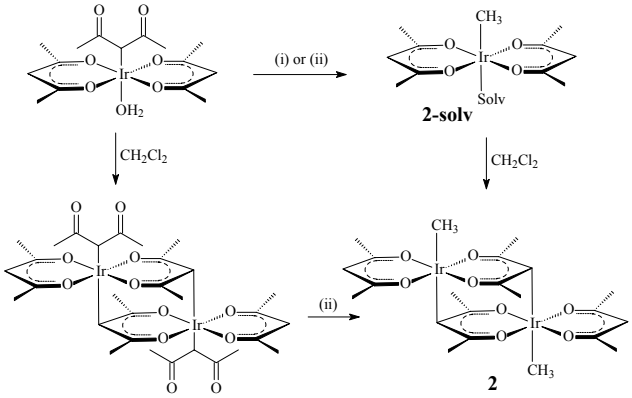

Conditions: (i) excess $HgMe_2$, MeOH/acetone, 60°C; (ii) 1.1 $ZnMe_2$, THF/toluene, 90°C

Heating a yellow suspension of **2** (**2-solv** can also be utilized but is less soluble) in mesitylene at 130 °C for 3h results in the formation of a clear yellow solution. ^{1}H and ^{13}C NMR analysis of the crude mixture in $CDCl_3$ shows clean formation of the dinculear complexe, bis-acac-O,O-Ir(III) mesityl, **3** (Eq 1). Only benzylic CH activation is observed; no activation is observed at the aromatic positions. If the reaction is run in a sealed NMR tube with mesitylene-d_{12}, only mono-deuterated methane is observed to form in the methane region. Heating **2** with cyclohexane as solvent yielded a crude solution of the corresponding dinuclear cyclohexyl complex, **4**. Treatment of this solution with excess pyridine afforded the mononuclear pyridine adduct, **4-py**, in quantitative yield based on **2** (Scheme 2).

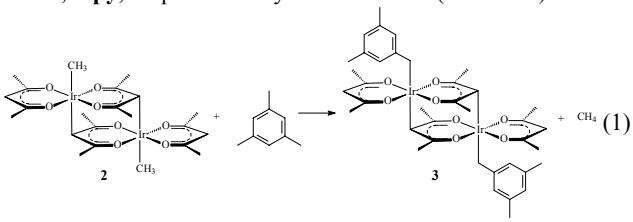

Some of the other substrates that react with **2** are shown in Table 1. As the facile equilibrium between mononuclear and dinuclear complexes in these systems can complicate analysis, the products of the reaction were dissolved in CD_3CN in order to ensure that only the mono-nuclear complexes were observed in solution.

These reactions unambiguously show that complexes based on the O-donor (acac)$_2$Ir(III) motif can activate alkane CH bonds. To our knowledge, this is first late-metal O-donor complex that shows this reactivity. Many systems show CH activation today. However, relatively fewer show catalysis with alkanes.[3,4,5,6,7,8,9] We are particularly interested in developing catalysis based on the CH activation reaction and it important to determine if the systems we are developing are sufficiently stable and selective to allow catalysis with alkanes. It is generally considered that O-donor ligands are kinetically labile, presumably due to the availability of a lone pair that is not present in P- or N-donor ligands. However, we find that complexes based on (acac)$_2$Ir(III) can be quite stable. For example, **1** can be refluxed in benzene or acetic acid for days without any signs

of decomposition. In acetic acid **1** is converted to the acetate analog. Another key key reason for examining the use of O-donor ligands with late metals for CH activation is that we anticipated that metal complexes based on O-donor ligands could be sterically and electronically different from those based on C, N or P-donor ligands. Specifically, given the higher electronegativity and "hardness" of O, it seemed likely that metal complexes would be less electron rich and if CH activation could be maintained could be more suited to oxidation catalysis. While this reduction in electron density might be expected to disfavor reaction such as oxidative addition, it could be expected that O-donor complexes could favor the oxidative functionalization reactions that are required in oxidation catalysis by facilitating conversion of M-R intermediates to functionalized RX products.

Scheme II. CH Activation of Cyclohexane

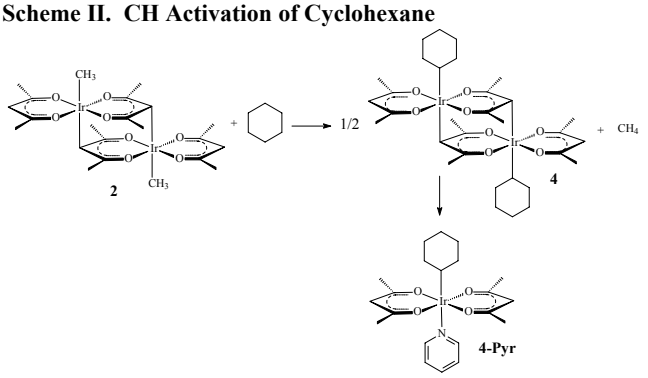

Table 1. C-H activation Products from Reaction of 2.

Entry	Substrate	Temp (°C)	Time	Product (major)
1		120	3 h	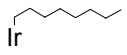
2		130	3 h	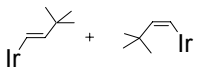
3		80	17 h	
4		100	1 h	

Indeed, consistent with the poorer electron-rich characteristics of O-donor complexes, we find that **1** will not bind olefin or CO except at high pressures. This is an important observations and most likely accounts for the efficient hydroarylation activity of **1**, more electron rich complexes would be expected to bind olefins more tightly and be inhibited.

To begin to explore alkane catalysis based on the CH activation reaction with O-donor ligated complexes, we examined the use of **2** to catalyze the H/D exchange between benzene-d_6 and various alkane substrates. Thus, an equimolar solution of benzene and cyclohexane was heated to160C with **1**. Analysis by GC/MS and NMR show that H/D exchange between C_6D_6 and RH cleanly occurs without any evidence of catalyst decomposition, except conversion of **2** in the phenyl analog, **1**. A likely catalytic cycle for this reaction is shown in Scheme II.

Preliminary experiments show that CH_4 exchanges with C_6D_6, Mesity-D_{12} or CD_3CO_2D solvents at ~160°C. These results show that the $(acac)_2Ir(III)$ motif is capable of catalysis with alkanes, including methane. The next step of research will be to explore the use of **2** to catalyze oxidation reactions, for example the conversion of methane to methyl products such as methanol or methyl acetate.

Scheme III. Proposed Mechanism for H/D Exchange

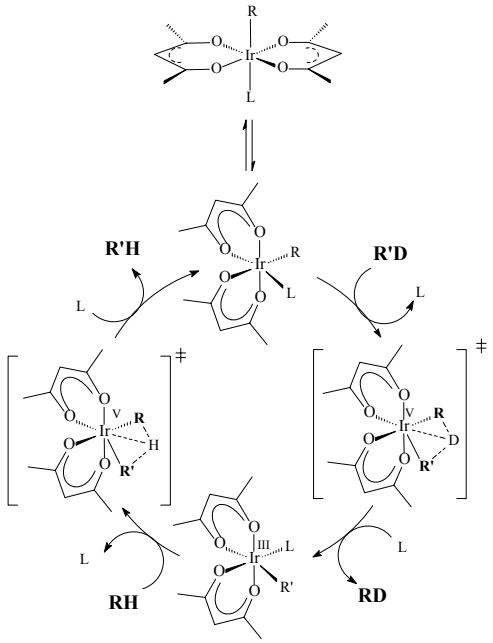

[1] (a) Jia, C.G.; Kitamura, T.; Fujiwara, Y. *Acc of Chem Res* **2001**, *34* 633. (b) "Isotope Effects in C-H Bond Activation Reactions by Transition Metals." Jones, W. D. *Accounts of Chemical Research* **2003**, *36*, 140-146

[2] (a) Periana, R. A.; Liu, X. Y.; Bhalla, G. *Chemical Communications* **2002**, 3000-3001. (b) Matsumoto, T.; Periana, R. A.; Taube, D. J.; Yoshida, H. *Journal of Molecular Catalysis a-Chemical* **2002**, *180*, 1-18. (c) Matsumoto, T.; Periana, R. A.; Taube, D. J.; Yoshida, H. *Journal of Catalysis* **2002**, *206*, 272-280. (d) Matsumoto, T.; Taube, D. J.; Periana, R. A.; Taube, H.; Yoshida, H. *Journal of the American Chemical Society* **2000**, *122*, 7414-7415

[3] (a) Chen. H. Y.; Schlecht, S.; Semple, T.C.; Hartwig, J. F. *Science*, **2000**, *287*, 1995.

[4] Periana, R. A.; Taube, D. J.; Gamble, S.; Taube, H.; Satoh, T.; Fuji, H. *Science*, **1998**, *280*, 560.

[5] (a) Kanzelberger, M; Singh, B; Czerw, M; Krogh-Jespersen, K; Goldman, A. S. *J. Am. Chem. Soc.* **2000**, *122,*11017

[6] (a) Lin, M; Shen, C; Garcia-Zayas, E. A.; Sen, A. *J. Am. Chem. Soc.* **2001**, *123*, 1000.

[7] Burk, M. J.; Crabtree, R. H. *J. Am. Chem. Soc.* **1987**, *109*, 8025

[8] (a) *Activation of Saturated Hydrocarbons by Transition Metals*, Shilov, A. E. Reidel: Dorrecht, 1984 and references therein

[9] Sakakura, T.; Sodeyama, T.; Sasaki, K.; Wada, K.; Tanaka, M. *J. Am. Chem. Soc.***1990**, *112*, 7221.

CATALYTIC PARTIAL OXIDATION OF METHANE TO METHANOL AND FORMALDEHYDE

Ayusman Sen and Minren Lin

Department of Chemistry
The Pennsylvania State University,
University Park, Pennsylvania 16802, U. S. A.
E-mail: asen@chem.psu.edu

Introduction

Methane is the least reactive and the most abundant member of the hydrocarbon family. Ethane comes second in both categories. Together, their known reserves approach that of petroleum [1]. Thus, the selective oxidative functionalization of these alkanes to more useful chemical products is of great practical interest [2-7]. The current technology for the conversion of alkanes to oxygenates involves *multi-step* processes. Clearly, the *direct* partial oxidation of the lower alkanes to oxygenates would be far more attractive from an economic standpoint. Of particular interest would be the formation of the *same* end product from different starting alkanes, thus obviating the need to separate the alkanes. For example, natural gas is principally methane with 5-10% ethane. A system that converts both to the same C_1 product, would not require the prior separation of the alkanes. We will discuss two catalytic systems for the direct partial oxidation of methane by dioxygen.

Results and Discussion

The first system involves the catalytic oxidation of methane to methanol by dioxygen in a mixture of water and trifluoroacetic acid [8,9]. A combination of metallic palladium and copper chloride acts as the catalyst and either carbon monoxide or dihydrogen is required as a coreductant. Studies indicate that the overall transformation encompasses three catalytic steps in tandem (Scheme 1). The first is the water gas shift reaction involving the oxidation of carbon monoxide to carbon dioxide with the simultaneous formation of dihydrogen. It is possible to bypass this step by replacing carbon monoxide with dihydrogen. The second catalytic step involves the combination of dihydrogen with dioxygen to yield hydrogen peroxide (or its equivalent). The final step involves the metal catalyzed oxidation of the alkane by hydrogen peroxide (or its equivalent). The activation parameters for the overall reaction, determined under the condition when the rate is first-order in both methane and carbon monoxide, are: $A = 2 \times 10^4\ s^{-1}$; $E_a = 15.3$ kcalmol^{-1}.

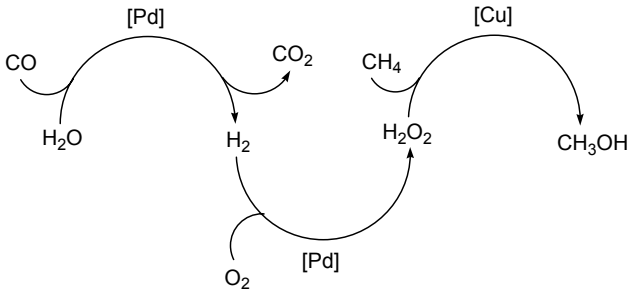

Scheme 1. Proposed catalytic three-step mechanism for methane oxidation.

The role of metallic palladium is two-fold. First, it generates hydrogen peroxide (or its equivalent). Second, it causes non-specific overoxidation of the substrate using the hydrogen peroxide thus generated. This latter reaction is suppressed when copper chloride is added; instead, copper chloride appears to catalyze the selective hydroxylation of the alkane by hydrogen peroxide. An interesting reactivity pattern exhibited by the bimetallic system is the preference for C-C cleavage over C-H cleavage for higher alkanes. Indeed, we are unaware of any other catalytic system that effects the oxidative cleavage of alkane C-C bonds under such mild conditions.

A curious aspect of the bimetallic system is that, apart from its ability to simultaneously activate both dioxygen and alkane, it requires a coreductant: carbon monoxide or dihydrogen. Thus, there is a striking resemblance with monooxygenases. In nature, while the dioxygenases utilize the dioxygen molecule more efficiently, it is the monooxygenases that carry out "difficult" oxidations, such as hydroxylation of alkanes. In the latter, one of the two oxygen atoms of dioxygen is reduced to water in a highly thermodynamically favorable reaction and the free-energy gained thereby is employed to generate a high-energy oxygen species, such as a metal-oxo complex, from the second oxygen atom.

The second catalytic procedure involves the gas-phase partial oxidation of methane and ethane to formaldehyde by dioxygen [10]. NO_x acts as catalyst and is ***not*** consumed in the reaction. The yield of oxygenates from methane is over 11%. The yield increases to over 16% when a trace of ethane (0.7%) is added to the gas mixture (Table 1). As might be expected, the yield of oxygenates from ethane is higher: over 24%. A catalytic cycle involving NO_2 as the C-H activating species is proposed (Scheme 2). The results that we have obtained thus far are noteworthy in several respects. First, the same C_1 product (formaldehyde) is obtained from both methane and ethane. Thus, the prior separation of the latter alkane is not required for this process. Second, in the context of partial oxidation of methane to oxygenates by dioxygen, there are few other system in the open literature that simultaneously exhibits such high conversion and selectivity.

Table 1. Methane Oxidation in Presence of Trace Ethane

Experiment No.	1	2
Temperature, °C.	600	600
Flow rate, mL/sec	2.26	5.65
Yield of CH_3OH[1], %	---	1.00
Yield of CH_2O[1], %	13.96	15.30
Yield of HCO_2H[1], %	2.27	0.64
Yield of CO[1], %	14.26	8.50
Total conversion[1], %	30.5	25.4
Selectivity[2], %	53.2	66.5
Yield[3], %	16.2	16.9
Total products, mmol.	3.08	6.21
[CH_4 (inlet) – CH_4 (outlet)] + CH_3CH_3 x 2, mmol	3.23	5.82

Gas mixture: CH_4, (16.6%); CH_3CH_3, (0.7%); NO, (11.0%); O_2, (5.5%); N_2, (16.6%); He, (49.7%).

1. Based on total carbon in CH_4 and CH_3CH_3.
2. Selectivity: $\Sigma(CH_2O + CH_3OH + HCO_2H)/\Sigma$(total products).
3. Yield: Total conversion x Selectivity.

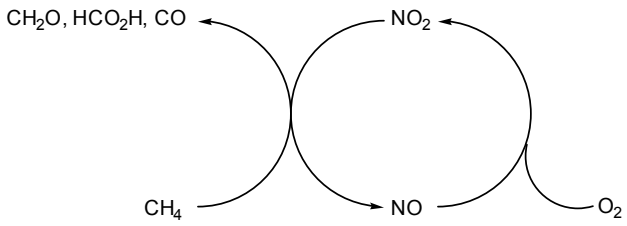

Scheme 2. Proposed mechanism for NO_x-catalyzed methane oxidation.

References

(1) M. G. Axelrod, A. M. Gaffney, R. Pitchai, and J. A. Sofranko, In *Natural Gas Conversion II*, H. E. Curry-Hyde and R. F. Howe (eds.), Elsevier, Amsterdam, **1994**, p. 93.
(2) A. Sen, *Top. Organomet. Chem*., **1999**, *3*, 81.
(3) G. A. Olah, A. Molnár, *Hydrocarbon Chemistry*, Wiley, New York, **1995**.
(4) R. H. Crabtree, *Chem. Rev*., **1995**, *95*, 987.
(5) T. J. Hall, J. S. J. Hargreaves, G. J. Huchings, R. W. Joyner, and S. H. Taylor, *Fuel Process. Technol*., **1995**, *42*, 151.
(6) J. L. G. Fierro, *Catalysis Lett*., **1993**, 2267.
(7) M. J. Brown and N. D. Parkyns, *Catalysis Today*, **1991**, 8305.
(8) M. Lin, T. Hogan, and A. Sen, *J. Am. Chem. Soc*., **1997**, *119*, 6048.
(9) A. Sen, *Acc. Chem. Res*., **1998**, *31*, 550.
(10) A. Sen and M. Lin, *Stud. Surf. Sci. Catal*., **2001**, *136*, 227.

Ni/ADM: A HIGH ACTIVTY AND SELECTIVTY TO C_{2+}OH CATALYST FOR CATALYTIC CONVERSION OF SYNTHESIS GAS TO HIGHER ALCOHOLS

Debao Li, Kan Zhang, Wenhuai Li, Yuhan Sun and Bing Zhong*

State Key Laboratory Coal Conversion, Institute of Coal Chemistry, Chinese Academy of Sciences, Taiyuan, P.R. China 030001

Introduction

Commonly, methyl tertiary butyl ether (MTBE) is the primary oxygenates used for reformulated gasoline (RFE), however, recent issues showed that the application of MTBE could cause some disadvantages such as contamination of drinking water.[1] For a long time, higher alcohols (C_1-C_5) are thought as an potential additive to gasoline to boost octane number and reduce emissions. The current interest is focused on the application of this process to produce high value gasoline octane enhancers in view of both utilization of resources and environmental protection.[2-3]

Catalysts used for the production of higher alcohols can be classified into the following categories: (i) modified high-pressure methanol–synthesis catalyst; (ii) modified low-pressure methanol–synthesis catalyst; (iii) alkali-doped molybdenum sulfide (ADM) catalysts.[3-5] Among the various catalysts, alkali-doped molybdenum sulfide (ADM) catalyst was one of the most promising systems due to its higher selectivity to alcohols, higher activity for water-gas shift. Previous studies revealed that the additions of Co could enhance the higher alcohols (C_2^+) selectivity due to its strong ability to promote carbon chain growth, however the studies of other F-T elements such as Ni and Fe were fairly rare.[6-7]

It was well known that nickel was excellent for methanation, but its other catalytic capabilities have been neglected for a long time. Recent investigates on Ni-SiO_2 catalyst revealed that strong ability of CO insertion reaction and excellent resistance to sulfur poisoning for feed gas.[8-9] In present paper, we reported ADM catalyst modified by Ni, which showed high performance for higher alcohol synthesis(HAS).

Experimental

Catalyst Preparation. Ni/ADM (Ni/K_2CO_3/MoS_2) catalyst was prepared by co-precipitation method. The solutions of nickel(II) acetate $Ni(CH_3COO)_2 \cdot 4H_2O$ and $(NH_4)_2MoS_4$ were dropped to the solution of acetic acid. After stirred and reacted thoroughly, the resulted solution was aged over night. After filtration, the precipitates was dried under vacuum followed by mixed with K_2CO_3 and thermal decomposed at 500℃ under N_2. ADM (K_2CO_3/MoS_2) catalyst was prepared by thermal decomposition of mixture of $(NH_4)_2MoS_4$ and K_2CO_3 at 500℃ under N_2. The catalysts were then pelleted and crushed to 40-60 mesh and stored in nitrogen for use.

Characterization Methods. X-ray powder diffraction (XRD) patterns of the tested catalysts were obtained on a Rigaku D/Max 2500 powder diffractometer using Cu Kα radiation as the X-ray source. SEM imagines were obtained using a LEO 438VP SEM (20KV).

CO Hydrogenation. The catalytic reactions were carried out using a stainless fixed-bed reactor with 2ml of catalyst. The products were analyzed by gas chromatographs The mass balance was based on carbon and the error of the balance of oxygen and hydrogen was within 5%. The activity of synthesis of alcohols was expressed as space-time-yield (STY), g ROH/Kg cat. h and the alcohols selectivity was based on carbon molar selectivity on a CO_2 free basis.

* Corresponding author. Fax: +86-351-4068405; E-mail:lwh@sxicc.ac.cn & leedebao@sohu.com

Results and Discussion

Table1 Performance of CO hydrogenation over Ni/ADM catalysts [a]

Catalyst	CO conv. (mol %)	STY (g/(ml • h))		Selectivity (mol%)	
		ROH	C_{2+}OH	Alc.	HC.
ADM	17.02	101	42	76.21	23.79
Ni-ADM					
Ni/Mo 1/4	20.31	119	77	73.44	26.56
1/3	34.11	160	130	69.89	30.11
1/2	28.02	138	113	70.78	29.22
1/1	18.68	124	60	76.90	23.10

[a]Reaction condition: T=573K, P=8.0MPa, GHSV=4000h^{-1} H_2/CO=1.0

Table 2 Alcohol distributions over Ni/ADM catalysts

Catalyst	Alcohols (C-atom %)				
	MeOH	EtOH	PrOH	BuOH	Others[b]
ADM	51.78	32.86	10.92	4.05	0.39
Ni-ADM					
Ni/Mo 1/4	29.20	47.23	17.15	6.01	0.41
1/3	13.27	33.84	27.11	23.26	2.53
1/2	13.28	35.36	28.97	19.92	2.46
1/1	36.66	47.42	11.63	3.68	0.61

[b] Includes C_{5+}OH, aldehydes, esters and ethers.

The results of CO hydrogenation were listed in **Table1** and **Table 2.** It can be seen that the promoter of Ni improved the CO conversion and STY of alcohols greatly. Moreover, the selectivity to higher alcohols (C_2-C_4) increased compared with that of traditional ADM catalyst. The remarkable effect of Ni promoter indicated that nickel had strong promotion for chain propagation. For the Ni/ADM catalyst, the optimum Ni/Mo ratio was about 1/3~1/2, at which the STY and CO conversion reached the maximum.

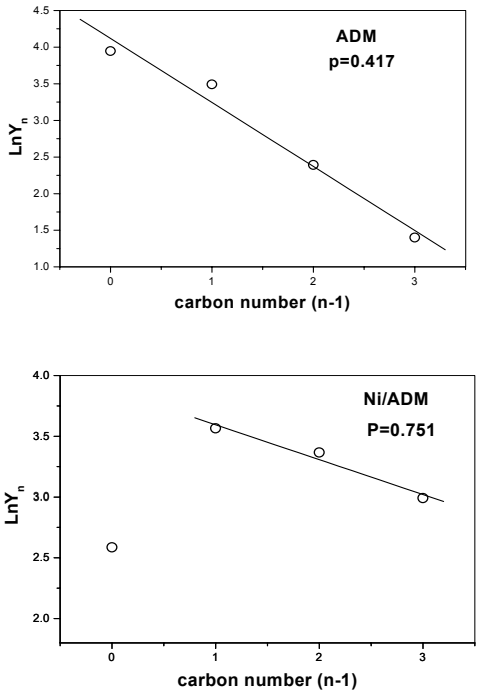

Fig. 1. A-S-F distributions of alcohol over ADM and Ni/ADM catalyst (Ni/Mo=1/2)

The individual distributions of alcohols over ADM and Ni/ADM catalysts were depicted in **Fig. 1**, as an A-S-F distribution:

$$Y_n = P^{n-1} (1 - P)$$

Where Y_n is the mole fraction of the alcohols with a carbon number of n and P is the chain-growth probability. Over ADM catalyst, the carbon number distribution of the alcohols obeyed the traditional A-S-F distribution. However, for Ni/ADM catalyst, methanol deviated the A-S-F distribution greatly. Moreover, the chain-growth probability P obtained through $C_2 - C_4$ alcohols was much higher than that of ADM catalyst. It seemed that the promoter Ni exerted strong promotion for carbon chain growth, especially for the step of C_1 to C_2.

For Ni/ADM catalyst, the morphology of Ni played an important role for the performances of HAS. The XRD patterns of Ni/ADM catalysts(**Fig.2**) showed clear crystal phases of Ni_2S_3. As the Ni/Mo ratio increased, the intensities of diffraction peaks also increased.

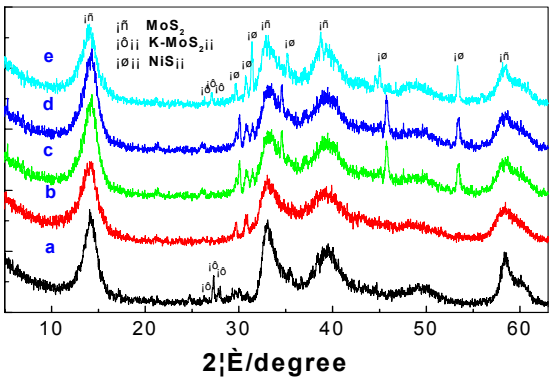

Fig. 2. The XRD patterns of catalysts a.K_2CO_3/MoS_2,b.Ni/Mo=1/4,c.Ni/Mo=1/3,d.Ni/Mo=1/2,e. Ni/Mo=1

Scanning electron microscope (SEM) micrographs of catalysts were shown in **Fig.3**. The morphological differences among these samples were evident. The Ni/ADM samples showed an irregular shape and significant porosity, and the surface of the MoS_2 appeared covered with a great deal of small-conglutinated particles. In these micrographs a progressive surface decoration is observed as a function of the concentration of promoter nickel. With high concentration of nickel, the conglutination became weaker and larger particles were formed on the surface of MoS_2. Studies of metal catalysts with various dispersion revealed that the structure of some active element (such as Ni, Pd) played an important role for CO hydrogenation: catalysts with small crystallites had advantage to produce alcohols while larger crystallites to methane.[10] For Ni/ADM catalyst, the promoter of Ni showed similar structure effect. At the optimum Ni/Mo ratio, namely 1/3~1/2, there must have strong synergy effect between Ni and Mo which was favorite for Higher alcohols synthesis.

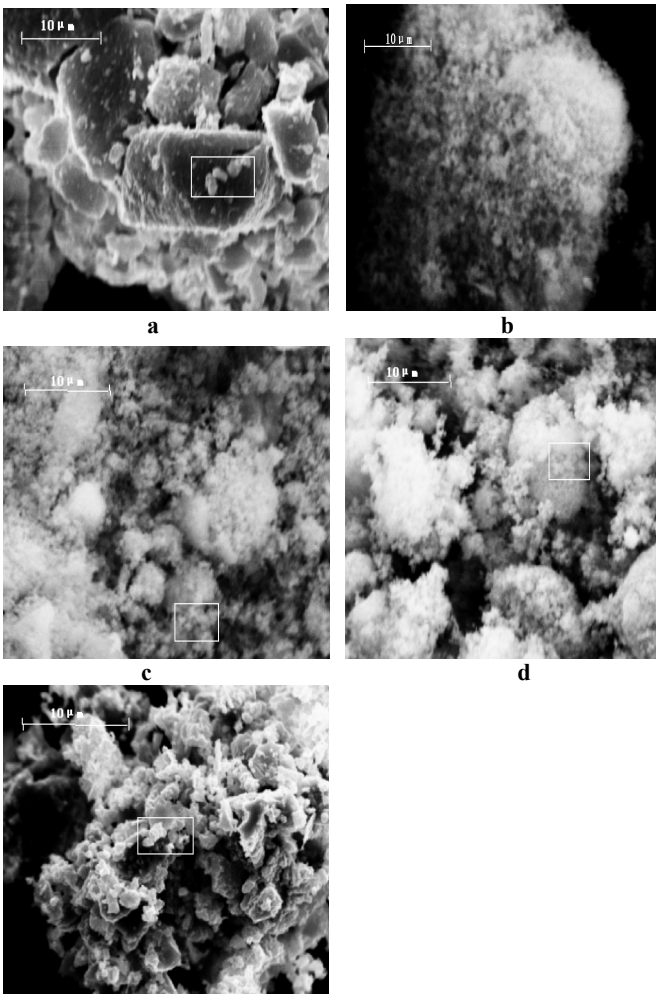

Fig. 3. SEM micrographs of catalysts a ADM, Ni/ADM: b Ni/Mo=1/4, c Ni/Mo=1/3, d Ni/Mo=1/2, e Ni/Mo=1.

Acknowledgment

This work was supported by State Key Fundation Project for Development and Research of China (G1999022404).

References

1. A. J. Lucero, R. E. Klepper, W. M. O'Keefe,and V. K. Sethi, *Fuel Chemistry Division Preprints*, **2001**, 46(2), 413.
2. A. Beretta, Q. Sun, R. G. Herman, K. Klier, *Ind. Eng. Chem. Res.*, **1997**, 36, 3085.
3. R. G. Herman, *Catal. Today*, **2000**, 55, 233.
4. Xiaoding Xu, B. M. Doesburg, J. F. Sckolen, *Catal. Today*, **1987**, 2, 125.
5. E. Tronconi, N. Ferlazzo, P. Forzatti, I. Pasquon, *Ind. Eng. Chem. Res.*, **1987**, 26, 2122.
6. G-Z Bian, Li Fan, Y-L Fu K.Fujimoto, *Ind. Eng. Chem. Res.*, **1998**,37, 1736.
7. J. Iranmahboob, D. O. Hill, H. Toghiani, *Appl. Catal.*, **2002**, 231, 99.
8. S. S. C. Chuang, S. I. Pien, *Catal, Lett.*, **1989**, 3, 323.
9. S. A. Hedrick, S. S. C. Chuang, A. Pant, A. G. Dastidar, *Catal. Today*, **2000**, 55 247.
10. Zhongrui Li, Yilu Fu et al., *Catal. Lett.*, **1989**, 65,43.

ATOM-ECONOMICAL REDUCTION OF CARBON MONOXIDE TO METHANOL: IS THE CATALYST SINGLE-SITE OR MULTI-SITE?

Devinder Mahajan

Energy Sciences and Technology Department, Brookhaven National Laboratory, Upton, New York 11973-5000 USA
and
Department of Materials Science & Engineering, Stony Brook University, Stony Brook, NY 11794 USA

Introduction

Hydrocarbons and methanol are considered the preferred products of catalytic reduction of carbon monoxide derived from clean natural gas. Pathways to these liquid energy carriers are collectively known as gas-to-liquid (GTL) technology. Methanol has particularly attractive attributes as a fuel, an additive in conventional fuels, and a versatile building block in the synthesis of chemicals[1,2]. Methanol is presently manufactured from synthesis gas using supported Cu/ZnO heterogeneous catalyst at 250 - 300°C and between 5 - 10 MPa operating pressure[3]. Methanol synthesis is highly exothermic (ΔH_{298} = - 128.6 kJ.mol^{-1}) that poses thermodynamic limitations and together with poor process heat control allows < 20% per pass gas conversion during the reaction[4]. A homogeneous catalyst that affords high reaction rates at low temperatures would offer superior reaction heat management, higher yields per pass, and may afford attractive economics. Efforts have been made to synthesize oxygenates from synthesis gas using homogeneous systems. The use of transition metal carbonyls specially those of Ru (5) and Rh (6) for synthesis of methanol, ethanol, other higher alcohols and ethylene glycol is well documented for synthesis gas conversion but with these systems the overall reaction parameters are not economically attractive.

We are investigating the use of single-site catalyst precursors to maximize CO conversion into methanol that may allow methanol production cheaply enough to consider methanol as a feedstock. We recently reported[5] the use of nickel complexes as versatile catalysts to homogeneously catalyze CO reduction to methanol under mild conditions of temperature (T: 80° - 130°C) and pressure (2000 - 5000 kPa). Under these conditions, CO conversion and methanol selectivity approach > 90% and > 95%, respectively. This paper describes the potential of the low temperature facile interconversion of various mono- and multi- nuclear Ni species under the reaction conditions and the role of such these species in defining the actual catalyst species in homogeneously catalyzed methanol synthesis.

Experimental

Materials. Potassium methoxide (>95% pure) and nickel complexes were purchased from Alfa and used as received. Methanol and p-dioxane were obtained from Aldrich and purified before use. Pure CO, H_2, and syngas mixture (66% H_2, 34% CO) were purchased from Scott Specialty Gases. Syngas mixtures were calibrated to reconfirm stoichiometries certified by the vendor.

Batch Studies. A commercially available stainless steel MagneDrive II Packless Zipperclave 0.5L reactor, manufactured by Autoclave Engineers, Inc. (AE) and modified for use in this study, is shown in Figure 1. The reactor was equipped with a Dispersamax six-blade impeller to ensure efficient gas/liquid mixing. Ports were provided for loading reactant gases, sampling vapor and liquid phases. The batch CSTR unit ratings were as follows: stirrer = O - 2000 rpm, T = 25 - 450 C, P = 100 - 14000 kPa.

Run Procedure. A specified amount of $KOCH_3$ and the Ni complex was weighed inside a Labconco glove box under N_2, mixed with the desired solvent mixture in the reactor and the reactor was quickly sealed after purging several times with N_2. The reactor was immediately pressurized with ~ 750 psig syngas, stirred and heated to the desired temperature. The temperature and pressure in the reactor were recorded until the pressure decreased to about 100 to 150 psig, at which time the reaction was quenched by replacing the heater with an ice-water bath. Once the reactor reached room temperature, the final pressure and temperature were recorded. Gas and liquid samples were taken for analysis and the final liquid volume was measured. Vapor and liquid phases were analyzed to obtain a mass balance for each run.

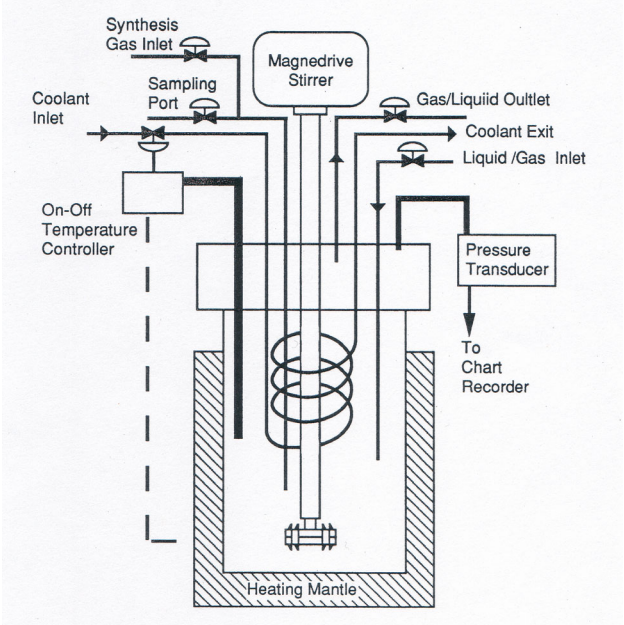

Figure 1. A modified AE Zipperclave batch unit for methanol synthesis.

Results and Discussion

Catalytic Activity Data. The activity data for homogeneous CO reduction to methanol catalyzed by various Ni complexes and activated by potassium methoxide base is shown in Table 1. The data show that the reaction is facile and CO, chloride and acetylacetonate (acac) ligated Ni complexes are versatile catalysts under mild temperature (120°C) and pressure (4700 kPa) conditions. In all 6 runs, the CO conversion per pass exceeded 90%. In Run 2, the triglyme co-solvent was replaced with tetrahydrofuran (THF) that resulted in an increase in reaction rate. The absence of potassium methoxide in Run 4 rendered the Ni catalyst totally inactive confirming the crucial role of the base in these reactions. The phosphine ligands are unsuitable for the reaction (Runs 6 and 7) and result in a totally inactive system. The selectivity to methanol was up to 99% and the by-products consisted of methyl formate (MF) and dimethyl ether (DME). Methane was observed only as a trace (< 0.001%). The rate data (mmol gas consumed/minute) in Table 1 were normalized to obtain batch rate data to yield a maximum rate of 20 g-mol MeOH.L Cat^{-1}.h^{-1} at 120°C and 4700 kPa. The rates are higher as compared to the commercial system (6 MeOH.L Cat^{-1}.h^{-1}/Lcat.h) that operates at a higher temperature of 250°C and a comparable pressure of 5000 kPa. It is to be emphasized that the solution remains homogeneous throughout the run.

Table 1. Catalytic activity of various Ni complexes for methanol synthesis.

Run	Catalyst	Batch Rate, mmol/min	Product Selectivity,% MeOH	MF	DME
1	$Ni(CO)_4$	54	>99	<1	Trace
2	$Ni(CO)_4$	66	95.7	4	0.3
3	$NiCl_2$	98	99.2	0.2	0.6
4	$NiCl_2$	-	-	-	-
5	$Ni(acac)_2$	72	98	1.4	0.6
6	$Ni(PPh_3)(CO)_3$	-	No activity		
7	$Ni(PPh_3)_2(CO)_2$	-	No activity		

0.5 L AE Zipperclave batch reactor, Solvent: 90% Triglyme/10% MeOH = 120 mL, [Ni] = 0.05 M, KOMe = 1.0 M, Syngas: 66% H_2/34% CO, T = 120°C, P_I = 4700 kPa.

Mechanistic Considerations. The low temperature concept of methanol synthesis has been the subject of research by several groups[6]. The mechanistic study on a catalyst system that is closely related to the catalyst system presented here has been reported in literature[7]. A mechanistic cycle, shown in Figure 2, has been

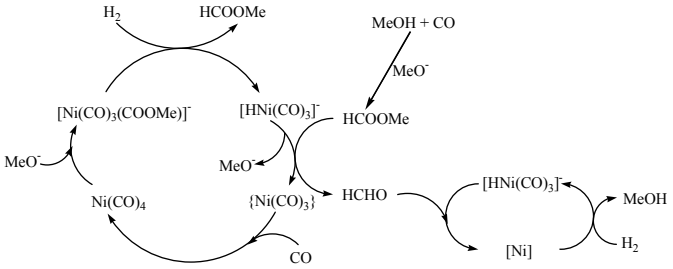

Figure 2. Proposed mechanistic pathway to methanol synthesis from balanced synthesis gas (H_2/CO = 2) catalyzed by homogeneous nickel complexes activated by sodium methoxide (from reference 6).

proposed based on the high-pressure infrared data[6]. This study emphasized FTIR as a tool to discern the mechanism of the $Ni(CO)_4$/NaOMe system. The proposed steps involve a nucleophilic attack of the methoxide anion ($^-$OMe) on a coordinated CO of $Ni(CO)_4$ followed by production of methyl formate (MF) and anionic hydridotricarbonylnickel species ($[HNi(CO)_3]^-$). Methyl formate is hydrogenated by the anionic Ni species to two moles of methanol via the intermediacy of formaldehyde and addition of CO regenerates $Ni(CO)_4$ to complete the catalytic cycle. The function of Ni is then primarily to hydrogenate methyl formate.

Though the proposed mechanistic cycle in Figure 2 is plausible, whether same intermediate species are involved during methanol synthesis catalyzed by the presented $Ni(CO)_4$/KOMe system needs to be confirmed. More importantly, it is suggested in Figure 2 that the mononuclear Ni species likely catalyzes CO reduction to methanol. We are presently investigating the role of

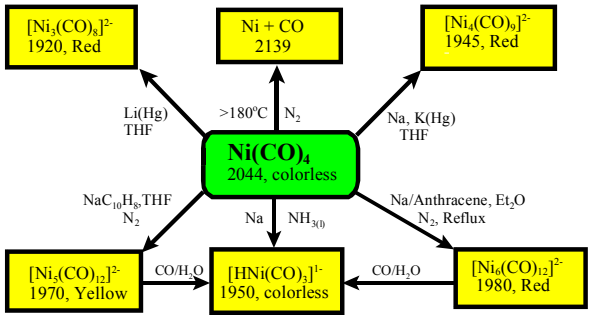

Figure 3. Possible interconversion of nickel carbonyl cluster anions (data from reference 8).

various Ni species that could potentially catalyze the methanol synthesis reaction at low temperatures. Related to this, a lot of work has been reported on the facile interconversion of Ni species[8,9] that is shown in Figure 3. The number in each box below the species represents the value of signature IR band and the cation associated with the anionic Ni species are selected from K^+, Na^+, Li^+, PPN^+, Me_4N^+. The Ni species in Figure 3 are mostly soluble in H_2O and are the result of the redox condensation reaction that is accompanied by a change in the oxidation state of Ni from Ni^0 to Ni^{2+}. A facile equilibrium may set up in the reactions shown in figure 3 as follows:

$$Ni(CO)_4 \rightleftharpoons [Ni_x(CO)_y]^{2-}$$
$$[Ni_x(CO)_y]^{2-} + H^+(H_2O) \rightleftharpoons [HNi_x(CO)_y]^{1-}$$

The foregoing information shows that the identification of the active catalytic species remains a challenge. Work is presently under to truly establish a pathway that makes the Ni based catalyst system so active for homogeneous methanol synthesis.

Acknowledgment. This work was supported by the U.S. Department of Energy under Contract No. DE-AC02-98CH10886.38. A start-up grant (to DM) from the State University of New York at Stony Brook is gratefully acknowledged.

References

1. Keim, W., Editor. Catalysis in C_1 Chemistry, D. Reidel Publishing Company, Dordrecht, 1983. Keim, W. J. Organomet. Chem. **372** (1989), 15.
2. I. Wender, I. Catal. Rev. Sci. Eng. **26** (1985) 3.
3. Lee, S. Methanol Synthesis Technology, CRC Press, Inc., Boca Raton, Florida, 1990.
4. Strelzoff, S. Chem. Eng. Prog. Symp. Ser. **66** (1970) 98.
5. Mahajan, D., Krisdhasima, V., Sproull, R.D. Can. J. Chem. **79** (5/6) (2001) 848.
6. Marchionna, M., Lami, M., Raspolli Galletti, A.M. CHEMTECH, April 1997, 27 and references therein.
7. Marchionna, M., Basini, L., Arogno, A., Lami, M., Ancilloti, F. J. Mol. Catal. **75** (1992) 147.
8. Longoni, G., Chini, P., Cavalieri, A. Inorg. Chem. **15(12)** (1976) 3025.
9. Beattie, J.K., Hambley, T.W., Masters, A.F., Meyers, J.T. Inorg. Chim. Acta. **213** (1993) 49.

IN SITU ATR/FTIR OBSERVATION OF TRANSFORMATION OF THE NICKEL SPECIES IN LOW TEMPERATURE METHANOL SYNTHESIS

Seiichi Ohyama

Centra Research Institute of Electric Power Industry
2-11-1 Iwado-kita Komae-shi,
Tokyo 201 8511, Japan

Introduction

Low-temperature methanol synthesis rapidly proceeds in liquid media at temperatures of around 373 K over appropriate catalytic systems. Brookhaven National Laboratory claimed two active catalytic systems: the catalyst prepared from nickel acetate, *tert*-amyl alcohol and NaH (denoted as $Ni(OCOCH_3)_2$/*tert*-amyl alcohol/NaH)[1] and a mixture of $Ni(CO)_4$ and CH_3OK (denoted as $Ni(CO)_4/CH_3OK$).[2] Over these catalysts, methanol (MeOH) are considered to be formed through the carbonylation of MeOH to methyl formate (MF), followed by the subsequent hydrogenation of MF to MeOH:

$$CH_3OH + CO \rightarrow HCOOCH_3,$$
$$HCOOCH_3 + 2H_2 \rightarrow 2CH_3OH.$$

The author provided an illustration to indicate the above reaction pathway in $Ni(CO)_4/CH_3OK$ and showed that hydridocarbonylnickel anion ($[HNi(CO)_3]^-$ or $[HNi_2(CO)_6]^-$) derived from $Ni(CO)_4$ was responsible for the latter step of the reaction.[3] With regard to $Ni(OCOCH_3)_2$/*tert*-amyl alcohol/NaH, the catalytically active species still remains unknown. This study aims to identify the catalytically active form of $Ni(OCOCH_3)_2$ and also to clarify the relation between the two nickel precursors, *i.e.*, $Ni(OCOCH_3)_2$ and $Ni(CO)_4$ based on in situ ATR/FTIR observation.

Experimental

In place of $Ni(OCOCH_3)_2$/*tert*-amyl alcohol/NaH, $Ni(OCOCH_3)_2/CH_3OK$, *i.e.*, a mixture of $Ni(OCOCH_3)_2$ (5 mmol) and CH_3OK (20 mmol) was employed for the reaction. Also, $Ni(CO)_4/CH_3OK$ was employed for reference, which was composed of 5 mmol of $Ni(CO)_4$ and 20 mmol of CH_3OK. CH_3OK was employed in the form of 30% CH_3OK solution in methanol, 5 cm^3 of which contained 20 mmol of CH_3OK and 105 mmol of methanol. The catalysts were dispersed in triethylene glycol dimethyl ether (triglyme), forming 50 cm^3 of the solution.

The reaction was carried out in batch operation in an autoclave (175 cm^3), which housed an attenuated total reflectance (ATR) accessory. Syngas with a ratio of $H_2/CO = 2$ was pressurized into the reactor up to 3.0 MPa at 333 K. The gas and liquid components after the run were analyzed by GC. In situ FTIR spectra were collected on Nicolet Magna 560 FTIR spectrometer equipped with an MCT detector and the ATR probe (TerminatIR from ASI Applied Systems), the crystal of which was immersed in the liquid in the autoclave. The experimental details are described elsewhere.[3]

Results and Discussion

Figure 1 (A) illustrates the time courses of temperature and pressures during the run over $Ni(OCOCH_3)_2/CH_3OK$ and its corresponding FTIR spectra are shown in Fig. 1 (B). The reaction was conducted at 333 K, a lower temperature than usual, which retarded the reaction rate to observe transformations in the liquid phase. The pressure decreased immediately after charging syngas at 333 K. The reactor was held at 333 K for 21 h and the pressure fell to 0.45 MPa. Upon charging the syngas, the absorption at 1730 cm^{-1} assigned to the ν(CO) of MF was immediately generated (Fig. 1 (b)) and enlarged (Fig. 1 (c)-(d)), which was observed during the reaction (Fig. 1 (c)-(f)) except for the end of the run (Fig. 1 (g)).

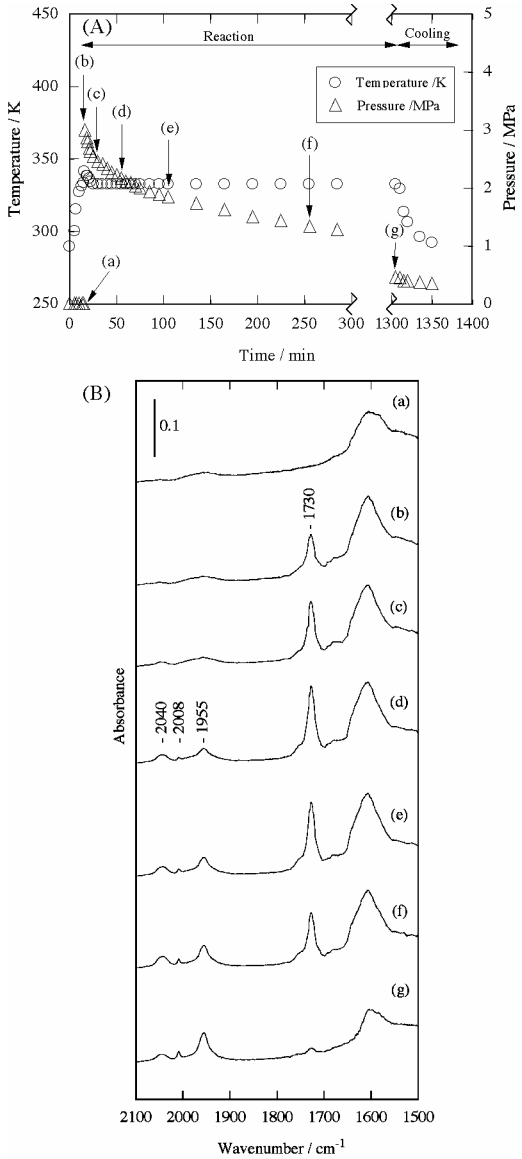

Figure 1. Time courses of temperature and pressure (A) and FTIR spectra (B) of $Ni(OCOCH_3)_2/CH_3OK$. The spectra (a)-(g) were collected at the corresponding points in figure (A).

For the first 10 min after charging the syngas, no absorptions were observed in the region of 2100-1800 cm^{-1} as shown in Fig. 1 (b)-(c). However, after 10 min, three small absorptions were recognized simultaneously at 2040, 2008 and 1955 cm^{-1} (Fig. 1 (d)). The bands showed a slight and monotonous increase (Fig. 1 (e)-(g)). The band at 2040 cm^{-1} was assigned to $Ni(CO)_4$, whereas the other bands at 2008 and 1955 cm^{-1} would be assigned to hydridocarbonylnickel anions ($[HNi(CO)_3]^-$ or/and $[HNi_2(CO)_6]^-$).[4] These two hydridocarbonylnickel anions have similar IR frequencies in the region and are labile and interchangeable with each other.[4] Thus, it is uncertain whether the bands represent $[HNi(CO)_3]^-$, $[HNi_2(CO)_6]^-$ or a mixture of both. To simplify the discussion, we just refer them to the hydridocarbonylnickel anion. Consequently, in situ observation of the solution revealed that the homogeneous nickel

species, i.e., $Ni(CO)_4$ and the hydridocarbonylnickel anion were simultaneously generated from $Ni(OCOCH_3)_2$ under the reaction condition.

Figure 2 illustrates time courses of MeOH and MF concentrations during the run, which were determined from the absorptions at 3500 and 1730 cm^{-1}, respectively. MF showed a rapid and immediate increase after the syngas charge. After the MF concentration became high and saturated (10 min after the syngas charge), the MeOH concentration began to increase sluggishly and showed a monotonous increase through the run. Meanwhile, MF gradually diminished and quite low at the end of the run. These products profiles showed a pattern typical of a consecutive reaction involving MF as an intermediate for the formation of MeOH, which indicates that in $Ni(OCOCH_3)_2/CH_3OK$, MeOH is produced on the same pathway as in $Ni(CO)_4/CH_3OK$.[4] Furthermore, formation of the nickel anion corresponded to the increase of the MeOH concentration. This supports the fact that the nickel anion catalyzes the hydrogenation of MF to MeOH, because we have already confirmed that $Ni(CO)_4$ itself does not catalyze the hydrogenation of MF.[4] Thus, the low-temperature methanol synthesis proceeds as homogeneous liquid phase reaction even in $Ni(OCOCH_3)_2/CH_3OK$ as well as in $Ni(CO)_4/CH_3OK$.

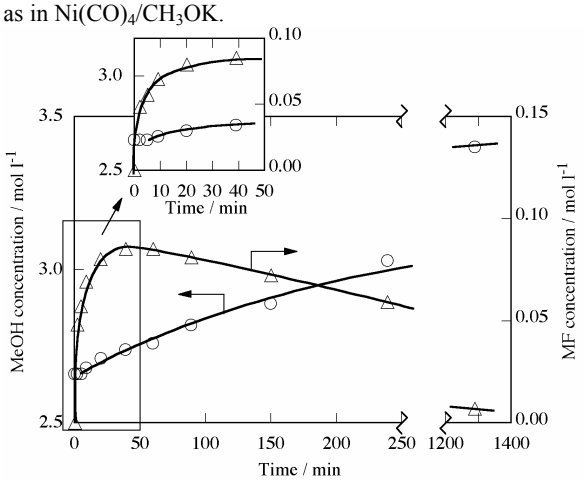

Figure 2. Variations in the concentrations of MeOH and MF during the run. The charging point of syngas was set at 0 min in the time scale.

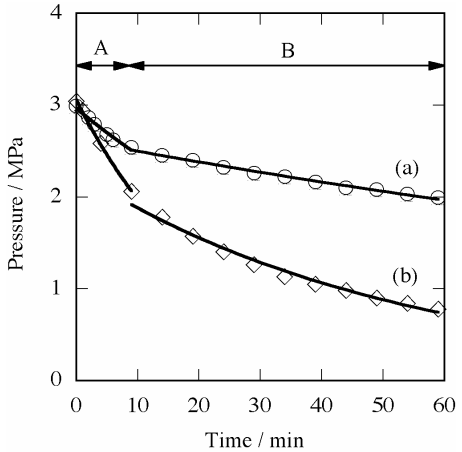

Figure 3. Time courses of pressure during the run. Catalyst: (a) $Ni(OCOCH_3)_2/CH_3OK$; (b) $Ni(CO)_4/CH_3OK$.

Figure 3 compares pressure profiles over $Ni(OCOCH_3)_2/CH_3OK$ and $Ni(CO)_4/CH_3OK$ with the runs performed at 333 K and 3 MPa. $Ni(CO)_4/CH_3OK$ exhibited a larger pressure drop than $Ni(OCOCH_3)_2/CH_3OK$. Assuming that the reaction rate obeys the first-order kinetics, two different fitting curves were applied to each pressure drop profile. The profiles were classified into two regions (denoted as A and B in Fig. 3). Good first-order rate plots were obtained over the both regions for the both catalysts. Based on in situ FTIR observations, it is apparent that the carbonylation of MeOH to MF exclusively proceeded over region A (the first 10 minutes after the syngas charge), whereas the hydrogenation of MF to MeOH limits the overall reaction rate in region B. The rate constants over region A are similar; 3.1×10^{-4} and 7.3×10^{-4} sec^{-1} for $Ni(OCOCH_3)_2/CH_3OK$ and $Ni(CO)_4/CH_3OK$, respectively. This is reasonable because the both catalytic systems employed the same amount of CH_3OK as a catalyst component for the carbonylation of MeOH. In contrast, in region B, the rate constant for $Ni(CO)_4/CH_3OK$ was 4 times higher than that for $Ni(OCOCH_3)_2/CH_3OK$ ($3.\square\times10^{-4}$ and 8.0×10^{-5} sec^{-1}, respectively). The difference in the rate constant would be attributed to the amount of the catalytically active nickel species, i.e., the hydridocarbonylnickel anion. As shown in **Figure 4**, the absorptions assigned to the nickel anion (2008 and 1955 cm^{-1}) is 5 times larger in $Ni(CO)_4/CH_3OK$ than in $Ni(OCOCH_3)_2/CH_3OK$, whereas the absorption assigned to $Ni(CO)_4$ (2040 cm^{-1}) was similar in intensity for both the catalytic systems. Thus, the ratio of the rate constants over the region B roughly agrees with the ratio of the absorptions assigned to the nickel anion, which indicates that the nickel anion is responsible for the hydrogenation of MF.

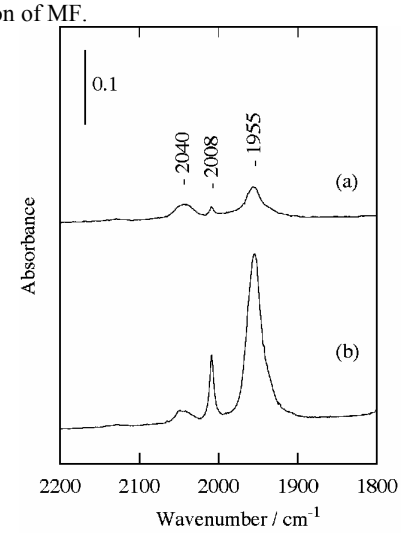

Figure 4. In situ FTIR spectra of (a) $Ni(OCOCH_3)_2/CH_3OK$ and (b) $Ni(CO)_4/CH_3OK$ at 333 K.

In summary, we concluded that under the reaction condition, part of $Ni(OCOCH_3)_2$ was converted into tetracarbonylnickel ($Ni(CO)_4$) and the hydridocarbonylnickel anion, the latter of which was responsible for the MF hydrogenation step in the low-temperature methanol synthesis. The difference in the catalytic activity between $Ni(OCOCH_3)_2/CH_3OK$ and $Ni(CO)_4/CH_3OK$ was explained by the concentrations of the hydridocarbonylnickel anion.

References

(1) R.S. Sapienza, W.A. Slegeir, T.E. O'Hare and D. Mahajan, *US Patent* 4,614,749, **1986**; 4,619,946, **1986**; 4,623,634, **1986**.

(2) D. Mahajan, R.S. Sapienza, W.A. Slegeir and T.E. O'Hare, *US Patent* 4,992,480, **1991**.

(3) S. Ohyama, *Appl. Catal. A*, 2001, **220**, 235.

(4) M. Marchionna, L. Basini, A. Aragno, M. Lami and F. Ancillotti, *J. Mol. Catal.*, **1992**, 75, 147.

MAPPING METAL CATALYSTS USING SYNCHROTRON COMPUTED MICROTOMOGRAPHY (CMT) and MICRO X-RAY FLUORESCENCE (μXRF)

K. W. Jones[1], H. Feng[2], and D. Mahajan[3]

[1]Laboratory for Earth and Environmental Sciences, Environmental Sciences Department, Brookhaven National Laboratory, Upton, New York 11973-5000 USA
[2]Department of Earth and Environmental Studies, Montclair State University, Montclair, NJ 07043 USA
[3]Energy Sciences & Technology Department, Brookhaven National Laboratory, Upton, NY 11973-5000, USA and Department of Materials Science & Engineering, Stony Brook University, Stony Brook, NY 11794 USA

Introduction

Gas-to-liquids (GTL) remains a viable pathway to synthesize clean fuels that are derived from natural gas, a clean energy source. There have been technological advances in natural gas conversion technology to a point that, for example, has led several companies to make investment in the Fischer-Tropsch route to synthesize clean hydrocarbon fuels. But a highly efficient gas conversion process that will allow companies to capitalize on remote natural gas in Alaska and other parts of the world still remains elusive. A major breakthrough is sought in developing a new catalyst that combines the environmentally sound process design.

Heterogeneous catalyst assemblies are typically utilized in the GTL conversion reactions. An in-depth characterization of catalytic materials is needed to design the next-generation catalyst. Computed Microtomography (CMT) and micro X-ray fluorescence (μXRF), techniques available at the National Synchrotron Light Source (NSLS), Brookhaven National Laboratory (BNL), are complementary techniques that allow mapping of catalyst constituents.

CMT is a non-invasive method that produces visualization of the interior of specimens based either on their linear x-ray attenuation coefficients or on the emission of characteristic x-rays from specific elements. The XRF technique uses a micrometer-size beam to make point-by-point measurements on elemental distributions in a thin section of a sample. This is a destructive method, but is valuable since the minimum-detection limits are superior to other methods.

Catalysts proposed for GTL work include Fe, Co, and Mn micron-sized or nano-sized particles supported on subtrates of γ-alumina, silica, and potentially polymeric compounds. A schematic representation of the material is shown in Figure 1. While the individual catalyst particles are less than .001 mm in size, the presence of larger-sized clusters and the distribution in the support matrix can be effectively measured using CMT and XRF. Here, we draw attention to previous work on catalysts using these techniques through the presentation of results obtained on several catalytic materials. Improvements to the CMT apparatus now make possible high-spatial resolution measurements that show the microstructure of supported catalysts on mm-size scales. Methods of data analysis have also developed rapidly so that it is now possible to determine porosity, pore structures and connectivities for these 3-dimensional data sets. It is also feasible to determine property changes following use of the catalysts in a GTL reactor. This capability will have direct applications in the development and tests of GTL reactors.

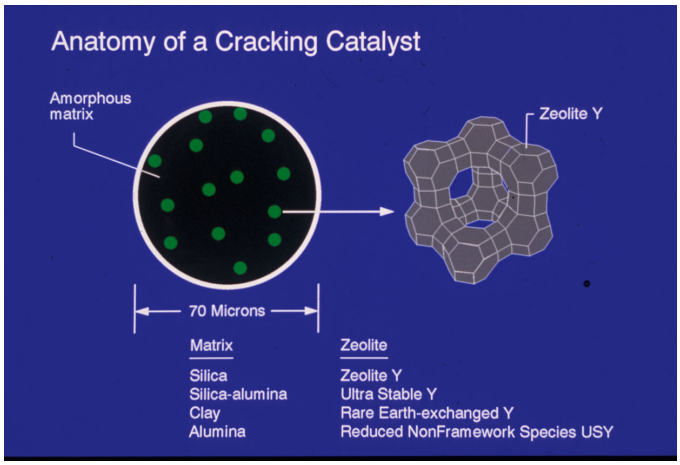

Figure 1. This schematic diagram shows the components of a supported catalyst particle.

Experimental

Apparatus. The experiments were performed at the National Synchrotron Light Source (NSLS) at BNL using several bending magnet beam lines. The synchrotron x-ray source provides high-intensity beams of x-rays that are the key to making measurements that are not feasible with conventional x-ray apparatus. The CMT work was done using a collimated beam of x rays to produce images with a scan-translate approach. The XRF work was also performed by accumulating images during a raster scan over an area of a thin section of the supported catalyst of interest. The spatial resolutions for the measurements were less than .010 mm.

Sample Preparation for CMT Measurements. The experiments were done at atmospheric pressure. The sample size was generally of the order of 1 - 10 mm. Thin sections were obtained using a microtome. We used two types of samples: Ni-Mo hydro-treating catalysts and Cr-SiO_2 polyethylene polymerization particles[1-4].

Results and Discussion

The work on the Ni-Mo hydrotreating catalysts made non-destructive sections through used and unused catalysts. As can be seen in Figure 2, the used catalyst shows evidence for an increase of the linear x-ray attenuation coefficient at the periphery of the particle and an increase in the amount of porosity in the interior of the particle when compared to the section through the unused particle. The distribution of Mo in these particles can be found by making measurements just above and just below the Mo K-x ray absorption edge and then subtracting the two images to determine the Mo contribution. The result of this experiment is shown in Figure 3.

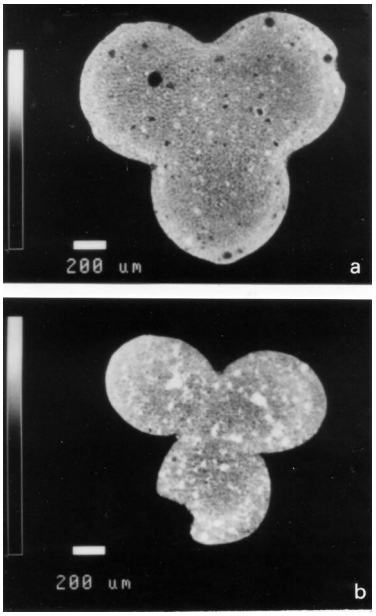

Figure 2. The tomographic slice obtained for a used Ni-Mo hdyrotreating catalyst is shown in Figure 2a and for an unused catalyst in Figure 2b.

The production of polymerization particles with the silica-based Cr catalyst is one that relies on fragmentation of the catalyst and a subsequent distribution through the polymer. Measurements were made on the particles using the CMT techniques described above. Thin sections were also made of a particle and maps were made of the distribution of the Cr using μXRF. The detection limit for Cr was roughly 10 parts-per-million by weight. The map obtained for the Cr distribution is shown in Figure 4. It can be seen that there is a rather constant concentration of Cr observed over the entire section with the exception of two regions where the enhance Cr concentration is evidence for only a partial disintegration of the catalyst.

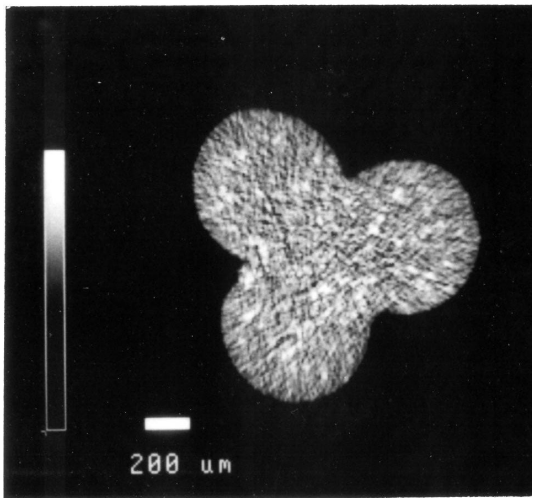

Figure 3. Mo concentration found is tomographic section of an unused Ni-Mo hydrotreating catalyst.

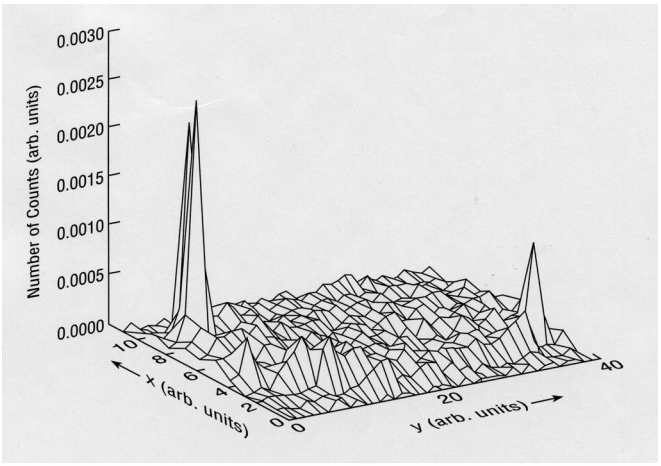

Figure 4. Distribution of Cr observed in a section of a polyethylene polymerization particle.

Conclusions

We have presented data illustrating the application of synchrotron based x-ray techniques to the study of hydrotreating and polyethylene polymerization catalyst. The CMT is a versatile technique for mapping changes in the composition of the catalyst constituents that in turn affects the catalytic activity. It is especially the case of F-T products that produce a significant amount of high molecular weight waxes that can clog the catalyst pores and adversely affect the catalyst performance over time. We are now focusing our work on imaging F-T catalysts. We hope to measure the changes in catalyst porosity that is so crucial to control the reactant gases to pass through the catalyst material to reach the active catalyst sites. The versatility of the CMT technique will allow us to monitor changes in the catalyst composition before and after the F-T reaction. The presented results show that the application of present state-of-the-art methods will be of great importance for work on GTL processes.

Acknowledgment. This work supported by the U. S. Department of Energy under Contract No. DE-AC02-98CH10886.

References

1. Conner, W. C., Webb, S. W., Spanne, P., and Jones, K. W. The use of x-ray microscopy and synchrotron microtomography to characterize polyethylene polymerization particles. Macromolecules 23, 4742-7 (1990).
2. Jones, K. W., Spanne, P., Webb, S. W., Conner, W. C., Beyerlein, R. A., Reagan, W. J., and Dautzenberg, F. M. Catalyst analysis using synchrotron x-ray microscopy. Nucl. Instrum. Methods B56/57, 427-32 (1991).
3. Ferrero, M. A., Sommer, R., Spanne, P., Jones, K. W., and Conner, W. C. X-ray microtomography studies of nascent polyolefin particles polymerized over magnesium chloride-supported catalysts. J. Polymer Science: Part A: Polymer Chemistry 31, 2507-12 (1993).
4. Jones, K. W., Berry, W. J., Borsay, D. J., Cline, H. T., Conner, W. C., Jr., and Fullmer, C. S. Applications of synchrotron radiation-induced x-ray emission (SRIXE). X-Ray Spectrometry 26, 350-8 (1997).

CATALYTIC CONVERSION OF METHANE TO METHANOL OVER LANTHANUM-COBALT-OXIDE SUPPORTED MOLYBDENUM BASED CATALYSTS

Xin Zhang, Dehua He, Qijian Zhang, Boqing Xu and Qiming Zhu*

State Key Laboratory of C_1 Chemistry and Technology,
Department of Chemistry, Tsinghua University
Beijing 100084, P.R. China

Introduction

Selective oxidation of methane is one of the most attractive potential industrial processes for the use of abundant natural gas resources. In the past decades, a great deal of effort has been made to develop catalysts and understand catalytic properties [1-2]. The MoO_3/SiO_2 and V_2O_5/SiO_2 catalysts have been reported to be the most active in the production of methanol [1-2]. The Mo(V)-loading has significant effects on the properties such as structure and reducibility of the catalysts, which determine the catalytic performance [1-2]. Generally speaking, the catalysts with the low Mo(V)-loading (high dispersion) show good activity and selectivity compared to the catalysts with the high Mo(V)-loading [1-2]. The participation of the lattice oxygen species (O^{2-}) or the adsorbed oxygen species (O^-) playing important roles on the formation of C_1-oxygenate has not been clear [1-2]. Other carriers such as Al_2O_3, Al_2O_3-SiO_2, MgO, TiO_2, TiO_2-SiO_2, SnO, ZnO_2, HZSM-5 and US-Y etc. have been used to support MoO_3 (V_2O_5), but their catalytic performances are quite poor [1-2]. Therefore, it is necessary to develop the effective catalysts for selective oxidation of methane to methanol.

The pervoskite-type oxide such as $LaCoO_3$ has high ability to activate and diffuse oxygen, due to its structure deficient. To our knowledge, such oxide catalysts showed good activity in combustion of methane, partial oxidation of methane to syngas, and oxidative coupling of methane etc. The pervoskite-type oxide supported Mo-based catalysts for selective oxidation of methane to C_1-oxygenate have been scarcely studied so far. Here, we report the catalytic performance of MoO_x/La-Co-oxide catalysts with the low Mo-loading in selective oxidation of methane, and characterize the properties of the catalysts so as to establish their relation to catalytic performance.

Experimental

Catalysts preparation. La-Co-oxide was prepared by using citric acid sol-gel method as described in elsewhere [3]. The Mo/La-Co-oxide catalysts (described as n-MLC, in which n express wt% of Mo) were prepared by impregnation of La-Co-oxide powder with different amount of $(NH_4)_6Mo_7O_{24}$ (Tianjing Chemical Co. Ltd., A.R.) aqueous solution. The precursor was dried at 383 K for 8 h, and calcined at 773 K for 8 h.

Catalytic test. Catalytic test was carried out in a continuous vertical-flow fixed-bed reactor, which was a 460 mm long quartz line tube (6.7 mm *i.d.*) tightly fixed in a stainless steel tube. Flow rate of reactant was controlled by a mass flow controller (Brooks 5850E serried) and pressure was controlled by a back-pressure regulator (Tescom Co.). Effluent gas kept at 423 K was analyzed by on-line gas-chromatograph (SHIMADZU, GC-8A, TCD) equipped with two columns: GDX-403 for separating CH_3OH, HCHO, C_2H_4, C_2H_6, H_2O, CO_2, and TDX-01 for N_2, O_2, CH_4, CO. The addition of N_2 in feed gas acted as both diluent and internal standard.

Characterization methods. The BET surface areas of catalysts were measured by using nitrogen adsorption/desorption isotherms method in ASAP-2010C adsorptionmeter. XRD measurement was carried out by BRUKER D8 Advanced X-rays powder diffractometer with Cu *K*α (λ=0.15046 nm). LR spectra were recorded on RENISHAW RM1000 Raman spectrometer quipped with He^+/Ne^+ laser (λ=514 nm, W=15 mW). TPR experiments of the samples were carried out in home-buildt TPR apparatus. XPS measurements were performed by PE PHI-5300 ESCA spectrometer, Al *K*α (1486.6 eV, 10.1 kV).

Results and Discussion

The results of catalytic test are shown in **Table 1**. Firstly, the effect of gas-phase homogeneous oxidation of methane was investigated. The reactor packed with quartz wool at constant temperature zoon (blank test) showed 4.9% CH_3OH selectivity at low CH_4 conversion, indicating that the gas-phase oxidation of methane had no great contribution to the formation of CH_3OH under such reaction conditions. In order to minimize the contribution of any gas-phase reactions, the space of up and down the catalyst bed (0.5 g, 20~40 mesh) was filled with quartz wool. The La-Co-oxide alone demonstrated the activity in combustion of methane. MoO_3 showed 6.9% HCHO selectivity with 1.6% CH_4 conversion. Catalytic performance of MoO_x/La-Co-oxide catalysts strongly depended on the Mo-loading. The highest CH_3OH selectivity (*ca.* 60%) and yield (*ca.* 6.7%) were achieved on the 7%wt Mo/La-Co-oxide. The results suggest that the synergetic effect between molybdenum oxide and La-Co-oxide occurred, and molybdenum oxide might be active sites for the formation of methanol.

It can be seen from **Table 1** that the BET surface areas of the MLC catalysts slightly increased with increasing Mo-loading. XRD results show that both La-Co-oxide and MoO_x/La-Co-oxide catalysts were mainly composed of $LaCoO_3$ and Co_3O_4 (**Figure 2**). LRS was used to determine the molecular structure of molybdenum oxide. The molybdenum oxide on the 3%wt Mo/La-Co-oxide catalyst was the isolated $[MoO_4]^{2-}$ species (889 and 858 cm^{-1}) [4]; likewise, the isolated and distorted $[MoO_4]^{2-}$ species (912, 821 and 322 cm^{-1}) located on the 7%wt Mo/La-Co-oxide catalyst [4]. The $[Mo_7O_{24}]^{6-}$ species (930 cm^{-1}) were detected on the 10%wt Mo/La-Co-oxide catalyst [4]. The XRD and LRS results indicate that molybdenum oxide was amorphous and its molecular structure depended on the Mo-loading. Considering the results of catalytic test, the studies reveal that the isolated and distorted $[MoO_4]^{2-}$ species enhanced the production of CH_3OH since Mo-OCH_3 intermediate might easily generate and transfer to CH_3OH on the species.

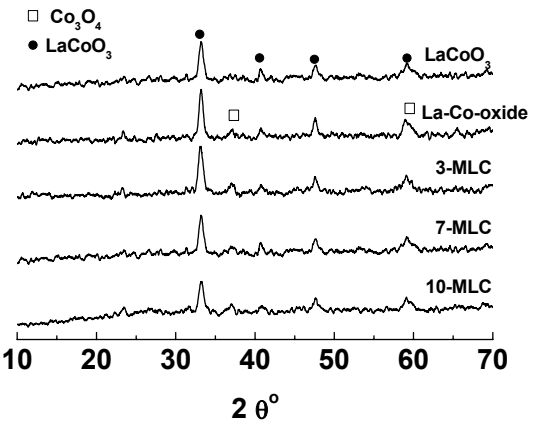

Figure 1. XRD patterns of the catalysts

Table 1 Catalytic performance of these catalysts in selective oxidation of methane to methanol

Catalysts	$S_{BET}(m^2/g)$	Temp (°C)	Conv CH_4 (%)	Selectivity %			Yield % CH_3OH
				CH_3OH	CO	CO_2	
Reactor	-	420	0.9	4.9	43.1	51.8	0.04
La-Co-oxide	10.8	420	4.2	-	8.6	91.4	-
3-MLC	10.8	420	8.9	28.8	11.2	60.0	2.6
5-MLC	10.6	420	10.2	41.6	21.5	36.8	4.2
7-MLC	11.2	380	5.0	5.0	59.1	35.7	0.3
		400	9.2	31.4	41.8	26.6	2.9
		420	11.2	60.0	21.8	18.2	6.7
		460	11.4	38.2	36.5	25.3	4.3
10-MLC	11.8	420	11.6	33.2	31.7	34.8	3.9
MoO_3	-	420	1.6	6.9HCHO	40.8	52.2	0.1HCHO

Reaction conditions: 4.2 MPa, $CH_4/O_2/N_2$=9/1/1, 14400 ml/(g.cat).h^{-1}.

XPS studies indicate a slight increases of binding energy of Co_{2p}, La_{3d} and Mo_{3d} with increasing Mo-loading. The results imply that the deficient sites gradually reduced in the catalysts with the Mo-loading, leading to weaken the electron shield for the nucleus of ions. Detailed analysis and Lorentizian curve fitting of the O_{1s} XPS spectra reveal the existence of oxygen species in mixed value state on the catalysts: $O^{2-}{}_{1s}$ at 528.8~529.0 eV, $O^{-}{}_{1s}$ at 530.1~530.2 eV and OH^-/CO_3^{2-} at 532.1~532.5 eV [3, 5]. The O^-/O^{2-} ratio can be estimated according to the area of these sub-peaks. It is worth of noticing, the O^-/O^{2-} ratio gradually reduced with the increase of Mo-loading.

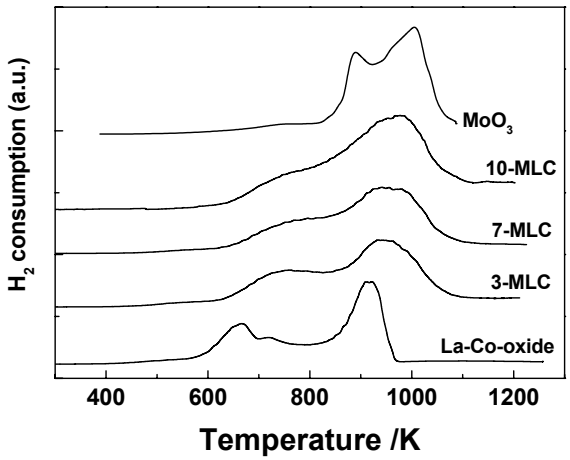

Figure 2. H_2-TPR profiles of the catalysts

Figure 2. gives some useful information of the reducibility of the catalysts. The TPR peaks temperature shifted toward the high temperature with the increase of Mo-loading. And, the TPR profiles of the MoO_x/La-Co-oxide catalysts were different from those of both La-Co-oxide and MoO_3. The results further indicate that the interaction between molybdenum oxide and La-Co-oxide occurred, which modified the reducibility of the catalysts. In addition, the reducibility of MoO_x/La-Co-oxide catalysts gradually reduced with the increase of the Mo-loading. The H_2 consumption of the MLC catalysts slightly increased with the Mo-loading, probably due to the increase of the reducible oxide species.

The results obtained in this work clearly show that molybdenum oxide loading on the carrier La-Co-oxide induced some change of properties such as molybdenum oxide structure, reducibility, oxidation state of ions, and surface composition, which in turn determined the catalytic performance. The effects were a function of the Mo-loading.

The changes of properties of the MLC catalysts might be due to the occurrence of interaction between molybdenum oxide and the La-Co-oxide. The electronegativity of Mo^{6+} is 2.16, Co^{3+} is 1.88 and La^{3+} is 1.08 [6]. Hence, the differences of the ions electronegativity resulted in the interaction. The catalysts with the low Mo-loading showed the strong interaction compared to the catalysts with the high Mo-loading, leading to more deficient sites and high reducibility. The deficient sites and reducibility influenced the activation and transform of oxygen species as the sequence: $O_{2\ (gas)} \Leftrightarrow O_{2\ (surface)} \Rightarrow O^{2-}{}_{(surface)} \Rightarrow O_2^{2-}{}_{(surface)} \Leftrightarrow O^{-}{}_{(surface)} \Rightarrow 2O^{2-}{}_{(lattice)}$ [3, 5], therefore, the O^-/O^{2-} ratio varied with the Mo-loading.

The reducibility and the O^-/O^{2-} ratio were close relation to the catalytic performance. It is well known that both O^- species and O^{2-} species are active in selective oxidation of methane to methanol [1-2]. And, it seems that the O^- species are more active than the O^{2-} species [1-2]. However, the O^- species also have high activity in oxidation of methanol [3]. Likewise, the proper improvement of reducibility can enhance the activation of methane [1-2]. The much high reducibility can result in deep oxidation of methane and methanol [1-2]. Hence, it is necessary that the catalysts with the proper reducibility and the O^-/O^{2-} ratio enhanced the production of methanol in selective oxidation of methane.

Acknowledgment. We acknowledge the financial support from the National Key Fundamental Research Project Foundation of the Ministry of Science and Technology of China (G199902240-06) and the Research Foundation of Tsinghua University.

References

1. Tabata K, Teng Y, Takemoto T, Suzuki E, Banares M.A, Pena M.A, and Fierro J.L, *Catal. Rev.*, **2002,** *44(1)*, 1-58
2. Faraldos M, Banares M.A, Anderson J.A, Hu H, Wachs I.E, Fierro J.L.G, *Fuel.Process.Tech*. **1995,** *42,* 214-225.
3. Wang W, Zhang H.B, Lin G.D, Xiong Z.T, *Appl.Catal. B.*, **2000**, *24*, 219-232.
4. Mestl G, Srinivasan T.K.K, *Catal. Rev-Sci. Eng.*, **1998,** *40(4)*, 451-570.
5. Wan H.L, Zhou X.P, Weng W.Z, Long R.Q, Chao Z.S, Zhang W.D, Chen M.S, Luo J.Z, Zhou S.Q, *Catalysis Today* **1999**, *51 (1)*, 161-175.
6. Weast R.C, Astle M.J.A, Beyer W.H, *CRC Handbook of Chemistry and Physics*, 64th EDITION, CRC Press, Inc. Boca Raton, Florida.

PrOx Reactor Startup and Transient Control Options

Michael A. Inbody, Rodney L. Borup, and José I. Tafoya

Fuel Cell Team, MST-11
Los Alamos National Laboratory
MS J-579, P.O. Box 1663
Los Alamos, NM 87545

Introduction

Low-temperature polymer electrolyte membrane (PEM) fuel cells require a hydrogen-rich fuel stream that has a carbon monoxide (CO) concentration less than 10 to 100 ppm, depending on the CO tolerance of the fuel cell. Fuel processing systems for PEM fuel cells that do not use separation processes to purify the hydrogen-rich fuel stream typically use a final CO removal step to meet the CO tolerance requirements of the fuel cell stack. A common method of final CO removal is by Preferential Oxidation (PrOx) of CO by oxygen from injected air over a catalyst. The selection of the catalyst and operating conditions such as temperature are critical to oxidize CO preferentially or selectively instead of oxidizing hydrogen, a parasitic loss of the fuel cell system fuel.

The PrOx reactor component of the fuel processor is used to remove the remaining CO from the outlet of the water-gas shift (WGS) reactor stages, in the range of 2% CO to 5000 ppm CO. The PrOx design inlet CO concentration reflects a trade-off between size of the WGS reactor stages and the efficiency penalty of the PrOx removal of CO. The efficiency penalty can be offset by adding system complexity through the use of multiple stages of PrOx. Because the CO and H_2 oxidation reactions are exothermic and selectivity for CO decreases with increasing temperature, achieving high CO conversions can increase the parasitic loss of hydrogen. Multiple stages with lower CO conversion per stage can be used to achieve a higher overall conversion with reduced parasitic loss of hydrogen by maintaining the catalyst in each stage in a temperature range where it is more selective for CO oxidation.

Transportation applications and some stationary applications of fuel cell systems require that the fuel processor respond to transient power demands. Transportation fuel cell systems, in particular, may undergo frequent startup/shutdown cycles. The PrOx reactor component, as the final stage in the fuel processor, is critical for maintaining the outlet CO concentration within the fuel cell stack tolerance through the startup transient and the transition to normal operation and then during subsequent system power transients.

In the PrOx reactor research at Los Alamos National Laboratory, we conduct experiments on laboratory PrOx reactor components to identify the performance of catalysts and PrOx reactors under steady-state and transient operating conditions. We have examined the response of PrOx reactors and catalysts to three types of transients, power, composition, and startup.

A power transient is a change in the total flow through the fuel processor as it responds to changes in the hydrogen demand of the fuel cell. Power transient experiments are used to identify the air injection and temperature control requirements to maintain specified outlet CO levels.

A composition transient is a change in the gas composition such as variations in the CO concentration caused by instabilities or variations in the fuel processor inlet flows. Composition transient experiments were conducted to measure the sensitivity of the PrOx reactor to variations in the inlet CO composition and the requirements to control the outlet CO concentration. These experiments can be used to identify requirements for a CO sensor for a control system input.

The PrOx startup transient is difficult to define and simulate because the character of the transient will vary depending on the particular fuel processor and startup strategy. However, the desired end in all cases is to deliver a fuel cell quality gas as quickly as possible. To achieve this end in the PrOx reactor, the mass of the catalysts and components in the flow need to be minimized, the catalyst should have a low light-off temperature for CO oxidation so that CO oxidation can begin before the fuel processor has completely warmed up, and should have good CO selectivity over a wide temperature range from low temperature at startup to normal operating temperature at steady-state. An additional desired characteristic is the capability to oxidize higher than normal concentrations of CO. Then, with proper design and controls, the PrOx reactor may be able to compensate for off-design performance of the upstream WGS reactors to maintain the required system outlet CO concentration.

We report here on our experimental approach to measure single-stage PrOx reactor response to composition transients and startup transients. The results of the composition transients are presented showing an option to controlling varying CO concentrations. The startup transient results also are presented showing a rapid decrease to steady-state outlet CO levels.

Experimental Approach

PrOx Reactor Test Facility and Hardware. PrOx reactor components were tested in a facility capable of simulating the outlet stream and conditions from a fuel processor. The major components of reformate, hydrogen, nitrogen, carbon dioxide, and water (as steam) along with carbon monoxide as a trace component, were metered with mass flow controllers. The reformate flow was heated with inline gas heaters to simulate the outlet temperatures from a fuel processor. Fuel processor operating pressures were obtained using a back pressure regulator. Computer control and measurement of these functions allowed for simulation of a variety of fuel processor configurations and transient operating conditions. CO, CO_2, and CH_4 concentrations were measured with NDIR analyzers and O_2 concentrations were measured with a paramagnetic O_2 analyzer.

Experiments reported here were conducted with a single-stage PrOx reactor set up with a 3 inch diameter by 5 inch long 600 cpsi monolith coated with a precious-metal-based catalyst.

Composition Transient Experiments. The response of the single-stage PrOx reactor was measured with a modulated inlet CO concentration with an overall steady flow with composition, 38.1% H_2, 27.3% N_2, 15.7% CO_2, and 17.1% H_2O. The space velocity was set to 38,000 hr^{-1} with an inlet gas temperature set to 97 ºC. In one set of experiments simulating an inlet stage, the CO concentration was modulated between 8000 ppm and 12000 ppm with a 60 s period sine wave. The air stoichiometry was set for a steady-state value at 10000 ppm CO. In a second experiment simulating an outlet stage, the CO concentration was varied between 0 and 2000 ppm again with a 60 s period sine wave. The air injection was held constant with the stoichiometry set for 2000 ppm.

Startup Transient Experiments. The startup response of the PrOx reactor catalyst from room temperature was measured by establishing a room temperature gas flow through the reactor and then injecting air at time = 0.0 s. A dry gas flow with 46.0% H_2, 32.9% N_2, and 19.0% CO_2 was established with a GHSV = 31,000 hr^{-1} at an inlet temperature of 20 ºC. Experiments were conducted with inlet CO concentrations of 1.2% and 2350 ppm. Outlet CO concentration and the temperature profile of the catalyst monolith were recorded from before the start of air injection to approximately steady-state. Temperatures in the catalyst monolith were monitored by 0.020" K-type thermocouples inserted at 1.0" depth intervals.

Results and Discussion

Composition Transient Experiments. Figure 1 shows the outlet CO concentration from the PrOx catalyst in response to a modulated inlet CO concentration from 8000 to 12000 ppm. The air stoichiometry (λ) is set to 1.44 for the mean CO level of 10000 ppm and held constant through the modulation. The peak-to-peak outlet CO variation is 1350 ppm and the mean is 506 ppm. As the air stoichiometry is increased the magnitude of the peak-to-peak variation and the mean outlet CO concentration both decrease. At λ=1.24, the peak-to-peak CO was 2700 ppm and the mean CO = 1300 ppm. At λ=1.65, the peak-to-peak CO was 460 ppm and the mean CO=235 ppm.

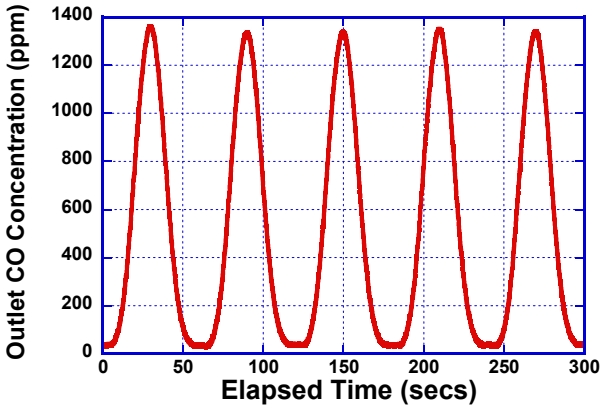

Figure 1. Outlet CO concentration as a function of time for a modulated CO input from 8000 to 12000 ppm.

The second set of composition transient experiments examined a hypothetical inlet to a second stage with a modulated inlet CO from 0 to 2000 ppm. With λ=2.4, the outlet CO was held in the range of 10 ppm. The combination of this second stage with the first stage performance at λ=1.44 suggests that the overall stoichiometry of 1.84 could control an 8000 to 12000 ppm variation at these flow rates.

Startup Transient Experiments. Figure 2 shows the outlet CO concentration measured as a function of time from the start of air injection for an inlet CO concentration of 1.2% at λ=1.09. The outlet CO concentration drops rapidly within 15 s of the start of air injection and reaches 730 ppm at 30 s. A similar test with inlet CO concentration of 2350 ppm CO at λ=2.4 shows a similar response of rapid CO decrease within 15 s and reaches 30 ppm at 30 s. Some of the delay in the outlet CO concentration response is due to sampling line delays in the gas analyzers.

Figure 3 shows the monolith temperature response for the 1.2% CO case. The temperature rise moves down the monolith in the 60 s shown as the temperature response takes longer to reach steady-state than the CO concentration. The catalyst used here has a low light-off temperature that facilitates its use in startup.

The rapid decline in outlet CO concentration at low inlet temperatures before the temperature profile has reached steady-state suggests that the thermal response of the PrOx catalyst substrate may not be a major factor in the startup of a PrOx reactor. In these experiments, low CO concentrations can be reached in 15 s after the start of air injection.

Conclusions

The response of a PrOx reactor catalyst to composition transients and to startup transients has been measured. The composition transient experiments suggest that variations in the inlet CO concentration can be tolerated without additional controls if the inlet stages of the PrOx reactor can bring the inlet CO to the final stage to within 2000-1000 ppm. At these low concentrations, the excess air does not generate a significant temperature rise to increase the reverse water-gas shift kinetics. Simple control of CO variations at constant flow can be achieved at the expense of additional H_2 consumption.

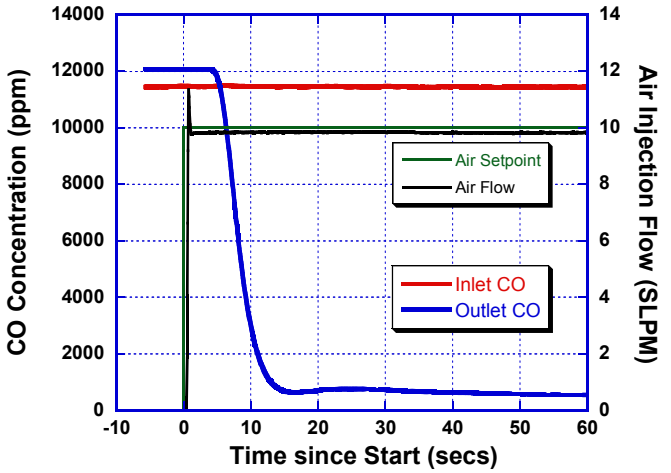

Figure 2. Outlet CO concentration measured as a function of time since the start of air injection.

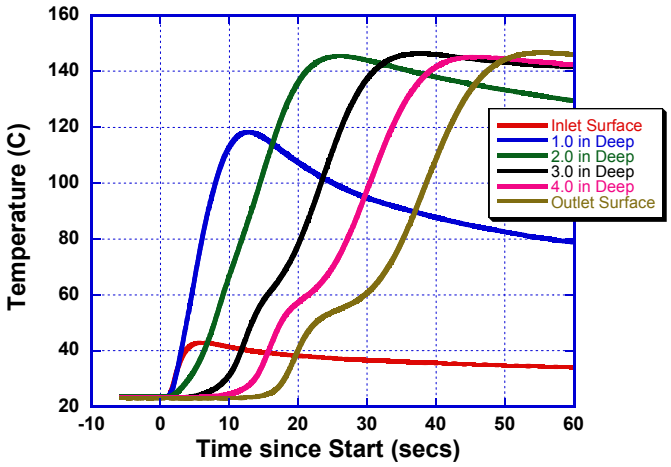

Figure 3. Temperature response at various depths in the monolith during startup.

The startup transient experiments demonstrate that the outlet CO concentration can be decreased rapidly. A low catalyst light-off temperature makes this feasible. Based on the rapid response within 15 s, a fast start less than 30 s appears feasible. Quantification of the sampling delays is needed and the startup performance needs to be confirmed in a multi-stage reactor.

Future experiments will examine the composition and startup transient response of multi-stage PrOx reactors to confirm the feasibility of CO control using these methods. Startup at higher inlet CO concentrations will be examined to determine the feasibility of high CO startup.

Acknowledgement. This work was funded through the DOE Office of Hydrogen, Fuel Cells and Infrastructure Technologies Program, Program Manager Nancy Garland.

STRUCTURE SENSITIVITY OF SELECTIVE CO OXIDATION IN H_2 OVER WATER-PRETREATED Pt/γ-Al_2O_3

In Hyuk Son, Soon Cheon Byeon, and Alan M. Lane*

Department of Chemical Engineering, University of Alabama, Tuscaloosa, AL, 35487, USA *Center for Materials for Information Technology (MINT), University of Alabama, Tuscaloosa, AL 35487

Introduction

Carbon monoxide must be removed from the hydrogen feed to Polymer Electrolyte Fuel Cells (PEFCs) because it poisons the anode. A new pretreatment method, involving saturation of the catalyst with liquid water during reduction (water-pretreatment), improved activity and selectivity of Pt/γ-Al_2O_3 in the low-temperature preferential oxidation (PROX) of CO in H_2[1]. TEM, XRD, and CO/H_2-TPD experiments confirmed that the improvements were due to smaller (~2 nm) Pt particles with an alloy-like interaction between the Pt and Al atoms, making them particularly stable against sintering. The stabilization of Pt particles is related to increased H_2 spillover during water-pretreatment[2]. This catalyst has a strong SMSI that increases the reducibility of alumina. Structure sensitivity is quite controversial concerning supported Pt catalysts and depends on the oxide support and the Pt dispersion. Evidences by XPS will show that the water-pretreated Pt/γ-Al_2O_3 is structure sensitive in the selective CO oxidation in H_2 rich condition.

Experimental

Activity tests: The following notation identifies the catalysts: (*W*)*X*Pt/Al where *W* is Water-pretreatment, *X* is wt%, and Al is γ-Al_2O_3. Four kinds of pretreatments were applied to 5Pt/Al: calcination at 400°C in air (After Cal. 5Pt/Al), reduction at 400°C in H_2 after at 120°C in He (LR5Pt/Al), conventional reduction in H_2 at 500°C (5Pt/Al), and water-pretreatment (W5Pt/Al)[1]. For various pretreated catalysts, CO conversion and selectivity were measured in the simulated reforming gases (1% CO, 1% O_2, H_2 balance, and total flow rate: 100 ml/min).

Characterization methods: Pt dispersions and their particle size were measured by CO chemisorption, TEM, and XRD. To investigate the oxidation state of Pt and alumina after different treatments, X-ray photoelectron spectroscopy (XPS) was used. A Kratos Axis 165 was used with an Al anode as the X-ray source.

Results and Discussion

After preferential oxidation (PROX) of CO in H_2, the average particle sizes of 5Pt/Al and W5Pt/Al are 16 and 2 nm, respectively[1, 2]. The dispersion of 5Pt/Al is 0.16 (CO/Pt mol ratio). Due to large amounts of H_2 spillover, the dispersion of W5Pt/Al cannot be measured accurately[1]. For After Cal. 5Pt/Al, its average particles size and dispersion were not measured. For LR5Pt/Al, the dispersion and average particle size are around 0.41 (CO/Pt) and 3 nm, respectively[3]. Thus, W5Pt/Al and LR5Pt/Al have better dispersions and smaller Pt particles. While, 5Pt/Al has less dispersed bigger Pt particles. Activity and selectivity of CO oxidation in H_2 were tested over the various pretreated catalysts as a function of temperature and the data were obtained after 1 hour for the steady-state reaction (Figure 1). The CO oxidation activity of After Cal. 5Pt/Al was low due to the oxide type Pt particles. W5Pt/Al showed higher CO oxidation activity and selectivity over the entire temperature range, particularly at low temperatures (below 100°C).

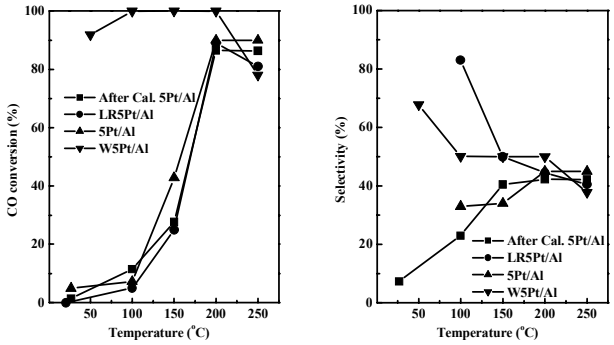

Figure 1. CO conversion, O_2 conversion, and selectivity for the catalysts after calcination at 400°C (After Cal. 5Pt/Al), lower temperature reduction at 400°C (LR5Pt/Al), reduction at 500°C (5Pt/Al), and water-pretreatment (W5Pt/Al) (1% CO, 1% O_2, H_2 balance, and total flow rate: 100 ml/min).

LR5Pt/Al, although it has more highly dispersed, small Pt particles (similar to W5Pt/Al), it showed the lowest activity over the entire temperature range. Over 100°C, the less dispersed bigger Pt particles on 5Pt/Al have a higher CO oxidation activity compared to the better dispersed smaller Pt particles on LR5Pt/Al, agreeing with previous studies[3]. In flowing He (as opposed to H_2), larger Pt particles on alumina have a higher CO oxidation rate because bridged CO adsorption, a weaker interaction caused by a weaker "strong metal-support interaction" (SMSI), facilitates oxygen adsorption on Pt. Highly dispersed small Pt particles have a lower CO oxidation rate because linearly adsorbed CO, a stronger interaction caused by stronger SMSI, blocks oxygen adsorption on Pt.

Thus, on W5Pt/Al, the highly dispersed, small Pt particles are different. Due to the H_2 spillover, the CO oxidation activity was higher under hydrogen-rich reaction conditions [2]. The controversy of structure-sensitivity/insensitivity of the CO oxidation reaction in H_2 over Pt on alumina catalysts cannot be determined simply based on particle size and dispersion. We hypothesize that much larger SMSI caused the greater H_2 spillover. The following XPS and H_2-TPR studies will illustrate the different interactions between Pt and alumina according to their oxidation states.

XPS tests were performed for understanding the differences in the interaction between Pt particles and alumina after the reaction. The states of Pt (metal Pt, Pt^0, PtO, PtO_2, or Pt-Al alloy) over catalysts were analyzed using the BE line positions of Pt 4*d* and Al 2*s* spectra (Figures 2 and 3). For After Cal. 5Pt/Al, the highest Pt $4d^{5/2}$ line position (317 eV) assigns to PtO_2 which is lower CO oxidation activity sites. The Pt $4d^{5/2}$ line positions of LR5Pt/Al, 5Pt/Al, and W5Pt/Al are 0.4, 1.1, and 1 eV higher than Pt metal. Thus, for LR5Pt/Al, the state of Pt is much closer to metallic Pt. The Pt $4d^{5/2}$ BEs of 5Pt/Al and W5Pt/Al are centered at similar positions (315.2 and 315.1 eV, respectively), while that of W5Pt/Al is skewed toward higher BEs. For W5Pt/Al, the positive shift is caused by the electron-deficiency of Pt from the Pt-Al alloy. Under reducible reaction conditions, the positive shift effect is less because of the oxidized Pt state (PtO_2)[4]. Thus, W5Pt/Al has the characteristics of Pt-Al alloy states.

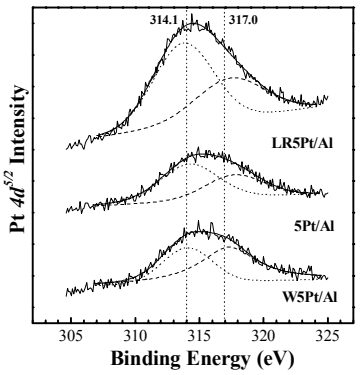

Figure 2. Deconvolution of Pt $4d^{5/2}$ XPS spectra.

The following analysis of Al 2*s* states supports the hypothesis of Pt-Al alloy formation on W5Pt/Al. Mecoville et al[5]. reported that Al 2*p* BEs chemically shift up 2.5-2.7 eV from metallic Al (72.5 eV) in an O_2 atmosphere due to surface oxides on Al (111). In the same way, the higher BEs of After Cal. 5Pt/Al (119.4 eV) and 5Pt/Al (118.7 eV) were caused by the oxide state from chemically adsorbed O_2 (highest dash line area in Figure 3). For W5Pt/Al, the shape of Al 2*s* is similar to LR5Pt/Al. But, its higher Al 2*s* BEs (119.1) indicates a higher Pt-Al alloy states. Thus, Pt particles on W5Pt/Al have a Pt-Al alloy type of interaction with stronger SMSI, while those on LR5Pt/Al are metallic Pt with a weaker SMSI.

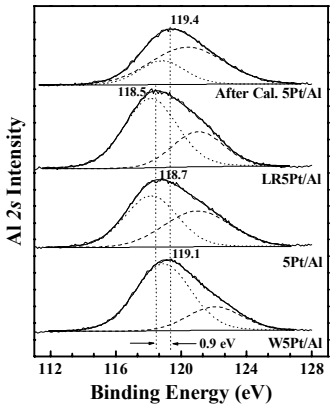

Figure 3. Deconvolution of Al 2*s* XPS spectra.

Conclusion

The low temperature reduction method and the water-pretreatment method generated highly dispersed small Pt particles over γ-Al_2O_3. The water-pretreated catalyst showed particularly high activity for low-temperature selective CO oxidation under H_2 rich conditions. XPS analysis showed that highly dispersed small Pt particles with a Pt-Al alloy character existed on the W5Pt/Al with stronger SMSI that increasd the reducibility of alumina. Thus, the water-pretreated Pt/γ-Al_2O_3 is structure sensitive in selective CO oxidation under H_2 rich conditions.

Acknowledgement.

The work presented in this paper is supported by the Center for Advanced Vehicle Technologies at the University of Alabama, which is funded by the U.S. Department of Transportation Federal Highway Administration under Grant DTFH61-99-X-00007 and by the DOE EPSCoR Implementation Grant DE-FG02-ER45867.

References

(1) Son, I. H.; Shamsuzzoha, M.; and Lane, A. M. *J. Catal.* **2002**, *210 (2)*, 460.
(2) Son, I. H.; and Lane, A. M. 2nd Topical Conference on Fuel Cell Technology, AIChE 2003 annual meeting, April, **2003**, New Orleans, Louisiana, U.S.A.,.
(3) Sarkany, J.; and Gonzaleg, R. D. *Appl. Catal.* **1982**, *4*, 53.
(4) Bouwman, R.; and Biloen, P. *J. Catal.* **1997**, *48*, 209.
(5) Mcconville, C. F.; Seymour, D. L.; Woodruff, D. P.; and Bao, S. *Surf. Sci.* **1987**, *188*, 1.

PREFERENTIAL CATALYTIC OXIDATION (PROX) OF CO FROM MODEL REFORMATES FOR PEM FUEL CELLS

*Bong-Kyu Chang and Bruce J. Tatarchuk**

Center for Microfibrous Materials Manufacturing (CM^3)
Department of Chemical Engineering,
Auburn University, Auburn, AL 36849

Introduction

During the last several decades, there has been a significant increase in the research on fuel cells since it can offer a cleaner alternative for conventional internal combustion engines. Due to both kinetic and thermodynamic constrains of hydrocarbons (e.g.: methanol) reforming, however, significant concentration of CO are produced from the hydrogen producing catalytic reformers. And there is a limit, unfortunately, regarding the thermodynamic conversion of the water-gas shift reaction (WGSR), so that a CO concentration which is sufficiently low to be acceptable by the PEMFC system cannot be achieved using WGSR only. The reformate coming from the fuel processing section contains 50~65 vol% H_2, 25~40 vol% CO_2, 2~5 vol% H_2O, and 1 vol% CO. The fuel cell performance significantly deteriorates if the feed stream contains even trace amount of CO (more than 20 ppm) since the Pt or Pt-Ru anodes are poisoned by CO, which strongly chemisorbs on the active sites, thus blocking the sites where the dissociation/oxidation of H_2 takes place. Among the many approaches to reduce CO concentration in the reformed gas mixture, selective catalytic oxidation of CO to CO_2 has been found to be the most effective way to remove the trace amount of CO from hydrogen.

In our previous study[1], over 150 catalysts were evaluated for selective oxidation of CO in model reformate in the temperature range of from room temperature to 250°C. Based on the amount of catalyst used, Pt/γ-Al_2O_3, promoted Pt-M/γ-Al_2O_3, Au/α-Fe_2O_3, and CuO-CeO_2, showed complete CO conversion activity in model reformate in integral reactor conditions. In the present study, catalytic activities of the four catalysts are investigated in differential reactor conditions and reveal that the promoted Pt-M/γ-Al_2O_3 catalyst is a superior candidate compared to other catalysts. The promoted Pt-M/γ-Al_2O_3 catalyst is, then, examined in the presence of excess water for practical PEM fuel cell applications and the result indicates that the promoted Pt-M/γ-Al_2O_3 catalyst retains its highest activity even in the presence of 30vol% water in the feed gas.

Experimental

Catalysts are prepared by conventional co-precipitation or incipient-wetness method followed by drying and calcination processes.

Differential reactor experiments are carried out using a 4mm I.D. quartz tube reactor. 0.01g (10mg) of catalysts are diluted with 0.1g of inert support material (α-Al_2O_3) to make the reactor isothermal. The particle size is 150-250 μm (60-100 mesh). Dry feed gas consists of 1% CO, 1% O_2, 20.6% CO_2, 40% H_2, and balance N_2 and feed flow rate is controlled by gas mass flow controller. The total feed flow rate is changed from 50 to 200 (ml/min) to produce the differential reactor conditions. The temperature range investigated in the differential reactor study is 100 to 180°C.

The reaction products were analyzed with gas chromatograph (TCD-GC);

Conversion of CO to CO_2 (%) = $(C_{CO}^{in} - C_{CO}^{out}) / C_{CO}^{in} \times 100\%$

Selectivity for CO oxidation over H_2 oxidation (%) = O_2 consumption by CO oxidation / Total O_2 consumption × 100%
= $\frac{1}{2}(C_{CO}^{in} - C_{CO}^{out}) / (C_{O2}^{in} - C_{O2}^{out}) \times 100\%$

Results and Discussion

(1) Integral reactor

In our previous study[1], over 150 catalysts were evaluated for selective oxidation of CO in H_2-rich gas in the temperature range of from room temperature to 250 °C.

Among the catalysts investigated Pt/γ-Al_2O_3, promoted Pt-M/γ-Al_2O_3, Au/α-Fe_2O_3, and CuO-CeO_2, showed extremely high CO conversion activity in model reformate in integral reactor conditions based on the amount of catalyst loaded. Figure 1 shows the results of the integral reactor study.

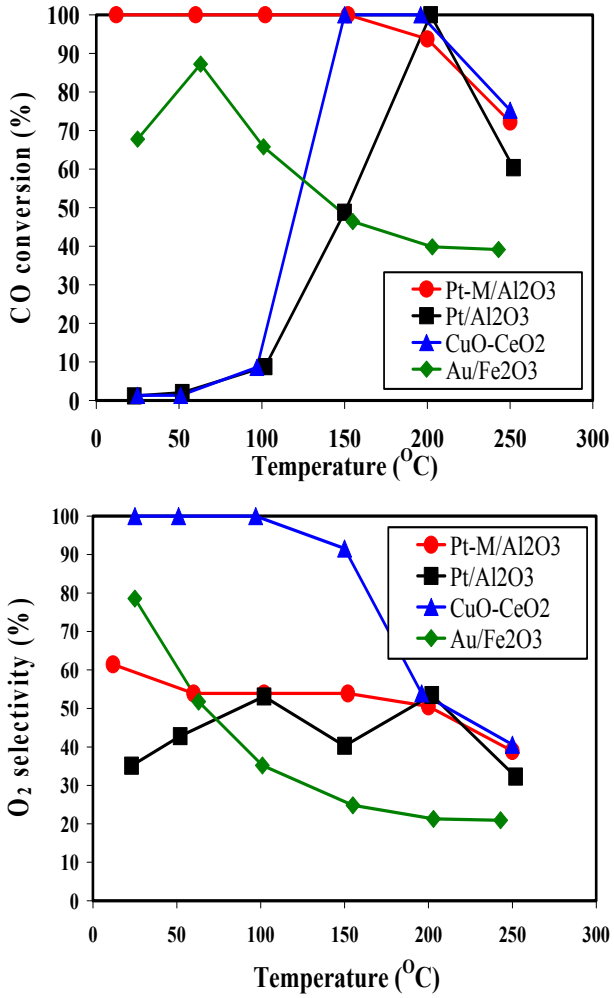

Figure 1. Comparison of the performance of Pt-M/Al_2O_3 (1.1wt%Pt), Pt/Al_2O_3 (1.1wt%Pt), Au/α-Fe_2O_3 (5at%Au), and CuO-CeO_2 (5.7% Cu, Cu:Ce = 0.143:1) in the presence of CO_2 and H_2O. *(1.1% CO, 1.1% O_2, 20.6 % CO_2, 40% H_2, 2.9% H_2O, and balance N_2 in the reactant feed, 0.1g catalyst, total flow rate 100 ml/min)*

And table 1 summarizes the comparison of the four catalysts in integral reactor in terms of active reaction temperature range, CO conversion, and O_2 selectivity.

Table 1. Comparison of the performance of Pt-M/Al_2O_3 (1.1wt%Pt), Pt/Al_2O_3 (1.1wt%Pt), Au/α-Fe_2O_3 (5at%Au), and CuO-CeO_2 (5.7% Cu, Cu:Ce = 0.143:1) in the presence of CO_2 and H_2O. (*1.1% CO, 1.1% O_2, 20.6 % CO_2, 40% H_2, 2.9% H_2O, and balance N_2 in the reactant feed, 0.1g catalyst, total flow rate 100 ml/min*)

Catalyst	Temp. (^{O}C)	CO conversion (%)	O_2 selectivity (%)
Pt-M/Al_2O_3	RT – 200	90 – 100	50 – 60
Pt/Al_2O_3	200	80 – 100	20 – 50
Au/α-Fe_2O_3	RT – 50	65 – 95	50 – 80
CuO-CeO_2	120 – 200	80 – 100	50 – 95

(2) Differential reactor

A differential reactor is defined in which the reaction rate is almost constant throughout the reactor due to the minimal changes in the reactant concentration. The reaction rate (r) thus can be calculated according to $\frac{W}{F} = \frac{X}{r}$ *or* $X = r\left(\frac{W}{F}\right)$

Since reaction rate is a constant, a plot of reaction conversion (X) versus inverse space velocity (W/F) should be linear with the slope equal to the reaction rate (r).

Figure 2 demonstrates differential reactor conditions at conversions below 15% for Pt-M/γ-Al_2O_3, Pt/γ-Al_2O_3, Au/α-Fe_2O_3, CuO-CeO_2, respectively. The purpose of this study is to compare the catalytic activity of the four catalysts in differential reactor conditions since all the four catalysts show complete CO conversion activity in integral reactor conditions in which the true catalytic activity of the four catalysts cannot be readily compared. As it can be clearly seen, the reaction rate (slope) increases as temperature increases from 100 to 180^{o}C for all four catalysts. Figure 3 compares Pt-M/γ-Al_2O_3, Pt/γ-Al_2O_3, Au/α-Fe_2O_3, CuO-CeO_2 catalysts in differential reactor conditions at 150^{o}C. The catalytic activity for the selective catalytic oxidation of CO in H_2 decreases in differential reactor conditions in the following order; Pt-M/γ-Al_2O_3 > CuO-CeO_2 > Au/α-Fe_2O_3 > Pt/γ-Al_2O_3.

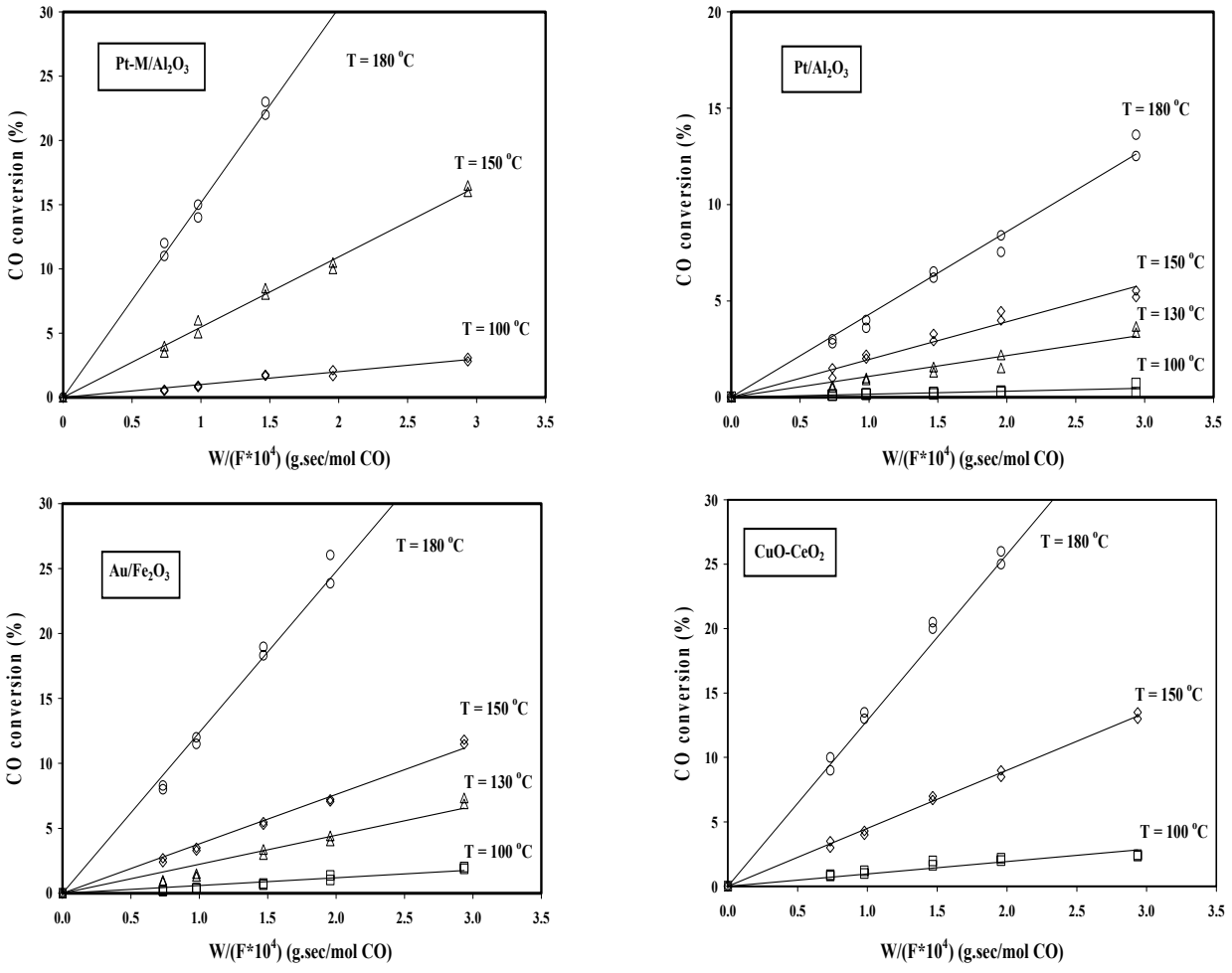

Figure 2. Demonstration of differential reactor conditions for Pt-M/Al_2O_3 (1.1wt%Pt), Pt/Al_2O_3 (1.1wt%Pt), Au/α-Fe_2O_3 (5at%Au), and CuO-CeO_2 (5.7% Cu, Cu:Ce = 0.143:1). *(1.1% CO, 1.1% O_2, 20.6 % CO_2, 40% H_2, and balance N_2 in the reactant feed)*

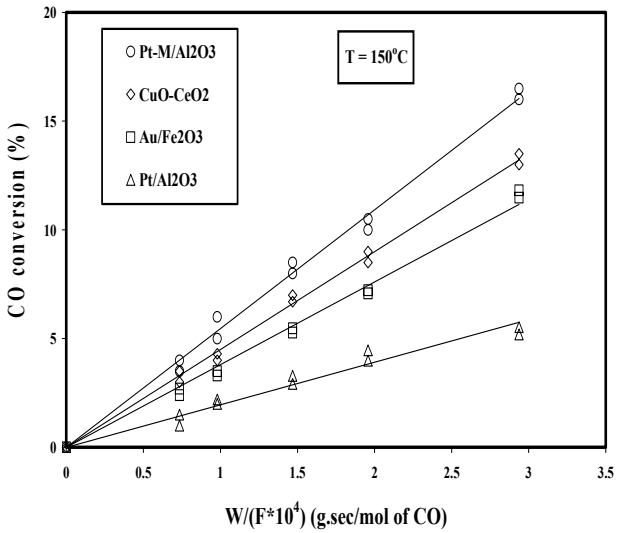

Figure 3. Comparison of the four catalysts in the differential reactor conditions *(T = 150°C)*

Conclusions

Pt/γ-Al_2O_3, promoted Pt-M/γ-Al_2O_3, Au/α-Fe_2O_3, and CuO-CeO_2 have demonstrated promising catalytic activities for selective CO oxidation in integral reactor conditions in the temperature range from 298 to 523K with up to 30% H_2O. Catalytic activities of these four systems have been further evaluated in differential reactor studies in the absence of heat and mass transfer limitations. Specific activities occur in the order: promoted Pt-M/γ-Al_2O_3 > CuO-CeO_2 > Au/α-Fe_2O_3 > Pt/γ-Al_2O_3. Comparison of specific activities and selectivities over the temperature range from 298 to 473K indicate that promoted Pt-M/γ-Al_2O_3 is the best candidate for operation with up to 30% H_2O from 298 to 373K.

References

1. Chen. L.; Chang. B-K.; Lu. Y.; Yang. W.; and Tatarchuk. B. J. Prepr. Pap. - *Am. Chem. Soc., Div. Fuel Chem.*, **2002**, *47* (2), 609.

---

* Corresponding Author. Tel: 1-334-844-2023; Fax: 1-334-844-2065
E-mail address: brucet@eng.auburn.edu

Preferential oxidation of CO in a microreactor with a single channel

L. Bednarova, X. Ouyang, H. Chen, W. Y. Lee, R. S. Besser

Department of Chemical, Biochemical and Materials Engineering, Stevens Institute of Technology, Hoboken, NJ 07030, USA

Introduction

Fuel cells have been extensively studied in the last two decades for different stationary and mobile applications. Hydrogen-rich reformate is the preferred feed for fuel cells and can be produced in a reformer by partial oxidation or steam reforming followed by water–gas shift reaction to reduce CO to about 1%. The remaining CO in the H_2-rich reformate is further decreased to less than 10 ppm CO by selective catalytic oxidation/preferential oxidation of CO ("PrOx") using O_2 or air to avoid poisoning of the Pt anode in the fuel cell.

Therefore, the conversion of CO during PrOx must be at least 99.9% in order to achieve a concentration of 10 ppm or less. Furthermore, the PrOx unit should be operated between 80°C and 200°C to minimize additional heating of cooling steps. Operation at low temperature is also very important for start-up in transportation application fuel cells. Therefore, the PrOx system must operate over a wide temperature range to be practical (1).

Research in the microreactor technologies has been extensive and intensive in the past several years. We have been deeply involved in this research and have now designed a simple, robust microreactor with a single channel for rapid catalyst characterization. The advantage over a multichannel reactor is that possible maldistribution of flow is eliminated. The channel length was estimated by preliminary modeling to be sufficient for treating approximately 5 Ncm^3/min of reformate. This microreactor is also suitable for acquisition of appropriate kinetic data which can be used for design of future PrOx microreactors and for scale up for higher throughputs. The fabrication is inexpensive and straight forward which makes the technology attractive because the microreactors can be disposed after single use.

Catalysts for PrOx usually consist of Pt (2), Au (3) or promoted Pt, Ru, Rh, Pd, alloys of Pt–Sn or Pt–Ru, or Rh (4) supported on alumina (2, 3, 4), silica (4), or zeolites (2). Copper catalysts on alternative supports such as ceria, ceria–samaria, or other ceria-promoted supports are also being developed in an attempt to provide selective surface oxygen for CO oxidation at low temperatures (3).

We fabricated silicon microreactors and deposited a thin-film of Pt/Al_2O_3 catalyst that was prepared by sol-gel technique. Different sequences were used to deposit the catalyst on the microreactor walls. The microreactor was tested for preferential oxidation of CO to reduce CO in reformate. The goal was to reduce CO content in the stream from 1.7% to below 10 ppm using the microchannel reactor.

Experimental

The micro-scale chemical reactors were successfully fabricated on p-type <100> 4 and 8 inch silicon wafers without any oxide layer by using state-of-the-art silicon bulk micromachining techniques. The reactor is comprised of dual gas inlets, a mixing region, and a single reaction channel with outlet. Two different microreactors with different dimensions were tested: the first one had a channel 4.5 cm long, 500 µm wide and 610 µm deep channel (Figure 1a) and the channel in the second one was 21.9 cm long and 500 µm wide and 75 µm deep. Each individual silicon chip was anodically bonded with a Pyrex™ glass piece for hermeticity. The catalyst was deposited in the microchannel either before the silicon chip was sealed with a Pyrex™ glass or after anodic bonding (AB) of chip with the glass.

Platinum supported on alumina was synthesized using a sol-gel technique (5, 6, 7). Alumina support was prepared from aluminum isopropoxide (Aldrich, 99.99+%) by adding it to deionized water at 85 °C to start the hydrolysis reaction resulting in a sol. After 45 min under continuous stirring, HNO_3 was added. Platinum metal was introduced by using a solution of $H_2PtCl_6.xH_2O$ (Aldrich, 99.9+%) in 1,3-butanediol (Aldrich, 99%, anhydrous) at room temperature. The platinum content in the catalyst was 2 wt%.

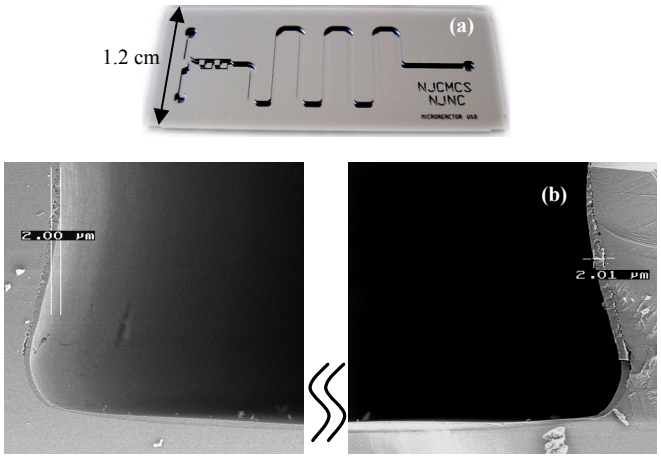

Figure 1. (a) Silicon microreactor for reaction characterization (BL_A3, BL_D7 and BL_ C3 in Table 1); (b) Cross-section of left and right side of microchannel with 2µm layer of catalyst (BL_A3)

The gel (liquid catalyst precursor) deposited in the microchannel was dried in air at 120 °C for 12 hours or at 40 °C for 24 hours, respectively (Table 1), and then calcined at 500 °C for 2 hours. The samples were investigated by XRD (Siemens D5000).

Table 1. Summary of microreactors

Reactor ID	Microchannel length [cm]	Catalyst deposition	Catalyst [mg]	Drying temperature [°C]
BL_A3	4.5	Before AB	0.54	120
BL_D7	4.5	Before AB	0.97	120
BL_C3	4.5	After AB	0.45	120
IT_A2	21.9	After AB	N/A (0.2)[1]	40

The microreactor was tested in a microkinetic array test rig wherein more than one reactor could be characterized simultaneously. In order to begin testing, the reactor was evacuated at room temperature for 30 minutes followed by heating (10°C/min) in pure H_2 (5 Ncm^3/min) to 450 °C and kept at this temperature for 4 hours, then allowed to cool to room temperature. Feed was introduced and temperature was stepwise increased at 10 °C/min from 20 °C to 100 °C, 120 °C, 140 °C, 160 °C, 180 °C, 200 °C, 240 °C, 260 °C, 280 °C and 300 °C. The temperature was kept at each set point for 40-60 min. The feed consisted of simulated reformate (1.7% ^{13}CO, 49.3% H_2 and N_2 as balance) and dry air (78.1% N_2 and 21.9% O_2). The flow of the reformate was kept at 5 Ncm^3/min and dry air at 0.5 Ncm^3/min ($\lambda = 2.57$). The reformate passes through the reaction zone in the microreactor designated "BL" in about 0.1 second and through microreactor "IT" in about 0.9 second. The products were analyzed by gas chromatograph (Varian CP-4900) and mass spectrometer (Stanford Research Systems QMS-200).

[1] estimated to 0.2 mg

Results and Discussion

The surface area of the catalyst is 480 cm^2/g. No peaks were observed on the XRD pattern, which indicates that the alumina structure was amorphous. The adhesion of the catalyst to the microchannel walls is excellent and fairly uniform (Figure 1b).

The feed was introduced at room temperature and no CO conversion was observed. The conversion of CO increased with increasing temperature; however, the activity of the catalyst in all microreactors was low (1st cycles in Figure 2). There did not appear to be a significant difference between performance of the microreactors. Each microreactor after being tested to up to 300 °C was reduced again in pure hydrogen. A new testing cycle was performed (2nd cycles in Figure 2) and CO conversion was monitored. The conversion increased with temperature and catalyst activity improved dramatically for some of them (BL_A3, BL_D7). The differences will be discussed further.

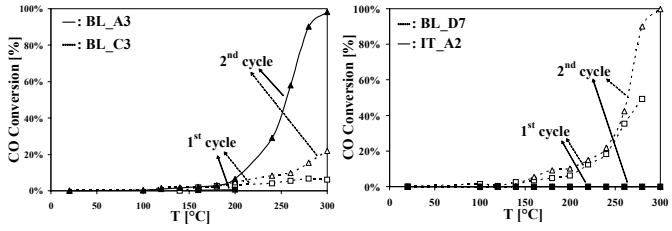

Figure 2. The effect of temperature on CO conversion in microreactors: a/ BL_A3, BL_C3; b/ BL_D7, IT_A2. Feed: 5 Ncm^3/min reformate (1.7% ^{13}CO, 49.3% H_2 and N_2 as balance), 0.5 Ncm^3/min air

Microreactor BL_A3 contains about the same amount of the catalyst as BL_C3 (Table 1) and the geometry of both reactors is identical. The difference between them is that microreactor BL_A3 had the catalyst deposited before being sealed while the other was first sealed and then the catalyst was infiltrated into the closed channel. That means that the microreactor BL_A3 has catalyst deposited on the silicon microreactor as well as on the glass on the top while BL_C3 contains catalyst only on three walls (the silicon part of microreactor). Because the catalyst amount is the same in the reactors, the catalyst layer is thicker in BL_A3 than in BL_C3. However, it is believed that this difference cannot be attributed to the difference in catalytic activity. It is proposed that the catalytic activity is rather enhanced due to performed pretreatment. The microreactor BL_A3 with catalyst was exposed during anodic bonding to 450 °C in furnace without controlled environment followed by *in-situ* reduction at 450 °C in the test rig (oxidation-reduction pretreatment). The latter microreactor (BL_C3) was pretreated only by reduction.

The microreactors were tested across a wide temperature range, starting at room temperature and increasing in steps to up to 300 °C. As mentioned before, the catalyst activity was low in the investigated temperature range. The microreactors with the thin-film catalyst were studied further. The microreactors were reinstalled in the microkinetic array and reduced again as they were exposed to air while stored. Reformate was introduced again at room temperature and stepwise increased to 300 °C as during previous testing (Figure 3a). The activity of catalysts in all microreactors was higher than during the first cycle of testing. There can be at least two explanations: (a) platinum was not fully reduced during the first testing cycle; (b) the catalyst behavior changed, possibly due to catalyst structural changes. We believe that the second possibility is more likely because the platinum was reduced before each cycle following the same procedure and the microreactors were exposed to air before each reduction. It appears that repeated catalyst exposure to higher temperature is likely an important factor in enhancing the catalyst activity.

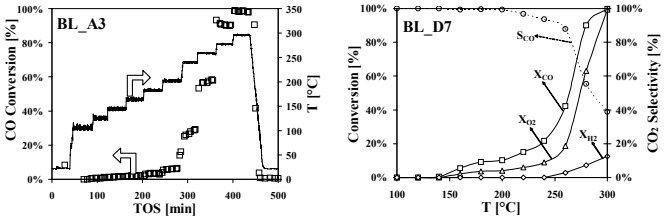

Figure 3. a/ CO conversion as a function of temperature and time on stream (reactor BL_A3); b/ Effect of temperature on conversion of CO, O_2 and H_2 (microreactor BL_D7). Feed: 5 Ncm^3/min reformate (1.7% ^{13}CO, 49.3% H_2 and N_2 as balance), 0.5 Ncm^3/min air

It should be noted that the microreactors with a highly active catalyst show a characteristic behavior. The conversion of CO increases with increasing temperature fairly linearly and there is a characteristic temperature at which we observe a steep increase in conversion reaching almost 100%. This is in agreement with previous studies (8). When the conversion of CO reached almost 100% we observed that hydrogen starts to oxidize, thus, the selectivity towards CO_2 decreases dramatically (Figure 3b). Therefore, there is a narrow temperature window at which high CO conversion can be obtained and consumption of hydrogen is not yet significant.

Conclusions

Thin-film Pt/Al_2O_3 catalyst was deposited on walls of microreactors with two methods and its activity was evaluated after different pretreatments. It was found that a more active catalyst is obtained after oxidation-reduction pretreatment than after only reduction. Moreover, the catalysts became more active after repeated catalytic testing.

Acknowledgement. The authors gratefully acknowledge the support of DARPA (Contract No. N66001-01-X-6039) and Stevens Institute of Technology. They also thank Dr. Stanley Pau of the New Jersey Nanotechnology Consortium (NJNC) at Bell Labs for fabricating some of the reactors.

References

(1) Thomas, C. E.; James, B. D.; Lomax Jr., F. D.; Kuhn Jr., I. F. *Int. J. Hydrogen Energy* **2000**, *25*, 551.
(2) Igatashi, H. ; Uchida, H.; Suzuki, M. ; Sasaki, Y.; Watanabe, M. *Appl. Cat. A:General* **1997**, *159*, 159.
(3) Avgouropoulos, G.; Ioannides, T. ; Papadopoulou, Ch.; Batista, J.; Hocevar, S.; Matralis, H. K. *Catalysis Today* **2002**, *75*, 157.
(4) Dudfield, C. D. ; Chen, R.; Adcock, P. L. *Int. J. Hydrogen Energy* **2001**, *26*, 763.
(5) Yoldas, B. E. *Am. Ceramic Soc. Bul.*, **1975**, *54(3)*, 289.
(6) Manasilp, A.; Gulari, E. *Appl. Cat. B: Environmental* **2002**, *37,* 17
(7) Besser, R.S.; Zhao, S. *Proc. 6th Int. Conf. Microreac. Techn. - IMRET VI*, **2002**, 289.
(8) Kahlich, M. J., Gasteiger, H. A., Behm, R. J. *J. Catal.* **1997**, *171*, 93.

PREFERENTIAL OXIDATION OF CO ON A NOBLE-METAL CATALYST COATED CERAMIC MONOLITH

*Rajesh K. Ahluwalia, Qizhi Zhang, and Michael A. Inbody**

Argonne National Laboratory, Argonne, IL
*Los Alamos National Laboratory, Los Alamos, NM

Introduction

Whereas the anode catalyst, typically Pt-Ru, in the polymer electrolyte fuel cells has low tolerance for carbon monoxide, 10-100 ppm, reforming of gasoline and other hydrocarbon fuels generally produces 1-2% of CO. Of the many methods of removing CO from the reformer gas, such as membrane separation of H_2 and methanation, preferential oxidation (PrOx) of CO over noble-metal catalysts is practiced most frequently.[1, 2] One index for characterizing the performance of a PrOx catalyst is CO selectivity (*S*) defined as the ratio of oxygen consumed by the desired CO reaction to the total oxygen consumed by the parallel CO and H_2 oxidation reactions. Another related index is the process stoichiometry λ which is the ratio of oxygen used in relation to the theoretical amount needed for complete conversion of CO.

From the standpoint of process efficiency, it is desirable to select the PrOx catalyst and operating conditions that lead to *S* and λ being as close to unity as possible. Additional considerations arise if reforming is to be carried out onboard a vehicle. For fast start, the PrOx reactor must be compact and, in particular, the thermal mass of the catalyst and the components in contact with the flow should be minimized. The catalyst should maintain the fuel processor outlet CO concentration within the fuel cell stack tolerances through the startup transient and transition to normal operation. For cold start, it helps if the catalyst has low light-off temperature for CO oxidation. The catalyst should retain CO selectivity over the range of temperatures representative of cold start and normal operation. It should be capable of oxidizing high concentrations of CO if the upstream water gas shift reactor is not operating at its optimal temperature as at start-up and during up-load transients.

The purpose of this paper is to present recent results on a low temperature, supported PrOx catalyst that has shown light-off for CO oxidation at room temperature. The focus is on taking data from single-stage PrOx experiments under steady-state conditions and applying them to multi-stage reactors.

Experimental

Engelhard Spectra-PROX I catalyst was coated on a 600-cpsi (cells per square inch) Corning monolith, 7.62 cm in diameter by 12.7 cm long, and evaluated in a single-stage test reactor shown in Fig. 1. The coated monolith, 297 g in mass, was instrumented with 0.02" K-type thermocouples inserted to various depths from the top of the monolith. The tests were conducted with a reformed gas of nominal composition 1.3% CO, 48.0% H_2, 19.8% CO_2, and 30.9% N_2 at inlet temperature of 85–100°C, the variation in temperature being caused by the injection of steam. The major gas flows were set and the air injection was varied to obtain measurements over a wide range of oxygen stoichiometry usually to identify the minimum CO concentration and limited to an outlet temperature below 300°C. The experiments were conducted at the same pressure, ~1.5 bar.

In all nine series of tests were conducted by varying CO concentration, H_2O concentration, and space velocity. The test matrix included three levels of CO concentration (0.2%, 1% and 2.6%), two levels of H_2O concentration (0 and 20%), and two levels of space velocity (15,000 and 30,000/h). Addition of steam and air resulted in the inlet CO concentration varying between 0.17 and 0.2% in the low range and between 1% and 1.3% in the medium range and in the space velocity varying between 31,300/h and 38,000/h at high flow rates and between 14,800/h and 19,000/h at low flow rates.

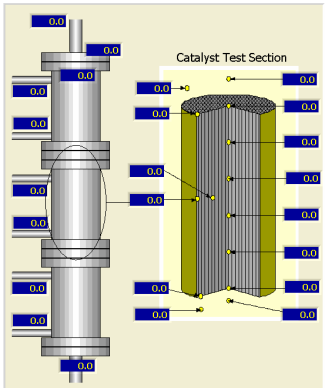

Figure 1. PrOx single-stage configuration for measurement of catalyst temperature response.

Within each series of tests oxygen stoichiometry was the variable. In all tests, the outlet oxygen concentration was below the detection limit. Tests with and without steam showed little change in the outlet CO concentration suggesting that the kinetics of water-gas shift reaction over the Pt catalyst formulation in the temperature range 100-300°C is quite slow in comparison to the oxidation reactions. Figure 2 presents typical axial temperature profiles from a test series with dry reformate, 1.3% inlet CO concentration and 30,000/h space velocity. These suggest that the oxidation reactions are essentially complete half way across the reactor for λ = 2 but continue down the length for λ < 1.

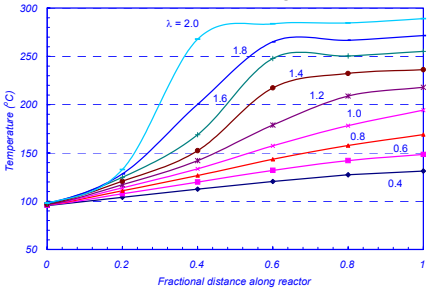

Figure 2. Measured temperature profiles for different oxygen stoichiometry at 1% inlet CO concentration and 30,000/h nominal space velocity.

We attempted to develop a correlation for CO selectivity at 30,000/h space velocity by analyzing the data at high flow rates. A plot of selectivity as a function of stoichiometry for different inlet CO concentrations revealed that *S* can be represented as a function of the reduced parameter $\lambda X^{1/4}$, where *X* is %CO concentration at inlet. A second-order polynomial in $\lambda X^{1/4}$ gave an adequate correlation of selectivity with the coefficients themselves second-order polynomials in *X*. In developing the correlation given below it was assumed that the selectivity approaches one as $\lambda X^{1/4}$ goes to zero and λS was constrained to be always less than one.

$$S = 1 - (0.6394 - 0.6004X + 0.1352X^2)(\lambda X^{1/4}) + (0.0825 - 0.1554X + 0.0251X^2)(\lambda X^{1/4})^2$$

Figure 3 compares the correlation with the data and shows that CO selectivity decreases with λ and increases with CO concentration for λ < 0.8, but the behavior with respect to CO concentration is more complex for λ > 0.8.

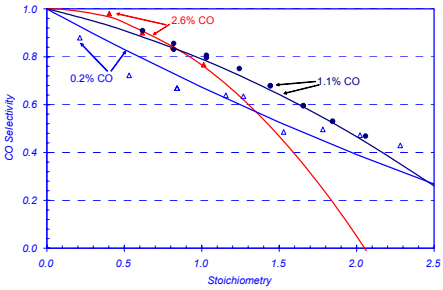

Figure 3. Correlation of selectivity data for 30,000/h nominal space velocity.

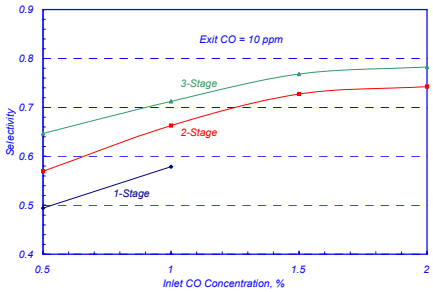

Figure 5. Optimum CO selectivities in one-, two-, and three-stage reactors with gas cooled to 100°C between the stages.

Results and Discussion

Figure 4 shows CO conversion and selectivity in a single-stage PrOx reactor calculated using the above correlation for 100°C inlet gas temperature. For 1% inlet CO concentration, the exit CO concentration decreases monotonically with oxygen stoichiometry, becoming vanishingly small at λ = 1.8, and increases thereafter. We conclude that for inlet CO concentration less than 1%, a single-stage reactor is capable of reducing CO to any level and should always be operated at λ < 1.8. A different behavior is seen at 1.5% inlet CO concentration. Here, the exit CO concentration decreases with λ until it reaches a minimum of 300 ppm at λ = 1.5 and begins to rise as λ is raised further. The CO selectivity actually goes to zero at λ = 2.6 and all added O_2 is consumed by the oxidation of H_2. Thus, more than one stage is required to reduce CO concentration to less than 300 ppm if the inlet CO concentration is 1.5% or higher.

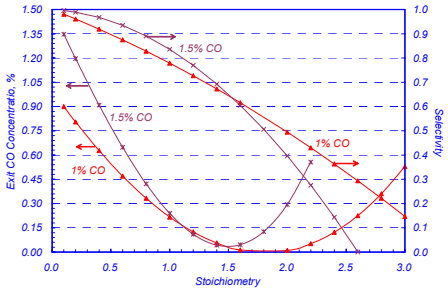

Figure 4. CO conversion and selectivity in a single-stage monolith reactor.

We have used an optimization algorithm to determine the operating conditions of an intercooled multi-stage PrOx reactor that can reduce CO concentration to 10–100 ppm at highest selectivity. It is assumed that the reformed gas is cooled to 100°C between stages. Typical results for 10-ppm exit CO concentration, shown in Fig. 5, confirm that the highest CO concentration that can be handled in a one-stage monolith reactor is about 1%. The CO selectivity in a one-stage reactor is 48% at X = 0.5% and 58% at X = 1%. A two-stage reactor can achieve optimum selectivities of 57% at X = 0.5%, 66% at X = 1%, and 75% at X = 2%. With a three-stage reactor, it is possible to obtain selectivities of 65%, 71% and 78% at inlet CO concentrations of 0.5%, 1% and 2%, respectively. At 1% inlet CO concentration, the optimum stoichiometries are 1.0 for stage 1, 1.1 for stage 2 and 2.3 for stage 3. The first stage has a selectivity of 77% and reduces the CO concentration to 0.2% from 1%. The second stage has a selectivity of 64% and reduces the CO concentration to 0.07% from 0.2%. The third stage has a selectivity of 42% and reduces CO concentration to 10 ppm from 0.07%. Together, the three stages have a combined overall stoichiometry of 1.4 and selectivity of 71%.

For more general application, the experimental data was used to derive a kinetic model of CO conversion. It was found that the intrinsic kinetics for CO and H_2 oxidation on the catalyst could be represented by the following power-law expressions.

$$r_{CO} = A_{cat} k_{CO} e^{-E_{CO}/RT} P_{CO}^{\alpha_1} P_{O_2}^{\beta_1}$$

$$r_{H_2} = A_{cat} k_{H_2} e^{-E_{H_2}/RT} P_{H_2} P_{CO}^{\alpha_2} P_{O_2}^{\beta_2}$$

where r is the reaction rate (mol/m^3.s) and A_{cat} is the specific internal and external area of the catalyst (m^2/m^3). From data fitting and experience of others with noble metal catalysts,

$E_{CO} = 83$ kJ/mol, $E_{H_2} = 107.6$ kJ/mol, $k_{CO} = 2.95x10^6$ mol/m^2.s,

$k_{H_2} = 1.4x10^8$ mol/m^2.s, $\alpha_1 = -0.5$, $\beta_1 = 0.85$, $\alpha_2 = -1.0$, and

$\beta_2 = 0.75$. We found that CO and H_2 oxidation on the coated ceramic monolith are affected by both the intrinsic kinetics and mass transfer. At low CO concentration, CO conversion and selectivity are determined by the mass transfer limitation. The model also indicates that CO selectivity decreases with gas temperature.

Conclusions

It is feasible to conduct preferential oxidation of CO on a noble-metal catalyst coated ceramic monolith at 100°C to produce a PEFC quality gas at space velocities in excess of 38,000/h. A single-stage reactor can reduce CO concentration from 1% to 10 ppm or lower at a selectivity of 58%; more than one stage is needed for inlet CO concentration higher than 1.5%. Under the same conditions a two-stage reactor yields a selectivity of 66%. The selectivity can be further improved to 71% by incorporating a third stage. The CO selectivity decreases as CO concentration is lowered. With a three-stage reactor, it is preferable to operate stages one and two under near-stoichiometric conditions and use excess oxygen in the last stage where the CO concentration is the lowest. Numerical simulations show that at low CO concentration, conversion is limited by diffusion of CO from the bulk phase to the surface of the catalyst. Under this condition, parallel oxidation of H_2 can only be controlled by also limiting the diffusion of O_2 to the catalyst. Finally, the activation energy is higher for H_2 oxidation than for CO oxidation so that CO selectivity always decreases with temperature.

Acknowledgement. This work is supported by the Office of Hydrogen, Fuel Cell and Infrastructure Technologies (HFCIT), U.S. Department of Energy. Dr. Nancy Garland is the program manager.

References

(1) Kahlich, M. J.; Gasteiger, H. A.; Brehm, R. J.; *J. Catalysis*, **1997**, 171, p. 93-105.

(2) Dudfield, C.D.; Chen, R.; Adcock, P.L.; *J. Power Sources*, **2000**, 86, p. 214-222.

PROCESSING OF GOLD NANOPARTICLES AS FUEL CELL CATALYSTS

*Jin Luo, Mathew M. Maye, Vivian W. Jones[+], Chuan- Jian Zhong**

Department of Chemistry, State University of New York at Binghamton, Binghamton, NY 13902. [+] 3M Corporate Analytical Technology Center, 3M Center, St. Paul. Minnesota 55144.
*cjzhong@binghamton.edu

Introduction

The study of nanosized gold catalysis has attracted increasing interest because of the discovery of unprecedented catalytic activity and specificity of gold at nanometer sizes [1,2]. The catalytic activity of such materials requires the ability to manipulate the interparticle spatial and surface access properties [3]. This ability is inherently linked to the controllable activation of the core-shell nanostructure, or removal or reconstitution of the shell components. We report here recent findings of an investigation of core-shell assembled gold and alloy nanoparticles as catalysts for electrooxidation of carbon monooxide and methanol. This investigation is aimed at understanding the structural and morphological evolution upon catalytic activation.

Experimental

We synthesized gold nanoparticles of 2-nm core size (1.9 ±0.7 nm, $Au_{2\text{-nm}}$) capped with decanethiolate (DT) monolayer shell using two-phase method [4]. The particles were assembled as a thin film on freshly-cleaved mica or polished glassy carbon (GC) substrates (0.5 cm^2) by exchange-crosslinking-precipitation route using 1,9-nonanedithiolate (NDT) as a linking or wiring agent [5]. Such a film consists of both wiring NDT and capping DT molecules. The thickness was controlled by assembling time and monitored by surface plasmon resonance absorbance and mass loading [5], which was equivalent to a few monolayers or sub-monolayer coverages.

Results and Discussion

Figure 1 shows a typical set of AFM phase images for a thin film on mica surface to compare the morphology before and after the thermal treatment at 225 °C for 30 min. The particles are clustered into wire or chain-like morphologies. From cross-section data of corresponding topographic images, we found that there was an overlapping of ~3 nanoparticles in average [6]. The outline of individual nanoparticles is slightly blurred or not well resolved. After the treatment, not only the outline of individual particles is better resolved, but also the chain-like feature remains intact. The removal of thiolates at this temperature was clearly supported by the tapping-mode phase imaging data. This set of data reveals that the phase contrast, which is associated with the thiollate monolayer on the gold nanoparticle, is change upon thermal activation. Before thermal treatment, it was dark contrast (Figure 1 a); After thermal treatment, the dark contrast disappeared (Figure 1 b). In addition, our height analysis of the cross-section data reveal 11.1 ±3.9 nm and 13.1 ±3.4 nm (not shown), respectively, suggesting little change in height. The small increase in particle size is believed to be due to localized aggregation largely from the overlapped particles. The unchanged interparticle spatial feature in the xy-plane demonstrates that the interparticle spatial property can be controlled even if there is a local aggregation from the overlapped nanoparticles. The combination of the initial molecular wiring and the subsequent adhesive interaction of the particle to the substrate must have played an important role in the spatial fixation. The results of infrared reflection spectroscopic analysis (Figure 2) provide the further evidence for the removal of hydrocarbons. Our XPS data (not shown) also supported the removal of sulfur species after the thermal treatment.

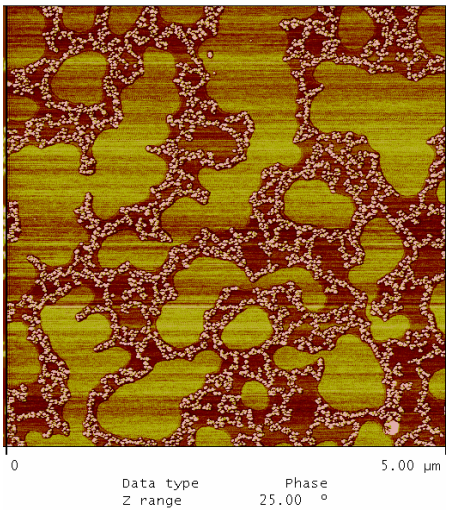

(a)

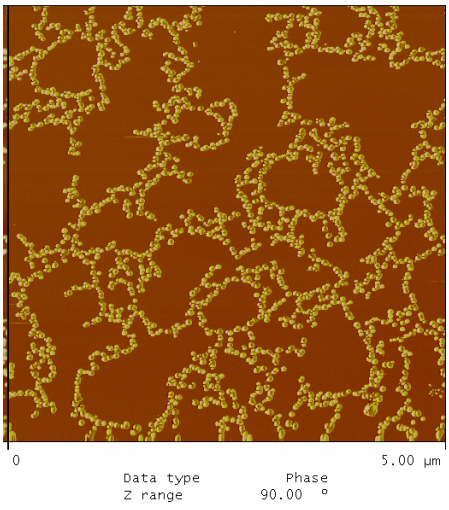

(b)

Figure 1. In-situ AFM phase images of a NDT-$Au_{2\text{-nm}}$/mica film (a) before and (b) after heating to 225 °C for 30 min.

The catalytic activity of the activated nanoparticles was examined for the electroxidation of CO and methanol. We note that AFM feature of the film on the conductive GC substrate is largely

similar to that on mica except for a much rougher morphology due to the substrate effect. We compare the electrocatalytic activity between the thermally activated gold catalysts with the electrochemically activated catalysts based on voltammetric data. The anodic current density for the thermally-activated film is twice as large as the electrochemically-activated catalyst (same film thickness), with the oxidation potential being slightly less positive than the electrochemically-activated film. The results demonstrate that the nanostructured catalytic activity can be thermally activated by the controlled temperature.

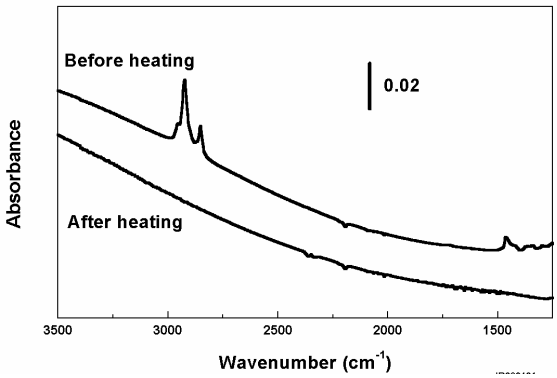

Figure 2. IRS spectra for an NDT-$Au_{2\text{-nm}}$/Au/glass film before and after heating at 250 °C for 30 min. The spectral background for the entire spectral region is not corrected.

In conclusion, we have shown that the activation of the catalytic activity of the catalysts can be controlled by manipulation of the core-shell structure, interfacial reactivity, and adhesions to the supporting substrate. These findings have important implications to the design and processing of nanostructured catalysts. We are currently investigating different molecular structures of the wiring agents, and developing an in-depth understanding of the size evolution as a function of temperature and substrate properties.

References

(1) Haruta, M. *Catal. Today*, **1997,** *36*, 153.
(2) Valden, M.; Lai, X.; Goodman, D. W. *Science*, **1998**, *281*, 1647.
(3) Zhong, C. J.; Maye, M. M. *Adv. Mater.*, **2001**, *13*, 1507.
(4) Brust, M.; Walker, M.; Bethell, D.; Schiffrin, D. J.; Whyman, R. *J. Chem. Soc., Chem. Comm*. **1994**, 801.
(5) (a) Leibowitz, F. L.; Zheng, W. X.; Maye, M. M.; Zhong, C. J. *Anal. Chem.*, **1999**, *71*, 5076. (b) Zheng, W. X.; Maye, M. M.; Leibowitz, F. L.; Zhong, C. J. *Anal. Chem*., **2000,** *72*, 2190.
(6) Luo, J.; Jones, V. W.; Maye, M. M.; Han, L.; Kariuki, N. N.; Zhong, C. J. *J. Am. Chem. Soc.*, **2002**, *124*, 13988.

LANTHANIDE-PROMOTED SOL-GEL Ni-BASED CATALYSTS FOR STEAM REFORMING OF PROPANE

Sittichai Natesakhawat, Okan Oktar, and Umit S. Ozkan

Department of Chemical Engineering
The Ohio State University
140 W. 19th Ave.
Columbus, OH 43210

Introduction

Steam reforming of hydrocarbons to produce hydrogen is a well-established industrial process.[1,2] It is usually performed at high temperatures (500-950 ^{o}C) over Ni-based catalysts. However, these catalysts suffer from coke formation more severely when higher hydrocarbons are reformed at low steam/carbon ratios. Recently, on-board steam reforming of hydrocarbons for proton exchange membrane (PEM) fuel cell-powered vehicles has attracted much attention. Widespread applications of fuel cells in transportation will depend on the development of an effective and efficient fuel processing technology from existing liquid fuels. Therefore, development of novel catalysts with improved catalytic activity and stability for the steam reforming process is essential.

There is evidence in the literature pointing to an increase in the coking resistance of Ni-based catalysts with an addition of lanthanide elements.[3,4] Zhuang et al.[3] investigated the effect of cerium oxide as the promoter in supported nickel catalysts for methane steam reforming at 550 ^{o}C. It showed a beneficial effect by not only decreasing the rate of carbon deposition but also increasing the catalytic activity. Su and Guo[4] reported an improvement in the stability and high-temperature steam resistance of Ni/α-Al_2O_3 catalysts doped with rare earth oxides in methane steam reforming. The growth of Ni particles and the formation of inactive NiO and $NiAl_2O_4$ phases were suppressed by the addition of rare earth oxides (4 wt%). In addition, oxides of heavy rare earth elements (Gd, Er, and Dy) exhibited a more pronounced effect than that of the light ones (La, Pr, Nd).

This paper presents results of propane steam reforming over sol-gel Ni-based catalysts promoted with La, Ce, and Yb. The effect of adding these lanthanide elements on reaction performance and properties of the catalysts will be discussed.

Experimental

Catalyst preparation. Sol-gel Ni/Al_2O_3 catalysts promoted with La, Ce, and Yb were prepared by a sol-gel technique. Metal nitrates (99.999 wt%, Aldrich) and aluminum tri-*sec*-butoxide (ATB) (Aldrich) were used as metal precursors. Ethanol (Alfa Aesar) of 130 cm^3 was used as a solvent. The H_2O/ATB molar ratio was kept constant at 3.6. Initially, ATB was added into ethanol and the mixture was subsequently mixed vigorously. The aqueous solutions of metal nitrates were then added dropwise to the ATB-ethanol mixture using a syringe pump at the flow rate of 0.49 cm^3/min. The pH of the resulting gel was measured and adjusted to pH = 4.8 by adding HNO_3 or NH_4OH. The samples were stirred for an additional 15 min and were kept at the room temperature for 30 min. The samples were subsequently dried in the oven at 110 ^{o}C overnight. The dry samples were ground into a fine powder and were calcined in flowing O_2 at 450 ^{o}C for 4 hr. It is noted that Ni and lanthanide contents were 20 wt% and 2 wt%, respectively for all catalysts prepared. For simplicity, all the catalysts prepared were denoted to indicate compositions: for example, 20Ni2YbAl represents 20%Ni-2%Yb/Al_2O_3 catalyst.

Reaction studies. Steam reforming of C_3H_8 was carried out in a 1/4 in. O.D. stainless steel flow reactor at 400-550 ^{o}C at atmospheric pressure. The total flow rates were 300-400 cm^3(STP)/min. The feed stream consisted of C_3H_8, H_2O, and N_2 as a diluent. The catalyst weight was varied between 30 and 50 mg in order to keep the total surface area in the reactor constant at 9 m^2. Prior to the reaction, catalysts were reduced *in situ* in flowing 20% H_2/N_2 of 50 cm^3/min at 600 ^{o}C for 2 hr. The catalysts were flushed with N_2 and then cooled to the desired reaction temperature. The effluent from the reactor was analyzed using an automated Shimadzu GC-14A equipped with FID and TCD detectors. A GOW- MAC 069-50 ruthenium methanizer operated at 350 ^{o}C was used with the FID for acurate determination of CO and CO_2. Reaction experiments were conducted for 20 hr until it reached a steady state. The product distributions maintained a carbon balance of 100% (±5%).

Catalyst Characterization. BET surface areas, pore volumes, and pore size distributions of sol-gel Ni-based catalysts were determined by N_2 adsorption-desorption at 77 K using a Micromeritics ASAP 2010 instrument. Temperature-programmed reduction (TPR) experiments were performed using a laboratory-made gas flow system. 10% H_2/Ar was used as a reducing gas at the total flow rate of 40 cm^3/min. The temperature of the catalyst samples was raised using the temperature program as follows: 10 min at room temperature, ramp rate of 10 ^{o}C/min to 900 ^{o}C, and 10 min at 900 ^{o}C. H_2 consumption was measured using a thermal conductivity detector (TCD) connected to a data-acquisition computer. The XRD analysis was carried out using a Scintag PAD-V diffractometer using Cu K_α radiation operated at 45 kV and 20 mA.

Results and Discussion

C_3H_8 conversion at 500 ^{o}C as a function of time on stream for different sol-gel Ni-based catalysts is plotted in Figure 1. It is clearly seen that the 20Ni2YbAl and 20Ni2CeAl catalysts showed significant improvement in both catalytic activity and stability compared to the monometallic 20NiAl catalyst.

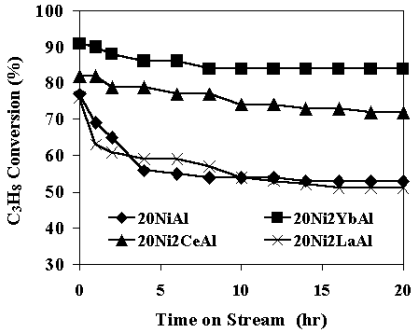

Figure 1. C_3H_8 conversion as a function of time on stream for different sol-gel Ni-based catalysts [Reaction conditions: 500 ^{o}C, 1 atm, total flow rate = 300 cm^3(STP)/min, $C_3H_8/H_2O/N_2$ = 1:4:95, equal surface area reactions (9 m^2), GHSV > 250,000 hr^{-1}].

On the other hand, the activity of the 20Ni2LaAl catalyst was comparable to that of the 20NiAl catalyst. The catalytic activity of C_3H_8 steam reforming at 500 ^{o}C decreased in the following order:

20Ni2YbAl > 20Ni2CeAl > 20Ni2LaAl ≈ 20NiAl

It is noted that all bimetallic catalysts have higher BET surface areas (230-300 m^2/g) than the monometallic catalyst (209 m^2/g). The TPR profiles of sol-gel Ni-based catalysts are shown in Figure 2. The position of the peak maximum shifted towards lower temperatures (570-600 ^oC) for all bimetallic catalysts. This high-temperature (HT) broad reduction peak may be due to bulk reduction of Ni in crystalline NiO or $NiAl_2O_4$ phase. On the other hand, a small low-temperature (LT) reduction peak around 400 ^oC could be attributed to the reduction of a well-dispersed and possibly amorphous NiO phase on the alumina support surface. However, the LT reduction peak could not be observed for the Ce-promoted catalyst. It is concluded that the reduction of Ni species is facilitated by the presence of lanthanide elements in the Al_2O_3-supported Ni catalysts.

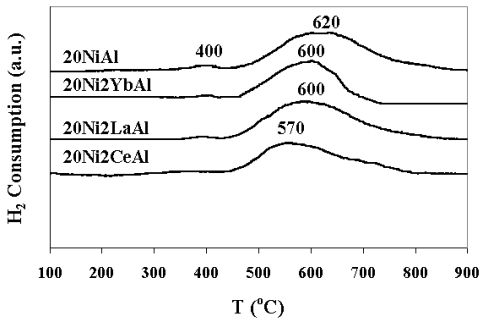

Figure 2. The TPR profiles of sol-gel Ni-based catalysts.

The XRD patterns of sol-gel Ni-based catalysts were obtained after calcination under O_2 at 450 °C. The major crystalline phases correspond to NiO, $NiAl_2O_4$, and γ-Al_2O_3. However, it is difficult to distinguish between $NiAl_2O_4$ and γ-Al_2O_3 because the diffraction lines of these two phases overlap, as evidenced by broad peaks.[5] No lanthanide-related crystalline phases could be detected. It is suggested that the lanthanide species could be well-dispersed or could exist in the form of a two-dimensional overlayer on the alumina support undetectable by XRD.[6]

It is known that metallic nickel is the active site for steam reforming reaction. As shown in Figure 3, after reduction under 20%H_2/N_2 at 600 ^oC, the metallic Ni crystalline phases [(111), (200), (220)] were observed at 2θ = 44.5, 51.8, and 76.4^o, respectively. Moreover, the NiO phase seemed to disappear while the diffraction lines of $NiAl_2O_4$ spinel were retained.

TPR results suggested that the activity of sol-gel Ni-based catalysts depended on the catalyst reducibility. More detailed reaction experiments and catalyst characterization are underway to investigate the promotion effect of lanthanide elements on sol-gel Ni-based catalysts.

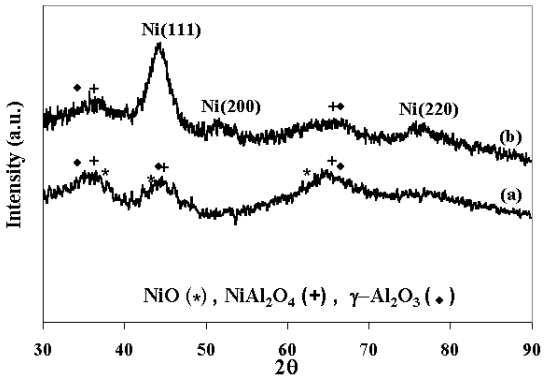

Figure 3. The XRD patterns of the sol-gel bimetallic 20Ni2YbAl catalysts after: (a) calcination at 450 ^oC (b) reduction at 600 ^oC.

Conclusions

Sol-gel Ni-based catalysts promoted with lanthanide elements such as La, Ce, and Yb have been synthesized and tested in steam reforming of propane at 500 ^oC and H_2O/C_3H_8 = 4. It was found that the addition of Yb or Ce (2 wt%) into the Ni/Al_2O_3 catalyst improved both catalytic activity and stability significantly. TPR results further revealed that the catalytic activity was influenced by catalyst reducibility.

Acknowledgement. The financial support provided by Honda Research Institute, USA Inc. is gratefully acknowledged.

References

(1) Rostrup-Nielsen, J.R. In *Catalysis: Science and Technology*; Anderson, J.R. and Boudart, M., Eds.; Springer: New York, 1984, pp. 3-117.
(2) Ridler, D.E. and Twigg M.V., in: M.V. Twigg (Eds.), Catalyst Handbook, Wolfe, London, 1989, pp. 225-282.
(3) Zhuang, Q.; Qin Y.; and Chang L. Appl. Catal. **1991**, *70*, 1.
(4) Su, B.-L. and Guo, S.-D, In *Catalyst Deactivation*; Delmon, B. and Froment, G.F., Eds.; Elsevier: Amsterdam, 1999; pp. 325-*.
(5) Vos, B.; Poels, E.; and Bliek, A. J. Catal. **2001**, *198*, 77.
(6) Bettman, M.; Chase, R.E.; Otto, K.; and Weber, W.H. J. Catal. **1989**, *117*, 447.

OPERATION OF DIRECT CARBONATE FUEL CELL WITH PROPANE

Sai P. Katikaneni, C.Y. Yuh, T.W. Lee and M. Farooque*

FuelCell Energy, Inc.
3 Great Pasture Road
Danbury, CT 06813, USA

skatikaneni@fce.com
Phone: (203) 825-6067
Fax: (203) 825-6273

Carbonate fuel cells are new generation of power plants that provide electricity at very high efficiency and low environmental emissions. FCE's "direct carbonate fuel cell" operates on a variety of hydrocarbon fuels such as natural gas, biogas, coal gas, diesel and LPG. Conventionally, an external reformer is used to supply hydrogen rich gas to fuel cell. FuelCell Energy's DFC™ technology has adopted an internal reforming approach that eliminates the need for an external reformer, resulting in increased efficiency, compactness, better thermal management and lower cost.

DFC operation on natural gas, peak shaving gas, LPG, digester gas, syngas, coal bed methane, and liquid fuels such as diesel, methanol and ethanol has been already demonstrated. Fuel clean-up and fuel processing operation varies based on the nature of fuel. However, the fuel thus supplied to the fuel cell has a two-step refinement approach. Step 1 involves fuel clean up system to remove impurities such as sulfur, halides, solid particulates, aromatic hydrocarbons, and oxygen. The second step is pre-reforming desulfurized fuel to knock out higher hydrocarbons in order to eliminate coke formation during reforming inside the fuel cell. Methane-rich gas obtained from pre-reformer is thus fed into fuel cell for internal reforming to produce hydrogen in DFC stacks which in turn is electrochemically converted to water, thereby producing DC power. At each stage of this operation, catalysts are used to facilitate production of desirable fuel cell fuel.

Fuel clean-up considerations vary with type of fuel and its constituents. The nature of impurities and their concentration will be considered to design suitable clean-up processor for each type of fuel for DFC applications. Table 1 indicates various fuels specification including type of impurities and their levels for designing clean-up processor. The impurities present in fuels will impact the performance of reforming catalysts, cell performance and overall life of fuel cell. Ni-based catalysts are used for internal reforming and prereforming of higher hydrocarbons. Nickel catalysts are sensitive for sulfur, chloride and particulate poisoning, thus, require impurity-free fuel for fuel cell applications. The tolerance level of these impurities on both catalyst and fuel cell components are significantly lower than conventional fuel processing operations. Also, the tolerance level is based on the type of impurity. Although worldwide standards favor a gradually lowering sulfur and other impurity levels in transportation fuels, it is necessary to further reduce the sulfur levels in fuel cells to sub-ppm levels prior to use in fuel cell power plants. Depending on the nature of fuel and impurity levels, an appropriate fuel clean-up process with suitable adsorbents/catalysts is required in DFC balance of power plant operation.

FCE has designed propane clean-up processor and propane prereformer to meet DFC fuel cell grade fuel. This presentation will discuss FCE's experience with operation of DFC on propane and focusing on clean-up considerations, LPG compositions and its effect on fuel processing operations, prereforming results, steam to carbon effects on prereforming and 30 kW stack operation with propane.

SIMULATION TOOLS FOR THE DESIGN OF VISION 21 ENERGY PLANTS

Thomas J. O'Brien[†], *Stephen E. Zitney*[‡], *William Rogers*[†], *and Anthony Cugini*[†]

[†]National Energy Technology Laboratory
3610 Collins Ferry Road
Morgantown, WV 26507-0880

[‡]Fluent, Inc.
3647 Collins Ferry Road
Morgantown, WV 26505

Introduction

The development of energy systems that use fossil fuels efficiently is needed to achieve the energy goals of the U.S. through the twenty-first century. The demands of environmental stewardship require placing a greater emphasis on clean energy options while, at the same time, global competitiveness creates a market atmosphere that rewards cost-effectiveness. In addition, the time and expense of developing and demonstrating new technological systems must be reduced. With tightening research budgets, the use of numerical simulation offers an effective supplementary approach to aid in the design, development, and evaluation of new clean energy technologies.

Currently, many modeling and simulation tools are being used for energy technology development. These are being integrated into platforms for performing complete virtual demonstrations of advanced fossil energy systems. Integration of existing modeling tools is the largest development need. At present, most process engineering applications for systems architectural and engineering designs, heat and mass constitutive simulations, cost estimations, and synthetic environment visualizations are self-contained, and each provides its own user interface. Integration of these tools within a virtual reality structure will provide a powerful cost-reducing tool to examine Vision 21 energyplex options.

At the heart of this development is the challenge of bridging the time and length scales that relate microscopic scientific understanding to macroscopic engineering design, an issue frequently addressed by quantum chemists[1,2]. For example, continuum solvation models based on quantum chemical calculations of the individual compounds in a mixture are being used to calculate thermodynamic properties of fluid mixtures[3]. Such fundamental models should become a valuable supplement for the well-established methods used in engineering design, namely group contribution methods, other activity coefficient models, and equation-of-state models. In addition, it should now be feasible to use the results of quantum chemical calculations to predict rate constants and thermodynamic data required for chemically reactive computational fluid dynamics, which can now be coupled with process simulation. This process requires the systematic reduction of higher-order models to consistent lower-order models, which can then be utilized in analysis at the larger scale.

For example, Vision 21 simulations of fuel cell processes consider a hierarchy of models ranging from molecular-level models to component-level models to overall system models. Molecular-level models are focused on phenomena occurring at the surface of the fuel cell membrane. Component models (e.g., fuel cell, reformer, gasifier) range from models based on engineering correlations to complex computational fluid dynamics (CFD) models that consider the hydrodynamics, heat transfer, multicomponent transport, electrochemical kinetics, and current distribution in a fuel cell[4,5]. Such models are required to optimize the design of individual components in a fuel cell process (e.g., reactor geometry, fuel distributor design, temperature distribution). System-level models or process simulations describe the combined performance of all the components in the fuel cell process[6,7,8,9]. Process simulators are primarily used to perform material and energy balances on the tightly integrated fuel cell flowsheets. Such models are useful for addressing system-level design questions (e.g., recycle stream options, heat integration, overall system efficiency).

Integration of CFD and Process Simulation

Two potential strategies for bridging the gap between component-level models (i.e., CFD) and system-level models (i.e., process simulation) include:

1) The CFD package and process simulator model *different components* and exchange consistent physical properties (e.g., density, viscosity, heat capacity, thermal conductivity) and reaction kinetics (e.g., Arrhenius rate parameters), as well as stream information (e.g., flow rate, composition, temperature, pressure) at flow boundaries[10].
2) The CFD package and process simulator model the *same component*, but different physical phenomena[11]. In this case, the process simulation model typically sends physical and transport property data (e.g., density, viscosity) to the CFD model, which in turn sends back flow-dependent information (e.g., turbulent kinetic energy). This strategy also includes the case where a CFD model of a single unit operation is represented by an interconnected network of models in the process simulator[12].

In this paper we present a framework for coupling two widely used simulation tools: FLUENT™ for CFD modeling and Aspen Plus® for process simulation. The software integration is accomplished using the standard CAPE-OPEN interfaces[13] (see www.colan.org). Osawe et al.[14] presented the details of the integration. Zitney and Syamlal[10] presented an example of a reaction-separation-recycle flowsheet coupled with a CFD stirred tank reactor model. They determined an optimum shaft speed (a CFD model parameter) for maximizing the overall rate of production of one of the products – a task that could not have been done by using either of the tools alone. On going work on simulating a power plant using the integrated software system is described by Sloan et al.[15].

Example Applications

Several applications are presented below which illustrate the present capability of this framework for integrating simulations tools for the design of potential Vision 21 components.

PEM Fuel Cell. As shown in Figure 1, this Aspen Plus application is a natural gas based PEM (proton exchange membrane) fuel cell power system, consisting of a reformer, shift converter, fuel cell, anode exhaust combustor and heat exchangers.

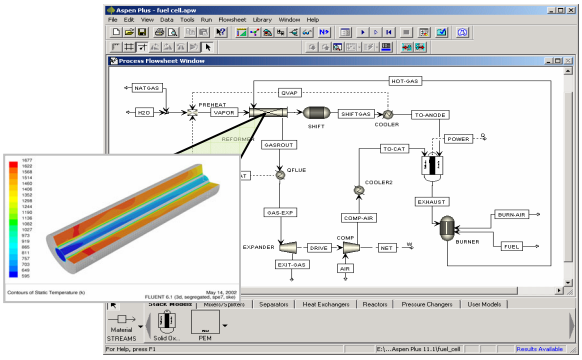

Figure 1. PEM Fuel Cell Power System

The reformer is heated with hot gases from the anode exhaust burner. The reformer is modeled with a single-step Arrhenius reaction: $CH_4 + H_2O \rightarrow CO + 3\ H_2$ and simulated using a 3D CFD model that predicts conversions that account for the limitations imposed by the heat transfer to the catalyst bed. The use of the integrated CFD and process simulation enables the design engineer to study the effect of the recycled hot gases on the PEM CFD model performance[16].

SOFC Fuel Cell. Prinkey et al.[17,18] and Rogers et al.[19] describe the development and validation of the NETL solid-oxide fuel cell (SOFC) model based on the FLUENT CFD code. The models for electrochemistry, electron transport (current) and porous media diffusion were implemented using the user-defined functions capability of FLUENT. Figure 2 shows the SOFC power system flowsheet in Aspen Plus, along with the distribution of H_2 mole fractions in the fuel stream passing along the fuel cell anode[16]. The hydrogen-rich flow enters from the bottom left and is gradually depleted as it proceeds towards the exhaust ports.

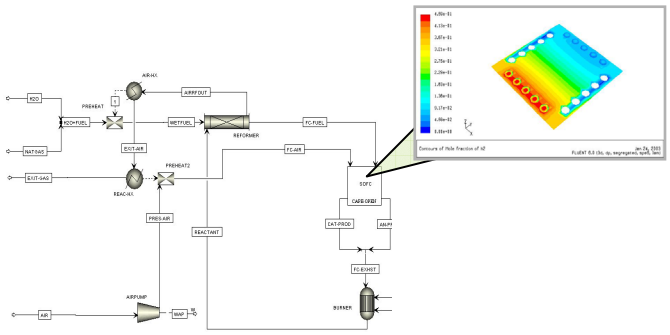

Figure 2. SOFC Fuel Cell Power System

Since the SOFC CFD model applied in this example represents a single cell, the other flowsheet components have been downscaled accordingly. Future work will include fuel cell stacks that produce electrical output on a more useful scale.

Coal Gasification. Gasification technology is essential for many schemes for the efficient and environmentally benign generation of power from a range of fuels, including coal and biomass. Specifically, they are the central component of several large-scale Integrated Gasification and Combined Cycle (IGCC) demonstration plants. Currently, detailed CFD gasification simulations are being performed which are being used for the analysis of large-scale facilities[20].

The CFD simulations account for the gas and particle dynamics, chemical reactions and heat transfer. They are used to study the flow of hot gas and unburned solids as it moves from the mixing zone into the riser of a circulating fluidized bed. The hydrodynamics of both the gas and solid phases are tracked, along with heat transfer between the two phases and production of gas species, such as methane, carbon monoxide and carbon dioxide. Design engineers use the CFD simulations to see how design changes affect the hydrodynamics and the chemistry in the gasifier. Future work will include integrating CFD models for gasification and fuel cell stacks into overall Vision 21 plant simulations.

Conclusions

This paper described the integration of CFD and process simulation tools for use in the design of energy plants. Such integrated simulations offer the ability to optimize individual components in the context of the entire power system rather than in isolation. Early results have demonstrated the potential for improved process design. Continued focus on seamless integration between process simulation, CFD, and other simulation tools will present many new opportunities to design Vision 21 plants based on the fundamental principles of fluid flow, heat and mass transfer, chemical reactions, and other related phenomena, further enhancing the performance and efficiency of future energy plants.

Acknowledgement

This work was supported by U.S. Department of Energy, Office of Fossil Energy, National Energy Technology Laboratory.

References

(1) Wang, Q.; Johnson, J.K.; Broughton J.Q., *Computers in Physics*, **1998**, *12* (6), 538.
(2) Clementi, E., *Philos. Trans. R. Soc. London, Ser. A*, **1988**, *326*, 445.
(3) Klamt, A., Presented at *Thermodynamics 2003*, Cambridge, UK, April 9-11, 2003.
(4) Um, S.; Wang, C.-Y.; Chen, K. S., *Journal of The Electrochemical Society*, **2000**, *147*(12), 4485-4493.
(5) Prinkey, M.T.; Gemmen, R.S.; Rogers, W.A., *American Flame Research Committee (AFRC) International Symposium*, Newport Beach, CA, USA, September 2000.
(6) Fontes, E.; Nilsson, E., *The Industrial Physicist*, August/September, **2001**, 14-17.
(7) Fuller, T.A.; Chaney, L.J.; Wolf, T.L.; Kesseli, J.; Nash, J.; Hartvigsen, J., Presented at the *2000 Fuel Cell Seminar*, Portland, OR, October 30 – November 2, 2000.
(8) Keegan, K.; Khaleel, M.; Chick, L; Recknagle, K; Simner, S.; Deibler, J., Presented at the *SAE 2002 World Congress*, Detroit, MI, March 4-7, 2002.
(9) Virji, M.B.V.; Adcock, P.L.; Mitchell, P.J.; Cooley, G., *Journal of Power Sources*, **1998**, *71*, 337-347.
(10) Zitney, S.E.; Syamlal, M., *Proc. of the European Symposium on Computer Aided Process Engineering –12*, ESCAPE-12, Grievink. J.; van Schijndel, J., Eds., **2002**, 397-402.
(11) Bezzo, F.; Macchietto, S.; Pantelides, C.C., *Computers and Chemical Engineering*, **2000**, *24*, 653.
(12) Urban, Z.; Liberis, L., Presented at *Chemputers Europe 5 Conference*, October 21-23, Dusseldorf, Germany, 1999.
(13) Braunschweig, B.L.; Pantelides, C.C.; Britt, H.I.; Sama, S., *Chem. Eng. Progress*, **2000**, *96*(9), 65.
(14) Osawe, M.O.; Felix, P.; Syamlal, M.; Lapshin, I.; Cleetus, K.J.; Zitney, S.E., Paper No. 250c, Presented at the *AIChE 2002 Annual Meeting*, Indianapolis, IN, November 3-8, 2002.
(15) Sloan, D.G.; Fiveland, W.A.; Zitney, S.E.; Syamlal, M., Presented at *The 27th International Technical Conference on Coal Utilization & Fuel Systems*, Clearwater, Florida, March 4-7, 2002.
(16) Syamlal, M.; Madsen, J.I.; Zitney S.E.; Rogers, W., Presented at the AIChE Spring National Meeting, Session [102], New Orleans, LA March 30 - April 3, 2003.
(17) Prinkey, M.; Gemmen, R.; Rogers, W., In *Proceedings of IMECE: ASME 2001 International Mechanical Engineering Congress and Exposition*, New York, NY, November 11-16, **2001**, No. 2-6-4-3.
(18) Prinkey, M.T.; Gemmen, R.S.; Rogers, W.A., *American Flame Research Committee (AFRC) International Symposium*, Newport Beach, CA, USA, September 2000.
(19) Rogers, W.A.; Gemmen, R.; Johnson, C.; Prinkey, M.; Shahnam, M., Presented at U.S. DOE NETL, RIT Meeting, 2003.
(20) Guenther, C.; Shahnam, M.; Syamlal, M.; Longanbach, J.; Cicero, D.; Smith, P., *Proceedings of the 19th Annual Pittsburgh Coal Conference*, Pittsburgh, PA, Sept. 23-27, 2002.

Effect of Hydrogen Donor on the Morphology of Carbon Formed During Pyrolytic Stressing of JP-8 Jet Fuel

*James J. Strohm, Abraham J. Brandt, Semih Eser and Chunshan Song**

The Energy Institute and The Dept. of Energy and Geo-Environmental Engineering, The Pennsylvania State University
209 Academic Projects Building, University Park, PA 16802
*E-mail: csong@psu.edu

Introduction

In the future, jet fuel used by high-Mach aircraft will be expected to perform a dual role as a coolant for mechanical and electrical systems, raising temperatures experienced by the fuel to greater than 480°C.[1] Current jet fuels are derived from petroleum sources resulting in a predominately paraffinic fuel. At these temperatures, linear paraffins are highly susceptible to pyrolytic degradation leading to the formation of carbon deposits[2] on metal surfaces within the aircraft through bulk and/or catalytic reactions.

Bulk deposits that are formed are generally due to the condensation of alkyl benzenes either present in the fuel or formed from pyrolytic dehydrogenation reactions, which results in deposits that have a general structure of 6 to 7 aromatic rings.[3] Previous work has shown hydrogen donors such as tetralin and α-tetralol can reduce such pyrolytic reactions under non-oxidative conditions, thus effectively reducing the formation of bulk deposits.[4,5] The presence of dissolved oxygen in the fuel dramatically lowers the effectiveness of such hydrogen donors in the pyrolytic regime, rendering them useless.[5] Recently, a binary hydrogen donor consisting of α-tetralone and tetralin has shown excellent oxidative resistance while significantly preventing the formation of polyaromatics.[6,7]

Catalytic deposition is associated with adsorption and subsequent reactions on metal surfaces resulting in filament or amorphous carbon growth. Composition of the metal surface has a profound effect on the formation rate and structure of deposits.[8,9] Superalloys based on the group VIIIA elements were developed for high-temperature applications in corrosive environments, and have been used successfully in aircraft parts and nuclear reactors.[10] However, these alloys still contain Ni and Fe, which are known to catalyze the growth of carbon filaments.[11]

The current study seeks to investigate the effect of the previously developed binary hydrogen donor on the morphology of carbon deposits formed on the superalloy, Inconel 718, during stressing of JP-8 under pyrolytic conditions while dissolved oxygen is present in the fuel.

Experimental

Thermal stressing of JP-8 fuels was performed in the presence of Inconel 718 foils, whose elemental composition is listed in Table 1. For each experiment a foil having dimensions of 10 x 3 x 0.1 mm was placed at the bottom of a 1/4" o.d. isothermal flow reactor, lined with a Silcosteel® coating developed by Restek Corporation. Prior to introducing fuel into the system, the reactor was heated to 500°C wall temperature under argon flow at 500 psig.

Table 1. Elemental Composition of Inconel 718[a,b]

Al	Cr	Cu	Fe	Mn	Mo
5000	19%	1500	18.5%	1800	3.05%
Nb+Ta	Ni	Si	Ti	C	S
5.13%	52.5%	1800	9000	400	80

[a]From Goodfellow Co. and expressed in weight percent. [b]Al, Cu, Mn, Si, Ti, C and S in ppm.

The fuels used in this study were 1 L of JP-8 with and without a 2 wt% addition of the binary hydrogen donor consisting of equal amounts of α-tetralone (THNone) and tetralin (THN). Each fuel was circulated through the reactor at a rate of 4 mL/min for a period of 24 hrs. The fuel was heated to 200°C before entering the reactor, and the bulk outlet temperature of the fuel was maintained at 500°C. Pressure was held constant at 500 psig, and liquid fuel samples were taken at six-hour intervals.

Carbon deposits on the metal foils were analyzed using a LECO R412 Carbon Analyzer to determine total amounts of carbon on the surface in $\mu g/cm^2$. Morphology of deposits was characterized by a Hitachi S-3500N scanning electron microscope. A Shimadzu GC-174 gas chromatograph with a Restek Xti-5 column coupled to a Shimadzu QP-5000 mass spectrometer was used to examine liquid samples. Solution state ^{13}C-NMR analysis was conducted on a Bruker AMX360 with a field of 8.4 T equivalent to a 90 MHz resonance frequency for ^{13}C. Approximately 0.2 mL of sample was diluted in 1 mL $CDCl_3$ and charged into a 5 mm tube. A pulse delay of 90 seconds was required to obtain a quantitative spectrum.

Results and Discussion

Impact on Fuel Reactions. Previous investigations of binary hydrogen donors have shown large improvements in preventing pyrolytic reactions leading to polyaromatic formation and bulk deposits. In a separate flow reactor system JP-8 was stressed with and without the binary hydrogen donor added to the fuel. Silcosteel was used to passivate the surface, in order to minimize catalytic decomposition of the fuel. The reactor utilized higher space velocities, leading to higher temperature conversions, which allowed direct examination of fuel and hydrogen donor interactions. Figure 1 shows the impact of the binary hydrogen donor on the final fuel composition when the fuel was stressed up to a bulk outlet temperature of 772°C (with a LHSV = 450 hr^{-1}).

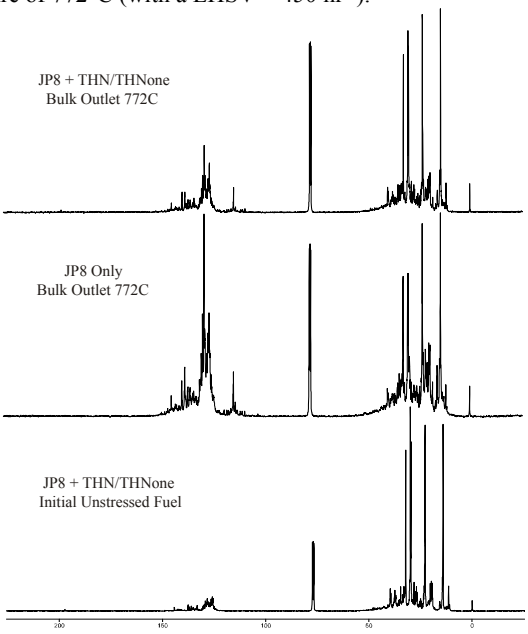

Figure 1. Impact of a binary hydrogen donor on the stabilization of pyrolytic reactions leading to the formation of PAHs as illustrated by ^{13}C-NMR analysis of the stressed fuels.[12]

As Figure 1 illustrates, there is a clear increase in the prevention of the total aromatic carbon that is formed when the binary hydrogen donor is added (32% reduction). More significantly, there is a 62% reduction in the formation of bridgehead carbon associated with PAH formation. In the base of the aliphatic region of the spectra, there is

an increased broadening indicating increased cyclization of the initial fuel. Overall, the signature of the JP-8 remains more intact upon stressing when the hydrogen donors are added to the fuel; clearly this indicates a decrease in the decomposition of the fuel, and subsequent formation of precursors to bulk deposits.

Impact on Carbon Formation. TPO investigation of carbon produced on the surface of the Inconel 718 foils showed no difference in the total amount of carbon produced when the binary hydrogen donor was added to the JP-8. The TPO profiles, however, indicated that carbon produced when the hydrogen donor was added were indeed different from the carbon produced in its absence. To further examine the morphology of the carbon produced, SEM analysis was conducted and is presented in Figure 2.

With the addition of the binary hydrogen donor to JP-8, there is enhanced formation of filamentous carbon when compared to the stressing of JP-8 only. Previous work has shown

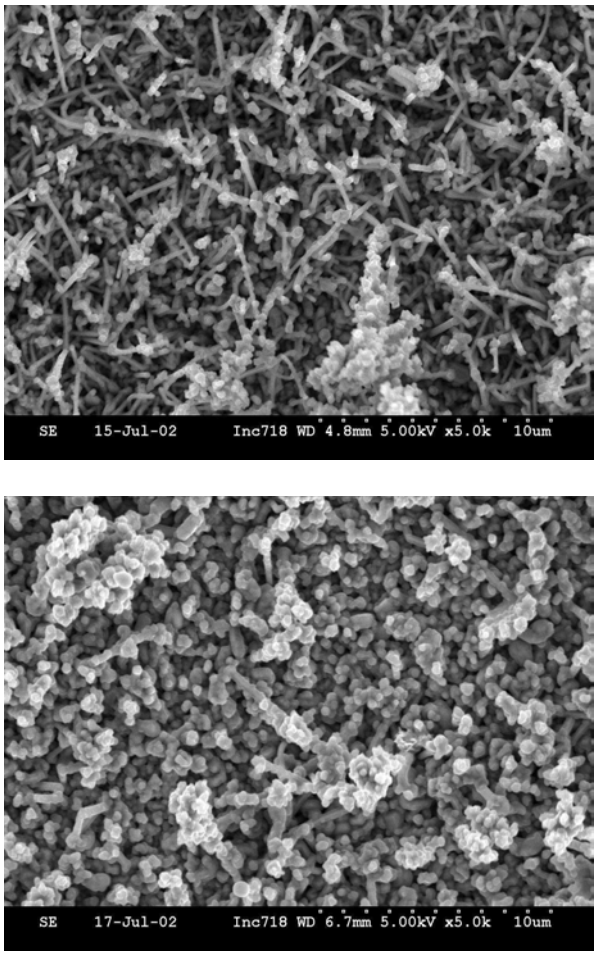

Figure 2. Scanning Electron Micrographs of deposits on the surface of Inconel 718 after thermal stressing for 24 hrs in the presence of JP-8 with (top) and without (bottom) hydrogen donors.

that filamentous carbon is due to catalytic reactions of metals such as nickel and iron with reactive species from thermal decomposition of the fuel.[9] Research in the field of steam reforming of hydrocarbons over nickel catalyst have shown that filament growth is due to the adsorption and diffusion of carbon through nickel particles.[13] When the particles of nickel are encapsulated by polymeric carbon, the activity (and growth of the filaments) is reduced. A similar explanation is given here for the observed differences in the carbon produced from the thermal stressing of JP-8 with and without hydrogen donor addition.

Stressing of JP-8 without the hydrogen donor shows very short and fat carbon filaments with regions of highly amorphous carbon. It is proposed that the reason for the short filaments and amorphous carbon is due to the lay-down of polyaromatics on the surface. This lay-down of polyaromatics will terminate the catalytic activity of active metals such as nickel, resulting in the termination of filament growth. In addition, the initial lay-down of polyaromatics will facilitate an increase in amorphous deposits, due to increasing condensation and dehydrogenation reactions propagating on the surface that is already coated with amorphous deposits. This also accounts for the "regions" rather than irregular coverage of amorphous carbon that was observed on the surface when hydrogen donor is added to the fuel.

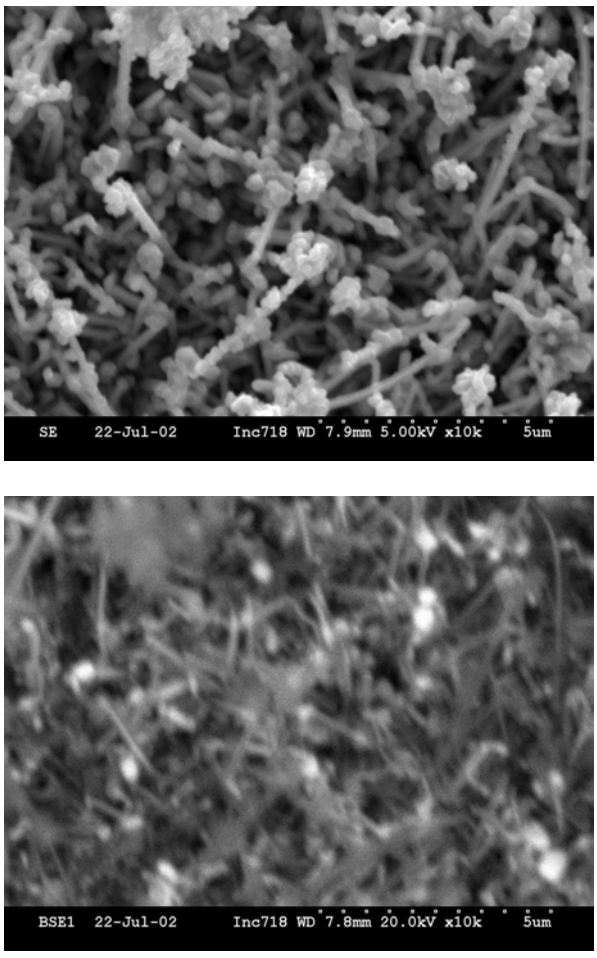

Figure 3. Scanning Electron Micrographs using secondary electrons (top) and back-scattered electrons (bottom) of deposits on the surface of Inconel 718 after thermal stressing for 24 hrs in the presence of JP-8 plus a 1% mixture of α-tetralone and tetralin.

Without the encapsulation of the active metal particles by polyaromatic lay-down, or by active hydrocarbon species from the degradation of the fuel polymerizing, the filaments can continue to grow. This is the case that is observed when hydrogen donors are added to the fuel. The decrease in the formation of polyaromatics, and the suppression of radical reactions that serve to enhance carbon

deposition prevent the encapsulation of active metals, thus allowing enhanced filament growth.

To confirm that metal species were present at the tips of the filaments that were growing, back-scattered electron (BSE) images from SEM analysis were investigated. Figure 3 shows a typical SEM image (top) of the surface after stressing of JP-8 with hydrogen donor addition and the corresponding BSE image of the same area. The light areas of the BSE image correspond to heavy elements that are present on the surface. It is seen that the ends of some of the filaments observed from the SEM image have light areas associated with them in the BSE image. Since the only heavy elements that would be present in the system would be metals, it is shown that these filaments do have metals located near their tips. Not all of the filaments show light areas near their tips, and this is due to some of the filaments being encapsulated by carbon, thus terminating the filament growth as seen in the SEM image of Figure 3.

Conclusions

The effect on the morphology of carbon produced from thermal stressing of JP-8 over Inconel 718 after adding a binary hydrogen donor, comprised of tetralin and α-tetralone, has been examined. Hydrogen donor addition can significantly improve the detrimental pyrolytic reactions leading to the formation of polyaromatics and other reactive species, which results in the formation of bulk and amorphous deposits on the surface. However, the reductions of such compounds being formed will allow the enhanced formation of filamentous carbon. The enhanced production of filamentous carbon is caused by the metal particles on the tips of the filaments remaining active, since they are not being encapsulated by pyrolytic carbon. To effectively reduce the formation of carbon during the pyrolytic decomposition of paraffinic-based fuels, a dual approach to the problem is needed. The first step is to passivate the surface so that the metals, such as nickel that can lead to filamentous carbon, do not interact with the fuel. Secondly, to eliminate the formation of amorphous carbon from bulk reactions, hydrogen donors can be added to the fuel to reduce the formation of polyaromatics, which are the precursors to the formation of amorphous carbon.

Acknowledgement. We are grateful for the U.S. Air Force Office of Scientific Research for financial support. Thanks go to Prof. Harold H. Schobert and Dr. Orhan Altin of Penn State University, and to Mr. William Harrison III, Dr. Cindy Obringer and Dr. Tim Edwards of the U.S. Air Force Wright Laboratory for helpful discussions.

References

(1) Edwards, T. and Zabarnick, S. *Ind. Eng. Chem. Res.* **1993**, *32*, 3117.
(2) Song, C; Eser, S.; Schobert, H.H.; Hatcher, P.G. *Energy & Fuels* **1993**, *7,* 234.
(3) Andresen, J.M.; Strohm, J.J.; Sun, L.; Song, C. *Energy & Fuels* **2001**, *15(3)*, 714.
(4) Song, C; Lai, W.-C.; Schobert, H.H. *Ind. Eng. Chem. Res.* **1994**, *33*, 548.
(5) Strohm, J.J.; Andresen, J.M.; Song, C. Prepr. Pap. – *Am. Chem. Soc., Div. Petro. Chem.* **2000**, *45(3)*, 449.
(6) Strohm, J.J.; Andresen, J.M.; Song, C. Prepr. Pap. – *Am. Chem. Soc., Div. Fuel Chem.*, **2001**, *46(2)*, 487.
(7) Strohm, J.J.; Andresen, J.M.; and Song C. Prepr. Pap. – *Am. Chem. Soc., Div. Fuel Chem.*, **2002**, *47* (3), 189.
(8) Atria, J.; Li, J.; Eser, S.; Schobert, H.H.; and Cermignani, W. *Carbon '97, 23rd Biennial Conf. Carbon* **1997**, *2*, 312.
(9) Altin, O.; Eser, S. *Ind. Eng. Chem. Res.* **2001**, *40*, 589.
(10) Sims, C.T.; Stoloff, N.S.; and Hagel, W.C. *Superalloys*, John Wiley and Sons: New York, 1987.
(11) Baker, R.T.K. *Carbon* **1989**, *27* (3), 315.
(12) Strohm, J.J. *Novel Hydrogen Donors for the Improved Thermal Stability of Advanced Aviation Jet Fuels*, M.S. Thesis, The Pennsylvania State University, **2002**.
(13) Rostrup-Nielsen, J.R. In *Catalysis Science and Technology*; Andersen, J.R.; Boudart, M., Ed.; Springer-Verlag, New York, **1984**, *4*, 34.

CHARACTERIZATION AND COMPARISON OF CARBON DEPOSITION FROM THERMAL STRESSING OF JP-8 MILITARY JET FUEL AND JET-A COMMERCIAL AVIATION JET FUEL OVER PURE METAL, BINARY ALLOY AND SUPER ALLOY SURFACES

Ramya Venkataraman, Orhan Altin, and Semih Eser

The Energy Institute
&
Department of Energy and Geo-Environmental Engineering
230 Hosler Building
The Pennsylvania State University, University Park, PA
16802, USA

Introduction

Jet fuel produces significant amounts of carbon deposits over the metal surfaces of aircraft engines due to the high temperatures encountered from thermal loads during its application as coolant[1,2]. This phenomena is a very important issue in the design of advanced aircrafts and is further complicated by the metal surface effects and composition of various types of jet fuel particularly the sulfur content[3]. Pure metals such as Ni and Fe have been observed to catalyze the deposit formation to a greater extent than super alloys[4] however the nature of the sulfur compounds present in the fuel in some cases promotes and in other cases inhibits the deposit formation[3]. Metal catalyzed carbon deposits are more structurally ordered than thermally formed carbon. The former can also promote formation of the latter due to increased surface area[5].

The objective of this study is to compare the nature and amount of carbon deposits from the thermal stressing of two different types of petroleum derived jet fuels, JP-8 and Jet A over a range of contemporary metal and alloy surfaces in order to understand the change in the nature of the deposition with change in fuel and catalytic surface effects.

Experimental

Thermal stressing experiments were carried out at 480 °C and 500 psig in an isothermal, glass lined flow reactor of OD 1/4". The above reaction conditions are supercritical[6]. The substrates used were two pure metals Ni and Fe, one binary alloy Fe-Ni (55/45) and a super alloy Inconel 600. The composition of Inconel 600 alloy wt% is Ni:72%, Fe:8%, Cr:15.5%, Mn: 1.0%, Cu:5000 ppm, C:1500 ppm, Si:5000 ppm, S:150 ppm. The fuels used were JP-8 which is an advanced military application fuel and Jet A which is commercial aviation jet fuel. According to the U.S turbine fuel specifications Jet A typically has a lower sulfur content than JP-8 however the in the batch received at Penn State both fuels had a comparable high sulfur content. The fuels were analyzed using GC/MS before and after the stressing experiments to study their composition. The sulfur content was obtained using GC/PFPD. The substrate foils were all cut into 13 cm X 3 mm coupons and rinsed in ethanol before being placed in the reactor. The duration of each of the experiments was 5 hours. The morphology of the carbon deposited samples was then studied under an SEM and the characterization and quantification of the deposits was done using Temperature Programmed Oxidation (TPO) in the LECO Multiphase Carbon Analyzer[7].

Results and Discussion

The total amounts of carbon deposition over each of the samples is shown in Table 1. Characterization of these deposits using TPO reveals that all four substrates, Ni, Fe, Ni-Fe, and Inconel 600 facilitate the formation of more than one type of carbon deposit through various complex mechanisms.

Table 1. Carbon deposits in (μg/cm^2) collected over Ni, Fe, Fe-Ni and Inconel 600 surfaces from JP-8 & Jet A.

	Carbon Deposits (μg/cm^2)			
Fuel	Ni	Fe	Fe-Ni (55/45)	Inconel 600
JP-8	66	124	29	176
Jet A	12.5	15	11	111

As can be seen in Table 1 overall JP-8 forms more carbon deposition than Jet A over pure metals, binary alloy and super alloy surfaces however both low temperature and high temperature carbon peaks seem to be occurring at nearly the same temperature for a particular substrate in both fuels. The pure metals Ni and Fe individually form more carbon deposits than their combined binary (Fe-Ni 55/45) alloy. Inconel 600 showed a significantly different behavior compared to the pure metals and binary alloy. It had the highest peak for highly ordered carbon in both cases and formed the maximum amount of carbon deposition in both fuels, followed by Fe and then Ni.

The crystalline structures seen in the SEM micrograph of Fe for both JP-8 and Jet A are most likely Fe sulfide crystals with highly ordered carbon growing over its surface which in turn gives rise to small amorphous carbon structures over it The Fe-Ni binary alloy produced a lot of filamentous carbon as well as amorphous carbon on its surface for both JP-8 and Jet A, as did the Ni surface with JP-8. The morphology of the carbon structures over Ni surface for Jet A seem mainly amorphous growing over the Ni sulfide crystals[3]. The Inconel 600 substrate mainly produced small spherical amorphous carbon when stressed with JP-8 and formed highly ordered filamentous carbon as well as amorphous carbon deposits with Jet A.

The carbon peak observed before 200 °C over Ni, Fe and Fe-Ni with JP-8 and over Inconel 600 with Jet A are mostly due to the adsorbed hydrocarbons on the surface of the amorphous carbon deposits. These usually have a lot of hydrogen associated with them and hence get oxidized much easier than the deposits themselves. Ni and Fe are very good substrates for the formation of catalytic carbon[5]. These may further develop secondary amorphous carbon in association with them by providing a greater surface area. Therefore we find a varied nature of carbon deposits over these substrates with both JP-8 and Jet A. The burn off temperatures for low temperature carbon increases in the order Fe-Ni, Fe, Inconel 600, Ni for JP-8 and Fe-Ni, Ni, Fe, Inconel 600 for Jet A. The high temperature carbon oxidation temperatures in increasing order are Ni, Ni-Fe, Inconel 600, Fe for JP-8 and Fe, Ni, Fe-Ni and Inconel 600 for Jet A. Although Ni is a better dehydrogenation catalyst[8] Fe is a very good oxidation catalyst[9], aiding in the better removal of carbon deposits, hence the CO_2 signal recorded by the carbon analyzer may be greater than that recorded over the Ni substrate. However the combination of these pure metals in the binary alloy (Fe-Ni) in a ratio of 55/45 seems to decrease the carbon deposits over the surface. According to the study by Zhang F[4] the presence of a homogenous one phase alloy (γFe, Ni) particularly at a 55/45 ratio of Fe/Ni in the binary alloy produces substantially lower amounts of deposits. The behavior of Inconel 600 is very interesting in the case of both fuels particularly Jet A. The

presence of trace elements on the Inconel 600 surface are expected to make it less susceptible to roughening by sulfur compounds[10] and carbon deposition. However, the sulfur compounds present in this batch of JP-8 and Jet A probably inhibit the formation of carbon deposits[3]. Ni, Fe and their binary alloy can easily form metal sulfides from the sulfur compounds in jet fuel whereas the resistance of Inconel 600 to this particular type of sulfur attack probably makes it more conducive to carbon deposit formation on its surface. The SEM micrograph of Ni surface after thermal stressing of Jet A suggests that the smooth crystalline structures in them may be Ni sulfides specific to benzylphenylsulfide which seem to inhibit carbon deposits on pure metals but increase deposition over super alloy surfaces[3]. The additives in JP-8 added for enhanced performance in military applications probably cause extensive degradation of the fuel during thermal stressing producing more solid deposits overall on different surfaces compared to Jet A.

Conclusions

The nature of carbon deposits on metal/alloy surfaces depends extensively on the nature of the substrate and can vary greatly with substrate composition but is relatively similar for similar fuels. Although pure metals are most susceptible to destruction by carbon deposition this may not the case always. The combination of Ni and Fe in a particular ratio can decrease the carbon deposition compared to the individual metals themselves. Although the trace elements in superalloys are added to make them more resistant to attack by carbon deposits the composition of the fuel particularly the sulfur compounds can aid the formation of the same.

Acknowledgment. This work is part of a project funded by the Air Force Office of Scientific Research under contract F49620-99-1-0290.

References

1. Orhan Altin, Geoffrey Bock and Semih Eser, "Thermal Stressing of Petroleum and Coal-Derived Jet Fuels On Inconel 718" *Division of Petroleum Chemistry, Inc., ACS 221st National Meeting*, Boston, August, 2001.
2. Strohm J. J.; Butnark S.; Keyser T.L.; Andersen J. M.; Badger M. W.; Schobert, H. H.; Song C. *Fuel Chemistry Division preprints* 2002, 47, 177-178.
3. Encarnacion Raymundo-Pinero, Orhan Altin, and Semih Eser, "Effects of Sulfur Compounds on Solid Deposition on Metals and Inconel 718 from Thermal Decomposition of N-Dodecane" *Division of Petroleum Chemistry, ACS 221st National Meeting*, Boston, August, 2001.
4. Zhang, F., *Carbon Deposition on Heated Alloy Surfaces From Thermal Decomposition of Jet Fuel*, M.S. Thesis, 2000, Pennsylvania State University, University Park.
5. Li, J., *Metal Surface Effects on Deposit Formation from Thermally Stressed Jet Fuel and Model Compounds*, Ph.D. Thesis, 1998, Pennsylvania State University, University Park.
6. Edwards T.; Zabarnick S.; *Ind. Eng. Chem. Res*. 1993, 32, 3117-3122.
7. Altin, O.; Eser, S.; *Ind. Eng. Chem. Res.*, 1999, 39(3), 642.
8. Yu J.; Eser S.; *Ind. Eng. Chem. Res*. 1997, 36, 534-584.
9. Thrower, P.A. *Chemistry and Physics of Carbon*. Marcel Dekker, INC, 1981, Vol 16.
10. Zhang F.; Altin O.; Eser S.; *Prepr. Pap- ACS Fuel Division Preprints* 2000, 220.

Carbon deposits from the thermal stressing of JP-8 over Ni, Fe, Fe-Ni (55/45) and Inconel 600 surfaces at supercritical conditions.

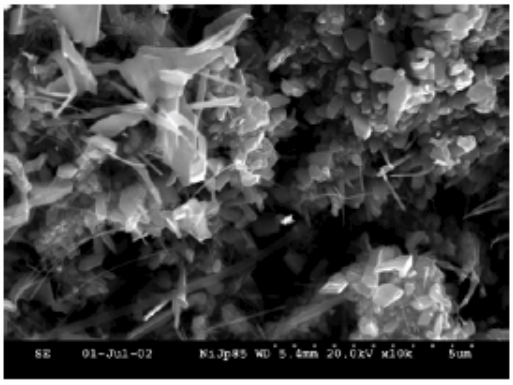

(**Fig.1**) SEM micrograph of JP-8 stressed over Ni for 5 hrs.

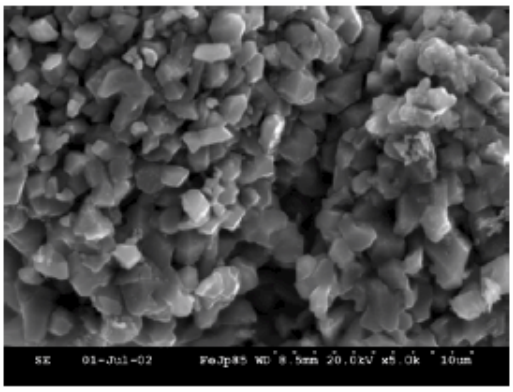

(**Fig.2**) SEM micrograph of JP-8 stressed over Fe for 5 hrs.

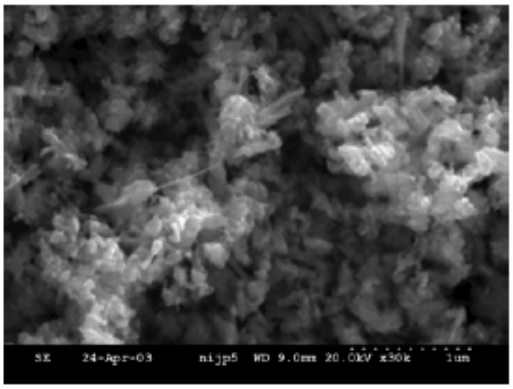

(**Fig.3**) SEM micrograph of JP-8 stressed over Fe-Ni (55/45) for 5 hrs.

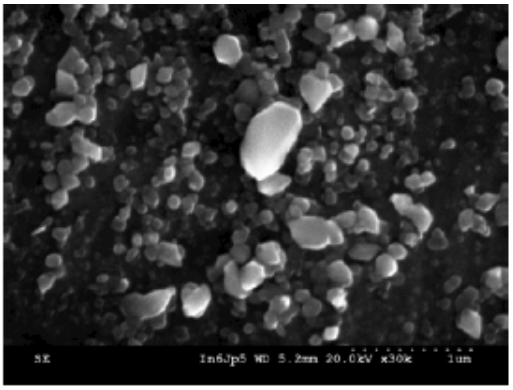

(**Fig.4**) SEM micrograph of JP-8 stressed over Inconel 600 for 5 hrs.

Carbon deposits from the thermal stressing of Jet A over Ni, Fe, Fe-Ni (55/45) and Inconel 600 surfaces at supercritical conditions.

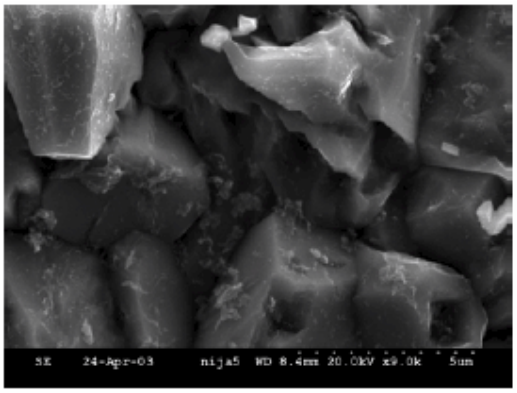

(**Fig.5**) SEM micrograph of Jet A stressed over Ni for 5 hrs.

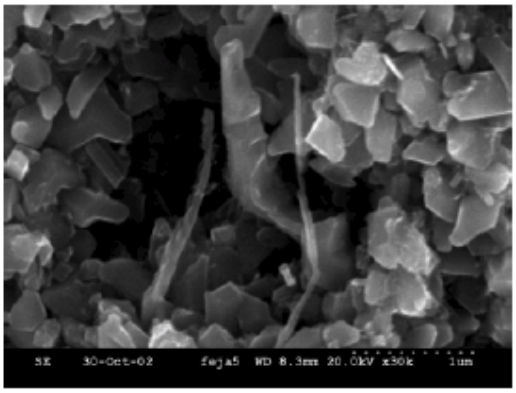

(**Fig.6**) SEM micrograph of Jet A stressed over Fe for 5 hrs.

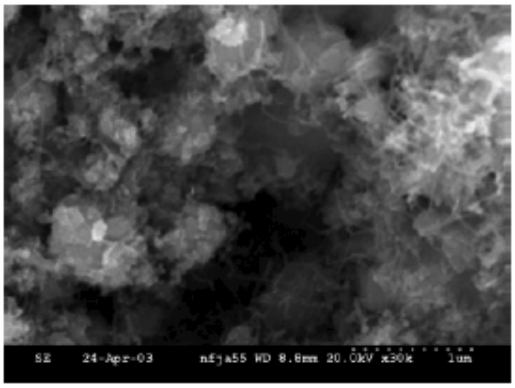

(**Fig.7**)
SEM micrograph of Jet A stressed over Fe-Ni (55/45) for 5 hrs

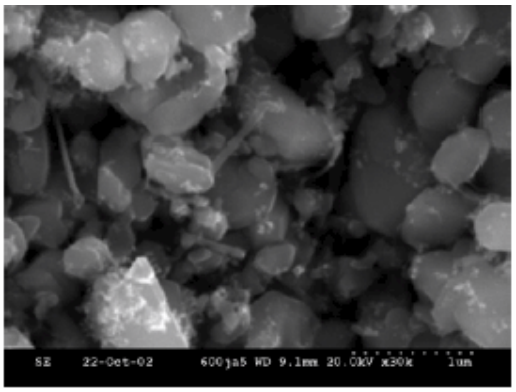

(**Fig.8**)
SEM micrograph of Jet A stressed over Inconel 600 for 5 hrs.

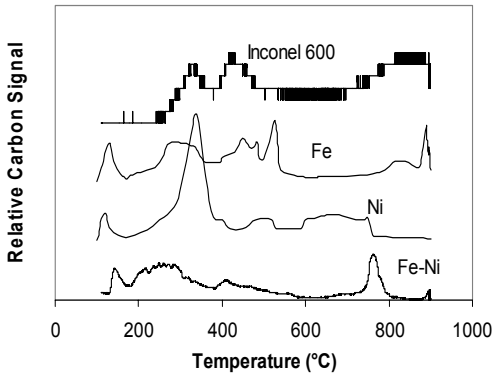

Figure 9. TPO profile of the deposits collected on JP-8 over Ni, Fe, Fe-Ni and Inconel 600 at 480°C, 500 psig and 4 ml/min flow rate for 5 hours.

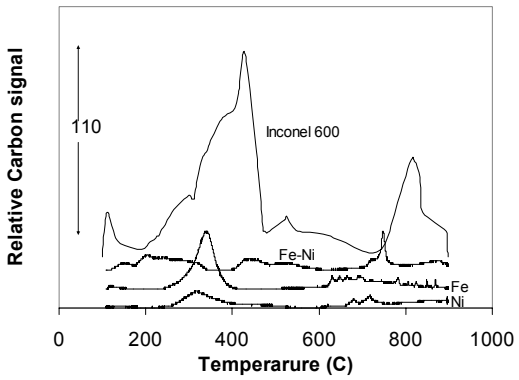

Figure 10. TPO profile of the deposits collected on Jet A over Ni, Fe, Fe-Ni and Inconel 600 at 480°C, 500 psig and 4 ml/min flow rate for 5 hours.

ENERGETIC CATALYST-HYDROGEN PLASMA REACTION AS A POTENTIAL NEW ENERGY SOURCE

R. L. Mills, P. Ray, M. Nansteel, J. He, X. Chen, A. Voigt, and B. Dhandapani

BlackLight Power, Inc.
493 Old Trenton Road
Cranbury, NJ 08512

Introduction

A new chemically generated or assisted plasma source based on a resonant energy transfer mechanism (rt-plasma) has been developed that may be a new power source. One such source operates by incandescently heating a hydrogen dissociator and a catalyst to provide atomic hydrogen and gaseous catalyst, respectively, such that the catalyst reacts with the atomic hydrogen to produce a plasma. It was extraordinary that intense extreme ultraviolet (EUV) emission was observed by Mills et al.[1,2] at low temperatures (e.g. $\approx 10^3$ K) and an extraordinary low field strength of about 1–2 V/cm from atomic hydrogen and certain atomized elements or certain gaseous ions which singly or multiply ionize at integer multiples of the potential energy of atomic hydrogen, 27.2 eV. A number of independent experimental observations confirm that the rt-plasma is due to a novel reaction of atomic hydrogen which produces as chemical intermediates, hydrogen in fractional quantum states that are at lower energies than the traditional "ground" ($n = 1$) state. Power is released, and the final reaction products are novel hydride compounds or lower-energy molecular hydrogen as reported herein. The supporting data include EUV spectroscopy,[1–6,8–10] characteristic emission from catalysts and the hydride ion products,[2,6,9] lower-energy hydrogen emission,[3–5] chemically formed plasmas,[1,2,6,8,9] extraordinary (>100 eV) Balmer α line broadening,[1–3,6,7,9] population inversion of H lines,[9,10] elevated electron temperature,[7] anomalous plasma afterglow duration,[8] power generation,[3,4] and analysis of novel chemical compounds.[11]

The theory given previously[1,3–6,12] is based on applying Maxwell's equations to the Schrödinger equation. The familiar Rydberg equation (Eq. (1)) arises for the hydrogen excited states for n > 1 of Eq. (2).

$$E_n = -\frac{e^2}{n^2 8\pi\varepsilon_o a_H} = -\frac{13.598\,eV}{n^2} \tag{1}$$

$$n = 1,2,3,... \tag{2}$$

An additional result is that atomic hydrogen may undergo a catalytic reaction with certain atoms, excimers, and ions which provide a reaction with a net enthalpy of an integer multiple of the potential energy of atomic hydrogen, $m \cdot 27.2$ eV wherein m is an integer. The reaction involves a nonradiative energy transfer to form a hydrogen atom that is lower in energy than unreacted atomic hydrogen that corresponds to a fractional principal quantum number. That is

$$n = \frac{1}{2},\frac{1}{3},\frac{1}{4},...,\frac{1}{p};\quad p \text{ is an integer} \tag{3}$$

replaces the well known parameter $n =$ integer in the Rydberg equation for hydrogen excited states. The $n = 1$ state of hydrogen and the $n = \frac{1}{\text{integer}}$ states of hydrogen are nonradiative, but a transition between two nonradiative states, say $n = 1$ to $n = 1/2$, is possible via a nonradiative energy transfer. Thus, a catalyst provides a net positive enthalpy of reaction of $m \cdot 27.2$ eV (i.e. it resonantly accepts the nonradiative energy transfer from hydrogen atoms and releases the energy to the surroundings to affect electronic transitions to fractional quantum energy levels). As a consequence of the nonradiative energy transfer, the hydrogen atom becomes unstable and emits further energy until it achieves a lower-energy nonradiative state having a principal energy level given by Eqs. (1) and (3). Processes such as hydrogen molecular bond formation that occur without photons and that require collisions are common. Also, some commercial phosphors are based on resonant nonradiative energy transfer involving multipole coupling.

Two H(1/p) atoms may react to form the corresponding molecule $H_2(1/p)$ that has a bond energy and vibrational levels that are p^2 times those of H_2 comprising uncatalyzed atomic hydrogen where p is an integer. The theory was given previously.[4,5,12] Since the υ = 0 to υ = 1 vibrational transition of H_2 is a resonant state of the corresponding transition of $H_2(1/2)$, emission due to the reaction $2H(1/2) \rightarrow H_2(1/2)$ is possible with vibronic coupling within the transition state at

$$E_{D+vib} = p^2 E_{D\,H_2} \pm \left(\frac{\upsilon^*}{3}\right) E_{vib\,H_2(\upsilon=0\rightarrow\upsilon=1)},\quad \upsilon^* = 1,2,3... \tag{4}$$

where $E_{D\,H_2}$ and $E_{vib\,H_2(\upsilon=0\rightarrow\upsilon=1)}$ are the experimental bond and vibrational energies of H_2, respectively.

Atomic and molecular hydrogen are predicted to form stable states of lower energy than traditionally thought possible. Substantial spectroscopic and physical differences are anticipated. For example, novel EUV atomic and molecular spectral emission lines from transitions corresponding to energy levels given by Eqs. (1) and (3) and Eq. (4), respectively, are predicted. He^+ fulfills the catalyst criterion—a chemical or physical process with an enthalpy change equal to an integer multiple of 27.2 eV since it ionizes at 54.417 eV which is $2 \cdot 27.2$ eV. Thus, microwave discharges of helium–hydrogen mixtures were studied by EUV spectroscopy to search for line emission from transitions to fractional Rydberg states of atomic hydrogen and due to the formation of molecular hydrogen corresponding to fractional Rydberg states of atomic hydrogen. In addition, helium–hydrogen (90/10%) and helium–deuterium (90/10%) plasma gases were flowed through a high-vacuum (10^{-6} Torr) capable, liquid nitrogen cryotrap, and the condensed gas was characterized by gas chromatography (GC), mass spectroscopy (MS), visible and EUV optical emission spectroscopy (OES), and ^{1}H nuclear magnetic resonance (NMR) of the liquid-nitrogen-condensable gas dissolved in $CDCl_3$. Since the electronic transitions are very energetic, power balances were measured to determine whether this reaction has sufficient kinetics to merit its consideration as a practical power source.

Experimental

EUV spectroscopy was recorded on microwave discharge plasmas of hydrogen, nitrogen, oxygen, carbon dioxide, ammonia, helium, neon, argon, krypton, xenon, or 2% hydrogen mixed plasmas as well as nitrogen-methane (96/4%) according to the methods given previously.[3,4] Each ultrapure gas alone or mixture was flowed through a half inch diameter quartz tube at an inlet pressure of 1 Torr. The gas pressure to the cell was maintained during differential pumping by flowing the mixture while monitoring the pressure with a 10 Torr and 1000 Torr MKS Baratron absolute pressure gauge. The tube was fitted with an Opthos coaxial microwave cavity (Evenson cavity). The microwave generator was an Opthos model MPG-4M generator (Frequency: 2450 MHz). The input power to the plasma was set at 85 watts with forced air cooling of the cell. Extreme ultraviolet emission spectra were also obtained on these plasmas maintained in a glow discharge cell that comprised a five-

way stainless steel cross that served as the anode with a hollow stainless steel cathode according to the methods given previously.[5,7] For spectral measurement, the light emission was introduced to a normal incidence McPherson 0.2 meter monochromator (Model 302) equipped with a 1200 lines/mm holographic grating with a platinum coating. The wavelength region covered by the monochromator was 2–560 nm. The EUV spectrum was recorded with a channel electron multiplier (CEM) at 2500–3000 V or a photomultiplier tube (PMT) at -1000 V and a sodium salicylate scintillator. The wavelength resolution was about 0.2 nm (FWHM) with an entrance and exit slit width of 50 μm. The increment was 0.2 nm and the dwell time was 500 ms. The PMT (Model R1527P, Hamamatsu) used has a spectral response in the range of 185–680 nm with a peak efficiency at about 400 nm. The increment was 0.4 nm and the dwell time was 1 s. Peak assignments were based on a calibration against the known He I, He II, and Lyman series lines.

To achieve higher sensitivity at the shorter EUV wavelengths, the light emission was recorded with a McPherson 4° grazing incidence EUV spectrometer (Model 248/310G) equipped with a grating having 600 lines/mm with a radius of curvature of ≈ 1m. The angle of incidence was 87°. The wavelength region covered by the monochromator was 5–65 nm. The wavelength resolution was about 0.1 nm (FWHM) with an entrance and exit slit width of 300 μm. The increment was 0.1 nm and the dwell time was 500 ms. The light was detected by a CEM at 2400 V.

Condensable gas from helium–hydrogen (90/10%) microwave plasmas maintained in the Evenson cavity was collected in a high-vacuum (10^{-6} Torr) capable, liquid nitrogen cryotrap as described previously.[13] After each plasma run the cryotrap was pumped down to 10^{-5} Torr to remove any non-condensable gases in the system. The pressure was recorded as a function of time as the cryotrap was warmed to room temperature. Typically, about 3 Torr of condensed gas was collected in a 3 hr plasma run. Controls were hydrogen and helium alone.

The mass spectra ($m/e = 1$ to $m/e = 200$) of ultrahigh purity hydrogen (Praxair) control samples and samples of the condensable gas from the helium–hydrogen microwave plasmas were recorded with a residual gas analyzer. In addition, the ion current as a function of time of the mass to charge ratio of two ($m/e = 2$) was recorded while changing the electron gun energy from 30 to 70 to 100 eV for ultrapure hydrogen and the condensable gas from the helium–hydrogen plasma reaction.

Cryogenic gas chromatography was performed on a Hewlett Packard 5890 Series II gas chromatograph equipped with a thermal conductivity detector and a 60 meter, 0.32 mm ID fused silica Rt-Alumina PLOT column (Restek, Bellefonte, PA). The chromatographic column was submerged in liquid nitrogen, and samples were run at -196° C using Ne as the carrier gas.

OES was performed on the condensable gas from helium–hydrogen (90/10%) microwave plasmas to search for atomic hydrogen lines from plasma-decomposed $H_2(1/p)$. A sample tube was fitted with the Evenson cavity, and the visible spectrum was recorded during a discharge maintained at 80 W input power at about 2 Torr as described previously.[13]

EUV OES was performed on the condensable gas from helium–hydrogen (90/10%) and helium–deuterium (90/10%) microwave plasmas by flowing the gas through a needle valve from a gas collection tube to the half inch diameter quartz tube fitted with the Evenson cavity. The microwave system and EUV spectrometer was as given *supra.*, except that the differential pumping was enhanced using a 2 mm diameter pin-hole optic between the plasma tube and chamber, and only the turbo pump was used. With the typical pressure in the 20 cm^3 gas collection tube of 5–20 Torr, the plasma could be maintained for up to 30 minutes before the flowing gas was depleted. Peak assignments were based on a calibration against standard lines obtained before and after each run as given previously.[13]

Sealed ^1H NMR samples were prepared by collecting the condensed gas from the cryotrap in an NMR tube (5 mm OD, 23 cm length, Wilmad) which was then sealed as described previously.[13] Control NMR samples comprised ultrahigh purity hydrogen (Praxair) and the helium–hydrogen (90/10%) mixture with $CDCl_3$ solvent. The NMR spectra were recorded with a 300 MHz Bruker NMR spectrometer that was deuterium locked. The chemical shifts were referenced to the frequency of tetramethylsilane (TMS) at 0.00 ppm.

The excess power was measured by water bath calorimetry on helium–hydrogen (90/10%) plasmas maintained in a microwave discharge cell compared to control plasmas with the same input power. The water bath was calibrated by a high precision heater and power supply. A high precision linear response thermistor probe (Omega OL-703) recorded the temperature of the 45 L water bath as a function of time for the stirrer alone to establish the baseline. The heat capacity was determined for several input powers, 30, 40, and 50 W ± 0.01 W, and was found to be independent of input power over this power range within ± 0.05%. The temperature rise of the reservoir as a function of time gave a slope in °C/s. This slope was baseline corrected for the negligible stirrer power and loss to ambient. The constant known input power (J/s), was divided by this slope to give the heat capacity in J/°C. Then, in general, the total power output from the cell to the reservoir was determined by multiplying the heat capacity by the rate of temperature rise (°C/s) to give J/s.

Since the cell and water bath system were adiabatic, the general form of the power balance equation with the possibility of excess power is:

$$P_{in} + P_{ex} - P_{out} = 0 \tag{5}$$

where P_{in} is the microwave input power, P_{ex} is the excess power generated from the hydrogen catalysis reaction, and P_{out} is the thermal power loss from the cell to the water bath. Since the cell was surrounded by water that was contained in an insulated reservoir with negligible thermal losses, the temperature response of the thermistor T as a function of time t was determined to be

$$\dot{T}(t) = \left(1.907 \times 10^5 \text{ J/°C}\right)^{-1} \times P_{out} \tag{6}$$

where 1.907×10^5 J/°C is the heat capacity for the least square curve fit of the response to power input for the control experiments ($P_{ex} = 0$). The slope was recorded for about 2 hours after the cell had reached a thermal steady state, to achieve an accuracy of ± 1%.

Results and Discussion

The EUV emission was recorded from microwave and glow discharge plasmas of (1) hydrogen, helium, krypton, and xenon alone, and (2) krypton and xenon with 2% hydrogen over the wavelength range 5–125 nm. No peaks were observed in these controls except hydrogen peaks at wavelengths greater than about 80 nm for hydrogen alone or hydrogen mixed with krypton or xenon. Neither krypton or xenon satisfy the catalyst condition; thus, no novel lines were predicted. Similarly, only He I and He II peaks were observed for helium alone.

The EUV spectrum (5–100 nm) of the microwave cell emission of the helium–hydrogen (98/2%) mixture is shown in Figure 1.

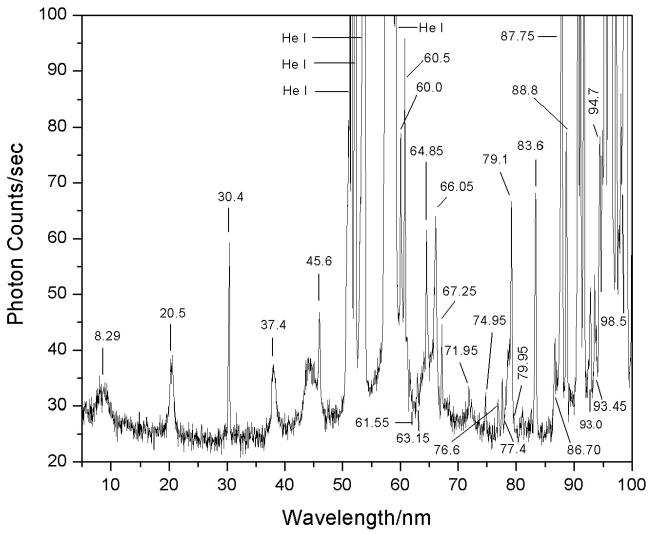

Figure 1. The EUV spectrum (5–100 nm) of the microwave cell emission of the helium–hydrogen (98/2%) mixture recorded with a normal incidence EUV spectrometer and a CEM. Reproducible novel emission lines were observed at 45.6 nm, 30.4 nm, and 8.29 nm with energies of $q \cdot 13.6$ eV where $q = 2$, 3, or 11 and at 37.4 nm and 20.5 nm with energies of $q \cdot 13.6$ eV where $q = 4$ or 6 that were inelastically scattered by helium atoms wherein 21.2 eV was absorbed in the excitation of He ($1s^2$) to He ($1s^12p^1$). In addition, a novel series of sharp wavelength-labeled peaks were observed in the 60–100 nm region that were assigned to members of peaks predicted at $E_{D+vib} = 17.913 \pm (\upsilon^*/3)\ 0.515902$ eV due to the reaction $2H(1/2) \rightarrow H_2(1/2)$ with vibronic coupling.

Reproducible novel emission lines were observed at 45.6 nm, 30.4 nm, and 8.29 nm with energies of $q \cdot 13.6\,\text{eV}$ where $q = 2,3,\text{or}\,11$ and at 37.4 nm, and 20.5 nm with energies of $q \cdot 13.6\,eV$ where $q = 4\,\text{or}\,6$ that were inelastically scattered by helium atoms wherein 21.2 eV was absorbed in the excitation of He ($1s^2$) to He ($1s^12p^1$) as discussed previously.[3,4,13] Additional spectra extended the series to $q = 1,2,3,4,6,7,8,9,\text{or}\,11$ as discussed before.[3,4,13] In addition, a series of peaks were observed in the 60–100 nm region of Figure 1. The wavelength-labeled peaks in Figure 1 match members of peaks predicted at $E_{D+vib} = 17.913 \pm \left(\frac{\upsilon^*}{3}\right) 0.515902\,eV$, $\upsilon^* = 1,2,3...$ due to the reaction $2H(1/2) \rightarrow H_2(1/2)$ with vibronic coupling. Hydrogen has no peaks below 80 nm. The peaks of the series also do not match helium as shown in control spectra and NIST tables[14] except for a distinguishable peak at 97.2 nm.[4] Figure 2 shows the plot of the theoretical emission vacuum wavelengths E_{DH_2} due to the reaction $2H(1/2) \rightarrow H_2(1/2)$ with vibronic coupling at energies of $E_{D+vib} = p^2 E_{DH_2} \pm \left(\frac{\upsilon^*}{3}\right) E_{vibH_2(\upsilon=0\rightarrow\upsilon=1)}$ ($p = 2$) and the wavelengths observed over multiple spectra as partially shown in Figure 1. The data matched (Eq. (4)) to longer wavelengths for $\upsilon^* = 2$ to $\upsilon^* = 32$ and to shorter wavelengths for $\upsilon^* = 1$ to $\upsilon^* = 16$ to within the spectrometer resolution of about ± 0.05%.

Helium–hydrogen (90/10%) gas was flowed through the microwave tube and the cryosystem for 2 hours with the trap cooled to liquid nitrogen temperature. No change in pressure over time was observed when the dewar was removed, and the system was warmed to room temperature. The experiment was repeated under the same conditions but with a plasma maintained with 60 W forward microwave power and 10 W reflected. In contrast to the control case, a liquid-nitrogen-condensable gas was generated in the helium–hydrogen plasma reaction since the pressure due to the reaction product rose from 10^{-5} Torr to 3 Torr as the cryotrap warmed to room temperature.

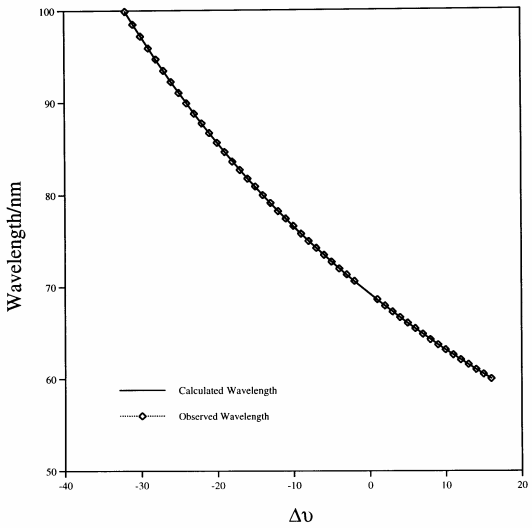

Figure 2. The plot of the theoretical (Eq. (4)) emission vacuum wavelengths E_{DH_2} due to the reaction $2H(1/2) \rightarrow H_2(1/2)$ with vibronic coupling at energies of $E_{D+vib} = p^2\, E_{DH_2} \pm (\upsilon^*/3)\, E_{vib\,H_2}$ (υ=0 →υ=1) (p=2) and the wavelengths observed such as those shown in Figure 1. The data matched to longer wavelengths for $\upsilon^* = 2$ to $\upsilon^* = 32$ and to shorter wavelengths for $\upsilon^* = 1$ to $\upsilon^* = 16$ to within the spectrometer resolution of about ± 0.05%.

The mass spectrum over the range $m/e = 1$ to $m/e = 200$ showed that the condensable gas was highly pure hydrogen. The $m/e = 2$ ion current as a function of time was recorded while changing the electron gun energy from 30 to 70 to 100 eV for ultrapure hydrogen and the condensed gas from the helium–hydrogen plasma reaction. The relative changes in the $m/e = 2$ ion current with increasing electron-beam energy indicated that the condensable gas has a higher ionization potential than ultrapure hydrogen. Upon increasing the ionization potential from 30 eV to 70 eV, the $m/e = 2$ ion current for the control hydrogen increased by a factor of about 30%; whereas, the gas collected under liquid nitrogen from the helium–hydrogen plasma increased by a factor of about 10 under the same pressure condition as that of the control.

The only known gases that show peaks on the liquid nitrogen-cooled Rt-Alumina PLOT column are helium and para-hydrogen and ortho-hydrogen, and these gases can be identified by their retention times of 13.7 min., 17.1 min., and 18.9 min., respectively. Trace helium (0.4%) and small peaks at the position of hydrogen were observed for the condensed gas that had the same 1:3 para-ortho ratio as H_2. However, two additional larger peaks were observed at 18.9 min. and 28.9 min. that had the same 1:3 relative ratio and were less thermally conductive than the neon carrier gas. The negative peaks could result from an on-column pressure change associated with the analyte gas.

With sufficient input power, the electrons at the tail of the Maxwellian distribution of a microwave plasma may be sufficiently energetic to ionize and decompose $H_2(1/2)$ (65 eV). The high resolution (± 0.1 nm) visible optical emission spectrum recorded on a

microwave discharge plasma of the liquid-nitrogen-condensable helium–hydrogen (90/10%) microwave discharge plasma gas showed strong Balmer α, β, γ, and δ lines of atomic hydrogen at 656.28 nm, 486.13 nm, 434.05 nm, and 410.17 nm, respectively, which indicated that the gas contained hydrogen.

The EUV optical emission spectra (45-100 nm) recorded on two separate microwave discharge plasmas of the liquid-nitrogen-condensable helium–hydrogen (90/10%) microwave discharge plasma gases collected over 48 hours are shown in Figure 3. A reproducible series of evenly spaced peaks were observed with a higher energy separation of 0.74 eV compared to the vibrational energy of H_2 ($E_{vib\,H_2(\upsilon=0\rightarrow\upsilon=1)} = 0.5159\,eV$) which is the highest known vibration transition energy. The series was similar to that shown in Figure 1, except that the energy spacing is about four times larger. Hydrogen has no emission below 80 nm. The peaks from the condensable gas did not match those of hydrogen for wavelengths >80 nm as well. The series of evenly spaced peaks did not match the He I and He II peaks observed from the helium gas discharge. The series of lines shown in Figure 3 was assigned to mixed vibration-rotational transitions of an electronically excited state of $H_2(1/p)$.

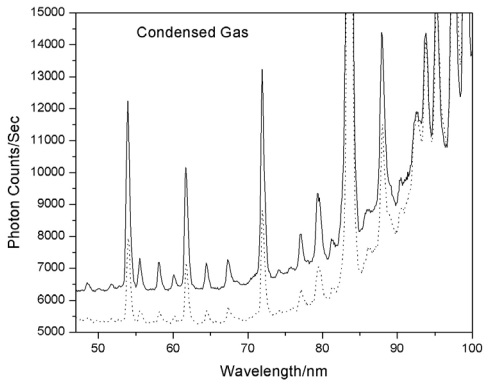

Figure 3. The EUV optical emission spectra (45–100 nm) recorded with a normal incidence EUV spectrometer and a CEM on two separate microwave discharge plasmas of the liquid-nitrogen-condensable helium–hydrogen (90/10%) microwave discharge plasma gases. A reproducible series of evenly spaced peaks were observed with a higher energy separation of 0.74 eV compared to the vibrational energy of H_2 ($E_{vib\,H_2}$ (υ=0 → υ=1) = 0.5159 eV) which is the highest known vibration transition energy. The series of lines was assigned to mixed vibration-rotational transitions of an electronically excited state of $H_2(1/p)$.

Deuterium substitution offers a method of definitively making the assignment of the condensed gas to a hydrogen-type molecule by the observation of a predicted shift of the spectral lines relative to the hydrogen spectrum. The EUV optical emission spectra (50-80 nm) recorded on microwave discharge plasmas of the liquid-nitrogen-condensable helium–hydrogen (90/10%) and helium–deuterium (90/10%) microwave discharge plasma gases are shown in Figure 4 (top) and (bottom), respectively. The isotope shift of the lines identified the series as belonging to $H_2(1/p)$ and supported the assignment of mixed vibration-rotational transitions of an electronically excited state of $H_2(1/p)$. The energy difference of 0.44 eV between the hydrogen and deuterium-based gases at 71.9 nm and 73.8 nm gives a good match to p=2 if anharmonicity and the increased electronic energy ΔE_{ele} of deuterium compared to hydrogen is considered as discussed previously.[13]

An exhaustive list of even remotely possible alternative assignments was considered for the EUV results for the reaction plasma EUV emission shown in Figure 1 and the liquid-nitrogen condensable H_2 shown in Figures 3 and 4. The only known species in a helium–hydrogen plasma, H^+, H_2^+, H_3^+, H^-, H, H_2, He_2^*, HeH^+, and remotely possibly HeH were eliminated since the spectra did not match or the species could not exist under the reaction conditions. Other exotic possibilities such as He_2^+, HHe_2^+, HHe_n^+ and He_n were eliminated due to the extremely specialized conditions required for their formation such as extremely low temperatures that were unlike those in the helium–hydrogen microwave plasmas.[15,16] Air contaminants were also eliminated. Emission from plasmas of nitrogen, oxygen, carbon dioxide, and ammonia or these gases with 2% hydrogen showed no emission in the region < 80 nm. In addition, water vapor present in the oxygen-hydrogen plasma showed no emission in this region. The spectrum of the nitrogen–methane (96/4%) plasma to form CN, C_x, and C_xH_y species (confirmed by visible spectra) showed no emission in this region. Emission of argon, krypton, and xenon as helium contaminants was eliminated. No emission was observed in the region <80 nm for krypton, krypton-hydrogen, xenon, xenon-hydrogen, and argon. Neon was eliminated based on spectral line mismatches and absences since only the Ne I lines were observed. Cl I, Br I, I I, and S I lines given by the NIST tables[14] were not detected in the visible or shorter wavelength regions. Silicon from the quartz tube wall was eliminated based on the NIST tables.[14] No pump contaminants were possible.

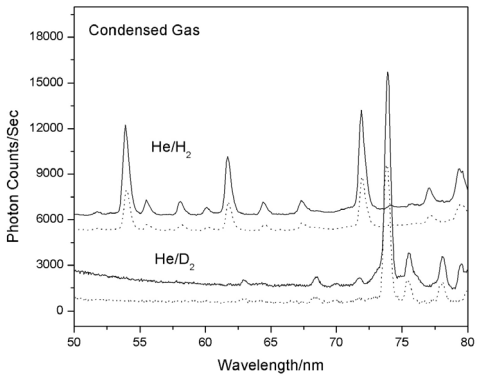

Figure 4. The EUV optical emission spectra (50–80 nm) recorded with a normal incidence EUV spectrometer and a CEM on two microwave discharge plasmas of the liquid-nitrogen-condensable helium–hydrogen (90/10%) (top) and helium–deuterium (90/10%) (bottom) microwave discharge plasma gases. The observation that the novel EUV emission spectrum shifted with deuterium substitution in a region where no hydrogen emission has ever been observed strongly supported the existence of lower-energy molecular hydrogen. The isotope shift of the lines also identified the series as belonging to mixed vibration-rotational transitions of an electronically excited state of $H_2(1/p)$.

^{1}H NMR spectra on sealed samples of condensable helium–hydrogen plasma gases dissolved in $CDCl_3$ relative to tetramethylsilane (TMS) are shown in Figure 5. Peaks observed in the 0 to 10 ppm region were a singlet peak at 7.26 ppm with side bands which matched $CDCl_3$ and two novel singlet peaks at 3.22 and 3.47 ppm. In addition, an H_2 peak was observed at 4.63 ppm. NMR chemical shifts of common laboratory solvents as trace impurities are given by Gottlieb et al.[17] All of the possible assignments were eliminated based on a mismatch between the observed and literature values for the chemical shifts, or in cases where the shifts matched to within ± 0.05 ppm, the known compound was eliminated based on a

mismatch between the multiplicity of the peak and/or the absence of other peaks of the known compound.

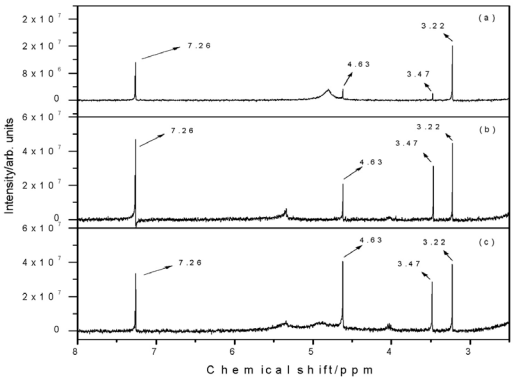

Figure 5. The ^{1}H NMR spectrum (2–7.5 ppm) on sealed samples of liquid-nitrogen-condensable helium–hydrogen plasma gases dissolved in $CDCl_3$ relative to tetramethylsilane (TMS). In each case, an H_2 peak was observed at 4.63 ppm. A singlet peak was observed at 7.26 ppm which matched $CHCl_3$. Two novel singlet peaks were observed at 3.22 ppm and 3.47 ppm which could not be assigned to a known compound. These upfield peaks relative to H_2 were assigned to $H_2(1/p)$ in two p quantum states.

The upfield peaks relative to H_2 only formed during the helium–hydrogen plasma reaction. The 3.22 ppm and 3.47 ppm peaks that could not be assigned to any known compound was assigned to $H_2(1/p)$ in two different quantum states. Even though the radii of corresponding states are related by inverse integers, the anticipated shifts are relatively small and matched those anticipated as discussed previously.[13] The assignments were further consistent with the EUV OES, GC, and MS results.

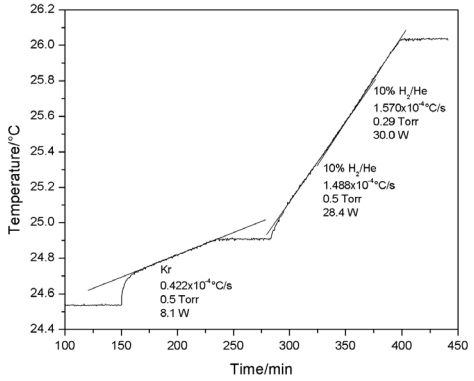

Figure 6. The *T(t)* water bath response to stirring and then with selected panel meter readings of the constant forward and reflected microwave input power to krypton was recorded. The microwave input power was determined to be 8.1 ± 1 W. A helium–hydrogen (90/10%) mixture was run at identical microwave input power readings as the control, and the excess power was determined to be 21.9 ± 1 W from the *T(t)* response.

The water bath calorimetry is an absolute standard and indicated $P_{in} = 8.1 \pm 1$ W input power at the selected diode settings for all control plasmas. From these results, power input to the helium–hydrogen plasma was confidently known as the diode readings identically matched those of the controls. For example, the $T(t)$ water bath response to stirring and then with selected panel meter readings of the constant forward and reflected microwave input power to krypton was recorded as shown in Figure 6. Using the corresponding $\dot{T}(t)$ in Eq. (6), the microwave input power was determined to be 8.1 ± 1 W. A helium–hydrogen (90/10%) mixture was run at the same microwave input power readings as the control which corresponded to $P_{in} = 8.1 \pm 1 W$ in Eq. (5). The $T(t)$ response was significantly increased for helium–hydrogen (90/10%) as shown in Figure 6. At 350 minutes, the pressure was changed from 0.5 Torr to 0.29 Torr. A slight increase in $\dot{T}(t)$ was observed at the lower pressure, possibly due to an increase in atomic hydrogen and He^+. The excess power was determined to be 21.9 ± 1 W from the corresponding $\dot{T}(t)$ using Eq. (6) and Eq. (5). The sources of error were the error in the calibration curve (± 0.05 W) and the measured microwave input power (± 1 W). The propagated error of the calibration and power measurements was ± 1 W. Given an excess power of 21.9 W in 3 cm^3 and a helium–hydrogen (90/10%) flow rate of 10.0 sccm, the excess power density and energy balance were high, 7.3 W/cm^3 and -2.9×10^4 kJ/mole H_2 (150 eV/H atom), respectively. The reaction of hydrogen to form water which releases -241.8 kJ/mole H_2 (1.48 eV/H atom) is about 100 times less than that observed. The results indicate that a new power source based on the catalysis of atomic hydrogen is not only possible, but is competitive with gas turbine combustion.

References

(1) Mills, R.L, Nansteel, M., Ray, P., *IEEE Trans. Plasma Sci.*, **2002**, *30* (2), 639.
(2) Mills, R.L, Nansteel, M., Ray, P., *New J. Phys*., **2002**, *4*, 70.1.
(3) Mills, R.L., Ray, P., Dhandapani, B, Nansteel, M., Chen, X., He, J., *J Mol. Struc*t., **2002**, *643* (1–3), 43.
(4) Mills, R.L., Ray, P., Dong, J., Nansteel, M., Dhandapani, B., He, J., *Vib. Spectrosc*., **2003**, *31* (2), 195.
(5) Mills, R.L., Ray, P., *Int. J. Hydrogen Energy,* **2002**, *27* (5), 533.
(6) Mills, R.L., Ray, P., *Int. J. Hydrogen Energy,* **2003**, *28* (8), 825.
(7) Mills, R.L., Ray, P., Dhandapani, B., Mayo, R.M., He, J., *J. Appl. Phys.*, **2002**, *92* (12), 7008.
(8) Conrads, H. Mills, R.L., Wrubel, Th., *Plasma Sources Sci. Technol*., in press.
(9) Mills, R.L., Ray, P., Mayo, R.M., *IEEE Trans. Plasma Sci*., **2003**, *31* (2), 236.
(10) Mills, R.L., Ray, P., Mayo, R.M., *Appl. Phys. Lett*., **2003**, *8*2 (11), 1679.
(11) Mills, R.L., Dhandapani, B, Nansteel, M., He, J., Shannon, T., Echezuria, A., *Int. J. Hydrogen Energy*, **2001**, *26* (4), 339.
(12) Mills, *The Grand Unified Theory of Classical Quantum Mechanics*, September 2001 Edition, BlackLight Power, Inc., Cranbury, New Jersey, Distributed by Amazon.com; January (2003) Edition posted at www.blacklightpower.com.
(13) Mills, R.L., Dhandapani, B, Nansteel, M., He, J., Ray, P., *J. Phys. Chem. B*, submitted.
(14) NIST Atomic Spectra Database, www.physics.nist.gov/cgi-bin/AtData/display.ksh.
(15) Baccarelli, I., Gianturco, F. A., Schneider, F., *J. Phys. Chem. A*, **1997**, *101*, 6054.
(16) Higgins, J., Callegari, C., Reho, J., Stienkemeier, F., Ernst, W.E., Gutowski, M., Scoles, G., *J. Phys. Chem. A*, **1998**, *102*, 4952.
(17) Gottlieb, H.E., Kotlyar, V., Nudelman, A., *J. Org. Chem.*, **1997**, *62*, 7512.

VALORIZATION OF LIGHT ALKANES FOR THE PRODUCTION OF LPG AND QUALITY GASOLINE

N. Viswanadham[1], Uday T. Turaga[2], and Lalji Dixit[1]*

[1]Indian Institute of Petroleum, Dehra Dun 248005, India
[2]Fuel Science Program, The Pennsylvania State University, State College, PA 16802
[*]E-Mail: nvish@iip.res.in

Introduction

Environmental legislation is restricting the use of light petroleum fractions such as light naphtha (LN) and natural gas liquid (NGL) for gasoline blending because these feeds have high Reid Vapor Pressure (~70) and low octane numbers (65-70). Consequently, such feedstocks are not being consumed and becoming available in surplus quantities. Existing refinery processes like catalytic reforming are not effective as the feedstocks mainly contain *n*-pentane and *n*-hexane that are non-reformable by simple dehydro-cyclization reactions. On the other hand, demand for propane and butane (Liquefied Petroleum Gas) is increasing at a growth rate of over 14% every year in India, where it is widely used in homes for cooking. LPG demand is expected to accelerate further in the future because of its potential use as a clean transportation fuel. Current petroleum production and refining capacities are not sufficient to meet the deficit and growing need for LPG [1,2]. This situation suggests the need for a new process that seeks to add value to light alkane feeds by converting them into LPG or low-benzene, high octane gasoline, or both simultaneously.

The conversion of hydrocarbons over acid catalyst involves carbocation intermediates and takes place at rates which are governed by the nature, number, and strength of acid sites suggesting that acid-catalyzed reactions on a given catalyst take place on sites of a narrow range of energies [3]. The zeolite, ZSM-5, is well known for its tailorable properties, in particular, acidity and shape selectivity facilitated by the medium-sized pore channels. Such features have made ZSM-5 a suitable catalyst for a number of hydrocarbon transformations such as xylene isomerization, toluene disproportionation, and methanol to gasoline and olefins [4,5]. The number and strength of acid sites are controlled by amount and distribution of aluminum in the zeolite framework which depends on the silica-alumina ratio of the gel during zeolite synthesis. The silica-alumina ratio could also be modified post-synthesis, e.g., by hydrothermal treatment.

It has been known that ZSM-5 increases LPG-range products when used as an FCC additive. Further, earlier studies in our laboratory have led to the development of zinc-aluminosilicate of MFI structure, which has good activity for the conversion of NGL to aromatics [6-8]. The knowledge of these systems led us to study the possibility of exploiting ZSM-5-based catalysts for the production of LPG and gasoline by suitable modification of catalytic properties. In this quest, we have developed a novel zeolite-based catalyst whose efficacy for conversion of light alkane/NGL feedstocks to LPG and gasoline has been thoroughly evaluated on both model compounds and commercial feedstocks. The catalyst and process—designated Naphtha to Gas and Gasoline (NTGG)—is relevant to refiners because of its ability to consume potentially surplus light alkane feedstocks and produce supply-constrained products such as LPG along with high-octane, low-benzene gasoline.

Experiments

ZSM-5 zeolite with Si/Al ratio of 35 was synthesized from the silica-alumina-sodium-water gel system in a stainless steal reactor. Its acidity properties were tailored by treating it with steam, nitric acid, and the incorporation of metal ions such as Zn and Pt. Steam treatment was conducted in a shallow bed reactor with 100% steam at controlled water flow rate and reactor temperatures ranging from 300 to 600 ^{0}C, for a duration of 3 hours. Acid leaching was conducted with 3N nitric acid at 100 ^{0}C, while metal incorporation was carried out by incipient wet impregnation of metal salts [8].

The as-synthesized and modified zeolite samples were characterized using nitrogen adsorption/desorption, XRD, XRF, IR, and microcalorimetric ammonia adsorption. The performance of these catalysts was evaluated in two phases. The first phase was used to select one catalyst out of several several formulations using *n*-heptane as a model reaction, while the second phase involved further testing on the selected catalyst using industrial feedstocks such as light naphtha (LN), natural gas liquid (NGL), and udex raffinate. The catalyst evaluation was conducted in a fixed-bed micro reactor at reaction temperatures of 400 to 500^o C, 10 kg/cm^2 pressure using nitrogen as carrier gas with N_2/HC molar ratio of 2.

Results and Discussion

X-ray diffraction patterns of the synthesized ZSM-5 samples revealed the formation of ZSM-5 without any impurity phases. The steamed and acid-treated samples had some changes in the intensities of major peaks suggesting increased hydrophobicity because of framework dealumination [9]. X-ray fluorescence, Si^{29}, and Al^{27} NMR studies indicated variations in the amount and nature of alumina in the ZSM-5 samples after steaming and acid treatment. Si^{29} MAS NMR was used to determine the framework Si/Al ratios and the phenomenon of steam dealumination was identified from higher Si/Al ratios and the presence of octahedral alumina.

Microcalorimetric adsorption of ammonia on the zeolites and resulting enthalpy of adsorption, as a function of volume of ammonia adsorbed were determined. The initial heat of adsorption indicates the maximum strength of acid site. As expected, the total amount of ammonia adsorbed per gram of catalysts decreased with steam dealumination. However, at a certain degree of dealumination, the samples exhibited a high value of initial heat of adsorption related with the involvement of extra-framework alumina in the creation of very strong acid sites.

Performance of various ZSM-5 catalysts towards *n*-heptane conversion is given in Figure 1, where based on the nature of utilization the product was broadly classified into five groups, namely, (1) fuel gas (methane, ethane and ethylene), (2) LPG (propane and butane), (3) BTX (benzene, toluene and xylenes), (4) C_5+ paraffins (pentane, hexane and heptane), and (5) C_{9+} (higher aromatics).

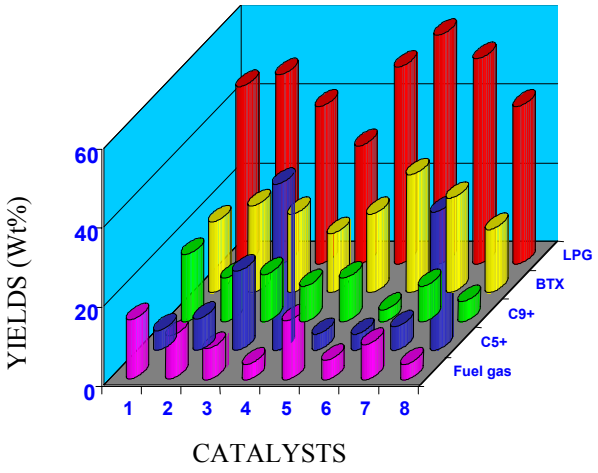

Figure 1. Effect of catalyst properties on product distribution

The results indicated a change in product selectivities after the modification of ZSM-5 properties by pre- and post-synthesis modifications. A general trend was the decrease in selectivity to fuel gas with simultaneous increase in LPG and aromatics, which is advantageous for achieving the desired product quality. However, careful analysis of the data suggests the influence of various factors on the product selectivity such as the amount and nature of extra-framework in zeolites. The criteria of catalyst selection is to maximize the production of LPG and BTX with minimal amount of fuel gas and C_5+ paraffins, where the catalyst HZ-6 exhibited the best performance with 56 wt% LPG and 36 wt% BTX in n-hepane conversion. Further testing with commercial feedstocks on this catalyst was also performed whose results are presented in Table 1. The lower IBP (initial boiling point) and FBP (Final boiling point) of the feedstocks indicate the lower average carbon number of the feed.

Table 1. Performance towards industrial feedstocks

Feed	*n*-C_7	NGL	UR*	LN-1	LN#-2
Feed Characteristics					
IBP	98.0	65.1	46.1	70.0	87.0
FBP	98.0	90.0	131.9	90.0	137.0
Density	0.68	0.70	0.68	0.72	0.79
Product Yield (wt%)					
Fuel gas	2.2	4.5	9.2	5.6	3.1
LPG	56.0	55.4	52.0	55.0	51.2
BTX	36.0	28.2	29.8	32.5	39.0
C_5+	3.0	9.8	7.0	3.0	2.0
C_9+	2.8	2.1	2.0	3.9	4.7

*Udex raffinates; #Light naphtha

The product analysis indicates that the catalyst exhibits high conversions for all the industrial feedstocks with minor changes in selectivities for LPG and aromatics irrespective of the minor differences in feed characteristics caused by hydrocarbon composition. The higher aromatic yield observed in LN-2 conversion can be ascribed to the higher FBP of the feed. It is interesting to see that the decrease in aromatic yield was always accompanied by a simultaneous increase in LPG.

Conclusions

The authors have demonstrated the development of zeolite-based catalysts using novel modifications for the utilization of light alkane feedstocks for the production of LPG and low benzene-containing gasoline. The total yield of LPG and aromatics over this catalyst was found to be more than 80 wt% and is highly attractive for commercial applications.

References

1. Haun, R.R., Otto, K.W., and Whitley, S.C., Oil Gas J., 13 June 1994, 92(24), 54.
2. LPG News of India, March 1996, p 17.
3. R.B. Borade, S.G. Hegde, S.B. Kulkarni, and P. Ratnasamy, Appl. Catal., 13 (1984) 27.
4. S.L. Meisel, J.C. Mc Cullough, C.H. Lechthaler, P.B. Weisz, Chem. Tech., 6 (1976) 86.
5. D.H. Olson, and W.O. Haag, Am. Chem. Soc. Symp. Ser., (1984) 248-275.
6. A.R. Pradhan, N. Viswanadham, S. Suresh, N. Ray, Uma Shanker and T.S.R. Prasada Rao. US Patent No. 6177374
7. A.R. Pradhan, N. Viswanadham, Mohanlal Sharma, Uma Shanker, N. Ray, and T.S.R. Prasada Rao, *US Patent No. 5961818*
8. N. Viswanadham,, A.R. Pradhan, N. Ray, S.C. Vishnoi, Uma Shanker and T.S.R. Prasada Rao, *Applied Catalysis: A*, 137, 1996, 225.
9. N. Viswanadham**,** Takafumi Shido, Takehiko Sasaki, and Yasuhiro Iwasawa *J.Phy.Chem. B,* 106 (2002) 10955-10963

KINETIC STUDY ON SOLVENT SWELLING OF SINGLE COAL PARTICLES IN PYRIDINE

Satoru Murata, Tomohiro Yokoyama, Toshifumi Sako, Hong Gao, Koh Kidena, and Masakatsu Nomura

Department of Applied Chemistry, Faculty of Engineering, Osaka University, 2-1 Yamada-oka, Suita, Osaka 565-0871, Japan

Introduction

Coal is a very complicated mixture of organic and inorganic materials, organic portions of which are believed to consist of numerous polycyclic aromatic compounds linked to each other by methylenes, ethers, and naphthenes. In order to obtain the structural information, many studies have been conducted including spectroscopic studies, destructive conversions and detailed analyses of the resulting products, and measurements of physical properties. Density of cross-link is one of the most important structural factors affecting physical properties and chemical reactivities of coal. In general, measurements of solvent swelling have been conducted to obtain the information of three-dimensional arrangement of organic portions of coals. Major methods for getting the data of swelling are (1) volumetric measurement based on packed bed and (2) gravimetric method using solvent sorption from vapor phase. Both methods have several advantages and shortcomings. One of the most important drawbacks in both methods, the authors think, is that these can give only the average values for each parameter such as kinetic parameters, activation energy, cross-link density, etc. Coal is considered to be a complicated heterogeneous mixture, therefore, all structural features should have a kind of distribution. A microscopic observation of swelling of coal particles is one of the methods to solve the above problem. Using this orthogonal microscope coupled with an image analysis system, the authors conducted swelling measurements of four kinds of coal particles to examine the distribution of kinetic parameters, and estimation of coal structural features such as average number of carbons between cross-link points.[1-2] One drawback of the apparatus employed in these studies is the lack of the method to control the temperature of the solvent. This may lead to ambiguity of the data obtained. Therefore, an improvement of the apparatus for enabling the measurement of the solvent swelling at different temperature was conducted in the present study to re-examine the kinetic parameters. The authors also tried to obtain the activation energy of the solvent swelling and the effects of pretreatments of coal on the rate and activation energy of swelling.

Experimental

Samples and reagents. Witbank coal sample was provided by the Iron and Steel Institute, Japan (ISIJ), whose ultimate analysis was as follows; C 82.5, H5.0, N 2.0, O+S (by diff.) 10.5 wt%, daf. The sample was ground to coarse particles ranging from 0.20 to 0.25 mm of a diameter and dried at 40 ^{o}C *in vacuo* for a night before use. Pyridine (solvent for swelling experiments) was commercially available as a reagent grade and used without further purification.

Experimental apparatus and procedure. Details of the experimental apparatus used in this study were described elsewhere. Basically, it consists of a pair of microscopes connected with color video camera systems to monitor orthogonally the behavior of the coal particles in a sealed solvent cell (made from a transparent quartz glass). This image analysis system was used for sampling the time-resolved images and evaluating the time-resolved volumetric swelling ratio of the coal particles quantitatively. In order to carry out the kinetic study, a brand-new cell was developed (see **Figure 1**). Here, the temperature of the water could be controlled with 0.5 ^{o}C from the determined one.

Under the conditions of atmospheric pressure and the controlled temperature, 3 mL of pyridine was injected into the cell and the system was kept for at least 30 min until the temperature of pyridine approached to the determined temperature. Then, the coal particles (typically 5 pieces) were randomly placed into cell, and sampling of images was started until a quasi-equilibrium state of swelling was attained (about 24 h, in the case of Witbank coal). The recorded images were directly examined and analyzed on an Apple Power Macintosh computer with an image processing software, NIH Image (ver. 1.61, from NIH, USA). The time-resolved volumetric swelling ratios of coal particles at time t ($Q_{v,t}$) were defined as the average value calculated with the equivalent volume converted from the two projection areas of the particles measured orthogonally by two cameras. Detailed expressions for calculation of the volumetric swelling ratio of the coal particles can be found elsewhere.

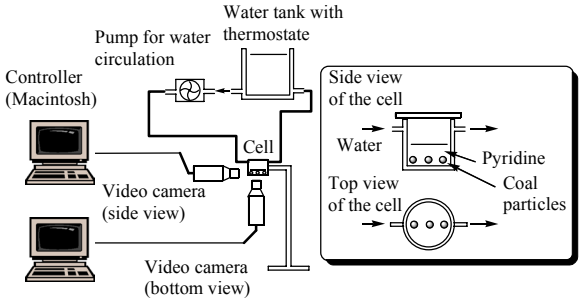

Figure 1. Schematic view of the apparatus for swelling experiments.

Results and Discussion

Kinetics of Witbank coal particles in pyridine. By using a newly prepared cell, swelling experiments of 35 particles of Witbank coal were conducted in pyridine at 20 ^{o}C. Swelling kinetics could be simulated by using the following empirical equations.

$$M_t / M_e = kt^n \quad (1)$$

$$(Q_{v,t} - 1) / (Q_{v,e} - 1) = M_t / M_e \quad (2)$$

$$(Q_{v,t} - 1) / (Q_{v,e} - 1) = kt^n \quad (3)$$

$$ln\,[(Q_{v,t} - 1) / (Q_{v,e} - 1)] = ln(k) + nln(t) \quad (4)$$

where, M_t and M_e mean amounts of the solvent penetrated into coal particles both at *time=t* and at *quasi*-equilibrium stage, respectively, $Q_{v,t}$ and $Q_{v,e}$ indicate volumetric swelling ratios at *time=t* and at *quasi*-equilibrium stage, respectively, k is rate constant for swelling, and n is a number that crudely indicates the nature of the solvent diffusion.

By using these equations, 35 sets of k, n, and $Q_{v,e}$ were obtained for 35 particles of Witbank coal.

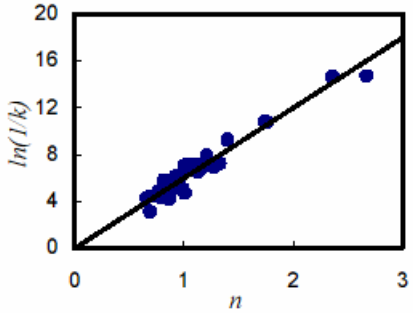

Figure 2. Correlation between n and *ln(1/k)* in swelling of Witbank coal particles in pyridine at 20 ^{o}C.

Then, the authors investigated the correlation of these swelling parameters and found that the parameter $ln(1/k)$ is proportional to the parameter n as shown in **Figure 2**. Using a proportional constant, β, **eq. 4** can be replaced with **eq. 6**.

$$ln(1/k) = n\beta \quad (5)$$

$$ln\,[(Q_{v,t} - 1) / (Q_{v,e} - 1)] = nln(t) - n\beta \quad (6)$$

The authors also found that the parameter n changed from 0.6 to 2.6 and its distribution could be simulated by double exponential function as shown in **Figure 3**, the latter findings were reported previously.

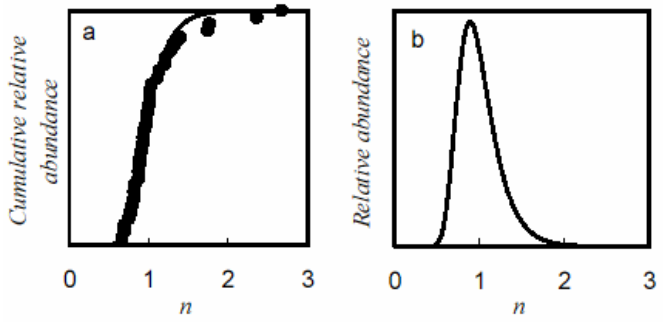

Figure 3. Distribution of n and curve fitting results (a) and differential form of fitting function (b).

Activation energy of swelling. The authors conducted the swelling experiments of Witbank coal particles in pyridine at 30 and 40 °C for evaluation of its activation energy. By using the same methods as mentioned above, kinetic parameters for swelling at 30 and 40 °C were obtained. Activation energy can be calculated by using a well-known equation:

$$ln(k) = -E_{act} / RT + ln\,(A) \quad (7)$$

Using **eq. 5**, **eq. 7** can be transformed into **eq. 8**.

$$E_{act} = - Rd[ln(k)]/d(1/T) = nRd\beta/d(1/T) \quad (8)$$

Eq. 8 indicates that activation energy can be calculated based on the value of $d\beta/d(1/T)$. The value $d\beta/d(1/T)$ can be obtained from the slope of the plots of β vs. reciprocal of temperature as shown in **Figure 4**.

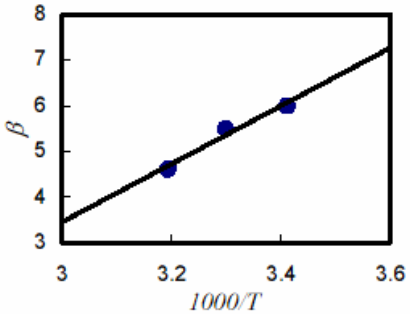

Figure 4. Temperature-dependence of the parameter, β, from the solvent swelling of Witbank coal in pyridine at 20-40 °C.

The value, $d\beta/d(1/T)$, was estimated to be 6.33 x 10^3 from **Figure 4**. From **eq. 8** and $d\beta/d(1/T)$, E_{act} for swelling of Witbank coal particles in pyridine could be estimated to be:

$$E_{act} = 12.8 \text{ x } n \text{ (in kcal/mol)} \quad (9)$$

As shown in **Figure 3**, the parameter n had some distribution from 0.6 to 2.6, and the authors reported that the distribution of n could be simulated by double exponential distribution function. Based on these results, the authors simulated the distribution of activation energies, the results being shown in **Figure 5**.

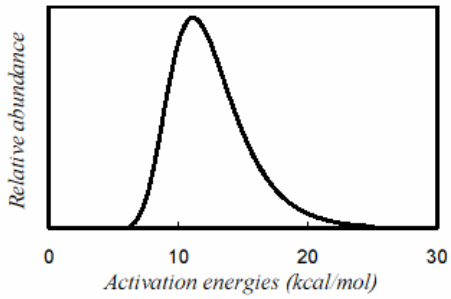

Figure 5. Distribution of the activation energies of swelling of Witbank coal particles in pyridine.

Effects of pretreatments on the kinetics of swelling.
The authors examined the effects of pretreatments of coal particles on the kinetics of solvent swelling. Pyridine pre-extraction, *O*-acetylation by acetic anhydride in pyridine, and HCl-leaching were employed as pretreatments of coal. These pretreatments were found to enhance the rate of swelling. It is interesting to note that distribution of n of the particles after *O*-acetylation and pyridine pre-extraction changed drastically.

Figure 6 shows the distribution of the activation energies of the swelling of original and treated Witbank coal particles.

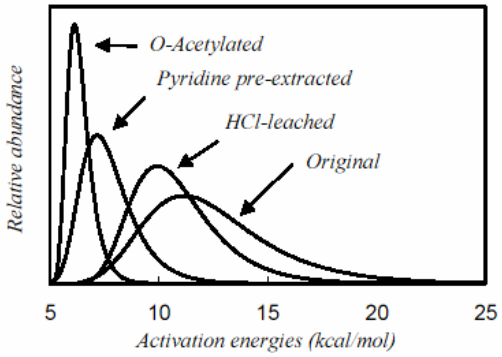

Figure 6. Distribution of Activation Energies from swelling of original and treated Witbank coal particles in pyridine.

Average and dispersion of activation energies also changed by these pretreatments. Changes of average values of E_{act} may result from the change of non-bonding interactions in the coal. O-Acetylation cleaves the hydrogen bondings. HCl-leaching cleaves ionic bonding by inorganic salts. Pyridine extraction may remove interaction *via* low-molecular weight compounds. Therefore, energy barriers for solvent penetration were reduced. Origin of the change of dispersion was not clear. One possibility is the induced rearrangement of three-dimensional structure of the coal by pyridine, because *O*-acetylation and extraction treatment used pyridine.

References

(1) Gao, H.; Artok, L.; Kidena, K.; Murata, S.; Nomura, M. *Energy Fuels*, **1998**, *12*, 881.
(2) Gao, H.; Nomura, M.; Murata, S.; Artok, L. *Energy Fuels*, **1999**, *13*, 518.

Biomimetic Oxidation Studies: Alkane Functionalization in Aqueous Solution Utilizing Methane Monooxygenase Model Enzyme Assemblies

Karine Neimann,[a] *Ronny Neumann,*[a] *Alain Rabion,*[b] *and Richard H. Fish* [b]

[a]Department of Organic Chemistry, Weizmann Institute of Science, Rehovot, Israel 76100 [b]Lawrence Berkeley National Laboratory, University of California, Berkeley, California, 94720

Introduction

Methane monooxygenase (MMO) and cytochrome P-450 enzymes, although active in aqueous media, have a structure wherein the diiron non-porphyrin and iron porphyrin active sites, respectively, are embedded within a hydrophobic pocket, which enables the uptake and subsequent functionalization (hydroxylation) of alkanes. In the continuing search for biomimetic models for these metalloenzyme oxidation catalysts, the emphasis is usually placed on the structure of the active site, and if this biomimic can perform alkane functionalization chemistry. Generally, the macroenvironment and the efficacy of the oxidation process in aqueous media with the various monooxygenase model complexes has not been a focus of the bioinorganic catalysis community. Nevertheless, for metalloporphyrins, some significant research has been directed toward alkene epoxidation and alkane functionalization in aqueous media, by embedding the active site model compounds within lipid bilayers, thermotropic liquid crystals, and micelles. However, in the more nascent field of MMO biomimetic catalysis, the question of the macroenvironment and the possibility of alkane functionalization in aqueous media has not been extensively studied.[1]

In order to study the functionalization of hydrophobic alkanes in aqueous media using a biomimetic MMO enzyme assembly, including the active site and a hydrophobic pocket, we have developed both a derivatized amorphous silica, which allows one to balance the hydrophilicity and the hydrophobicity of a silicate surface, and a classically formed aqueous micelle system utilizing a cationic surfactant, cetyltrimethylammonium hydrogensulfate.[1] In our derivatized amorphous silica technique, hydrophilic poly(ethylene) oxide (PEO) and/or hydrophobic poly(propylene) oxide (PPO) were covalently attached to siloxane monomers. The siloxane monomers were then polymerized using sol-gel synthesis that yields an amorphous silicate with PEO and/or PPO anchored to the silica surface. The PEO/PPO phases are to be considered comparable to anchored solvents, where the anchoring of the solvent is somewhat analogous to the use of bonded phase columns in gas chromatography in place of simple, physically adsorbed phases. Therefore, active MMO biomimetic complexes, such as *in situ* formed $[Fe_2O(\eta^1\text{-}H_2O)(\ (\eta^1\text{-}OAc)(TPA)_2]^{3+}$, **1**, TPA = tris[(2-pyridyl)methyl]amine), from the $[Fe_2O(\mu\text{-}OAc)(TPA)_2]^{3+}$ analog, **2**, at pH = 4.2, can then be embedded into the PEO and PPO tethered silica (Figure 1). Thus, the placement of the precatalyst into the anchored solvents allows one to potentially functionalize alkanes in aqueous solution with *t*-butyl hydroperoxide (TBHP) in the presence of oxygen gas (O_2) and, in this paper, we compare this former MMO model enzyme system to the latter mentioned technique, where the precatalyst, alkane, and oxidants were dissolved within the hydrophobic layers of the aqueous micelle dispersions (Figure 2).[1]

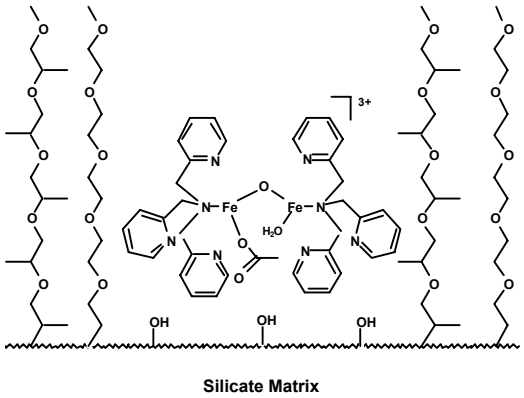

Figure 1: A schematic representation of *in situ* formed $[Fe_2O(\eta^1\text{-}H_2O)(\ (\eta^1\text{-}OAc)(TPA)_2]^{3+}$, **1**, embedded in the PEO, PPO derivatized silica, for alkane functionalization in water at pH 4.2.

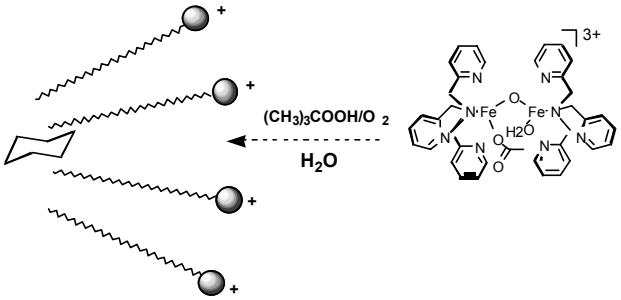

Figure 2: A schematic representation of *in situ* formed **1** diffusing, along with the oxidants, TBHP/O_2, into aqueous micelles formed with the surfactant, cetyltrimethylammonium hydrogensulfate, for alkane functionalization in water at pH 4.2.

Results and Discussion

Alkane Functionalization Studies with Surface Derivatized Silicates

As an initial example of alkane functionalization using various surface derivatized silicates, the oxidation of cyclooctane was carried out with *in situ* formed (pH = 4.2) $[Fe_2O((\eta^1\text{-}H_2O)(\eta^1\text{-}OAc)(TPA)_2]^{3+}$, **1**, as the precatalyst, in the presence of TBHP/O_2. From the results presented in Table 1, one can clearly observe that silicates with both hydrophobic PPO and hydrophilic PEO tethers provided a significantly improved reaction medium, compared to either PEO or PPO alone, with ~140 turnovers (TON, mmol of product/mmol of catalyst) being observed with 10 mol% PPO and 10 mol% PEO–SiO_2, while approximately 25 TON were observed with PPO–SiO_2 or PEO–SiO_2. It is interesting to note that $Fe(ClO_4)_3$ showed no alkane functionalization activity when impregnated in 10 mol% PPO and 10 mol% PEO–SiO_2, which indicates that the TPA ligands might be necessary for solubilization in the anchored polyether solvents, and therefore, for catalysis to occur.

The reaction selectivity also differed as a function of the silicate support. For example, with PPO–SiO_2 or PEO–SiO_2, the major product was cyclooctanone and the minor product was cyclooctene, formed consistently in a ratio of ~1.2:1. Futhermore, very minor amounts (<5%) of cyclooctanol and the mixed dialkylperoxide, cyclooctyl-*t*butylperoxide, were also formed. For 10 mol% PPO and 10 mol% PEO–SiO_2, about 25% of the products formed was the dehydrogenated cyclooctene, while the remaining 75% of oxygenated products, cyclooctanol, cyclooctanone, and cyclooctyl-*t*-butylperoxide, were formed in approximately a 1:3:2 ratio. The reaction was carried out at pH = 4.2 and, as in previous studies, the solution turned colorless from its original yellow color with formation of the proposed $[(TPA)Fe^{2+}(\mu\text{-}OH)Fe^{3+}(TPA)]$ complex that designates a Haber-Weiss process in the decomposition of TBHP. This observation is further supportive of the Haber-Weiss process in that after the TBHP oxidant was completely decomposed, the yellow color returned.

Table 1. **Oxidation of Cyclooctane with Complex 1 Embedded in Surface Derivatized Silica.**[a]

Silica Support	Total TON (hr^{-1})	Products[b]
10% PEO–SiO_2	19 (6.3)	43%, 55%, 1%, 1%
20% PEO–SiO_2	25 (8.3)	42%, 56%, 1%, 1%
10% PPO,10% PEO–SiO_2	142 (47.3)	26%, 35%, 13%, 25%
10% PPO–SiO_2	24 (8.0)	40%, 55%, 0%, 5%
20% PPO–SiO_2	21 (7.0)	37%, 49%, 0%, 4%
none	< 1	na

[a]Reactions were carried out by mixing 0.38 mmol cyclooctane, 3.8 mmol TBHP in 5 mL water at pH 4.2 and 0.38 μmol of *in situ* formed (as 1% wt. $[Fe_2O((\eta^1\text{-}H_2O)(\eta^1\text{-}OAc)(TPA)_2]^{3+}$ on derivatized silica) for 3 h at room temperature. [b]Mol% total products for cyclooctene, cyclooctanone, cyclooctanol, and cyclooctyl-*t*-butyl peroxide, respectively. Yields based on TBHP were 80-90%.

Thus, it is clearly evident that alkane functionalization reactions with TBHP/O_2 as oxidants, and in the presence of MMO biomimetic complexes, such as **1**, as well as other metal complexes, are initiated by formation of *t*-BuO• and *t*-BuOO• radicals.[1] In this case, by invoking the Haber-Weiss mechanism, the intermediate cyclooctyl radical can react with either dioxygen leading to the formation of cyclooctanone and cyclooctanol, via the proposed cyclooctyl hydroperoxide, or with a *t*-BuOO• radical to form the mixed dialkyl peroxide. Interestingly, and uniquely for cyclooctane, cyclooctene was formed as a significant product, plausibly by an intramolecular oxidative dehydrogenation pathway from the cyclooctyl radical. Moreover, cyclooctene is *not* formed by dehydration of cyclooctanol as its use as a substrate, under typical reaction conditions, yielded no cyclooctene, but was converted to cyclooctanone.

The scope of the alkane functionalization reaction in aqueous solution with TBHP/O_2 and complex **1** in 10 mol% PPO and 10 mol% PEO–SiO_2 was extended to additional substrates (Table 2). For cycloalkanes, it was found that the activity sequence was: cyclohexane > cycloheptane ~ cyclooctane. However, in contrast to the reaction with cyclooctane, no alkene dehydrogenation products were observed, but the product ratios, ketone:alcohol:dialkyl peroxide, were similar. Alkyl aromatic compounds were also oxidized to benzylic ketones and alcohols. Furthermore, a representative linear alkane, nonane, yielded ketones and secondary alcohols in a 2:1 ratio (Table 2).

Table 2. **The Oxidation of Alkanes with 1% wt. Complex 1, 10 % PPO, 10% PEO–SiO_2.**[a]

Substrates	Total TON	Products[b,c]
cyclohexane	238	cyclohexanone 51% cyclohexanol 16% cyclohexyl-*t*-butyl peroxide 33%
cycloheptane	146	cycloheptanone 55% cycloheptanol 19% cycloheptyl-*t*-butyl peroxide 26%
tetrahydronaphthalene	141	α–tetralone 94% α–tetralol 6%
ethylbenzene	157	acetophenone 72% 1-phenylethanol 28%
n-nonane	31	2-, 3-, 4-nonanone 68% 2-, 3-, 4-nonanol 32%

a) Reactions were carried out by mixing 0.38 mmol alkane, 3.8 mmol TBHP in 5 mL water at pH 4.2 with 0.38 μmol precatalyst (as 1% wt. **1** on 10% PPO, 10% PEO–SiO_2) for 3 h at room temeperature. b) products as mol% total products. c) Yields based on TBHP were 80-90%.

Alkane Functionalization Studies with Aqueous Micelles

We chose cetyltrimethylammonium hydrogensulfate (CTAHS) to create micelles for the oxidation of cyclohexane with TBHP/O_2 in aqueous solution with precatalyst, $[Fe_2O((\eta^1\text{-}H_2O)(\eta^1\text{-}OAc)(BPIA)_2]^{3+}$, **3**, (BPIA = bis[(2-pyridyl)methyl][2-(1-methylimidazolyl)methyl]amine) (Figure 2). The results show that as the concentration of cyclohexane and TBHP were varied, a dependence on the TON of the products for each reactant was observed with catalyst **3**. We also observe that an increase in the cyclohexane concentration from 150 to 750 mmols concomitantly increases the amount of oxidation products from 11 TON to 32 TON and, more importantly, an increase in the CyOH/CyONE ratio from 0.47 to 0.82. By halving the amount of TBHP, we observe a decrease in the amount of oxidation products by a factor ~1.8, while the CyOH/CyONE ratio does not change. *These overall results strongly suggest that the cyclohexane oxidation occurs within the micelles.* We also evaluated other substrates, such as toluene (500 mmol) and octanol (500 mmol), in our aqueous micelle system, under similar conditions. We found that toluene provided only benzyl alcohol and benzaldehyde in a ratio of 1.5 with a total TON of 7, while octanol provided only octanal with a total TON of 3. It is intertesting to note, in the latter result, that in the absence of the surfactant (CTAHS) that ~ 1 TON was observed..

In conclusion, we have demonstrated the first example of the functionalization of hydrocarbon substrates with MMO biomimetic complexes embedded in a derivatized surface silica system and compared this synthesized macroenvironment with an aqueous micelle system using TBHP/O_2 as the oxidants. These free radical, alkane functionalization reactions were presumably initiated by the favorable redox chemistry of complexes **1** and **3** in both of the above-mentioned macroenvironments that provided *t*-BuO• and *t*-BuOO• radicals (Haber-Weiss process).

Acknowledgments. Funded by the U. S.-Israel Binational Science Foundation, Elf Aquitaine Inc, and DOE.

Reference

Neimann, K.; Neumann, R.; Rabion, A.; Buchanan, R. M.; Fish, R. H. *Inorg. Chem.* **1999**, *38*, 3575 and references therein.

SINGLE-CRYSTAL NEUTRON DIFFRACTION: A VALUABLE TOOL FOR PROBING BOND ACTIVATION IN σ COMPLEXES

Thomas F. Koetzle and Arthur J. Schultz

IPNS Division
Argonne National Laboratory
Argonne, IL 60439

Introduction

Neutron diffraction has the unique capacity to provide precise hydrogen atom positions in crystalline solids. For more than 20 years, this capability has been exploited in a series of single-crystal studies that shed light on bond activation in σ complexes. Topics investigated include H–H activation in molecular hydrogen complexes,[1] C–H activation in agostic systems[2] and, most recently, B–H activation in a catecholborane metal complex.[3] This paper illustrates some of these results, drawing upon studies carried out using both steady-state monochromatic beam and pulsed time-of-flight Laue diffraction techniques.

Despite its noteworthy successes including those that we illustrate here, single-crystal neutron diffraction generally has seen limited application to date due to the need for very large crystals. Revolutionary improvements are anticipated with the advent of a new generation of sources now under construction or in the planning stage, including the Spallation Neutron Source (SNS) that is scheduled to become operational at Oak Ridge in 2006. Some speculations will be offered on the exciting possibilities envisioned for the single-crystal diffractometer (SCD) that is being planned for SNS.[4]

Experimental

Large, well-formed crystals of the compounds under investigation were mounted on an SCD instrument at the High Flux Beam Reactor[5] (HFBR) at Brookhaven National Laboratory or at the Intense Pulsed Neutron Source (IPNS) at Argonne National Laboratory. The samples were generally cooled to temperatures of 100 K or below for intensity data collection using a closed-cycle helium refrigerator. At HFBR, measurements were carried out sequentially with a steady-state monochromatic beam technique and a neutron wavelength near 1 Å, employing a point detector. Measurements at IPNS utilize a white beam time-of-flight Laue technique with a time- and position-sensitive detector[6] to sample many reflections in parallel (see **Figure 1** for a schematic view of IPNS SCD). These single-crystal neutron diffraction experiments can require a considerable amount of beam time. For example the catecholborane complex mentioned above, which is triclinic and has a unit-cell volume of 642 Å^3, required 14 d for intensity measurement on IPNS SCD using a 4 mm^3 single crystal. Data collection times for our experiments at HFBR were generally similar.

Neutron intensity data were corrected for background, for the Lorenz effect, and for absorption. Time-of-flight data from IPNS were also corrected for the incident neutron spectrum and for the wavelength-dependent detector efficiency. Extinction corrections were included in the least-squares structure refinements, as required.

Results and Discussion

Molecular Hydrogen (η-H_2) Complexes. The discovery by Kubas in 1984 that transition metals can bind molecular hydrogen forming η-H_2 complexes, also termed "non-classical hydrides," has opened a new field of investigation and has allowed some earlier reaction mechanisms or reactivity patterns to be more precisely

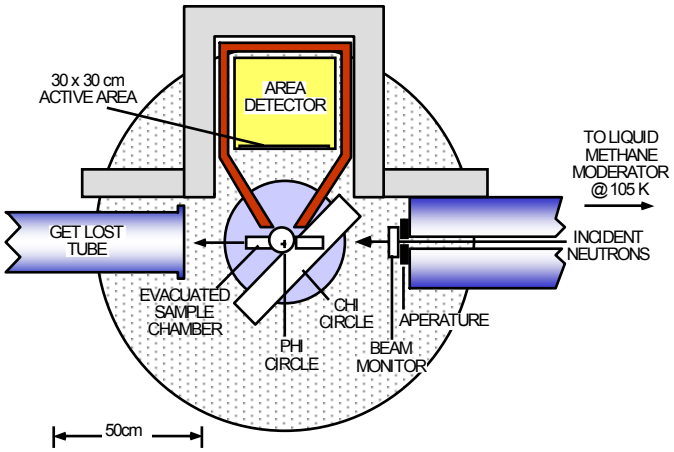

Figure 1. Schematic view of IPNS SCD instrument.

defined or even reconsidered.[7] The crucial step in the hydrogenation reaction path is the coordination to the metal center of an H_2 molecule and its activation via the formation of a non-classical η-H_2 complex, with the subsequent cleavage of the H–H bond (oxidative addition) leading to a classical M(H)$_2$ hydrido complex (**Figure 2**).

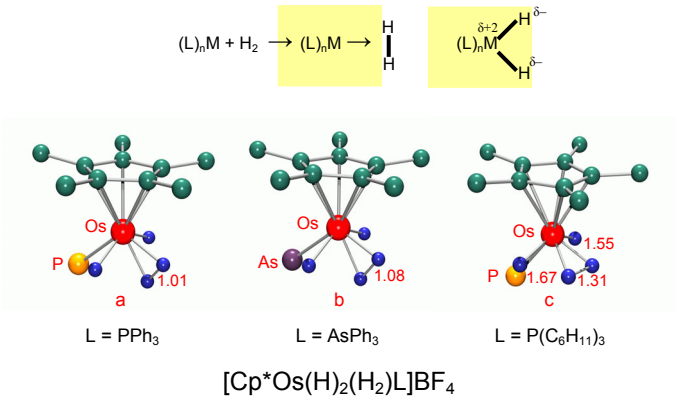

Figure 2. Molecular structures of three cationic osmium molecular hydrogen complexes. The phenyl and cyclohexyl groups bound to phosphorus and arsenic, and the methyl group hydrogens on the pentamethylcyclopentadienyl ligand, are not shown for clarity.

A detailed knowledge of the metal-hydrogen bonding interaction is essential for a better understanding of these reactions. To this end, single-crystal neutron diffraction studies of (H_2) complexes at low temperatures (< 25 K) have established that the H–H separation can cover a wide range of distances, from ~ 0.8 Å (strong H–H bond) to ~1.4 Å (weak H–H bond), thus neatly spanning the oxidative addition pathway and giving support to the mechanistic studies of this most important reaction. Single-crystal neutron diffraction provided the first unambiguous experimental proof of the existence of the so-called "stretched" (i.e., activated) H–H bonds (>1.0 Å).[1,7] Recently a series of cationic osmium complexes (see **Figure 2**) containing

hydrides and dihydrogen in varying degrees of activation has been studied.[8] The reason for the rotation and activation of the H_2 ligand is not completely clear from just these three structures. In order to understand the relative contributions of electronic and steric properties of the ancillary ligands, a question still open to discussion, the series needs to be expanded to include other ligands such as trimethylphosphine. To date, it has not been possible to produce suitably large crystals for neutron diffraction. In the future we hope to be able to tackle this problem at SNS using 0.1 mm^3 crystals, which are readily available, and to use the experimentally observed trends as a check of high-level quantum mechanical calculations.

Agostic Systems. Three-center, two-electron, C–H–metal interactions (agostic bonds) provide models for intermediates in the metal assisted activation of C–H bonds. The molecule shown in **Figure 3** is a possible transition state model for the β-elimination reaction of a metal-allyl to a metal-dienehydride complex. The C–H–Mn interaction is characterized by a very long C–H distance of 1.19(1) Å, compared to a normal value of 1.09 Å. Formation of a 2-electron, 3-center C–H–Mn bond allows the complex to achieve an 18 electron configuration.[2]

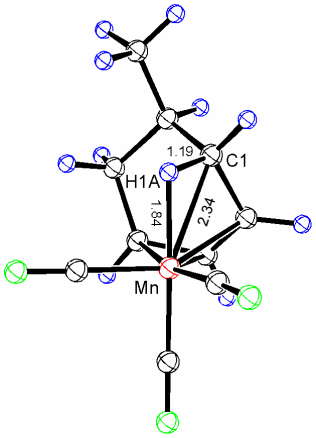

Figure 3. Molecular structure of $(C_7H_{11})Mn(CO)_3$.

Our neutron diffraction study[3] of $(MeCp)Mn(CO)_2(HBCat)$, HBCat=Catecholborane, illustrated in **Figure 4** below, indicates that this σ-borane possesses an extremely elongated B–H bond (1.384(6) Å). This type of highly activated σ-complex is expected to be typical of reaction intermediates that precede oxidative addition of substrates in catalytic hydroborations. The molecular geometry found here features a lateral configuration of the borane (Mn–H–B = 88.8(3)°) and a four-legged piano-stool arrangement with OC–Mn–CO = 90.7(2)°.

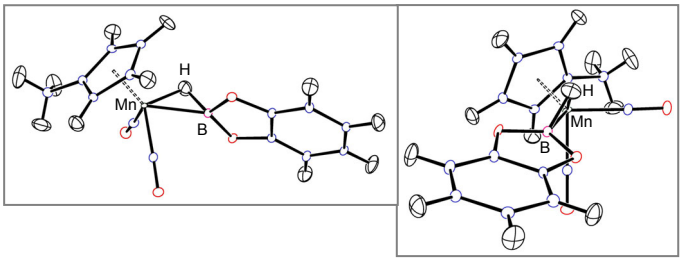

Figure 4. Structure of $(MeCp)Mn(CO)_2(HBCat)$, HBCat= Catecholborane, viewed approximately normal to the Mn–H–B plane (left) and perpendicular to this plane (right).

Future Developments. As we have noted above, revolutionary advancements are anticipated with the advent of a new generation of neutron sources now under construction or in the planning stage. These include the SNS at Oak Ridge, which will generate approximately two orders of magnitude more neutron flux than is now available at IPNS (see **Figure 5**). The SCD instrument planned for SNS[4] will include an extensive area detector array and will be optimized for rapid data collection on moderate size unit cells with up to ca. 50 Å axial repeats. A major objective is to be able to study small, 0.1 mm^3, samples approaching the size that are routinely used in many laboratories for single-crystal X-ray studies. A schematic layout of the instrument conceptual design is shown in **Figure 6**.

In order to maximize scientific impact, SNS SCD includes provision for magnetic scattering experiments, using polarized neutron beams to study unpaired electron distributions, and for diffuse scattering measurements to attack problems involving short-range order. *By greatly expanding the range of materials that can be explored, SNS SCD is expected to revolutionize single-crystal neutron diffraction as we know it, especially from the viewpoint of the practicing synthetic chemist.*

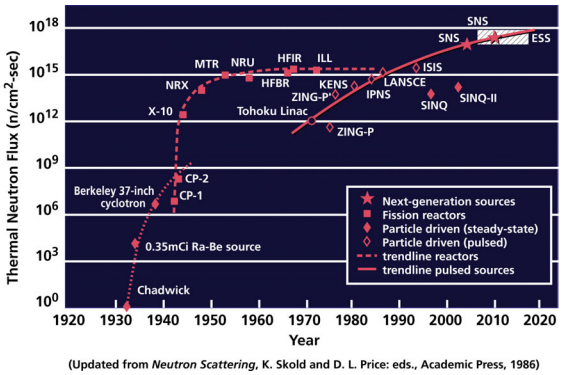

Figure 5. Flux increase at neutron sources, 1930 - .

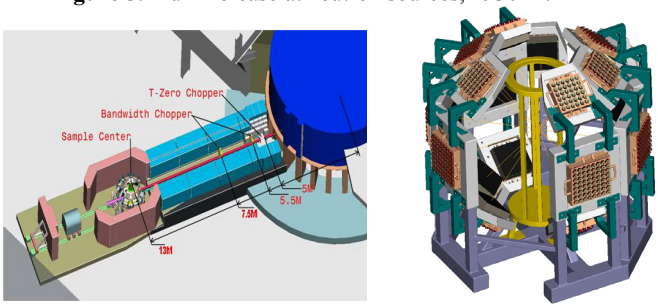

Figure 6. Conceptual design of SNS SCD with the beam line layout (left), and a detail of the sample enclosure and detector array (right). Top access is provided for mounting auxiliary equipment, including cryostats and magnets.

Acknowledgment. This work was supported by the Office of Basic Energy Sciences, U.S. Department Of Energy, under contract W-31-109-ENG-38. Additional support was provided to T.F.K. by NATO under grant PST.CLG.976225.

References

(1) Koetzle, T. F. *Trans. Am. Crystallogr. Assoc.* **1995**, *31*, 57-68.
(2) Schultz, A. J.; Teller, R. G.; Beno, M. A.; Williams, J. M.; Brookhart, M.; Lamana, W.; Humphrey, M. B. *Science* **1983**, *220*, 197-199.
(3) Koetzle, T. F.; Schultz, A. J.; Wang, X. P.; Hartwig, J. F.; Schlecht, S.; Albinati, A. *Am. Crystallogr. Assoc. Meeting Abstracts, Los Angeles, CA,* 2001.
(4) Hoffmann, C. *Conceptual Design for a Single Crystal Diffractometer at SNS*, 2002.
(5) The HFBR facility was permanently shut down in 1999.
(6) Schultz, A. J. *Trans. Am. Crystallogr. Assoc.* **1993**, *29*, 29-41.
(7) Kubas, G. J. *Metal Dihydrogen and σ-Bond Complexes*, Kluwer Academic: Dordrecht, 2001.
(8) Gross, G. L.; Young, D. M.; Schultz, A. J.; Girolami, G. S. *J. Chem. Soc., Dalton Trans.* **1997**, *18*, 3081-3082.

METHANOL AND HYDROGEN FROM METHANE, WATER, AND LIGHT

Charles E. Taylor

U.S. Department of Energy
National Energy Technology Laboratory
P.O. Box 10940
Pittsburgh, PA 15236-0940

Introduction

Research on the conversion of natural gas (methane) has been an ongoing effort at the National Energy Technology Laboratory (NETL) for over 20 years. A long-term goal of our research team is to explore novel pathways for the direct conversion of methane to liquid fuels, chemicals, and intermediates.

Literature reports have indicated that photochemical oxidation of methane may be a commercially feasible route to methanol [1, 2]. In these studies, methane, water and light are reacted at moderate temperatures and pressures.

Research in our laboratory [3] has shown that, methane, dissolved in water, at temperatures > 70 °C, with a semiconductor catalyst, can be converted to methanol and hydrogen. The use of three relatively abundant and inexpensive reactants - light, water, and methane - to produce methanol is an attractive process option. The main advantage of using a photocatalyst to promote the photoconversion of methane to methanol is that the presence of the catalyst, in conjunction with an electron transfer agent, allows reaction to occur with visible light instead of with ultraviolet. This greatly simplifies reactor design and will permit flexibility in the selection of the light source. The products of the reaction of interest, methanol and hydrogen, are both commercially desirable as fuels or chemical intermediates. The limiting factor for conversion of methane appears to be the solubility of methane in water. We hypothesized that if the concentration of methane in water can be increased, conversion should also increase. Methane hydrates might provide a method of increasing the amount of methane dissolved in water, because at standard temperature and pressure (STP), one volume of saturated methane hydrates contains approximately 180 volumes of methane.

Methane hydrates were first observed in the laboratory in 1810. It wasn't until nearly 150 years later that they were observed in nature. Hydrates can occur in permafrost, in sediment where gas exists under moderate to high pressure and low temperatures, and offshore beneath deep water. Hydrates are a problem in the oil and gas production industry because they can form in the well or pipelines, thereby blocking the flow of fuel. Estimates by the U.S. Geological Survey project that world hydrate deposits contain approximately 2×10^4 trillion cubic meters of methane [4]. Estimates of methane hydrate deposits off the coast of the United States is approximately 9×10^3 trillion cubic meters of methane with an additional 17 trillion cubic meters of methane in the permafrost on the north slope of Alaska [1].

Our vision is to immobilize methane and water in close proximity by formation of the methane hydrate. The reaction will involve the formation of hydroxyl radical (•OH) within the methane hydrate by photochemical means. The proximity and restricted mobility of the •OH and the CH_4 would then favor the formation of CH_3OH. Successful demonstration of this principle would then open the possibility of using hydrates to immobilize reactants in a way that favors the desired selectivity. This is the basis of our Patent [5].

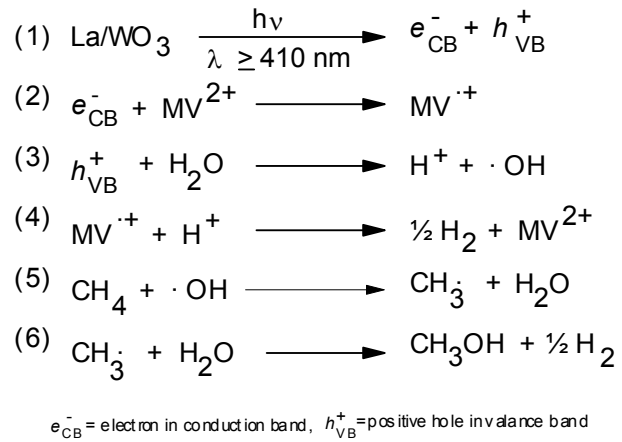

e^-_{CB} = electron in conduction band, h^+_{VB} = positive hole in valance band

Scheme 1: Proposed pathway for the photocatalytic conversion of methane and water

EXPERIMENTAL

The tungsten oxide semiconductor photocatalysts were synthesized following a modification of the procedure in the literature [6]. Four dopants, copper, lanthanum, platinum, and a mixture of copper and lanthanum, were selected for study on the tungsten oxide catalyst base. The titania photocatalyst used in this study is a proprietary sol-gel TiO_2 catalyst obtained from Attia Corporation.

The 1.0 MPa, a commercially supplied 1-liter quartz photochemical reaction vessel, was fitted to meet the needs of this research. This included use of a Teflon-coated magnetic stirring bar in the reactor, a fritted glass sparger, a nitrogen line used to cool the UV lamp, and an injection port.

In a typical 1.00 MPa pressure experiment, the sintered catalyst is suspended, by mechanical stirring, in double-distilled water (~750 mL) containing an electron-transfer reagent, methyl viologen dichloride. A mixture of methane (5 mL/min) and helium (16 mL/min) is sparged through the photocatalytic reactor. The helium is an internal standard for on-line analysis of the reactor effluent. The reaction temperature is maintained at ~371 K by circulation of heated (~393 K) silicone oil in the outer jacket of the reactor. A high-pressure mercury-vapor quartz lamp is used as the light source.

All pressurized and hydrate reactions were conducted in a high-pressure view cell. The cell is constructed of 316 stainless steel 6.35 cm (2.5 inches) OD and 27.4 cm (11 inches) in length. The internal volume of the cell is ~ 40 mL. The cell is fitted with 2 machined endcaps, one which contains a sapphire window to allow for observation of the contents of the cell using a CCD camera. The cell is fitted with ports to accommodate the fill gas inlet and reaction product outlet, a pressure transducer to monitor the internal pressure of the gas inside the cell, and a thermocouple that terminates inside the cavity of the cell to monitor the temperature of the liquid/hydrate mixture. While the working pressure of the cell is rated at 220 MPa (32,000 psia), all experiments were conducted at 13.8 MPa (2000 psig) or less. The temperature of the cell is controlled by the flow of a glycol/water solution from an external circulating temperature bath through a coil of 0.64 cm (¼ inch) copper tubing that is wrapped around the outside of the cell. Several layers of insulating material are wrapped around the cell to help maintain constant temperature.

A typical experiment involves filling the cell with 40 mL of double-distilled water. A Teflon® coated stir bar is added, followed by portions of the photocatalyst. The endcap is placed on the cell and tightened to specifications. An external magnetic stirrer is used to obtain a high degree of vortex mixing inside the cell. The cell is connected to the gas manifold and purged several times with

methane. Following the purge procedure, the cell is charged with methane at pressures of 5.5 – 13.8 MPa (800-2000 psig). Using the external circulating temperature bath, the temperature of the water in the cell is lowered until formation of the methane hydrate is observed. After formation of the hydrate, the temperature of the cell is lowered to -5 °C and held constant. Illumination of the hydrate is then performed using a high-pressure 350-watt mercury-vapor lamp, with the light directed toward the sapphire window. After illumination for a set period of time, the cell is allowed to warm slowly to room temperature. When the cell and its contents have reached room temperature, the contents of the cell are vented and a gas chromatograph and/or a mass spectrometer are used to analyze the products.

RESULTS

Of the four-tungsten oxide (doped with platinum, lanthanum, copper, and a 50/50 molar mixture of copper and lanthanum) and the sol-gel titania catalysts studied, the tungsten oxide catalyst doped with lanthanum exhibited the largest methane conversion and methanol yield. This catalyst was the one chosen for use in this study (Figure 1).

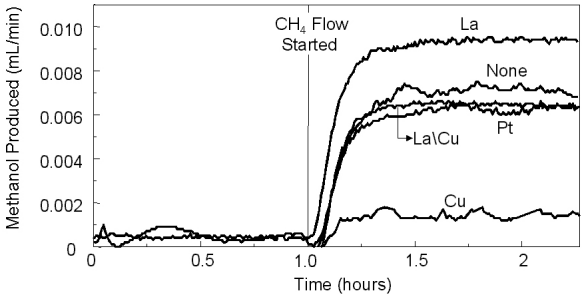

Figure 1. Methanol production with various promoted tungsten oxide photocatalysts.

Figure 2 shows the results of a typical photocatalytic methane conversion experiment at 1.0 MPa. Methane conversions are ~4% with hydrogen and methanol as the main products of reaction. Note that after the UV lamp is turned off, the detected flow of methanol decreases slowly to zero (over ~2 hours). It was hypothesized that this behavior was due to stripping of methanol from the water in the reactor by the reactant gases. To confirm this, methanol was injected into the reactor, previously filled with 750 mL water at the operating temperature, and the concentration of methanol in the gas flow from the reactor was measured as a function of time. A decrease in methanol concentration over several hours, similar to that observed in experiments undergoing methane photoconversion, was observed.

As noted previously, the proposed reaction sequence of interest initially produces hydroxyl radical, which then reacts with methane to produce methanol. To test the validity of this hypothesis, a 30% solution of hydrogen peroxide, a good source of hydroxyl radicals, was injected into the reactor during photocatalytic methane conversion. After peroxide injection, conversion of methane increases from ~4% to ~10%, methanol production increases 17 fold, and carbon dioxide increases 5 fold, along with modest increases in hydrogen and carbon monoxide. A drop in methane conversion to zero for approximately 12 min after injection of the hydrogen peroxide solution was observed in all experiments. This drop in methane conversion can be explained by assuming that prior to injecting hydrogen peroxide solution; a steady-state condition existed between the methane dissolving in the water and methane being consumed. It is likely that the introduction of excess hydroxyl radicals depleted the dissolved methane. At the temperature where the reactions were conducted, the solubility of methane in water is very low (0.017 ml of methane per ml of water [7]). This low solubility results in little methane available for conversion until steady-state conditions could be re-established.

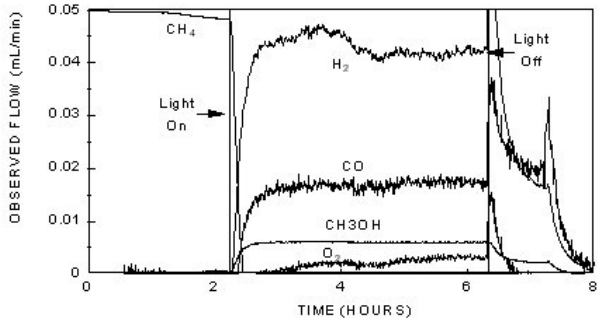

Figure 2. Products of the photocatalytic conversion of methane in water at 1.00 MPa and 370 K.

Note that in Figure 2, after the UV lamp is turned off, the detected flow of methanol decreases slowly to zero (over ~2 h). This is due to stripping of dissolved methanol from the water in the reactor by the reactant gases. Gas chromatographic analysis of the liquid product that had condensed in the trap at 273 K revealed the presence of methanol and acetic acid. Further analysis to identify other components by GC-MS was not possible due to the low concentration of products in the trap. The products were diluted by water carried over from the reactor in the flow of helium that is used as an internal standard.

The tungsten oxide photocatalyst is reported to function at wavelengths >410 nm. All results reported above were obtained using the UV lamp's total spectrum output In order to separate reactions initiated by radiation with UV light from reactions initiated by visible light, a filter was constructed to block the UV portion of the lamp's energy output. The filter, a Pyrex ® sleeve fitted around the lamp, absorbs nearly all radiation below ~310 nm. The total energy output of the lamp with the filter in-stalled is ~50% of that without the filter. Experiments using the filter around the lamp were conducted under conditions described above. The results of experiments conducted with the UV filter installed gave similar conversions and product selectivities as those observed using the full spectrum of the lamp (Figure 3).

Photocatalytic conversion of methane and water at 10.1 MPa produced a product slate similar to that obtained at atmospheric pressure. What is of note is that while no conversion of methane was observed for the experiments conducted at atmospheric pressure at temperatures less than 343 K, at 10.1 MPa conversion occurred at 323 K.

The majority of the photocatalytic research, including the photocatalytic conversion of methane in methane hydrates, was performed with the lanthanum-promoted tungsten oxide photocatalyst. Figure 3 shows the results of photocatalytic conversion of methane dissolved in water at atmospheric pressure and 97°C for various dopants. As is shown, the catalyst doped with lanthanum out performs the other doped catalyst for the production of methanol.

Photocatalytic conversion of the methane contained within the methane hydrate molecule produced results similar to the two previously described experiments; methanol and hydrogen were the main products. This is an interesting result as at atmospheric pressure, no photocatalytic conversion of methane dissolved in water is observed at temperatures below 70°C. The photocatalytic conversions of the methane hydrate occurred at temperatures of –5°C and below.

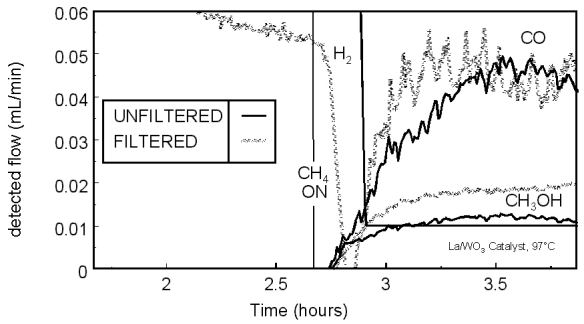

Figure 3. Products of the photocatalytic reaction of methane dissolved in water at atmospheric pressure and 97°C with full spectrum and filtered (visible) light.

Analysis, by mass spectrometry (Figure 4), of the gas contained in the headspace of the cell after illumination revealed the presence of methanol, hydrogen, ethane, oxygen, formic acid, and carbon dioxide. The formation of methanol and hydrogen are the primary products of reaction. The other products observed are formed by side reactions. Photocatalytic splitting of water (a side reaction not shown but observed in our laboratory when using this catalyst) forms oxygen. Ethane is formed by the combination of two methyl radicals (produced in Equation 5), and the formic acid and carbon dioxide are the result of further reactions of methanol.

The results of photocatalytic conversion of methane contained within methane hydrates with a sol-gel titanium dioxide photocatalyst are similar to the tungsten oxide photocatalyst with the exception that while methanol and hydrogen are produced by the reaction, oxygen is the main product of the titanium sol-gel photocatalyst.

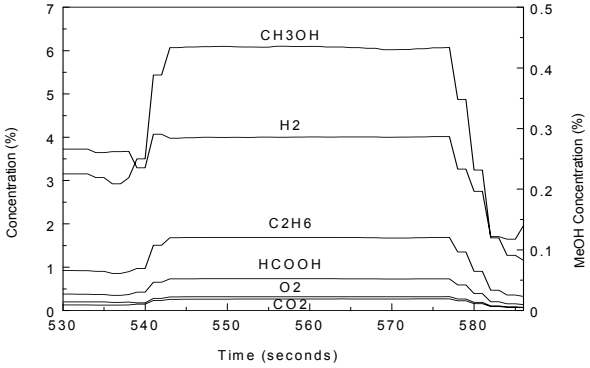

Figure 4. Products of the photocatalytic conversion of methane in methane hydrate with lanthanum-promoted tungsten oxide photocatalyst.

CONCLUSIONS

By use of a photocatalyst and electron-transfer reagent, we have been able to convert methane and water to methanol and hydrogen. Products of conversion at atmospheric pressure and 10.1 MPa were similar. While photoconversion of methane and water to methanol and hydrogen did not occur below 343 K at 1.0 MPa, conversion was observed at 323 K at 10.1 MPa and at temperatures as low as 258 K in methane hydrates. We also observe several side reactions of methane conversion in all instances, the production of ethane, oxygen, formic acid and carbon dioxide.

Under the conditions used in the 1 MPa experiments, the photocatalytic reaction produced 1.7 g of methanol-per gram of catalyst-per hour in the steady-state mode and produced 43 g of methanol-per gram of catalyst-per hour when hydrogen peroxide solution was added.

The use of a filter removed the UV component from the lamp. Experimental results show that little difference between the filtered and unfiltered lamp was observed in the case of the platinum-doped tungsten oxide sample. This indicates that the photocatalyst is operating using visible light, the UV portion of the lamp's output is negligible in the photocatalytic con-version of methane to methanol, and that a limiting factor in conversion may be the solubility of methane in water.

In all experiments, conversion of methane and the production of methanol are augmented by the addition of hydrogen peroxide solution, consistent with the postulated mechanism that invokes a hydroxyl radical as an intermediate in the reaction sequence. The use of other radical initiators would be of interest to deter-mine if the enhanced conversion could be sustained.

After the hydrate had formed and the pressure in the cell equilibrated, the UV lamp was turned on to initiate the photocatalytic conversion process. During illumination, a decrease in the pressure of the cell is observed. Following illumination, the cell was maintained at -2°C for several hours before warming to room temperature. Also of note is that the final pressure of methane is less than the starting methane pressure due to conversion of the methane within the hydrate.

Mass spectrometric analysis of the gas vented from the cell after illumination revealed the presence of methanol, hydrogen, ethane, oxygen, formic acid, and carbon dioxide, as shown in Figure 4. Side reactions that occur during the photocatalytic conversion process are responsible for producing these additional species. Photocatalytic splitting of water forms oxygen, ethane is formed by the combination of two methyl radicals, and the formic acid and carbon dioxide are the result of further reactions of methanol.

Attempts to use GC to identify products dissolved in the water after reaction were of limited value. In an effort to detect these products dissolved in the water, the cell and its contents were heated to 70°C prior to venting. Analysis of the gas headspace resulted in the detection of similar products as those obtained at room temperature. If products dissolved in the water were present, their concentration was too low to be detected with our setup. We are currently refining our detection system to correct this problem.

Experiments were also performed where the double-distilled water was replaced with simulated seawater. The results of these experiments were similar to those performed with double-distilled water.

DISCLAIMER. Reference in this report to any specific commercial product, process, or service is to facilitate understanding and does not necessarily imply its endorsement or favoring by the United States Department of Energy.

ACKNOWLEDGEMENTS. The author would like to acknowledge the technical assistance of Jennifer Bennett, Bradley C. Bockrath, Helen M. Borlan, Joseph D'Este, Edward P. Ladner, Dirk D. Link, and Richard P. Noceti

REFERENCES

(1) Ashokkumar, M. and Maruthamuthu, P. *J. Mat. Sci. Le*tt.**1988**, 24, 2135-39.
(2) Ogura, K. and Kataoka, M. *J. Mol. Cat.* **1988**, 43, 371-79.
(3) Noceti, R.P. and Taylor, C.E. U.S. Patent 5,720,858 **February 24, 1998**.
(4) Collett, T.S. and Kuuskraa, V.A. *Oil and Gas J.* **May 11, 1998**, 90.
(5) Taylor, C.E., Noceti, R.P., and Bockrath, B.C. U.S. Patent *6,267,849* **July 31, 2001**.
(6) P. Maruthamuthu, M. Ashokkumar, Int. J. Hydrogen Energy 14(4) (1989) 275.
(7) J.A. Dean (Ed.), Lange's Handbook of Chemistry, 13th Ed., 1985, p. 10-5.

NEUTRON REFLECTIVITY STUDIES OF THE GAS/SOLID/LIQUID INTERFACE

Miriam Rafailovich, Tadanori Koga, Young Soo Seo, Devinder Mahajan, Jonathan Sokolov

Department of Materials Science and Engineering, Stony Brook University, Stony Brook, NY 11794 USA

Benjamin Chu
Department of Chemistry, Stony Brook University, Stony Brook, NY 11794 USA

Sushil Satija
NIST, Gaithersburg, MD 20879 USA

Introduction

Polymer films form convenient matrices catalysis. In particular when highly reactive Fe or Co nanoparticles are encapsulated in polymer films the polymer can serve both as mechanical support as well as protective coating against fouling. On the other hand, since many of the reactions are gas phase, the same protective properties inhibit flow of the reactants and reduce the efficiency of the catalyst. Recently, using neutron reflectivity (NR), it has been demonstrated that $scCO_2$ may serve as a "universal solvent" near polymer surfaces and in thin films within a narrow temperature and pressure regime, known as the "density fluctuation ridge"[1,2]. Even thin films of glassy polymers, such as polystyrene (PS) and poly(methyl methacrylate), the films were observed to swell up to 40 % along the ridge near the critical temperature of CO_2 (T_c=31.3 ºC),[3] at temperature well below their glass transition temperatures (T_g ~ 100 ºC), while the bulk swelling was less than 10 %. In addition, we found that the effect could be frozen by a flash evaporation of CO_2 via the polymer vitrification process[4] without the formation of voids[5,6] as previously reported in the bulk.[7,8] Since CO_2 is a "green solvent" which does not react with many of the catalytic particle inclusions, one can in principal use this process to produce polymer films with high throughput for the reactants which also provide a protective support for the catalyst. Here we will report on the physical properties of theses films, such as density and melting and explore the effects of nanoparticle additions on the interactions between the polymer and CO_2.

Experimental

The films qualities were investigated by using x-ray reflectivity (XR), where the XR is more sensitive than NR to concentration profiles over small distances, and spectroscopic ellipsometry. Samples used in this study were two kinds of hydrogenated PS (PS1:M_w=2.0×10^5, PS2:M_w=6.5×10^5). Both polymers were obtained from Polymer Lab. and their polydispersity indices were 1.05. The thin films were spun cast on HF etched Si substrates and were pre-annealed for 5 hours in vacuum of 10^{-6} Torr at 150 °C. The films were first placed in the high-pressure chamber and immersed in $scCO_2$ at the ridge condition (T = 36 ºC and P = 8.2 MPa) for an annealing time of 2 hours, and then quickly depressurized to atmospheric pressure within 10 sec. It should be noted that the surface remained flat even after the quick evaporation with the root-mean-square (rms) roughness (σ =. 6Å) between the polymer/air interface, which is identical to that of the unswollen film.[5] The XR measurements have been carried out at the X10B beamline of the National Synchrotron Light Source (NSLS), Brookhaven National Laboratory (BNL) using photon energy of 11 keV. In order to obtain the density profile in the direction normal to the surface, we performed the Fourier transformation (FT) analysis for the XR data.[9] FT is powerful tool to analyze even a low x-ray contrast interface of multilayers. A H-VASE spectroscopic ellipsometry (J.A. Woollam Co., Inc.) was used to study the freezing samples with a wide spectral range of 300-800 nm with 10 nm increments. The angles of incidence for all the measurements were varied from 60 to 75º with 5º increments from the vertical.

Results and Discussion

Figure 1(a) shows the representative XR profile $I(q_z)$ for freezing PS1 (unswollen film thickness (L_0 = 110 Å), where the reflectivity is plotted as a function of the momentum transfer normal to the surface, $q_z = 4\pi \sin\theta / \lambda$ with θ being the glancing angle of incidence and λ, the x-ray wavelength, respectively. Figure 1 (b) shows the FT profile of XR data shown in Fig. 1(a), which is related to the corresponding one-dimensional Patterson function, i.e.,

$$F(d, q_1) = \left| \int_{q1}^{q2} q_z^4 I(q_z) \exp(iq_z d) dq_z \right|^2 \qquad (1)$$

where q_1 is the lower q limit, q_2 is the higher q limit and d is the film thickness. The q_1 value, which is sensitive to the shape of the FT, and the q_2 value, which is given by the q_z-range of the data, were set as q_1=0.053 Å^{-1} and q_2=1.0 Å^{-1}, respectively, for the integration in q_z-space. From the figure we can see two small peaks (shown by asterisks), which indicate an existence of two layers having different thickness and density in the film, and one large peak, which is equivalent to the total thickness of the freezing film (164 Å). It is noteworthy that no small peaks are seen in the unswollen film, i.e., the film is thoroughly homogenous, as previously discussed.[9] In order to refine these XR and FT data simultaneously, we used a four-layer model, i.e., silicon substrate, native oxide and two PS layers having the different densities. As shown in Fig. 1 (c), the best-fit result showed that the film was incorporating a constrained 30 Å layer at the Si interface having the bulk PS dispersion value δ of 1.92×10^{-6}) in the refractive index for x-ray[10] and an intermediate layer of 134 Å thickness with δ = 1.27×10^{-6} between air and the constraint layer. Surprisingly, the latter δ value corresponds to an approximately 35 % lower density than the bulk PS density. Hence, we can easily produce tailor-made lower density films as exposed to $scCO_2$ and subsequent quick evaporation.

Next, we shall focus on the optical index of refraction of the vitrified films, which is a density-dependent physical property, by using spectroscopic ellipsometry. The polymer used was PS2 in order to clarify whether the production of the lower-density layer was specific to the polymer. The sample preparation for the vitrified films was exactly same as that for the PS1 films. Fig. 2 shows the refractive indices of the mobile layers as a function of the unswollen thickness. From the figure we can clearly see that the indices of refraction for the mobile layers decreased with increasing S_f values over the wide wavelength range of 450-800 nm. It is noted that this trend is in good agreement with the previous report for PMMA-CO_2 mixtures using ellipsometry experiments.[18]

In conclusion, we found a novel method for producing stable low density and low index of refraction polymer films by using supercritical carbon dioxide. Furthermore, the density-fluctuation-induced swelling may be not specific to either the gas or the polymer

system. Experiments are currently in progress on polymer films containing Fe and Co nanoparticles. Since these particles provide high x-ray contrast, the XR reflectivity yields both the density of the film as well as the distribution of the particles within the films. We, therefore, are able to study the effects of nanoparticle size, concentration, and chemical nature on the on the interactions of supercritical solvents such as ethane and $scCO_2$ with polymer support films.

Acknowledgements

Support of this work by the NSF-MRSEC (DMR 9632525) is gratefully acknowledged.

References

1. McHugh, M. A.; Krukonis, V. Supercritical Fluids Extraction Principles and Practice; Woburn, MA, 1994.
2. Koga, T.; Seo, Y.-S.; Zhang, Y.; Shin, K.; Kusano, K.; K., N.; Rafailovich, M. H.; Sokolov, J. C.; Chu, B.; Peiffer, D.; Occhiogrosso, R.; Satija, S. K. Phys. Rev. Lett. **2002**, 89, 125506.
3. Koga, T.; Seo, Y.; Shin, K.; Zhang, Y.; Rafailovich, M.; Sokolov, J.; Chu, B.; Peiffer, D.; Satija, S. K. Submitted to Macromolecules.
4. Koga, T.; Seo, Y.; Hu, X.; Kwanwoo, S.; Zhang, Y.; Rafailovich, M. H.; Sokolov, J. C.; Chu, B.; Satija, S. K. Europhys. Lett. in press.
5. Koga, T.; Shin, K.; Zhang, Y.; Seo, Y.-S.; Rafailovich, M. H.; Sokolov, J. C.; Chu, B.; Satija, S. K. J. Phys. Soc. Jpn, **2001**; 70, 347.
6. RamachandraRao, V. S.; Gupta, R. R.; Russell, T. P.; Watkins, J. J. Macromolecules **2001**, 34, 7923.
7. Arora, K. A.; Lesser, A. J.; McCarthy, T. J. Macromolecules **1998**, 31, 4614.
8. Stafford, C. M.; Russell, T. P.; McCarthy, T. J. Macromolecules **1999**, 32, 7610.
9. Seeck, O. H.; Kaendler, I. D.; Tolan, M.; Shin, K.; Rafailovich, M. H.; Sokolov, J. C.; Kolb, R. Appl. Phys. Lett. **2000**, 75, 2713.
10. δ is expressed by $\delta = r_e N_A/(2\pi)\rho\sum_i (Z_i/A_i)$ where r_e is the classical electron radius, N_A is Avogadro's number, ρ is the density, A_i and Z_i are atomic weight and atomic number of the element i.
11. DeMaggio, G. B.; Frieze, W. E.; Gidley, D. W.; Zhu, M.; Hristov, H. A.; Yee, A. F. Phys. Rev. Lett. **1997**, 78, 1524.
12. Polymer Handbook 4th Ed.; John Wiley & Sons, Inc.: NY, 1999.
13. S_f was calculated from the equation $S_f = (L-L_0)/(L_0-x)$, where L is the measured thickness of the swollen films and x is the thickness of the constrained layer, respectively.
14. The maximum thickness for four-layer model was approximately 650 Å for PS2. The difference between two PS could be due to the R_g scaled swelling behavior.
15. Koga, T. et al, manuscript in preparation.
16. Philipp, E. D., 1. In Handbook of Optical Constants of Solids; Palik, E. D., Ed,; Harcourt Brace Javanovich:Orland, 1985; Vol. 1.
17. Jellison, G. E. J. Appl. Phys. **1991**, 69, 7627.
18. Sirard, S. M.; J., Z. K.; Sanchez, I. C.; Green, P. F.; Johnston, K. P. Macromolecules **2002**, 35, 1928.

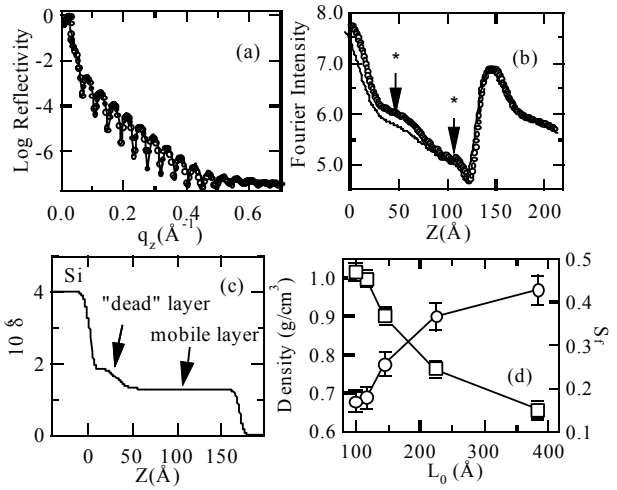

Figure 1. (a) Measured RF (symbols) and refinement (solid line) of the freezing PS1 (L_0=110 Å) film. (b) FT of measured (symbols) and calculated (solid) RFs. (c) Dispersion profile used for the refinement. (d) Thickness dependence of ρ(○) and S_f (□).

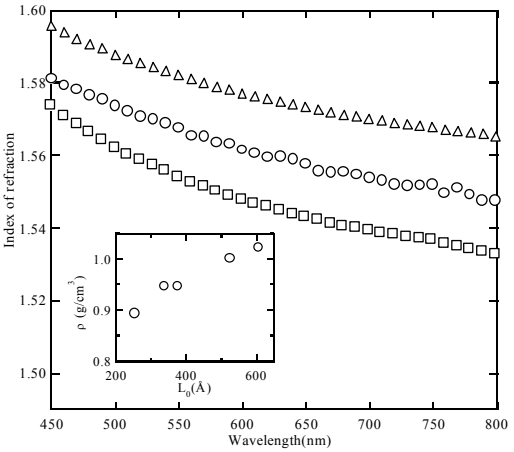

Figure 2 Index of refraction for PS2: Unswollen (Δ), L_0=523 Å (S_f=0.16) (○) and L_0=337 Å (S_f= 0.21) (□). In the inset, thickness dependence of ρ for PS2 is shown.

KINETIC REPRODUCIBILITY OF METHANE PRODUCTION FROM METHANE HYDRATES

Phillip Servio & Devinder Mahajan

Energy Sciences and Technology Department
Brookhaven National Laboratory
Upton, New York 11973-5000, USA

Introduction

Natural gas is the cleanest of all available fossils fuels and its use is increasing globally. This increasing demand is raising concerns regarding the long-term supply of this precious resource. Recent estimates have put the amount of stored methane in methane hydrates at several orders of magnitude higher than all presently known sources of methane. In order to pursue this abundant reserve, technological hurdles must be solved which will allow the safe capture of methane from dispersed hydrate sources around the world.

Experimental

A new experimental apparatus has been developed for the measurement of hydrate formation and decomposition kinetics, see figure 1. The main component of the hydrate phase equilibrium apparatus is a high-pressure reactor fabricated from 316 stainless steel. The vessel has rectangular viewing windows constructed from borosilicate and is immersed in a temperature-controlled bath consisting of an equal volume mixture of ethylene glycol and water. Experimental gas and water are brought into contact, in the reactor, in a countercurrent fashion. Water enters from the top, while the gas enters from the bottom to help agitate the liquid and clay sediments and achieve a uniform system. The experimental temperature of both the gas and liquid phases are measured with the aid of type K thermocouples. The pressure is measured by differential pressure transducers. The experimental methane gas flow rate into the system is measured and regulated by a mass flow controller (Brooks) with a range of 0-2000 ml per minute. A back pressure regulator is used to ensure constant pressure during both a formation and decomposition experiment. A dry test meter is used on the back pressure regulator side to measure the amount of gas exiting the high pressure vessel

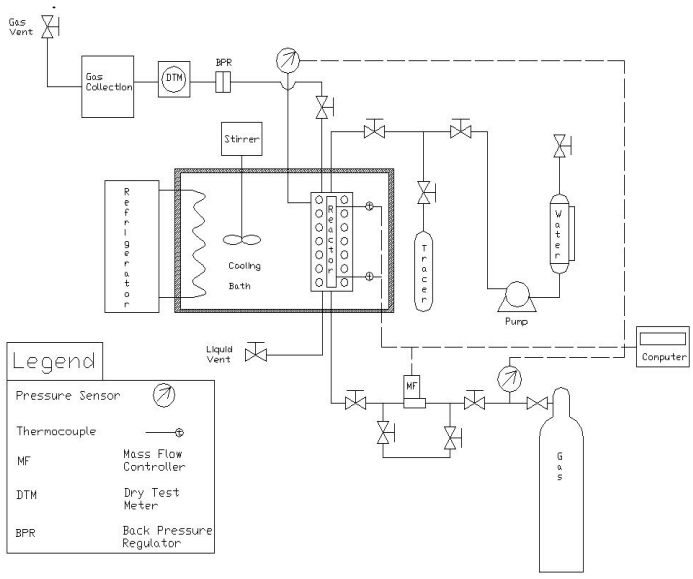

Figure 1. Newly Commissioned Unit for Hydrate Kinetic Study at BNL.

during the formation or decomposition process. Tracers may also be injected in order to determine sediment stability during the cycle of hydrate formation and decomposition.

Results and Discussion

The Kinetics of hydrate formation can be described in two steps, nucleation and growth. Nucleation is characterized as the time required for hydrate crystals to achieve a critical size nucleus that can sustain growth. The nucleation time is believed to be a stochastic phenomenon that cannot be predicted (Parent and Bishnoi, 1996). Hydrate growth is the process where hydrate nuclei have achieved the necessary critical size and continue to grow and form hydrate crystals. The driving force for hydrate growth is the difference in the fugacity of the dissolved gas and the three-phase equilibrium fugacity at the experimental temperature. Figure 2 shows a typical plot of moles of gas consumed vs. time during a hydrate formation experiment.

.

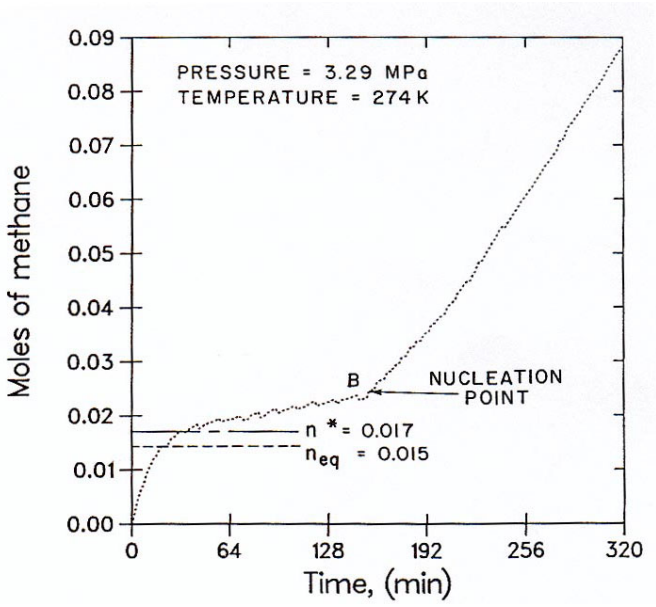

Figure 2. Moles of gas consumed vs. time for a methane hydrate formation experiment (adapted from Englezos et al., 1990).

In figure 2, the onset of hydrate formation occurs at the nucleation point, B, which is known as the turbidity time. The turbidity time denotes the first appearance of stable hydrate crystals and is the beginning of the hydrate growth phase. n* is the number of moles of methane gas corresponding to a vapor-liquid water equilibrium. This equilibrium is hypothetical because hydrates form at these conditions. This would be the solubility of methane in water in the absence of hydrates. n_{eq} is the number of moles of methane dissolved in liquid water corresponding to a vapor-liquid-hydrate equilibrium pressure at the system temperature (Servio and Englezos, 2002). At the system temperature**,** the pressure is known as the incipient equilibrium hydrate formation pressure, P_{eq}. The value of n_{eq} is less then n* in the hydrate formation region because it corresponds to a lower pressure, P_{eq}, then the experimental pressure. Experimental work by Servio and Englezos (2002) validated these results. It was hypothesized that the difference in moles of gas between point B (n_B) and n_{eq} accounts for the amount of gas consumed in the formation of hydrate nuclei as postulated by Englezos et al. (1987).

The hydrate decomposition process has not been as extensively studied as that of hydrate growth; fortunately the two processes have many similarities. A decomposition process can be viewed as decomposing particles surrounded by a desorption "reaction" layer, followed by a cloud of evolved gas (Kim et al, 1987). The decomposition of solid hydrates is an endothermic process that gives gas and liquid water as its products. Hydrate decomposition is thought to consist of the following two steps:

1) The destruction of the clathrate host lattice at the surface of the particle followed by the desorption of the guest molecule from the surface into the reaction layer.
2) The diffusion of gas from the reaction layer into the bulk liquid

The driving force is represented by the difference in fugacity of the gas at the three-phase equilibrium conditions (equilibrium temperature and pressure) and the dissolved gas fugacity at the experimental temperature and pressure. The latter fugacity is assumed to be equivalent to the fugacity of the gas at the solid particle surface.

Our current study relates to the methane hydrate formation and decomposition cycle in a recently commissioned unit. First, the baseline kinetic study is being carried out with CH_4/H_2O mixture under the temperature/pressure conditions that mimic the methane hydrate stability zone in the subsurface environment to establish data reproducibility. The baseline study will be followed by a kinetic study in the Euxinic seawater/CH_4 mixture to mimic seafloor environment. The known kinetic models will be reviewed with respect to their relevance to the measured data.

Typical models that will be evaluated for the production of methane gas from methane hydrate include those of Yousif et al. (1991) and Goel et al. (2001). Figure 3 shows the molar ratio of methane gas trapped at various dissociation pressures (Goel et al., 2001). Figure 4 gives the cumulative gas produced from hydrates at

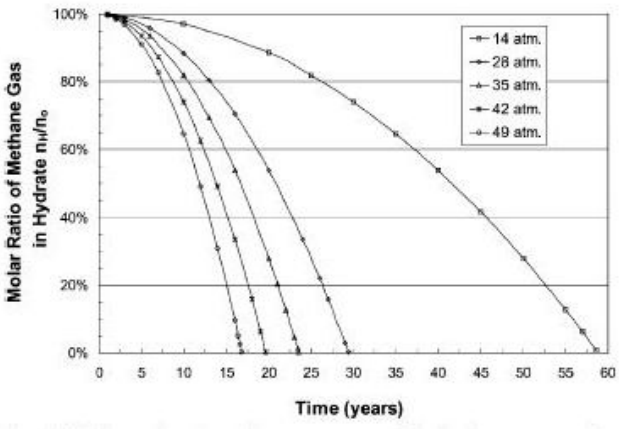

Figure 3. Molar ratio of methane trapped in hydrates at various dissociation pressure drops (adapted from Goel et al., 2001).

various dissociation pressure drops. It is important to note that figures 3 and 4 were produced under the assumption that the pressure drop is constant through the dissociation of the hydrates. In a reservoir the pressure drop is variable and is taken into consideration in the model of Goel et al. (2001).

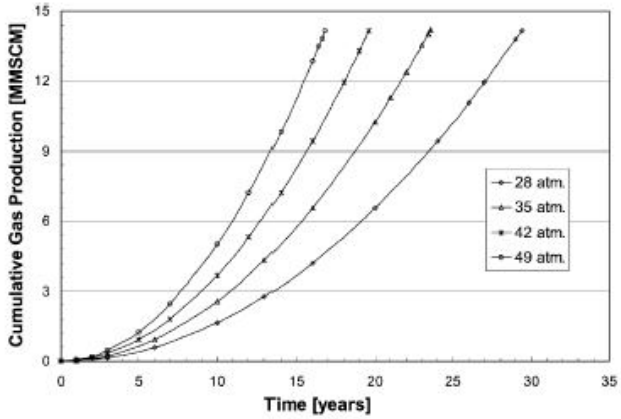

Figure 4. Cumulative gas produced from hydrates at various dissociation pressure drops (adapted from Goel et al., 2001).

The results obtained from this work will give valuable insight into the current state of existing models for the formation and dissociation of hydrates in porous media. These results will also provide us with information concerning the stability of sea floor hydrates and sediments under dissociation conditions.

Acknowledgment

This work was supported by Brookhaven National Laboratory under the Laboratory Directed Research and Development (LDRD) Program. A start-up grant (to DM) from the State University of New York at Stony Brook is gratefully acknowledged.

References

1. Englezos, P., *Gas Hydrate Equilibria*, M.Sc Thesis, U. Calgary, 1990.

2. Englezos, P., Kalogerakis, N., Dholabhai, P. D., Bishnoi, P. R., *Kinetics of Formation of Methane and Ethane Gas Hydrates*, Chem. Eng. Sci., 42 (11), 2647-2658, 1987.

3. Goel, N., Wiggins, M., Shah, S., *Anayltic modeling of gas recovery from in situ hydrate dissociation,* Journal of Petroleum Sci. & Eng., 29,115-127, 2001.

4. Kim, H. C.,Bishnoi, P. R., Heidemann, R. A., Rizvi, S. S. H. *Kinetics of methane Hydrate decomposition*, Chem. Eng. Sci, 42 (7), 1645-1653, 1987.

5. Parent, J.S. and P.R. Bishnoi, *Investigations into the nucleation behavior of natural gas hydrates,* Chemical Engineering Communications (CEC), 144, 51-64, 1996.
6. Servio, P., Englezos, P., *Measurement of the amount of dissolved methane in water in equilibrium with its Hydrate*, J. Chem. Eng. Data, *47*(1), 87-90, 2002.

7. Yousif, M.H., Abass, H.H., Selim, M.S., Sloan, E.D., *Experimental and theoretical investigation of methane-gas-hydrate dissociation in porous media*, SPE Reservoir Eng., 69-76, February 1991.

STABILIZATION OF COPPER/ZIRCONIA BASED CATALYSTS FOR ALCOHOL SYNTHESIS

*Cheng Yang, Guisheng Wu, Wenhuai Li, Yuhan Sun**

State Key Laboratory of Coal Conversion,
Institute of Coal Chemistry, Chinese Academy of Sciences,
Taiyuan 030001 P.R.China

Introduction

Among other technologies based on syngas, direct alcohols synthesis represents a promising natural gas upgrading objective. It is widely recognized that higher alcohols together with methanol can be produced from syngas by appropriate modification of methanol synthesis catalysts and reaction conditions [1-2]. The conventional methanol synthesis is a highly exothermic process with 6-8 MPa, 260-280°C as operating conditions and a conversion of CO about 60% performed on CuZnAl catalyst. The synthesis of higher alcohols is a combination of parallel and consecutive reactions. The formation of alcohols becomes more exotherm with higher carbon number. In comparison with the other alcohols, methanol formation is limited thermodynamically at substantial lower temperature. Qualitatively, in the reaction of syngas to methanol and higher alcohols only the conversion of the reaction to methanol can be limited by the position of the thermodynamic equilibrium in the range of 10-30MPa and 300-420°C, whereas a similar situation is not expected in the case of ethanol, n-propanol and isobutanol [3]. However, such reaction conditions are hardly consistent with the preservation of a high dispersion of reduced copper.

Palladium is also well known as an active phase for CO hydrogenation. Indeed, an alkalized PdZnMrZrO$_2$ catalyst has been developed for methanol-isobutanol synthesis, as ZrO$_2$ was claimed to be active for iso-synthesis [4]. The catalyst for the process also requires high temperatures (>400°C) and pressures (>12 MPa) and produce isobutanol with relatively low productivity (<100 g/kg-cat·h). Moreover, the addition of palladium into other metal catalysts can lead to a substantial improvement in catalytic properties due to its excellent candidates of activate hydrogen, which could then spread over the neighboring phases through a hydrogen-spillover mechanism. It has been demonstrated that active catalyst for the synthesis of methanol can be prepared by dispersing Cu on ZrO$_2$ [5]. Thus, the objective of this work is first to stabilize a Cu/ZrO$_2$ catalyst by introducing La and Mn. Then, the most efficient catalyst for methanol synthesis is shifted towards higher alcohols under mild conditions using K as a promoter. The modification is further made in the catalyst composition by Pd to increase the production of higher alcohols without simultaneously increasing unwanted methanation and other hydrocarbon by-products.

Experimental

Catalysts preparation. Catalytic formulations were prepared by co-precipitation in constant pH conditions about 10-11 using the corresponding metal nitrates as precursors (Cu:Mn/La:Zr molar ratio = 1:0.5/0.1:2) with aqueous sodium carbonate solution, followed by aging, washing and drying. Pd and K were doped by wetness impregnation K_2CO_3 and $Pd(NO_3)_2$ with the precipitates, and then the samples were calcined at 350℃ for 4 hr under air. The Pd and K loading in the prepared catalysts were 0.5wt% and 5.0wt%, respectively.

Catalytic activity test. CO hydrogenation tests were carried out using a stainless steel fixed-bed reactor, which contained 1.0ml catalyst. All the catalysts were reduced in H_2 (5% in N_2) flow at 300 ℃ and atmospheric pressure for 6 hr before syngas exposure. Shimazu-8A GC was used to analyze the products. H_2, CO, CH_4 and CO_2 were determined by thermal conductivity detector(TCD) equipped with a TDX-101 column. The water and methanol in liquids were also detected by TCD with a GDX-401 column. The alcohols and hydrocarbons were analyzed by flame ionization detector(FID) with a Propake-Q column.

Characterization Methods. The surface area of the catalysts was measured at -196 ℃ by nitrogen adsorption using a BET apparatus (ASAP 2000). The dispersion degree of Cu was calculated by N_2O-adsorption performed in a micro-reactor, followed with MS. The transmission EXAFS measurements were conducted in the 4B9A beamline in Beijing Synchrotorm Radiation Facility operating at 30-50mA and 2.2GeV. X-ray power diffraction was carried out with a Rigaku D/Max diffractometer equipped with a Cu target and Ni filter. TG-MS was used to determine the amount of carbon deposited on a TGA-92 from TA Instruments.

Results and Discussion

Table 1. The structural parameters of La and Mn modified Cu/ZrO$_2$ catalysts

Catalyst	S_{BET} (m^2/g)	D_{Cu} (%)	CuO fitting parameter [a]	
			N	R/(Å)
Cu/ZrO$_2$	128.86	2.92	3.60	1.948
Cu/La/ZrO$_2$	144.16	4.12	3.57	1.952
Cu/Mn/ZrO$_2$	171.01	5.54	1.83	1.945

a: The coordination number and Cu-O bond length of pure CuO is 4.0 and 1.96, respectively.

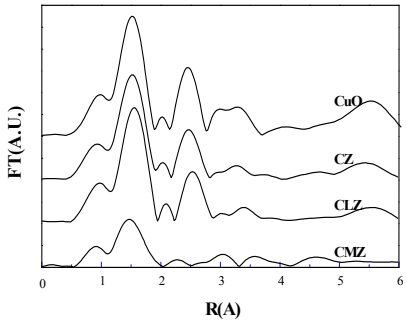

Figure1. The RSF profile of La and Mn modified Cu/ZrO$_2$ catalysts

The catalyst structure greatly changed with the Mn and La addition (see **Table 1**). The surface area increased and highly dispersed copper appeared suggested that both Mn and La could promote the dispersion of the active phase. The radial structure functions (RSF) obtained around Cu atom are shown in **Figure 1**. The coordination number of Cu-O in Cu/Mn/ZrO$_2$ was much lower than that in Cu/La/ZrO$_2$, indicating that a CuMnOx complex formed [6], though only a broad peak could be detected in XRD patterns (not presented). On the contrary, La was facile to enter the lattice of ZrO$_2$ crystals and enhanced the Cu-ZrO$_2$ interaction [7]. Sun [5] found that the strength and nature of the interaction between the dispersed Cu and ZrO$_2$ rather than their surface area is decisive for the activity of CO hydrogenation. Clearly, the addition of La and Mn both promoted the

* Corresponding author. Fax: +86-351-4041153. E-mail address: yhsun@sxicc.ac.cn, yangch68@sxicc.ac.cn

activity of Cu/ZrO_2 for methanol synthesis, and methanol yield on $Cu/La/ZrO_2$ was much higher than that on $Cu/Mn/ZrO_2$ catalyst (see **Figure 2**). It could be interpreted that La and Mn played different roles in influencing the interaction of the components, besides increased the dispersion of active phase Cu. More interestingly, it was found that La and Mn in the co-modified Cu/ZrO_2 catalyst performed a synergistic promotion in improving the catalytic activity for methanol synthesis (see **Figure 3**). The yield of methanol reached 1.8 g/ml-cat.h under 6.0MPa at the GHSV of $7000h^{-1}$.

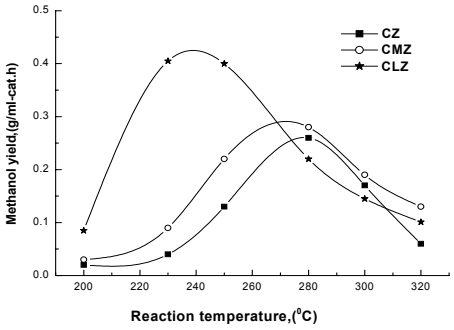

Figure 2. Activity of La and Mn modified Cu/ZrO_2 catalysts for methanol synthesis, Reaction conditions: P=6.0MPa, GHSV=3000 h^{-1}, H_2/CO (molar)=2.0: 1

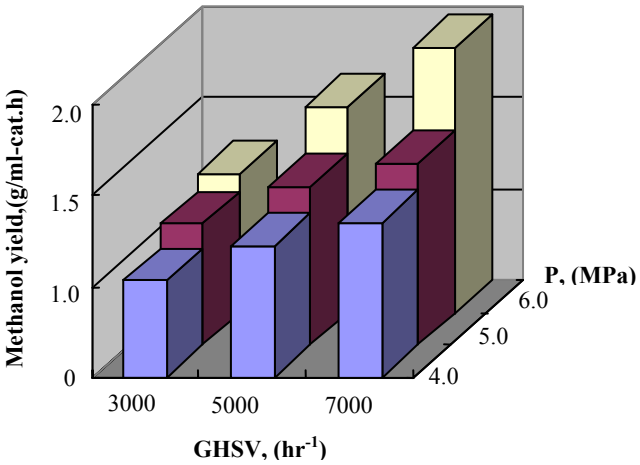

Figure 3. Catalytic performance of La and Mn co-modified Cu/ZrO_2 catalysts for methanol synthesis

K was usually used as a promoter for methanol synthesis shifted towards higher alcohols. As shown in **Table 2** and **Figure 4**, K-CLMZ catalyst showed high performance for higher alcohols synthesis. Naturally, the BET surface area of the alkalized catalyst was drastically decreased as K doped in the pore. The activity of K-CLMZ was also decreased comparing with that of CLMZ catalyst, but it was successfully shifted methanol synthesis towards higher alcohols with amount of CO_2 and hydrocarbons as the by-products. It was noticed that the texture of K-CLMZ catalyst was seriously destroyed during the catalytic test and amount of carbon was deposited on the surface. This suggested that the alkalized catalyst could not serve the relatively severe conditions, i.e. lower H_2/CO radio and high reaction temperature and pressure.

Apparently, the activity was remarkably promoted by Pd addition to K-CLMZ catalyst. Though the selectivity of alcohols and the amount of $C^{2+}OH$ was slightly increased, their yields were both

Table 2. Activity and selectivity of alkalized $CuMnLaZrO_2$ (CLMZ) and $PdCuLaMnZrO_2$ (PCLMZ) catalysts for higher alcohols synthesis

Catalyst	CO Conv (%)	Selectivity, (C-atom%)			Alc.STY (g/ml/h)
		CHx	CO_2	ROH	
K-CLMZ	32.04	28.42	29.32	42.26	0.596
K-PCLMZ	57.38	31.89	24.37	43.74	0.716

Reaction conditions: T=360℃, P=12.0MPa, GHSV=8000 h^{-1}, H_2/CO (molar)=1.0: 1

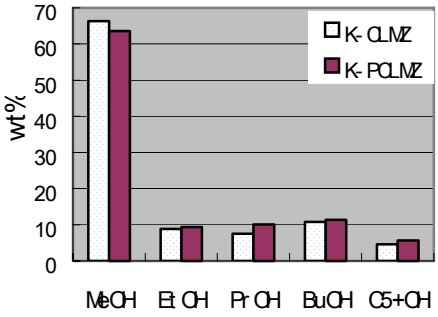

Figure 4. Alcohol distributions over K-CLMZ and K-PCLMZ

remarkably improved. This might due to Pd as an excellent candidate of activate hydrogen, which could spread over the neighboring phases through a hydrogen-spillover mechanism, then improved the rate of carbon hydrogenation and retarded the carbon deposit. Fujimoto and Yu [8] investigating the spillover effect of hydrogen on Pd or Pt promoted Cu/ZnO-based catalysts, arrived at a conclusion that the introduction of Pd led to an increase in the activity as well as the stability of the catalysts poisoning by water. This might be the reason that the texture of K-PCLMZ only slightly destroyed comparing with that of K-CLMZ catalyst. The catalysts performed the similar behavior as Fujimoto and Yu observed.

Table 3. The texture of alkalized $CuMnLaZrO_2$ (CLMZ) and $PdCuLaMnZrO_2$ (PCLMZ) catalysts and carbon deposit

Catalyst		S_{BET} (m^2/g)	V_P (ml/g)	d_P (nm)	Carbon (wt%)
K-CLMZ	Fresh	94.66	0.100	4.24	-
	Tested	27.85	0.039	6.73	0.51
K-PCLMZ	Fresh	88.91	0.141	4.62	-
	Tested	41.80	0.647	5.73	0.27

References

1. Herman, R. G., *Catal. Today*, **2000**, *55*, 233-245
2. Stiles, A. V., et. Al., *Ind. Eng. Chem. Res*., **1991**, 30, 811-821
3. Verkerk, K. A. N., Jaeger, B., Finkeldei, C. H., Keim, W., *Appl. Catal.,* **1999**, 186, 407-431.
4. Wilhelm, K., Wolfang, F., **1989**, 3, 59-64.
5. Sun,Y. H., Sermon, P. A., *J.Chem.Soc.Chem.Commun*., **1993**, 16, 1242-1244.
6. Porta, P., Moretti, G., Musicanti, M., Nardella, A., Catal. Today, **1991**, 9, 211-218.
7. Andriamasinoro, D., Poix, P., Kiennemann, A., Kieffer, R., Appl. Catal. A: General, **1993**, 106, 201-207.
8. K. Fujimoto, Y. Yu, *Stud. Surf. Sci. Catal.*, **1993**, 77, 393-396.

INFLUENCE OF PREPARATION ON STRUCTURAL AND CATALYTIC PROPERTIES OF PALLADIUM PROMOTED COPPER/ZIRCONIA CATALYSTS

Minggui Lin[1], Cheng Yang[2], Yongkui Shan[1], Wei Wei[2], Yuhan Sun[1,2], Mingyuan He[1]*

[1] Department of Chemistry, East China Normal University, Shanghai 200062 P. R. China
[2] The State Key Laboratory of Conversion, Institute of Coal Chemistry, Chinese Academy of Sciences, Taiyuan 030001 P.R.China

Introduction

The traditional low-temperature low-pressure methanol synthesis catalysts, based on $CuO/ZnO/Al_2O_3$ by BASF, were still the subject of extensive fundamental studies, which allowed recently to envisage other supports and in particular, zirconia. Indeed, ZrO_2 is of special interest because of its character of abundant oxygen vacancy, redox property, thermal mechanical stability, high specific surface area, and intrinsic catalytic properties. In recent years, a number of zirconia-containing catalysts have been developed. Especially, metal/zirconia based systems showed interesting catalytic behavior for hydrogenation reaction. For example, zirconia supported copper catalyst has been found to exhibit excellent properties for the methanol synthesis from syngas [1]. Palladium is also well known as an active phase for CO hydrogenation. Moreover, the addition of palladium into other metal catalysts could lead to a substantial improvement in catalytic properties due to its excellent candidates of activate hydrogen, which could then spread over the neighboring phases through a hydrogen-spillover mechanism. Fujimoto and Yu [2], investigating the spillover effect of hydrogen on Pd or Pt promoted Cu/ZnO-based catalysts, arrived at a conclusion that the introduction of palladium led to an increase in the activity as well as the stability of the catalysts poisoning by water. Similar observation has been made by Sahibzada *et al.* and Melian-Cabrera *et al.* [3,4].

The present study focuses on the influence of preparation variables on the structural and catalytic properties of palladium promoted copper/zirconia catalysts for methanol synthesis from CO/H_2. The catalysts were characterized by means of nitrogen adsorption, X-ray powder diffraction (XRD), temperature-programmed reduction (TPR) and nitrous oxide titration.

Experimental

Catalyst preparation. The copper/zirconia (Cu:Zr molar radio =1:2) catalyst were prepared by conventional co-precipitation from a solution of $Cu(NO_3)_2$, $ZrOCl_2$, with Na_2CO_3 under electromagnetic stirring at 70℃. The precipitate was aged, washed with distilled water free of Cl^-, then dried overnight at 120℃ and calcined at 350℃ for 3 hr in air. The catalysts containing 0.2 wt% Pd were prepared by the wetness impregnation method using $Pd(NO_3)_2$ as the precursor. One was dried and the other further calcination following procedures as above, denoting with PCZ-d and PCZ-c respectively.

Catalytic activity test. Activity tests were carried out using a stainless fixed-bed flow reactor with I.D. of 8mm. The catalyst evaluated was hold in the middle of the microreactor, then was reduced in a gas of H_2/N_2 mixture (10% in N_2) at 290℃ for 8 hr with temperature-programmed controller before exposure to syngas. The composition of feed gas was $H_2/CO=2$ with trace amount of CO_2. CO hydrogenation was employed at 8.0MPa overall pressure and with a space velocity of $8000h^{-1}$. H_2, CO, CH_4, and CO_2 were separated by using a carbon size column and were monitored by thermal conductivity detector. The liquid products were separated by using Porapak Q column and detected by a flame ionization detector.

Characterization Methods. The surface area of the samples was determined at -196℃ by nitrogen adsorption using a BET apparatus (ASAP 2000). The powder X-ray diffraction were performed on a D/max-γA diffractmeter. The amount of exposed copper was measured using a nitrous oxide chemisorption method called reactive frontal chromatography (RFC). TPR experiments were carried out at a heating rate of $10℃min^{-1}$ with a programmable temperature controller. An H_2/Ar mixture (5% in Ar) was passed over the catalyst at a total flow-rate of 50 cm^3min^{-1} and hydrogen consumption was monitored by a thermal conductivity detector.

Results and Discussion

Table 1. Morphological properties of catalysts

Samples		S_{BET} m^2/g	V_p cm^3/g	d_P nm	D_{Cu} (%)
CZ	Flesh	148.9	0.127	3.423	2.89
	Used	45.0	0.047	4.236	1.30
PCZ-d	Flesh	131.2	0.134	4.074	1.12
	Used	67.2	0.069	4.130	1.45
PCZ-c	Flesh	117.8	0.117	3.981	1.31
	Used	46.4	0.051	4.433	1.14

The addition of 0.2wt%Pd into copper/zirconia system led to a slight change in BET surface area as shown in **Table 1**. A further loss of special surface area for palladium promoted Cu/ZrO_2 catalyst was followed with calcinations of pre-dried sample at 350℃ under air. After exposure to hydrogenation condition, all samples suffered from a sharply decrease of BET surface area compared to the fresh ones. Considering the loss of the porous volume of all samples (**Table 1**), one should consider that this might be resulted partially from the plugging of microporous fraction of samples by coke deposition on the catalyst surface originated from the Boudouard reaction:

$$2CO\ (g) = CO_2\ (g) + C\ (s)$$

Moreover, it is worth noting that PCZ-d catalyst seems to exhibit more effective capability of coke deposition resistance than that of other catalysts, therefore possesses larger porous volume. Because of its ability of activate hydrogen followed spread over the neighboring phase through spillover mechanism, the existence of palladium causes more abundant hydrogen resource required for CO hydrogenation on Cu/ZrO_2 catalyst surface. Therefore, this will reduce the coke deposition to some extent due to sufficient hydrogen pressure on the catalyst surface [5].

The results of copper dispersion were also presented in **Table 1**. Similar to the trend in BET surface area, a large loss of metal Cu dispersion can be observed after CZ catalyst underwent CO hydrogenation, decreasing from 2.89% to 1.30%. In the case of palladium promoted Cu/ZrO_2 catalysts, there is essentially no difference between the flesh catalysts and the used ones, even PCZ-d with better dispersion.

XRD measurements were operated to investigate the phase composition and the changes induced by the pretreatment of the precursors. In all samples, the zirconia phase gave rise to a very broad peak (not presented), indicating either a state of very low

* Corresponding author. Fax: +86-351-4041153. E-mail address: yusun@sxicc.ac.cn yangch68@sxicc.ac.cn

crystallinity or the presence of very small zirconia crystallites before reaction as well as after exposure to CO hydrogenation condition.

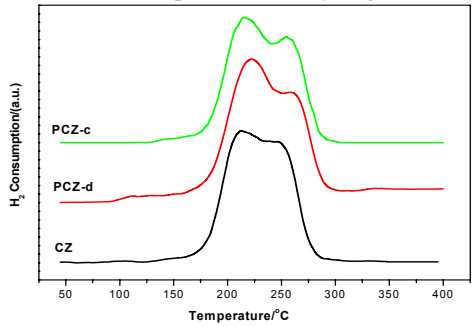

Figure 1. The TPR profiles of the catalysts

Before catalytic activity test, catalysts have been characterized by TPR with hydrogen as the reducing gas, and the resulting TPR profiles are shown in **Figure 1**. For all samples, only two reducing peaks can be seen at 215-220℃and 250-260℃, which are agreement with the results of Shimokawabe *et al.*[6], who have demonstrated that the lower temperature peak centered at 220℃ is due to the reduction of the highly dispersed cupric oxide with an octahedral environment while the higher temperature one corresponding to 242-290 ℃ ascribed to these of the bulk-like CuO. Compared with binary copper/zirconia catalyst, the ternary catalysts exhibited a higher intensity of the peak of lower temperature at the expense of the magnitude of higher temperature peak. This must be attributed to the typical effect of hydrogen spillover as a result of Pd addition between the palladium component and zirconia support, although it also occurred in the interphase of copper and zirconia. On this phenomenon, hydrogen atoms activated by palladium and/or copper components spread over zirconia on layer and sublayer surface at lower temperature, and then were released for reduction of CuO through the reverse spillover function at elevated temperature, a mechanism observed by R.Burch *et al.* [7] over Cu/ZnO catalyst. These authors proposed that ZnO can act as a reservoir for spillover hydrogen, and that reverse spillover may account for the higher rate of methanol synthesis on Cu when ZnO is present in the catalyst. Accordingly, it must be the spillover/reserve spillover mechanism partially responsible for high activity (discussed below) of the ternary catalysts. Hydrogen spillover and inverse spillover function were also reported over rhodium-based catalysts [8].

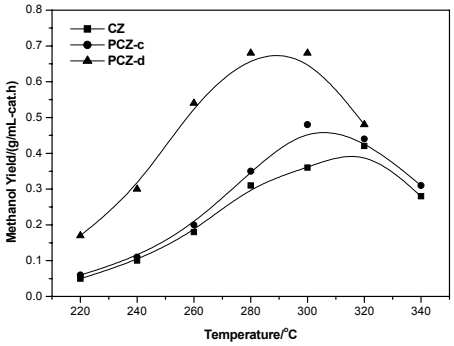

Figure 2. Catalytic activity of samples as a function of reaction temperature. Reaction conditions: P=8.0MPa; GVSH=8000h^{-1}.

The catalytic performances of samples were investigated after drying as well as after calcination at 350℃. It can be observed from **Figure 2** that zirconia supported copper catalysts, either alone or combined with palladium promoter, exhibit highly active properties for methanol synthesis. Surprisingly, space time yield (STY) increased from 0.42g/mL-cat.h at 320℃ for CZ catalyst to 0.68g/mL-cat.h at 280℃ for PCZ-d catalyst while that of PCZ-c was only influenced slightly, revealing clearly that the various pretreatment of the catalyst precursors causes a disproportionately significant effect in methanol synthesis activity. Palladium promotion in traditional Cu/ZnO-based catalysts for methanol synthesis from CO_2 has been studied by several groups [3,4].

Apparently, it is established that catalytic properties of samples does not correlate with measured BET surface area, and these textural changes therefore cannot explain the unexpected increase in activity observed over PCZ-d catalyst. Moreover, there is no apparent correlation of the activity rise with the changes in the amount of exposed copper of ternary catalysts, especially, PCZ-d catalyst. We suggest that high activity is related to the presence of amorphous zirconia as proposed by R. A. Koeppel *et al.* [9]. In the work, these authors suggested that the presence of anions like acetate, formate or nitrate in the precursors could result in a distortion of the oxide structure of zirconia due to the partial replacement of oxygen ions by these anions, and therefore inhibit the phase transformation of amorphous zirconia. And in their opinions, the crystallization of the amorphous zirconia is likely to result in a drastic decrease of the copper/zirconia interfacial area, which is decisive factor of methanol activity.

In summary, on the basis of the present findings that the Pd promotion in methanol production varied greatly with pretreatment method employed, single phenomenon cannot be responsible for this trend in catalytic activity. On the one hand, the structural modification of zirconia support by dopant anions must be considered according to other publications reported, and the resort of NO_3^- in the zirconia lattice causing distortion of structure appeared to be cause of the activity change of PCZ-d catalyst; on the other hand, hydrogen spillover mechanism should not be ruled out judging by the discussion above. However, further experiment work is required to confirm such hypothesis and provide a definite interpretation.

Acknowledgment. This work was supported by State Key Foundation Project for Development and Research of China (G1999022400) and Academic Innovation Project for Acknowledge and Engineering of China (KGCX2-302).

References

1. Y. H. Sun, P. A. Sermon, *J. Chem. Soc. Chem. Commun.,* **1993**, 16, 1242-1244.
2. K. Fujimoto, Y. Yu, *Stud. Surf. Sci. Catal.*, **1993**, 77, 393-396.
3. M. Sahibzada, K. Chadwick, I. S. Metcalfe, *Catal. Today*, **1996**, 29, 367-372.
4. I. Melian-Cabrera, M. Lopez Granados, J. L. G. Fierro, *Catal. Lett.*, **2002**, 79, 165-170.
5. J. T. Sun, I. S. Metcalfe, M. Sahibzada, *Ind. Eng. Chem. Res.*, **1999**, 38, 3868-3872.
6. M. Shimodawabe, H. Asakawa, N. Takezawa, *Appl. Catal.*, **1990**, 59, 45-58.
7. R. Burch, S. E. Golunski, M. S. Spencer, *J. Chem. Soc. Faraday Trans.*, **1990**, 86 (15), 2683-2691.
8. T. Inui, T. Uamanoto, M. Inoue, H. Hara, T. Takeguchi, J. Kim, *Appl. Catal., A: General*, **1999**, 186, 395-406.
9. R. A. Koeppel, A. Baiker, C. Shild, A. Wokaun, *Stud. Surf. Sci. Catal.*, **1991**, 63, 59-68.

Fuel Cells Operating in the "Gap" Temperature Regime

Eugene S. Smotkin

Department of Chemistry
University of Puerto Rico @ Rio Piedras
San Juan, Puerto Rico 00931
Department of Chemical Engineering
Illinois Institute of Technology
Chicago, IL 60616

Introduction

Low temperature fuel cells are based on solid polymer electrolyte membranes (PEMs), e.g. Nafion™. The thickness of Nafion™ membranes (25–175μm) permits compact series stacking of cells enabling high power and energy density systems. PEM electrolytes require sufficient hydration of the anchored sulfonate groups to support the Grottus hopping proton conduction mechanism (1). The maintenance of adequate hydration (e.g. about 3 water molecules per proton exchange site) requires precise water management, which sets the upper limit of practical PEM operation at about 90°C. Pt based electrocatalysts are poisoned by CO, which is an intermediate in the formation of hydrogen prepared by steam reforming of commodity fuels such as gasoline or methane. Although CO can be removed by the addition of a water-gas-shift (WGS) reactor and a preferential oxidation (PROX) unit to the reformer, the overall power density of the fuel cell system is substantially reduced and, more significantly, the interfacing of a 1000°C reformer to a 90°C fuel cell is daunting process control task. Finally, the kinetics of the four-electron oxygen reduction reaction (ORR) at the cathode of PEM fuel cells demands about 400 mV of polarization to obtain 1 mA/cm^2 of Pt. The surface area of Pt catalysts is typically about 25 cm^2 per mg. Thus low temperature fuel cell membrane electrode assemblies (MEAs) require substantial Pt loadings. A 50 kW traction power fuel cell requires over 125 g of Pt.

An intermediate temperature electrolyte system enabling fuel cell operation between 250°C and 400°C—i.e. in the gap between the PEM fuel cell and the molten carbonate fuel cell (MCFC)—has the benefits of enhanced ORR kinetics, CO tolerance, and a simplified fuel processor without the materials thermal instability problems of the high temperature systems. Additionally the gap temperature region enables downward scalability for portable power, a power regime not accessible by MCFCs. A "gap" electrolyte would radically change the paradigm of fuel cell engineering. Inorganic electronically insulating proton conductors (EIPCs) are the most likely candidates for gap electrolytes and are widely studied.(2, 3, 4, 5, 6, 7) The best inorganic EIPCs in the gap regime have conductivities ranging from 10^{-3} to 10^{-2} S/cm. For comparison the conductivity of hydrated Nafion 117 (175 μm) at 100ºC is approximately 10^{-1} S/cm.

Thus a membrane based on an inorganic proton conductor must be about 5–20 μm thick in order to achieve the same conductivity as Nafion™. Until now, there have been no reports of fuel cell performance using inorganic EIPCs in the gap range. Researchers have failed to prepare freestanding films of inorganic EIPCs that can withstand the mechanical stresses associated with fuel cell assembly. The EIPC must simultaneously serve as an electrolyte and as a separator of the fuel and oxidant streams.

We report the first demonstration of a fuel cell operating in the gap regime. The innovation is a support structure that enables the use of very thin inorganic EIPCs. Figure 1 shows a schematic of a fuel cell assembly using a supported EIPC. The composite electrolyte system is based on an EIPC supported on a thin metal hydride membrane—e.g. Pd (8), a Pd alloy (9), or a group Vb alloy coated with a thin layer of Pd (10, 11, 12, 13)—that is strong, flexible, and has excellent hydrogen transport properties. The metal hydride is coated on one or both sides with a thin film of the inorganic EIPC. By themselves, neither the metal hydride foil nor the EIPC can make an acceptable fuel cell membrane. The metal alone, being an electronic conductor, would short circuit the cathode and anode; the EIPC alone has poor mechanical properties and may also be fuel-permeable. Together, the two components form an electronically insulating, mechanically strong, fuel impermeable thin membrane that is ideally suited to the intermediate temperature regime.

We exemplify the support structure using ammonium polyphosphate/silica as the EIPC and Pd as the metal hydride support structure. Ammonium polyphosphate, which has the maximum conductivity of 5×10^{-3} S/cm at 300ºC, is made proton-conductive by the thermal decomposition to polyphosphoric acid (2). Silica is added to the framework material to keep the composite material in the solid state up to 400ºC. While this EIPC has been studied in pellet form, until now, freestanding films have never been studied because the EIPC is brittle and difficult to work with.

Experimental

The composite membrane electrolyte was prepared as follows: ammonium polyphosphate and silica spheres were stirred in methanol for two days. The slurry was sprayed onto one side of a 25 μm palladium foil. The coated foil was sintered in an ammonium atmosphere to melt and mix the ammonium polyphosphate with the silica spheres. The thickness of the EIPC layer can be varied by repetitive spraying and sintering. In this study, the EIPC thickness is 20 μm. The hybrid membrane, with the EIPC facing the cathode oxygen flow fields, was assembled into a fuel cell with Pt electrodes (4 mg/cm^2 Pt black with 10 wt% ammonium polyphosphate) contacting both faces of the ITEC system. The fuel cell assembly was placed in a press equipped with electrically insulated heating platens.

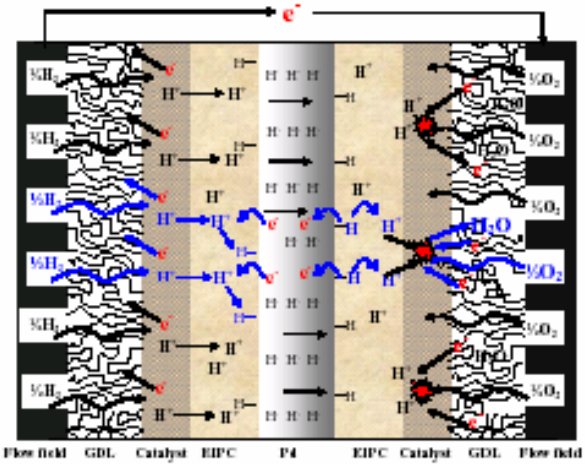

Figure 1. Schematic of an intermediate temperature hybrid electrolyte composite incorporated into a fuel cell. The metal hydride foil could be Pd, a Pd alloy, or a group Vb alloy coated with Pd. An EIPC layer covers the foil on one or both sides. The catalytic area is prepared in a "solid state ink" incorporated into the EIPC.

Results and Discussion

Figure 2 shows the fuel cell performance at 250˚C using humidified fuel. The fuel was either hydrogen or a reformate simulant containing 5% CO balanced with hydrogen. Both fuel compositions were studied with oxygen at the cathode. In both cases, the CO had no effect on the performance curve: The ITEC shows

complete tolerance to CO. The use of air instead of pure O_2 results in a decrease of OCV and cell performance due to the lower partial pressure. Increasing the air flow-rate from 100 sccm to 200 sccm causes an increase in the OCV from 0.66 V to 0.71 V.

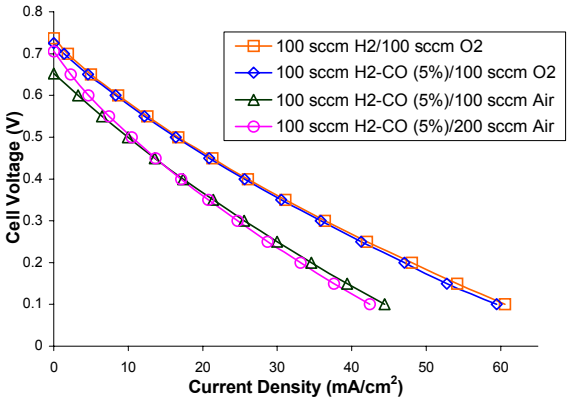

Figure 2. I-V curves obtained at 250°C for a hydrogen/oxygen fuel cell containing a poly-phosphate-silica (4:1) 20 µm thick EIPC on the cathode side of a 25µm thick Pd foil. Pt catalysts were used on both the anode and cathode sides of the cell.

Conclusions

We have demonstrated the first example of a fuel cell operating in the "gap" regime. Within the gap regime, the water-gas-shift reactor and the PROX reactor will not be needed. Further, the intermediate temperature operation will permit downward scalability for portable power, not available to higher temperature fuel cell systems such as the MCFC or solid oxide fuel cell (SOFC).

Acknowledgement. Funding for this work was provided by NuVant Systems Inc. and the Army Research Office through the STTR program.

References

1. P. Atkins, *Physical Chemistry*, 6th ed., Freeman, New York, 1999, p. 741.
2. T. Kenjo, Y. Ogawa, *Solid State Ionics*, **76**, 29 (1995).
3. Y. Du, A. S. Nowick, *Solid State Ionics*, **91**, 85 (1996).
4. K. D. Kreuer, *Solid State Ionics*, **97**, 1 (1997).
5. A. S. Nowick, Y. Du, *Solid State Ionics* , **77**, 137 (1995).
6. B. Gross, *et al*, *Solid State Ionics*, **125**, 107 (1999).
7. S. M. Haile, D. A. Boysen, C. R. I. Chisholm, R. B. Merle, *Nature*, **410**, 910 (2001).
8. T. Graham, *Phil. Trans. Roy. Soc.*, **156**, 399 (1866).
9. J. B. Hunter, *U. S. Patent*, 2,773,561 (1956).
10. A. C. Makrides, M. A. Wright, D. N. Jewett, *U. S. Patent* 3,350,846 (1967).
11. C. Nishimura, M. Komaki, S. Hwang, M. Amano, *Journal of Alloys and Compounds*, **330-332**, 902 (2002).
12. R. E. Bexbaum, A. B. Kinney, *Ind. Eng. Chem. Res.*, **35**, 530 (1996).
13. N. M. Peachey, R. C. Snow, R. C. Dye, *J. Membrane Sci.*, **111**, 123 (1996).

Application of Sulfonated Diels-Alder Polyphenylenes in Hydrogen Based PEM Fuel Cells.

Cy H. Fujimoto and Christopher J. Cornelius

Chem and Bio Technologies. Sandia National Laboratories, Albuquerque, New Mexico 87185-0888.

Introduction:

The limitations of perfluoronated PEMs (i.e. Nafion) such as, low performance at temperatures above 80 ^{o}C, high fuel permeation in DMFCs, cost and environmental processing issues have spurred the search for a cheaper and efficient alternative.[1,2,3]

Polyphenylenes represent a promising class of thermoplastics that show potential as a PEM fuel cell material. Moreover, polyphenylene synthesized though Diels Alder (DA) polymerization has advantages of thermal stability, organic solubility and mechanically robust films.[4,5,6]

Until now DA polyphenylenes have not been applied towards polyelectrolyte usage, even though this class of polymer exhibits promising physical properties such as, easily tunable backbone/lateral groups and the potential of incorporating three acidic functional groups per repeat unit compared to one in most poly(arylene) systems. We report here the physical properties and preliminary hydrogen fuel cell performance data of this class of polymer.

Experimental:

Membrane Preparation. 0.5 g of sulfonated DA polymer was casted on a clean glass plate as the sodium salt form in 10 mL of NMP. The cast was left to evaporate at 80 ^{o}C under a constant flow of N_2 for 12 hrs. The film was then dried at 100 ^{o}C under vacuum for 24 hrs and acidified (soak in 2M H_2SO_4 for 24 hrs)

Ion-Exchange Capacity. 0.2 g of acidified polymer was dried and weighed. The sample was then treated with 10 mL of 0.1 M NaOH and stirred for 24 hrs. The sample was then filtered and titrated against 0.01 M HCl.

Water Uptake. The acidified films were immersed in DI water for 24 hrs. at 25 ^{o}C. They were then blotted dry and weighed (W_s). The films were then dried and weighted until a constant weight was achieved (W_d). Water uptake was calculated by:

Water uptake =[$W_s - W_d / W_d$] x 100%

Proton Conductivity. The conductivities were determined in fully hydrated films by AC impedance spectroscopy over a frequency range of $1x10^3$ Hz to $1x10^6$ Hz using a Solartron 1260 gain phase analyzer.

Fuel Cell Testing. Polarization curves of the membranes were taken on a Fuel Cell Technologies instrument using UP H_2 and O_2 as reactant gases.

Results and Discussion.

Sulfonated DA polymers were readily cast into films from NMP. These films were robust and showed no forms of brittleness even when dried.

The films displayed proton conductives ranging from 10-80 mS/cm while still maintaining mechanical stability (swelling under 50%).

IEC	Swelling	Conductivity (mS/cm)
0.92	10%	10
1.03	15%	19
1.51	27%	29
1.70	35%	49
2.25	50%	62

Fuel cell performance data indicted that the sulfonated DA polymers could obtain high power levels and current densities of 342 mW/cm^2 at 800 mA/cm^2.

References:

1. Savadogo, O. J. New Mater. *Electrochem. Syst.* **1998**, 1, 47.
2. Rikukawa, M.; Sanui, K. *Prog. Polym. Sci*. **2000**, 25, 1463.
3. Steck, A.; Stone, C. Proceedings of the Second International Symposium on New Materials for Fuel Cell and Modern Battery Systems.
4. Stille, J. K. *J. Macromol. Sci. Chem*. **1969**, 3, 1043.
5. Neenan, T. X.; Kumar, U. *Macromolecules*. **1995**, 28, 124.
6. Fujimoto, C. H.; Loy, D. A.; Wheeler, D. R.; Jamison, G. M.; Cornelius, C. J. *Polymer Preprints*. **2002**, 43, 2, 1376.

SCREENING AND PERFORMANCE EVALUATION TESTING OF MATERIALS FOR PROTON EXCHANGE MEMBRANE FUEL CELL STACK SEALING

Lawrence E. Frisch

Engineered Elastomers Science & Technology,
Dow Corning Corporation,
3901 S Saginaw Rd, Building 2202 E-3 Mail 131, Midland, MI 48686, larry.frisch@dowcorning.com

The economic viability of PEM Fuel Cells requires significant reduction in the cost of assembling and sealing the PEM stack. Resistance to the range of fuels, reactants, coolants and other system components is critical to the seal material performance. Additionally the stack sealing system or method must last the life of the stack, is often used to enhance the structural strength of the stack and provide performance-enhancing functionality. This paper discusses Dow Corning's Proton Exchange Membrane Fuel Cell (PEMFC) stack sealing material development. Specifically the selection and development of appropriate test methods for screening and long-term performance assessments are presented. Standard and accelerated testing of sealing materials is discussed as well as specifications for key life testing of the sealing materials and stack assembly for sealing integrity. Key parameters for materials to be used in various sealing methods are discussed.

TUNGSTEN CARBIDES AS POTENTIAL ELECTROCATALYSTS

Jingguang G. Chen, Henry H. Hwu, Michael B. Zellner*

Center for Catalytic Science and Technology (CCST)
Department of Chemical Engineering
Department of Materials Science and Engineering
University of Delaware
Newark, Delaware 19716

Introduction

As the global supply of fossil fuels predictably diminishes, there have been overwhelming interests in developing the fuel cell technology. While there exist many types of fuel cells each requiring different electrocatalysts and fuels, systems involving the oxidation of methanol to obtain hydrogen fuel or electrons appear to exhibit potential advantages over others [1, 2]. In the case of the direct methanol fuel cell (DMFC), the ideal chemistry at the anode involves the oxidation of methanol in the presence of water to produce CO_2, electrons, and protons

Currently, the electrocatalyst of choice for the DMFC system is the bimetallic system of Pt/Ru; this material is favored because it demonstrates significant activity for methanol oxidation *as well as* the dehydrogenation of water, which is critical for the removal of adsorbed CO species [1, 4-6]. Aside from its activity, however, the Pt/Ru system is disadvantageous in terms of its prohibitively high costs and its susceptibility to be poisoned by CO [7]. As a result, the discovery of less expensive and more CO-tolerant alternatives to the Pt/Ru electrocatalysts would greatly facilitate the commercialization of the methanol-based fuel cell systems.

The carbides of Groups IV-VI early transition metals often show catalytic properties similar to that of the Pt-Group metals, especially in hydrogenation and dehydrogenation reactions involving unsaturated hydrocarbons [8, 9]. In particular, there have been numerous studies on tungsten carbides (WC and W_2C) since Levy and Boudart suggested that WC displayed Pt-like behavior in a variety of catalytic reactions in 1973 [10]. There have also been several attempts to utilize tungsten carbides as an electrocatalyst [11-16], as it is resistant to acid solutions at anodic potentials [13, 14].

In this presentation we will provide a comparison of the general trend in the activity and product selectivity of methanol and water on C/W(111), Pt/C/W(111), O/C/W(111), and C/W(110). We will also compare the desorption temperature of CO from these surfaces. Finally, we will briefly compare our results on tungsten carbides to those on the surfaces of Pt(111) and Ru(0001) under identical UHV conditions.

Experimental

The UHV chamber used in the current study has been described in detail previously [21]. Briefly, it is a three-level stainless steel chamber equipped with Auger electron spectroscopy (AES), low-energy electron diffraction (LEED), and temperature-programmed desorption (TPD) in the top two levels, and high-resolution electron energy loss spectroscopy (HREELS) in the bottom level. For TPD experiments the W(111) and W(110) samples were heated with a linear heating rate of 3 K/s.

Clean W(110) and W(111) crystal surfaces were prepared by cycles of Ne^+ bombardment at 500K (sample current ~6 □A) and flashing to 1200K, as described previously [17, 20]. The procedures for preparing the carbide-modified W surfaces using ethylene or other unsaturated hydrocarbon molecules as a carbon source are described elsewhere [21, 22]. The carbide surfaces will be referred to as C/W(110) or C/W(111). The preparation of oxygen-modified C/W(111) involved first making the carbide layer and then dosing 1L of oxygen at 900K; this surface will be referred to as O/C/W(111). For the Pt-modified C/W(111) surface, submonolayer coverages of Pt was achieved by heating Pt wire (0.127 mm in diameter, 99.9% from Alfa Aesar) that was wrapped tightly on W heating wires, as described elsewhere [23].

Results and Discussion

Recently our group has published several papers to demonstrate that tungsten carbide surfaces possess characteristics that are desirable for fuel cell electrocatalysts. In particular, we show that carbide-modified W(111), or C/W(111), is significantly more active toward the decomposition of methanol and water than Pt-group metals [17, 18]. We further modified the C/W(111) surface with submonolayer coverages of Pt and oxygen to examine possible synergistic or deactivating effects [17-19]. Lastly, we explored the effect of substrate structure by performing identical experiments on carbide-modified W(110) [20].

This preprint compares and summarizes a series of studies on the reactions of CH_3OH, H_2O, and CO over several model tungsten carbide surfaces. Our results demonstrate that methanol and water readily dissociate on C/W(111), Pt/C/W(111), O/C/W(111), and C/W(110). Although the presence of submonolayer Pt on C/W(111) reduces the activity toward the dissociation of methanol, the added Pt leads to a complete suppression of the undesirable methane product. When the C/W(111) surface is modified by oxygen, significant activities toward the decomposition of methanol and water are maintained while the CO desorption temperature is reduced to below room temperature (242K). Finally, comparative studies of the C/W(111) and C/W(110) surfaces show only minor differences regarding the reactions with CH_3OH, H_2O, and CO.

Table 1. Reactivity of methanol on different C/W Surfaces

Surfaces	*Total Number Of CH_3OH Reacting per W Atom*
W(111) [17]	0.411
C/W(111) [17]	0.280
0.6ML Pt/C/W(111) [19]	0.177
O/C/W(111) [17]	0.236
C/W(110) [20]	0.304
Pt(111) [33, 34]	~0
Ru(0001)† [35]	N/A

Table 2. Reactivity of water on different C/W Surfaces

Surfaces	*Activity (H_2O Molecules per W atom)*
W(111) [18]	0.320
C/W(111) [18]	0.180
0.6ML Pt/C/W(111) [19]	0.056
O/C/W(111) [18]	0.095
C/W(110) [20]	0.153
Pt(111) [36, 37]	~0
Ru(0001) [38, 39]	~0

Overall, as shown in Tables 1, 2, and 3, the tungsten carbide surfaces exhibit characteristics more favorable toward DMFC applications than Pt or Ru surfaces in two important aspects: (1) The tungsten carbide surfaces are more active toward the dissociation of methanol and water. (2) The CO desorption temperature is at least 100 degrees lower, suggesting that tungsten carbides might be more resistant to CO-poisoning. As a result, the current study demonstrates the feasibility for potential application of tungsten carbides as electrocatalysts. We are currently using physical vapor deposition (PVD) films of tungsten carbides and Pt-modified to correlate surface science studies with electrochemical performance.

Table 3. Desorption temperature of CO from different C/W Surfaces

Surfaces	*CO Desorption Temperature[a] (K)*
W(111) [18]	292, 874
C/W(111) [18]	330, 355
0.3ML Pt/C/W(111) [19]	357
O/C/W(111) [18]	242, 284
C/W(110) [20]	284, 335
Pt(111) [27, 28]	~460
Ru(0001) [25, 26]	~475

Acknowledgment
We acknowledge financial support from the Basic Energy Sciences, Department of Energy (DOE/BES Grant No. DE-FG02-00ER15014). HHH also acknowledges financial support from the Presidential Fellowship at the University of Delaware and the American Vacuum Society Graduate Student Fellowship. MBZ acknowledges partial financial support from a National Aeronautics and Space Administration (NASA) Graduate Fellowship.

References
[1] R. Parsons and T. VanderNoot, J. Electroanal. Chem. **257**, 9 (1988).
[2] A. Hamnett, Catal. Today **38**, 445 (1997).
[3] G. J. K. Acres, et. al. Catal. Today **38**, 393 (1997).
[4] A. Hamnett and B. J. Kennedy, Electrochim. Acta. **33**, 1613 (1988).
[5] M. M. P. Janssen and J. Moolhuysen, Electrochim. Acta. **21**, 869 (1976).
[6] S. A. Campbell and R. J. Parsons, Chem. Soc. Faraday Trans. **88**, 833, (1992).
[7] P. Stonehart in *Electrochemistry and Clean Energy*, edited by J. Drake (Royal Society of Chemistry, Cambridge, 1994).
[8] S. T. Oyama, *The Chemistry of Transition Metal Carbides and Nitrides* (Blackie Academic and Professional, Glasgow, 1996).
[9] J. G. Chen, Chem. Rev. **96,** 1477 (1996).
[10] R. Levy and M. Boudart, Science **181**, 547 (1973).
[11] H. Okamoto, G. Kawamura, A. Ishikawa, and T. Kudo, J. Electrochem. Soc. **134**, 1645 (1987).
[12] G. Kawamura, H. Okamoto, A. Ishikawa, and T. Kudo, J. Electrochem. Soc. **134**, 1653 (1987).
[13] H. Boehm and F. A. Pohl, Wiss. Ber. AEG-Telefunken **41**, 46 (1968).
[14] H. Binder, A. Koehling, and G. Sandstede, Am. Chem. Soc. Div. Fuel Chem. Prepr. **13**, 99 (1969).
[15] R. Fleischmann and H. Boehm, Ber. Bunsenges, Phys. Chem. **84**, 1023 (1980).
[16] P. N. Ross, Jr. and P. Stonehart, J. Catal. **48**, 42 (1977).
[17]H. H. Hwu, J. G. Chen, K. Kourtakis, and G. Lavin, J. Phys. Chem. B **105**, 10037 (2001).
[18]H. H. Hwu, B. D. Polizzotti, and J. G. Chen, J. Phys. Chem. B **105**, 10045 (2001).
[19]N. Liu and J. G. Chen, J. Catal. accepted (2003).
[20]H. H. Hwu and J. G. Chen, J. Phys. Chem. B **107**, 2029 (2002).
[21] B. Fruhberger and J. G. Chen, J. Am. Chem. Soc. **118**, 11599 (1996).
[22] N. Liu, S. A. Rykov, H. H. Hwu, M. T. Buelow, and J. G. Chen, J. Phys. Chem. B **105**, 3894 (2001).
[23]N. Liu and J. G. Chen, Catal. Lett. **77**, 35, (2001).
[24]K. D. Childs, et. al., *Handbook of Auger Electron Spectroscopy; Physical Electronics, Third Edition* (1995).
[25]F. Bautier de Mongeot, M. Scherer, B. Gleich, E. Kopatzki, and R. J. Behm, Surf. Sci. **411**, 249 (1998).
[26]K. L. Kostov, H. Rauscher, and D. Menzel, Surf. Sci. **278**, 62 (1992).
[27]A. Crossley and D. A. King, Surf. Sci. **68**, 528 (1977).
[28]G. Ertl, M. Neuman, and K. M. Streit, Surf. Sci. **64**, 393 (1977).
[29]E. Iglesia, F.H. Ribeiro, M. Boudart and J.E. Baumgartner, Catal. Today **15**, 307 (1992); E. Iglesia, J.E. Baumgartner, F.H. Ribeiro and M. Boudart, J. Catal. **131** 523 (1991).
[30]E.A. Blekkan, C.C. Pham-Huu, M.J. Ledoux, and J. Guille, Ind. Eng. Chem. Res. **33**, 1657 (1994).
[31]N. Liu, S. A. Rykov, and J. G. Chen, Surf. Sci. **487**, 107 (2001).

MEMBRANE-ELECTRODE ASSEMBLY FOR HIGH-TEMPERATURE PEMFC

Chao-Yi Yuh, Ludwig Lipp, Pinakin Patel and Ray Kopp

FuelCell Energy, Inc.
3 Great Pasture Road
Danbury, CT 06813

Introduction

Fuel cells offer the best alternative to conventional fossil fuel combustion power generation technologies. However, for fuel cells to be commercially viable, issues such as cost, size, and functionality need to be addressed. A natural-gas fueled PEMFC system for stationary application desires near atmospheric pressure operation, >35% HHV efficiency, >100°C operation for cogeneration, simple construction, reliable >40,000h life, and low system cost (<$1500/kW). A PEMFC system for transportation application requires <3 atm pressure operation, >5,000h life and <$10/kW MEA cost. Although research efforts so far have advanced PEMFC technology significantly, substantial performance and endurance improvements beyond the current state-of-the-art are required before the above goals can be achieved.

At present, the state-of-the-art PEMFC is operated at ~60 to 80°C. CO poisoning of its anode precious metal catalyst is a major barrier for its commercialization utilizing hydrocarbon feedstock[1]. Various approaches to mitigate CO poisoning such as alternative anode catalysts, PROX, or air bleeding have not completely alleviate the issue. Since the chemisorption of CO weakens considerably with temperature, one approach to mitigate the CO poisoning is to operate at higher temperatures. Additional advantages such as faster electrode kinetics and higher quality waste heat for cogeneration can also be realized. Operating at >100°C also mitigates cathode flooding by the liquid water reaction product and allows a greater ability to remove waste heat. Therefore, MEA operating above 100°C (preferably >120°C) is highly desired. The ultimate MEA goals for commercial use include: 1) higher membrane proton conductivity with negligible electronic conductivity, area specific resistance less than 100 $m\Omega cm^2$; 2) improved humidification properties (minimal water transport and low hydration) and dimensional stability (low swelling); 3) high mechanical strength; 4) low gas permeability (less than 0.1 percent gas crossover); 5) long life of 40,000h for stationary and 5,000h for transportation applications; 6) cell performance >0.7 V (0.8V preferred) at 400-500 mA/cm^2; 7) low cost.

Challenges with high-temperature operation

Most developers presently use perfluorosulfonic acid (PFSA) polymer membrane such as Nafion® made by DuPont. It is deficient in terms of ionic conductivity at temperatures above 100°C and at low relative humidity (R.H.). High-temperature operation dries out the membrane, drastically reducing proton conduction. To operate Nafion® beyond 100°C, pressurization is needed to maintain high R.H., requiring complicated compressor system. Dried Nafion® is also more permeable to gases, resulting in increased cross-leakage. Furthermore, the loss of liquid water embrittles the membrane and could cause membrane cracking and poor electrode-membrane contact. Another important challenge for >100°C operation of the baseline Nafion®-base MEA is the significantly reduced cell voltage, mainly due to a large cathode polarization increase. This increase is mainly caused by a loss of proton conductivity and catalyst utilization in the cathode catalyst layer. Membrane improvement alone is not sufficient to achieve the PEMFC commercialization goal.

Advanced Proton-Conducting Membranes

Proton-conducting mechanisms have been extensively discussed by Kreuer[2,3]. Literature survey has showed that a useable proton conducting membrane material with desired proton conductivity comparable to fully hydrated Nafion® (>0.1 S/cm) between 100-150°C is not yet available[4-6]. Because useable 100-150°C proton-conducting materials are not yet available, many new high-temperature proton-conducting materials are being actively developed. The reported approaches include:

Mechanical Support to enhance high-temperature mechanical strength for ultra-thin membranes
Solid Proton Conductor to enhance proton conductivity at low R.H.
New High-Temperature Proton-Conducting Ionomer
Substitutes for Water in Nafion to reduce humidity effect
Ultra-thin membrane or Pt Doping for Self Humidification

The solid proton conductors (superacid) under evaluation include PTA (phosphotungstic acid), ZHP (zirconium hydrogen phosphate), zeolite, silica, etc. These materials are brittle inorganics and therefore are generally incorporated into a composite structure containing flexible polymeric ionomer phases. However, although to a lesser extent than Nafion®, they also lose water at high temperatures, with reduced proton conductivity. Considerable modifications of their morphologies (such as fine nano-size) may be needed to effectively enhance proton conductivity. New high-temperature iomomers are in general sulfonated or phosphonated polymers, usually containing aromatic backbone[7-9], including sulfonated polyphosphazene, polysulfone, or PEEK. So far, long-term high-temperature proton conductivity and durability under low R.H. have yet to be demonstrated. These liquid acid (less volatile than water) impregnated membranes may adsorb at the Pt surface, resulting n high cathode polarization. The liquid acids may also evaporate away slowly during long-term use, limiting their high-temperature durability. Because water dry-out is the main cause of proton-conductivity loss in many materials at high temperatures, substitutes for water in the ionomers with high boiling-point proton-conducting liquid such as pyrazole or imidazole have been evaluated. However, these liquid proton conductors may adsorb on the Pt catalyst surface, interfering ORR and resulting in high cathode polarization. The liquid proton conductor may also slowly evaporate away. The composite approaches are adopted by many researchers because few single-component monolithic materials have all the desired properties. So far, few composite materials have sufficient proton conductivity comparable to a fully hydrated Nafion®.

Many of the membrane materials reported above were studied for their proton-conducting and mechanical properties. However, very little performance data of MEA incorporating the advanced membranes at high temperatures were reported. The reported performance data were usually obtained with non-system conditions (e.g., very high R.H. or stoichs). The electrode Pt catalyst loading level was also usually too high (such as using Pt black, $>1mg/cm^2$ per electrode), not practical for commercial use.

In order for the Pt catalyst in the cathode to be utilized, its surface needs to be accessed by the proton-conducting phases and reactant oxygen. Therefore, an ionomer of high proton conductivity is not sufficient to guarantee a high cathode performance. The acid groups (ionic clusters) of the ionomers have to be situated right at the Pt for it to be active for the ORR. The water in the acidic ionic

clusters is also needed to facilitate ORR[1]. Furthermore, high oxygen permeability is needed to reduce mass-transfer loss. The baseline Nafion® ionomer if well humidified has a very high oxygen permeability[1]. Any new proton-conducting phase in the cathode catalyst layer also needs to have similarly high oxygen permeability.

This paper detailed the MEA work performed at FCE focusing on improving high-temperature membrane durability and cathode catalyst layer activity.

MEA EVALUATION

A number of composite membrane and MEA have been developed to improve water retention and proton conduction at 120°C. The experimental MEA are all less than 75 μm thick. The composite membranes consist of ionomer and solid superacid. Fine additives/modifiers with high-proton conductivity have been incorporated into the MEA (membrane and/or cathode). The proton-conducting additives include: PTA, sulfated nano-oxide, ZHP and several types of zeolites. The ionomer phase under study in the composite MEAs include Nafion® of various EW as well as low EW experimental ionomers. Cross-linking approach is also adopted to strengthen membrane mechanical strength. The fabricated MEAs were tested in laboratory-scale 25cm^2 cells at 80-140°C to evaluate promising MEA formulations.

FCE has achieved significant performance and endurance improvements[10] under atmospheric pressure operation, hydrogen/air atmosphere, at 400mA/cm^2. The cross-linking approach has enhanced membrane durability significantly, by reducing MEA OCV decay rate. The CO tolerance was significantly improved (at least to 100ppm CO) as illustrated in Figure 1, demonstrating the benefit of >100°C operation. Detailed MEA test results will be presented at the meeting.

Acknowledgement

This study was supported by the Office of Energy Efficiency and Renewable Energy, U.S. Department of Energy, under Contract DE-FC02-99EE27567. And by U.S. National Science Foundation, under Contract DMI-0232574.

References

1. Gottesfeld, G. and Zawodzinski, Z. in Electrochemical Science and Engineering, R. Alkire, H. Gerischer, D. Kolb and C. Tobias, Editors, Wiley-VCG, New York, 1994, **5**, p.195-301,
2. Kreuer, K., Solid State Ionics, 2000, **136-137**, 149.
3. Kreuer, K., Solid State Ionics, 1997, **94**, 55.
4. Roziere, J. and Jones, D., in 1st European PEFC Forum, F. Buchi, G. Scherer and A. Wokaun, Editors, 2001, p. 145.
5. Zawodzinski, T., et al., in 2002 US DOE Hydrogen and Fuel Cell Joint Program Review, May 6-10, 2002.
6. Norby, N., Solid-State Ionics, 1999, **125**, 1.
7. Kerres, J., J. Membrane Science, 2001, **185**, 3.
8. Jones, D. and Roziere, J., J. Membrane Science, 2001, **185**, 41.
9. Kreuer, K., J. Membrane Science, 2001, **185**, 29.
10. Yuh, C, FY2002 Progress Report, Hydrogen, Fuel Cell and Infrastructure Technologies, Energy Efficiency and Renewable Energy, IV.B.5, 297-299.

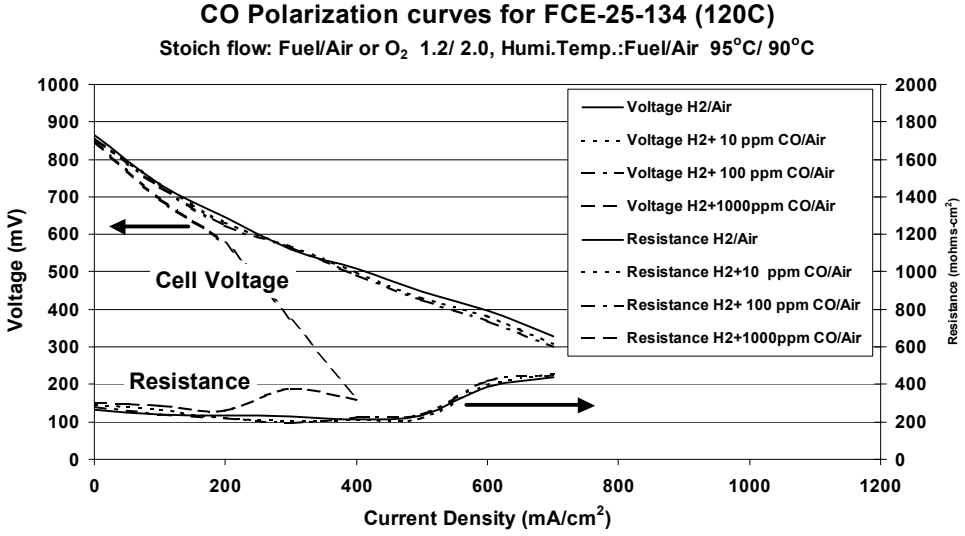

Figure 1. Significant tolerance to 100ppm CO was achieved at 120°C.

TOWARDS THE DEVELOPMENT OF A MEMBRANE ELECTRODE ASSEMBLY (MEA) STYLE BIOFUEL CELL

Nick L. Akers and Shelley D. Minteer

Department of Chemistry
Saint Louis University
3501 Laclede Ave.
St. Louis, MO 63103

Introduction

A biofuel cell is an electrochemical device in which electrical energy is produced from chemical reactions by means of the catalytic activity of living cells and/or their enzymes. Enzyme-based biofuel cells were introduced in the 1960's [1], but the technology has not developed at the rate of traditional fuel cells for a number of reasons. The main problems that have plagued the technology have been the inability to immobilize the enzyme at the electrode surface, the lack of stability of the enzyme, and the lack of stability of the redox mediator (if a redox mediator is necessary).

Recent research in our group has focused on developing biofuel cells where the enzyme is immobilized in a membrane that buffers the pH and confines the enzyme to an area that helps maintains its structural integrity [2]. A secondary aspect of our biofuel cell has been to immobilize and stabilize the redox mediator at the electrode surface using electropolymerization. Alcohol/O_2 biofuel cells were fabricated using dehydrogenase enzyme-immobilized membranes that were cast on the surface of poly(methylene green)-modified anodes. The alcohol fuels are oxidized to aldehydes in the presence of alcohol dehydrogenase and NAD^+. The NADH product is the redox mediator for the fuel cell. NADH oxidation on platinum and carbon electrodes has poor reaction kinetics and occurs at large overpotentials [3]. Therefore, a polymer-based electrocatalyst was used to regenerate NAD^+ and to shuttle electrons from the NADH to the electrode. The electrocatalyst employed in this study is methylene green. Cyclic voltammetric studies of poly(methylene green)-coated glassy carbon electrodes have shown that poly(methylene green) is an electrocatalyst for NADH [4].

The enzyme-immobilization membrane is a quaternary ammonium salt modified Nafion® membrane that maintains the advantageous electrochemical properties of Nafion®. The immobilization membrane protects the enzyme from elevated temperatures experienced during heat pressing and allows for the biofuel cell to be tested under the same conditions that a traditional fuel cell is tested. Therefore, these new biofuel cell electrodes are optimal for the formation a membrane electrode assembly (MEA) style biofuel cell.

Experimental

Reagents. Methylene green (Sigma), sodium nitrate (Fisher), sodium borate (Fisher), Nafion® 1100 suspension (Aldrich) and Nafion® 117 (Aldrich) were purchased and used as received. Enzymes employed include alcohol dehydrogenase (E.C. 1.1.1.1, initial activity of 300-500 Units/mg), aldehyde dehydrogenase (E.C. 1.2.1.5, initial activity of 2-10 Units/mg), formaldehyde dehydrogenase (E.C. 1.2.1.2, initial activity of 1-6 Units/mg), and formate dehydrogenase (E.C. 1.2.1.46, initial activity of 5-15 Units/mg). Enzymes were purchased from Sigma (St. Louis, MO) and Rosche Applied Science (Indianapolis, IN), stored at 0° C, and used as received. Additionally, NAD^+ was purchased from Sigma and used as received.

Preparation of the Bioanode. The bioanode consists of 1cm x 1cm square GAT expanded graphite worms (Superior Graphite CO.) that are compressed at pressures varying from 1500 psi to 10000 psi depending on conditions and requirements. Before hydraulic pressing, the expanded graphite is pretreated with methylene green by allowing the material to soak in the methylene green buffer solution. After pressing, methylene green is electropolymerized onto the pressed GAT material. Polymerizing a thin film of poly(methylene green) was accomplished by performing cyclic voltammetry using a CH Instruments 810 or 620 potentiostat (Austin, TX) from -0.3 Volts to 1.3 Volts for 12 sweep segments at a scan rate of 0.05 V/s in a solution containing 0.4 mM methylene green and 0.1 M sodium nitrate in 10 mM sodium tetraborate. The electrode was rinsed and then allowed to dry overnight before further modification.

Nafion® membranes incorporated with quaternary ammonium salts were formed in a two-step process. The first step was to co-cast the quaternary ammonium salt with 5% by wt. Nafion® suspension into a weighing boat. All mixture-casting solutions were prepared so the concentration of quaternary ammonium salt is in a three-fold excess of the concentration of sulfonic acid sites in the Nafion® suspension. Previous studies had shown that all of the salt ions that were introduced into a membrane were ejected from the membrane upon soaking in water [5]. Therefore, 18 MΩ water was added to the weighing boats and allowed to soak overnight. The water was removed and the films were rinsed thoroughly with 18 MΩ water. The films were resuspended in lower aliphatic alcohols, which were then employed in forming the enzyme casting solutions.

Enzyme/ Nafion®casting solutions with an enzyme to quaternary ammonium salt/ Nafion®casting solution ratio of 2:1 (usually 1200 µL of 1.0 µM enzyme: 600 µL Nafion® suspension) and 0.03g NAD^+ were vortexed in preparation for coating on electrode. The solution was pipeted onto the surface of the methylene green coated graphite support, and the solution was allowed to thoroughly dry before the MEA was fabricated.

MEA Fabrication. The cathode material is an ELAT electrode with 20% Pt on Vulcan XC-72 (E-Tek). The anode construction is previously described. Assembly of the MEA occurs at custom heating elements connected to the platens of a hydraulic laboratory press (Carver). First, a piece of Kapton (American Durafilm) is laid down, followed by the cathode, Nafion® 117 membrane, bioanode, and finally another piece of Kapton. This MEA assembly is placed between the heating elements. Pressure is typically applied to 3000 psi but can differ depending on conditions. Concurrently to pressing, the heating elements are elevated to a temperature of 125°C as measured by external thermistors. The MEA remains at temperature for three minutes, after which the pressure is released and the MEA is allowed to cool. A schematic of the completed MEA cell can be seen in Figure 1.

Electrochemical Measurements. All data were collected and analyzed for the test cell with a CH Instruments 810 potentiostat interfaced to a PC computer. The potentiostat functions to measure open circuit potentials and can apply varying loads to the test cell. The MEA is contained in a custom fabricated test apparatus with compartments for fuel delivery for the anode and ventilation for the cathode. Electrical connection to the anode and cathode is achieved with stainless steel wire mesh.

Results and Discussion

Previous research has shown that it is possible to immobilize oxidase enzymes (such as: glucose oxidase) in Nafion®while maintaining enzyme activity by diluting Nafion®. However, diluting Nafion® makes unstable and non-uniform films [6-7]. The most recent approach by Karyakina and coworkers has been to neutralize Nafion® and dilute it to a lesser degree in ethanol [8]. However, both

of these approaches are problematic as the pH environment in the solution around the Nafion® decreases, Nafion® will exchange protons back into the membrane and re-acidify the membrane.

Previous research in our group has shown that we can immobilize dehydrogenase enzymes (a group of enzymes that have been more difficult to immobilize) in a quaternary ammonium salt doped Nafion® membrane while prolonging the active lifetime of the enzyme to 60-90 days [2]. The quaternary ammonium salt doped Nafion® suspension buffers the pH of the membrane to neutral levels, while the micellar structure of the polymer acts to protect the enzymes. Initial enzyme activity studies of dehydrogenase enzymes immobilized in quaternary ammonium salt doped Nafion® membranes have shown that the dehydrogenase enzymes remain active after heat treatment in an oven at 130 °C for 10 minutes. These preliminary results have shown the feasibility of forming a MEA style biofuel cell. MEA style fuel cells have the advantage of a zero gap format that increases power outputs.

Currently, we are optimizing the system for hydraulic pressures and heating element temperatures. Ideally, the amount of time the MEA spends at elevated temperatures should be no longer than is necessary to bind the anode and cathode to the Nafion®.

Preliminary results from a completed biofuel cell MEA have shown open circuit potentials ranging from 0.34 - 0.21 V with currents from 3.6 - 1.4 mA. Optimization of the heat pressing conditions should result in open circuit potentials and current densities at least equaling non-MEA biofuel cells, and most likely surpassing them due to the advantages of zero gap between the electrodes.

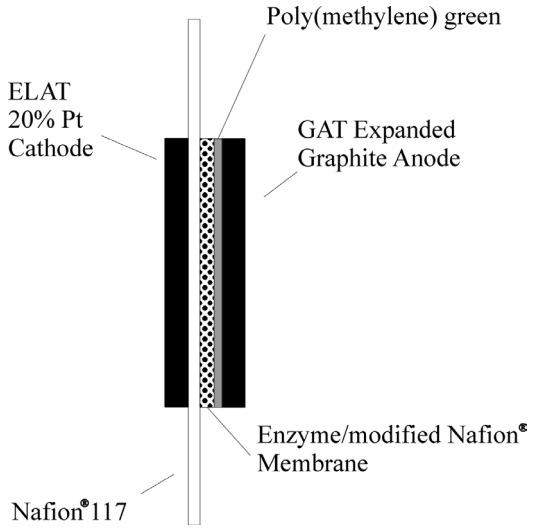

Figure 1. A schematic of how the MEA is assembled. Schematic is not to scale.

Conclusions

Biofuel cells with high current densities have previously been characterized in a non-MEA format by the authors [2]. The desire is to further increase the power densities of these biofuel cells by creating an MEA biofuel cell. MEA's offer advantages of zero gap between the anode and cathode, improving the power densities. Previously, it has not been possible to create a biofuel cell MEA due to denaturing of the enzymes that would occur at high temperatures. The protective environment created by the quaternary ammonium salt modified Nafion® is sufficient for the enzymes to retain activity after exposure to high temperatures. This allows for the creation of the first known MEA based on biofuel cell technology. Future work will focus on optimizing experimental conditions to fully capitalize on the advantages of the MEA format.

Acknowledgement. The authors wish to thank the Office of Naval Research and the Saint Louis University Beaumont Faculty Development Fund for funding this research. The authors would also like to thank Christine M. Moore for her help with heat treatment studies.

References

(1) Yahiro, A.T.; Lee, S.M.; Kimble, D.O. *Biochim. Biophys. Acta* **1964**, 88, 375.
(2) Akers, N.L.; Moore, C.M.; Minteer, S.D. *Electrochim. Acta* **2003**, *in press*.
(3) Blaedel, W.J.; Jenkins, R.A. *Analytical Chemistry* **1975**, 47, 1337-1338.
(4) Zhou, D.; Fang, H.Q.; Chen, H.; Ju, H.; Wang, Y. *Analytica Chimica Acta* **1996**, 329, 41-48.
(5) Schrenk, M.; Villigram, R.; Torrence, N.; Brancato, S.; Minteer, S.D. *J. Membrane Sci.* **2002**, 205, 3-10.
(6) Fortie, G; Vaillancourt, M.; Belanger, D. *Electroanalysis*, **1992**, 4, 275.
(7) Rishpon, J.; Gottesfeld, S.; Campbell, C.; Davey, J.; Zawodzinski, T.A.J. *Electroanalysis*, **1994**, 6, 17.
(8) Karyakin, A.A.; Kotel'nikova, E.A.; Lukachova, L.V.; Karyakina, E.E. *Anal. Chem.*, **2002**, 74, 1597.

ALTERNATE METHANOL TOLERANT CATHODES FOR PEMFC APPLICATIONS

Vadari Raghuveer and Balasubramaniam Viswanathan

Department of Chemistry
Indian Institute of Technology, Madras
Chennai 600 036, India

Introduction

The application of fuel cells to electric vehicles requires a PEMFC offering a high power density and low noble metal catalyst loading or cheap electrocatalyst, to reduce weight, volume and cost. However, at high potentials the formation of adsorbed species on the platinum surface inhibit the oxygen reduction reaction and hence result in loss of fuel cell performance[1]. The most commonly employed solid polymer electrolyte, Nafion 117, has the drawback of methanol permeation across the membrane[2-4], which poisons the platinum catalyst at the cathode. Attempts are therefore being made to find methanol tolerant oxygen reduction electrocatalyst for SPE-DMFCs. Many mixed oxide systems such as spinels, perovskites[5] have been investigated for the possible application as cathode materials. These are restricted to alkaline medium as they are not stable in acids. The Pb-Ru pyrochlore is known to be stable in acid, but at high cathodic potentials, the topotactic extrusion of lead takes places. They exhibit better stability if bonded to any solid polymer proton-exchange membrane[7] that is exposed to an aqueous electrolyte reservoir on the opposite side of the membrane. The Pb-Ru pyrochlore prepared by convention ceramic method shows quite low activity for oxygen reduction. Upon dispersing on the carbon matrix, significant enhancement in the activity was observed[7].

The activity of the electrochemical charge transfer reaction across the electrode/electrolyte interface depends on the density of states of the electrode. Hence the Pb-Ru pyrochlore oxide, when prepared in the nanocrystalline form, can be expected to exhibit altered electrochemical behaviour by virtue of an enhanced surface to volume factor as well as due to alterations in the density of states, because of the broken bonds, in the diffuse space charge region inside the solid[8-10].

In the present study, the electrochemical reduction of oxygen was carried out using the nanocrystalline Pb-Ru pyrochlore sample of composition $Pb_2Ru_{1.95}Pb_{0.05}O_7$ which was prepared by polymer modified sol-gel method (PMSGpyro) as cathode electrocatalyst, by gas diffusion mode using proton exchange membrane (Nafion 117) as electrolyte. The nanomaterial thus obtained was characterized by XRD and transmission electron microscopy. The activity and stability comparison of the nancyrstalline oxide and commercial platinum were made using cyclic voltammetry and chronoamperometry respectively, at RT and 70^{o}C.

Experimental

Preparation of Nanocrystalline Pb-Ru pyrochlore

The chemicals used for the synthesis of nanocrystalline Pb-Ru pyrochlore of composition $Pb_2Ru_{1.95}Pb_{0.05}O_7$ are Lead nitrate (CDH, 99.1%), Ruthenium chloride (s.d.fine chemicals Ltd.). Polyacrylamide gel was used as protecting agent to prevent crystal growth. High molecular weight polyacrylamide was prepared by radical polymerization of the monomer using H_2O_2 as radical generator.

The polyacrylamide gel solution was prepared by taking 2 g of gel in 500 ml distilled water and the resulting solution was kept aside for two days to obtain sufficient viscosity. The optimized concentration of the polymer gel solution taken is 0.4%. The stoichiometric amounts of metal nitrates and chlorides were taken in one burette and in another burette 5% KOH solution was taken. The solutions from the two burettes were released into the gel solution maintained at 75-80^{o}C with vigorous stirring, by maintaining the pH 7.5-8.5. After the completion of precipitation, the precipitate was aged for 30 min. at 75-80^{o}C, followed by filtration and dried in an air oven maintained at 373 K for 2 h. The precursor was calcined at 500^{o}C for 2 h in air.

Characterization methods. The thermograms of the samples were obtained using Perkin Elmer TGA (Delta Series, TGA 7) instrument with a steady heating rate and flow of 20 ml min^{-1} of nitrogen. The XRD measurements were obtained using a Philips PW 1130 at room temperature. The radiation used is Ni filtered Cu k_α (λ = 1.5405 A^o). The C, H and N analysis were obtained using Heraeus CHN analyzer. The microscopic analyses was carried out using Philips EM430ST operated at 300 kV. The sample was dispersed in ethanol by sonication and dropped on to a carbon grid and imaged. All the electrochemical measurements were performed using Wenking potentioscan (POS 73) with a Philips digital X-Y recorder (PM 8033). A Pt (1.5 cm^2) and saturated Ag/AgCl was used as counter and reference electrode respectively. Chronoamperometric responses were obtained by fixing the potential and recording the current response with time using Philips X-t recorder. The flow rate of the oxygen gas in the gas diffusion electrodes was controlled using mass flow controller.

Gas diffusion electrode and Membrane electrode assembly. The gas diffusion electrode was prepared by mixing the Pb-Ru pyrochlore oxide catalyst with carbon (Vulcan XC 72R) in 1:3 ratio and suspended in water with 5% Nafion. For, the commercial catalyst, the platinum supported carbon (20% Pt/C, Arora Mathey) was taken as such and suspended in water and 5% Nafion solution. The mixture was thoroughly homogenenized with a ultrasonicator before and a dilute PTFE dispersion was added, for 30 minutes. The active layer contains 20 wt% of PTFE. The resulting semi-solid paste was then spread onto the previously treated Teflon containing uncatalysed carbon coated carbon cloth and leveled by roller.

The membrane electrode assembly was constructed based on the literature[7]. The carbon cloth containing the catalyst layer side was bonded to a previously treated Nafion 117 membrane by placing the Nafion membrane on top of the coated surface, the assembly was then hot pressed for 3 min. The other side of the carbon cloth which contains Teflon containing uncatalysed carbon was used as gas diffusion layer. The geometric area of the carbon cloth with the catalyst layer used in the present study is 2.5 cm^2.

Results and Discussion

The TGA/DTG (figure not shown) obtained for the the assynthesized sample before calcination, show peaks corresponding to 110^{o}C and 475^{o}C attributed to the removal of physisorbed water, condensation process for the formation of oxide framework and polymer decomposition. The decomposition of polyacrylamide takes place at 450^{o}C. The water removal during the condensation process as well as decomposition of the polymer takes place at almost the same temperature. Thus the calcinations temperature chosen is 500^{o}C in air. The XRD pattern observed for pyrochlore in **Figure 1** confirms the formation of single phase material with well defined superstructure reflections

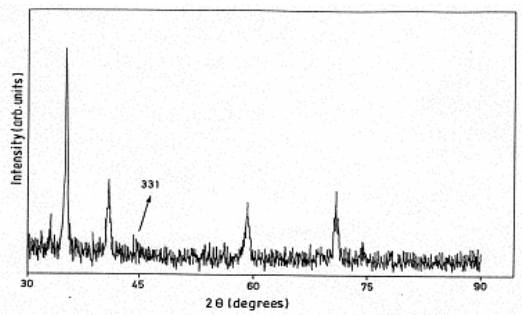

Figure 1 X-ray diffraction pattern obtained for nanocrystalline Pb-Ru pyrochlore sample

corresponding to the pyrochlore order (331 reflection). The pattern is matching well with JCPDS standard file No. 34-472. The XRD peaks observed are characteristically broader which is normally expected for the nanosized crystallites. The percentage of C (< 0.5%), H (<0.08%) and N (<0.5%) are considerably low confirming the removal of the polyacrylamide during calcination at 500^{oC} for 2h. The TEM micrograph of the nanocrystalline Pb-Ru pyrochlore sample is shown in **Figure 2**. The sample was imaged at different regions. It is seen from the micrograph that the overall particle size ranges from 1-15 nm and the particles are spherical in nature, confirming the particles are in nanosize region.

The nanocrystalline Pb-Ru pyrochlore sample was found to be stable in the test cell where the catalyst was bonded to one side of the Nafion 117 membrane and 2.5 M sulphuric acid solution contacted to the other side. The cyclic voltammograms taken in the presence of nitrogen and oxygen gas on the back side of the Pb-Ru pyrochlore sample (PMSGpyro) and commercial platinum (20%Pt/C), electrode in the potential range of +0.8 to -0.5 V vs Ag/AgCl, at room temperature, at a scan rate of 25 mV/s, are shown in **Figure 3** and **Figure 4** respectively. The higher current response in the presence of oxygen compared to that of the nitrogen, suggests that the oxygen reduction reaction is taking place on the nanocrystalline oxide and platinum surface. The magnitude of the current during the forward and reverse scan are almost equal. The current density at +0.2 V vs Ag/AgCl, during the forward cathodic scan, provides a measure of electrocatalytic activity and is tabulated in Table 1. The oxygen reduction onset potential is almost same for the nanocrystalline pyrochlores (**Figure 4a**) and commercial platinum (**Figure 4b**). The nanocrystalline pyrochlore exhibited better activity compared to that of the same material prepared by conventional ceramic method (Sspyro). This may be due to the increase in the density of states upon decrease in the particle size[10]. No change in the cyclic voltammetric response was observed upon the addition of methanol in the sulphuric acid with respect to time, suggesting that the pyrochlore is methanol tolerant. The chronoamperometric response of the sample PMSGpyro and commercial platinum electrodes for the oxygen reduction at +0.2V vs Ag/AgCl for 1.5h, at room temperature and 70^{o}C (**Figure 5)** shows comparable stability during the oxygen reduction reaction.

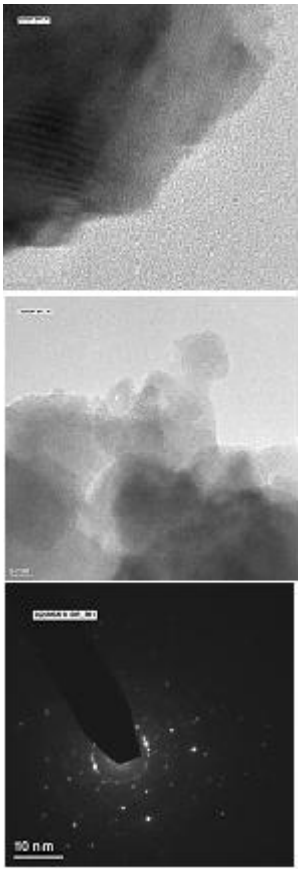

Figure 2 TEM micrograph of nanocrystalline Pb-Ru pyrochlore prepared by polymer modified sol-gel method taken in different t regions

Table 1. Comparison of electrocatalytic activity for the oxygen reduction using pyrochlore and commercial platinum as cathode

Electocatalyst	OCV (V vs Ag/AgCl)	Activity at +0.2 V vs Ag/AgCl I (A/2.5 cm^2)
SSpyro	-	1.6
PMSGpyro	0.500	16.4
Commercial Pt (20%Pt/C)	0.520	14.0

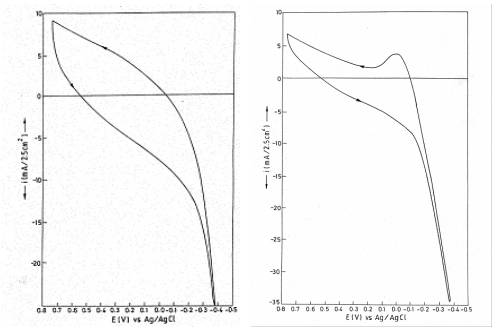

Figure 3 Cyclic voltammogram obtained for (a) Nanocrystalline Pb-Ru pyrochlore and (b) commercial platinum (20%Pt/C) bonded to Nafion 117 membrane in the presence of nitrogen gas

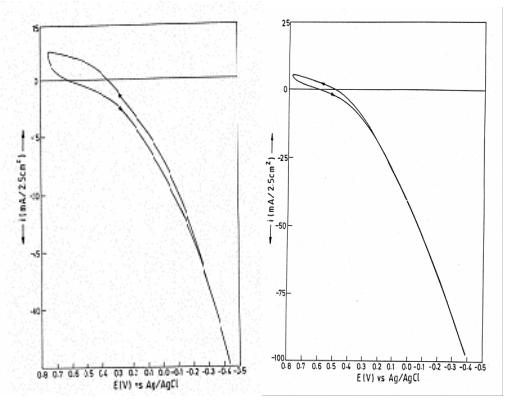

Figure 4 Cyclic voltammogram obtained for (a) Nanocrystalline Pb-Ru pyrochlore and (b) commercial platinum (20%Pt/C) bonded to Nafion 117 membrane in 12 ml/min flow rate of oxygen gas on the back side of the electrode at a scan rate of 25 mV/s at RT

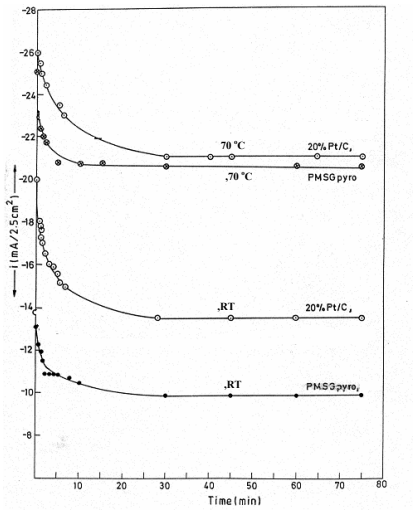

Figure 5 Chronoamperometric response of nanocrystalline Pb-Ru pyrochlore sample and commercial platinum (20%Pt/C) for the oxygen reduction polarization potential at +0.2V vs Ag/AgCl in the presence of oxygen gas.

Conclusions

The nanocrystalline Pb-Ru pyrochlore prepared by polymer modified sol-gel method has been evaluated as the electrode for the oxygen reduction reaction in proton exchange membrane (PEM) medium. The oxide particle obtained are nanocrystalline in nature, which is evident from the XRD and TEMmeasurements. The nanocrystalline Pb-Ru pyrochlore (2.05 mg/2.5 cm^2) exhibits comparable activity with that of the commercial platinum catalyst (0.6 mg/2.5 cm^2), for oxygen reduction reaction in the proton exchange membrane medium. The chrono amperometric measurements reveal that the nanocrystalline pyrochlore exhibits comparable stability to that of commercial platinum electro catalyst for oxygen reduction reaction. The enhancement in the activity exhibited by the nanocrystalline Pb-Ru pyrochlore may be due to the enhanced surface to volume ratio.

References

(1) Burke, L. D.; Casey, J. J.; Morrissey, J. A.; Sullivan, J. F. O'. *J. Appl. Electrochem.* **1994**, *24*, 30.
(2) Kauranen, P. S.; Skou, D. *J. Electroanal. Chem.* **1996**, *408*, 189.
(3) Scott, K.; Taama, W. M.; Argyropolous, P.; Sundmacher, K. *J. Power Sources.* **1999**, *83*, 204.
(4) Longo, J. W.; Stround, R. M.; Swikur-Lyons, K. E.; Rolison, D. R. *J. Phys. Chem. B.* **2000**, *104*, 9772.
(5) Hayashi, M.; Hyodo, T.; Miura, N.; Yamazoe, N. *Electrochemistry*, **2000**, *68*, 112.
(6) Goodenough, J. B.; Manoharan, R.; Paranthaman, M. *J. Am. Chem. Soc.,* **1990,** *112,* 2076.
(7) Zen, J.-M.; Manoharan, R.; Goodenough, J. B. *J. Appl. Electrochem.* **1992**, *22*,140.
(8) Memming, R. *Solid State Ionics***, 1997**, *94*, 131.
(9) Kuznetsov, A. M.; Ulstrup, J. *Electrochim. Acta.* **2000**, *45*, 2339.
(10) Raghuveer, V.; Viswanathan, B. *Fuel*, **2002**, *81*, 2191

Production of Pure Hydrogen and Novel Carbon Nanotube Structures by Catalytic Decomposition of Propane and Cyclohexane

Yuguo Wang, Naresh Shah, and Gerald P. Huffman

University of Kentucky, 107 Whalen Building, 533 South Limestone Street, Lexington, KY 40506-0043

Introduction

The U.S. Department of Energy has recently announced its intention to develop "FreedomCar", a hydrogen-powered vehicle. Such vehicles would likely use polymer electrolyte membrane (PEM) fuel cells, which require very pure hydrogen. Currently, the most common method of producing high purity hydrogen is a multi-step process, involving steam reforming or partial oxidation of natural gas or gasification of hydrocarbons (including coal and biomass) to produce synthesis gas ($CO + H_2$), water-gas shift reactions to convert CO to CO_2 and H_2, and various purification steps to reduce the CO to ppm levels. Direct non-oxidative catalytic decomposition of hydrocarbons into hydrogen and carbon is an alternative, one-step process to produce hydrogen of the required purity.

In previous work[1-4], we have investigated the decomposition of methane and ethane into hydrogen and carbon nanotubes using nano-scale, binary Fe-based catalysts supported on high surface area alumina (M-Fe/Al_2O_3, M=Mo, Pd or Ni). These binary catalysts exhibited high activity for the catalytic decomposition of undiluted methane into pure hydrogen and carbon nanotubes, while ethane was decomposed into hydrogen, methane, and carbon nanotubes. In certain temperature ranges, the catalytic decomposition of ethane produced carbon nanotubes with a novel structure that resembled stacked traffic cones[3]. This is a very open structure that appears to have potential as a hydrogen storage material. In this work, we present the results for the production of hydrogen by catalytic decomposition of propane and cyclohexane.

Experimental

Supported catalysts were prepared by co-precipitation or incipient wetness methods by adding aqueous solutions of appropriate catalyst metal (Fe, Mo, Ni and Pd) salts in the desired proportions to γ-alumina (150 m^2/g). The composition of the binary metal catalysts, M-Fe (M= Mo, Pd or Ni) was 0.5 wt% M and 4.5 wt% Fe with respect to the alumina support.

The propane experiments were carried out as described previously[1], in a fixed bed, plug-flow quartz reactor. The cyclohexane experiments were carried out in a fixed bed, plug-flow stainless steel reactor. Prior to reaction, the catalysts were reduced in flowing hydrogen (50 mL/min) for 2 h at 700 °C. After reduction, the reactor was flushed with an inert gas until the GC showed no residual hydrogen peak (~ 15 min.). The gaseous decomposition products of propane were analyzed by an online GC with a TCD detector, while the products from decomposition of cyclohexane were analyzed in the gas state online by two GC's, the first for hydrocarbon analysis and the second downstream for hydrogen analysis.

Results and Discussions

The product distributions of thermal and catalytic cracking of propane using a (0.5%Pd-4.5%Fe)/γ-Al_2O_3 catalyst are shown in Figures 1 and 2, respectively. It is seen that the thermal cracking starts at about 525 ºC and catalytic decomposition starts at about 375 ºC. At approximately 475 ºC, propane is catalytically completely decomposed into a mixture of methane and hydrogen. Propane is not completely decomposed by thermal cracking until a temperature of 725 ºC is reached. Moreover, thermal cracking of propane produces a mixture of ethane, ethylene, methane, and hydrogen, while only hydrogen and methane are produced by catalytic cracking.

Not surprisingly, hydrogen production at higher temperatures is similar to that of pure methane. The most active of the current suite of catalysts was the 0.5%Ni-4.5%Fe/Al_2O_3 catalyst, which yielded approximately 85 volume% of hydrogen at a fairly modest temperature of 625 ºC. Time on stream studies (TOS) were carried out at 625 ºC to determine the rate of deactivation of the various pre-reduced (at 700 °C) catalysts (Figure 3). The activities of the Mo-Fe and Ni-Fe catalysts decrease relatively slowly at rates of ~1-2% per hour. This rate of deactivation is considerably slower than that of a 5% Fe/Al_2O_3 catalyst (shown in Fig. 3). However, a considerable loss in activity for the Pd-Fe catalyst is seen at 625 °C after only about 1.5 hours. The reason for this is not known at this time, but may be clarified by investigation of the structure of the catalyst by XAFS and Mössbauer spectroscopy, which is currently in progress. Our previous investigations have indicated that the most active form of the M-Fe catalysts is a mixture of an active austenitic Fe-M-C alloy phase and support binding iron aluminate[4]. It may be that these structures were not achieved in the current Pd-Fe catalysts for some reason.

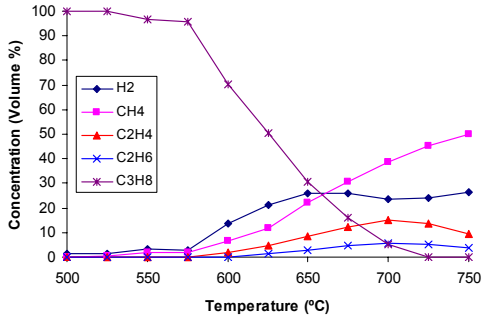

Figure 1. Product distribution of thermal cracking of propane at different temperatures.

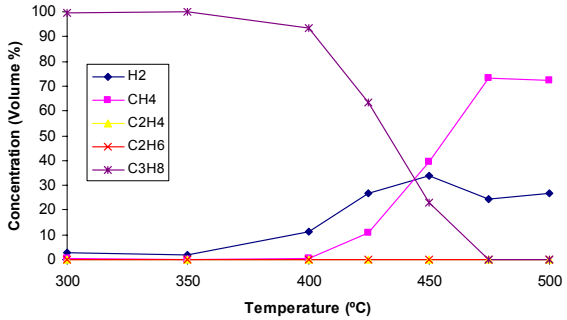

Figure 2. Product distribution of catalytic cracking of propane.

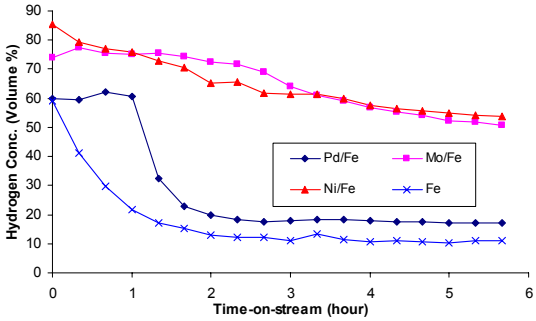

Figure 3. Time-on-stream catalytic decomposition of propane at a reactor temperature of 625 ºC.

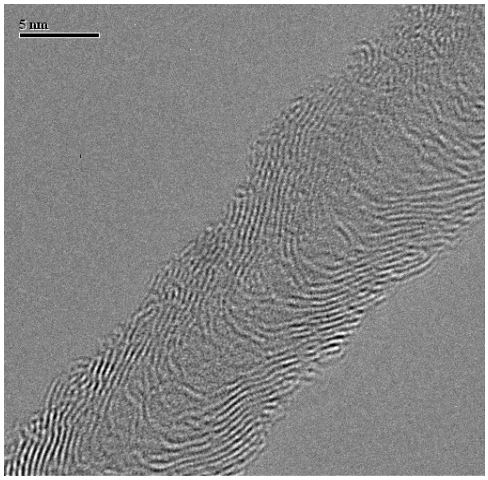

Figure 4. HRTEM image of MWNT grown by decomposing undiluted propane at 475 ºC over Pd-Fe/Al_2O_3 pre-reduced at 700 ºC.

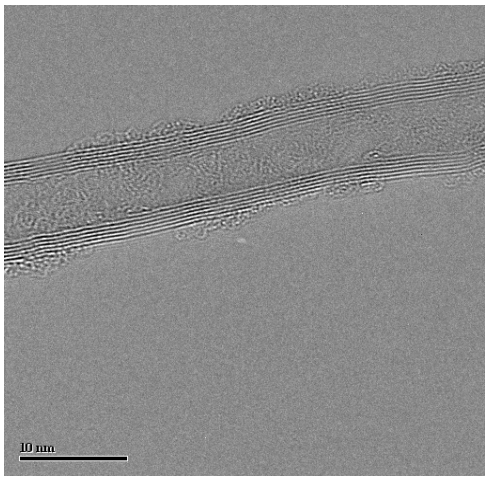

Figure 5. HRTEM image of MWNT grown by propane decomposition at 625 ºC over Mo-Fe/Al_2O_3 (pre-reduced at 700 ºC).

An HRTEM image of carbon multiwalled nanotubes (MWNT) grown by decomposing undiluted propane over the Pd-Fe catalyst at 475 ºC is shown in Figure 4. Decomposition of ethane with Pd-Fe also produced the same type of MWNT [2,3], with an interesting structure resembling nested cones stacked over one another. Because there are many more side openings in these novel MWNTs, they have more potential for hydrogen storage than conventional MWNTs, whose walls are parallel and cylindrical. The hydrogen storage capability of these nanotubes is currently under investigation. The MWNTs produced by decomposition of propane over the Ni-Fe and Mo-Fe catalysts at 625 ºC were predominantly the more conventional type, consisting of parallel concentric hollow cylinders (Figure 5).

Preliminary experiments have also been conducted using the Ni-Fe/Al_2O_3 for hydrogen production from cyclohexane. Figure 6 shows the distribution of different products in the outgoing gas flow from the reactor as a function of temperature. No reaction products were observed below 400 ºC and the only products produced above that temperature were methane, benzene, and hydrogen. It appears that the Ni-Fe/Al_2O_3 catalyst mainly cleaves carbon-carbon bonds to produce hydrogen, methane and carbon nanotubes. At 475 ºC, benzene production reaches its highest point, but is still insignificant (~3 vol.%) compared to the production of methane. Consequently, it appears that the catalyst is not effective in dehydrogenating cyclohexane to benzene. At 500 ºC, no benzene is observed in the outgoing gas flow from the reactor, which is consistent with results obtained by Otsuka et al.[5] using a Ni/SiO_2 catalyst to produce hydrogen from C6 hydrocarbons.

The results for a TOS run of cyclohexane with Ni-Fe/Al_2O_3 are shown in Figure 7. The reaction was stopped after about one hour because the carbon produced in the stainless steel reactor prevented accurate flow control of cyclohexane through the catalyst bed. Within this one hour period, hydrogen is about 60% of the outgoing gas flow. Methane production increases after about 50 minutes, and at the same time, the remaining cyclohexane in the outgoing gas flow decreases. This may be because carbon deposits on the catalyst bed decreases the flow of cyclohexane through the bed. Preliminary HRTEM observations of carbon build up on the catalyst bed showed similar "nested cone" structure MWNTs.

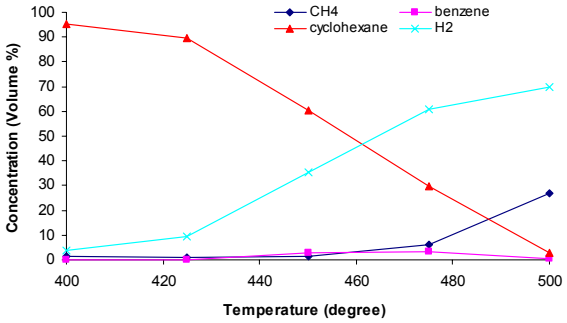

Figure 6. Product distribution of Ni-Fe/Al_2O_3 catalytic conversion of cyclohexane at different temperatures.

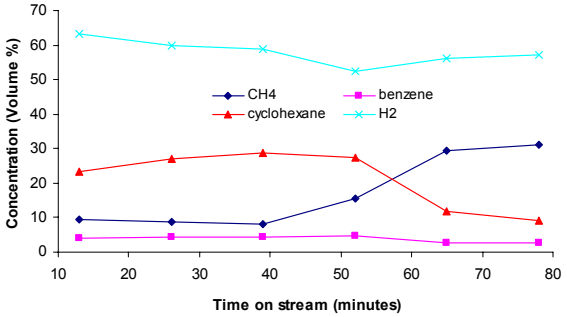

Figure 7. Product distribution of cyclohexane conversion on Ni-Fe/Al_2O_3 at 475 ºC.

Acknowledgement. This research was supported by the U.S. Department of Energy through the Office of Fossil Energy (FE) under the National Energy Technology Laboratory (NETL) under DOE contract No. DE-FC26-02NT4159.

References

(1) Shah, N.; Panjala, D.; Huffman G. P. *Energy & Fuels*, **2001**, *15(6)*, 1528.

(2) Makkuni, A.; Panjala D.; Shah N.; Huffman G. P. Prepr. Pap. - *Am. Chem. Soc., Fuel Chem. Div. Preprints*, **2002**, 47(2), 782-783.

(3) Shah, N.; Wang, Y.; Panjala, D.; Huffman, G.P. "Production of High Purity Hydrogen and Novel Carbon Nanostructures by Non-Oxidative Catalytic Dehydrogenation of Ethane", submitted to *J. Phys. Chem. B*.

(4) Shah, N.; Pattanaik, S.; Huggins, F.E.; Panjala, D.; Huffman, G.P. "XAFS and Mössbauer spectroscopy characterization of supported binary catalysts for non-oxidative dehydrogenation of methane", *Fuel Proc. Tech.*, in press.

(5) Otsuka K.; Shigeta Y.; Takenaka S. *Int J Hydrogen Energy*, **2002**, 27, 11.

SHAPE SELECTIVE METHYLATION OF 4-METHYLBIPHENYL WITH METHANOL OVER MgO/HZSM5

Xinwen Guo[a], Jian-Ping Shen[b], Lu Sun[b], Chunshan Song[b] and Xiangsheng Wang[a]*

[a]State Key Laboratory of Fine Chemicals, Dalian University of Technology, Dalian 116012, China
[b]Clean Fuels and Catalysis Program, The Energy Institute and Department of Energy & Geo-Environmental Engineering, The Pennsylvania State University, 209 Academic Projects Building, University Park, PA 16802, USA

Introduction

Shape-selective alkylation of polycyclic hydrocarbons has been the focus of many recent studies [1-9] for preparation of symmetric intermediates such as 4,4'-dialkylbiphenyl (4,4'-DABP) or 2,6'-dialkylnaphthalene (2,6'-DAN), the important precursors for advanced polymer materials [1]. In the preparation of 4,4'-DABP, the alkylation agents can be either large group like isopropyl or the small one such as ethyl and methyl groups. The results in literature show that it is extremely difficult to obtain shape selectivity to 4,4'-dimethylbiphenyl [8,9]. Recently, some breakthrough on the methylation of 4-methylbiphenyl with methanol was achieved in which the selectivity to 4,4'-DMBP can be up to as high as 65% over HZSM-5 modified with inorganic P compound [10]. Over MgO modified HZSM-5 catalyst, the selectivity to 4,4'-DMBP is up to 80% [11]. In this paper, effects of catalyst activation and the reaction conditions on the methylation of 4-MBP with methanol over MgO/CBV8020 were investigated.

Experimental

HZSM-5 (CBV8020, 80) was obtained from PQ Corporation and calcined at 540 °C for 5 h.

The MgO/CBV8020 was prepared as follows: a solution was prepared from 1.101 g $Mg(NO_3)_2$•$6H_2O$ and 20 ml distilled water, 3 g CBV8020 was added into the solution under stirring at room temperature. After 15 minutes, the mixture was placed into an oven (120 °C) and dried overnight, and then calcined at 450 °C for 5 hrs. The loading of MgO is about 5.6 wt%.

The acidic properties of MgO/CBV8020 sample were measured by TPD of ammonia on Autosorb 2910 apparatus. The samples were outgassed at 250 °C prior to BET sorption of N_2 to measure surface areas and total pore volumes (Autosorb-1). Micropore and mesopore volumes were calculated using the t-plot method.

Methylation of 4-methylbiphenyl was carried out in a fixed-bed, quartz flow reactor. About 0.30 g catalyst is placed in between quartz beads and activated at 450 °C for 1 h, then cooled down to 300 °C. The typical reaction conditions are as follows: feed 4-methylbiphenyl: methanol: mesitylene = 1:5:5 (mol ratio), reaction temperature 300 °C, N_2 flow 20 ml/min. Analysis of products was carried out by GC-MS and GC with BETA DEX® 120 column (60 m *0.25 mm). The typical analysis conditions are as follows: He flow 1.5 ml/min inside the capillary column, 300 °C for both detector and injector, the initial GC oven temperature 145 °C, the ramp 1 °C/min to final 190 °C, and then kept at the final temperature for 15 min.

Results and discussion

SEM of CBV8020 shows that the crystal size is about 1~3 μm. XRD spectra of CBV8020 and MgO/CBV8020 show that MgO modification leads to the decrease of the relative crystallinity, no crystalline MgO. According to the literature [12], the XRD-undetectable part of MgO can be highly dispersed onto the surface of ZSM-5. TPD curves of CBv8020 and MgO/CBV8020 show that the weak acidity in HZSM-5 decreases after MgO modification.
During the preparation of MgO/CBV8020, Mg nitrate is decomposed at 330 °C. So, the effect of calcination temperature on the methylation of 4-MBP over the catalyst was investigated.

Table 1 Effect of calcination temperature on methylation of 4-MBP with methanol (Reaction time is 75 min)

Calcination temperature (°C)		450	500	550	600	650
Conversion (%)		8.3	8.1	9.7	6.1	7.8
Yield (%)	BP	0.6	0.6	0.6	0.5	0.7
	MBPs	2.3	2.5	2.6	1.2	1.6
	DMBPs	5.3	5.1	6.4	4.3	5.5
	others	0.0	0.0	0.0	0.0	0.1
MBP composition (%)	2-	0.3	0.0	0.5	0.1	0.1
	3-	2.2	2.6	2.4	1.2	1.6
	4-	97.5	97.4	97.2	98.7	98.3
DMBP composition (%)	2,2'-	3.8	0.0	0.0	4.7	5.0
	3,3'-	1.5	0.0	1.7	1.4	1.7
	3,4'-	13.6	15.6	14.8	17.2	12.7
	4,4'-	78.1	80.7	79.7	74.5	76.3
	2,3'-	3.0	3.7	3.8	3.3	3.5
	others	0.0	0.0	0.0	0.9	0.9

It can be seen from Table 1 that with an increase in the calcination temperature of MgO/HZSM-5, the selectivity to 4,4'-DMBP increases to 80.7% when the calcination temperature is 500 °C, and the conversion of 4-MBP is 9.7% when that calcination temperature is 550 °C. The optimum scope is between 450-550 °C.

Table 2 lists the effect of reaction temperature on methylation of 4-MBP with methanol over MgO/CBV8020 zeolite catalyst. It can be seen that with an increase in the reaction temperature, the conversion of 4-MBP decreases and the selectivity to 4,4'-DMBP first increases, then decreases. The selectivity to 4,4'-DMBP is up to 79.7% when the reaction temperature is 300 °C. With an increase in the reaction temperature, the isomerization of 4-MBP into 3-MBP increases, and the isomerization of 4,4'-DMBP into 2,3'- and 3,4'-DMBP increases.

Table 2. Effect of reaction temperature on methylation of 4-MBP with methanol (Reaction time is 75 min)

Reaction temp (°C)		275	300	325	350	375	400
Conversion (%)		7.1	9.7	9.4	10.7	12.7	13.3
Yield (%)	BP	0.6	0.6	0.5	0.6	0.6	0.6
	MBPs	1.2	2.6	3.5	5.7	7.2	8.4
	DMBPs	5.3	6.4	5.2	4.4	4.6	4.0
	others	0.0	0.0	0.0	0.0	0.0	0.0
MBP composition (%)	2-	0.0	0.5	0.2	0.0	0.2	0.1
	3-	1.3	2.4	3.6	6.0	7.4	8.7
	4-	98.7	97.2	96.3	94.0	92.4	91.2
DMBP composition (%)	2,2'-	5.8	0.0	4.6	2.3	3.1	4.7
	3,3'-	1.3	1.7	2.1	2.8	3.3	3.5
	3,4'-	14.5	14.8	15.5	20.0	21.6	23.3
	4,4'-	75.8	79.7	72.7	70.0	66.0	61.9
	2,3'-	2.6	3.8	4.3	5.3	6.1	6.7
	others	0.0	0.0	0.8	0.0	0.0	0.0

* Corresponding author. Email: guoxw@dlut.edu.cn; Fax: 86-411-3689065; Tel:86-411-3689065

The effect of WHSV of feed on the methylation of 4-MBP with methanol was also investigated, when the WHSV increases from 2 ml/h to 6 ml/h, the selectivity to 4,4'-DMBP decreases from 79.7% to 70.0%, and the conversion of 4-MBP decreases from 9.7% to 3.6%.

The effect of reaction time on the methylation of 4-MBP with methanol shows that both the conversion of 4-MBP and the selectivity to 4,4'-DMBP decrease with reaction time. Moreover, the addition of water in the feed does not favor methylation of 4-MBP with methanol.

The effect of the amount of mesitylene on the methylation of 4-MBP was investigated, and the results are listed in Table 3.

Table 3 Effect of the amount of mesitylene on methylation of 4-MBP with methanol (Reaction time is 75 min)

4-MBP:mesitylene (molar ratio)		1:5	1:14.26
Conversion (%)		9.7	10.0
Yield (%)	BP	0.6	0.9
	MBPs	2.6	4.6
	DMBPs	6.4	4.5
	others	0.0	0.0
MBP composition (%)	2-	0.5	0.0
	3-	2.4	4.9
	4-	97.2	95.1
DMBP composition (%)	2,2'-	0.0	0.0
	3,3'-	1.7	0.0
	3,4'-	14.8	18.6
	4,4'-	79.7	81.4
	2,3'-	3.8	0.0
	others	0.0	0.0

From Table 3, it can be seen that with an increase in the amount of mesitylene, both the selectivity to 4,4'-DMBP and 4-MBP conversion increase a little. However, the activity stability improves a lot, after 375 min reaction, the selectivity to 4,4'-DMBP is about 80%, and 4-MBP conversion is about 8% (Figure 1). 4-MBP conversion decreases to 2% after 700 min. After regeneration by calcinating at 550 °C for 4 h, 4-MBP conversion is about 8%, while the selectivity to 4,4'-DMBP is up to 86% (Figure 2). The results of N_2 physical absorption (Table 4) show that both the total surface area and micro-porosity decrease after reaction due to the coke, while the meso-porosity keeps constant. After regeneration, both the surface area and the porosity are the same as those of fresh catalyst.

Table 4 Properties of MgO/CBv8020 before and after reaction and after regeneration

Sample	Surface area / $m^2 \cdot g^{-1}$			Porosity / $ml \cdot g^{-1}$		
	Total	Micro	Meso	Total	Micro	Meso
Fresh	314	267	47	0.21	0.13	0.08
After reaction	200	160	40	0.14	0.08	0.06
After regenaration	312	257	55	0.21	0.13	0.08

Acknowledgements. The project was sponsored by the Scientific Research Foundation for the Returned Overseas Chinese Scholars, Ministry of Education, and the Pennsylvania State University.

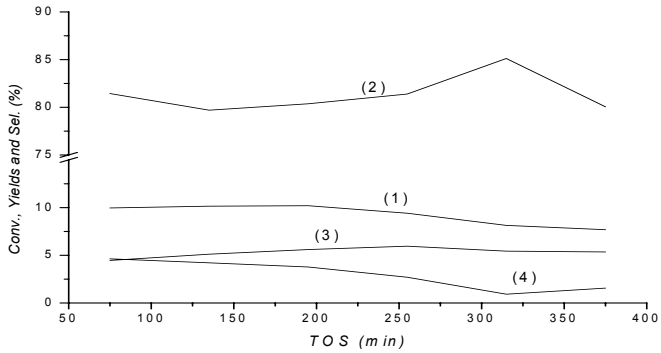

Figure 1 Methylation of 4-MBP with methanol over Mg/CBV8020 (4-MBP: methanol: mesitylene=1:5:14.26)

(1) Conversion of 4-MBP; (2) 4,4'-DMBP Selectivity; (3) DMBP Yield of; (4) MBP Yield

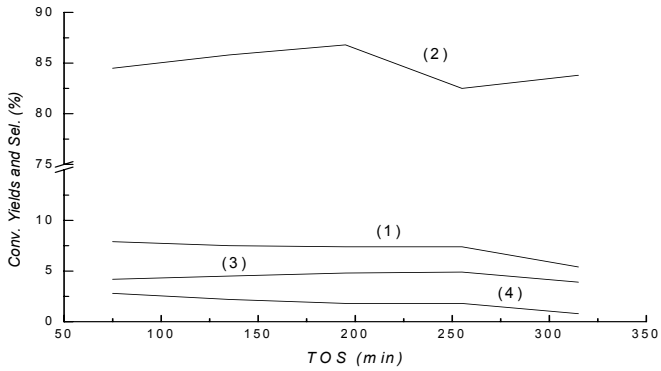

Figure 2 Methylation of 4-MBP with methanol over Mg/CBV8020 after regeneration (4-MBP: methanol: mesitylene=1:5:14.26)
(1) Conversion of 4-MBP; (2) 4,4'-DMBP Selectivity; (3) DMBP Yield of; (4) MBP Yield

References

[1] C. Song, J.M.Graces and Y. Sugi, eds., Shape-selective Catalysis. Chemicals Synthesis and Hydrocarbon Processing, ACS Symp. Ser., **2000**, Vol. 738(Am. Chem. Soc., Washington, DC) p.410; C. Song, Cattech, **2002**, 6 (2), 64.
[2] D. Fraenkel, M. Cherniavsky, B. Ittah and M. Levy, J. Catal. **1986**, 101, 273.
[3] G.S. Lee, J.J.Maj, S.C. Rocke and J.M.Garces, Catal. Lett. **1989**, 2, 243.
[4] C. Song and S. Kirby, Micropor. Mater. **1994**, 2, 467.
[5] A.D. Schmitz and C. Song, Catal. Today, **1996**, 31, 59;
A.D. Schmitz and C. Song, Catal. Lett. **1996**, 40, 59.
[6] Y.Sugi and M. Toba, Catal Today, **1994**,19, 187.
[7] J.P.Shen, J. Ma, D. Jiang and E. Min,Chem. Res. Chin. Uni. **1993**, 14, 845; J.P.Shen, J. Ma, D. Jiang and E. Min,Chem. Res. Chin. Uni. **1993,** 14, 1135.
[8] Y.Sugi, Y. Kubota, K. Nakajima, K. Kunimori, H. Hanaoka and T. matsuzaki, Am. Chem. Soc. Div. Petrol. Chem. Prepr. **1998**, 43, 264.
[9] C. Brechtelsbaur and G.Emig, Appl. Catal. **1997**, 161, 79.
[10] J.P. Shen, L. Sun, C. Song, Catal. Lett. **2000**, 65, 147; J.P. Shen, L. Sun, C. Song, Stud. Surf. Sci. Catal. **2001**, 135, 151.
[11] X.W. Guo, J.P. Shen, S. Lu, C. Song, X. S. Wang, Catal. Lett. 2003, 87, 25.
[12] D. E. Jiang, B. Y. Zhao, Y C Xie, et al., Applied Catalysis A: General, **2001**, 219, 69-78.

PLASMA ENHANCED PREPARATION OF Pt/NaZSM-5 CATALYSTS FOR NO REDUCTION BY METHANE

*Neng Zhu[1] and Yue-ping Zhang[2,3] **

[1]College of Environmental Science and Engineering, [2]Department of Chemistry, [3] ABB Plasma Greenhouse Gas Chemistry Laboratory, Tianjin University, Tianjin 300072, China

Introduction

An intensive investigation has been conducted to reduce nitrogen oxides that are extremely harmful pollutants. The reported investigations include catalytic reduction by hydrocarbons (esp., methane)[1-5], plasma reduction [6,7] and the combination of plasma and catalytic reduction [8-13]. The catalytic reduction has a higher selectivity but the lifetime of catalysts needs to be improved. Plasma conversion shows a high conversion rate for removing nitrogen oxides (NO_x). But the poor selectivity limits its application. The combination of plasma and heterogeneous catalyst has been found recently to be a promising technology for NO_x reduction [8-13]. In general, the investigated combination includes single stage plasma catalytic reactor system and two-step plasma catalytic reactor system. The first reactor system employs a direct interaction between catalyst and plasma species during NO_x reduction. The catalyst must show some field-dependent structural and electronic properties that can response effectively to the influence of plasmas. The two-step system normally uses plasma in the first step to convert NO to other nitrogen oxides that are easier to be converted catalytically in the second step. Evidently, for either single stage or two-step combination technology, a good catalyst is very important. In this work, we report a different technology: the plasma is used first to prepare catalyst and then the prepared catalyst is applied for NO reduction by methane. The experiment confirms that a better catalyst has been achieved. A remarkable improvement in the stability has been achieved by this plasma treatment.

Experimental

A Pt/NaZSM-5 catalyst was prepared by incipient wetness impregnation method. The support NaZSM-5 was commercially obtained (Nankai University Catalyst Plant, China) and was applied as received. This support was first impregnated in an aqueous solution of chloroplatinic acid (H_2PtCl_6) for 18 hours. After impregnation, the resulted sample was dried at 110 °C for eight hours. The obtained sample was then treated by plasma at room temperature for 30 minutes before further calcination at 500 °C for four hours. We have successfully utilized a dc glow discharge for plasma treatment of catalyst. During plasma treatment, the catalyst powder (40-60 mesh) was held in a container that is placed in the discharge tube. The glow discharge [14], one of cold plasma phenomena, is initiated by a dc high voltage generator at low pressure. The catalyst was located in the "positive column" of glow discharge [14] that was generated at ca. 120 Pa using argon as the plasma-forming gas. This region is characterized by its high-energy electrons. The applied voltage to the electrode was measured using a high voltage probe (Tektronix P6015A) with a Tektronix TDS210 digital real-time oscilloscope. The loading amount of Pt is 0.1%, 0.2%, 0.3% and 0.5%, respectively. The effect of the Pt loading amount on the NO reduction by methane has been investigated in this work.

The catalytic NO reduction by methane was carried out in a quartz tube reactor. The inner diameter of the quartz tube is 6 mm. The catalyst loaded is 0.1 g. The feed gas contained 3989.1 ppm NO, 7845.2 ppm CH_4 and helium makes the balance. The total flow rate was kept at 100 Nml/min (GHSV= 47922 h^{-1}). Before reaction, the catalyst was pretreated at 773 K under the flowing hydrogen at a flow rate of 20 Nml/min for 1 hour. Then the temperature was reduced to 573 K and the gas helium was fed into the reactor for half hour.

The feed gas and the effluent were analyzed by a GC (Agilent 4890D) with a TCD detector using a column of HP-Plot Molecular Sieve 5A. The column ID is 0.53 mm and the length is 15 m.

Results and Discussion

Figure 1 shows an effect of Pt loading amount on the NO conversion of NO reduction by methane. Evidently, almost all the catalysts exhibit an excellent low temperature activity. Except the catalyst 0.1% Pt/NaZSM-5, all the catalysts show a 100% NO conversion at the temperatures tested. For the catalyst 0.1% Pt/NaZSM-5, the NO conversion is less than 100% at the temperatures below 410 °C. This means that the loading amount has an effect on the catalytic activity.

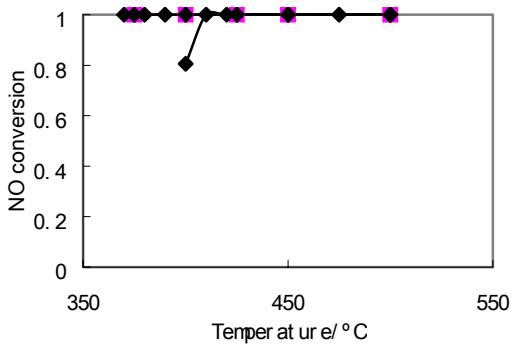

Figure 1. Comparison of activity of Pt/NaZSM-5 with different Pt loading amount (◆: 0.1%Pt; ■: 0.2%Pt; ●: 0.3%Pt; ▲: 0.5% Pt)

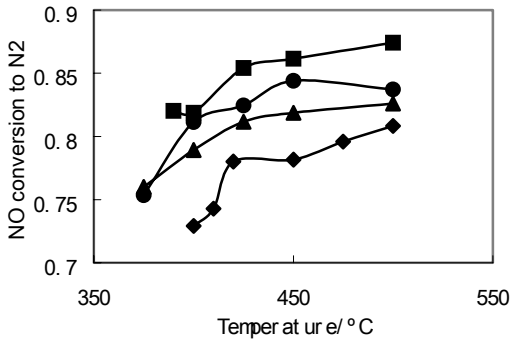

Figure 2. The NO conversion to N_2 over catalysts wuth different Pt loading amount (◆: 0.1%Pt; ■: 0.2%Pt; ●: 0.3%Pt; ▲: 0.5% Pt)

Figure 2 presents the effect of Pt loading amount on the selectivity of NO reduction to N_2. It is very interesting to find that the best selectivity of the catalysts tested is presented over the catalyst

0.2%Pt/NaZSM-5. The Pt loading amount less or higher than 0.2% is not favored for the NO reduction to nitrogen. Further catalyst characterization is being conducted for a better understanding of the reactions.

Conclusions

The present investigation confirms the glow discharge plasma-enhanced preparation will lead to a better catalyst for NO reduction to nitrogen. The Pt loading amount has a little effect on the catalytic conversion if the loading amount of Pt is larger than 0.1%. However, the Pt loading amount has a significant influence on the selectivity of NO reduction to nitrogen. The best loading amount of Pt over the NaZSM-5 zeolite support is 0.2% for NO reduction to nitrogen. We have previously found that the plasma enhanced preparation of catalyst has led to an increased stability of the catalyst. Further investigation will lead to a practical application of Pt/NaZSM-5 catalyst for NO reduction to nitrogen.

Acknowledgement. The support from the Tianjin City Committee of Science and Technology is greatly appreciated. Part of instrument and equipment applied in this investigation was donated by ABB Switzerland Ltd., which is deeply appreciated.

References

(1) Loughran C.J.; Resasco D.E. *Appl. Catal. B* **1995**, *5*, 351.
(2) Ozkan U.S.; Kumthekar M.W.; Karakas G. *Catal. Today* **1998**, *40*, 3.
(3) Xie S.; Rosynek M.P.; Lunsford J.H. *J. Catal.* **1999**,*188*, 32.
(4) Adelman B.J.; Sachtler W.M.H. *Appl. Catal. B* **1997**,*14*, 1.
(5) Balint I.; Miyazaki A.; Aika K.-I. *Appl. Catal. B* **2002**, *37*, 217.
(6) Luo J.; Suib S.L.; Marquez M.; Hayashi Y.; Matsumoto H. *J. Phys. Chem. A* **1998**,*102*,7954.
(7) Kim H.H.; Prieto G.; Takashima K.; Katsura S.; Mizuno A. *J. Electrostatics* **2002**, *55*, 25.
(8) Kim H.H.; Takashima K.; Katsura S.; Mizuno A. *J. Physics D* **2001**, *34*, 604.
(9) Rajanikanth B.S.; Ravi V. *Plasma Sci. & Tech*. **2002**, *4*, 1399.
(10) Yoon S.; Panov A.G.; Tonkyn R.G.; Ebeling A.C.; Barlow S.E.; Balmer M.L. *Catal. Today* **2002**, *72*, 243.
(11) Roh H.-S.; Park Y.-K.; Park S.-E. *Chem. Lett*. **2000**, 578.
(12) Francke K.P.; Miessner H.; Rudolph R. *Catal. Today* **2000**, *59*, 411.
(13) Bröer S.; Hammer T. *Appl. Catal. B* **2002**, *28*, 101.
(14) Liu C.-J.; Vissokov G.P.; Jang B. *Catal. Today*, **2002**, *72*,173.

CATALYTIC SYNTHESIS OF DIETHYL CARBONATE FROM CARBON MONOXIDE AND ETHYL NITRITE ON SUPPORTED Pd CATALYSTS

Xinbin Ma, Haifeng Shi, Zhen Zhang, Baowei Wang, Shengping Wang, Genhui Xu

State Key Laboratory of C1 Chemistry and Technology, School of Chemical Engineering and Technology, Tianjin University, Tianjin 30072, China

Introduction

Diethyl carbonate (DEC) is one of the important green chemicals and widely used for organic synthesis because of having various functional groups in its molecule. DEC is a better octane blending fuel, and has more oxygen in the molecule than *tert*-butyl ether (MTBE), 40.6% versus 18.2%, which reduces emissions from gasoline and diesel engine [1]. For these reasons many studies on the production of DEC have been extensively carried out, e.g., reactions between phosgene and ethanol, oxidative carbonylation of ethanol and trans-esterification reaction. Among them, a novel type of catalytic synthesis of DEC over supported Pd catalysts using ethyl nitrite as substitutes for ethanol and oxygen was developed, which is similar to the synthesis of diethyl oxalate (DEO) in which DEC is generated as a by-product [2].

In this synthesis procedure, two separated reactions are involved. The first reaction is DEC synthesis from ethyl nitrite and CO over Pd catalysts and the second reaction is a gas-liquid reaction of ethyl nitrite synthesis from nitrogen monoxide produced in the first step, oxygen and ethanol. Ethyl nitrite produced in the second step is recycled in the process.

$$CO+2C_2H_5ONO \longrightarrow CO(OC_2H_5)_2+2NO$$

$$2C_2H_5OH+2NO+1/2O_2 \longrightarrow 2C_2H_5ONO+H_2O$$

It was showed that the catalysts Pd on activated carbon have high activities and the better selectivity for the DMC synthesis [3]. Herein, we reported the activities of palladium catalysts for the DEC synthesis. The reason for deactivation of catalyst $PdCl_2/CuCl_2$/a.c. was also investigated.

Experimental

Catalyst Preparation. A catalyst component solution containing Pd, Cu was prepared by heat-dissolving 0.437g of palladium chloride ($PdCl_2$) and 0.839g of cupric chloride ($CuCl_2.2H_2O$) in 40 ml methanol at a temperature of 40℃ to 50℃. Separately, particulate activated carbon in an amount 8.725g was immersed in the solution, and the resultant mixture was stirred at room temperature for an hour. Then methanol was evaporated away from the mixture at a temperature of 50℃ under a reduced pressure. The resultant mixture was dried in a nitrogen gas atmosphere at a temperature of 200℃, to provide a solid catalyst. In the resultant catalyst, a mixture of $PdCl_2$ and $CuCl_2$ was carried on a carrier consisting of the activated carbon. The total content of the metal compound in terms of metallic palladium was 3wt % by weight based on the weight of the carrier, and the atomic ratio of Pd, Cu in the catalysis was Pd: Cu=1:2.

Diethyl Carbonate Synthesis. The above solid catalyst in an amount of 3.0 ml was placed in a gas phase reaction tube having an inside diameter of 20mm and equipped with an outside jacket. The tube filled with catalyst was fixed vertically and a heating system was used to maintain the inside temperature of the reaction tube between 110℃ and 120℃. A mixed gas containing ethyl nitrite (EN) prepared from ethanol, sulfuric acid and sodium nitrite, carbon monoxide and nitrogen, consisting of 15% by volume of ethyl nitrite, 20% by volume of carbon monoxide and 65% by volume of nitrogen, was fed into the reaction tube through a top end thereof at a space velocity of $2000h^{-1}$ under the ambient atmosphere pressure, to cause the carbon monoxide to react with the ethyl nitrite. The reaction products passed through a cooling trap and uncondensed gas products were analyzed by gas chromatographs with TCD detector. The liquid products collected in the cooling trap were taken out every hour, and were analyzed by GC (4890D, Agilent) with FID detector. The by-product includes diethyl oxalate (DMO), CO_2, ethyl formate (EF), and diethoxyethane (DEE). The CO and EN selectivities to DEC were calculated on the basis of the CO or EN consumed, respectively.

CO selectivity (%) = DEC/[DEC+2DEO+CO_2] ¡Á100

EN selectivity (%) =DEC/[DEC+DEO+DEE+2EF] ¡Á100

Catalyst Characterization. The specific surface areas of the catalysts were determined using a constant volume adsorption apparatus (CHEMBET-3000) by the N_2 BET method at the liquid nitrogen temperature. The XPS analysis of the catalysts was carried out on a Perkin-Elmer PHI 1600 ESCA system operated at pass energy of 29.35 eV with an aluminum X-ray source (E=1486.6 eV). The samples were mounted on the specimen holder by means double-sided adhesive tape. Spectra were recorded in steps of 0.25 eV. The C1s peak (284.6 eV) was used as the internal standard for binding-energy calibration. The deviation of the binding energy was ±0.15 eV. The pressure during the measurements did not exceed 1.6×10^{-8} Torr and the temperature was approximately 293 K.

Results and Discussion

Effect of Solvent. Table 1 shows the catalytic activities and properties of the catalysts $PdCl_2$-$CuCl_2$/a.c., which were made by using the same activated carbon and have the same amount of Pd and Cu. Nevertheless, $PdCl_2$ and $CuCl_2$ are dissolved in different solvent (hydrochloric acid or methanol).

Table1 The Effect of the Dissolved Solvent on the Activity and Specific Surface Area of Catalyst

Solvent	Specific surface area (m^2/g)		Conv. (%)	Selectivity (%)	STY (g/lcat.h)
	B	A			
HCl	583	286	16.3	91	199
CH_3OH	680	322	28.5	92	392

B, before reaction; A, after reaction.

As the result showed in the **Table1**, $PdCl_2$ and $CuCl_2$ dissolved by methanol make the catalyst have a larger specific area and we conclude it is because that using methanol to dissolve $PdCl_2$ and $CuCl_2$ enable Pd metal to be adsorbed in smaller particle on the surface of the carrier than using hydrochloric acid, therefore the catalyst showed higher catalytic behavior on terms of conversion of CO and STY of DEC, PH of the solvent used to dissolve $PdCl_2$ and $CuCl_2$ may also have effect on the catalytic behavior of the catalyst. Since the synthesis of DEC is under normal pressure, the STY of DEC is not very high. However, the specific area of the catalyst decreases greatly after reaction. Palladium species supported on activated carbon or metal oxides have been reported to aggregate easily to form Pd metal particles, especially in the presence of CO or H_2 [4]. Deactivation of supported Pd catalysts is often a consequence of reduction and migration of Pd species and the resultant growth of Pd metal. The reason responsible for the decrease of the specific area

may be because atom Pd gets to conglomerate during the reaction and the cluster of atom Pd clogged the hole of the carrier.

Catalyst Lifetime Test. The deactivation behavior of 3wt.% Pd/C for DEC synthesis reaction was studied at 388K to examine the stability of the catalysis. The relation between the formation rate of DEC, ethyl formate (EF) and DEO and the selectivity of CO and ethyl nitrite(EN) to DEC and reaction time are shown in **Figure1**.

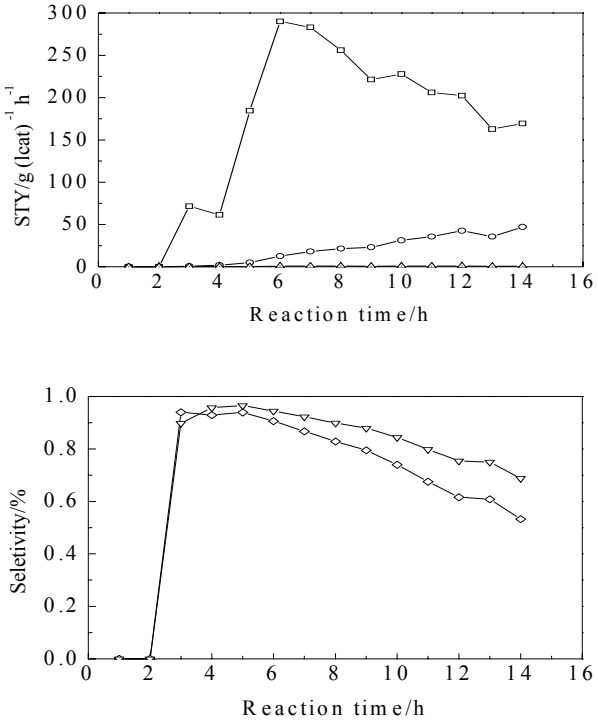

Figure 1. Catalytic behavior of 3 wt.% Pd/C for DEC synthesis as a function of reaction time. (a) Formation rates of DEC (□), EF (△) and DEO (○) and (b) Selectivity of CO (◇) and EN (▽) to DEC.

The STY of DEC reached the maximum of 290 g(lcat.h)$^{-1}$ after 6 h then gradually decreased and reached a steady state activity 220 g(lcat. h)$^{-1}$. Meantime, the DEO and EF formation increased slowly. The selectivity to DEC on the basis of CO and EN consumed decreased with the increase of the reaction time. The rate of deactivation of the catalyst in the reaction was relatively higher than in the UBE progress. It is partly because we did not add HCl gas into the system, atom Pd could not be reoxidized fully, which resulted in the deactivation of the catalyst.

Effect of Reaction Temperature. The relation between the reaction temperature and the catalytic activity of Pd/C was also investigated. The catalytic activity and the selectivity of DEC on the basis of CO consumed are shown in the **Figure 2**.

Clearly, the selectivity of DEC based on CO increased with the increase of the reaction temperatures from 100℃ to 125℃. The STY of DEC gradually increased with the increase of the reaction temperature from 100℃ to 120℃, beyond which the STY of DEC decreased greatly, the decomposition of ethyl nitrite is responsible for this because the decomposition point of ethyl nitrite is 116℃ under normal pressure [3].

XPS Characterization. It is demonstrated in **Table 2** that there is a peak of Cl^- at the binding energy 200 eV before reaction but after reaction the peak of Cl^- disappeared on the surface of the catalyst. As showed in **Figure 1** the catalytic behavior of catalyst also deactivated with the loss of Cl^-, this is the main reason for the deactivation of the catalyst. While the amount of Pd increased after reaction, it was perhaps that Pd got congregated during reaction.

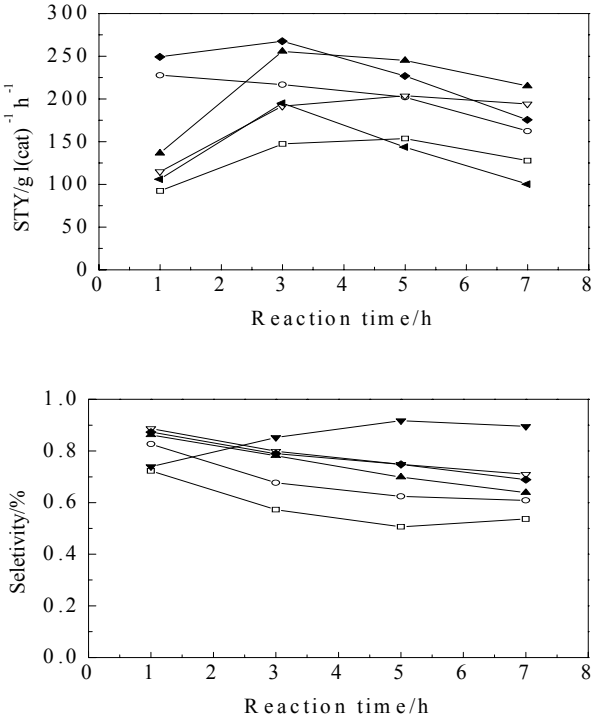

Figure 2. Effect of reaction temperature on the catalytic activity of Pd/C for DEC synthesis. 100℃ (□), 105℃ (○), 110℃ (▲), 115℃ (▽), 120℃ (◆), 125℃ (▼)

Table 2. The Surface Composition of Catalyst Detected by XPS

Catalyst		Surface composition (mol%)				
		C	O	Pd	Cl	Cu
3 wt.% Pd/C	B	64.0	29.2	0.6	3.4	2.8
	A	54.6	38.7	5.6	0	5.6

B before reaction; A after reaction

Conclusions

$PdCl_2$ and $CuCl_2$ dissolved in methanol can make the catalysts have a larger specific surface area and show better activity than dissolved in hydrochloric acid. The catalysts have relatively high selectivity and STY of DEC when reaction temperature is about 110 ℃. The loss of chloride ion is the main reason for the deactivation of the catalysts. So how to fix chloride ion or supply chloride ion during reaction to maintain the activity of catalysts is the key problem.

References

(1) Pacheco, M. A., Marshall, C. L., *Energy & Fuels*, **1997**, 11, 2-29.
(2) Jiang, X. Z., Su, Y. H., Chien, S. H., *Catalysis Letter*, **2000**, 69, 153-156
(3) Matsuzaki, T., Nakamura A., *Catalysis Surveys of Japan*, **1997**, 1, 77-88.
(4) Yamamoto, Y., Matsuzaki, T., Tanaka, S., Nishihira, K., Ohdan, K., Nakamura, A., Okamoto, Y. *J. Chem. Soc., Faraday Trans.*, **1997**, 93, 3721-3727.

THE INFLUENCE OF POTASSIUM PROMOTER ON SYNTHESIS OF DIETHYL CARBONATE BY OXIDATIVE CARBONYLATION OF ETHANOL

Xinbin Ma, Zhen Zhang, Shengping Wang, Haifeng Shi, Hengjin Zhang

State Key Laboratory of C1 Chemistry and Technology, School of Chemical Engineering and Technology, Tianjin University, Tianjin 300072, China

Introduction

Diethyl carbonate (DEC) is one of the important green chemicals in carbonate ester and widely used for organic synthesis because it has versatile chemical properties as a nontoxic carbonylating and ethylating agent by the presence of a carbonyl group and two ethoxy groups in its molecule. Diethyl carbonate can be used as solvent, surfactant, additive of lithium cell electrolyte etc. In recent years, diethyl carbonate is found to substitute for methyl *tert*-butyl ether (MTBE), which is used as an oxygen-containing fuel additive. It has more favorable gasoline/water distribution coefficient and lower volatility than dimethyl carbonate [1], which is another promising substitute of MTBE.

Several reaction routes have been known for DEC production so far such as the traditional phosgene process, the ester exchange process, the carbon monoxide–ethyl nitrite process and the oxidative carbonylation of ethanol. The synthesis of DEC from oxidative carbonylation of ethanol can be carried out in both liquid- and gas-phases. The gas-phase process is more attractive because it avoids the drawbacks of the liquid-phase process, such as the halide corrosion and the difficulty in separating catalyst from the products. The overall reaction is:

$$2C_2H_5OH+CO+\frac{1}{2}O_2 \xrightarrow{Cu^{2+}/Pd^{2+}} O=C(OC_2H_5)_2+H_2O$$

Dunn [4] reported that the yield and selectivity of DEC were improved when the $CuCl_2/PdCl_2$/activated carbon catalyst is treated with KOH by using a batch reactor. Roh et al. [5] used a pulse-quench-flow reactor to investigate the influence of the amounts of reactant and the reaction condition on continuous production of DEC.

Dunn concluded that the catalyst $CuCl_2/PdCl_2$/activated carbon treated with KOH is better than other metal alkali compounds, and explained that potassium promote the reaction. In order to further enhance the conversion rate of reactants and the yield of DEC, the effects of various potassium salts promoters in catalyst $CuCl_2/PdCl_2$/activated carbon on the reaction performance were studied in this paper. The reason for deactivation of catalyst $CuCl_2/PdCl_2$/activated carbon was also investigated.

Experimental

Catalyst Preparation. The catalyst was prepared by impregnating activated carbon with methanol solution of $CuCl_2$, $PdCl_2$ and a sort of potassium salts (potassium acetate, potassium citrate tribasic monohydrate, potassium sorbic, potassium chloride). Then the mixture was refluxed with vigorous stirring for 4h at 60 ℃, and the methanol was removed by vacuum distillation and the catalyst was dried at 80 ℃ for 4h in a vacuum oven. The Cu and Pd content in the catalyst are 3wt. % Cu and 0.25wt. % Pd measured as metals. The molar ratio of the K/Cu was 1. The catalyst sample was then impregnated in a sodium hydroxide methanol solution (Cu/OH=1, molar ratio), and again treated in the above method. The BET specific surface area of the activated carbon employed here is 900 m^2/g.

Catalyst Evaluation. Catalytic activity was measured in a computer-controlled continuous micro reactor system (MRCS-8004B) with a stainless steel tubular reactor of 8mm inner diameter. A thermocouple was placed inside the catalyst bed for accurate temperature control. The reaction products passed through a cooling trap and uncondensed gas products were analyzed by gas chromatographs (GC-8A, Shimadzu) with TCD detector, which employed a column packed with TDX-01 and Propak-Q. The liquid products collected in the cooling trap were taken out every hour, and were analyzed by GC (4890D, Agilent) with FID detector. The reaction conditions were as follows, 2g catalyst, 0.1ml/min ethanol (as liquid), 4 sccm O_2, 40 sccm CO, 20 sccm N_2, reaction temperature 150℃ and reaction pressure 0.64 MPa.

Catalyst Characterization. The XPS analysis of the catalysts was carried out on a Perkin-Elmer PHI 1600 ESCA system operated at a pass energy of 187.85 eV for survey spectra with a Al Kα X-ray source (E=1486.6 eV). The samples were mounted on the specimen holder by means of double-sided adhesive tape. Spectra were recorded in steps of 0.80 eV. The C1s peak (284.6 eV) was used as the internal standard for binding-energy calibration. The pressure during the measurements controlled under 1.6×10^{-8} Torr and the temperature was approximately 293 K.

Results and Discussion

Dunn [4] reported that potassium promoter is better than any other promoter such as sodium, calcium, etc. In the process of synthesis dimethyl carbonate, Jiang et al. [6] concluded that potassium acetate is the most active promoter than other potassium promoter. We use different potassium salt to investigate the catalytic activity of the catalyst.

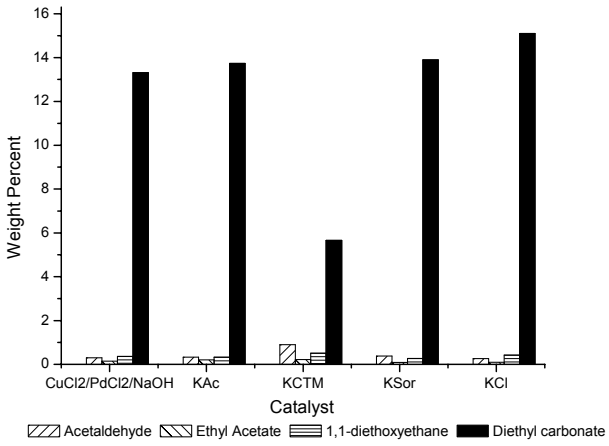

Figure 1. Influence of treating an activated carbon-supported $CuCl_2$ + $PdCl_2$ + NaOH catalyst with various potassium salts on the product yields. Conditions: 2g catalyst, 0.1ml/min ethanol (as liquid), 4 sccm O_2, 40 sccm CO, 20 sccm N_2, reaction temperature 150℃, reaction pressure 0.64 MPa

The most of the catalysts show better activity except the catalyst in which potassium citrate tribasic monohydrate was added as a promoter as shown in **Figure 1**. The selectivity of the reaction kept steady. When KCl was added as a promoter in the catalyst $CuCl_2/PdCl_2$/NaOH/a.c., the reaction shows the best activity. However, the selectivity of DEC dropped down slightly. This result is consistent with previously reported research conducted on the

oxidative carbonylation of methanol [6]. The formation of byproducts is independent on the main reaction of DEC synthesis. According to GC-MS analysis, the mechanism of the production of byproducts was put forward as follows:

$$CH_3CH_2OH + 1/2O_2 \rightarrow CH_3CHO + H_2O$$

$$CH_3CHO + 1/2O_2 \rightarrow CH_3COOH$$

$$CH_3COOH + CH_3CH_2OH \rightarrow CH_3COOCH_2CH_3$$

$$CH_3CHO + 2CH_3CH_2OH \rightarrow C_2H_5O(CH)(CH_3)OC_2H_5 + H_2O$$

The four steps mechanism makes it easy to carry out thermodynamic calculation and analysis.

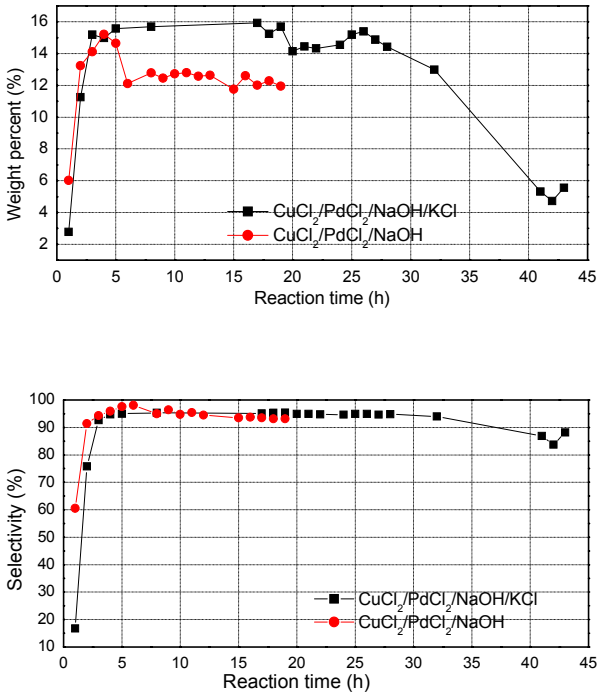

Figure 2. The difference of the product yield and the selectivity to DEC between the catalyst $CuCl_2/PdCl_2/NaOH/KCl/a.c.$ and the catalyst $CuCl_2/PdCl_2/NaOH/a.c.$ (40h lifetime test.)

As shown in **Figure 2,** the catalytic activity maintained steady within 30 hours after adding KCl on the catalyst, and the catalyst without adding potassium chloride deactivated after six hours run. The conversional rate dropped down about twenty percent to twelve percent. However, the selectivity of both these two kinds of catalysts kept high level. The selectivity to DEC didn't increase significantly after potassium chloride was added as a promoter. The potassium chloride can improve the catalytic activity of the catalyst without influence on the selectivity of the diethyl carbonate. Through XPS analysis shown in **Figure 3**, the percentage of chlorine dropped from 12.6 % to 6.5 % of the catalyst $CuCl_2/PdCl_2/NaOH/KCl/a.c.$ after the reaction. The results indicate that chloride ion is an important component in the catalysts, and therefore must be playing a key role in forming DEC. The chlorine ion run away is the main reason of the deactivation of the catalyst. How to fix the chlorine ion becomes the key to prolong the lifetime of the catalysts. Because potassium can apply the chlorine ion, the activity of the catalyst can be increased and maintain more hours.

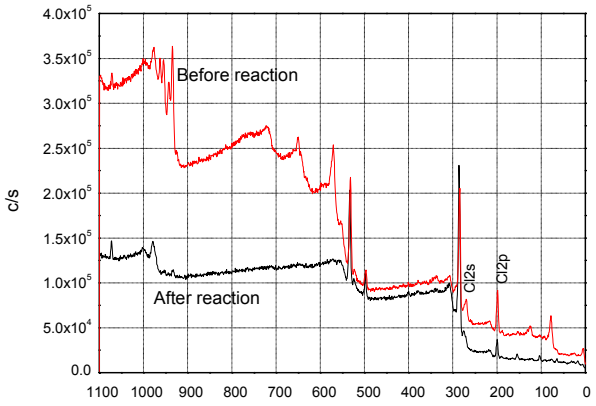

Figure 3. Comparison of the XPS spectrum of $CuCl_2/PdCl_2/NaOH/KCl/a.c.$ catalyst before reaction and after reaction.

Conclusions

Diethyl carbonate can be prepared with high selectivity using a catalyst $CuCl_2/PdCl_2/NaOH$ supported on activate carbon. When potassium salts was added as a promoter, the conversion of ethanol and the formation of diethyl carbonate increased. Through XPS analysis, we can conclude that potassium chloride shows the best activity because chloride ion is an important component in the catalysts, and therefore it must be playing a key role in forming DEC. The production of by-products are independent on the main reaction, it just because the oxidative of ethanol. The four steps mechanism is given to make the thermodynamic calculation and analysis easy.

Reference

(1) Pacheco, M. A., Marshall, C. L. *Energy & Fuel,* **1997**, 11,2~29.
(2) Mo, W. L., Li, G. X., Zhu, Y. Q. *Chinese Journal of Catalysis,* **2003**, 24, 3~4.
(3) Wang, Y. J., Zhao, X. Q., Yuan, B. G. *Applied Catalysis A: General,* **1998**, 171, 255-260.
(4) Dunn, B. C., Guenneau, C., Hilton, S. A., Pahnke, J., Eyring, E. M. *Energy & Fuels* 2002,16(1): 177-181.
(5) Roh, N. S., Dunn, B. C., Eyring, E. M. Prepr. Pap. - *Am. Chem. Soc., Div. Fuel Chem.*, **2002**, 47(1), 142-143.
(6) Jiang, R. X., Wang Y. J., Zhao, X. Q. *Journal of Molecular catalysis A: Chemical,* **2002**, 185, 159~166.

Studies on Conversion of FCC Gasoline to Light Olefins and High Octane Number Gasoline with Low Olefin Content

Xiaohong Li, Chunyi Li, Qimin Yuan, Chaohe Yang, Honghong Shan, and Jianfang Zhang
State Key Laboratory of Heavy Oil Processing, University of Petroleum, Dongying 257061, Shandong, China

Introduction

Light olefins, such as ethylene, propylene, butylene, are major basic chemical materials. With the development of global economy the demand for ethylene and propylene increases greatly, and it is estimated that the increasing rates may be 4.8% and 5.6% per year within coming years, respectively[1]. Presently 90% ethylene[1] and 70% propylene[2] are produced by thermal cracking of hydrocarbons, which operates at about 800 ^{o}C, in some cases even higher than 1000 ^{o}C. Obviously, the energy consumption is very large. Furthermore, limited by the reaction mechanism, the ratio of propylene/ethylene is hardly regulated. In order to improve the production of light olefins, many studies have been carried out worldwide, where catalytic pyrolysis is a very important field [3~6].

FCC processes provide about 80% commercial gasoline in China. FCC gasoline contains too much olefin and can not meet the gasoline specifications limiting the olefin content not more than 35% (vol). The current methods of reducing olefin content may lead to a significant loss of octane number, as the octane number of olefins is higher.

In catalytic pyrolysis, olefins are more active than other hydrocarbons, such as alkanes, naphthenes, aromatics. Thus, if the olefins in FCC gasoline can be selectively cracked to light olefins by using specially made catalysts at appropriate conditions, then on one hand light olefins can be produced, and on the other hand the octane number of gasoline may be retained or even enhanced as aromatics content increases. Here we will introduce the abecedarian results in this aspect.

Experimental

In the experiments the HZSM-5/Al_2O_3 catalyst was prepared by the semi-synthesis method. The particle size of the catalyst is 20~100mm. During the reaction H_2O and feed were pumped into the fixed-bed micro-reactor from the upside respectively. In the atmosphere of N_2 and/or stream the feed was cracked over the catalyst bed, which was placed in the middle of the reactor and the free space was filled with quartz sand to shorten the residence time of oil gas. After reaction, N_2 was used to sweep the reactor to ensure all the oil gas to be out. The effluent from the reactor was collected with a condenser immersed in ice/water bath. The uncondensed gas was collected by draining-water method and analyzed with Varian 3800 chromatograph. The hydrocarbon composition of the gasoline and the octane number were analyzed with HP5890 chromatogram.

Results and Discussion

In order to confirm the feasibility of the above idea, the experiments of thermal cracking and catalytic pyrolysis were conducted. In Table 1, the conversion in the catalytic pyrolysis is 12.91 percent points lower than that in the thermal cracking, while the yield of ethylene + propylene in the former is 2.99 percent points higher and the selectivity is 21.32 percent points higher, and the yields of the byproducts including H_2, CH_4, C_2H_6 and coke in the catalytic pyrolysis are much lower than that in the later. This may be caused by selective catalysis of the catalyst and the restraining effect of lower temperature on the free radical mechanism of thermal cracking. Furthermore, the ratio of propylene/ethylene in the catalytic pyrolysis is 2.12, which is much higher than the value 0.90 in the thermal cracking.

Table 1. Comparison of thermal cracking and catalytic pyrolysis

Process	Thermal Cracking		Catalytic Pyrolysis	
Temperature, ^{o}C	750		600	
Conversion, %	57.33		44.42	
Catalyst	Quartz sand		HZSM-5/Al_2O_3	
	Y, %	S, %	Y, %	S, %
Hydrogen	0.30		0.06	
Methane + Ethane	15.22	26.56	1.78	4.10
Ethylene	15.10	26.33	10.17	22.89
Propylene	13.67	23.84	21.59	48.60
Butylene	8.17	14.25	7.73	17.40
Coke	0.24		0.03	
Ethylene + Propylene	28.77	50.17	31.76	71.49

Reaction conditions: mass of catalyst: 7g, reaction time: 1h, H_2O/Oil ratio (wt/wt): 0.55, feed: Daqing gasoline, input rate of feed: 150g/h

Table 2. RON, MON and antiknock index of feed and product after catalytic pyrolysis

	RON	MON	Antiknock Index
Feed	91.0	78.1	84.5
Pruduct	95.7	83.1	89.4

Reaction conditions are the same as that of Table 1.

Table 3. Hydrocarbon composition of feed and product after catalytic pyrolysis (wt%)

	Alkanes	Naphthenes	Aromatics	Olefins
Feed	38.67	8.50	17.54	35.27
Product	41.70	10.67	37.76	10.39

Reaction conditions are the same as that of Table 1.

After the catalytic pyrolysis, the RON, MON and antiknock index of the remaining gasoline (Table 2) rise by 4.7, 5.0 and 4.9, respectively. The increase of octane number has close relation with the hydrocarbon composition listed in table 3. After the catalytic reaction, although the olefin content drops from 35.27% to 10.39%, the aromatics, whose syncretic octane number are about 110, rise more than 20 percent points. The conversion of olefins is more than 85%, and is much more than that of the other hydrocarbons. The reason maybe ascribes to two aspects: one is the reaction rate of olefins is much faster, and the other is that the pore size of the HZSM-5 only allows alkanes and olefins to enter.

The effects of temperature, residence time, H_2O/Oil ratio (wt/wt) and reaction time in catalytic pyrolysis were also investigated. In Fig. 1, we can see the conversion of the reaction and the yield of ethylene + propylene rise with temperature, while the selectivity to ethylene + propylene drops because the thermal cracking plays an increasing role. The yield increase of ethylene is larger than that of propylene with temperature. Thus, the ratio of propylene to ethylene can be adjusted by varying the reaction temperature.

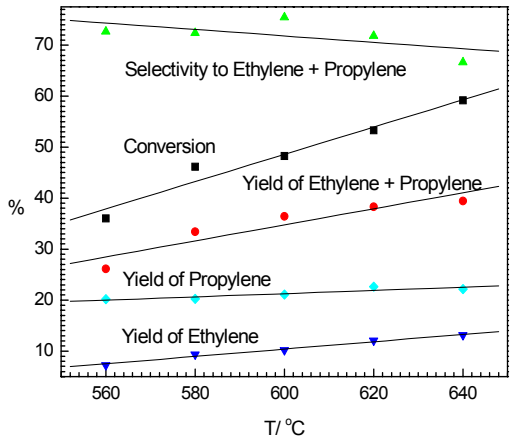

Figure 1. Trends of conversion, yield of products and selectivity to products with temperature (Mass of catalyst: 7g, Reaction time: 1h, Input rate of feed: 150g/h, H_2O/Oil ratio: 0.50).

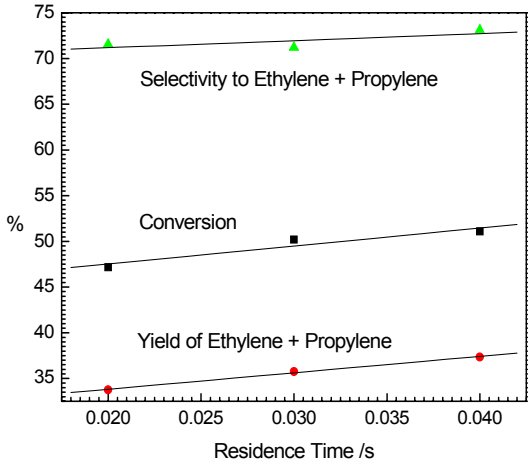

Figure 2. Conversion, yield of products and selectivity to products with residence time (Mass of catalyst: 7g, Temperature: 600°C, Reaction time: 1h, Input rate of feed: 150g/h, H_2O/Oil ratio: 0.34).

As shown in Fig. 2, the conversion of the reaction and the yield of ethylene + propylene increase from 47.17% to 51.09% and from 33.75% to 37.35% with the residence time of oil gas in the reactor varying from 0.02s to 0.04s, respectively. It seems that the longer time is more favorable. However, it is well known that olefins may be saturated due to hydrogen transfer, therefore, the residence time should not be too long.

Steam can reduce the partial pressure of hydrocarbons and restrain coking of the catalyst[7]. On no steam participation, the conversion, the yield of ethylene + propylene and the selectivity to ethylene + propylene are 20.61%, 37.44%, 55.05%, respectively. However, when the H_2O/Oil ratio is 0.28 (Fig. 3), the yield of ethylene + propylene and the selectivity to it increase by 15.0 and 32.0 percent points, respectively. The reason that the conversion decreases with H_2O/Oil ratio may be due to the reduction of the partial pressure of oil gas. In addition, producing high temperature steam will consume very large amount of energy. So the appropriate H_2O/Oil is crucial for producing light olefins economically. In order to study the effect of the reaction time, some experiments were carried out. In Fig. 4, the conversion and the yield of ethylene + propylene fall quickly by 14.4 and 9.8 percent points respectively when the reaction time were prolonged from 20min to 120min, which is caused by the coking deactivation. However, the selectivity of the catalyst to ethylene + propylene keeps about 72%, and even after reacting for 120min the yield of ethylene + propylene is still higher than 30%.

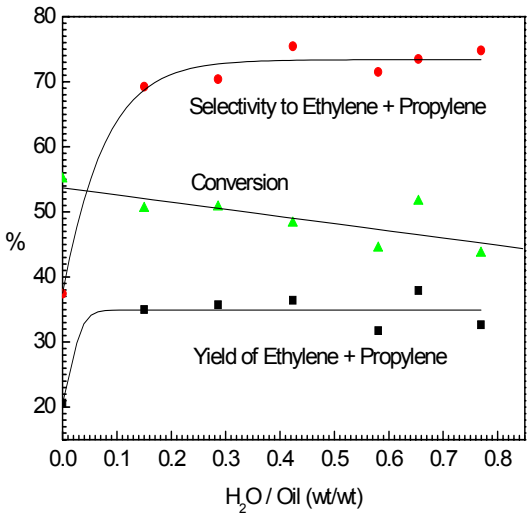

Figure 3. Curves for conversion, yield of products and selectivity to products with H_2O/Oil ratio (Mass of catalyst: 7g, Temperature: 600°C, Reaction time: 1h, Input rate of feed: 150g/h).

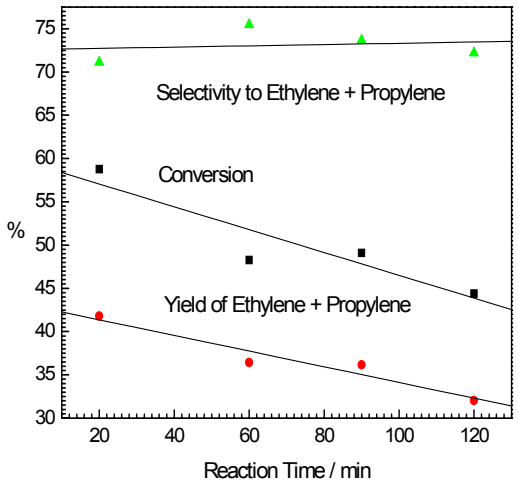

Figure 4. Effect of reaction time on the catalytic pyrolysis of FCC gasoline (Mass of catalyst: 7g, Temperature: 600°C, H_2O/Oil ratio: 0.50, Input rate of feed: 150g/h).

The catalytic pyrolysis of FCC gasoline is a new and effective method to produce light olefins. One of its prominent advantages is that high octane number gasoline with low olefins content can be obtained simultaneously. Certainly, the appropriate reaction conditions and the special catalyst should be studied further.

Acknowledgement

This work was supported by PetroChina, Corp., under contract 020802-05-2.

References

1. Yi, H. L.; Shi, Zh. C.; Li, C. Y.; Wang, X. Q.. *Petroleum Processing and Petrochemicals*, **2002**, *33(3)*, 38.
2. Zhou, Q.; Hu, J. L.. *Shihua Jishu*, **2001**, *8(4)*, 244.
3. Zhang, Zh. G.; Xie, Ch. G.; Shi, Zh. Ch.; Wang, Y. M.. *Petroleum Processing and Petrochemicals*, **2001**, *32(5)*, 21.
4. Xie, Ch. G.; Pan, R. N.. *Petroleum Processing and Petrochemicals*, **1994**, *25(6)*, 30.
5. Powers, D. H.; Webber, K. M.. W.O. Pat., No. 0,181,280, **2001.**
6. Chester, A. W.; Degnan, T. F.; Kiu, K.; Timken. H. K. C.; Mathias. M. F.; Woolery, G.L.. W.O. Pat., No. 0,031,215, **2000.**
7. Cheng, Y. G.; Mao, W. X.; He, Y. K.. *Petrochemical Technology*, **2001**, *30(4)*, 311.

CS_2-SOLUBLE FRACTIONS FROM MACERALS AND EXTRACTION KINETICS

Yugui Zhang [1] *Yajun Tian*[2] *Wang Baojun*[1] *Xie Kechang*[1] *Xianyong Wei*[3]

1. State Key Lab of C1 Chemistry and Technology, Taiyuan University of Technology, Taiyuan, 030024, P. R. China
2. College of Chemistry and Chemical Engineering, Nanjing University, Nanjing 210093,P.R China
3. Department of Applied Chemistry, School of Chemical Engineering, CUMT, Xuzhou , Jiangsu 221008, China

Introduction

The solvent extraction techniques have long become of valid methods to study properties, constitutes and structures of coal. Coal extracts have been used to obtain coal material in solution form that can readily be characterized[1, 2]. In general terms, the mechanism of coal extraction seems to consist in substitution: electron-donating solvent molecules replace the coal electron donor participants in the forces [3]. Numerous organic solvents used for coal extraction had been characterized by quantitative measures[3, 4, 5] of their electron-donor (DN) and electron-acceptor (AN) properties (Gutmann's[6] donor and acceptor numbers) as well as by Hildebrand's solubility parameter and Snyder's polarity index. Correlations were found between the extract yields on one hand and donor numbers of the solvents as well as the differences (DN_AN), on the other. Though extract yield with solvent CS_2 is generally lower, solvent CS_2 is available for use to extraction of many low weight molecular compounds in coal. However, for long time, not much attention had been paid to Studying the law of extract process of coal and investigating the kinetic of the extraction.

In this work, fractions and kinetics of extraction for several macerals with solvent CS_2 were studied, origin and occurrence of the low molecular compound were discussed.

Experimental

Coal Samples. Three groups of coal samples used in this study respectively were taken from Fushun west strip mine (FS) in Liaoning province, Datong Sitai mine (DT) and Pingshou strip mine (PS) in Shanxi province, included a resinite, two inertinte and three vitrinite concentrates. Individual maceral concentrates were drawn from the same coal seam for each couple samples in each mine, and maceral purities were all higher than 95%. Proximate and ultimate analyses data of coal samples used in this study are presented in **Table 1.**

Table 1 Proximate and ultimate analyses data of coal samples

Coal samples	$\%A_{ad}$	$\%V_{daf}$	$\%C_{daf}$	$\%H_{daf}$	$\%N_{daf}$	$\%O^*_{daf}$	%S
FS vitrinite	2.46	41.50	79.90	5.82	1.00	13.28	0.51
FS resinite	0.89	99.01	81.40	10.10	0.14	7.71	0.13
DT vitrinite	10.02	31.98	—	—	—	—	0.97
DT fusinite	15.27	27.50	—	—	—	—	—
PS vitrinite	5.54	40.38	79.89	5.32	1.78	13.23	0.58
PS fusinite	8.36	28.24	84.73	3.96	9.89	0.66	0.76

O^*: by difference

Solvent extraction. Approximately 10 g of coal with 200 ml carbon disulfide was extracted in the Soxhlet extractor. In order to determinate the weight of extract as a function of time, the solvent contained extract fraction was frequently replaced by fresh solvent, and a series of solvable fractions of the certain time range were obtained. The liquid of each fraction was distillated to 3-5ml concentrated liquids in the vacuum rotatory evaporator and then dried in air at 35°C until partially dry and then dried to constant weight in a vacuum drying oven.

The extraction yield is the weight of extract divided by the weight of organic substance in coal sample.

Results and Discussion

Extract yield. Table 2 is extract yields of PS and DT coal samples in different ranges of time. **Table 3** is extract yields and family constitutes of FS coal in different ranges of time.

Table 2 Extract yields of PS and DT coal samples in different ranges of time (on the basis of dry ash free)

Time range	PS fusinite	PS vitrinite	DT fusinite	DT vitrinite
0-1	0.42	0.80	0.62	0.74
1-3	0.11	0.11	0.17	0.36
3-7	0.14	0.16	0.13	0.17
7-15	0.17	0.17	0.18	0.28
15-31	0.27	0.18	0.21	0.35
31-64	0.17	0.14	0.14	0.19
64-103	0.10	0.10	0.10	0.11
0-103	1.39	1.65	1.54	2.20

Table 3 Extract yields of FS coal sample in different ranges of time (on the basis of dry ash free)

Time range	Vitrinite	Time range	Resinite
0—2	0.71	0—2	15.38
2—9	0.33	2—7	2.67
9—22	0.16	7—25	0.97
22—46	0.15	25—49	0.47
46—70	0.10	49—73	0.29
70—94	0.11	0—73	19.78
0—94	1.56		

Table 2 and table 3 show that the variety of extract yields is very small after long time, therefore the sum of yield during all ranges is regarded as the theoretic extraction yield.

Normalization of extract yiled. Normalized ratio is defined as the fraction of an extract yield to the theoretic extraction yield. **Figure 1** is a plot of normalized ratio vs. time for FS vitrinite and FS resinite, and **figure 2** for PS and DT coals.

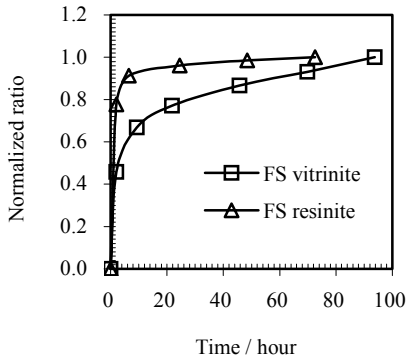

Figure 1. The curve of the normalized ratio of extraction yield vs. time for FS vitrinite and resinite coal

In generally, the extract rate of all macerals is high at beginning few hours, and then decelerates gradually. The extract rate of FS resinite is faster than that of FS vitrinite. Although their biggest yield shows little difference, their rates do notable difference. However, for DT vitrinite and DT inertinite, their extract yields have notable difference, but little difference for their rates.

Extract kinetic. Studying the process of extraction and investigating the kinetic of the extraction is very important for the probable

industrialization. Also, it may be beneficial to understand the mechanism of the extraction.

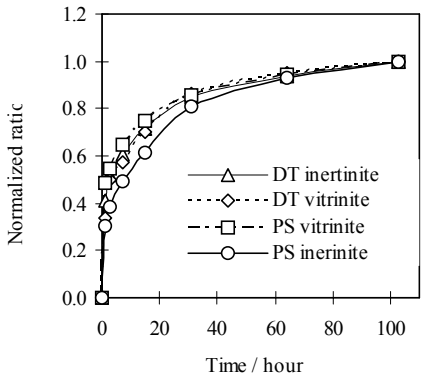

Figure 2. The curve of the normalized ratio of extraction yield vs time for DT and PS coals

Assume the extract rate is first order of the extractable content in coal, that is:

$$\frac{d\alpha}{d\tau} = k(1-\alpha) \quad (1)$$

where, α, the normalized ratio of extract yield

k, the constant of extract rate

τ, time of extraction

its integral formula is

$$-\ln(1-\alpha) = k\tau \quad (2)$$

In theory, its plot should be a beeline to past the origin drop, and the slope of beeline is *k*, the constant of extract rate.

For instance, with DT vitrinite, the result of –ln(1-α) vs. τ displays in **Figure 3**, and the plot is not a beeline to pass the origin, which illuminates that process of extraction is not the process of first order process. However, the whole process can be divided into two first order stages to describe, the critical time of the two stages is about 3.08 hour, the slopes of two stages are 0.25 and 0.038 respectively.

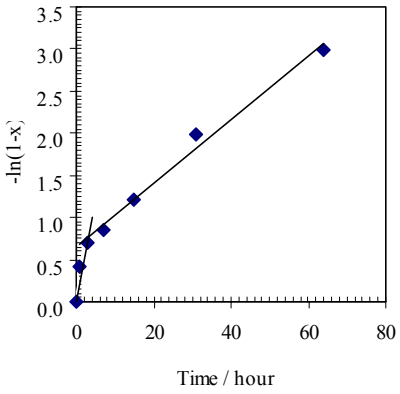

Figure 3. Kinetic curves of extraction of FS vitrinite.

Above all, we can describe the extraction process with two first order sub-processes. A group of general formulae are shown as **Formula** (3) and (4).

For the first stage,

$$\alpha = 1 - e^{-k_1\tau} \quad (0 \leqslant \tau < a) \quad (3)$$

For the second stage,

$$\alpha = 1 - e^{-[k_2(\tau-a)+b]} \quad (\tau \leqslant a) \quad (4)$$

where, k_1 is extract rate constant of the first stage,

k_2 is extract rate constant of the second stage,

a is the critical time between the first stage and second stage,

b is value of formula –ln(1-α), when τ = a, that is b=k1×a.

After regression, corresponding parameters is obtained, so the extraction process of FS vitrinite could be simulated by **Formula** (5) and (6).

For the first stage,

$$\alpha = 1 - e^{-0.25\tau} \quad (0 \leqslant \tau < 3.08) \quad (5)$$

For the second stage,

$$\alpha = 1 - e^{-[0.038(\tau-3.02)+0.755]} \quad (3.08 \leqslant \tau) \quad (6)$$

It is found in **Figure 4** that the prediction values match the experimental results very well. The confidence of simulation is 0.9904.

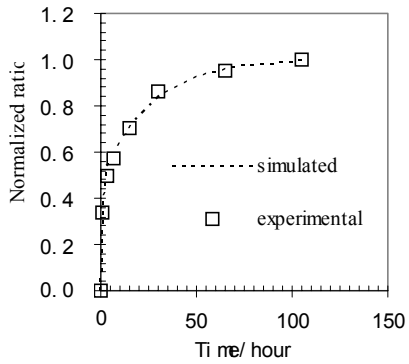

Figure 4. Comparison of simulation with experimental results for DT vitrinite

In a similar way, the parameters of other samples are obtained and presented in **Table 4**. For most cases, their extraction process could be described by two first order producers, except FS resinte.

Table 4 Kinetic parameters of extraction of CS_2 solvent

samples	k_1	k_2	a	b	Confidence
DT vitrinite	0.25	0.038	3.02	0.755	0.9904
DT fusinite	0.27	0.033	3.02	0.817	0.9774
PS vitrinite	0.31	0.033	3.00	0.930	0.9640
PS fusinite	0.18	0.036	2.90	0.522	0.9872
FS vitrinite	0.13	0.025	8.68	1.128	0.9614
FS resinte	0.41	0.043	5.98	2.451	0.7734

Acknowledgment. BASIG NATURES AND PURPOSES in The Key Technologies Research and Development program, under contract G1999022101, supported this work.

References

1. Y.G. Zhang, B.J. Wang, Y.J. Tian et al. Journal of China University of Mining and Technology, 2003(3)
2. Z M Zong, X H Wang, X H Gu, et al. Proceedings of the 7th China-Japan Symposium on Coal and C1 Chemistry, 2001, 347-350.
3. A. Marzec, M. Jozwa, K. Betlej. Fuel Processing Technology. 1979,2(1), 35– 44.
4 M. Nishioka. Fuel, 1993, 72 (12): 1719-1723
5. V. Gutmann, The Donor– Acceptor Approach to Molecular Interactions, Plenum, New York, 1978.
6. A. Marzec. Fuel Processing Technology , 2002,77–78, 25–32.

OVERVIEW OF UTILIZATION PROSPECTS FOR COAL MINE METHANE

Ray Zahradnik and Charles D. Estes

Appalachian-Pacific, LLC.
1401 Wilson Boulevard
Suite 1101
Arlington, VA 22209

Introduction

Coal Mine Methane (CMM) refers to methane that is released from coal mines as a consequence of the mining operation. CMM has historically been perceived as a safety hazard in mining operations. It can be released during operations at the mining face, where it is generally removed by circulating air that maintains methane concentrations well below safety standards. It can be released after mining has occurred, as in the case of longwall mining, and is generally vented to the atmosphere by means of drilled openings that are referred to as gob wells. It can also be released after a mine has been decommissioned and shut in. In this instance, it is released to the atmosphere by means of vent wells and/or natural fissures in the surrounding rock formation.

It is estimated that in the United States over 300 million cubic feet of CMM are released to the atmosphere every day. Methane is a potent greenhouse gas and contributes to environmental problems such as global warming, retropospheric ozone formation, and potentially stratospheric ozone depletion. The Intergovernmental Panel on Climate Change estimates the potency of methane to be 22 to 24.5 times that of carbon dioxide. On this basis, the daily discharge of CMM is equivalent to the exhaust of between 5 and 6 1000MW power stations.

Apart from being hazardous and environmentally dangerous, CMM represents a potentially attractive raw material, and its recovery and utilization can be a profitable venture under certain conditions. At a value of $1/MCF, the worth of the vented CMM in the United States represents $100 million annually. Whether the capital expenditure needed to capture and utilize CMM is economically justified has been the subject of a long-term investigation by Appalachian-Pacific, LLC. (AP)

Technologies for Recovering and Utilizing CMM

The composition of CMM varies, depending upon how it is obtained. In a mine ventilation shaft, where much of the CMM is released, the methane concentration is 1 or 2 %, with the remainder being air. In gob wells, the methane concentration ranges from 50 to 80 %. CMM released from shut-in mines varies from 60 to 90 % methane, with nitrogen and carbon dioxide comprising the rest. Both the composition and the flow of CMM from all of these sources vary with time and conditions, presenting a problem for potential utilization.

The simplest recovery system consists in capturing CMM as it is released from gob wells or from shut in mines by means of collection lines attached to the wells. The gas is at atmospheric pressure and generally saturated with water. Such gas can be introduced into natural gas pipeline with a minimum of processing, which would include drying and pressurization. CMM is often below pipeline standards, but because it is such a small quantity in relation to the pipeline flow, pipeline companies often accept it.

A second utilization procedure is to use the CMM as a fuel for electrical generation. Depending upon the system used to generate power, the CMM may need little additional processing. However, the uneven nature of the flow and composition presents operational problems for the power system, and both gas clean up and storage may be required for optimal economic advantage.

A third utilization scheme is to liquefy the methane in CMM to produce LNG for sale as an alternate transportation fuel. This represents the highest value-added use for CMM, but requires the most elaborate and expensive processing facilities. AP has been involved in a cost-shared project with the US DOE to determine an appropriate technology and marketing plan for the production and sale of LNG from CMM for the past several years.

The Production and Sale of LNG from CMM

In order to produce LNG from CMM in a cost competitive manner, technologies that are compatible with the production rates and composition variability of CMM are necessary. AP has developed process designs that satisfy these requirements. A critical element in the design is a small-scale liquefier that is both efficient and inexpensive. AP plans to use a Thermoacoustic liquefier being developed by Praxair, Inc., based upon initial investigations by LASL.

The basis of the Thermoacoustic liquefier is the use of a Thermoacoustic engine to provide the power for a refrigeration cycle. (1) A 100 gpd pilot unit to liquefy methane was constructed and tested with good results in the late 90's, and a 500 gpd unit is currently undergoing testing and verification. (2) A photograph of this experimental unit is provided in Figure 1.

Figure 1. Photograph of Prototype 500 gpd Thermoacoustic Liquefier.

If these tests are successful, AP plans to incorporate a 10,000 gpd Thermoacoustic refrigeration unit into a CMM recovery and processing facility to be located in West Virginia. The LNG produced would be sold into the heavy-duty transportation market.

A process design for this facility has been completed, based upon a feed stream of CMM from a shut-in mine. Alternative gas conditioning systems have been considered. The purpose of the gas conditioning system is to remove CO_2 and water vapor prior to entering the refrigeration unit. In some cases oxygen is present in the CMM, which also must be removed.

Both amine scrubbing and cryogenic removal have been considered for this operation. Depending upon the conditions of the feed stream and the overall system balances, either option may be employed.

A process schematic for the overall system is provided in Figure 2. The details for this design and for the Liquefier will be provided in the complete paper.

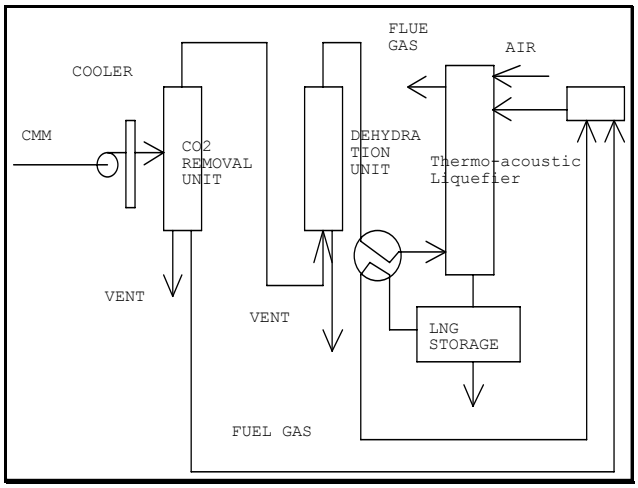

Figure 2. Process schematic for producing LNG from CMM.

In general, a portion of the CMM feed stream can be used to provide the combustion gas for the Thermoacoustic liquefier, as shown in Figure 2.

Fuel gas may also be needed for the onsite generation of electrical power. Depending upon the availability and composition of the CMM and the decision to generate electricity, the overall system material balances must support these options.

CMM itself may be used directly as a fuel gas. In this case, the separation scheme following the liquefier is somewhat more involved, as shown in Figure 3.

Various cost projections for the venture will also be presented, along with a discussion of the economic sensitivities.

Because LNG has not become generally accepted in the West Virginia area as an alternative fuel, AP plans to conduct a market priming program, aimed at providing information to potential users about the features of LNG utilization as well as initial sales. AP is being aided in this effort by West Virginia University

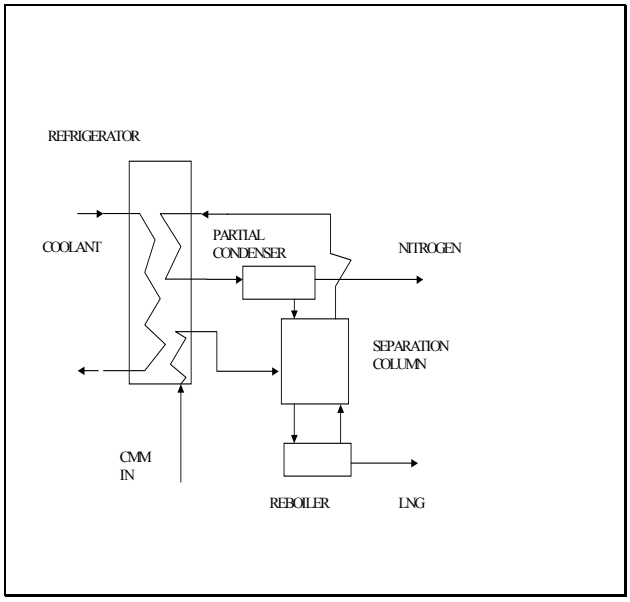

Figure 3. Schematic of Refrigerator, showing how nitrogen can be rejected at tail end of process.

.

Conclusions

CMM represents both an environmental problem and an economic opportunity. There are problems involved with its capture and utilization that are technical, economic, and institutional. The complete paper will include a discussion of these problems.

There are other projects underway under the DOE cooperative program that provide additional perspective on the utilization of CMM. These will also be discussed.

Acknowledgement.

This work has been carried out as part of a DOE contract No. DE-AC21-95MC32185 and DOE Cooperative Agreement DE-FC28-00NT40978.

References

1. Swift, G. W., Thermoacoustics: A Unifying Perspective for some Engines and Refrigerators. *Acoustical Society of America Publications, Sewickley, PA* 2002.

2. Wollan, J. Praxair, Inc. Private Communications

OPPORTUNITIES FOR CLEAN FUELS FROM LAND FILL GAS

James Wegrzyn

Energy Sciences and Technology Department
Brookhaven National Laboratory
Upton, New York 11973-5000, USA

Introduction

The US Department of Energy estimates that if bioreactor technology were applied to 50% of the waste that's currently being deposited in landfills, it would provide over 270 billion cubic feet of methane annually. Bioreactors are defined as any landfill cell where liquid and/or air is added in a controlled fashion to accelerate bio-stabilization. However besides providing waste stabilization, bioreactors also increase the production rate of methane. This presents the opportunity for making clean fuels from a sustainable energy source (*i.e.* municipal solid waste). Although 270 billion cubic feet of methane might seem like a large number, it's small when compared with the US annual fuel consumption. The interest therefore in clean fuels from landfill gas is not to address the countries energy security problem, but rather in developing a market driven and environmentally sound approach for converting LFG to liquid fuel. This paper suggests the replacement of the biomass gasification and hot gas cleanup route to GTL with a bioreactor and cold gas cleanup process.

Description

The four major subsystems of converting wastes to clean fuels are; 1) bioreactor, 2) gas cleanup, 3) methane steam reforming or partial oxidation, and 4) gas to liquid technologies. Information on each of these four components can be readily found in the open literature. A brief review is being given here for the purpose of completeness.

Bioreactor. The bioreactor landfill is an emerging technology for solid waste management, although it has been a subject of research since the 1960s. More recent and complete reviews are available [1,2,3]. This paper will attempt to simplify a very complex biological system by starting with Equation (1).

$$\mathbf{C + H_20 \rightarrow 1/2CO_2 + 1/2CH_4} \quad \text{anaerobic} \quad [1]$$

But in fact a consortium of microorganisms (fermentative, acetogenic and methanogenic) is necessary to convert organic material into methane and carbon dioxide. Justification for using Eqn. (1) is that the typical LFG composition follows Equation (1) as being 50% methane; 40% carbon dioxide; and 10% nitrogen, oxygen and VOCs. Also aerobic bioreactors can stabilize waste and compliments the anaerobic activity. The optimum bioreactor appears to be a hybrid bioreactor which combines the positive features of both the anaerobic and aerobic reactions. The major difference between a bioreactor and a "dry tomb" conventional landfill is the controlled addition of moisture. "The recirculation system employed to distribute moisture throughout the waste mass is the most critical operational component in the bioreactor process [4]". US EPA has identified six advantages of bioreactors over dry tomb landfills.

- Waste stabilization in years vs. decades
- Lower waste toxicity and mobility
- Reduced leachate disposal costs
- Significant increased LFG generation
- Reduced post-closure cost

This paper looks at taking advantage of this increased LFG generation rate for the production of 5,000 to 10,000 gallons per day of clean synthetic fuels.

Landfill Gas Cleanup Landfill gas has become a marketable energy resource. Projects include power generation, pipe line grade natural gas and more recently the production of liquefied natural gas. In the case of LNG there are currently three cleanup technologies being considered; adsorbents, chilled methanol[5] and liquid CO_2 wash[6]. The first two gas cleanup technologies are well document in the literature, so discussion will be limited to applying the CO_2 wash technology for LFG cleanup. The Acrion CO_2 wash technology is an absorbent column that utilizes the excellent solvent property of liquid CO_2. The process requires water and hydrogen sulfide removal prior to compression. Nominal operating conditions are -50°C and 25 bar pressure. At these conditions approx. 10% of the CO_2 is condensed at the top of the reactor (Figure 1) and flows down a high surface area packed bed removing all contaminants. Independent analysis was not able to detect any contaminants in the process stream. Gas composition by volume at the outlet was measured to be; 63.4% methane, 27.8% carbon dioxide, 07.4% nitrogen and 01.4% oxygen. Detection sensitivity was at the ppm or better level. This feed stock of high purity gas offers wider selections of catalysts and longer catalysts life for the subsequent GTL process.

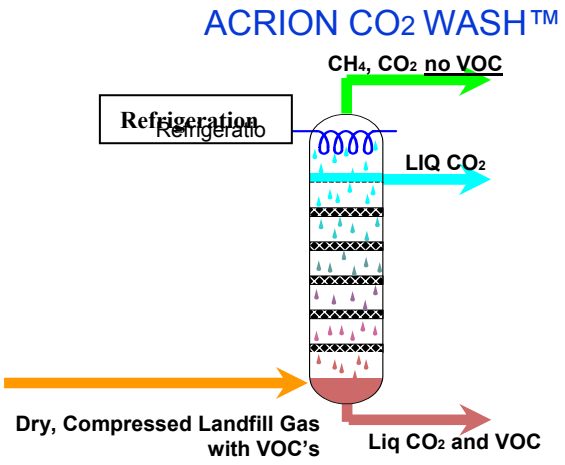

Figure 1. Liquid CO_2 wash technology for the removal of volatile organic contaminants (VOC) from a LFG process stream

Stream/Dry Reforming Natural Gas The two methods of producing syn-gas from natural gas are partial oxidation and reforming. The reforming of natural gas requires higher temperatures than partial oxidation (steam reforming ~ 800°C equation (2) and dry reforming ~ 1200°C Equation (3)). However since landfills have a flaring system to incinerate the VOCs, access to high temperatures is not a major problem. Also it's worth noting that the use of dry reforming reduces the atmospheric venting of CO_2 by incorporating it into the fuel process stream.

$$\mathbf{CH_4 + H_2O \rightarrow CO + 3H_2} \quad [2] \quad \text{steam reforming}$$

$$\mathbf{1/2CO_2 + 1/2CH_4 \rightarrow CO + H_2} \quad [3] \quad \text{dry reforming}$$

The reformer is the major capital cost item in the production of syn-gas. Using the heat from incineration for reforming will require a separate engineering/cost study.

Gas to Liquid Technologies GTL is both a mature and emerging technology. Equations (4-6) represent GTL technologies in its simplest form without the associated catalyst roles and activities.

$$CO + 2H_2 \rightarrow CH_3OH \quad [4] \quad \text{methanol synthesis}$$

$$2CO + 4H_2 \rightarrow (CH_3)_20 + H_2O \quad [5] \quad \text{dimethylether}$$

$$nCO + 2nH_2 \rightarrow -(CH_2)_n- + nH_2O \quad [6] \quad \text{Fischer-Tropsch}$$

Equation (6) assumes the cessation of water-gas shift activity[7], but the hydrocarbon product distribution will still follow the observed Anderson, Schutz and Flory (ASF) distribution.

Proposed Process Flow

The problem at hand is to link the various subsystems into an energy efficient and environmentally sensitive system that will also make a business case to attract investment. There are multiple approaches to solving to this problem. The process flow diagram shown in Figure 2 was selected based on simplicity, waste stabilization and product optimization. No attempt was made to determine a return on investment (ROI) for the proposed process.

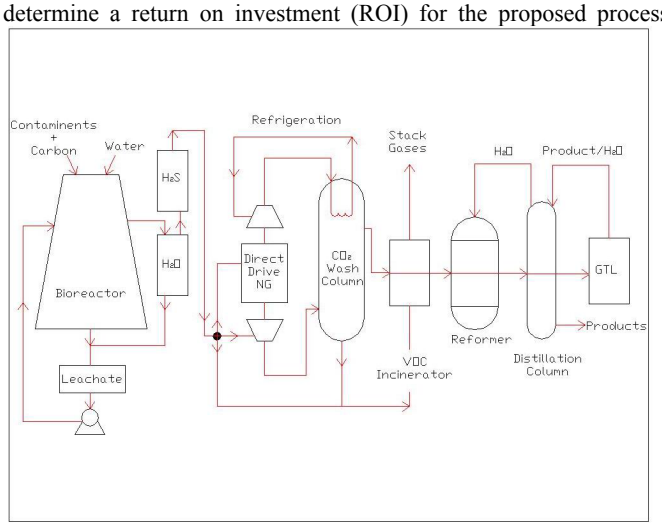

Figure 2. Waste to clean fuel process flow diagram for 5,000-10,000 diesel equivalent gallon per day output.

The clean gas composition from the outlet of the wash column is nominally three parts methane to one part carbon dioxide. The criteria of one part CO with two part H_2 for optimum liquid fuel synthesis, see Equation (6), requires the addition one part water, see Equation (7). This water can be recycled from the distillation column. The remaining water from the distillation column can help meet the water demand of the bioreactor.

$$3/4CH_4 + 1/4CO_2 + 1/2H_2O \rightarrow -CH_2- + H_2O \quad [7]$$

Other features of the proposed design are:

- The use of a direct drive natural gas engine to power the compressors, reducing the electrical load requirements
- The use of the heat from incineration for steam reforming
- The use of the hot syn-gas from the reformer for distillation
- No waste water treatment necessary
- Emissions limited to the effluents of the incinerator

Discussion

Because of the economy of scale GTL projects have been limited to large gas fields. Large projects require large investments. This paper attempted to identify the opportunity of down sizing to the scale of 5,000 to 10,000 gal per day by taking advantage of low cost LFG and associated emission credits. Most the processes discussed in this paper has been greatly simplified. In fact the process calls for inputting only organic waste and water, and then waiting 200 days before producing a reasonable quantity of syn-fuel without any electrical load requirement. The process also minimizes and contains all waste products. The opportunity is here. The challenge is to make a business case with a more thorough engineering/cost study.

Acknowledgment

This work was performed under DOE Contract No. DE-AC02-98CH10886 for the Office of Freedom Car and Vehicle Technology.

References

1. Reinhart, D.R., Townsend, T.G. *Landfill Bioreactor Design and Operation*, Lewis Publishers, Boca Raton, FL. 1998.

2. Komillis, D.P., Ham R.K., Stegmann R., *The Effect of Landfill Design and Operation Practices on Waste Degradation Behavior:A Review,* Waste Management Res., 17, 20-26, 1999.

3. Komillis, D.P., Ham, R.K., Stegmann, R., *The Effect of Municipal Solid Waste Pretreatment on Landfill Behavior: A Literature Review,* Waste Management Res., 17, 10-19, 1999.

4. *The Bioreactor Landfill; Next Generation of Landfill Management*, A White Paper from Waste Management, Inc.

5. Vandor, D., *Liquid Natural Gas (LNG): An Alternative Fuel from Landfill Gas and Wastewater Digester Gas*, Technical Report Brookhaven Nat. Lab., 1999.

6. Acrion Technologies, Inc., Cleveland, Ohio; US Patent 5,681,360 Landfill Gas Recovery, 28 Oct. 1997.

7. Mahajan, D., Koyayaashi, A., Gupta, N., *Fischer-Tropsch Synthesis Catalyzed by Ultrafine Particles of Iron: Cessation of water-Gas Shift Activity*, Chem. Commun., p. 795, 1994.

SELECTIVE CHEMICAL SENSORS FOR COMBUSTION PROCESSES

Arun K Prasad, Hongwen Zhou, Pelagia I Gouma

Dept of Material Science and Engineering
SUNY at Stony Brook
314, Old Engineering Bldg,
Stony Brook, NY 11794-2275

Introduction

Semiconducting metal oxides have been studied as suitable materials for gas sensors for the past few decades because they are easy to fabricate, give fast response to gases and are robust even while operating under harsh environments. There has been various reports on these materials used as thin film gas sensors in automotive exhausts for monitoring the products of combustion processes such as nitrogen dioxide, nitric oxide, carbon monoxide, hydrocarbons etc. Traditionally, gas sensors reported till date, utilize various methods to achieve selectivity such as addition of dopants, varying the processing technique use of mixed metal oxides etc. It is shown that it is possible to achieve the desired sensing properties by altering the polymorphic phase of a single oxide material.

Experimental

Ion Beam Deposition. Thin films of tungsten trioxide were reactively sputter-deposited onto alumina substrates in a dual ion beam deposition system. Ion-beam sputtering from the 6" diameter tungsten target was done using a filamentless radio-frequency inductively coupled plasma (RFICP) primary source, with the film partially oxidized during growth using a RFICP assist source directed at the substrate. The ratio of oxygen to argon in the secondary plasma was maintained at 1:1 and the overall process pressure was 1.6×10^{-4} Torr. A more extensive description of the deposition chamber is given elsewhere [1].

Sol-gel Preparation. Thin films of sol-gel WO_3 was prepared using tungsten isopropoxide obtained from Chemat Technology. The solutions were prepared by mixing it with n-butanol to obtain 0.1M solution. After mixing, the sol was mechanically agitated for 5 min and then ultrasonic agitation was performed for 2 hours. The sol was then allowed to age and settle. A transparent yellow liquid was obtained after 24 hours of aging. The sol was dropped on sensor substrate which consists of alumina substrate with gold interdigitated electrodes (200 μm width and 150 μm separation). The substrate was spun at 2500 rpm for 30 s in a spin coater (Chemat Technology KW-4A). The films were then sintered for 8 hours at 500°C.

Sensor Testing. The sensing tests were carried out inside a tube furnace (Lindberg/Blue), which was heated at a programmed rate. The sensor was placed inside the tube furnace in a quartz tube (1 in. diameter and 24 in. length) and is connected to external leads. The sensing tests were performed at 450°C. The gases used for sensing are nitrogen dioxide and ammonia. The gases were controlled using MKS flow controllers. Synthetic air was used as background gas. Electrical resistance measurements of the sensing films as a function of gas concentration were recorded using Agilent 34401 digital multimeter.

Characterization. TEM investigations were performed using a Philips CM12 transmission electron microscope with LaB_6 cathode and incident energy of electrons of 120keV. XRD was performed on a Philips CM1728 diffractometer, to identify the phases in the sol-gel films during various stages of the study. DSC/TGA studies were carried out using NETSCH Analyzer STA 441C.

Results and Discussion

Figure 1 shows the sensing response of the IBD WO_3 deposited on the sensor substrates. The response shows the shift in resistance of the WO_3 IBD films upon exposure to various concentration pulses from 400 ppm down to 100 ppm of various gases such as ammonia, and nitrogen dioxide. It is seen that the WO_3 films are more sensitive to nitrogen dioxide than ammonia (a 200% increase in case of NO_2 as opposed to less than 5% decrease in case of NH_3). The average grain size found by TEM analysis is around 50 nm. Phase determination by electron and x-ray diffraction studies revealed the presence of orthorhombic phase of β-WO_3 phase.

Figure 2 shows the DSC/DTA data for sol-gel WO_3 films. We observed a peak near 320°C which is probably associated with water removal. XRD investigations showed no peaks associated with WO_3 phases. The next broad peak which was observed at around 500°C is probably associated with the formation of metastable orthorhombic phase of β-WO_3. Heat treatments were done at this temperature for 8 hours with the sol-gel deposited on sensor substrates and sensing tests were carried out. **Figure 3a** shows the response of sol-gel WO_3 film to various concentrations of NO_2 from 100 ppm down to 20 ppm. **Figure 3b** shows the response of sol-gel WO_3 film to various concentrations of NH_3. There is found to be a 25% decrease in resistance with NO_2 as opposed to only less than 0.1% decrease with ammonia. The inverse response with NO_2 as compared with that obtained from IBD films can probably explained due to the change in carrier concentration from n to p type of the semiconducting oxide and is discussed in detail elsewhere[1].

Figure 4 shows the TEM bright field image of sol-gel films after sensing. The grain size as observed is found out to be in the range of 20-30 nm.

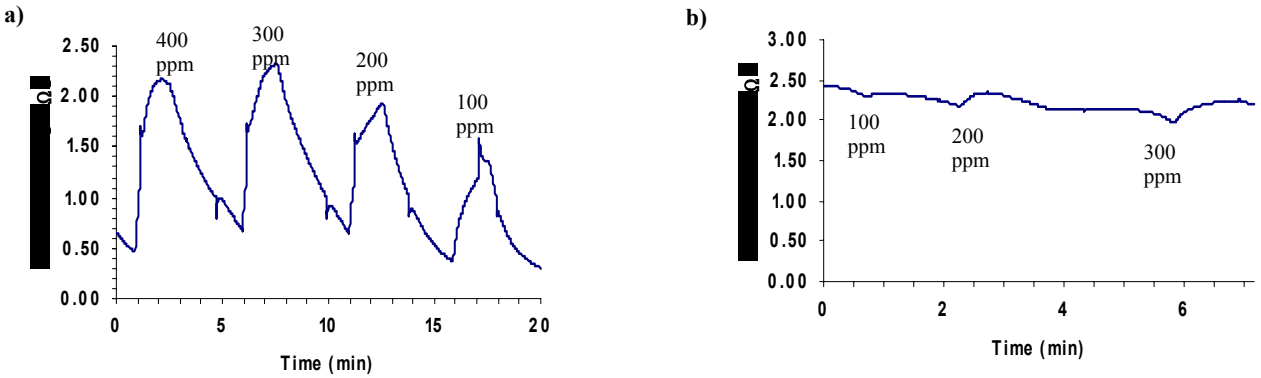

Figure 1. Sensing response of IBD WO_3 to a) NO_2 and b) NH_3

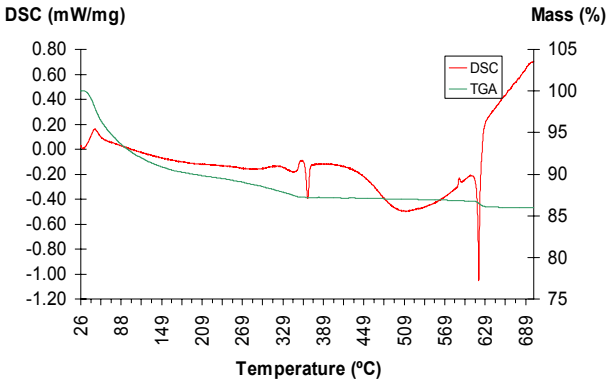

Figure 2. DSC/TGA curve for sol-gel WO_3

3a)

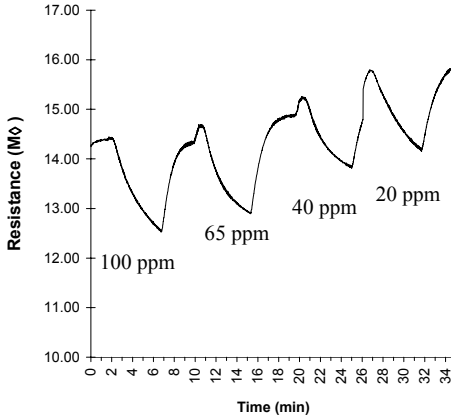

3b)

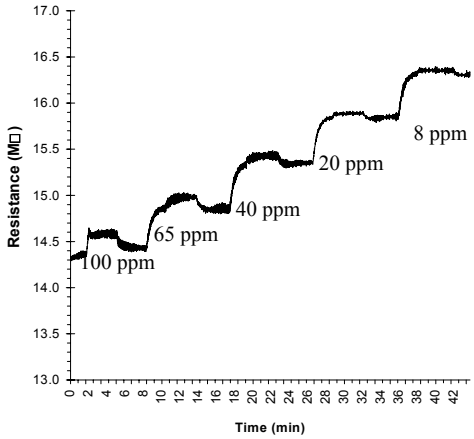

Figure 3
a) Response of sol-gel WO_3 to various concentrations of NO_2
b) Response of sol-gel WO_3 films to various concentrations of NH_3

It is shown that the orthorhombic phase of WO_3 which possesses a distorted ReO_3 structure is selective to NO_2 in comparison to NH_3. In our other work with MoO_3 [2], we have shown that he existence of β-MoO_3 phase (monoclinic) which has a similar structure to that of β-WO_3 (orthorhombic)[3]. Sol-gel technique is better suited to applications in microhotplates because it allows easier method of depositing film on desired areas in the microhotplates.

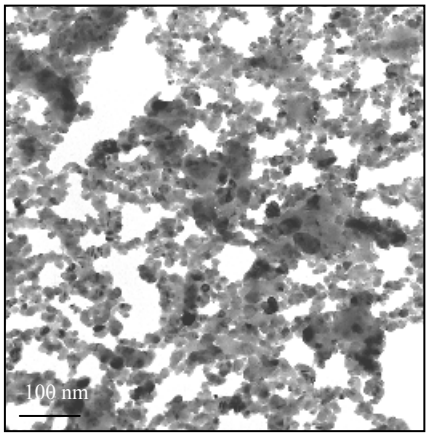

Figure 4. TEM bright field image of sol-gel films after sensing

Current work focuses on processing of thin films made of a single oxide material which show preferential selectivity which depends upon the polymorphs chosen as the sensing element. The hotplates used are fabricated and copyrighted by NIST. Future work will report on these results.

Conclusions

Selective NO_2 sensors were fabricated using IBD films of tungsten trioxide. The films were characterized and the microstructure of the films which are sensitive to NO_2 are identified. Using sol-gel technique, thin films of the same oxide material are fabricated possessing similar microstructure. Sensing tests performed using the sol-gel WO_3 films showed selective response to NO_2 in comparison to ammonia. Incorporation of these sol-gel films on microhotplates is currently under study and will be reported in future work.

Acknowledgement. This work has been partially funded by an ACS-PRF grant. The authors would wish to acknowledge Prof. Richard Gambino for use of IBD facilities.

References

(1) Prasad, A. K.; Kubinski, D.; Gouma, P. I. *Sensor Actuat B-Chem* **In Print**.
(2) Prasad, A. K.; Gouma, P. I. *Journal of Materials Science* **Submitted**.
(3) Mccarron, E. M. *J Chem Soc-Chem Comm* **1986**, *4*, 336-338.

METHANOL SYNTHESIS FROM SYNGAS IN A SLURRY REACTOR

Fei Ren, Hansheng Li, Dezheng Wang and Jinfu Wang
Department of Chemical Engineering, Tsinghua University, Beijing 100084, China
Weixiong Pan and Jinlu Li
Department of Chemistry, Tsinghua University, Beijing 100084, China

Introduction

The synthesis of methanol from CO and H_2 has become more important since methanol is one of the materials that can substitute the forthcoming depletion of petroleum. Industrially, methanol is produced catalytically on copper-containing catalysts such as $Cu/ZnO/Al_2O_3$ and $Cu/ZnO/Cr_2O_3$ from synthesis gas containing carbon monoxide, carbon dioxide and hydrogen in a gas-phase process at high pressures and temperatures. The synthesis gas is usually produced by the steam reforming of natural gas or other hydrocarbons or coals.

In the gas phase process, syngas reacts on the surface of the catalysts in a fixed bed reactor. In this type of reactor, the control of the reaction temperature uses the recycling of excess synthesis gas for the removal of reaction heat. H_2-rich synthesis gas is the preferred media for heat removal because the heat capacity of H_2 is much larger than that of CO. Therefore, the one-pass CO conversion is kept at a relatively low level. The recycling and compression of synthesis gas result in a huge energy consumption [1].

To overcome these disadvantages of the gas phase process, liquid phase processes for methanol production have been developed.[2] A higher one-pass CO conversion is obtained in the liquid phase processes, and these new processes also confer technical advantages when CO-rich synthesis gas is used as the feedstock.

In this work, we report the development of a new catalyst (denoted LP201) which gives a high CO conversion without any decrease in activity in 1000 hour operation in a slurry reactor for the synthesis of methanol. The syntheses of methanol in a slurry reactor and a fixed bed reactor are compared and the deactivation of the catalyst in the gas-phase process is discussed.

Experimental

Catalyst preparation. The catalyst, denoted as LP201, has a molar ratio of copper, zinc, aluminum and zirconium of 5:4:0.8:0.2 and was prepared by a co-precipitation method described elsewhere.

Catalyst characterization. The BET specific area of the catalyst samples were measured in a Micrometrics ASAP 2400 apparatus by nitrogen adsorption. The specific area of the catalyst LP201 is 93 m^2/g. Thermogravimetric analysis was performed on a WCT-2A thermogravimetric apparatus and infrared spectroscopy on a Nicolet FT-IR spectrometer.

Catalyst activity. CO (containing 4.2% CO_2) and H_2 were mixed and fed into a 1000 ml stirred autoclave with a series of controllers which provide precise control and measurement of temperature (± 1 K), agitator speed and pressure (Autoclave Engineers, USA). After reaction, the mixture is processed by a high-pressure gas-liquid separator. The gas phase flows out through a back-pressure regulator and is analyzed on-line by gas chromatography. The flow rate is measured with a wet flow meter. The liquid phase flows through a needle valve and enters a normal-pressure gas-liquid separator. The liquid product (methanol) is weighed and its composition is analyzed by gas chromatography. The solvent is liquid paraffin, whose distillation cut-off temperature is higher than 573 K. The catalysts are LP201 or C302 (manufactured in China) used with particle sizes of 150-180 mesh. Before use for methanol synthesis, they were reduced in H_2/N_2 (3.4%H_2) at 240℃ and 0.8 MPa.

Results and Discussion

The activities of the LP201 and commercial C302 catalysts in a mechanical agitated slurry reactor are compared. The result is shown in Figure 1. It can be seen that the activity of the LP201 catalyst is much higher than that of the commercial C302 catalyst. When LP201 is used, its syngas conversion at the lower pressure of 4 MPa is higher than that of C302 at 6 MPa. This indicates that the LP201 catalyst is suitable for the large scale synthesis of methanol in a slurry reactor.

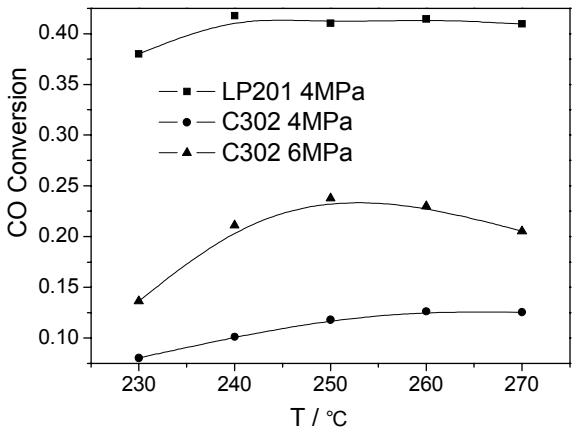

Figure 1. Comparison of the activities of LP201 and C302 at a space velocity of 3000 $ml.gcat^{-1}.hr^{-1}$ and $H_2/(CO+CO_2)$ of 2

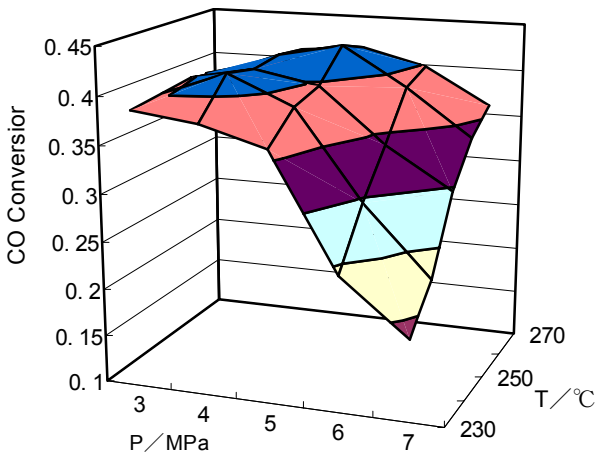

Figure 2. Influence of temperature and pressure on CO conversion at a space velocity of 3000 $ml.gcat^{-1}.hr^{-1}$ and $H_2/(CO+CO_2)$ of 2

Figure 2 shows the influence of temperature and pressure on CO conversion in a slurry reactor. There exist different phenomena at high and low pressure conditions. When the pressure is relatively low, with an increase in temperature, the change in CO conversion is not monotonic, and the trend is that of an increase followed by a decrease, with the maximum conversion appearing near 250 ℃. This

phenomenon is in agreement with many works in the literature[3, 4] and our previous works.[5] As the reaction temperature increases, the reaction rate gets higher and leads to the increase of CO conversion. However, methanol synthesis is an exothermic reaction, and a low temperature is more beneficial for methanol synthesis. With continual increase in the reaction temperature, the conversion does not continue to increase because of thermodynamic limitation, but a decreasing trend will even appear. When the system pressure is relative high, because of the relatively low CO conversion, the system is far from thermodynamic equilibrium and under the control of reaction kinetics. In this case, CO conversion increases monotonically with an increase in temperature.

In the whole temperature range studied, with an increase in pressure, CO conversion first increases and the decreases. Methanol synthesis is a volume-decreasing reaction, and a high pressure benefits methanol generation, but when the pressure increases beyond a certain pressure, methanol accumulates in the liquid phase, which leads to a check on methanol synthesis and the CO conversion decreases.

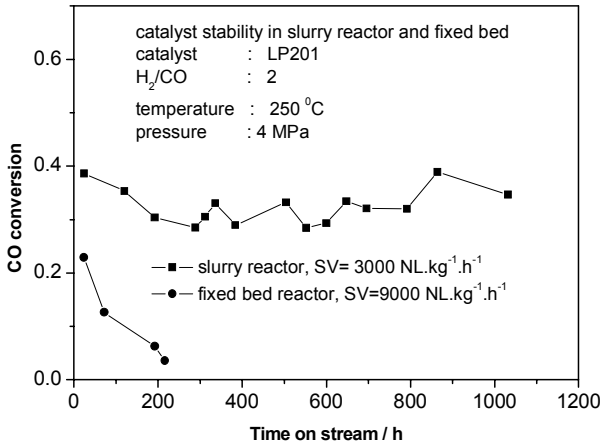

Figure 3. Stability of LP201 catalyst in a slurry reactor and a fixed bed reactor.

LP201 has a higher catalytic activity and good stability in a slurry reactor, as shown in Figure 3. The one-pass CO conversion is still higher than 30% after a 1000-hour lifetime experiment. However, in a fixed bed reactor, the catalyst activity shows an obvious decreasing trend at a space velocity of 9000 $L.kg^{-1}.h^{-1}$. This phenomenon shows the advantage of a slurry reactor compared with a fixed bed, and the liquid phase methanol synthesis is more suitable for the large-scale industrial application.

To understand the deactivation of catalyst LP201 in the fixed bed, thermogravimetric analysis (TGA) and infrared spectroscopy studies were carried out. Figure 4 shows the results of TGA. The TG curve shows three regions of weight loss: 20~110, 110~300 and 600~800℃, which are attributed to water loss and carbon combustion of the deactivated catalyst, respectively. Meanwhile, an endothermal peak around 80℃, and two exothermal peaks around 300 and 700℃ appear in differential thermal analysis (DTA) that are related to the thermo-gravity losses. These indicate the existence of carbon on the deactivated sample and the two exothermal peaks around 300 and 700℃ in DTA represent different types of carbon[6]. Figure 5 shows the FT-IR spectra of LP201 catalyst before reduction (A), after reduction (B), after deactivation (C) and the sample after TGA of the deactivated catalyst (D). The surface structure of the deactivated catalyst is very different from the LP201 catalyst after reduction and before methanol synthesis and the change in the structure of the deactivated catalyst is irreversible. This suggests that an irreversible change in the structure of catalyst and carbon deposition during the gas-phase methanol synthesis led to the deactivation of the catalyst.

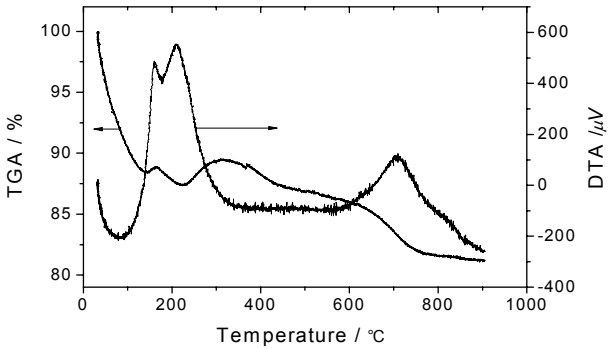

Figure 4. TGA and DTA of deactivated LP201 catalyst

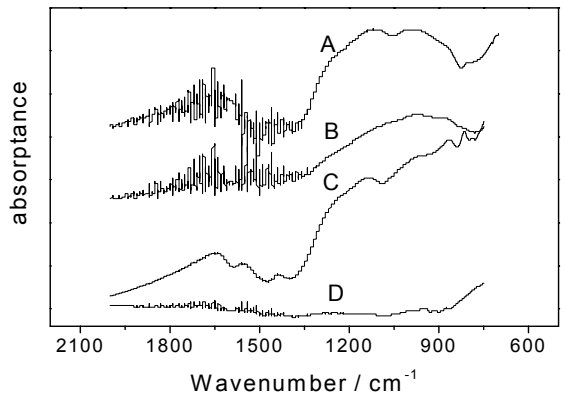

Figure 5. Infrared spectra of LP201 catalyst
A-before reduction, B-after reduction, C-after deactivation, D-the sample after TGA of the deactivated catalyst

References

(1) Zhang Kai, Song Huisen, Sun Dongkai, Li Shunfen, Yang Xiangui, Zhao Yulong, Huang Zhe, Wu Yutang. Fuel, **2003**, 82(2): 233-239.

(2) H. Mabuse, K. Hagihara, T. Watanabe, M. Saito. Energy Conversion and Management **1997**, V38, pp. S437-S442.

(3) Inui T., Li J.-L. Applied Catalysis A. **1996**, 139(1-2): 87-96.

(4) Liaw B.J., Chen Y.Z. Applied Catalysis A. **2001**, 206(2): 245-256.

(5) Yuwei Wang, Zhiliang Wang, Jinfu Wang, Yong Jin, Petrochemical Technology. **2002** 31(8): 597-601.

(6) Liu H M, Li T, Xu Y D. Chem. J. Chin. Univ., 2002, 23(8): 1556-1561.

BIOCHEMICAL ENHANCEMENT OF COALBED METHANE (CBM) RECOVERY AND ITS POTENTIAL FOR TREATMENT OF PRODUCED WATER

Mow S. Lin and Eugene T. Premuzic

Energy Sciences & Technology Department
Brookhaven National Laboratory
Building 815
Upton, NY 11973-5000

Introduction

Exploration and production of coal bed methane (CBM) resources has been increasing rapidly in recent years. In the United States, the CBM resource is estimated to be between 275 to 649 trillion cubic feet (TCF). The current production amounts to 7.5 percent of the total natural gas production in the US.[1] Along with CBM, water is co-produced during the process and compared to conventional natural gas wells, the amount of produced water is significantly higher. With increasing CBM production, the produced water is expected to increase accordingly. Currently, the water produced is either disposed or reused. If this water, after treatment, meets the requirements of several State and Federal regulations such as Clean Water Act, Resource Conservation and Recovery Act and Drinking Water Act, it may be added to the local water supply. Some source dependent produced water may contain salts, dissolved organic compounds and metals including radioactive elements, which require expensive treatment, before it is disposed to surface or compatible subsurface formations. In contrast to the oil industry, the water is not reinjected into the reservoir to enhance recovery as practiced in many oil fields. In this study, the feasibility of biochemically-enhanced recovery of CBM will be discussed.

Experimental

Bioabsorption of dissolved metals. All microorganisms were purchased from ATCC and grown to maximum growth according to published procedures.[2] The cells were harvested by centrifugation and washed with isotonic water, then stored at 4 ^{o}C. The samples were resuspended in synthesized salts solution and allowed to equilibrate at 25 ^{o}C for 30 minutes. The concentrations of metals in the samples were analyzed by atomic absorption spectroscopy (Perkin-Elmer model 560) calibrated according to the manufacture's manual.

Degradation of dissolved organics. Heavy crude oil was added to a mineral medium of 2 g NH_4Cl and 5.57g Na_2HPO_4, 2.44g KH_2PO_4, 0.2g $MgCl_2$, 0.001g $CaCl_2{\bullet}H_2O$ and 0.001g $FeCl_3{\bullet}H_2O$ per liter up to a saturation of 25 ^{o}C. 5% (v/v) of fully-grown *Acinetobacter sp* ATCC 31012 was added to the sample and incubated at 30 ^{o}C aerobically. The reaction was monitored by UV-VIS spectrophotometer at 260 nm.

Biochemical conversion of coals. Coals were ground by mortar and pestle into a powder under 80 mesh and stored in a desiccator. A dried sample was suspended as 2 % (w/v) of powder in the above described mineral medium in an Erlenmeyer flask. The sample was inoculated with 5% of *Acinetobacter* culture (10^8/ml) and incubated aerobically on a rotary shaker at 30^{o}C for 7 days. A control sample without inoculation was prepared and treated under the same conditions. After treatment the samples were filtered and dried in a desiccator for analysis.

Pyrolysis-gas chromatography-mass spectrometry analysis. A CDC 150 pyroprobe was fitted with the inlet of a Perkins Elmer gas chromatograph with a 30m DB1 capillary column (J&W Co). The sample was heated from 30^{o}C at a rate of 20 ^{o}C /m sec to 800 ^{o}C and held for 10 sec. The pyrolysate was analyzed with a temperature program set at 50 ^{o}C initially for 4 minutes, then ramped at a rate of 8 ^{o}C/min to 320 ^{o}C and held for 20 min. The effluent was split and analyzed by a Pulse flame photometric detector (PFPD) for sulfur and by an ion trap detector (ITD) for simultaneous mass spectrometric analysis. PFPD measures the sulfur emissions, was used to selectively analyze the fragments containing sulfur.

Results and Discussion

Dissolved metals are known to accumulate in either cellular organelles or on cell surfaces and membranes.[2,3] The former process is associated with cellular functions and cell growth. The latter process is due to interaction with functional groups i.e. carboxylate hydroxyl, and amino groups which are integral parts of the cell surface. These groups form strong and specific chelating complexes that can be released by changing pH. In principle the cells can be used to adsorb and release the metals in cycles. The cells can be immobilized and engineered in a column or bed to facilitate filtration processes.

Data shown in **Table 1** indicates that different microorganisms can adsorb substantial amounts of metals both metal selectively and species specifically. [2]

Table 1. **Selective adsorption of metals by different microorganisms as measured by grams of metal adsorbed/dry weight (g) of microorganisms.**

Microorganism	Pb	U	Th	Cr	Mn	Sn
E. coli	0.32	0.05	0.03	0.36	0.001	0.11
S. cerevisiae	0.16	0.02	0.04	0.04	0.001	0.09
P. aeruginosa sp	0.08	0.14	0.90	0.008	0	0.1
P. fluorescens	0.08	0.02	0.56	0.1	0.05	0.02

Data shown in **Figure 1** indicate that there is a maximum adsorption of lead, U/Th decay product by *E. coli* near pH 6 and little adsorption outside the pH 3.5 to 9.5 ranges. Therefore, the bioadsorbent can be used to adsorb metals at pH 6 and release it outside the pH range for example.

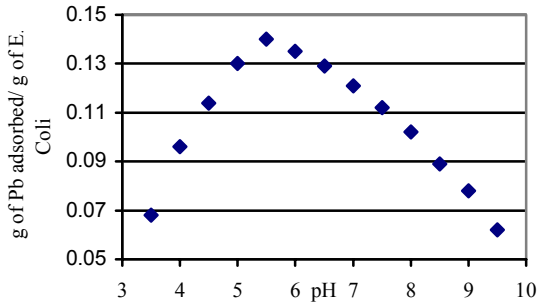

Figure 1. Effect of pH on the adsorption of lead

The chemical structure representing heavy crude oils rich in asphaltenes, resemble to a certain extent, the chemical structures of coal. Many studies of the biodegradation of petroleum oils have been reported. [4] For example as shown in **Figure 2** a fast biodegradation of a heavy crude oil occurs over a period of 16 days. The oil concentration was reduced by 70%. Under aerobic condition, the products were identified to be small acids and alcohols i.e. acetic and ethanol.[5]

Coal is a complex mixture of macromolecular hydrocarbons cross-linked by nitrogen, sulfur and oxygen (NSO) bridges as well as metals within organometallic complexes. To analyze such complex

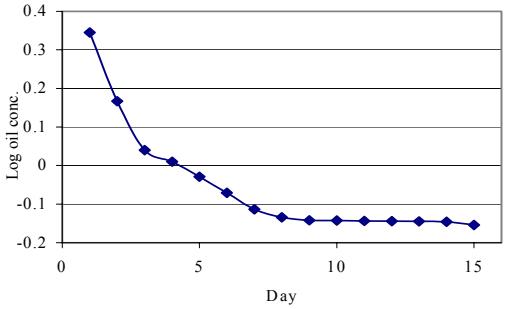

Figure 2. Biodegradation of heavy crude oil in water at 30 ^{o}C,Y axis is log oil concentration in 30 mg/liter

metrics several multipurpose analytical technique must be used.[6] In this work GC-MS, Py-GC-MS interfaced with PFPD has been used throughout (see Experimental Section) under identical conditions for untreated and biotreated samples. For example, in **Figure 3**, the result of a Py-GC analysis using the sulfur specific detector (PFPD) shows significant changes in the organosulfur components of the untreated and treated coal samples. In the treated sample, smaller molecular weight sulfur compounds appear in the retention time region of 3-7 min., accompanied with reduction of substituted thiophenes in the 6-11 min. region, dibenzothiophenes in the 10-25 min. and larger organosulfur compounds in the 30-60 min. region. The results suggest that the coal matrix structures was broken at the cross-linking bridges yielding smaller molecular weight fractions.

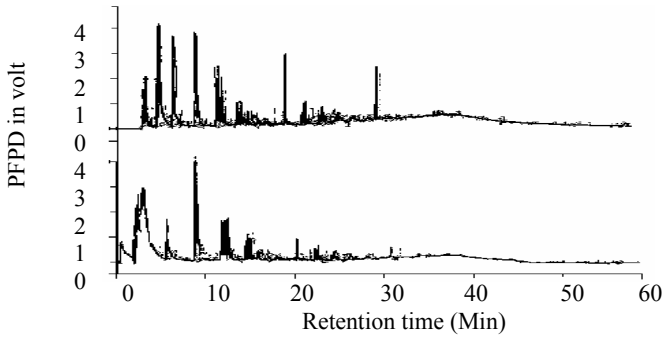

Figure 3. Py-GC-PFPD selective analysis of sulfur compounds of untreated Wyodak coal (top) and aerobically biotreated coal (bottom) samples.

Shown in **Figure 4,** the Py-GC-MS analysis of untreated coal pyrolysate with standards identify hydrocarbon compounds from retention time 5-10 min. as C_6-C_{12} fraction, 10-25 min. as C_{12}-C_{18} diesel fraction, 25-40 min. as C_{18}-C_{32} fractions and 40-60 min. as C_{32}-C_{50} fractions correspondingly. Under identical analytical conditions, the treated sample shows 40% more of C_{10}-C_{16} fractions and 20% more of C_{28}-C_{82} fractions, which further supports the observation shown in **Figure 3**.

Anaerobic transformation of coal has been reported as a potential source of methane from coal [7]. Biochemical reactions enrich the lighter carbon isotope in the product. It is recognized that the isotope effects measured as $\delta^{13}C$ of thermogenic CH_4 and biogenic CH_4 are in the range from –50 to -20 ‰ and –110 to -50 ‰ respectively.[8] Isotopic studies of $\delta^{13}C$ from gases produced from two wells in Alberta, Canada measured ranging from –56.4 to –48.4. The results of these gases, rich in lighter carbon (^{12}C) indicate that they are biogenic in origin. Attempts to incubate the microbes from cores isolated from these wells were not successful. However, laboratory studies were able to produce significant amounts of biogenic methane using coal as the only substrate. [9]

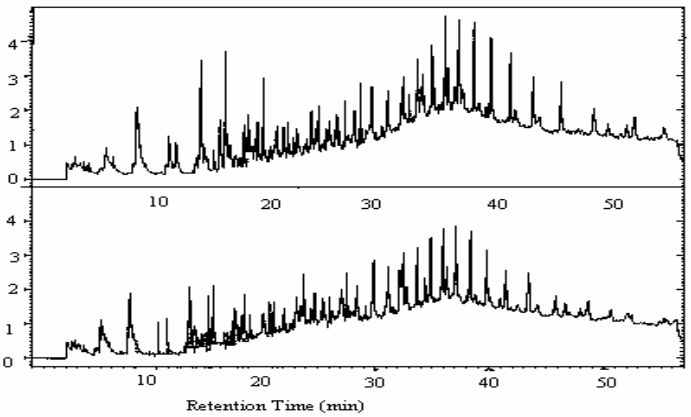

Figure 4. The Py-GC-MS analysis of hydrocarbons of treated Wyodak coal (top) and untreated sample (bottom). Y axis is detector response of unit in Mega counts.

Conclusion

The data presented in this paper indicate that coal under certain conditions can be biodegraded and the initial and produced material can be analyzed for. This implies that the biodegradation of coals under aerobic and anaerobic condition can be monitored, which is essential to the development of a processing technology. Currently, the assumption that the produced waters may also be biotreated in a manner similar to processing of coal by either biosorption and/or further biotreatment in an attractive possibility and is being further explored.

Acknowledgment. This work bas been supported in part by the U.S. Department of Energy, under Contract No. DE-ACO2-98CH10886; and by the Office of Sciences, U.S. Department of Energy, under CCI program. We also wish to express gratitude to Mr. Frank Clementi for technical support.

References

1. USGS Fact Sheet FS-156-00, November **2000**.
2. Premuzic, E. T., Lin, M., Zhu, H. L., and Gremme, A. M., *ArchEnviron. Contam. Toxicon.*,**1991**, 20, 234-240.
3. Beveridge, T. J.; Koval, S. F., *Appl. Environ Microbiol* **1981**, 42(2): 325-335.
4. Altas, R. M. Bartha, R.,*biotechnol Bioeng,* **1972,** 14, pp. 309-317.
5. Premuzic, E. T., Lin, M. S., *Resources, Conservation and Recycling*, **1991**, 5, pp. 277-284
6. Lin, M. S., Premuzic, E. T., Manowitz, B., Jeon, Y., and Racaniello, L., *Fuel,* **1993,** 72, No. 12, pp. 1667-1672
7. Deobald, L. A.,**1993** in: *Microbial transformation of low rank coals,* pp/ 111-138, Crawford, D. L. (Ed). CRC press, Inc. Boca Raton, FL.
8. Whiticar, M.J. **1999**, *Chem. Geology*, 161, 291.
9. Budwill, K., 4th Annual unconventional Gas and Coalbed Methane Conference, **2002**, Oct. 24, Alberta Research Council

REDUCTIVE DECHLORINATION OF CHLORINATED SOLVENTS IN GROUNDWATER : A CASE STUDY

Eric Rodriguez[1], Kevin A. McGuinness[1], and Duke U. Ophori[2]

[1]ARCADIS G&M
1200 MacArthur Blvd
Mahwah, NJ

[2]Department of Earth and Environ. Studies
Montclair State University
Upper Montclair, NJ 07043

Introduction

In groundwater contaminated by chlorinated aliphatics, remediation by reductive dechlorination is a well-documented process that occurs given the appropriate groundwater environment[1,2]. The first microbiologically mediated reductive dechlorination of perchloroethene (PCE) and trichloroethene (TCE) was observed in the early 1980s, and the first evidence of complete dechlorination of PCE to ethane under methanogenic conditions was reported in 1989[3]. According to Sutherson[3], even where a strongly reducing natural groundwater environment is not present, complete and effective reductive dechlorination of chlorinated volatile organic compounds (CVOCs) can still be accomplished by artificially driving an aquifer to a strongly reduced state that is maintained throughout the remedial process. The injection of a reagent solution (electron donor) to serve as a carbohydrate substrate can enhance microbial activity (biostimulation) by providing a carbon source[3].

In this study, an experiment was conducted, in which a carbohydrate solution (molasses) was injected into groundwater wells at a site impacted with CVOCs, in an attempt to create strongly anaerobic and reducing conditions that might cause Enhanced Reductive Dechlorination (ERD). A post-experiment evaluation of the site was performed to ascertain: 1) if a strongly anaerobic and reducing zone was created successfully, and 2) if reductive dechlorination was enhanced.

Site Description

The site occupies approximately 1.8 acres of land in the metropolitan New York. Locally, the site is underlain by fill material consisting of sand, silt, gravel, bricks, marble fragments, and boulders. Regionally, the bedrock is composed of the Manhattan Formation Schist, Inwood Marble, and Fordham Gneiss.

Manufacturing operations at the site were initiated in 1951 and ceased in 1998. Operations consisted of electroplating and the use of degreasers, which are believed to be the source of a CVOC plume, mainly TCE, at the site. An initial review of available site-specific data showed that high concentrations of TCE were present in the upper 10 feet of the aquifer, and that reductive dechlorination was already occurring at the site but because of only aerobic to slightly anaerobic conditions, complete dechlorination was not occurring.

Pre-Experiment Evaluation

The focus of this study was to create conditions that would enhance or drive reductive dechlorination to completion at the site. Prior to creating such anaerobic conditions, it was necessary to assess the existing natural background conditions of groundwater at the site. The conditions would assist in the creation and implementation of an In-situ Reactive Zone (IRZ), defined as an area in a groundwater system where strongly reducing and anaerobic conditions have been created for the purpose of reducing chlorinated compounds in groundwater. These data would also serve as the background with which post-experiment results could be compared. The background evaluation was performed to identify key electron acceptors and donors available, and to establish existing oxidation-reduction potential (REDOX) conditions. These data were obtained by collecting and analyzing groundwater samples from wells, and by collecting wellhead field parameters during low-flow well purging[4].

Groundwater levels in wells were measured to characterize the groundwater flow field. Results of these measurements indicate that groundwater flows to the south and southwest at the site.

Groundwater sampling was performed using the low-flow methodology[4]. Wells were purged using a Grundfos Rediflow 2 submersible pump at a purge rate between 0.2 and 0.5 liters/min. Trichloroethene (TCE) was found to be the diagnostic constituent of concern at the site. The highest concentrations of total CVOCs in groundwater were detected in the upper unconsolidated unit between the depth range of 10 to 20 feet. Concentrations of TCE ranged from not detected to 28,000 ppb.

Field parameters were collected during low flow purging using a flow-through-cell. A YSI 600XL water meter was used to measure water-quality and field parameters such as DO, REDOX, temperature, specific conductance, pH, total organic carbon (TOC) and dissolved organic carbon (DOC). Samples were submitted to a certified laboratory for analysis, except for ferrous iron and sulfide that were analyzed directly in the field using a HACH spectrophotometer.

The field parameters and biogeochemical analysis were used to determine the DO and REDOX conditions of the site, and to evaluate the presence of electron acceptors and donors. Dissolved oxygen is the most thermodynamically favored acceptor used by microbes for the biodegradation of organic carbon. After depletion of DO, microbes will preferentially use nitrate as an electron acceptor, followed by iron (III), sulfate (sulfanogenesis), and carbon dioxide (methanogenesis) in that order[1].

During the pre-experiment assessment, one up-gradient well (MW-HP-8S), three side-gradient wells (GP-106, MW-2, MW-4S), seven mid-plume wells (GP-107, PTW-1, GP-105, MW-HP-1S, MW-HP-1D, GP-104), and three distal-plume wells (GP-103, MW-7S, GP-102S), were sampled as in literature[1].

A summary of relevant field and analytical data from this assessment showed DO and REDOX values which indicated aerobic and oxidizing groundwater conditions in the up-gradient well, transitional to aerobic conditions in the side-gradient and mid-plume wells, and anaerobic to aerobic conditions in the distal-plume wells. Sufficient concentrations of electron acceptors such as nitrate, manganese, Fe(III), sulfate and carbon dioxide were available for microbial respiration, once oxygen was depleted, to support reductive pathways.

Experiment

A 20-month in-situ bioremediation experiment was conducted by injecting a carbohydrate substrate (molasses) into the groundwater to increase microbial activity and thus to deplete the electron acceptors. The goal was to create an IRZ that would possibly enhance reductive dechlorination of CVOCs in groundwater at the site. Monitoring well GP-107 was selected as the substrate injection point because it is located in the center of the TCE plume area, that has historically shown elevated concentrations of TCE. The substrate injections were performed on a biweekly schedule to create and maintain the IRZ. Fifty substrate injection events were performed between September 2000 and August 2002.

The concentration of substrate used for the first three injections into well GP-107 had a water to molasses ratio of 20:1, with a volume of approximately 100 gallons. Substrate

injections were performed using a centrifugal pump. The water and molasses were mixed using the pump and stirring rod in 55-gallon drums. Following a thorough mixing of the solution, it was injected under low pressure (approximately 2 to 12 psi) into the injection point.

Results from the pre-experiment analyses were continuously reviewed throughout the experiment to adjust the reagent strength and volume to ensure that the injections would not initiate excessive fermentation processes that can lower the pH.

To track the establishment, growth and progress of the IRZ, performance monitoring of select wells (PTW-1, PTW-2, GP-104, MW-HP-1S) immediately down-gradient and side-gradient of well GP-107 was conducted on a biweekly schedule. This allowed parameters such as DO, REDOX potential, specific conductivity, TOC and DOC to be monitored. These wells which are within and immediately surrounding the IRZ were sampled and analyzed for a targeted list of specific electron acceptors and byproducts to document that anaerobic microorganisms were depleting the acceptors, and that reduced byproducts (i.e., sulfide, ferrous iron, dissolved iron, methane) were present and accumulating. Daughter products of TCE such as cis-1,2 DCE, vinyl chloride, and ethane were also analyzed to track the anticipated increase of these compounds. This synergy of data collected is sufficient to document the occurrence of reductive dechlorination and its level of occurrence.

Results and Discussion

In-Situ Reactive Zone (IRZ). Reducing conditions were established at the injection point GP-107 two weeks after the first substrate injection was performed. The minimum target TOC concentration of 1,000 mg/L was reached approximately 1.5 months after the first injection. It was observed that the created IRZ encompassed an area down-gradient of GP-107 that included wells PTW-1, PTW-2, and MW-HP-1S, after 1.5, 5, and 10 months of the first injection respectively. Encompassment of the IRZ is characterized by increases in TOC and conductivity, and by decreases in DO and REDOX potential (Fig. 1).

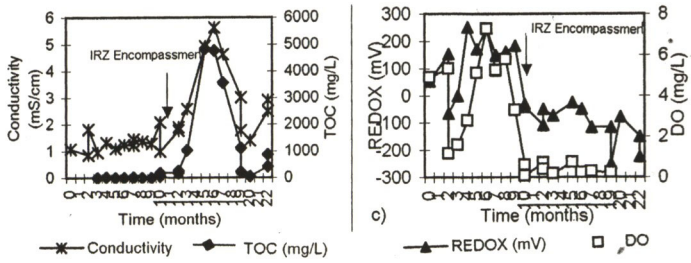

Figure 1. Example patterns of TOC, conductivity, DO and REDOX from well MW-HP-1S.

Enhanced Reductive Dechlorination (ERD). Results of the experiment provided evidence that ERD was occurring at the site due to the alteration of the groundwater environment. Factors for evaluating the occurrence of ERD include depletion of electron acceptors and increase in their byproducts as illustrated by biogeoch-
emical monitoring results, a decrease in parent (source) TCE concentrations, and the accompanying increase in daughter products. Analytical results indicated that concentrations of TCE decreased in wells PTW-1, PTW-2, MW-HP-1S, and GP-104 while daughter products, primarily cis-1,2 DCE, vinyl chloride, and ethene increased in concentration. Based on the field data and TOC results summarized in the preceding section, the IRZ has encompassed monitoring points PTW-1, PTW-2, and MW-HP-1S, and is believed to be the catalyst for the ERD of TCE. The monitoring results from the three wells encompassed by the IRZ were similar, thus only those from PTW-2 are summarized here. Monitoring well PTW-2 is located approximately 30 feet down gradient of injection well GP-107. Concentrations of TCE detected in well PTW-2 showed a significant decrease from 8,400 ug/L (pre-experiment) to 400 ug/L (post-experiment) (Fig. 2). In May and June 2001, concentrations of TCE

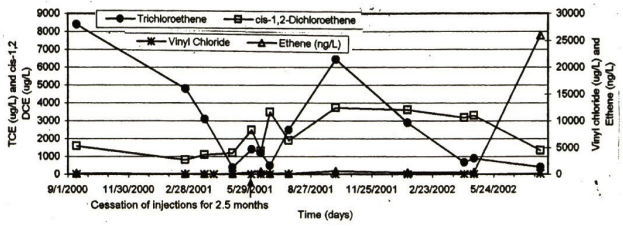

Figure 2. Distribution of TCE, DCE, Ethene and Vinyl Chloride from well PTW-2

had decreased to 380 and 480 ug/L respectively and subsequently increased to 2,500 ug/L (July 2001) and then to 6440 ug/L (October 2001). Note that the experiment was conducted in the mid-plume area, therefore a mass of TCE continues to flow into the study area, which may be responsible for the TCE concentration rebound. Additionally, a temporary cessation of injections was done to quantify how long the organic carbon in the up gradient injection well (GP-107) would remain during injection #20, which may be partially responsible for the rebound. However, following re-initiation of injections, concentrations of TCE again decreased significantly.

With the decrease of TCE, concentrations of cis-1,2-DCE increased from 1,600 (pre-experiment) to 3730 ug/L (October 2001) providing evidence of ERD of TCE and not TCE dilution processes. Following October 2001, cis-1,2 DCE decreased to 1340 ug/L at the conclusion of the pilot test demonstrating that continued and complete reductive dechlorination is occurring. This process is further supported by the detection of vinyl chloride (118 ug/L) during the last groundwater sampling event. Concentrations of ethene have also illustrated a significant increasing trend from 209 ng/L (pre-experiment) to 26,000 ng/L (post-experiment) demonstrating that the mass of TCE in groundwater has been reduced and that the final degradation product (ethene) has been achieved. The complete degradation sequence (TCE to ethene) for dechlorination of TCE has been observed.

There was more evidence from the analysis of field data and biogeochemical indicators that supported the occurrence of anaerobic and reducing conditions, as well as ERD at the site. These include: low dissolved oxygen (< 1 mg/L) and REDOX (< 0 mV) concentrations, reduced nitrate and sulfate, and increased nitrite and sulfide concentrations. Methane concentrations increased continually, suggesting that the environment could have approached and achieved methanogenic conditions.

References

1. Wiedemeier, T.H., Swanson, M.A., Moutoux, D.E., Gordon, E.K., Wilson, J.T., Wilson, B.H., Kampbell, D.H., Hansen, J.E., Haas, P., Chapelle, F.H., *Technical protocol for evaluating natural attenuation of chlorinated solvents in groundwater;* Air Force Center for Env. Excel. Tech. Transfer Div., **1996**.
2. Carr, C.S., Hughes, J.B., *Env. Sci. Tech*., **1998**, 32, 1817-1824.
3. Sutherson, S.S., *Natural and enhanced remediation systems*, CRC Press, Inc., Boca Raton, Florida, **2002**.
4. U.S. EPA., *Groundwater sampling standard operating Procedures*, U.S. EPA., Region II, New York, **1998**.

EFFECT OF THE ADDITION OF Fe AND Mn ON STRUCTURAL AND CATALYTIC PROPERTIES OF Cu/ZrO_2 CATALYSTS FOR CO HYDROGENATION

*Run Xu, Zhongyi Ma, Cheng Yang, Wei Wei, Yuhan Sun**

The State Key Laboratory of Conversion
Institute of Coal Chemistry
Chinese Academy of Science
Taiyuan 030001 P.R.China
*Corresponding author. Fax: +86-351-4041153. E-mail address:
yhsun@sxicc.ac.cn, yangch68@sxicc.ac.cn

Introduction

Since the last century's oils crises, higher alcohol synthesis from natural gas via syngas has received increasing attention because it can be used as gasoline blend or alternative motor fuel [1]. The preparation of more effective catalysts is still a subject for practical purposes. The catalysts most frequently used contain copper as active component, zinc oxide and alumiana or chromium oxide as a structural promoter. Several metal oxides have been tested as alternative support materials for CO/CO_2 hydrogenation catalysts. Among them, ZrO_2 is of special interest because of its mechanical and thermal stability, its high specific surface area and its intrinsic catalytic properties. In the previous work, Fischer-Tropsch elements (Fe, Co, Ni, Ru) were introduced to Cu/ZrO_2 based system, which successfully shifted methanol synthesis towards higher alcohols [2]. More recently, a $FeCu/MnZrO_2$ bimetallic system was designed and the interaction of molecule in the catalyst for higher alcohols synthesis was studied [3]. The interactions that occur between the active phases or metal-support generally affected the surface and structure of the catalyst and hence its catalytic performance. However, regarding the interplay of $FeCu/MnZrO_2$ catalysts, very few data was available contrasted with Cu/ZrO_2. The aim of the present work was to study the effect of group I and groupΓ metal oxides, i.e. through iron or manganese derivates, addition to a $CuZrO_2$ catalyst.

Experimental

Catalysts preparation. Catalyst were prepared by co-precipitation from a solution of $Cu(NO_3)_2{\cdot}3H_2O$, $ZrOCl_2{\cdot}8H_2O$ and/or $Mn(NO_3)_2$, $Fe(NO_3)_3{\cdot}9H_2O$ with a solution of Na_2CO_3 under electromagnetic stirring at 343K and pH=10. Then the precipitates were aged at 343K for 2h. After washed thoroughly with distilled water, the precipitates were dried and calcined. The prepared catalyst composition was as follows: Cu:Mn:Zr:Fe = 1:0.5:2:0.1(mole ratio).

Characterization Methods. The BET surface areas of catalysts were determined by N_2 adsorption at 77K using the Tristar 3000 Chemical Adsorption Instrument (Micromeritics). The temperature programmed reduction (TPR) of catalysts was carried out in the flowing of 5% H_2 in Ar. The catalysts were heated at the rate of 10K min^{-1} and the amounts of H_2 consumption were determined by a gas chromatograph with a TCD detector. The diffuse reflectance FTIR (DRIFT) spectra were recorded with a resolution of $8cm^{-1}$ and accumulation of 400 on a Nicolet Magna-II 550 FTIR spectrometer supplied with a TGS detector and a diffuse reflectance attachment. The CO temperature programmed desorption (TPD) of catalysts was carried out in the flowing of Ar. The catalysts were heated at the rate of 10K min^{-1} and the analysis of the gas was determined by mass spectrometer. The copper surface area (S_{Cu}) was determined by applying a nitrous oxide pulse method as described by Evans et al. [4]. The exit gas was analyzed by mass spectrometer. The amount of surface copper was calculated from the amount of nitrogen evolved, assuming the dissociation of nitrous oxide takes place on surface copper (average atom density : $1.49 \cdot 10^{19}$atoms/m^2) :

Catalytic test. The activity tests were conducted with a fixed-bed, stainless flow micro reactor with I.D. of 6 mm. All catalysts were reduced before syngas exposure. The analysis of the gaseous and liquid products was made by shimazu-8A gas chromatographs. CO, CO_2, CH_4 and H_2 were analyzed by a thermal conductivity detector (TCD) on a carbon seize column. C1-C5 hydrocarbons and the alcohols were analyzed by a flame ionization detector (FID) on a Chromosorb 101 column.

Results and Discussion

Cu/ZrO_2 has been reported to show high activity and high selectivity for methanol synthesis under mild reaction conditions [5]. As Stiles [6] proposed, the modifications would be made in the catalyst composition and operating conditions to increase the production of higher alcohols. Indeed, the catalytic activity and selectivity over Cu/ZrO_2 was not high at relatively high temperature (see **Table 1**). This might due to the sinter of Cu on the surface [7]. The addition of iron greatly influenced on the performance of the Cu/ZrO_2 catalyst. The catalytic activity decreased. But the content of higher alcohols in the liquid products increased as well as the selectivity to CO conversion to alcohols. This indicated that the effect of Fe could be ascribed to giving the activity sites for carbon chain growth and stabilization the catalyst against sintering. It was interesting to find the $Cu/MnZrO_2$ catalyst showed a higher activity and selectivity for alcohols synthesis [2]. The space-time yield reached 0.849 g • mL^{-1} • h^{-1} and methanol was the primary alcohol component. It was considered that Mn could mainly enhance the activity of methanol synthesis through increase the degree of Cu dispersion. As a result, contrary to the result of the bimetallic catalyst $FeCu/ZrO_2$, the performance of the Mn modified $FeCu/ZrO_2$ catalyst had a drastic change. The space-time yield increased to 0.42 g • mL^{-1} • h^{-1}. At the same time, the higher alcohols fraction represented 15.3% of the total alcohol production.

Table 1 The CO hydrogenation performances of various catalysts

Catalysts	CO Con. (%)	Selectivity [a] (%)		ROH Yield (g • mL^{-1} • h^{-1})	Alcohols Distribution (wt.-%)				
		CH_x	ROH		C_1	C_2	C_3	C_4 (i-C_4)	C_5^+
Cu/ZrO_2	13.05	42.79	57.21	0.209	98.01	1.33	0.66	---	---
$FeCu/ZrO_2$	7.80	24.99	75.01	0.19	95.11	2.65	0.91	1.09(0.94)	0.24
$Cu/MnZrO_2$	37.28	21.79	78.21	0.849	94.01	2.41	1.61	1.4(0.96)	0.58
$FeCu/MnZrO_2$	26.3	40.17	59.83	0.42	84.7	7.65	3.12	3.49(1.48)	1.04

Reaction conditions: 573K, 8.0MPa, $8000h^{-1}$ a: selectivity based on number of atoms per gram carbon = [number of CO converted to given product / total number of CO converted] × 100%

The surface areas and copper dispersion of catalysts are given in **Table 2**. The Cu/ZrO_2 showed a lower BET surface area of all catalysts. But this was obviously increased on the bimetallic catalyst $FeCu/ZrO_2$. It can be seen that a high surface areas was achieved in Mn modified catalysts. And the area of $FeCu/MnZrO_2$ catalyst was enhanced ulteriorly than Mn modified alone. The Cu dispersion and surface areas of Cu/ZrO_2 slightly improved via the addition Fe promoter. The Cu-dispersion degrees in the $Cu/MnZrO_2$ catalyst system increased greatly. This might account for the catalytic results that the activity for methanol synthesis on $Cu/MnZrO_2$ catalyst was much higher than Cu/ZrO_2 catalyst and the $FeCu/MnZrO_2$ catalyst showed a good performance on higher alcohols synthesis.

Table 2 BET surface areas and Cu dispersion of various catalysts

Catalysts	S_{BET} ($m^2 \cdot g^{-1}$)	D_{Cu} (%)	S_{Cu} ($m^2 \cdot g^{-1}$)
Cu/ZrO_2	61.16	1.07	1.35
$FeCu/ZrO_2$	112.14	1.13	1.41
$Cu/MnZrO_2$	193.32	5.67	6.32
$FeCu/MnZrO_2$	196.6	6.55	7.15

Figure 1 illustrates TPR curves for the copper catalysts with different promoters, such as Cu/ZrO_2, $FeCu/ZrO_2$, $Cu/MnZrO_2$ and $FeCu/MnZrO_2$. Only one peak was seen at 543 K on bulk CuO (not shown in figure). This peak was considered to the reduction of CuO to Cu. Over Cu/ZrO_2 catalyst, the peaks shifted to lower temperature and two peaks were discerned at 473K and 528K, according to the reduction of highly dispersed CuO and bulky CuO, respectively [8]. The peak shifted to higher temperature when Fe was added. The reduction of CuO in $FeCu/ZrO_2$ occurred at the temperature range 420-600K with only one peak at 508 K. It indicated that single state of Cu^{2+} existed in $FeCu/ZrO_2$ catalyst, and the interaction between copper and other components was enhanced, which hindered the reduction of CuO. For Mn-promoted Cu/ZrO_2, the intensity of former peak increased and shifted to higher temperatures, while the latter peak decreased. On $FeCu/MnZrO_2$ catalyst, the former reduction peak shifted to higher temperatures with the maximum at 513K, and the latter one disappeared. It was in line with the results that the addition of iron improved the dispersion of Cu.

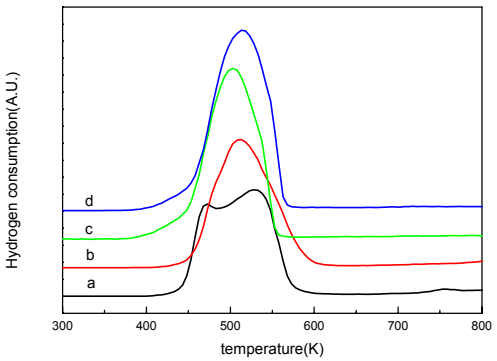

Figure 1. The H_2-TPR curves of iron and manganese modified Cu/ZrO_2 catalysts.
a: $CuZrO_2$ b: $FeCu/ZrO_2$ c:$CuMnZrO_2$ d: $FeCuMnZrO_2$

The IR bands of CO adsorbed on various catalysts are shown in **Table 3**. CO has been extensively used to identify the nature of adsorption sites in copper catalysts [9]. According to the research of Fisher and Bell [10], the bands of CO adsorption with the frequencies of 2095-2120 cm^{-1} could be attributed to linearly adsorbed CO on Cu sites. Noteworthy was that the band of CO adsorbed on monometallic catalysts shifted to high frequency when addition Fe promoter. And the intensity of the bands above mentioned also enhanced in consistent with Cu dispersion and surface areas improved. Furthermore, the interaction between Cu and Fe resulted in the antibonding of the metal d-electrons to the $2\pi^*$-orbital of the CO molecule decrease, thus weakening of the carbon-metal bond in the chemisorbed CO molecule on Cu, which leaded to the band of CO adsorbed shift to high frequency.

The results of CO-TPD are also listed in **Table 3**. It could be seen that the amounts of CO desorption on monometallic catalysts were few. Only a small amount of CO_2 was desorbed from Cu/ZrO_2. Contrary to the monometallic catalysts, the addition of Fe improved the CO adsorption. The amount of CO_2 desorption was almost three times than Cu/ZrO_2. Moreover, these phenomena became obviously on Mn modified catalysts. This result indicated that the number of CO adsorption sites and the interplay between CO and metal were all increased.

Table 3 The CO adsorbed on various catalysts

Catalysts	Wavenumber[a](cm^{-1})	CO ($\mu mol \cdot g^{-1}$)	CO_2($\mu mol \cdot g^{-1}$)
Cu/ZrO_2	2101_w	115[b]	45
$FeCu/ZrO_2$	2108_w	197	130
$Cu/MnZrO_2$	2109_m	317	175
$FeCu/MnZrO_2$	2113_s	475	255

[a] the wavenumber are the bands of CO adsorption on Cu
[b] the values are those of desorbed gases during the TPD

Conclusion

C_1-C_5 alcohols could efficiently be produced by modification a typical methanol catalyst (e.g. Cu/ZrO_2) from syngas by addition of iron and manganese compounds. It was found that the addition of iron could improve the selectivity of higher alcohols because of its strong chain growth ability and strong interaction with copper. The synergistic effect of manganese with bimetallic catalyst might play an important role in increase the activity for alcohols synthesis.

Acknowledgment. This work was supported by the State Key Foundation Project for Development and Research of China (G1999022400) and Knowledge Innovation Program of CAS (KGCX2-302).

References

1. X. D. Xu, E. B. M. Doesberg, J. J. F. Scholten, *Catalyst. Today*, 2 (1987) 125
2. N. Zhao, R. Xu, W. Wei, Y.H. Sun, *React. Kinet. Catal. Lett.*, 75 (2002) 297
3. R. Xu, Z.Y. Ma, C. Yang, W. Wei, Y.H. Sun, *Molecule.* (In press)
4. J. W. Evans, M. S.Wainwright, A. J.Bridgewater, D. J.Youny, *Appl. Catal.*, 1983, 7:75
5. Y. H. Sun, P.A. Sermon, *J. Chem. Soc. Chem. Commun.*, (1993) 1242
6. A. B. Stiles, F. Chen, J. B. Harrison, X.D. Hu, D. A. Storm, H. X. Yang, Ind. Eng. Chem. Res. 30 (1991) 811
7. Y. H. Sun, P.A. Sermon, *Catal. Lett.*, 29 (1994) 361
8. M. Shimokawabe, H. Asakawa, N. Takezawa, *Appl. Catal.*, 59 (1990) 45.
9. J. Ryczkowski, *Catalysis Today*, 68 (2001) 263
10. I. A. Fisher, A. T. Bell, *J. Catal.*, 178 (1998) 153

Analysis of the Distributed Feed IRSOFC

Ayman M. Al-Qattan and Donald J. Chmielewski

Department of Chemical & Environmental Engineering
Illinois Institute of Technology
10 West 33rd Street, Chicago, IL 60616

Background

The electrochemical reactions occurring within a SOFC are: $H_2 + O^{=} \rightarrow H_2O + 2e^{-}$ at the anode and $\frac{1}{2}O_2 + 2e^{-} \rightarrow O^{=}$ at the cathode. As these reactions proceed, a certain mount of energy is released. Unfortunately, only a portion of this released energy can be converted to electrical power, the balance showing up as heat. In steam reforming, the endothermic reforming reaction ($CH_4 + H_2O \rightarrow 3H_2 + CO$) is followed by the equilibrium dominated exothermic shift reaction ($CO + H_2O \leftrightarrow H_2 + CO_2$).

It was concluded by Yakabe *et al.*[1] that thermal stresses are a significant issue in IRSOFCs. Peters *et al.*[2] also state that ``Large temperature gradients … can cause damage to one or more of the components …" These thermal stresses are due to a mismatch in reaction kinetics (i.e., reforming is fast and the electrochemistry is slow). Thus, a severe "cold spot" is created at the stack inlet. Another important issue is the need to feed excess pre-heated steam with the hydrocarbon fuel (a typical rule of thumb is an inlet steam-to-carbon ratio (SCR) of 2:1). This steam is required to guard against the occurrence of carbon depositing side reactions (a typical example being $CO + H_2 \leftrightarrow C + H_2O$). If we can safely reduce the amount of steam fed to the IRSOFC, then a significant reduction in operating cost can be achieved due a reduction in pre-heating duty and cooling costs.

Model Development

The local electrochemical reaction rate can be derived from the local current density *j*, given by $j = \frac{E - V}{R}$, where *E* is the local Nernst potential obtained from the expression $E = E^o + \frac{\Re T_s}{n\boldsymbol{F}} \ln\left(\frac{p_{H_2} p_{O_2}^{0.5}}{p_{H_2O}}\right)$. The ratio $\frac{p_{H_2}}{p_{H_2O}}$ can be simply exchanged for a ratio of concentrations, as we will assume the ideal gas law to hold throughout. The local rate of hydrogen generation can be expressed in terms of current density: $r_{H_2} = -\frac{j}{hn\boldsymbol{F}}$, where *h* is the fuel cell channel height. Combining the above concepts yields the following expression for the electrochemical reaction rate: $-r_{H_2} = \alpha(T_s) + \beta(T_s)\ln(\rho)$, where $\rho = \left(\frac{C_{H_2}}{C_{H_2O}}\right)$. In the literature we find a number of expressions aimed at describing the kinetics of steam reforming[1,2,3]. Using the results of Achenbach[4] we define the CH_4 generation rate as: $r_{CH_4} = -k_r C_{CH_4}$ where $k_r = k_{ro} \exp\left(\frac{-\Delta E}{RT}\right)$. It should be noted that this expression was determined under excess steam conditions (i.e., a SCR above two). The rate expression for the generation of $C0_2$ due to the shift reaction is assumed to be[1]: $r_{CO_2} = k_{s,f}\left(C_{CO}C_{H_2O} - \frac{C_{CO_2}C_{H_2}}{K_{eq}}\right)$.

In the development of mass balance equations we allow for the introduction of distributed feeds[5] along the length of the channel.

To highlight these terms a hat (^) notation will be used for all distributed feed terms. An overall molar balance leads to $\frac{dF}{dz} = \hat{F} - \left(\frac{2}{C}\right)Ar_{CH_4}$ where $\hat{F}$ is the distributed feed volumetric flow rate per reactor length. Species balance equations are given as: $\frac{d}{dz}(FC_i) = \hat{F}\hat{C}_i + A\sum_j \gamma_{ij} r_j$ where $\hat{C}_i$ is the molar concentration in the distributed feed for species *i*, r_j is the reaction rate and γ_{ij} is the appropriate stoichiometric coefficient. Although the carbon deposition reactions will have a great impact on the activity of the anode, it is assumed that they will have negligible impact on the material balance of the gas stream. In the simulation section, we will describe how the above model will be used to indicate the potential of accelerated carbon deposition.

Distributed Feed Design

The goal of the design scheme is to select the distributed feed flow rate profile such that the HSR will be spatially uniform. Define the desired (or set-point) HSR as: $\rho_{sp} = \exp\left[\frac{1}{\beta(T_s)}\left(\frac{j_{sp}}{hn\boldsymbol{F}} - \alpha(T_s)\right)\right]$ where j_{sp} is the desired current density. Next we make the following assumptions: 1) the reaction surface temperature is spatially constant, 2) the shift reaction proceeds infinitely fast to the equilibrium condition. In the simulations, both of these assumptions will be removed. Now we enforce the condition $\frac{d\rho}{dz} = 0$. After a number of algebraic manipulations a spatially constant value of $\hat{F}$ is determined, which will depend on $\rho_{sp}, K_{eq}, k_r, \alpha, \beta, \hat{C}_i$ and A. Clearly, the assumptions used to derive this expression will not be valid in the

actual operation of the stack, however as we will see in the next section it does provide sufficient guidance such that the performance of the stack will be greatly improved.

Simulation Analysis

In **figure 1**, the reaction surface temperatures of the two configurations are compared. The first two curves represent the conventional SOFC design under inlet SCR's of 2:1 and 1:1. The third curve is for the distributed feed configuration with a minimal amount steam in the feed (i.e., inlet SCR=1:10). Clearly, this profile is a significant improvement over the conventional design. Unfortunately, the concept of a spatially continuous distributed feed is possible only as a mathematical construct. To face this issue we propose a discrete injection design aimed at approximating the continuous distributed feed case. The fourth profile of **figure 1** shows the discrete injection results, again with a SCR=1:10. As discussed earlier, we do not consider carbon deposition kinetics explicitly. Instead, we define the carbon monoxide plus methane to steam ratio (CMMSR), which is proposed as a measure of carbon deposition rates. **Figure 2** compares the CMMSR for the two designs under various inlet SCR conditions. **Figure 3** compares the stack designs under various air stream flow rates. It is clearly seen that the distributed feed configuration requires much less heat from the air flow stream.

Acknowledgements. Support provided by IIT and the Kuwait Institute for Scientific Research.

References

(1) Yakabe, H.; Ogiwara, T.; Hishinuma, M.; and Yasuda, I. *Journal of Power Sources*, ``3-D Model Calculation for Planar SOFC", **2001,** vol. 102, pp 144-154.

(2) Peters, R.; Dahl, R.; Kluttgen, U.; Palm, C.; and Stolten, D. *Journal of Power Sources*, "Internal Reforming of Methane in Solid Oxide Fuel Cell Systems", **2002**, vol. 106, pp 238-244.

(3) Selimovic, A. *Licentiate Thesis, Lund Institute of Technology*, "Solid Oxide Fuel Cell Modelling for SOFC/Gas Turbine Combined Cycle Simulations", **2000**.

(4) Achenbach, E. *Journal of Power Sources*, "Three-Dimensional and Time-Dependent Simulation of a Planner Solid Oxide Fuel Cell Stack", **1994**, vol. 49, pp 333-348.

(5) Al-Qattan, A.; Chmielewski, D.J.; Al-Hallaj, S.; and Selman, J.R. *Chemical Engineering Science*, "A Novel Design for Solid Oxide Fuel Cell Stacks" submitted September, **2002**.

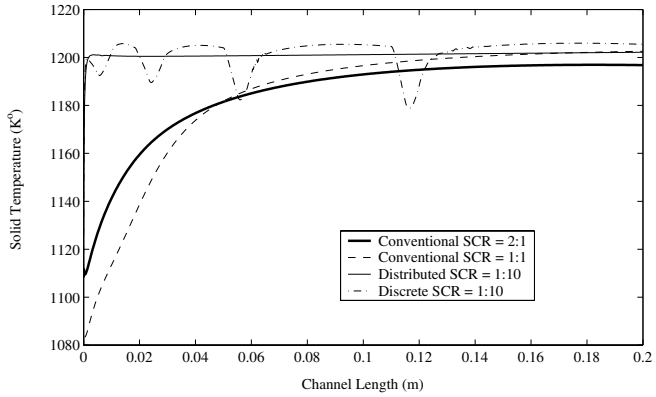

Figure 1. Temperature profiles under various stack designs and inlet conditions.

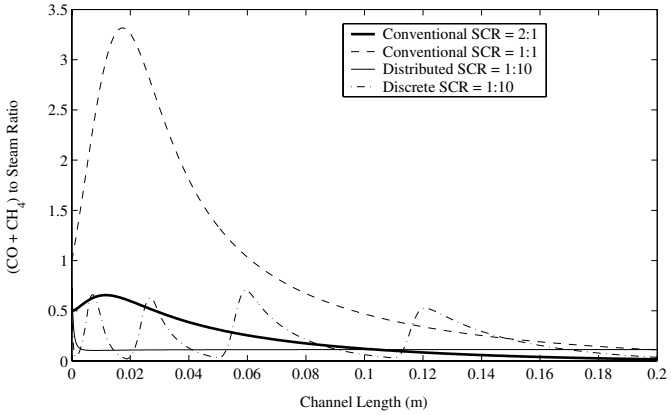

Figure 2. CMMSR profiles under various stack designs and inlet conditions.

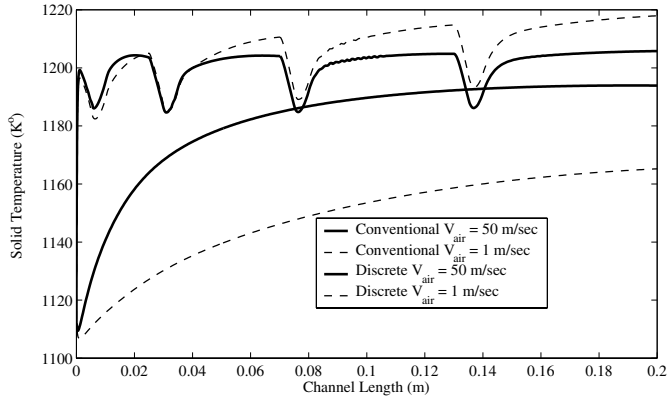

Figure 3. Temperature profiles under various stack designs and air flow conditions.

TEMERATURE EFFECTS ON THE FORMATION OF CARBON DURING PRE-REFROMING OF LOGISTIC FUELS OVER NOBEL METAL CATALYSTS FOR SOFC APPLICATIONS

*James J. Strohm, Jian Zheng and Chunshan Song**

Clean Fuels and Catalysis Program, The Energy Institute, and
Department of Energy and Geo-Environmental Engineering
The Pennsylvania State University
209 Academic Project Building, University Park, PA 16802
*E-mail: csong@psu.edu

Introduction

The demand for on-site/on-board hydrogen production is increasing with growing interest in fuel cell applications. Reforming of logistic fuels provide a viable means for hydrogen production due to the existing infrastructure and higher energy density. However, the use of such hydrocarbon based fuels in the kerosene and diesel boiling ranges dramatically increase the risk of carbon formation during reforming operations both prior to the catalyst bed (during pre-heating and mixing) and on the catalyst leading to catalyst deactivation[1,2].

Currently the most widely used reforming catalysts are based on supported nickel. Nickel catalysts are infamous for high levels of carbon formation leading to deactivation even with use of light hydrocarbons (C_1-C_4). Numerous studies have dealt with carbon formation on nickel catalyst and various ways to prevent carbon growth during steam reforming of light hydrocarbons.[3-5] Nobel metal catalysts have shown reduced carbon filament formation due carbon not being able to dissolve into the metal.[6] Pre-reforming allows for the production of a methane and hydrogen rich gas at lower temperatures (~500°C) helping alleviate the risk of carbon formation[6].

Much of the current focus on pre-reforming (or reforming) of higher hydrocarbons is based on the use of oxidative steam reforming.[7,8] Although this method allow for high conversion with minimal risk of carbon formation, the product gases are usually more dilute resulting in decreased efficiency of the fuel cell system.[9] Recently, work has shown rhodium supported catalysts can be effective in pre-reforming using only steam for model logistic fuels.[10,11]

The focus of the present work is to expand on the previous work on the use of noble metal supported catalyst in the pre-reforming of logistic fuels. The effect of temperature on the formation and type of carbon during pre-reforming of a model jet fuel is examined.

Experimental

Catalyst preparation. A support of CeO_2-Al_2O_3 was prepared by calcination at 650°C in air for 6 hours of a physical mixture of $Ce_2(CO_3)_3 \bullet 8H_2O$, $Al(OH)_3$ and polyvinylalcohol (Aldrich) as described by Suzuki and coworkers[12]. Wet impregnation of $RhCl_3$ (Aldrich) was used to give a nominal metal content of 2wt%. After thoroughly washing the sample, the catalyst was treated with 7M NH_3-H_2O at room temperature for 2 hours. The final catalyst pellets have a measured BET surface area of 64 m^2 per gram of catalyst.

Reaction system. One gram of catalyst with particle size of 18-35 mesh was placed into the middle of an Inconel 800H stainless steel reactor tube (0.375" I.D. and length of 24"). On either side of the catalyst bed, one inch of α-alumina beads (4-5 mm diameter) were isolated to examine the carbon deposition before and after the catalyst bed. The remaining volume of the reactor tube was filled with α-alumina beads with between 3.5-7 mm in diameter.

Catalyst reduction was conducted *in situ* with 20 ml/min hydrogen flow at 500°C for 12 hours. The carrier gas was then switched to nitrogen. Once the desired furnace temperature was reached, steam was introduced for 30 minutes followed by the introduction of the fuel stream as outlined elsewhere[13]. A thermocouple was placed on the outer-wall of the reactor tube and results are reported in terms of the measured wall temperature. The steam to carbon ratio was held constant at 3:1 with volumetric flow rates of 1.38 and 4.02 ml/hr for the fuel and water, respectively. The reaction was conducted at various furnace temperatures while the pressure and time on stream was held constant at 1 atm and 10 hours.

A model jet fuel was used comprising of approximately 20 wt% (10% trimethyl benzene, 5% ethyl benzene and 5% butyl benzene) aromatics in dodecane.

Carbon analysis. Temperature programmed oxidation (TPO) was conducted using a LECO RC-412 multiphase carbon analyzer equipped with an IR detector for CO_2 and H_2O. The temperature programmed used was a 30°C/min heating rate from 100 to 900°C with a 5 minute hold under UHP oxygen flow. TPD experiments were also conducted using the LECO RC-412 carbon analyzer. For TPD experiments two separate temperature programs were used (i.) heating rate of 30°C/min from 100 to 350°C with a 5 minute hold and (ii.) heating rate of 30°C/min from 100 to 900°C with a 5 minute hold. After the furnace cooled, the gas stream was switched from UHP nitrogen to oxygen. TPO analysis was then conducted in the same manner described above.

Since the TPD equipment used can only detect CO_2 to measure the carbon coming off of the system, it was desired to look at the carbon species being removed. In this case, a pyrolysis GCMS (Py-GCMS) was used to determine carbon being desorbed or being removed during TPD analysis. Once again, two separate temperature programs were used for the Py-GCMS; the pyro-probe was either held at 350°C or 900°C for 90 seconds. During the heating of the sample in the pyro-probe, liquid nitrogen was used to cold-trap any elutants in the column. The GCMS was equipped with a Restek RXTI5 column and the oven was then heated from 40 to 340°C at 6°C/min with an initial hold of 5 minutes and final hold time of 10 minutes.

Results and Discussion

Carbon formation prior to the catalyst bed. To avoid carbon formation during mixing of the fuel, a pre-heater was designed using a wick and heated steam to vaporize the fuel. By carefully controlling the temperatures at each zone of the pre-heater, experiments in excess of 10 days have been achieved with minimal carbon formation due to fuel pre-heating and mixing. Further explanation of the pre-heater design can be found in one of our previous publications.[14]

As the fuel and steam mixture enters the higher temperature reaction furnace, coking on the alumina beads was observed prior to the mixture reaching the catalyst bed. To quantify the amount of carbon that is being coked prior to the catalyst bed, the alumina beds within one inch on either side of the catalyst bed were analyzed for any carbon formation. Figure 1 shows the effect of reaction temperature on the gas-phase carbon deposition prior to the catalyst bed. As shown in Figure 1, there is significant carbon formation from the model jet fuel prior to reaching the catalyst bed. With just an increase in less than 50°C, the amount of carbon formed on the alumina beads increases by over 100%. The carbon formed is due to gas-phase pyrolysis of the fuel and steam mixture and this is further supported by an increase in ethylene in the gaseous product stream as the temperature of pre-reforming is increased.

Previous work on thermal decomposition of pure jet fuels at similar temperatures have shown the formation of carbon is due to condensation and dehydration reactions of aromatics and once ring sizes greater than 4 is reached solid deposits are observed. From modeling of these results, Andresen and co-workers were able to determine that the coke formed consists mainly of 6-7 aromatic rings which can be linked by aliphatic side chains.[14] It is postulated here that a similar structure of carbon is most likely formed during the gas-phase pyrolysis of the steam and jet fuel mixture. It is apparent from the above figure that lower temperatures provide some relief from extensive carbon formation prior to the catalyst bed.

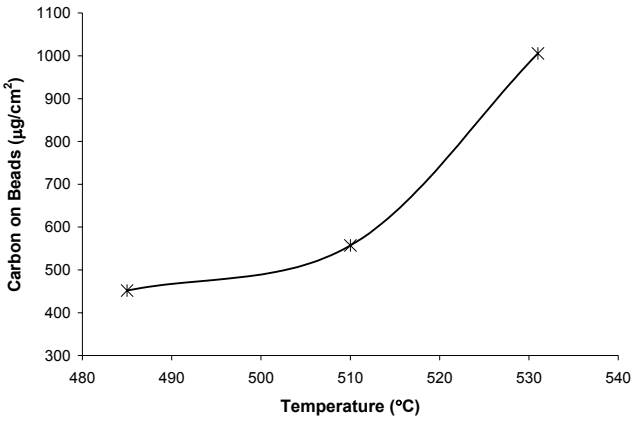

Figure 1. The impact of reaction temperature on the formation of carbon (in amount of carbon per unit surface area) on alumina beads directly before the catalyst bed.

In addition to examining the formation of carbon prior to the catalyst bed, the beads directly after the catalyst bed was also examined. At slightly lower temperatures of 485°C, there was some carbon detected (<100 µg/cm^2) whereas at elevated temperatures of 510 and 531°C no carbon was detected. This implies that as pre-reforming nears completeness, the risk of carbon formation after the catalyst bed is minimized due to little to no slippage of higher hydrocarbons.

Temperature effect on conversion. As can be seen in Figure 2, as the temperature is increased slightly the conversion can be significantly enhanced. It should be noted that the conversion plotted in Figure 2 is the final conversion observed after 10 hours on stream. Initially for all temperatures the conversion was very close to 100%. After only one hour, at an outer-wall temperature of 485°C the conversion dropped to 90% and continued to decline to a final conversion of 74%. Similarly at an outer-wall temperature of 510°C the conversion dropped after 5 hours to 97% and continued to slightly fall to 96% after 10 hours on stream. At the last temperature studied, 531°C outer-wall temperature, the conversion remained constant at nearly 100% for the duration of the run with no measurable deactivation.

Carbon formation on the catalyst. Figure 2 also illustrates the total amount of carbon measured on the catalyst after being on stream for 10 hours at each temperature. A maximum amount of carbon (in wt% of catalyst) is observed at 510°C. By going to temperatures either higher or lower a reduction in the total amount of carbon is achieved. At higher temperatures, this can be related to the catalyst activity. If the reaction on the catalyst surface occurs at sufficient rates, the adsorbed carbon species will not have the time to polymerize on the surface or spill-over to the support and polymerize. However at these elevated temperatures, gas-phase pyrolysis if more of a concern and can lead to enhanced formation of carbon on the support (and prior to the catalyst bed). Further evidence is from looking at the product distribution of the reformed gas, the increase in temperature shows enhanced ethylene formation which can be attributed to β-scission reactions during gas-phase pyrolysis of the hydrocarbon chains.

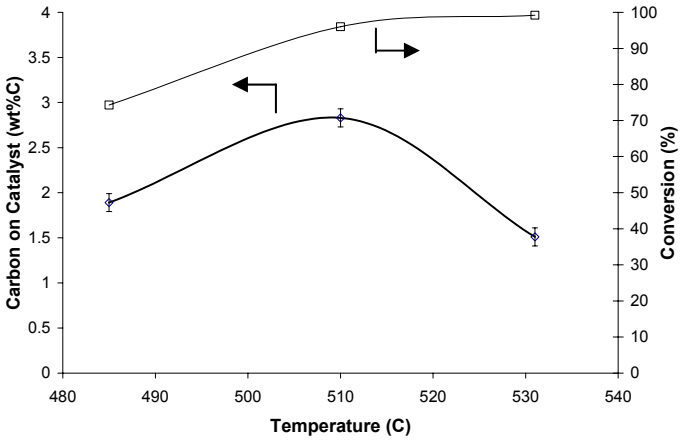

Figure 2. Temperature dependence on conversion of the model jet fuel and the total carbon formed on the catalyst.

Figure 3 shows the TPO profiles obtained from oxidation of the total carbon on the spent catalysts at the various temperatures examined. Peak I is attributed to CO_2 desorption from the catalyst which is supported by TPD at 350°C where the peak disappears. Upon exposing the catalyst sample that underwent TPD at 350°C to the air, peak I reappears. During TPD at 350°C, peaks II, III and part of IV are reduced indicating adsorbed hydrocarbon species. To further understand and identify peaks II-IV, py-GCMS was used to identify the species being desorbed. The first set of py-GCMS analysis was conducted with the pyro-probe being held at 350°C. The major products found desorbing at these temperatures were un-reacted hydrocarbons (dodecane and aromatics) as well as some partially reacted hydrocarbons such as toluene and naphthalene. After py-GCMS analysis, the catalyst samples were then analyzed using TPO. TPO results showed a large reduction in peaks II and III with minor reduction in peak IV.

At the pre-reforming temperature of 531°C, Figure 3 does not exhibit peak II. From the py-GCMS analysis of the same catalyst, the only major product observed was some dodecane, with a large reduction when compared to the other temperatures. Thus indicating that peak II is adsorbed alkyl-benzenes either initially in the fuel or formed from partial reaction in the gas phase or the catalyst surface. This also corresponds to the boiling range of the alkyl-benzenes such as butyl benzene. This also implies that peak III is dodecane being desorbed from the catalyst, whose boiling point is 212°C.

To further support this, the fresh catalyst was exposed to JP-8 (military aviation fuel) and then dried in a vacuum oven at 150°C overnight. TPO analysis of this sample then showed an increase in peaks II, III and IV; further supporting that peaks II through IV are adsorbed hydrocarbon species rather than coke. At the pre-reforming temperature of 485°C, peak IV is more defined and py-GCMS

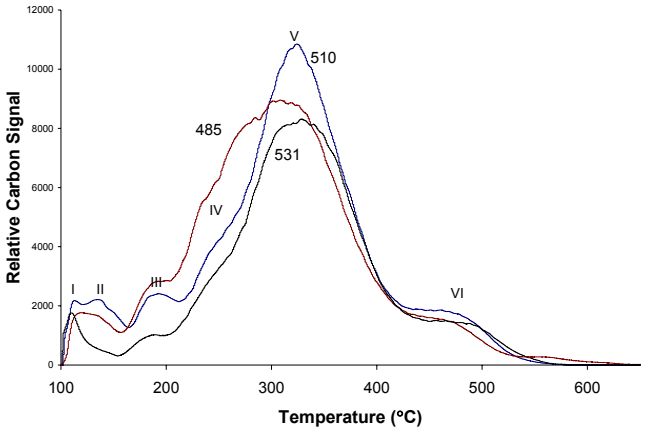

Figure 3. TPO profiles of the catalyst after 10 hours of pre-reforming of a model jet fuel at measured outer-wall temperatures of 485, 510 and 531°C.

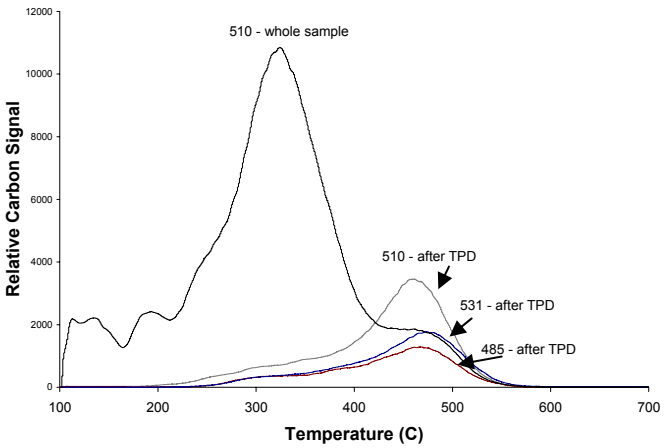

Figure 4. TPO profiles of the catalyst sample after pre-reforming at 485, 510 and 531°C after TPD at 900°C compared with the TPO profile of the whole spent catalyst (510°C pre-reforming temperature).

showed high amounts of naphthalene and alkylated naphthalenes being desorbed indicating that peak IV is adsorbed naphthalenes that are formed from gas-phase pyrolysis or on the catalyst.

Peak V is being tentatively identified as highly amorphous carbon. Py-GCMS analysis with the pyro-probe being held at 900°C for 90 sec yielded a significant reduction in peak V. The major compounds being formed after flash pyrolysis of the sample were 3 to 7 ringed aromatic structures along with some light gaseous products. This indicates that the major building blocks of the carbon detected in peak V is large aromatic units that maybe connected with short aliphatic linkages. Due to the short time the pyro-probe is able to be held at 900°C, not all of the carbon was removed from peak V indicating insufficient heat transfer through the catalyst sample. To get an accurate estimation of the amount of amorphous (or easily removed) carbon on the surface, TPD analysis was conducted at 900°C. Figure 4 shows the resulting carbon remaining on the surface of the catalyst after TPD analysis at 900°C.

From Figure 4 it is shown that some of the initial peak V is still present. This could be due to there being an additional peak embedded in peak V or that some of the aromatic units contributing to the amorphous carbon are of extremely large ring sizes that are not volatile even at 900°C. Another important note is that the peak located between 400 and 550°C (peak VI) is enhanced after TPD at 900°C for the catalyst samples after pre-reforming at 510 and 531°C. This is most likely due to some of the amorphous carbon of peak V being transformed, during the TPD analysis, to peak VI.

For pre-reforming temperature of 485°C there is very little increase in peak VI after TPD analysis. This implies that the aromatic structure of the amorphous coke is of smaller ring size than at the higher temperatures. Py-GCMS verified that the majority of the decomposition of peak V for the pre-reforming temperature of 485 was 2-3 member aromatic rings as apposed to the higher member rings observed for the higher temperatures. This is further shown by Figure 3 where the maximum for peak V (and IV) is slightly shifted towards lower temperatures. Further py-GCMS analysis of all of the samples after TPD at 900°C shows no compounds coming off when the pyro-probe is taken to 1200°C, indicating that the carbon remaining on the sample is highly aromatic and is approaching a more graphitic carbon.

Conclusions

The effect of temperature was studied on the formation of carbon on rhodium supported catalyst during pre-reforming of a model jet fuel. At pre-reforming temperatures of 510°C, maximum carbon formation was observed. By increasing the pre-reforming temperature to 531°C the amount of carbon formed on the catalyst is significantly reduced due to higher activity of the catalyst. However by increasing the reaction temperature the amount of carbon formed during gas-phase pyrolysis prior to the catalyst bed increased dramatically. To avoid carbon formation prior to the catalyst bed, without fuel modification, the pre-reforming temperature should be kept below 510°C thus requiring catalysts with higher activity at these temperatures.

Acknowledgement. We are grateful to the DoD/DARPA Palm Power Program and management team for supporting this work. We also wish to thank Dr. Mehdi Namazian of Altex Technologies Inc. for helpful discussions on the pre-mixing. Thanks also go to Ms. Lu Sun for BET surface measurements and Mr. Ronald Copenhaver for setting up the reactor system.

References

(1.) Rostrup-Nielsen, J.R. *Cat. Today*, **1997**, 37, 225.
(2.) Song, C. *Cat. Today*, **2002**, 77, 17.
(3.) Rostrup-Nielsen, J.R. In *Catalysis Science and Technology*; Andersen, J.R.; Boudart, M., Ed.; Springer-Verlag, New York, **1984**, Vol. 4, pp.34.
(4.) Trimm, D.L. *Catal. Rev. – Sci. Eng.*, **1977**, 16(2), 155.
(5.) Rostrup-Nielsen, J.R. *J. Cat.*, **1974**, 33, 184.
(6.) Rostrup-Nielsen, J.R. Christensen, T.S. Dybkjaer, I. *Stud. Surf. Sci. Catal.*, **1998**, 113, 81.
(7.) Borup, R.; Perry, L.; Inbody, M.; Tafoya, J. Prepr. Pap. – *Am. Chem. Soc., Div. Fuel Chem.,* **2002**, 47(2), 548.
(8.) Trimm, D.L.; Onsan, Z.I. *Catal. Rev. – Sci. Eng.*, **2001**, 43, 31.
(9.) Larminie, J.; Dicks, A. *Fuel Cell Systems Explained*; John Wiley: New York, **2000**.
(10.) Zheng, J.; Strohm, J.J.; Song, C. Prepr. Pap. – *Am. Chem. Soc., Div.. Fuel Chem.,* **2003**, 48(2), to be accepted.
(11.) Zheng, J.; Strohm, J.J.; Song, C. Prepr. Pap. – *Am. Chem. Soc., Div.. Fuel Chem.,* **2003**, 48(2), to be accepted
(12.) Suzuki, H.; Iwanami, H.; Iwanami, O.; Kitahara, T. *Int. J. Hydrogen Energy*, **2001***, 26*, 935.
(13.) Zheng, J.; Shen, J.-P.; Song, C.; Pan, W.; Strohm, J.J. Prepr. Pap. – *Am. Chem. Soc., Div.. Fuel Chem.,* **2003**, 48(1), 374.
(14.) Andresen, J.M.; Strohm, J.J.; Sun, L.; Song, C. *Energy & Fuels*, **2001**, 15(3), 714.

CATALYTIC ELECTRODES FOR HIGH PERFORMANCE SOLID OXIDE FUEL CELLS OPERATED AT INTEMEDIATE AND LOW TEMPERATURES

Xiangrong Liu[a, b], Zhigang Zhu[b], Bin Zhu[a, b], Ingvar Albinsson[c] and Bengt-Erik Mellande[c]*

[a]Department of Chemical Engineering & Technology, Royal Institute of Technology (KTH), S-100 44 Stockholm, Sweden; [b]Goeta Technology Developer International, S-17160, Solna, Sweden; [c]Physics and Engineering Physics, Chalmers University of Technology, S-412 96 Göteborg, Sweden

Introduction

During recent years many efforts have been contributed to the reduced temperature (800 to 1000°C) and intermediate temperature (IT, 400 –700°C) solid oxide fuel cells (SOFCs). Challenges to develop high performance ITSOFCs rest on both electrolyte and electrodes. Recent research showed that the development in functional anode materials is one of the keys to enhance the fuel cell performance at lower temperatures. It has been reported in a number of publications that the ceria- composite electrodes (especially for the anode) could greatly enhance the YSZ SOFC performances for intermediate temperature operation.[1-3] Our approach to use the ceria-composite ceramic materials for both electrolyte and electrodes (anode and cathode) has shown promising performances.

Fuel cells that can be operated for hydrocarbon fuels, e.g., coal gas, natural gas and biomass fuels for the stationary power generation; alcohol (methanol, ethanol etc.) and gasoline/diesel oil for the tractionary power applications, have significant importance for the social sustainable development and further for an urgent marketing demand. The SOFC may in some respects be seen as an ideal source to generate electricity due to its high efficiency and flexibility regarding choice of the fuels, especially for the hydrocarbon fuels. However, when the hydrocarbon type fuels are adopted, the electrode catalytic function is strictly requested to be suitable for various gas or liquid fuels. There is thus an imperative need to develop efficient catalytic electrodes for ITSOFCs in both stationary and tractionary applications.

Experimental

Materials and preparation. Commercial $Gd_{0.1}Ce_{0.9}O_{1.95}$ (GDC) powder was purchased from Seattle Specialty Ceramics, USA. Alkaline hydroxides, e.g., MOH and M_2CO_3 (M = Li, Na) (A. R., Aldrich Chemical Company, Inc., USA), were used to prepare the composites with GDC for the electrolytes; NiO (Merck, A. R.) and $La_{0.6}Sr_{0.4}Co_{0.8}Fe_{0.2}O_3$ (LSCF) (Seattle Specialty Ceramics, Seattle, WA, USA) were used in the ceria-composite electrodes. Platinum (Leitplatin 308A, Hanau, Germany) and silver (Leitsilber 200, Hanau, Germany) pastes were also investigated for the electrodes for comparison. Stainless steel was adopted for the fuel cell device holder.

The ceria-composite electrolyte samples were prepared by mixing GDC with MOH or M_2CO_3 in a 10 to 20 wt.% of the total weight and grinding well. The mixtures were heat-treated at 600-680°C for one hour depending on the salts. The resulting materials were grounded again thoroughly for use. The ceria-composite electrodes, e.g., the ceria-composite anode were prepared through a mixture of the ceria with 20-30 wt.% LiOH (or Li_2CO_3) composite (50 vol.%) and anode, NiO (50 vol.%). This mixture was grounded and then heat-treated at 700°C for 1 hour. After heat-treatment a 20 vol.% active carbon was added, then ground thoroughly for use. The ceria-composite cathode was prepared in the same procedure in replacement of the NiO by LSCF.

Fuel cell construction. The composite anode-supported ITSOFCs were constructed by directly pressing the composite anode, electrolyte and cathode in one step. The cathode was much thinner compared to the anode thickness. To avoid cracking and separation of the ITSOFC components (anode, electrolyte and cathode) during heating, complete ITSOFC assemblies were heat-treated using a program- controlled furnace to carefully adjust the temperature rise and holding time, e.g., for minimum 30 minutes at 600°C. The finally completed fuel cell assembly for tests has a dimension of 1-2 mm in thickness and 13 mm in diameter. In some cases, the electrolyte support fuel cell assembly was also investigated for comparison. In this case, about 1 mm thick electrolyte disc was pasted by Pt paste.

Characterisation. Material characterisation of the electrical properties was carried with the help of a.c. impedance analysis. The impedance analysis was performed with a computerised Hewlett-Packard HP4274A LCR-meter. The measured frequency range covers from 0.1 Hz to 100 kHz with an applied signal of 20 mV. The temperature of the sample (holder) was controlled by an Eurotherm temperature controller and the sample temperature was measured with a Platinum thermocouple attached at the position of the sample. In most cases, the measurements were carried out between 400 and 650°C. At the same time the fuel cell was employed as an in-situ characterisation method for the materials as suggested before.[4]

Results and Discussion

Performance for hydrogen fuelled ITSOFCs using the ceria-composite electrode have been reported elsewhere.[5,6] The maximum power densities 0.8 Wcm^{-2} could be reached at 600°C. In some cases the ITSOFCs can even function at temperature as low as 200°C depending on the catalyst function of the ceria-composite electrodes. These advanced ITSOFC performances are contributed by excellent electrode function.

This electrode function, both catalyst and electrical/electro-chemical property. This electrode function is marked by the non-polarization effects in I-V characteristics. Due to the interface between two fuel cell components, electrode and electrolyte, there is always a significant electrode polarization, can be normally observed. This is due to the fact of a discontinuous transport process between the electrons (external circuit) and ions (in the electrolyte and electrodes, internal circuit). However, if there is a continuous transporting process, i.e., the electrolyte is the ionic and electrodes are the electronic and ionic concentration gradient materials, the interfacial polarization would fade away. This effect was studied by the electrochemical characterization on the ITSOFC electrode activation and polarization with the help of the ceria-composite electrodes. **Figure 1** shows I-V characterizations during the in- situ OCV set up accompanying with the cell discharging processes. The freshly constructed ITSOFC at the immediate I-V measurement shows a rather high resistance, 4.2 Ω, deduced from its I-V characteristic. Accompanying with the reduction of NiO in the ceria-composite anode during the fuel cell (OCV) set-up process, the polarisation caused by the electrode activation and reaction kinetics in the I-V characteristics is removed significantly, thus decreasing the cell resistance from 4.2 to around 1 Ω during the first half an hour. The discharge reduces the polarisation more effectively and in turn improves the cell interfaces. After discharging under 200 $mAcm^{-2}$ for 5 and 10 minutes, the cell resistance drops rapidly from about 1 Ω to 0.5 Ω. Correspondingly the polarisationion effect in the I-V characteristic partially and completely disappears for 5 and for 10

minutes discharge, respectively. It can be seen from Fig. 3 that there is a noteworthy polarisation loss in the electrode process reflected by the non-linearity in the I-V characteristics for the fresh fuel cell before discharge. This polarisation effect depends largely on the cell construction technique, mainly the interfacial structures between the electrolyte and electrodes, and also on the electrode materials. For example, the platinum electrode ITSOFCs always exhibit much stronger polarisation effects than that of the composite electrodes, to be further discussed below. The all-ceria-composite ITSOFCs with both ceria-composite electrolyte and electrodes may provide a continuous electronic and ionic transporting route in the electrolyte/electrode interfaces, and continuous ionic transport from the interface to the electrolyte, the interface being totally connected by electron and ion conducting bridge, making no observable electrode polarisation eventually for all-ceria-component ITSOFCs. This concept is further supported by studying the ITSOFCs constructed by different electrodes.

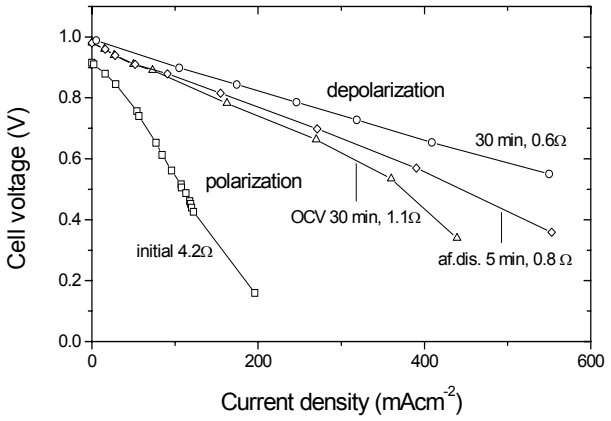

Figure 1. In-situ I-V characteristics

High catalyst function to methanol and ethanol liquid fuels. ITSOFCs devices based on the ceria-composite materials showed the OCV around 0.95 V for 2 M methanol, 0.91 V for 1 M ethanol and 0.78 V for 1 M acetone at 600°C. When these liquid fuels were adopted directly, the ITSOFCs operated under 300 to 450 $mAcm^{-2}$ (180 to 280 $mWcm^{-2}$) at 600°C demonstrate a peak power density around 330 $mWcm^{-2}$ and 300 $mWcm^{-2}$ methanol and ethanol fuel cells, respectively, as shown in Figure 6. The performance of the liquid fuelled ITSOFCs can be certainly improved greatly by developing suitable catalysts as demonstrated for DMPEFCs. For example, very recently the CuO was found to be especially active for the direct liquid ceramic fuel cells. The CuO additives in the electrodes can significantly promote the electrode reaction for methanol and ethanol, and improve the DMSOFCs (direct methanol SOFCs) and DESOFCs (direct ethanol SOFCs) performances.

Electrode catalytic function to other hydrocarbon fuels. **Figure 2** exhibits some typical I-V characteristics of the ITSOFCs for using the biomass syngas composition. The ITSOFC performances obtained in **Figure 2** are rather comparable with that obtained for the hydrogen fuel excluding some voltage/power loss caused by the lower cell voltage due to the hydrocarbon fuel very much related to the catalyst function of the anode when facing the hydrocarbone fuels.

Our ITSOFCs based on ceria-based composite electrolyte and electrodes have the advantages to directly operate various existing fuels, e.g. various hydrocarbon fuels: synthesized coal gas, biomass, nature gas, alcohol as well as ammonia. Hydrocarbon fuels can be easily thermally decomposed, e.g. methanol: CH_3OH (g) --- 2 H_2 + CO. This process can theoretically deliver a product stream containing up to 67 vol% H_2.[7] This type fuels can be directly operated in LTSOFCs. Ceria is known to perform functions, including the promotion of water-gas shift and steam-reforming reactions, stabilization of the surface area of the catalyst and maintenance of the dispersion of the catalytic metals. All these functions have provided the ceria-composite electrodes the efficient ways to improve the cell performances.

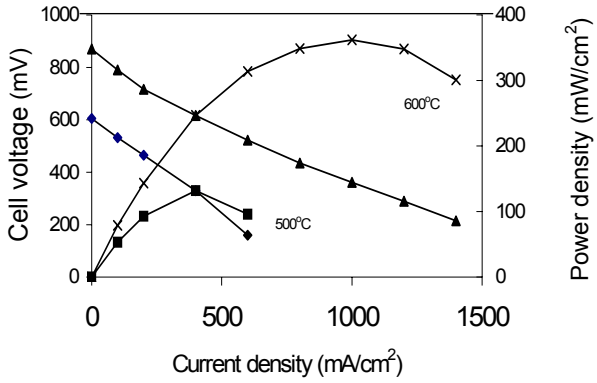

Figure 2. FC performance using the biomass syngas composition fuel

Advantages of the ITSOFCs using the ceria-composite electrodes and electrolytes.

The major advantages of the ceria-composite materials may be summarised as follows: i) The ceria-composite electrodes are highly catalytic and conductive for both ion and electrons; ii) The ceria-composite electrolytes are highly electrolytic, which means that oxygen atoms can be oxidized as the ions as efficient as possible and transport as fast as possible, based on the high ionic conductivity and ionic entire transport ability of the ceria-composite electrolyte; iii) excellent compatibility between the electrodes and the electrolyte based on the use of one kind ceria composite material with different components. In addition, using the same ceria-based composite materials, there are excellently compatible without problems for the mechanical and thermal expansion compatibility. Compared to the case when ceria was used only as the anode to improve/enhance performance of the YSZ thin film electrolyte SOFCs, the all-ceria-composite ITSOFC systems are more promising. All these mentioned unique advantages, e.g., super ionic conductivity, highly catalyst and compatibility among all cell components make the ceria-composite ITSOFCs more efficient and more promising than the YSZ SOFCs.

Acknowledgement. This work is supported by Carl Tryggers Stiftelse for Vetenskap Forskning (CTS) and the Swedish Research Council (VR). Some experiments were completed by Goeta R&D base in China.

References

(1). Murray, E. P.; Tsai, T.; Barnett, S. A., *Nature,* **1999**, *400*, 649.
(2). Hibino, T.; Tsunekawa, H.; Tanimoto, S.; Sano, M., *J. Electrochem. Soc*. **2000**, *147*, 1338.
(3). Seungdoo, P.; John, M. V.; Raymond, J. G., *Nature*, **2000**, *404*, 265.
(4). Zhu, B., *Electrochemistry Communication*, **1999**, *1*, 242-249.
(5). Zhu, B., *J. Power Sources,* **2001**, *93*, 82-88.
(6). Zhu, B., *J. Power Sources,* **2003**, *114* , 1-9.
(7). Pettersson, L.; Sjöström, K.; *Combust. Sci. Technol*., **1991**, *80*, 265.

Microkinetic Modeling of Ammonia Synthesis and Decomposition on Ruthenium and Microreactor Design for Hydrogen Production

Soumitra R. Deshmukh, Ashish B. Mhadeshwar and Dionisios G. Vlachos

Department of Chemical Engineering and Center for Catalytic Science and Technology (CCST)
University of Delaware, Newark, DE 19716-3110

Introduction

The overall objective of this work is to develop design rules for production of hydrogen from ammonia at the small scale. While ammonia synthesis is one of the most extensively studied processes in catalysis, due to its use in the manufacturing of fertilizers, ammonia decomposition has only recently become of interest due to its potential use in CO-free hydrogen production for fuel cells. Ruthenium is one the better catalysts for the latter but the kinetics of decomposition is not as well understood. Noting the shortcomings of the literature models, we develop a complete microkinetic model to describe the ammonia synthesis as well as decomposition on Ru. An easy to implement reduced model is developed using a novel *computer-aided reduction methodology*. Computational fluid dynamics (CFD) simulations are then performed in a microreactor. Optimization of a microreactor for hydrogen production for fuel cell applications is also discussed.

Chemistry Modeling

Although ammonia synthesis ($2NH_3 \leftrightarrow N_2 + 3H_2$) is one of the better-studied reactions in the literature, decomposition kinetics on Ru is not as well established. Partial mechanisms and reduced rate expressions have been proposed[1,2] to qualitatively describe experimental trends. These reduced rate expressions have been derived based on the traditional Langmuir-Hinshelwood approximations where a posteriori validation has occasionally been done. As seen in Fig. 1, these models fail to capture the experimental data in a microreactor.

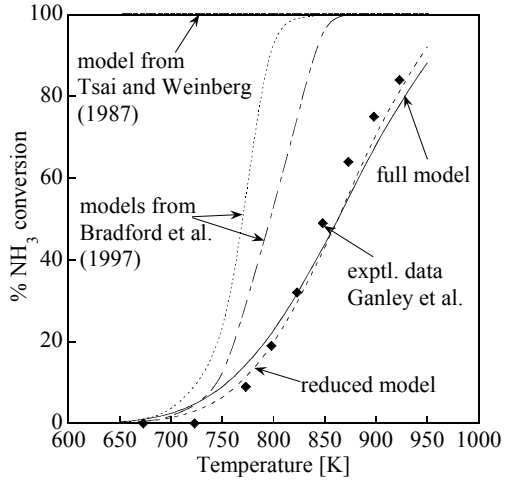

Figure 1. PFR simulations with full and reduced reaction models compared to the experimental data of Ganley et al.[3] The reaction model can describe faithfully the experimental data without any adjustment in rate parameters. The reduced reaction model is in very good agreement with the full model and the experimental data. Literature, reduced reaction models are not as accurate.

A detailed reaction mechanism for ammonia decomposition on Ru has been developed. Specifically, the multistep methodology described in Aghalayam et al.[4] is employed to construct a surface reaction mechanism for ammonia decomposition on Ru. In particular, 6 reversible elementary steps for ammonia decomposition are laid down, which include adsorption/desorption of NH_3, N_2, and H_2, and hydrogen abstraction steps from NH_x intermediates and their reverse. Order of magnitude estimates of pre-exponential factors are determined using Transition State Theory (TST)[5], whereas activation energies are calculated using the semi-empirical Bond Order Conservation (BOC) technique[6,7] with input from quantum mechanical density functional theory (DFT) as well as surface science experiments. Adsorbate-adsorbate interactions, shown in Table 1, are also taken into account through the BOC framework in desorption and surface reactions. The mechanism, shown in Table 2, is enthalpically consistent at 300 K. The entire semi-empirical framework has been integrated with surface CHEMKIN to enable transparent, easy use in computing the reaction rates. Simulations have then been carried out and compared to targeted experiments in order to slightly optimize the reaction mechanism against uncertainties. The reaction mechanism is able to predict well atmospheric ammonia decomposition and high-pressure ammonia synthesis data, along with various ultra-high vacuum temperature programmed desorption (TPD) and reaction (TPR) data.

Table 1. Heat of Chemisorption Data.
θ indicates coverage of surface species.

Species	Heat of chemisorption (kcal/mole)	References
N*	$135\text{-}35\theta_N$	[8, 9]
H*	63	[10, 11]
NH_3*	18.23	[10, 11]
NH*	86.79	Our BOC calcns.
NH_2*	59.95	Our BOC calcns.

Table 2: Screening surface reaction mechanism of ammonia decomposition on Ru at 300 K.
The activation energies are in kcal/mol, calculated in the zero coverage limit (θ_*=1). All activation energies are coverage dependent as determined from the BOC framework (see Table 1).

No.	Reaction	Sticking coefficient or pre-exponential [s^{-1}]	Activation energy at θ_*=1
1	$H_2 + 2* \rightarrow 2H*$	1	1.9
2	$2H* \rightarrow H_2 + 2*$	1.0×10^{13}	23.7
3	$N_2 + 2* + \rightarrow 2N*$	1	6.2
4	$2N* \rightarrow N_2 + 2*$	1.0×10^{13}	50.3
5	$NH* + * \rightarrow H* + N*$	1.0×10^{11}	5.8
6	$H* + N* \rightarrow NH* + *$	1.0×10^{11}	37.2
7	$NH_2^* + * \rightarrow H* + NH^*$	1.0×10^{11}	19.1
8	$H* + NH^* \rightarrow NH_2^* + *$	1.0×10^{11}	17.4
9	$NH_3^* + * \rightarrow H* + NH_2^*$	1.0×10^{11}	17.5
10	$H* + NH_2^* \rightarrow NH_3^* + *$	1.0×10^{11}	13.2
11	$NH_3 + * \rightarrow NH_3^*$	1	0
12	$NH_3^* \rightarrow NH_3 + *$	1.0×10^{13}	18.2

Armed with a predictive reaction mechanism, we employ a systematic *computer-aided reduction methodology* based on reaction path analysis and small parameter asymptotics, the results of which are also depicted in Fig. 1.

Computational Fluid Dynamics Modeling

The microreactor, fabricated for hydrogen production for portable applications, consists of an 11x25 array of diamond shaped posts (coated with Ru/Al_2O_3 catalyst) each of size 300 μm x 300 μm x 3000 μm. Two-dimensional CFD simulations of the microreactor is carried out using the reduced kinetic model for ammonia decomposition. The elliptic Navier-Stokes equations are solved for the flow, along with the continuity, and species and enthalpy conservation equations. The computational mesh involves ~100,000 nodes (typical discretization of 220x575) and results in 800,000 unknowns, requiring about 1 hr of CPU time. The velocity and concentration contours for one such calculation are shown in Fig. 2.

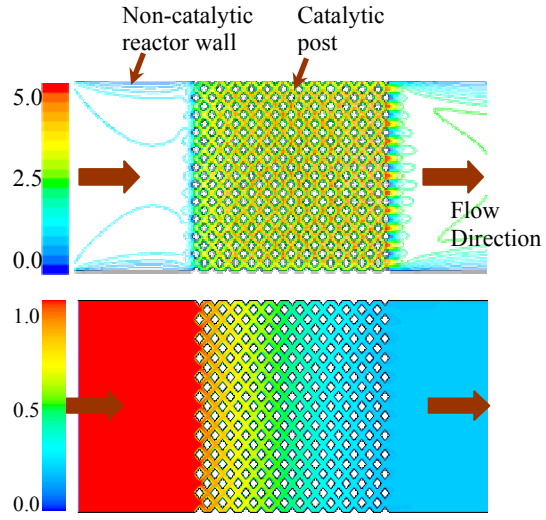

Figure 2. Flow (top) and mass fraction (bottom) contours for a full microreactor CFD simulation.

Results and Discussion

Computational results are in excellent agreement with recent experiments on the effect of temperature on conversion. Comparing the results with those obtained for a tubular reactor we see that the posts play a significant role in reducing the mass transfer effects and thereby increasing the conversion considerably. Microreactor performance was also evaluated for various post geometries such as diamonds, triangles and circles keeping the active area per unit volume constant. The shapes of posts show no significant effect on the conversion in the microreactor but show significant influence on the flow patterns and therefore the pressure drop in these devices. It is found that the circular posts have a lower pressure drop by about a factor of 30%, which is of significant importance given the large pressure drop in these devices for high flow rates. It was found that the conversion in the microreactor decreased with increase in the flow velocity. Boundary layer separation is observed in the microreactor under certain flow conditions. Dimensionality effects will also be discussed.

Conclusions

A complete microkinetic model for ammonia decomposition and synthesis on Ru is proposed and validated with experimental TPR and TPD data. Reduced models are developed for both cases. CFD

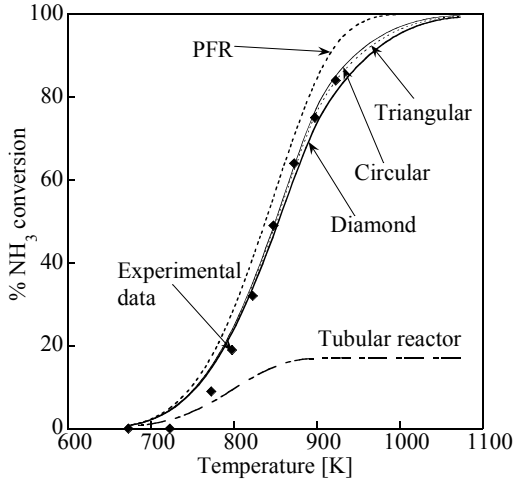

Figure 3. Comparison of conversion of PFR, tubular reactor, and microreactor with various post shapes to experimental data.

modeling is carried out for the microreactor to determine the influence of various geometric factors on ammonia conversion and pressure drop. Insights into the optimization of these microreactors are developed.

Acknowledgement. This work was supported by the Army Research Office under contract DAAD 19-01-1-0582. Any opinions, findings, and conclusions or recommendations expressed are those of the authors and do not necessarily reflect the views of the Army Research Office.

References

(1) Bradford, M. C. J.; Fanning, P. E.; Vannice, M. A., Kinetics of NH_3 decomposition over well dispersed Ru. *Journal of Catalysis* **1997,** 172, 479-484.

(2) Tsai, W.; Weinberg, W. H., Steady-state decomposition of ammonia on the Ru(001) surface. *Journal of Physical Chemistry* **1987,** 91, (20), 5302-5307.

(3) Ganley, J. C.; Seebauer, E. G.; Masel, R. I., Porous anodic alumina posts as catalyst support in microreactors for production of hydrogen from ammonia. *AIChE Journal* submitted.

(4) Aghalayam, P.; Park, Y. K.; Vlachos, D. G., Construction and optimization of detailed surface reaction mechanisms. *AIChE J.* **2000,** 46, (10), 2017-2029, *This paper was selected in the highlights of Chem. Eng. Progress (paper of the month), p., Oct. issue, 2000.*

(5) Dumesic, J. A.; Rudd, D. F.; Aparicio, L. M.; Rekoske, J. E.; Trevino, A. A., *The Microkinetics of Heterogeneous Catalysis*. ed.; American Chemical Society: Washington, D.C., 1993.

(6) Shustorovich, E., Bond-order conservation approach to chemisorption and heterogeneous catalysis: Applications and implications. *Advances in Catalysis* **1990,** 37, 101-164.

(7) Shustorovich, E.; Sellers, H., The UBI-QEP method: A practical theoretical approach to understanding chemistry on transition metal surfaces. *Surface Science Reports* **1998,** 31, 1-119.

(8) Jacobi, K., Nitrogen on Ruthenium single-crystal surfaces. *Physica Status Solidi (a)* **2000,** 177, 37-51.

(9) Zhang, C. J.; Luynch, M.; Hu, P., A density functional theory study of stepwise addition reactions in ammonia synthesis on Ru(0001). *Surface Science* **2002,** 496, (3), 221-230.

(10) Shustorovich, E.; Bell, A. T., Synthesis and decomposition of ammonia on transition metal surfaces: Bond-order-conservation-Morse-potential analysis. *Surface Science Letters* **1991,** 259, L791-L796.

(11) Savargaonkar, N.; Narayan, R. L.; Pruski, M.; Uner, D. O.; King, T. S., Structure sensitive hydrogen adsorption: Effect of Ag on Ru/SiO_2 catalysts. *Journal of Catalysis* **1998,** 178, 26-33.

SYNTHESIS OF SODIUM BOROHYDRIDE FOR ENERGY APPLICATIONS

Ying Wu, Jason C. Brady, Michael T. Kelly, Jeffrey V. Ortega, Jonathan L. Snover

Millennium Cell Inc.
1 Industrial Way West, Eatontown, NJ 07724, USA

Introduction

Sodium borohydride ($NaBH_4$) has been demonstrated as an effective hydrogen storage material. Its hydrolysis generates high purity humidified hydrogen suitable for use in PEM fuel cells. Although the technology can be scaled and tailored for many different applications from very small portable power to fuel cell vehicles, the current high cost of $NaBH_4$ is limiting early adoption of the technology to premium power applications. The utilization of $NaBH_4$ in high demand, continuous power generation and fuel cell vehicles will not be economically feasible until the production cost of $NaBH_4$ can be significantly reduced.

Discussion

Sodium borohydride is a structurally simple, yet complex chemical. It does not occur in nature; therefore it has to be synthesized from sodium and boron containing raw materials. The production of $NaBH_4$ requires the combination of three elements, Na, B, H, and a large amount of energy input. Intrinsically, the level of complexity is derived from significant enthalpic and entropic barriers associated with the strength of the boron-oxygen bond. Low cost $NaBH_4$ will depend on the availability of a production process that combines the necessary raw materials (borates, hydrogen, and sodium) in a pathway of optimum overall energy efficiency.

The current sate-of-the-art $NaBH_4$ production process is based on the reduction of the trialkyiborate, $B(OCH_3)_3$, with NaH, known as the Schlesinger Process [1] . The following chemical equations describe the synthetic pathway to$NaBH_4$.

$$Na_2B_4O_7 + H_2SO_4 + 5\ H_2O \rightarrow 4\ H_3BO_3 + Na_2SO_4 \quad (1.1)$$

$$H_3BO_3 + 3\ CH_3OH \rightarrow B(OCH_3)_3 + 13\ H_2O \quad (1.2)$$

$$NaCl \rightarrow Na + \tfrac{1}{2}\ Cl_2, \text{ by electrolysis.} \quad (1.3)$$

$$4\ Na + 2\ H_2 \rightarrow 4\ NaH \quad (1.4)$$

$$B(OCH_3)_3 + 4\ NaH \rightarrow NaBH_4 + 3\ NaOCH_3 \quad (1.5)$$

$$3\ NaOCH_3 + 3\ H_2O \rightarrow 3\ CH_3OH + 3\ NaOH \quad (1.6)$$

Overall Reaction:

$$Na_2B_4O_7 + 16\ Na + 8\ H_2 + H_2SO_4 + 5\ H_2O \rightarrow 4\ NaBH_4 + 12NaOH + Na_2SO_4 \quad (1.7)$$

The various steps of the Schlesinger Process are fragmented among various chemical producers, lacking integration and producing undesirable by-products. Although the process provides high purity $NaBH_4$, the individual reaction steps are not optimized for energy efficiency. An examination of the primary energy input for the process versus the eventual chemical energy stored in $NaBH_4$ will be provided to identify areas for energy efficiency improvements. For example, the process uses large amounts of Na metal. This subjects the overall energy efficiency to the limitations in energy efficiency of the Na process. The current NaCl electrolysis process for Na metal is less than 50% energy efficient. Additionally, reactions (1.4) and (1.5) are both exothermic, losing a significant portion of the original energy input to reaction heat. Compounded together, the overall reaction of (1.7) is less than 20% energy efficient. Clearly, for $NaBH_4$ to become an effective energy carrier, the energy efficiency of its production process has to be significantly improved.

In light of the multi-step nature of the synthetic process, it is important to improve the energy efficiency of each step. The single most costly raw material is Na metal. It follows that major improvements in Na production will have a significant impact on the $NaBH_4$ production efficiency. Alternatively, an intermediate other than NaH may be considered to avoid the large enthalpic loses associated with reactions 1.4 and 1.5.

In the first approach, we propose an electrochemical reaction utilizing an anodic reducing agent to lower the operating voltage of the electrochemical cell, thereby achieving overall energy savings in the production of Na. In the second approach, we propose an alternative synthetic pathway that proceeds through diborane (B_2H_6), an energy-rich hydride intermediate that is closer in energy to $NaBH_4$. The interconversion of B_2H_6 and $NaBH_4$ can be manipulated by the appropriate selection of reagent. For example, the reaction of $NaBH_4$ with certain oxidizing agents generates B_2H_6[2], and B_2H_6 can be converted to $NaBH_4$ with a variety of Na containing salts [3]. In this approach, the overall process will include the following proposed reaction steps:

$$4NaBO_2 + 2CO_2 + 12ROH \rightarrow 2\ Na_2CO_3 + 4\ B(OR)_3 + 6H_2O \quad (2.1)$$

$$4\ B(OR)_3 + 12\ H_2 \rightarrow 2\ B_2H_6 + 12\ ROH \quad (2.2)$$

$$2B_2H_6 + 2Na_2CO_3 \rightarrow 3NaBH_4 + NaBO_2 + 2CO_2 \quad (2.3)$$

Overall Reaction:

$$NaBO_2 + 4\ H_2 \rightarrow NaBH_4 + 2\ H_2O \quad (2.4)$$

Experimental

In the first step, Reaction 2.1, relatively inexpensive sodium borates was used as the starting material. Building upon existing knowledge of alkylborate synthesis, we have developed an improved reaction for the preparation of $B(OR)_3$, including trimethyl and tributyl borates, from the discharged product of the Hydrogen on Demand™ system. Other precursors investigated include borax and anhydrous sodium metaborate, and could be extended to any inexpensive borate salts. The reactions were carried out under reflux conditions in alcohol under a CO_2 atmosphere. The use of CO_2 produces Na_2CO_3 as a byproduct, which is used in Reaction 2.3 to form $NaBH_4$ from B_2H_6.

We also report here some preliminary results on Reaction 2.3, which was developed based on the knowledge that Na-containing Lewis bases can react with B_2H_6 to form $NaBH_4$. Initial experiments were modeled after those described by Davis and Gottbrath [4], who conducted the reaction of B_2H_6 with aqueous NaOH. In our experiments, Na_2CO_3 was used instead of NaOH. Yields ranged from 6% to 25%, with higher concentration Na_2CO_3 and greater ratio of Na_2CO_3 to B_2H_6 giving rise to higher yields. Product characterization carried out by infrared spectroscopy (IR), proton and boron nuclear magnetic resonance (^1H NMR and ^{11}B NMR), and by powder X-ray diffraction (XRD) confirmed that $NaBH_4$ was indeed synthesized.

The technique of ball-milling was then employed to study the direct interaction of the gaseous diborane and the solid Lewis bases. At the same time, the competing borane decomposition pathway with water was removed by avoiding the aqueous medium. Using this method, higher yields of $NaBH_4$ were achieved, from 15% to 65%. The yield was further increased by increasing B_2H_6 pressure within

the reaction vessel. Additionally, diglyme was added to the ball mill to facilitate the dissolution of product $NaBH_4$, thereby exposing more Na_2CO_3 surfaces for further reaction. Pressures up to 40 psig were employed, and yields up to 72.8% were obtained at these increased pressures along with the utilization of diglyme.

Reaction 2.2 involves the hydrogenolysis of trialky borate, $B(OR)_3$, to give the intermediate $HB(OR)_2$, which subsequently disproportionate to generate B_2H_6. The details of this reaction is beyond the scope of this paper, and will be address in future publications.

Conclusions

We have successfully demonstrated the feasibility of converting diborane to borohydride, which represents an important step towards developing a new $NaBH_4$ synthesis process. Various reducing agents are being studied for the conversion of B-O bonds to B-H bonds.

Reference

(1) Schlesinger, H. I.; Brown, H. C.; Finholt, A. E. *J. Am. Chem. Soc.* **1953**, *75*, 205.

(2) Kanth, J. V. B.; Brown, H. C. *Inorg. Chem.* **2000,** *39,* 1795-1802.

(3) Narayana, C.; Periasamy, M. *J. Organome. Chem*. **1987**, *323*, 145-147.

(4) Davis, R. E.; Gottbrath, J. A. *Chem. Ind.* **1961**, 1961.

SODIUM BOROHYDRIDE FOR HYDROGEN STORAGE

Ying Wu, Richard M. Mohring

Millennium Cell Inc.
1 Industrial Way West, Eatontown, NJ 07724, USA

Introduction

The hydrolysis of sodium borohydride ($NaBH_4$) is an exothermic reaction that releases hydrogen gas [1] as in Equation 1:

$$NaBH_4(aq) + 2H_2O \xrightarrow[cat]{} 4H_2 + NaBO_2(aq) + \sim 300\ kJ \qquad (1)$$

$NaBH_4$ can be dissolved in water and stabilized via the addition of base (NaOH). In order to have any appreciable reaction, a catalyst is necessary for activation and control of the release of hydrogen gas. Based on this concept, Millennium Cell has developed a technology known commercially as Hydrogen on Demand™ fuel systems (HOD system) [2]. Hydrogen generated in this manner is of high purity and free of carbon, sulfur, or nitrogen containing impurities that poison the fuel cell catalyst. Scheme 1 illustrates the HOD system integrated with a PEM fuel cell, whose water is recycled back to the fuel mixture.

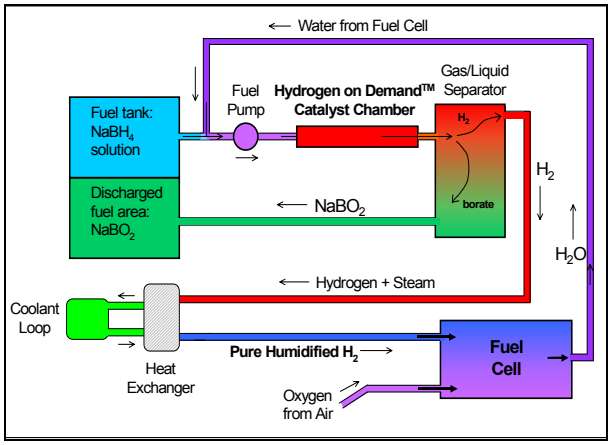

SCHEME 1. Integrated HOD and Fuel Cell System.

The reaction of Equation 1 allows for storage of hydrogen in aqueous solutions at high gravimetric density. In a stoichiometric mixture of $NaBH_4$ and H_2O, the amount of H_2 stored represents 10.8% of the mixture weight. The higher the $NaBH_4$ concentration, the more hydrogen is stored in a given volume. Table 1 compares the volumetric storage efficiency of a 30wt% $NaBH_4$ solution to compressed and cryogenic hydrogen storage. The advantage of $NaBH_4$ is obvious.

Table 1. Volumetric Storage Efficiency Comparisons.

Storage Method	Storage Specifications	Volumetric Storage Efficiency
$NaBH_4$	30 wt% solution	~ 63 g H_2/L
Liquid H_2	cryogenic	~ 71 g H_2/L
Compressed H_2	5,000 psi	~ 23 g H_2/L
	10,000 psi	~ 39 g H_2/L

Results and Discussion

A number of functioning prototype systems have been constructed and operated by Millennium Cell. One example is an 18 SLM system designed to be coupled to a Ballard Nexa® 1.2 kWe fuel cell. The rate at which H_2 is generated is directly proportional to the rate at which $NaBH_4$ solution is pumped into the catalyst chamber. This operational simplicity translates into relatively straightforward control strategies [3]. When the fuel cell demand for hydrogen gas increases, the system pressure begins to drop. The control system detects the load signal and the drop in pressure and responds by increasing the rate at which fuel is pumped into the catalyst chamber. As fuel reaches the catalyst, H_2 gas is generated causing the pressure to increase, and the fuel pump is regulated accordingly. Examples of load following data will be presented.

Another important HOD application is in fuel cell vehicles. DaimlerChrysler's Natrium® and Peugeot-Citroën's H_2O® are two examples. For automotive applications, system pressure can vary from 0-13 bar (0-190 psi) and the rated power output reaches 75 kWe. These specifications demand much higher hydrogen flow rates, up to ~1000 SLM of H_2.

Figure 1 shows the results of a testing on an automotive-scale HOD system, designed to operate a H_2 powered internal combustion engine vehicle (>50 kWe) at Millennium Cell [3].

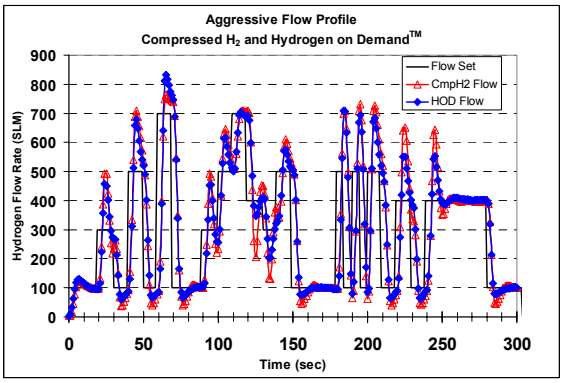

Figure 1. Data taken on an automotive scale Hydrogen on Demand™ system, compared to a baseline of compressed hydrogen.

The figure shows an "aggressive flow profile" where the hydrogen flow (directly related to the engine output power) was varied over a wide range of flows and steps to simulate a driving cycle. The HOD system response is shown by the solid diamond symbols. For comparison, a bank of manifolded 2200 psig compressed hydrogen cylinders was also run through the same profile, shown in open triangle symbols. The compressed hydrogen and HOD system response curves are essentially identical; both are clearly capable of supplying the required hydrogen for the application.

Conclusion

In summary, $NaBH_4$ has a high intrinsic gravimetric and volumetric hydrogen storage density for practical hydrogen generation. The Hydrogen on Demand™ technology has been successfully demonstrated over a wide range of hydrogen delivery flow rates and delivery pressures. Research progress is being made on improving current $NaBH_4$ synthesis technology so that markets such as transportation can be accessed.

Reference

1. Schlesinger, H. I.; Brown, H. C.; Finholt, A. E. *et. al.*, *J. Am. Chem. Soc.* **1953**, *75*, 215.
2. Amendola, S., *et al.*, "System for Hydrogen Generation", WO Publication WO 01/51410 A1. US patent pending.
3. Mohring, R. M.; Eason, I. A.; Fennimore, K. A. SAE World Congress, SAE Technical Paper Number 2002-01-0098, 2002.

Improvement of Hydrogen Storage and Hydrogen Release Properties of Magnesium by in-situ Catalyst Deposition

*Xiaochun Xu, and Chunshan Song**

Clean Fuels and Catalysis Program, The Energy Institute, and Department of Energy & Geo-Environmental Engineering, The Pennsylvania State University, 209 Academic Projects Building, University Park, PA 16802, USA
* Corresponding author. E-mail: csong@psu.edu; Tel: 814-863-4466; Fax: 814-865-3248

Introduction

Because of its high theoretical hydrogen storage capacity (7.6 wt%), magnesium is amongst the most attractive materials for hydrogen storage. From thermodynamical view, the magnesium hydride should form readily at ambient temperature. However, this never occurs in practice.[1] The major problem of magnesium as a rechargeable hydrogen carrier has been its very slow hydriding/dehydriding kinetics. In order to improve the hydriding/dehydriding kinetic, attempts have been made in changing the microstructure of the magnesium and adding a promotoer into the magnesium.[2-5] For the catalytic hydriding/dehydriding of magnesium, the catalyst should preferrably deposited on the outer surface of the metal particles. However, the conventional techniques, such as ball milling, mechanic alloying and melt-spinning, etc., can not finely control the deposition of the catalyst. Some more complicated process, such as sputtering, etc., has been used.[5] In this paper, a novel in-situ catalyst deposition method was developed for depositing various catalysts on the outer surface of the magnesium particles through a simple wet chemical process. The hydrogen storage and release properties of the catalyst-modified magnesium are reported.

Experimental

The catalyst-modified magnesium was prepared by auto-reduction of a metal salt in ethylene glycol[6] and in-situ deposited the metal on the magnesium powder (Aldrich, 99.8%, 325 mesh). The precursors for the preparation of the metal particles (catalysts) were palladium chloride, ruthenium chloride and hexachloroplatinic acid. The desired amount of catalyst deposited on the magnesium was 0.5 mol%. After preparation, the mixture dispersion was washed several times with anhydrous butanone and ether, centrifuged, and the collected precipitate was dried at room temperature. All the above processes were carried out under Ar atmosphere in a glove box.

The phase and microstructure of the as-prepared materials were characterized by X-ray diffraction (XRD) and Scanning electron microscopy (SEM). The XRD patterns were obtained on a Scintag Pad V using Cu K_α radiation. The SEM images were photographed on a Hitachi S-3500N. The hydriding/dehydring properties of the materials were measured in an apparatus similar to that in reference 7.[7] The hydriding properties of the materials were measured by monitoring the pressure change in an autoclave at desired temperatures and pressures. The dehydriding properties of the materials were measured by counting the volume of the blow-off hydrogen through a gas burette at ambient pressure and desired temperatures.

Results and Discussion

1. Preparation and characterization of Pd-modified magnesium

Figure 1 shows the XRD patterns of magnesium and Pd-modified magnesium. From the XRD patterns, it can be learned that (1) magnesium was stable in the preparation procedures and did not transform into other phases, e.g., magnesium oxide or magnesium hydroxide; (2) palladium was deposited on the magnesium particle. Since the desired amount of palladium was only 0.5 mol% in palladium-modified magnesium, the diffraction intensity for palladium was weak. In addition, the width of the diffraction patterns of palladium is broad, which indicate that the particle size of the palladium is small. Under a similar preparation condition, Bonet et al[6] reported that the particle size of palladium was about 19 nm.

Figure 2 shows the SEM images of magnesium and Pd-modified magnesium. By comparing the two SEM images, it can be found that palladium particles were uniformly dispersed on the outer surface of the magnesium particles. The particle size of palladium was around 50-100 nm.

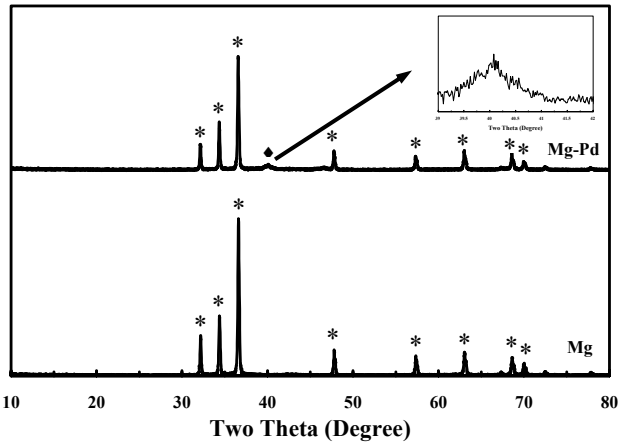

Figure 1. XRD patterns of magnesium and palladium-modified magnesium. (*) Magnesium; (♦) Palladium.

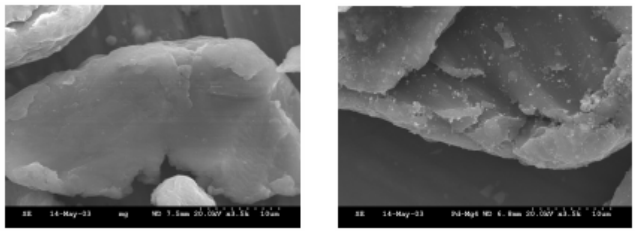

(a) (b)

Figure 2. SEM image of magnesium (a) and palladium-modified Magnesium (b).

2. Hydriding/dehydriding kinetics of Pd-modified Mg

Figure 3 and Figure 4 compare the absorption and desorption kinetics of magnesium and Pd-modified magnesium, respectively. At high temperature, e.g., 573 K, depositing the palladium on the magnesium dose not shows any obvious catalytic effect on hydride kinetic. However, at a lower temperature, e.g., 523 K, the catalytic effect of palladium becomes significant. The palladium-modified magnesium readily absorbs hydrogen, while the un-modified magnesium absorbs hydrogen after 45 minutes. The amount of hydrogen absorbed is 2.13 wt.% for palladium-modified magnesium and 1.02 wt.% for un-modified magnesium after 4 hours absorption. The effect of palladium on desorption is more pronounced than that of on absorption. At 613 K, the rate of dehydide of palladium-modified magnesium is much faster than that of the un-modified magnesium. For example, the palladium-modified magnesium hydride desorbs 5.12 wt.% hydrogen after 20 minutes desorption, which is 10 times faster than that of the un-modified magnesium hydride. Even at 593 K, the palladium-modified magnesium hydride

can still fully dehydride in 4 hours, while the un-modified magnesium hydride only desorbs 0.50 wt% hydrogen at the same desorption condition.

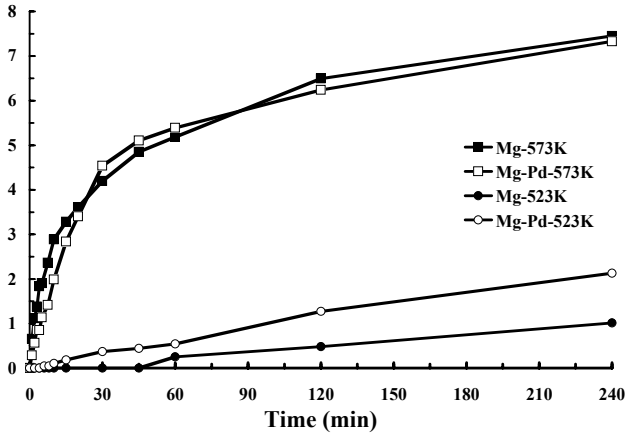

Figure 3. Comparative H_2 absorption kinetics of magnesium and Pd-modified magnesium under 400 Psi at 523 K and 573K.

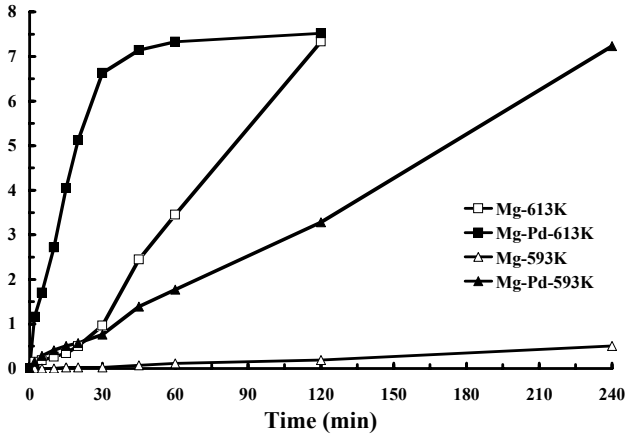

Figure 4. Comparative H_2 desorption kinetics of magnesium and Pd-modified magnesium at 593 K and 613K under ambient pressure.

3. The types of catalysts

Figure 5 and Figure 6 compare the absorption and desorption kinetics of magnesium and Pd, Pt and Ru-modified magnesium, respectively. After the magnesium is modified with Pd, Pt and Ru, the hydriding and dehydriding kinetics of the magnesium are all improved. At 523 K and 400 Psi, the Pd, Pt and Ru-modified magnesium all readily absorb the hydrogen. The rate of absorption decreases in the following order: Pd > Pt ≈ Ru > Un-modified. The rate of desorption at 593 K shows different trend at different desorption time. At the beginning, the rate of desorption decreases in the following order: Pd ≈ Pt > Ru > Un-modified. The desorption rate of Pt-modified magnesium hydride becomes slowly after 120 minutes desorption.

Conclusions

A novel in-situ catalyst deposition method that improves hydrogen uptake and release kinetics, was developed for depositing various catalysts (Pd, Pt and Ru) on the magnesium particles through a simple wet chemistry process. XRD and SEM characterizations indicated that nano-sized metal particles were deposited on the outer surface of the magnesium particles. Both the hydriding and dehydriding kinetics of magnesium were improved significantly after depositing the catalysts on the outer surface of the magnesium particles. Among Pd, Pt and Ru, Pd showed the best catalytic effect.

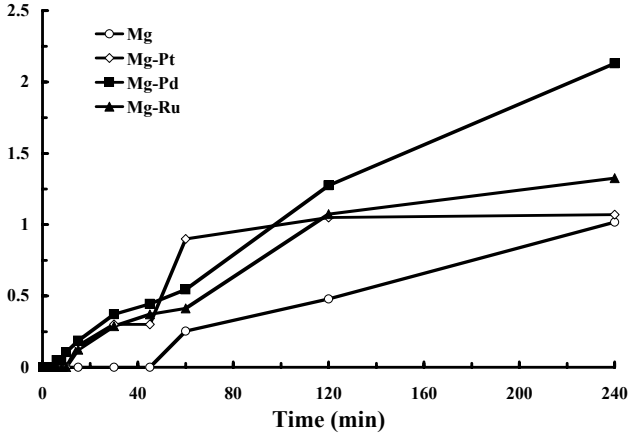

Figure 5. Comparative H_2 absorption kinetics of magnesium and Pd, Pt, Ru-modified magnesium under 400 Psi at 523 K.

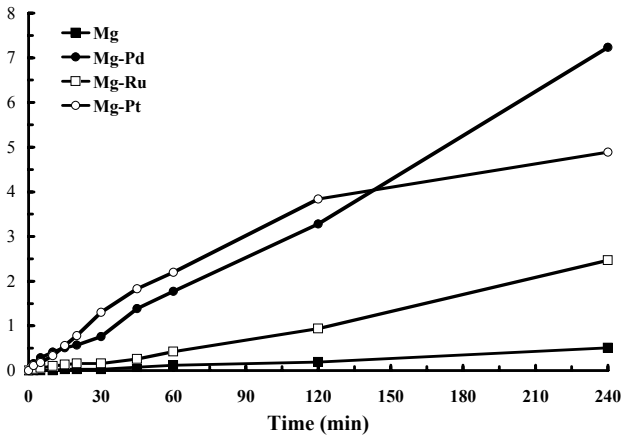

Figure 6. Comparative H_2 desorption kinetics of magnesium and Pd, Pt, Ru-modified magnesium at 593 K under ambient pressure.

Acknowledgement. We gratefully acknowledge the financial support by a Seed Grant from the Hydrogen Energy Center of the Pennsylvania State University.

References

(1) Zaluska, A.; Zaluski, L.; Strom-Olsen, J.O. *J. Alloy. Comp.* **1999**, *289*, 197-206.
(2) Hout, J.; Tremblay, M.-L.; Schulz, R. *J. Alloy. Comp.* **2003**, *in press*.
(3) Gross, K.J.; Chartouni, D.; Leroy, E.; Züttel, A.; Schlapbach, L. *J. Alloy. Comp.* **1998**, *269*, 259-270.
(4) Yin, J.T.; Yamada, T.; Yoshinari, O.; Tanaka, K. *Materials Transactions* **2001**, *42*, 712-716.
(5) Higuchi, K.; Yamamoto, K.; Kajioka, H.; Toiyama, K.; Honda, M; Orimo, S.; Fujii, H. *J. Alloy. Comp.* **2002**, *330-332*, 526-530.
(6) Bonet, F; Delmas, V.; Grugeon, S.; Herrera Urbina, H; Silvert, P.Y.; Tekaia-Elhsissen, K. *Nano. Mater.* **1999**, *8*, 1277-1284.
(7) Bogdanovic, B.; Schwickardi, M. *J. Alloy. Comp.* **1997**, *253-254*, 1-9.

Can Heteroatoms be the activators for hydrogen storage in carbon nanotubes?

B.Viswanathan, M.Sankaran and R.Ganesan

Department of chemistry, Indian Institute of Technology, Madras 600036.

Introduction

The studies on the storage of hydrogen took a dramatic turn in 1998-99, when Rodriguez et al [1,2] reported exotic values of hydrogen absorption by carbon nano structures up to 10-12 hydrogen molecules per carbon atom, though in a sequent communication they have reduced this up to 4 molecules per atom of carbon. This is nearly twice (0.4 g H_2/g C) of the most hydrogenated carbon compound namely CH_4 where the hydrogen to carbon weight ratio is 0.25 g H_2/g C. Subsequently there have been various reports in literature to substantiate these observations [3-7] and none of them in any way could realize the expected (DOE standards) 6.5 weight percent leave alone repeating the original adsorption capacity claimed.

The present investigation has therefore been undertaken with the following objectives and postulates (i) Hydrogen adsorption on carbon materials especially nanotubes, is possible only when it contains some sites wherein hydrogen molecule can be activated. Taking the clue from nature, it is postulated that the presence of heteroatoms in the carbon nanotubes may be the appropriate sites for activation of hydrogen and (ii) If heteroatom containing carbon nanotubes were to be one of the materials appropriate for hydrogen storage, then the questions to be addressed are: (a) what is the gradation of materials containing various heteroatoms? (b) What are the geometrical positions in the nanotubes that are active? In order to understand the interaction of hydrogen molecule in pure carbon nanotubes and heteroatoms (N, P, S and B) substituted carbon nanotubes, cluster model calculations have been carried out using Density Functional Theory (DFT). From the analysis of the reports in literature, it is clear that the hydrogen molecule is interacting at the interstitial positions of the carbon nanotubes than inside the nanotubes. The cluster model, which describes the interface of the three tubes, is considered in these studies (Fig.1).

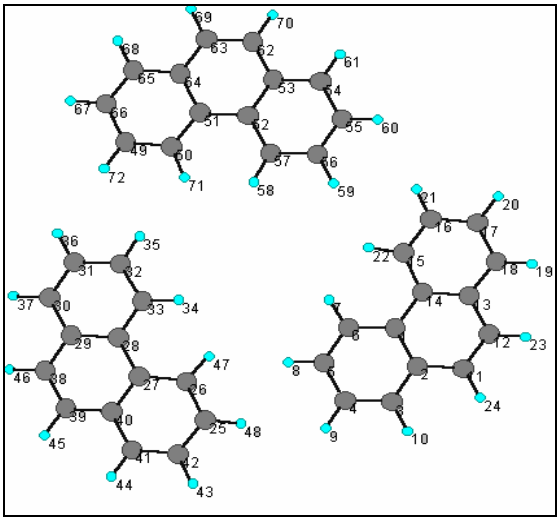

Figure 1. The Cluster model (the heteroatoms are substituted in positions (26,33,50,57,15 and 6)

Theoretical methods

The terminal sites of the cluster are saturated with hydrogen in order to avoid the edge effect [8]. The geometry of the cluster is optimized using Universal Force Field (UFF 1.02) approach. The hydrogen molecule is allowed to interact with optimized cluster and the geometry of the system is optimized. Cerius2 software was used for force field calculations. Using force field optimized parameters, DFT single point energy and bond population calculations were done by Becke's three parameter hybrid functional with LYP correlation functional (B3LYP) and 6-31G(d) basis set using Gaussian98W. Similar procedure was adopted for heteroatom substituted cluster models.

Results and discussions

The hydrogen molecule is allowed to interact with the carbon atoms of the unsubstituted nanotube and the dissociation energy of hydrogen was calculated (Table 1). The dissociation energy of hydrogen in its free state is 4.74 eV, and remains unaltered when it is placed in between the pure carbon nanotubes (4.76 eV). In order to study the influence of heteroatoms toward the activation of hydrogen, various heteroatoms (N, P and S) are substituted at different positions of the cluster as shown in Fig 1. The substitutional positions for heteroatoms as given in brackets (26,33,50,57,15,6) are chosen based on the fact that these interstitial positions offer minimum potential energy for the cluster. In the presence of heteroatoms, the dissociation energy of hydrogen molecule is considerably decreased compared to that of pure carbon nanotubes as can be seen from the values presented in Table 1. This indicates that heteroatom can activate the hydrogen molecule and its presence favors the dissociation of hydrogen. This conclusion can also be arrived from the redox potential values of the couples involved. For instance, redox potentials of heteroatoms are higher than that of carbon (S/S^{2-}, N/N^{3-}, P/P^{3-}, C/C^{4-} are respectively, 0.171, 0.057, -0.111 and -0.132 V). The same fact can be further independently supported by the Ellingham diagram which indicates that free energy of formation for N-H bond is more favourable than that of C-H bond. The bond length of the hydrogen molecule is elongated in heteroatom substituted carbon nanotube compared to that of pure carbon nanotubes, indicating that there is considerable activation of hydrogen molecule in heteroatom containing carbon nanotubes.

In order to understand the role of hetero atoms in hydrogen activation in carbon nanotubes the calculations have been carried out to estimate the value of activation energy value of each of the steps of hydrogen activation and migration (Fig 2) within the framework of Transition state theory and the essential results are given in Table 2. These results also support our contention that heteroatoms may be appropriate for activation of hydrogen on carbon nanotubes.

Conclusions

Heteroatom containing carbon nanotubes are able to activate the hydrogen compared to pure carbon nanotubes. This activated hydrogen can migrate to other sites and opens up another avenue in the search of material for the hydrogen storage.

Table 1. The Bond length and dissociation energy of hydrogen on the clusters.

Heteroatom	Mode of substitution	Bond length (H-H) (Å)	H_2 dissociation energy (eV)
Hydrogen	-	0.708	4.74
Un substituted CNT	-	0.708	4.76
Nitrogen substituted CNT			
	1 N + 1 H_2	0.84	0.31
(Each ring 1N)	3 N + 1 H_2	0.84	0.32
	3 N + 3 H_2	0.84	0.33
(Each ring 2N)	6 N + 1 H_2	1.08	0.56
	6 N + 3 H_2	1.08	0.50
Phosphorus substituted CNT			
	1 P + 1 H_2	0.81	2.06
(Each ring 1P)	3 P + 1 H_2	0.82	1.36
	3 P + 3 H_2	0.82	1.51
Sulphur substituted CNT			
	1 S + 1 H_2	0.81	0.27
(Each ring 1S)	3 S + 1 H_2	0.81	1.03
	3 S + 3 H_2	0.81	0.25

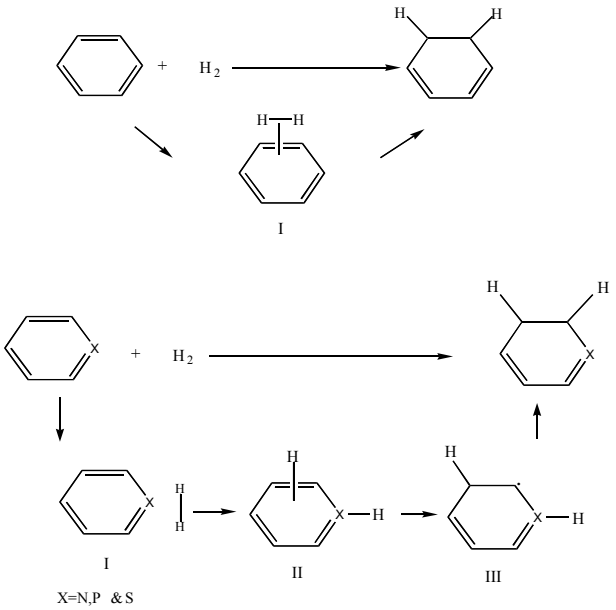

Figure 2. Proposed transition state path ways for hydrogen storage in carbon nanotubes and hetroatom (N,Pand S) containing carbon nanotubes.

References

1. A. Chambers, C. Parks, R.T.K. Baker and N.M. Rodriguez *J.Phys. Chem.*B **1998,**102, 4253.
2. C. Park, P. E. Anderson, C. D. Tan, R. Hidalgo, A. Chambers and N. M. Rodriguez, *J.Phys. Chem.*B **1999,** 103, 10572.
3. C.C. Ahn, Y. Ye, B.V. Ratnakumar, C. Witham, R.C. Bowman, Jr. and B. Fultz *Appl. Phys. Lett.* **1998,** 73, 3378.
4. R. Ströbel, L. Jörissen, T. Schliermann, V. Trapp, W. Schütz, K. Bohmhammel, G. Wolf and J. Garche *J. Power Sources* **1999,** 84, 221.
5. Y. Ye, C.C. Ahn, C. Witham, B. Fultz, J. Liu, A.G. Rinzler, D. Colbert, K.A. Smith and R.E. Smalley *Appl. Phys. Lett.* **1999,** 74, 2307.
6. C. Liu, Y.Y. Fan, M. Liu, H.T. Cong, H.M. Cheng and M.S. Dresselhaus *Science* **1999**, 286, 1127.
7. M. Hirscher, M. Becher, M. Haluska, A. Quintel, V. Skakalova, Y. -M. Choi, U. Dettlaff-Weglikowska, S. Roth, I. Stepanek, P. Bernier. *J. Alloys. Comp*. **2002,** 330, 654.
8. F.H.Yang and R.T.Yang, *Carbon* **2002,** 40, 437.

Table 2. The transition state optimized parameters for various clusters and energy of activation for each pathway.

Substitution	Ea[c] I (eV)	Ea II (eV)	Ea III (eV)	H-H (Å)	X-H (Å)	C_2-H[b] (Å)	C_2-H[a] (Å)	C_3-H (Å)
Carbon	15.08	-	-	0.65	-	-	-	-
Nitrogen	3.91	8.50	1.30	1.69	1.19	1.39	1.16	1.13
Phosphorus	3.15	8.84	2.24	2.11	1.62	1.74	1.12	1.26
Sulphur	4.27	9.30	3.58	2.18	1.51	2.32	1.58	1.67

a - after migration, b - before migration, c - Ea=TE (each transition state) – TE (reactant)